

PRINCIPLES of SOLAR ENGINEERING

THIRD EDITION

D. Yogi Goswami



CRC Press
Taylor & Francis Group

THIRD EDITION

PRINCIPLES OF

SOLAR

ENGINEERING

THIRD EDITION

PRINCIPLES OF SOLAR ENGINEERING

D. Yogi Goswami



CRC Press
Taylor & Francis Group
Boca Raton London New York

CRC Press is an imprint of the
Taylor & Francis Group, an **informa** business

CRC Press
Taylor & Francis Group
6000 Broken Sound Parkway NW, Suite 300
Boca Raton, FL 33487-2742

© 2015 by Taylor & Francis Group, LLC
CRC Press is an imprint of Taylor & Francis Group, an Informa business

No claim to original U.S. Government works
Version Date: 20141017

International Standard Book Number-13: 978-1-4665-6379-7 (eBook - PDF)

This book contains information obtained from authentic and highly regarded sources. Reasonable efforts have been made to publish reliable data and information, but the author and publisher cannot assume responsibility for the validity of all materials or the consequences of their use. The authors and publishers have attempted to trace the copyright holders of all material reproduced in this publication and apologize to copyright holders if permission to publish in this form has not been obtained. If any copyright material has not been acknowledged please write and let us know so we may rectify in any future reprint.

Except as permitted under U.S. Copyright Law, no part of this book may be reprinted, reproduced, transmitted, or utilized in any form by any electronic, mechanical, or other means, now known or hereafter invented, including photocopying, microfilming, and recording, or in any information storage or retrieval system, without written permission from the publishers.

For permission to photocopy or use material electronically from this work, please access www.copyright.com (<http://www.copyright.com/>) or contact the Copyright Clearance Center, Inc. (CCC), 222 Rosewood Drive, Danvers, MA 01923, 978-750-8400. CCC is a not-for-profit organization that provides licenses and registration for a variety of users. For organizations that have been granted a photocopy license by the CCC, a separate system of payment has been arranged.

Trademark Notice: Product or corporate names may be trademarks or registered trademarks, and are used only for identification and explanation without intent to infringe.

Visit the Taylor & Francis Web site at
<http://www.taylorandfrancis.com>

and the CRC Press Web site at
<http://www.crcpress.com>

Contents

Preface.....	xiii
Author.....	xvii
1. Introduction to Solar Energy Conversion.....	1
1.1 Global Energy Needs and Resources.....	2
1.1.1 Present Status and Potential of RE	3
1.1.2 Wind Power	4
1.1.3 Biomass.....	5
1.1.4 Ocean Energy Conversion	8
1.2 Solar Energy.....	8
1.2.1 Thermal Conversion	11
1.2.2 Photovoltaic Conversion	12
1.2.3 Limitations of Solar Energy.....	13
1.3 Energy Storage.....	14
1.4 Economics of Solar Systems.....	17
1.4.1 Present Worth.....	18
1.4.2 Series of Payments	18
1.4.3 Levelized Cost of Energy.....	19
1.4.4 Internal Rate of Return	19
1.5 Summary of RE Resources	24
1.6 Forecast of Future Energy Mix.....	25
References	27
2. Fundamentals of Solar Radiation	29
2.1 The Physics of the Sun and Its Energy Transport	29
2.2 Thermal Radiation Fundamentals.....	30
2.2.1 Black-Body Radiation	31
2.2.2 Radiation Function Tables	32
2.2.3 Intensity of Radiation and Shape Factor	35
2.2.4 Transmission of Radiation through a Medium	38
2.3 Sun–Earth Geometric Relationship.....	39
2.3.1 Solar Time and Angles.....	42
2.3.2 Sun-Path Diagram.....	55
2.3.3 Shadow-Angle Protractor	57
2.4 Solar Radiation	61
2.4.1 Extraterrestrial Solar Radiation	61
2.5 Estimation of Terrestrial Solar Radiation	64
2.5.1 Atmospheric Extinction of Solar Radiation	65
2.5.2 Clear-Sky Radiation Model	66

2.5.3	Solar Radiation on a Tilted Surface	68
2.5.4	Monthly Solar Radiation Estimation Models	76
2.6	Models Based on Long-Term Measured Horizontal Solar Radiation	80
2.6.1	Monthly Solar Radiation on Tilted Surfaces.....	80
2.6.2	Circumsolar or Anisotropic Diffuse Solar Radiation.....	84
2.6.3	Hourly and Daily Solar Radiation on Tilted Surfaces	85
2.6.4	Spectral Models.....	99
2.7	Measurement of Solar Radiation	99
2.7.1	Instruments for Measuring Solar Radiation and Sunshine.....	100
2.7.2	Detectors for Solar Radiation Instrumentation.....	104
2.7.3	Measurement of Sunshine Duration.....	105
2.7.4	Measurement of Spectral Solar Radiation.....	106
2.7.5	Wide Band Spectral Measurements	106
2.7.6	Solar Radiation Data.....	107
2.8	Solar Radiation Mapping Using Satellite Data	109
2.8.1	Estimation of Solar Resource from Satellite Data	110
	References	115
3.	Solar Thermal Collectors	119
3.1	Radiative Properties and Characteristics of Materials	119
3.1.1	Selective Surfaces.....	123
3.1.2	Reflecting Surfaces.....	127
3.1.3	Transparent Materials	127
3.2	Flat-Plate Collectors	129
3.2.1	Liquid-Type Collectors	130
3.2.2	Air-Type Collectors.....	130
3.2.3	Glazings.....	131
3.2.3.1	Absorbers.....	133
3.2.4	Energy Balance for a Flat-Plate Collector	134
3.2.4.1	Collector Heat-Loss Conductance	135
3.2.5	Thermal Analysis of Flat-Plate Collector–Absorber Plate.....	139
3.2.6	Collector Efficiency Factor	143
3.2.7	Collector Heat-Removal Factor	144
3.2.8	Transient Effects.....	148
3.2.9	Air-Cooled Flat-Plate Collector Thermal Analysis	151
3.2.9.1	Air-Collector Efficiency Factor	152
3.2.9.2	Air-Collector Heat-Removal Factor	152
3.3	Tubular Solar Energy Collectors.....	154
3.3.1	Evacuated-Tube Collectors.....	155
3.3.2	Thermal Analysis of a Tubular Collector	157

3.4	Experimental Testing of Collectors	158
3.4.1	Testing Standards for Solar Thermal Collectors	161
3.4.1.1	Time Constant.....	162
3.4.1.2	Thermal Performance	162
3.4.1.3	Incidence Angle Modifier	162
3.5	Concentrating Solar Collectors	162
3.5.1	Thermodynamic Limits to Concentration.....	164
3.5.2	Optical Limits to Concentrations	168
3.5.3	Acceptance of Diffuse Radiation.....	168
3.5.4	Ray Tracing Diagrams.....	169
3.5.5	Concentrator Types.....	172
3.5.6	Fixed Concentrators.....	173
3.6	Parabolic Trough Concentrator	174
3.6.1	Optical Analysis of PTC.....	174
3.6.2	Thermal Losses from PTC.....	178
3.6.3	Thermal Performance of PTC Collector	181
3.7	Compound-Curvature Solar Concentrators.....	182
3.7.1	Paraboloidal Concentrators	182
3.7.2	Spherical Concentrators	186
3.7.3	Compound Parabolic Concentrator.....	187
3.7.4	Optical Analysis of CPC Collector	188
3.7.5	Thermal Performance of the CPC Collector	192
3.8	Central Receiver Collector	193
3.9	Fresnel Reflectors and Lenses	193
3.10	Solar Concentrator Summary.....	195
	References	202
	Suggested Reading	204
4.	Thermal Energy Storage and Transport	205
4.1	Thermal Energy Storage	205
4.2	Types of TES.....	206
4.2.1	Sensible Heat Storage	206
4.2.2	Latent Heat Storage.....	207
4.2.3	Thermochemical Energy Storage	211
4.3	Design of Storage System.....	213
4.3.1	Selection of Storage Material.....	213
4.3.1.1	Solar Collection System.....	213
4.3.1.2	Application.....	213
4.3.1.3	Additional Considerations.....	214
4.3.2	Design of Containment.....	214
4.3.3	Heat-Exchanger Design.....	216
4.3.3.1	Packed Bed Storage	216
4.3.3.2	Pressure Drop in a Packed Bed	223

4.3.3.3	Flow across Tube Banks	225
4.3.3.4	Performance of Packed Bed TES Systems.....	226
4.4	Energy Transport Subsystems	229
4.4.1	Piping Systems	229
4.4.2	Pressure Drop.....	230
4.4.3	Heat Loss.....	233
4.4.4	Heat Exchangers	235
	References	252
5.	Solar Heating Systems.....	255
5.1	Calculations of Heating and Hot-Water Loads in Buildings.....	255
5.1.1	Calculation of Heat Loss.....	257
5.1.2	Internal Heat Sources in Buildings	260
5.1.3	Degree-Day Method.....	260
5.1.4	Service Hot-Water Load Calculation.....	264
5.2	Solar Water-Heating Systems	266
5.2.1	Natural Circulation Systems	266
5.2.2	Forced-Circulation Systems.....	269
5.3	Liquid-Based Solar Heating Systems for Buildings	271
5.3.1	Physical Configurations of Active Solar Heating Systems	272
5.3.2	Solar Collector Orientation.....	273
5.3.3	Fluid Flow Rates.....	273
5.3.4	Thermal Storage	274
5.3.5	Other Mechanical Components.....	276
5.3.6	Controls in Liquid Systems	277
5.3.7	Load Devices in Liquid Solar Heating Systems	277
5.4	Solar Air-Heating Systems.....	280
5.4.1	Heating System Physical Configuration.....	281
5.4.2	Collector Designs.....	283
5.4.3	Fluid Flow Rates.....	285
5.4.4	Other Mechanical Components.....	285
5.4.5	Unglazed Transpired Wall System for Air Preheating ...	286
5.5	Methods of Modeling and Design of Solar Heating Systems	288
5.5.1	Design of a Liquid-Based Solar Heating System by <i>f</i> -Chart.....	288
5.6	Long-Term Performance of Solar Heating Systems.....	302
5.6.1	Critical Solar Intensity Ratio X	302
5.6.2	Utilizability Method	303
5.6.3	Example Calculation	305
5.6.4	Collection Period (Δt_c)	307
5.6.5	Long-Term Performance of Collector Systems with Storage	308
5.7	TRNSYS Computer Simulation Program	311

5.8	Solar Industrial Process Heat	312
5.9	Examples of SIPH Systems	318
5.9.1	SIPH for Textile Industries	318
5.9.2	SIPH System for Milk Processing	322
	References	326
6.	Solar Cooling and Dehumidification	329
6.1	Solar Space Cooling and Refrigeration	329
6.1.1	Cooling Requirements for Buildings	331
6.1.2	Vapor-Compression Cycle	336
6.1.3	Absorption Air Conditioning	339
6.1.4	Mass Balance Equations.....	347
6.1.5	Ammonia–Water Refrigeration System.....	349
6.2	Solar Desiccant Dehumidification	355
6.2.1	Solid Desiccant Cooling System	356
6.2.2	Liquid Desiccant Cooling System.....	357
6.3	Summary	361
	References	365
7.	Passive Solar Heating, Cooling, and Daylighting	367
7.1	Introduction	367
7.1.1	Current Applications and Costs	367
7.2	Passive Space Heating Systems.....	368
7.2.1	Types of Passive Heating Systems.....	368
7.2.2	Fundamental Concepts for Passive Heating Design	371
7.2.3	Generalized Passive Design Methods	372
7.2.4	First Level: Rule of Thumb	373
7.2.4.1	Load.....	373
7.2.4.2	Solar Savings Fraction	373
7.2.4.3	Load Collector Ratio	373
7.2.4.4	Storage.....	374
7.2.5	Second Level: LCR Method	375
7.2.6	Third Level: SLR Method	376
7.3	Passive Space Cooling Systems	379
7.3.1	Controlling the Solar Input	379
7.3.2	Movement of Air	379
7.3.3	Evaporative Cooling	382
7.3.4	Nocturnal and Radiative Cooling Systems.....	382
7.3.5	Earth Contact Cooling (or Heating)	384
7.3.5.1	Heat Transfer Analysis	384
7.3.5.2	Soil Temperatures and Properties	387
7.3.5.3	Generalized Results from Experiments	387
7.4	Daylighting Design Fundamentals	388
7.4.1	Lighting Terms and Units.....	389

7.4.2	Economics of Daylighting.....	389
7.4.3	Daylighting Design Fundamentals	391
7.4.3.1	Architectural Features.....	391
7.4.3.2	Daylighting Geometry.....	391
7.4.4	Design Methods	393
7.4.5	Lumen Method of Sidelighting (Vertical Windows).....	393
7.4.6	Lumen Method of Skylighting.....	398
7.5	Further Information.....	405
7.5.1	General Background Information	405
7.5.2	Technical Publication Information	405
	References	408
	Suggested Readings.....	409
8.	Solar Thermal Power	411
8.1	Historical Perspective.....	411
8.2	Thermodynamic Power Cycles	414
8.2.1	Rankine Cycle.....	415
8.2.2	Supercritical Rankine Cycle	424
8.2.3	Components of a Rankine Power Plant	424
8.2.4	Choice of Working Fluid.....	425
8.3	Design of Parabolic Trough-Based Power Plants.....	428
8.3.1	Sizing and Layout of the Solar Field	428
8.3.1.1	I Field Layout	432
8.3.1.2	H Field Layout	433
8.3.2	Pressure Drop in the Solar Field.....	435
8.3.3	Expansion Tank.....	437
8.3.4	Power Block.....	438
8.3.5	Condenser	438
8.3.5.1	Air-Cooled Condensers.....	440
8.4	Examples of PTC Solar Thermal Power Plants	442
8.5	Parabolic Dish Systems	449
8.6	Stirling Cycle.....	449
8.6.1	Thermodynamics of Stirling Cycle	450
8.6.2	Piston/Displacer Drives.....	456
8.6.3	Kinematic or Free-Piston Engines	456
8.6.4	Examples of Solar Stirling Power Systems	457
8.7	Central Receiver Tower Systems	460
8.7.1	Heliostats.....	460
8.7.2	Receiver	464
8.7.2.1	External Receiver.....	464
8.7.2.2	Cavity Receivers	468
8.7.2.3	Volumetric Receivers	471
8.7.3	Design of Heliostat Field.....	473
8.7.3.1	Reflection Factor ($\eta_{\text{reflection}}$).....	475
8.7.3.2	Cosine Factor (η_{\cosine}).....	475

8.7.3.3	Atmospheric Attenuation Factor ($\eta_{\text{attenuation}}$)	476
8.7.3.4	Interception Factor ($\eta_{\text{interception}}$).....	476
8.7.3.5	Shading and Blocking Factor ($\eta_{\text{shading \& blocking}}$)	477
8.7.4	Field Layout	478
8.8	Central Receiver System (CRS) Design	480
8.9	Recent Developments in Solar Thermal Power Cycles.....	482
8.9.1	Hybrid and Combined Cycles.....	483
8.9.2	Kalina Cycle.....	484
8.9.3	Aqua–Ammonia Combined Power/Absorption Cycle...	485
8.9.4	Combined Power/Cooling Cycle	485
8.9.5	Supercritical CO ₂ Power Cycle	486
8.10	Solar Distillation of Saline Water.....	490
8.10.1	Solar-Driven Reverse Osmosis.....	496
8.10.2	RO Mathematical Model.....	497
8.11	Nonconvecting Solar Ponds.....	500
8.11.1	Introduction.....	500
8.11.2	Solar Pond Stability Criteria.....	502
8.11.3	Thermal Performance of Solar Ponds	504
	References	510
9.	Photovoltaics.....	515
9.1	Semiconductors	516
9.1.1	<i>p</i> – <i>n</i> Junction	518
9.1.2	PV Effect.....	519
9.2	Analysis of PV Cells	525
9.2.1	Efficiency of Solar Cells	530
9.2.2	Maximum Power Point Tracking.....	531
9.2.3	Multijunction Solar Cells	532
9.2.4	Thin-Film Solar Cells	533
9.2.5	Dye-Sensitized Solar Cells and Polymer Solar Cells.....	535
9.2.5.1	Fabrication of DSSC	536
9.2.6	Design of a PV System	537
9.3	Manufacture of Solar Cells and Panels.....	540
9.3.1	Single-Crystal and Polycrystalline Cells	540
9.3.2	Amorphous Silicon and Thin-Film Fabrication	543
9.4	Design for Remote PV Applications.....	544
9.4.1	Estimation of Loads and Load Profiles.....	545
9.4.2	Estimation of Available Solar Radiation.....	547
9.4.3	PV System Sizing	547
9.4.4	Water Pumping Applications.....	549
	References	557
10.	Solar Photochemical Applications	559
10.1	Photocatalytic Reactions	559
10.2	Solar Photocatalytic Detoxification	563

10.3	Solar Reactors	564
10.3.1	Concentrator Reactors	565
10.3.2	Nonconcentrating Reactors	567
10.3.3	Flat-Plate Reactors.....	568
10.3.4	Tubular Reactors	568
10.3.5	Shallow Solar Ponds	569
10.3.6	Falling Film.....	571
10.4	Kinetic Models.....	571
10.5	Useful Insolation	577
10.6	Catalyst Development	579
10.7	System Design Methodology.....	580
10.7.1	Catalyst Life	585
10.8	Gas-Phase Photocatalytic Detoxification	585
10.8.1	Photoreactors	586
10.9	Commercial/Industrial Applications	587
10.10	Solar Disinfection of Water and Air.....	590
10.11	Summary	591
	References	592
	Appendix 1: International System of Units, Fundamental Constants, and Conversion Factors.....	597
	Appendix 2: Solar Radiation Data.....	601
	Appendix 3: Supplementary Material for Chapter 3.....	669
	Appendix 4: Supplementary Material for Chapter 4.....	687
	Appendix 5: Supplementary Material for Chapter 5.....	693
	Appendix 6: Thermodynamic Data for Cooling Systems	709
	Appendix 7: Supplementary Material for Chapter 7.....	723
	Appendix 8: Supplementary Material for Chapter 8.....	751
	Appendix 9: Economic Data Tables.....	763

Preface

Almost 15 years have passed since the last edition of *Principles of Solar Engineering* was published. During this period, the price of photovoltaic (PV) panels has dropped 10 times and global deployment has increased 30 times. Of course, some of this development has occurred because of governmental incentives and economies of scale; however, a large part of the advancement has been attributed to scientific and technological developments that have improved not only conversion efficiencies but also manufacturing technologies. There have been many improvements in solar thermal technologies as well. A number of concentrating solar thermal power plants (CSPs), as large as 400 MW, have been built or are under construction or under planning stages. Developments in higher-temperature CSPs are leading to a number of other advances, especially higher-temperature heat transfer fluids and thermodynamic power cycles. Since solar power is becoming a significant part of the grid power, energy storage has assumed increased importance. As the commercial deployment of solar technologies increases, it necessitates the need for better solar resource assessment, including modeling and forecasting. All of these developments have necessitated a new edition of the book, which is thoroughly revised and updated.

The new edition has been thoroughly revised to make it useful to students all over the world, by including examples and problems for both northern and southern latitudes. Solar radiation data in the book cover most of the world and examples have been chosen to cover countries in the Northern as well as Southern Hemisphere. The book contains many examples and homework problems and is designed to be both a textbook and a reference for scientists and practicing engineers, architects, and building design and construction professionals.

Chapter 1 introduces the global energy situation and changes taking place in the distribution of available energy resources to fulfill society's needs. Significantly, the highest increase has been in the areas of wind and solar PV power installed capacities in the world. Another significant change in the first chapter from the last edition is the addition of an economic analysis of solar energy systems now with a number of solved examples. This change reflects the author's cogent practical experience in solar energy systems from the small residential scale to the multi-megawatt scale. It is critical for students to understand the importance of economic analysis of solar energy systems in addition to the science and technology. With the introduction of this economic analysis in the first chapter, as students learn about the solar energy systems in Chapters 5 through 10, they will be able to analyze these systems from an economic standpoint as well.

There are significant changes in the second chapter on solar radiation. As global investment in solar power increases, there is a realization to accurately assess solar resources. Long-term measurements provide the best “bankable” data; however, they are not available for most of the locations in the world. Therefore, solar radiation modeling methods validated with long-term measured values are very important. The revised chapter describes the modeling methods accepted by the experts in solar resource assessment.

Chapter 3 covers concentrating and nonconcentrating solar thermal collectors. Although the fundamentals are the same as in the last edition, the new edition covers the latest developments in collector materials as well as new correlations for heat transfer and thermal performance analysis. The revised chapter covers concentrating collectors in much more depth than before, especially the parabolic trough concentrator and the central receiver heliostat and its receiver/absorber. Chapter 4 covers thermal energy storage, another area that has seen significant development in the last 15 years. The new developments, including materials, analysis, and design, are thoroughly covered in the revised Chapter 4. Solar industrial process heat has been moved from Chapter 8 in the previous edition to Chapter 5 in the current edition, since these systems are more appropriate in this chapter together with the other solar heat systems. Solar refrigeration, cooling, and dehumidification are covered in Chapter 6. This chapter covers the fundamentals of the refrigeration and dehumidification cycles and their applications to building cooling and dehumidification. Chapter 7 covers passive methods of water and space heating, passive cooling, and daylighting. The revision includes a section on various computer codes and sources of information on passive system design and daylighting.

Chapters 8 and 9, covering CSP and PV power, respectively, are thoroughly edited covering the latest advancements and what students need to learn for future upcoming developments in these areas. Since solar central receiver systems, commonly known as power towers, are expected to become more prevalent in the industry than before, the new Chapter 8 covers this topic in detail, including the design of a solar heliostat field, receiver/absorber, and higher-temperature thermodynamic power cycles, especially the supercritical CO₂ cycle. Chapter 8 also covers solar desalination in detail, including thermal and reverse osmosis desalination and desalination integrated with thermodynamic power cycles as a bottoming cycle. Chapter 9 covers the latest developments in thin film solar cells, including dye-sensitized solar cells. The revised chapter also includes additional topics, such as maximum power point tracking. Since engineers use software packages for the design of solar CSP and PV plants, information about those packages is included in the chapters as well as an appendix. Finally, Chapter 10 covers environmental applications of solar energy, such as photocatalytic oxidation of environmental pollutants. This book is the only solar energy textbook that covers this topic including the fundamentals and design methods.

Because of the comprehensiveness of this book, a single course on solar energy cannot cover the entire book. Experience shows that at least two courses are necessary to cover the book, one focused on the fundamentals and the other focused on the design of systems for one or more applications, such as building heating and cooling, industrial process heat, electric power plants, or environmental applications. On the other hand, a single course could be offered covering the fundamentals and emphasis on selected applications depending on the background of the students.

The author would like to thank the coauthors of the earlier edition, Frank Kreith and Jan Kreider, for writing the original first edition that helped in the education of a large number students and professionals in the 1970s to the year 2000 when the second edition was published. The author would also like to thank Dr. Jeffrey Morehouse for writing the chapter on passive methods for heating, cooling and daylighting. Another group of persons that deserves the gratitude of the author is his current and former graduate students, colleagues, assistants, and coworkers who have helped in various ways in the revision of this book including solving examples and homework problems, updating tables of values and figures, drawing figures, combing the equations, checking reference citations, and updating the solution manual. Some of them include Ricardo Vasquez Padilla, Saeb Besarati, Gokmen Demirkaya, Chennan Li, Jamie Trahan, Phil Myers, Rachana Vidhi, Antonio Archibald Ramos, Rajeev Kamal, Samantha Wijewardane, Gunnar Tamm, Sanjay Vijayaraghavan, Chatura Wikramaratne, Mehdi Zeyghami, Yangyang Zhang, Mohammad Abutayeh, Tanvir Alam, and Abhinav Bhardwaj. The author would like to give special thanks to Gunnar Tamm and Sanjay Vijayaraghavan for preparing the solutions manual and Phil Myers for updating it for the third edition. The author would also like to thank his colleagues, Elias Stefanakos and Chand Jotshi, for numerous discussions on various topics covered in the book, and his editorial assistant, Barbara Graham, for help in the drafts of the chapters and tables.

Finally, the author would like to thank his wife, Lovely Goswami, for her encouragement, support, and patience during the preparation of this and a number of other books.

Author



D. Yogi Goswami is a Distinguished University Professor and Director of the Clean Energy Research Center at the University of South Florida. He conducts fundamental and applied research on solar thermal power and cooling, photocatalytic detoxification and disinfection, thermodynamics, third-generation photovoltaics, and hydrogen production and storage. Professor Goswami is the editor in chief of *Solar Energy* and *Progress in Solar Energy*. He has published as an author or editor 17 books and more than 350 refereed technical papers. He also holds 16 patents, some of which have been successfully commercialized.

Dr. Goswami has developed successful industrial ventures based on his inventions and other innovations and has served on the boards of many companies.

A recognized leader in professional scientific and technical societies, Prof. Goswami has served as a governor of ASME-International, president of the International Solar Energy Society (ISES), senior vice president of ASME, and president of the International Association for Solar Energy Education.

Dr. Goswami is a recipient of the highest awards of many professional societies related to solar energy including the Farrington Daniels Award from ISES, the Frank Kreith Energy award and medal from ASME, the John Yellott Award for Solar Energy from ASME, and the Charles Greely Abbott Award and Hoyt Clark Hottel Award from the American Solar Energy Society (ASES). He is a charter fellow of the National Academy of Inventors and a fellow of the American Association for the Advancement of Science, ASME International, and the ASES.

Contributing Authors

Chapter 7

Jeffrey H. Morehouse
Emeritus Professor
University of South Carolina
Columbia, South Carolina

Sections 3.6 and 8.3

Ricardo Vasquez Padilla
CSRIO
Melbourne, Australia

Section 4.33

Jamie Trahan
Clean Energy Research Center
University of South Florida
Tampa, Florida

Sections 8.7–8.9

Saeb Besarati
Clean Energy Research Center
University of South Florida
Tampa, Florida

Section 8.10

Chennan Li
GE Power & Water
Schenectady, New York

1

Introduction to Solar Energy Conversion

A thing that will assume enormous importance quite soon is the exhaustion of our fuel resources. Coal and oil have been accumulating in the earth over five hundred million years, and at the present rates of demand for mechanical power, the estimates are that oil will be all gone in about a century, and coal probably in a good deal less than five hundred years. For the present purpose, it does not matter if these are underestimates; they could be doubled or trebled and still not affect the argument. Mechanical power comes from our reserves of energy, and we are squandering our energy capital quite recklessly. It will very soon be all gone, and in the long run we shall have to live from year to year on our earnings (Darwin 1953).

Charles Galton Darwin
(grandson of Charles Darwin)

The only energy earnings or income we have is the direct radiative energy from the sun (Daniels 1964). Fossil fuels are the stored form of the sun's energy, representing our energy savings or energy capital. In addition, we have the indirect forms of solar energy (wind, biomass, ocean, and hydro), geothermal energy, and nuclear energy in radioactive materials. It is clear that we have been using the energy capital at unsustainable rates over the last 100 years while throwing away our energy earnings, the direct energy from the sun. However, there is concerted effort throughout the world to change it. As we move toward a future where solar energy will play a far greater role, education of students in the science and engineering of solar energy has become extremely important and urgent. This book fills that need.

This book assumes that the reader is familiar with traditional thermodynamics, basic heat transfer, and fluid mechanics and has knowledge of calculus and ordinary differential equations. Some elements of radiation, fluid mechanics, and heat transfer specific to solar engineering are presented in the text. The design and analysis of solar utilization schemes are approached from a systems-analysis viewpoint, which combines technical design with economic analysis. There is no single solution to a given task in solar energy utilization and each problem must be analyzed separately from fundamental principles.

1.1 Global Energy Needs and Resources

Global energy consumption in the last half-century has rapidly increased and is expected to continue to grow over the next 50 years but with significant differences. The past increase was stimulated by relatively “cheap” fossil fuels and increased rates of industrialization in North America, Europe, and Japan; yet while energy consumption in these countries continues to increase, additional factors make the picture for the next 50 years more complex. These additional complicating factors include China’s and India’s rapid increase in energy use as they represent approximately one-third of the world’s population, the expected depletion of oil resources in the near future, and the effect of human activities on global climate change. On the positive side, the renewable energy (RE) technologies of wind, biofuels, solar thermal, and photovoltaics (PV) are finally showing maturity and the ultimate promise of cost competitiveness.

The total primary energy demand in the world increased from 5536 million tons of oil equivalent (MTOE) in 1971 to 10,345 MTOE in 2002, representing an average annual increase of 2% (Figure 1.1).

By 2008, the world energy demand had increased to 12,271 MTOE, representing an average annual increase of approximately 3%. The main reason for a 50% increase in the annual rate is the fast-growing energy demand in the Asia Pacific, more specifically China. Since the per capita energy used in the most populous countries (China and India) is still very small, the global energy use may continue to increase at this extremely high rate. Since 2008,

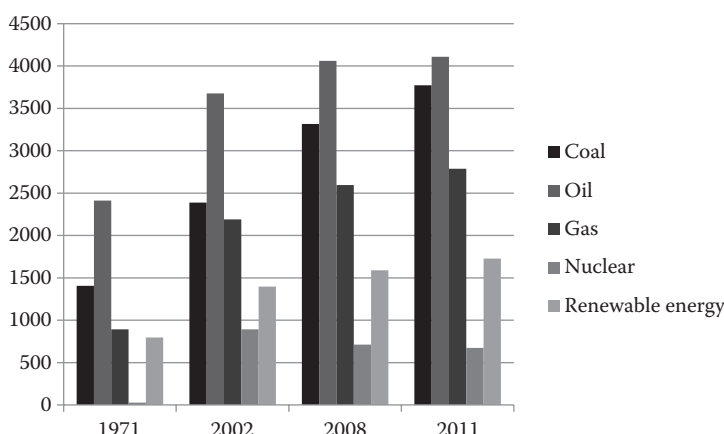


FIGURE 1.1

World primary energy demand (MTOE). (Data from IEA, *World Energy Outlook 2005*, International Energy Agency, Paris, France, 2005; IEA, *World Energy Outlook 2010*, International Energy Agency, Paris, France, 2010; IEA, *World Energy Outlook 2013*, International Energy Agency, Paris, France, 2013.)

the average annual energy increase dropped to approximately 2.1%, mainly because of the deep recession in the United States and Europe where the energy use actually went down.

Even at a 2% increase per year, the primary energy demand of 12,271 MTOE in 2008 would double by 2043 and triple by 2063. Of course, the global energy use cannot continue to increase at the same rate forever. The International Energy Agency (IEA 2010) estimated that the global energy use will increase at an average annual rate of 1.2% up to 2035. Even at that optimistic rate, the global energy use will increase by 38% by 2035, reaching a value of 16,934 MTOE per year. A review of the present energy resources and their availability (Kreith and Goswami 2007; WBGU 2003) shows that as much as 50% of the global energy use in 2050 will have to come from RE sources, a vast majority being from solar energy and wind. With a view to meet the future demand of primary energy in 2050 and beyond, it is important to know the extent of available RE resources and their ability to fulfill our energy needs for buildings, food, water, transportation, industry, and electrical power. This book presents the availability of solar energy, methods of conversion to useful forms, various applications, methods of design, and economic analysis.

1.1.1 Present Status and Potential of RE

According to the data in Table 1.1, RE accounted for 13.2% of the world's total primary energy supply in 2011. However, approximately 75% of the RE supply was from biomass, and in developing countries, it is mostly converted by traditional open combustion, which is very inefficient. Because of its inefficient use, biomass resources presently supply only approximately 20% of what they could if converted by modern, more efficient, available technologies.

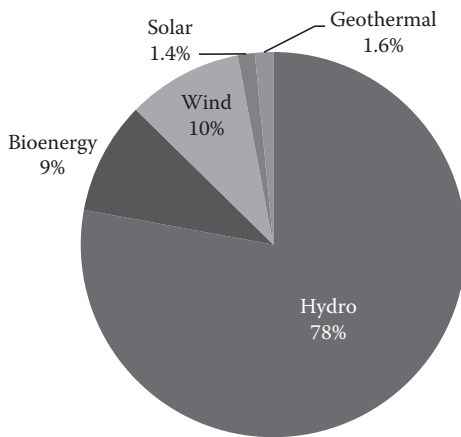
The total share of all renewables for electricity production in 2011 was approximately 20.1%, a vast majority (78%) of it being from hydroelectric power (Figure 1.2). Even though worldwide solar power capacity represented only 1.4% of the total electricity capacity, it was growing at an average annual rate of approximately 50%.

TABLE 1.1

2011 Fuel Shares in World Total Primary Energy Supply

Source	Share
Oil	31.4%
Natural gas	21.3%
Coal	28.9%
Nuclear	5.2%
Renewables	13.2%

Source: IEA, *World Energy Outlook 2013*, International Energy Agency, Paris, France, 2013.

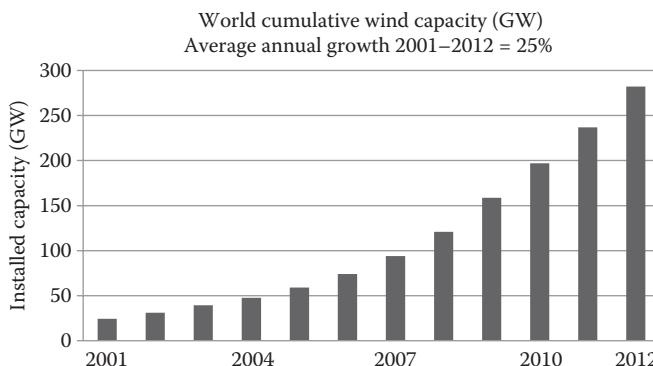
**FIGURE 1.2**

2011 Renewable resource shares in world electricity capacity. (Data from IEA, *World Energy Outlook 2013*, International Energy Agency, Paris, France, 2013.)

1.1.2 Wind Power

The utilization of wind power has been widespread since medieval times. Windmills were used in rural United States to power irrigation pumps and drive small electric generators used to charge batteries that provided electricity during the last century. A windmill or wind turbine converts the kinetic energy of moving air into mechanical motion, usually in the form of a rotating shaft. This mechanical motion can be used to drive a pump or to generate electric power. The energy content of the wind increases with the third power of the wind velocity and wind power installations are economical in regions where winds of sufficient strength and regularity occur.

Wind energy technology has progressed significantly over the last two decades. The technology has been vastly improved and capital costs have come down to as low as \$1000/kW. At this level of capital costs, wind power is already economical at locations with fairly good wind resources. Therefore, the average annual growth in worldwide wind energy capacity from 2001 to 2012 was over 25% (Figure 1.3). The average growth in the United States over the same period was 37.7%. The total worldwide installed wind power capacity, which was 24 GW in 2001 (Figure 1.3), reached a level of 282 GW in 2012 (WWEA 2012). The world's total theoretical potential for onshore wind power is around 55 TW with a practical potential of at least 2 TW (UNDP 2004), which is approximately 40% of the entire present worldwide generating capacity. The offshore wind energy potential is even larger.

**FIGURE 1.3**

World total wind power installed capacity. (From WWEA 2012, http://www.wwindea.org/webimages/WorldWindEnergyReport2012_final.pdf.)

Wind power is an indirect form of solar energy; however, it will not be covered in this book. Instead, it will be covered in detail in a companion book on RE being published separately.

1.1.3 Biomass

Although theoretically harvestable biomass energy potential is of the order of 90 TW, the technical potential on a sustainable basis is of the order of 8–13 TW or 270–450 exajoules/year. This potential is 3–4 times the present electrical generation capacity of the world. It is estimated that by 2025, even municipal solid waste (MSW) could generate up to 6 exajoules/year.

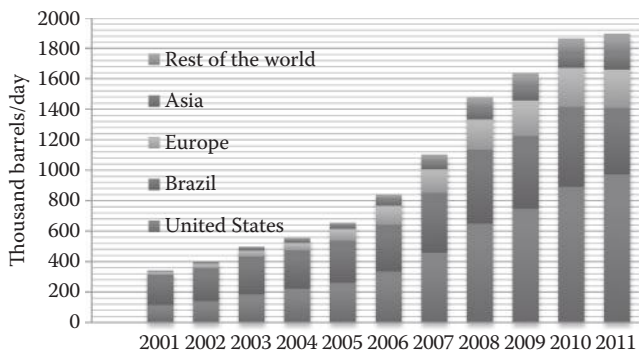
The biggest advantage of biomass as an energy resource is its relatively straightforward transformation into transportation fuels. Biofuels have the potential to replace as much as 75% of the petroleum fuels in use for transportation in the United States (Worldwatch Institute 2006). This is especially important in view of the declining oil supplies worldwide. Biofuels will not require additional infrastructure development. Therefore, development of biofuels is being viewed very favorably by governments around the world. Biofuels, along with other transportation options such as electric vehicles and hydrogen, will help diversify the fuel base for future transportation. Table 1.2 and Figure 1.4 show the global production of biofuels from 2001 to 2011. United States, Brazil, and Europe are the top producing countries and region of the world. Biofuel production grew more than 5 times in 10 years, although it started from a much smaller base. In 2005, the world ethanol production had reached approximately 36 billion liters per year while biodiesel production topped 3.5 billion liters during the same year.

TABLE 1.2

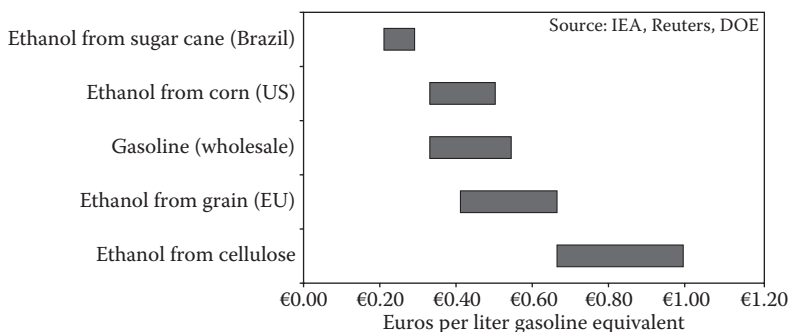
Total Biofuel Production (Thousand Barrels per Day)

	2001	2002	2003	2004	2005	2006	2007	2008	2009	2010	2011
United States	115.7	140.3	183.9	223.3	260.6	335.0	457.3	649.7	747.1	889.8	971.7
Brazil	197.6	216.9	249.4	251.7	276.4	307.3	395.7	486.3	477.5	527.1	438.1
Europe	21.2	29.3	39.3	48.9	76.8	123.9	153.8	198.1	233.2	255.2	250.5
Asia	3.1	8.3	17.2	21.1	28.2	44.9	49.2	75.6	93.8	99.8	118.2
Rest of the world	5.3	8.6	9.6	9.8	14.2	29.6	47.3	67.7	83.8	93.3	118.8
World	342.9	403.5	499.4	554.8	656.3	840.6	1103.3	1477.3	1635.4	1865.4	1897.2

Source: Enerdata, *Global Energy Statistical Yearbook 2013*, Enerdata Information Services, London, UK, 2013, <http://www.enerdata.net>; IEA, *World Energy Outlook 2013*, International Energy Agency, Paris, France, 2013.

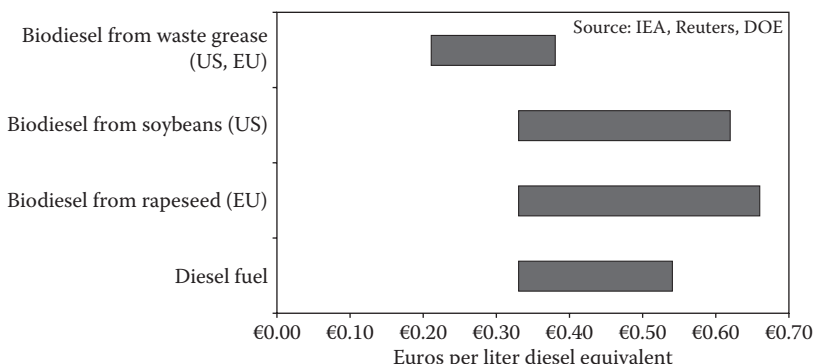
**FIGURE 1.4**

World biofuel production, 2001–2011. (From IEA, *World Energy Outlook 2013*, International Energy Agency, Paris, France, 2013.)

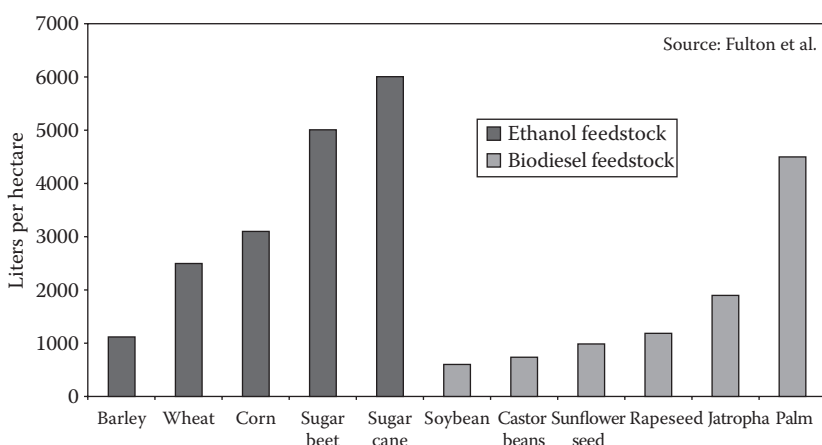
**FIGURE 1.5**

Cost ranges for ethanol and gasoline production, 2006. (From Worldwatch Institute, *Biofuels for Transportation—Global Potential and Implications for Sustainable Energy in the 21st Century*, Worldwatch Institute, Washington, DC, 2006.)

The present cost of ethanol production ranges from approximately 25 Euro cents to approximately 1 Euro per gasoline equivalent liter, as compared to the wholesale price of gasoline, which is between 40 and 60 Euro cents per liter (Figure 1.5). Biodiesel costs, on the other hand, range between 20 Euro cents to 65 Euro cents per liter of diesel equivalent (Figure 1.6). Figure 1.7 shows the feedstock used for these biofuels. An important consideration for biofuels is that the fuel should not be produced at the expense of food while there are people going hungry in the world. This would not be of concern if biofuels were produced from MSW or nonfood forest resources.

**FIGURE 1.6**

Cost ranges for biodiesel and diesel production, 2006. (From Worldwatch Institute, *Biofuels for Transportation—Global Potential and Implications for Sustainable Energy in the 21st Century*, Worldwatch Institute, Washington, DC, 2006.)

**FIGURE 1.7**

Biofuel yields of selected ethanol and biodiesel feedstock. (From Worldwatch Institute, *Biofuels for Transportation—Global Potential and Implications for Sustainable Energy in the 21st Century*, Worldwatch Institute, Washington, DC, 2006.)

According to the Worldwatch Institute report, a city of 1 million people produces approximately 1800 tons of MSW and 1300 tons of organic waste every day, which using the present-day technology could produce enough fuel to meet the needs of 58,000 persons in the United States, 360,000 in France, and nearly 2.6 million in China at current rates of per capita fuel use (Worldwatch Institute 2006).

1.1.4 Ocean Energy Conversion

Almost 71% of the world's surface is covered by oceans. Oceans serve as a tremendous storehouse of solar energy because of the temperature differences produced by the sun as well as the kinetic energy stored in the waves. There are a number of places in the ocean where temperature differences of the order of 20–25 K exist at depths of less than 1000 m, and these temperature differences could be used to operate low-pressure heat engines. Although the thermodynamic efficiency of a heat engine operating on such a small temperature difference is low, the available amount of thermal energy is very large. However, putting this energy-conversion method into practice requires the development of efficient and cheap heat exchangers that can withstand the rough marine conditions. Since heat-exchange equipment is the most expensive part of any ocean thermal conversion scheme, the cost of using the temperature gradients in the ocean for practical solar energy utilization depends largely on this development.

The second method of utilizing the oceans for energy generation is through ocean waves. Energy in ocean currents and waves is kinetic energy, which can be converted to power by specially designed turbines. Energy from tides can be harnessed by constructing a dam to hold seawater at a higher elevation when the tide is high and letting it run a turbine when the tide is low. According to an Electric Power Research Institute study, the total ocean wave and tidal power resource potential for the United States is approximately 2100 TWh/year (EPRI 2007), of which approximately 260 TWh/year could be credibly harnessed. Ocean energy conversion will not be treated in this text. Instead, it will be covered in detail in a companion text on RE conversion.

1.2 Solar Energy

The amount of solar radiant energy falling on a surface per unit area and per unit time is called *irradiance*. The mean extraterrestrial irradiance normal to the solar beam on the outer fringes of the earth's atmosphere is approximately 1.36 kW/m^2 . Since the earth's orbit is elliptical, the sun-to-earth distance varies slightly with time of year, and the actual extraterrestrial irradiance varies by $\pm 3.4\%$ during the year. The angle subtended by the sun when viewed from the earth is only 0.0093 rad (approximately 32 min of arc); the direct

beam radiation reaching the earth is therefore almost parallel. Although the brightness of the solar disc decreases from center to edge, for most engineering calculations, the disc can be assumed to be of uniform brightness. The radiant energy from the sun is distributed over a range of wavelengths, and the energy falling on a unit surface area per unit time within a particular spectral band is known as the *spectral irradiance*; its value is usually expressed in watts per square meter per nanometer of bandwidth. The extraterrestrial spectral irradiance is shown in Figure 1.8. It can be approximated by the spectrum of a black body at 5800 K. In the upper part of Figure 1.8, the wave bands typically useable for different solar applications are shown, and the lowest curve shows the spectral direct-beam irradiance at sea level on earth under clear sky conditions with the sun overhead.

The amount of sunlight striking the earth's atmosphere continuously is 1.75×10^5 TW. Considering a 60% transmittance through the atmospheric cloud cover, 1.05×10^5 TW reaches the earth's surface continuously. If the irradiance on only 1% of the earth's surface could be converted into electric energy with a 10% efficiency, it would provide a resource base of 105 TW,

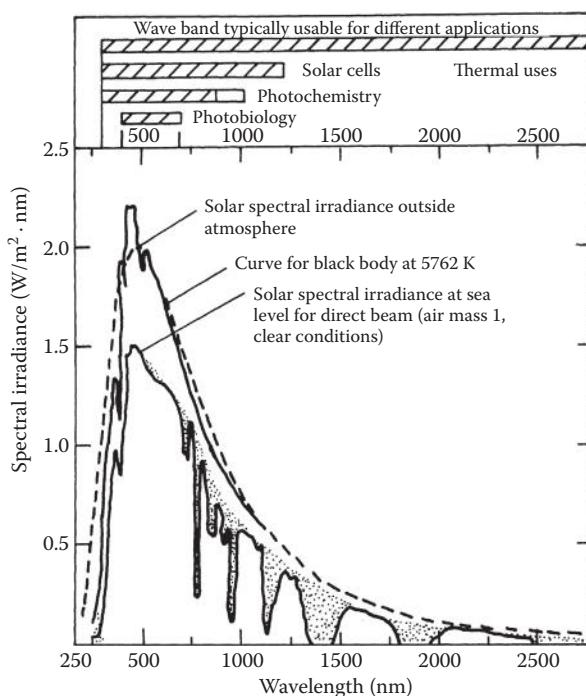


FIGURE 1.8

Spectral irradiance curves for direct sunlight are extraterrestrial and at sea level with the sun directly overhead. Shaded areas indicate absorption owing to atmospheric constituents, mainly H_2O , CO_2 , and O_3 . Wavelengths potentially utilized in different solar energy applications are indicated at the top.

while the total global energy needs for 2050 are projected to be approximately 25–30 TW. The present state of solar energy technologies is such that commercial solar panel efficiencies have reached more than 20%, laboratory multijunction solar cell efficiencies under concentrating sun have exceeded 40%, and solar thermal systems provide efficiencies of 40%–60%.

Solar PV panels have come down in cost from approximately \$30/W to approximately \$0.50/W in the last three decades. At \$0.50/W panel cost, the overall system cost is around \$2/W, which is already lower than grid electricity in the Caribbean island communities. Of course, there are many off-grid applications where solar PV is already cost-effective. With net metering and governmental incentives, such as feed-in laws and other policies, grid-connected applications such as Building-Integrated PV have become cost-effective even where grid electricity is cheaper. As a result, the worldwide growth in PV production has averaged more than 43% per year from 2000 to 2012 and 61% from 2007 to 2012 (Figure 1.9) with Europe showing the maximum growth.

Solar thermal power using concentrating solar collectors was the first solar technology that demonstrated its grid power potential. A 354 MW_e concentrating solar thermal power (CSP) plant has been operating continuously in California since 1988. Progress in solar thermal power stalled after that time because of poor policy and lack of research and development (R&D). However, the last 10 years have seen a resurgence of interest in this area and a number of solar thermal power plants around the world are under construction. The largest CSP plant with a capacity of 400 MW came on line in Nevada in February 2014. The cost of power from these plants (which is so far in the range of 12 to 16 US cents/kWh_e) has the potential to go down to 5 US cents/kWh_e with scale-up and creation of a mass market. An advantage of solar thermal power is that thermal energy can be stored efficiently, and fuels

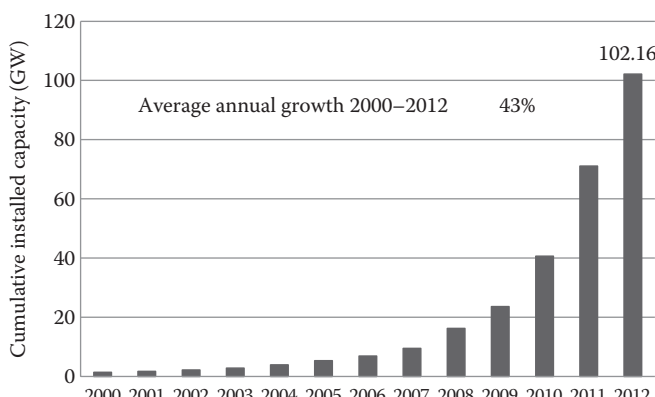


FIGURE 1.9

World solar PV production 2000–2012 (GWp). (From EPIA, *Global Market Outlook for Photovoltaics*, European Photovoltaic Industries Association, Brussels, Belgium, <http://www.epia.org/>.)

**FIGURE 1.10**

Deployment of solar heat (glazed) collectors, MW_{th}.

such as natural gas or biogas may be used as backup to ensure continuous operation. If this technology is combined with power plants operating on fossil fuels, it has the potential to extend the time frame of the existing fossil fuels.

Low-temperature solar thermal systems and applications have been well developed for quite some time. They are being actively installed wherever the policies favor their deployment. Figure 1.10 gives an idea of the rate of growth of solar thermal systems in the world.

We shall now describe, briefly, the important conversion methods.

1.2.1 Thermal Conversion

Thermal conversion is an engineering conversion method that utilizes a familiar scientific phenomenon. When a dark surface is placed in sunshine, it absorbs solar energy and heats up. Solar energy collectors working on this principle consist of a surface facing the sun, which transfers part of the energy it absorbs to a working fluid in contact with it. To reduce heat losses to the atmosphere, one or two sheets of glass are usually placed over the absorber surface to improve its efficiency. These types of thermal collectors suffer from heat losses owing to radiation and convection, which increase rapidly as the temperature of the working fluid increases. Improvements such as the use of selective surfaces, evacuation of the collector to reduce heat losses, and special kinds of glass are used to increase the efficiency of these devices.

The simple thermal conversion devices described above are called flat-plate collectors. They are available today for operation over a range of temperatures up to approximately 365 K (200°F). These collectors are suitable mainly for providing hot water service and space heating and possibly are also able to operate absorption-type air-conditioning systems.

The thermal utilization of solar radiation for the purpose of generating low-temperature heat is at the present time technically feasible and economically

viable for producing hot water and heating swimming pools. In some parts of the world, thermal low-temperature utilization is also used for heating and cooling buildings.

The generation of higher working temperatures as needed, for example, to operate a conventional steam engine requires the use of focusing devices in connection with a basic absorber–receiver. Operating temperatures as high as 4000 K (6740°F) have been achieved, and the generation of steam to operate pumps for irrigation purposes has also proved technologically feasible. At the present time, a number of focusing devices for the generation of steam to produce electric power are under construction in different regions of the world, and the cost estimates suggest that the cost of solar power in favorable locations will be no more than that of conventional thermal power when the development of these plants has been completed.

1.2.2 Photovoltaic Conversion

The conversion of solar radiation into electrical energy by means of solar cells was developed as a part of satellite and space-travel technology. The present technology utilizes the band gap of semiconductor materials to generate electrons and conduct them in a preferred direction using a p–n junction (described in detail later in the book). The theoretical maximum efficiency of single solar cells is approximately 33%, and in practice, efficiencies as high as 25% have been achieved with silicon photovoltaic devices. Multijunction solar cells can utilize a much broader spectrum of solar energy at a higher efficiency. Efficiencies as high as 44% have been achieved in the laboratory (Green et al. 2013) and the present research is aimed at efficiencies of around 50%. The overall system efficiencies of the commercially available photovoltaic panels today are in the range of 10% to 20%. With the development of thin film solar photovoltaic technologies, the costs of panels have come down from approximately \$30/W_p to as low as \$0.50/W_p. Here, W_p stands for peak watt, which means that the stated output would be expected when the solar irradiance on the panel is 1000 W/m² at standard atmospheric conditions. This level of solar radiation would be expected at a sunny location on a clear day around noon while the panel is directly facing the sun. With costs of the panels being lower than \$1/W_p, the total PV system costs are in the range of \$1.50/W_p (for multi-megawatt scale systems) to approximately \$3/W_p for residential-scale systems. Because of the reduction in costs, improvements in reliability and lifetimes, and preferential public policies, the PV industry is growing at an average annual rate of more than 50%.

Another way of direct conversion of sunlight to electricity takes advantage of the electromagnetic wave nature of sunlight as opposed to the quantum nature used in the conventional PV. This concept proposes to use nanoscale and microscale antennas (size of the order of the wavelength of radiation) to convert solar and ambient radiation into electricity (Goswami et al. 2004). The proposed panel would consist of billions of such antennas coupled with

rectifiers. The combined antenna and rectifier structure is known as a *rectenna*. The theoretical efficiency of a rectenna is in the range of 80% to 90%. An efficiency of greater than 80% was demonstrated for a rectenna converting radiation at a frequency of 2.4 GHz to electricity (Brown 1984). However, since the frequency of visible solar radiation is in the range of 300 THz, which would require a five-orders-of-magnitude size reduction of antennas and a totally different concept of the rectifier, development of this concept for converting solar energy is no simple task and is expected to take probably a decade or longer to become practical.

1.2.3 Limitations of Solar Energy

The first problem encountered in the engineering design of equipment for solar energy utilization is the low flux density, which makes necessary large surfaces to collect solar energy for large-scale utilization. Also, the larger the surfaces, the more expensive the delivered energy becomes. When the sun is directly overhead on a cloudless day, 10 m^2 of surface could theoretically provide energy at a 70% efficiency of collection and 30% conversion efficiency at a rate of approximately 2 kW. Several factors reduce this amount in practice, however.

The total solar energy reaching the earth is made up of two parts: the energy in the direct beam and the diffuse energy from the sky. The amount of direct energy depends on the cloudiness and the position of the sun and is obviously greatest on clear days. Some solar radiation falling on clouds is diffused by scattering, but clouds do not absorb all of the energy. The effect of clouds is mainly to increase the percentage of diffuse energy in the total energy reaching the surface, and diffuse irradiance in summer months with high and broken clouds can be as high as 400 W/m^2 . Thick clouds let less energy pass than thin clouds and scatter proportionally more of the total energy back into space.

The second practical limitation that is not apparent from the macroscopic energy view is that most of the solar energy falls on remote areas and would therefore require some means of transmission to be useful to the industrialized nations. The mean amount of energy available on a horizontal plane is greatest in the continental desert areas around latitudes 25°N and 25°S of the equator and falls off toward both the equator and the poles. The highest annual mean irradiance is 300 W/m^2 in the Red Sea area. Clouds reduce the mean global irradiance considerably in equatorial regions. However, whereas in northern climates the mean horizontal surface global irradiance varies from season to season, it remains relatively constant in equatorial regions. Typical values of mean annual horizontal surface irradiance are as follows: Australia, approximately 200 W/m^2 ; United States, 185 W/m^2 ; United Kingdom, 105 W/m^2 .

Table 1.3 shows the total solar electric energy potential for the solar energy-rich areas of the world. It is important to note that many of these parts of the world, for example, Saudi Arabia, central Australia, and parts of South Africa and India, are flat deserts that are practically unusable for agriculture.

TABLE 1.3

Solar-Electric Energy from Earth's High-Insolation Areas

Desert	Nominal Areas [km ²]	Nominal Annual Thermal Energy Flux [GW h(th)/km ²]	Percentage of Area Assumed Useable	Electric Energy Extracted at 25% Efficiency [GW h/year]
North Africa	7,770,000	2300	15 ^a	670,000,000
Arabian Peninsula	1,300,000	2500	30 ^b	244,000,000
Western and central Australia	1,550,000	2000	25	194,000,000
Kalahari	518,000	2000	50	129,000,000
Thar (northwest India)	259,000	2000	50	65,000,000
Mojave, southern California	35,000	2200	20	3,900,000
Vizcaino, Baja, California (Mexico)	15,500	2200	25	2,100,000
Total/average	11,447,500	2190 (average)	31 (average)	1,308,000,000

^a Parts of Arabian and Libyan deserts.^b Approximately 60% of Rub'al Khali desert.

At the same time, it should be noted that these are also regions with little or no water, which point to the need to develop dry cooling options for solar thermal electric power. Although the global distribution of solar energy does not favor the industrialized parts of the world, it is important to note that these are the regions, especially Europe, that have led in the deployment of solar power over the last decade.

The third limitation of solar energy as a large-scale source of power and heat is its intermittency. Solar energy has a regular daily cycle owing to the turning of the earth around its axis and a regular annual cycle owing to the inclination of the earth axis with the plane of the ecliptic and to the motion of the earth around the sun, and is also unavailable during periods of bad weather. It is obvious that these daily and seasonal variations in irradiance, exacerbated by variations owing to weather, introduce the need for storage or a supplementary fuel.

1.3 Energy Storage

Widespread use of solar energy systems requires satisfactory means of storing the energy once it has been collected and converted. Storage is becoming especially important for areas where grid-connected photovoltaic power capacity is increasing rapidly. Distributed grid-connected solar electric power systems require storage as a part of a *smart grid* management of

disparity between supply and demand. There are various options available for storage of solar energy before conversion to the final useful form as well as after conversion. Some are economically viable at this time, while others need more R&D and reduction in costs.

For applications such as heating and cooling of buildings, sensible heat storage in water or rocks is a reasonable solution. Passive storage in "thermal mass" in buildings is a clever method of integrating storage with buildings by incorporating additional stone, bricks, or even phase-change materials in the building components.

For electrical energy production systems, however, storage systems must be specially designed and built. Figure 1.11 shows a comparison of the energy densities of various options including liquid fuels. Figure 1.12 presents a comparison of possible energy-storage systems for various applications. The first group of storage possibilities is batteries, but only lead-acid batteries are currently available at reasonable cost, although considerable R&D is ongoing to develop more advanced battery systems. Development of supercapacitors would help in smoothing out short-term intermittency problems of storage

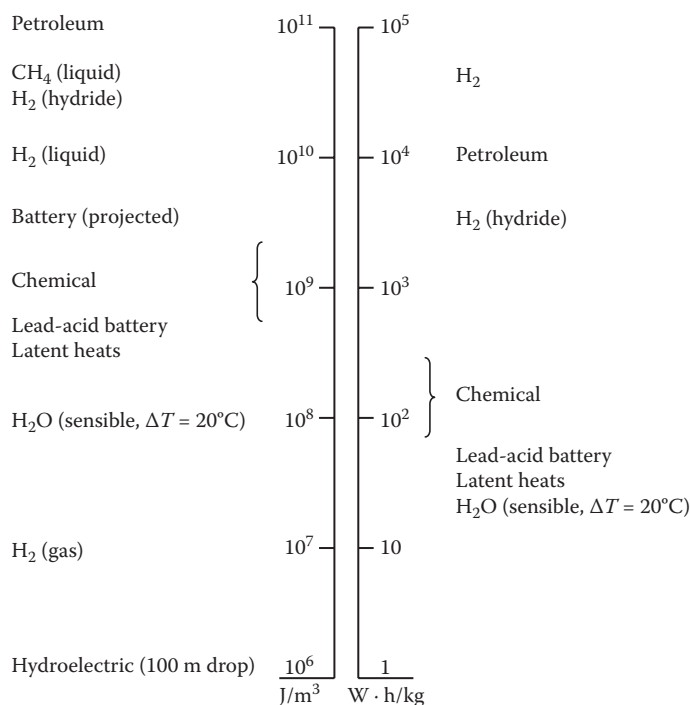
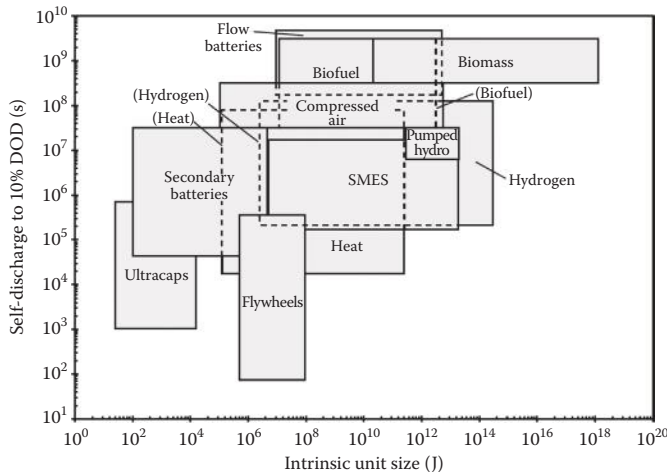


FIGURE 1.11

Mass and volumetric energy densities for typical energy-storage media. (Redrawn from Offenhardt, P.O.D., Classical methods of storing thermal energy. In: K.W. Bör (ed.), *Sharing the Sun-Solar Technology in the Seventies*, vol. 8, Solar Energy Society of Canada, Winnipeg, 1976.)

**FIGURE 1.12**

A comparison of storage technologies, mapped by self-discharge time and unit size. (Adapted from Kreith, F. and Goswami, D.Y., *Handbook of Energy Efficiency and Renewable Energy*, Chapter 18, CRC Press, Boca Raton, FL, 2007.)

especially for PV systems. However, cost-effective supercapacitors would have to be available for this to happen. Conventional electric power plants currently use hydro storage or compressed air storage where applicable. These methods could possibly be used for large solar power applications also but the plants would have to be at locations suitable for such storage systems, which put additional constraints on solar power plants. Therefore, it is unlikely that these storages would be adopted for solar power plants.

Another possibility is using solar energy to generate hydrogen and storing the energy in the gaseous or liquid phase. There appear to be no technical difficulties to the large-scale production, storage, and subsequent use of hydrogen in either liquid or gaseous form, but the hydrogen production efficiency is relatively low and, consequently, the cost of hydrogen storage and delivery systems is quite high at the present time.

High-temperature thermal energy storage is especially appropriate for concentrating solar thermal power, also known as CSP, and is already being used in large scale commercially. The present capital cost of high-temperature thermal energy storage is around \$30–\$50/kWh_{th}, which is expected to go down to below \$10/kWh_{th} with the ongoing R&D. With the capital costs of CSP plants going down from approximately \$3 M/MW_e to less than \$1.5 M/MW_e and with 6–10 h of thermal energy storage at a capital cost of approximately \$10/kWh_{th}, electricity from CSP plants can achieve grid parity in many parts of the world.

Parabolic trough-based solar thermal power plants typically operate in the range of 300°C–400°C and can use synthetic oil as the sensible heat storage

medium as well as a heat transfer fluid. However, the high cost of synthetic oil has made it necessary to look for alternatives. Molten salt, usually a mixture of potassium nitrate and sodium nitrate, is a cheaper alternative that is being considered by a number of solar power companies. Latent heat storage in phase-change materials is under development, which is expected to reduce the cost of storage to less than \$10/kWh_{th} from the present commercial storage costs of approximately \$30–\$50/kWh_{th}. Although adding storage to a CSP plant increases the capital costs of a plant, it actually reduces the leveled cost of energy (LCOE) because it allows the power block of a CSP to be used for longer number of hours. Details of these and other storage materials, components, systems, and design methods are described in detail in Chapter 4. Central receiver tower systems, also known as power tower, can achieve temperatures from 500°C to more than 1000°C, which allows them to convert thermal energy to power at much higher efficiencies than parabolic trough-based systems. Therefore, most of the future R&D and commercial activity is directed toward the power tower system.

1.4 Economics of Solar Systems

Although solar energy systems have environmental benefits that have monetary value in terms of reduced health care costs and other global climate benefits, decisions about investing in solar energy systems are rarely based on these benefits. Since these are societal benefits, sometimes the governments provide financial incentives to encourage investments in such systems. A solar energy system differs fundamentally from a fossil fuel system in a manner that requires an economic analysis reflecting the benefits accrued by solar usage throughout the lifetime of the system. Fossil fuel-based systems usually have relatively small initial costs and relatively large annual operating costs reflecting fuel costs. Solar energy systems, on the other hand, cost more initially but have much lower costs during their lifetime. Therefore, a life cycle costing approach has to be adopted to compare investment in a solar energy system with the conventional energy system.

The concept of life cycle costing includes both the initial capital costs and the year-to-year operating costs in making economic decisions. The life cycle cost of any energy system is defined as the total of the following cost components over the life of a system:

1. Initial costs including equipment, construction/installation, and land costs (if any)
2. Operating costs
3. Interest charges if money is borrowed

4. Periodic maintenance, insurance, and miscellaneous recurring charges
5. Taxes
6. Salvage value (usually a negative cost)

The costs of a solar energy system have to be weighed against the benefits, which accrue in the future as the system produces its intended output (heat, electricity, etc.). Therefore, it is necessary to convert the future benefits to their present worth (PW). The financial performance parameters most commonly used for comparing economics are *payback period*, mostly for residential and small commercial systems, and *internal rate of return* (IRR), which is used by investors for large-scale solar electric systems. These and other important concepts are described in the following.

1.4.1 Present Worth

Just as the future value X of a sum of money P invested at an annual interest rate i is

$$X = P(1 + i)^t, \quad (1.1)$$

in which t is the future time expressed in years (or other time unit corresponding to the time basis of the interest rate i), a future sum of money X with a discount rate i has a present worth P given by

$$P = X(1 + i)^{-t} = X \cdot \text{PWF}(i, t), \quad (1.2)$$

where PWF is called the present worth factor, tabulated in Table A9.1 in the Appendix. The effect of inflation on the future value of an invested sum is to reduce the future value by a factor $(1 + j)$ per year, where j is the inflation rate per year. This is important for figuring out the future savings in terms of fuel costs that are increasing at an inflation rate of j . Considering an inflation rate of j , the PWF is given by

$$\text{PWF}(i', t) = (1 + i')^{-t}, \text{ where } i' = (i - j)/(1 + j). \quad (1.3)$$

The total life cycle costs (TLCC) include the initial costs and the future costs, such as operations and maintenance, repair, and replacement costs and interest payments, all discounted to a PW.

1.4.2 Series of Payments

In many cases, a solar energy system is financed by a loan, S , at an annual interest rate of i , to be paid back with annual payments, P_{ann} over a period t years. The annual payment, P_{ann} , in such cases, is given by

$$S = P_{\text{ann}}[(1 + i)^{-1} + (1 + i)^{-2} + (1 + i)^{-3} + \dots] \quad (1.4)$$

or

$$P_{\text{ann}} = S[i/(1 - (1 + i)^{-t})] = S \cdot \text{CRF}(i, t). \quad (1.5)$$

The term in brackets in Equation 1.5 is called the *capital recovery factor*, $\text{CRF}(i, t)$, which is tabulated in Table A9.2.

1.4.3 Levelized Cost of Energy

Many governments around the world are offering *feed-in tariffs* for solar power producers, which remain fixed for certain periods, such as 10 to 25 years. In order to determine the benefit of the feed-in tariff, it is important to know the LCOE of the solar power plant. The LCOE is the cost of a unit of energy (e.g., \$/kWh_e from a PV system) produced or saved by the system over the useful life of the system, discounted back to the present. The LCOE for a system with a useful life of N years is given by the following relation:

$$\text{LCOE} = \frac{\text{TLCC}}{\sum_{n=1}^N (E_n / (1 + i)^n)}, \quad (1.6)$$

where E_n is the energy produced by the solar energy system in year n . If the solar energy system output is assumed to be the same every year, E_n in Equation 1.6 can be taken out of the summation. In that case, the remaining summation is the series $[(1 + i)^{-1} + (1 + i)^{-2} + \dots]$, which is equivalent to the ratio $[1 - (1 + i)^{-n}] / i$ or the inverse of the capital recovery factor ($\text{CRF}(i, n) = i / [1 - (1 + i)^{-n}]$). Therefore, the LCOE simplifies to

$$\text{LCOE} = \frac{\text{TLCC}}{E_n} \text{CRF}(i, n). \quad (1.7)$$

1.4.4 Internal Rate of Return

IRR is the rate of return on the initial investment needed to convert future cash flow from a project equal to the initial investment. If the initial investment is considered a negative cash flow, then IRR is the discount rate that makes the sum of all cash flows discounted to their PW equal to zero.

$$0 = \sum_{n=1}^N \frac{\text{CF}_n}{(1 + \text{IRR})^n} + \text{CI}, \quad (1.8)$$

where CF_n is the net cash flow in year n , CI is the initial capital investment, and N is the number of years of useful life of the project. CF_n is the net of the revenues (or savings) and expenses during the year n .

IRR is used by investors to compare their potential investment in a solar energy project to the same investment in another project to determine if the solar energy investment is better. For large projects, investors usually finance in part by their equity investment and the rest by debt. In such cases, the periodic debt payments including the principal and interest are considered as a part of the expenses during that year. Therefore, the IRR for the equity investment is leveraged by the debt. Since the interest on the debt is lower than the rate of return, leveraging improves the IRR of the equity investment.

Example 1.1

A homeowner in Tampa, Florida, installed a 5 kW_p PV system using crystalline silicon panels for a total cost of \$27,500. The system is connected to the grid with a net metering plan (i.e., the homeowner pays for the difference in the electricity used and that produced by the system). The system produced 7300 kWh_e in the first year. If the effective electricity rate is \$0.15/kWh and assuming the rate will increase at a rate of 5%/year, find the payback period for the system. Assume the discount rate to be 5%.

Solution

For future output from a solar system, normally we have to model the solar resource for the location and the orientation of the panels, which is covered in Chapter 2, and use it to find the output based on the system model (covered in Chapters 5 through 10 depending on the application). Since it is known in the present case that the system produced 7300 kWh_e in the first year, it is fair to assume that it will produce that amount in the future as well, modified by any expected degradation in the panel efficiency. Since the panels are crystalline silicon, their degradation will be small. Assuming that the panels will degrade at a rate of 0.25% per year, the output in the succeeding years will be

$$\text{Second year output} = 7300 \times (100 - 0.25)/100 = 7300 \times 0.9975 = 7282 \text{ kWh}_e$$

$$\text{Third year output} = 7300 \times (0.9975)^2 = 7264 \text{ kWh}_e, \text{ and so on.}$$

Since the electric rate is increasing at 5%/year, it will be $0.15 \times (1.05) = \$0.1575$ the second year. The annual savings are $7300 \text{ kWh}_e \times \$0.15/\text{kWh}_e = \$1095$ the first year and so on.

Figure 1.13 shows the calculations for 28 years, assumed as the life of the system.

On the basis of Figure 1.13, it will take approximately 17 years for a simple payback of the initial investment. However, since the investment is made in year 1, the savings must be accounted for in their PW. The PW of the savings 5 years from the initial year (taken as 0 year here) from Equation 1.2 = $\$1318 \times (1 + 0.05)^{-5} = \$1318 \times 0.7835 = \$1032$.

The factor 0.7835 can also be found from Table A9.1 as PWF(5%, 5). On the basis of the PW, the system payback time is approximately 28 years.

Year	kWh	\$/kWh	Annual savings (\$)	Cumulative annual savings (\$)	PW annual savings	PW cumulative annual savings (\$)
1	7300	0.15	1095	1095	1043	1043
2	7282	0.158	1147	2242	1040	2083
3	7264	0.165	1201	3443	1038	3121
4	7245	0.174	1258	4701	1035	4156
5	7227	0.182	1318	6019	1032	5188
6	7209	0.191	1380	7399	1030	6218
7	7191	0.201	1446	8845	1027	7245
8	7173	0.211	1514	10,359	1025	8270
9	7155	0.222	1586	11,944	1022	9292
10	7137	0.233	1661	13,605	1020	10,312
11	7120	0.244	1740	15,345	1017	11,329
12	7102	0.257	1822	17,167	1015	12,344
13	7084	0.269	1908	19,075	1012	13,356
14	7066	0.283	1999	21,074	1009	14,365
15	7049	0.297	2093	23,167	1007	15,372
16	7031	0.312	2193	25,360	1004	16,376
17	7013	0.327	2296	27,656	1002	17,378
18	6996	0.344	2405	30,061	999	18,378
19	6978	0.361	2519	32,580	997	19,375
20	6961	0.379	2638	35,219	994	20,369
21	6944	0.398	2763	37,982	992	21,361
22	6926	0.418	2894	40,877	989	22,351
23	6909	0.439	3032	43,908	987	23,338
24	6892	0.461	3175	47,083	985	24,322
25	6874	0.484	3326	50,409	982	25,304
26	6857	0.508	3483	53,892	980	26,284
27	6840	0.533	3648.14	57,540	977	27,261
28	6823	0.560	3820.97	61,361	975	28,236

FIGURE 1.13

Annual output and savings from the PV system in Example 1.1.

Example 1.2

The homeowner in Example 1.1 gets a rebate of \$2/W from the electric power company and a 30% federal income tax credit. What is the payback period now?

Solution

Total rebate for the 5 kW system = $\$2/\text{W} \times 5 \text{ kW} \times 1000 \text{ W/kW} = \$10,000$

$$\begin{aligned}\text{Federal income tax credit} &= (\text{Net total cost}) \times 0.30 \\ &= (\$27,500 - \$10,000) \times 0.3 = \$5250\end{aligned}$$

$$\text{Net total cost after tax credit} = \$17,500 - \$5250 = \$12,250.$$

Therefore, from Figure 1.13, the payback time on the basis of PW is reduced to approximately 12 years.

Example 1.3

A solar power company invests in a 1 MW_p PV system at a sunny location, where the system output is expected to be 6 MWh_e/day on the average for the whole year. The company will minimize the system degradation to less than 0.15%/year by aggressive maintenance and repairs. The company expects that the system will be down for 7 days/year for maintenance or repair. The total initial costs of the system are expected to be \$2.5 M, and the average annual maintenance/repair costs are expected to be 3% of the initial costs. The company plans to invest 30% equity and finance 70% of the capital costs as debt at 6%/year. The company expects to get feed-in tariff of \$0.22/kWh_e for 20 years. What is the LCOE for this system? What is the IRR for the system?

Solution

Capital investment for this 1 MW_e system is $\$2.5 \text{ M} \times 0.3 = \0.75 M . The rest (\$1.75 M) is debt at a rate of 6% for 20 years.

$$\text{Year 1: MWh}_e \text{ produced} = 6 \text{ MWh}_e \cdot (365 - 7) = 2148 \text{ MWh}_e$$

$$\begin{aligned} \text{Revenue} &= 2148 \text{ MWh}_e \cdot \$0.22/\text{kWh}_e \cdot (1000 \text{ kWh}_e/\text{MWh}_e) = \$472,560 \\ &\text{or } \$0.47256 \text{ M} \end{aligned}$$

$$\begin{aligned} \text{Annual debt payment from Equation 1.5, } P_{\text{ann}} &= S[i/(1 - (1 + i)^{-t})] = \\ &S \cdot CRF(i, t) \end{aligned}$$

$$P_{\text{ann}} = \$1.75 \text{ M} [0.06/(1 - (1.06)^{-20})] = \$152,573 \text{ or } \$0.152573 \text{ M}$$

$$\text{Repairs and maintenance} = \$2.5 \text{ M} \cdot 0.003 = \$0.0075 \text{ M}$$

$$\text{Cash flow} = -\$750,000 + \$472,560 - \$152,573 - \$7500 = -\$311,403$$

Year 2: Assuming that the system performance degrades 0.15% and the maintenance costs increase 5%, the calculations are as follows:

$$\text{MWh}_e \text{ produced} = 6 \text{ MWh}_e \cdot (365 - 7) (1 - 0.0015) = 2145 \text{ MWh}_e$$

$$\text{Revenue} = 2145 \text{ MWh}_e \cdot \$0.22/\text{kWh}_e \cdot (1000 \text{ kWh}_e/\text{MWh}_e) = \$471,851$$

$$\text{Repairs and maintenance} = \$2.5 \text{ M} \cdot (0.003) (1.05) = \$7875$$

$$\text{Cash flow} = \$471,851 - \$152,573 - \$7875 = \$311,403$$

Table 1.4 shows the values calculated for 20 years. The IRR calculated from Equation 1.8 is 41.26%.

For LCOE, we need to use Equation 1.6,

$$\text{LCOE} = \frac{\text{TLCC}}{\sum_1^N (E_n / (1 + i)^n)}. \quad (1.6)$$

Assuming a discount rate of 5%, the PW of the capital and interest payments is \$2,651,397, and the PW of all the repairs and maintenance costs is \$142,857.

TABLE 1.4
Annual Outputs, Revenues, Costs and Cash Flow for Example 1.3

Year	MWh _e	\$/kWh _e	Annual Revenue (\$M)	Cumulative Revenue (\$M)	PW Annual Revenue (\$M)	Cumulative Revenue (\$M)	PW Capital and Debt Payments (\$M)	Repairs and Maintenance (\$M)	Cash Flow (\$M)
1	2148	0.22	0.473	0.473	0.461	0.461	0.153	0.008	-0.750
2	2145	0.22	0.472	0.944	0.439	0.900	0.153	0.008	0.312
3	2142	0.22	0.471	1.416	0.417	1.317	0.153	0.008	0.311
4	2138	0.22	0.470	1.886	0.397	1.713	0.153	0.009	0.309
5	2135	0.22	0.470	2.356	0.377	2.090	0.153	0.009	0.308
6	2132	0.22	0.469	2.825	0.359	2.449	0.153	0.010	0.307
7	2129	0.22	0.468	3.293	0.341	2.790	0.153	0.010	0.306
8	2126	0.22	0.468	3.761	0.324	3.114	0.153	0.011	0.304
9	2122	0.22	0.467	4.228	0.308	3.423	0.153	0.011	0.303
10	2119	0.22	0.466	4.694	0.293	3.716	0.153	0.012	0.302
11	2116	0.22	0.466	5.159	0.279	3.995	0.153	0.012	0.301
12	2113	0.22	0.465	5.624	0.265	4.260	0.153	0.013	0.299
13	2110	0.22	0.464	6.088	0.252	4.513	0.153	0.013	0.298
14	2106	0.22	0.463	6.552	0.240	4.752	0.153	0.014	0.297
15	2103	0.22	0.463	7.014	0.228	4.980	0.153	0.015	0.295
16	2100	0.22	0.462	7.476	0.217	5.197	0.153	0.016	0.294
17	2097	0.22	0.461	7.938	0.206	5.404	0.153	0.016	0.292
18	2094	0.22	0.461	8.398	0.196	5.600	0.153	0.017	0.291
19	2091	0.22	0.460	8.858	0.187	5.786	0.153	0.018	0.289
20	2088	0.22	0.459	9.318	0.177	5.964	0.153	0.019	0.288
E _n							IRR		41.26%

Therefore,

$$\text{TLCC} = \$2,651,397 + \$142,857 = \$2,794,254$$

$$E_n = 42,353 \text{ MWh}_e$$

$$\text{LCOE} = \frac{\$2,794,254}{26,454.1 \text{ MWh}} = \$105.63/\text{MWh}_e \text{ or } \$0.105/\text{kWh}_e.$$

In the above example, taxes and insurance costs have been neglected.

1.5 Summary of RE Resources

By definition, the term *reserves* does not apply to renewable resources; hence, we need to look at the annual “potential” of each resource. Figure 1.14 summarizes the resource potential and the present costs and the potential future costs for each renewable resource.

Technology	Annual potential	Operating capacity 2005	Investment costs US\$ per kW	Current energy cost	Potential future energy cost
Biomass energy	276–446 EJ total or 8–13 TW MSW ~ 6 EJ				
Electricity Heat Ethanol Biodiesel		~44 GW _e ~225 GW _{th} ~36 billion lit. ~3.5 billion lit.	500–6000/kW _e 170–1000/kW _{th} 170–350/kW _{th} 500–1000/kW _{th}	3–12 ¢/kWh 1–6 ¢/kWh 25–75 ¢/lit.(ge) [*] 25–85 ¢/lit.(de)**	3–10 ¢/kWh 1–5 ¢/kWh 6–10 \$/GJ 10–15 \$/GJ
Wind power	55 TW theo. 2 TW practical	59 GW _e	850–1700	4–8 ¢/kWh	3–8 ¢/kWh
Solar energy Photovoltaics Thermal power Heat	>100 TW	5.6 GW _e 0.4 GW _e	5000–10,000 2500–6000 300–1700	25–160 ¢/kWh 12–34 ¢/kWh 2–25 ¢/kWh	5–25 ¢/kWh 4–20 ¢/kWh 2–10 ¢/kWh
Geothermal	600,000 EJ useful resource base 5000 EJ economical in 40–50 years				
Electricity Heat		9 GW _e 11 GW _{th}	800–3000 200–2000	2–10 ¢/kWh 0.5–5 ¢/kWh	1–8 ¢/kWh 0.5–5 ¢/kWh
Ocean energy Tidal Wave OTEC	2.5 TW 2.0 TW 228 TW	0.3 GW	1700–2500 2000–5000 8000–20,000	8–15 ¢/kWh 10–30 ¢/kWh 15–40 ¢/kWh	8–15 ¢/kWh 5–10 ¢/kWh 7–20 ¢/kWh
Hydroelectric	1.63 TW theo. 0.92 TW econ.	690 GW	1000–3500	2–10 ¢/kWh	2–10 ¢/kWh
Large Small		25 GW	700–8000	2–12 ¢/kWh	2–10 ¢/kWh

* ge—gasoline equivalent liter.

** de—diesel equivalent liter.

FIGURE 1.14

Potential and status of RE technologies. (From UNDP, *World Energy Assessment: Energy and The Challenge of Sustainability*, New York, 2004 [updated from the other sources].)

As in the case of other new technologies, it is expected that RE technology cost competitiveness will be achieved with R&D, scale-up, commercial experience, and mass production. Experience shows industry-wide cost reductions in the range of 10%–20% for each cumulative doubling of production for wind power, PV, ethanol, and gas turbines. Similar declines can be expected in CSP and other renewable technologies. Wind energy technologies have already achieved market maturity, and PV technologies are well on their way. CSP is expected to achieve the cost target of approximately \$0.05/kWh by the time it has an installed capacity of approximately 40 GW (GEF 2005). As a reference point, wind power achieved that capacity milestone in 2003.

1.6 Forecast of Future Energy Mix

On the basis of the information about limited oil, natural gas and nuclear resources, and the serious environmental concerns about coal, it seems logical that the RE technologies of solar, wind, and biomass not only will be essential but also will be able to fill the gap and provide a clean and sustainable energy future. There are many differing views on the future energy mix. However, we agree with the WBGU, which estimates that as much as 50% of the world's primary energy in 2050 will have to come from RE (Figure 1.15). However, achieving that level of RE use by 2050 will require a worldwide commitment and an unprecedented global effort.

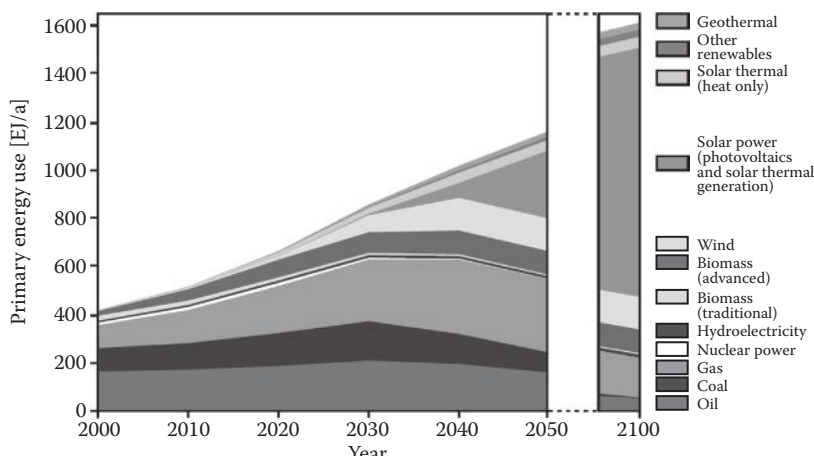


FIGURE 1.15

The global energy mix for year 2050 and 2100 according to WBGU (2003).

PROBLEMS

1. In 2011, RE provided 20.1% of the total electricity capacity of the world. Of the total electricity capacity from RE, solar power accounted for 1.4%, geothermal 1.6%, biomass 9%, and wind power accounted for 10%, the rest 78% being from hydro. On the basis of the IEA data, the annual growth rate of solar power was 50%, whereas that for biomass, wind, geothermal, and hydropower was 12%, 25%, 4%, and 2%, respectively. Assuming these annual growth rates to continue to 2025, find the fractions of each of these renewable energies in electrical power capacity in 2025, if the annual growth rate of total electricity capacity is 2.4% (based on IEA growth scenario).
2. If the total world electrical power capacity grows at a rate of 3% during this period (based on IEA growth scenario), what fraction of the total electricity capacity in 2030 will be from (a) RE and (b) solar energy?
3. Keeping the assumptions from Problem 1, find the fractions of solar, wind, biomass, and hydropower in the world electrical capacity during the present year. Compare your data with the actual available data from some source. Discuss the reasons for the differences.
4. A homeowner paid \$4000 for a solar water heater and received a tax credit of 30%. The system saves \$450 per year. Find a simple payback time. Assuming a discount rate of 5%, find the payback time based on the PW analysis.
5. A solar power company plans to build a 50 MWe solar power plant with the following information. Find the LCOE and IRR for this investment.

Location: Daggett, California (Lat. $34^{\circ} 51.8'$)
Capital costs, including site prep and construction = \$125 M (30% equity, 70% debt at 5%)
Repairs and maintenance = \$150,000/year (plant shutdown 10 days/year for maintenance and repairs)
Yearly electrical output = 300 MWh_e/day
Tariff received = \$0.15/kWh_e for the first year, with 5%/year escalation after that
Life of system = 25 years
6. Calculate the IRR if the power company gets a fixed feed-in tariff of \$0.25/kWh_e for 20 years and the salvage value of the plant after 20 years is \$20 M.

References

- Brown, W.C. 1984. The history of power transmission by radio waves. *IEEE Trans. Microw. Theory Techn.* 32: 1230–1242.
- Daniels, F. 1964. *Direct Use of Sun's Energy*. Yale University Press, New Haven, CT.
- Darwin, C.G. 1953. *The Next Million Years*. Greenwood Press Publishers, Westport, CT. Reprinted in 1973 from original publication in 1953.
- Enerdata. 2013. *Global Energy Statistical Yearbook 2013*. Enerdata Information Services, London, UK. Available at <http://www.enerdata.net>.
- EPIA (European Photovoltaic Industries Association). 2014. *Global Market Outlook for Photovoltaics*. EPIA, Brussels, Belgium. Available at <http://www.epia.org>.
- EPRI (Electric Power Research Institute). 2007. *Primer: Power from Ocean Waves and Tides*. EPRI, Palo Alto, CA. Available at <http://www.snpud.com/site/content/documents/tidal/tidalprimer.pdf>.
- Fulton, L., Hawes, T., and Hardy, J. 2004. *Biofuels for Transport—An International Perspective*. International Energy Agency, Paris, France.
- GEF (Global Environmental Facility). 2005. Assessment of the World Bank/GEF strategy for the market development of concentrating solar thermal power. GEF Report GEF/c.25/inf.11. GEF, Washington, DC.
- Goswami, D.Y. et al. 2004. New and emerging developments in solar energy. *Sol. Energy J.* 76: 1–3, 33–43.
- Green, M.A. et al. 2013. Solar cell efficiency tables. *Prog. Photovolt: Res. Appl.* 21: 1–11.
- IEA (International Energy Agency). 2005. *World Energy Outlook 2005*. International Energy Agency, Paris, France.
- IEA (International Energy Agency). 2010. *World Energy Outlook 2010*. International Energy Agency, Paris, France.
- IEA (International Energy Agency). 2013. *World Energy Outlook 2013*. International Energy Agency, Paris, France.
- Kreith, F., and D.Y. Goswami. 2007. *Handbook of Energy Efficiency and Renewable Energy*, Chapter 1. CRC Press, Boca Raton, FL.
- Offenhartz, P.O.D. 1976. Classical methods of storing thermal energy. In *Sharing the Sun-Solar Technology in the Seventies*, Vol. 8, K.W. Böer, ed. Solar Energy Society of Canada, Winnipeg.
- UNDP (United Nations Development Programme). 2004. *World Energy Assessment: Energy and The Challenge of Sustainability*. UNDP, New York.
- WBGU (German Advisory Council on Global Change). 2003. *World in Transition—Towards Sustainable Energy Systems*. WBGU, Berlin. Available at <http://www.wbgu.de>.
- Worldwatch Institute. 2006. *Biofuels for Transportation—Global Potential and Implications for Sustainable Energy in the 21st Century*. Worldwatch Institute, Washington, DC.
- WWEA (World Wind Energy Association). 2012. Available at <http://www.wwindea.org>.

2

Fundamentals of Solar Radiation

2.1 The Physics of the Sun and Its Energy Transport

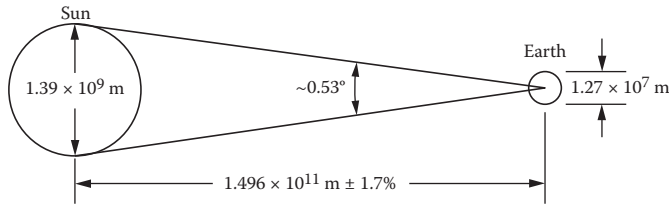
The nature of energy generation in the sun is still an unanswered question. Spectral measurements have confirmed the presence of nearly all the known elements in the sun. However, 80% of the sun is hydrogen and 19% is helium. Therefore, the remaining 100-plus observed elements make up only a tiny fraction of the composition of the sun. It is generally accepted that a hydrogen-to-helium thermonuclear reaction is the source of the sun's energy. Yet, because such a reaction has not been duplicated in the laboratory, it is unclear precisely what the reaction mechanism is, what role the turbulent flows in the sun play, and how solar prominences and sunspots are created.

The nature of the energy-creation process is of no importance to terrestrial users of the sun's radiation. Of interest is the amount of energy, its spectral and temporal distribution, and its variation with time of day and year. These matters are the main subject of this chapter.

The sun is a 13.9×10^5 km diameter sphere composed of many layers of gases, which are progressively hotter toward its center. The outermost layer, that from which energy is radiated into the solar system, is approximately at an equivalent black-body temperature of 5760 K (10,400°R). The center of the sun, however, may be at 20×10^6 K. The rate of energy emission from the sun is 3.8×10^{23} kW, which results from the conversion of 4.3×10^9 g/s of mass to energy. Of this total, only a tiny fraction, approximately 1.7×10^{14} kW, is intercepted by the earth, which is located approximately 150 million km from the sun (Figure 2.1).

Solar energy is the world's most abundant permanent source of energy. The amount of solar energy intercepted by the planet earth is 5000 times greater than the sum of all other inputs (terrestrial nuclear, geothermal and gravitational energies, and lunar gravitational energy). Of this amount, 30% is reflected to space, 47% is converted to low-temperature heat and reradiated to space, and 23% powers the evaporation/precipitation cycle of the biosphere. Less than 0.5% is represented in the kinetic energy of the wind and waves and in photosynthetic storage in plants.

Total terrestrial radiation is only approximately one-third of the extraterrestrial total during a year, and 70% of that falls on the oceans. However,

**FIGURE 2.1**

Relationship between the sun and the earth.

the remaining 1.5×10^{17} kW·h that falls on land is a prodigious amount of energy—approximately 6000 times the total energy usage of the United States in 2009. However, only a small fraction of this total can be used because of physical and socioeconomic constraints as described in Chapter 1.

2.2 Thermal Radiation Fundamentals

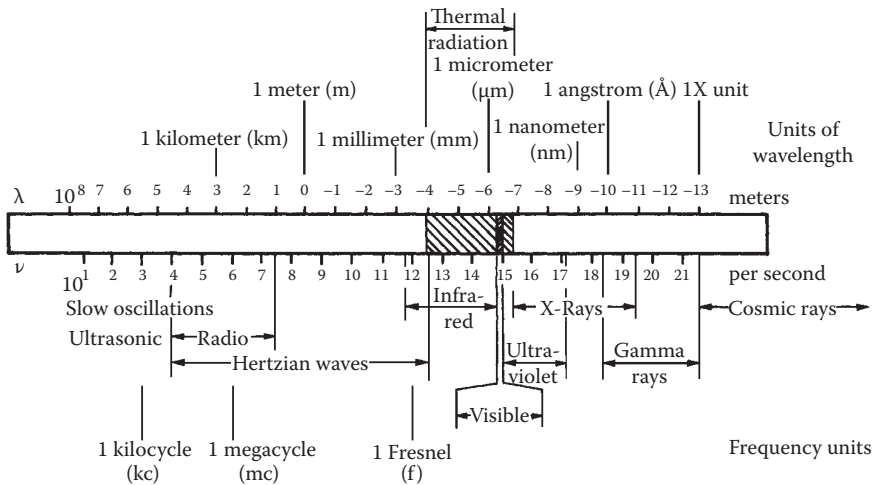
The material presented in this section has been selected from textbooks on heat transfer and radiation (e.g., Howell and Siegel 1992; Iqbal 1983; Kreith and Bohm 1993; Sparrow and Cess 1978). It provides the background needed to understand the nature of solar radiation for the engineering analysis of solar energy systems.

To begin then, all radiation travels at the speed of light, which is equal to the product of the wavelength and the frequency of radiation. The speed of light in a medium equals the speed of light in a vacuum divided by the refractive index of the medium through which it travels:

$$c = \lambda\nu = \frac{c_0}{n}, \quad (2.1)$$

where λ is the wavelength in meters (or micrometers [μm], $1 \mu\text{m} = 10^{-6}$ m), ν is the frequency (in s^{-1}), c is the speed of light in a medium (m/s), c_0 is the speed of light in a vacuum (m/s), and n is the index of refraction of the medium.

Thermal radiation is one kind of electromagnetic energy, and all bodies emit thermal radiation by virtue of their temperature. When a body is heated, its atoms, molecules, or electrons are raised to higher levels of activity called excited states. However, they tend to return to lower-energy states, and in this process, energy is emitted in the form of electromagnetic waves. Changes in energy states result from rearrangements in the electronic, rotational, and vibrational states of atoms and molecules. Since these rearrangements involve different amounts of energy changes and these energy changes are related to the frequency, the radiation emitted by a body is distributed over a range of wavelengths. A portion of the electromagnetic spectrum is shown in Figure 2.2. The wavelengths associated with the various mechanisms are not sharply defined; thermal radiation

**FIGURE 2.2**

Electromagnetic radiation spectrum.

is usually considered to fall within the band from approximately 0.1 to 100 μm , whereas solar radiation has most of its energy between 0.1 and 3 μm .

For some problems in solar energy engineering, the classical electromagnetic wave theory is not suitable. In such cases, for example, in photovoltaic or photochemical processes, it is necessary to treat the energy transport from the point of view of quantum mechanics. In this view, energy is transported by particles or *photons*, which are treated as energy units or quanta rather than waves. The energy of a photon, E_p , of frequency ν_p is

$$E_p = h\nu_p \quad (2.2)$$

where h is Planck's constant ($6.625 \times 10^{-34} \text{ J}\cdot\text{s}$).

2.2.1 Black-Body Radiation

The energy density of the radiation emitted at a given wavelength (monochromatic) by a perfect radiator, usually called a black body, is given according to the relation

$$E_{b\lambda} = \frac{C_1}{(e^{C_2/\lambda T} - 1)\lambda^5 n^2}, \quad (2.3)$$

where

$$C_1 = 3.74 \times 10^8 \text{ W}\cdot\mu\text{m}^4/\text{m}^2 \quad (1.19 \times 10^8 \text{ Btu}\cdot\mu\text{m}^4/\text{h}\cdot\text{ft}^2)$$

$$C_2 = 1.44 \times 10^4 \mu\text{m}\cdot\text{K} \quad (2.59 \times 10^4 \mu\text{m}\cdot^\circ\text{R})$$

n = refractive index of the medium = 1.0 for vacuum; n is taken to be approximately equal to 1 for air

The quantity $E_{b\lambda}$ has the unit $\text{W/m}^2\cdot\mu\text{m}$ ($\text{Btu/h}\cdot\text{ft}^2\cdot\mu\text{m}$) and is called the monochromatic emissive power of a black body, defined as the energy emitted by a perfect radiator per unit wavelength at the specified wavelength per unit area and per unit time at the temperature T .

The total energy emitted by a black body, E_b , can be obtained by integration over all wavelengths. This yields the Stefan–Boltzmann law

$$E_b = \int_0^\infty E_{b\lambda} d\lambda = \sigma T^4, \quad (2.4)$$

where σ is the Stefan–Boltzmann constant $= 5.67 \times 10^{-8} \text{ W/m}^2\cdot\text{K}^4$ ($0.1714 \times 10^{-8} \text{ Btu/h}\cdot\text{ft}^2\cdot\text{R}^4$) and T is the absolute temperature in Kelvin (or $R = 460 + {}^\circ\text{F}$).

The concept of a black body, although no such body actually exists in nature, is very convenient in engineering because its radiation properties can readily be related to those of real bodies.

2.2.2 Radiation Function Tables

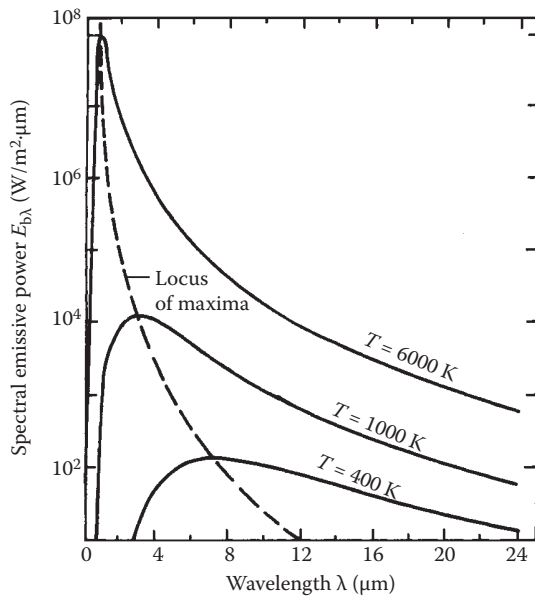
Engineering calculations of radiative transfer are facilitated by the use of radiation function tables, which present the results of Planck's law in a more convenient form than Equation 2.3. A plot of the monochromatic emissive power of a black body as a function of wavelength as the temperature is increased is given in Figure 2.3. The emissive power shows a maximum at a particular wavelength. These peaks, or inflection points, are uniquely related to the body temperature. By differentiating Planck's distribution law (Equation 2.3) and equating to zero, the wavelength corresponding to the maximum value of $E_{b\lambda}$ can be shown to occur when

$$\lambda_{\max}T = 2897.8 \mu\text{m K} \quad (5215.6 \mu\text{m R}). \quad (2.5)$$

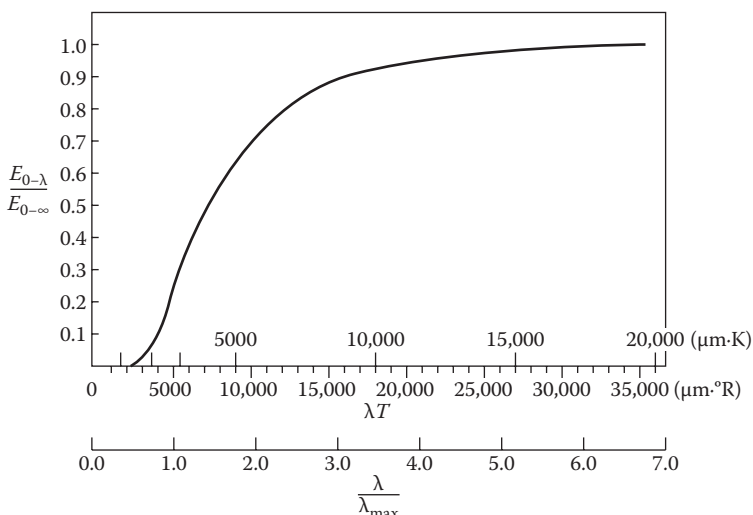
Frequently, one needs to know the amount of energy emitted by a black body within a specified range of wavelengths. This type of calculation can be performed easily with the aid of the radiation functions mentioned previously. To construct the appropriate radiation functions in dimensionless form, note that the ratio of the black-body radiation emitted between 0 and λ and between 0 and ∞ can be made a function of the single variable (λT) by using Equation 2.3 as shown below (for $n = 1$):

$$\frac{E_{b,0-\lambda}}{E_{b,0-\infty}} = \frac{\int_0^\lambda E_{b\lambda} d\lambda}{\int_0^\infty E_{b\lambda} d\lambda} = \frac{\int_0^{\lambda T} \frac{C_1 d(\lambda T)}{\sigma(\lambda T)^5 (e^{C_2/\lambda T} - 1)}}{\int_0^\infty \frac{C_1 d(\lambda T)}{\sigma(\lambda T)^5 (e^{C_2/\lambda T} - 1)}}. \quad (2.6)$$

The above relation is plotted in Figure 2.4 and the results are also shown in tabular form in Figure 2.5. In this table, the first column is the ratio of λ to

**FIGURE 2.3**

Spectral distribution of black-body radiation.

**FIGURE 2.4**

Fraction of total emissive power in spectral region between $\lambda = 0$ and λ as a function of λT and λ/λ_{\max} .

λ/λ_{\max}	$\frac{E_{b\lambda}}{E_{b\lambda,\max}}$	$\frac{E_{b\lambda,0-\lambda}}{\sigma T^4}$	λ/λ_{\max}	$\frac{E_{b\lambda}}{E_{b\lambda,\max}}$	$\frac{E_{b\lambda,0-\lambda}}{\sigma T^4}$	λ/λ_{\max}	$\frac{E_{b\lambda}}{E_{b\lambda,\max}}$	$\frac{E_{b\lambda,0-\lambda}}{\sigma T^4}$
0.00	0.0000	0.0000	1.50	0.7103	0.5403	2.85	0.1607	0.8661
0.20	0.0000	0.0000	1.55	0.6737	0.5630	2.90	0.1528	0.8713
0.25	0.0003	0.0000	1.60	0.6382	0.5846	2.95	0.1454	0.8762
0.30	0.0038	0.0001	1.65	0.6039	0.6050	3.00	0.1384	0.8809
0.35	0.0187	0.0004	1.70	0.5710	0.6243	3.10	0.1255	0.8895
0.40	0.0565	0.0015	1.75	0.5397	0.6426	3.20	0.1141	0.8974
0.45	0.1246	0.0044	1.80	0.5098	0.6598	3.30	0.1038	0.9045
0.50	0.2217	0.0101	1.85	0.4815	0.6761	3.40	0.0947	0.9111
0.55	0.3396	0.0192	1.90	0.4546	0.6915	3.50	0.0865	0.9170
0.60	0.4664	0.0325	1.95	0.4293	0.7060	3.60	0.0792	0.9225
0.65	0.5909	0.0499	2.00	0.4054	0.7197	3.70	0.0726	0.9275
0.70	0.7042	0.0712	2.05	0.3828	0.7327	3.80	0.0667	0.9320
0.75	0.8007	0.0960	2.10	0.3616	0.7449	3.90	0.0613	0.9362
0.80	0.8776	0.1236	2.15	0.3416	0.7565	4.00	0.0565	0.9401
0.85	0.9345	0.1535	2.20	0.3229	0.7674	4.20	0.0482	0.9470
0.90	0.9725	0.1849	2.25	0.3053	0.7777	4.40	0.0413	0.9528
0.95	0.9936	0.2172	2.30	0.2887	0.7875	4.60	0.0356	0.9579
1.00	1.0000	0.2501	2.35	0.2731	0.7967	4.80	0.0308	0.9622
1.05	0.9944	0.2829	2.40	0.2585	0.8054	5.00	0.0268	0.9660
1.10	0.9791	0.3153	2.45	0.2447	0.8137	6.00	0.0142	0.9790
1.15	0.9562	0.3472	2.50	0.2318	0.8215	7.00	0.0082	0.9861
1.20	0.9277	0.3782	2.55	0.2197	0.8290	8.00	0.0050	0.9904
1.25	0.8952	0.4081	2.60	0.2083	0.8360	9.00	0.0033	0.9930
1.30	0.8600	0.4370	2.65	0.1976	0.8427	10.00	0.0022	0.9948
1.35	0.8231	0.4647	2.70	0.1875	0.8490	20.00	0.0002	0.9993
1.40	0.7854	0.4911	2.75	0.1780	0.8550	40.00	0.0000	0.9999
1.45	0.7477	0.5163	2.80	0.1691	0.8607	50.00	0.0000	1.0000

λ = wavelength in micrometer.

λ_{\max} = wavelength at $E_{b\lambda,\max}$ in micrometer = $2898/T$.

$E_{b\lambda}$ = monochromatic emissive power in $\text{W}/\text{m}^2 \cdot \mu\text{m}$

$$= 374.15 \times 10^6 / \lambda^5 [\exp(14,387.9/\lambda T) - 1],$$

$E_{b\lambda,\max}$ = maximum monochromatic emissive power in $\text{W}/\text{m}^2 \cdot \mu\text{m}$

$$= 12.865 \times 10^{-12} T^5,$$

$$E_{b\lambda,0-\lambda} = \int_0^\lambda E_{b\lambda} d\lambda,$$

$$\sigma T^4 = E_{b\lambda,0-\infty} = 5.670 \times 10^{-8} T^4 \text{ W/m}^2, \text{ and}$$

T = absolute temperature in Kelvin.

FIGURE 2.5

Thermal radiation functions.

λ_{\max} from Equation 2.5, and the third column is the ratio of $E_{b,0-\lambda}$ to σT^4 from Equation 2.6. For use on a computer, Equation 2.6 can be approximated by the following polynomials:

$$\text{for } v \geq 2 \quad \frac{E_{b,0-\lambda}}{\sigma T^4} = \frac{15}{\pi^4} \sum_{m=1,2,\dots} \frac{E^{-mv}}{m^4} \left\{ [(mv+3)mv+6]mv+6 \right\}, \quad (2.7a)$$

and

$$v < 2 \quad \frac{E_{b,0-\lambda}}{\sigma T^4} = \frac{15}{1-\pi^4} v^3 \left(\frac{1}{3} - \frac{v}{8} - \frac{v^2}{60} - \frac{v^4}{5040} + \frac{v^6}{272,160} - \frac{v^8}{13,305,600} \right), \quad (2.7b)$$

where $v = C_2/\lambda T$.

2.2.3 Intensity of Radiation and Shape Factor

The emissive power of a surface gives the total radiation emitted in all directions. To determine the radiation emitted in a given direction, we must define another quantity, the radiation intensity I . This quantity is defined as the radiant energy passing through an imaginary plane in space per unit area per unit time and per unit solid angle perpendicular to the plane as shown in Figure 2.6. I is defined by the relation

$$I = \lim_{\begin{subarray}{l} dA \rightarrow \infty \\ d\omega \rightarrow \infty \end{subarray}} \frac{dE}{dA \, d\omega} \quad (2.8)$$

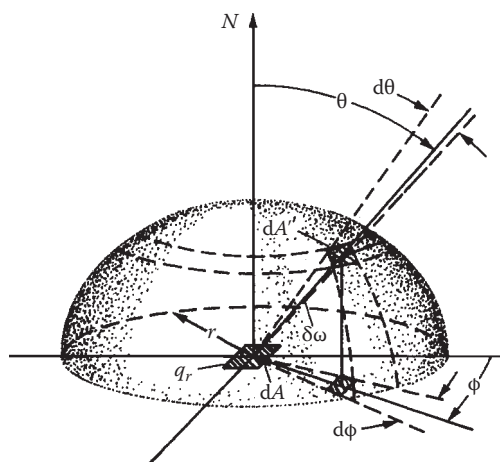


FIGURE 2.6

Schematic diagram illustrating radiation intensity and flux.

Radiation intensity has both magnitude and direction. It can be related to the radiation flux, defined as the radiant energy passing through an imaginary plane per unit area per unit time in all directions. Note that, whereas for the intensity, the area dA' is perpendicular to the direction of the radiation; for the flux, the area dA is at the base in the center of a hemisphere through which all of the radiation passes. Recalling that the definition for the solid angle between dA' and dA is $d\omega = dA/r^2$, the radiation flux q_r emanating from dA can be obtained by integrating the intensity over the hemisphere. As shown in Figure 2.6, the unit projected area for I is $dA \cos \theta$ and the differential area dA' on the hemisphere is $r^2 \sin \theta d\theta d\phi$; thus,

$$q_r = \int_0^{2\pi} \int_{\pi/2}^0 I \cos \theta \sin \theta d\theta d\phi. \quad (2.9)$$

If the area dA is located on a surface, the emissive power E can also be obtained from Equation 2.9. For the special case of a diffuse surface, for which I is the same in all directions, Equation 2.9 gives

$$q_r = \pi I. \quad (2.10)$$

Since all black surfaces are diffuse,

$$E_b = \pi I_b. \quad (2.11)$$

Equation 2.11 can, of course, also be written for monochromatic radiation as

$$E_{b\lambda} = \pi I_{b\lambda}. \quad (2.12)$$

In the evaluation of the rate of radiation heat transfer between two surfaces, not only their temperatures and their radiation properties but also their geometric configurations and relationships play a part. The influence of geometry in radiation heat transfer can be expressed in terms of the *radiation shape factor* between any two surfaces 1 and 2 defined as follows:

F_{1-2} is the fraction of radiation leaving surface 1 that reaches surface 2.

F_{2-1} is the fraction of radiation leaving surface 2 that reaches surface 1.

In general, F_{m-n} is the fraction of radiation leaving surface m that reaches surface n . If both surfaces are black, the energy leaving surface m and arriving at surface n is $E_{bm} A_m F_{m-n}$ and the energy leaving surface n and arriving at m is $E_{bn} A_n F_{n-m}$. If both surfaces absorb all the incident energy, the net rate of exchange $q_{m \leftrightarrow n}$ will be

$$q_{m \leftrightarrow n} = E_{bm} A_m F_{m-n} - E_{bn} A_n F_{n-m}. \quad (2.13)$$

If both surfaces are at the same temperature, $E_{bm} = E_{bn}$ and the net exchange is zero, $q_{m \leftrightarrow n} = 0$. This shows that the geometric radiation shape factor must obey the reciprocity relation

$$A_m F_{m-n} = A_n F_{n-m}. \quad (2.14)$$

The net rate of heat transfer can therefore be written in two equivalent forms:

$$q_{m \leftrightarrow n} = A_m F_{m-n}(E_{bm} - E_{bn}) = A_n F_{n-m}(E_{bm} - E_{bn}). \quad (2.15)$$

The evaluation of geometric shape factors is in general quite involved. For a majority of solar energy applications, however, only a few special cases are of interest. One of these is a small convex object of area A_1 surrounded by a large enclosure A_2 . Since all radiation leaving A_1 is intercepted by A_2 , $F_{1-2} = 1$ and $F_{2-1} = A_1/A_2$.

Another case is the exchange of radiation between two large parallel surfaces. If the two surfaces are near each other, almost all of the radiation leaving A_1 reaches A_2 and vice versa. Thus, $F_{1-2} = F_{2-1} = 1.0$, according to the definition of the shape factor. A third case of importance is the exchange between a small surface ΔA_1 and a portion of space A_2 , for example, the exchange between a flat-plate solar collector tilted at an angle β from the horizontal and the sky it can see. For this situation, we refer to the definition of radiation flux (see Figure 2.6). The portion of the radiation emitted by ΔA_1 that is intercepted by the surrounding hemisphere depends on the angle of tilt. When the surface is horizontal, $F_{1-2} = 1$; when it is vertical, $F_{1-2} = 1/2(\beta = 90^\circ)$. For intermediate values, it can be shown that (Sparrow and Cess 1978)

$$F_{1-2} = \frac{1}{2}(1 + \cos\beta) = \cos^2 \frac{\beta}{2}. \quad (2.16)$$

If the diffuse sky radiation is uniformly distributed and assumed to be black, then a small black area A_1 receives radiation at the rate

$$A_1 F_{1-sky} E_{sky} = \frac{A_1}{2}(1 + \cos\beta)\sigma T_{sky}^4 \quad (2.17)$$

whereas the net radiation heat transfer is given by

$$q_{sky-1} = A_1 F_{1-sky} \sigma (T_{sky}^4 - T_1^4). \quad (2.18)$$

If the receiving area is gray with an absorptance $\bar{\alpha}$ equal to the emittance $\bar{\epsilon}$, the net exchange is given by

$$q_{\text{sky} - 1} = A_1 F_{1-\text{sky}} \bar{\alpha} \sigma (T_{\text{sky}}^4 - T_1^4). \quad (2.19)$$

2.2.4 Transmission of Radiation through a Medium

When radiation passes through a semitransparent medium such as glass or the atmosphere, the decrease in intensity can be described by Bouger's law that assumes that the attenuation is proportional to the local intensity in the medium. If $I_\lambda(x)$ is monochromatic intensity after radiation has traveled a distance x , the law is expressed by the equation

$$-dI_\lambda(x) = I_\lambda(x) K_\lambda dx, \quad (2.20)$$

where K_λ is the monochromatic extinction coefficient assumed to be a constant of the medium. If the transparent medium is a slab of thickness L and the intensity at $x = 0$ is designated by the symbol $I_{\lambda,0}$, the monochromatic transmittance τ_λ is equal to the ratio of the intensity at $x = L$ to $I_{\lambda,0}$. An expression for $I_\lambda(L)$ can be obtained by integrating Equation 2.20 between 0 and L , which gives

$$\ln \frac{I_\lambda(L)}{I_{\lambda,0}} = -K_\lambda L \quad \text{or} \quad I_\lambda(L) = I_{\lambda,0} e^{-K_\lambda L}. \quad (2.21)$$

Then,

$$\tau_\lambda = \frac{I_\lambda(L)}{I_{\lambda,0}} = e^{-K_\lambda L}. \quad (2.22)$$

The extinction coefficient K_λ is a complex property of the medium since it combines the effects of absorption, emission, and scattering by the molecules and particles that make up the medium. Fortunately, for materials such as glass and plastics with known compositions, this coefficient can be determined accurately. Transmission of radiation through such materials will be discussed further in Chapter 3. In the present chapter, we are concerned about the transmission of solar radiation through the atmosphere. The atmosphere consists of the molecules of gases in it, such as N_2 , O_2 , CO_2 , H_2O , and so on, and aerosols such as dust particles, water droplets, and ice crystals. The extinction processes of the atmosphere consist of (a) absorption and emission by the molecules and aerosols, (b) scattering by the molecules, and (c) scattering by aerosols.

Since the atmosphere consists of a large number of components whose concentration changes as a function of time and location, determining the extinction coefficient of the atmosphere presents a formidable challenge. A major research effort is underway by scientists trying to predict global climate change. Some early attempts for the estimation of extinction coefficient for "average atmospheric conditions" were combined with an empirical approach to use the above equation for the estimation of terrestrial solar radiation resource. This approach is described later in this chapter.

2.3 Sun–Earth Geometric Relationship

Figure 2.7 shows the annual orbit of the earth around the sun. The distance between the earth and the sun changes throughout the year, the minimum

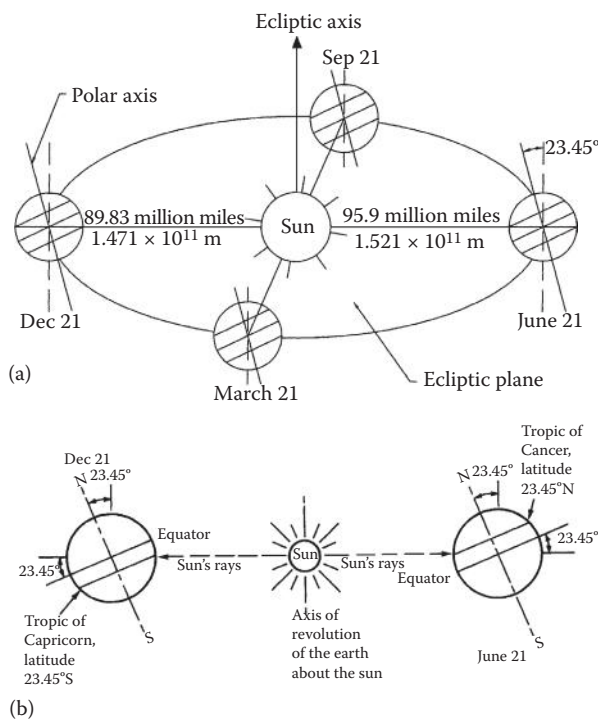


FIGURE 2.7

(a) Motion of the earth about the sun. (b) Location of tropics. Note that the sun is so far from the earth that all the rays of the sun may be considered as parallel to one another when they reach the earth.

being 1.471×10^{11} m at winter solstice (December 21) and the maximum being 1.521×10^{11} m at summer solstice (June 21). The year-round average earth–sun distance is 1.496×10^{11} m. The amount of solar radiation intercepted by the earth, therefore, varies throughout the year, the maximum being on December 21 and the minimum on June 21.

The axis of the earth's daily rotation around itself is at an angle of 23.45° to the axis of its ecliptic orbital plane around the sun. This tilt is the major cause of the seasonal variation of the solar radiation available at any location on the earth. The angle between the earth–sun line (through their centers) and the plane through the equator is called the *solar declination*, δ_s . The declination varies between -23.45° on December 21 to $+23.45^\circ$ on June 21. Stated another way, the declination has the same numerical value as the latitude at which the sun is directly overhead at solar noon on a given day. The tropics of Cancer (23.45°N) and Capricorn (23.45°S) are at the extreme latitudes where the sun is overhead at least once a year as shown in Figure 2.7. The Arctic and Antarctic circles are defined as those latitudes above which the sun does not rise above the horizon plane at least once per year. They are located, respectively, at $66\frac{1}{2}^\circ\text{N}$ and $66\frac{1}{2}^\circ\text{S}$. Declinations north of the equator (summer in the Northern Hemisphere) are designated as positive; those south, negative. The solar declination may be estimated by the relation*

$$\delta_s = 23.45^\circ \sin[360(284 + n)/365^\circ], \quad (2.23)$$

where n is the day number during a year with January 1 being $n = 1$. Approximate values of declination may also be obtained from Figure 2.8 or Figure 2.9. For most calculations, the declination may be considered constant during any given day.

For the purposes of this book, the Ptolemaic view of the sun's motion provides a simplification to the analysis that follows. It is convenient to assume the earth to be fixed and to describe the sun's apparent motion in a coordinate system fixed to the earth with its origin at the site of interest. Figure 2.10 shows an apparent path of the sun to an observer. The position of the sun can be described at any time by two angles, the altitude and azimuth angles, as shown in Figure 2.10. The *solar altitude angle*, α , is the angle between a line collinear with the sun's rays and the horizontal plane. The *solar azimuth angle*, a_s , is the angle between a due south line and the projection of the site to sun line on the horizontal plane. The sign convention used for the azimuth angle is positive west of south and negative east of south. The *solar zenith angle*, z , is the angle between the site to sun line and the vertical at the site:

$$z = 90^\circ - \alpha. \quad (2.24)$$

* A more accurate relation is $\sin \delta_s = \sin(23.45^\circ) \sin[360(284 + n)/365]^\circ$. Because the error is small, Equation 2.23 is generally used.

Date	Declination		Equation of time		Date	Declination		Equation of time	
	Deg	Min	Min	Sec		Deg	Min	Min	Sec
Jan	1	-23	4	-3	14	Feb	1	-17	19
	5	-22	42	-5	6		5	-16	10
	9	-22	13	-6	50		9	-14	55
	13	-21	37	-8	27		13	-13	37
	17	-20	54	-9	54		17	-12	15
	21	-20	5	-11	10		21	-10	50
	25	-19	9	-12	14		25	-9	23
	29	-18	9	-13	5				
Mar	1	-7	53	-12	38	Apr	1	+4	14
	5	-6	21	-11	48		5	5	46
	9	-5	48	-10	51		9	7	17
	13	-3	14	-9	49		13	8	46
	17	-1	39	-8	42		17	10	12
	21	-0	5	-7	32		21	11	35
	25	+1	30	-6	20		25	12	56
	29	3	4	-5	7		29	14	13
May	1	+14	50	+2	50	Jun	1	+21	57
	5	16	2	3	17		5	22	28
	9	17	9	3	35		9	22	52
	13	18	11	3	44		13	23	10
	17	19	9	3	44		17	23	22
	21	20	2	3	24		21	23	27
	25	20	49	3	16		25	23	25
	29	21	30	2	51		29	23	17
Jul	1	+23	10	-3	31	Aug	1	+18	14
	5	22	52	-4	16		5	17	12
	9	22	28	-4	56		9	16	6
	13	21	57	-5	30		13	14	55
	17	21	21	-5	57		17	13	41
	21	20	38	-6	15		21	12	23
	25	19	50	-6	24		25	11	2
	29	18	57	-6	23		29	9	39
Sep	1	+8	35	-0	15	Oct	1	-2	53
	5	7	7	+1	2		5	-4	26
	9	5	37	2	22		9	-5	58
	13	4	6	3	45		13	-7	29
	17	2	34	5	10		17	-8	58
	21	1	1	6	35		21	-10	25
	25	0	32	8	0		25	-11	50
	29	-2	6	9	22		29	-13	12

FIGURE 2.8

Summary of solar ephemeris. Since each year is 365.25 days long, the precise value of declination varies from year to year. *The American Ephemeris and Nautical Almanac*, published each year by the US Government Printing Office, contains precise values for each day of each year.

(Continued)

Date	Declination		Equation of time			Date	Declination		Equation of time		
	Deg	Min	Min	Sec			Deg	Min	Min	Sec	
Nov	1	-14	11	+16	21	Dec	1	-21	41	11	16
	5	-15	27	16	23		5	-22	16	9	43
	9	-16	38	16	12		9	-22	45	8	1
	13	-17	45	15	47		13	-23	6	6	12
	17	-18	48	15	10		17	-23	20	4	47
	21	-19	45	14	18		21	-23	26	2	19
	25	-20	36	13	15		25	-23	25	+0	20
	29	-21	21	11	59		29	-23	17	-1	39

FIGURE 2.8 (CONTINUED)

Summary of solar ephemeris. Since each year is 365.25 days long, the precise value of declination varies from year to year. *The American Ephemeris and Nautical Almanac*, published each year by the US Government Printing Office, contains precise values for each day of each year.

The solar altitude and azimuth angles are not fundamental angles. Hence, they must be related to the fundamental angular quantities *hour angle*, *latitude*, and *declination*. The three angles are shown in Figure 2.11. The solar hour angle h_s is based on the nominal time of 24 h required for the sun to move 360° around the earth or 15° per hour. Therefore, h_s is defined as

$$h_s = (15^\circ/h) \cdot (\text{hours from local solar noon}) = \frac{\text{minutes from local solar noon}}{4 \text{ min/degree}}. \quad (2.25)$$

Again, values east of due south, that is, morning values, are negative; and values west of due south are positive.

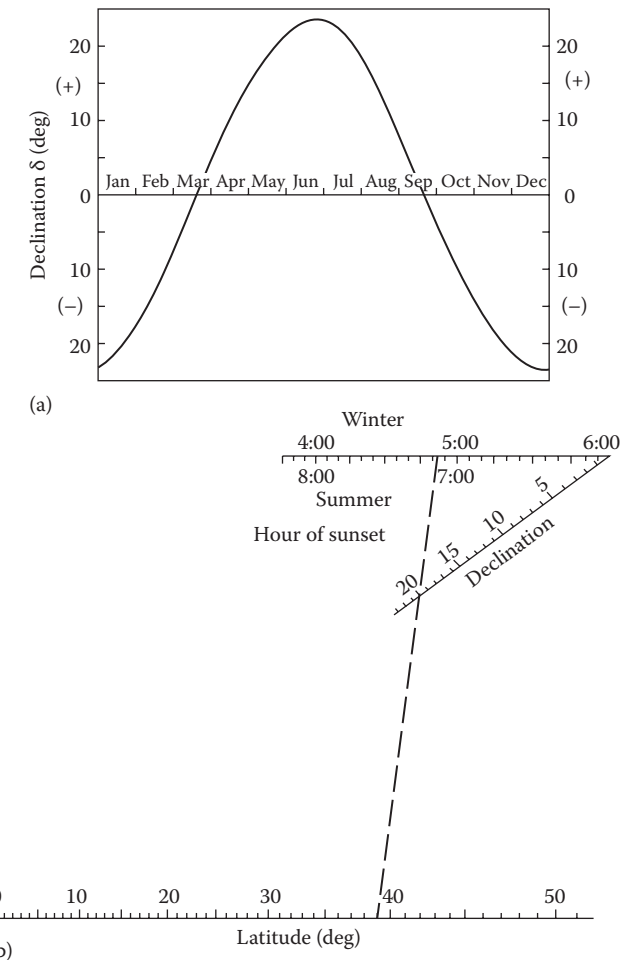
The latitude angle L is the angle between the line from the center of the earth to the site and the equatorial plane. The latitude may be read from an atlas and is considered positive north of the equator and negative south of the equator.

2.3.1 Solar Time and Angles

The sun angles are obtained from the local solar time, which differs from the local standard time (LST). The relationship between the local solar time and the LST is

$$\text{Solar time} = \text{LST} + ET + (l_{st} - l_{local}) \cdot 4 \text{ min/degree}. \quad (2.26)$$

ET is the equation of time, which is a correction factor that accounts for the irregularity of the speed of earth's motion around the sun; l_{st} is the standard

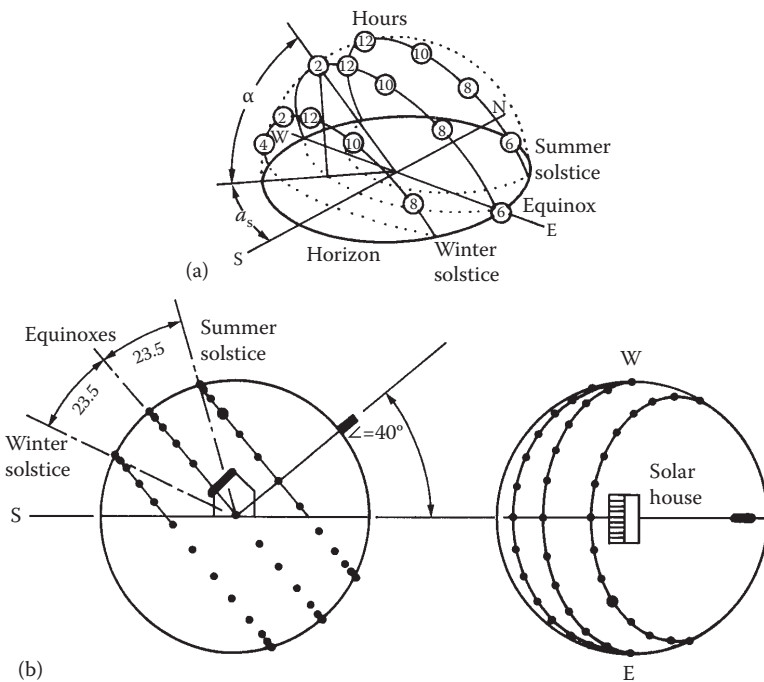
**FIGURE 2.9**

(a) Graph to determine the solar declination. (b) Sunset nomograph example. Example b shows determination of sunset time for summer (7:08 p.m.) and winter (4:52 p.m.) when the latitude is 39°N and the solar declination angle is 20°. (From Whillier, A., *Sol Energy* 9, 165–166, 1965.)

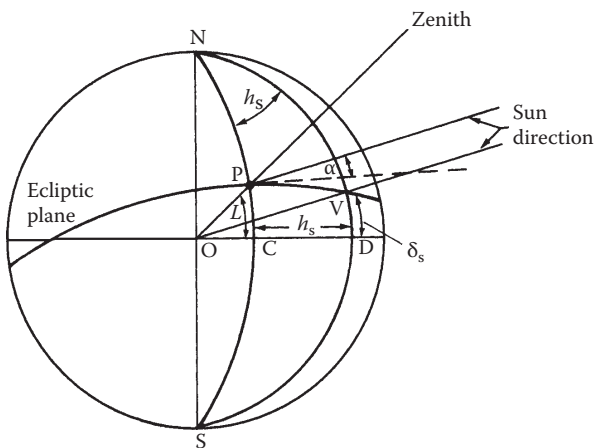
time meridian, and l_{local} is the local longitude. ET may be estimated from Figure 2.8 or calculated from the following empirical equation:

$$\text{ET (in minutes)} = 9.87 \sin 2B - 7.53 \cos B - 1.5 \sin B \quad (2.27)$$

where $B = 360(n - 81)/364$ degrees.

**FIGURE 2.10**

Sun paths for the summer solstice (6/21), the equinoxes (3/21 and 9/21), and the winter solstice (12/21) for a site at 40°N: (a) isometric view; (b) elevation and plan views.

**FIGURE 2.11**

Definition of solar hour angle h_s (CND), solar declination δ_s (VOD), and latitude L (POC); P, site of interest. (Modified from Kreider, J.F. and F. Kreith, *Solar Heating and Cooling*, Washington, DC: Hemisphere Publ. Corp., 1982.)

The solar altitude angle, α , can be found from the application of the law of cosines to the geometry of Figure 2.11 and simplification as

$$\sin \alpha = \sin L \sin \delta_s + \cos L \cos \delta_s \cos h_s. \quad (2.28)$$

Using a similar technique, the solar azimuth angle, a_s , can be found as

$$\sin a_s = \cos \delta_s \sin h_s / \cos \alpha. \quad (2.29)$$

At local solar noon, $h_s = 0$; therefore, $\alpha = 90 - |L - \delta_s|$, and $a_s = 0$.

In calculating the solar azimuth angle from Equation 2.29, a problem occurs whenever the absolute value of a_s is greater than 90° . A computational device usually calculates the angle as less than 90° since $\sin a_s = \sin(180 - a_s)$. The problem can be solved in the following way:

For $L > \delta_s$, the solar times when the sun is due east (t_E) or due west (t_W) can be calculated by t_E or $t_W = 12:00$ noon $\mp (\cos^{-1}[\tan \delta_s / \tan L])/(15^\circ/h)$ ($-$ for t_E , $+$ for t_W).

For solar times earlier than t_E or later than t_W , the sun would be north (south in the Southern Hemisphere) of the east–west line and the absolute value of a_s would be greater than 90° , which may be calculated as $a_s = +$ or $- (180^\circ - |a_s|)$.

For $|L| \leq |\delta_s|$, the sun remains north (south in the Southern Hemisphere) of the east–west line and the true value of a_s is greater than 90° .

Sunrise and *sunset* times can be estimated by finding the hour angle for $\alpha = 0$. Substituting $\alpha = 0$ in Equation 2.28 gives the hour angles for sunrise (h_{sr}) and sunset (h_{ss}) as

$$h_{ss} \text{ or } h_{sr} = \pm \cos^{-1}[-\tan L \cdot \tan \delta_s]. \quad (2.30)$$

It should be emphasized that Equation 2.30 is based on the center of the sun being at the horizon. In practice, sunrise and sunset are defined as the times when the upper limb of the sun is on the horizon. Because the radius of the sun is $16'$, the sunrise would occur when $\alpha = -16'$. Also, at lower solar elevations, the sun will appear on the horizon when it is actually $34'$ below the horizon. Therefore, for apparent sunrise or sunset, $\alpha = -50'$.

Example 2.1a

Find the solar altitude and azimuth angles at solar noon in Gainesville, Florida, on February 1. Also find the sunrise and sunset times in Gainesville on that day.

Solution

For Gainesville,

Latitude $L = 29^\circ + 41' N$ or $29.68^\circ N$.

Longitude $l_{\text{local}} = 82^\circ + 16' W$ or $82.27^\circ W$.

On February 1, day number

$$n = 32.$$

Therefore, declination

$$\begin{aligned}\delta_s &= 23.45 \sin[360(284 + 32)/365]^\circ \\ &= -17.5^\circ\end{aligned}$$

At solar noon, $h_s = 0$. Therefore,

$$\begin{aligned}\sin \alpha &= \cos L \cos \delta_s \cos h_s + \sin L \sin \delta_s \\ &= \cos(29.68^\circ) \cos(-17.5^\circ) \cos(0) + \sin(29.68^\circ) \sin(-17.5^\circ),\end{aligned}$$

or

$$\alpha = 42.82^\circ$$

$$\sin a_s = \cos(-17.5^\circ) \sin(0) / \cos(42.8^\circ) = 0,$$

or

$$a_s = 0.$$

At solar noon, α can also be found as

$$\begin{aligned}\alpha &= 90 - |L - \delta_s|^\circ \\ &= 90 - |29.68 + 17.5|^\circ = 42.82^\circ \\ h_{ss} \text{ or } h_{sr} &= \pm \cos^{-1}[-\tan L \cdot \tan \delta_s] \\ &= \pm \cos^{-1}[-\tan(29.68^\circ) \tan(-17.5^\circ)] \\ &= \pm 79.65^\circ.\end{aligned}$$

$$\text{Time from solar noon} = \pm(79.65^\circ)(4 \text{ min/degree})$$

$$= \pm 319 \text{ min or } \pm (5 \text{ hr } 19 \text{ min}).$$

$$\text{Sunrise time} = 12:00 \text{ Noon} - (5 \text{ hr } 19 \text{ min})$$

$$= 6 \text{ hr } 41 \text{ min a.m. (solar time).}$$

$$\text{Sunset time} = 12:00 \text{ Noon} + (5 \text{ hr } 19 \text{ min})$$

$$= 5 \text{ hr } 19 \text{ min p.m. (solar time).}$$

To convert these times to local times, we need to find ET:

$$ET = (9.87 \sin 2B - 7.53 \cos B - 1.5 \sin B) \text{ min.}$$

$$\begin{aligned} B &= \frac{360}{364}(n - 81) = \frac{360}{364}(32 - 81) \\ &= -48.46^\circ. \end{aligned}$$

Therefore,

$$ET = -13.67 \text{ min.}$$

$$LST = \text{Solar time} - ET - 4(l_{st} - l_{local}).$$

Gainesville, Florida, is in the Eastern Standard Time (EST) zone, where $l_{st} = 75^\circ\text{W}$. Therefore,

$$\begin{aligned} LST &= \text{Solar time} - (-13.67 \text{ min}) - 4(75 - 82.27) \text{ min} \\ &= \text{Solar time} + 42.75 \text{ min}. \end{aligned}$$

Therefore,

$$\begin{aligned} \text{Sunrise time} &= 6:41 \text{ a.m.} + 43 \text{ min} \\ &= 7:24 \text{ a.m. EST}, \end{aligned}$$

and

$$\begin{aligned} \text{Sunset time} &= 5:19 \text{ p.m.} + 43 \text{ min} \\ &= 6:02 \text{ p.m. EST}. \end{aligned}$$

Note: Since the sunrise and sunset times are calculated when the center of the sun is at the horizon, they differ from the apparent times. If we use $\alpha = -50'$, the apparent sunrise and sunset times would be 7:20 a.m. EST and 6:06 p.m. EST, respectively.

Example 2.1b

Repeat the calculations of Example 2.1a for Canberra, Australia.

Latitude $L = 35^\circ - 18\text{ S}$ or 35.3°S .

Longitude $l_{local} = 149^\circ - 11\text{ E}$ or 149.18°E .

Standard Meridian = 150°E .

Solution

Using the values of δ_s and ET calculated in Example 2.1a, and taking the latitude and longitude as -35.3° and -149.18° , respectively, the solar angles α and a_s are found as

$$\sin \alpha = \cos(-35.3^\circ) \cos(-17.5^\circ) \cos(0) + \sin(-35.3^\circ) \sin(-17.5^\circ)$$

or

$$\alpha = 72.2^\circ.$$

$$\sin a_s = \cos(-17.5^\circ) \sin(0) / \cos(72.2^\circ)$$

or

$$a_s = 0^\circ,$$

α may also be found as

$$\begin{aligned} \alpha &= 90^\circ - |-35.3^\circ + 17.5^\circ| \\ &= 72.2^\circ. \end{aligned}$$

The hour angles for sunrise and sunset are found as

$$\begin{aligned} h_{ss}, h_{sr} &= \pm \cos^{-1}[-\tan(-35.3^\circ) \cdot \tan(-17.5^\circ)] \\ &= \pm 102.9^\circ. \end{aligned}$$

$$\begin{aligned} \text{Time from solar noon} &= \pm(102.9^\circ) \cdot (4 \text{ min/degree}) \\ &= \pm 412 \text{ min or } \pm (6 \text{ h } 52 \text{ min}). \end{aligned}$$

Sunrise time = 5:08 a.m. (solar time), and

Sunset time = 6:52 p.m. (solar time).

Take l_{st} for Canberra as -150° .
Therefore,

$$\begin{aligned} \text{LST} &= \text{Solar time} - (-13.67 \text{ min}) - 4(-150^\circ + 149.18^\circ) \text{ min} \\ &= \text{Solar time} + 17 \text{ min}. \end{aligned}$$

Therefore,

Sunrise time = 5:25 a.m. (LST)

Sunset time = 7:09 p.m. (LST)

(As explained in the previous example, the apparent sunrise and sunset times would be 5:21 a.m. and 7:13 p.m., respectively.)

Example 2.2

Find the solar altitude and azimuth angles in Tocumen (Panamá) on (a) June 1 at 7 a.m. and (b) December 1 at 2 p.m. Also find the sunrise and sunset times on these days.

Solution

For Tocumen (Panamá):

$$L = 9.05^\circ \text{ N} (+), l_{\text{local}} = 79.37^\circ \text{ W} (+), \text{ and } l_{\text{st}} = 75^\circ \text{ W} (+)$$

a. For June 1, $n = 152$.

The declination angles for this day are

$$\delta_s = 23.45^\circ \sin \frac{360}{365} (284 + 152)$$

$$\delta_s = 22.04^\circ.$$

The local time is 7:00 a.m. The solar time is given by

$$ST = LST + ET + (l_{\text{st}} - l_{\text{local}}) \cdot 4 \frac{\text{min}}{1^\circ}$$

The equation of time is

$$B = \frac{360}{364} (152 - 81) = 70.22^\circ$$

$$\begin{aligned} ET(\text{min}) &= 9.87 \sin(2 \cdot 70.22^\circ) - 7.53 \cos(70.22^\circ) - 1.5 \sin(70.22^\circ) \\ &= 2.32 \text{ min}. \end{aligned}$$

Then, the solar time is

$$\begin{aligned} ST &= 7:00 + 2.32 \text{ min} + (75^\circ - 79.37^\circ) \cdot 4 \text{ min} \\ &= 7:00 - 15.16 \text{ min} \\ &= 6:44.84 \text{ a.m.} \end{aligned}$$

The hour angle is

$$\begin{aligned} h_s &= (ST - 12) \frac{15^\circ}{h} = (6.7474 - 12) \frac{15^\circ}{h} \\ &= -78.78^\circ. \end{aligned}$$

The solar altitude angle is

$$\sin \alpha = \cos \delta_s \cos L \cos h_s + \sin \delta_s \sin L$$

$$\sin \alpha = \cos(22.04^\circ) \cos(9.05^\circ) \cos(-78.78^\circ) + \sin(22.04^\circ) \sin(9.05^\circ)$$

and

$$\alpha = 13.71^\circ.$$

The solar azimuth angles are defined by

$$\begin{aligned} \sin a_s &= \cos \delta_s \sin h_s / \cos \alpha \\ &= \cos(22.04^\circ) \sin(-78.78^\circ) / \cos(13.71^\circ) \end{aligned}$$

and

$$a_s = -69.37^\circ.$$

We need to find out if $|a_s|$ is greater than 90° . For $|L| \leq |\delta_s|$, sun is north, and $|a_s| > 90^\circ$. Therefore, the real value of a_s is

$$a_s = -180^\circ + |a_s| = -110.62^\circ.$$

The sunrise and sunset are obtained from:

$$\begin{aligned} h_{ss} \text{ or } h_{sr} &= \pm \cos^{-1}[-\tan L \tan \delta_s] \\ &= \pm 93.697^\circ \\ &= 6.247 \text{ h} \end{aligned}$$

$$h_{sr} = 12:00 - 6.247 = 5.753 \text{ a.m. (solar time)}$$

$$h_{ss} = 12:00 + 6.247 = 18.247 \text{ p.m. (solar time)}$$

$$\text{LST} = \text{ST} - \text{ET} - (L_{st} - L_{local}) \cdot 4 \frac{\text{min}}{1^\circ}$$

Then,

$$\begin{aligned} h_{sr} &= 5.753 - (-15.16) \text{ min} \\ &= 6:00:20 \text{ a.m. (local time)} \end{aligned}$$

$$\begin{aligned} h_{ss} &= 18.247 - (-15.16) \text{ min} \\ &= 18:30 \text{ p.m. (local time).} \end{aligned}$$

(As explained in the previous example, the apparent sunrise and sunset times would be 5:56 a.m. and 6:34 p.m., respectively.)

- b. For December 1, $n = 335$.

The declination angles for this day are

$$\delta_s = 23.45^\circ \sin \frac{360}{365} (284 + 335)$$

$$\delta_s = -22.10^\circ.$$

The local time is 2:00 p.m. (or 14:00 p.m.). The solar time is given by

$$ST = LST + ET + (l_{st} - l_{local}) \cdot 4 \frac{\text{min}}{1^\circ}.$$

The equation of time is

$$B = \frac{360}{364} (335 - 81) = 251.21^\circ$$

$$\begin{aligned} ET(\text{min}) &= 9.87 \sin(2 \cdot 251.21^\circ) - 7.5 \cos(251.21^\circ) - 1.5 \sin(251.21^\circ) \\ &= 9.9 \text{ min.} \end{aligned}$$

Then, the solar time is

$$\begin{aligned} ST &= 14:00 + 9.9 \text{ min} + (75^\circ - 79.37^\circ) \cdot 4 \text{ min} \\ &= 14:00 - 7.58 \text{ min} \\ &= 13:52:25 \text{ pm} \end{aligned}$$

The hour angle is

$$\begin{aligned} h_s &= (ST - 12) \frac{15^\circ}{\text{h}} = (13.873 - 12) \frac{15^\circ}{\text{h}} \\ &= 28.09^\circ. \end{aligned}$$

The solar altitude angle is

$$\begin{aligned}\sin \alpha &= \cos \delta_s \cos L \cos h_s + \sin \delta_s \sin L \\ &= \cos(-22.10^\circ) \cos(9.05^\circ) \cos(28.09^\circ) + \sin(-22.10^\circ) \sin(9.05^\circ)\end{aligned}$$

and

$$\alpha = 49.29^\circ.$$

The solar azimuth angles are defined by

$$\begin{aligned}\sin a_s &= \cos \delta_s \sin h_s / \cos \alpha \\ &= \cos(-22.10^\circ) \sin(28.09^\circ) / \cos(49.29^\circ)\end{aligned}$$

and

$$a_s = 41.99^\circ.$$

We need to find out if $|a_s|$ is greater than 90° . For $L \leq \delta_s$:

$$t_E, t_W = 12:00 \pm \cos^{-1} \frac{\tan \delta_s}{\tan L} \frac{h}{15^\circ}.$$

For this problem, $|\tan \delta_s| > |\tan L|$, which means that there is no solution for t_E or t_W . Therefore, the sun remains south and the value of a_s is the same:

$$a_s = 41.99^\circ.$$

The sunrise and sunset are obtained from

$$\begin{aligned}h_{ss} \text{ or } h_{sr} &= \pm \cos^{-1} [\tan L \tan \delta_s] \\ &= \pm 86.29^\circ \\ &= \pm 5.753 \text{ h}\end{aligned}$$

$$h_{sr} = 12:00 - 5.753 = 6.247 \text{ a.m. (solar time)}$$

$$h_{ss} = 12:00 + 5.753 = 17.753 \text{ p.m. (solar time)}$$

$$\text{LST} = \text{ST} - \text{ET} - (l_{st} - l_{local}) \cdot 4 \frac{\text{min}}{1^\circ}.$$

Then,

$$\begin{aligned} h_{sr} &= 6.247 - (-7.58) \text{ min} \\ &= 6:22:24 \text{ a.m. (local time)} \end{aligned}$$

$$\begin{aligned} h_{ss} &= 17.753 - (-7.58) \text{ min} \\ &= 17:52:46 \text{ p.m. (local time).} \end{aligned}$$

(As explained in the previous example, the apparent sunrise and sunset times would be 6:18 a.m. and 5:57 p.m., respectively.)

Knowledge of the solar angles is helpful in the design of passive solar buildings, especially the placement of windows for solar access and the roof overhang for shading the walls and windows at certain times of the year. The following example illustrates this point.

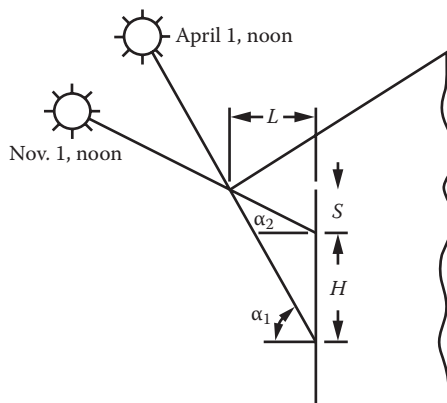
Example 2.3a

Find the roof overhang L of a south-facing window of height $H = 1 \text{ m}$, such that the window is completely shaded at solar noon on April 1 and not shaded at all at noon on November 1. Assume that the roof extends far beyond the window on either side. Location: Gainesville, Florida. Also, find the overhang if $S = 1.3 \text{ m}$.

Solution

From the geometry of the figure,

$$L = S / \tan \alpha_2.$$



Also,

$$L = (S + H)/\tan \alpha_1.$$

On April 1,

$$n = 91.$$

$$\delta_s = 23.45^\circ \sin[360(284 + 91)/365] = 4.02^\circ$$

Therefore, at solar noon,

$$\alpha_1 = 90 - |29.68 - 4.02| = 64.34^\circ.$$

On November 1,

$$n = 305.$$

$$\delta_s = 23.45^\circ \sin[360(284 + 305)/365] = -15.4^\circ.$$

Therefore,

$$\begin{aligned}\alpha_2 &= 90^\circ - |29.68^\circ + 15.4^\circ| \\ &= 44.9^\circ\end{aligned}$$

$$L = \frac{H}{\tan \alpha_1 - \tan \alpha_2} = \frac{1}{\tan(64.43^\circ) - \tan(44.9^\circ)} = 0.92 \text{ m.}$$

$$S = L \tan \alpha_2 = 0.92 \times \tan(44.9^\circ) = 0.92 \text{ m.}$$

If $S = 1.3 \text{ m}$, then,

$$L = 1.3/\tan 44.9^\circ = 1.3 \text{ m.}$$

Also,

$$L = 2.3/\tan 64.34^\circ = 1.1 \text{ m.}$$

Therefore, $1.1 \text{ m} \leq L \leq 1.3 \text{ m}$.

Example 2.3b

Repeat the above example for Canberra, Australia, for a north-facing window, such that the window is completely shaded at noon on November 1 and completely lit at noon on April 1.

Solution

The figure shown in Example 2.3a may be used if we take the solar angles α_1 and α_2 as shown in the figure to be on November 1 and April 1, respectively. From Example 2.3a,

$$\begin{aligned}\delta_s &= 4.02^\circ \text{ on April 1, and} \\ &= -15.4^\circ \text{ on November 1.}\end{aligned}$$

For Canberra, Australia, Latitude = -35.3° .
Therefore, at solar noon,

$$\begin{aligned}\alpha_1 &= 90^\circ - |-35.3^\circ + 15.4^\circ| \\ &= 70.1^\circ\end{aligned}$$

and

$$\begin{aligned}\alpha_2 &= 90^\circ - |-35.3^\circ - 4.02^\circ| \\ &= 50.68^\circ.\end{aligned}$$

Following the procedure in Example 2.3a, therefore,

$$\begin{aligned}L &= \frac{1}{\tan(70.1^\circ) - \tan(50.68^\circ)} \\ &= 0.65 \text{ m}\end{aligned}$$

and

$$\begin{aligned}S &= 0.65 \tan(50.68^\circ) \\ &= 0.79 \text{ m.}\end{aligned}$$

If S is given as 1.3 m, then,

$$L = 1.3 / \tan(50.68^\circ) = 1.07 \text{ m.}$$

Also,

$$L = 2.3 / \tan(70.1^\circ) = 0.83 \text{ m;}$$

therefore, $0.83 \text{ m} \leq L \leq 1.07 \text{ m.}$

2.3.2 Sun-Path Diagram

The projection of the sun's path on the horizontal plane is called a *sun-path diagram*. Such diagrams are very useful in determining shading phenomena

associated with solar collectors, windows, and shading devices. As shown earlier, the solar angles (α , a_s) depend upon the hour angle, declination, and latitude. Since only two of these variables can be plotted on a two-dimensional graph, the usual method is to prepare a different sun-path diagram for each latitude with variations of hour angle and declination shown for a full year. A typical sun-path diagram is shown in Figure 2.12 for 30°N latitude.

Sun-path diagrams for a given latitude are used by entering them with appropriate values of declination δ_s and hour angle h_s . The point at the intersection of the corresponding δ_s and h_s lines represents the instantaneous location of the sun. The solar altitude can then be read from the concentric circles in the diagram; the azimuth, from the scale around the circumference of the

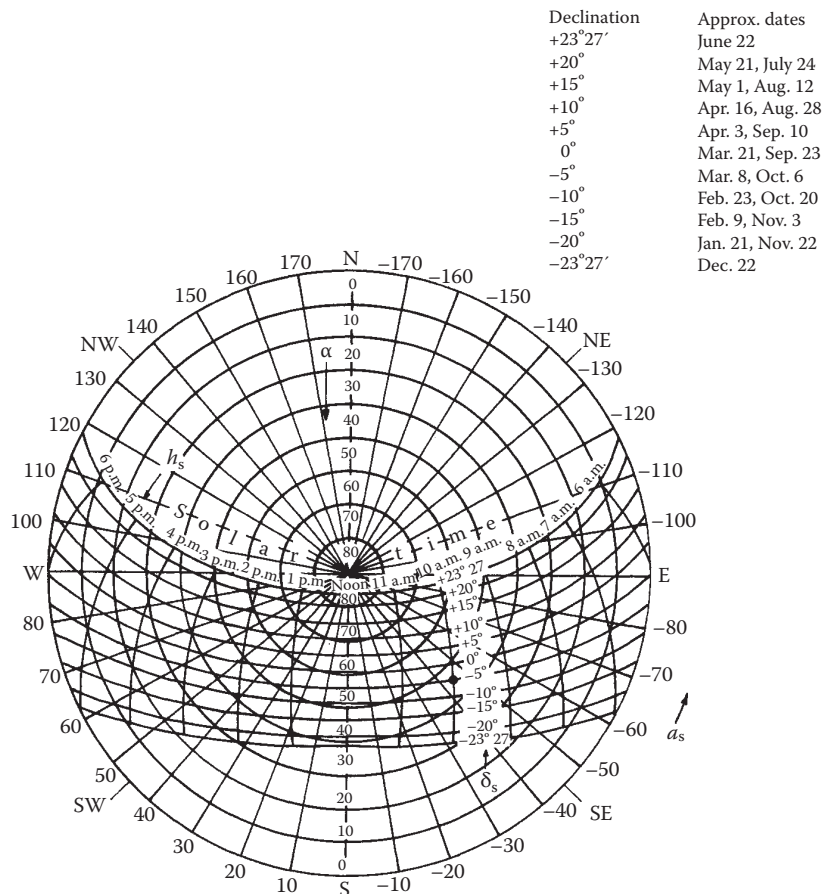


FIGURE 2.12

Sun-path diagram for 30°N latitude showing altitude and azimuth angles. (Modified from Kreider, J.F. and F. Kreith, *Solar Heating and Cooling*, revised 1st ed. Washington, DC: Hemisphere Publ. Corp., 1977.)

diagram. A complete set of sun-path diagrams is contained in Appendix 2 (Figure A2.1).

Example 2.4

Using Figure 2.12, determine the solar altitude and azimuth for March 8 at 10 a.m. Compare the results to those calculated from the basic equations (Equations 2.28 and 2.29).

Solution

On March 8, the solar declination is -5° ; therefore, the -5° sun path is used. The intersection of the 10 a.m. line and the -5° declination line in the diagram represents the sun's location; it is marked with a heavy dot in Figure 2.12. The sun position lies midway between the 40° and 50° altitude circles, say at 45° , and midway between the -40° and -50° azimuth radial lines, say at -45° . Thus, $\alpha \cong 45^\circ$ and $a_s \cong -45^\circ$. Equations 2.28 and 2.29 give precise values for α and a_s :

$$\sin \alpha = \sin(30^\circ) \sin(-5^\circ) + \cos(30^\circ) \cos(-5^\circ) \cos(-30^\circ)$$

$$\alpha = 44.7^\circ$$

$$\sin a_s = \frac{\cos(-5^\circ) \sin(-30^\circ)}{\cos(44.7^\circ)}$$

$$a_s = -44.5^\circ$$

Therefore, the calculated values are within $\pm 0.5^\circ$ (1%) of those read from the sun-path diagram.

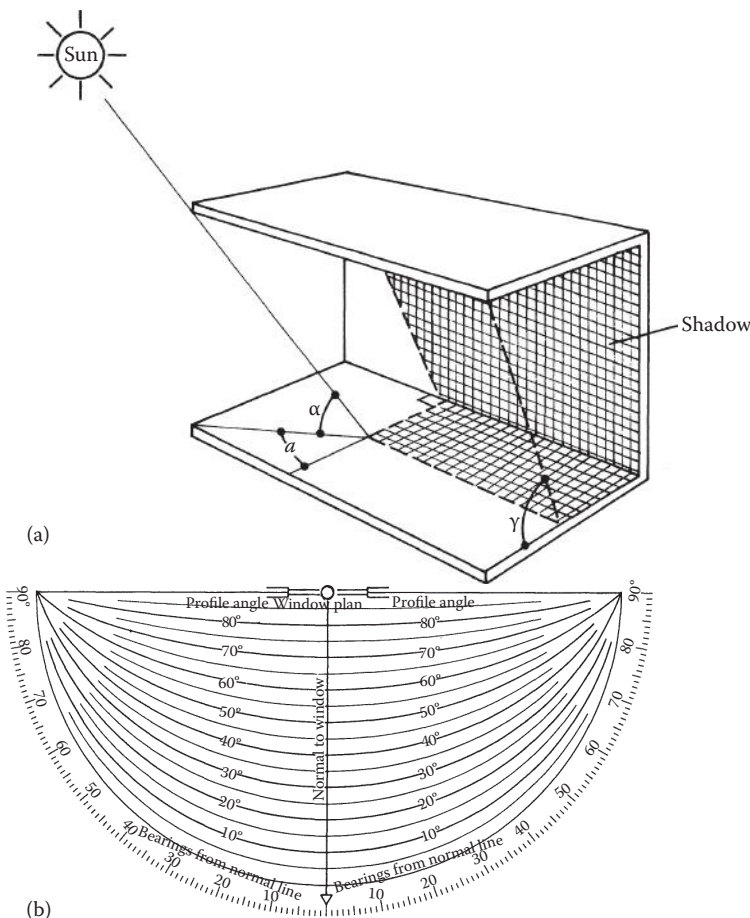
2.3.3 Shadow-Angle Protractor

The shadow-angle protractor used in shading calculations is a plot of solar altitude angles, projected onto a given plane, versus the solar azimuth angle. The projected altitude angle is usually called the *profile angle* γ . It is deemed as the angle between the normal to a surface and the projection of the sun's rays on a vertical plane normal to the same surface. The profile angle is shown in Figure 2.13a with the corresponding solar altitude angle. The profile angle, which is always used in sizing shading devices, is given by

$$\tan \gamma = \sec a \tan \alpha, \quad (2.31)$$

where a is the solar azimuth angle with respect to the wall normal.

Figure 2.13b shows the shadow-angle protractor to the same scale as the sun-path diagrams in Figure 2.12 and Appendix 2. It is used by plotting the limiting values of profile angle γ and azimuth angle a , which will start to cause shading of a particular point. The shadow-angle protractor is usually

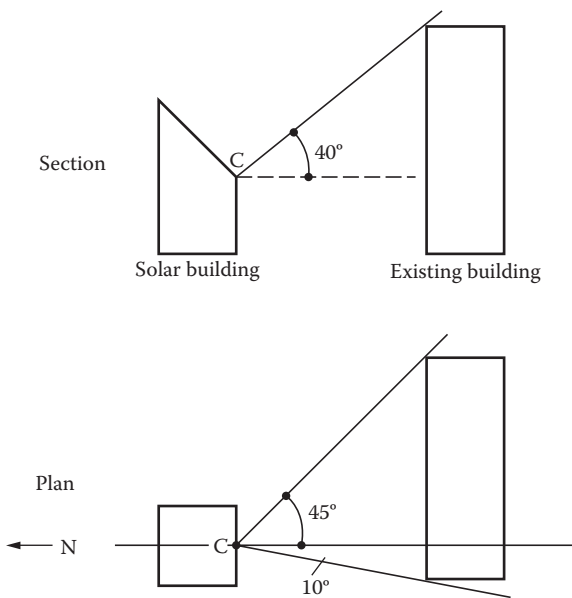
**FIGURE 2.13**

(a) Sketch showing the profile angle γ and the corresponding solar altitude angle α for a window shading device; (b) the shadow-angle protractor. (With permission from the Libby–Owens–Ford Glass Co.)

traced onto a transparent sheet so that the shadow map constructed on it can be placed over the pertinent sun-path diagram to indicate the times of day and months of the year during which shading will take place. The use of the shadow-angle protractor is best illustrated by an example.

Example 2.5

A solar building with a south-facing collector is sited to the north–northwest of an existing building. Prepare a shadow map showing what months of the year and what part of the day point C at the base of the solar collector will be shaded. Plan and elevation views are shown in Figure 2.14. Latitude = 40°N.

**FIGURE 2.14**

Plan and elevation view of proposed solar building and existing building, which may shade solar collector at point C.

Solution

The limiting profile angle for shading is 40° and the limiting azimuth angles are -45° and $+10^\circ$ as shown in Figure 2.14. These values are plotted on the shadow-angle protractor (Figure 2.15a). The shadow map, when superimposed on the sun-path diagram (Figure 2.15b), shows that point C will be shaded during the following times of day for the periods shown:

Declination	Date	Time of Day
$-23^\circ 27'$	Dec 22	8:45 a.m.–12:40 p.m.
-20°	Jan 21, Nov 22	8:55 a.m.–12:35 p.m.
-15°	Feb 9, Nov 3	9:10 a.m.–12:30 p.m.

In summary, during the period from November 3 to February 9, point C will be shaded between 3 and 4 hours. It will be shown later that this represents approximately a 50% loss in collector performance for point C, which would be unacceptable for a collector to be used for heating a building in winter.

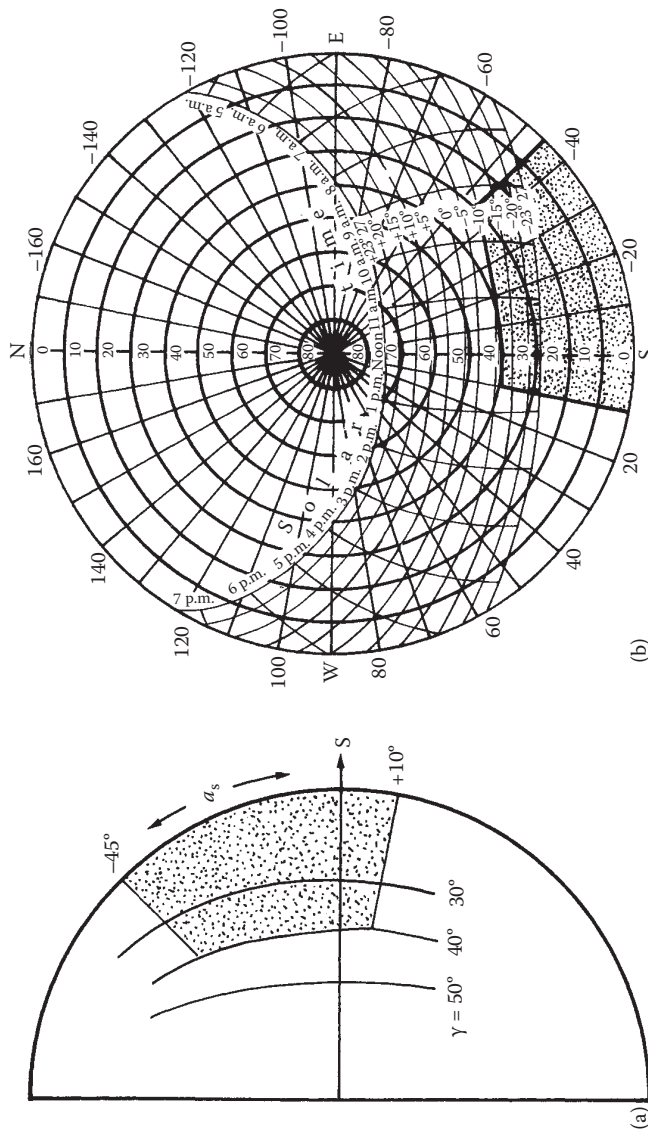


FIGURE 2.15
(a) Shadow map constructed for the example shown in Figure 2.14; (b) sun-path diagram.

2.4 Solar Radiation

Detailed information about solar radiation availability at any location is essential for the design and economic evaluation of a solar energy system. Long-term measured data of solar radiation are available for a large number of locations in the United States and other parts of the world. Where long-term measured data are not available, various models based on available climatic data can be used to estimate the solar energy availability. Solar energy is in the form of electromagnetic radiation with the wavelengths ranging from approximately $0.3\text{ }\mu\text{m}$ (10^{-6} m) to over $3\text{ }\mu\text{m}$, which correspond to ultraviolet (less than $0.4\text{ }\mu\text{m}$), visible (0.4 and $0.7\text{ }\mu\text{m}$), and infrared (over $0.7\text{ }\mu\text{m}$). Most of this energy is concentrated in the visible and the near-infrared wavelength range (see Figure 2.16). The incident solar radiation, sometimes called *insolation*, is measured as irradiance, or the energy per unit time per unit area (or power per unit area). The units most often used are watts per square meter (W/m^2), British thermal units per hour per square foot ($\text{Btu}/\text{h}\cdot\text{ft}^2$), and Langleys per minute (calories per square centimeter per minute, $\text{cal}/\text{cm}^2\cdot\text{min}$).

2.4.1 Extraterrestrial Solar Radiation

The average amount of solar radiation falling on a surface normal to the rays of the sun outside the atmosphere of the earth (extraterrestrial) at mean earth-sun distance (D_0) is called the *solar constant*, I_0 . Measurements by NASA indicated the value of the solar constant to be 1353 W/m^2 ($\pm 1.6\%$), $429\text{ Btu/h}\cdot\text{ft}^2$ or

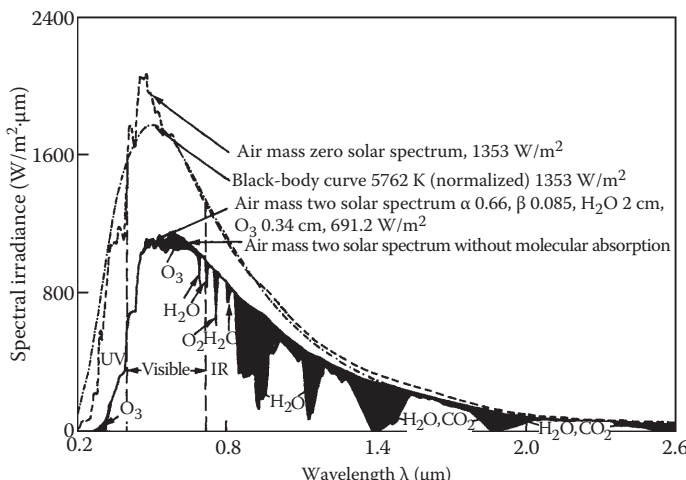


FIGURE 2.16

Extraterrestrial solar radiation spectral distribution. Also shown are equivalent black-body and atmosphere-attenuated spectra.

1.94 cal/cm²·min (Langleys/min). This value was revised upward by Frohlich et al. (1973) to 1377 W/m² or 437.1 Btu/h·ft² or 1.974 Langleys/min, which was the value used in compiling SOLMET data in the United States (Quinlan 1977, 1979). Recently, new measurements have found the value of the solar constant to be 1366.1 W/m². A value of 1367 W/m² is also used by many references.

The variation in seasonal solar radiation availability at the surface of the earth can be understood from the geometry of the relative movement of the earth around the sun. Since the earth's orbit is elliptical, the earth–sun distance varies during a year, the variation being $\pm 1.7\%$ from the average. Therefore, the extraterrestrial radiation, I , also varies by the inverse square law as below:

$$I = I_0(D_0/D)^2 \quad (2.32)$$

where D is the distance between the sun and the earth and D_0 is the yearly mean earth–sun distance (1.496×10^{11} m). The $(D_0/D)^2$ factor may be approximated as (Spencer 1971)

$$(D_0/D)^2 = 1.00011 + 0.034221 \cos(x) + 0.00128 \sin(x) \\ + 0.000719 \cos(2x) + 0.000077 \sin(2x), \quad (2.33)$$

where

$$x = 360(n - 1)/365^\circ, \quad (2.34)$$

and n = day number (starting from January 1 as 1). The following approximate relationship may also be used without much loss of accuracy:

$$I = I_0[1 + 0.034 \cos(360n/365.25)^\circ]. \quad (2.35)$$

Figure 2.17 also shows the relationship of the extraterrestrial solar radiation to the solar constant. For many solar energy applications, such as photovoltaics and photocatalysis, it is necessary to examine the distribution of energy within the solar spectrum. Table 2.1 shows the spectral irradiance at

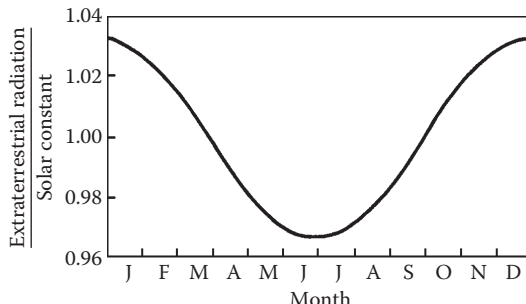


FIGURE 2.17

Effect of the time of year on the ratio of extraterrestrial radiation to the nominal solar constant.

TABLE 2.1
Extraterrestrial Solar Irradiance

λ (μm)	E_λ (W/m ² μm)	D_λ (%)	λ (μm)	E_λ (W/m ² μm)	D_λ (%)	λ (μm)	E_λ (W/m ² μm)	D_λ (%)
0.115	0.00799	3.76E-04	0.43	1.389	11.98	0.90	889.60	63.91
0.14	0.07694	1.07E-03	0.44	1848	13.25	1.00	730.70	69.84
0.16	0.20640	1.25E-03	0.45	2131	14.72	1.2	488.60	78.55
0.18	2.06	2.45E-03	0.46	2092	16.26	1.4	342.90	84.58
0.20	7.93	8.68E-03	0.47	2010	17.79	1.6	247.70	88.89
0.22	51.91	0.05	0.48	2102	19.32	1.8	168.20	91.88
0.23	59.09	0.08	0.49	2072	20.78	2.0	115.90	93.91
0.24	42.19	0.12	0.50	1932	22.24	2.2	82.58	95.35
0.25	62.28	0.16	0.51	1915	23.66	2.4	58.47	96.36
0.26	90.16	0.22	0.52	1864	25.00	2.6	43.54	97.10
0.27	297.50	0.38	0.53	1938	26.38	2.8	33.25	97.65
0.28	78.46	0.52	0.54	1813	27.78	3.0	25.60	98.08
0.29	617.70	0.74	0.55	1905	29.16	3.2	20.08	98.42
0.30	416.60	1.14	0.56	1812	30.52	3.4	15.75	98.68
0.31	464.80	1.56	0.57	1803	31.86	3.6	12.83	98.89
0.32	836.30	2.08	0.58	1818	33.19	3.8	10.39	99.06
0.33	1162	2.72	0.59	1716	34.51	4.0	8.30	99.19
0.34	1133	3.42	0.60	1737	35.80	4.5	5.03	99.43
0.35	1081	4.12	0.62	1681	38.29	5.0	3.27	99.58
0.36	1188	4.84	0.64	1591	40.68	6.0	1.64	99.75
0.37	1376	5.67	0.66	1517	42.94	7.0	0.90360	99.84
0.38	1096	6.50	0.68	1474	45.14	8.0	0.53890	99.89
0.39	1301	7.26	0.70	1413	47.25	10.0	0.22720	99.94
0.40	1727	8.12	0.72	1361	49.29	15.0	0.04418	99.98
0.41	1610	9.39	0.75	1273	52.16	20.0	0.01385	99.99
0.42	1787	10.71	0.80	1129	56.54	50.0	0.00036	100.0

Source: Adapted from Gueymard, C., *Sol Energy* 76, 423-453, 2003.

Note: Solar constant = 1366.1 W/m²; E_λ is the solar spectral irradiance; D_λ is the percentage of the solar constant associated with wavelengths shorter than λ .

the mean earth–sun distance for a solar constant of 1366.1 W/m^2 as a function of wavelength according to the standard spectrum data published by NASA. Use of the data is illustrated in the following example.

Example 2.6

Calculate the fraction of solar radiation within the visible part of the spectrum, that is, between 0.40 and $0.70 \mu\text{m}$.

Solution

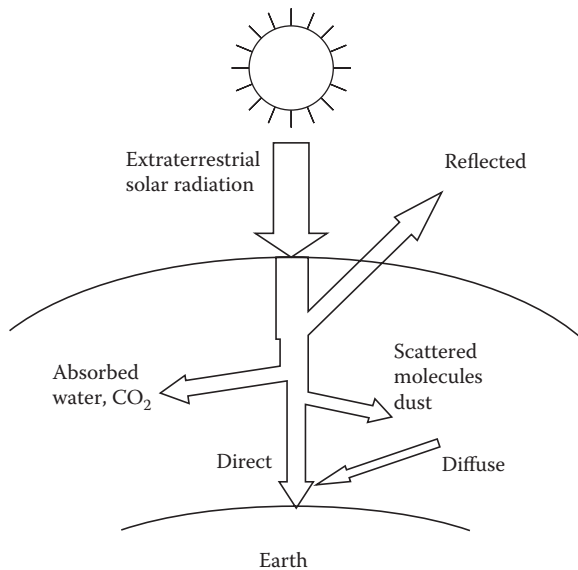
The first column in Table 2.1 gives the wavelength. The second column gives the averaged solar spectral irradiance in a band centered at the wavelength in the first column. The fourth column, $D\lambda$, gives the percentage of solar total radiation at wavelengths shorter than the value of λ in the first column. At a value of $0.40 \mu\text{m}$, 8.12% of the total radiation occurs at shorter wavelengths. At a wavelength of 0.70 , 47.25% of the radiation occurs at shorter wavelengths. Consequently, 39.13% of the total radiation lies within the band between 0.40 and $0.70 \mu\text{m}$, and the total energy received outside the earth's atmosphere within that spectral range is 534.6 W/m^2 ($169.6 \text{ Btu/h}\cdot\text{ft}^2$).

2.5 Estimation of Terrestrial Solar Radiation

As extraterrestrial solar radiation, I , passes through the atmosphere, a part of it is reflected back into space, a part is absorbed by air and water vapor, and some gets scattered by molecules of air, water vapor, aerosols, and dust particles (Figure 2.18). The part of solar radiation that reaches the surface of the earth with essentially no change in direction is called *direct* or *beam radiation*. The scattered diffuse radiation reaching the surface from the sky is called the sky *diffuse radiation*.

Although extraterrestrial radiation can be predicted with certainty,* radiation levels on the earth are subject to considerable uncertainty resulting from local climatic interactions. The most useful solar radiation data are based on long-term (30 years or more) measured average values at a location, which unfortunately are not available for most locations in the world. For such locations, an estimating method (theoretical model) based on some measured climatic parameter may be used. This chapter describes several ways of estimating terrestrial solar radiation; all have large uncertainties (as much as $\pm 30\%$) associated with them.

* The effect of sunspots, which may cause up to 0.5% variation, is neglected.

**FIGURE 2.18**

Attenuation of solar radiation as it passes through the atmosphere.

2.5.1 Atmospheric Extinction of Solar Radiation

As solar radiation I travels through the atmosphere, it is attenuated because of absorption and scattering. If K is the local extinction coefficient of the atmosphere, the beam solar radiation at the surface of the earth can be written according to Bouger's law (Equation 2.21) as

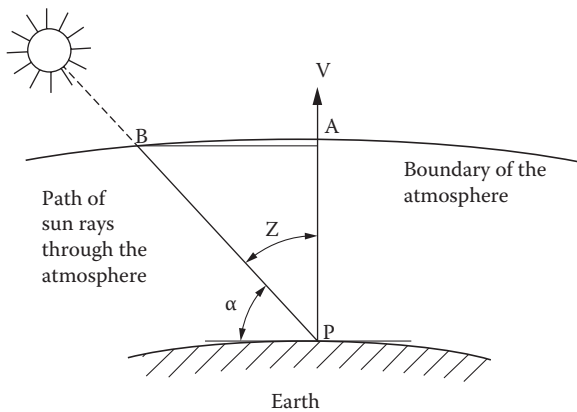
$$I_{b,N} = I e^{-\int K dx}, \quad (2.36)$$

where $I_{b,N}$ is the instantaneous beam solar radiation per unit area normal to the sun's rays and x is the length of travel through the atmosphere. If L_o is the vertical thickness of the atmosphere and

$$\int_0^{L_o} K dx = k, \quad (2.37)$$

the beam normal solar radiation for a solar zenith angle of z will be

$$I_{b,N} = I e^{-k \sec z} = I e^{-k/\sin \alpha} = I e^{-km}, \quad (2.38)$$

**FIGURE 2.19**

Air mass definition; air mass $m = BP/AP = \text{cosec } \alpha$, where α is the altitude angle. The atmosphere is idealized as a constant thickness layer.

where m is a dimensionless path length of sunlight through the atmosphere, sometimes called the *air mass ratio* (Figure 2.19).

$$m = \frac{BP}{AP} \approx \frac{1}{\cos z} \approx \frac{1}{\sin \alpha} \quad (2.39)$$

The following equation gives a more accurate value of air mass according to Kasten and Young (1989)

$$m \approx \frac{1}{\sin \alpha + 0.50572(6.07995 + \alpha)^{-1.6364}}, \quad (2.40)$$

where α is expressed in degrees.

When the solar altitude angle is 90° (sun is overhead), $m = 1$.

2.5.2 Clear-Sky Radiation Model

Gueymard and Thevenard (2009) have described a model that can be used to model solar radiation for clear days for a large number of locations in the world. This model was developed for ASHRAE to calculate the solar heat gain for fenestration; therefore, they named it the ASHRAE Clear Sky Model. This is a simple model that was developed based on a large number of simulations using sophisticated spectral simulations using the SMARTS spectral code developed by Gueymard (2000, 2005, 2008) and validating with ground-based measurements. On the basis of the detailed simulations, Gueymard developed a simple two-band solar irradiance model REST2 (Reference

evaluation of solar transmittance, 2) that can model clear-sky solar irradiance very accurately. The proposed model was developed in two steps.

1. Solar transmittance of clear sky was modeled based on two spectral bands, the first band from 0.29 to 0.7 μm , characterized by absorption by molecules and aerosols, and the second band from 0.7 to 4 μm , characterized by absorption by water vapor and CO_2 . The two-band clear-sky radiation model was used to calculate clear-sky solar irradiance for a large number of “typical” cases and compared with the data covering a large part of the world. Figure 2.20 shows the global sites used in the validation.
2. The second step consisted in developing a condensed model depending on only two monthly parameters described later in this section.

According to the ASHRAE model, the beam and diffuse components are calculated as

$$I_{b,N} = I \left(e^{-\tau_b m^b} \right) \quad (2.41)$$

$$I_{d,h} = I \left(e^{-\tau_d m^d} \right), \quad (2.42)$$

where

$I_{b,N}$: beam normal irradiance per unit area normal to the sun rays

$I_{d,h}$: diffuse horizontal irradiance per unit area on a horizontal surface

I : extraterrestrial normal irradiance

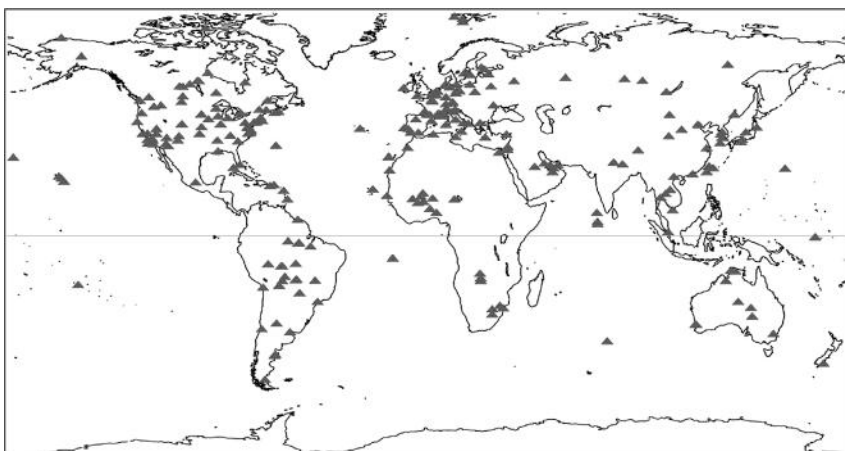


FIGURE 2.20

World sites of interest used in the model. (From Gueymard, C.A. and D. Thevenard, *Sol Energy* 83, 1998–2018, 2009.)

m: air mass

τ_b , τ_d : beam and diffuse optical depths (τ_b and τ_d are more correctly termed pseudo-optical depths, because optical depth is usually employed when the air mass coefficient is unity)

b, d: beam and diffuse air mass exponents

Values of τ_b and τ_d are location specific and vary during the year. They embody the dependence of clear-sky solar radiation upon local conditions, such as elevation, precipitable water content, and aerosols. Their average values are tabulated for the 21st day of each month for all the locations in the tables of climatic design conditions (ASHRAE NIR Fundamentals). Tables A2.2a and A2.2b give values of τ_b and τ_d for various locations in the United States and around the world, respectively.

Air mass exponents *b* and *d* are correlated to τ_b and τ_d through the following empirical relationships:

$$b = 1.219 - 0.043\tau_b - 0.151\tau_d - 0.204\tau_b \cdot \tau_d \quad (2.43)$$

$$d = 0.202 + 0.852\tau_b - 0.007\tau_d - 0.357\tau_b \cdot \tau_d \quad (2.44)$$

This radiation model describes a simple parameterization of a sophisticated broadband radiation model and provides accurate predictions of $I_{b,N}$ and $I_{d,h}$ even at sites where the atmosphere is very hazy or humid most of the time.

Solar radiation on a horizontal surface is given by

$$I_h = (I_{b,N} \sin \alpha + I_{d,h}). \quad (2.45)$$

2.5.3 Solar Radiation on a Tilted Surface

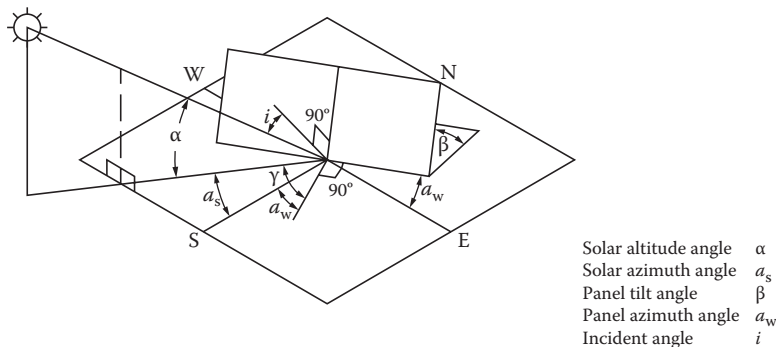
Solar radiation on an arbitrary tilted surface having a tilt angle of β from the horizontal and an azimuth angle of a_w (assumed + west of south), as shown in Figure 2.21, is the sum of components consisting of beam ($I_{b,c}$), sky diffuse ($I_{d,c}$), and ground reflected solar radiation ($I_{r,c}$):

$$I_c = I_{b,c} + I_{d,c} + I_{r,c}. \quad (2.46)$$

If *i* is the *angle of incidence* of the beam radiation on the tilted surface, it is simple to show that the instantaneous beam radiation on the surface per unit area is

$$I_{b,c} = I_{b,N} \cos i. \quad (2.47)$$

From the geometry in Figure 2.21, it can be shown that the angle of incidence *i* for the surface (angle between the normal to the surface and a line collinear with the sun's rays) is related to the solar angles as

**FIGURE 2.21**

Definitions of solar angles for a tilted surface.

$$\cos i = \cos \alpha \cos(a_s - a_w) \sin \beta + \sin \alpha \cos \beta. \quad (2.48)$$

The diffuse radiation on the surface ($I_{d,c}$) can be obtained by multiplying the sky diffuse radiation on a horizontal surface by the view factor between the sky and the surface*:

$$\begin{aligned} I_{d,c} &= I_{d,h}(1 + \cos \beta)/2 \\ &= I_{d,h} \cos^2(\beta/2). \end{aligned} \quad (2.49)$$

The ground reflected solar radiation can be found from the total solar radiation incident on a horizontal surface and the ground reflectance ρ as

$$I_{r,c} = I_h \rho. \quad (2.50)$$

The part of I_r intercepted by the tilted surface can be found by multiplying the ground reflected radiation by the view factor between the surface[†] and the ground:

$$\begin{aligned} I_{r,c} &= \rho I_h (1 - \cos \beta)/2 = \rho I_h \sin^2(\beta/2) \\ &= \rho (I_{b,N} \sin \alpha + I_{d,h}) \sin^2(\beta/2). \end{aligned} \quad (2.51)$$

For ordinary ground or grass, ρ is approximately 0.2, and for snow-covered ground, it can be taken as approximately 0.8.

* The surface has been assumed infinitely large for this view factor. See Section 2.2.3.

[†] The tilted surface and the ground in front of it have been assumed to be infinitely large for this view factor.

Example 2.7a

Find the instantaneous solar radiation at 12:00 noon EST on a solar collector surface ($\beta = 30^\circ$, $a_w = +10^\circ$) on February 1 in Tampa, Florida.

Solution

For Tampa International Airport: $L = 27.96^\circ \text{ N}$ (+), $l_{\text{local}} = 82.54^\circ \text{ W}$ (+) and $l_{\text{st}} = 75^\circ \text{ W}$ (+).

For February 1, $n = 32$.

The declination angles for this day are

$$\delta_s = 23.45^\circ \sin \frac{360}{365}(284 + 32)$$

$$\delta_s = -17.51^\circ.$$

The local time is 12:00 p.m. The solar time is given by

$$ST = LST + ET + (l_{\text{st}} - l_{\text{local}}) \cdot 4 \frac{\text{min}}{1^\circ}.$$

The equation of time is

$$B = \frac{360}{364}(32 - 81) = -48.46^\circ$$

$$\begin{aligned} ET (\text{min}) &= 9.87 \sin(2 \times (-48.46^\circ)) - 7.53 \cos(-48.46^\circ) - 1.5 \sin(-48.46^\circ) \\ &= -13.66 \text{ min}. \end{aligned}$$

Then, the solar time is

$$ST = 12:00 - 13.66 \text{ min} + (75^\circ - 82.54^\circ) \times 4 = 11:16 \text{ a.m.}$$

The hour angle is

$$h_s = (ST - 12) \frac{15^\circ}{h} = (11.26 - 12) \frac{15^\circ}{h} = -11.1^\circ.$$

The solar altitude angle is

$$\begin{aligned} \sin \alpha &= \cos \delta_s \cos L \cos h_s + \sin \delta_s \sin L \\ &= \cos(-17.51^\circ) \cos(27.96^\circ) \cos(-11.1^\circ) + \sin(-17.51^\circ) \sin(27.96^\circ) \end{aligned}$$

and

$$\alpha = 43.30^\circ.$$

The solar azimuth angle is calculated as

$$\sin a_s = \cos \delta_s \sin h_s / \cos \alpha = \cos(-17.51^\circ) \sin(-11.1^\circ) / \cos(43.30^\circ)$$

and

$$a_s = -14.61^\circ.$$

We need to find out if $|a_s|$ is greater than 90° .

For $L > \delta_s$,

$$\begin{aligned} t_E &= 12:00 - \cos^{-1} \frac{\tan \delta_s}{\tan L} \frac{h}{15^\circ} \\ &= 12:00 - \cos^{-1} \frac{\tan(-17.51^\circ)}{\tan(27.96^\circ)} \frac{h}{15^\circ} \\ &= 3.5689 \text{ h} \end{aligned}$$

Given that $ST > t_E$, the sun is south, and $a_s = -14.61^\circ$. The air mass is as follows:

$$\begin{aligned} m &= \frac{1}{\sin(43.30^\circ) + 0.50572 (6.07995 + 43.30^\circ)^{-1.6364}} \\ &= 1.4565. \end{aligned}$$

The data for the Tampa International AP, Florida, are shown in the following table:

Data for Tampa International AP, Florida

Lat: 27.96°N Long: 82.54°W Elev: 3 m

Month	Jan	Feb	Mar	Apr	May	Jun	Jul	Aug	Sep	Oct	Nov	Dec
τ_b	0.344	0.364	0.391	0.403	0.47	0.473	0.509	0.493	0.445	0.398	0.36	0.346
τ_d	2.531	2.403	2.271	2.272	2.029	2.07	1.95	2.01	2.19	2.356	2.488	2.512
$I_{b,N}$, noon (W/m^2)	902	908	899	895	831	823	793	805	836	861	876	882
$I_{d,h}$, noon (W/m^2)	94	113	134	137	174	167	188	175	143	116	97	93

Source: Data taken from ASHRAE. 2009. *Handbook of Fundamentals*. American Society of Heating Refrigeration and Air Conditioning Engineers, Atlanta, GA.

The “pseudo” optical depths are tabulated for the 21st day of each month for all the locations in the tables of climatic design. Values for other days of the year should be found by interpolation. For this example, by using linear interpolation between January and February, the pseudo optical depths are as follows:

$$\tau_b = 0.35109$$

$$\tau_d = 2.48558$$

The parameters for air mass are as follows:

$$b = 1.219 - 0.043\tau_b - 0.151\tau_d - 0.204\tau_b\tau_d = 0.6506$$

$$d = 0.202 + 0.852\tau_b - 0.007\tau_d - 0.357\tau_b\tau_d = 0.1722.$$

The extraterrestrial solar radiation is given by

$$\begin{aligned} I &= I_0 \cdot 1 + 0.034 \cos \frac{360n}{365.25} {}^\circ \\ &= 1366.1 \cdot 1 + 0.034 \cos \frac{360 \times \frac{32}{365.25}}{360} {}^\circ = 1406 \text{ W/m}^2. \end{aligned}$$

The direct solar radiation component is

$$\begin{aligned} I_{b,N} &= I e^{-\tau_b m^b} \\ &= 1406 \exp(-0.35109 \cdot 1.4565^{0.6506}) \\ &= 898 \text{ W/m}^2. \end{aligned}$$

The diffuse solar radiation on a horizontal surface is

$$\begin{aligned} I_{d,h} &= I e^{-\tau_d m^d} \\ &= 1406 \exp(-2.48558 \cdot 1.4565^{0.1722}) \\ &= 99 \text{ W/m}^2. \end{aligned}$$

The instantaneous beam radiation on the surface per unit area is given by

$$I_{b,c} = I_{b,N} \cos i.$$

For this geometry, the cosine of the angle of incidence is

$$\begin{aligned} \cos i &= \cos \alpha \cos(a_s - a_w) \sin \beta + \sin \alpha \cos \beta \\ &= \cos(43.30^\circ) \cos(-14.61^\circ - (+10^\circ)) \sin(30^\circ) + \sin(43.30^\circ) \cos(30^\circ) \\ &= 0.9248. \end{aligned}$$

Then, the beam radiation is

$$I_{b,c} = 898 \times 0.9248 = 830 \text{ W/m}^2.$$

The diffuse radiation on the collector surface will be

$$\begin{aligned} I_{d,c} &= I_{d,h} \cos^2 \frac{\beta}{2} \\ &= 99 \cos^2 \frac{30^\circ}{2} \\ &= 92 \text{ W/m}^2. \end{aligned}$$

The ground reflected solar radiation is

$$I_{r,c} = \rho(I_{b,N} \sin \alpha + I_{d,h}) \sin^2 \frac{\beta}{2} .$$

Assuming that the solar collector is surrounded by ordinary ground or grass, then $\rho \approx 0.2$

$$\begin{aligned} I_{r,c} &= 0.2(898 \sin(43.30^\circ) + 99) \sin^2 \frac{30^\circ}{2} \\ &= 10 \text{ W/m}^2. \end{aligned}$$

Finally, the total radiation on a tilted collector surface is

$$I_c = I_{b,c} + I_{d,c} + I_{r,c} = 830 + 92 + 10 = 932 \text{ W/m}^2.$$

Example 2.7b

Repeat the calculations in Example 2.6a for a north-facing solar collector ($\beta = 30^\circ$, $a_w = 10^\circ$) in Canberra, Australia (latitude = $35^\circ 18' S$, longitude = $149^\circ 11' E$, Standard Meridian = $150^\circ E$).

Solution

As the day number has not been changed, the values of the δ_s and ET remain the same.

$$\delta_s = -17.51^\circ$$

$$ET = -13.66 \text{ min.}$$

The local time is 12:00 p.m. The solar time is given by

$$ST = 12:00 - 13.66 \text{ min} + (-150^\circ + 149.18^\circ) \times 4 \frac{\text{min}}{1^\circ} = 11:43 \text{ a.m.}$$

The hour angle is

$$h_s = (ST - 12) \frac{15^\circ}{h} = (11.72 - 12) \frac{15^\circ}{h} = -4.2^\circ.$$

The solar altitude angle is

$$\begin{aligned}\sin \alpha &= \cos \delta_s \cos L \cos h_s + \sin \delta_s \sin L \\ &= \cos(-17.51^\circ) \cos(-35.3^\circ) \cos(-4.2^\circ) + \sin(-17.51^\circ) \sin(-35.3^\circ)\end{aligned}$$

and

$$\alpha = 71.82^\circ.$$

The solar azimuth angle is calculated as

$$\sin a_s = \cos \delta_s \sin h_s / \cos \alpha = \cos(-17.51^\circ) \sin(-4.2^\circ) / \cos(71.82^\circ)$$

and

$$a_s = -12.93^\circ.$$

The air mass is as follows:

$$m = \frac{1}{\sin(71.82^\circ) + 0.50572(6.07995 + 71.82^\circ)^{-1.6364}} = 1.052.$$

The data for the Canberra airport are shown in the following table:

Data for Canberra Airport

Lat: 35.30°S Long: 149.20°E Elev: 580 m

Month	Jan	Feb	Mar	Apr	May	Jun	Jul	Aug	Sep	Oct	Nov	Dec
τ_b	0.363	0.340	0.326	0.313	0.299	0.291	0.292	0.297	0.315	0.318	0.334	0.342
τ_d	2.403	2.559	2.606	2.638	2.730	2.747	2.702	2.678	2.582	2.609	2.520	2.519
$I_{b,N}$, noon (W/m ²)	972	974	952	908	871	853	869	915	948	986	995	998
$I_{d,h}$, noon (W/m ²)	126	104	94	82	69	64	70	78	94	98	111	113

Source: Data taken from ASHRAE. 2009. *Handbook of Fundamentals*. American Society of Heating Refrigeration and Air Conditioning Engineers, Atlanta, GA.

By using linear interpolation between January and February, the pseudo optical depths are as follows:

$$\tau_b = 0.3548$$

$$\tau_d = 2.4584$$

The parameters for air mass are as follows:

$$b = 1.219 - 0.043\tau_b - 0.151\tau_d - 0.204\tau_b\tau_d = 0.6546$$

$$d = 0.202 + 0.852\tau_b - 0.007\tau_d - 0.357\tau_b\tau_d = 0.1722$$

The extraterrestrial solar radiation is given by

$$I = I_0 \cdot 1 + 0.034 \cos \frac{360n}{365.25}^\circ = 1406 \text{ W/m}^2$$

The direct solar radiation component is

$$\begin{aligned} I_{b,N} &= I e^{-\tau_b m^b} \\ &= 1406 \exp(-0.3548 \times 1.052^{0.6546}) \\ &= 974 \text{ W/m}^2. \end{aligned}$$

The diffuse solar radiation on a horizontal surface is

$$\begin{aligned} I_{d,h} &= I e^{-\tau_d m^d} \\ &= 1406 \exp(-2.4584 \times 1.0521^{0.1722}) \\ &= 118 \text{ W/m}^2. \end{aligned}$$

The cosine of the angle of incidence is

$$\begin{aligned} \cos i &= \cos \alpha \cos(a_s - a_w) \sin \beta + \sin \alpha \cos \beta \\ &= \cos(71.82^\circ) \cos(-12.93^\circ - (+10^\circ)) \sin(30^\circ) + \sin(71.82^\circ) \cos(30^\circ) \\ &= 0.9665. \end{aligned}$$

Then, the beam radiation is

$$I_{b,c} = I_{b,N} \cos i$$

$$I_{b,c} = 974 \times 0.9665 = 941 \text{ W/m}^2.$$

The diffuse radiation on the collector surface will be

$$\begin{aligned} I_{d,c} &= I_{d,h} \cos^2 \frac{\beta}{2} \\ &= 118 \cos^2 \frac{30^\circ}{2} \\ &= 110 \text{ W/m}^2. \end{aligned}$$

The ground reflected solar radiation is

$$I_{r,c} = \rho(I_{b,N} \sin \alpha + I_{d,h}) \sin^2 \frac{\beta}{2} .$$

Assuming that the solar collector is surrounded by ordinary ground or grass, then $\rho \approx 0.2$

$$\begin{aligned} I_{r,c} &= 0.2(974 \sin(71.82^\circ) + 118) \sin^2 \frac{30^\circ}{2} \\ &= 14 \text{ W/m}^2 . \end{aligned}$$

Finally, the total radiation on a tilted collector surface is

$$I_c = I_{b,c} + I_{d,c} + I_{r,c} = 941 + 110 + 14 = 1065 \text{ W/m}^2.$$

2.5.4 Monthly Solar Radiation Estimation Models

One of the earliest methods of estimating solar radiation on a horizontal surface was proposed by the pioneer spectroscopist Angström. It was a simple linear model relating average horizontal radiation to clear-day radiation and to the sunshine level, that is, percent of possible hours of sunshine. Since the definition of a clear day is somewhat nebulous, Page (1966) refined the method and based it on extraterrestrial radiation instead of the ill-defined clear day:

$$\begin{aligned} \bar{H}_h &= \bar{H}_{o,h} - a + b \frac{\bar{n}}{\bar{N}} \\ &= \bar{H}_{o,h} - a + b \frac{\bar{PS}}{100} , \end{aligned} \tag{2.52}$$

where \bar{H}_h and $\bar{H}_{o,h}$ are the horizontal terrestrial and horizontal extraterrestrial radiation per day averaged for a month, \bar{PS} is the monthly averaged percent of possible sunshine (i.e., hours of sunshine/maximum possible duration of sunshine $\times 100$), a and b are constants for a given site, and \bar{n} and \bar{N} are the monthly average numbers of hours of bright sunshine and day length, respectively. The ratio \bar{n}/\bar{N} is also equivalent to the monthly average percent sunshine (\bar{PS}). $\bar{H}_{o,h}$ can be calculated by finding $H_{o,h}$ from Equation 2.53, using Equations 2.35 and 2.48 and averaging $H_{o,h}$ for the number of days in each month, or data in Appendix 2 (Table A2.1) can be used, which was developed based on I_o equal to 1366.1 W/m^2 .

$$H_{o,h} = \int_{t_{sr}}^{t_{ss}} I \sin \alpha \, dt \quad (2.53)$$

which can be written as

$$H_{o,h} = \frac{24I}{\pi} (\cos(L) \cos(\delta) \sin(h_{ss}) + h_{ss} \sin(L) \sin(\delta)) \quad (2.53a)$$

Some typical values of a and b are given in Table 2.2 (Löf et al. 1966). Additional values for worldwide locations are given in Appendix 2 (Table A2.4).

Example 2.8

Using the predictive method of Angström or Page, estimate the monthly solar radiation for the North Central Sahara Desert (Tamanrasset, Algeria, area) at latitude = 25°N. Percentages of possible sunshine and extraterrestrial radiation for this site are given in the table below.

Solution

Using the climate data given, the expected monthly average horizontal radiation for the North Sahara is calculated in the following table using $a = 0.30$ and $b = 0.43$ from Table 2.2.

Month	$\bar{H}_{o,h}^a$		\bar{H}_h	
	$\overline{PS} / 100$	$\text{kJ/m}^2\cdot\text{day}$	$\text{kJ/m}^2\cdot\text{day}$	$\text{Btu/ft}^2\cdot\text{day}$
Jan	0.88	23,902	16,215	1425
Feb	0.83	28,115	18,469	1626
Mar	0.90	32,848	22,143	1950
Apr	0.85	37,111	24,697	2174
May	0.80	39,356	25,345	2231
Jun	0.76	40,046	25,101	2210
Jul	0.86	39,606	36,528	2336
Aug	0.83	37,832	24,852	2188
Sep	0.77	34,238	21,608	1902
Oct	0.86	29,413	19,701	1735
Nov	0.85	24,909	16,577	1460
Dec	0.80	22,669	14,599	1285

^a Monthly averaged, daily extraterrestrial radiation.

TABLE 2.2Coefficients a and b in the Angström–Page Regression Equation

Location	Climate	Sunshine Hours in Percentage of Possible		a	b
		Range	Average		
Albuquerque, New Mexico	BS-BW	68–85	78	0.41	0.37
Atlanta, Georgia	Cf	45–71	59	0.38	0.26
Blue Hill, Massachusetts	Df	42–60	52	0.22	0.50
Brownsville, Texas	BS	47–80	62	0.35	0.31
Buenos Aires, Argentina	Cf	47–68	59	0.26	0.50
Charleston, South Carolina	Cf	60–75	67	0.48	0.09
Dairen, Manchuria	Dw	55–81	67	0.36	0.23
El Paso, Texas	BW	78–88	84	0.54	0.20
Ely, Nevada	BW	61–89	77	0.54	0.18
Hamburg, Germany	Cf	11–49	36	0.22	0.57
Honolulu, Hawaii	Af	57–77	65	0.14	0.73
Madison, Wisconsin	Df	40–72	58	0.30	0.34
Malange, Angola	Aw-BS	41–84	58	0.34	0.34
Miami, Florida	Aw	56–71	65	0.42	0.22
Nice, France	Cs	49–76	61	0.17	0.63
Poona, India (monsoon)	Am	25–49	37	0.30	0.51
(dry)		65–89	81	0.41	0.34
Stanleyville, Congo	Af	34–56	48	0.28	0.39
Tamanrasset, Algeria	BW	76–88	83	0.30	0.43

Source: Löf, G.O.G. et al., World distribution of solar energy. *Eng. Expt. Station Rept.* 21, University of Wisconsin, Madison, 1966. With permission.

Note: Af = tropical forest climate, constantly moist, rainfall all through the year; Am = tropical forest climate, monsoon rain, short dry season, but total rainfall sufficient to support rain forest; Aw = tropical forest climate, dry season in winter; BS = steppe or semiarid climate; BW = desert or arid climate; Cf = mesothermal forest climate, constantly moist, rainfall all through the year; Cs = mesothermal forest climate, dry season in winter; Df = microthermal snow forest climate, constantly moist, rainfall all through the year; Dw = microthermal snow forest climate, dry season in winter.

A number of researchers found Angström–Page-type correlations for specific locations, which are listed in Figure 2.22. Some of these include additional parameters such as relative humidity and ambient temperature. Correlations listed in the table may be used for the specific locations for which they were developed.

Another meteorological variable that could be used for solar radiation prediction is the opaque cloud cover recorded at many weather stations around the world. This quantity is a measure of the percent of the sky dome obscured by opaque clouds. Because this parameter contains even less solar information than sunshine values, it has not been useful in predicting long-term solar radiation values.

Authors	Measured data correlated	Correlation equations
Iqbal (1979)	Canada, 3 locations	$\frac{\bar{D}_h}{\bar{H}_h} = 0.791 - 0.635 \left(\frac{\bar{n}}{N} \right)$ $\frac{\bar{H}_d}{\bar{H}_h} = 0.163 + 0.478 \left(\frac{\bar{n}}{N} \right) - 0.655 \left(\frac{\bar{n}}{N} \right)^2$ $\frac{\bar{H}_b}{\bar{H}_{o,h}} = -0.176 + 1.45 \left(\frac{\bar{n}}{N} \right) - 1.12 \left(\frac{\bar{n}}{N} \right)^2$
Garg and Garg (1985)	India, 11 locations, 20 years' data	$\frac{\bar{H}_h}{\bar{H}_{o,h}} = 0.3156 + 0.4520 \left(\frac{\bar{n}}{N} \right)^2$ $\frac{\bar{D}_h}{\bar{H}_{o,h}} = 0.3616 - 0.2123 \left(\frac{\bar{n}}{N} \right)$ $\frac{\bar{D}_h}{\bar{H}_h} = 0.8677 - 0.7365 \left(\frac{\bar{n}}{N} \right)$
Hussain (1994)	India	$\frac{\bar{H}_h}{\bar{H}_{o,h}} = 0.394 + 0.364 \left[\frac{\bar{n}}{N'} \right] - 0.0035 W_{at}$ $\frac{\bar{D}_h}{\bar{H}_{o,h}} = 0.306 - 0.165 \left[\frac{\bar{n}}{N'} \right] - 0.0025 W_{at}$
Coppolino (1994)	Italy	$\frac{\bar{H}_h}{\bar{H}_{o,h}} = 0.67 \left(\frac{\bar{n}}{N} \right)^{0.45} \sin(\alpha_{sn})^{0.05}$ <p style="text-align: center;">α_{sn} = Solar elevation at noon on the 15th of each month, degrees</p> $0.15 \leq \frac{\bar{n}}{N} \leq 0.90$
Akinoglu and Ecevit (1990)	Italy	$\frac{\bar{H}_h}{\bar{H}_{o,h}} = 0.145 + 0.845 \left(\frac{\bar{n}}{N} \right) - 0.280 \left(\frac{\bar{n}}{N} \right)^2$
Ögelman et al. (1984)	Turkey, 2 locations, 3 years' data	$\left(\frac{\bar{H}_h}{\bar{H}_{o,h}} \right) = 0.204 + 0.758 \left(\frac{\bar{n}}{N} \right) - 0.250 \left\{ \left(\frac{\bar{n}}{N} \right)^2 + \sigma \frac{\frac{2}{n}}{N} \right\}$ $\sigma \frac{\frac{2}{n}}{N} = 0.035 + 0.326 \left(\frac{\bar{n}}{N} \right) - 0.433 \left(\frac{\bar{n}}{N} \right)^2$
Gopinathan (1988)	40 locations around the world	$\frac{\bar{H}_h}{\bar{H}_{o,h}} = a + b \left(\frac{\bar{n}}{N} \right)$ $a = -0.309 + 0.539 \cos L - 0.0639 h + 0.290 \left(\frac{\bar{n}}{N} \right)$ $b = 1.527 - 1.027 \cos L + 0.0926 h + 0.359 \left(\frac{\bar{n}}{N} \right)$

FIGURE 2.22

Angström–page-type correlations for specific locations. (\bar{H}_a , \bar{H}_b , $\bar{H}_{o,h}$, and \bar{D}_h are monthly averaged daily values; \bar{N} = maximum duration for which the Campbell–Stokes recorder can be active, that is, solar elevation $>5^\circ$; W_{at} = relative humidity $\times (4.7923 + 0.3647T + 0.055T^2 + 0.0003T^3)$; T = ambient temperature ($^\circ\text{C}$); W_{at} = g moisture/ m^3 ; h = elevation in kilometers above sea level; L = latitude.)

2.6 Models Based on Long-Term Measured Horizontal Solar Radiation

Long-term measured solar radiation data are usually available as monthly averaged total solar radiation per day on horizontal surfaces. In order to use these data for tilted surfaces, the total solar radiation on a horizontal surface must first be broken down into beam and diffuse components. A number of researchers have proposed models to do that, prominent among them being Liu and Jordan, Collares-Pereira and Rabl, and Erbs, Duffie and Klein.

2.6.1 Monthly Solar Radiation on Tilted Surfaces

In a series of papers, Liu and Jordan (1960, 1961a,b, 1963, 1967) have developed an essential simplification in the basically complex computational method required to calculate long-term radiation on tilted surfaces. This is called the LJ method. The fundamental problem in such calculations is the decomposition of long-term measured total horizontal radiation into its beam and diffuse components.

If the decomposition can be computed, the trigonometric analysis presented earlier can be used to calculate incident radiation on any surface in a straightforward manner. Liu and Jordan (LJ) correlated the diffuse-to-total radiation ratio (\bar{D}_h/\bar{H}_h) with the *monthly clearness index* \bar{K}_T , which is defined as

$$\bar{K}_T = \frac{\bar{H}_h}{\bar{H}_{o,h}}, \quad (2.54)$$

where \bar{H}_h is the monthly averaged terrestrial radiation per day on a horizontal surface. $\bar{H}_{o,h}$ is the corresponding extraterrestrial radiation, which can be calculated from Equation 2.53 by averaging each daily total for a month. The original LJ method was based upon the extraterrestrial radiation at mid-month, which is not truly an average.

The LJ correlation predicts the monthly diffuse (\bar{D}_h) to monthly total \bar{H}_h ratio. It can be expressed by the empirical equation

$$\frac{\bar{D}_h}{\bar{H}_h} = 1.390 - 4.027\bar{K}_T + 5.531\bar{K}_T^2 - 3.108\bar{K}_T^3. \quad (2.55)$$

Note that the LJ correlation is based upon a solar constant value of 1394 W/m^2 ($442 \text{ Btu/h}\cdot\text{ft}^2$), which was obtained from terrestrial observations, whereas the newer value, based on satellite data, is 1366.1 W/m^2 . The values of \bar{K}_T must be based on this earlier value of the solar constant to use the LJ method.

Collares-Pereira and Rabl (1979) conducted a study and concluded that although Liu and Jordan's approach is valid, their correlations would predict significantly smaller diffuse radiation components. They also concluded that Liu and Jordan were able to correlate their model with the measured data because they used the measured data that were not corrected for the shade ring (see solar radiation measurements). Collares-Pereira and Rabl (C-P&R) also introduced the sunset hour angle h_{ss} in their correlation to account for the seasonal variation in the diffuse component. The C-P&R correlation is

$$\frac{\bar{D}_h}{\bar{H}_h} = 0.775 + 0.347 \left(h_{ss} - \frac{\pi}{2} \right) - 0.505 + 0.0261 \left(h_{ss} - \frac{\pi}{2} \right) \cos(2\bar{K}_T - 1.8), \quad (2.56)$$

where h_{ss} is the sunset hour angle in radians. The C-P&R correlation agrees well with the correlations for India (Choudhury 1963), Israel (Stanhill 1966), and Canada (Ruth and Chant 1976) and is, therefore, preferred to Equation 2.55.

The monthly average beam component \bar{B}_h on a horizontal surface can be readily calculated by simple subtraction since \bar{D}_h is known:

$$\bar{B}_h = \bar{H}_h - \bar{D}_h. \quad (2.57)$$

It will be recalled on an instantaneous basis from Equations 2.45 and 2.47 and Figure 2.21 that

$$I_{b,N} = \frac{I_{b,h}}{\sin \alpha}, \quad (2.58)$$

$$I_{b,c} = I_{b,N} = \cos i, \quad (2.47)$$

where $I_{b,h}$ is the instantaneous horizontal beam radiation. Solving for $I_{b,c}$, the beam radiation on a surface,

$$I_{b,c} = I_{b,h} \frac{\cos i}{\sin \alpha}. \quad (2.59)$$

The ratio in parentheses is usually called the beam radiation *tilt factor* R_b . It is a purely geometric quantity that converts instantaneous horizontal beam radiation to beam radiation intercepted by a tilted surface.

Equation 2.59 cannot be used directly for the long-term beam radiation \bar{B}_h . To be strictly correct, the instantaneous tilt factor R_b should be integrated over a month with the beam component $I_{b,h}$ used as a weighting factor to

calculate the beam tilt factor. However, the LJ method is used precisely when such short-term data as $I_{b,h}$ are not available. The LJ recommendation for the monthly mean tilt factor \bar{R}_b is simply to calculate the monthly average of $\cos i$ and divide it by the same average of $\sin \alpha$. In equation form for south-facing surfaces, this operation yields

$$\bar{R}_b = \frac{\cos(L - \beta) \cos \delta_s \sin h_{sr} + h_{sr} \sin(L - \beta) \sin \delta_s}{\cos L \cos \delta_s \sin h_{sr}(\alpha = 0) + h_{sr}(\alpha = 0) \sin L \sin \delta_s}, \quad (2.60)$$

where the sunrise hour angle $h_{sr}(\alpha = 0)$ in radians is given by Equation 2.30 and h_{sr} is the min $|h_s(\alpha = 0)|, |h_s(i = 90^\circ)|$, respectively, and is evaluated at midmonth. Non-south-facing surfaces require numerical integration or iterative methods to determine \bar{R}_b . The long-term beam radiation on a tilted surface \bar{B}_c is then,

$$\bar{B}_c = \bar{R}_b \bar{B}_h, \quad (2.61)$$

which is the long-term analog of Equation 2.47. Values of \bar{R}_b are tabulated in Appendix 2, Table A2.5.

Diffuse radiation intercepted by a tilted surface differs from that on a horizontal surface, because a tilted surface does not view the entire sky dome, which is the source of diffuse radiation. If the sky is assumed to be an isotropic source of diffuse radiation, the instantaneous and long-term tilt factors for diffuse radiation, R_d and \bar{R}_d , respectively, are equal and are simply the radiation view factor from the plane to the visible portion of a hemisphere. In equation form:

$$R_d = \bar{R}_d = \cos^2 \frac{\beta}{2} = (1 + \cos \beta)/2. \quad (2.62)$$

In some cases where solar collectors are mounted near the ground, some beam and diffuse radiation reflected from the ground can be intercepted by the collector surface. The tilt factor \bar{R}_r for reflected total radiation ($\bar{D}_h + \bar{B}_h$) is then calculated to be

$$\bar{R}_r = \frac{\bar{R}}{\bar{D}_h + \bar{B}_h} = \rho \sin^2 \frac{\beta}{2} = \rho(1 - \cos \beta)/2, \quad (2.63)$$

in which ρ is the diffuse reflectance of the surface south of the collector assumed uniform and of infinite extent.

For snow, $\rho \cong 0.75$; for grass and concrete, $\rho \cong 0.2$. A more complete list of reflectances is provided in Table A2.7 of Appendix 2. The total long-term

radiation intercepted by a surface \bar{H}_c is then the total of beam, diffuse, and diffusely reflected components:

$$\bar{H}_c = \bar{R}_b \bar{B}_h + \bar{R}_d \bar{D}_h + \bar{R}_r (\bar{D}_h + \bar{B}_h). \quad (2.64)$$

Using Equations 2.62 and 2.63, we have

$$\bar{H}_c = \bar{R}_b \bar{B}_h + \bar{D}_h \cos^2 \frac{\beta}{2} + (\bar{D}_h + \bar{B}_h) \rho \sin^2 \frac{\beta}{2}, \quad (2.65)$$

in which \bar{R}_b is calculated from Equation 2.60.

Example 2.9

Using the \bar{H}_h data calculated in Example 2.7 in place of the long-term measured data for the North Central Sahara Desert at latitude 25°N, find the monthly averaged insolation per day on a south-facing solar collector tilted at an angle of 25° from the horizontal.

Solution

The solution below is for the month of January. Values for the other months can be found by following the same method.

$$\bar{H}_h = 16,215 \text{ kJ/m}^2 \cdot \text{day}.$$

From Table A2.1:

$$\bar{H}_{o,h} = 24,199.$$

Therefore,

$$\bar{K}_T = \bar{H}_h / \bar{H}_{o,h} = 0.67.$$

δ_s and h_{sr} can be found for the middle of the month (January 16).

$$\begin{aligned} \delta_s &= 23.45^\circ \sin[360(284 + 16)/365^\circ] \\ &= -21.1^\circ 1'. \end{aligned}$$

$$h_{sr}(\alpha = 0) - \cos^{-1}(-\tan L \tan \delta)$$

$$= -79.6^\circ \text{ or } -1.389 \text{ rad}$$

and $h_{ss} = 1.389$

Using CP&R correlation,

$$\begin{aligned}\frac{\bar{D}_h}{\bar{H}_h} &= 0.775 + 0.347(1.389 - 1.5708) \\ &\quad - [0.505 + 0.0261(1.389 - 1.5708)] \cos(2 \times 0.67 - 1.8) \\ &= 0.211\end{aligned}$$

Therefore,

$$\bar{D}_h = 0.211 \times 16,215 = 3421 \text{ kJ/m}^2 \cdot \text{day}$$

and

$$\bar{B}_h = \bar{H}_h - \bar{D}_h = 12,794 \text{ kJ/m}^2 \cdot \text{day}.$$

Insolation on a tilted surface can be found from Equation 2.64. We need to find \bar{R}_b from Equation 2.60.

Therefore,

$$\begin{aligned}\bar{R}_b &= \frac{\cos(0)\cos(-21.1^\circ)\sin(-79.6^\circ) - 1.389\sin(0)(-21.1^\circ)}{\cos(25^\circ)\cos(-21.1^\circ)\sin(-79.6^\circ) - 1.389\sin(25^\circ)\sin(-21.1^\circ)} \\ &= 1.47.\end{aligned}$$

$$\bar{R}_d = \cos^2(25/2) = 0.953.$$

$$\begin{aligned}\bar{R}_r &= \rho \sin^2(\beta/2) \text{ (Assume } \rho = 0.2) \\ &= 0.2 \sin^2(12.5^\circ) \\ &= 0.009.\end{aligned}$$

Therefore,

$$\begin{aligned}\bar{H}_c &= (1.47)(12,794) + 0.953(3421) + 0.009(16,215) \\ &= 22,213 \text{ kJ/m}^2\end{aligned}$$

2.6.2 Circumsolar or Anisotropic Diffuse Solar Radiation

The models described in the above sections assume that the sky diffuse radiation is isotropic. However, this assumption is not true because of circumsolar radiation (brightening around the solar disk). Although the assumption of isotropic diffuse solar radiation does not introduce errors in the diffuse values on horizontal surfaces, it can result in errors of 10% to 40% in the

diffuse values on tilted surfaces. A number of researchers have studied the anisotropy of the diffuse solar radiation because of circumsolar radiation. Temps and Coulson (1977) introduced an anisotropic diffuse radiation algorithm for tilted surfaces for clear-sky conditions. Klucher (1979) refined the Temps and Coulson algorithm by adding a cloudiness function to it:

$$R_d = \frac{1}{2}(1 + \cos\beta)M_1M_2, \quad (2.66)$$

where

$$M_1 = 1 + F \sin^3(\beta/2), \quad (2.67)$$

$$M_2 = 1 + F \cos^2 i \sin^3(z), \quad (2.68)$$

and

$$F = 1 - (D_h/H_h)^2. \quad (2.69)$$

Examining F , we find that under overcast skies ($D_h = H_h$), R_d in Equation 2.66 reduces to the isotropic term of Liu and Jordan. The Klucher algorithm reduces the error in diffuse radiation to approximately 5%.

In summary, monthly averaged, daily solar radiation on a surface is calculated by first decomposing total horizontal radiation into its beam and diffuse components using Equation 2.55 or 2.56. Various tilt factors are then used to convert these horizontal components to components on the surface of interest.

2.6.3 Hourly and Daily Solar Radiation on Tilted Surfaces

Accurate determination of the hourly solar radiation received during the average day of each month is a prerequisite in different solar energy applications. In the early 1950s, Whillier introduced the “utilizability” method to analytically predict the performance of active solar collectors. This method used a simple formulation to estimate the mean hourly radiation during each hour of an average day of the month, based on the ratio of the hourly to daily irradiation received by a horizontal surface outside of the atmosphere. The long-term models provide the mean hourly distribution of global radiation over the average day of each month.

Three methods are described below:

- Collares-Pereira and Rabl Model, CPR (Collares-Pereira and Rabl 1979)
- Collares-Pereira and Rabl Model modified by Gueymard, CPRG (Gueymard 1986)
- Daily Integration or DI Model by Gueymard (Gueymard 2000)

Given the long-term average daily total and diffuse irradiation on a horizontal surface \bar{H}_h and \bar{H}_d , it is possible to find the long-term average hourly irradiances \bar{I}_d , \bar{I}_h , and \bar{I}_b .

The ratio of the hourly diffuse to the long-term average daily diffuse irradiation on a horizontal surface, r_d , is given by (Figure 2.23)

$$r_d = \frac{I_d}{\bar{H}_d} = \frac{\pi}{24} \frac{\cos h_s - \cos h_{ss}}{\sin h_{ss} - \frac{\pi}{180} h_{ss} \cos h_{ss}}. \quad (2.70)$$

The ratio of hourly total to the long-term average daily total irradiation on a horizontal surface, r_t , is given by

$$r_t = \frac{I_h}{\bar{H}_h} = (a + b \cos(h_s)) r_d, \quad (2.71)$$

with

$$a = 0.409 + 0.5016 \sin(h_{ss} - 60^\circ)$$

$$b = 0.6609 - 0.4767 \sin(h_{ss} - 60^\circ).$$

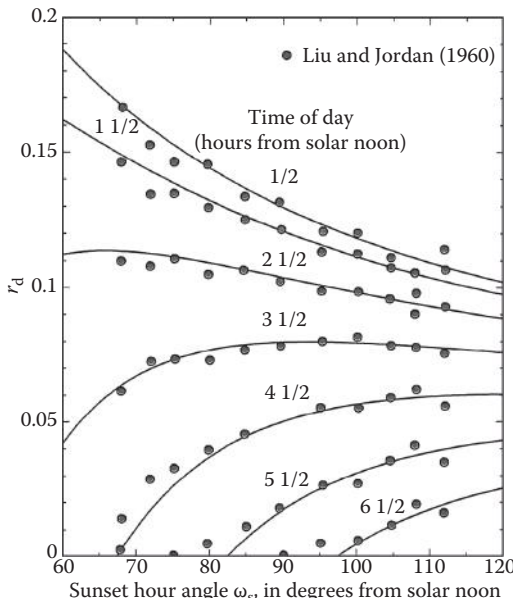


FIGURE 2.23

Collares-Pereira and Rabl Model, CPR. (Adapted from Collares-Pereira, M. and A. Rabl, *Sol Energy* 22, 155–166, 1979; Liu, B.H.Y. and R.C. Jordan, *Sol Energy* 4, 1–19, 1960. See also Liu, B.Y.H., Characteristics of solar radiation and the performance of flat plate solar energy collectors, PhD dissertation, University of Minnesota, Minneapolis, 1960.)

This fit satisfies, within 1% for all h_{ss} , the normalization condition

$$\int_{-t_s}^{t_s} I_h \, dt = \bar{H}_h. \quad (2.72)$$

For the CPRG method, the ratio of hourly total to the long-term average daily total irradiation on a horizontal surface, r_t , is given by (Gueymard 1986) (Figure 2.24)

$$r_t = \frac{I_h}{\bar{H}_h} = \frac{(a + b \cos h_s) r_d}{f_c}, \quad (2.73)$$

with

$$f_c = a + kb - \frac{\pi}{180} \left(h_{ss} - \frac{1}{2} \sin 2h_{ss} \right) \quad (2.74)$$

$$k = 2 \sin h_{ss} - \frac{\pi}{180} h_{ss} \cos h_{ss}^{-1}. \quad (2.75)$$

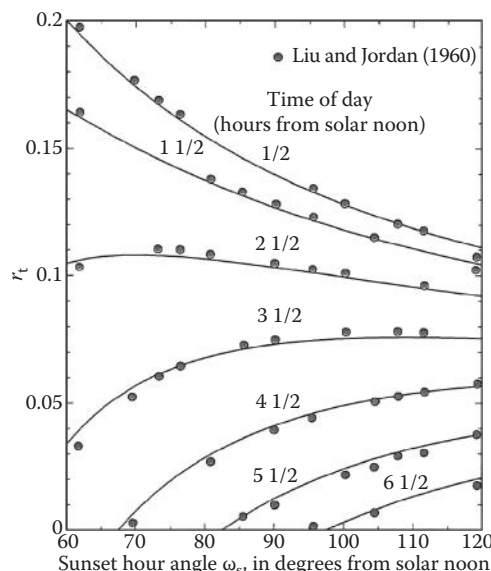


FIGURE 2.24

Collares-Pereira and Rabl Model modified by Gueymard (1986). (Adapted from Collares-Pereira, M. and A. Rabl, *Sol Energy* 22, 155–166, 1979; Liu, B.Y.H. and R.C. Jordan, *Sol Energy* 4, 1–19, 1960. See also Liu, B.Y.H., Characteristics of solar radiation and the performance of flat plate solar energy collectors, PhD dissertation, University of Minnesota, Minneapolis, 1960.)

The normalization condition is expressed by

$$\int_{-t_s}^{t_s} r_t \, dt = 1. \quad (2.76)$$

For the DI Model:

Gueymard (2000) developed the daily integration approach to predict the monthly average hourly global irradiation by using a large data set of 135 stations with diverse geographic locations (82.58°N to 67.68°S) and climates. Gueymard compared his proposed model with previous hourly radiation models, Collares-Pereira and Rabl Model CP&R (Collares-Pereira and Rabl 1979) and Collares-Pereira and Rabl Model modified by Gueymard (Gueymard 1986), and concluded that the daily integration model is the most accurate compared to the other models.

The DI model uses the same expression for r_d as above (Equation 2.70). The expression for r_t is given by

$$r_t = r_d \frac{1 + q(a_2/a_1)A(h_{ss})r_d(24/\pi)}{1 + q(a_2/a_1)B(h_{ss})/A(h_{ss})}, \quad (2.77)$$

where (a_2/a_1) represents the atmospheric extinction effect. a_1 and a_2 were obtained from a multiple least-squares fit:

$$a_1 = 0.41341K_t + 0.61197K_t^2 - 0.01886K_tS_o + 0.00759S_o \quad (2.78)$$

$$a_2 = \text{Max}(0.054, 0.28116 + 2.2475K_t - 1.7611K_t^2 - 1.84535 \sin h_o + 1.681 \sin^3 h_o) \quad (2.79)$$

and $B(h_{ss})$ is defined as

$$B(h_{ss}) = \omega_s(0.5 + \cos^2 h_{ss}) - 0.75 \sin(2 h_{ss}) \quad (2.80)$$

For all three DI, CPR, and CPRG models:

The instantaneous solar beam radiation on a horizontal surface, $I_{b,h}$, is given by

$$I_{b,h} = r_t \bar{H}_h - r_d \bar{H}_d. \quad (2.81)$$

The instantaneous solar beam radiation on a tilted surface, $I_{b,c}$, is

$$I_{b,c} = I_{b,h} \frac{\cos i}{\sin \alpha}. \quad (2.59)$$

Then, the total radiation on a tilted surface, I_c , is

$$I_c = (r_t \bar{H}_h - r_d \bar{H}_d) \frac{\cos i}{\sin \alpha} + r_d \bar{H}_d \cos^2 \frac{\beta}{2} + \rho r_t \bar{H}_h \sin^2 \frac{\beta}{2}. \quad (2.82)$$

The following websites give information about long-term database either measured or satellite solar radiation.

- Surface Meteorology and Solar Energy (Version 6.0) [<https://eosweb.larc.nasa.gov/sse/>]
- Energy Plus Weather Data [http://apps1.eere.energy.gov/buildings/energyplus/weatherdata_about.cfm?CFID=777061&CFTOKEN=999ebda95de32b46-A8949F8C-E3B6-3771-7E42A53F29DDF35C]
- National Solar Radiation Data Base, 1961–1990: Typical Meteorological Year 2 [http://webcache.googleusercontent.com/search?q=cache:http://rredc.nrel.gov/solar/old_data/nsrdb/tmy2/]
- National Solar Radiation Data Base, 1991–2005 Update: Typical Meteorological Year 3 [http://rredc.nrel.gov/solar/old_data/nsrdb/1991-2005/tmy3/]
- The Solar and Wind Energy Resource Assessment (SWERA) [<http://en.openei.org/apps/SWERA/>]
- National Renewable Laboratory (NREL) [http://www.nrel.gov/international/geospatial_toolkits.html http://www.nrel.gov/international/geospatial_toolkits.html#HOMER]

Example 2.10

Find the instantaneous solar radiation at 12:00 noon solar time on a solar collector surface (β = Latitude, $a_w = 0^\circ$) on March 21 in Las Vegas, Nevada.

Solution

For Las Vegas Mccarran Intl Ap, Nevada:

$$L = 36.08 \text{ N (+)}, l_{\text{local}} = 115.16 \text{ W (+)}, \text{ and } l_{\text{st}} = 120 \text{ W (+)}.$$

For March 21:

The declination angle for this day is

$$\delta_s = 0^\circ.$$

The hour angle is

$$h_s = (\text{ST} - 12) \frac{15^\circ}{\text{h}} = (12 - 12) \frac{15^\circ}{\text{h}} = 0^\circ.$$

The solar altitude angle is

$$\sin \alpha = \cos \delta_s \cos L \cos h_s + \sin \delta_s \sin L$$

$$\sin \alpha = \cos(0^\circ) \cos(36.08^\circ) \cos(0^\circ) + \sin(0^\circ) \sin(36.08^\circ);$$

then,

$$\alpha = 53.92^\circ.$$

The solar azimuth angle is defined by

$$\sin a_s = \frac{\cos \delta_s \sin h_s}{\cos \alpha}$$

$$\sin a_s = \frac{\cos(0^\circ) \sin(0^\circ)}{\cos(53.92^\circ)};$$

then,

$$a_s = 0^\circ.$$

We need to find out if a_s is greater than 90° .

For $L > \delta_s$,

$$t_E = 12:00 - \cos^{-1} \frac{(\tan \delta_s)}{\tan L} \frac{h}{15^\circ}$$

$$t_E = 12:00 - \cos^{-1} \frac{(\tan(0^\circ))}{\tan(36.08^\circ)} \frac{h}{15^\circ}$$

$$t_E = 6 \text{ h.}$$

Given that $ST > t_E$, the sun is south, and a_s . The air mass is calculated from

$$m = \frac{1}{\sin \alpha + 0.50572(6.07995 + \alpha^\circ)^{-1.6364}}$$

$$m = \frac{1}{\sin(53.92^\circ) + 0.50572(6.07995 + 53.92^\circ)^{-1.6364}}$$

$$m = 1.2363.$$

The data for Las Vegas Mccarran Intlp Ap, Nevada, are shown in the table below:

Data for Las Vegas Mccarran Intlp Ap, Nevada

Lat: 36.086°N Long: 115.16°W Elev: 665 m

Month	Jan	Feb	Mar	Apr	May	Jun	Jul	Aug	Sep	Oct	Nov	Dec
τ_b	0.314	0.333	0.355	0.382	0.404	0.412	0.55	0.56	0.407	0.38	0.317	0.304
τ_d	2.386	2.277	2.211	2.099	2.062	2.059	1.674	1.674	2.084	2.096	2.388	2.417
$I_{b,N}$, noon (W/m ²)	881	902	911	899	880	870	752	752	844	831	869	868
$I_{d,hv}$, noon (W/m ²)	99	119	136	159	166	167	243	243	152	139	97	92

Source: Data taken from ASHRAE. 2009. *Handbook of Fundamentals*. American Society of Heating Refrigeration and Air Conditioning Engineers, Atlanta, GA.

The pseudo optical depths are tabulated for the 21st day of each month for all the locations in the tables of climatic design. Values for other days of the year should be found by interpolation. For this example, by using linear interpolation between January and February, the pseudo optical depths are as follows:

$$\tau_b = 0.355$$

$$\tau_d = 2.211.$$

The parameters for air mass are as follows:

$$b = 1.219 - 0.043\tau_b - 0.151\tau_d - 0.204\tau_b\tau_d = 0.7097$$

$$d = 0.202 + 0.852\tau_b - 0.007\tau_d - 0.357\tau_b\tau_d = 0.2087.$$

The extraterrestrial solar radiation is given by (for March 21, $n = 80$)

$$I = I_0 \frac{D_0}{D}^2$$

$$x = \frac{360}{365} (80 - 1) = 77.91^\circ$$

$$\frac{D_0}{D}^2 = 1.00011 + 0.034221 \cos x + 0.00128 \sin x + 0.000719 \cos 2x + 0.000077 \sin 2x$$

$$\frac{D_0}{D}^2 = 1.0079.$$

Then,

$$I = 1366.1(1.0079) \frac{W}{m^2} = 1377 \frac{W}{m^2}.$$

The direct solar radiation component is

$$I_{b,N} = I e^{-\tau_b m^b}$$

$$I_{b,N} = 1377 \exp(-0.355 \times 1.2363^{0.7097}) = 911 \frac{W}{m^2}.$$

The diffuse solar radiation on a horizontal surface is

$$I_{d,h} = I e^{-\tau_d m^d}$$

$$I_{d,h} = 1377 \exp(-2.211 \times 1.2363^{0.2087}) = 137 \frac{W}{m^2}.$$

The instantaneous beam radiation on the surface per unit area is given by

$$I_{b,c} = I_{b,N} \cos i.$$

For this geometry, the cosine of the angle of incidence is

$$\cos i = \cos \alpha \cos(a_s - a_w) \sin \beta + \sin \alpha \cos \beta$$

$$\cos i = \cos(53.92^\circ) \cos(0^\circ) \sin(36.08^\circ) + \sin(53.92^\circ) \cos(36.08^\circ) = 1.0.$$

Then, the beam radiation is

$$I_{b,c} = 911(1.0) = 911 \frac{W}{m^2}.$$

The diffuse radiation on the collector surface is

$$I_{d,c} = I_{d,h} \cos^2(\beta/2)$$

$$I_{d,c} = 137 \cos^2(36.08^\circ/2) = 124 \frac{W}{m^2}.$$

The ground reflected solar radiation is

$$I_{r,c} = \rho(I_{b,N} \sin \alpha + I_{d,h}) \sin^2(\beta/2).$$

Assuming that the solar collector is surrounded by ordinary ground or grass, then $\rho \sim 0.2$

$$I_{r,c} = 0.2(911 \sin(53.92^\circ) + 137) \sin^2(36.08^\circ/2) = 17 \frac{\text{W}}{\text{m}^2}.$$

Finally, the total radiation on tilted collector surface is

$$I_c = I_{b,c} + I_{d,c} + I_{r,c}$$

$$I_c = 911 + 124 + 17 = 1052 \frac{\text{W}}{\text{m}^2}.$$

Solution by using CPRG

The sunset is given by

$$h_s = (ST - 12) \frac{15^\circ}{h} = (12 - 12) \frac{15^\circ}{h} = 0^\circ.$$

The ratio of hourly diffuse to the long-term average daily diffuse irradiation on a horizontal surface, r_d , is given by

$$r_d = \frac{\pi}{24} \frac{\cos h_s - \cos h_{ss}}{\sin h_{ss} - \frac{\pi}{180} h_{ss} \cos h_{ss}}$$

$$r_d = \frac{\pi}{24} \frac{\cos 0^\circ - \cos 90^\circ}{\sin 90^\circ - \frac{\pi}{180} 90^\circ \cos 90^\circ} = 0.1308.$$

The parameters a and b are as follows:

$$a = 0.409 + 0.5016 \sin(h_{ss} - 60^\circ)$$

$$a = 0.409 + 0.5016 \sin(90^\circ - 60^\circ) = 0.6598$$

$$b = 0.6609 - 0.4767 \sin(h_{ss} - 60^\circ)$$

$$b = 0.6609 - 0.4767 \sin(90^\circ - 60^\circ) = 0.8992$$

For CPRG, the ratio of hourly total to the long-term average daily total irradiation on a horizontal surface, r_t , is given by

$$r_t = \frac{I_h}{H_h} = \frac{a + b \cos h_s}{f_c} r_d$$

$$f_c = a + kb \frac{\pi}{180} h_{ss} - \frac{1}{2} \sin 2h_{ss} ,$$

with

$$k = 2 \sin h_{ss} - \frac{\pi}{180} h_{ss} \cos h_{ss}$$

$$k = 2 \sin 90^\circ - \frac{\pi}{180} 90^\circ \cos 90^\circ = 0.5.$$

Then,

$$f_c = 0.6598 + 0.5 \times 0.8992 \frac{\pi}{180} 90^\circ - \frac{1}{2} \sin 2 \times 90^\circ = 1.3660.$$

r_t is

$$r_t = \frac{0.6598 + 0.8992 \times \cos 0^\circ}{1.3660} \times 0.1308 = 0.1493.$$

The long-term average daily total and diffuse radiation are obtained from NASA-SSE (<http://eosweb.larc.nasa.gov/sse/>):

$$\bar{H}_h = 5.24 \frac{\text{kWh}}{\text{m}^2 \cdot \text{day}} \quad \bar{H}_d = 1.26 \frac{\text{kWh}}{\text{m}^2 \cdot \text{day}}$$

The beam radiation is

$$I_{b,c} = (r_t \bar{H}_h - r_d \bar{H}_d) \frac{\cos i}{\sin \alpha}$$

$$I_{b,c} = (0.1493 \times 5.24 - 0.1308 \times 1.26) \frac{1}{\sin 53.92^\circ} = 765 \frac{\text{W}}{\text{m}^2}.$$

The diffuse radiation on the collector surface is

$$I_{d,c} = r_d \bar{H}_d \cos^2(\beta/2)$$

$$I_{d,c} = 0.1308 \times 1.26 \cos^2(36.08^\circ/2) = 149 \frac{\text{W}}{\text{m}^2}.$$

The ground reflected solar radiation is

$$I_{r,c} = \rho r_t \bar{H}_h \sin^2(\beta/2)$$

$$I_{r,c} = 0.2 \times 0.1493 \times 5.24 \sin^2(36.08^\circ/2) = 15 \frac{\text{W}}{\text{m}^2}.$$

The total radiation on tilted collector surface is

$$I_c = I_{b,c} + I_{d,c} + I_{r,c}$$

$$I_c = 765 + 149 + 15 = 929 \frac{\text{W}}{\text{m}^2}.$$

Solution by using DI

The sunset is given by

$$h_s = (ST - 12) \frac{15^\circ}{h} = (12 - 12) \frac{15^\circ}{h} = 0^\circ.$$

The ratio of hourly diffuse to the long-term average daily diffuse irradiation on a horizontal surface, r_d , is given by

$$r_d = \frac{\pi}{24} \frac{\cos h_s - \cos h_{ss}}{\sin h_{ss} - \frac{\pi}{180} h_{ss} \cos h_{ss}}$$

$$r_d = \frac{\pi}{24} \frac{\cos 0^\circ - \cos 90^\circ}{\sin 90^\circ - \frac{\pi}{180} 90^\circ \cos 90^\circ} = 0.1308.$$

The daily-average extraterrestrial irradiation on a horizontal surface, H_o , may be calculated as a function of the solar constant, E_{sc} , as

$$H_o = \frac{24}{\pi} h_{ss} R E_{sc} \sin h_o,$$

with

$$E_{sc} = 1367 \text{ W/m}^2$$

$$R = (D_o/D)^2 = 1.0079$$

h_o is the daily average solar elevation outside of the atmosphere, defined by

$$\sin h_o = q A(h_{ss}) / h_{ss}$$

and

$$\begin{aligned} q &= \cos L \cos \delta_s = 0.8617 \\ A(h_{ss}) &= \sin h_{ss} - h_{ss} \cos h_{ss} = 1.0. \end{aligned}$$

Then,

$$\sin h_o = qA(h_{ss})/h_{ss} = 0.5485,$$

and

$$H_o = \frac{24}{\pi} h_{ss} R E_{sc} \sin h_o = 9.070 \text{ kWh/m}^2.$$

The long-term average daily total and diffuse radiation are obtained from NASA-SSE (<http://eosweb.larc.nasa.gov/sse/>):

$$\bar{H}_h = 5.24 \text{ kWh/m}^2 \cdot \text{day}$$

$$\bar{H}_d = 1.26 \text{ kWh/m}^2 \cdot \text{day}.$$

The daily average clearness index, K_t , is given by

$$K_t = \bar{H}_h / H_o = 0.5777.$$

The day length (in hours) is obtained as

$$S_o = \frac{24}{\pi} h_{ss} = 12 \text{ h}.$$

(a_2/a_1) represents the atmospheric extinction effect. a_1 and a_2 were obtained from a multiple least-squares fit:

$$a_1 = 0.41341 K_t + 0.61197 K_t^2 - 0.01886 K_t S_o + 0.00759 S_o = 0.4034$$

$$a_2 = \text{Max}\left(0.054, 0.28116 + 2.2475 K_t - 1.7611 K_t^2 - 1.84535 \sin h_o + 1.681 \sin^3 h_o\right) = 0.2569$$

$B(h_{ss})$ is defined as

$$B(h_{ss}) = \omega_s (0.5 + \cos^2 h_{ss}) - 0.75 \sin(2 h_{ss}) = 0.7853.$$

The ratio of the horizontal hourly radiation to the total horizontal daily radiation, r_t , is given by

$$r_t = r_d \frac{1 + q(90)A(h_{ss})r_d(24/\pi)}{1 + q(a_2/a_1)B(h_{ss})/A(h_{ss})}$$

$$r_t = 0.1416.$$

The beam radiation is

$$I_{b,c} = (r_t \bar{H}_h - r_d \bar{H}_d) \frac{\cos i}{\sin \alpha}$$

$$I_{b,c} = (0.1416 \times 5.24 - 0.1308 \times 1.26) \frac{1}{\sin 53.92^\circ} = 711 \frac{W}{m^2}.$$

The diffuse radiation on the collector surface is

$$I_{d,c} = r_d \bar{H}_d \cos^2(\beta/2)$$

$$I_{d,c} = 0.1308 \times 1.26 \cos^2(36.08^\circ/2) = 149 \frac{W}{m^2}.$$

The ground reflected solar radiation is

$$I_{r,c} = \rho r_t \bar{H}_h \sin^2(\beta/2)$$

$$I_{r,c} = 0.2 \times 0.1416 \times 5.24 \sin^2(36.08^\circ/2) = 14 \frac{W}{m^2}.$$

The total radiation on tilted collector surface is

$$I_c = I_{b,c} + I_{d,c} + I_{r,c}$$

$$I_c = 711 + 149 + 14 = 874 \frac{W}{m^2}.$$

Example 2.11

Calculate the monthly average normal beam radiation for Jaipur, India (Vasquez-Padilla 2011).

Solution

For Jaipur: Lat = 26°55'N and Long = 75°49'E

The input data are as follows:

Jaipur, India

Month	\bar{H}_h^a (kWh/m ² ·day)	\bar{H}_d^b (kWh/m ² ·day)
Jan	4.00	1.01
Feb	4.71	1.27
Mar	5.46	1.64
Apr	6.11	1.97
May	6.38	2.22
Jun	6.24	2.36
Jul	5.09	2.47
Aug	4.71	2.30
Sep	5.12	1.90
Oct	4.79	1.44
Nov	4.16	1.08
Dec	3.74	0.95
Annual	5.04	1.72

Source: Data taken from <http://eosweb.larc.nasa.gov/sse/>.

a Mean monthly global solar radiant exposure.

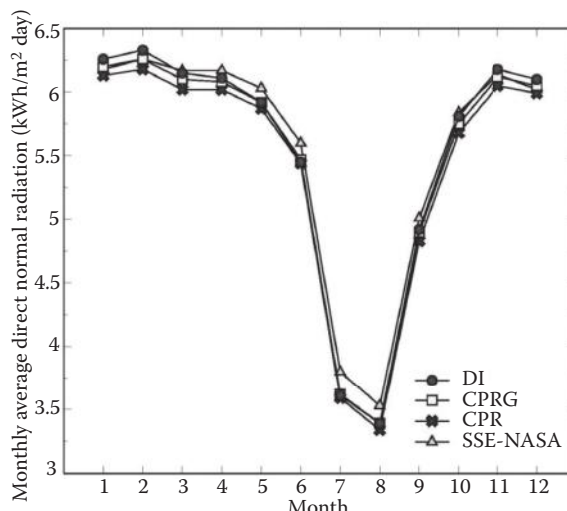
b Mean monthly diffuse solar radiant exposure.

The monthly average normal beam radiation is calculated by

$$\bar{H}_{b,N} = \int_{-t_s}^{t_s} r_t \bar{H}_h - r_d \bar{H}_d \frac{\cos i}{\sin \alpha} dt.$$

The results obtained for CPR, CPRG, and DI are as follows:

Results for Jaipur, India



2.6.4 Spectral Models

Many biological, chemical, and physical processes are activated more powerfully at some wavelengths than at others. Therefore, it is important to know the spectral characteristics of the incident radiation. In order to model spectral solar radiation at a location, radiation needs to be modeled as it travels through the atmosphere. These models are complex to begin with and are made more complex since different wavelengths are absorbed, reflected, and scattered differently in the atmosphere. Examples of radiative transfer numerical model include the Santa Barbara DISORT, atmospheric radiative transfer code (SBDART), and the moderate resolution transmission code MODTRAN. SBDART, developed at the University of California at Santa Barbara, is relatively simpler to use than MODTRAN, is freely accessible, and even has a convenient user interface online (<http://arm.mrcsb.com/sbdart/>).

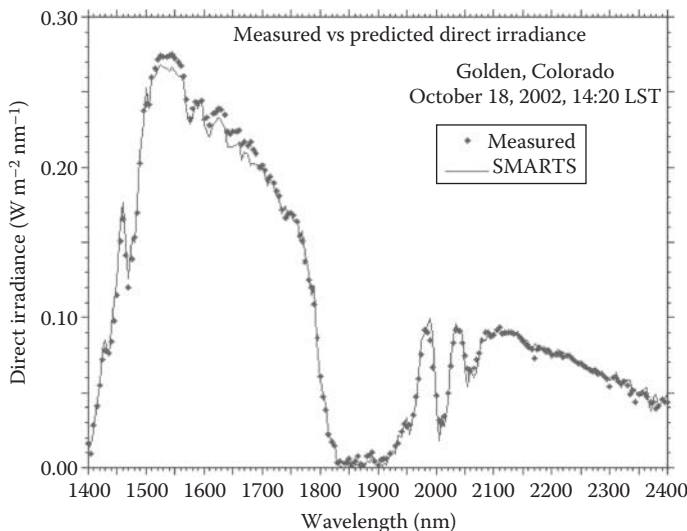
MODTRAN, developed by the Air Force Geophysical Laboratory, has a much higher resolution and is considered as the standard in atmospheric applications.

These models, however, are not convenient for solar energy or other engineering-type applications.

Bird's simple spectral model (SPCTRAL2), the spectral model of the atmospheric radiative transfer of sunshine (SMARTS), and REST2 can be used for solar engineering applications. Even though these models are limited to clear-sky conditions, they can also be empirically modified to predict spectra under cloudy conditions. The SMARTS model offers fast and accurate predictions of spectral irradiance on any tilted surface without the difficulties and limitations associated with the atmospheric models mentioned above. Sample outputs produced by SMARTS, compared with actual spectroradiometric measurements from high-performance instruments, are shown in Figures 2.25 and 2.26.

2.7 Measurement of Solar Radiation

Solar radiation measurements of importance to most engineering applications, especially thermal applications, include total (integrated over all wavelengths) direct or beam and sky diffuse values of solar radiation on instantaneous, hourly, daily, and monthly bases. Some applications such as photovoltaics, photochemical, and daylighting require knowledge of spectral (wavelength specific) or band (over a wavelength range—e.g., ultraviolet, visible, infrared) values of solar radiation. This section describes some of the instrumentation used to measure solar radiation and sunshine and some sources of long-term measured data for different parts of the world. Also described briefly in this section is the method of satellite-based measurements.

**FIGURE 2.25**

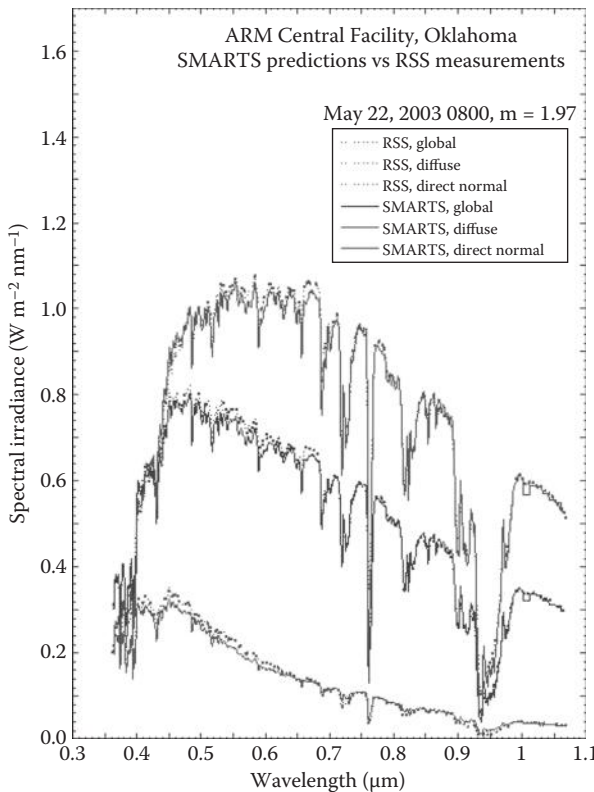
A sample spectral irradiance prediction compared with measured data for Golden, Colorado. (Taken from <http://www.solarconsultingservices.com/smarts.php>.)

2.7.1 Instruments for Measuring Solar Radiation and Sunshine

There are two basic types of instruments used to measure solar radiation, *pyranometer* and *pyrheliometer*. A pyranometer has a hemispherical view of the surroundings and therefore is used to measure total, direct, and diffuse solar radiation on a surface. A pyrheliometer, on the other hand, has a restricted view (approximately 5°) and is, therefore, often used to measure the direct or beam solar radiation by pointing it toward the sun. Pyranometers are also used to measure the sky diffuse radiation by using a shadow band to block the direct sun view. A detailed discussion of the instrumentation and calibration standards is given by Iqbal (1983) and Zerlaut (1989).

A pyranometer consists of a flat sensor/detector (described later) with an unobstructed hemispherical view, which allows it to convert and correlate the total radiation incident on the sensor to a measurable signal. The pyranometers using thermal detectors for measurements can exhibit serious errors at tilt angles from the horizontal owing to free convection. These errors are minimized by enclosing the detector in double hemispherical high-transmission glass domes. The second dome minimizes the error attributed to infrared radiative exchange between the sensor and the sky. A desiccator is usually provided to eliminate the effect of condensation on the sensor or the dome. Figure 2.27 shows pictures of typical commercially available precision pyranometers.

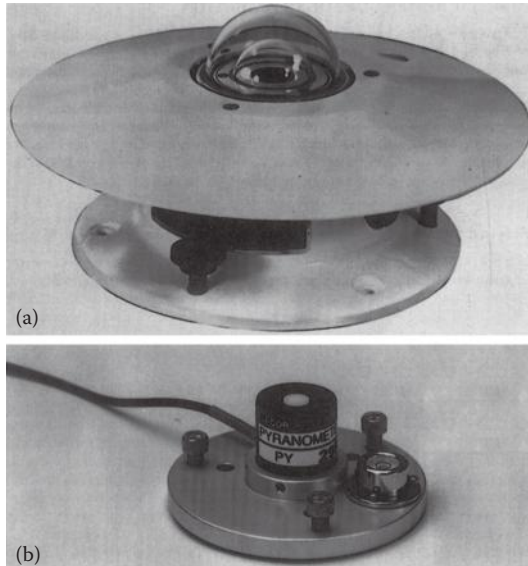
A pyranometer can be used to measure the sky diffuse radiation by fitting a shade ring to it, as shown in Figure 2.28, in order to block the beam

**FIGURE 2.26**

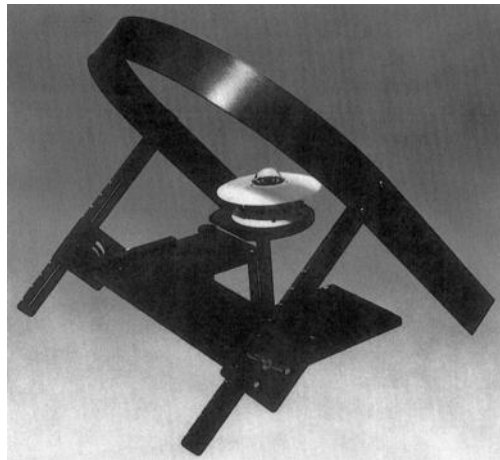
A sample prediction for direct normal, diffuse and global horizontal spectral irradiance. (Taken from <http://www.solarconsultingservices.com/smarts.php>.)

radiation throughout the day. The position of the shade ring is adjusted periodically as the declination changes. Since the shade ring obstructs some diffuse radiation from the pyranometer, correction factors must be applied.

Geometric correction factors (GCFs) that account for the part of the sky obstructed by the shade ring can be easily calculated. However, a GCF assumes isotropic sky, which results in errors because of the circumsolar anisotropy. Eppley Corp. recommends the following additional correction factors to account for anisotropy: +7% for clear sky, +4% for partly cloudy condition, and +3% for cloudy sky. Mujahid and Turner (1979) determined that these correction factors gave less than 3% errors on partly cloudy days but gave errors of -11% for clear-sky conditions and +6% on overcast days. They suggested correction factors owing to anisotropy as tabulated in Table 2.3, which reduce the errors to less than $\pm 3\%$. It must be remembered that these correction factors are in addition to the GCFs. Recently, a sun occulting disk has been employed for shading the direct sun.

**FIGURE 2.27**

Typical commercially available pyranometers with (a) thermal detector and (b) photovoltaic detector.

**FIGURE 2.28**

A pyranometer with a shade ring to measure sky diffuse radiation.

Beam or direct solar radiation is usually measured with an instrument called a pyrheliometer. Basically, a pyrheliometer places the detector at the base of a long tube. This geometry restricts the sky view of the detector to a small angle of approximately 5° . When the tube points toward the sun, the detector measures the beam solar radiation and a small part of the diffuse

TABLE 2.3

Shading Band Correction Factors Owing to Anisotropy

Solar Altitude	k_T									
Angle	0	0.1	0.2	0.3	0.4	0.5	0.6	0.7	0.8	0.9
<20°	0.0	0.0	0.0	0.0	0.015	0.06	0.14	0.23	0.24	0.24
20° to 40°	0.0	0.0	0.0	0.0	0.006	0.05	0.125	0.205	0.225	0.225
40° to 60°	0.0	0.0	0.0	0.0	0.003	0.045	0.115	0.175	0.205	0.205
>60°	0.0	0.0	0.0	0.0	0.0	0.035	0.09	0.135	0.17	0.17

Source: Mujahid, A. and Turner, W.D., Diffuse sky measurement and model. ASME Pap. no. 79-WA/Sol-5, 1979.

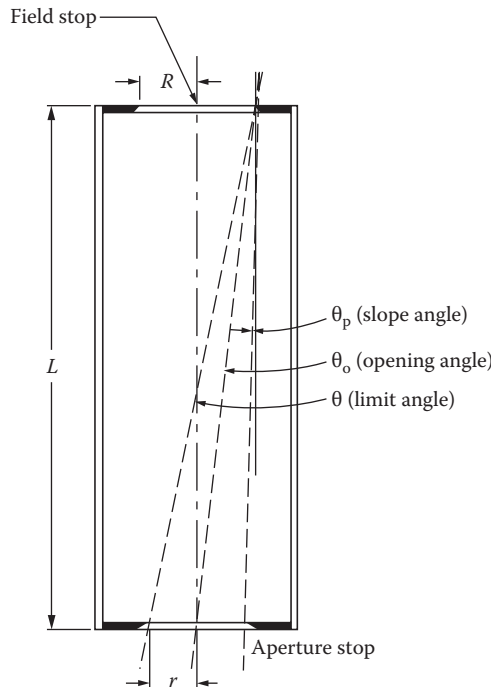
solar radiation within the view angle. Figure 2.29 shows the geometry of a pyrheliometer sky occulting tube.

In this figure, the opening half angle is

$$\theta_o = \tan^{-1} R/L. \quad (2.83)$$

The slope angle is

$$\theta_p = \tan^{-1}[(R - r)/L]. \quad (2.84)$$

**FIGURE 2.29**

Geometry of a pyrheliometer sky occulting tube.

The limit half angle is

$$\theta = \tan^{-1}[(R + r)/L]. \quad (2.85)$$

The field of view is $2\theta_0$. The World Meteorological Organization (WMO) recommends the opening half angle θ_0 to be 2.5° (Zerlaut 1989) and the slope angle θ_p to be 1° .

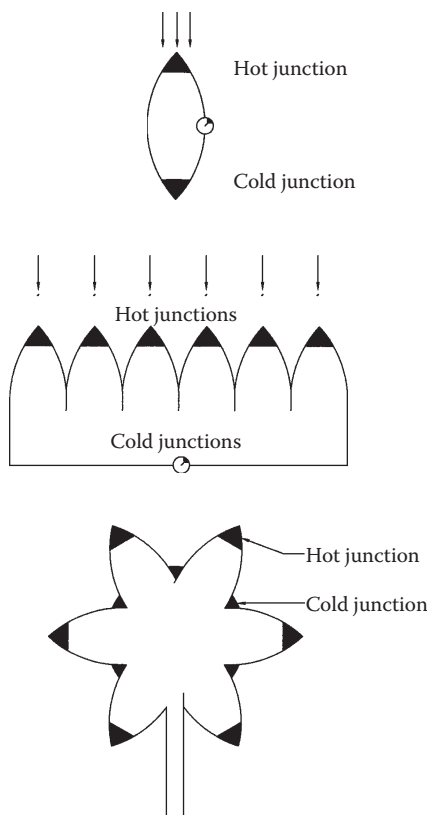
Continuous tracking of the sun is required for the accuracy of the measurements. This is obtained by employing a tracking mechanism with two motors, one for altitude and the other for azimuthal tracking. Another problem is that the view angle of a pyrheliometer is significantly greater than the angle subtended by the solar disk (approximately 0.5°). Therefore, the measurements using a pyrheliometer include the beam and the circumsolar radiation. These measurements may present a problem in using the data for central receiver systems that use only direct beam radiation. However, this is not a significant problem for parabolic trough concentrators that, in most cases, have a field of view of the order of 5° .

2.7.2 Detectors for Solar Radiation Instrumentation

Solar radiation detectors are of four basic types (Iqbal 1983; Zerlaut 1989): thermomechanical, calorimetric, thermoelectric, and photoelectric. Of these, thermoelectric and photoelectric are the most common detectors in use today.

A *thermoelectric detector* uses a thermopile that consists of a series of thermocouple junctions. The thermopile generates a voltage proportional to the temperature difference between the hot and cold junctions, which, in turn, is proportional to the incident solar radiation. Figure 2.30 shows different types of thermopile configurations. The Eppley black and white pyranometer uses a radial differential thermopile with the hot junction coated with 3M Velvet Black and the cold junction coated with a white barium sulfate paint.

Photovoltaic detectors normally use silicon solar cells measuring the short circuit current. Such detectors have the advantage of being simple in construction. Because heat transfer is not a consideration, they do not require clear domes or other convection suppressing devices. They are also insensitive to tilt as the output is not affected by natural convection. One of the principal problems with photovoltaic detectors is their spectral selectivity. Radiation with wavelengths greater than the band gap of the photovoltaic detector cannot be measured. Silicon has a band gap of 1.07 eV corresponding to a wavelength of $1.1 \mu\text{m}$. A significant portion of the infrared part of solar radiation has wavelengths greater than $1.1 \mu\text{m}$. Therefore, photovoltaic detectors are insensitive to changes in the infrared part of solar radiation.

**FIGURE 2.30**

Various thermopile configurations. (From Zerlaut, G., Solar radiation instrumentation. In *Solar Resources*, R.L. Hulstrom, ed., Cambridge, MA: MIT Press, 1989.)

2.7.3 Measurement of Sunshine Duration

The time duration of bright sunshine data is available at many more locations in the world than the solar radiation. That is why a number of researchers have used these data to estimate the available solar radiation. Two instruments are widely used to measure the sunshine duration. The device used by the US National Weather Service is called a *sunshine switch*. It is composed of two photovoltaic cells—one shaded, the other not. During daylight, a potential difference is created between the two cells, which in turn operates a recorder. The intensity level required to activate the device is that just sufficient to cast a shadow. The other device commonly used to measure the sunshine duration is called the *Campbell–Stokes sunshine recorder*. It uses a solid, clear glass sphere as a lens to concentrate the solar beam on the opposite side of the sphere. A strip of standard treated paper marked with time graduations is mounted on the opposite side of the sphere where the solar



FIGURE 2.31
Campbell-Stokes sunshine recorder.

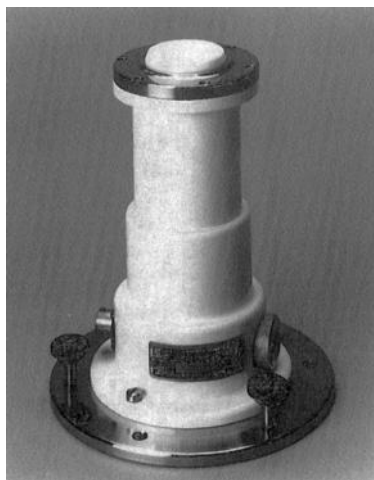
beam is concentrated. Whenever the solar radiation is above a threshold, the concentrated beam burns the paper. The length of the burned part of the strip gives the duration of bright sunshine. The problems associated with the Campbell-Stokes sunshine recorder include the uncertainties of the interpretation of burned portions of the paper, especially on partly cloudy days, and the dependence on the ambient humidity. Figure 2.31 shows a Campbell-Stokes sunshine recorder.

2.7.4 Measurement of Spectral Solar Radiation

Spectral solar radiation measurements are made with spectroradiometers. Full spectrum scanning is difficult, requires constant attention during operation, and is therefore expensive. Zerlaut (1989) has described a number of solar spectroradiometers. These instruments consist basically of a monochromator, a detector-chopper assembly, an integrating sphere, and a signal conditioning/computer package. They have the capability of measuring solar radiation in the wavelength spectrum of 280–2500 nm.

2.7.5 Wide Band Spectral Measurements

Some applications of solar energy require solar radiation data in wide band wavelength ranges such as visible, ultraviolet, and infrared rather than

**FIGURE 2.32**

Eppley TUVR Total UV Radiometer. (Courtesy of Eppley Lab.)

complete spectral data. For example, solar photocatalytic detoxification using TiO_2 as the catalyst needs data in the UV wavelength range while passive solar applications need data in the infrared wavelength range. Instruments such as pyranometers and pyrheliometers can be adapted for wide band spectral measurements by using cut-on and cut-off filters. Eppley instruments provide standard cut-off filters at the following wavelengths: 530 nm (orange), 630 nm (red), and 695 nm (dark red). They are provided as plain filters at the aperture of a pyrheliometer tube and as outer glass domes for pyranometers. Instrument manufacturers provide various interference filters peaking at different wavelengths in the solar spectrum.

Solar UV measurements are important in general since prolonged exposure to solar UV can cause skin cancer, fading of colors, and degradation of plastic materials. Such measurements have become even more important because the photocatalytic effect based on TiO_2 as a catalyst depends only on the solar UV wavelength range. Figure 2.32 shows an Eppley Model TUVR (total ultraviolet radiometer) that measures total hemispherical UV radiation from 295 to 385 nm. This radiometer uses a selenium photoelectric cell detector, a pair of band-pass filters to allow wavelengths from 295 to 385 nm to pass through, and a beveled teflon diffuser.

2.7.6 Solar Radiation Data

Measured solar radiation data are available at a number of locations throughout the world. Data for many other locations have been estimated based on measurements at similar climatic locations. Some of the available data from various locations in the world are presented in Appendix 2 (Tables A2.3a

and A2.3b). This Appendix also provides tables of modeled clear-sky data for various latitudes (Table A2.6).

Solar radiation data for the United States are available from the National Climatic Data Center of the National Oceanic and Atmospheric Administration (NOAA) and the National Renewable Energy Laboratory (NREL). In the mid-1970s, NOAA compiled a database of measured hourly global horizontal solar radiation for 28 locations for the period 1952–1975 (called SOLMET) and of data for 222 additional sites (called ERSATZ) estimated from SOLMET data and some climatic parameters such as sunshine duration and cloudiness. NOAA also has two data sets of particular interest to engineers and designers: the typical meteorological year (TMY) and the Weather Year for Energy Calculations (WYEC) data sets. The TMY data set represents typical values from 1952 to 1975 for hourly distribution of direct beam and global horizontal solar radiation. The WYEC data set contains monthly values of temperature, direct beam and diffuse solar radiation, and estimates of *illuminance* (for daylighting applications). Illuminance is solar radiation in the visible range to which the human eye responds. Recently, NREL compiled a National Solar Radiation Data Base (NSRDB) for 239 stations in the United States (Maxwell 1998; NSRDB 1992). NSRDB is a collection of hourly values of global horizontal, direct normal, and diffuse solar radiation based on measured and estimated values for the period 1961–1990. Since long-term measurements were available for only approximately 50 stations, measured data make up only approximately 7% of the total data in the NSRDB. A typical meteorological year data set from NSRDB is available as TMY2.

The data for other locations in the world are available from national government agencies of most countries of the world. Worldwide solar radiation data are also available from the World Radiation Data Center (WRDC) in St. Petersburg, Russia, based on worldwide measurements made through local weather service operations (Voeikov Main Geophysical Observatory 1999). WRDC, operating under the auspices of the WMO, has been archiving data from over 500 stations and operates a worldwide website in collaboration with NREL (<http://wrdc.mgo.nrel.gov>). Data for some cities of the world from WRDC are given in Appendix 2 (Table A2.3). An International Solar Radiation Data Base was also developed by the University of Lowell (University of Lowell Photovoltaic Program 1990).

- Surface Meteorology and Solar Energy (Version 6.0) [<http://eosweb.larc.nasa.gov/sse/>]
- Energy Plus Energy Weather Data [http://apps1.eere.energy.gov/buildings/energyplus/weatherdata_about.cfm?CFID=5019287&CFTOKEN=b54041e7be537f1f-B598302C-5056-BC19-15C492F462EE1BAC]
- National Solar Radiation Data Base, 1961–1990: Typical Meteorological Year [http://rredc.nrel.gov/solar/old_data/nsrdb/] [<http://rredc.nrel.gov/solar/pubs/NSRDB/>]

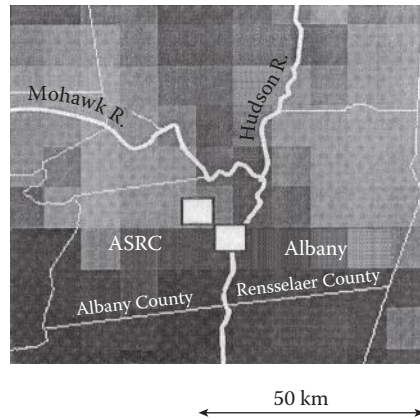
- National Solar Radiation Data Base, 1991–2005 Update: Typical Meteorological Year 3 [http://rredc.nrel.gov/solar/old_data/nsrdb/] [<http://www.nrel.gov/docs/fy12osti/54824.pdf>]
 - The Solar and Wind Energy Resource Assessment (SWERA) [[http://en.openei.org/wiki/Solar_and_Wind_Energy_Resource_Assessment_\(SWERA\)](http://en.openei.org/wiki/Solar_and_Wind_Energy_Resource_Assessment_(SWERA))]
 - National Renewable Laboratory (NREL) [<http://www.nrel.gov/>]
-

2.8 Solar Radiation Mapping Using Satellite Data

Remote sensing satellite data have been used since the early 1960s to extract quantitative and qualitative cloud data. The most important application of cloud cover mapping has been for the observation of storms, hurricanes, and so on. Recently, however, considerable interest has been developed in using the cloud mapping data to estimate terrestrial solar radiation. Since meteorological satellites from a number of countries can now cover most of the earth, the data can be used to estimate solar radiation where no measured data exist or none is being measured.

Weather satellites are available in three main orbiting configurations—equatorial, polar, and geostationary. The equatorial satellites are low-level orbiting satellites (~600 km altitude) that generally orbit the earth in a west-to-east direction in a sinusoidal path that crosses the equator at least twice per orbit. Polar satellites are also low-orbit satellites that orbit the earth from the North Pole to the South Pole while the earth rotates underneath. Sun synchronous polar orbits have their orbits synchronized with the sun such that the same point on the earth is viewed at the same time each day. Low-orbit satellites are capable of gathering high-resolution spatial data. A geostationary satellite orbits in such a way that it is always over the same point on the earth's surface. Geostationary satellites have very high altitudes (approximately 36,000 km) and can provide high temporal resolution images over a large portion of the earth's surface. A number of countries maintain geostationary satellites including the United States (GOES, longitudes 70°W and 140°W), Europe (METEOSAT, longitude 0°), India (INSAT, longitude 70°E), and Japan (GMS, longitude 140°E).

Various types of high-resolution radiometers collect radiative data images of the earth's atmosphere below. These radiometers scan spectral measurements in the wavelength ranges of shortwave (0.2–3.0 μm), longwave (6.5–25 μm), and total irradiance (0.2–100 μm). The spatial resolution of images from the satellite is given by a *pixel*, which represents the smallest area of data, generally of the order of 2 km × 2 km. However, several pixels of data are required to derive a surface value giving a surface resolution of

**FIGURE 2.33**

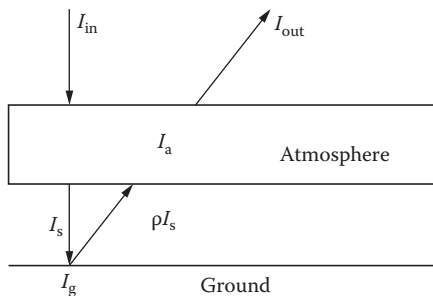
GOES-8 Intermediate resolution image close-up around Albany. (From Perez, R. et al., The strengths of satellite based resource assessment. *Proc. of the 1997 ASES Annual Conf*, pp. 303–308, Washington, DC, 1997.)

the order of $10 \text{ km} \times 10 \text{ km}$. Figure 2.33 shows an example of an intermediate resolution GOES-8 image around Albany, New York, overlaid on a local map.

2.8.1 Estimation of Solar Resource from Satellite Data

The signal recorded by a radiometer on a satellite measures the solar radiation flux reflected back from the earth's atmosphere. The basic method behind estimation of ground solar radiation from these data is to apply the principle of energy conservation in the earth-atmosphere system (Noia et al. 1993), as shown in Figure 2.34. From this figure, we can write

$$I_{\text{in}} = I_{\text{out}} + I_a + I_g \quad (2.86)$$

**FIGURE 2.34**

Solar radiation in the earth-atmosphere model.

where I_{in} represents the solar radiation incident on the atmosphere, I_{out} represents the outward radiation from the atmosphere, I_a is the radiation absorbed by the atmosphere, and I_g is the radiation absorbed by the ground.

I_g can be expressed in terms of the surface albedo* ρ (reflectivity) and the solar radiation I_s , incident on the earth's surface:

$$I_g = I_s(1 - \rho). \quad (2.87)$$

From Equations 2.82 and 2.83, we can obtain

$$I_s = (I_{\text{in}} - I_{\text{out}} - I_a)/(1 - \rho). \quad (2.88)$$

I_{out} is measured by the satellite radiometers. I_{in} depends on the sun-earth distance and the solar zenith angle and can be calculated using Equation 2.32 as

$$I_{\text{in}} = I_0(D_0/D)^2 \cdot \cos(z). \quad (2.89)$$

If we could estimate I_a , and ρ were known a priori, I_s could be estimated using Equation 2.88 from the value of I_{out} measured by a satellite. However, I_a cannot be estimated easily since it depends on the atmospheric conditions such as cloud cover, dust particles, and air mass, and surface albedo (reflectance) ρ varies for every point of the region under consideration. In order to deal with these factors, two types of empirical methods are under development. These are known as statistical and physical methods. These methods have been reviewed in detail by Schmetz (1989), Hay (1993), Noia et al. (1993), Islam (1994), and Pinker et al. (1995).

Statistical Methods. Statistical methods are based on finding a relationship between the radiative flux measured by a satellite radiometer and the simultaneous solar radiation value measured at the earth's surface in the area under consideration. Some of the models developed on statistical approach include those by Hay and Hanson (1978), Tarpley (1979), Justus et al. (1986), Cano et al. (1986), and Sorapipatana et al. (1988).

Physical Methods. Physical methods are based on the analysis of radiative processes in the atmosphere as the solar radiation passes through it. Some of the models developed with this approach include those by Gautier (1980), Moeser and Raschke (1984), Dedieu et al. (1987), and Marullo et al. (1987).

The simplest of the above models is by Hay and Hanson (1978), which gives the atmospheric transmittance T as

$$T = \frac{I_s}{I_{\text{in}}} = a - b \frac{I_{\text{out}}}{I_{\text{in}}}, \quad (2.90)$$

or $I_s = aI_{\text{in}} - bI_{\text{out}}.$

* The term *albedo* is used mostly in the field of meteorology.

The values of regression coefficients given by Hay and Hanson (1978) are as follows: $a = 0.79$, $b = 0.71$. This method is simple; however, the coefficients, particularly b , vary considerably with parameters such as cloud reflectivity. More recent investigations suggest that it is necessary to determine coefficients a and b for different locations.

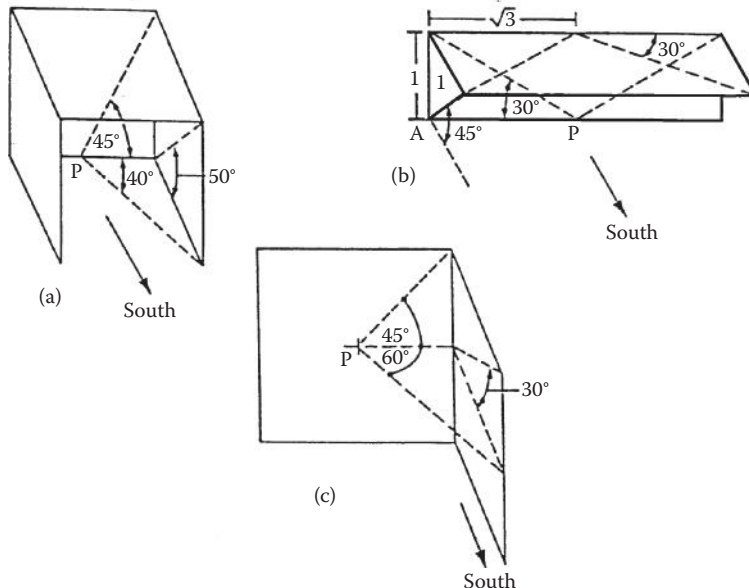
It is beyond the scope of this book to discuss all the models. It suffices, however, to point out that all the models, including the Hay and Hanson model, more or less give values within 10% of the ground measured values (Noia et al. 1993). The methods usually break down under partly cloudy conditions and under snow-covered ground conditions.

PROBLEMS

1. Spectroscopists make use the concept of wavenumber, $\tilde{\nu}$ (number of waves per unit length, $\tilde{\nu} = 1/\lambda$, to study the spectral absorption, emission, etc., of electromagnetic radiation).
 - a. For radiation in a vacuum ($n = 1$), derive an alternative form of the Planck distribution (Equation 2.3) in terms of wavenumber.
 - b. Using the results of part A, show that Wien's displacement law (Equation 2.5) can be alternatively expressed as $\tilde{\nu} = 1.93 T \text{ cm}^{-1}\text{K}$ ($3.47 \text{ cm}^{-1}\text{R}$).
2. Calculate the declination, the zenith angle, and the azimuth angle of the sun for New York City (latitude 40.77°N) on October 1 at 2:00 p.m. solar time.
3. A solar energy system in Tampa, Florida, requires two rows of collectors facing south and tilted at a fixed 30° angle. Find the minimum normalized distance at which the second row should be placed behind the first row for no shading at noon solar time at winter solstice. What percentage of the second row is shaded on the same day at 9:00 a.m. solar time?
4. Find the sunrise and sunset times for a location of your choice on September 1.
5. Construct a table of hourly sun angles for the 15th day of each month for a location of your choice. Also show the sunrise and sunset times for those days.
6. Referring to Figure 2.21, prove Equation 2.48 for the angle of incidence. (Hint: use direction cosines of the sun-ray vector and a vector normal to the tilted surface to find the angle between them. The dot product of two unit vectors gives the cosine of the angle between them.)
7. Show that the angle of incidence for a south-facing cylindrical surface (e.g., a tubular detector) can be obtained from the equation \cos^2

$i = 1 - [(\sin(\beta - L) \cos \delta_s \cos h_s + \cos(\beta - L) \sin \delta_s)]^2$. (Hint: integrate over the surface of the cylinder.)

8. Determine the following for a south-facing surface at 30° slope in Tampa, Florida (latitude = 27.97°N , longitude = 82.46°W) on September 21 at noon solar time:
 - a. Zenith angle
 - b. Angle of incidence
 - c. Beam radiation
 - d. Diffuse radiation
 - e. Reflected radiation
 - f. Total radiation
 - g. Local time
9. Show that the hourly averaged, extraterrestrial radiation for a given hour is the same, to within 1%, as instantaneous radiation at the hour's midpoint.
10. Prepare shadow maps for point P on the sun-path diagrams for 35°N and 40°N for the three geometries shown in (a), (b), and (c) below. Determine the hours of shading that occur each month.



11. Repeat Problem 10c if the surface containing point P faces due west instead of due south for a 40°N location.

12. Calculate the incidence angle at noon and 9 a.m. solar time on a fixed, south-facing flat-plate collector located at 40°N latitude and tilted 70° up from the horizontal. Find i for June 21 and December 21.
13.
 - a. If the surface in Problem 12 faces S 45°E , what are the incidence angles?
 - b. Using the results of Problem 7, determine the incidence angles for the collector in Problem 12 if it had a cylindrical surface.
14. Using a one-term Fourier cosine series, develop an empirical equation for solar declination as a function of day number counted from January 1 (see Figures 2.8 and 2.9).
15. Derive an equation for the lines of constant declination in a sun-path diagram, for example, Figure 2.12. Check your equation by plotting a few declination lines on a piece of polar coordinate graph paper.
16. Derive Equation 2.31 relating profile angle γ to azimuth angle α and altitude angle α .
17. Based on Equation 2.48, what value of β would result in the annual minimum value of the incidence angle i ? Note that this tilt angle would result in maximum collection of beam radiation on a fixed, flat, south-facing surface. (Hint: use a double integration procedure.)
18. At what time does the sun set in Calcutta (23°N) on May 1 and December 1?
19. What is the true solar time in Sheridan, Wyoming (107°W) at 10:00 a.m. Mountain Daylight Time on June 10? What is the true solar time at 10:00 a.m. Mountain Standard Time on January 10?
20. Using the Angström–Page method, calculate the average horizontal insolation in Miami, Florida, in May and in October with \bar{P}_S 60% and 70%, respectively. Compare these results to the predicted value for the 15th days of those months obtained from the ASHRAE Clear Sky Model.
21. Equation 2.55 is based on an early solar constant value of 1394 W/m^2 . Derive a modified form of Equation 2.55 based on a solar constant of 1366.1 W/m^2 .
22. Predict the hourly beam and diffuse radiation on a horizontal surface for Denver (40°N) on September 9 at 9:30 a.m. on a clear day.
23. Derive an expression for the minimum allowable distance between east–west rows of solar collectors that will assure no shading of one row by the row immediately to the south. Use the law of sines and express the result in terms of the collector tilt and face length and the controlling value of the solar profile angle.

References

- Akinoglu, B.G., and A. Ecevit. 1990. Construction of a quadratic model using modified angstrom coefficients to estimate global solar radiation. *Sol. Energy* 45: 85.
- ASHRAE. 2009. *Handbook of Fundamentals*. American Society of Heating, Refrigeration and Air Conditioning Engineers, Atlanta, GA.
- Cano, D. et al. 1986. Method for the determination of the global solar radiation from meteorological satellite data. *Sol. Energy* 37(1): 31–39.
- Choudhury, N.K.O. 1963. Solar radiation at New Delhi. *Sol. Energy* 7(44).
- Collares-Pereira, M., and A. Rabl. 1979. The average distribution of solar radiation—correlation between diffuse and hemispherical. *Sol. Energy* 22: 155–166.
- Coppolino, S. 1994. New correlation between clearness index and relative sunshine. *Renew. Energ.* 4(4): 417–423.
- Dedieu, G., P.Y. Deschamps, and Y.H. Kerr. 1987. Satellite estimation of solar irradiance at the surface of the earth and of surface albedo using a physical model applied to METEOSAT data. *J. Clim. Appl. Meteorol.* 26: 79–87.
- Frohlich, C. et al. 1973. The third international comparison of pyrheliometers and a comparison of radiometric scales. *Sol. Energy* 14: 157–166.
- Garg, H.P., and S.N. Garg. 1985. Correlation of the monthly average daily global, diffuse and beam radiation with bright sunshine hours. *Energy Convers. Manage.* 25(4): 409–417.
- Gautier, C. 1980. Simple physical model to estimate solar radiation at the surface from GOES satellite data. *J. Appl. Meteorol.* 19(8): 1005–1012.
- Gopinathan, K. 1988. A general formula for computing the coefficients of the correlation connecting global solar radiation to sunshine duration. *Sol. Energy* 41: 499.
- Gueymard, C. 1986. Mean daily averages of beam radiation received by tilted surfaces as affected by the atmosphere. *Sol. Energy* 37: 262–267.
- Gueymard, C. 2000. Prediction and performance assessment of mean hourly global radiation. *Sol. Energy* 68: 285–303.
- Gueymard, C.A. 2005. SMARTS code, version 2.9.5 User's Manual. Solar Consulting Services. Available at: <http://www.solarconsultingservices.com/smarts.php>.
- Gueymard, C.A. 2008. REST2: High performance solar radiation model for cloudless-sky irradiances, illuminance and photosynthetically active radiation; Validation with a benchmark dataset. *Sol. Energy* 82: 272–285.
- Gueymard, C.A., and D. Thevenard. 2009. Monthly average clear-sky broadband irradiance database for worldwide solar heat gain and building cooling load calculations. *Sol. Energy* 83: 1998–2018.
- Hay, J.E. 1993. Satellite based estimates of solar irradiance at the earth's surface: I. Modelling approaches. *Renew. Energ.* 3: 381–393.
- Hay, J.E., and K.J. Hanson. 1978. A satellite-based methodology for determining solar irradiance at the ocean surface during GATE. *Bull. Am. Meteorol. Soc.* 59: 1549.
- Howell, J.R., and R. Siegel. 1992. *Thermal Radiation Heat Transfer*. McGraw-Hill Book Co, New York.
- Hussain, M. 1994. Estimation of the global and diffuse irradiation from sunshine duration and atmospheric water vapor content. *Sol. Energy* 33(2): 217–220.
- Iqbal, M. 1979. Correlation of average diffuse and beam radiation with hours of bright sunshine. *Sol. Energy* 23: 169–173.

- Iqbal, M. 1983. *An Introduction to Solar Radiation*. Academic Press, New York.
- Islam, M.R. 1994. Evolution of methods for solar radiation mapping using satellite data. *RERIC Int. Energ.* J. 16(2).
- Justus, C., M.V. Paris, and J.D. Tarpley. 1986. Satellite-measured insolation in the United States, Mexico and South America. *Remote Sens. Environ.* 20: 57–83.
- Kasten, F., and A.T. Young. 1989. Revised optical air mass tables and approximation formula. *Appl. Optics* 28: 4735–4738.
- Klucher, T.M. 1979. Evaluation of models to predict insolation on tilted surfaces. *Sol. Energy* 23(2): 111–114.
- Kreith, F., and M. Bohm. 1993. *Principles of Heat Transfer*, 5th ed. West Publishing Co, St. Paul, MN.
- Liu, B.Y.H., and R.C. Jordan. 1960. The interrelationship and characteristic distribution of direct, diffuse and total solar radiation. *Sol. Energy* 4: 1–19. See also Liu, B.Y.H. 1960. Characteristics of solar radiation and the performance of flat plate solar energy collectors. PhD dissertation, University of Minnesota, Minneapolis, MN.
- Liu, B.Y.H., and R.C. Jordan. 1961a. Daily insolation on surfaces titled toward the equator. *Trans. ASHRAE* 67: 526–541.
- Liu, B.Y.H., and R.C. Jordan. 1961b. Daily insolation on surface titled toward the equator. *Trans. ASHRAE* 3(10): 53–59.
- Liu, B.Y.H., and R.C. Jordan. 1963. A rational procedure for predicting the long-term average performance of flat-plate solar energy collectors. *Sol. Energy* 7: 53–74.
- Liu, B.Y.H., and R.C. Jordan. 1967. Availability of solar energy for flat-plate solar heat collectors, Chapter 1. In *Low Temperature Engineering of Solar Energy*. ASHRAE, New York; see also 1977 revision.
- Löf, G.O.G., J.A. Duffie, and C.O. Smith. 1966. World distribution of solar energy. Eng. Expt. Station Rept. 21, University of Wisconsin, Madison.
- Marullo, S., G. Dalu, and A. Viola. 1987. Incident short-wave radiation at the surface from METEOSAT data. *Il Nuovo Cimento* 10C: 77–90.
- Maxwell, E.L. 1998. METSTAT—The solar radiation model used in the production of the national solar radiation data base (NSRDB). *Sol. Energy* 62: 263–279.
- Moeser, W., and E. Raschke. 1984. Incident solar radiation over Europe estimated from METEOSTAT data. *J. Clim. Appl. Meteorol.* 23(1): 166–170.
- Mujahid, A., and W.D. Turner. 1979. Diffuse sky measurement and model. ASME Pap. no. 79-WA/Sol-5, ASME, NY.
- Noia, M., C. Ratto and R. Festa. 1993. Solar irradiance estimation from geostationary satellite data: I. statistical models; II. physical models. *Sol. Energy* 51: 449–465.
- NSRDB. 1992. *Volume 1: Users Manual: National Solar Radiation Data Base (1961–1990), Version 1.0*. National Renewable Energy Laboratory, Golden, CO.
- Ögelman, H., A. Ecevit, and E. Tasdemiroglu. 1984. A new method for estimating solar radiation from bright sunshine data. *Sol. Energy* 33(6): 619–625.
- Page, J.K. 1966. The estimation of monthly mean values of daily total short-wave radiation on vertical and inclined surfaces from sunshine records or latitudes 40°N–40°S. *Proc. U.N. Conf. New Sources Energy* 4: 378.
- Perez, R. et al. 1997. The strengths of satellite based resource assessment. *Proc. of the 1997 ASES Annual Conf*, Washington, DC, pp. 303–308.
- Pinker, R.T., R. Frouin, and Z. Li. 1995. A review of satellite methods to derive surface shortwave irradiance. *Remote Sens. Environ.* 51: 108–124.

- Quinlan, E.T., ed. 1977. *SOLMET Vol. 1: Hourly Solar Radiation Surface Meteorological Observations*. NOAA, Asheville, NC.
- Quinlan, F.T., ed. 1979. *SOLMET Vol. 2: Hourly Solar Radiation Surface Meteorological Observations*. NOAA, Asheville, NC.
- Ruth, D.W., and R.E. Chant. 1976. The relationship of diffuse radiation to total radiation in Canada. *Sol. Energy* 18: 153.
- Schmetz, J. 1989. Towards a surface radiation climatology: Retrieval of downward irradiances from satellites. *Atmos. Res.* 23: 287–321.
- Sorapipatana, C., R.H.B. Exell and D. Borel. 1988. A bispectral method for determining global solar radiation from meteorological satellite data. *Sol. Wind Technol.* 5(3): 321–327.
- Sparrow, E.M., and R.D. Cess. 1978. *Radiation Heat Transfer*. Wadsworth Publ. Co., Belmont, CA.
- Spencer, J.W. 1971. Fourier series representation of the position of the sun. *Search* 2: 172.
- Stanhill, G. 1966. Diffuse sky and cloud radiation in Israel. *Sol. Energy* 10: 66.
- Tarpley, J.D. 1979. Estimating incident solar radiation at the surface from geostationary satellite data. *J. Appl. Meteorol.* 18(9): 1172–1181.
- Temps, R.C., and K.L. Coulson. 1977. Solar radiation incident upon slopes of different orientations. *Sol. Energy* 19(2): 179–184.
- University of Lowell Photovoltaic Program. 1990. *International Solar Irradiation Database, Version 1.0*. University of Lowell Research Foundation, Lowell, MA.
- Vasquez-Padilla, R. 2011. Simplified methodology for designing parabolic trough solar power plants. PhD dissertation, University of South Florida, Tampa, FL, USA.
- Voeikov Main Geophysical Observatory. 1999. Worldwide daily solar radiation. Available at <http://www.mgo.rssi.ru>.
- Whillier, A. 1965. Solar radiation graphs. *Sol. Energy* 9: 165–166.
- Zerlaut, G. 1989. Solar radiation instrumentation. In *Solar Resources*, R.L. Hulstrom, ed., MIT Press, Cambridge, MA.

3

Solar Thermal Collectors

Converting the sun's radiant energy to heat is very common from historical times and has evolved into a well-developed solar conversion technology today. The basic principle of solar thermal collection is that when solar radiation strikes a surface, a part of it is absorbed, thereby increasing the temperature of the surface. The efficiency of that surface as a solar collector depends not only on the absorption efficiency but also on how the thermal and reradiation losses to the surroundings are minimized and how the energy from the collector is removed for useful purposes. Various solar thermal collectors range from unglazed flat plate-type solar collectors operating at approximately 5°C–10°C above the ambient to central receiver concentrating collectors operating at above 1000°C. Table 3.1 lists various types of solar thermal collectors and their typical temperature and concentration ranges.

This chapter analyzes in detail the thermal and optical performance of several solar thermal collectors. They range from air- and liquid-cooled non-concentrating, flat-plate types to compound-curvature, continuously tracking types with concentration ratios up to 3000 or more. Applications of the energy converted by solar thermal collectors are described in Chapters 5 through 8. Section 3.1 describes some fundamental radiative properties of materials, knowledge of which helps in the design of solar thermal collectors.

3.1 Radiative Properties and Characteristics of Materials

When radiation strikes a body, a part of it is reflected, a part is absorbed and, if the material is transparent, a part is transmitted, as shown in Figure 3.1.

The fraction of the incident radiation reflected is defined as the reflectance ρ , the fraction absorbed as the absorptance α , and the fraction transmitted as the transmittance τ . According to the first law of thermodynamics, these three components must add up to unity, or

$$\alpha + \tau + \rho = 1. \quad (3.1)$$

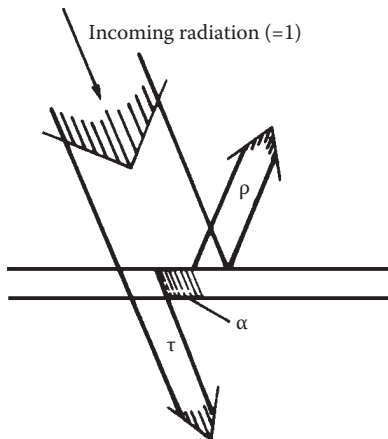
Opaque bodies do not transmit any radiation and $\tau = 0$.

The reflection of radiation can be *specular* or *diffuse*. When the angle of incidence is equal to the angle of reflection, the reflection is called specular;

TABLE 3.1

Types of Solar Thermal Collectors and Their Typical Temperature Range

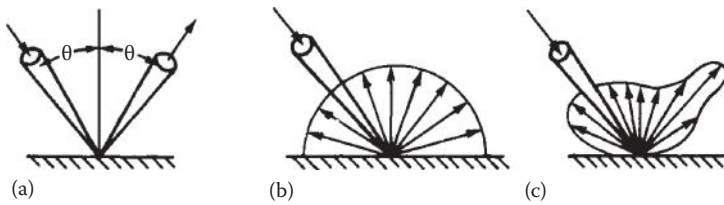
Type of Collector	Concentration Ratio	Typical Working Temperature Range (°C)
Flat-plate collector	1	≤ 70
High efficiency flat-plate collector	1	60–120
Fixed concentrator	3–5	100–150
Parabolic trough collector	10–50	150–350
Parabolic dish collector	200–500	250–700
Central receiver	500 to >3000	500 to >1000

**FIGURE 3.1**Schematic representation of transmittance τ , absorptance α , and reflectance ρ .

when the reflected radiation is uniformly distributed into all directions, it is called diffuse (see Figure 3.2). No real surface is either specular or diffuse, but a highly polished surface approaches specular reflection, whereas a rough surface reflects diffusely.

Another important radiative property is called emittance ϵ , which is the ratio of the radiative emissive power of a real surface to that of an ideal "black" surface as defined in Chapter 2.

All of the radiative properties of materials, α , τ , ρ , and ϵ , can be functions of the wavelength and direction. In fact, such dependence is used in the design of solar energy devices and systems. For example, selective absorbers are used for solar collectors and passive heating systems, and glazing materials are used for daylighting and solar collectors.

**FIGURE 3.2**

Reflections from (a) ideal specular, (b) ideal diffuse, and (c) real surfaces.

Referring to Figure 2.6, the monochromatic directional emittance of a surface at a wavelength λ , $\varepsilon_\lambda(\theta, \phi)$, in a direction signified by an azimuth angle ϕ and a polar angle θ , is

$$\varepsilon_\lambda(\theta, \phi) = \frac{I_\lambda(\theta, \phi)}{I_{b\lambda}}. \quad (3.2)$$

From the above, the total directional emittance $\varepsilon(\theta, \phi)$ over all the wavelengths or the monochromatic hemispherical emittance ε_λ can be obtained by integration of $\varepsilon_\lambda(\theta, \phi)$ over all the wavelengths or the entire hemispherical space, respectively. The overall emittance ε is found by integrating the hemispherical emittance over all the wavelengths.

$$\varepsilon = \frac{1}{\sigma T^4} \int_0^\infty \varepsilon_\lambda E_{b\lambda} d\lambda. \quad (3.3)$$

Observe that both ε_λ and ε are properties of the surface.

The next most important surface characteristic is the absorptance. We begin by defining the monochromatic directional absorptance as the fraction of the incident radiation at wavelength λ from the direction θ, ϕ that is absorbed, or

$$\alpha_\lambda(\theta, \phi) = \frac{I_{\lambda,a}(\theta, \phi)}{I_{\lambda,i}(\theta, \phi)}, \quad (3.4)$$

where the subscripts "a" and "i" denote absorbed and incident radiation, respectively. The monochromatic directional absorptance is also a property of the surface.

More important than $\alpha_\lambda(\theta, \phi)$ is the overall directional absorptance $\alpha(\theta, \phi)$, defined as the fraction of the total radiation from the direction θ, ϕ that is absorbed, or

$$\alpha(\theta, \phi) = \frac{\int_0^\infty \alpha_\lambda(\theta, \phi) I_{\lambda,i}(\theta, \phi) d\lambda}{\int_0^\infty I_{\lambda,i}(\theta, \phi) d\lambda} = \frac{1}{I_i(\theta, \phi)} \int_0^\infty \alpha_\lambda(\theta, \phi) I_{\lambda,i}(\theta, \phi) d\lambda. \quad (3.5)$$

The overall absorptance is a function of the characteristics of the incident radiation and is, therefore, unlike the monochromatic absorptance, not a property of a surface alone. It is this characteristic that makes it possible to have selective surfaces that absorb the radiation from one source at a higher rate than from another. In other words, even though according to Kirchhoff's law the monochromatic emittance at a wavelength λ must equal the monochromatic absorptance at the same wavelength

$$\alpha_\lambda(\theta, \phi) = \varepsilon_\lambda(\theta, \phi), \quad (3.6)$$

the overall emittance is not necessarily equal to the overall absorptance unless thermal equilibrium exists, and the incoming and outgoing radiation have the same spectral characteristics.

The effect of incidence angle on the absorptance is illustrated in Table 3.2 where the angular variation of the absorptance for a nonselective black surface, typical of those used on flat-plate collectors, is shown. The absorptance of this surface for diffuse radiation is approximately 0.90.

The third characteristic to be considered is the reflectance. Reflectance is particularly important for the design of focusing collectors. As mentioned previously, there are two limiting types of reflection: specular and diffuse.

TABLE 3.2

Angular Variation of Absorptance of Lampblack Paint

Incidence Angle i (°)	Absorptance $\alpha(i)$
0–30	0.96
30–40	0.95
40–50	0.93
50–60	0.91
60–70	0.88
70–80	0.81
80–90	0.66

Source: Adapted from Löf, G.O.G. and R.A. Tybout, Model for optimizing solar heating design, ASME Paper 72-WA/SOL-8, 1972.

As illustrated in Figure 3.2a, when a ray of incident radiation at an angle θ is reflected at the same polar angle and the azimuthal angles differ by 180° , as for a perfect mirror, the reflection is said to be specular. The reflection is said to be diffuse if the incident radiation is scattered equally in all directions, as shown in Figure 3.2b.

3.1.1 Selective Surfaces

Two types of special surfaces of great importance in solar collector systems are selective absorbers and reflecting surfaces. Selective absorber surfaces combine a high absorptance for solar radiation (short wavelengths) with a low emittance for the normal operating temperature of the surface. This combination of surface characteristics is possible because 98% of the energy in incoming solar radiation is contained within wavelengths below 3 μm , whereas 99% of the radiation emitted by black or gray surfaces at 400 K is at wavelengths longer than 3 μm . The dotted line in Figure 3.3 illustrates the spectral reflectance of an ideal, selective semigray surface having a uniform reflectance of 0.05 below 3 μm , but 0.95 above 3 μm . Real surfaces do not approach this performance. Figure 3.4 lists properties of some selective coatings in the normal temperature range of solar thermal collectors (below 250°C), which are reproduced from a detailed review of selective absorbers by Kennedy (2002). Performance of selective absorber coatings degrades as the temperatures increase to 400°C and above. Since the interest in concentrating solar thermal power has increased and plants as large as 300 MWe are under construction, there is a need for selective solar absorbers capable of maintaining high performance at temperatures of 400°C and above. Figure 3.5 lists some of the high-temperature selective surfaces based on the research summarized by Kennedy (2002).

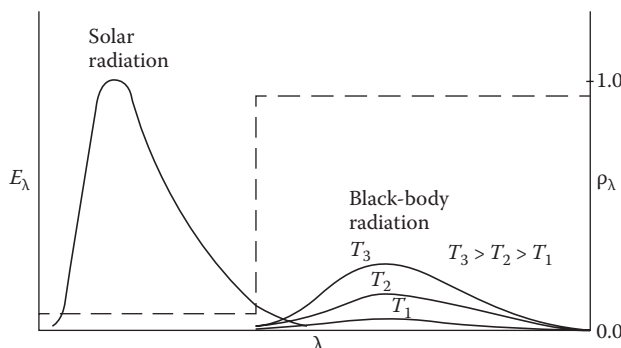


FIGURE 3.3

Illustrations of reflectance characteristics of an ideal selective surface. The figure shows radiation from ideal surfaces at different temperatures and solar radiation.

Material	Substrate	Fabrication	Stability (°C)	
			Absorptance α	Emissance ϵ (100°C)
Ni–Sn	Cu	Electrodeposition/sol–gel	0.92–0.98	0.08–0.25
Graphitic films	Cu	MF-pulsed	0.92	0.025
α -C/H/Cr	Al	PVD/PECVD	0.876	0.061
α -C/H				250
Ge in silicon binder	Cu or SS	Paint	0.91	0.7
Si			0.83	0.7
PbS			0.96	0.7
Ag dielectric	Al	Biomimetic sol–gel		300
Black copper	Cu	Electrodeposition	0.97–0.98	0.02
BiCu–Cu ₂ O/Cu				370
Black chrome	Ni–Cu	Electrodeposition	0.97	0.09
Cr–Cr ₂ O ₃	CU steel			400
Mo/Cr ₂ O ₃			0.95	<0.30
TiN _x O _y	Cu	ARE	0.92	0.06
Cr, Fe, Mo, SS, Ta, Ti, W silicides	Bulk Cu Sputtered Cu	DC reactive sputtering	0.76–0.82 0.81–0.86	0.02–0.3 400 250
Cr, Fe, Mo, SS, Ta, Ti, W carbides	Bulk Cu Sputtered Cu	DC reactive sputtering	0.76–0.81 0.84–0.90	0.02 0.035–0.06 400 250
Ni–NiO _x	Al	Reactive sputtering	0.96	0.10
Ni-pigmented Al ₂ O ₃	Al	Anodization	0.85–0.97	0.08–0.21 300–400

FIGURE 3.4

Mid-temperature selective surfaces. (Adapted from Kennedy, C.E., Review of mid- to high-temperature solar selective absorber materials. Report NREL/TP-520-31267, National Renewable Energy Laboratory, Golden, CO, 2002.)

Material	Substrate	Fabrication	Absorptance α	Emissance ϵ (100°C)*	Stability (°C)	
					Vacuum	Air
Mo-Al ₂ O ₃	Ni or Al Steel	RF sputtering	0.96	0.16 (350) 0.1–0.07 (400)	350–500	
W-Al ₂ O ₃		RF sputtering	0.97–0.98	0.04	600	
W-Al ₂ O ₃	Cu	CVD	0.85	0.08	600	
Pt-Al ₂ O ₃		RF sputtering	0.90–0.98			
Al ₂ O ₃ -Pt-Al ₂ O ₃						
Double						
Mo-Al ₂ O ₃	Cu	DC sputtering	0.96	0.06 (350 _c)	500	
Mo-AlN			0.92–0.94	0.08–0.10 (350 _c)	350–500	
W-AlN					500	
Quasi-crystals multilayer cement	Cu, Si		0.90 0.86–0.92	0.025 0.031–0.05	500 500	400
Si ₃ N ₄ /Si-Ge/Ag	SS, Al	CVD	0.890	0.0389 (300) 0.545 (500)	650 (He)	
Ni:SiO ₂ Cr:SiO	Al, Cu	Reactive DC sputtering	0.90–0.96	0.03–0.14		400–800 (Ar)
Al-AlN _x -AlN	SS	Reactive DC	0.97	0.10	500	
Ag/CuO/Rh ₂ O ₃ /CeO ₂ //	SS	Organic-metallic Spray	0.9 0.86–0.88	0.1 0.1	700 775	500 550
CeO ₂ // Ag/Pt/CuO// Rh/Rh ₂ O ₃ // Ag/Pt			0.88	0.06–0.12	700	500
CeO ₂ // CuO/CoO						
Mn ₂ O ₃ /Pt						
Black cobalt						
Co ₃ O ₄ /Co			0.96–0.92	0.71–0.017		400–650
Ni-Co ₃ O ₄ /Co			0.95	0.10		

FIGURE 3.5
High-temperature selective surfaces.

(Continued)

Material	Substrate	Fabrication	Absorptance α	Emittance $\epsilon(100^\circ\text{C})^*$	Stability ($^\circ\text{C}$)	
					Vacuum	Air
Black moly		CVD	0.94	0.30 (500 _c)	500	350
Mo-MoO ₂						
Black tungsten		CVD	0.83	0.25	800	
W-WO _x						
AU/TiO ₂	SS	Sol-gel	0.85	0.01 (400 _c)	>500	
AU/MgO	Mo/SS	RF sputtering	0.90–0.93	0.04–0.1		400
ZrC _x N _y	Al		0.85	0.074 (325 _c)	600	125
Al ₂ O ₃ /ZrC _x N _y /Ag			0.91	0.05 (325 _c)	700	175
ZrO _x /ZrC _x /Zr	SS		0.90	0.05 (20)	700	
TIN	Cu, Al	DC reactive Sputtering	0.80	0.14–0.40		500
Ti _{1-x} Al _x N						750–900
M ₃ O _c + M'Fe ₂ P ₄	Ni-Mo alloy	Painting Arc plasma	>0.90	>0.45		700 1060
VB ₂ , NbB ₂ , TaB ₂ , TiB ₂ , ZrB ₂ , LaB ₆ , WS ₂ , TiSi ₂	Glass	DC reactive sputtering	0.99	0.95–0.97	2300–3040 (MP)	
Si ₃ N ₄ AR-ZrB ₂	ZrB ₂	CVD	0.88–0.93	0.08–0.10		500
Masterbeads “paint”			0.93			<1000
Textured SS	SS		0.93 ± 0.02	0.22 ± 0.02	>440	
Textured Cr	Cr		0.80–0.90	0.10–0.30	550	<500
W whiskers			0.98	>0.26		
Mo, Rh, Pt, W, HfC, Au					>600	
NiO _x , CoO _x					800	

* Emittance values at 100 °C unless indicated by a number in parenthesis. Subscript c means calculated.

FIGURE 3.5 (CONTINUED)

High-temperature selective surfaces. (Adapted from Kennedy, C.E., Review of mid- to high-temperature solar selective absorber materials. Report NREL/TP-520-31267, National Renewable Energy Laboratory, Golden, CO, 2002.)

TABLE 3.3

Specular Reflectance Values for Solar Reflector Materials

Material	ρ
Silver (unstable as front surface mirror)	0.94 ± 0.02
Gold	0.76 ± 0.03
Aluminized acrylic, second surface	0.86
Anodized aluminum	0.82 ± 0.05
Various aluminum surfaces, range	0.82–0.92
Copper	0.75
Back-silvered water-white plate glass	0.88
Aluminized type-C Mylar (from Mylar side)	0.76

3.1.2 Reflecting Surfaces

Concentrating solar collectors require the use of reflecting surfaces with high specular reflectance in the solar spectrum or refracting devices with high transmittance in the solar spectrum. Reflecting surfaces are usually highly polished metals or metal coatings on suitable substrates. With opaque substrates, the reflective coatings must always be front surfaced, for example, chrome plating on copper or polished aluminum. If a transparent substrate is used, however, the coating may be front or back surfaced. In any back-surfaced reflector, the radiation must pass through the substrate twice and the transmittance of the material becomes very important.

Table 3.3 presents typical values for the normal specular reflectance of new surfaces for beam solar radiation.

3.1.3 Transparent Materials

The optical transmission behavior can be characterized by two wavelength-dependent physical properties—the index of refraction n and the extinction coefficient k . The index of refraction, which determines the speed of light in the material, also determines the amount of light reflected from a single surface, while the extinction coefficient determines the amount of light absorbed in a substance in a single pass of radiation as described in Chapter 2.

Figure 3.6 defines the angles used in analyzing reflection and transmission of light. The angle i is called the *angle of incidence*. It is also equal to the angle at which a beam is specularly reflected from the surface. Angle θ_r is the *angle of refraction*, which is defined as shown in the figure. The incidence and refraction angles are related by Snell's law:

$$\frac{\sin(i)}{\sin(\theta_r)} = \frac{n_r}{n_i} = n_r \quad (3.7)$$

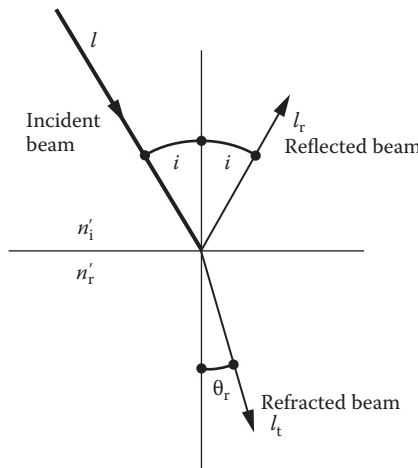
**FIGURE 3.6**

Diagram showing incident, reflected, and refracted beams of light and incidence and refraction angles for a transparent medium.

where n_i and n_r are the two refractive indices and n_r is the index ratio for the two substances forming the interface. Typical values of refractive indices for various materials are shown in Table 3.4. For most materials of interest in solar applications, the values range from 1.3 to 1.6, a fairly narrow range.

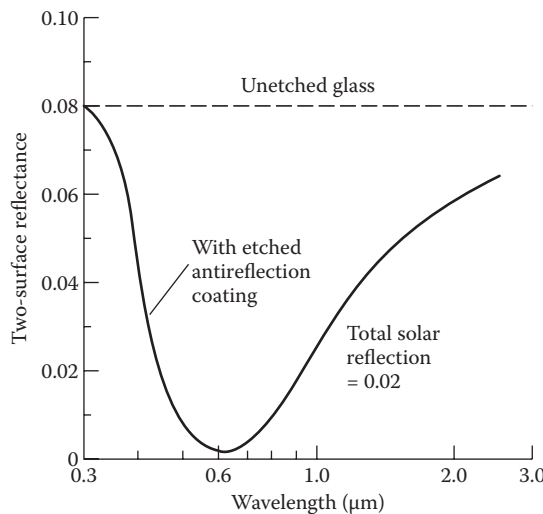
By having a gradual change in index of refraction, reflectance losses are reduced significantly. The reflectance of a glass-air interface common in solar collectors may be reduced by a factor of 4 by an etching process. If glass is

TABLE 3.4

Refractive Index for Various Substances in the Visible Range Based on Air

Material	Index of Refraction
Air	1.000
Clean polycarbonate	1.59
Diamond	2.42
Glass (solar collector type)	1.50–1.52
Plexiglass ^a (polymethyl methacrylate, PMMA)	1.49
Mylar ^a (polyethylene terephthalate, PET)	1.64
Quartz	1.55
Tedlar ^a (polyvinyl fluoride, PVF)	1.45
Teflon ^a (polyfluoroethylene-propylene, FEP)	1.34
Water—liquid	1.33
Water—solid	1.31

^a Trademark of the duPont Company, Wilmington, Delaware.

**FIGURE 3.7**

Reflection spectra for a sample of glass before and after etching.

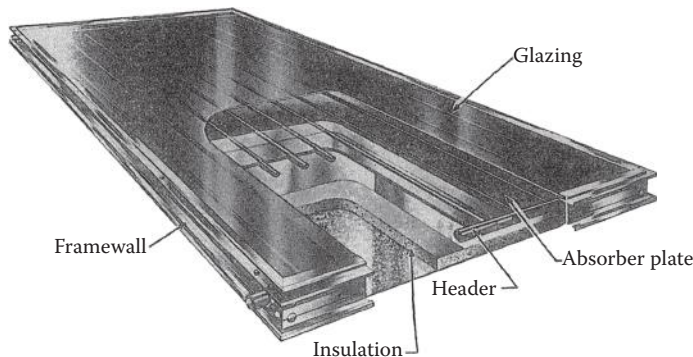
immersed in a silica-supersaturated fluosilicic acid solution, the acid attacks the glass and leaves a porous silica surface layer. This layer has an index of refraction intermediate between glass and air. Figure 3.7 shows the spectral reflectance of a pane of glass before and after etching.

3.2 Flat-Plate Collectors

A simple flat-plate collector consists of an absorber surface (usually a dark, thermally conducting surface); a trap for reradiation losses from the absorber surface (such as glass, which transmits shorter-wavelength solar radiation but blocks the longer-wavelength radiation from the absorber); a heat-transfer medium such as air, water, and so on; and some thermal insulation behind the absorber surface. Flat-plate collectors are used typically for temperature requirements up to 75°C, although higher temperatures can be obtained from high-efficiency collectors. These collectors are of two basic types based on the heat-transfer fluid:

Liquid type: where heat-transfer fluid may be water, mixture of water and antifreeze oil, and so on

Air type: where heat-transfer medium is air (used mainly for drying and space heating requirements)

**FIGURE 3.8**

Typical liquid-type flat-plate collector. (Courtesy of Morning Star Corp., Orange Park, FL.)

3.2.1 Liquid-Type Collectors

Figure 3.8 shows a typical liquid-type flat-plate collector. In general, it consists of the following:

1. *Glazing*: one or more covers of transparent material like glass, plastics, and so on. Glazing may be left out for some low-temperature applications.
2. *Absorber*: a plate with tubes or passages attached to it for the passage of a working fluid. The absorber plate is usually painted flat black or electroplated with a selective absorber.
3. *Headers* (or manifolds): to facilitate the flow of heat-transfer fluid.
4. *Insulation*: to minimize heat loss from the back and the sides.
5. *Container*: box or casing.

3.2.2 Air-Type Collectors

Air types of collectors are more commonly used for agricultural drying and space heating applications. Their basic advantages are twofold: (1) low sensitivity to leakage and (2) there is no need for an additional heat exchanger for drying and space heating applications. However, because of the low heat capacity of the air and the low convection heat-transfer coefficient between the absorber and the air, a larger heat-transfer area and higher flow rates are needed. Figure 3.9 shows some common configurations of air heating collectors. Common absorber materials include corrugated aluminum or galvanized steel sheets, black metallic screens, or simply any black painted surface.

Unglazed, transpired solar air collectors offer a low-cost opportunity for some applications such as preheating of ventilation air and agricultural drying

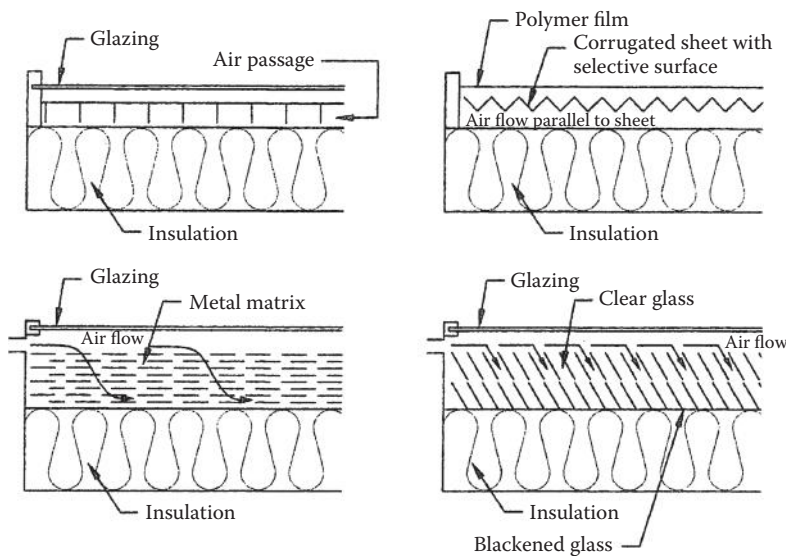


FIGURE 3.9
Some common configurations of air heating collectors.

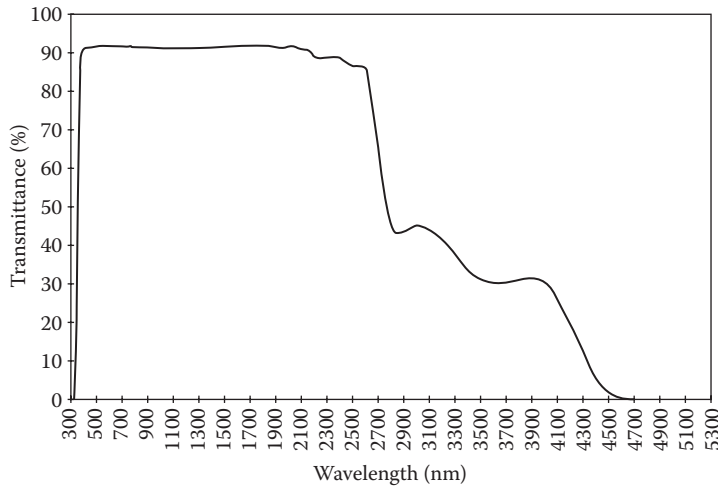
and curing (Kutcher 1996). Such collectors consist of perforated absorber sheets that are exposed to the sun and through which air is drawn. The perforated absorber sheets are attached to the vertical walls, which are exposed to the sun. Kutcher and Christensen (1992) have given a detailed thermal analysis of unglazed transpired solar collectors. (See Section 5.4.5 for additional details.)

The most important components, whose properties determine the efficiency of solar thermal collectors, are glazings and absorbers.

3.2.3 Glazings

The purpose of a glazing or transparent cover is to transmit the shorter-wavelength solar radiation but block the longer-wavelength reradiation from the absorber plate and to reduce the heat loss by convection from the top of the absorber plate. Consequently, an understanding of the process and laws that govern the transmission of radiation through a transparent medium is important. Section 3.1 describes in brief the transmission of radiation through materials.

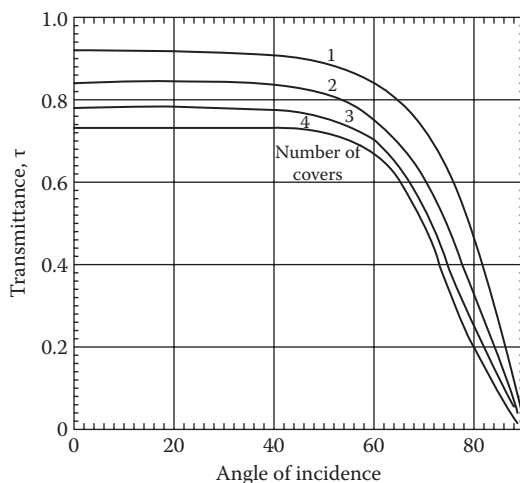
Glass is the most common glazing material. Figure 3.10 shows transmittance of glass as a function of wavelength. Transparent plastics, such as polycarbonates and acrylics, are also used as glazings for flat-plate collectors. The main disadvantage of plastics is that their transmittance in the longer wavelength is also high; therefore, they are not as good a trap as glass. Other disadvantages include deterioration over a period attributed to ultraviolet

**FIGURE 3.10**

Spectral transmittance of a 3-mm low-iron float glass.

solar radiation. Their main advantage is resistance to breakage. Although glass can break easily, this disadvantage can be minimized by using tempered glass.

In order to minimize the upward heat loss from the collector, more than one transparent glazing may be used. However, with the increase in the number of cover plates, transmittance is decreased. Figure 3.11 shows the effect of number of glass cover plates on transmittance.

**FIGURE 3.11**

Transmittance of multiple glass covers having an index of refraction 1.526".

3.2.3.1 Absorbers

The purpose of the absorber is to absorb as much of the incident solar radiation as possible, reemit as little as possible, and allow efficient transfer of heat to a working fluid. The most common forms of absorber plates in use are shown in Figure 3.12. The materials used for absorber plates include copper, aluminum, stainless steel, galvanized steel, plastics, and rubbers. Copper seems to be the most common material used for absorber plates and tubes because of its high thermal conductivity and high corrosion resistance. However, copper is quite expensive. For low-temperature applications (up to approximately 50°C or 120°F), a plastic material called ethylene propylene polymer (trade names EPDM, HCP, etc.) can be used to provide inexpensive absorber material. To compensate for the low thermal conductivity, a large surface area is provided for heat transfer. Figure 3.13 shows a typical collector made from such material.

In order to increase the absorption of solar radiation and to reduce the emission from the absorber, the metallic absorber surfaces are painted or coated with flat black paint or some selective coating. A selective coating has high absorptivity in the solar wavelength range (0.3 to 3.0 μm). Absorptivities and emissivities of some common selective surfaces are given in Figures 3.4 and 3.5.

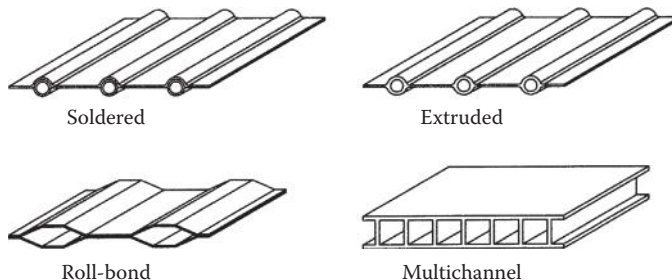


FIGURE 3.12
Common types of absorber plates.

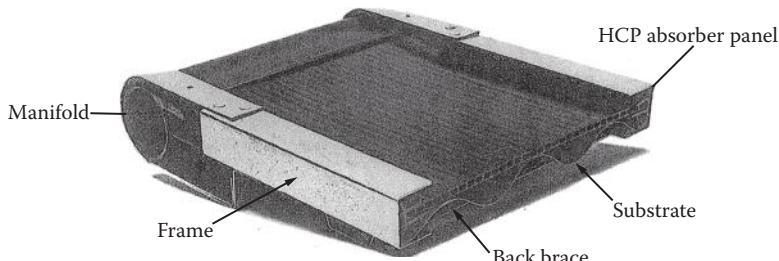


FIGURE 3.13
Cutaway view of a typical collector made from ethylene propylene polymer. (Courtesy of Sealed Air Corp., Saddle Brook, NJ.)

A simple and inexpensive collector consists of a black painted corrugated metal absorber on which water flows down open, rather than enclosed in tubes. This type of collector is called a *trickle collector* and is usually built on-site. Although such a collector is simple and inexpensive, it has the disadvantages of condensation on the glazing and a higher pumping power requirement.

3.2.4 Energy Balance for a Flat-Plate Collector

The thermal performance of any type of solar thermal collector can be evaluated by an energy balance that determines the portion of the incoming radiation delivered as useful energy to the working fluid. For a flat-plate collector of an area A_c , this energy balance on the absorber plate is

$$I_c A_c \tau_s \alpha_s = q_u + q_{\text{loss}} + \frac{de_c}{dt}, \quad (3.8)$$

where I_c is the solar irradiation on a collector surface, τ_s is the effective solar transmittance of the collector cover(s), α_s is the solar absorptance of the collector-absorber plate surface, q_u is the rate of heat transfer from the collector-absorber plate to the working fluid, q_{loss} is the rate of heat transfer (or heat loss) from the collector-absorber plate to the surroundings, and de_c/dt is the rate of internal energy storage in the collector.

The instantaneous efficiency of a collector η_c is simply the ratio of the useful energy delivered to the total incoming solar energy, or

$$\eta_c = \frac{q_u}{A_c I_c}. \quad (3.9)$$

In practice, the efficiency must be measured over a finite time period. In a standard performance test, this period is on the order of 15 or 20 min, whereas for design, the performance over a day or over some longer period t is important. Then, we have for the average efficiency

$$\eta_c = \frac{\int_0^1 q_u dt}{\int_0^1 A_c I_c dt}, \quad (3.10)$$

where t is the time period over which the performance is averaged.

A detailed and precise analysis of the efficiency of a solar collector is complicated by the nonlinear behavior of radiation heat transfer. However, a simple linearized analysis is usually sufficiently accurate in practice. In addition, the simplified analytical procedure is very important because it illustrates the parameters of significance for a solar collector and how these parameters interact. For a proper analysis and interpretation of these test results, an understanding

of the thermal analysis is imperative, although for design and economic evaluation, the results of standardized performance tests are generally used.

3.2.4.1 Collector Heat-Loss Conductance

In order to obtain an understanding of the parameters determining the thermal efficiency of a solar collector, it is important to develop the concept of *collector heat-loss conductance*. Once the collector heat-loss conductance U_c is known, and when the collector plate is at an average temperature T_c , the collector heat loss can be written in the simple form

$$q_{\text{loss}} = U_c A_c (T_c - T_a). \quad (3.11)$$

The simplicity of this relation is somewhat misleading because the collector heat-loss conductance cannot be specified without a detailed analysis of all the heat losses. Figure 3.14 shows a schematic diagram of a single-glazed collector, while Figure 3.15a shows the thermal circuit with all the elements that must be analyzed before they can be combined into a single conductance element shown in Figure 3.15b. The analysis in the following shows an example of how this combination is accomplished.

In order to construct a model suitable for a thermal analysis of a flat-plate collector, the following simplifying assumptions will be made:

1. The collector is thermally in steady state.
2. The temperature drop between the top and bottom of the absorber plate is negligible.
3. Heat flow is one-dimensional through the cover as well as through the back insulation.

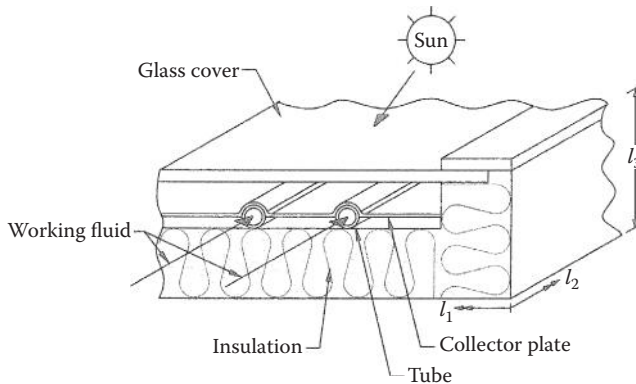
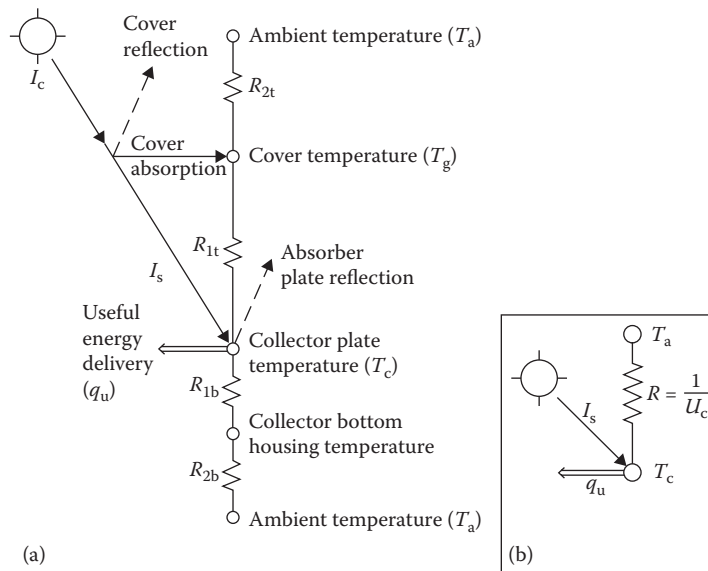


FIGURE 3.14

Schematic diagram of a solar collector.

**FIGURE 3.15**

Thermal circuits for a flat-plate collector shown in Figure 3.14: (a) detailed circuit; (b) approximate, equivalent circuit to (a). In both circuits, the absorbed energy is equal to $\alpha_s I_s$, where $I_s = \tau_s I_c$. Collector is assumed to be at uniform temperature T_c .

4. The headers connecting the tubes cover only a small area of the collector and provide uniform flow to the tubes.
5. The sky can be treated as though it were a black-body source for infrared radiation at an equivalent sky temperature.
6. The irradiation on the collector plate is uniform.

For a quantitative analysis, let the plate temperature be T_c and assume solar energy is absorbed at the rate $I_s \alpha_s$ or $I_c A_c \tau_s \alpha_s$. Part of this energy is then transferred as heat to the working fluid, and if the collector is in the steady state, the other part is lost as heat to the ambient air if $T_c > T_a$. Some of the heat loss occurs through the bottom of the collector. It passes first through the back to the environment. Since the collector is in steady state, according to Equation 3.8,

$$q_u = I_c A_c \tau_s \alpha_s - q_{\text{loss}}, \quad (3.12)$$

where q_{loss} can be determined using the equivalent thermal circuit as shown in Figure 3.15.

$$q_{\text{loss}} = U_c A_c (T_c - T_a) = \frac{A_c (T_c - T_a)}{R}. \quad (3.13)$$

There are three parallel paths to heat loss from the hot collector-absorber plate at T_c to the ambient at T_a : the top, bottom, and edges. Because the edge losses are quite small compared to the top and the bottom losses, they are quite often neglected. However, they can be estimated easily if the insulation around the edges is of the same thickness as the back. The edge loss can be accounted for by simply adding the areas of the back (A_b) and the edges (A_e) for back heat loss.

Therefore, the overall heat-loss coefficient is

$$U_c A_c = \frac{A_c}{R} = \frac{A_c}{R_{1t} + R_{2t}} + \frac{A_c + A_e}{R_{1b} + R_{2b}}. \quad (3.14)$$

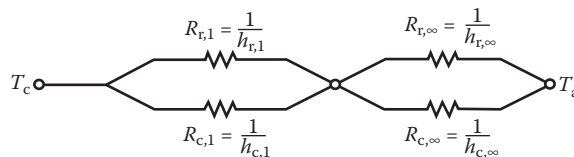
The thermal resistances can be found easily from the definition. For example,

$$R_{1b} = \frac{l_i}{k_i} \quad \text{and} \quad R_{2b} = \frac{1}{h_{c,\text{bottom}}}, \quad (3.15)$$

where k_i and l_i are, respectively, the thermal conductivity and thickness of the insulation and $h_{c,\text{bottom}}$ is the convective heat-transfer coefficient between the collector and the air below the collector. In a well-insulated collector, R_{2b} is much smaller than R_{1b} and usually neglected. Referring to Figure 3.14,

$$A_e = 2(l_1 + l_2)l_3. \quad (3.16)$$

Since the heat loss from the top is by convection and radiation, it is more complicated than the bottom heat loss. Convection and radiation provide two parallel paths for heat loss from the absorber plate at T_c to the glass cover at T_g and from the glass cover to the ambient. That is, the series resistance of R_{1t} and R_{2t} consists of



Therefore,

$$\frac{1}{R_{1t}} = \frac{1}{R_{r,1}} + \frac{1}{R_{c,1}} = h_{r,1} + h_{c,1} \quad \text{and} \quad (3.17)$$

$$\frac{1}{R_{2t}} = \frac{1}{R_{r,\infty}} + \frac{1}{R_{c,\infty}} = h_{r,\infty} + h_{c,\infty}. \quad (3.18)$$

Since thermal radiative heat transfer is proportional to the fourth power of the temperature, R_r and h_r are found as follows:

Radiative heat transfer from the plate to the glass cover

$$q_{f_{c \rightarrow R}} = \sigma A_c \frac{(T_c^4 - T_g^4)}{\left(1/\epsilon_{p,i} + 1/\epsilon_{s,i} - 1\right)} = h_{r,1} A_c (T_c - T_g), \quad (3.19)$$

where $\epsilon_{p,i}$ is the infrared emittance of the plate and $\epsilon_{g,i}$ is the infrared emittance of the glass cover.

Therefore,

$$h_{r,1} = \frac{\sigma(T_c + T_g)(T_c^2 + T_g^2)}{\left(1/\epsilon_{p,i} + 1/\epsilon_{g,i} - 1\right)}. \quad (3.20)$$

Similarly, from the radiative heat transfer between the glass plate (at T_g) and the sky (at T_s), we can find that

$$q_{r_{g \rightarrow \text{sky}}} = \epsilon_{g,i} \sigma A_c (T_g^4 - T_s^4) = h_{r,\infty} A_c (T_g - T_a), \quad (3.21)$$

or

$$h_{r,\infty} = \epsilon_{g,i} \sigma (T_g^4 - T_s^4) / (T_g - T_a). \quad (3.22)$$

Evaluation of the collector heat-loss conductance defined by Equation 3.14 requires iterative solution of Equations 3.19 and 3.21, because the unit radiation conductances are functions of the cover and plate temperatures, which are not known a priori.

Several books (Duffie and Beckman 1980; Kreith and Kreider 2012) suggest using a simplified empirical equation proposed by Klein (1975) and Agarwal and Larson (1981). However, recent studies by several researchers (Akhtar and Mullick 1999, 2007; Mahboub and Moummi 2012; Samdarshi and Mullick 1991) have shown that the empirical equation for top heat-loss coefficient could result in large errors. Therefore, Mullick and Samdarshi (1988) suggested a method to evaluate T_g accurately, which has been modified by later publications for multiple covers, large tilt angles, and V-shaped absorber surface. According to this method, the top heat-loss coefficient U_t [in $\text{W}/(\text{m}^2 \cdot \text{K})$] is

$$U_t^{-1} = \frac{\sigma(T_c^2 + T_g^2)(T_c + T_g)}{\frac{1}{\epsilon_{p,i}} + \frac{1}{\epsilon_{g,i}} - 1} + \frac{kNu}{L}^{-1} + \frac{\sigma \epsilon_{g,i} (T_g^4 - T_s^4)}{T_g - T_a}^{-1} + h_{c,\infty}^{-1} + L_g/k_g, \quad (3.23)$$

where

$$T_g = \frac{(fT_c + CT_a)}{(1+f)},$$

where

$$C = \frac{\frac{T_s}{T_a} + \frac{h_{c,\infty}}{3.5}}{1 + \frac{h_{c,\infty}}{3.5}}.$$

According to Swinbank (1963), for clear sky, T_s may be assumed to be equal to $0.0552(T_a)^{1.5}$. If T_s is assumed equal to T_a , C becomes equal to 1.

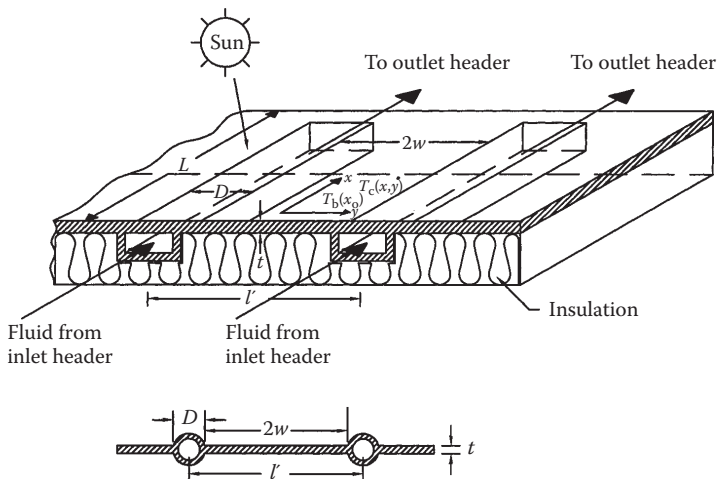
$$f = \frac{12 \times 10^{-8}(T_a + 0.2T_c)^3 + h_{c,\infty}^{-1} + 0.3L_g}{6 \times 10^{-8}(\epsilon_{p,i} + 0.028)(T_c + 0.5T_a)^3 + 0.6L^{-0.2}\{(T_c - T_a)\cos\beta\}^{0.25}^{-1}} \quad (3.24)$$

$$\text{Nu} = 1 + 1.44[1 - 1708/Ra']^+ \left\{ 1 - 1708(\sin 1.8\beta)^{1.6}/Ra' \right\}^+ + (Ra'/5830)^{1/3} - 1^+, \quad (3.25)$$

where the exponent “+” means that only positive values of the term in brackets are to be used; $Ra' = Ra \cos \beta$, where β is the collector tilt angle; k and k_g are the thermal conductivity of air and glass, respectively, in $\text{W}/(\text{m}\cdot\text{K})$; and L and L_g are the thickness of the air gap and glass, respectively, in meters.

3.2.5 Thermal Analysis of Flat-Plate Collector–Absorber Plate

In order to determine the efficiency of a solar collector, the rate of heat transfer to the working fluid must be calculated. If transient effects are neglected (Hottel and Whillier 1958; Klein 1975), the rate of heat transfer to the fluid flowing through a collector depends on the temperature of the collector surface from which heat is transferred by convection to the fluid, the temperature of the fluid, and the heat-transfer coefficient between the collector and the fluid. To analyze the rate of heat transfer, consider first the condition at a cross section of the collector with flow ducts of rectangular cross sections as shown in Figure 3.16. Solar radiant energy impinges on the upper face of the collector plate. A part of the total solar radiation falls on the upper surface of the flow channels, while another part is incident on the plates connecting any two adjacent flow channels. The latter is conducted in a transverse direction toward the flow channels. The temperature is a maximum at any midpoint between adjacent channels, and the collector plate acts as a fin attached

**FIGURE 3.16**

Sketch showing coordinates and dimensions for collector plate and fluid ducts.

to the walls of the flow channel. The thermal performance of a fin can be expressed in terms of its efficiency. The fin efficiency η_f is defined as the ratio of the rate of heat flow through the real fin to the rate of heat flow through a fin of infinite thermal conductivity, that is, a fin at a uniform temperature. We shall now derive a relation to evaluate this efficiency for a flat-plate solar collector.

If U_c is the overall unit conductance from the collector-plate surface to the ambient air, the rate of heat loss from a given segment of the collector plate at x, y in Figure 3.16 is

$$q(x, y) = U_c[T_c(x, y) - T_a] \, dx \, dy, \quad (3.26)$$

where T_c is the local collector-plate temperature ($T_c > T_a$), T_a is the ambient air temperature, and U_c is the overall unit conductance between the plate and the ambient air.

U_c includes the effects of radiation and free convection between the plates, the radiative and convective transfer between the top of the cover and the environment, and conduction through the insulation. Its quantitative evaluation has been previously considered.

If conduction in the x direction is negligible, a heat balance at a given distance x_0 for a cross section of the flat-plate collector per unit length in the x direction can be written in the form

$$\alpha_s I_s dy - U_c(T_c - T_a)dy + \left. -kt \frac{dT_c}{dy} \right|_{y, x_0} - \left. -kt \frac{dT_c}{dy} \right|_{y+dy, x_0} = 0. \quad (3.27)$$

If the plate thickness t is uniform and the thermal conductivity of the plate is independent of temperature, the last term in Equation 3.27 is

$$\frac{dT_c}{dy} \Big|_{y+dy, x_0} = \frac{dT_c}{dy} \Big|_{y, x_0} + \frac{d^2T_c}{dy^2} \Big|_{y, x_0} dy,$$

and Equation 3.27 can be cast into the form of a second-order differential equation:

$$\frac{d^2T}{dy^2} = \frac{U_c}{kt} T_c - T_a + \frac{\alpha_s I_s}{U_c} . \quad (3.28)$$

The boundary conditions for the system described above at a fixed x_0 are as follows:

1. At the center between any two ducts, the heat flow is 0, or at $y = 0$, $dT_c/dy = 0$.
2. At the duct, the plate temperature is $T_b(x_0)$, or at $y = w = (l' - D)/2$, $T_c = T_b(x_0)$ where $T_b(x_0)$ is the fin-base temperature.

If we let $m^2 = U_c/kt$ and $\phi = T_c - (T_a + \alpha_s I_s/U_c)$, Equation 3.28 becomes

$$\frac{d^2\phi}{dy^2} = m^2\phi, \quad (3.29)$$

subject to the boundary conditions

$$\frac{d\phi}{dy} = 0 \text{ at } y = 0, \text{ and}$$

$$\phi = T_b(x_0) - T_a + \frac{\alpha_s I_s}{U_c} \text{ at } y = w.$$

The general solution of Equation 3.29 is

$$\phi = C_1 \sinh my + C_2 \cosh my. \quad (3.30)$$

The constants C_1 and C_2 can be determined by substituting the two boundary conditions and solving the two resulting equations for C_1 and C_2 . This gives

$$\frac{T_c - (T_a + \alpha_s I_s/U_c)}{T_b(x_0) - (T_a + \alpha_s I_s/U_c)} = \frac{\cosh mw}{\cosh my}. \quad (3.31)$$

From the Equation 3.31, the rate of heat transfer to the conduit from the portion of the plate between two conduits can be determined by evaluating the temperature gradient at the base of the fin, or

$$q_{\text{fin}} = -kt \frac{dT_c}{dt} \Big|_{y=w} = \frac{1}{m} \{\alpha_s I_s - U_c [T_b(x_0) - T_a] \tanh mw\}. \quad (3.32)$$

Since the conduit is connected to fins on both sides, the total rate of heat transfer is

$$q_{\text{total}}(x_0) = 2w \{\alpha_s I_s - U_c [T_b(x_0) - T_a]\} \frac{\tanh mw}{mw}. \quad (3.33)$$

If the entire fin were at the temperature $T_b(x_0)$, a situation corresponding physically to a plate of infinitely large thermal conductivity, the rate of heat transfer would be a maximum, $q_{\text{total,max}}$. As mentioned previously, the ratio of the rate of heat transfer with a real fin to the maximum rate obtainable is the fin efficiency η_f . With this definition, Equation 3.33 can be written in the form

$$q_{\text{total}}(x_0) = 2w\eta_f \{\alpha_s I_s - U_c [T_b(x_0) - T_a]\}, \quad (3.34)$$

where $\eta_f \equiv (\tanh mw)/mw$.

The fin efficiency η_f is plotted as a function of the dimensionless parameter $w(U_c/kt)^{1/2}$ in Figure 3.17. When the fin efficiency approaches unity, the

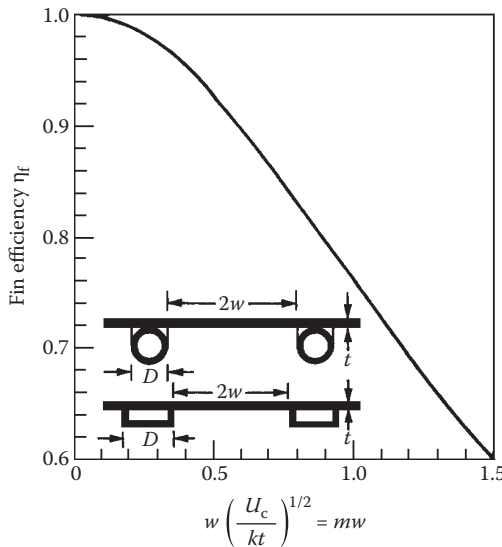


FIGURE 3.17

Fin efficiency for tube and sheet flat-plate solar collectors.

maximum portion of the radiant energy impinging on the fin becomes available for heating the fluid.

In addition to the heat transferred through the fin, the energy impinging on the portion of the plate above the flow passage is also useful. The rate of useful energy from this region available to heat the working fluid is

$$q_{\text{duct}}(x_0) = D\{\alpha_s I_s - U_c[T_b(x_0) - T_a]\}. \quad (3.35)$$

Thus, the useful energy per unit length in the flow direction becomes

$$q_u(x_0) = (D + 2w\eta)\{\alpha_s I_s - U_c[T_b(x_0) - T_a]\}. \quad (3.36)$$

The energy $q_u(x_0)$ must be transferred as heat to the working fluid. If the thermal resistance of the metal wall of the flow duct is negligibly small and there is no contact resistance between the duct and the plate, the rate of heat transfer to the fluid is

$$q_u(x_0) = P\bar{h}_{c,i}[T_b(x_0) - T_f(x_0)]. \quad (3.37)$$

where P is the perimeter of the flow duct, which is $2(D + d)$ for a rectangular duct. Contact resistance may become important in poorly manufactured collectors in which the flow duct is clamped or glued to the collector plate. Collectors manufactured by such methods are usually not satisfactory.

3.2.6 Collector Efficiency Factor

To obtain a relation for the useful energy delivered by a collector in terms of known physical parameters, the fluid temperature, and the ambient temperature, the collector temperature must be eliminated from Equations 3.36 and 3.37. Solving for $T_b(x_0)$ in Equation 3.37 and substituting this relation in Equation 3.36 gives

$$q_u(x_0) = l'F'\{\alpha_s I_s - U_c[T_f(x_0) - T_a]\}, \quad (3.38)$$

where F' is called the collector efficiency factor (Bliss 1959) and $l' = (2w + D)$. F' is given by

$$F' = \frac{1/U_c}{l - 1/(U_c(D + 2w\eta_f)) + 1/(\bar{h}_{c,i}P)}. \quad (3.39)$$

For a flow duct of circular cross section of diameter D , F' can be written as

$$F' = \frac{1/U_c}{l - 1/(U_c(D + 2w\eta_f)) + 1/(\bar{h}_{c,i}\pi D)}.$$

TABLE 3.5

Typical Values for the Parameters That Determine the Collector Efficiency Factor F' for a Flat-Plate Collector in Equation 3.39

	U_c	
2 glass covers	4 W/m ² ·K	0.685 Btu/h·ft ² ·°F
1 glass cover	8 W/m ² ·K	1.37 Btu/h·ft ² ·°F k_t
Copper plate, 1 mm thick	0.38 W/K	0.72 Btu/h·°F
Steel plate, 1 mm thick	0.045 W/K	0.0866 Btu/h·°F
		\bar{h}_{ci}
Water in laminar flow forced convection	300 W/m ² ·K	52 Btu/h·ft ² ·°F
Water in turbulent flow forced convection	1500 W/m ² ·K	254 Btu/h·ft ² ·°F
Air in turbulent forced convection	100 W/m ² ·K	17.6 Btu/h·ft ² ·°F

Physically, the denominator in Equation 3.39 is the thermal resistance between the fluid and the environment, whereas the numerator is the thermal resistance between the collector surface and the ambient air. The collector-plate efficiency factor F' depends on U_c , \bar{h}_{ci} , and η_f . It is only slightly dependent on temperature and can, for all practical purposes, be treated as a design parameter. Typical values for the factors determining the value of F' are given in Table 3.5.

The collector efficiency factor increases with increasing plate thickness and plate thermal conductivity, but it decreases with increasing distance between flow channels. Also, increasing the heat-transfer coefficient between the walls of the flow channel and the working fluid increases F' , but an increase in the overall conductance U_c will cause F' to decrease.

3.2.7 Collector Heat-Removal Factor

Equation 3.38 yields the rate of heat transfer to the working fluid at a given point x along the plate for specified collector and fluid temperatures. However, in a real collector, the fluid temperature increases in the direction of flow as heat is transferred to it. An energy balance for a section of flow duct dx can be written in the form

$$\dot{m}c_p \left(T_f|_{x+dx} - T_f|_x \right) = q_u(x)dx. \quad (3.40)$$

Substituting Equation 3.38 for $q_u(x)$ and $T_f(x) + (dT_f(x)/dx)dx$ for $T_f|_{x+dx}$ in Equation 3.40 gives the differential equation

$$\dot{m}c_p \frac{dT_f(x)}{dx} = l F \{ \alpha_s I_s - U_c [T_f(x) - T_a] \}. \quad (3.41)$$

Separating the variables gives, after some rearranging,

$$\frac{dT_f(x)}{T_f(x) - T_a - \alpha_s I_s / U_c} = \frac{l F U_c}{\dot{m} c_p} dx. \quad (3.42)$$

Equation 3.42 can be integrated and solved for the outlet temperature of the fluid $T_{f,out}$ for a duct length L and for the fluid inlet temperature $T_{f,in}$ if we assume that F' and U_c are constant, or

$$\frac{T_{f,out} - T_a - \alpha_s I_s / U_c}{T_{f,in} - T_a - \alpha_s I_s / U_c} = \exp \left(-\frac{U_c l F L}{\dot{m} c_p} \right). \quad (3.43)$$

To compare the performance of a real collector with the thermodynamic optimum, it is convenient to define the heat-removal factor F_R as the ratio between the actual rate of heat transfer to the working fluid and the rate of heat transfer at the minimum temperature difference between the absorber and the environment.

The thermodynamic limit corresponds to the condition of the working fluid remaining at the inlet temperature throughout the collector. This can be approached when the fluid velocity is very high. From its definition, F_R can be expressed as

$$F_R = \frac{G c_p (T_{f,out} - T_{f,in})}{\alpha_s I_s - U_c (T_{f,in} - T_a)}, \quad (3.44)$$

where G is the flow rate per unit surface area of collector \dot{m}/A_c . By regrouping the right-hand side of Equation 3.44 and combining with Equation 3.43, it can easily be verified that

$$\begin{aligned} F_R &= \frac{G c_p}{U_c} \left(1 - \frac{\alpha_s I_s / U_c - (T_{f,out} - T_a)}{\alpha_s I_s / U_c - (T_{f,in} - T_a)} \right) \\ &= \frac{G c_p}{U_c} \left(1 - \exp \left(-\frac{U_c l F}{G c_p} \right) \right). \end{aligned} \quad (3.45)$$

Inspection of the above relation shows that F_R increases with increasing flow rate and approaches as an upper limit F' , the collector efficiency factor. Since the numerator of the right-hand side of Equation 3.44 is q_u , the rate of useful heat transfer can now be expressed in terms of the fluid inlet temperature, or

$$q_u = A_c F_R [\alpha_s I_s - U_c (T_{f,in} - T_a)]. \quad (3.46)$$

If a glazing above the absorber plate has transmittance τ_s , then

$$q_u = A_c F_R [\tau_s \alpha_s I_c - U_c (T_{f,in} - T_a)], \quad (3.47)$$

and instantaneous efficiency η_c is

$$\eta_c = \frac{q_u}{I_c A_c} = F_R \tau_s \alpha_s - U_c (T_{f,in} - T_a) / I_c. \quad (3.48)$$

Equation 3.48 is also known as the *Hottel–Whillier–Bliss* equation. This is a convenient form for design, because the fluid inlet temperature to the collector is usually known or can be specified.

Example 3.1

Calculate the averaged hourly and daily efficiency of a water solar collector on January 15, in Boulder, Colorado. The collector is tilted at an angle of 60° and has an overall conductance of $8.0 \text{ W/m}^2\text{K}$ on the upper surface. It is made of copper tubes, with a 1-cm ID, 0.05 cm thick, which are connected by a 0.05-cm-thick plate at a center-to-center distance of 15 cm. The heat-transfer coefficient for the water in the tubes is $1500 \text{ W/m}^2\text{K}$, the cover transmittance is 0.9, and the solar absorptance of the copper surface is 0.9. The collector is 1 m wide and 2 m long, the water inlet temperature is 330 K, and the water flow rate is 0.02 kg/s. The horizontal insolation (total) I_h and the environmental temperature are tabulated in the following. Assume that the diffuse radiation accounts for 25% of the total insolation.

Solution

The total radiation received by the collector is calculated from Equation 2.46 and neglecting the ground reflected radiation:

$$I_c = I_{d,c} + I_{b,c} = 0.25 I_h \cos^2 \frac{60}{2} + (1 - 0.25) I_h R_b.$$

Time (h)	$I_h (\text{W/m}^2)$	$T_{amb} (\text{K})$
7–8	12	270
8–9	80	280
9–10	192	283
10–11	320	286
11–12	460	290
12–13	474	290
13–14	395	288
14–15	287	288
15–16	141	284
16–17	32	280

The tilt factor R_b is obtained from its definition in Chapter 2 (see Equation 2.60):

$$R_b = \frac{\cos i}{\sin \alpha} = \frac{\sin(L - \beta)\sin \delta_s + \cos(L - \beta)\cos \delta_s \cos h_s}{\sin L \sin \delta_s + \cos L \cos \delta_s \cos h_s},$$

where $L = 40^\circ$, $\delta_s = -21.1$ on January 15, and $\beta = 60^\circ$. The hour angle h_s equals 15° for each hour away from noon.

The fin efficiency is obtained from Equation 3.34:

$$\eta_f = \frac{\tanh m(l - D)/2}{m(l - D)/2}$$

where

$$m = \frac{U_c}{kt}^{1/2} = \frac{8}{390 \times 5 \times 10^{-4}}^{1/2} = 6.4, \text{ and}$$

$$\eta_f = \frac{\tanh 6.4(0.15 - 0.01)/2}{6.4(0.15 - 0.01)/2} = 0.938.$$

The collector efficiency factor F' is, from Equation 3.39,

$$F' = \frac{\frac{1/U_c}{l - 1/(U_c(D + 2w\eta_f)) + 1/(h_{c,i}\pi D)}}{\frac{1/8.0}{0.15 \cdot 1/8.0(0.01 + 0.14 \times 0.938) + 1/1500\pi \times 0.01}} = 0.92.$$

Then, we obtain the heat-removal factor from Equation 3.45:

$$F_R = \frac{Gc_p}{U_c} \left[1 - \exp \left(-\frac{U_c F}{Gc_p} \right) \right].$$

Time (h)	I_h (W/m ²)	R_b	$I_{d,c}$ (W/m ²)	$I_{b,c}$ (W/m ²)	I_c (W/m ²)	q_u (W)	T_{amb} (K)	η_c
7–8	12	4.46	2	40	42	0	270	0.000
8–9	80	2.71	15	163	178	0	280	0.000
9–10	192	2.28	36	328	364	0	283	0.000
10–11	320	2.11	60	507	567	182	286	0.160
11–12	460	2.07	86	714	800	554	290	0.346
12–13	474	2.11	89	751	840	609	290	0.363
13–14	395	2.28	74	675	749	457	288	0.305
14–15	287	2.71	54	584	638	305	288	0.239
15–16	141	4.46	26	471	498	60	284	0.060
16–17	32	0	6	0	0	0	280	0.000

$$F_R = \frac{0.001 \times 4184}{8.0} \left(1 - \exp\left(-\frac{8.0 \times 0.922}{0.01 \times 4184}\right)\right) = 0.845$$

From Equation 3.47, the useful heat delivery rate is

$$q_u = 2 \times 0.845 [I_c \times 0.81 - 8.0(T_{f,in} - T_{amb})].$$

The efficiency of the collector is $\eta_c = q_u / A_c I_c$ and the hourly averages are calculated in the table above.

Thus, $\sum I_c = 4676 \text{ W/m}^2$ and $\sum q_u = 2167 \text{ W}$. The daily average efficiency is obtained by summing the useful energy for those hours during which the collector delivers heat and dividing by the total insolation between sunrise and sunset. This yields

$$\eta_{c,day} = \frac{\sum q_u}{\sum A_c I_c} = \frac{2167}{2 \times 4676} = 0.232 \text{ or } 23.2\%.$$

3.2.8 Transient Effects

The preceding analysis assumed that steady-state conditions exist during the operation of the collector. Under actual operating conditions, the rate of insolation will vary and the ambient temperature and the external wind conditions may change. To determine the effect of changes in these parameters on the performance of a collector, it is necessary to make a transient analysis that takes the thermal capacity of the collector into account.

As shown in Klein et al. (1974), the effect of collector thermal capacitance is the sum of two contributions: the *collector storage* effect, resulting from the heat required to bring the collector up to its final operating temperature, and the *transient* effect, resulting from fluctuations in the meteorological conditions. Both effects result in a net loss of energy delivered compared with the predictions from the zero capacity analysis. This loss is particularly important on a cold morning when all of the solar energy absorbed by the collector is used to heat the hardware and the working fluid, thus delaying the delivery of useful energy for some time after the sun has come up.

Transient thermal analyses can be made with a high degree of precision (Kreith 1975), but the analytical predictions are no more accurate than the weather data and the overall collector conductance. For most engineering applications, a simpler approach is therefore satisfactory (Duffie and Beckman 1980). For this approach, it will be assumed that the absorber plate, the ducts, the back insulation, and the working fluid are at the same temperature. If back losses are neglected, an energy balance on the collector plate and the working fluid for a single-glazed collector delivering no useful energy can be written in the form

$$(\bar{mc})_p \frac{d\bar{T}_p(t)}{dt} = A_c I_s \alpha_s + A_c U_p (\bar{T}_g(t) - \bar{T}_p(t)) , \quad (3.49)$$

where $(\bar{mc})_p$ is the sum of the thermal capacities of the plate, the fluid, and the insulation; I_s is the insolation on the absorber plate; and U_p is the conductance between the absorber plate at \bar{T}_p and its cover at \bar{T}_g . Similarly, a heat balance on the collector cover gives

$$(mc)_g \frac{d\bar{T}_g(t)}{dt} = A_c U_p (\bar{T}_p(t) - \bar{T}_g(t)) - A_c U_\infty (\bar{T}_g(t) - T_a) , \quad (3.50)$$

where $U_\infty = (h_{c,\infty} + h_{r,\infty})$ (see Equation 3.18) and $(mc)_g$ is the thermal capacity of the cover plate.

Equations 3.49 and 3.50 can be solved simultaneously and the transient heat loss can then be determined by integrating the instantaneous loss over the time during which transient effects are pronounced. A considerable simplification in the solution is possible if one assumes that at any time the collector heat loss and the cover heat loss are equal, as in a quasi-steady state, so that

$$U_\infty A_c (\bar{T}_g(t) - T_a) = U_c A_c (\bar{T}_p(t) - T_a) . \quad (3.51)$$

Then, for a given air temperature, differentiation of Equation 3.51 gives

$$\frac{d\bar{T}_g(t)}{dt} = \frac{U_c d\bar{T}_p(t)}{U_\infty dt} . \quad (3.52)$$

Adding Equations 3.50, 3.51, and 3.52 gives a single differential equation for the plate temperature

$$(\bar{mc})_p + \frac{U_c}{U_\infty} (mc)_R \frac{d\bar{T}_p(t)}{dt} = \alpha_s I_s - U_c (\bar{T}_p(t) - T_a) A_c . \quad (3.53)$$

Equation 3.53 can be solved directly for given values of I_s and T_a . The solution to Equation 3.53 then gives the plate temperature as a function of time, for an initial plate temperature $T_{p,0}$, in the form

$$\bar{T}_p(t) - T_a = \frac{\alpha_s I_s}{U_c} - \frac{\alpha_s I_s}{U_c} (T_{p,0} - T_a) \exp \left(-\frac{U_c A_c t}{(\bar{mc})_p + (U_c/U_\infty)_c (mc)_g} \right) . \quad (3.54)$$

Collectors with more than one cover can be treated similarly, as shown in Collares-Pereira et al. (1977).

For a transient analysis, the plate temperature \bar{T}_p can be evaluated at the end of a specified period if the initial value of \bar{T}_p and the values of α_s , I_s , U_c , and T_a during the specified time are known. Repeated applications of Equation 3.54 provide an approximate method of evaluating the transient effects. An estimate of the net decrease in useful energy delivered can be obtained by multiplying the effective heat capacity of the collector, given by $(\bar{mc})_p + (U_c/U_\infty)(mc)_g$, by the temperature rise necessary to bring the collector to its operating temperature. Note that the parameter $[(\bar{mc})_p + (U_c/U_\infty)(mc)_g]/U_c A_c$ is the *time constant* of the collector (Collares-Pereira and Rabl 1979; Kreith 1975) and small values of this parameter will reduce losses resulting from transient effects.

Example 3.2

Calculate the temperature rise between 8 and 10 a.m. of a $1 \text{ m} \times 2 \text{ m}$ single-glazed water collector with a 0.3-cm-thick glass cover if the heat capacities of the plate, water, and back insulation are 5, 3, and 2 kJ/K , respectively. Assume that the unit surface conductance from the cover to ambient air is $18 \text{ W}/\text{m}^2 \cdot \text{K}$ and the unit surface conductance between the collector and the ambient air is $U_c = 6 \text{ W}/\text{m}^2 \cdot \text{K}$. Assume that the collector is initially at the ambient temperature. The absorbed insolation $\alpha_s I_s$ during the first hour averages $90 \text{ W}/\text{m}^2$, and that between 9 and 10 a.m., $180 \text{ W}/\text{m}^2$. The air temperature between 8 and 9 a.m. is 273 K , and that between 9 and 10 a.m., 278 K .

Solution

The thermal capacitance of the glass cover is $(mc)_g = (\rho V c_p)_g = (2500 \text{ kg}/\text{m}^3)(1 \text{ m} \times 2 \text{ m} \times 0.003 \text{ m})(1 \text{ kJ}/\text{kg} \cdot \text{K}) = 15 \text{ kJ}/\text{K}$. The combined collector, water, and insulation thermal capacity is equal to

$$(\bar{mc})_p + \frac{U_c}{U_\infty}(mc)_g = 5 + 3 + 2 + 0.3 \times 15 = 15.5 \text{ kJ}/\text{K}.$$

From Equation 3.54, the temperature rise of the collector given by

$$T_p - T_a = \frac{\alpha_s I_s}{U_c} - \frac{\alpha_s I_s}{U_c} (T_{p,0} - T_a) \exp \left[-\frac{U_c A_c t}{(\bar{mc})_p + (U_c/U_\infty)(mc)_g} \right].$$

At 8 a.m., $T_{p,0} = T_a$; therefore, the temperature rise, between 8 and 9 a.m., is

$$= \frac{90}{6} \left(1 - \exp \left[-\frac{2 \times 6 \times 3600}{15,500} \right] \right) = 15 \times 0.944 = 14.2 \text{ K}.$$

Thus, at 9 a.m., the collector temperature will be 287.2 K. Between 9 and 10 a.m., the collector temperature will rise as shown below:

$$= 278 + \frac{180}{6} - (30 - 9.2)0.056 = 306 \text{ K}$$

Thus, at 10 a.m., the collector temperature has achieved a value sufficient to deliver useful energy at a temperature level of 306 K.

3.2.9 Air-Cooled Flat-Plate Collector Thermal Analysis

The basic air-cooled flat-plate collector shown in Figure 3.18 differs fundamentally from the liquid-based collectors described in preceding sections because of the relatively poor heat-transfer properties of air. For example, in turbulent flow in a given conduit for a fixed value of Reynolds number, the convection heat-transfer coefficient for water is approximately 50 times greater than that for air. As a result, it is essential to provide the largest heat-transfer area possible to remove heat from the absorber surface of an air-heating collector.

The most common way to achieve adequate heat transfer in air collectors is to flow air over the entire rear surface of the absorber as shown. The heat-transfer analysis of such a collector does not involve the fin effect or the tube-to-plate bond conductance problem, which arises in liquid collectors. The heat-transfer process is essentially that of an unsymmetrically heated duct of large aspect ratio (typically 20–40).

Malik and Buelow (1976a,b) surveyed the fluid mechanics and heat-transfer phenomena in air collectors. They concluded that a suitable expression for the Nusselt number for a smooth air-heating collector is

$$\text{Nu}_{\text{sm}} = \frac{0.0192 \text{ Re}^{3/4} \text{ Pr}}{1 + 1.22 \text{ Re}^{-1/8} (\text{Pr} - 2)} . \quad (3.55)$$

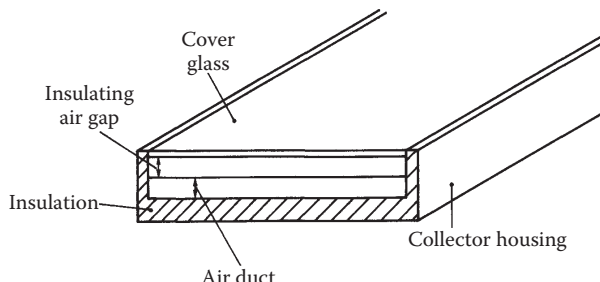


FIGURE 3.18

Schematic diagram of a basic air-heating flat-plate collector with a single glass (or plastic) cover.

If the surface is hydrodynamically rough, they recommended multiplying the smooth-surface Nusselt number by the ratio of the rough-surface friction factor f to the smooth-surface friction factor f_{sm} from the Blasius equation

$$f_{sm} = 0.079 \text{ Re}^{-1/4}. \quad (3.56)$$

The convective coefficient h_c in the Nusselt number is based on a unit absorber area but the hydraulic diameter D_H in the Nusselt and Reynolds numbers is based on the *entire duct perimeter*.

3.2.9.1 Air-Collector Efficiency Factor

The collector efficiency factor F' is defined as the ratio of energy collection rate to the collection rate if the absorber plate were at the local fluid temperature. F' is particularly simple to calculate, since no fin analysis or bond-conductance term is present for air collectors. For the collector shown in Figure 3.18, F' is given by

$$F' = \frac{\bar{h}_c}{\bar{h}_c + U_c}, \quad (3.57)$$

where U_c is calculated from Klein's equation and the duct convection coefficient h_c is calculated from Equation 3.55.

3.2.9.2 Air-Collector Heat-Removal Factor

The collector heat-removal factor is a convenient parameter, since it permits useful energy gain to be calculated by knowledge of only the easily determined fluid inlet temperature as shown in Equation 3.45. The heat-removal factor F_R for a typical air collector such as the one shown in Figure 3.18 is given by

$$F_R = \frac{\dot{m}_a c_{p,a}}{U_c A_c} \left(1 - \exp \left(- \frac{F U_c A_c}{\dot{m}_a c_{p,a}} \right) \right), \quad (3.58)$$

where F' is given by Equation 3.57, \dot{m}_a is the air flow rate (kg/s), and $c_{p,a}$ is its specific heat. The heat-removal factor for air collectors is usually significantly less than that for liquid collectors because \bar{h}_c for air is much smaller than that for a liquid such as water.

Example 3.3

Calculate the collector-plate efficiency factor F' and heat-removal factor F_R for a smooth, 1-m-wide, 5-m-long air collector with the following design. The flow rate per unit collector area is $0.7 \text{ m}^3/\text{min} \cdot \text{m}_c^2$ ($2.1 \text{ ft}^3/\text{minft}_c^2$).

The air duct height is 1.5 cm (0.6 in), the air density is 1.1 kg/m^3 (0.07 lb/ft^3), the specific heat is $1 \text{ kJ/kg}\cdot\text{K}$ ($0.24 \text{ Btu/lb}\cdot^\circ\text{F}$), and the viscosity is $1.79 \times 10^{-5} \text{ kg/m}\cdot\text{s}$ ($1.2 \times 10^{-5} \text{ lb}\cdot\text{ft}\cdot\text{s}$). The collector heat-loss coefficient U_c is $18 \text{ kJ/h}\cdot\text{m}^2\cdot\text{K}$ ($5 \text{ W/m}^2\cdot\text{K}$; $0.88 \text{ Btu/h}\cdot\text{ft}^2\cdot^\circ\text{F}$).

Solution

The first step is to determine the duct heat-transfer coefficient h_c from Equation 3.55. The Reynolds number is defined as

$$\text{Re} = \frac{\rho \bar{V} D_H}{\mu},$$

in which the average velocity \bar{V} is the volume flow rate divided by the flow area.

$$\bar{V} = \frac{0.7 \times 1 \times 5}{1 \times 0.015} = 233 \text{ m/min} = 3.89 \text{ m/s},$$

and the hydraulic diameter D_H is

$$D_H = \frac{4(0.015 \times 1)}{1 + 1 + 0.015 + 0.015} = 0.0296 \text{ m, and}$$

$$\text{Re} = \frac{(1.1)(3.89)(0.0296)}{1.79 \times 10^{-5}} = 7066.$$

From Equation 3.55, the Nusselt number is

$$\text{Nu} = \frac{0.0192(7066)^{3/4}(0.72)}{1 + 1.22(7066)^{-1/8}(0.72 - 2.0)} = 22.0.$$

The heat-transfer coefficient is

$$h_c = \text{Nu} \frac{k}{D_H} = \frac{\text{Nu} c_p}{\text{Pr} D_H}.$$

The Prandtl number for air is ~ 0.72 . Therefore,

$$\begin{aligned} h_c &= \frac{(22.0)(1.0)(1.79 \times 10^{-5})}{(0.72)(0.0296)} = 0.0185 \text{ kJ/m}^2\cdot\text{s}\cdot\text{K} \\ &= 66.5 \text{ kJ/m}^2\cdot\text{h}\cdot^\circ\text{C} (3.26 \text{ Btu/h}\cdot\text{ft}^2\cdot^\circ\text{F}). \end{aligned}$$

The plate efficiency is then, from Equation 3.57,

$$F = \frac{66.5}{66.5 + 18} = 0.787,$$

and the heat-removal factor F_R can be calculated from Equation 3.58. The mass flow rate per unit area is

$$\frac{\dot{m}}{A_c} = \rho(q/A_c) = \frac{1.1 \times 0.7}{60} = -0.128 \text{ kg/s} \cdot \text{m}_c^2.$$

Then,

$$F_R = \frac{(0.0128)(1)}{(18/3600)} \cdot 1 - \exp \left(-\frac{(0.787)(18/3600)}{(0.0128)(1)} \right) = 0.677.$$

That is, the particular collector in question can collect 67.7% of the heat it could collect if its surface were at the air-inlet temperature. F_R varies weakly with the fluid temperature through the temperature effect upon U_c .

3.3 Tubular Solar Energy Collectors

Two general methods exist for significantly improving the performance of solar collectors above the minimum flat-plate collector level. The first method increases solar flux incident on the receiver. It will be described in Section 3.5 on concentrators. The second method involves the reduction of parasitic heat loss from the receiver surface. Tubular collectors, with their inherently high compressive strength and resistance to implosion, afford the only practical means for completely eliminating convection losses by surrounding the receiver with a vacuum on the order of 10^{-4} mm Hg. The analysis of evacuated tubular collectors is the principal topic of this section.

Tubular collectors have a second application. They may be used to achieve a small level of concentration (1.5 to 2.0) by forming a mirror from a part of the internal concave surface of a glass tube. This reflector can focus radiation on a receiver inside this tube. Since such a receiver is fully illuminated, it has no parasitic "back" losses. The performance of a nonevacuated tubular collector may be improved slightly by filling the envelope with high-molecular-weight noble gases. External concentrators of radiation may also be coupled to an evacuated receiver for improvement of performance over the simple evacuated tube. Collectors of this type are described briefly below.

3.3.1 Evacuated-Tube Collectors

Evacuated-tube devices have been proposed as efficient solar energy collectors since the early 20th century. In 1909, Emmett proposed several evacuated-tube concepts for solar energy collection, two of which are being sold commercially today (Emmett 1911). Speyer (1965) also proposed a tubular evacuated flat-plate design for high-temperature operation. With the recent advances in vacuum technology, evacuated-tube collectors can be reliably mass produced. Their high-temperature effectiveness is essential for the efficient operation of solar air-conditioning systems and process heat systems.

Figure 3.19 shows schematic cross sections of several glass evacuated-tube collector concepts. The simplest design is basically a small flat-plate collector housed in an evacuated cylinder (Figure 3.19a). If the receiver is metal, a glass-to-metal seal is required to maintain a vacuum. In addition, a thermal short may occur from inlet to outlet tube unless special precautions are taken.

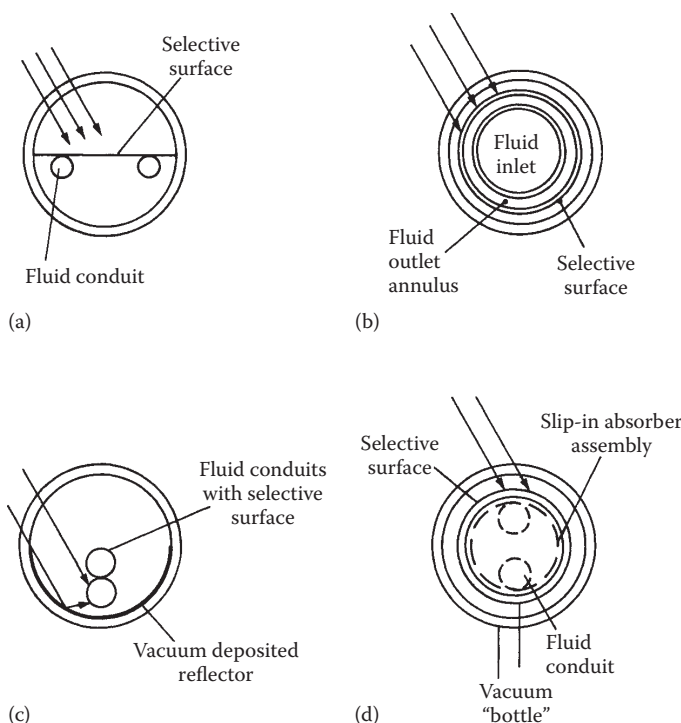


FIGURE 3.19

Evacuated-tube solar energy collectors: (a) flat plate, (b) concentric tubular, (c) concentrating, (d) vacuum bottle with slip-in heat exchanger contacting rear surface of receiver.

Mildly concentrating, tubular collectors can be made using the design of Figure 3.19c. Either a single flow-through receiver with fins or a double U tube as shown can be used.

One of Emmett's designs is shown in Figure 3.19d. It consists of an evacuated vacuum bottle much like an unsilvered, wide-mouth Dewar flask into which a metal heat exchanger is inserted. The outer surface of the inner glass tube is the absorber. The heat generated is transferred through the inner glass tube to the metal slip-in heat exchanger. Since this heat transfer is through a glass-to-metal interface that has only intermittent point contacts, significant axial temperature gradients can develop, thereby stressing the glass tube. In addition, a large temperature difference can exist between the inner and outer glass tubes. At the collector ends where the tubes are joined, a large temperature gradient and consequent thermal stress can exist.

The level of evacuation required for suppression of convection and conduction can be calculated from basic heat-transfer theory. As the tubular collector is evacuated, reduction of heat loss first occurs because of the reduction of the Rayleigh number. The effect is proportional to the square root of density. When the Rayleigh number is further reduced below the lower threshold for convection, the heat-transfer mechanism is by conduction only. For most gases, the thermal conductivity is independent of pressure if the mean free path is less than the heat-transfer path length.

For very low pressure, the conduction heat transfer in a narrow gap (Dushman 1962) is given by

$$q_k = \frac{k\Delta T}{g + 2p}, \quad (3.59)$$

where g is the gap width and p is the mean free path. For air, the mean free path at atmospheric pressure is approximately 70 μm. If 99% of the air is removed from a tubular collector, the mean free path increases to 7 mm, and conduction heat transfer is slightly affected. However, if the pressure is reduced to 10^{-3} torr, the mean free path is 7 cm, which is substantially greater than the heat-transfer path length, and conduction heat transfer is effectively suppressed. The relative reduction in heat transfer as a function of mean free path can be derived from Equation 3.59:

$$\frac{q_{vac}}{q_k} = \frac{1}{1 + 2p/g}, \quad (3.60)$$

where q_k is the conduction heat transfer if convection is suppressed and q_{vac} is the conduction heat transfer under a vacuum.

3.3.2 Thermal Analysis of a Tubular Collector

The heat loss from a tubular collector occurs primarily through the mechanism of radiation from the absorber surface. The rate of heat loss per unit absorber area q_L can then be expressed as

$$q_L = U_c(T_r - T_a). \quad (3.61)$$

Total thermal resistance $1/U_c$ is the sum of three resistances:

R_1 = radiative exchange from absorber tube to cover tube

R_2 = conduction through glass tube

R_3 = convection and radiation to environment

The overall resistance is then

$$\frac{1}{U_c} = R_1 + R_2 + R_3. \quad (3.62)$$

The conductances R_i^{-1} are given by

$$R_1^{-1} = \frac{1}{1/\epsilon_r + 1/\epsilon_e - 1} \sigma(T_r + T_{ei})(T_r^2 + T_{ei}^2), \quad (3.63)$$

$$R_2^{-1} = \frac{2k}{D_r \ln(D_{eo}/D_{ei})}, \text{ and} \quad (3.64)$$

$$R_3^{-1} = h_c + \sigma\epsilon_e(T_{eo} + T_a)(T_{eo}^2 + T_a^2) \frac{D_{eo}}{D_r}, \quad (3.65)$$

where the subscript "e" denotes envelope (tube) properties, subscripts "i" and "o" denote inner and outer surfaces of the envelope (tube), T_r is the receiver (absorber) temperature, and h_c is the external convection coefficient for the envelope. Test data have shown that the loss coefficient U_c is between 0.5 and 1.0 W/m²°C, thus confirming the analysis.

The energy delivery rate q_u on an aperture area basis can be written as

$$q_u = \tau_e \alpha_r I_{eff} \frac{A_t}{A_c} - U_c(T_r - T_a) \frac{A_r}{A_c}, \quad (3.66)$$

where I_{eff} is the effective solar radiation both directly intercepted and intercepted after reflection from the back reflector, A_t is the projected area of a

tube (its diameter), and A_r is the receiver or absorber area. The receiver-to-collector aperture area ratio is $\pi D_r/d$, where d is the center-to-center distance between the tubes. Therefore,

$$q_u = \frac{D_r}{d} [\tau_e \alpha_r I_{\text{eff}} - \pi U_c (T_r - T_a)]. \quad (3.67)$$

Beekley and Mather (1975) have shown that a tube spacing one envelope diameter D_{eo} apart maximizes daily energy gain. A specularly reflecting cylindrical back surface improves performance by 10% or more.

3.4 Experimental Testing of Collectors

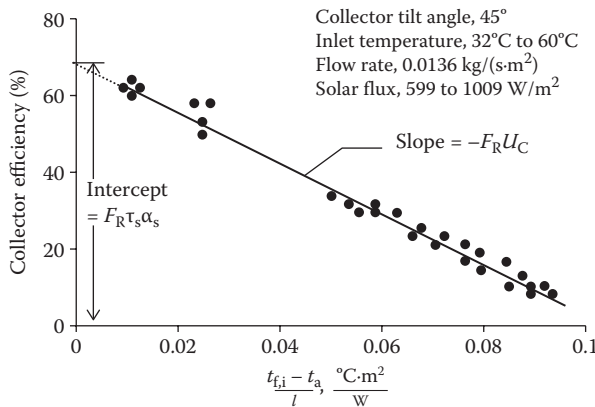
The performance of solar thermal systems for heating and cooling depends largely on the performance of solar collectors. Therefore, experimental measurement of thermal performance of solar collectors by standard methods is important and necessary. The experimentally determined performance data are needed for design purposes and for determining the commercial value of the collectors. The thermal performance of a solar collector is determined by establishing an efficiency curve from the measured instantaneous efficiencies for a combination of values of incident solar radiation, ambient temperature, and inlet fluid temperature. An instantaneous efficiency of a collector under steady-state conditions can be established by measuring the mass flow rate of the heat-transfer fluid, its temperature rise across the collector ($T_{f,out} - T_{f,in}$), and the incident solar radiation intensity (I_c) as

$$\eta_c = \frac{q_u}{A_c I_c} = \frac{\dot{m} C_p (T_{f,out} - T_{f,in})}{A_c I_c}. \quad (3.68)$$

The efficiency, η_c , of a collector under steady state can also be written according to the Hottel–Whillier–Bliss equation (Equation 3.48) as

$$\eta_c = F_R \tau_s \alpha_s - F_R U_c \frac{(T_{f,in} - T_a)}{I_c}. \quad (3.48)$$

Equation 3.48 suggests that for constant values of F_R and U_c , if η_c is plotted with respect to $(T_{f,in} - T_a)/I_c$, a linear curve will result, with a "y" intercept of $F_R \tau_s \alpha_s$ and a slope of $-F_R U_c$. Figure 3.20 shows a typical thermal performance curve for a flat-plate collector. Since τ_s and α_s can be measured independently,

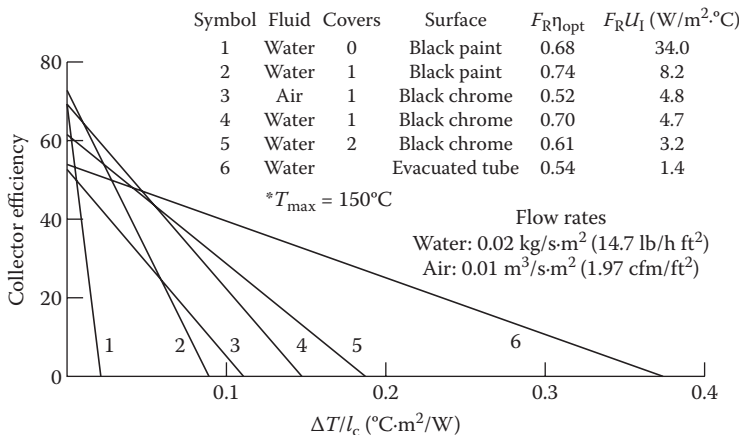
**FIGURE 3.20**

Thermal efficiency curve for a double-glazed flat-plate liquid type of solar collector.

a thermal performance curve of a flat-plate collector allows us to establish the value of F_R and U_c also. Figure 3.21 shows typical performance curves of various glazed and unglazed flat-plate solar collectors.

In Equation 3.48, the product $\tau_s \alpha_s$ will change with the angle of incidence. Since flat-plate collectors are normally fixed, the angle of incidence changes throughout the day. A relationship can be written between the actual or effective $(\tau_s \alpha_s)$ and $(\tau_s \alpha_s)_n$ for normal incidence as

$$(\tau_s \alpha_s) = (\tau_s \alpha_s)_n K_{\tau \alpha} \quad (3.69)$$

**FIGURE 3.21**

Typical performance curves for various flat-plate solar collectors.

where $(\tau_s \alpha_s)_n$ is the value of the product for normal angle of incidence and K_{ta} is called the incidence angle modifier. Therefore, the thermal performance of a flat-plate collector may be written as

$$\eta_c = F_R K_{ta} (\tau_s \alpha_s)_n - U_c \frac{(T_{f,in} - T_a)}{I_c} . \quad (3.70)$$

The thermal performance of collectors is usually found experimentally for normal angles of incidence in which case $K_{ta} = 1.0$. The incidence angle modifier is then measured separately. It has been established that K_{ta} is of the form

$$K_{ta} = 1 - b \frac{1}{\cos i} - 1 , \quad (3.71)$$

where b is a constant and i is the angle of incidence. Figure 3.22 shows a typical curve for K_{ta} .

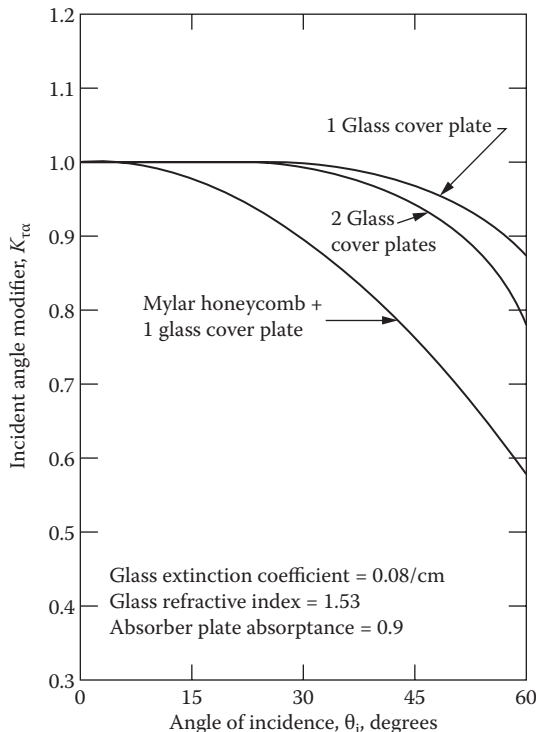


FIGURE 3.22

Incident angle modifier for three flat-plate solar collectors. (Reprinted from ASHRAE Standard 93-77, Methods of testing to determine the thermal performance of solar collectors. With permission from the American Society of Heating, Refrigerating and Air-Conditioning Engineers, Inc., Atlanta, GA.)

3.4.1 Testing Standards for Solar Thermal Collectors

Standard testing procedures adopted by regulating agencies in various countries establish ways of comparing the thermal performance of various collectors under the same conditions. In the United States, the thermal performance standards established by the American Society of Heating, Refrigeration and Air-Conditioning Engineers (ASHRAE) have been accepted for thermal performance testing of solar thermal collectors (ASHRAE 1980, 2003). Similar standards have been used in a number of countries (EN 12975-2). The standards established by ASHRAE include the following:

ASHRAE Standard 93-2003, "Methods of Testing to Determine the Thermal Performance of Solar Collectors" (ASHRAE 2003)

ASHRAE Standard 96-1980, "Methods of Testing to Determine the Thermal Performance of Unglazed Solar Collectors" (ASHRAE 1980)

ASHRAE Standard 93-2003 specifies the procedures for determining the time constant, thermal performance, and the incidence angle modifier of solar thermal collectors using a liquid or air as a working fluid. Figure 3.23 shows a schematic of a standard testing configuration for thermal performance testing. The tests are conducted under quasi-steady-state conditions

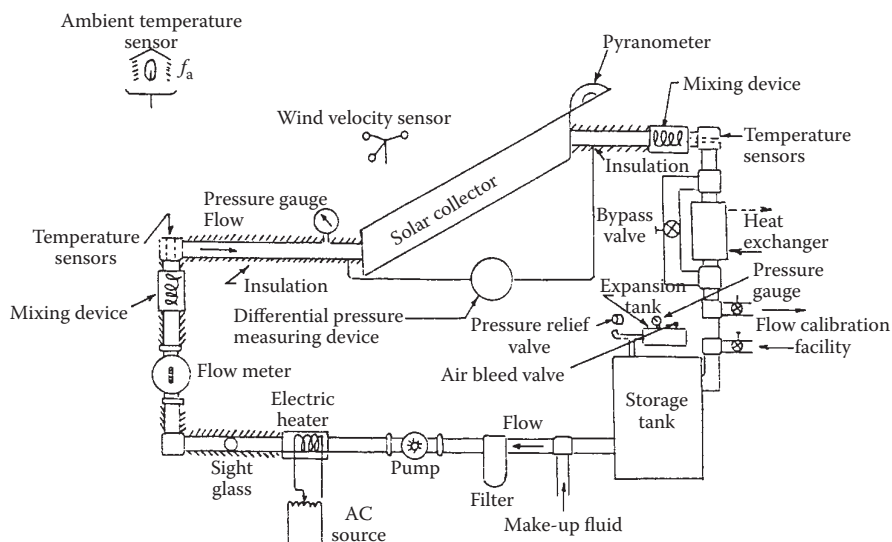


FIGURE 3.23

A testing configuration for a liquid-type solar collector. (Reprinted from ASHRAE Standard 93-77, Methods of testing to determine the thermal performance of solar collectors. With permission from the American Society of Heating, Refrigerating and Air-Conditioning Engineers, Inc., Atlanta, GA.)

3.4.1.1 Time Constant

In order to avoid the transient effects, performance of a collector is measured and integrated over at least the time constant of the collector. The time constant is measured by operating the collector under steady or quasi-steady conditions with a solar flux of at least 790 W/m^2 and then abruptly cutting the incident flux to zero, while continuing to measure the fluid inlet ($T_{f,i}$) and exit ($T_{f,e}$) temperatures. The fluid inlet temperature is maintained at $\pm 1^\circ\text{C}$ of the ambient temperature. The time constant is then determined as the time required to achieve

$$\frac{T_{f,e} - T_{f,i}}{T_{f,e,\text{initial}} - T_{f,i}} = 0.30. \quad (3.72)$$

3.4.1.2 Thermal Performance

For determining the thermal performance of a collector, ASHRAE Standard 93-2003 specifies test conditions to get at least four data points for the efficiency curve. The test conditions include the following:

1. Near normal incidence ($i \leq 5^\circ$) angle tests close to solar noon time
2. At least four tests for each $T_{f,i}$, two before and two after solar noon
3. At least four different values of $T_{f,i}$ to obtain different values of $\Delta T/I_c$, preferably to obtain ΔT at 10%, 30%, 50%, and 70% of stagnation temperature rise under the given conditions of solar intensity and ambient conditions

3.4.1.3 Incidence Angle Modifier

ASHRAE 93-2003 specifies that a curve for incidence angle modifier be established by determining the efficiencies of a collector for average angles of incidence of 0° , 30° , 45° , and 60° while maintaining $T_{f,i}$ at $\pm 1^\circ\text{C}$ of the ambient temperature. Since $(T_{f,i} - T_a) = 0$, the incident angle modifier according to Equation 3.70 is

$$K_{ta} = \frac{\eta_c}{F_R(\tau_s \alpha_s)_n}. \quad (3.73)$$

The denominator is the y intercept of the efficiency curve.

3.5 Concentrating Solar Collectors

Concentration of solar radiation is achieved by reflecting or refracting the flux incident on an aperture area A_a onto a smaller receiver/absorber area A_r .

An optical concentration ratio, CR_o , is defined as the ratio of the solar flux I_r on the receiver to the flux, I_a , on the aperture, or

$$CR_o = I_r/I_a, \quad (3.74)$$

while a geometric concentration ratio CR is based on the areas, or

$$CR = A_a/A_r. \quad (3.75)$$

CR_o gives a true concentration ratio because it accounts for the optical losses from the reflecting and refracting elements. However, since it has no relationship to the receiver area, it does not give an insight into the thermal losses that are proportional to the receiver area. In the analyses in this book, only geometric concentration ratio CR will be used.

Concentrators are inherently more efficient at a given temperature than are flat-plate collectors, since the area from which heat is lost is smaller than the aperture area. In a flat-plate device, both areas are equal in size. A simple energy balance illustrates this principle. The useful energy delivered by a collector q_u is given by

$$q_u = \eta_o I_c A_a - U_c (T_r - T_a) A_r, \quad (3.76)$$

in which η_o is the optical efficiency and other terms are as defined previously. The instantaneous collector efficiency is given by

$$\eta_c = \frac{q_u}{I_c A_a}, \quad (3.77)$$

from which, using Equation 3.76,

$$\eta_c = \eta_o - \frac{U_c (T_r - T_a)}{I_c} \frac{1}{CR}. \quad (3.78)$$

For a flat plate $CR \approx 1$, and for concentrators, $CR > 1$. As a result, the loss term (second term) in Equation 3.78 is smaller for a concentrator and the efficiency is higher. This analysis is necessarily simplified and does not reflect the reduction in optical efficiency that frequently, but not always, occurs because of the use of imperfect mirrors or lenses in concentrators. The evaluation of U_c in Equation 3.78 in closed form is quite difficult for high-temperature concentrators, because radiation heat loss is usually quite important and introduces nonlinearities ($\propto T^4$). One disadvantage of concentrators is that they can collect only a small fraction of the diffuse energy incident at their aperture. This property is an important criterion in defining the geographic limits to the successful use of concentrators.

3.5.1 Thermodynamic Limits to Concentration

A simple criterion is developed below for the upper limit of concentration (Rabl 1975) of a solar collector. Figure 3.24 is a schematic diagram of any concentrating device in which the source, aperture, and receiver are shown. The source represents a diffuse source or a diffuse-like source that could be formed by a moving point source, that is, the sun. The evaluation of the maximum achievable concentration ratio CR_{max} uses the concept of radiation exchange factors described in Chapter 2.

The factor \mathfrak{J}_{12} is defined as the fraction of radiation emitted from surface 1 that reaches surface 2 by whatever means—direct exchange, reflection, or refraction. It is shown in Chapter 2 that reciprocity relations exist for area exchange factors; for this analysis, the second law of thermodynamics requires, in addition, that

$$A_s \mathfrak{J}_{sa} = A_a \mathfrak{J}_{as} \quad (3.79)$$

and

$$A_s \mathfrak{J}_{sr} = A_r \mathfrak{J}_{rs}, \quad (3.80)$$

where “a” denotes aperture, “r” denotes receiver, and “s” denotes the source. Here, we use \mathfrak{J} symbols for exchange factor between nonblack surfaces and F symbols for black surfaces. By means of these expressions, the concentration ratio CR can be expressed as

$$CR = \frac{A_a}{A_r} = \frac{\mathfrak{J}_{sa} \mathfrak{J}_{rs}}{\mathfrak{J}_{as} \mathfrak{J}_{sr}}. \quad (3.81)$$

For the best concentrator possible, all radiation entering the aperture A_a reaches the receiver A_r ; that is,

$$\mathfrak{J}_{sa} = \mathfrak{J}_{sr}. \quad (3.82)$$

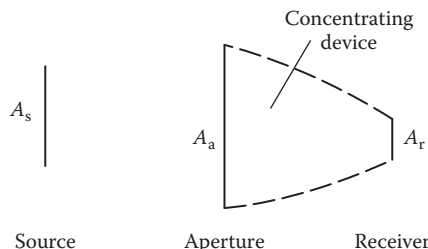


FIGURE 3.24

Generalized schematic diagram of any two-dimensional solar energy concentrating device showing source of radiation A_s , aperture A_a , and receiver A_r areas.

In addition, if the source is representable as a black body,

$$\mathfrak{F}_{as} = F_{as}, \quad (3.83)$$

where F_{as} is the radiation shape factor between two black surfaces. Using Equations 3.81 and 3.83, we have

$$CR = \frac{\mathfrak{F}_{rs}}{F_{as}}. \quad (3.84)$$

Because $\mathfrak{F}_{rs} \leq 1$ by the second law,

$$CR \leq CR_{max} = \frac{1}{F_{as}}. \quad (3.85)$$

Equation 3.85 states the simple and powerful result that the maximum concentration permitted by the second law is simply the reciprocal of the radiation shape factor F_{as} .

The shape factor F_{as} for a solar concentrator in two dimensions can be calculated from the diagram in Figure 3.25. This sketch represents a trough-like or single-curvature concentrator formed from mirrors or a linear (cylindrical) lens. It is illuminated by a line source of light of length $2r$ representing a portion of the sun's virtual trajectory. By reciprocity, we have

$$F_{as} = F_{sa} \frac{A_s}{A_a}. \quad (3.86)$$

If an angle $2\theta_{max}$ is defined as the maximum angle within which light is to be collected, we have

$$F_{as} = \sin \theta_{max} \quad (3.87)$$

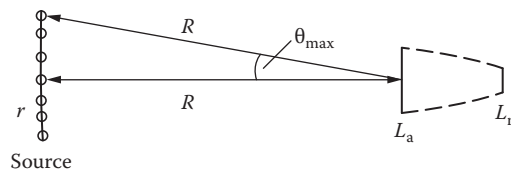


FIGURE 3.25

Schematic diagram of two-dimensional sun-concentrator geometry used to calculate shape factor F_{as} and showing acceptance half-angle θ_{max} and several positions of the sun.

from Hottel's crossed-string method (Hottel and Sarofim 1967) for $L \ll r$. The angle θ_{\max} is called the *acceptance half-angle*. From Equation 3.85, the maximum concentration is then

$$CR_{\max,2D} = \frac{1}{\sin \theta_{\max}}. \quad (3.88)$$

The term acceptance half-angle denotes coverage of one-half of the angular zone within which radiation is accepted (that is, "seen") by the receiver of a concentrator. Radiation is said to be accepted over an acceptance angle $2\theta_{\max}$ because radiation incident within this angle reaches the absorber after passing through the aperture. Practical acceptance angles range from a minimum subtending the sun's disk (approximately $1/2^\circ$) to 180° , a value characterizing a flat-plate collector accepting radiation from a full hemisphere.

Double-curvature or dish-type concentrators have an upper limit of concentration that can be evaluated by extending the method used above to three dimensions. The result of such a calculation for a compound-curvature device is given by

$$CR_{\max,3D} = \frac{1}{\sin^2 \theta_{\max}}. \quad (3.89)$$

In the above analyses, if the concentrator has an index of refraction $n > 1$, the maximum concentration will be (Welford and Winston 1989)

$$CR_{\max,2D} = \frac{n}{\sin \theta_{\max}} \quad (3.90)$$

and

$$CR_{\max,3D} = \frac{n^2}{\sin^2 \theta_{\max}}. \quad (3.91)$$

The second law prescribes not only the geometric limits of concentration as shown above but also the operating temperature limits of a concentrator. The radiation emitted by the sun and absorbed by the receiver of a concentrator q_{abs} is

$$q_{\text{abs}} = \tau \alpha_s A_s F_{\text{sa}} \sigma T_s^4, \quad (3.92)$$

where T_s is the effective temperature of the sun and τ is the overall transmittance function for the concentrator, including the effects of any lenses,

mirrors, or glass covers. If the acceptance half-angle θ_{\max} is selected to just accept the sun's disk of angular measure $\theta_s (\theta_s \sim 1/4^\circ)$, we have, by reciprocity (Equation 3.86), for a concentrator with compound curvature,

$$q_{\text{abs}} = \tau \alpha_s A_a \sin^2 \theta_s \sigma T_s^4. \quad (3.93)$$

If convection and conduction could be eliminated, all heat loss q_L is by radiation, and

$$q_L = \varepsilon_{\text{ir}} A_r \sigma T_r^4, \quad (3.94)$$

where ε_{ir} is the infrared emittance of the receiver surface. Radiation inputs to the receiver from a glass cover or the environment can be ignored for this upper limit analysis.

An energy balance on the receiver is then

$$q_{\text{abs}} = q_L + \eta_c q_{\text{abs}}, \quad (3.95)$$

where η_c is the fraction of energy absorbed at the receiver that is delivered to the working fluid. Substituting for Equations 3.93 and 3.94 in Equation 3.95, we have

$$(1 - \eta_c) \tau \alpha_s A_a \sin^2 \theta_s \sigma T_s^4 = \varepsilon_{\text{ir}} A_r \sigma T_r^4. \quad (3.96)$$

Because $CR = A_a/A_r$ and $CR_{\max} = 1/\sin^2 \theta_s$,

$$T_r = T_s (1 - \eta_c) \tau \frac{\alpha_s CR}{\varepsilon_{\text{ir}} CR_{\max}}^{1/4}. \quad (3.97)$$

In the limit as $\eta_c \rightarrow 0$ (no energy delivery) and $\tau \rightarrow 1$ (perfect optics), we have

$$\lim T_r \rightarrow T_s \frac{CR}{CR_{\max}}^{1/4}. \quad (3.98)$$

Since $\varepsilon_{\text{ir}} \rightarrow \alpha_s$ as $T_r \rightarrow T_s$, Equation 3.98 shows that

$$T_r \leq T_s, \quad (3.99)$$

as expected for an optically and thermally idealized concentrator. Equation 3.99 is equivalent to the Clausius statement of the second law for a solar concentrator.

3.5.2 Optical Limits to Concentrations

Equations 3.88 through 3.91 define the upper limit of concentration that may be achieved for a given concentration viewing angle. Of interest are the upper and lower limits of concentration defined by practical viewing angle limits—the maximum CR limited only by the size of the sun's disk and achieved by continuous tracking and the minimum CR, based on a specific number of hours of collection with no tracking.

The upper limit of concentration for two- and three-dimensional concentrators is on the order of

$$\text{CR}_{\max,2D} = \frac{1}{\sin 1/4^\circ} \approx 216 \text{ in air,}$$

$$= \frac{1.5}{\sin 1/4^\circ} \approx 324 \text{ in glass } (n = 1.5),$$

and

$$\text{CR}_{\max,3D} = \frac{1}{\sin^2 1/4^\circ} \approx 46,000 \text{ in air,}$$

$$= \frac{(1.5)^2}{\sin^2 1/4^\circ} \approx 103,500 \text{ in glass.}$$

In practice, these levels of concentration are not achievable because of the effects of tracking errors and imperfections in the reflecting- or refracting-element surface, as described later. Gleckman et al. (1989) are reported to have achieved the highest concentration of 56,000.

3.5.3 Acceptance of Diffuse Radiation

Diffuse or scattered radiation is not associated with a specific direction as is beam radiation. It is expected, therefore, that some portion of the diffuse component will fall beyond the acceptance angle of a concentrator and not be collectable. The minimum amount of diffuse radiation that is collectable can be estimated by assuming that the diffuse component is isotropic at the aperture. The exchange factor reciprocity relation shows that

$$A_a \mathfrak{I}_{as} = A_r \mathfrak{I}_{rs}. \quad (3.100)$$

For most practical concentrating devices that can accept a significant fraction of diffuse radiation, $\mathfrak{J}_{rs} = 1$. That is, all radiation leaving the receiver reaches the aperture and the environment eventually. Then,

$$\mathfrak{J}_{as} = \frac{A_r}{A_a} = \frac{1}{CR} \quad (3.101)$$

for any concentrator. Equation 3.101 indicates that at least $1/CR$ of the incident diffuse radiation reaches the receiver. In actual practice, the collectable diffuse portion will be greater than $1/CR$, since diffuse radiation is usually concentrated near the solar disk except during the cloudiest of days (see Chapter 2).

3.5.4 Ray Tracing Diagrams

Ray tracing diagrams are helpful in understanding the distribution of concentrated flux on the receiver and to design the receiver-absorber configurations. They are drawn by tracing a beam of parallel rays specularly reflected from the reflector surface. Figure 3.26 shows simple examples of ray tracing diagrams for a circular reflector and a parabolic reflector. From this figure, it is easy to understand that a receiver for a linear parabolic trough could be designed as a small diameter tube, while a larger-area rectangular surface would be required for a linear circular trough. Figure 3.27 demonstrates that the size of the receiver can be reduced, and therefore concentration increased, by using a smaller rim angle. A three-dimensional concentrator can be visualized by rotating each reflector profile about its axis. If a parabolic or circular reflecting concentrator tracks the sun in such a way that the axis of symmetry is always parallel to the solar beam, the reflected flux will be incident on the receiver. However, if the tracking is not perfect or if the concentrator is not designed to track, the beam may

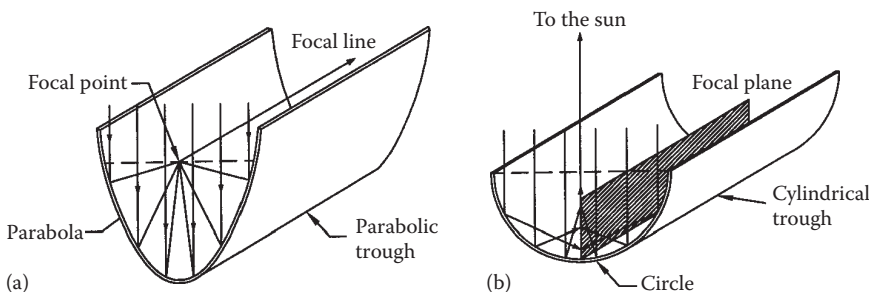
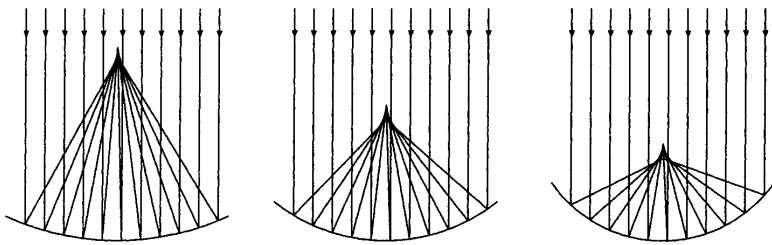
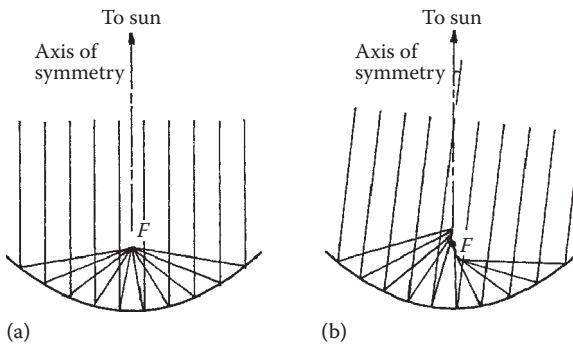


FIGURE 3.26

Examples of ray tracing diagrams for (a) a parabolic reflector and (b) a circular reflector.

**FIGURE 3.27**

Focusing of parallel rays of light using circular mirrors with different rim angles.

**FIGURE 3.28**

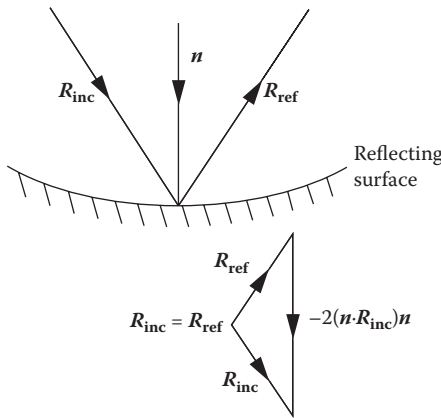
Concentration by parabolic reflector for a beam (a) parallel to the axis of symmetry and (b) at an angle to the axis.

make an angle with the axis of symmetry. In which case, the incident beam will not focus on the receiver, as demonstrated in Figure 3.28, unless the receiver design is modified. As seen from this figure, tracking errors will penalize a parabolic concentrator more severely than a circular concentrator. Therefore, a parabolic concentrator requires more accurate sun tracking for best utilization.

In order to formulate a ray tracing procedure suitable for numerical computation, laws of reflection and refraction are used in vector form as explained in detail in Welford and Winston (1989). Figure 3.29 shows the incident and reflected rays as unit vectors \mathbf{R}_{inc} and \mathbf{R}_{ref} , and a unit vector along the normal pointing into the reflecting surface is shown as \mathbf{n} . Then, according to the laws of reflection,

$$\mathbf{R}_{\text{ref}} = \mathbf{R}_{\text{inc}} - 2(\mathbf{n} \cdot \mathbf{R}_{\text{inc}})\mathbf{n}. \quad (3.102)$$

Thus, to trace a ray, we first find the incidence point at the reflecting surface, then a unit normal to the surface, and finally the reflected ray using

**FIGURE 3.29**

Vector formulation of reflection. (Adapted from Welford, W.T. and R. Winston, *High Collection Nonimaging Optics*, Academic Press, San Diego, CA, 1989.)

Equation 3.102. For example, if the reflecting surface is an ideal paraboloid with a focal length F , it can be expressed in an x, y, z coordinate system as

$$Z = \frac{x^2 + y^2}{4F}, \quad (3.103)$$

or

$$f(x, y, z) = 4Fz - x^2 - y^2. \quad (3.104)$$

The normal vector or gradient to this surface is defined as

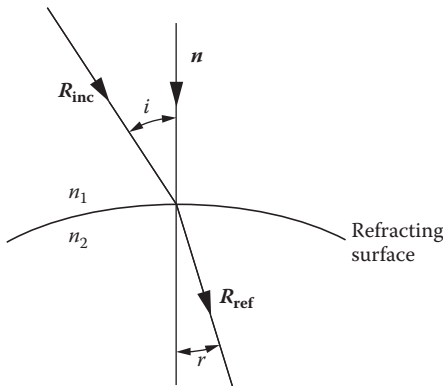
$$\mathbf{f} = \frac{df}{dx} \mathbf{i} + \frac{df}{dy} \mathbf{j} + \frac{df}{dz} \mathbf{k}. \quad (3.105)$$

Upon evaluation of the derivative ∇f from Equation 3.105, a normal to the paraboloid at x, y, z is

$$\nabla f = -2xi - 2yj + 4Fk, \quad (3.106)$$

and a unit normal is defined as

$$\mathbf{n} = \frac{\mathbf{f}}{|\mathbf{f}|}. \quad (3.107)$$

**FIGURE 3.30**

Vector formulation of refraction. (Adapted from Welford, W.T. and R. Winston, *High Collection Nonimaging Optics*, Academic Press, San Diego, CA, 1989.)

After finding n at the incidence point, R_{ref} can be found from Equation 3.102. For a refracting surface, the vector relationship between the incident and the refracted rays can be expressed as (Figure 3.30)

$$n_2 \mathbf{R}_{\text{ref}} \times \mathbf{n} = n_1 \mathbf{R}_{\text{inc}} \times \mathbf{n}. \quad (3.108)$$

The procedure to follow is similar to that for reflection. Welford (1974) gives details of the application to lens systems.

3.5.5 Concentrator Types

Concentrators can be classified according to the following:

1. Amount of tracking required to maintain the sun within the acceptance angle
2. Type of tracking—single or double axis

As shown in the preceding sections, tracking requirements depend on the acceptance half-angle θ_{max} ; the larger the θ_{max} , the less frequently and less accurately the tracker must operate. Two tracking levels may be identified:

1. Intermittent tilt change or completely fixed.
2. Continuously tracking reflector, refractor, or receiver. If oriented east–west, it requires an approximate $\pm 30^\circ/\text{day}$ motion; if north–south, an approximately $15^\circ/\text{h}$ motion.

Both must accommodate to a $\pm 23 1/2^\circ/\text{year}$ declination excursion.

The least complex concentrators are those not requiring continuous accurate tracking of the sun. These are necessarily of large acceptance angle, moderate concentration ratio, and usually single-curvature design. Because the smallest diurnal, angular excursion of the sun is in a north-south plane, the fixed or intermittently turned concentrators must be oriented with the axis of rotation perpendicular to this plane, that is, in an east-west direction, in order to capitalize on the large acceptance angles.

3.5.6 Fixed Concentrators

A simple fixed-concentrator concept is based on using flat reflectors to boost the performance of a flat-plate collector as shown in Figure 3.31. Other variations of this concept are shown in Figure 3.32. The concentration ratio of these

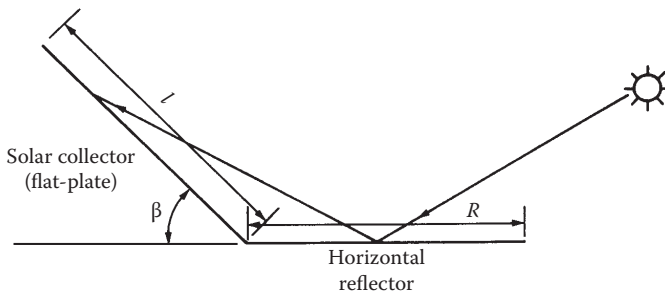


FIGURE 3.31

Horizontal reflecting surface used to boost flat-plate collector performance.

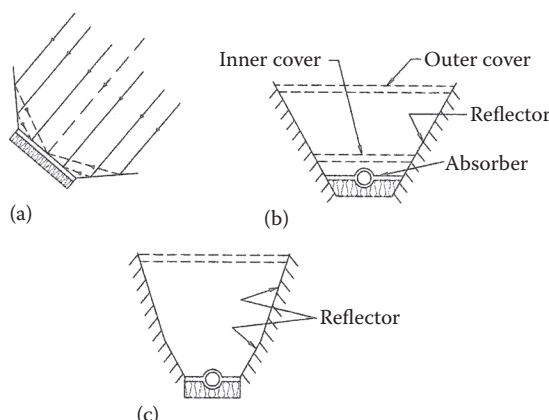


FIGURE 3.32

Examples of flat reflectors used to concentrate sunlight. (a) Flat-plate collector with reflective wings. (b) Trapezoidal design. (c) Two-facet design. (From ASHRAE 93-2003, Methods of testing to determine the thermal performance of solar collectors, ASHRAE, Atlanta, GA.)

concentrators is of the order of 1.5 to 3. For higher concentrations, spherical or parabolic reflecting or refracting surfaces are used.

3.6 Parabolic Trough Concentrator

The most common commercially available solar concentrator is the parabolic trough concentrator (PTC). Figure 3.33 shows a photograph of a commercial PTC and Figure 3.34 shows sketches of a commercial LS3 PTC. PTC collectors usually track the sun with one degree of freedom using one of three orientations: east–west, north–south, or polar. Sun tracking can be done for each by programming computers that control the tracking motors. The east–west and north–south configurations are the simplest to assemble into large arrays but have higher incidence angle cosine losses than the polar mount. Also, the polar mount intercepts more solar radiation per unit area. The absorber of a PTC is usually tubular, enclosed in a glass tube to reduce radiative and convective losses. The convective losses can be minimized by creating a vacuum in the annular space between the absorber and the glass cover.

3.6.1 Optical Analysis of PTC

The peak *optical efficiency*, η_o , of a collector is the ratio of the solar radiation absorbed in the absorber to that intercepted by the collector aperture directly facing the sun. The following major optical characteristics give the optical efficiency η_o :

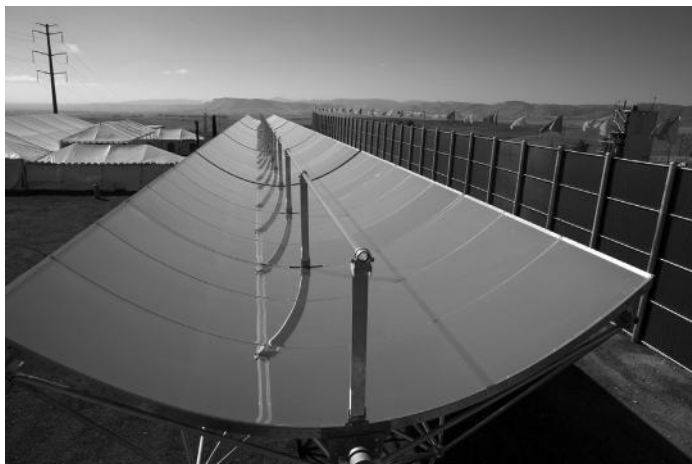
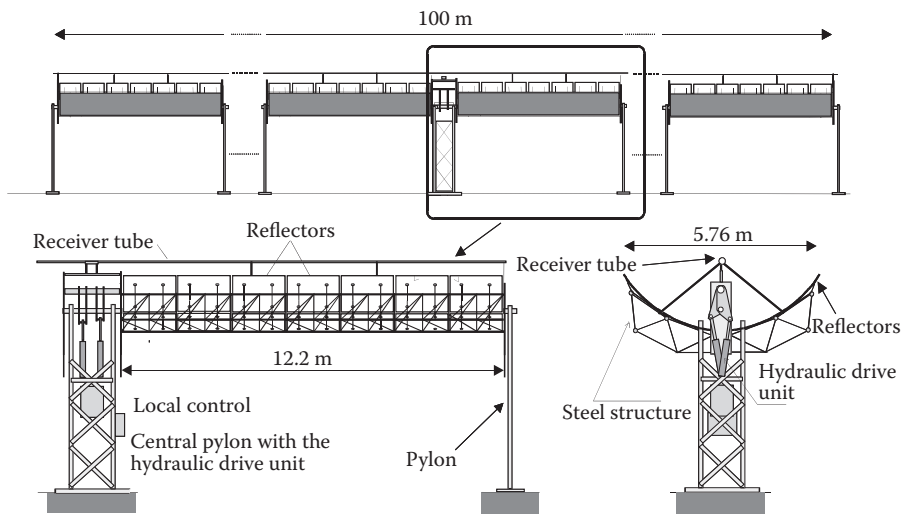


FIGURE 3.33

Commercial PTC. (Courtesy of Skyfuel, Inc., Arvada, CO.)

**FIGURE 3.34**

Sketches of a commercial LS3 Parabolic Trough Collector. (Adapted from Romero-Alvarez and Zarza, Concentrating Solar Power, Chapter 19 in Energy Conversion, Goswami and Kreith, eds., CRC Press, 2008.)

1. Reflectance of clean mirror, ρ . Typical clean silvered glass mirrors used in PTC have reflectance of around 0.93–0.94.
2. Transmittance of glass envelope of absorber, τ . A typical value of transmittance is 0.93. However, it can be increased to more than 0.96 by applying antireflective coatings to both sides of glass.
3. Absorptance of receiver/absorber, α . Typical values of α for selective absorbers are 0.94–0.95.
4. Intercept factor, γ , defined as the fraction of the rays reflected from the mirror that reach the absorber. A fraction of the rays reflected from the mirror do not reach the absorber because of mirror imperfections, geometrical errors in the parabolic reflector shape, mechanical deformations of the PTC during tracking, and shadowing owing to flexible bellows and the receiver supports. Neglecting the mirror imperfections, the intercept for 0° angle of incidence can be considered as made up of three factors (Vasquez-Padilla 2011): geometrical errors in parabolic trough shape, γ_1 ; shadowing by flexible bellows and receiver supports, γ_2 ; and mechanical deformation of the support structure during tracking, γ_3 . The intercept factor γ is then given by

$$\gamma = \gamma_1 \gamma_2 \gamma_3. \quad (3.109)$$

Typical values for clean PTCs are as follows: $\gamma_1 = 0.97\text{--}0.98$, $\gamma_2 = 0.96\text{--}0.97$, and $\gamma_3 = 0.99$, which gives the intercept factor γ in the range of 0.92–0.94.

Therefore, the peak optical efficiency of a parabolic trough at 0° angle of incidence

$$\eta_{o,peak} = \rho\tau\alpha\gamma. \quad (3.110)$$

During operation, the optical efficiency of a PTC is much less than peak owing to the angle of incidence, soiling of the mirrors and the glass envelope of the receiver, and end losses, which account for the fraction of a receiver, which is not illuminated by the rays incident on the aperture.

The incidence angle of the beam on the PTC aperture affects all four parameters comprising the optical efficiency. The effect is quantified by the incidence angle modifier, $K(i)$, for an angle of incidence, i , which is defined by

$$K(i) = \frac{\eta_o(i)}{\eta_o(i=0)}. \quad (3.111)$$

Table 3.6 gives the expressions for incidence angle modifiers for some popular commercially available PTC collectors (also Figure 3.35).

Another geometric factor is the end losses attributed to angle of incidence, which accounts for the fraction of the receiver tube not illuminated by the reflected radiation. From Figure 3.36, the end loss factor F_{el} is given by

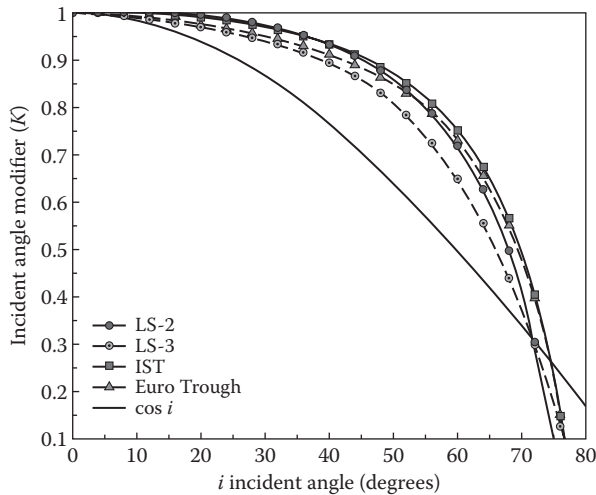
$$F_{el} = \frac{(L_c - z)}{L_c} = 1 - \frac{r}{L_c} \tan i, \quad (3.112)$$

TABLE 3.6

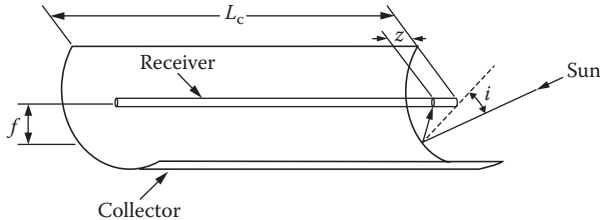
Incident Angle Modifier for Different PTC Solar Collectors

Solar Collector	Incident Angle Modifier Function, $K(i)$
LS-2	$1 + 0.000884 \frac{i}{\cos i} - 0.00005369 \frac{i^2}{\cos i}$
LS-3	$1 - 2.2307 \times 10^{-4} i - 1.1 \times 10^{-4} i^2$ + $3.18596 \times 10^{-6} i^3 - 4.85509 \times 10^{-8} i^4$
IST	$1 + 0.0003178 \frac{i}{\cos i} - 0.00003985 \frac{i^2}{\cos i}$
Euro Trough	$1 - 5.25097 \times 10^{-4} \frac{i}{\cos i} - 2.859621 \times 10^{-5} \frac{i^2}{\cos i}$

Source: Adapted from Vasquez-Padilla, R., Simplified methodology for designing parabolic trough solar power plants, PhD dissertation, University of South Florida, Tampa, FL, 2011.

**FIGURE 3.35**

Incidence angle modifier for different parabolic trough solar collectors—LS-2, LS-3, IST, and Euro Trough 9. (Adapted from Vasquez-Padilla, R., Simplified methodology for designing parabolic trough solar power plants, PhD dissertation, University of South Florida, Tampa, FL, 2011.)

**FIGURE 3.36**

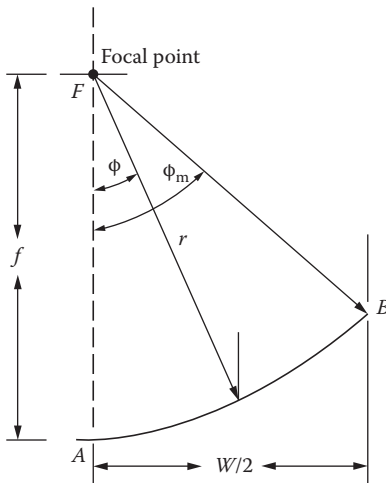
Geometrical end losses of a PTC.

where r is shown in Figure 3.37. Lippke (1995) proposed using $r = f$, which is used in many simulations (Patnode 2006; Stuetzle 2002).

Therefore,

$$F_{el} \approx 1 - \frac{f}{L_c} \tan i. \quad (3.113)$$

Gaul and Rabl (1979) suggest using an average value of r , which for a PTC of aperture width W , gives F_{el} as

**FIGURE 3.37**

Parabola geometry of a rim angle of ϕ_m . (Adapted from Lippke, F., Simulation of the part-load behavior of a 30 MWe SEGS plant. Tech. Rep., SAND-95-1293, Sandia National Labs., Albuquerque, NM, United States, 1995.)

$$F_{el} = 1 - \frac{f}{L_c} \cdot \frac{W^2}{1 + \frac{W^2}{48f^2}} \tan i. \quad (3.114)$$

Figure 3.38 shows that Gaul and Rabl's model gives slightly lower values of F_{el} .

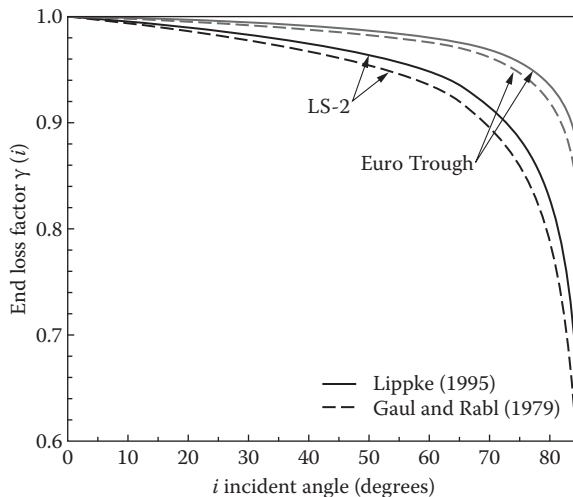
Finally, soiling of the mirror over time results in a loss, quantified by the soiling factor F_s . It is defined as the ratio of the average mirror reflectance in operation to the nominal reflectance when the mirror is clean (Zarza Moya 2012). For example, if the reflectance of the clean mirror is 0.95 and the mirror is washed when the reflectance falls to 0.9, then the average mirror reflectance is 0.925 and the F_s is $0.925/0.95 = 0.97$. Table 3.7 gives radiative properties of some heat collection elements.

Therefore, the optical efficiency of a PTC becomes

$$\eta_o = \eta_{o,peak} F_{el} F_s K(i) = \rho \tau \alpha \gamma F_{el} F_s K(i). \quad (3.115)$$

3.6.2 Thermal Losses from PTC

A major difference between a flat-plate collector and a concentrating collector, such as PTC, is that the losses for a PTC are from the receiver surface whose area is much smaller than the aperture area. However, the radiative

**FIGURE 3.38**

End loss factor for different PTC collectors based on Lippke (1995) and Gaul and Rabl (1979). (Adapted from Vasquez-Padilla, R., Simplified methodology for designing parabolic trough solar power plants, PhD dissertation, University of South Florida, Tampa, FL, 2011.)

TABLE 3.7

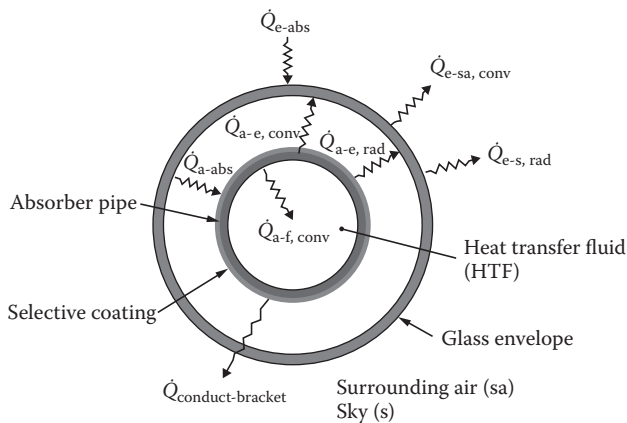
Radiative Properties for Different Heat Collection Elements

Selective Coating	Envelope Transmittance	Coating Absorptance	Coating Emittance	
			100°C	400°C
Luz black chrome	0.935	0.940	0.110	0.27
Luz cermet	0.935	0.920	0.060	0.15
Solel UVAC cermet a	0.965	0.960	0.070	0.13
Solel UVAC cermet b	0.965	0.950	0.080	0.15
Solel UVAC avg	0.965	0.955	0.076	0.14
Schott PTR70	0.96	0.95	—	0.1

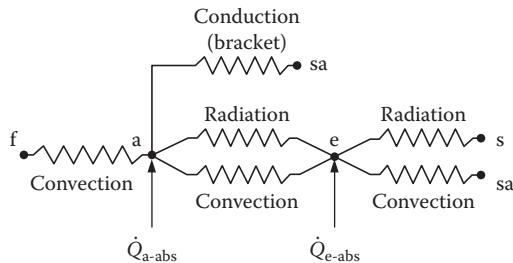
Source: Adapted from ASHRAE 96-1980, Methods of testing to determine the thermal performance of unglazed solar collectors, ASHRAE, Atlanta, GA.

losses are much higher since the receiver temperature T_r is much higher and the radiative losses are proportional to the fourth power of T_r . Figure 3.39 shows a cross section of the receiver-absorber indicating the energy transfers to and from the absorber.

A detailed heat-transfer model (see Figure 3.40) would consider the heat transfer from the absorber surface to the heat-transfer fluid (HTF) by conduction through the absorber tube and convection ($Q_{a-f, \text{conv}}$), heat loss from the

**FIGURE 3.39**

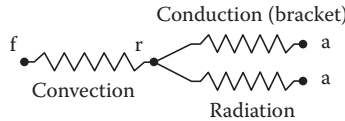
Heat transfer in a heat collection element. (Adapted from Adapted from Vasquez-Padilla, R., Simplified methodology for designing parabolic trough solar power plants, PhD dissertation, University of South Florida, Tampa, FL, 2011.)

**FIGURE 3.40**

Thermal resistance model.

absorber surface to the glass envelope by convection ($Q_{r-e, \text{conv}}$) and radiation ($Q_{r-e, \text{rad}}$), and heat transfer from the glass envelope to the ambient by convection ($Q_{e-a, \text{conv}}$) and radiation ($Q_{e-a, \text{rad}}$) including the radiative heat transmitted from the absorber through the glass. In addition, there is heat loss to the support brackets by conduction $Q_{\text{conduct-bracket}}$.

For simplification, if convective heat loss from the absorber is neglected because of vacuum, and the absorption of the glass envelope is neglected, the heat transfer could be represented by Figure 3.41 and the heat loss q_L may be written as

**FIGURE 3.41**

Simplified thermal resistance model.

$$q_L = A_k \frac{T_r - T_a}{R_k} + \varepsilon_r \sigma (T_r^4 - T_a^4) A_r, \quad (3.116)$$

where R_k is the composite thermal resistance of the support brackets and A_k is the effective area for conduction heat transfer.

3.6.3 Thermal Performance of PTC Collector

The thermal performance of a PTC collector can be analyzed similarly to that of a flat-plate collector by assuming an overall heat-loss coefficient U_c for the receiver/absorber. Therefore, the instantaneous efficiency η_c can be written as

$$\begin{aligned} \eta_c &= \frac{q_u}{I_c A_a} = \frac{q_{\text{absorbed}} - q_L}{I_c A_a} \\ &= \eta_o - U_c (T_r - T_a) A_r / I_c A_a \\ &= \eta_o - U_c \frac{T_r - T_a}{I_c} \cdot \frac{A_r}{A_a}, \end{aligned} \quad (3.117)$$

where T_r and A_r are the temperature and the area of the receiver and A_a is the aperture area of the collector.

The heat loss from a PTC depends on the absorber tube temperature and is typically measured experimentally at several temperatures in its working temperature range. Variation in the overall heat-loss coefficient is usually expressed as a second-degree polynomial equation:

$$U_c = a + b(T_r - T_a) + c (T_r - T_a)^2 \text{ W/m}^2\text{K}, \quad (3.118)$$

where coefficients a , b , and c are found experimentally. Table 3.8 gives these values for LS-3 collectors (Zarza Moya 2012). Typically, U_c for absorber tubes with good vacuum is less than 5 W/m².K.

TABLE 3.8Values of Coefficients a , b , and c for an LS-3 Collector

$T_{\text{absorber}} (\text{°C})$	a	b	c
<200	0.687257	0.001941	0.000026
>200; <300	1.433242	-0.00566	0.000046
>300	2.895474	-0.0164	0.000065

Source: Adapted from Lippke, F., Simulation of the part-load behavior of a 30 MWe SEGS plant, Tech. Rep., SAND-95-1293, Sandia National Labs., Albuquerque, NM, 1995.

3.7 Compound-Curvature Solar Concentrators

The collectors used for high-temperature solar processes are of the double-curvature type and require a tracking device with two degrees of freedom. Concentration ratios above 50 are generally used. Examples of concentrator designs include the following: spherical mirror, CR = 50–150; paraboloidal mirror, CR = 500–3000; Fresnel lens, CR = 100–1000; and Fresnel mirror, CR = 1000–3000. These concentrator types will be discussed briefly in this section.

3.7.1 Paraboloidal Concentrators

The surface produced by rotating a parabola about its optical axis is called a paraboloid. The ideal optics of such a reflector is the same, in cross section, as those of the parabolic trough described earlier in this chapter. However, owing to the compound curvature, the focus occurs ideally at a point instead of along a line. Figure 3.42 shows a commercial paraboloid collector.

**FIGURE 3.42**

Commercial paraboloidal solar concentrator.

The optical efficiency η_o (defined relative to the direct-normal solar flux) of a paraboloid is the product of six terms:

$$\eta_o = \rho \tau \alpha f \gamma(\psi_1, \psi_2) F(\psi_3), \quad (3.119)$$

where ρ is the mirror reflectance, τ is the receiver cover (if any) transmittance, α is the receiver absorptance, f is the fraction of the aperture not shaded by supports and absorber, γ is the intercept factor depending on mirror slope errors ψ_1 and the solar beam ψ_2 , and $F(\psi_3)$ is the tracking error factor where (ψ_3) is the angle between the solar direction and the aperture normal. The optical intercept factor for a paraboloid is given by (Ramsay et al. 1977)

$$\gamma(\psi_1, \psi_2) = 1 - \exp \left(-\frac{\pi D_r^2}{4\sigma^2} \right), \quad (3.120)$$

where D_r is the receiver diameter and σ^2 is the beam spread variance at the receiver. For a spherical segment receiver, σ^2 is given by (Duff and Lameiro 1974)

$$\sigma^2 = 2A_a \left(4\sigma_{\psi_1}^2 + \sigma_{\psi_2}^2 \right) (2 + \cos\phi)/3\phi\sin\phi, \quad (3.121)$$

where A_a is the aperture area, ϕ is the paraboloid rim half-angle, and σ_{ψ_1} and σ_{ψ_2} are the beam variances due to mirror surface errors and solar beam spread, respectively.

For a flat receiver with paraboloid optics, σ^2 is given by (Duff and Lameiro 1974)

$$\sigma^2 = 2A_a \left(4\sigma_{\psi_1}^2 + \sigma_{\psi_2}^2 \right) / \sin^2 \phi. \quad (3.122)$$

The concentration ratio of paraboloids can be determined easily from basic geometry. The aperture area is πR^2 , where R is the aperture radius and the area for a spherical receiver is $4\pi R_r^2$, where R_r is the spherical receiver radius. If the receiver is only a spherical segment, not a complete sphere, the receiver area to be used below is ΩR_r^2 , where Ω is the segment included solid angle, instead of $4\pi R_r^2$. The receiver radius for perfect optics is sized to collect all rays with the acceptance half-angle θ_{max} . Hence,

$$R_r = (R/\sin \phi)\sin \theta_{max}. \quad (3.123)$$

Therefore, the concentration CR is

$$CR = (\pi R^2) / [4\pi \times (R/\sin \phi)^2 \sin^2 \theta_{max}],$$

or

$$CR = \sin^2 \phi / (4\sin^2 \theta_{max}). \quad (3.124)$$

The small effect of absorber shading of the mirror is ignored. Its inclusion would reduce CR given by Equation 3.124. For $\theta_{max} = 1/4^\circ$ (the sun's half-angle), $CR \sim 13,000$ if $\phi = 90^\circ$. For $\theta_{max} = 1/2^\circ$, $CR \sim 3300$, and for $\theta_{max} = 1^\circ$, $CR \sim 800$. Note

that concentrations for this configuration are one-fourth the thermodynamic limit, which is $(\sin \theta_{\max})^{-2}$ for compound-curvature collectors. See Equation 3.89.

For a flat absorber, the concentration for perfect optics is

$$CR = \sin^2 \phi \cos^2 (\phi + \theta_{\max}) / \sin^2 \theta_{\max}, \quad (3.125)$$

where the small effect of mirror shading by the absorber is again ignored.

Example 3.4

Calculate the concentration ratio and diameter of a flat receiver for a 10-m-diameter paraboloid concentrator that is designed to accept 90% of the incident beam radiation. The rim half-angle is 90° and the mirror surface variance $\sigma_{\psi_1}^2$ is expected to be $(0.25^\circ)^2$. Assume that the standard deviation for the sun's disk is 0.125° .

Solution

From Equation 3.120,

$$\pi D_r^2 / 4\sigma^2 = -\ln(1 - 0.90) = 2.303,$$

and from Equation 3.122,

$$\begin{aligned} \sigma^2 &= 2A_a \left(4\sigma_{\psi_1}^2 + \sigma_{\psi_2}^2 \right) / \sin^2 \phi \\ &= 2 \times (\pi/4 \times 10^2) \cdot 4 \times (0.25)^2 + (0.125)^2 \cdot (\pi/180)^2 / \sin^2 90^\circ \\ &= 0.0127 \text{ m}^2 (\sigma = 11.3 \text{ cm}). \end{aligned}$$

Solving the first equation for D_r ,

$$D_r = [2.303 \times 4 \times \sigma^2 / \pi]^{1/2} = 0.193 \text{ m.}$$

The concentration ratio is

$$CR = A_a / A_r = \frac{\pi \times 10^2 / 4}{\pi (0.193)^2 / 4} = 2685.$$

Note that the effect of tracking error ψ_3 can be included in the intercept factor $\gamma(\psi_1, \psi_2)$ by defining an appropriate $\sigma_{\psi_3}^2$ and adding it to the slope and solar image variances in Equations 3.121 and 3.122.

The thermal losses from a paraboloid are quite small and primarily radiative. Since the absorber area is so small, it is generally not worthwhile to use any type of convection-suppressing cover. For example, consider the thermal losses from a planar absorber of $CR = 1500$ paraboloid with a receiver surface temperature of 600°C . For a cavity absorber ($\epsilon_{ir} \sim 1.0$), the radiation heat loss is approximately 20 W/m^2 aperture if the ambient temperature is 60°C . For a typical convection coefficient in light winds of $25 \text{ W/m}^2\text{ }^\circ\text{C}$, the convection loss is approximately 10 W/m^2

aperture. If the insolation is 900 W/m^2 and the optical efficiency is 65%, the total heat loss at 600°C represents less than 6% of the absorbed flux. Stated another way, the collector loss coefficient U_c at 600°C is only $0.064 \text{ W/m}^2\text{°C}$. The performance of high-concentration paraboloids is, therefore, much more sensitive to optical properties than to thermal losses.

Recent developments in paraboloidal concentrators include multifaceted mirror concentrators, single-faceted stretched-membrane mirror concentrators, and multifaceted stretched-membrane mirror concentrators. Figure 3.43 shows examples of such commercially developed paraboloidal concentrators.



(a)



(b)

FIGURE 3.43

Examples of commercially developed multifaceted and stretched-membrane paraboloidal concentrators: (a) multifaceted mirror, (b) stretched single membrane (Schlaich Bergermann & Partner, Germany).

3.7.2 Spherical Concentrators

A second type of compound-curvature collector uses spherical geometry instead of parabolic geometry. Figure 3.44c shows ray traces in a plane of symmetry for normal incidence (two-axis tracking) on a spherical concentrator. Spherical aberration is seen to be present and causes the reflected flux to be along a line instead of at a point as is the case for other compound-curvature mirrors. It is also clear that rays intercepted near the pivot end of

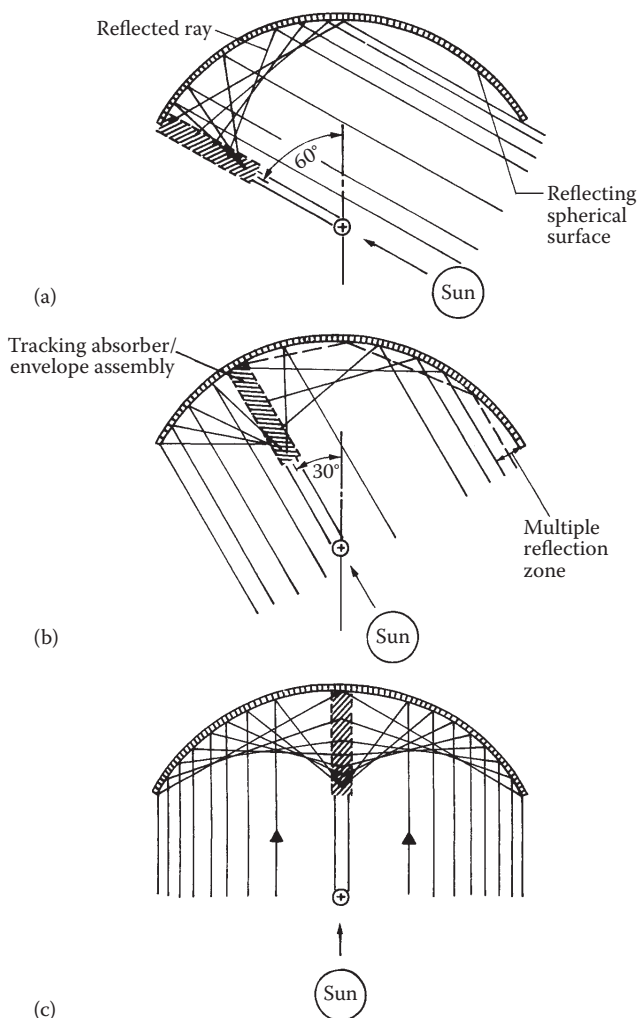


FIGURE 3.44

Ray traces for a fixed spherical concentrator for three incidence angles: (a) normal incidence for two-degree-of-freedom tracking of the mirror; (b and c) off-normal incidence for a fixed mirror and a moving absorber.

the absorber intercept the absorber at very large incidence angles. Therefore, an absorber envelope with very low reflectance or no envelope at all is used to avoid severe penalties to the optical efficiency.

The concentration ratio of a spherical concentrator can be calculated from the definition of CR:

$$CR = A_a / A_r = \pi R_o^2 \sin^2 \phi / \pi D_r L_r. \quad (3.126)$$

Taking the receiver length $L_r = R_o/2$,

$$CR = (2R_o / D_r) \sin^2 \phi. \quad (3.127)$$

If the absorber is a cylinder and is to intercept all singly reflected rays within the acceptance half-angle θ_{\max} ,

$$D_r = 2R_o \sin \theta_{\max}, \quad (3.128)$$

and

$$CR = \sin^2 \phi / \sin \theta_{\max}, \quad (3.129)$$

if the acceptance half-angle is $1/4^\circ$ for $\phi = 90^\circ$, $CR = 229$; for $\theta_{\max} = 1/2^\circ$, $CR = 115$ for perfect optics. It is obvious that the spherical concentrator cannot achieve concentration ratios approaching those of paraboloids owing to spherical aberration and hence this concentrator is much more sensitive to operating temperature than the point-focus type.

The efficiency of this concentrator is lower than that of other compound-curvature devices, because of smaller CR values; therefore, the unit cost of solar heat will be higher. One method of reducing the unit cost is to use the concentrator with a *fixed mirror*, thereby eliminating the expensive mirror tracking and structural components. This configuration is known as a stationary reflector tracking absorber (SRTA) concentrator. The collector is kept "in focus" by tracking only the absorber, aiming it directly at the sun's center. However, the effective aperture in this fixed mirror mode is reduced by the cosine of the incidence angle. Hence, the saving in cost by eliminating the reflector tracker is partly offset by reduced energy capture. If a value of rim half-angle $\phi = 60^\circ$ is used as shown in Figure 3.44 and if the fixed aperture faces the sun directly at noon, then the daylong cosine penalty will reduce the captured flux by approximately 17%. Of course, if the aperture does not directly face the sun at noon, the cosine loss will be larger.

3.7.3 Compound Parabolic Concentrator

A nonimaging concentrator concept called the compound parabolic concentrator (CPC) was developed by Winston (1974, 1975) and Rabl (1975, 1976a,b)

and described by Baranov and Melnikov (1966). The CPC can approach the thermodynamic limit of concentration discussed earlier; that is,

$$CR_{CPC} = CR_{max,2D} = 1/\sin \theta_{max}.$$

Figure 3.45 shows a schematic cross section of the original CPC concept. It is seen to be formed from two distinct parabolic segments, the foci of which are located at the opposing receiver surface end points. The axes of the parabolic segments are oriented away from the CPC axis by the acceptance angle θ_{accept} . The slope of the reflector surfaces at the aperture is parallel to the CPC optical axis. Figure 3.46 is a photograph of a CPC collector.

Different types of planar and tubular receivers have been proposed for CPCs. Of most interest in this book is the tubular-type receiver shown in Figure 3.47 since high-pressure heat-transfer fluid can flow through it.

3.7.4 Optical Analysis of CPC Collector

A number of the optical losses present in tracking collectors described above are negligible in CPC collectors because of their broad acceptance band and ability to use imprecise optical elements. Some of the optical loss mechanisms listed in Section 3.6.1 are reduced or nonexistent in CPCs.

The three optical parameters—mirror reflectance, cover transmittance, and absorber absorptance—are first-order effects for CPCs. Mirror reflectance

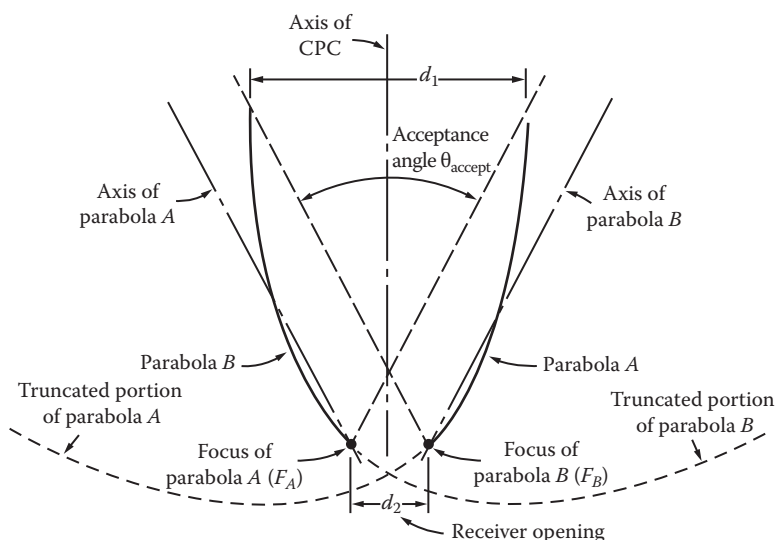
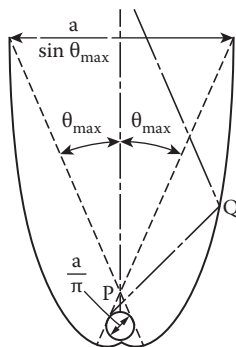


FIGURE 3.45

Schematic cross section of a CPC showing parabolic segments, aperture, and receiver.

**FIGURE 3.46**

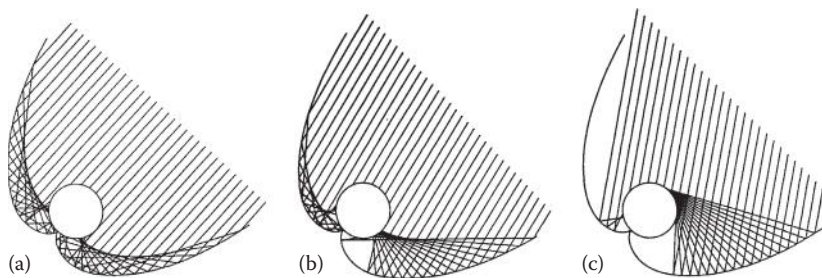
Commercial CPC collector module using an evacuated tubular receiver. (Courtesy of MHG Heating, UK.)

**FIGURE 3.47**

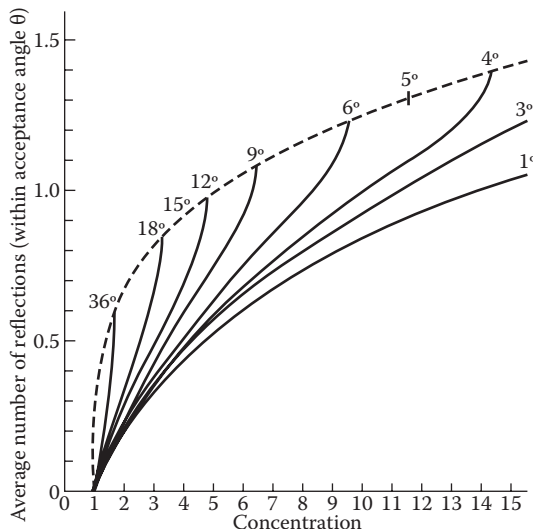
CPC collector concept with tubular receiver.

effects are slightly different for a CPC than for other line-focus reflectors since the CPC does not form a sharp image of the sun at the absorber. Figure 3.48 shows that some solar radiation incident near the aperture edges is reflected more than once on its way to the absorber. The effect of multiple reflectance can be simply accounted for in optical efficiency calculations, to lowest order, by using $\rho_m^{\bar{n}}$, where \bar{n} is the average number of reflections of all incident rays over the aperture. Some effect of incident angle on \bar{n} has been noted but Rabl (1976a) recommends the use of a constant \bar{n} for engineering purposes.

Figure 3.49 can be used to determine the average number of reflections \bar{n} for various concentration ratios CR for the basic CPC in Figure 3.45. For tubular receiver CPCs (Figure 3.47), \bar{n} should be increased by approximately 0.5 over the Figure 3.49 values. The dashed line in Figure 3.49 represents \bar{n} for a fully developed CPC. Since the upper half of the reflector for most CPCs is

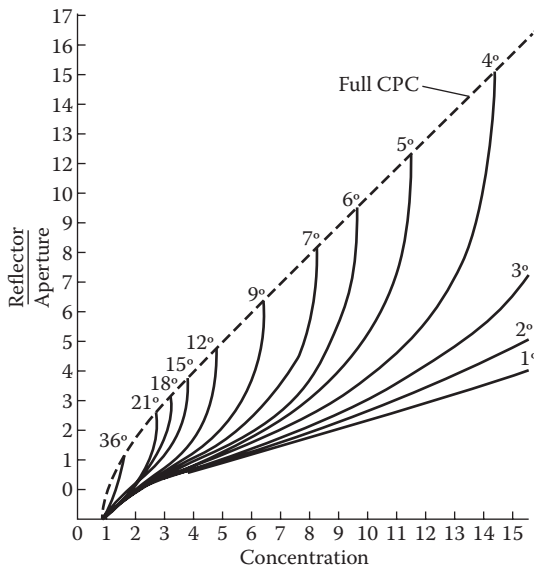
**FIGURE 3.48**

Ray trace diagrams of the tubular CPC collector at three values of incidence angle: (a) normal incidence, (b) intermediate, and (c) the limit of acceptance. (Courtesy of W. McIntire, Argonne National Laboratory.)

**FIGURE 3.49**

Average number of reflections for the basic CPC as a function of CR. The dashed line represents a full CPC. The number reflections for various truncations can be determined by using Figure 3.53 along with this figure. Values of acceptance angle are shown on the upper curve. (From Hsieh, C.K., *Sol. Energy* 27: 19, 1981.)

nearly parallel to the optical axis, it affords little concentration effect. In practice, the upper portion (approximately 40%–60% of the mirror) is normally eliminated to reduce CPC size and cost. Figure 3.50 shows the concentration achievable for various truncation amounts. This CR value and the corresponding value of acceptance angle then determine a point on the \bar{n} – CR map (Figure 3.49), and \bar{n} can be evaluated for any truncation. For careful designs, a ray trace procedure must be used to find \bar{n} and its dependence on incidence angle.

**FIGURE 3.50**

Effect of truncation on the basic CPC concentration ratio for various values of acceptance angle. (From Hsieh, C.K., *Sol. Energy* 27: 19, 1981.)

A final consideration in the optical analysis of the CPC family is the effect of partial acceptance of diffuse radiation. Equation 3.101 showed that at least $(CR)^{-1}$ of the incident diffuse flux reached the absorber. Since CPC collectors operate in the concentration range of 2 to 10 to capitalize on the corresponding reduced tracking requirement, from one-half to one-tenth of the incident diffuse radiation is accepted. This property of CPCs is conveniently included in the CPC optical efficiency by defining the intercept factor γ used for PTC analysis somewhat differently. If γ is defined as the fraction of total radiation accepted by a CPC, it can be expressed as

$$\gamma = [I_{b,c} + I_{d,c}/CR]/I_{tot,c} \quad (3.130)$$

where subscripts "b," "d," and "tot" refer to beam, diffuse, and total flux incident on the collector aperture, respectively.

The optical efficiency of a CPC can then be written as*

$$\eta_o = \rho_m^{\bar{n}} \tau_r \alpha_r \gamma. \quad (3.131)$$

* For the tubular receiver CPC, a small gap of width g is required between the mirror cusp and the absorber pipe to accommodate the absorber envelope. Some otherwise collectable rays escape the receiver at this point, reducing the optical efficiency by the factor $(1 - g/p_r)$, where p_r is the absorber perimeter. Other design details are given in Collares-Pereira and Rabl (1979).

γ depends on the characteristics of local solar flux and is not a purely geometric factor such as $\gamma(\psi_1, \psi_2)$. For the tubular CPC, $\bar{n} \sim 1.2$, $\rho_m \sim 0.85$, $\alpha_r \sim 0.95$, $\gamma \sim 0.95$, and $\tau_r \sim 0.90$. Therefore, $\eta_o \sim 0.67$. If an etched glass cover is used, $\eta_o \sim 0.71$. These values of optical efficiency are 7%–8% greater than those for a PTC device. Improved optical efficiency partially offsets the lower concentration and associated heat loss effect usually imposed on CPCs ($CR < 10$) in order to benefit from their reduced tracking requirements.

3.7.5 Thermal Performance of the CPC Collector

For a tubular receiver CPC, the same heat-loss analysis can be used as for a PTC collector with a tubular receiver. Some uncertainty in the convection heat loss from the tube to the environment exists, since the tube is in a partial enclosure and protected from the environment.

The thermal efficiency of a CPC (based on total beam and diffuse collector plane flux) is given by

$$\eta_c = \rho_m^{\bar{n}} \tau_r \alpha_r \gamma - U_c (T_r - T_a) / (I_c CR), \quad (3.132)$$

where U_c is based on the aperture area.

By analogy with the PTC analysis developed earlier for an evacuated receiver,

$$U_c = \epsilon_e \sigma (T_r^2 + T_a^2) (T_r + T_a) + (A_k / A_a) (1/R_k) (CR), \quad (3.133)$$

where R_k is the conduction heat-transfer resistance for all conduction paths of total effective area A_k . Hsieh (1981) and Hsieh and Mei (1983) presented a detailed thermal analysis of a CPC with an evacuated tubular selective coated receiver and the entire collector covered with a transparent cover. They proposed the following empirical equations for the heat-loss coefficient U_c .

$$\text{For } 29^\circ\text{C} \leq (T_r - T_a) \leq (137 + 0.0283T_a - 0.0000616T_a^2), \\ U_c = (0.18 + 16.95\epsilon_r)[0.212 + 0.00255T_a + (0.00186 + 0.000012T_a)(T_r - T_a)], \quad (3.134a)$$

$$\text{and for } (137 + 0.0283T_a - 0.0000616T_a^2) \leq (T_r - T_a) \leq 260^\circ\text{C}, \\ U_c = (0.168 + 17.16\epsilon_r)[0.086 + 0.00225T_a + (0.00278 + 0.000014T_a)(T_r - T_a)], \quad (3.134b)$$

where U_c is the collector loss coefficient (W/Km^2) of the absorber area, T_r is the receiver (absorber) temperature ($^\circ\text{C}$), T_a is the ambient temperature ($^\circ\text{C}$), and ϵ_r is the emissivity of the absorber surface.

These empirical equations are valid under the following conditions: $\epsilon_r = 0.05$ to 0.2, wind velocity $V = 0$ to 10 m/s, concentration $C = 1.5$ to 6; correspondingly, average number of reflections $\bar{n} = 0.55$ to 1.05, ambient temperature $T_a = -10^\circ\text{C}$ to 35°C , total radiation $I_t = 720$ to 1200 W/m^2 aperture area, diffuse-to-beam radiation ratio $I_d/I_b = 0.1$ to 0.5.

3.8 Central Receiver Collector

A central receiver collector consists of a large field of mirrors on the ground that track the sun in such a way that the reflected radiation is concentrated on a receiver/absorber on top of a tower. The mirrors are called *heliostats*. Central receivers can achieve temperatures of the order of 1000°C or even higher. Therefore, a central receiver concentrator is suitable for thermal electric power production in the range of 10–1000 MW. The concept of a central receiver solar thermal power has been known for a long time. Francia (1968) built a pilot model of a solar power tower plant in 1967 at the University of Genoa, Italy. Since the early 1970s, when the power tower concept was first proposed by Hildebrandt and Vant-Hull (1974), the central receiver technology has been actively developed in the United States. Since then, the technology has been pursued in Germany, Spain, Switzerland, France, Russia, Italy, and Japan (DeLaquil et al. 1993).

A central receiver collector consists of a heliostat field, a receiver/absorber, and the tracking controls for the heliostats. Since central receiver collectors are used to produce very high temperatures, which are used to produce thermal power, this topic is dealt in detail in Chapter 8.

3.9 Fresnel Reflectors and Lenses

If the smooth optical surface of a reflector or a lens can be broken into segments to achieve essentially the same concentration, the resulting concentrator is called the Fresnel concentrator. Figure 3.51 shows examples of a Fresnel mirror and a Fresnel lens. Use of Fresnel reflectors for large collectors reduces the wind load and simplifies manufacture. A Fresnel lens can achieve a concentration close to a corresponding plano convex lens with far less material and lower manufacturing costs. However, a disadvantage is that the facet edges become rounded in the manufacturing process, which makes the edges ineffective.

Off-normal incidence effects are present in a Fresnel device owing to the change in focal length with incidence angle.

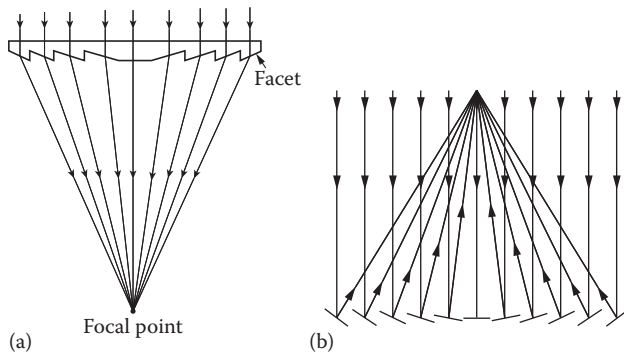


FIGURE 3.51
Fresnel concentrators: (a) lens, (b) mirror.

Figure 3.52 shows the focal point for normal and nonnormal incidence. Note that the effect of the shortened focal length is to cause the sun's image to appear wider at the nominal focal plane during off-normal periods. Figure 3.53 shows the decrease in focal length that occurs for various off-normal conditions (Collares-Pereira et al. 1977; Rabl 1978). It is seen that a $\pm 60^\circ$ excursion, which would be encountered for 8 h of collection at the equinoxes in an east–west axis alignment, would diminish the focal length by two-thirds. Hence, the Fresnel line-focus device with $CR > 10$ is restricted to a north–south orientation ($\pm 35^\circ$ excursion over a year) if the majority of daylight hours are to be collection hours.

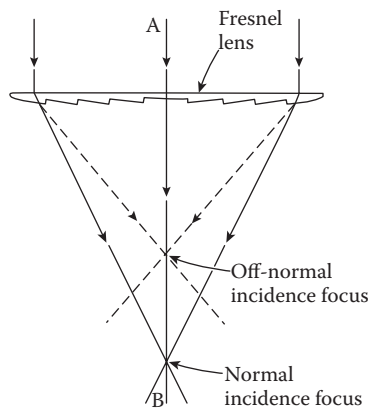
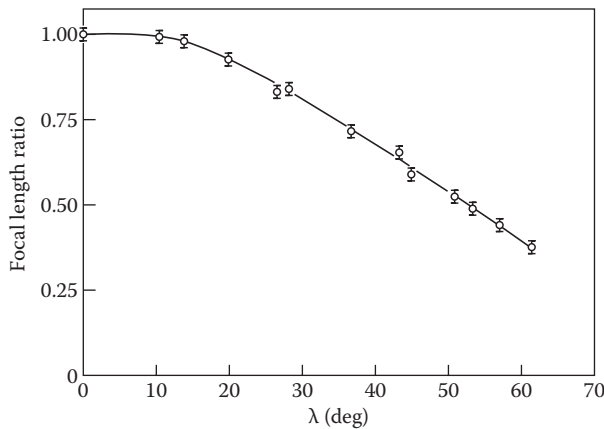


FIGURE 3.52
Line-focus Fresnel lens concentrator section showing nominal focus for normal incidence and shortened focal length at off-normal incidence.

**FIGURE 3.53**

Effect of off-normal incidence angle λ (measured in plane AB out of the plane of Figure 3.52) on apparent focal length of a line-focus Fresnel lens. The focal length ratio is the focal length at $\lambda \neq 0$ divided by the focal length at $\lambda = 0$ (i.e., normal incidence). (From Rabl, A., *Proc. Sol. Thermal Cone. Coll. Tech. Symp.*, B. Gupta, ed. Denver, CO, 1–42, 1978.)

3.10 Solar Concentrator Summary

Figure 3.54 contains a summary of all important optical properties of the common reflecting solar concentrators:

Concentration ratio, CR

Average number of reflections, \bar{n}

Capture parameter, γ

Beam spread variance, σ^2

The CR standard of comparison is the thermodynamic limit derived in Section 3.5.1. It is seen that all concentrators except the CPC family fall short of the ideal limit by a factor of 3 or more. For any meaningful concentration and rim half-angles $\phi > 45^\circ$, the SRTA is seen to fall short of the ideal limit by the greatest amount because of its focal aberration.

The optical parameter γ and its independent variable σ have been developed using analyses analogous to that used for the PTC collector. Duff and Lameiro (1974) have also derived expressions for σ for reflector systems with flat mirror segments instead of curved ones. They are slightly different in form from those in Figure 3.54 but are developed by using the same analysis method.

Collector parameter	Single curvature			Compound curvature		
	Nonimaging CPC family	Parabolic mirror	Cylindrical receiver	Spherical receiver	Paraboloidal mirror	Spherical mirror cylindrical receiver
CR/CR _{max} for perfect optics	1.0	$\frac{\sin \phi^a}{\pi}$	$\sin \phi \cos(\phi + \theta_{\max})$ $- \sin \theta_{\max}$	$\frac{\sin^2 \phi^a}{4}$	$\sin^2 \phi \cos^2 (\phi + \theta_{\max})$ $- \sin^2 \theta_{\max}$	$2 \sin^2 \phi \sin^2 \theta_{\max}$
\bar{n}	0.7–1.2	1.0	1.0	1.0	1.0	1.0
γ	$\frac{1}{1 + \sigma_\theta \cot \theta_{\max}}^b$	$\frac{1}{\sqrt{2\pi}\sigma} \int_{L_c/2}^{L_c/2} \exp\left[-\frac{1}{2} \left(\frac{y}{\sigma_y}\right)^2\right] dy$	#	$1 - e^{-\left(\frac{L_c/\sigma}{\sigma}\right)}$		(No closed-form expression)
σ^2	—	$\frac{A_a^2 \sigma_0^2 (2 + \cos \phi)}{12 \phi \sin \phi}$		$\frac{2 A_a^2 \sigma_0^2 (2 + \cos \phi)}{3 \phi \sin \phi}$	$\frac{2 A_a^2 \sigma_0^2}{\sin^2 \phi}$	(No closed-form expression)
L_c	$\frac{D_r}{2}$	$\frac{D_r}{2}$	$\frac{D_r}{2}$	$\frac{\pi D_r^2}{4}$	$\frac{\pi D_r^2}{4}$	$\frac{D_r}{2}$
A_a	Aperture width	Aperture width	Aperture width	Aperture area		

^a For Fresnel mirror arrangements or power towers, multiply expressions given by the ground cover fraction. It is usually on the order of 1/2.
^b Approximate expression for radiation incident near the limits of acceptance only; otherwise, $\delta = 1.0$.

$$\left\{ A_a^2 \left(4\sigma_{\psi_1}^2 + \sigma_{\psi_2}^2 \right) \left[\frac{-1}{3\sin^2 \phi \cos \phi} + \frac{2}{3\sin^3 \phi} + \frac{2}{\sin \phi} - \frac{\cos \phi}{3\sin \phi} - \frac{2\phi}{\sin \phi} + \frac{4\sin \phi}{3\cos \phi} - \ln \tan \left(\frac{\pi}{4} + \frac{\phi}{2} \right) + \ln \tan \left(\frac{\pi}{4} - \frac{\phi}{2} \right) \right] \right\}^{1/2}$$

Duff (1976) has given an alternative expression for ϕ^2 in which a different integration procedure was used.

FIGURE 3.54

Comparison of design parameters of solar concentrators. CR_{max} = thermodynamic limit to concentrations (see Equations 3.90 and 3.91); L_c = characteristic dimension of receiver; D_r = receiver diameter or width; θ_{max} = acceptance angle; φ = mirror rim half-angle; σ₀² = 4σ_{ψ₁}² + σ_{ψ₂}²; γ = optical capture factor; \bar{n} = average number of reflections. (Adapted from Duff, W.S., and G.F. Lameiro, A performance comparison method for solar concentrators, ASME Paper 74-WA/Sol-4, New York, 1974.)

Thermal properties of concentrators cannot be summarized conveniently since they are complex functions of surface properties, geometry, and conduction-convection suppression techniques. Each collector concept must be analyzed using the approach described in detail for the PTC.

Figure 3.55 summarizes the equations most often used for calculation of the incidence angles of beam radiation on the aperture of all common types of solar collectors. These equations are used to calculate daylong energy delivery of both concentrators and flat-plate collectors. A complete discussion of incidence angles is contained in Chapter 2.

In order to apply the method of Section 2.6.1 to find monthly averaged daily solar radiation on a tracking solar concentrator, the tilt factors in Equation 2.64 must be continuously changed owing to tracking. Collares-Pereira and Rabl have given expressions for various modes of tracking that can be used to calculate \bar{H}_c as

$$\bar{H}_c = \bar{r}_T - \bar{r}_d (\bar{D}_h / \bar{H}_h) \bar{H}_h. \quad (3.135)$$

Equations for \bar{r}_T and \bar{r}_d are given in Figure 3.56. The collection start (or stop) time, h_{coll} , used in Figure 3.56 represents the time measured from solar noon at which the collector starts (or stops) operating.

Orientation of collector	Incidence factor $\cos i$
Fixed, horizontal, plane surface	$\sin L \sin \delta_s + \cos \delta_s \cos h_s \cos L$
Fixed plane surface tilted so that it is normal to the solar beam at noon on the equinoxes	$\cos \delta_s \cos h_s$
Rotation of a plane surface about a horizontal east–west axis with a single daily adjustment permitted so that its surface normal coincides with the solar beam at noon every day of the year	$\sin^2 \delta_s + \cos^2 \delta_s \cos h_s$
Rotation of a plane surface about a horizontal east–west axis with continuous adjustment to obtain maximum energy incidence	$\sqrt{1 - \cos^2 \delta_s \sin^2 h_s}$
Rotation of a plane surface about a horizontal north–south axis with continuous adjustment to obtain maximum energy incidence	$[(\sin L \sin \delta_s + \cos L \cos \delta_s \cos h_s)^2 + \cos^2 \delta_s \sin^2 h_s]^{1/2}$
Rotation of a plane surface about an axis parallel to the earth's axis with continuous adjustment to obtain maximum energy incidence	$\cos \delta_s$
Rotation about two perpendicular axes with continuous adjustment to allow the surface normal to coincide with the solar beam at all times	1

FIGURE 3.55

Incidence angle factors for various orientations and motions of solar collectors. The incidence factor denotes the cosine of the angle between the surface normal and the solar beam.

Collector type	r_T^{abc}	r_d^d
Fixed aperture concentrators that do not view the foreground	$[cos(L - \beta)]/(d cos L) \{ -ah_{coll}cos h_{sr}(i = 90) + [a - b cos h_{sr}(i = 90) sin h_{coll} + (b/2)(sin h_{coll} cos h_{coll} + h_{coll})]$	$(sin h_{coll}/d) \{ [cos(L + \beta)/cos L] - [1/(CR)] \} + (h_{coll}/d) \{ [cos h_{sr}(\alpha = 0)/(CR)] - [cos(L + \beta)/cos h_{sr}(i = 90)] \}$
East–west axis tracking ^e	$\frac{1}{d} \int_0^{h_{coll}} \{[(a + b cos x)/cos L] \times \sqrt{\cos^2 x + \tan^2 \delta_s} dx$	$\frac{1}{d} \int_0^{h_{coll}} \{[1/cos L] \times \sqrt{\cos^2 x + \tan^2 \delta_s} - [1/(CR)] [\cos x - \cos h_{sr}(\alpha = 0)]\} dx$
Polar tracking	$(ah_{coll} + b sin h_{coll})/(d cos L)$	$(h_{coll}/d) \{[1/cos L] + [cos h_{sr}(\alpha = 0)/(CR)] - \sin h_{coll}/[d(CR)]\}$
Two-axis tracking	$(ah_{coll} + b sin h_{coll})/(d cos \delta_s cos L)$	$(h_{coll}/d) \{[1/cos \delta_s cos L] + [cos h_{sr}(\alpha = 0)/(CR)] - \sin h_{coll}/[d(CR)]\}$

^a $a = 0.409 + 0.5016 \sin[h_{sr}(\alpha = 0) - 60^\circ].$

^b $b = 0.6609 - 0.4767 \sin[h_{sr}(\alpha = 0) - 60^\circ].$

^c $d = \sin h_{sr}(\alpha = 0) - h_{sr}(\alpha = 0) \cos h_{sr}(\alpha = 0).$

^d CR is the collector concentration ratio.

^e Elliptic integral tables to evaluate terms of the form of $\int_0^h \sqrt{\cos^2 x + \tan^2 \delta_s} dx$ contained in r_T and r_d are given in the Appendix. Use the identity $\cos \delta_s = \sin(90^\circ - \delta_s)$ and multiply the integral by $\cos \delta_s$ a constant. For computer implementation, a numerical method can be used. For hand calculations, use Weddle's rule or Cote's formula.

FIGURE 3.56

Parameters r_T and r_d used to calculate monthly solar flux incident on various collector types. (From Collares-Pereira, M. and A. Rabl, *Sol. Energy* 23: 235–254, 1979.) (The collection hour angle value h_{coll} not used as the argument of trigonometric functions is expressed in radians. Note that the total interval $2 h_{coll}$ is assumed to be centered about solar noon.)

PROBLEMS

- Calculate the heat-removal factor for a collector having an overall heat-loss coefficient of $6 \text{ W/m}^2\text{K}$ and constructed of aluminum fins and tubes. Tube-to-tube centered distance is 15 cm; fin thickness is 0.05 cm; tube diameter is 1.2 cm; fluid tube heat-transfer coefficient is $1200 \text{ W/m}^2\text{K}$. The cover transmittance to solar radiation is 0.9 and is independent of direction. The solar absorptance of the absorber plate is 0.9, the collector is 1 m wide and 3 m long, and the water flow rate is 0.02 kg/s . The water temperature is 330 K.
- Calculate the efficiency of the collector described in Problem 1 on March 1 at a latitude of 40°N between 11 a.m. and 12 noon. Assume that the total horizontal insolation is 450 W/m^2 , the ambient temperature is 280 K, and the collector is facing south.
- Calculate the plate temperature in Example 3.2 at 10 a.m., if the absorbed insolation during the first 3 h is 0, 150, and 270 W/m^2 and the air temperature is 285 K.
- Calculate the overall heat-transfer coefficient, neglecting edge losses, for a collector with a double glass cover, with the following specifications:

Plate-to-cover spacing	3 cm
Plate emittance	0.9
Ambient temperature	275 K
Wind speed	3 m/s
Glass-to-glass spacing	3 cm
Glass emittance	5 cm
Back insulation thickness	5 cm
Back insulation thermal conductivity	$0.04 \text{ W/m}\cdot\text{K}$
Mean plate temperature	340 K
Collector tilt	45°

- The graph in Figure 3.20 gives the results of an ASHRAE standard performance test for a double-glazed flat-plate collector. If the transmittance for the glass is 0.90 and the absorptance of the surface of the collector plate is 0.92, determine the following:

The collector heat-removal factor F_R

The overall heat-loss conductance of the collector U_c in $\text{W/m}^2\text{K}$

The rate at which the collector can deliver useful energy in W/m^2 when the insolation incident on the collector per unit area is 600 W/m^2 , the ambient temperature is 5°C , and inlet water is at 15°C

The maximum flow rate through the collector, with cold water entering at a temperature of 15°C, that will give an outlet temperature of at least 60°C if this collector is to be used to supply heat to a hot-water tank. Area of the collector is 4 m².

6. Standard tests on a commercially available flat-plate collector gave a thermal efficiency of

$$\eta = 0.7512 - 0.138(T_{f,in} - T_a)/I_c$$

$$K_{ra} = 1 - 0.15(1/\cos(i) - 1)$$

where $(T_{f,in} - T_a)/I_c$ is in °C·m²/W.

Find the useful energy collected from this collector each hour and for the whole day in your city on September 15.

Assume that all the energy collected is transferred to water storage with no losses. Calculate the temperature of the storage for each hour of the day. Assume a reasonable ambient temperature profile for your city.

Given:

Collector area = 6 m²

Collector tilt = 30° (south facing in the Northern Hemisphere, north facing in the Southern Hemisphere)

Storage volume = 0.3 m³ (water)

Initial storage temperature = 30°C

7. What is the second law efficiency of a flat-plate collector operating at 70°C if the environmental temperature is 10°C and the collector efficiency is 50%? Compare with a single-curvature concentrator operating at 200°C and with a double-curvature concentrator operating at 2500°C, all with first law efficiencies of 50%.
8. Show that the plate efficiency F' for an air-cooled flat-plate collector is given by Equation 3.57.
9. The heat-removal factor F_R permits solar collector delivery to be written as a function of collector fluid *inlet* temperature T_f in Equation 3.48. Derive the expression for a factor analogous to F_R , relating collector energy delivery to fluid *outlet* temperature.
10. In nearly all practical situations, the argument of the exponential term in Equation 3.45 for F_R is quite small. Use this fact along with a Taylor's series expansion to derive an alternate equation for F_R . Determine the range where the alternate equation and Equation 3.45 agree to within 1%.
11. The stagnation temperature $T_{c,max}$ of a solar collector corresponds to the temperature at the zero efficiency point, that is, the no net

energy delivery point. Using Equation 3.76, calculate the stagnation temperature of a flat-plate collector with 75% optical efficiency and a U_c value of 4.5 W/m²K if the insolation is 900 W/m² and the ambient temperature is 20°C.

12. Calculate the stagnation temperature of the collector in Problem 12 if it were used with an optical booster of concentration ratio 2.0 having an optical efficiency of 70%.
13. What is the operating temperature for an evacuated-tube collector operating at 50% efficiency if the insolation is 800 W/m²? Use data from Figure 3.21.
14. A method of reducing heat loss from a flat-plate collector is to pull a partial vacuum in the dead air spaces between cover plates. What vacuum level is required to completely eliminate convection in a single cover flat-plate collector operating at 85°C and tilted at 45° if the cover plates are at 40°C and are spaced 2 cm apart? See Equation 3.57.
15. Derive an expression for the heat-loss conductance U_c for a flat-plate collector in which convection and conductance are completely eliminated in the air layers by use of a hard vacuum.
16. The effect of air flow rate in an air-cooled flat-plate collector appears in the heat-removal factor F_R (Equation 3.58). Calculate the effect of doubling the flow rate on the heat-removal factor for the collector analyzed in Example 3.3. What percentage increase in energy delivery would be achieved by doubling the fan size?
17. What are the maximum concentration ratios for trough concentrators with acceptance angles of 10°, 25°, and 36°?
18. What is the maximum achievable temperature of a double-curvature concentrator with a concentration ratio of 5000, a nonselective surface, and an 80% transmittance function?
19. Calculate the depth of a full CPC collector if the aperture is 1 m and CR = 5. Repeat for an aperture of 1 cm.
20. What is the reflectance loss in a 50% truncated CPC collector using silver mirrors if it has a 36° acceptance half-angle? What is the loss for an anodized aluminum reflector?
21. Compare the average number of reflections for a full and 50% truncated CPC if the acceptance half-angle is 9°.
22. How much concentration effect is lost by truncating a 7° half-angle CPC by 1/4, 1/3, and 1/2?
23. Explain how Figures 3.49 and 3.50 could be used to prepare a map showing the effect of truncation on average number of reflectors of a CPC collector. Sketch qualitatively what such a map would look like.

24. A parabolic trough 1 m wide and 10 m long with no end support plates is 30 cm deep and has a focal length of 20.83 cm. Calculate its optical efficiency at a 30° incidence angle for perfect optics and tracking if its reflector reflectance is 80%, $\tau\alpha$ product is 75%, and if the receiver supports shade 5% of the aperture.
 25. Calculate the maximum concentration ratio for a parabolic trough collector with a 50 cm aperture, which captures 92% of the incident radiation if the rim half-angle is 50° and the surface is accurate to 2 mrad in slope. What is the receiver diameter?
-

References

- Agarwal, V.K., and D.C. Larson. 1981. Calculation of the top loss coefficient of a flat plate collector. *Sol. Energy* 27: 69–71.
- Akhtar, N., and S.C. Mullick. 1999. Approximate method for computation of glass cover temperature and top heat-loss coefficient of solar collectors with single glazing. *Sol. Energy* 66: 349–354.
- Akhtar, N., and S.C. Mullick. 2007. Computation of glass cover temperatures and top heat loss coefficient of flat plate solar collectors with double glazing. *Energy* 32: 1067–1074.
- ASHRAE 93-2003. *Methods of Testing to Determine the Thermal Performance of Solar Collectors*. ASHRAE, Atlanta, GA.
- ASHRAE 96-1980. *Methods of Testing to Determine the Thermal Performance of Unglazed Solar Collectors*. ASHRAE, Atlanta, GA.
- Baranov, V.K., and G.K. Melnikov. 1966. Study of the illumination characteristics of hollow focons. *Sov. J. Opt. Technol.* 33: 408–411. Also 1975. Parabolocylindric reflecting unit and its properties. *Geliotekhnika* 11: 45–52.
- Beekley, D.C., and G.R. Mather. 1975. *Analysis and Experimental Tests of a High Performance, Evacuated Tube Collector*. Owens-Illinois, Toledo, OH.
- Bliss, R.W. 1959. The derivations of several plate efficiency factors useful in the design of flat-plate solar-heat collectors. *Sol. Energy* 3: 55.
- Collares-Pereira, M., and A. Rabl. 1979. Simple procedure for predicting long term average performance of nonconcentrating and of concentrating solar collectors. *Sol. Energy* 23: 235–254.
- Collares-Pereira, M., A. Rabl, and R. Winston. 1977. Lens mirror combinations with maximal concentration. Enrico Fermi Institute Rept. No. EFI 77–20. University of Chicago Press, Chicago.
- DeLaquil, III, P. et al. 1993. Solar thermal electric technology. In *Renewable Energy-Sources for Fuels and Electricity*, T. Johansson et al., eds. Island Press, Washington, DC, pp. 213–296.
- Duff, W.S. 1976. Optical and thermal performance of three line focus collectors. ASME Paper 76-WA/HT-15. ASME, New York.
- Duff, W.S., and G.F. Lameiro. 1974. A performance comparison method for solar concentrators. ASME Paper 74-WA/Sol-4. ASME, New York.

- Duffie, J.A., and W.A. Beckman. 1980. *Solar Energy Thermal Processes*. John Wiley & Sons, New York.
- Dushman, S. 1962. *Scientific Foundations of Vacuum Technology*, 2nd ed., J.M. Lafferty ed. John Wiley & Sons, New York.
- Emmett, W.L.R. 1911. Apparatus for utilizing solar heat. U.S. Patent 980, 505.
- EN 12975-2. 2006. *Thermal Solar Systems and Components—Solar Collectors—Part 2: Test Methods*. European Committee for Standardization, Brussels, Belgium.
- Francia, G. 1968. Pilot plants of solar steam generating stations. *Sol. Energy* 12: 51–64.
- Gaul, H.W., and A. Rabl. 1979. Incidence angle modifier and average optical efficiency of parabolic trough collectors. In *Sun II: Proceedings of the International Solar Energy Society, Silver Jubilee Congress*, Vol. 1, Atlanta, GA, May 1979, K.W. Boer, and B.H. Glenn, eds. Pergamon Press, New York, pp. 547–551.
- Gleckman, P., J. O'Gallagher, and R. Winston. 1989. Concentration of sunlight to solar surface levels using non-imaging optics. *Nature* 339: 198–200.
- Hildebrandt, A.F., and L.L. Vant-Hull. 1974. Tower top focus solar energy collector. *Mech. Eng.* 23(9): 23–27.
- Hottel, H.C., and A.F. Sarofim. 1967. *Radiative Transfer*. McGraw-Hill, New York.
- Hottel, H.C., and A. Whillier. 1958. Evaluation of flat-plate collector performance. *Trans. Conf. Use Sol. Energy* 2(Pt 1): 74.
- Hsieh, C.K. 1981. Thermal analysis of CPC collectors. *Sol. Energy* 27: 19.
- Hsieh, C.K., and F.M. Mei. 1983. Empirical equations for calculation of CPC collector loss coefficients. *Sol. Energy* 30: 487.
- Kennedy, C.E. 2002. Review of mid- to high-temperature solar selective absorber materials. Report NREL/TP-520-31267. National Renewable Energy Laboratory, Golden, CO.
- Klein, S.A. 1975. Calculation of flat-plate collector loss coefficients. *Sol. Energy* 17: 79–80.
- Klein, S.A., J.A. Duffie, and W.A. Beckman. 1974. Transient considerations of flat-plate solar collectors. *J. Eng. Power* 96A: 109–114.
- Kreith, F. 1975. Evaluation of focusing solar energy collectors. *ASTM Stand. News* 3: 30–36.
- Kreith, F., and J.F. Kreider. 2012. *Principles of Sustainable Energy*. CRC Press, Boca Raton, FL.
- Kutcher, C.F. 1996. Transpired solar collector systems: A major advance in solar heating. Paper presented at the *World Engineering Congress*, Atlanta, GA, November 6–8, 1996.
- Kutcher, C.F., and C.B. Christensen. 1992. Unglazed transpired solar collectors. In *Advances in Solar Energy*, Vol. 7, K. Böer, ed., pp. 283–307. American Solar Energy Society, Boulder, CO.
- Lippke, F. 1995. Simulation of the part-load behavior of a 30 MWe SEGS plant. Tech. Rep., SAND-95-1293. Sandia National Labs., Albuquerque, NM.
- Löf, G.O.G., and R.A. Tybout. 1972. Model for optimizing solar heating design. ASME Paper 72-WA/SOL-8. ASME, New York.
- Mahboub, C., and N. Maummi. 2012. Calculation of the glass cover temperature and the top heat loss coefficient for 60°C vee corrugated solar collectors with single glazing. *Sol. Energy* 86: 804–808.
- Malik, M.A.S., and F.H. Buelow. 1976a. Hydrodynamic and heat transfer characteristics of a heat air duct. In *Helio-technique and Development*, (COMPLES 1975), Vol. 2. Development Analysis Associates, Cambridge, MA, pp. 3–30.

- Malik, M.A.S., and F.H. Buelow. 1976b. Heat transfer in a solar heated air duct-a simplified analysis. In *Heliotherapy and Development*, (COMPLES 1975), Vol. 2. Development Analysis Associates, Cambridge, MA, pp. 31–37.
- Mullick, S.C., and S.K. Samdarshi. 1988. An improved technique for computing the top heat loss factor of flat-plate collector with a single glazing. *ASME J. Sol. Energy Eng.* 110: 262–267.
- Patnode, A.M. 2006. Simulation and performance evaluation of parabolic trough solar power plants. Master's thesis, University of Wisconsin-Madison, College of Engineering, Madison, WI.
- Rabl, A. 1975. Comparison of solar concentrators. *Sol. Energy* 18: 93–111.
- Rabl, A. 1976a. Optical and thermal properties of compound parabolic concentrators. *Sol. Energy* 18: 497. See also Rabl, A. 1977. Radiation through specular passages. *Int. J. Heat Mass Trans.* 20: 323.
- Rabl, A. 1976b. Ideal two dimensional concentrators for cylindrical absorbers. *Appl. Opt.* 15: 871.
- Rabl, A. 1978. In *Proc. Sol. Thermal Conc. Coll. Tech. Symp.*, B. Gupta, ed. Denver, CO, pp. 1–42. SERI, Golden, CO.
- Ramsay, J.W., B.P. Gupta, and G.R. Knowles. 1977. Experimental evaluation of a cylindrical parabolic solar collector. *J. Heat Transfer* 99: 163.
- Samdarshi, S.K., and S.C. Mullick. 1991. An analytical equation for top heat loss factor of a flat plate solar collector with double glazing. *ASME J. Sol. Energy Eng.* 113: 117–122.
- Speyer, F. 1965. Solar energy collection with evacuated tubes. *J. Eng. Power* 87: 270.
- Stuetzle, T. 2002. Automatic control of the 30 MWe SEGS VI parabolic trough plant. Master's thesis, University of Wisconsin-Madison, Madison, WI.
- Swinbank, W. 1963. Long wave radiation from clear skies. *Quart. J. Roy. Meteor. Soc.* 89(381): 339–348.
- Vasquez-Padilla, R. 2011. Simplified methodology for designing parabolic trough solar power plants. Ph.D. dissertation, University of South Florida, Tampa, FL.
- Welford, W.T. 1974. *Aberrations of the Symmetrical Optical System*. Academic Press, New York.
- Welford, W.T., and R. Winston. 1989. *High Collection Nonimaging Optics*. Academic Press, San Diego, CA.
- Winston, R. 1974. Solar concentrators of a novel design. *Sol. Energy* 16: 89–95. Includes references of early CPL work from 1966.
- Winston, R. 1975. Radiant energy collection. U.S. Patent 3,923,381.
- Zarza Moya, E. 2012. Parabolic trough concentrating solar power (CSP) systems, Chapter 7. In *Concentrating Solar Power Technology: Principles, Developments and Applications*, K. Lovegrove, and W. Stein, eds. Woodhead Publishing Lt, Cambridge, UK.

Suggested Reading

- Forristall, R. 2003. *Heat Transfer Analysis and Modeling of a Parabolic Trough Solar Receiver Implemented in Engineering Equation Solver*. National Renewable Energy Laboratory (NREL), Golden, CO.

4

Thermal Energy Storage and Transport

Energy storage becomes necessary whenever there is a mismatch between the energy available and the demand (ASHRAE 2011). Storage is especially important in solar energy applications because of the seasonal, diurnal, and intermittent nature of solar energy. Nature provides storage of solar energy in a number of ways, such as plant matter, also known as biomass, ocean thermal energy, and hydro-potential at high elevation by evaporation from water bodies and subsequent condensation (Jensen 1980). In fact, even fossil fuels are a stored form of solar energy because they are produced from biomass. Natural solar energy storage provides a longer-term buffer between supply and demand. Since solar energy availability varies by the time of the day and also by the time of the year (seasonal), and can have intermittency even during a day owing to clouds, energy storage systems can be short term or long term depending on the objective:

1. *Buffering* with the objective of overcoming cloudiness for short periods from a few minutes to a couple of hours.
2. *Delivery Period Displacement*, such as collection during the day for delivery during peak load period of evening hours.
3. *Delivery Period Extension* by storing enough during the day to have storage available for hours before sunrise and after sunset or even for longer times of non-sunshine hours of a day to a number of days.
4. *Seasonal Storage*, which would store heat during summer for usage during winter.

Energy can be stored as heat, electrochemical energy in batteries, mechanical energy in flywheels, or potential energy as pumped hydro or compressed air (Glendenning 1981). In this chapter, we will examine thermal energy storage (TES) in detail.

4.1 Thermal Energy Storage

TES in various solid and liquid media is used for solar water heating, space heating, and cooling as well as high-temperature applications such as solar thermal power (Garg et al. 1985). Important parameters in a storage system

include the *duration of storage*, *energy density* (or specific energy), and the *charging and discharging* (storage and retrieval) characteristics (Tomlinson and Kannberg 1990). The energy density is a critical factor for the size of a storage system (Swet 1987). The rate of charging and discharging depends on thermophysical properties such as thermal conductivity and design of the storage system (Beckman and Gilli 1984). The following sections describe the types of TES, materials, and storage system design.

4.2 Types of TES

Thermal energy can be stored as sensible heat, as latent heat, or as the heat of chemical reaction (thermochemical) (Jotshi and Goswami 1998).

4.2.1 Sensible Heat Storage

Sensible heat, Q , is stored in a material of mass m and specific heat c_p by raising the temperature of the storage material from T_1 to T_2 and is expressed by Equation 4.1:

$$\begin{aligned} Q &= \int_{T_1}^{T_2} mc_p dT \\ &= \int_{T_1}^{T_2} \rho V c_p dT, \end{aligned} \quad (4.1)$$

where ρ and V are density and volume of the storage material, respectively. For moderate temperature changes, such as for solar space and water heating systems, the density and specific heat may be considered constants (deWinter 1975). Therefore, $Q = \rho V c_p \Delta T$. Most common sensible heat storage materials are water, organic oils, rocks, ceramics, and molten salts (Yang and Garimella 2010). Some of these materials, along with their physical properties, are listed in Figure 4.1. Water has the highest specific heat value of 4190 J/kg·°C.

The most common medium for storing sensible heat for use with low- and medium-temperature solar systems is water. Water is cheap and abundant and has a number of particularly desirable properties. Table 4.1 lists the advantages and disadvantages of aqueous storage of thermal energy (Kreider 1979).

Water is the standard storage medium for solar heating and cooling systems for buildings today. For these systems, useful energy can be stored below the boiling point of water.

Storage medium	Temperature range, °C	Density (ρ), kg/m ³	Specific heat (C), J/kg K	Energy density (ρC) kWh/m ³ K	Thermal conductivity (W/m K)
Water	0–100	1000	4190	1.16	0.63 at 38°C
Water (10 bar)	0.180	881	4190	1.03	—
50-ethylene glycol-50-water	0–100	1075	3480	0.98	—
Dowtherm A® (Dow Chem. Co.)	12–260	867	2200	0.53	0.122 at 260°C
Therminol 66® (Monsanto Co.)	−9–343	750	2100	0.44	0.106 at 343°C
Draw salt (50NaNO ₃ -50KNO ₃) ^a	220–540	1733	1550	0.75	0.57
Molten salt (53KNO ₃ /40NaNO ₃ /7NaNO ₃) ^a	142–540	1680	1560	0.72	0.61
Liquid sodium	100–760	750	1260	0.26	67.5
Cast iron	mp. 1150–1300°C	7200	540	1.08	42.0
Taconite	—	3200	800	0.71	—
Aluminum	m.p. 660	2700	920	0.69	200
Fireclay	—	2100–2600	1000	0.65	1.0–1.5
Rock	—	1600	880	0.39	—

^a Composition in percent by weight.

Note: m.p. = melting point.

FIGURE 4.1

Physical properties of some sensible heat storage materials.

TABLE 4.1

Advantages and Disadvantages of Water as a Thermal Storage Medium

Advantages	Disadvantages
Abundant, low cost	High vapor pressure
Non-toxic	Difficult to stratify
Not combustible	Low surface tension, leaks easily
Excellent transport properties	Corrosive medium
High specific heat	Freezing and consequent destructive expansion
High density	Nonisothermal energy delivery
Good combined storage medium and working fluid	
Well-known corrosion control methodology	

4.2.2 Latent Heat Storage

Thermal energy can be stored as latent heat in a material that undergoes phase transformation at a temperature that is useful for the application. If a material with phase change temperature T_m is heated from T_1 to T_2 such that $T_1 < T_m < T_2$, the thermal energy Q stored in a mass m of the material is given by Equation 4.2:

$$Q = \int_{T_1}^{T_m} mc_p dT + m\lambda + \int_{T_m}^{T_2} mc_p dT, \quad (4.2)$$

where λ is the heat of phase transformation.

Four types of phase transformations useful for latent heat storage are as follows: solid \rightleftharpoons liquid, liquid \rightleftharpoons vapor, solid \rightleftharpoons vapor, and solid \rightleftharpoons solid. Since phase transformation is an isothermal process, thermal energy is stored and received at a fixed temperature known as the transition temperature. Some common phase change materials (PCMs) used for thermal storage are paraffin waxes, nonparaffins, inorganic salts (both anhydrous and hydrated), and eutectics of organic or inorganic compounds. For high-temperature storage, even metals may be used as PCMs. Table 4.2 lists some PCMs with their physical properties.

Most common PCMs used for solar energy storage undergo solid \rightleftharpoons liquid transformation. For such materials, the thermal energy stored may be written from Equation 4.2 as, approximately (Equation 4.3),

$$Q = m \bar{c}_{ps}(T_m - T_1) + \lambda + \bar{c}_{pl}(T_2 - T_m) , \quad (4.3)$$

where \bar{c}_{ps} and \bar{c}_{pl} are the average specific heats in the solid and liquid phases, respectively.

Example 4.1

A company is interested in 2 h of buffer storage for a 1.5 MW_{th} solar thermal power plant that operates between 285°C and 380°C. Estimate the amount of material that is needed if sodium nitrate, NaNO₃, is used as the latent heat storage medium.

Solution

The melting temperature, average solid and liquid specific heats, and the latent heat of sodium nitrate can be found from Table 4.2:

$$\bar{c}_{ps} = 1.27 \text{ kJ/kg}\cdot^\circ\text{C}$$

$$\bar{c}_{pl} = 1.64 \text{ kJ/kg}\cdot^\circ\text{C}$$

$$T_m = 307^\circ\text{C}$$

$$\lambda = 177 \text{ kJ/kg}$$

The energy that is required for 2 h of storage is

$$\begin{aligned} Q &= \text{number of hours of storage} \times \text{thermal power requirement} \\ &= 2 \text{ h} \times 1500 \text{ kW} = 3000 \text{ kWh} \\ &= 3000 \text{ kWh} \times \frac{3600 \text{ s}}{\text{h}} = 10.8 \times 10^6 \text{ kJ.} \end{aligned}$$

TABLE 4.2
Physical Properties of Latent Heat Storage Materials or PCMs

Storage Medium	Melting Point (°C)	Latent Heat (kJ/kg)	Specific Heat (kJ/kg·°C)		Density (kg/m ³)		Energy Density (kWh/m ³ ·K)	Thermal Conductivity (W/m·K)
			Solid	Liquid	Solid	Liquid		
<i>n</i> -Tetradecane	5.5	228	—	—	825	771	48	0.15
LiClO ₃ ·3H ₂ O	8.1	253	—	—	1720	1530	108	—
<i>n</i> -Octadecane	28	244	2.16	—	814	774	52.5	0.15
Na ₂ SO ₄ ·1OH ₂ O (Glauber's salt)	32.4	251	1.76	3.32	1460	1330	92.7	2.25
Na ₂ S ₂ O ₃ ·5H ₂ O	48	200	1.47	2.39	1730	1665	92.5	0.57
NaCH ₃ COO·3H ₂ O	58	180	1.9	2.5	1450	1280	64	0.5
Steric acid	70	203	—	2.35	941	347	48	0.1721
Ba(OH) ₂ ·8H ₂ O	78	301	0.67	1.26	2070	1937	162	0.6531
Mg(NO ₃) ₂ ·6H ₂ O	90	163	1.56	3.68	1636	1550	70	0.611
HDPE (cross-linked)	126	180	2.88	2.51	960	900	45	0.361
LiNO ₃	252	530	2.02	2.041	2310	1776	261	1.35
NaNO ₃	307	177	1.27	1.64	2260	1900	93	0.5
NaOH/NaCl/Na ₂ CO ₃ (77.2:16.2:6.6) ^b	318	290	—	—	—	—	—	—
LiCl/BaCl ₂ /KCl (54.2:6.4:39.4) ^b	320	170	—	—	—	—	—	—
KNO ₃	335	266	0.5	—	2110	1865	138	0.5
Zn/Mg (52:48) ^a	340	180	—	—	—	—	—	—
LiCl/KCl (58:42) ^b	348	170	—	—	—	—	—	—

(Continued)

TABLE 4.2 (CONTINUED)
Physical Properties of Latent Heat Storage Materials or PCMs

Storage Medium	Melting Point (°C)	Latent Heat (kJ/kg)	Specific Heat (kJ/kg/°C)			Density (kg/m ³)	Energy Density (kWh/m ³)	Thermal Conductivity (W/m·K)
			Solid	Liquid	Solid			
KOH	380	149.7	—	—	—	—	—	0.5
MgCl ₂ /KCl/NaCl (45:4:21:6:33) ^b	380	284	—	—	—	—	—	—
Zn/Al (96:4) ^a	381	138	—	—	—	—	—	—
LiCO ₃ /K ₂ CO ₃ /Na ₂ CO ₃ (32:35:33) ^a	397	277	1.34	1.76	2300	2140	165	—
Na ₂ CO ₃ /K ₂ CO ₃ /Li ₂ CO ₃ (37:35:31) ^a	397	275	1.67	1.63	2300	—	175	2.04
Al/Mg/Zn (59:35:6) ^a	443	310	—	—	—	—	—	—
NaCl/MgCl ₂ (48:52) ^a	450	430	0.92	1	2230	—	266	0.96
KCl/MgCl ₂ (36:64) ^a	470	388	0.84	0.96	2190	—	236	0.83
Na ₂ CO ₃ /Li ₂ CO ₃ (56:44) ^a	487	368	1.8	2.09	2320	—	237	2.11
NaCl/CaCl ₂ (33:67) ^a	500	281	0.84	1	2780	—	217	1.02
LiCO ₃ /K ₂ CO ₃ (35:65) ^a	505	345	1.68	1.63	2265	1960	1.88	—
LiBr	550	203	—	—	—	2528	142	—
LiF/NaF ₂ /MgF ₂ (46:44:10) ^a	632	858	1.4	—	2240	—	534	1.2
Al	660	398	—	—	—	2375	262	2.5
MgCl ₂	714	452	—	—	2140	1680	210	—

Note: 1 liquid.

^a Composition in percent by weight.

^b Composition in percent by mole.

By rearranging Equation 4.3, the mass requirement for 10.8×10^6 kJ of storage is

$$m = \frac{Q}{\bar{c}_{ps}(T_m - T_1) + \lambda + \bar{c}_{pl}(T_2 - T_m)}$$

$$m = \frac{10.8 \times 10^6 \text{ kJ}}{1.27 \frac{\text{kJ}}{\text{kg} \cdot ^\circ\text{C}} (307^\circ\text{C} - 285^\circ\text{C}) + 177 \frac{\text{kJ}}{\text{kg}} + 1.64 \frac{\text{kJ}}{\text{kg} \cdot ^\circ\text{C}} (380^\circ\text{C} - 307^\circ\text{C})}$$

$$= 33,265.6 \text{ kg.}$$

Actual mass required will be more since some of the heat in the system can not be recovered economically and in a reasonable amount of time.

4.2.3 Thermochemical Energy Storage

Thermochemical energy can be stored as heat of reaction in reversible chemical reactions. In this mode of storage, the reaction in the forward direction is endothermic (storage of heat), while the reverse action is exothermic (release of heat). For example,



The amount of heat Q stored in a chemical reaction depends on the heat of reaction and the extent of conversion as given by Equation 4.5:

$$Q = a_r m \Delta H, \quad (4.5)$$

where a_r is fraction reacted, ΔH is the heat of reaction per unit mass, and m is mass.

Chemical reaction is generally a highly energetic process. Therefore, a large amount of heat can be stored in a small quantity of a material. Another advantage of thermochemical storage is that the products of reaction can be stored at room temperature and need not be insulated. For sensible and latent heat storage materials, insulation is very important. Examples of reactions include decomposition of metal hydrides, oxides, peroxides, ammoniated salts, carbonates, sulfur trioxide, and so on (Harrison and Pelanne 1977). Some useful chemical reactions are reported in Table 4.3.

TABLE 4.3
Properties of Thermochemical Storage Media

Compound	Temperature (°C)	Pressure (bar)	Reaction	ΔH (kJ/mol)	ΔH (kWh/m ³)
Manganese oxide	530	1	$\text{MnO}_2 + \Delta H \leftrightarrow 0.5\text{Mn}_2\text{O}_3 + 0.25\text{O}_2$	42	336
Calcium hydroxide	505	1	$\text{Ca}(\text{OH})_2 + \Delta H \leftrightarrow \text{CaO} + \text{H}_2\text{O}$	112	364
Calcium carbonate	896	1	$\text{CaCO}_3 + \Delta H \leftrightarrow \text{CaO} + \text{CO}_2$	167	113
Magnesium hydride	250–500	—	$\text{MgH}_2 + \Delta H \leftrightarrow \text{Mg} + \text{H}_2$	75	111
Ammonia	400–500	—	$\text{NH}_3 + \Delta H \leftrightarrow 1/2\text{N}_2 + 3/2\text{H}_2$	67	675
Methane/water	500–1000	—	$\text{CH}_4 + \text{H}_2\text{O} \leftrightarrow \text{CO} + 3\text{H}_2$	206	—
Magnesium oxide	250–400	—	$\text{MgO} + \text{H}_2\text{O} \leftrightarrow \text{Mg}(\text{OH})_2$	81	—
Iron carbonate	180	—	$\text{FeCO}_3 \leftrightarrow \text{FeO} + \text{CO}_2$	—	—
Methanolation-demethanolation	200–250	1–5	$\text{CH}_3\text{OH} \leftrightarrow \text{CO} + 2\text{H}_2$	98	—
Mg_2FeH_6	500	66	$\text{Mg}_2\text{FeH}_6 + \Delta H \leftrightarrow \text{Mg}_2\text{Fe} + 3\text{H}_2$	77.4	160
Magnesium carbonate	427–327	1	$\text{MgCO}_3 + \Delta H \leftrightarrow \text{MgO} + \text{CO}_2$	101.1	187
Sulfur trioxide	520–960	1	$\text{SO}_3 + \Delta H \leftrightarrow \text{SO}_2 + 1/2\text{O}_2$	99.6	280

4.3 Design of Storage System

Design of a storage system involves the selection of a storage material, design of containment, and heat exchangers for charging and discharging (Cole et al. 1980).

4.3.1 Selection of Storage Material

Selection of the storage material is the most important part of the design of a TES system. The selection depends on a number of factors. Below are some of those factors.

4.3.1.1 Solar Collection System

The solar collection system determines the temperature at which the storage material will be charged and the maximum rate of charge. Thermophysical properties of the storage material at this temperature are important in determining the suitability of the material. For example, flat plate liquid-type collectors may use water as the storage material, while air-type flat plate collectors for space heating may use a rock or pebble bed as the storage medium. If the storage material can be used as the heat-exchanger fluid in the collector, it avoids the need of a collector-to-storage heat exchanger. This criterion favors liquid storage materials. Water and glycol–water mixtures are the most common storage materials for flat plate and moderately concentrating collector systems. For parabolic trough concentrators, high-temperature oils are more appropriate. For higher-concentration and higher-temperature collectors such as central receiver tower, molten salts may be used.

Molten nitrate salt (50 wt% NaNO_3 /50 wt% KNO_3), also known as Draw salt, which has a melting point of 222°C, has been used as a storage and a heat-transfer fluid in an experiment in Albuquerque, New Mexico. It was the first commercial demonstration of generating power from storage (Delameter and Bergen 1986). Solar Two, a 10-MW solar thermal power demonstration project in Barstow, California, was also designed to use this molten salt to store solar energy (Chavez et al. 1995). Another molten nitrate salt is 40 wt% NaNO_2 /7 wt% NaNO_3 /53 wt% KNO_3 , known as HTS (heat-transfer salt) with a melting point of 142°C. This salt has been widely used in the chemical industry.

4.3.1.2 Application

The application determines the temperature at which the storage will be discharged and maximum rate of discharge. For hot water applications and moderate-temperature industrial process heat, water would be an obvious choice for heat storage. A PCM may be used if space considerations are very important.

For applications in heating and cooling of buildings, the containment of PCM can become an integral part of the building. It may be part of the ceiling, wall, or floor of the building and may serve a structural or a non-structural function. Tubes, trays, rods, panels, balls, canisters, and tiles containing PCMs have been studied in the 1970s and 1980s for space-heating applications (Rabl 1977). The PCMs used were mostly salt hydrates such as $\text{Na}_2\text{SO}_4 \cdot 10\text{H}_2\text{O}$ (Glauber's salt), $\text{Na}_2\text{S}_2\text{O}_3 \cdot 5\text{H}_2\text{O}$ (Hypo), $\text{NaCH}_3\text{COO} \cdot 3\text{H}_2\text{O}$, $\text{Na}_2\text{HPO}_4 \cdot 12\text{H}_2\text{O}$, $\text{Ba(OH)}_2 \cdot 8\text{H}_2\text{O}$, $\text{MgCl}_2 \cdot 6\text{H}_2\text{O}$, and $\text{Mg}(\text{NO}_3)_2 \cdot 6\text{H}_2\text{O}$. Paraffin mixtures have been used for thermal storage in wallboards.

4.3.1.3 Additional Considerations

Other considerations include space requirements, cost, long-term cycling stability, corrosivity, complexity of containment system, and complexity of heat-exchanger design for maximum rates of charge and discharge.

4.3.2 Design of Containment

Containment design is especially important for liquid and phase change storage materials. Water can be stored in any tank able to withstand the expected pressure. Some commonly used tanks for water storage include steel tanks with glass, epoxy or stone lining, fiberglass reinforced polymer, concrete with plastic liner, and wooden tanks.

Containment of PCMs can be problematic, since phase change is accompanied by a large change in volume and other thermophysical properties (Potter 1959). PCMs may be bulk stored in tanks or be micro- or macroencapsulated. Bulk storage requires special attention to the design of heat exchangers for charging and discharging. *Microencapsulation* involves very small particles of a PCM dispersed in a single phase matrix. It is usually considered a way of introducing high TES in building materials (Moses and Lane 1986). Some examples include PCMs encapsulated in concrete, floor tiles, and wallboard. The US Department of Energy sponsored the development of a composite wallboard by mixing up to 35% paraffin waxes in gypsum. The waxes contain *n*-octadecane as the main constituent with a melting point of 23°C and a heat of fusion of 184 kJ/kg.

Most of the successful developments to date have been made in *macroencapsulation* of PCMs. Capsules may be made out of plastics for low-temperature applications and metals for higher temperatures. They may be shaped as spherical balls, cylindrical rods, rectangular panels, or flexible pouches. Some of the materials used for macroencapsulation are listed in Table 4.4. Figure 4.2 shows some examples of commercially developed, macroencapsulated PCMs (Makansi 1994).

TABLE 4.4

Thermal Conductivity of Potential Containment Materials

Materials	Thermal Conductivity ^b	
	(W/m·K)	(Btu/h·ft·°F)
<i>Plastics^a</i>		
ABS	0.17–0.33	0.1–0.2
Acrylic	0.19–0.43	0.11–0.25
Polypropylene	0.12–0.17	0.07–0.1
Polyethylene (high density)	0.43–0.52	0.25–0.3
Polyethylene (medium density)	0.30–0.42	0.17–0.25
Polyethylene (low density)	0.30	0.17
Polyvinyl chloride	0.13	0.08
<i>Metals^c</i>		
Aluminum	237	137
Copper	401	232
Carbon steel (AISI 1095)	45	26

^a *Plastics, a Desk-top Data Bank*, 5th Ed., Book A, The International Plastics Selector, Inc., San Diego, CA, 1980.

^b As measured by ASTM C-177.

^c *CRC Handbook of Chemistry and Physics*, 88th Ed. 2007–2008.

**FIGURE 4.2**

Examples of commercially developed PCM capsules.

4.3.3 Heat-Exchanger Design

For liquid storage media, heat exchangers of the shell and tube type or submerged coil type are generally used for charging and discharging. These types of heat exchangers are described later in this chapter.

For solid storage media or macroencapsulated PCM, normally a packed bed type of storage configuration is designed. In this case, the heat is transferred to or from a heat-transfer fluid by flowing the heat-transfer fluid through the voids in the bed. Clark (1986) has reviewed research on heat transfer and pressure drop for flow through such storage systems. More recently, such systems have been reviewed for their applications in higher-temperature applications, such as CSP and industrial process heat (Karlekar and Desmond 1977; Kuravi et al. 2013).

4.3.3.1 Packed Bed Storage

Figure 4.3 shows a schematic of a packed bed storage system. Table 4.5 gives average void fractions for packed beds (Clark 1986). Packed bed storage systems are often designed by employing numerical models that rely on experimentally derived correlations. These models solve the relevant equations for a system such as the momentum and energy equations for the storage material and heat-transfer fluid. The results of the model can provide transient temperature and velocity data as well as performance characteristics such as efficiency and cyclic behavior.

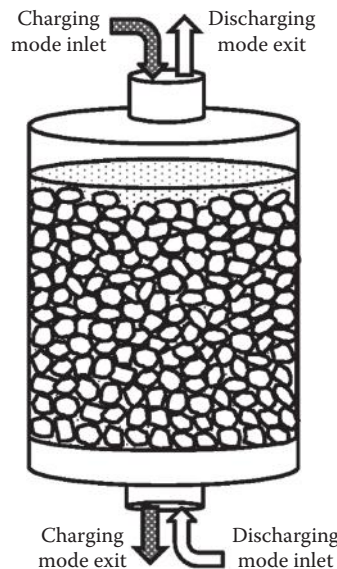


FIGURE 4.3
Schematic of a packed bed TES.

TABLE 4.5Representative Average Void Fractions, $\bar{\varepsilon}$, for Packed Beds

Particle Type	Packing	Average Void Fraction
Sphere	Rhombohedral	0.26
Sphere	Tetragonal spheroidal	0.30
Sphere	Orthorhombic	0.40
Sphere	Cubic	0.48
Sphere	Random	0.36–0.43
Crushed rock	Granular	0.44–0.45
Sphere	Very loose, random	0.46–0.47
Sphere	Poured, random	0.37–0.39
Sphere	Close, random	0.36–0.38

Source: Adapted from Clark, J.A., Thermal design principles. In: *Solar Heat Storage: Latent Heat Materials*, Lane, G.A. (ed.), Chapter 5, CRC Press, pp. 185–223, 1986.

Recently, Sanduja et al. (2013) illustrated the use of a numerical model to design a sensible heat packed bed storage system for a solar thermal power plant. The model was validated with the numerical and experimental results presented by Hanchen et al. (2011) and Meier et al. (1991). They considered the storage system consisting of an axisymmetric tank with 1D plug flow assumption. The 1D assumption is valid when radial effects play a minor role in the velocity and temperature distribution of the bed and thus can be neglected. The unsteady governing energy equations for the storage material and heat-transfer fluid are, respectively:

Solid phase:

$$\rho_s c_s (1 - \varepsilon) \frac{\partial T_s}{\partial t} = h_v (T_f - T_s) + K_{\text{eff}} \frac{\partial^2 T_s}{\partial x^2} \quad (4.6)$$

Fluid phase:

$$\rho_f c_f \varepsilon \frac{\partial T_f}{\partial t} + c_f G \frac{\partial T_f}{\partial x} = h_v (T_s - T_f) + \frac{U_{\text{loss}} P}{A} (T_{\text{inf}} - T_f) \quad (4.7)$$

where K_{eff} is the effective thermal conductivity of the solid phase, h_v is the volumetric heat-transfer coefficient, ε is the porosity or void fraction of the packed bed, U_{loss} is the overall heat loss coefficient, A is the cross-sectional area of the bed, P is the perimeter of the tank (πD for a cylindrical tank of diameter D ; and $W \cdot D$ for a rectangular tank shown in Figure 4.3), T_{inf} is the ambient temperature, and c and ρ are the specific heat capacity and density

of the respective materials (Figure 4.4). G is defined as the superficial mass flow rate of HTF per unit bed cross-sectional area, or air mass flux:

$$G = \frac{\dot{m}}{A_{\text{bed}}} = \rho V = \rho \varepsilon v, \quad (4.8)$$

where \dot{m} is the mass flow rate of the heat-transfer fluid, V is the superficial velocity of the bed, and v is the interstitial particle velocity. The temperature of the storage material, T_s , and the temperature of fluid, T_f , are solved for with the numerical model.

They developed a numerical solution based on forward difference for temporal discretization and upwind difference for the first-order and central difference for the second-order space discretization. For guidance on numerical modeling, refer to Jaluria and Torrance (2003). The initial conditions are as follows:

Charging cycle:

$$T_f(t=0) = T_s(t=0) = T_{\text{initial}}. \quad (4.9)$$

Discharging cycle:

$$T_f(t=0) = T_f(t_{\text{end}}); \quad T_s(t=0) = T_s(t_{\text{end}}). \quad (4.10)$$

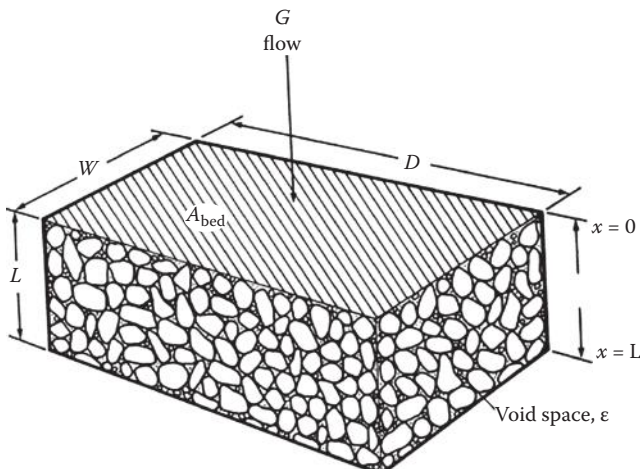


FIGURE 4.4

Representative element of the packed bed model. (Adapted from Clark, J.A., Thermal design principles, Chapter 5 in *Solar Heat Storage: Latent Heat Materials*, Lane, G.A. (ed.), CRC Press, pp. 185–223, 1986.)

The boundary conditions for the charging–discharging cycle are as follows:

$$\begin{aligned} T_f(x = 0) &= T_{\text{inlet}} \\ \frac{\partial T_f(x = H)}{\partial x} &= 0 \\ \frac{\partial T_s(x = 0)}{\partial x} &= \frac{\partial T_s(x = H)}{\partial x} = 0. \end{aligned} \quad (4.11)$$

Following validation, the model was used to predict the performance of a storage system under operating conditions that were specific to their application. The operating conditions are shown in Table 4.6. For a single-cycle analysis, the system is charged for 1 h, and for a multiple-cycle analysis, the system is continuously charged and discharged for 1 h each. Figure 4.5 shows the solid temperature distribution along the height of the bed for single and multiple cycles.

In the energy equations, the effective thermal conductivity, overall heat loss coefficient, and volumetric heat-transfer coefficient, h_v , are typically calculated from correlations that were experimentally developed. Various heat-transfer correlations are available in the literature that may be used to simulate the system temperature distribution. Sanduja et al. (2013) employed a heat-transfer coefficient developed by Coutier and Farber (1982):

$$h = \frac{700}{6(1 - \varepsilon)} G^{0.76} D_p^{0.24}, \quad (4.12)$$

TABLE 4.6

Input Parameters Used in the Model Simulations of Sanduja et al. (2013)

Parameter	Value
Charging inlet air temperature, T_c (K)	873
Discharging inlet air temperature, T_d (K)	383
Ambient temperature, T_{inf} (K)	293
Air mass flow rate, \dot{m} (kg/s)	0.568
Tank height (m)	4
Tank diameter (m)	1
Particle diameter (m)	0.009
ε , porosity	0.4
Overall heat loss coefficient, U (W/m ² ·K)	0.678
Particle density, ρ_s (kg/m ³)	3200
Particle specific heat, c_s (J/kg·K)	1158
Particle thermal conductivity, k_s (W/m·K)	6.14

where h is the particle surface heat-transfer coefficient and D_p is the equivalent diameter of the storage particle. The volumetric heat-transfer coefficient can be related to the surface heat-transfer coefficient, h , by Kim (1994):

$$h_v = h \frac{A_e}{V_e} , \quad (4.13)$$

where the ratio A_e/V_e represents the superficial particle surface area per unit bed volume. In Equation 4.13, it is important to find the active surface area of the elements and it is often difficult to predict this area for irregular shaped particles and irregular arrangement in a packed bed. For a bed of spheres or cylindrical particles with aspect ratio of unity, the volumetric heat-transfer coefficient is simply calculated using the following equation:

$$h_v = \frac{6(1-\varepsilon)}{D_p h} . \quad (4.14)$$

For a bed of randomly packed spheres, Clark (1986) recommends a correlation by Beasley and Clark (1984) for the heat-transfer coefficient h for air flow through the bed (Figure 4.4), valid for Reynolds numbers of 10–10,000.

$$\frac{hD_p}{k} = 2.0 + 1.354\text{Re}_o^{1/2}\text{Pr}^{1/3} + 0.0326\text{Re}_o\text{Pr}^{1/2}, \quad (4.15)$$

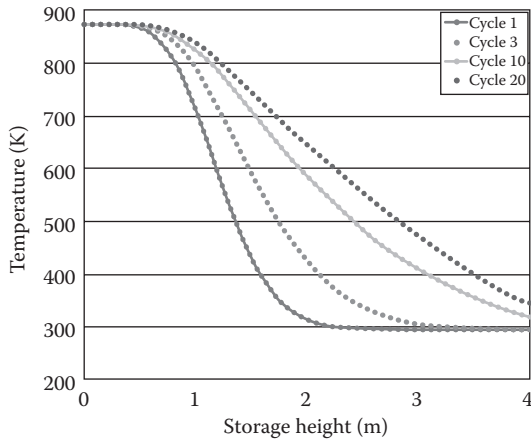
where Re_o and Pr are Reynolds and Prandtl numbers, respectively, as defined below:

$$\text{Re}_o = \frac{D_p G}{\mu}, \quad \text{Pr} = \frac{c_p}{k}. \quad (4.16)$$

D_p is the diameter of the storage particle and μ , c_p and k are the viscosity, specific heat, and thermal conductivity, respectively, of the heat-transfer fluid (air). This correlation may be used for low-temperature TES.

Kuravi et al. (2013) conducted an experimental study with a bed of solid bricks of *feelite* (an iron ore) arranged with channels for air flow (Figure 4.5) and found that the correlation shown in Equation 4.17 by Coutier and Farber (1982) with a modification proposed by Li and Ma (2011) for sphericity can predict the experimental results more accurately compared to other correlations. On the basis of this finding and their experimental study, they proposed the following correlation, which could be used for a packed bed system with channels for air flow:

$$h = \frac{1060}{6(1-\varepsilon)} G^{0.76} D_e^{0.24} \psi^{-0.56}. \quad (4.17)$$

**FIGURE 4.5**

Temperature distribution of the solid phase across the storage height (1.6 m) at the end of a single and multiple 1-h charge and discharge cycles. (Adapted from Sanduja, P. et al., Numerical analysis of a packed bed thermal storage system for concentrated solar power. *Energy Procedia, Proceedings of the ISES 2013 Solar World Congress*, 2013.)

The equivalent element diameter, D_e is given by the equation

$$D_e = \frac{6}{\pi} V_e^{(1/3)}, \quad (4.18)$$

where V_e is the volume of the element. The sphericity, ψ is given by

$$\psi = \frac{a_s}{a_e}, \quad (4.19)$$

where a_s is the surface area of a sphere having a volume equal to the material element and a_e is the surface area of the material element.

Similar to modeling of sensible heat storage systems, latent heat storage modeling requires a solution of the governing mass, momentum, and energy equations. Latent heat storage modeling is more complicated, however, because the interface between the two phases moves with time as latent heat is absorbed or released during the phase change process. An external heat-transfer coefficient is no longer sufficient since the assumption of a constant temperature distribution within the material is not accurate. To account for the additional thermal resistance during the phase change process within a spherical particle, Arkar and Medved (2005) employed an effective heat-transfer coefficient adopted from Jeffreson (1972):

$$h_{\text{eff}} = \frac{h}{1 + 0.2Bi}, \quad (4.20)$$

where h is the particle surface heat-transfer coefficient and Bi is the Biot number, a dimensionless number defined as

$$\text{Bi} = \frac{hD_p}{k_s}. \quad (4.21)$$

The effective heat-transfer coefficient replaces the surface heat-transfer coefficient in the energy equations. For additional details on various phase change modeling techniques, see Idelsohn (1994) and Voller (1996).

Example 4.2

A company is interested in designing a sensible heat storage system for a low-temperature waste heat application. Air is to be used as the heat-transfer fluid and crushed rock is to be used as the storage medium. A laboratory-scale system was first constructed and the experimental data were compared to the results of a numerical model that solves Equations 4.6 and 4.7 for the storage material and air temperatures. It was found that when the heat-transfer coefficient of Equation 4.15 was used, the model closely predicted the temperature distribution of the experimental packed bed. Following validation, the model is to be used to determine the optimum particle diameter for a large-scale system. The following table provides the design conditions of the large-scale system:

Design Parameter	Value
Tank height (m)	8
Tank diameter (m)	4
Mass flow rate (kg/s)	1.5
Particle diameters under consideration (m)	0.025, 0.035, 0.045
Charging air temperature (K)	373
Discharging air temperature (K)	301

Calculate the heat-transfer coefficient using Equation 4.15 for the particle diameter of 0.025 m. Air properties based on an average temperature of 648 K are assumed: $c_p = 1009 \text{ J/kg}\cdot\text{K}$, density = 1.049 kg/m^3 , $\mu = 2.081 \times 10^{-5} \text{ kg/m}\cdot\text{s}$, $k = 0.0292 \text{ W/m}\cdot\text{K}$.

Solution

To calculate h , the particle Reynolds number, Prandtl number, and air mass flux, G , must be calculated:

$$G = \frac{\dot{m}}{A_{\text{bed}}} = \frac{1.5 \text{ kg/s}}{\pi(4 \text{ m}^2)/4} = 0.1194 \text{ kg}/(\text{m}^2\text{s})$$

$$\text{Re}_o = \frac{D_p G}{\mu} = \frac{0.025 \text{ m} \times 0.1194 \text{ kg}/(\text{m}^2\text{s})}{2.081 \times 10^{-5} \text{ kg}/(\text{m} \cdot \text{s})} = 143.441$$

$$\text{Pr} = \frac{c_p}{k} = \frac{1009 \frac{\text{J}}{\text{kg} \cdot \text{K}} \times \frac{2.081 \times 10^{-5} \text{ kg}}{\text{m} \cdot \text{s}}}{0.0292 \frac{\text{W}}{\text{m} \cdot \text{K}}} = 0.7190.$$

Therefore, the particle surface heat-transfer coefficient is

$$\begin{aligned} h &= \frac{k}{D_p} \left(2.0 + 1.354 \text{Re}_o^{1/2} \text{Pr}^{1/3} + 0.0326 \text{Re}_o \text{Pr}^{1/2} \right) \\ &= \frac{0.0292 \frac{\text{W}}{\text{mK}}}{0.025 \text{ m}} \left(2.0 + 1.354(143.441)^{1/2}(0.719)^{1/3} + 0.0326(143.441)(0.719)^{1/2} \right) \\ &= 23.936 \frac{\text{W}}{\text{m}^2\text{K}}. \end{aligned}$$

The heat-transfer coefficient must be calculated for each particle diameter that is under investigation. Before solving the energy equations for the packed bed, the surface heat-transfer coefficient must be converted to the volumetric heat-transfer coefficient given in Equation 4.13.

4.3.3.2 Pressure Drop in a Packed Bed

To find the pressure drop in packed beds, the following equation developed by Ergun (1952) may be used:

$$\Delta p = f \frac{L}{D_p} \rho V^2 \frac{1-\varepsilon}{\varepsilon^3}, \quad (4.22)$$

where ε is the average void fraction (Table 4.5) and the friction factor f is given by

$$f = \frac{150(1-\varepsilon)}{\text{Re}_o} + 1.75. \quad (4.23)$$

Trahan et al. (2013) conducted an experimental study on pressure drop in a packed bed system and used the correlations of Ergun (1952), Eisfeld and

Schnitzlein (2001), and Singh et al. (2006) to determine the particle sphericity of crushed rock. They found that Ergun's equation showed the same power dependence of pressure drop on velocity in the Reynolds numbers range of 300 to 6000. Therefore, they proposed the following correlation for the pressure drop for nonspherical particles:

$$\frac{\Delta P}{L} = 150 \frac{(1-\varepsilon)^2}{\psi^2 \varepsilon^3} \frac{U}{D_e^2} + 1.75 \frac{1-\varepsilon}{\psi \varepsilon^3} \frac{\rho U^2}{D_e}, \quad (4.24)$$

where D_e is the equivalent diameter of the particles as defined in Equation 4.18.

Example 4.3

An estimate of the pressure drop of a packed bed is needed in order to determine the pumping energy and thus the pump size that is required to move fluid through a storage system. The company in Example 4.1 would like to encapsulate sodium nitrate in spherical capsules and place them in a random configuration in a storage tank that is 4 m tall. Air is used as the heat-transfer fluid and the diameter of the particles is 0.05 m. If the superficial bed velocity is 0.75 m/s, calculate the pressure drop of the packed bed. Assume an air density of 0.600 kg/m³ and a dynamic viscosity of 3.058×10^{-5} kg/m·s.

Solution

The sphericity is unity and the porosity of the bed can be determined from Table 4.5. Since the bed consists of spheres that are randomly poured in the tank, a porosity of 0.38 can be assumed. Equation 4.24 can then be used to calculate the pressure drop of the packed bed:

$$\begin{aligned} \frac{\Delta P}{L} &= 150 \frac{(1-\varepsilon)^2}{\varepsilon^3} \frac{U}{D_p^2} + 1.75 \frac{1-\varepsilon}{\varepsilon^3} \frac{\rho U^2}{D_p} \\ &= 150 \frac{(1-0.38)^2}{0.38^3} \frac{(3.058 \times 10^{-5} \text{ kg/m}\cdot\text{s}) \times 0.75 \frac{\text{m}}{\text{s}}}{(0.05 \text{ m})^2} \\ &\quad + 1.75 \frac{(1-0.38)}{(0.38)^3} \frac{(0.600 \text{ kg/m}^3) 0.75 \frac{\text{m}}{\text{s}}}{0.05 \text{ m}}^2 \\ \frac{\Delta P}{L} &= 9.64 + 133.47 = 143.11 \frac{\text{kg}}{\text{m}^2 \text{s}^2}. \end{aligned}$$

The height of the tank is 4 m; therefore, the estimated pressure drop is

$$\Delta P = 4 \text{ m} \times 143.11 \frac{\text{kg}}{\text{m}^2 \text{s}^2} = 572 \text{ Pa.}$$

4.3.3.3 Flow across Tube Banks

Figure 4.6 shows a schematic of flow across a tube bank. For flow of air across tube banks of 10 rows deep and Reynolds numbers from 2000 to 40,000, McAdams (1954) recommends a mean Nusselt number, Nu , as

$$\text{Nu} = \frac{hD_o}{k_f} = A \left(\frac{D_o G_{\max}}{f} \right)^{0.6} \text{Pr}_f^{1/3}, \quad (4.25)$$

where $A = 0.33$ for staggered tubes and 0.26 for in-line tubes. The subscript “f” indicates that the thermal property is to be determined at the film temperature or the average of the tube and the air temperatures. G_{\max} is defined as

$$G_{\max} = \frac{\dot{m}}{A_{\min}} \quad (4.26)$$

or the mass flow rate of air divided by the minimum free flow area (Singh et al. 2006).

For latent heat storage systems, sometimes a shell and tube arrangement is used such that the heat-transfer fluid flows through the tubes while the PCM

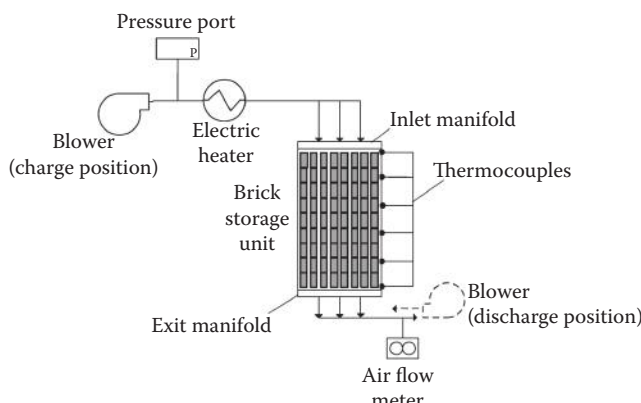


FIGURE 4.6

Schematic diagram of experimental sensible heat storage system. (From Kuravi, S. et al., *Progress in Energy and Combustion Science*, 39, 285–319, 2013.)

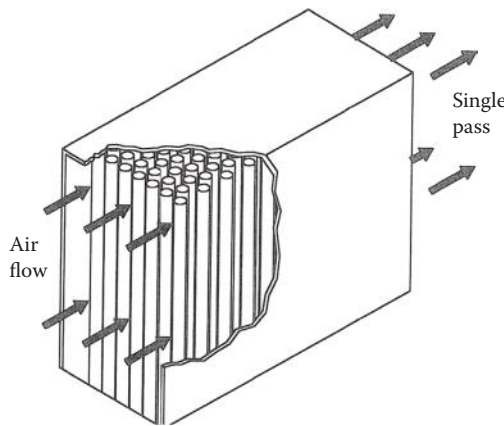


FIGURE 4.7
Schematic of a system with flow across tubes containing PCM.

fills the rest of the shell (Figure 4.7). For such systems, Zhang and Faghri (1996) suggest that the Nusselt number for flow within the tube is given by Edwards and Jensen (1994) as

$$\text{Nu} = \frac{0.023(l_c/D)^{0.2}}{1.32 - \frac{0.35l_c}{D}} \text{Re}^{0.8} \text{Pr}^{0.4}. \quad (4.27)$$

Pressure drop for flow through tubes is found from Equation 4.28, which is explained in detail in Section 4.4.

$$\Delta p = f \cdot 4(L/D) \cdot \frac{1}{2\rho} \bar{V}^2. \quad (4.28)$$

4.3.3.4 Performance of Packed Bed TES Systems

To evaluate the performance of a TES system, the charging and discharging efficiency can be calculated. The charging efficiency is based on the ratio of energy stored in the solid media to the energy input into the system and can be defined as

$$\eta_{\text{charging}} = \frac{E_{\text{stored}}}{E_{\text{Net Input}} + E_{\text{pump,charge}}}, \quad (4.29)$$

where E_{stored} accounts for the internal energy of the solid particles (Hanchen et al. 2011):

$$E_{\text{stored}} = \int_0^L \rho_{\text{solid}} c_{p,\text{solid}} A (T_{s(x)} - T_o) dx. \quad (4.30)$$

The temperature difference of the solid is calculated relative to a reference state, T_o , such as ambient temperature or the initial temperature of the bed.

The net energy input or removed from the system is calculated on the basis of the change of internal energy of the HTF and can be calculated as

$$E_{\text{input/output}} = \int_0^{t_{\text{end}}} \int_0^{T_{\text{HTF}}(t)} A \cdot G \cdot c_{p,\text{HTF}} dT dt, \quad (4.31)$$

where A is the cross-sectional area of the bed. The discharging efficiency is defined as

$$\eta_{\text{discharging}} = \frac{E_{\text{recovered/output}}}{E_{\text{stored}} + E_{\text{pump,discharge}}}. \quad (4.32)$$

The discharging efficiency is of particular interest since the design criteria of the TES system is based on the amount of energy that is needed during the discharging process. Yang and Garimella (2010) define the discharging efficiency with respect to a threshold value that characterizes the minimum temperature of HTF that exits the system. This value, Θ_o , is defined by the specific application, and any thermal energy that is delivered above the threshold temperature qualifies as useful energy. The dimensionless variable is given as

$$\Theta_o = \frac{T_o - T_c}{T_h - T_c}, \quad (4.33)$$

where T_h is the hot temperature of the HTF from the solar collector and T_c is the cold temperature of the HTF before entering the TES system during discharging. For example, if a value of 0.90 is chosen for Θ_o , T_h is 390°C and T_c is 285°C, then HTF exiting the TES system above 379.5°C during discharging is considered useful. Yang and Garimella (2010) defined the discharging efficiency as

$$\eta_{\text{discharging}} = \frac{\text{Energy retrieved with } \Theta > \Theta_o \text{ in a discharge half-cycle}}{\text{Energy delivered from the collector field in a charge half-cycle}} \quad (4.34)$$

and developed a correlation for discharging efficiency based on simulations that use molten salt as the HTF and $\Theta_o = 0.95$. The efficiency is a function of the Reynolds number, Re_o , and dimensionless tank height:

$$\eta = 1 - 0.1807 Re_o e^{0.1801} \frac{H}{100}^x, \quad (4.35)$$

where $x = 0.00234 Re_o^{-0.6151} + 0.00055 Re_o - 0.485$. This efficiency correlation can be used for Reynolds numbers between 1 and 50 and H between 10 and 800, where H is defined as

$$H = \frac{\text{tank height}}{\text{particle diameter}}. \quad (4.36)$$

The overall system efficiency is expressed as

$$\eta_{\text{overall}} = \eta_{\text{charging}} \cdot \eta_{\text{discharging}}. \quad (4.37)$$

Example 4.4

Calculate the discharging efficiency of a packed bed TES system that uses quartzite as the storage media and a molten salt mixture of 60 wt% $NaNO_3$ and 40 wt% KNO_3 as the HTF. The system must deliver energy to a central receiver power plant at a maximum temperature of $T_h = 600^\circ C$ and no less than $584^\circ C$ to prevent the turbine from shutting down. The temperature of the molten salt entering the bed during discharging is $285^\circ C$ and the superficial mass flow rate per unit area of the bed is $0.927 \text{ kg/s}\cdot\text{m}^2$. The height of the tank is 13 m and the equivalent particle diameter of the quartzite is 32.5 mm. The molten salt viscosity as a function of temperature (in $^\circ C$) is given as

$$\mu(\text{kg/m}\cdot\text{s}) = [22.714 - 0.12T + (2.281 \times 10^{-4})T^2 - (1.474 \times 10^{-7})T^3] \times 10^{-3}.$$

Solution

The viscosity of the molten salt can be calculated based on the average temperature of the bed ($T_{\text{ave}} = (285 + 600)/2 = 442.5^\circ C$):

$$\begin{aligned} &= [22.714 - 0.12(442.5^\circ C) + (2.281 \times 10^{-4})(442.5^\circ C)^2 - (1.474 \times 10^{-7})(442.5^\circ C)^3] \times 10^{-3} \\ &= 0.001506 \frac{\text{kg}}{\text{m}\cdot\text{s}}. \end{aligned}$$

The Reynolds number is then calculated as

$$\text{Re} = \frac{GD_p}{\mu} = \frac{(0.927 \text{ kg/m}^2\text{s})(0.0325 \text{ m})}{0.001506 \text{ kg/ms}} = 20.$$

In order to determine if Equation 4.8 can be used for the analysis, the threshold value and dimensionless tank height must be determined:

$$\Theta_o = \frac{T_o - T_c}{T_h - T_c} = \frac{584 - 285}{600 - 285} = 0.95$$

$$H = \frac{\text{tank height}}{\text{particle diameter}} = \frac{13 \text{ m}}{0.0325 \text{ m}} = 400.$$

Since the threshold value of the dimensionless temperature is 0.95, H lies between 10 and 800, and the Reynolds number falls between 1 and 50, Equation 4.8 may be used. To calculate the discharging efficiency, the value of x must be determined:

$$x = 0.00234(20^{-0.6151}) + 0.00055(20) - 0.485 = -0.4736.$$

Thus the discharging efficiency is

$$\eta = 1 - 0.1807 \text{Re}^{0.1801} \left(\frac{H}{100} \right)^x = 1 - 0.1807(20^{0.1801}) \left(\frac{400}{100} \right)^{-0.4736} = 0.839 \times 100 = 83.9\%.$$

4.4 Energy Transport Subsystems

To transport solar heat from a solar collector to storage, and then to an end use, an energy transport subsystem is used. It consists of pipes, pumps, expansion tanks, valves of various types, and heat exchangers. Heat exchangers are treated in Section 4.4.4, and pipes and pumps, in this section. Valves and expansion tanks are standard items and are not described in detail.

4.4.1 Piping Systems

In most solar thermal processes considered in this book, standard circular pipes of steel, copper, aluminum, or special alloys are used to transport heat in the form of internal energy in the pumped fluid. Two parasitic losses occur in pipes—pressure drop and heat loss. Both losses are treated briefly herein.

4.4.2 Pressure Drop

Friction at the pipe walls, bends, valves, and so on results in flow resistance and pressure drop. To overcome the pressure drop, pumps are required. The sizing of pumps is a routine engineering exercise and is done by calculating two quantities, the friction factor at a given flow rate and the pipe length (Kent 1978). The friction factor f can be read from Figure 4.8 as a function of the Reynolds number and roughness ratio shown in Figure 4.9. The Darcy friction factor is defined as

$$f = \Delta p / \left(4(L/D) \frac{1}{2} \rho \bar{V}^2 \right), \quad (4.38)$$

where Δp is the pressure drop; D is the diameter; L is the pipe length including the equivalent length of smooth pipe for all fittings, expansions, and contractions; and \bar{V} is the space averaged velocity.

Churchill (1977) finds that the curves in Figure 4.10 can all be represented by one equation for the laminar, transition, and turbulent regimes:

$$f = 8[(8/\text{Re})^{1/2} + (A + B)^{-3/2}]^{1/12}, \quad (4.39)$$

where

$$A = -2.457 \ln \left(\frac{7}{\text{Re}} \right)^{0.9} + \frac{0.27 \epsilon}{D}^{16}; \quad B = \frac{37,530}{\text{Re}}^{16} \quad (4.40)$$

and ϵ is the average height of surface irregularities.

Pump motor horsepower P_p can be calculated using Equation 4.38 to be

$$P_p = f(L/D) \frac{1}{2} \rho A \bar{V}^3 / \eta_p \eta_m, \quad (4.41)$$

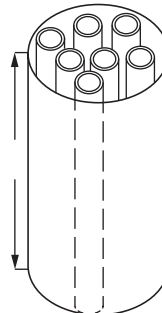


FIGURE 4.8

TES system with embedded tubes for increased heat-transfer area.

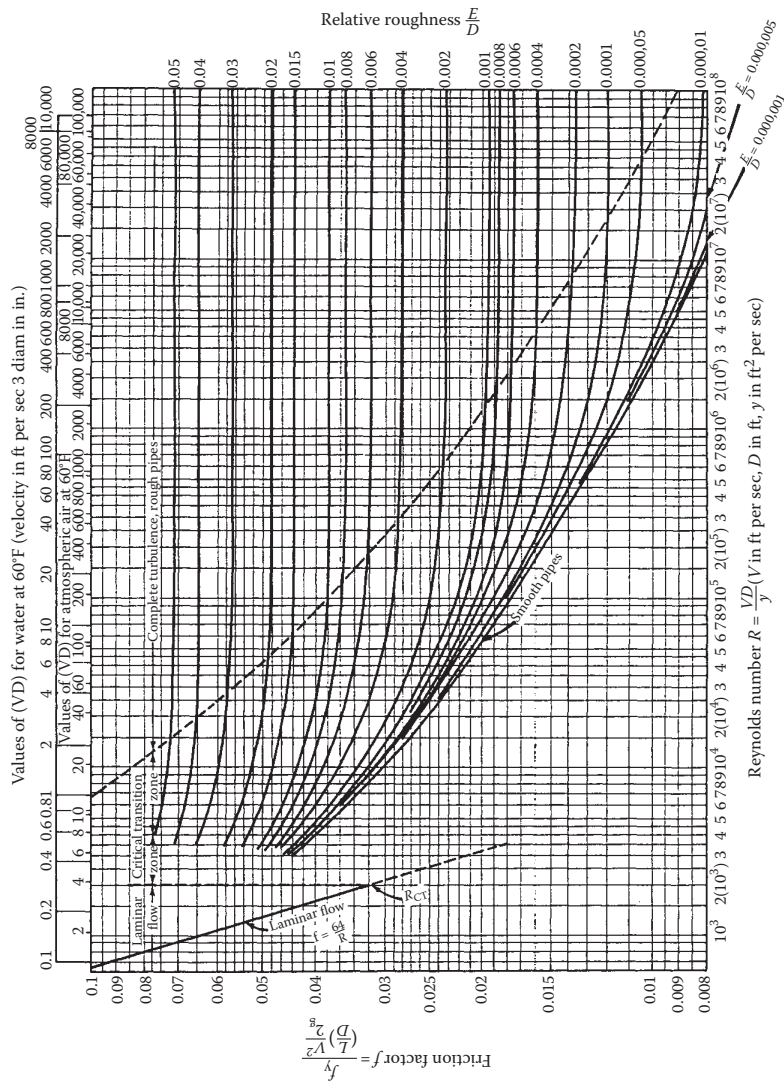
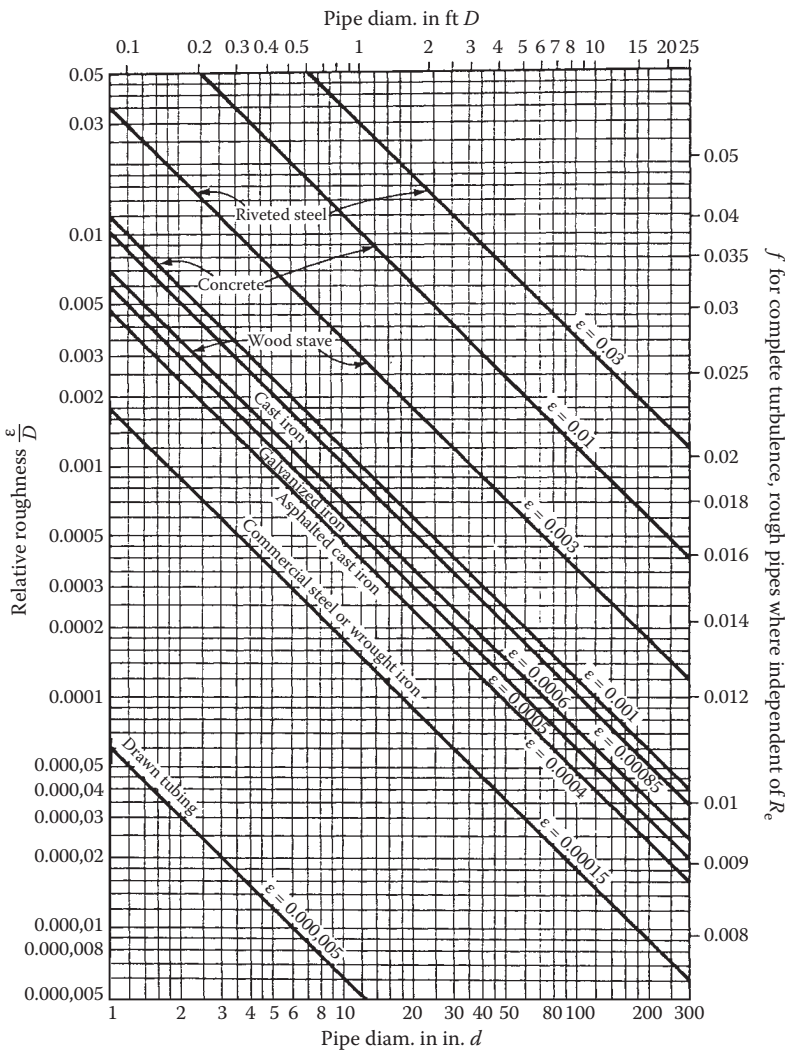


FIGURE 4.9
Friction factor for pipe flow as a function of Reynolds number and roughness ratio ϵ/D . (From Potter, P.J., *Power Plant Theory and Design*, Ronald Press, New York, 1959.)

**FIGURE 4.10**

Roughness ratio ϵ/D for various types of commercial pipe. (From Potter, P.J., *Power Plant Theory and Design*, Ronald Press, New York, 1959.)

where A is the flow area, η_p is the pump efficiency, η_m is the motor efficiency, and the average velocity \bar{V} is related to the volumetric flow as $\dot{Q} = \bar{A}\bar{V}$.

Although the fluid circuits in most parts of solar thermal systems are quite simple, the collector field is frequently connected in a complex series-parallel arrangement as dictated by trade-offs between piping costs, pump size, and fluid temperature rise. The flow in series-parallel arrays can be calculated using iterative techniques such as the Hardy-Cross method. However, for

preliminary design, a closed form solution has been developed for flow through arrays of solar collectors connected in parallel. For $j + 1$ identical collectors with the same flow rate connected in parallel with constant diameter D headers or manifolds, the array pressure drop (inlet header inlet port to outlet header outlet port) is given by

$$\Delta P = \frac{K_f \dot{m}^2}{6} [j(2j+1)(j+1)] \Delta p_{\text{coll}} \quad (4.42)$$

where Δp_{coll} is the collector pressure drop, \dot{m} is the mass flow rate per collector, and

$$K_f = 8 \bar{f} L / (\pi^2 \rho D^5). \quad (4.43)$$

The average friction factor, \bar{f} in the header is evaluated at one-half the total array flow, $(j+1)\dot{m}/2$, and the collectors are all connected into the manifold at a uniform distance L apart. It is noted that identical flow \dot{m} through each header does not occur automatically, but can be accomplished to within a few percent by requiring 90% or more of the total array pressure drop to occur across the collector; that is,

$$\Delta p_{\text{coll}} \geq 0.9 \Delta P. \quad (4.44)$$

In the design of piping systems, the absolute pressure must not be permitted to drop below the boiling point to avoid vapor lock, boiling, or pump cavitation. The critical design point is where the fluid is hottest and the pressure lowest—often at a circulating pump inlet port. Some common fluids used for high-temperature solar systems are shown in Table 4.7. The fluid manufacturer should be consulted for precise viscosity values to be used for system design. Typical values are in the range 0.2 to 5.0 c_p . Most are quite temperature sensitive.

4.4.3 Heat Loss

Parasitic heat losses from storage tanks, pipes, and pumps can be calculated from equations given in any heat-transfer text. For cylindrical insulation of thermal conductivity k , length L , inner diameter D , and thickness t for pipes and tanks,

$$q_{\text{cyl}} = \frac{2\pi k L}{\ln \frac{D+2t}{D}} (T_f - T_a), \quad (4.45)$$

TABLE 4.7
Properties of Liquid Heat-Transfer Media

Material	Composition	Density (kg/m ³)	Specific Heat (kJ/kg·°C)	Boiling Point (°C)	Manufacturer
Water		~1000	~4.2	~100	
Therminal VP-1	Diphenyl oxide 73.5% Biphenyl oxide 26.5 wt%	1060 (25°C)	2.18 (250°C)	257	Solutia Inc.
Dowtherm A	Diphenyl oxide 73.5% Biphenyl oxide 26.5 wt%	1056 (25°C)	2.23 (255°C)	257	Dow Chemical
Hitec	40% NaNO ₂ , 7% NaNO ₃ , 53% KNO ₃	1640 (300°C)	1.6 (300°C)	—	Coastal Chemical
Caloria HT-43	Hydrotreated heavy paraffinic 99%	880 (15.6°C)	2.1 (100°C)	293	Exxon Company
Diethylene glycol		1180 (20°C)	2.3 (25°C)	245	Dow Chemical
Tetraethylene glycol		1124 (20°C)	2.2 (25°C)	327	Dow Chemical
Xceltherm MK1	Diphenyl oxide 73% Biphenyl oxide 27%	1062 (25°C)	2.2 (260°C)	257	Radco
Dynalene MS-1	Potassium nitrate and sodium nitrate	1900 (300°C)	1.40 (300°C)	—	Dynalene
Syltherm XLT	Dimethyl polysiloxane	852 (25°C)	2.32 (280°C)	—	Dow Chemical

Source: Data collected from various manufacturers' brochures, MSDS, and online resources.

where T_f is the fluid temperature and T_a is the ambient temperature. For spherical storage tanks, the heat loss is

$$q_{\text{sph}} = \frac{\pi k D(D + 2t)}{t} (T_f - T_a). \quad (4.46)$$

In the above, it is assumed that the principal resistance to heat loss occurs in the insulation.

Although heat losses can be made arbitrarily small, the law of diminishing returns applies and a point is reached where added insulation costs more than the value of the extra heat retained. It can be shown that the optimum distribution of a given volume of insulation over all the components of a solar thermal system occurs when the surface heat flux is the same everywhere; note that this does not imply equal insulation thickness t (Harrison and Pelanne 1977).

For low-temperature applications such as heating, cooling, and domestic hot water, foam rubber or polyurethane foam insulation is normally used. For higher-temperature applications, the principal insulations include calcium silicate, mineral fiber, expanded silica (perlite), and fiberglass. Table 4.8 lists the properties of industrial-grade insulations useful in elevated temperature solar systems (Harrison and Pelanne 1977). Calcium silicate is a mixture of lime and silica reinforced with fibers and molded into shape. It has good compressive strength. Mineral fiber consists of rock and slag fibers bonded together and are useful up to 1200°F (650°C). The compressive strength is less than calcium silicate but is available in both rigid and flexible, shaped segments.

Perlite is expanded volcanic rock consisting of small air cells enclosed by a mineral structure. Additional binders are added to decrease moisture migration and to reduce shrinkage. Cellular glass is available in flexible bats or rigid boards and shaped sections. It has very low moisture absorption.

For very high temperatures, the selection of materials is quite limited. In addition to mineral fiber and calcium silicate noted above, ceramic fibers (to 1400°C), castable ceramic insulation (to 1600°C), Al_2O_3 or ZrO_2 fibers (to 1600°C), and carbon fibers (to 2000°C) are available. It is to be noted that these temperatures correspond to the refractory range of metals where service conditions are very severe.

An excellent summary of industrial insulation practice and design methods and economics analysis is contained in Harrison and Pelanne (1977).

4.4.4 Heat Exchangers

Heat exchangers are devices in which two fluid streams exchange thermal energy: one stream is heated while the other is cooled. There are a number of arrangements used to transfer heat from one fluid to another. The simplest

TABLE 4.8

Properties of Pipe Insulation for Elevated Temperatures

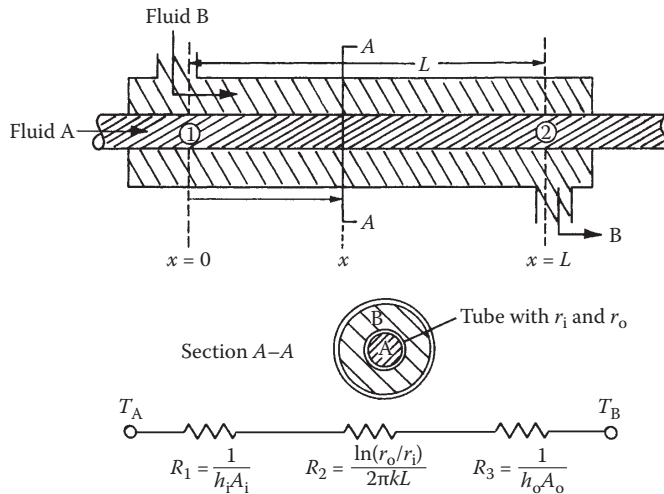
Insulation Type	Temperature Range (°F)	Conductivity k [Btu/(h) (ft²)(°F/in.)]	Density (lb/ft³)	Applications
Urethane foam	-300 to 300	0.11 to 0.14	1.6 to 3.0	Hot and cold piping
Cellular glass blocks	-350 to 500	0.20 to 0.75	7.0 to 9.5	Tanks and piping
Fiberglass blanket for wrapping	-120 to 550	0.15 to 0.54	0.60 to 3.0	Piping and pipe fittings
Fiberglass preformed shapes	-60 to 450	0.22 to 0.38	0.60 to 3.0	Hot and cold piping
Fiberglass mats	150 to 700	0.21 to 0.38	0.60 to 3.0	Piping and pipe fittings
Elastomeric preformed shapes and tape	-40 to 220	0.35 to 0.27	4.5 to 6.0	Piping and pipe fittings
Fiberglass with vapor barrier jacket	20 to 150	0.20 to 0.31	0.65 to 2.0	Refrigerant lines, dual-temperature lines, chilled-water lines, fuel-oil piping
Fiberglass without vapor barrier jacket	to 500	0.20 to 0.31	1.5 to 3.0	Hot piping
Cellular glass blocks and boards	70 to 900	0.20 to 0.75	7.0 to 9.5	Hot piping
Urethane foam blocks and boards	200 to 300	0.11 to 0.14	1.5 to 4.0	Hot piping
Mineral—fiber preformed shapes	to 1200	0.24 to 0.63	8.0 to 10.0	Hot piping
Mineral—fiber blankets	to 1400	0.26 to 5.60	8.0	Hot piping
Fiberglass field applied jacket for exposed lines	500 to 800	0.21 to 0.55	2.4 to 6.0	Hot piping
Mineral—wool blocks	850 to 1800	0.36 to 0.90	11.0 to 18.0	Hot piping
Calcium silicate blocks	1200 to 1800	0.33 to 0.72	10.0 to 14.0	Hot piping

Source: Harrison, M. and C. Pelanne, Cost effective thermal insulation, *Chem. Eng.*, 84, 62, 1977.

Note: 1 Btu/(h)(ft²)(°F/in.) = 1/12 Btu/h·ft·°F = 0.144 W/m·°C.

arrangement is the double-pipe heat exchanger shown in Figure 4.11. It will be discussed first.

In this system, fluid A flows inside a tube of inner radius r_i and the outer radius r_o . Fluid B flows in the annulus formed between the outer surface of the inner tube, A_o , and the inner surface of the outer tube. An overall heat-transfer coefficient U can be calculated from the thermal circuit shown in Figure 4.11. It may be based on any convenient area of the exchanger, but

**FIGURE 4.11**

Schematic diagram of a double-pipe heat exchanger in parallel flow.

usually the outside area $A_o = 2\pi r_o L$ of the inner tube is most convenient (Karlekar and Desmond 1977). Then,

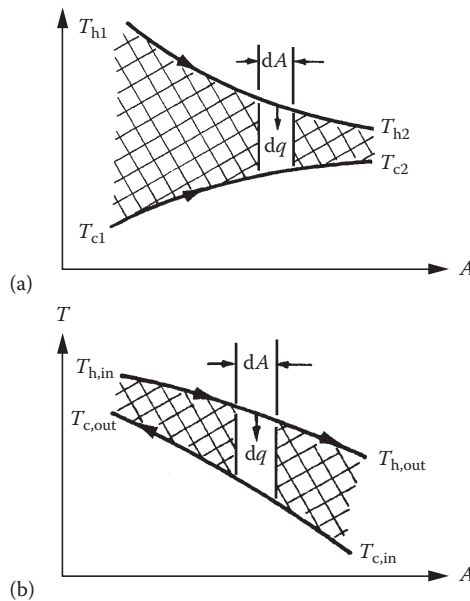
$$U_o A_o = \frac{1}{\frac{1}{h_i A_i} + \frac{\ln(r_o/r_i)}{2\pi k L} + \frac{1}{h_o A_o}}. \quad (4.47)$$

And at any cross section, the local rate of heat transfer across the tube is

$$dq = U_o dA_o (T_A - T_B) = U_o 2\pi r_o dx (T_A - T_B). \quad (4.48)$$

Simplifications in the evaluation of U_o are possible when one or two of the thermal resistances dominate. For example, the thermal resistance of the tube wall, R_2 in Figure 4.11, is often small compared to the convective resistances and sometimes one of the two convective resistances is negligible compared to the other.

The flow arrangement shown in Figure 4.9, where both fluids enter from the same end, is called parallel flow, and Figure 4.12a shows the temperature distribution for both fluid streams. If one of the two fluids were to enter at the other end and flow in the opposite direction, the flow arrangement would be *countercflow*. The temperature distribution for the latter case

**FIGURE 4.12**

(a) Parallel flow; (b) counterflow.

is shown in Figure 4.12b. If a counterflow arrangement is made very long, it approaches the thermodynamically most efficient possible heat-transfer condition. Figure 4.12 shows that the counterflow exchanger has the highest heat-transfer effectiveness and is therefore the preferred design for solar systems.

There are two basic methods for calculating the rate of heat transfer in a heat exchanger. One method employs a mean temperature difference between the two fluids in the exchanger ΔT_{mean} and then determines the rate of heat transfer from the relation (Karlekar and Desmond 1977)

$$q = UA\Delta T_{\text{mean}}. \quad (4.49)$$

This mean temperature difference is called the logarithmic mean temperature difference (LMTD). It can be evaluated directly only when the inlet and outlet temperatures of both fluid streams are specified. The use of the LMTD approach is explained in Karlekar and Desmond (1977). The other method is called the effectiveness-NTU method (ϵ -NTU). The ϵ -NTU method offers many advantages over the LMTD approach and will be discussed in the following.

First, we define the exchanger effectiveness ϵ :

$$\epsilon = \frac{\text{actual rate of heat transfer}}{\text{maximum possible rate of heat transfer}}. \quad (4.50)$$

The actual rate of heat transfer can be determined by calculating either the rate of internal energy loss of the hot fluid or the rate of internal energy gain of the cold fluid; that is,

$$\dot{q} = \dot{m}_h c_{p,h} (T_{h,in} - T_{h,out}) = \dot{m}_c c_{p,c} (T_{c,out} - T_{c,in}), \quad (4.51)$$

where the subscripts "h" and "c" denote the hot and cold fluid, respectively. The maximum rate of heat transfer possible for specified inlet fluid temperatures is attained when one of the two fluids undergoes the maximum temperature difference in the exchanger. This maximum temperature difference equals the difference in the entering temperatures for the hot and cold fluid. Which of the two fluids can undergo this maximum temperature change depends on the relative value of the product ($\dot{m}c_p$), the mass flow rate times the specific heat of the fluid at constant pressure, called the heat capacity rate \dot{C} . Since a thermodynamic energy balance requires that the energy given up by one fluid must be received by the other if there are no external heat losses, only the fluid with the smaller value of \dot{C} can undergo the maximum temperature change. Thus, the fluid that may undergo this maximum temperature change is the one that has the minimum value of the heat capacity rate; therefore, the maximum rate of heat transfer is

$$\dot{q}_{\max} = \dot{C}_{\min} (T_{h,in} - T_{c,in}), \quad (4.52)$$

where

$$\dot{C}_{\min} = (\dot{m}c_p)_{\min}.$$

The fluid with the minimum $\dot{m}c_p$ or \dot{C} value can be either the hot or the cold fluid. Using subscript "h" to designate the effectiveness when the hot fluid has the minimum \dot{C} and the subscript "c" when the cold fluid has the minimum \dot{C} value, we get

$$\varepsilon_{hx} = \frac{\dot{C}_h (T_{h,in} - T_{h,out})}{\dot{C}_h (T_{h,in} - T_{c,in})} = \frac{T_{h,in} - T_{h,out}}{T_{h,in} - T_{c,in}} \quad (4.53)$$

$$\varepsilon_{hx} = \frac{\dot{C}_c (T_{c,out} - T_{c,in})}{\dot{C}_c (T_{h,in} - T_{c,in})} = \frac{T_{c,out} - T_{c,in}}{T_{h,in} - T_{c,in}}, \quad (4.54)$$

where the subscripts "in" and "out" refer to the inlet and outlet of the fluid as shown in Figure 4.12.

Kays and London (1980) have calculated effectiveness values for many types of heat exchangers. They found that ε_{hx} can be expressed for a given

exchanger type as a function of two variables, the number of transfer units NTU,

$$\text{NTU} = UA_{\text{hx}} / (\dot{m}c_p)_{\text{min}} \quad (4.55)$$

and the capacitance ratio C ,

$$C = (\dot{m}c_p)_{\text{min}} / (\dot{m}c_p)_{\text{max}} = \dot{C}_{\text{min}} / \dot{C}_{\text{max}} \quad (4.56)$$

For boiling or condensation, $C = 0$.

Figure 4.13a through d shows effectiveness values for the common heat-exchanger types and Table 4.9 contains equations for calculating $\varepsilon_{\text{hx}}(\text{NTU}, C)$. For parallel flow and counterflow devices in which boiling or condensation occurs in one stream, $\varepsilon_{\text{hx}} = 1 - e^{-\text{NTU}}$. For the special case of $(\dot{m}c_p)_{\text{min}} = (\dot{m}c_p)_{\text{max}}$, a special effectiveness equation applies for counterflow heat exchangers.

$$\varepsilon_{\text{hx}} = \text{NTU} / (\text{NTU} + 1). \quad (4.57)$$

Figure 4.14 shows that the counterflow exchanger has the highest heat-transfer effectiveness and is therefore the preferred design for solar systems.

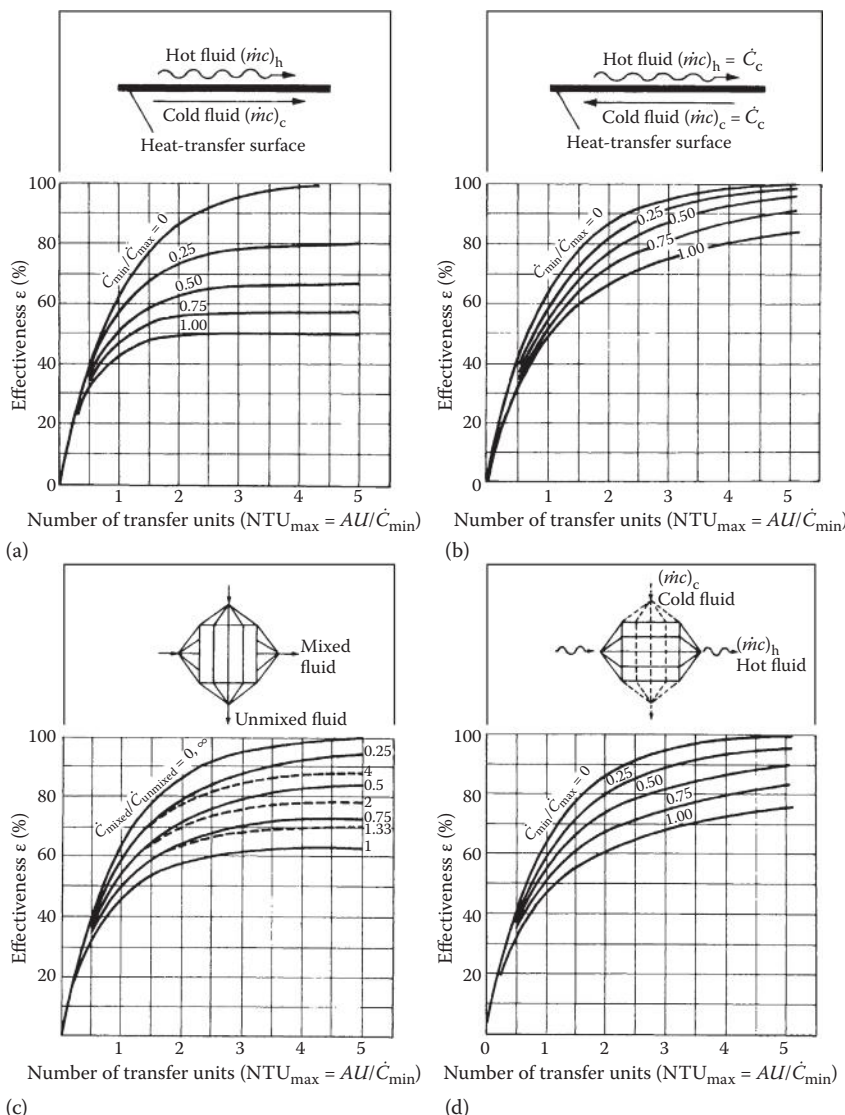
One of the most common uses of a heat exchanger is to isolate a fluid used in a solar collector field from the process fluid that conveys the heat energy to its end use as shown in Figure 4.15. If the required process inlet temperature is $T_{p,i}$, the collector outlet fluid must be at a temperature $T_{c,o}$ above $T_{p,i}$ because of the presence of the heat exchanger. Since collector efficiency decreases with increasing operating temperature, less energy is collected than if no heat exchanger were present. A heat-exchanger penalty factor F_{hx} , which can be applied to the linear collector model (Equation 3.46) developed earlier, has been calculated by deWinter (1975). Equation 3.46 can be rewritten in terms of the heat-exchanger inlet temperature (process return temperature) $T_{p,o}$ as

$$\eta_c = F_{\text{hx}} F_R [\eta_o - U_c (T_{p,o} - T_a) / I_c]. \quad (4.58)$$

The heat-exchanger factor is given by

$$F_{\text{hx}} = 1 + \frac{F_R U_c A_c}{(\dot{m}c_p)_c} \frac{(\dot{m}c_p)_c}{\varepsilon_{\text{hx}} (\dot{m}c_p)_{\text{min}}}^{-1}, \quad (4.59)$$

where c denotes collector properties and ε_{hx} is the heat-exchanger effectiveness. The collector loss coefficient U_c is evaluated at the mean collector operating temperature \bar{T}_c .

**FIGURE 4.13**

Heat-exchanger effectiveness as a function of NTU and C ; (a) parallel flow, (b) counterflow, (c) cross flow, one fluid mixed, and (d) cross flow, no mixing. (From Kays, W.M. and A.L. London, *Compact Heat-Exchangers*, McGraw-Hill, New York, 1980. Copyright 1964. With permission from McGraw-Hill Book Company.)

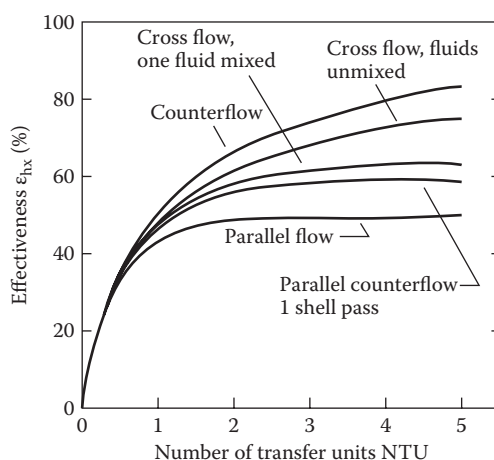
TABLE 4.9

Heat Exchanger Effectiveness Expressions

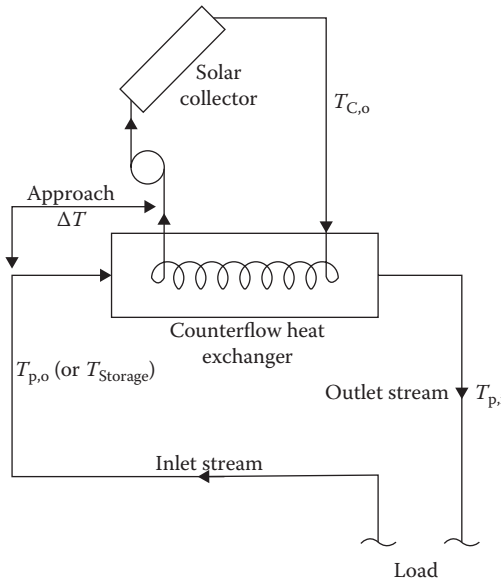
Flow Geometry	Relation
Double pipe; parallel flow	$\epsilon = \frac{1 - \exp[-N(1+C)]}{1+C}$
Counterflow	$\epsilon = \frac{1 - \exp[-N(1-C)]}{1 - C \exp[-N(1-C)]}$
Cross flow; both fluids unmixed	$\epsilon = 1 - \exp\{(C/n) [\exp(-NCn)-1]\}$ where $n = N^{-0.22}$
Both fluids mixed	$\epsilon = \frac{1}{1 - \exp(-N)} + \frac{C}{1 - \exp(-NC)} - \frac{1}{N}^{-1}$
C_{\max} mixed, C_{\min} unmixed	$\epsilon = (1/C)\{1 - \exp[C(e^{-N}-1)]\}$
C_{\max} unmixed, C_{\min} mixed	$\epsilon = 1 - \exp\{(1/C)[\exp(-NC) - 1]\}$
Shell and tube; one shell pass, 2, 4, 6 tube passes	$\epsilon = 2 \frac{1+C+(1+C^2)^{1/2}}{1+C-(1+C^2)^{1/2}} \frac{1+\exp -N(1+C^2)^{1/2}}{1-\exp -N(1+C^2)^{1/2}}^{-1}$

Source: Karlekar, B.V. and R.M. Desmond, *Engineering Heat Transfer*, West Publ., St. Paul, Minnesota, 1977.

Note: $N = NTU \equiv UA/\dot{C}_{\min}$, $C = \dot{C}_{\min}/\dot{C}_{\max}$.

**FIGURE 4.14**

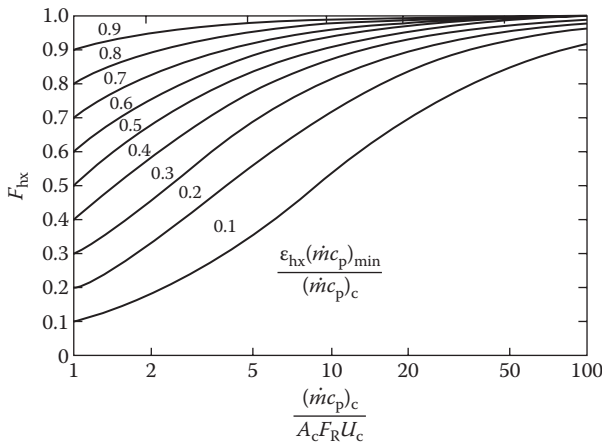
Heat-exchanger effectiveness as a function of NTU; effect of flow type for. (From Kays, W.M. and A.L. London, *Compact Heat-Exchangers*, McGraw-Hill, New York, 1980. Copyright 1964. With permission from McGraw-Hill Book Company.)

**FIGURE 4.15**

Use of a heat exchanger to isolate a collector from the thermal process.

Figure 4.16 shows F_{hx} for a range of operating conditions. Unless the collector flow is very low, $F_{hx} > 0.95$ for most high-performance collectors. For small $F_R U_C A_C / (\dot{m}c_p)_c$, F_{hx} is approximated closely by

$$F_{hx} = 1 - F_R U_C A_C \left\{ \frac{(\dot{m}c_p)_c - \varepsilon_{hx}(\dot{m}c_p)_{min}}{\varepsilon_{hx}(\dot{m}c_p)_{min}(\dot{m}c_p)_c} \right\}. \quad (4.60)$$

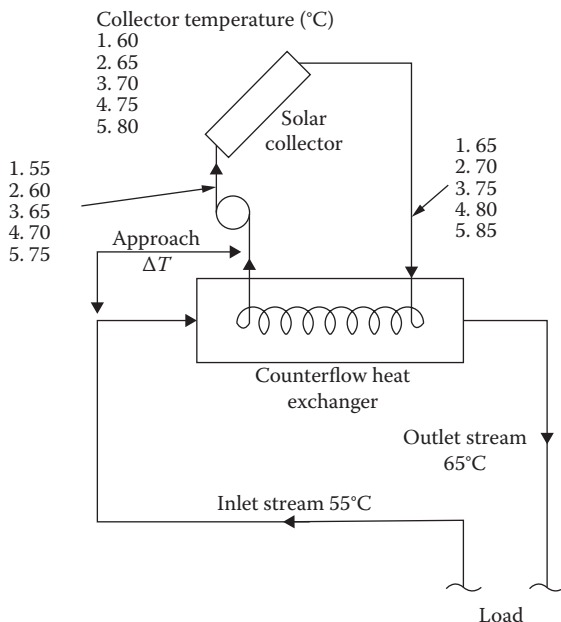
**FIGURE 4.16**

Heat-exchanger factor F_{hx} calculated from Equation 4.60.

Example 4.5

Calculate the efficiency at which the solar collector in Figure 4.17 operates in order to deliver energy to a working fluid at 65°C for several values of the approach temperature difference. The approach temperature is the difference between the incoming cool fluid and the exiting warm fluid at the heat exchanger (see Figure 4.17). The temperature rise through the heat exchanger is 10°C and is equal to the fluid temperature rise through the solar collector.

The collector has a $\tau\alpha$ product of 0.80 and loss coefficient U_c of 5 W/m²K. If the solar radiation normal to the collector surface is 500 W/m² and the ambient temperature T_a is 20°C, calculate the collector efficiency for the following five values of approach ΔT :



Case	Approach ΔT (°C)
1	0 (thermodynamic limit)
2	5
3	10
4	15
5	20

FIGURE 4.17

Fluid stream and solar collector temperatures for Example 4.5 (heat-exchanger problem).

Case	Approach ΔT (°C)
1	0 (thermodynamic limit)
2	5
3	10
4	15
5	20

Solution

Fluid stream temperatures are shown at several points for each case in Figure 4.17. The collector temperature T_c can be taken as the average of inlet and outlet fluid temperatures for purposes of the example as shown in the figure.

Collector efficiency can be calculated from the following equation (see Chapter 3):

$$\eta = \tau \alpha - U_c \frac{\Delta T}{I_c} ,$$

where

$$\Delta T = \bar{T}_c - T_a .$$

For the collector specified here,

$$\eta = 0.8 - 5 \frac{T}{I_c} \times 100\% .$$

The collector efficiency can be calculated in tabular form as shown in Table 4.10.

Note that the heat-exchanger design has a very strong effect on collector efficiency; for relatively small changes of approach temperature difference, efficiency, and therefore energy delivery, change significantly.

TABLE 4.10

Collector Efficiency Calculation for Example 4.5

Case	\bar{T}_c (°C)	ΔT (°C)	I_c (W/m ²)	$\Delta T/I_c$ (K·m ² /W)	η (%)
1	60	40	500	0.08	40
2	65	45	500	0.09	35
3	70	50	500	0.10	30
4	75	55	500	0.11	25
5	80	60	500	0.12	20

Example 4.6

Calculate the energy delivery penalty in a solar system caused by a required exchanger for values of effectiveness from 0.2 to 0.99. Compare the economic value of this energy penalty to the heat-exchanger cost if the annual amortized cost (see Section 1.4) of a heat exchanger per year is \$6/m²_{hx}. The economic value of the solar energy collection penalty is the value of nonsolar energy required to make up for the penalty resulting from the heat exchanger. The value of nonsolar, makeup energy is \$10/GJ for this example. System specifications are listed below. Water is the working fluid.

$$A_c = 100 \text{ m}^2$$

$$(\dot{m}c_p)_{\min} = (\dot{m}c_p)_{\max} = \frac{50 \text{ kg}}{\text{h} \cdot \text{m}_c^2} \times 4182 \frac{\text{J}}{\text{kg} \cdot \text{K}}$$

Energy delivery with no heat exchanger = 200 MJ/m_c²·year.

$$F_R U_c = 5 \text{ W/m}_c^2 \cdot {}^\circ\text{C} \left(= 5 \times 3600 \text{ J/h} \cdot \text{m}_c^2 \cdot {}^\circ\text{C} \right)$$

$$U_{hx} = 1400 \text{ W/m}_c^2 \cdot {}^\circ\text{C}$$

Solution

The heat-exchanger penalty factor F_{hx} with the above values substituted in Equation 4.59 is

$$F_{hx} = \frac{1}{1 + 0.0861 \frac{1}{\varepsilon_{hx}} - 1}.$$

Table 4.11 summarizes the thermal penalty from heat-exchanger use. Also shown is the heat-exchanger area required to provide a given effectiveness. The heat-exchanger area A_{hx} is evaluated by the use of Equation 4.55 and values of NTU required to provide a given effectiveness for counterflow heat exchangers from Table 4.11. The annual energy delivery Q_u in Table 4.12 is given by

$$Q_u = F_{hx} A_c (200) \text{ MJ/m}_c^2 \cdot \text{year}.$$

The solar energy penalty, which must be made up by the other fuels, is

$$Q_a = (1 - F_{hx}) A_c (200) \text{ MJ/m}_c^2 \cdot \text{year}.$$

TABLE 4.11

Counterflow Heat Exchanger Performance

NTU	ϵ_{hx} for Indicated Capacity Rate Ratios $(mc_p)_{min}/(mc_p)_{max}$							
	0	0.25	0.50	0.70	0.75	0.80	0.90	1.00
0	0	0	0	0	0	0	0	0
0.25	0.221	0.216	0.210	0.206	0.205	0.204	0.202	0.200
0.50	0.393	0.378	0.362	0.350	0.348	0.345	0.339	0.333
0.75	0.528	0.502	0.477	0.457	0.452	0.447	0.438	0.429
1.00	0.632	0.598	0.565	0.538	0.532	0.525	0.513	0.500
1.25	0.713	0.675	0.635	0.603	0.595	0.587	0.571	0.556
1.50	0.777	0.735	0.691	0.655	0.645	0.636	0.618	0.600
1.75	0.826	0.784	0.737	0.697	0.687	0.677	0.657	0.636
2.00	0.865	0.823	0.775	0.733	0.722	0.711	0.689	0.667
2.50	0.918	0.880	0.833	0.788	0.777	0.764	0.740	0.714
3.00	0.950	0.919	0.875	0.829	0.817	0.804	0.778	0.750
3.50	0.970	0.945	0.905	0.861	0.848	0.835	0.807	0.778
4.00	0.982	0.962	0.928	0.886	0.873	0.860	0.831	0.800
4.50	0.989	0.974	0.944	0.905	0.893	0.880	0.850	0.818
5.00	0.993	0.982	0.957	0.921	0.909	0.896	0.866	0.833
5.50	0.996	0.998	0.968	0.933	0.922	0.909	0.880	0.846
6.00			0.975	0.944		0.921	0.892	0.857
6.50			0.980	0.953		0.930	0.902	0.867
7.00			0.985	0.960		0.939	0.910	0.875
7.50			0.988	0.966		0.946	0.918	0.882
8.00			0.991	0.971		0.952	0.925	0.889
8.50			0.993	0.975		0.957	0.931	0.895
9.00			0.994	0.979		0.962	0.936	0.900
9.50			0.996	0.982		0.966	0.941	0.905
10.00			0.997	0.985		0.970	0.945	0.909
∞	1.000	1.000	1.000	1.000	1.000	1.000	1.000	1.000

Source: Kays, W.M. and A.L. London, *Compact Heat-Exchangers*, McGraw-Hill, New York, 1980. Copyright 1980 by McGraw-Hill Book Co. Used with permission of McGraw-Hill Book Co.

The economic value of the heat-exchanger energy penalty is

$$C_a = Q_a c_a,$$

where c_a is the cost of auxiliary energy in dollars per gigajoule. The host of heat-exchanger area C_{hx} is

$$C_{hx} = A_{hx} c_{hx},$$

where c_{hx} is the amortized cost per year of heat exchanger per unit in dollars per square meter per year (see Table 4.13).

TABLE 4.12

Thermal Performance Summary for Example 4.6

Effectiveness, ϵ_{hx}	Exchanger Penalty, F_{hx}	Energy Collection, Q_u (GJ/year)	NTU ^a	Exchanger Area, A_{hx} (m ²)
0.2	0.744	14.88	0.25	1.04
0.333	0.853	17.06	0.50	2.07
0.5	0.921	18.42	1.00	4.15
0.6	0.946	18.92	1.50	6.22
0.7	0.964	19.28	2.33	9.75
0.8	0.979	19.58	4.00	16.60
0.9	0.991	19.82	9.00	37.34
0.99	0.999	19.98	99.00	411.00
1.0 ^b	1.000 ^b	20.00 ^b	— ^c	0.00 ^b

^a Table 4.11 or Equation 4.57.^b Baseline.^c No exchanger baseline.**TABLE 4.13**

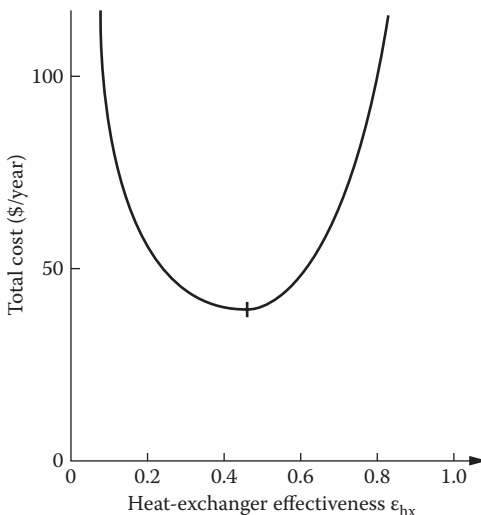
Economic Summary for Example 4.6

Effectiveness, ϵ_{hx}	Extra Nonsolar, Q_a (GJ/year)	Economic Value of Energy Penalty, C_a (\$/year)	Cost of Exchanger Area, C_{hx} (\$/year)	Total Cost ^a (\$/year)
0.2	5.12	51.20	6.24	57.44
0.333	2.94	29.40	12.42	41.82
0.5	1.58	15.80	24.90	40.70
0.6	1.08	10.80	37.32	48.12
0.7	0.72	7.20	58.50	65.70
0.8	0.42	4.20	99.60	103.80
0.9	0.18	1.80	224.04	225.85
0.99	0.02	0.20	2466.00	2466.20

^a $C_a + C_{hx}$.

The results of this example show that the cost of the extra exchanger area to provide increased effectiveness ϵ_{hx} rises rapidly. Since the heat-exchanger cost to provide the last few percent of solar energy delivery is high, the value of this energy is relatively small when compared with the additional exchanger cost. It is, therefore, not cost-effective to provide this energy. Likewise, small heat exchangers have a larger energy penalty, which has a correspondingly larger dollar value in replacement fuel. It is therefore cost-effective to add heat-exchanger area in order to recover a portion but not all of the solar energy required.

Figure 4.18 is a plot of the total extra cost required to provide a total demand of 20 GJ/year. This extra cost is required by the design stipulation that a heat exchanger be used. It is a cost above the basic solar and

**FIGURE 4.18**

Total cost of heat exchanger and nonsolar energy penalty for Example 4.6. Least-cost configuration has a heat-exchanger effectiveness of 0.46.

backup system costs. The least cost heat-exchanger configuration is for an effectiveness value of about 0.46. It is to be noted that this example considers only one component of the solar system. A complete system optimization requires making simultaneous trade-offs of many system components. This methodology is described later in this book. Note that the direct application of the F_{hx} factor to annual energy delivery instead of instantaneous delivery is correct only for the case of negligible loss from storage and no heat rejection by storage boiling or other means.

PROBLEMS

- On a clear day, the energy delivered by a solar system, Q_u , is approximately a sinusoidal function of time with a maximum, $Q_{u\max}$, near noon and a minimum at sunrise and sunset.
 - If this is a solar thermal system and thermal energy demand is a constant L_o , calculate the temperature history of storage for a day for the block system in Figure 4.19.
 - If this is a PV system with $Q_{u\max}$ from one solar panel at noon equal to 200 W_e and length of the day from sunrise to sunset as 10 h, how many solar panels would be needed to provide for a constant load of 1 kW_e for 24 h?
- A packed bed storage system consists of a bed of crushed rock. The average diameter of the particles is 35 mm, and the sphericity was

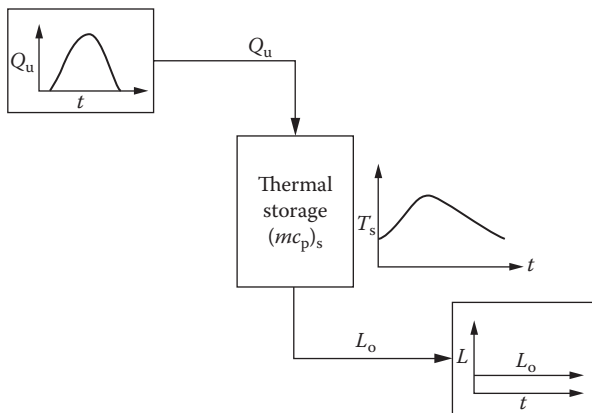
**FIGURE 4.19**

Figure for Problem 1.

determined to be 0.75. Air is used as the heat-transfer fluid and flows through the system with a superficial bed velocity of 0.90 m/s. Calculate the pressure drop per unit length, assuming the air density is 1.15 kg/m^3 and the air viscosity is $1.903 \times 10^{-5} \text{ kg/m}\cdot\text{s}$. How does this compare to the pressure drop when the particle diameter is 50 mm?

3. Compare the energy storage capability of sodium sulfate decahydrate (Glauber's salt) in a range from 30° to 60°C with that of water and rock in the same range. Also, compare the volumes of storage for the three media.
4. A 100-m^2 liquid solar collector (flat-plate type) is located 40 m from the building it serves. If the liquid pressure drop through the collector is 7 kPa, what is the total pressure drop in the collector fluid loop? What pipe size would you recommend for the collector loop? Why?

Assume:

1. Flow rate is 1.15 l/min per m^2 of collectors.
2. Pipe fittings add 20 equivalent m of pipe.
3. Fluid velocity in pipe is 1 m/s.
4. Actual pipe length is 2.5 times the distance of collector to building.
5. A cylindrical storage tank for the collector in Problem 2 is located in the basement of the dwelling it serves. If the basement temperature is 16°C and the storage tank is 70°C , what is the heat-loss rate from the tank? The tank is a cylinder with diameter equal to its height; it is insulated with a 15-cm-thick fiberglass batt.

6. How large should a water storage tank be if it is to supply the total daily heat load (1.5 GJ) of a building if the storage tank temperature may vary by 20°C ? Neglect parasitic transmission and conversion losses. If a 4-m³ carbon steel tank costs \$1000.00, what will this tank cost?
7. What is the pressure drop in 50 m of a 1-in pipe for fluid flowing at 0.4 m³/min?
8. If the fluid velocity in a pipe is to be kept below 4 ft/s, what pipe size should be used to flow 500 gal/min? What is the pressure drop in 500 ft of this pipe?
9. An array of twenty 40-ft² solar panels is connected in parallel. What is the pressure drop through the manifold if water is used at the rate of 0.03 gal/min ft² and the collectors are spaced 5 ft apart. Pipe with 1-in diameter is used.
10. A heat exchanger is used to isolate a collector loop from the storage loop in a solar-cooling system. Collector and storage fluid capacitance rates are $300 \text{ kJ/m}_c^2 \cdot \text{h} \cdot ^{\circ}\text{C}$ and the collector heat loss conductance is $5 \text{ kJ/kJ/m}_c^2 \cdot \text{h} \cdot ^{\circ}\text{C}$ with a heat removal factor $F_R = 0.9$. What is the energy delivery penalty from heat-exchanger use if the heat-exchanger effectiveness is 0.25, 0.5, and 0.9?
11. Water flowing at a rate of 70 kg/min is to be heated from 340 to 350 K in a counterflow double pipe heat exchanger by a 50% glycol solution that enters the heat exchanger at 360 K and exits at 345 K. If the overall heat-transfer coefficient is 300 W/m²·K, calculate the required heat-exchanger area.
12. A shell-and-tube heat exchanger with one shell pass and two tube passes, having an area of 4.5 m², is to be used to heat high-pressure water initially at 290 K with hot air initially at 400 K. If the exit water temperature is not to exceed 350 K, the air flow rate is 0.5 kg/s, and the overall heat-transfer coefficient is 300 W/m²·K, calculate the water flow rate.
13. A cross-flow fin-and-tube heat exchanger uses hot water to heat air from 290 to 300 K. Water enters the heat exchanger at 340 K and exits at 310 K. If the total heat-transfer rate is to be 300 kW and the average heat-transfer coefficient between the water and the air is 50 W/m²·K, calculate the area of the heat exchanger required and the mass rate of air flow through the exchanger.
14. A small steam condenser is to be designed to condense 0.8 kg/min steam at 80 kN/m² with cooling water at 290 K. If the exit temperature of the water is not to exceed 320 K, calculate the area required for a shell-and-tube heat exchanger with the steam making one shell pass and the water making two tube passes. The overall heat-transfer coefficient is 3000 W/m²·K.

References

- Arkar, C., and S. Medved. 2005. Influence of accuracy of thermal property data of a phase change material on the result of a numerical model of a packed bed latent heat storage with spheres. *Thermochim. Acta* 438: 192–201.
- ASHRAE. 2011. Thermal storage. In *ASHRAE Handbook, HVAC Application*. American Society of Heating, Refrigerating and Air-Conditioning Engineers, 1791 Tullie Circle, N.E., Atlanta, GA, p. 40.14.
- Beasley, D.E., and J.A. Clark. 1984. Transient response of a packed bed for thermal energy storage. *Int. J. Heat Mass Transfer* 27(9): 1659–1669.
- Beckman, G., and P.V. Gilli. 1984. *Topics in Energy—Thermal Energy Storage*. Springer-Verlag, New York.
- Chavez, J.M. et al. 1995. The solar two power tower project: A 10 MWe power plant. *Proceedings of the 1995 IECEC* 2: 469–475. ASME, New York.
- Churchill, S.W. 1977. Friction factor equation spans all fluid-flow regimens. *Chem. Eng.* 84(24): 91.
- Clark, J.A. 1986. Thermal design principles, Chapter 5. In *Solar Heat Storage: Latent Heat Materials*, G.A. Lane, ed. CRC Press, Boca Raton, FL, pp. 185–223.
- Cole, R.L. et al. 1980. *Design and Installation Manual for Thermal Energy Storage*, ANL-79-15, 2nd ed. Argonne National Lab., Argonne, IL.
- Coutier, J., and E. Farber. 1982. Two applications of a numerical approach of heat-transfer process within rock beds. *Sol. Energy* 29(6): 451–462.
- Delameter, W.R., and N.E. Bergen. 1986. Review of molten salt electric experiment: Solar central receiver project. SAND 86-8249. Sandia National Laboratory, Albuquerque, NM.
- deWinter, F. 1975. Heat exchanger penalties in double-loop solar water heating systems. *Sol. Energy* 17: 335.
- Edwards, D.P., and M.K. Jensen. 1994. Pressure drop and heat transfer predictions of turbulent flow in longitudinally finned tubes. *Adv. Enhanced Heat Transfer* 287: 17–23.
- Eisfeld, B., and K. Schnitzlein. 2001. The influence of confining walls on the pressure drop in packed beds. *Chem. Eng. Sci.* 56(14): 4321–4329.
- Ergun, S. 1952. Fluid flow through packed columns. *Chem. Eng. Prog.* 48: 89.
- Garg, H.P., S.C. Mullick, and A.K. Bhargava. 1985. *Solar Thermal Energy Storage*. D. Reidel, Boston.
- Glendenning, I. 1981. Advanced mechanical energy storage. In *Energy Storage and Transportation*, G. Beghe, ed. D. Reidel, Boston, pp. 50–52.
- Hanchen, M., S. Brückner, and A. Steinfeld. 2011. High-temperature thermal storage using a packed bed of rocks—Heat transfer analysis and experimental validation. *Appl. Therm. Eng.* 31: 1798–1806.
- Harrison, M., and C. Pelanne. 1977. Cost effective thermal insulation. *Chem. Eng.* 84: 62.
- Idelsohn, S.R., M.A. Storti, and L. Crivelli. 1994. Numerical methods in phase-change problems. *Arch. Computational Methods Eng.* 1: 49–74.
- Jaluria, Y., and K.E. Torrance. 2003. *Computational Heat Transfer*. Taylor & Francis Group, New York.
- Jeffreson, C.P. 1972. Prediction of breakthrough curves in packed beds: 1. Applicability of single parameter models. *AICHE J.* 18(2): 409–416.

- Jensen, J. 1980. *Energy Storage*. Newnes-Butterworth, Boston.
- Jotshi, C.K., and D.Y. Goswami. 1998. Energy storage. In *Mechanical Engineering Handbook*, F. Kreith, Editor-in-Chief. CRC Press, Boca Raton, FL, pp. 8–104.
- Karlekar, B.V., and R.M. Desmond. 1977. *Engineering Heat Transfer*. West Publ., St. Paul, MN.
- Kays, W.M., and A.L. London. 1980. *Compact Heat-Exchangers*. McGraw-Hill, New York.
- Kent, G.R. 1978. Preliminary pipeline sizing. *Chem. Eng.* 85: 199.
- Kim, L.V. 1994. Determination of the heat transfer coefficients in porous media. *J. Eng. Phys. Thermophys.* 65: 1168–1172.
- Kreider, J.F. 1979. *Medium and High Temperature Processes*. Academic Press, New York.
- Kuravi, S. et al. 2013. Thermal energy storage technologies and systems for concentrating solar power plants. *Prog. Energy Combust. Sci.* 39: 285–319.
- Li, L., and W. Ma. 2011. Experimental study on the effective particle diameter of a packed bed with non-spherical particles. *Transp. Porous Med.* 89: 35–48.
- Makansi, J. 1994. Energy storage reinforces competitive business practices. *Power* 138(9): 63.
- McAdams, W.H. 1954. *Heat Transmission*, 3rd ed. McGraw-Hill, New York.
- Meier, A., C. Winkler, and D. Wuillemin. 1991. Experiment for modeling high temperature rock bed storage. *Sol. Energy Mater.* 24: 255–264.
- Moses, P.J., and G.A. Lane. 1986. Encapsulation of PCMs. In *Solar Heat Storage: Latent Heat Materials*, Vol. II. G. A. Lane, Ed. CRC Press, Boca Raton, FL, pp. 93–152.
- Potter, P.J. 1959. *Power Plant Theory and Design*. Ronald Press, New York.
- Rabl, A. 1977. A note on the optics of glass tubes. *Sol. Energy* 19(2): 215.
- Sanduja, P. et al. 2013. Numerical analysis of a packed bed thermal storage system for concentrated solar power. *Energy Procedia, Proceedings of the ISES 2013 Solar World Congress*.
- Singh, R., R.P. Saini, and J.S. Saini. 2006. Nusselt number and friction factor correlations for packed bed solar energy storage system having large sized elements of different shapes. *Sol. Energy* 80(7): 760–771.
- Swet, C.J. 1987. Storage of thermal energy—Status and prospects. In *Progress in Solar Engineering*, D.Y. Goswami, ed. Hemisphere Publ., Washington, DC.
- Tomlinson, J.J., and L.F. Kannberg. 1990. Thermal energy storage. *Mech. Eng.* 9: 68–72.
- Trahan, J. et al. 2013. Evaluation of pressure drop and particle sphericity for an air-rock bed thermal energy storage system. *Energy Procedia, Proceedings of the 2013 ISES Solar World Congress*, Cancun, Mexico.
- Voller, V.R. 1996. An overview of numerical methods for solving phase change problems. In *Advances in Numerical Heat Transfer*, Vol. 1, Chapter 9. Taylor & Francis, London.
- Yang, Z., and S.V. Garimella. 2010. Thermal analysis of solar thermal energy storage in a molten-salt thermocline. *Sol. Energy* 84: 974–985.
- Zhang, Y., and A. Faghri. 1996. Heat transfer enhancement in latent heat thermal energy storage system by using the internally finned tube. *Int. J. Heat Mass Transfer* 39(15): 3165–3173.

5

Solar Heating Systems

For the well being and health ... the homesteads should be airy in summer and sunny in winter. A homestead promising these qualities would be longer than it is deep and the main front would face south.

Aristotle

The use of solar energy for heat production dates from antiquity. Historically, methods used for collecting and transferring solar heat were passive methods, that is, without active means such as pumps, fans, and heat exchangers. *Passive* solar heating methods utilize natural means such as radiation, natural convection, thermosyphon flow, and thermal properties of materials for collection and transfer of heat. *Active* solar heating methods, on the other hand, use pumps and fans to enhance the rate of fluid flow and heat transfer. Active methods for water heating, space heating, and industrial process heat (IPH) have been developed mainly in the last four decades. This chapter describes in detail the function and design of active systems for heating buildings and service water. Passive solar heating, cooling, and daylighting are covered in Chapter 7. Other applications, such as low-temperature solar heat for agriculture, agricultural drying, or aquaculture, can be analyzed with the principles set forth in this chapter and Chapters 3 and 4.

Energy for heating buildings and hot water consumes approximately one-quarter of the annual energy production in the United States. In many areas of the United States and the world, solar heating can compete economically with other types of fuel for heating, without even considering the environmental benefits.

5.1 Calculations of Heating and Hot-Water Loads in Buildings

Energy requirements for space heating or service water heating can be calculated from basic conservation of energy principles. For example, the heat required to maintain the interior of a building at a specific temperature is the total of all heat transmission losses from the structure and heat required to warm and humidify the air exchange with the environment by infiltration and ventilation.

Comfort in buildings has long been a subject of investigation by the American Society of Heating, Refrigerating and Air-Conditioning Engineers (ASHRAE). ASHRAE has developed extensive heat load calculation procedures embodied in the *ASHRAE Handbook of Fundamentals* (ASHRAE 2013). The most frequently used load calculation procedures will be summarized in this section; the reader is referred to the ASHRAE handbook for details.

Figure 5.1 shows the combinations of temperature and humidity that are required for human comfort. The shaded area is the standard US comfort level for sedentary persons. Many European countries have human comfort levels from 3°C to 7°C below US levels. If activity of a continuous nature

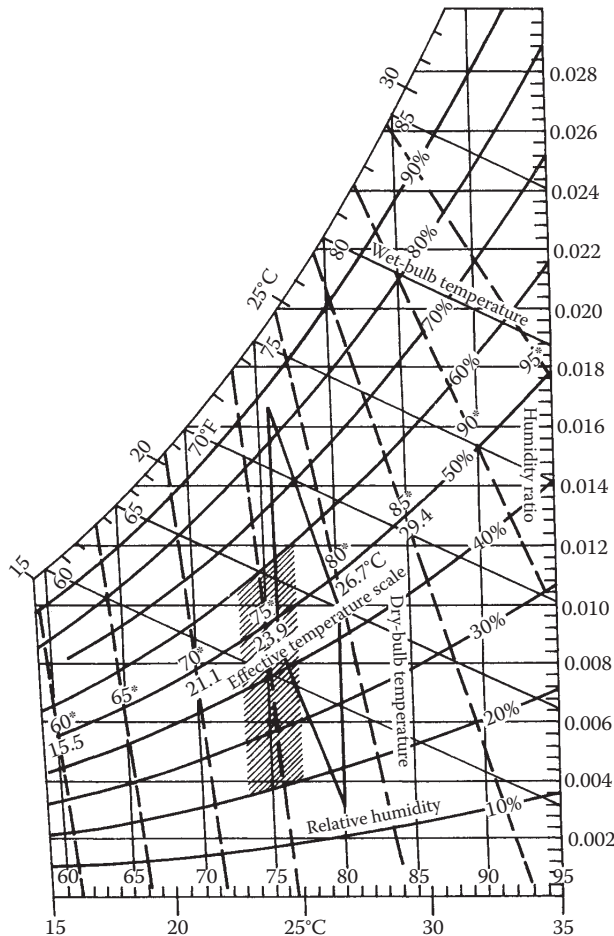


FIGURE 5.1
Heat-loss calculations for buildings.

is anticipated, the comfort zone lies to the left of the shaded area; if extra clothing is worn, the comfort zone is displaced similarly.

5.1.1 Calculation of Heat Loss

It is outside the scope of this book to describe the details of the heat load calculations for buildings. However, the method is described in brief in this section. For details, one should refer to the *ASHRAE Handbook of Fundamentals* (ASHRAE 2013) or some textbook on heating and air-conditioning. Table 5.1 lists the components of heat-loss calculations of a building.

Complete tables of thermal properties of building materials are given in Appendix 5. Appendix 5 also contains web addresses that list the average wind and design temperature data for many cities in the United States and the rest of the world.

Transmission heat losses through attics, unheated basements, and the like are buffered by the thermal resistance of the unheated space. For example, the temperature of an unheated attic lies between that of the heated space and that of the environment. As a result, the ceiling of a room below an attic is exposed to a smaller temperature difference and consequently would have lower heat loss than the same ceiling without the attic. The effective conductance of thermal buffer spaces can easily be calculated by forming an energy balance on such spaces.

The following example is an illustration of the heat-loss calculation method described in this section.

TABLE 5.1

Heating Load Calculations for Buildings

Heating Load Component	Equations 5.1 through 5.4	Descriptions/References
Walls, roof, ceilings, glass	$q = U \cdot A(T_i - T_o)$ (5.1)	T_i and T_o are inside and outside air temperature, respectively. U values of composite section are calculated from the thermal properties of components given in Appendix 5.
Basement floors and walls below ground level	$q_f = U_f A_f$ (5.2)	U_f has special units of W/m ² .
Concrete floors on ground	$q_{fe} = F_e P_e (T_i - T_o)$ (5.3)	P_e is the perimeter of the slab.
Infiltration and ventilation air	$q_{sensible} = Q \rho_a C p_a (T_i - T_o)$ or = $1200 * Q (T_i - T_o)$ watts $q_{latent} = Q \rho_a h_{fg} \Delta W$ or = $2808 * Q \Delta W$ watts (5.4)	Q is volume of air flow in m ³ /s. ρ_a and $C p_a$ are density and specific heat of air. h_{fg} is the latent heat of water at room temperature. ΔW is humidity ratio difference between inside and outside air.

* Assuming $\rho_a = 1.2 \text{ kg/m}^3$; $h_{fg} = 2340 \text{ J/kg}$, $C p_a = 1000 \text{ J/kg}\cdot^\circ\text{C}$.

Example 5.1

Calculate the heat load on a house for which the wall area is 200 m^2 , the floor area is 600 m^2 , the roof area is 690 m^2 , and the window area totals 100 m^2 . Inside wall height is 3 m. The construction of the wall and the roof is shown in Figure 5.2.

Solution

The thermal resistance of the wall shown in Figure 5.2 can be found by the electrical resistance analogy as

$$R_{\text{wa}} = R_{\text{outside air}} + R_{\text{wood siding}} + R_{\text{sheathing}} + R_{\text{comb}} + R_{\text{wall board}} + R_{\text{inside air}}$$

Combined thermal resistance for the studs and insulation (R_{comb}) is found as

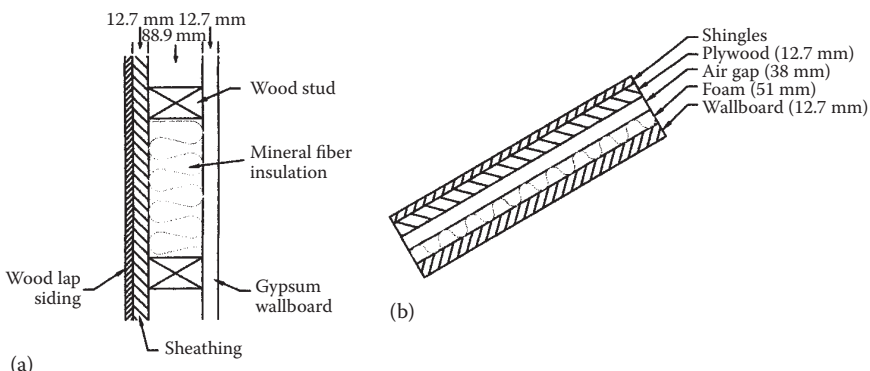
$$\frac{1}{R_{\text{comb}}} = \frac{A_{\text{stud}}}{R_{\text{stud}}} + \frac{A_{\text{insulation}}}{R_{\text{insulation}}} \frac{1}{A_{\text{stud}} + A_{\text{insulation}}}.$$

Assuming that the studs occupy 15% of the wall area,

$$\frac{1}{R_{\text{comb}}} = \frac{0.15}{0.77} + \frac{0.85}{1.94}$$

or

$$R_{\text{comb}} = 1.58 \frac{\text{m}^2 \cdot ^\circ\text{C}}{\text{W}}$$

**FIGURE 5.2**

Cross sections of the wall and the roof for Example 5.1. (a) Wall construction. (b) Roof construction.

Therefore, the wall thermal resistance, R_{wa} , can be found as

Element	Thermal Resistance (m ² ·°C/W)
Outside air (6.7 m/s wind)	0.030
Wood bevel lap siding	0.14
12.7 mm sheathing	0.23
88.9 mm combined wood stud and mineral fiber insulation	1.58
12.7 mm gypsum wallboard	0.079
Inside air (still)	0.12
$R_{wa} = 2.179$	

Therefore,

$$U_{wa} = \frac{1}{R_{wa}} = \frac{1}{2.179} = 0.46 \text{ W/m}^2 \cdot ^\circ\text{C.}$$

The heat loss through the windows depends on whether they are single or double glazed. In this example, single-glazed windows are installed, and a U factor equal to 4.7 W/m²·°C is used. (If double-glazed windows were installed, the U factor would be 2.4 W/m²·°C.)

The roof is constructed of 12.7 mm gypsum wallboard, 51 mm foam insulation board, 38 mm still air, 12.7 mm plywood, and asphalt shingles (wooden beams and roofing paper are neglected for the simplified calculations here). Therefore,

$$U_{rf} = \frac{1}{0.030 + 0.077 + 0.11 + 0.17 + 2.53 + 0.079 + 0.1} \\ \text{Outside Shingles Plywood Airgap Foam Wallboard Inside} \\ \text{air air} \\ = 0.32 \text{ W/m}^2 \cdot ^\circ\text{C}$$

If the respective areas and U factors are known, the rate of heat loss per hour for the walls, windows, and roof can be calculated.

$$\text{Walls: } q_{wa} = (200 \text{ m}^2) \times 0.46 \text{ W/m}^2 \cdot ^\circ\text{C} = 92 \text{ W/}^\circ\text{C}$$

$$\text{Windows: } q_{wi} = (100 \text{ m}^2) \times 0.47 \text{ W/m}^2 \cdot ^\circ\text{C} = 470 \text{ W/}^\circ\text{C}$$

$$\text{Roof: } q_{rf} = (690 \text{ m}^2) \times 0.32 \text{ W/m}^2 \cdot ^\circ\text{C} = 220 \text{ W/}^\circ\text{C}$$

$$\text{Total } q_{tr} = 782 \text{ W/}^\circ\text{C}$$

If double-glazed windows were used, the heat loss would be reduced to 552 W/°C.

The infiltration and ventilation rate Q for this building is assumed to be 0.5 ACH (air changes per hour). The sensible and latent heat loads of the infiltration air may be calculated using the equations given in Table 5.1. Therefore,

$$Q = 0.5 \times (600 \text{ m}^2 \times 3 \text{ m} \text{ (volume)}) = 900 \text{ m}^3/\text{h} = 0.25 \text{ m}^3/\text{s},$$

$$q_{\text{sensible}} = 0.25 \text{ m}^3/\text{s} \times (1.2 \text{ kg/m}^3)(1000 \text{ J/kg} \cdot ^\circ\text{C}) = 300 \text{ W}/^\circ\text{C}.$$

In residential buildings, humidification of the infiltration air is rarely done. Neglecting the latent heat, the total rate of heat loss q_{tot} is the sum of q_{sensible} and q_{tr} :

$$q_{\text{tot}} = (782 + 300) = 1082 \text{ W}/^\circ\text{C}.$$

This calculation is simplified for purposes of illustration. Heat losses through the slab surface and edges have been neglected, for example.

More refined methods of calculating energy requirements on buildings do not use the steady-state assumption used above (Klein et al. 1975). The thermal inertia of buildings may be expressly used as a load-leveling device. If so, the steady-state assumption is not met and the energy capacitance of the structure must be considered for accurate results. Many adobe structures in the US Southwest are built intentionally to use daytime sun absorbed by 1-ft-thick walls for nighttime heating, for example.

5.1.2 Internal Heat Sources in Buildings

Heat supplied to a building to offset energy losses is derived from both the heating system and internal heat sources. Table 5.2 lists the common sources of internal heat generation for residences. Commercial buildings such as hospitals, computer facilities, or supermarkets will have large internal gains specific to their function. Internal heat gains tend to offset heat losses from a building but will add to the cooling load of an air-conditioning system. The magnitude of the reduction in heating system operation will be described in Section 5.1.3.

5.1.3 Degree-Day Method

The preceding analysis of heat loss from buildings expresses the loss on a per-unit temperature difference basis (except for unexposed floor slabs). In order to calculate the peak load and total annual load for a building, appropriate design temperatures must be defined for each. The outdoor design temperature is usually defined statistically, such that the actual outdoor temperature will exceed the design temperature 97.5% or 99% of the time over a long period. The design temperature difference (ΔT) is then the interior building temperature minus the outdoor design temperature. The design ΔT is used for rating non-solar heating systems but is not useful for selection of solar systems, since solar systems rarely provide 100% of the energy demand of a building at peak conditions.

TABLE 5.2

Some Common Internal Sensible Heat Gains That Tend to Offset the Heating Requirements of Buildings

Type	Magnitude (W or J/s)
Incandescent lights	Total W
Fluorescent lights	Total W
Electric motors	$746 \times (\text{hp}/\text{efficiency})$
Natural gas stove	$8.28 \times \text{m}^3/\text{h}$
Appliances	Total W
A dog	50–90
People	
Sitting	70
Walking	75
Dancing	90
Working hard	170
Sunlight	$\text{Solar heat gain} \times \text{fenestration transmittance} \times \text{shading factor}^{\text{a}}$

Source: ASHRAE. *Handbook of Fundamentals*. ASHRAE, Atlanta, GA, 2013.

^a Shading factor is the amount of a window not in a shadow expressed as a decimal between 1.0 and 0.0.

A more useful index of heating energy demand is the total annual energy requirement for a building. This quantity is somewhat more difficult to calculate than the peak load. It requires knowledge of day-to-day variations in ambient temperature during the heating season and the corresponding building heat load for each day. Building heat loads vary with ambient temperatures as shown in Figure 5.3. The no-load temperature T_{nl} , above which no heat need be supplied to the building, is a few degrees below the required interior temperature T_i because of internal heat-generation effects.

The no-load temperature at which internal source generation q_i just balances transmission and infiltration losses can be determined from the energy balance

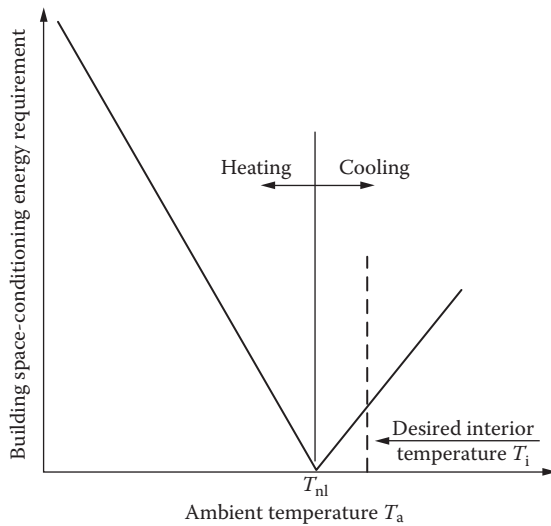
$$q_i = \overline{UA}(T_i - T_{nl}), \quad (5.5)$$

where \overline{UA} is the overall loss coefficient for the building (W/°C). Then,

$$T_{nl} = T_i - \frac{q_i}{\overline{UA}}. \quad (5.6)$$

The total annual heat load on the building, Q_T can be expressed as

$$Q_T = \int_{365 \text{ days}} \overline{UA}(T_{nl} - T_a)^+ dt, \quad (5.7)$$

**FIGURE 5.3**

Building load profile versus ambient temperature showing no-load temperature T_{nl} and desired interior temperature T_i .

in which all arguments of the integral are functions of time. The superscript “+” indicates that only positive values are considered. In practice, it is difficult to evaluate this integral; therefore, three simplifying assumptions are made:

1. \overline{UA} is independent of time.
2. T_{nl} is independent of time.
3. The integral can be expressed by the sum.

Thus,

$$\overline{UA} \sum_{n=1}^{365} (T_{nl} - \bar{T}_a)^+ \quad (5.8)$$

where n is the day number, and the daily average temperature \bar{T}_a can be approximated by $\frac{1}{2}(T_{a,\max} + T_{a,\min})$, in which $T_{a,\max}$ and $T_{a,\min}$ are the daily maximum and minimum temperatures, respectively.

The quantity $(T_{nl} - T_a)^+$ is called the *degree-day unit*. For example, if the average ambient temperature for a day is 5°C and the no-load temperature is 20°C, 15 degree C-days are said to exist for that day. However, if the ambient temperature is 20°C or higher, 0 degree-days exist, indicating 0 demand for

heating that day. Degree-day totals for monthly ($\Sigma_{\text{month}} (T_{\text{nl}} - T_a)^+$) and annual periods can be used directly in Equation 5.8 to calculate the monthly and annual heating energy requirements.

In the past, a single value of temperature has been used throughout the United States as a universal degree-day base, 65.0°F or 18.3°C.* This practice is now outdated, since many homeowners and commercial building operators have lowered their thermostat settings in response to increased heating fuel costs, thereby lowering T_{nl} . Likewise, warehouses and factories operate well below the 19°C level. Therefore, a more generalized database of degree-days to several bases (values of T_{nl}) has been created by the US National Weather Service (NWS).

A variable base degree-day method, which recognizes that T_{nl} may vary not only with location but also from building to building, is more accepted now (ASHRAE 2013). ASHRAE (2013) have listed heating degree days and cooling degree days for a number of worldwide locations.

Example 5.2

A building located in Denver, Colorado, has a heat-loss coefficient \overline{UA} of 1000 kJ/h·°C and internal heat sources of 4440 kJ/h. If the interior temperature is 20°C (68°F), what are the monthly and annual heating energy requirements? A gas furnace with 65% efficiency is used to heat the building.

Solution

In order to determine the monthly degree-day totals, the no-load temperature (degree-day basis) must be evaluated from Equation 5.6.

$$T_{\text{nl}} = 20 - \frac{4440}{1000} = 15.6^{\circ}\text{C} (60^{\circ}\text{F})$$

The monthly degree C-days for Denver are taken from the NWS and given in Table 5.3. The energy demand is calculated as

$$\text{Energy demand} = \overline{UA} \times 24 \frac{\text{h}}{\text{day}} \times \text{degree C-days}. \quad (5.9)$$

The monthly energy demand is given in Table 5.3.

* The degree-day base in SI units is defined as 19.0°C, not 18.3°C, which corresponds to 65.0°F. Therefore, precise conversion between the two systems is not possible by a simple multiplication by 5/9.

TABLE 5.3

Monthly and Annual Energy Demands for Example 5.2

Month	Degree C-days	Energy Demand ^a (GJ)
Jan	518	12.4
Feb	423	10.2
Mar	396	9.5
Apr	214	5.2
May	68	1.6
Jun	14	0.3
Jul	0	0
Aug	0	0
Sep	26	0.6
Oct	148	3.6
Nov	343	8.2
Dec	472	11.3
	2622	62.9

^a Energy demand equals $UA \times \text{degree C-days} \times 24 \text{ h/day}$.

The annual energy demand of 62.9 GJ is delivered by a 65% efficient device. Therefore,

$$\text{Average annual purchased energy} = \frac{62.9}{0.65} \text{ GJ} = 96.8 \text{ GJ}.$$

5.1.4 Service Hot-Water Load Calculation

Service hot-water loads can be calculated precisely with the knowledge of only a few variables. The data required for calculation of hot-water demand are as follows:

Water source temperature (T_s)

Water delivery temperature (T_d)

Volumetric demand rate (Q)

The energy requirement for service water heating q_{hw} is given by

$$q_{hw}(t) = \rho_w Q(t) c_{pw} [T_d - T_s(t)], \quad (5.10)$$

where ρ_w is the water density and c_{pw} is its specific heat. The demand rate, $Q(t)$, varies in general with time of day and time of year; likewise, the source temperature varies seasonally. Source temperature data are not compiled in

a single reference; local water authorities are the source of such temperature data.

Few generalized data exist with which to predict the demand rate Q . Table 5.4 indicates some typical usage rates for several common building types. Process water heating rates are peculiar to each process and can be ascertained by reference to process specifications.

Example 5.3

Calculate the monthly energy required to heat water for a family of four in Nashville, Tennessee. Monthly source temperatures for Nashville are shown in Table 5.5, and the water delivery temperature is 60°C (140°F).

Solution

For a family of four, the demand rate Q may be found using a demand recommended from Table 5.4:

$$Q = 4 \times 76 \text{ liters/day} = 0.30 \text{ m}^3/\text{day}.$$

The density of water can be taken as 1000 kg/m³, and the specific heat, as 4.18 kJ/kg·°C.

Monthly demands are given by

$$\begin{aligned} q_m &= (Q \times \text{days/month})(\rho_w c_{pw})[T_d - T_s(t)] \\ &= (0.30 \times \text{days/month})(1000 \times 4.18)[60 - T_s(t)]. \end{aligned}$$

The monthly energy demands calculated from the equation above with these data are tabulated in Table 5.5.

TABLE 5.4

Approximate Service Hot-Water Demand Rates

Usage Type	Demand per Person	
	Liters/day	Gallons/day
Retail store	2.8	0.75
Elementary school	5.7	1.5
Multifamily residence	76.0	20.0
Single-family residence	76.0	20.0
Office building	11.0	3.0

TABLE 5.5

Water Heating Energy Demands for Example 5.3

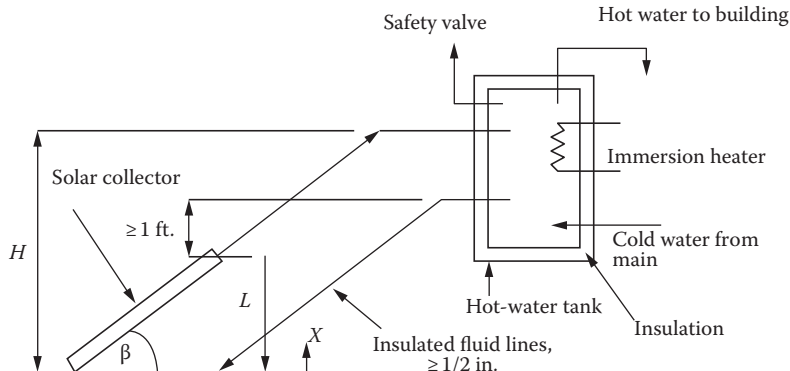
Month	Days/Month	Demand (m ³ /month)	Source Temperature (°C)	Energy Requirement (GJ/month)
Jan	31	9.3	8	2.0
Feb	28	8.4	8	1.8
Mar	31	9.3	12	1.9
Apr	30	9.0	19	1.5
May	31	9.3	17	1.7
Jun	30	9.0	21	1.5
Jul	31	9.3	22	1.5
Aug	31	9.3	24	1.4
Sep	30	9.0	24	1.4
Oct	31	9.3	22	1.5
Nov	30	9.0	14	1.7
Dec	31	9.3	12	1.9

5.2 Solar Water-Heating Systems

Solar water-heating systems represent the most common application of solar energy at the present time. Small systems are used for domestic hot-water applications while larger systems are used in IPH applications. There are basically two types of water-heating systems: *natural circulation* or passive solar system (thermosyphon) and *forced circulation* or active solar system. Natural circulation solar water heaters are simple in design and low cost. Their application is usually limited to nonfreezing climates, although they may also be designed with heat exchangers for mild freezing climates. Forced-circulation water heaters are used in freezing climates and for commercial and IPH.

5.2.1 Natural Circulation Systems

The natural tendency of a less dense fluid to rise above a denser fluid can be used in a simple solar water heater to cause fluid motion through a collector (Close 1962). The density difference is created within the solar collector where heat is added to the liquid. In the system shown in Figure 5.4, as water gets heated in the collector, it rises to the tank, and the cooler water from the tank moves to the bottom of the collector, setting up a natural circulation loop. It is also called a *thermosyphon loop*. Since this water heater does not use a pump, it is a passive water heater. For the thermosyphon to work, the storage tank must be located higher than the collector.

**FIGURE 5.4**

Schematic diagram of thermosyphon loop used in a natural circulation, service water-heating system. The flow pressure drop in the fluid loop must equal the buoyant force "pressure" $\int_0^L g\rho(x)dx - \rho_{stor}gL$, where $\rho(x)$ is the local collector fluid density and ρ_{stor} is the tank fluid density, assumed uniform.

The flow pressure drop in the fluid loop (ΔP_{FLOW}) must equal the buoyant force "pressure difference" ($\Delta P_{BUOYANT}$) caused by the differing densities in the hot and cold legs of the fluid loop:

$$\begin{aligned}\Delta P_{FLOW} &= \Delta P_{BUOYANT} \\ &= \rho_{stor}gH - \int_0^L \rho(x)g dx + \rho_{out}g(H-L) ,\end{aligned}\tag{5.11}$$

where H is the height of the legs and L is the height of the collector (see Figure 5.4), $\rho(x)$ is the local collector fluid density, ρ_{stor} is the tank fluid density, and ρ_{out} is the collector outlet fluid density; the latter two densities were assumed to be uniform. The flow pressure term ΔP_{FLOW} is related to the flow loop system head loss, which is in turn directly connected to friction and fitting losses and the loop flow rate:

$$\Delta P_{FLOW} = \oint_{LOOP} \rho d(h_L),\tag{5.12}$$

where $h_L = KV^2$, with K being the sum of the component loss velocity factors (see any fluid mechanics text) and V being the flow velocity.

Since the driving force in a thermosyphon system is only a small density difference and not a pump, larger-than-normal plumbing fixtures must be used to reduce pipe friction losses (Phillips and Cook 1975). In general,

one pipe size larger than normal used with a pump system is satisfactory. Figure 5.5 shows some passive water heaters.

Since the hot-water system loads vary little during a year, the angle of tilt is that equal to the latitude, that is, $\beta = L$. The temperature difference between the collector inlet water and the collector outlet water is usually 8°C - 11°C during the middle of a sunny day (Close 1962). After sunset, a thermosyphon system can reverse its flow direction and lose heat to the environment during the night. To avoid reverse flow, the top header of the absorber should be at least 30 cm below the cold leg fitting on the storage tank, as shown; otherwise, a check valve would be needed.

To provide heat during long cloudy periods, an electrical immersion heater can be used as a backup for the solar system. The immersion heater is located near the top of the tank to enhance stratification so that the heated fluid is at the required delivery temperature. Tank stratification is desirable in a thermosyphon to maintain flow rates as high as possible. Insulation must be applied over the entire tank surface to control heat loss.

Several features inherent in the thermosyphon design limit its utility. If it is to be operated in a freezing climate, a nonfreezing fluid must be used, which in turn requires a heat exchanger between collector and potable water storage. (If potable water is not required, the collector can be drained during cold periods instead.) Heat exchangers of either the shell-and-tube type or the immersion-coil type require higher flow rates for efficient operation than a thermosyphon can provide. Therefore, the thermosyphon is usually limited to nonfreezing climates. For mild freeze climates, a heat-exchanger

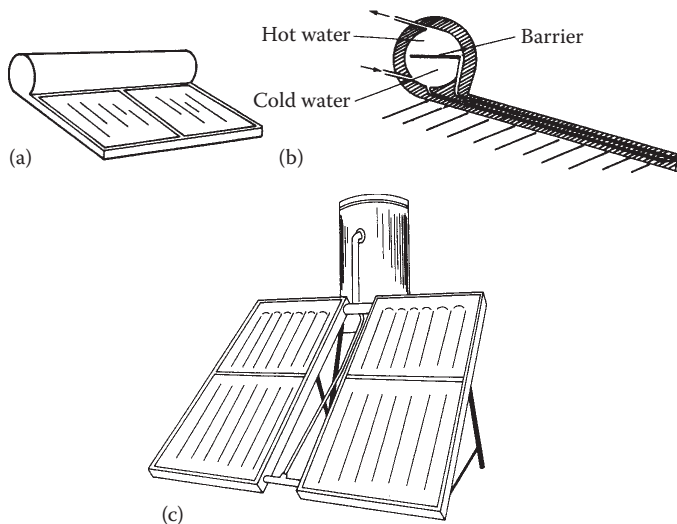


FIGURE 5.5

Passive solar water heaters: (a) compact model using combined collector and storage, (b) section view of the compact model, and (c) tank and collector assembly.

coil welded to the outer surface of the tank and filled with an antifreeze may work well.

Example 5.4

Determine the “pressure difference” available for a thermosyphon system with 1-m-high collector and 2-m-high legs. The water temperature input to the collector is 25°C and the collector output temperature is 35°C. If the overall system loss velocity factor (K) is 15.6, estimate the system flow velocity.

Solution

Equation 5.11 is used to calculate the pressure difference, with the water densities being found from the steam tables (see Appendix 3 and Tables 3.8 and 3.9).

$$\rho_{\text{stor}}(25^\circ\text{C}) = 997.009 \text{ kg/m}^3$$

$$\rho_{\text{stor}}(35^\circ\text{C}) = 994.036 \text{ kg/m}^3$$

$\rho_{\text{coll.ave.}}(30^\circ\text{C}) = 996.016 \text{ kg/m}^3$ (note: average collector temperature used in “integral”) and with $H = 2$ and $L = 1 \text{ m}$:

$$\begin{aligned}\Delta P_{\text{BUOYANT}} &= (997.009)9.81(2) - [(996.016)9.81(1) + (994.036)9.81(1)] \\ &= 38.9 \text{ N/m}^2(\text{pa}).\end{aligned}$$

The system flow velocity is estimated from the system K given, the pressure difference calculated above, taking the average density of the water around the loop (at 30°C) and substituting into Equation 5.12:

$$\Delta P_{\text{BUOYANT}} = (\rho_{\text{loop.ave.}})(h_L)_{\text{loop}} = (\rho_{\text{loop.ave.}})KV^2$$

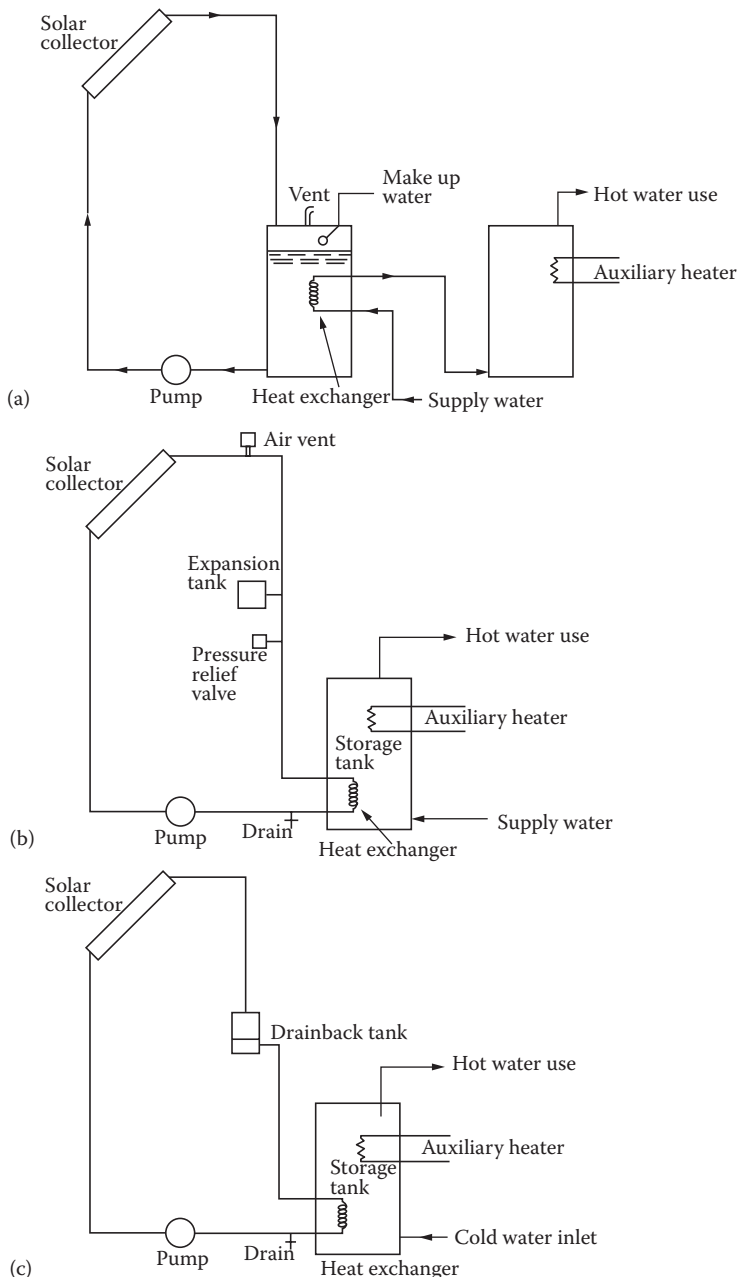
$$V^2 = 38.9/(996.016)(15.6)$$

$$V = 0.05 \text{ m/s.}$$

5.2.2 Forced-Circulation Systems

If a thermosyphon system cannot be used for climatic, structural, or architectural reasons, a forced-circulation system is required.

Figure 5.6 shows three configurations of forced-circulation systems: (1) open loop, (2) closed loop, and (3) closed loop with drainback. In an open loop system (Figure 5.6a), the solar loop is at atmospheric pressure; therefore, the collectors are empty when they are not providing useful heat. A disadvantage of this system is the high pumping power required to pump the water to the collectors every time the collectors become hot. This disadvantage is

**FIGURE 5.6**

Typical configurations of solar water-heating systems: (a) open loop system, (b) closed loop system, and (c) closed loop drainback system. (Adapted from Goswami, D.Y., *Alternative Energy in Agriculture*, Vol. 1, Boca Raton, FL, CRC Press, 1986.)

overcome in the pressurized closed loop system (Figure 5.6b) since the pump has to overcome only the resistance of the pipes. In this system, the solar loop remains filled with water under pressure.

In order to accommodate the thermal expansion of water from heating, a small (approximately 2-gallon capacity) expansion tank and a pressure relief valve are provided in the solar loop. Because water always stays in the collectors of this system, antifreeze (propylene glycol or ethylene glycol) is required for locations where freezing conditions can occur. During stagnation conditions (in summer), the temperature in the collector can become very high, causing the pressure in the loop to increase. This can cause leaks in the loop unless some fluid is allowed to escape through a pressure-release valve. Whether the result of leaks or of draining, air enters the loop causing the pumps to run dry. This disadvantage can be overcome in a closed loop drainback system that is not pressurized (Figure 5.6c). In this system, when the pump shuts off, the water in the collectors drains back into a small holding tank while the air in the holding tank goes up to fill the collectors. The holding tank can be located where freezing does not occur, but still at a high level to reduce pumping power. In all three configurations, a differential controller measures the temperature differential between the solar collector and the storage and turns the circulation pump on when the differential is more than a set limit (usually 5°C) and turns it off when the differential goes below a set limit (usually 2°C). Alternatively, a photovoltaic (PV) panel and a DC pump may be used. The PV panel will turn on the pump only when solar radiation is above a minimum level. Therefore, the differential controller and the temperature sensors may be eliminated.

5.3 Liquid-Based Solar Heating Systems for Buildings

The earliest active solar space-heating systems were constructed from enlarged water-heating components. Experiments beginning in 1938 at the Massachusetts Institute of Technology (MIT) showed that solar heating with liquid working fluids could be done without any major technical problems. The early MIT work formed the basis of many of the design techniques used today. Other experiments after World War II provided additional fundamental information on collector designs and storage operation for liquid-based heating systems. Figure 5.7 shows a modern solar-heated house in North Carolina.

Solar space-heating systems can be classified as active or passive depending on the method utilized for heat transfer. A system that uses pumps or blowers for fluid flow in order to transfer heat is called an active system. On the other hand, a system that utilizes natural phenomena for heat transfer is called a passive system. Examples of passive solar space-heating systems include direct gain, attached greenhouse, and storage wall (also called Trombe wall). Passive solar heating systems are described in Chapter 7. In

**FIGURE 5.7**

A picture of an active solar-heated house in North Carolina. (Picture courtesy of Jim Schmid, NREL.)

this section, configurations, design methods, and control strategies for active solar heating systems are described.

5.3.1 Physical Configurations of Active Solar Heating Systems

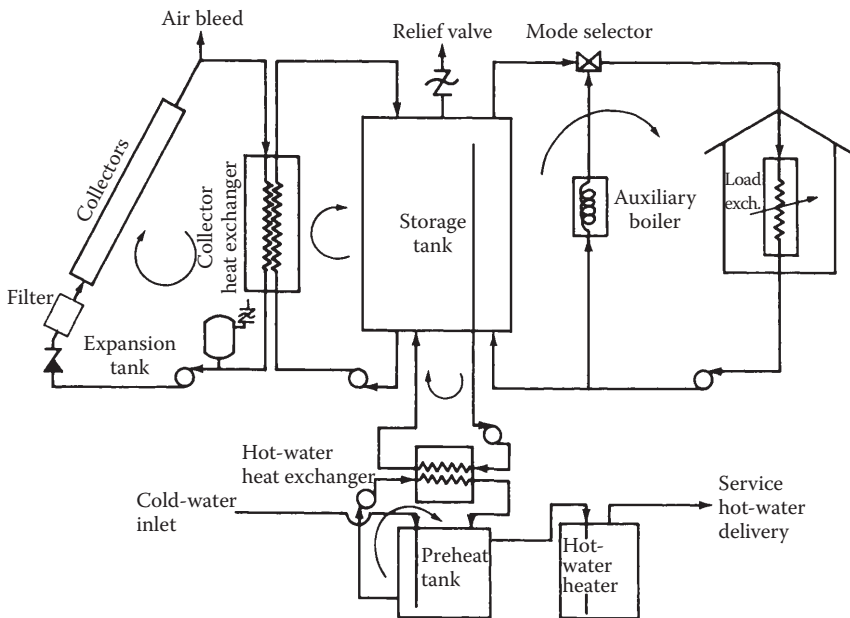
Figure 5.8 is a schematic diagram of a typical space-heating system. The system consists of three fluid loops—collector, storage, and load. In addition, most space-heating systems are integrated with a domestic water-heating system to improve the yearlong solar load factor.

Since space heating is a relatively low-temperature use of solar energy, a thermodynamic match of collector to task indicates that an efficient flat-plate collector or low-concentration solar collector is the thermal device of choice.

The collector fluid loop contains fluid manifolds, the collectors, the collector pump and heat exchanger, an expansion tank, and other subsidiary components. A collector heat exchanger and antifreeze in the collector loop are normally used in all solar space-heating systems, since the existence of a significant heating demand implies the existence of some subfreezing weather.

The storage loop contains the storage tank and pump as well as the tube side of the collector heat exchanger. To capitalize on whatever stratification may exist in the storage tank, fluid entering the collector heat exchanger is generally removed from the bottom of storage. This strategy ensures that the lowest temperature fluid available in the collector loop is introduced at the collector inlet for high efficiency.

The energy delivery-to-load loop contains the load device, baseboard heaters or fin-and-tube coils, and the backup system with a flow control (mode selector) valve.

**FIGURE 5.8**

Typical solar thermal system for space heating and hot-water heating showing fluid transport loops and pumps.

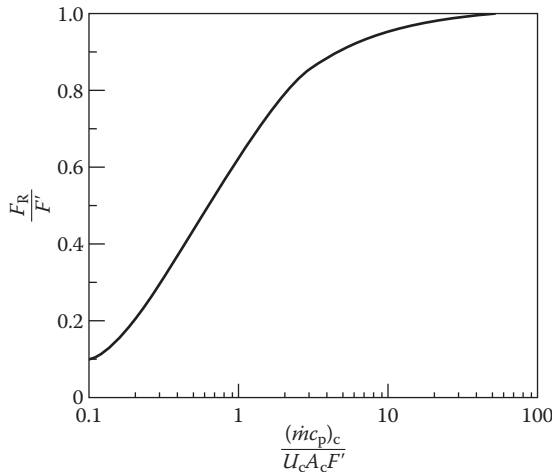
5.3.2 Solar Collector Orientation

The best solar collector orientation is such that the average solar incidence angle is smallest during the heating season. For tracking collectors, this objective is automatically realized. For fixed collectors in the Northern Hemisphere, the best orientation is due south (due north in the Southern Hemisphere), tilted up from the horizon at an angle of approximately 15° greater than the local latitude.

Although due south is the optimum azimuthal orientation for collectors in the Northern Hemisphere, variations of 20° east or west have little effect on annual energy delivery (Kreider and Kreith 1977). Off-south orientations greater than 20° may be required in some cases because of obstacles in the path of the sun. These effects may be analyzed using sun-path diagrams and shadow-angle protractors as described in Chapter 2.

5.3.3 Fluid Flow Rates

For the maximum energy collection in a solar collector, it is necessary that it operates as closely as possible to the lowest available temperature, which is the collector inlet temperature. Very high fluid flow rates are needed to maintain a collector-absorber surface nearly isothermal at the inlet temperature.

**FIGURE 5.9**

Effect of fluid flow rate on collector performance as measured by the heat-removal factor $F_R; F'$ is the plate efficiency factor (see Chapter 4).

Although high flows maximize energy collection, practical and economic constraints put an upper limit on useful flow rates. Very high flows require large pumps and excessive power consumption and lead to fluid conduit erosion.

Figure 5.9 shows the effect of mass flow rate on annual energy delivery from a solar system. It is seen that the law of diminishing returns applies and that flows beyond approximately $50 \text{ kg/h} \cdot \text{m}_c^2$ ($\sim 10 \text{ lb/h} \cdot \text{ft}_c^2$) have little marginal benefit for collectors with loss coefficients on the order of $6 \text{ W/m}_c^2 \cdot ^\circ\text{C}$ ($\sim 1 \text{ Btu/h} \cdot \text{ft}_c^2 \cdot ^\circ\text{F}$). In practice, liquid flows in the range of $50 - 75 \text{ kg/h} \cdot \text{m}_c^2$ ($10 - 15 \text{ lb/h} \cdot \text{ft}_c^2$) of water equivalent are the best compromise among collector heat-transfer coefficient, fluid pressure drop, and energy delivery. However, an infinitely large flow rate will deliver the most energy if pumping power is ignored for a nonstratified storage. If storage stratification is desired, lower flow rates must be used, since high flow destroys stratification.

In freezing climates, an antifreeze working fluid is recommended for collectors. Attempts to drain collectors fully for freeze protecting have usually been unsuccessful unless collector fluid conduits are very large and smooth and unless all piping is sloped to assure drainage. The potential damage risk from incomplete draining will usually dictate that additional investment in antifreeze be made.

5.3.4 Thermal Storage

Thermal storage tanks must be insulated to control heat loss, as described in Chapter 4. If a storage tank is located within a structure, any losses from

the tank tend to offset the active heating demands of the building. However, such storage loss is uncontrolled and may cause overheating in seasons with low heat loads. Some solar heating systems have used a ventilatable structure surrounding storage. This enclosure may be vented to the building interior in winter and to the environment in summer.

Safety concerns may cause storage to be located external to a building in some cases. Large volumes of hot water could be released to a building interior if a storage tank were to fail. Potential personal injury or property damage, which could result from an accident, must be assessed in siting storage tanks. Tank burial would seem to be the safest approach in some cases. Buried storage tanks must be sealed from ground moisture, insulated with waterproof insulation, and galvanically protected.

The amount of thermal storage used in a solar heating system is limited by the law of diminishing returns. Although larger storage results in larger annual energy delivery, the increase at the margin is small and hence not cost-effective. Seasonal storage is, therefore, usually uneconomical, although it can be realized in a technical sense. Experience has shown that liquid storage amounts of 50–75 kg H₂O/m² (10–15 lb/ft²) are the best compromise between storage tank cost and useful energy delivery. Klein (1976) has calculated the effect of storage size on annual energy delivery. The results of his study, shown in Figure 5.10, exhibit the expected diminishing returns to scale.

Since solar energy heating systems operate at temperatures relatively close to the temperatures of the spaces to be heated, storage must be capable of

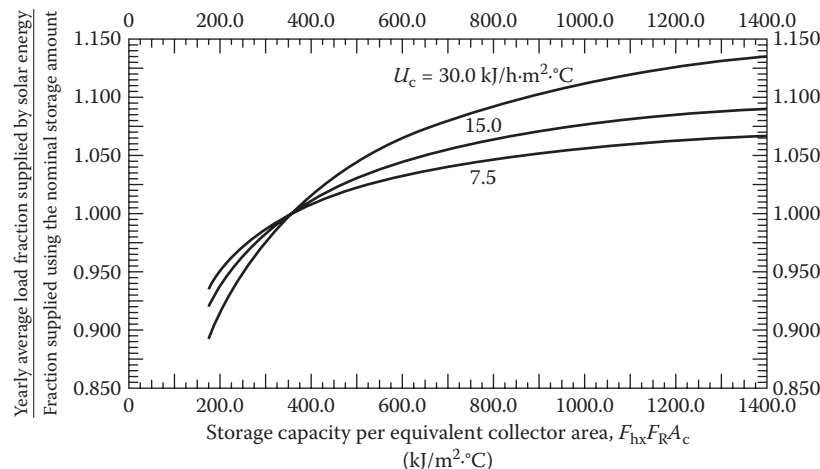


FIGURE 5.10

Effect of liquid storage capacity on liquid-based solar heating system energy delivery. (From Klein, S.A., A design procedure for solar heating systems, PhD dissertation, University of Wisconsin, Madison, WI, 1976.)

delivering and receiving thermal energy at relatively small temperature differences. The designer must consider the magnitude of these driving forces in sizing heat exchangers, pumps, and air-blowers. The designer must also consider the nonrecoverable heat losses from storage—even though storage temperatures are relatively low, surface areas of storage units may be large and heat losses therefore are appreciable.

Some investigators have proposed heating the storage medium with conventional fuels to maintain its temperature at useful levels during sunless periods. This approach has two major flaws:

1. If storage is heated with conventional fuels, it cannot be heated with solar energy when available; therefore, some collected solar energy cannot be used.
2. If storage is partially heated with conventional fuels, the collector inlet temperatures will be higher and efficiency will be lower than it would be if storage were not boosted. Therefore, the useful return on the solar system investment would be diminished.

In conclusion, it should be emphasized that storage heating with conventional fuels is uneconomical in any practical solar thermal system designed to date.

5.3.5 Other Mechanical Components

Other mechanical components in solar heating systems include pumps, heat exchangers, air bleed valves, pressure-release valves, and expansion tanks. Heat exchangers in solar systems are selected based on economic criteria described in Chapter 4. The best trade-off of energy delivery increase with increasing heat-exchanger size usually results from use of an exchanger with effectiveness in the range of 0.6–0.8. Counterflow heat exchangers are required for this level of effectiveness. A detailed example of heat-exchanger selection is contained in Chapter 4.

Achievement of the required effectiveness level may dictate fairly high flow rates in the storage tank side of the collector heat exchanger. Flows up to twice that in the collector side can improve exchanger performance significantly in many cases. Since the storage side loop is physically short and has a small pressure drop, increased flow in this loop increases pump energy requirements by a negligible amount. Typical solar heat-exchanger sizes range from 0.05 to 0.10 m² of heat-exchanger surface per square meter of net collector area.

In hydronic heating systems, it is essential that all air be pumped from the system. To facilitate this process, air bleed valves located at high points in a system are used. These are opened during system fill and later if air should collect. Air bleeds are required at points of low velocity in piping

systems where air may collect because the local fluid velocity is too low for entrainment.

5.3.6 Controls in Liquid Systems

Control strategies and hardware used in current solar system designs are quite simple and are similar in several respects to those used in conventional systems. The single fundamental difference lies in the requirement for differential temperature measurement instead of simple temperature sensing. In the space-heating system shown in Figure 5.8, two temperature signals determine which of three modes is used. The signals used are the collector-storage differential and room temperature. The collector-storage difference is sensed by two thermistors or thermocouples, the difference being determined by a solid-state comparator, which is a part of the control device. Room temperature is sensed by a conventional dual-contact thermostat.

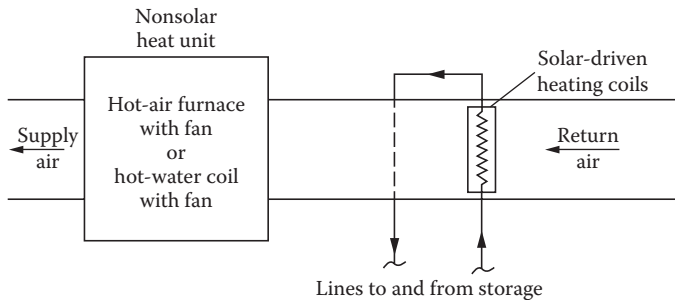
The control system operates as follows. If the first room thermostat contact closes, the mode selector valve and distribution pump are activated in an attempt to deliver the thermal demand from solar thermal storage. If room temperature continues to drop, indicating inadequate solar availability, the mode selector diverts flow through the backup system instead of the solar system, and the backup is activated until the load is satisfied.

The collector-storage control subsystem operates independently of the heating subsystem described above. If collector temperature, usually sensed by a thermistor thermally bonded to the absorber plate, exceeds the temperature in the bottom of the storage tank by 5°C – 10°C (9°F – 18°F), the collector pump and heat-exchanger pump (if present) are activated and continue to run until the collector and storage temperature are within approximately 1°C – 2°C (2°F – 4°F) of each other. At this point, it is no longer worthwhile to attempt to collect energy and the pumps are turned off. The collector-storage subsystem also has a high temperature cutout that turns the collector loop pump off when the storage temperature exceeds a set limit.

5.3.7 Load Devices in Liquid Solar Heating Systems

A heating load device transfers heat from the solar storage to the air in the space. Therefore, a liquid-to-air heat exchanger is sized on the basis of the energy demand of a building. Several generic types of load devices are in common use.

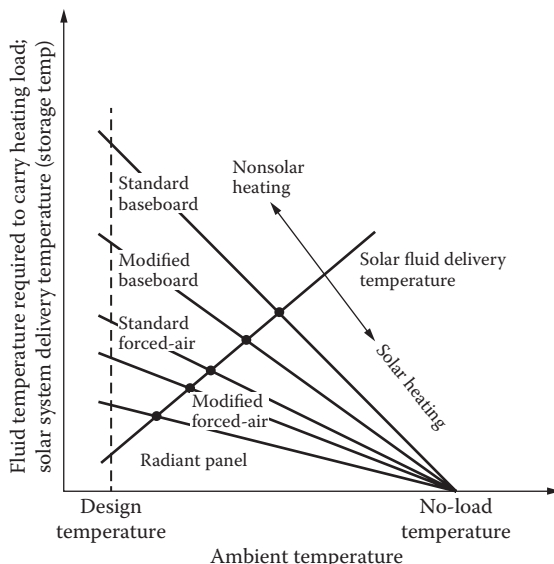
1. Forced-air systems—tube-and-fin coil located in the main distribution duct of a building or zone of a building (see Figure 5.11).
2. Baseboard convection systems—tube-and-fin coils located near the floor on external walls. These operate by natural convection from the convectors to the room air.

**FIGURE 5.11**

Forced-air heating system load device location upstream of nonsolar heat exchanger or furnace.

3. Heated floors or ceilings—water coils. These transfer heat to large thermal masses that in turn radiate or convect into the space. This heating method is usually called radiant heating.

Each load device requires fluid at a different temperature in order to operate under design load conditions as shown in Figure 5.12. Since baseboard heaters are small in heat-transfer area and rely on the relatively ineffectual

**FIGURE 5.12**

Heating load diagram for baseboard, forced-air, and radiant systems. Modified baseboard and forced-air systems are oversized in order to carry heating demands at lower temperature. Balance points are indicated by large dots at intersections.

mechanism of natural convection, they require the highest fluid temperature. Forced-air systems involve the more efficient forced-convection heat-transfer mode and, hence, are operable at lower fluid temperatures (see Figure 5.12). Radiant heating can use very large heat-transfer areas and is, therefore, operable at relatively low fluid temperatures.

In Figure 5.12 the intersection of the solar fluid temperature line and the load line for a specific configuration is called the *balance point*. At ambient temperatures below the balance point, solar energy cannot provide the entire demand, and some backup is required; above the balance point, solar capacity is sufficient to carry the entire load. Note that the load lines are specific to a given building. The solar fluid temperature line is not fixed for a building but depends on solar collector and storage size as well as local solar radiation levels. The line shown in Figure 5.12 is, therefore, an average line. The instantaneous solar line changes continuously in response to load and climatic forcing functions as described in Chapter 4.

It is possible to modify load devices to lower the balance point, as shown in Figure 5.12. For example, a forced-air tube-and-fin exchanger can be enlarged by adding one or more additional rows of tubes. This increased heat-transfer area will permit the same energy delivery at a lower fluid temperature. Figure 5.13 depicts the effect of forced-air load device size (heat-transfer

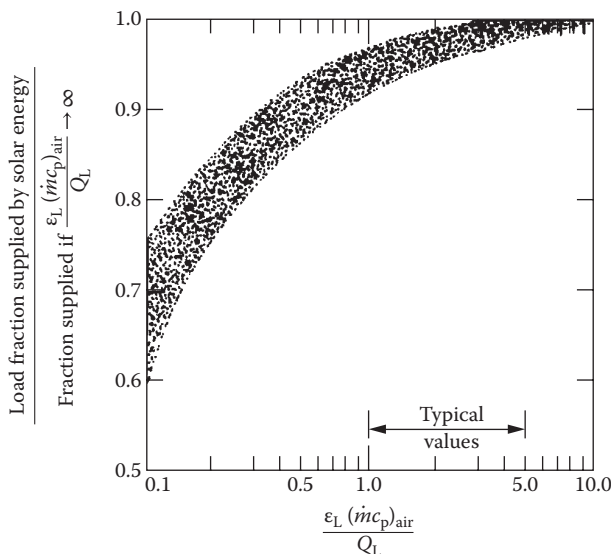


FIGURE 5.13

Effect of load device capacity for forced-air heating systems. Q_L is the building heat load expressed in units consistent with $(\dot{m}c_p)_{\text{air}}$. (From Klein, S.A., A design procedure for solar heating systems, PhD dissertation, University of Wisconsin, Madison, WI, 1976.)

effectiveness ε_L) on annual energy delivery. The law of diminishing returns is evident as increasing effectiveness returns progressively less energy. The effectiveness of a cross-flow heat exchanger of the type used in forced-air systems is calculated in Chapter 4 and shown in Figure 4.12.

5.4 Solar Air-Heating Systems

Air has been used as the working fluid in solar heating systems since World War II. Although demonstrated in fewer buildings than liquid systems, air systems have several advantages that can lead to their use in smaller installations in single-family and multifamily residences. In addition, air systems are well suited to crop drying and air preheating in certain processes.

Table 5.6 lists some of the advantages and disadvantages of air and liquid systems. Several of the disadvantages of an air system follow from the poor heat-transfer properties of air. Large space requirements for ducts preclude the use of air systems in large buildings because of space limitations. This is usually not a disadvantage in air systems used in residences. However, the

TABLE 5.6

Advantages and Disadvantages of Air and Liquid Space-Heating Systems

Advantages	Disadvantages
<i>Air Systems</i>	
No freezing problem	Space heating only
No internal corrosion problem with dry air	Large space requirements for ducts
Leaks of smaller consequence	Larger storage volume required for rocks
No heat exchanger between collector-storage and storage-building loops	Cannot store heat and heat building at the same time—major problem in low load seasons
No boiling or pressure problems	Low (ρc_p) product for air
Easy for do-it-yourselfers	
Simple and reliable	
<i>Liquid Systems</i>	
Higher transport energy density	Freezing problems
Better heat-transfer properties	Leakage problems
Water storage has higher energy density	Corrosion problem—water chemistry needs monitoring
Suitable for space heating and cooling	Heat exchanger required for collector-storage and storage-building loops
Small fluid conduits	Boiling and fluid expansion provisions required

thermal performance and costs for both systems are nearly identical if the air system does not have leaks.

In all air-based solar heating systems, a pebble-bed storage device is used. Although water offers a higher storage energy density than most solids, the difficulty of economically exchanging heat from an air stream to a liquid storage fluid stream precludes its use. Storage controls and operating parameters are described in detail in Section 5.4.1.

Flat-plate collectors are usually required for air-heating systems to provide sufficient area to transfer heat effectively from the absorber plate to the air stream. A flat-plate collector provides a good thermodynamic match for temperature demands in space-heating applications. Air-heating flat-plate collectors are described in Chapter 3.

5.4.1 Heating System Physical Configuration

In many ways, liquid-based and air-based solar systems are similar in operation. Figure 5.14 is a schematic diagram of a typical air-heating system.

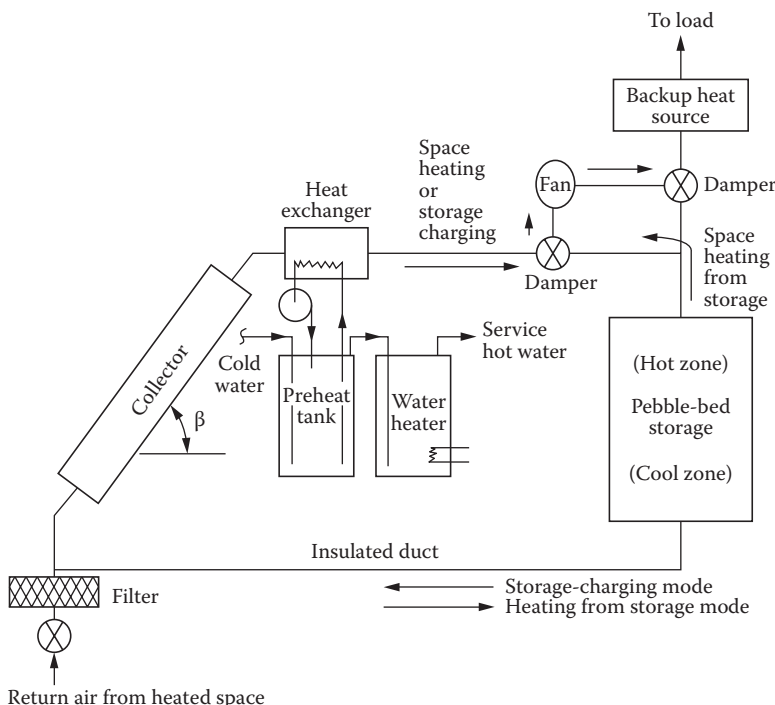


FIGURE 5.14

Typical air-based solar space-heating system showing directions of fluid flow and important components.

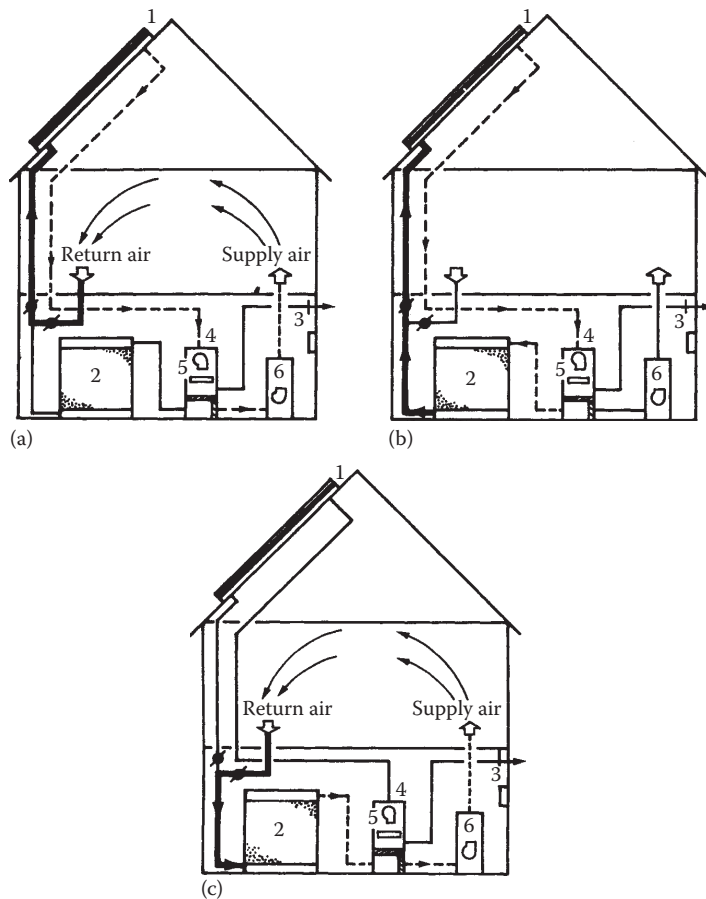
Similar flow regimes and collector orientations are used in both types of systems. The air system is simpler, however, since a collector heat exchanger and associated pumps, pipes, and expansion tanks are not present. The use of pebble-bed storage is advantageous because of the stratification that results. Stratification ensures a low inlet temperature to the collector; the collector inlet temperature is approximately the temperature of the cool zone of storage, which, in turn, is the building return air temperature ($\sim 15^\circ\text{C}$ – 20°C). Cool collector inlet temperatures are essential to efficient operation of an air system. Since stratification cannot be achieved with isothermal phase-change storage media, they are not suitable for use with air-based systems. Frequently, more dampers are required than shown in Figure 5.14 to prevent leakage and backflows through a cold collector via a leaky damper. Careful design of dampers and actuators is essential.

The collector-to-storage loop consists of insulated ducts, collector manifolds, and a hot-water preheat exchanger. These tube-and-fin exchangers provide some preheat to hot water if placed at the collector outlet to ensure their exposure to the hottest air available. Collector flow balancing is achieved by controlling the pressure drop through each collector and using equal duct lengths for each.

Figure 5.15 shows a hot-air system. During the storage-charging mode (Figure 5.15b), heated air flows through the rock bed at a low flow rate determined by the desired temperature rise in the collector, usually 10 – 15 liters/ $\text{s} \cdot \text{m}_c^2$. As progressively more heat is stored, the interface between the hot and cold regions of storage moves downward in the storage bin. The air returning to the collector is at the temperature of the cool region of storage.

During daytime heating on a sunny day (Figure 5.15a), air from the collector is diverted to the building instead of to storage. During sunny periods when no heating demand exists, storage is charged by warm air from the collector. During the nighttime or cloudy daytime heating modes, heat is removed from storage by a counterflow of air through the rock bed, as shown in Figure 5.15c. The outlet temperature from storage is close to the daytime collection (inlet) temperature, since the air being heated passes through the hottest zone of storage last. As progressively more heat is removed from storage, the interface between the hot and cold regions of storage moves upward.

The storage medium for air systems has typically been 25–50 mm diameter granite or river-bed rocks. An air filter is required between the heated space and storage to eliminate dust buildup in the gravel bed. Dust would reduce the heat-transfer coefficient to the rock pieces and increase the bed pressure drop. The recommended amount of storage to be used is roughly the same as for a liquid system—approximately 300 kg of rock per square meter of collector ($0.75 \text{ ft}^3/\text{ft}_c^2$, $0.25 \text{ m}^3/\text{m}_c^2$). Design information on the expected pressure drop through pebble-bed storage is contained in Chapter 4.

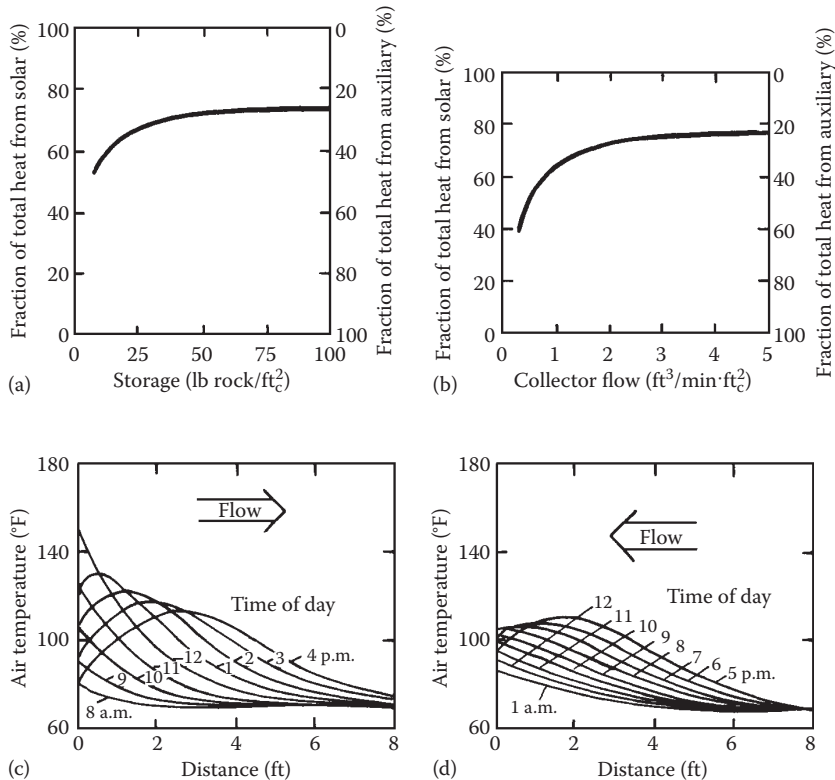
**FIGURE 5.15**

Schematic diagram of operating modes of solar air system: (a) space heating from collector; (b) storing solar heat, and (c) space heating from storage. The components are (1) collector, (2) storage, (3) control, (4) fan, (5) hot-water preheater (optional), and (6) backup heater. (Courtesy of the Solaron Corp.)

5.4.2 Collector Designs

Several air-heating collector designs are shown in Figure 3.7. However, relatively few performance data for such collectors have been published to provide designers with the information necessary to predict system performance and determine optimal system configurations reliably.

One of the early computer-aided design studies that does provide guidelines for the designer of air-collector systems was conducted by Balcomb et al. (1975, 1976). Figure 5.16 shows some of their practical results. Figure 5.16a depicts the variation of solar delivery with storage volume. It is clear that

**FIGURE 5.16**

Hot-air solar system operating parameters: (a) effect of storage size on annual energy delivery, (b) effect of collector air flow rate on annual energy delivery, (c) typical temperature distribution in rock bed during storage heating by solar energy, and (d) typical temperature distribution in rock bed during heat removal from storage. (Adapted from Balcomb, J.D. et al., *Solar Handbook for Los Alamos*, LASL, New Mexico, 1975; and Balcomb, J.D. et al., Design considerations of air-cooled collector/rock-bin storage solar heating systems, paper presented at the ISES Annual Meeting, Los Angeles, CA, 1975.)

storage volumes in excess of 60 lb rock/ft^2 (300 kg/m^2) improve the annual solar delivery by a negligible amount. Likewise, Figure 5.16b indicates that collector air flow rates greater than $15 \text{ liters/s} \cdot \text{m}^2$ increase delivery very little. Figure 5.16c and d show temperature profiles for a particular rock bed modeled for various times of day for both the storage-charging and storage-discharging modes. Any properly sized storage will have similar temperature distributions; the key property is that the outlet temperature from storage should be low to permit the inherently inefficient air collector to operate at as low a temperature as possible. The optimal geometric configuration of a storage bed is roughly cubical in order to minimize the air pressure drop.

5.4.3 Fluid Flow Rates

The flow rate through an air collector and storage loop is a compromise between pressure drop and energy transfer to the air stream. As shown in Figures 5.16 and 5.17, the effect of air capacitance rate $(\dot{m}c_p)_c$ can be significant. Apart from the beneficial effect of increased flow rate on the heat-removal factor F_R , which is usually quite low for air collectors (~ 0.6 – 0.7), increased flows tend to cause an offsetting decrease in storage bed stratification. Decreased stratification penalizes collector performance, since the collector inlet temperature is higher under these circumstances.

Nominal flow rates used in air collectors are approximately $10 \text{ liters}/\text{m}_c^2 \cdot \text{s}$ ($2 \text{ ft}^3/\text{min} \cdot \text{ft}_c^2$). This capacitance rate is well below that for liquid systems but is a compromise between the offsetting effects of stratification reduction and improved heat transfer from the absorber plate that would result from higher flow rates. This effect is not present in liquid systems, since storage stratification is generally of little consequence in liquid systems.

5.4.4 Other Mechanical Components

Air systems require fewer auxiliary components than liquid systems. Controls in air systems are similar in function to those in liquid systems and are not described in detail here. The controller operates one blower, one

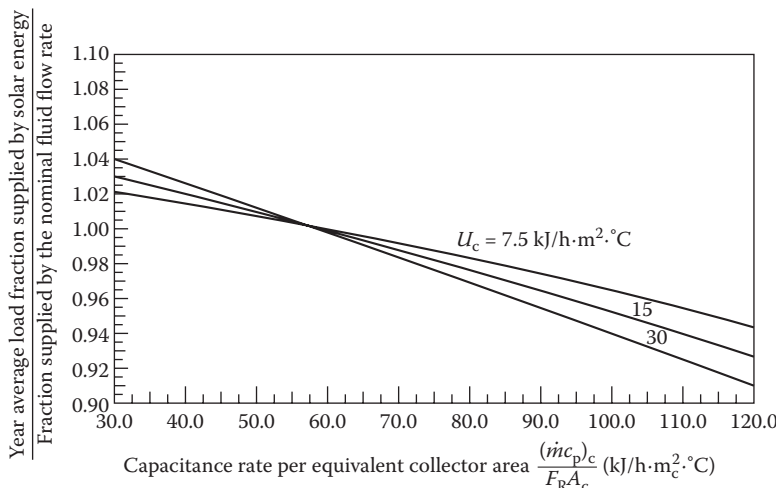


FIGURE 5.17

Effect of collector fluid flow rate on annual energy delivery in an air-based solar heating system. The effect of the collector loss coefficient U_c is also shown. The nominal fluid flow rate is $58 \text{ kg}/\text{m}_c^2 \cdot \text{°C} \cdot \text{h}$, based on the equivalent areas $F_R A_c (\dot{m}c_p)_{air}$. (Adapted from Klein, S.A., A design procedure for solar heating systems, PhD dissertation, University of Wisconsin, Madison, WI, 1976.)

pump (preheat), and two dampers, which are the analogs of valves in liquid systems. The dampers must seal tightly. For example, if the middle damper in Figure 5.15, controlling the air flow to the heated space, should leak, the fan could draw cold air from the nighttime collector through the damper to mix with warm air from storage. Such a leak could reduce the heating effect substantially.

Sizing of the blower and ducts in air systems can be done by conventional methods. Pressure-drop data for air ducts are presented in Appendix 4, in a convenient form for such calculations in Figure A4.4. In some cases, a two-speed blower is required in air systems if the system pressure drop in the collector-to-space heating mode is substantially different from the pressure drop through storage. Careful design can frequently avoid this problem, however.

5.4.5 Unglazed Transpired Wall System for Air Preheating

Ventilation air preheating systems using wall-mounted unglazed transpired solar air collectors are the only active solar air-heating systems that have found market acceptance in commercial and industrial buildings (Kutcher 1996). Such systems preheat the ventilation air in a once-through mode without any storage. Figure 5.18 shows a transpired wall system in which the air

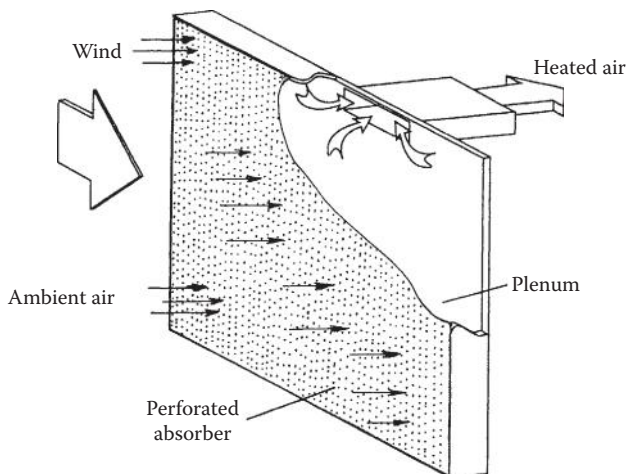


FIGURE 5.18

Unglazed transpired solar collector system for building ventilation preheat. Intake air is drawn by the building ventilation fan through the perforated absorber plate and up the plenum between the absorber and the south wall of the building. (Adapted from Kutcher, C.F. and C.B. Christensen. Unglazed transpired solar collectors. *Advances in Solar Energy*, K. Boer, ed., vol. 7, pp. 283–307, 1992.)

is drawn through a perforated absorber plate by the building ventilation fan. Kutcher and Christensen (1992) presented a thermal analysis of this system. From a heat balance on the transpired unglazed collector, the useful heat collected is

$$q_u = I_c A_c \alpha_s - U_c A_c (T_{\text{out}} - T_a). \quad (5.13)$$

The overall heat-loss coefficient U_c , which is attributed to radiative and convective losses, is given as

$$U_c = h_r / \varepsilon_{\text{hx}} + h_c \quad (5.14)$$

where ε_{hx} is absorber heat-exchanger effectiveness, h_r is a linearized radiative heat-transfer coefficient, and h_c is the convective heat-loss coefficient. The heat-exchanger effectiveness for air flowing through the absorber plate is defined as

$$\varepsilon_{\text{hx}} = \frac{T_{\text{out}} - T_a}{T_c - T_a}. \quad (5.15)$$

The forced convective heat-loss coefficient owing to a wind velocity of U_∞ is given as

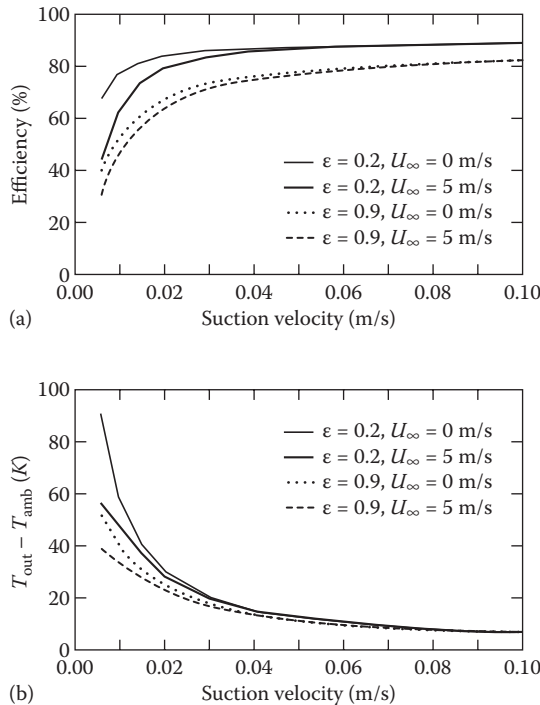
$$h_c = 0.82 \frac{U_\infty \nu c_p}{L v_0}, \quad (5.16)$$

where ν is the kinematic viscosity of air in m^2/s , c_p is the specific heat in $\text{J}/\text{kg}\cdot\text{K}$, v_0 is the section velocity, and L is the height of the collector.

Radiation heat loss occurs to both the sky and to the ground. Assuming the absorber is gray and diffuse with an emissivity ε_c , the radiative loss coefficient h_r is

$$h_r = \varepsilon_c \sigma \frac{\left(T_c^4 - F_{\text{cs}} T_{\text{sky}}^4 - F_{\text{cg}} T_{\text{gnd}}^4 \right)}{T_c - T_a}, \quad (5.17)$$

where F_{cs} and F_{cg} are the view factors between the collector and the sky and between the collector and the ground, respectively. For a vertical wall with infinite ground in front of it, both F_{cs} and F_{cg} will be 0.5 each. Using the above equations, Kutcher and Christensen (1992) showed that the predicted performance matches the measured performances well. Figure 5.19 shows their predicted thermal performances.

**FIGURE 5.19**

Predicted thermal performance of a vertical unglazed transpired solar collector as a function of suction velocity, absorber emissivity, and wind speed. Collector size = 3 m × 3 m, $T_{\text{amb}} = 10^\circ\text{C}$, $T_{\text{sky}} = T_{\text{amb}} - 15^\circ\text{C}$, $T_{\text{gnd}} = T_{\text{amb}}$, and $I_c = 700 \text{ W/m}^2$. (a) Efficiency versus suction velocity. (b) Suction air temperature rise versus suction velocity. (From Kutcher, C.F. and C.B. Christensen. Unglazed transpired solar collectors. *Advances in Solar Energy*, K. Boer, ed., vol. 7, pp. 283–307, 1992.)

5.5 Methods of Modeling and Design of Solar Heating Systems

Several methods of modeling and design of solar space and water heating have been developed including f -chart, TRNSYS, utilization, and SLR. The first three of these methods are described briefly in Sections 5.5.1 through 5.7. The SLR method is described in Chapter 7. Before design of a solar heating system can start, one must know the loads and the availability of solar radiation at the location. Estimation of solar radiation is described in Chapter 2 and estimation of the loads has been described briefly earlier in Chapter 5.

5.5.1 Design of a Liquid-Based Solar Heating System by f -Chart

Klein et al. (Beckman et al. 1977; Klein 1976; Klein et al. 1975, 1976a,b) developed a method of simplified prediction of the performance of a solar heating system

based on a large number of detailed simulations for various system configurations in various locations in the United States. The results from these simulations were then correlated with dimensionless parameters on charts that are general in form and usable anywhere. The charts are called *f*-charts, denoting a parameter f_s , the fraction of monthly load supplied by solar energy. The dimensionless groups used in the *f*-charts are derived from a nondimensionalization of the equations of governing energy flows; the groups therefore have a physical significance as described in the following. The *f*-chart method has been developed for standard solar heating and hot-water system configurations.

Schematic diagrams for standard solar heating systems based on liquid and air heat-transfer fluids are shown in Figures 5.8 and 5.14, respectively. Certain deviations from these configurations can be handled in the *f*-chart method. For example, the collector-to-storage heat exchanger in the liquid-based system may be eliminated. The domestic water heater in Figure 5.14 is shown as a two-tank system, which may be reconfigured as a one-tank system.

In the *f*-chart method, the fraction of load supplied by solar energy, f_s , is correlated with two dimensionless parameters, called the loss parameter P_L and the solar parameter P_s . Parameters P_L and P_s are defined as

$$P_L = \frac{A_c F_{hx} F_R U_c \Delta t (T_R - \bar{T}_a)}{L} \quad (5.18)$$

and

$$P_s = \frac{A_c F_{hx} F_R \bar{I}_c (\bar{\tau}\alpha)}{L}. \quad (5.19)$$

P_s and P_L are measures, respectively, of the long-term insolation gain by the collector and long-term thermal loss per unit load. The parameters in Equations 5.18 and 5.19 and in the *f*-chart are described in Table 5.7.

P_s may be rewritten as

$$P_s = \frac{A_c \bar{I}_c F_{hx} F_R (\bar{\tau}\alpha)_n}{L} \frac{(\bar{\tau}\alpha)}{(\tau\alpha)_n}. \quad (5.20)$$

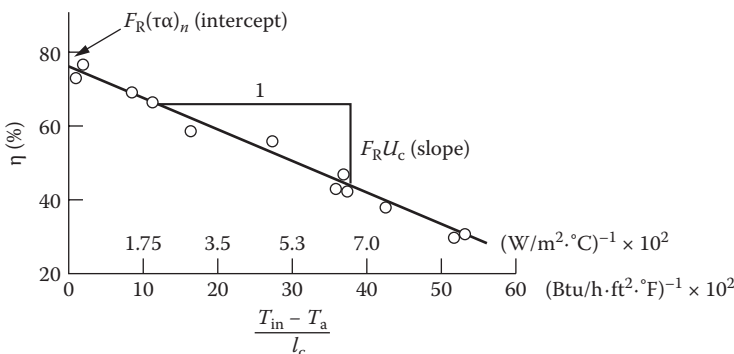
As shown in Chapter 3, $F_R U_c$ and $F_R(\tau\alpha)_n$ in the equations above can be determined directly from the slope and intercept of a collector efficiency curve plotted as shown in Figure 5.20. In addition, Klein suggests that the time-averaged value $F_R(\bar{\tau}\alpha)$ is related to the normal incidence value $F_R(\tau\alpha)_n$ as

$$\frac{F_R(\bar{\tau}\alpha)}{F_R(\tau\alpha)} = 0.95, \quad (5.21)$$

for a surface tilted within $\pm 20^\circ$ of the local latitude.

TABLE 5.7Definition of Parameters in *f*-Chart

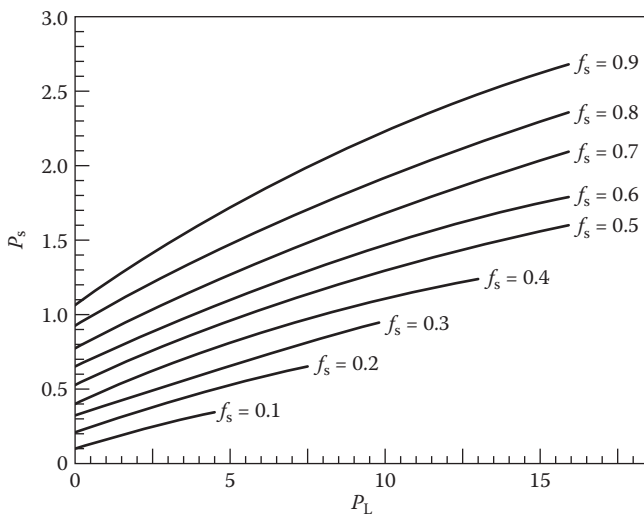
Parameter	Definition
A_c	Net collector aperture area (m^2)
f_s	The solar load fraction: fraction of monthly load carried by solar system
F_R	Collector heat-removal factor (see Equation 3.43)
F_{hx}	Collector loop heat-exchanger factor (see Equation 4.36) $F_{hx} = 1$ if no collector heat exchanger is used
\bar{I}_c	Total monthly collector-plane insolition ($\text{J}/\text{m}^2\cdot\text{month}$) (see Chapter 2)
L	Total monthly water-heating load (J/month) (see Example 5.3)
\bar{T}_a	Monthly average ambient temperature ($^\circ\text{C}$)
T_R	Reference temperature with a value of 100°C
U_c	Collector heat-loss coefficient ($\text{W}/\text{m}^2\cdot^\circ\text{C}$) (see Chapter 3)
Δt	Number of seconds per month (s/month)
$\bar{\tau}\alpha$	Monthly averaged collector transmittance-absorptance product

**FIGURE 5.20**

Typical flat-plate collector efficiency curve showing method of evaluating $F_R(\tau\alpha)_n$ and $F_R U_c$. (From Kreider, J.F. and F. Kreith, *Solar Heating and Cooling*, Hemisphere Publ. Corp., Washington, DC, revised 1st ed., 1977.)

Note that Figure 5.20 is a plot of efficiency versus collector *inlet* fluid temperature, as distinguished from *average* fluid temperature. Such curves are usually available from the collector manufacturers. Figure 5.21 shows the *f*-chart for a liquid-based solar heating and hot-water system. The results of the computer model used to generate the f_s curves in Figure 5.21 can also be expressed in the form of an empirical equation as (Klein et al. 1976a)

$$f_s = 1.029 P_s - 0.065 P_L - 0.245 P_s^2 + 0.0018 P_L^2 + 0.0215 P_s^3 \quad (5.22)$$

**FIGURE 5.21**

The f -chart for solar water-heating systems. (From Klein, S.A., A design procedure for solar heating systems, PhD dissertation, University of Wisconsin, Madison, WI, 1976.)

valid for the range

$$0 \leq P_s \leq 3.0; \quad 0 \leq P_L \leq 18.0; \quad \text{and} \quad 0 \leq f_s \leq 1.0.$$

It is further required that $P_s > P_L/12$ to ensure that the monthly insolation is above the useful threshold and that thermal losses are below an upper bound at which energy absorbed is equal to energy lost from the absorber plate.

The f -chart in Figure 5.21 is based on nominal values of collector flow rate, thermal storage mass, and load heat-exchanger effectiveness. It is possible to use the f -chart for other values of these important parameters if the loss parameter and a solar parameter are appropriately modified. Table 5.8 contains the nominal values used in generating the f -chart and the dimensionless groups that are used to modify the loss or the solar parameter for other system values. The f -chart in Figure 5.21 may be used for a water-heating-only system with the following modification for P_L :

$$P_L = \frac{F_{hx}R_cA_c\Delta t(11.6 + 1.18T_{w,o} + 3.86T_{w,i} - 2.32\bar{T}_a)}{L}, \quad (5.23)$$

where $T_{w,i}$ and $T_{w,o}$ are water supply and delivery temperatures, respectively. Klein (1976) has prepared f -charts for air-based solar heating systems also as

TABLE 5.8

Nominal Values of Physical Parameters and Modifying Groups for *f*-Chart Use for Liquid-Based Systems

Parameter	Nominal Value	Modified Parameter ^a	
Flow rate ^b	0.0128 liters H ₂ O equivalent	$P_L = P_{L,nom} \frac{F_{hx} F_R}{(F_{hx} F_R)_{nom}}$	(5.24)
$\frac{(mc_p)_c}{A_c}$	$s \cdot m_c^2$	$P_s = P_{s,nom} \frac{F_{hx} F_R}{(F_{hx} F_R)_{nom}}$	(5.25)
Storage volume (water)			
$V_s = \frac{M}{\rho A_c}$	75 liters H ₂ O/m _c ²	$P_L = P_{L,nom} \frac{V_s^{-0.25}}{75}$	(5.26)
Load heat exchanger ^c			
$\frac{\varepsilon_L (mc_p)_{air}}{Q_L}$	2.0	$P_s = P_{s,nom} \quad 0.393 + 0.651 \exp -0.139 \frac{Q_L}{\varepsilon (mc_p)_{air}}$	(5.27)
		0.651 exp -0.139	

Note: The table was prepared from data and equations presented in Beckman et al. (1977) and Klein (1976).

^a Multiply basic definition of P_s and P_L in Equations 5.18 and 5.19 by a factor for nonnominal group values; $(F_{hx} F_R)_{nom}$ refers to values of $F_{hx} F_R$ at collector rating or test conditions.

^b In liquid systems, the correction for flow rate is small and can usually be ignored if variation is no more than 50% below the nominal value.

^c $(mc_p)_{min}$ is the minimum fluid capacitance rate, usually that of air for the load heat exchanger; Q_L is the heat load per unit temperature difference between inside and outside of the building.

shown in Figure 5.22. Loss and solar parameters P_L and P_s are identical to those for liquid systems and are defined in Equations 5.18 and 5.19. Since air systems do not use a collector-to-storage heat exchanger, the heat-exchanger factor is given by $F_{hx} = 1.0$.

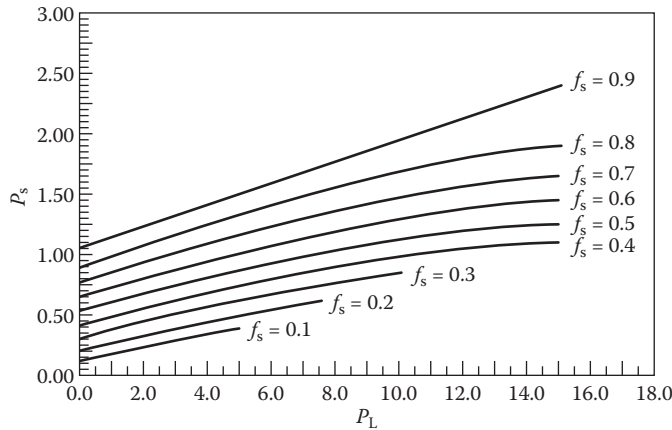
The data from which the *f*-chart was created can be expressed by an empirical equation as

$$f_s = 1.040 P_s - 0.065 P_L - 0.159 P_s^2 + 0.00187 P_L^2 - 0.0095 P_s^3 \quad (5.28)$$

valid for the following ranges:

$$0 \leq P_s \leq 3.0; \quad 0 \leq P_L \leq 18.0; \quad 0 \leq f_s \leq 1.0.$$

It is further required that $P_s > 0.07 P_L$ to ensure that the monthly insolation is above the useful threshold level and that thermal losses are below

**FIGURE 5.22**

The f -chart for air-based solar space-heating systems. (From Klein, S.A., A design procedure for solar heating systems, PhD dissertation, University of Wisconsin, Madison, WI, 1976.)

an upper bound at which energy absorbed is equal to energy lost from the absorber plate.

The f -chart for air systems is based on nominal values of air flow rate and storage capacity. Table 5.9 shows the nominal value of these two parameters and the dimensionless groups to be used to multiply the loss parameter to correct for flow rate or storage changes from the nominal value used to construct Figure 5.22.

TABLE 5.9

Factors for Storage Capacity and Air Flow Rate for f -Chart for Air-Based Systems

Parameter	Nominal Value ^a	Loss Parameter Multiplier
Storage capacity, V_s	$0.25 \text{ m}^3/\text{m}_c^2$	$\frac{0.25}{V_s}^{0.3}$
Fluid volumetric flow rate, Q_c	10.1 liters/s	$\frac{Q_c}{10.1}^{0.28}$

Sources: Adapted from Beckman, W.A. et al., *Solar Heating Design by the F-Chart Method*, John Wiley & Sons, New York, 1977; and Klein, S.A., A design procedure for solar heating systems, PhD dissertation, University of Wisconsin, Madison, WI, 1976.

^a Based on net collector area; fluid volume at standard atmosphere conditions.

Example 5.5

Calculate the annual heating energy delivery of a solar space-heating system using a double-glazed, flat-plate collector in Bismarck, North Dakota. The building and solar system specifications are given below.

Building Specifications

Location: 47°N latitude (see Appendix 2, Tables A2.2 and A2.3)

Space-heating load: 28,000 kJ/°C·day

Solar System Specifications

Collector loss coefficient: $F_R U_c = 4.44 \text{ W/m}^2 \cdot \text{K}$

Collector optical efficiency (average): $F_R (\overline{\tau\alpha}) = 0.70$

Collector tilt: $\beta = L + 15^\circ = 62^\circ$

Collector area: $A_c = 60 \text{ m}^2$

Collector fluid flow rate: $\dot{m}_c/A_c = 55 \text{ kg/h} \cdot \text{m}^2$

Collector fluid heat capacity: $c_{p_c} = 1.9 \text{ kJ}/^\circ\text{C} \cdot \text{kg}$ (antifreeze)

Storage capacity: 83 kg of $\text{H}_2\text{O}/\text{m}^2$

Storage fluid flow rate: $\dot{m}_s/A_c = 100 \text{ kg of H}_2\text{O/h} \cdot \text{m}^2$

Storage fluid heat capacity: $c_{p_s} = 4.187 \text{ kJ/kg} \cdot {}^\circ\text{C}$ (water)

Heat-exchanger effectiveness: 0.75

Load heat exchanger: $\epsilon_L (\dot{m} c_p)_{\text{air}}/Q_L = 2.0$

Climatic Data

Climatic data from the NWS are tabulated in Table 5.10.

Solution

The *f*-chart method is amenable to a step-by-step application. The following order is suggested:

TABLE 5.10

Climatic and Solar Data for Bismarck, North Dakota

Month	Average Ambient Temperature (°C)	Heating Degree C-days	Horizontal Solar Radiation (kJ/m ² ·day)
Jan	-13.2	978	6572
Feb	-10.3	801	10,465
Mar	-3.8	687	14,902
Apr	6.1	368	18,711
May	12.4	188	23,023
Jun	17.7	68	24,697
Jul	21.6	10	25,828
Aug	20.7	19	21,600
Sep	14.2	140	16,325
Oct	8.2	313	11,386
Nov	-1.7	601	6739
Dec	-9.1	851	5191

1. Calculate monthly collector-plane insolation for each month.
2. Calculate solar and loss parameters P_s and P_L (Equations 5.18 and 5.19) for each month and heat-exchanger penalty factor F_{hx} (Equation 4.36).
3. Evaluate f_s from the f -chart for each month.
4. Calculate total annual energy delivery from monthly totals.

Each of these steps is shown in Table 5.11.

The following are the calculations for the month of January. Results for the other months can be found similarly.

From Table A2.2 (by interpolation):

$$\bar{H}_{o,h} = 3048 \cdot \frac{\text{Wh}}{\text{m}^2 \cdot \text{day}} = 10,973 \frac{\text{kJ}}{\text{m}^2 \cdot \text{day}}.$$

From Table 5.10:

$$\bar{H}_h = 6572 \text{ kJ/m}^2 \cdot \text{day}.$$

Using Equation 2.54:

$$\bar{K}_T = \frac{\bar{H}_h}{\bar{H}_{o,h}} = 0.6.$$

TABLE 5.11

The f -Chart Summary for Example 5.5

Month	Collector-Plane Radiation (kJ/m ² ·day)	Monthly Energy Demand (GJ)	P_L	P_s	f_s
Jan	18,378	27.38	2.81	0.83	0.53
Feb	20,654	22.43	3.34	1.14	0.69
Mar	19,327	19.24	3.66	1.24	0.73
Apr	16,491	10.25	6.22	1.99	0.91
May	15,913	5.26	11.30	3.75	1.00
Jun	15,356	1.90	29.39	10.01	1.00
Jul	16,604	0.28	190.00	73.43	1.00
Aug	16,988	0.53	101.53	39.69	1.00
Sep	17,925	3.92	14.85	5.66	1.00
Oct	18,874	8.76	7.11	2.67	1.00
Nov	14,926	16.86	4.09	1.10	0.63
Dec	15,399	23.83	3.11	0.80	0.49
Annual	—	140.64	—	—	0.68

Note: $P_s > 3.0$ or $P_L > 18.0$ implies $f_s = 1.0$; no correction for storage size and flow rates is required.

By Equation 2.56:

$$\frac{\bar{D}_h}{H_h} = 0.775 + 0.347 \cdot h_{ss} - \frac{\pi}{2} - 0.505 + 0.0261 \cdot h_{ss} - \frac{\pi}{2} \cos(2\bar{K}_T - 1.8) = 0.2178$$

Therefore,

$$\begin{aligned}\bar{D}_h &= \frac{\bar{D}_h}{H_h} \times H_h = 0.2178 \times 6572 \text{ kJ/m}^2 \cdot \text{day} \\ &= 1431 \text{ kJ/m}^2 \cdot \text{day.}\end{aligned}$$

Using Equation 2.57:

$$\bar{B}_h = \bar{H}_h - \bar{D}_h = 5141 \frac{\text{kJ}}{\text{m}^2 \cdot \text{day.}}$$

From Equation 2.23, we can find

$$\delta_s = 23.45^\circ \sin[360(284 + 15)/365]^\circ = -21.27^\circ.$$

Using Equation 2.30:

$$\begin{aligned}h_{sr(\alpha=0)} &= -\cos^{-1}(-\tan L \cdot \tan \delta_s) \\ &= -\cos^{-1}[-\tan(47^\circ) \cdot \tan(-21.27^\circ)] \\ &= -65.3^\circ \text{ or } -1.14 \text{ rad.}\end{aligned}$$

Therefore, using Equation 2.60:

$$\begin{aligned}\bar{R}_b &= \frac{\cos(L - \beta) \cos \beta_s \sin h_{sr(\alpha=0)} + h_{sr} \sin(L - \beta) \sin \delta_s}{\cos L \cos \delta_s \sin h_{sr(\alpha=0)} + h_{sr(\alpha=0)} \sin L \sin \delta_s} \\ &= \frac{\cos(47^\circ - 62^\circ) \cos(-21.27^\circ) \sin(-65.3^\circ) - 1.14 \sin(47^\circ - 62^\circ) \sin(-21.27^\circ)}{\cos 47^\circ \cos(-21.27^\circ) \sin(-65.3^\circ) - 1.14 \sin 47^\circ \sin(-21.27^\circ)} \\ &= 3.36\end{aligned}$$

Using Equation 2.62:

$$\bar{R}_d = \cos^2(\beta/2) = \cos^2(62^\circ/2) = 0.7347.$$

Then, using Equation 2.64, neglecting reflection,

$$\begin{aligned}\bar{H}_c &= R_b \cdot \bar{B}_h + \bar{R}_d \cdot \bar{D}_h \\ &= 3.363 \times 5141 \text{ kJ/m}^2 \cdot \text{day} + 0.7347 \times 1431 \text{ kJ/m}^2 \cdot \text{day} \\ &= 18,341 \text{ kJ/m}^2 \cdot \text{day}.\end{aligned}$$

The monthly energy demand is

$$\begin{aligned}\text{Load} &= \overline{UA} \times {}^\circ\text{C days} \\ &= 28,000 \text{ kJ} \cdot {}^\circ\text{C} \times 978 {}^\circ\text{C day} \\ &= 27,384 \text{ GJ}.\end{aligned}$$

$$\begin{aligned}(\dot{m}c_p)_c &= (\dot{m}_c/A_c) \times A_c \times c_p \\ &= 55 \text{ kg/h} \cdot \text{m}^2 \times 60 \text{ m}^2 \times 1.9 \text{ kJ/kg} \cdot \text{K} \\ &= 6270 \text{ kJ/h} \cdot \text{K} \text{ or } 1742 \text{ W/K}\end{aligned}$$

$$\begin{aligned}(\dot{m}c_p)_s &= (\dot{m}_s/A_c) \times A_c \times c_{ps} \\ &= 100 \text{ kg/m}^2 \cdot \text{h} \times 60 \text{ m}^2 \times 4.187 \text{ kJ/kg} \cdot \text{K} \\ &= 25122 \text{ kJ/h} \cdot \text{K} \text{ or } 6978 \text{ W/K}\end{aligned}$$

$$(\dot{m}c_p)_{\min} = (\dot{m}c_p)_c.$$

Therefore, Equation 4.59 gives

$$\begin{aligned}F_{hx} &= \left\{ 1 + [F_R U_c A_c / (\dot{m}c_p)_c] [1/\epsilon_{hx} - 1] \right\}^{-1} \\ &= \left\{ 1 + 4.44 \text{ W/m}^2 \cdot \text{K} \times 60 \text{ m}^2 / 1742 \text{ W/K} [1/0.75 - 1] \right\}^{-1} \\ &= 0.951.\end{aligned}$$

Using Equation 5.18,

$$\begin{aligned}P_L &= \frac{A_c F_{hx} F_R U_c \Delta t (T_R - \bar{T}_a)}{\text{Load}} \\ &= \frac{60 \text{ m}^2 \times 0.951 \times 4.44 \frac{\text{W}}{\text{m}^2 \cdot \text{K}} \times (31 \times 24 \times 3600) \text{ s}}{27.384 \text{ GJ} \times (10^9 \text{ J}/1 \text{ GJ})} \\ &= 2.81.\end{aligned}$$

Using Equation 5.19,

$$P_s = \frac{A_c F_{hx} F_R \bar{I}_c(\bar{\tau}_a)}{\text{Load}}$$

$$= \frac{60 \text{ m}^2 \times 0.951 \times 0.7 \times 18,341 \frac{\text{kJ}}{\text{m}^2 \cdot \text{day}} \times 31 \text{ days}}{27.384 \text{ GJ} \times \frac{10^6 \text{ kJ}}{1 \text{ GJ}}}$$

$$= 0.83.$$

From Figure 5.21 or Equation 5.22,

$$f_s = 0.53.$$

Example 5.6

The cost of the solar heating system in Example 5.5 is \$25,000 and the building owner is allowed to take a 30% tax credit for this system. Find the payback period for the system in Example 5.5, if the backup system is a gas furnace with an efficiency of 95%. The average price of natural gas is \$1.20/therm. (Note: Since the density and heating value of natural gas vary depending on the source, natural gas is usually priced in terms of the heating value rather than volume or mass. In the United States, the unit used for natural gas is *therm*. A *therm* is 100,000 Btu, which is approximately equal to the heating value of 1000 ft³ of natural gas at standard conditions.)

Solution

The cost of the system = \$25,000

Tax credit = \$25,000 × 0.30 = \$7500

Effective cost of the system = \$25,000 – \$7500 = \$17,500

From Example 5.5, for January:

$$\text{Energy savings} = (\text{Energy demand})(f_s) = 27.38 \times 0.53 = 14.51 \text{ GJ}$$

$$\begin{aligned} \text{Natural gas savings} &= \text{Energy savings}/\eta_{\text{furnace}} = (14.51 \text{ GJ}/0.9) \\ &\quad (1000 \text{ MJ/GJ}) (1 \text{ therm}/105.5 \text{ MJ}) \\ &= 152.8 \text{ therms}. \end{aligned}$$

Table 5.12 gives the values for each month and for the whole year.

Assuming the life of the system to be approximately 20 years, the calculations are done for 25 years. It is assumed that the system performance will go down by approximately 0.25% per year, the price of

TABLE 5.12

Monthly and Yearly Natural Gas Savings Summary for Example 5.5

Month	Monthly Energy Demand (GJ)	f_s	Monthly Energy Savings (GJ)	Monthly Natural Gas Savings (therms)
Jan	27.38	0.53	14.51	152.8
Feb	22.43	0.69	15.48	163.0
Mar	19.24	0.73	14.05	147.9
Apr	10.25	0.91	9.33	98.2
May	5.26	1	5.26	55.4
Jun	1.9	1	1.90	20.0
Jul	0.28	1	0.28	2.9
Aug	0.53	1	0.53	5.6
Sep	3.92	1	3.92	41.3
Oct	8.76	1	8.76	92.3
Nov	16.86	0.63	10.62	111.9
Dec	23.83	0.49	11.68	123.0
Annual	140.64	0.68	96.31	1014.3

natural gas will go up by 5% per year, and the discount rate is 5%. The calculations are shown in Table 5.13.

For example, for the first year:

$$\text{Yearly savings} = (1014 \text{ therms})(\$1.2/\text{therm}) = \$1217$$

For the fifth year:

$$\text{Yearly natural gas savings} = (1014 \text{ therms})(0.9975)^{(5-1)} = 1004 \text{ therms}$$

$$\text{Price of natural gas} = (\$1.2)(1.05)^{(5-1)} = \$1.459/\text{therm}$$

$$\text{Savings for the year} = (1004 \text{ therms})(\$1.459/\text{therm}) = \$1465$$

$$\text{Present worth of savings} = \$1465/(1 + 0.05)^{(5-1)} = \$1205$$

According to Table 5.13, the payback period is 15 years.

Example 5.7

Find the payback period of the system in Example 5.6 if the backup system is an electric heat pump with the following information:

- The backup conventional system is an electric heat pump that operates on an average COP of 1.2 from November to March, and an average COP of 2.5 for the rest of the year.
- The effective price of electricity is \$0.15/kWh_e in the first year and is expected to increase at a rate of 5% per year.

TABLE 5.13

Energy Savings from the Solar Heating System Based on a Natural Gas Backup System

Year	Energy from Solar Heating System (GJ)	Natural Gas Savings (therms)	Natural Gas Price (\$/therm)	Annual Savings (\$)	Cumulative Annual Savings (\$)	PW Annual Savings (\$)	PW Cumulative Annual Savings (\$)
1	96.31	1014	1.2	1217	1217	1217	1217
2	96.07	1012	1.260	1275	2492	1214	2431
3	95.83	1009	1.323	1335	3827	1211	3642
4	95.59	1007	1.389	1398	5225	1208	4850
5	95.35	1004	1.459	1465	6690	1205	6055
6	95.11	1002	1.532	1534	8224	1202	7257
7	94.87	999	1.608	1607	9831	1199	8456
8	94.64	997	1.689	1683	11,514	1196	9652
9	94.40	994	1.773	1763	13,276	1193	10,845
10	94.16	992	1.862	1846	15,123	1190	12,035
11	93.93	989	1.955	1934	17,056	1187	13,222
12	93.69	987	2.052	2025	19,081	1184	14,406
13	93.46	984	2.155	2121	21,202	1181	15,587
14	93.23	982	2.263	2222	23,424	1178	16,766
15	92.99	979	2.376	2327	25,751	1175	17,941
16	92.76	977	2.495	2437	28,188	1172	19,113
17	92.53	974	2.619	2553	30,740	1169	20,282
18	92.30	972	2.750	2673	33,414	1166	21,449
19	92.07	970	2.888	2800	36,214	1163	22,612
20	91.84	967	3.032	2933	39,147	1161	23,773

Solution

Calculations for the first year:

$$\text{Savings for January} = 14.51 \text{ GJ}$$

Considering an average COP of 1.2 for January and conversion from GJ to kWh_e

$$\text{Monthly electric savings} = (14.51 \text{ GJ}/1.2)(1 \text{ kWh}_e/0.0036 \text{ GJ}) = 3359 \text{ kWh}_e$$

Calculations for the whole year are given in Table 5.14.

Calculations for the 20-year life of the system are shown in Table 5.15.

The payback period is 7 years.

TABLE 5.14

Monthly and Yearly Electric Savings Summary

Month	Monthly Energy Demand (GJ)	f_s	Monthly Energy Savings (GJ)	Monthly Electric Savings (kWh _e)
Jan	27.38	0.53	14.51	3359
Feb	22.43	0.69	15.48	3583
Mar	19.24	0.73	14.05	3251
Apr	10.25	0.91	9.33	1036
May	5.26	1	5.26	584
Jun	1.9	1	1.90	211
Jul	0.28	1	0.28	31
Aug	0.53	1	0.53	59
Sep	3.92	1	3.92	436
Oct	8.76	1	8.76	973
Nov	16.86	0.63	10.62	2459
Dec	23.83	0.49	11.68	2703
Annual	140.64	0.68	96.31	18,685

TABLE 5.15

Annual Savings from the Solar Heating System

Year	Energy from Solar Heating System (GJ)	Electricity Savings (kWh _e)	Electricity Tariff (\$/kWh _e)	Annual Savings (\$)	Cumulative Annual Savings (\$)	PW Annual Savings (\$)	PW Cumulative Annual Savings (\$)
1	96.31	18,685	0.15	2803	2803	2803	2803
2	96.07	18,638	0.158	2936	5738	2796	5598
3	95.83	18,592	0.165	3075	8813	2789	8387
4	95.59	18,545	0.174	3220	12,033	2782	11,169
5	95.35	18,499	0.182	3373	15,406	2775	13,944
6	95.11	18,453	0.191	3533	18,939	2768	16,712
7	94.87	18,406	0.201	3700	22,639	2761	19,473
8	94.64	18,360	0.211	3875	26,514	2754	22,227
9	94.40	18,315	0.222	4059	30,573	2747	24,974
10	94.16	18,269	0.233	4251	34,824	2740	27,714
11	93.93	18,223	0.244	4453	39,276	2733	30,448
12	93.69	18,178	0.257	4663	43,940	2727	33,174
13	93.46	18,132	0.269	4884	48,824	2720	35,894
14	93.23	18,087	0.283	5116	53,940	2713	38,607
15	92.99	18,042	0.297	5358	59,298	2706	41,313
16	92.76	17,996	0.312	5612	64,910	2699	44,013
17	92.53	17,951	0.327	5878	70,788	2693	46,706
18	92.30	17,907	0.344	6156	76,944	2686	49,392
19	92.07	17,862	0.361	6448	83,392	2679	52,071
20	91.84	17,817	0.379	6753	90,146	2673	54,743

5.6 Long-Term Performance of Solar Heating Systems

In order to assess the economic viability of any solar process, its cumulative energy delivery over its economic life (in years or decades) must be known. It is very difficult to calculate this number accurately since (1) solar systems and their energy delivery are subject to the vagaries of local microclimate, which can change on a time scale on the order of hours, and (2) future weather cannot be predicted at this level of detail. The standard approach used to estimate future performance of a solar system is to use a typical year of past weather data and assume that it will represent the future on the average, to engineering accuracy. Two common methods used to predict long-term performance of solar IPH (SIPH) systems are the utilizability method and the TRNSYS (Reddy 1987). These methods can also be used for the design of SIPH systems. Sections 5.6 and 5.7 describe both methods.

5.6.1 Critical Solar Intensity Ratio X

The instantaneous efficiency equation for many solar collectors has been shown to be of the form

$$\eta_c = F(\eta_o - U_c \Delta T^+ / I_c), (\eta_c > 0), \quad (5.29)$$

where ΔT^+ is the value of a collector to ambient temperature difference if positive and η_c is zero otherwise, and F is a heat-exchanger factor (F' , F_R), the expression for which depends on the definition of ΔT^+ . It is technically correct but not always economical to operate the solar collector system if $\eta_c > 0$. In practice, $\eta_c \geq \eta_{min} > 0$ is usually the system turn-on criterion since it is not worthwhile to operate collector loops for cases where η_c is very small.

Equation 5.29 can be used to determine the solar intensity level above which useful energy collection can take place. Solving Equation 5.29 for I_c ,

$$I_c \geq U_c \Delta T^+ / (\eta_o - \eta_{min}/F). \quad (5.30)$$

A dimensionless critical intensity ratio X is generally used and since $\eta_{min} \ll 1$ and F is close to 1, for convenience, the second term in the denominator above is dropped:

$$X \equiv U_c \Delta T^+ / \eta_o I_c \leq 1.0. \quad (5.31)$$

X is seen to be the ratio of collector heat loss to absorbed solar flux at $\eta_c = 0$, that is, at the no-net-energy-delivery condition. In many cases, the daily or monthly averaged daily critical intensity ratio X is of more interest and is defined as*

$$\bar{X} \equiv U_c \overline{\Delta T^+} \Delta t_c / \overline{\eta_o I_c}, \quad (5.32)$$

* Note that U_c can be defined to include pipe heat loss per collector array (Beckman 1978).

where $\bar{\eta}_o$ is the daily averaged optical efficiency and $\bar{\Delta T^+}$ is the daily mean temperature difference *during collection*. These can also be expressed as

$$\bar{\Delta T} = \frac{1}{\Delta t_c} \int_{t_o}^{t_o + \Delta t_c} (T_c - T_a) dt, \quad (5.33)$$

$$\bar{\eta}_o = \frac{\int_{t_o}^{t_o + \Delta t} \eta_o I_c dt}{\int_{t_o}^{t_o + \Delta t_c} I_c dt} \quad (5.34)$$

and

$$\bar{I}_c = \frac{1}{\Delta t_c} \int_{t_o}^{t_o + \Delta t_c} I_c dt. \quad (5.35)$$

The collector cut-in time t_o and cut-off time $t_o + \Delta t_c$ are described shortly. The time $t = [0, 24]$ h is related to the solar hour angle h_s by $t = (180 + h_s)/15$; Δt_c is the collection period in hours. In Equation 5.33, T_c can be collector surface, average fluid, inlet fluid, or outlet fluid temperature, depending upon the efficiency data basis.

5.6.2 Utilizability Method

Utilizability, ϕ , has been used to describe the fraction of solar flux absorbed by a collector, which is delivered to the working fluid. On a monthly time scale,

$$\bar{\phi} = \bar{Q}_u / F \bar{\eta}_o \bar{I}_c < 1.0, \quad (5.36)$$

where the overbars denote monthly average, \bar{Q}_u is the monthly averaged daily total useful energy delivery, and $\bar{\phi}$ is the fraction of the absorbed solar flux that is delivered to the fluid in a collector operating at a fixed temperature T_c . The $\bar{\phi}$ concept does not apply to a system composed of collectors, storage, and other components wherein the value of T_c varies continuously. The fixed temperature mode will occur if the collector is a boiler, if very high flow rates are used, if the fluid flow rate is modulated in response to flux variations to maintain a uniform T_c value, or if the collector provides only a minor fraction of the thermal demand. However, if the flow is modulated, note that the value of F (i.e., F' , F_R) may not remain constant to engineering accuracy.

When T_c is not constant in time as in the case of a collector coupled to storage, the $\bar{\phi}$ concept cannot be applied directly. However, for most concentrators for $CR > 10$, the value of U_c is small and the collector is relatively insensitive to a *small* range of operating temperatures. To check this assumption for a particular process, values of $\bar{\phi}$ at the extremes of the expected temperature excursion can be compared.

The value of $\bar{\phi}$ depends upon many system and climatic parameters. However, Collares-Pereira and Rabl (1979) have shown that only three are of first order—the clearness index \bar{K}_T (see Chapter 2), the critical intensity ratio \bar{X} (Equation 5.32), and the ratio r_d/r_T (see Chapter 2). The first is related to insolation statistics, the second to collector parameters and operating conditions, and the last to collector tracking and solar geometry.

Empirical expressions for $\bar{\phi}$ have been developed for several collector types (Collares-Pereira and Rabl 1979). For nontracking collectors,

$$\bar{\phi} = \exp \left\{ -\bar{X} - \left(0.337 - 1.76\bar{K}_T + 0.55r_d/r_T \right) \bar{X}^2 \right\} \quad (5.37)$$

for

$$\bar{\phi} > 0.4, \bar{K}_T = [0.3, 0.5], \text{ and } \bar{X} = [0, 1.2].$$

Also,

$$\bar{\phi} = 1 - \bar{X} + \left(0.50 - 0.67\bar{K}_T + 0.25r_d/r_T \right) \bar{X}^2 \quad (5.38)$$

for

$$\bar{\phi} > 0.4, \bar{K}_T = [0.5, 0.75], \text{ and } \bar{X} = [0, 1.2].$$

The $\bar{\phi}$ expression for tracking collectors ($CR > 10$) is

$$\bar{\phi} = 1.0 - (0.049 + 1.44\bar{K}_T)\bar{X} + 0.341\bar{K}_T\bar{X}^2 \quad (5.39)$$

for

$$\bar{\phi} > 0.4, \bar{K}_T = [0, 0.75], \text{ and } \bar{X} = [0, 1.2].$$

Also,

$$\bar{\phi} = 1.0 - \bar{X} \quad (5.40)$$

for $\bar{\phi} > 0.4$, $\bar{K}_T > 0.75$ (very sunny climate), and $\bar{X} = [0, 1.0]$ for any collector type.

Equations 5.37 through 5.40 were developed using curve-fitting techniques emphasizing large $\bar{\phi}$ values since this is the region of interest for most practical designs. Hence, they should be considered accurate to $\pm 5\%$ only for $\bar{\phi} > 0.4$. Empirical equations for utilizability were also given by Klein et al.; however, these equations were restricted to flat-plate collectors. Since SIPH systems may use concentrating solar collectors, equations given by Collares-Pereira and Rabl (1979) are used in this chapter.

5.6.3 Example Calculation

To illustrate the use of the long-term method, an example will be worked in stepwise fashion. The several steps used are as follows:

1. Evaluate \bar{K}_T from terrestrial \bar{H}_h data and extraterrestrial $\bar{H}_{o,h}$ data.
2. Calculate r_d/r_T for the concentration ratio and tracking mode for the collector.
3. Calculate the critical intensity ratio \bar{X} from Equation 5.32 using a long-term optical efficiency value $\bar{\eta}_o$ and monthly average collector-plane insolation.

$$\bar{I}_c = (r_T - r_d \bar{D}_h / \bar{H}_h) \bar{H}_h. \quad (5.41)$$

The collection time Δt_c may need to be determined in some cases for non-tracking, low-concentration collectors by an iterative method as described in Section 5.6.4.

Example 5.8

Find the energy delivery of a polar-mounted, parabolic trough collector operated for 8 h per day ($\Delta t_c = 8$) during March in Kabul, Afghanistan ($L = 34.5^\circ\text{N}$). The collector has an optical efficiency $\bar{\eta}_o$ of 60%, a heat-loss coefficient $U_c = 0.5 \text{ W/m}^2 \cdot ^\circ\text{C}$, CR = 20, and heat-removal factor $F_R = 0.95$. The collector is to be operated at 150°C . The mean, horizontal solar flux is $5.23 \text{ kWh/m}^2 \cdot \text{day}$ and the ambient temperature is 10°C .

Solution

Following the three-step procedure above, the clearness index is calculated:

$$\bar{H}_{o,h} = 8.22 \text{ kWh/m}^2 \cdot \text{day} \quad (\text{Table A2.1}) \quad \bar{K}_T = 5.23 / 8.22 = 0.64.$$

From Equation 2.52 and $h_{ss} = 90^\circ$ or $\pi/2$ radians

$$\bar{D}_h = 0.775 + 0.347(\pi/2 - \pi/2) - (0.505 + 0.0261(\pi/2 - \pi/2)) \cdot (\cos(2 \times 0.64 - 1.8))$$

$$\bar{H}_h = 0.34.$$

The geometric factors r_d and r_T are calculated from expressions in Table 3.13:

$$r_T = (ah_{coll} + b \sin h_{coll})/d \cos L,$$

$$r_d = (h_{coll}/d)(1/\cos L + \cos h_{sr}(\alpha = 0)/(CR)) - \sin h_{coll}/d(CR),$$

where

$$h_{coll} = (\Delta t_c/2) \times 15^\circ = 60^\circ = 1.047 \text{ rad.}$$

If the collection period is centered about solar noon,

$$h_{sr}(\alpha = 0) = 90^\circ = 1.571 \text{ rad, (for March 21)}$$

$$a = 0.409 + 0.5016 \sin 30^\circ = 0.66,$$

$$b = 0.6609 - 0.4767 \sin 30^\circ = 0.42,$$

$$d = \sin 90^\circ - 1.571 \cos 90^\circ = 1.0,$$

in which case

$$r_T = (0.66 \times 1.047 + 0.42 \times \sin 60^\circ)/1.0 \cos 34.5^\circ = 1.28,$$

$$r_d = (1.047/1.0)[1/\cos 34.5^\circ + \cos 90^\circ/20] - \sin 60^\circ/1.0 \times 20 = 1.31.$$

Finally, the critical intensity ratio is

$$\bar{X} = U_c \overline{\Delta T^+} \Delta t_c / \bar{\eta}_o \bar{I}_c,$$

and the collector-plane insolation \bar{I}_c from Equation 5.41 is

$$\bar{I}_c = (1.28 - 1.31 \times 0.34) \times 5.23 = 5.4 \text{ kWh/m}^2;$$

thus,

$$\bar{X} = 0.5 \times (150 - 10) \times 8 / 0.6 \times 5400 = 0.173.$$

The utilizability $\bar{\phi}$ from Equation 5.39 is

$$\bar{\phi} = 1.0 - (0.049 + 1.44 \times 0.64)(0.173) + 0.341 \times 0.64 \times (0.173)^2 = 0.84.$$

Finally, the useful energy is

$$Q_u = F_R \bar{\eta}_o \bar{I}_c \bar{\phi} = 0.95 \times 0.6 \times 5.4 \times 0.84 = 2.58 \text{ kWh/m}^2 \cdot \text{day}$$

for the month of March on the average.

5.6.4 Collection Period (Δt_c)

The collection period Δt_c can be dictated by either optical or thermal constraints. For example, with a fixed collector, the sun may pass beyond the acceptance limit or be blocked by another collector, and collection would then cease. Alternately, a high-efficiency solar-tracking concentrator operating at relatively low temperature might be able to collect from sunrise to sunset. A third scenario would be for a relatively low-concentration device operating at high temperature to cease to have a positive efficiency during daylight at the time that heat losses are equal to the absorbed flux. In this case, the cutoff time is dictated by thermal properties of the collector and the operating conditions.

Collares-Pereira and Rabl (1979) have suggested a simple procedure to find the proper value of Δt_c . Useful collection Q_c is calculated using the optical time limit first; that is, $\Delta t_c = 2 \min \{[h_{sr}(\alpha = 0), h_{sr}(i = 90)]/15\}$. Second, Q_u is calculated for a slightly shorter period, say, by one-half hour, than the optical limit. If this value of Q_u is larger than that for the first, optically limited case, the collection period is shorter than the optical limit. The period is then further reduced until the maximum Q_u is reached.

The above method assumes that collection time is symmetric about solar noon. This is almost never the case in practice since the heat collected for an hour or so in the morning is required to warm the fluid and other masses to operating temperature. A symmetric phenomenon does not occur in the afternoon. If the time constant of the thermal mass in the collector loop is known, the collection period may be assumed to begin at t_o , $\Delta t_c/2$ h (from above symmetric calculation) before noon decreased by two or three time constants. Another asymmetry can occur if solar flux is obstructed during low sun angle periods in winter. It is suggested that r_T and r_d from Table 3.13 under asymmetric collection conditions be calculated from

$$r_T = [r_T(h_{s,stop}) + r_T(h_{s,start})]/2 \quad (5.42)$$

$$r_d = [r_d(h_{s,stop}) + r_d(h_{s,start})]/2, \quad (5.43)$$

where the collection starting and stopping hour angles account for transients, shading, and so on, as described above:

$$h_{s,start} = 180 - 15t_o, \quad (5.44)$$

$$h_{s,stop} = 180 - 15(t_o + \Delta t_c). \quad (5.45)$$

Example 5.9

Calculations in Example 5.8 were based on $\Delta t_c = 8$ h. Repeat for 10 h to see the effect of collection time if a symmetric collection period about noon is used.

Solution

The values of r_T and r_d for $h_{\text{coll}} = 75^\circ = 1.31$ rad are

$$r_T = (0.66 \times 1.31 + 0.42 \times \sin 75^\circ) / 1.0 \cos 34.5^\circ = 1.98,$$

$$r_d = (1.31 / 1.0)(1 / \cos 34.5^\circ) - \sin 75^\circ / 20 = 1.54.$$

The collector-plane insolation is then

$$\bar{I}_c = (1.98 - 1.54 \times 0.34) \times 5.23 = 7.6 \text{ kWh/m}^2$$

and

$$\bar{X} = [0.5 \times (150 - 10) \times 10] / 0.6 \times 7600 = 0.154.$$

Then, $\bar{\phi}$ is 0.86 from Equation 5.39 and the useful energy delivery is 3.7 kWh/m²-day. Hence, it is worthwhile operating the collector for at least 10 h. The calculation can be repeated by the reader for an asymmetric case 4 h before noon and 6 h after to determine the effect of warm up.

5.6.5 Long-Term Performance of Collector Systems with Storage

Section 5.6.2 of this chapter described a method of predicting long-term performance of a solar collector operated at a temporally constant temperature. This situation is a good approximation of the operating conditions experienced by several types of generic thermal systems. Other systems, however, do not operate at constant temperature and the $\bar{\phi}$ method cannot be used. Although there is no simplified performance method now extant for varying temperature systems, Klein and Beckman (1979) have correlated some modeling results on collector-heat exchanger-storage subsystems coupled to a uniform, process-like load operating above some temperature T_{proc} . The method is called the $\bar{\phi}, f$ chart and is described below. Although the method was developed for flat-plate collectors and uses a different $\bar{\phi}$ calculation method than used above, it can be applied equally well to concentrators.

The calculation method requires first the determination of the utilizationability $\bar{\phi}$ from Equations 5.37 through 5.40. This represents the maximum energy deliverable to a load at T_{proc} . When storage is present and collected solar heat is greater than the demand, the temperature of storage, and hence

the collector inlet temperature, will rise. (The $\bar{\phi}, f$ method applies only to well-mixed, sensible heat storage with liquid heat-transfer fluids and storage media.) Hence, the monthly averaged, daily useful energy collected Q_u will be less than $F\bar{\eta}_o\bar{I}_c\bar{\phi}$, but storage may permit a greater fraction of the demand to be met by solar since the maximum amount of heat $F\bar{\eta}_o\bar{I}_c\bar{\phi}$ collectable may be more than can be used, depending on the demand amount. The $\bar{\phi}, f$ method can be employed to find Q_u in a system with storage.

The technical basis for the $\bar{\phi}, f$ method lies in the nondimensionalization of governing energy equations for a solar thermal system. Dimensionless groups, so identified, are used to correlate monthly thermal energy delivery-to-load for various systems simulated in various climates by an hourly time-scale computer model. The two dimensionless groups identified for use in the $\bar{\phi}, f$ method, in addition to $\bar{\phi}$ ($\bar{\phi}$ is defined in this context relative to the minimum temperature acceptable to the process T_{proc} , not relative to the collector temperature as in Section 5.6.2), are a solar parameter P_s , a measure of long-term solar gain by the collector receiver, and a collector heat-loss parameter P_L , a measure of long-term heat loss at a fixed collector-to-ambient temperature difference of 100°C. This 100°C value does not restrict the generality of the results, however. In equation form,

$$P_s = F_R \bar{\eta}_o \bar{I}_c A_c N_d / L, \quad (5.46)$$

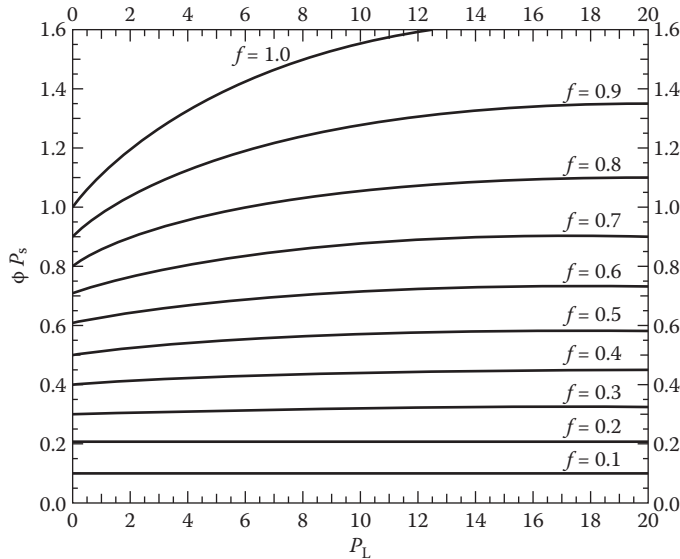
$$P_L = F_R U_c A_c N_h 100 / L, \quad (5.47)$$

in which F_R is given in Equations 3.44 and 3.46. L is the monthly thermal demand, and N_d and N_h are the number of days and hours in a month. The $\bar{\phi}, f$ chart predicts the monthly solar load fraction $f_s(\bar{\phi}, P_s, P_L) \equiv Q_u/L$ by an empirical equation (Klein and Beckman 1979)

$$f_s = \bar{\phi} P_s - a [e^{3.85 f_s} - 1] [1 - e^{-0.15 P_L}], \quad (5.48)$$

where $a = 0.015 \frac{Mc_p}{350A_c}^{-0.76}$, in which m is expressed in kg, c_p in kJ/kg·°C, and A_c in m².

Figure 5.23 is a $\bar{\phi}, f$ chart for a standard storage size of 350 kJ/°C·m² and is plotted with values of $\bar{\phi} P_s$ and P_L to give a monthly value of f_s . The calculation of $\bar{\phi} P_s$ and P_L is done once for each month of an average year, and the totals are added to give annual performance. Example 5.10 shows how the method is used. It is noted that $\bar{\phi} P_s$, the ordinate, is the ratio of maximum possible energy delivered by a collector operating at fixed T_{proc} , $(F\bar{\eta}_o\bar{I}_c\bar{\phi}A_c)$, to the monthly load L . At values of $f_s > 0.4$, the $\bar{\phi}, f$ curves are not independent of

**FIGURE 5.23**

The $\bar{\phi}, f$ chart used to calculate average, monthly solar fraction $f(f_s)$ of solar thermal systems.

X since at progressively higher load fractions, the average storage and collector temperatures are higher and collected solar heat per unit area is smaller because collector efficiency is lower at higher temperature.

This $\bar{\phi}, f$ chart is based upon several limiting assumptions that should be noted in interpreting f_s values:

1. The load L is distributed uniformly over the month between the hours of 6:00 and 18:00.
2. Standard storage amount is fixed at $350 \text{ kJ}/^\circ\text{C} \cdot \text{m}^2$ (approximately 2 gallons of $\text{H}_2\text{O}/\text{ft}^2$ or $84 \text{ l}/\text{m}^2$). For nonstandard storage, correction a (see Equation 5.48) is applied.
3. No energy is rejected from storage; therefore, the vessel is assumed to be designed for the peak temperature and pressure expected.
4. Storage is well mixed and no storage-to-load heat exchanger is used.
5. The load device uses solar heat at temperature-independent efficiency to meet the load L . Therefore, the load device cannot be a turbine, for example.
6. No parasitic heat losses from storage occur.

Some of these restrictions can be relaxed using work on the $\bar{\phi}, f$ method conducted by Klein and Beckman (1979). Users of the $\bar{\phi}$ methods must exercise caution in the proper choice of the $\bar{\phi}$ time scale. In the method presented

here, $\bar{\phi}$ and \bar{I}_c are calculated over the collection period Δt_c , not over all daylight hours. The method developed by Klein uses $\bar{\phi}$ and \bar{I}_c for all daylight hours. Although the Collares-Pereira $\bar{\phi}$ value can be used with the $\bar{\phi}, f$ chart, the two methods of finding $\bar{\phi}$ itself must not be confused.

Example 5.10

Repeat Example 5.8 from Section 5.6.3 for Kabul, Afghanistan, for a monthly averaged load of 260 kWh/day using a collector of 100 m². From the previous example, recall that $F_R \bar{\eta}_o = 0.57$, $F_R U_c = 0.475 \text{ W/m}^2 \cdot ^\circ\text{C}$, $\bar{I}_c = 5.4 \text{ kWh/m}^2$, and $\bar{\phi} = 0.84$. What is the effect of storage on energy delivery per unit collector area?

Solution

First calculate P_s and P_L , then use the $\bar{\phi}, f$ chart to find the solar fraction.

$$P_s = F_R \bar{\eta}_o \bar{I}_c A_c N_d / L = 0.57 \times 5.4 \times 100 \times 31 / (260 \times 31) = 1.18,$$

$$P_L = F_R U_c A_c N_h 100 / L$$

$$= 0.475 \times 100 \times (31 \times 24) \times 100 / (260 \times 31 \times 1000) = 0.44.$$

The value of f_s from the chart with $P_L = 0.44$ and $\bar{\phi} P_s = 0.99$ is $f_s = 0.97$. Therefore, the energy delivery per unit area is $0.97 \times 260 / 100 = 2.52 \text{ kWh/m}^2 \cdot \text{day}$, nearly identical to the result using the $\bar{\phi}$ method. This is a result of the low value of U_c for the concentrator and its resulting insensitivity to temperature fluctuations above T_{proc} . The reader may repeat the calculations for a 200-m² collector with $U_c = 2.0 \text{ W/m}^2 \cdot ^\circ\text{C}$ to show that $\bar{\phi} = 0.43$, $P_L = 1.75$, $P_s = 2.37$, and $f_s = 0.85$. The energy delivery per unit area is then 1.11 kWh/m²·day compared with 1.32 kWh/m²·day predicted by the $\bar{\phi}$ method. Hence, the effect of storage is to reduce the unit energy delivery by 16% for the more lossy collector.

5.7 TRNSYS Computer Simulation Program

TRNSYS (Transient System Simulation) is a sequential-modular transient simulation program developed at the Solar Energy Laboratory of the University of Wisconsin (Klein et al. 1979). It is a widely used, detailed, design tool involving hourly simulations of a solar energy system over an entire year. The TRNSYS computer program contains FORTRAN subroutines of almost all the components that are necessary to build a solar energy system. The component models, which are either empirical or analytical, describe the component performance with algebraic or differential equations. A system

simulation model is created by interconnecting the models of individual components. The resulting set of simultaneous algebraic or differential equations is solved by TRNSYS. This public domain software is constantly being upgraded and is backed by technical support.

5.8 Solar Industrial Process Heat

IPH consumed over 15 EJ (10^{18} J) of energy in 1972 in the United States and this amount grew to 23 EJ by 1994. Although detailed industry specific numbers such as in Table 5.16 are not available for the present use, the total amount of IPH for the world grew to 1748 MTOE or 73 EJ according to the IEA 2010

TABLE 5.16

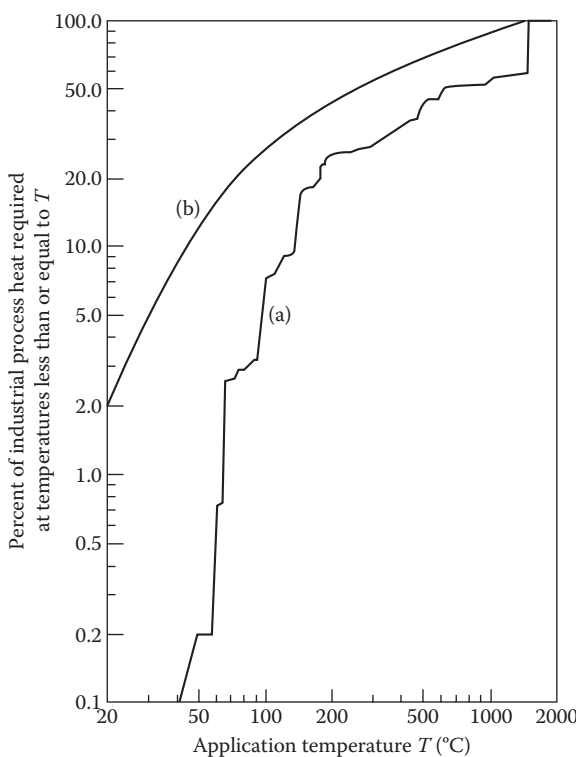
Summary of US Industrial Heat Usage by SIC Category for 1971 and 1994

SIC Group	Quantities in 10^{12} kJ	
	1971	1994
20. Food and kindred products	779	1254
21. Tobacco products	14	W
22. Textile mills	268	327
23. Apparel	22	W
24. Lumber and wood products	188	518
25. Furniture	37	73
26. Paper and allied products	2006	2812
27. Printing and publishing	16	118
28. Chemicals	2536	5621
29. Petroleum products	2576	6688
30. Rubber	158	303
31. Leather	19	W
32. Stone, clay and glass	1541	996
33. Primary metals	3468	2597
34. Fabricated metal products	295	387
35. Machinery	283	260
36. Electrical equipment	213	256
37. Transportation	310	383
38. Instruments	53	113
39. Miscellaneous	72	W
Subtotal	14,854	22,854

Source: Intertechology Corporation, Analysis of the economic potential of solar thermal energy to provide industrial process heat, ERDA Rep. No. COO/2829-1, 3 volumes, 1977.

Note: W, withheld to avoid disclosing data for individual establishments.

World Energy Outlook (IEA 2010). IEA projects the global IPH to grow to 2150 MTOE or 92 EJ by 2020. According to the latest studies (Taibi et al. 2012; Vajen et al. 2012), renewable energy could provide more than 20% of it. The economic outlook for industrial solar heat appears to be extremely favorable because process heat solar collectors could be used throughout the year and each system can be designed to fit the temperature level required for its specific applications, which is particularly important in the use of process heat. Table 5.16 shows the amount of heat used by selected industries in the United States. Majority of the heat is used in the mining, food, textiles, lumber, paper, chemicals, petroleum products, stone-clay-glass, and primary metals (Kreider 1979). The breakdown of industrial energy usage is as follows (Intertechology Corporation 1977): process steam, 41%; direct process heat, 28%; shaft drive, 19%; feedstock, 9%; and other, 3%. In addition to the quantity of heat, quality (i.e., temperature) is also very important to match the proper solar collection system to the application. Figure 5.24 shows the cumulative process heat use by temperature requirement (Intertechology Corporation 1977). It is seen that approximately 25% of the heat is used at

**FIGURE 5.24**

Distribution of US process heat use by required temperature level: (a) heat requirements; (b) IPH requirements plus preheat from 15°C.

temperatures below 100°C, which may be provided by flat-plate collectors, CPCs, or solar ponds, approximately 50% of the heat is used at temperatures below 260°C, and 60% is used below 370°C. Therefore, 50%–60% of all the US process heat could be delivered by parabolic trough collectors.

Since 50% of the IPH requirements that are below 260°C are provided by fossil fuels, it represents enormous waste of availability. Table 5.17 shows approximate second law efficiencies for IPH systems below 260°C assuming 80% first law efficiency for fossil fuel systems. Although the numbers in Table 5.17 are not precise, they do point out the potential to increase the efficiency of energy use by replacing the high-quality fossil fuels with SIPH. SIPH systems are quite simple and are based on the solar heating systems already discussed. The selection of the type of solar collectors depends on the process temperature requirements. Table 5.18 gives the temperature requirements and the type of solar collectors suitable for the process.

The material and type of storage depend on the temperature requirement, the design storage duration, the required energy density (space constraints), and the charging and discharging characteristics. These topics are discussed in detail in Chapter 4. The storage duration for SIPH systems is rarely more than 1 day since the solar systems are designed to displace part of the fossil fuel requirements. The size of storage must be evaluated based on a cost-benefit analysis. Land availability can be critical for SIPH for existing industries. However, in many cases, roofs of industrial buildings can be utilized for this purpose.

Since SIPH components and systems have already been described in Chapters 3 and 4 and this chapter, this section will give some examples of SIPH systems and a methodology for long-term performance prediction.

TABLE 5.17

Second Law Efficiencies for US Industrial Processes below 260°C (500°F)

Temperature	Fraction of US Process Heat (%)	Fossil Fuel (%) (η_2)	Solar (%) (η_2)
29.4°C (85°F)	10	<1	12
49°C (120°F)	5	6	52
65.6°C (150°F)	5	10	65
79.4°C (175°F)	5	13	71
98.9°C (210°F)	5	16	72
121.1°C (250°F)	5	20	77
148.9°C (300°F)	5	25	83
187.8°C (370°F)	5	30	85
237.8°C (460°F)	5	35	85
Total/averages	50	16	61

Source: Kreider, J.F., *Medium and High Temperature Solar Processes*, Academic Press, New York, 1979.

TABLE 5.18
IPH Applications and Types of Possible Solar Energy Systems

Industry/Process	Energy Form	Temperature (°C)	Shallow Ponds or Simple Air Heaters	Flat Plates	Fixed Compound Surfaces	Single-Tracking Troughs	Central Receivers
Aluminum							
Bayer process digestion	Steam	216				X	
Automobile and truck manufacturing							
Heating solutions	Steam (water) Air	49–82 21–29	X X				
Heating makeup air in paint booths							
Drying and baking	Air	163–218		X		X	
Concrete block and brick							
Curing product	Steam	74–177		X		X	
Gypsum							
Calcining	Air	160		X		X	
Curing plasterboard	Steam (air)	299		X		X	
Chemicals							
Borax, dissolving and thickening	Steam	82–99		X		X	
Borax, drying	Air	60–77	X		X		
Bromine, blowing brine/distillation	Steam	107				X	
Chlorine, brine heating							
Chlorine, caustic evaporation	Steam (water)	66–93		X		X	
Phosphoric acid, drying	Air	143–149 121				X	

(Continued)

TABLE 5.18 (CONTINUED)
IPH Applications and Types of Possible Solar Energy Systems

Industry/Process	Energy Form	Temperature (°C)	Shallow Ponds or Simple Air Heaters	Flat Plates	Fixed Compound Surfaces	Single-Tracking Troughs	Central Receivers
Phosphoric acid, evaporation	Steam	160		X	X		X
Potassium chloride, leaching	Steam	93		X	X	X	X
Potassium chloride, drying	Air	121					X
Sodium metal, salt purification	Steam	135		X			X
Sodium metal, drying	Steam (air)	116					X
Food							
Washing	Water	49–71		X	X		
Concentration	Steam (water)	38–43		X	X		
Cooking	Steam	121–188			X	X	
Drying	Steam (air)	121–232		X		X	
Glass							
Washing and rinsing	Water	71–93		X	X		
Laminating	Air	100–177			X	X	X
Drying glass fiber	Air	135–141			X	X	X
Decorating	Air	21–93		X			
Lumber							
Kiln drying	Air	66–99		X	X	X	
Glue preparation/plywood	Steam	99–177			X	X	
Hot pressing/fiberboard	Steam	199				X	X
Log conditioning	Water	82			X		
Mining (Frasch sulfur)	Presurized						
Extraction	Water	160–166				X	X

Source: Kreider, J.F., *Medium and High Temperature Solar Processes*, Academic Press, New York, 1979.

5.9 Examples of SIPH Systems

Most of the IPH systems below 200°C require hot water, steam, or hot air. A typical low-temperature SIPH system is shown schematically in Figure 5.25. If the heat is needed in process air, water-to-air heat exchangers may be used or air heating collectors and rock storage may be used. Hot air is needed typically in agricultural drying, which may be provided by passive solar air heaters. If a large body of water is available, solar ponds may be used for low-temperature applications. Solar ponds are described later in this chapter.

A high-temperature SIPH system may be designed to use low-temperature, medium-temperature, and high-temperature collectors in stages in order to minimize the cost and maximize the efficiency. A schematic of such a system designed for textile dyeing process is shown in Figure 5.26.

5.9.1 SIPH for Textile Industries

The textile industry is one of the 10 largest energy-consuming industries. Of all the energy used in the textile industry, 60%–65% is used in wet processing, including dyeing, finishing, drying, and curing. The energy for wet processing is used as hot water and steam. The textile industry in the United States uses approximately 500 billion liters of water per day and approximately 25% of this water is used at an average temperature of 60°C. Tables 5.19 and 5.20 show typical calculations for determining energy consumption for jet dyeing (Wagner 1977) and tenter frame drying (Hebrank 1975), respectively, for 100% textured polyester circular knit fabric (Goswami and Langley 1987). In the analysis in Table 5.19, Wagner assumed 40% moisture content in the fabric. In carpet dyeing, moisture may be as much as 300% (Lowery et al. 1977). Drying involves the use of high-pressure (6 atm) steam so that the condensed water may be used for other processes. There are no known examples of SIPH for textile drying, but there are a number of examples of

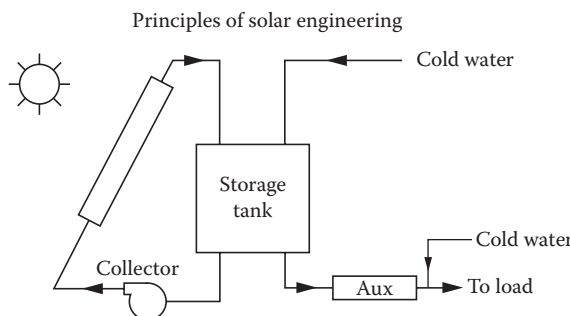
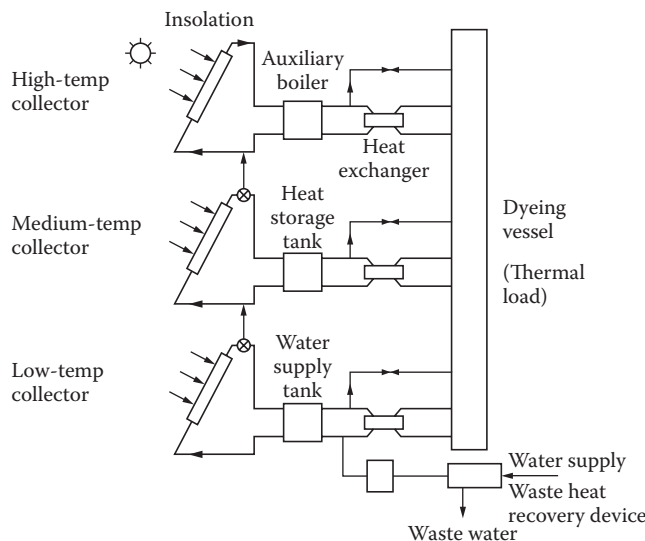


FIGURE 5.25

Schematic of a low-temperature SIPH system.

**FIGURE 5.26**

Schematic of a SIPH system for dyeing process.

TABLE 5.19Sample Calculations^a: Heat for Pressure Jet Dyeing

Scour	Energy Consumption GJ/100 kg Fabric
Heat bath, 21°C–60°C	163
Heat cloth, 21°C–60°C	9
Raise bath to 129°C	293
Raise cloth to 129°C	14
Replace heat loss from radiation	
During cycle 21°C–129°C	23
During dyeing at 129°C	65
Scour at 60°C	172
Total	739

Source: Goswami, B.C. and Langley, J., A Review of the Potential of Solar Energy in the Textile Industry, a chapter in *Progress in Solar Engineering*, Hemisphere Publishing Corporation, Washington, 1987; and Wagner, R., *Energy Conservation in Dyeing and Finishing, Textile Chemists and Colorists*, Vol. 9, p. 52, 1977.

^a Fabric load = 227 kg, bath ratio 10 of 1; cycle time = 2.75 h.

SIPH for textile dyeing. One of those is for a dyeing operation at the Riegel Textile Corp. plant in LaFrance, South Carolina (Goswami and Klett 1982; Goswami and Langley 1987). Figure 5.27 shows a schematic of the system.

The original system used evacuated tube collectors made by General Electric Corp. That system failed because of repeated tube breakage. Since

TABLE 5.20

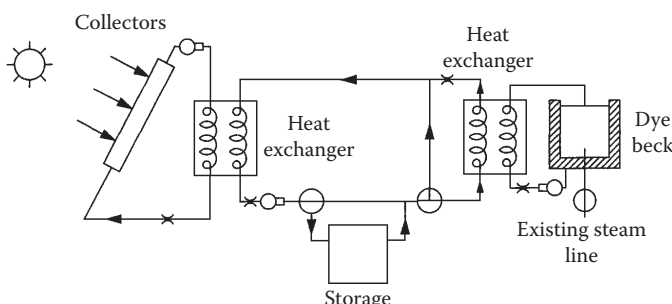
Energy Consumption during Tenter Frame Drying

Steps	Energy Requirements (MJ/100 kg H ₂ O)
Evaporate water	
$100 \text{ kg} \times 4.18 \text{ kJ/kg}\cdot\text{°C} (100\text{°C}-21\text{°C})$	33
Latent heat of vaporization	226
Raise steam temperature to 121°C	
$100 \text{ kg} \times 1.9 \text{ kJ/kg}\cdot\text{°C} (121\text{°C}-100\text{°C})$	4
Heat air (24 kg air/kg H ₂ O)	
$2400 \text{ kg} \times 1.015 \text{ kJ/kg}\cdot\text{°C} (121\text{°C}-21\text{°C})$	244
Heat fabric to 121°C	
$100 \text{ kg} \times 100/40 \times 2.08 \times (121\text{°C}-21\text{°C})$	52
Dryer run at 121°C	559
Dryer run at 149°C	647 (+15%)

Effect of Fabric Moisture Content on Tenter Frame Energy Demand

Steps	30%	80%
Evaporate water		
Raise temperature (21°C–100°C)	10.0	26.5
Latent heat of vaporization	67.7	180.5
Raise steam temperature to 121°C	1.4	3.5
Raise air to 121°C	73.3	195.2
Total	152.4	405.7

Source: Goswami, B.C. and Langley, J., A review of the potential of solar energy in the textile industry, a chapter in *Progress in Solar Engineering*, Hemisphere Publishing Corporation, Washington, DC, 1987; and Hebrank, W.H., *American Dyestuff Reporter*, Vol. 63, p. 34, April 1975.

**FIGURE 5.27**

Schematic of solar energy system at Riegel Textile Corporation plant at LaFrance, South Carolina.

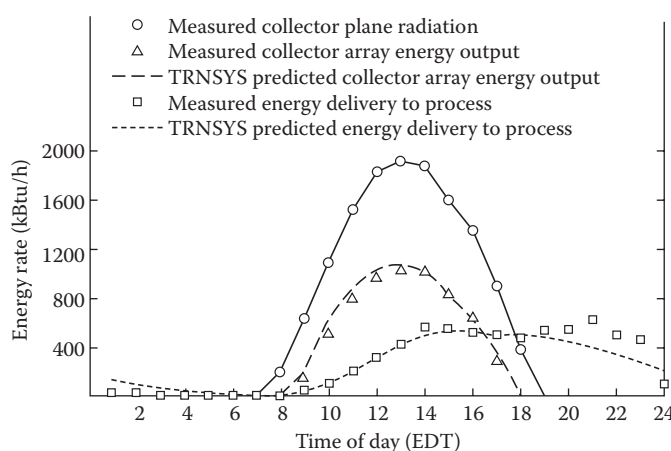
the dyeing process used water at a temperature of 70°C, the evacuated tube collectors were replaced with flat-plate collectors. The flat-plate collectors at this plant have copper absorbers and tubes painted flat black, low iron textured and tempered glass cover, and bronze-enamelled steel frames. The system has 621 m² of collector area.

The dyeing process at this plant is an atmospheric Dye Beck batch process at a maximum temperature of 90°C, which is also typical of the textile industry in the United States (Goswami and Langley 1987). The batch dyeing process involves heating of approximately 4500 liters of inlet water from 10°C–25°C to 90°C. The typical dye cycle is shown in Table 5.21. The refurbished SIPH system at Riegel Textile plant has been operating successfully. The system was simulated using the TRNSYS computer model (TRNSYS 1981). Figure 5.28 shows the actual performance of the system and that predicted by TRNSYS. According to the measured performance of the system from August 14 to October 8, 1983, the system operated with an efficiency of 46% (Goswami and Langley 1987).

TABLE 5.21

Typical Dye Beck Heat Requirements

Dye Process Operation	Temperature of Dye Beck (°C)	Time Interval of Cycle (h)	Percentage of Total Process Energy
Heat the initial load	16–32	0.5	7
Dyeing preparation	32–88	0.5	22
Dye period	88	7–9	68
Cool and reheat for dye fixation	32–43	1.0	3

**FIGURE 5.28**

Actual and predicted system operation, August 16, 1983.

5.9.2 SIPH System for Milk Processing

Food systems use approximately 17% of the US energy (Singh et al. 1986), almost 50% of which is for food processing as hot water (<100°C) or hot air. Proctor and Morse (1975) show that over 40% of the energy demand in the beverage industry in Australia was in the form of hot water between 60°C and 80°C. Considering the temperature and heat requirements of food processing, one would be tempted to conclude that SIPH would be ideal. However, many food processing requirements are seasonal, which may not be economical considering the present price of the conventional fuels unless the SIPH system can be used for the majority of the year. One application that is year-round is milk processing. Singh et al. (1986) simulated a SIPH system for milk processing in the United States using TRNSYS. The unit operations (and their respective temperatures) for this plant compatible with solar thermal energy are as follows:

1. Boiler feed make-up water (100°C)
2. Pasteurizer make-up water (21°C)
3. Case washer and rinsing (49°C)
4. Clean up (71°C)
5. High temperature short time clean up (79°C)
6. Bottle water (93°C)

They estimated that for a plant producing 170,000 kg/week of milk and 98,000 kg/week of orange juice, a total of 621.3 GJ (or 80%) of energy demand was compatible with solar energy in summer and 724.9 GJ (or 93%) of energy demand was compatible in winter. Simulating a solar system similar to the one in Figure 5.25, they found that a 4000 m² collector area could provide approximately 30%–35% solar fraction for the milk processing plant in Madison, Wisconsin; Fresno, California; or Charleston, South Carolina (Singh et al. 1986).

PROBLEMS

1. The no-load temperature of a building with internal heat sources is given by Equation 5.6. How would this equation be modified to account for heat losses through the surface of an unheated slab, the heat losses being independent of ambient temperature?
2. An unheated garage is placed on the north wall of a building to act as a thermal buffer zone. If the garage has roof area A_r , window area A_{wi} , door area A_d , and wall area A_{wa} , what is the effective U value for the north wall of the building if its area is A_n ? The garage floor is well insulated and has negligible heat loss. Express the effective

U value in terms of the *U* values and areas of the several garage surfaces.

3. What is the annual energy demand for a building in Denver, Colorado, if the peak heat load is 44 kJ/s based on a design temperature difference of 42°C? Internal heat sources are estimated to be 6 kJ/s and the design building interior temperature is 20°C.
4. What is the January solar load fraction for a water-heating system in Washington, DC, using 100 m² of solar collector if the water demand is 4 m³/day at 65°C with a source temperature of 12°C? No heat exchanger is used and the solar collector efficiency curve is given in Figure 5.20; the solar collector is tilted at an angle equal to the latitude.
5. Repeat Problem 4 for Albuquerque, New Mexico, in July if the water source temperature is 17°C.
6. Explain how the *f*-chart (Figure 5.21) can be used *graphically* to determine the solar load fraction for a range of collector sizes once the solar and loss parameters have been evaluated for only one system size. *Hint:* consider a straight line passing through the origin and the point (*P_s*, *P_L*).
7. The *f*-chart was generated using data for flat-plate collectors. What modifications would be necessary to use it for a compound parabolic concentrator collector? Describe the effect on each *f*-chart parameter in Table 5.7.
8. In an attempt to reduce cost, a solar designer has proposed replacing the shell-and-tube heat exchanger in Figure 5.8 with a tube coil immersed in the storage tank. The shell-and-tube heat exchanger originally specified had a surface area of 10 m² and a *U* value of 2000 W/m²·K to be used with a 100-m² solar collector. Using a Nusselt number correlation for free convection around a tube

$$\overline{\text{Nu}_D} = \frac{\overline{hD}}{k} = 0.53 (\text{Gr}_D \text{Pr})^{0.25}$$
 to estimate the *h* value of the submerged coil, find the length of a 12-mm-diameter copper pipe needed to achieve the same value of *UA* product as the shell-and-tube heat exchanger. What percentage of the storage tank volume would be consumed by this coil if 50 kg of water is used per square meter of collector? Use a storage water temperature of 60°C and a collector water outlet temperature of 70°C for the calculations.
9. If a solar system delivers 2500 MJ/m²·year with a water flow rate of 30 kg/m_c²·h and a plate efficiency factor *F'* = 0.93, how much energy will it deliver if the flow rate is doubled? Neglect the effect of flow rate on *F'*; the collector has a heat-loss conductance of 4 W/m²·°C.

10. How large (MJ/h) should a heat-rejection system be if it must dump the entire heat production of a 1000-m² solar collector array in Denver, Colorado, on August 21 if the collector is at 100°C and the ambient temperature is 35°C? Use solar collector data in Figure 5.20 and hourly solar radiation data in Appendix 2.
11. Use the *f*-chart to determine the amount of solar energy that can be delivered in Little Rock, Arkansas, in January for the following solar and building conditions:

Building

Load: 20 GJ/month

Latitude: 35°N

Solar System

Collector tilt: 55°, facing south

Area: 60 m²

Ambient temperature: 5°C

Collector efficiency curve: see Figure 5.20

No heat exchanger used

Nominal storage, flow rate, and load heat exchanger values used

12. Repeat Problem 11 if storage size is doubled and halved.
13. Repeat Problem 11 for an air-heating system for which $F_R U_c = 3.64 \text{ W/m}^2 \cdot \text{K}$ and $F_R(\tau\alpha)_n = 0.50$ (typical commercial values). Do air or liquid collectors deliver more energy per square meter in this case?
14. Repeat Problem 13 if collector fluid rate is doubled.
15. Using the data in Problem 11, calculate system performance for a horizontal and for a vertical collector. Assume Equation 5.22 applies to both cases.
16. Using the data in Problem 11, find the solar collector area and the size of the storage tank (assuming water storage) to provide f_s of 0.6 in January.
17. Calculate monthly energy requirements for hot-water supply for a residence in Tampa, Florida, with five occupants. Water source temperature, which is usually available from the city government, is presented in the table below and water delivery temperature is set to 60°C.
The building has a solar water-heating system consisting of two flat-plate collectors measuring 1.5 m × 2.5 m with the following performance characteristics, a 300-liter (~80 US gallons) water storage tank, and the associated controls:

$$F_R(\tau\alpha)_n = 0.75; F_R U_L = 0.13 \text{ W/m}^2 \cdot \text{K}; K_{\tau\alpha} = 1 - 0.15(1/\cos(i) - 1)$$

Using the *f*-chart method, find the total energy supplied by the solar energy system for the hot-water requirements.

Water Source Temperatures (°C)

Jan	Feb	Mar	Apr	May	Jun	Jul	Aug	Sep	Oct	Nov	Dec
16.5	18.5	20	23	26.5	29	30	30	29	25.5	20.5	18

18. The cost of the complete solar water-heating system described above is \$4000. The backup energy source is electricity with a tariff of \$0.14/kWh_e with an annual inflation rate for tariff of 4%.
- Find the payback period of the system assuming a discount rate of 5%. Assume that the system performance degrades at a rate of 0.3% per year.
 - Find the payback period, if the owner gets a rebate of \$1200 on this system.
 - If the owner finances the system with a 10-year loan from a bank at an interest rate of 4.5% per annum with equal monthly payments over the life of the loan, find the monthly payment. When does the monthly payment become less than the average monthly savings from the system?
 - Find the monthly payment due to the solar system only, if the system was included in the mortgage loan for the building at 5% for 25 years.
19. Using the following data for heating degree days for Little Rock, Arkansas, and the system described in Problem 11, find the monthly and yearly heating load provided by the solar heating system. If the cost of the system is \$25,000, find the payback period, given the following:
- The backup system is based on natural gas that costs \$1.20/therm and will increase at an average annual rate of 4%. Assume the discount rate to be 5%. How does the payback period change if the building owner gets a 30% tax credit for the solar energy system?
 - The backup system is electric heat pump that operates at an average COP of 1.3 during December to February and 2.5 during the rest of the heating season. Assume that the electricity tariff is \$0.15/kWh and will increase at an average annual rate of 4%. Assume the discount rate to be 5%.
 - If the homeowner can get financing from a bank at an annual interest rate of 5.5% for a 20-year loan, how will it affect the economics of the system?

Heating Degree C-Days for Little Rock, Arkansas (Base = 18.3°C)

Jan	Feb	Mar	Apr	May	June	July	Aug	Sept	Oct	Nov	Dec	Annual
403	300	204	78	11	0	0	0	7	66	211	372	1653

References

- ASHRAE. 2013. *Handbook of Fundamentals*. American Society of Heating, Refrigerating and Air Conditioning Engineers, Atlanta, GA.
- Balcomb, J.D. et al. 1975. *Solar Handbook for Los Alamos*. LASL, New Mexico; Balcomb, J.D. et al. 1975. Design considerations of air-cooled collector/rock-bin storage solar heating systems. Paper presented at the ISES Annual Meeting, Los Angeles, CA.
- Balcomb, J.D., and J.D. Hedstrom. 1976. Simulation analysis of passive solar heated buildings—Preliminary results. Los Alamos Rept. LA-UR-76-89; see also, under the same title, paper in *Sol. Energy* 19: 277–282, 1977.
- Beckman, W. 1978. Simulations of the performance of open cycle desiccant systems using solar energy. *Sol. Energy* 21: 531.
- Beckman, W.A., S.A. Klein, and J.A. Duffie. 1977. *Solar Heating Design by the F-Chart Method*. John Wiley & Sons, New York.
- Close, D.J. 1962. The performance of solar water heaters with natural circulation. *Sol. Energy* 6: 33.
- Collares-Pereira, M., and A. Rabl. 1979. Simple procedure for predicting long term average performance of nonconcentrating and of concentrating solar collectors. *Sol. Energy* 23: 235–253.
- Goswami, B.C., and J. Langley. 1987. A review of the potential of solar energy in the textile industry. In *Progress in Solar Engineering*, D.Y. Goswami, ed. Hemisphere Publishing Corporation, Washington, DC.
- Goswami, D.Y., and D.E. Klett. 1982. Solar industrial process heat for textile industries. Paper presented at the 1982 ASME, *Textile Industries Division Conference at Raleigh, NC*.
- Hebrank, W.H. 1975. Tenter frame drying. *Am. Dyestuff Rep.* 63: 34.
- IEA. *World Energy Outlook 2010*. International Energy Agency, Paris, France.
- Intertechnology Corporation. 1977. Analysis of the economic potential of solar thermal energy to provide industrial process heat, 3 Vols. ERDA Rep. No. COO/2829-1.
- Klein, S.A. 1976. A design procedure for solar heating systems. Ph.D. dissertation, University of Wisconsin, Madison, WI.
- Klein, S.A., and W.A. Beckman. 1977. General design method for closed loop solar energy systems, *Proc. 1977 ISES Meeting*.
- Klein, S.A., and W.A. Beckman. 1979. General design method for closed loop solar energy systems. *Sol. Energy* 22: 269.
- Klein, S.A., W.A. Beckman, and J.A. Duffie. 1976a. A design procedure for solar heating systems. *Sol. Energy* 18: 113.

- Klein, S.A., W.A. Beckman, and J.A. Duffie. 1976b. A design procedure for solar air heating systems. Paper presented at the 1976 ISES Conference, American Section, Winnipeg, Manitoba, August 15–20.
- Klein, S.A. et al. 1975. A method for simulation of solar processes and its application. *Sol. Energy* 17: 29–37.
- Klein, S.A. et al. 1979. TRNSYS—A transient system simulation. User's manual. Engineering Experiment Station Report 38-10. University of Wisconsin, Madison, WI.
- Kreider, J.F. 1979. *Medium and High Temperature Solar Processes*. Academic Press, New York.
- Kreider, J.F., and F. Kreith. 1977. *Solar Heating and Cooling*, revised 1st ed. Hemisphere Publ. Corp., Washington, DC.
- Kutcher, C.F. 1996. Transpired solar collector system: A major advance in solar heating. Paper presented at the *World Energy Engineering Congress*, Atlanta, GA, November 6–8.
- Kutcher, C.F., and C.B. Christensen. 1992. Unglazed transpired solar collectors. In *Advances in Solar Energy*, Vol. 7, K. Boer, ed. American Solar Energy Soc., Boulder, CO, pp. 283–307.
- Lowery, J.F. et al. 1977. Energy conservation in the textile industry. Technical Report of Department of Energy Project No. Ey-76S-05-5099. School of Textile Engineering, Georgia Institute of Technology, Atlanta, GA, p. 36. Report No. Ey-76-S-05-5099, 1978, 1979.
- Phillips, W.F., and R.D. Cook. 1975. Natural circulation from a flat plate collector to a hot liquid storage tank. ASME Paper 75-HT-53, ASME, NY.
- Proctor, D., and R.N. Morse. 1975. *Solar Energy for Australian Food Processing Industry*. CSIRO Solar Energy Studies, East Melbourne, Victoria, Australia.
- Reddy, T.A. 1987. *The Design and Sizing of Active Solar Thermal Systems*. Oxford University Press, Oxford.
- Singh, R.K., D.B. Lund, and E.H. Buelow. 1986. Compatibility of solar energy with food processing energy demands, Chapter 6. In *Alternative Energy in Agriculture*, Vol. I, D.Y. Goswami, ed. CRC Press, Boca Raton, FL.
- Taibi, E., D. Gielen, and M. Bazilian. 2012. The potential of renewable energy in industrial applications. *Renew. Sustain. Energy Rev.* 16: 735–774.
- TRNSYS. 1981. A transient simulation program, version 11.1. Engineering Experiment Station, Report 38. Solar Energy Laboratory, University of Wisconsin, Madison, WI.
- Vajen, K., C. Lauterbach, and B. Schmitt. 2012. Solar heat for industrial processes—Potential, technologies and applications. *Proceedings of the International Conference on Solar Energy for MENA Region (INCSOL)*, Amman, Jordan, October 22–23.
- Wagner, R. 1977. Energy conservation in dyeing and finishing. *Text. Chem. Color.* 9: 52.

6

Solar Cooling and Dehumidification

The real cycle you're working on is a cycle called yourself.

Robert Pirsig

6.1 Solar Space Cooling and Refrigeration

In some ways, solar energy is better suited to space cooling and refrigeration than to space heating, but this application of solar energy has not found much commercial success. The seasonal variation of solar energy is extremely well suited to the space-cooling requirements of buildings. The principal factors affecting the temperature in a building are the average quantity of radiation received and the environmental air temperature. Since the warmest seasons of the year correspond to periods of high insolation, solar energy is most available when comfort cooling is most needed. Moreover, as we have seen in Chapter 3, the efficiency of solar collectors increases with increasing insolation and increasing environmental temperature. Consequently, in the summer, the amount of energy delivered per unit surface area of collector can be larger than that in winter.

There are several approaches that can be taken to solar space cooling and refrigeration. Because of the limited operating experience with solar-cooling systems, their design must be based on basic principles and experience with conventional cooling systems. The material presented in this chapter will therefore stress the fundamental principles of operation of refrigeration cycles and combine them with special features of the components in a solar system.

The two principal methods of lowering air temperature for comfort cooling are refrigeration with actual removal of energy from the air or evaporation cooling of the air with adiabatic vaporization of moisture into it. Refrigeration systems can be used under any humidity condition of entering air, whereas evaporative cooling can be used only when the entering air has a comparatively low relative humidity.

The most widely used air-conditioning method employs a vapor-compression refrigeration cycle. Another method uses an absorption refrigeration cycle

similar to that of the gas refrigerator. The vapor-compression refrigeration cycle requires energy input into the compressor, which may be provided as electricity from a photovoltaic system or as mechanical energy from a solar-driven engine. Referring to Figure 6.1, the compressor raises the pressure of the refrigerant, which also increases its temperature. The compressed high-temperature refrigerant vapor then transfers its heat to the ambient environment in the condenser, where it condenses to a high-pressure liquid at a temperature close to (but higher than) the environmental temperature. The liquid refrigerant is then passed through the expansion valve where its pressure is suddenly reduced, resulting in a vapor–liquid mixture at a much lower temperature. The low-temperature refrigerant is then used to cool air or water in the evaporator where the liquid refrigerant evaporates by absorbing heat from the medium being cooled. The cycle is completed by the vapor returning to the compressor. If water is cooled by the evaporator, the device is usually called a chiller. The chilled water is then used to cool the air in the building.

In an absorption system, the refrigerant is evaporated or distilled from a less volatile liquid absorbent, the vapor is condensed in a water- or air-cooled condenser, and the resulting liquid is passed through a pressure-reducing valve to the cooling section of the unit. There, it chills the water as it evaporates, and the resulting vapor flows into a vessel, where it is reabsorbed in the stripped absorbing liquid and pumped back to the heated generator. The

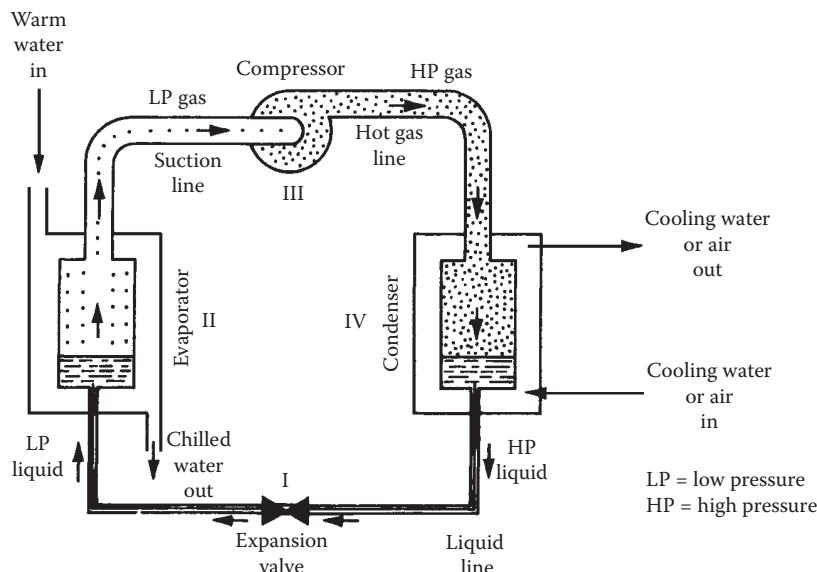
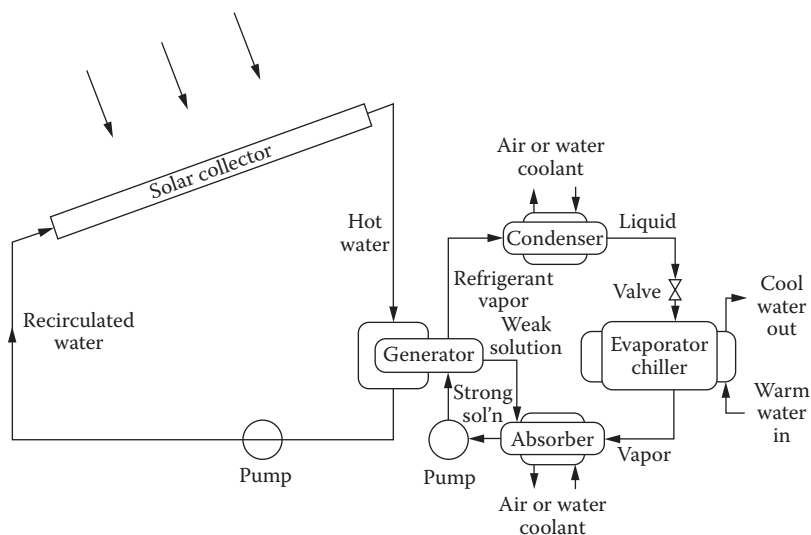


FIGURE 6.1

Schematic diagram illustrating the basic refrigeration vapor-compression cycle.

**FIGURE 6.2**

Schematic diagram of a solar-powered absorption refrigeration system.

heat required to evaporate the refrigerant in the generator can be supplied directly from solar energy as shown in Figure 6.2.

In humid climates, removal of moisture from the air represents a major portion of the air-conditioning load. In such climates, desiccant systems can be used for dehumidification, in which solar energy can provide most of the energy requirements. There are several passive space-cooling techniques, such as nocturnal cooling (night sky radiation), ground cooling, and underground air tunnels. These techniques are described in Chapter 7. The present chapter covers the active solar cooling techniques based on vapor-compression and vapor-absorption refrigeration cycles and desiccant humidification.

6.1.1 Cooling Requirements for Buildings

The cooling load of a building is the rate at which heat must be removed to maintain the air in a building at a given temperature and humidity. It is usually calculated on the basis of the peak load expected during the cooling season. For a given building, the cooling load depends primarily on

1. Inside and outside dry-bulb temperatures and relative humidities
2. Solar-radiation heat load and wind speed
3. Infiltration and ventilation
4. Internal heat sources

A method of calculating the cooling load is presented in detail in ASHRAE (2013).

The steps in calculating the cooling load of a building are as follows:

1. Specify the building characteristics: wall area, type of construction, and surface characteristics; roof area, type of construction, and surface characteristics; window area, setback, and glass type; and building location and orientation.
2. Specify the outside and inside wet- and dry-bulb temperatures.
3. Specify the solar heat load and wind speed.
4. Calculate building cooling load resulting from the following: heat transfer through windows; heat transfer through walls; heat transfer through roof; sensible and latent heat gains resulting from infiltration and ventilation; sensible and latent heat gains (water vapor) from internal sources, such as people, lights, cooking, and so on.

Equations 6.1 through 6.7 may be used to calculate the various cooling loads for a building. Cooling loads resulting from lights, building occupants, and so on may be estimated from ASHRAE (2013). For unshaded or partially shaded windows, the load is

$$\dot{Q}_{wi} = A_{wi} F_{sh} \bar{\tau}_{b,wi} I_{h,b} \frac{\cos i}{\sin \alpha} + \bar{\tau}_{d,wi} I_{h,d} \cos^2 \beta / 2 + \bar{\tau}_{r,wi} I_r + U_{wi} (T_{out} - T_{in}) . \quad (6.1)$$

$$I_r = \rho (I_{b,h} + I_{d,h}) \sin^2 (\beta / 2)$$

For shaded windows, the load (neglecting sky diffuse and reflected radiation) is

$$\dot{Q}_{wi,sh} = A_{wi,sh} U_{wi} (T_{out} - T_{in}). \quad (6.2)$$

For unshaded walls, the load is

$$\dot{Q}_{wa} = A_{wa} \bar{\alpha}_{s,wa} I_r + I_{h,d} \cos^2 \beta / 2 + I_{h,b} \frac{\cos i}{\sin \alpha} + U_{wa} (T_{out} - T_{in}) . \quad (6.3)$$

For shaded walls, the load (neglecting sky diffuse and reflected radiation) is

$$\dot{Q}_{wa,sh} = A_{wa,sh} [U_{wa} (T_{out} - T_{in})]. \quad (6.4)$$

For the roof, the load is

$$\dot{Q}_{rf} = A_{rf} \bar{\alpha}_{s,rf} I_r + I_{h,d} \cos^2 \beta / 2 + I_{h,b} \frac{\cos i}{\sin \alpha} + U_{rf} (T_{out} - T_{in}) . \quad (6.5)$$

Sensible cooling load owing to infiltration and ventilation is

$$\dot{Q}_i = \dot{m}_a(h_{\text{out}} - h_{\text{in}}) = \dot{m}_a C p_a (T_{\text{out}} - T_{\text{in}}). \quad (6.6)$$

Latent load owing to infiltration and ventilation is

$$\dot{Q}_w = \dot{m}_a (W_{\text{out}} - W_{\text{in}}) \lambda_w, \quad (6.7)$$

where

- \dot{Q}_{wi} = heat flow through unshaded windows of area A_{wi} ,
- $\dot{Q}_{wi,sh}$ = heat flow through shaded windows of area $A_{wi,sh}$,
- \dot{Q}_{wu} = heat flow through unshaded walls of area A_{wa} ,
- $\dot{Q}_{wu,sh}$ = heat flow through shaded walls of area $A_{wa,sh}$,
- \dot{Q}_{rf} = heat flow through roof of area A_{rf} ,
- \dot{Q}_i = heat load resulting from infiltration and ventilation,
- \dot{Q}_w = latent heat load,
- $I_{h,b}$ = beam component of insolation on horizontal surface,
- $I_{h,d}$ = diffuse component of insolation on horizontal surface,
- I_r = ground-reflected component of insolation,
- $W_{\text{out}}, W_{\text{in}}$ = outside and inside humidity ratios,
- U_{wi}, U_{wa}, U_{rf} = overall heat-transfer coefficients for windows, walls, and roof, including radiation,
- \dot{m}_a = net infiltration and ventilation mass flow rate of dry air,
- $C p_a$ = specific heat of air (approximately 1.025 kJ/kg-K for moist air),
- T_{out} = outside dry-bulb temperature,
- T_{in} = indoor dry-bulb temperature,
- F_{sh} = shading factor (1.0 = unshaded, 0.0 = fully shaded),
- $\bar{\alpha}_{s,wa}$ = wall solar absorptance,
- $\bar{\alpha}_{s,rf}$ = roof solar absorptance,
- i = solar-incidence angle on walls, windows, and roof,
- $h_{\text{out}}, h_{\text{in}}$ = outside and inside air enthalpy,
- α = solar-altitude angle,
- λ_w = latent heat of water vapor,
- ρ = ground reflectance,
- $\bar{\tau}_{b,wi}$ = window transmittance for beam (direct) insolation,
- $\bar{\tau}_{d,wi}$ = window transmittance for diffuse insolation, and
- $\bar{\tau}_{r,wi}$ = window transmittance for ground-reflected insolation.

Recent ASHRAE handbooks recommend the use of the CLTD (cooling load temperature difference) method. For more details of the method, one should refer to ASHRAE (2013).

Example 6.1

Determine the cooling load for a building in Phoenix, Arizona, with the specifications tabulated in Table 6.1.

TABLE 6.1

Building Specifications for Example 6.1

Factor	Description or Specification
Building characteristics	
Roof	
Type of roof	Flat, shaded
Area, $A_{rf,sh}$ (m^2)	240
Walls (painted white)	
Size, north and south	$3 \times 20 \text{ m}$ (two)
Size, east and west	$3 \times 12 \text{ m}$ (two)
Area, A_{wa} , north and south walls (m^2)	$60 - A_{wi} = 60 - 6 = 54 \text{ m}^2$ (two)
Area, A_{wa} , east and west walls (m^2)	$36 - A_{wi} = 36 - 6 = 30 \text{ m}^2$ (two)
Absorptance, $\bar{\alpha}_{s,wa}$ and $\bar{\alpha}_{s,rf}$, of white paint	0.12
Windows	
Size, north and south	$2 \times 1.5 \text{ m}$ (two)
Size, east and west	$2 \times 1.5 \text{ m}$ (two)
Shading factor, F_{sh}	0.20
Insolation transmittance	$\bar{\tau}_{b,wi} = 0.60; \bar{\tau}_{d,wi} = 0.81; \bar{\tau}_{r,wi} = 0.60$
Ground reflectance	0.2
Location and latitude	Phoenix, Arizona; 33°N
Date	August 1
Time and local-solar-hour angle, h_s	Noon; $h_s = 0$
Solar declination, δ_s (degree)	$17^\circ - 55'$
Wall surface tilt from horizontal, β	90°
Temperature, outside and inside ($^\circ\text{C}$)	$T_{out} = 38; T_{in} = 23$
Insolation, I (W/m^2)	$I_{h,b} = 200; I_{h,d} = 100; I_r = 70$
U factor for walls, windows, and roof	$U_{wa} = 0.19; U_{wi} = 1.09; U_{rf} = 0.061$
Infiltration ($\text{lbm dry air}/\text{h}$)	Neglect
Ventilation ($\text{lbm dry air}/\text{h}$)	Neglect
Internal loads	Neglect
Latent heat load, Q_w (%)	30% of wall sensible heat load

Solution

To determine the cooling load for the building just described, calculate the following factors in the order listed.

1. Incidence angle for the south wall i at solar noon can be written from Equations 2.44 and 2.28 as

$$\begin{aligned} \cos i &= \cos \beta \cos(L - \delta_s) + \sin \beta \sin(L - \delta_s) \\ &= 0.26. \end{aligned} \quad (6.8)$$

2. Solar altitude α at solar noon (from Equation 2.28)

$$\sin \alpha = \sin \delta_s \sin L + \cos \delta_s \cos L \cos h_s = \cos(L - \delta_s) = \cos 15^\circ = 0.966.$$

3. Insolation $I_{r,wa} = I_{r,wi} = 0.2(700 + 100)\sin^2(45^\circ) = 80 \text{ W/m}^2$

$$I_{r,rf} = 0.$$

4. South-facing window load (from Equation 6.1)

$$\begin{aligned} \dot{Q}_{wi} &= 2 \times 3 \quad 0.20 \times 0.6 \times 700 \frac{0.26}{0.966} + (0.81 \times 100 \cos^2(45^\circ)) + (0.60 \times 80) \\ &\quad + 1.09(38 - 23) \end{aligned} \Big\} = 765 \text{ W.}$$

5. Shaded-window load (from Equation 6.2)

$$\dot{Q}_{wi,sh} = (3 \times 6)[1.09(38 - 23)] = 295 \text{ W.}$$

6. South-facing wall load (from Equation 6.3)

$$\begin{aligned} \dot{Q}_{wa} &= (60 - 6) \quad 0.12 \quad 100 \cos^2(45^\circ) + 80 + 700 \frac{0.26}{0.966} + 0.19(38 - 23) \\ &= 2217 \text{ W.} \end{aligned}$$

7. Shaded-wall load (from Equation 6.4)

$$\dot{Q}_{wa,sh} = [(60 + 36 + 36) - (3 \times 6)] \times [0.19(38 - 23)] = 324 \text{ W.}$$

8. Roof load (from Equation 6.5)

$$\dot{Q}_{rf} = 240[\bar{\alpha}_{s,rf} \times 0 + 0.061(38 - 23)] = 220 \text{ W.}$$

9. Latent-heat load (30% of sensible wall load)

$$\dot{Q}_w = 0.3[(60 + 60 + 36 + 36) - (4 \times 60)][0.19(38 - 23)] = 144 \text{ W.}$$

10. Infiltration load

$$\dot{Q}_i = 0.$$

11. Total cooling load for the building described in the example

$$\begin{aligned} \dot{Q}_{tot} &= \dot{Q}_{wi} + \dot{Q}_{wi,sh} + \dot{Q}_{wa} + \dot{Q}_{wa,sh} + \dot{Q}_{rf} + \dot{Q}_w + \dot{Q}_i, \\ \dot{Q}_{tot} &= 3965 \text{ W.} \end{aligned}$$

6.1.2 Vapor-Compression Cycle

The principle of operation of a vapor-compression refrigeration cycle can be illustrated conveniently with the aid of a pressure–enthalpy diagram as shown in Figure 6.3. The ordinate is the pressure of the refrigerant in N/m² absolute, and the abscissa is its enthalpy in kJ/kg. The roman numerals in Figure 6.3 correspond to the physical locations in the schematic diagram of Figure 6.1.

Process I is a throttling process in which hot liquid refrigerant at the condensing pressure p_c passes through the expansion valve, where its pressure is reduced to the evaporator pressure p_e . This is an isenthalpic (constant enthalpy) process, in which the temperature of the refrigerant decreases. In this process, some vapor is produced and the state of the mixture of liquid refrigerant and vapor entering the evaporator is shown by point A. Since the expansion process is isenthalpic, the following relation holds:

$$h_{ve}f + h_{le}(1 - f) = h_{lc} \quad (6.9)$$

where f is the fraction of mass in vapor state, subscripts “v” and “l” refer to vapor and liquid states, respectively, and “c” and “e” refer to states corresponding to condenser and evaporator pressures, respectively. And,

$$f = \frac{h_{lc} - h_{le}}{h_{ve} - h_{le}}. \quad (6.10)$$

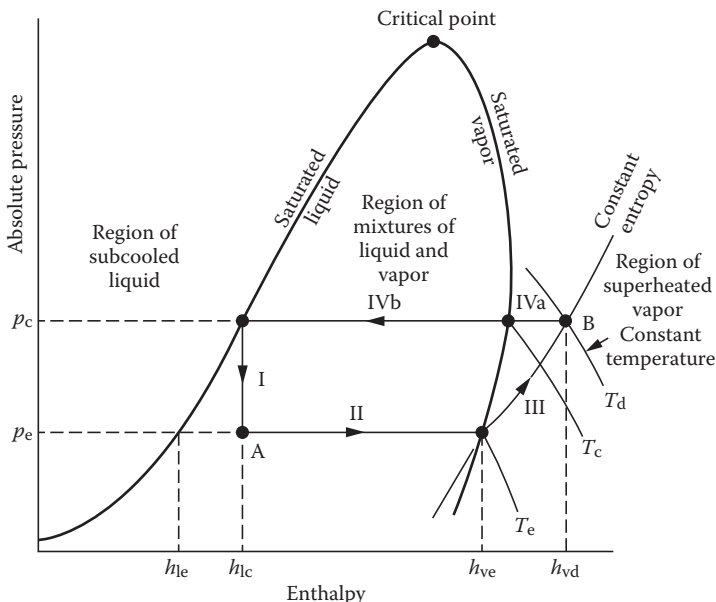


FIGURE 6.3
Simple refrigeration cycle on pressure–enthalpy diagram.

Process II represents the vaporization of the remaining liquid. This is the process during which heat is removed from the chiller. Thus, the specific refrigeration effect per kilogram of refrigerant q_r is

$$q_r = h_{ve} - h_{lc} \text{ in kJ/kg (Btu/lb).} \quad (6.11)$$

In the United States, it is still common practice to measure refrigeration in terms of *tons*. One ton is the amount of cooling produced if 1 ton of ice is melted over a period of 24 h. Since 1 ton = 907.2 kg and the latent heat of fusion of water is 334.9 kJ/kg,

$$1 \text{ ton} = \frac{(907.2 \text{ kg}) \times (334.9 \text{ kJ/kg})}{(24 \text{ h}) \times (3600 \text{ s/h})} = 3.516 \text{ kW} = 12,000 \text{ Btu/h.} \quad (6.12)$$

If the desired rate of refrigeration requires a heat-transfer rate of \dot{Q} , the rate of mass flow of refrigerant necessary \dot{m}_r is

$$\dot{m}_r = \frac{\dot{Q}_r}{(h_{ve} - h_{lc})}. \quad (6.13)$$

Process III in Figure 6.3 represents the compression of refrigerant from pressure p_e to p_c . The process requires work input from an external source, which may be obtained from a solar-driven expander turbine or a solar electrical system. In general, if the heated vapor leaving the compressor is at the condition represented by point B in Figure 6.3, the work of compression W_c is

$$W_c = \dot{m}_r(h_{vd} - h_{ve}). \quad (6.14)$$

In an idealized cycle analysis, the compression process is usually assumed to be isentropic.

Process IV represents the condensation of the refrigerant. Actually, sensible heat is first removed in subprocess IVa as the vapor is cooled at constant pressure from T_d to T_c and latent heat is removed at the condensation temperature T_c , corresponding to the saturation pressure p_c in the condenser. The heat-transfer rate in the condenser \dot{Q}_c is

$$\dot{Q}_c = \dot{m}_r(h_{vd} - h_{lc}). \quad (6.15)$$

This heat must be rejected into the environment, either to cooling water or to the atmosphere if no water is available.

The overall performance of a refrigeration machine is usually expressed as the ratio of the heat transferred in the evaporator \dot{Q}_r to the shaft work

supplied to the compressor. This ratio is called the *coefficient of performance* (COP), defined by

$$\text{COP} = \frac{\dot{Q}_c}{W_c} = \frac{h_{ve} - h_{lc}}{h_{vd} - h_{ve}}. \quad (6.16)$$

The highest coefficient of performance for any given evaporator and condenser temperatures would be obtained if the system were operating on a reversible Carnot cycle. Under these conditions,

$$\text{COP}(\text{Carnot}) = \frac{T_e}{T_d - T_e}. \quad (6.17)$$

However, frictional effects and irreversible heat losses reduce the COP of real cycles much below this maximum.

Example 6.2

Calculate the amount of shaft work to be supplied to a 1-ton (3.52-kW) refrigeration plant operation at evaporator and condenser temperatures of 273 K and 309 K, respectively, using Refrigerant 134a (R-134a) as the working fluid. The properties of R-134a are tabulated in Table 6.2. (More complete data are given in Appendix 6.) Also calculate the COP and the mass flow rate of the refrigerant.

Solution

From the property table, the enthalpies for process I are as follows:

$$\begin{aligned} \text{Saturated vapor at } 273 \text{ K} & \quad h_{ve} = 247.2 \text{ kJ/kg} \\ \text{Saturated liquid at } 309 \text{ K} & \quad h_{lc} = 100.3 \text{ kJ/kg} \\ \text{Saturated liquid at } 273 \text{ K} & \quad h_k = 50.0 \text{ kJ/kg} \end{aligned}$$

TABLE 6.2

Properties of R-134a for Example 6.2

Temperature (K)	Absolute Pressure (kPa)	Vapor-Specific Volume (m ³ /kg)	Liquid Enthalpy (kJ/kg)	Vapor Enthalpy (kJ/kg)	Vapor Entropy (kJ/kg·K)
<i>Saturated</i>					
273	292.8	0.0689	50.02	247.2	0.919
309	911.7	0.0223	100.25	266.4	0.9053
<i>Superheated</i>					
308.5	900	0.0226	—	266.18	0.9054
313	900	0.0233	—	271.3	0.9217
312.4	1000	0.0202	—	268.0	0.9043
313	1000	0.0203	—	268.7	0.9066

Therefore, from Equation 6.10,

$$f = \frac{100.3 - 50.0}{247.2 - 50.0} = 0.255.$$

The mass flow rate of refrigerant \dot{m}_r is obtained from Equation 6.13 and the enthalpies above, or

$$\dot{m}_r = \frac{3.52 \text{ kW}}{(247.2 - 100.3) \text{ kJ/kg}} = 0.024 \text{ kg/s.}$$

The specific shaft-work input required is

$$\frac{W_c}{\dot{m}_r} = h_{vd} - h_{ve}.$$

The entropy s_e of the saturated vapor entering the compressor at 273 K and 292.8 kPa is 0.919 kJ/kg-K. From the property table, superheated vapor at a pressure of 911.7 kPa has an entropy of 0.919 kJ/kg-K at a temperature of 313 K with an enthalpy of 270.8 kJ/kg. Thus, the energy input to the working fluid by the compressor is

$$W_c = 0.024(270.8 - 247.2) = 0.566 \text{ kW.}$$

Finally, the heat-transfer rate from the refrigerant to the sink, or cooling water in the condenser, is from Equation 6.15:

$$\dot{Q}_c = \dot{m}_r(h_{vd} - h_{lc}) = 0.024(270.8 - 100.3) = 4.09 \text{ kW.}$$

The COP of the thermodynamic cycle is

$$\text{COP} = \frac{247.2 - 100.3}{270.8 - 247.2} = 6.2,$$

whereas the Carnot COP is 273/36 or 7.6.

The above cycle has been idealized. In practice, the liquid entering the expansion valve is several degrees below the condensing temperature, while the vapor entering the compressor is several degrees above the evaporation temperature. In addition, pressure drops occur in the suction, discharge, and liquid pipelines, and the compression is not truly isentropic. Finally, the work required to drive the compressor is somewhat larger than W_c above, because of frictional losses. All of these factors must be taken into account in a realistic engineering design.

6.1.3 Absorption Air Conditioning

Absorption air conditioning is compatible with solar energy since a large fraction of the energy required is thermal energy at temperatures that currently available flat-plate collectors can provide.

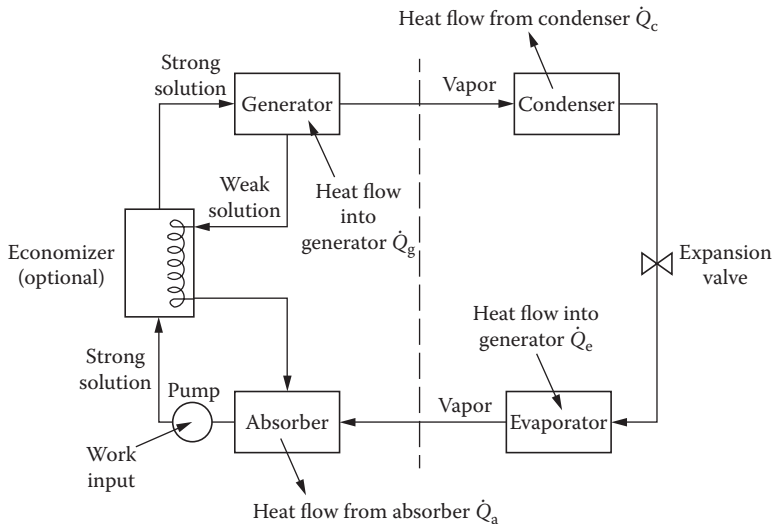
**FIGURE 6.4**

Diagram of heat and fluid flow of absorption air conditioner, with economizer. (From Kreider, J.F. and F. Kreith, *Solar Heating and Cooling*, Revised 1st Ed. Washington, DC: Hemisphere Publ. Corp., 1977.)

Solar absorption air conditioning has been the subject of investigation by a number of researchers (Chinnappa and Wijeyesundara 1992; Kochhar 1982; Macriss and Zawacki 1989; Manrique 1991; Siddiqui 1993; Thombloom and Nimmo 1996). Figure 6.4 shows a schematic of an absorption refrigeration system. Absorption refrigeration differs from vapor-compression air conditioning only in the method of compressing the refrigerant (left of the dashed line in Figure 6.4). In absorption air-conditioning systems, the pressurization is accomplished by first dissolving the refrigerant in a liquid (the absorbent) in the absorber section, then pumping the solution to a high pressure with an ordinary liquid pump. The low boiling refrigerant is then driven from solution by the addition of heat in the generator. By this means, the refrigerant vapor is compressed without the large input of high-grade shaft work that the vapor-compression air conditioning demands.

The effective performance of an absorption cycle depends on the two materials that comprise the refrigerant-absorbent pair. Desirable characteristics for the refrigerant-absorbent pair follow.

1. The absence of a solid-phase absorbent.
2. A refrigerant more volatile than the absorbent so that separation from the absorbent occurs easily in the generator.

3. An absorbent that has a strong affinity for the refrigerant under conditions in which absorption takes place.
4. A high degree of stability for long-term operations.
5. Nontoxic and nonflammable fluids for residential applications. This requirement is less critical in industrial refrigeration.
6. A refrigerant that has a large latent heat so that the circulation rate can be kept low.
7. A low fluid viscosity that improves heat and mass transfer and reduces pumping power.
8. Fluids that must not cause long-term environmental effects.

Lithium bromide–water ($\text{LiBr}-\text{H}_2\text{O}$) and ammonia–water ($\text{NH}_3-\text{H}_2\text{O}$) are the two pairs that meet most of the requirements. In the $\text{LiBr}-\text{H}_2\text{O}$ system, water is the refrigerant and LiBr is the absorber, while in the ammonia–water system, ammonia is the refrigerant and water is the absorber. Because the $\text{LiBr}-\text{H}_2\text{O}$ system has high volatility ratio, it can operate at lower pressures and, therefore, at the lower generator temperatures achievable by flat-plate collectors. A disadvantage of this system is that the pair tends to form solids. LiBr has a tendency to crystallize when air cooled, and the system cannot be operated at or below the freezing point of water. Therefore, the $\text{LiBr}-\text{H}_2\text{O}$ system is operated at evaporator temperatures of 5°C or higher. Using a mixture of LiBr with some other salt as the absorbent can overcome the crystallization problem. The ammonia–water system has the advantage that it can be operated down to very low temperatures. However, for temperatures much below 0°C , water vapor must be removed from ammonia as much as possible to prevent ice crystals from forming. This requires a rectifying column after the boiler. Also, ammonia is a safety Code Group B2 fluid (ASHRAE Standard 34-1992) which restricts its use indoors (ASHRAE 2013).

Other refrigerant–absorbent pairs include (Macriss and Zawacki 1989)

- Ammonia–salt
- Methylamine–salt
- Alcohol–salt
- Ammonia–organic solvent
- Sulfur dioxide–organic solvent
- Halogenated hydrocarbons–organic solvent
- Water–alkali nitrate
- Ammonia–water–salt

If the pump work is neglected, the COP of an absorption air conditioner can be calculated from Figure 6.4:

$$\text{COP} = \frac{\text{cooling effect}}{\text{heat input}} = \frac{\dot{Q}_c}{\dot{Q}_g}. \quad (6.18)$$

The COP values for absorption air conditioning range from 0.5 for a small, single-stage unit to 0.85 for a double-stage, steam-fired unit. These values are approximately 15% of the COP values that can be achieved by a vapor-compression air conditioner. It is difficult to directly compare the COP of an absorption air conditioner with that of a vapor-compression air conditioner because the efficiency of electric power generation or transmission is not included in the COP of the vapor-compression air conditioning. The following example illustrates the thermodynamics of a LiBr–H₂O absorption refrigeration system.

Example 6.3

A water–lithium bromide absorption refrigeration system such as that shown in Figure 6.5 is to be analyzed for the following requirements:

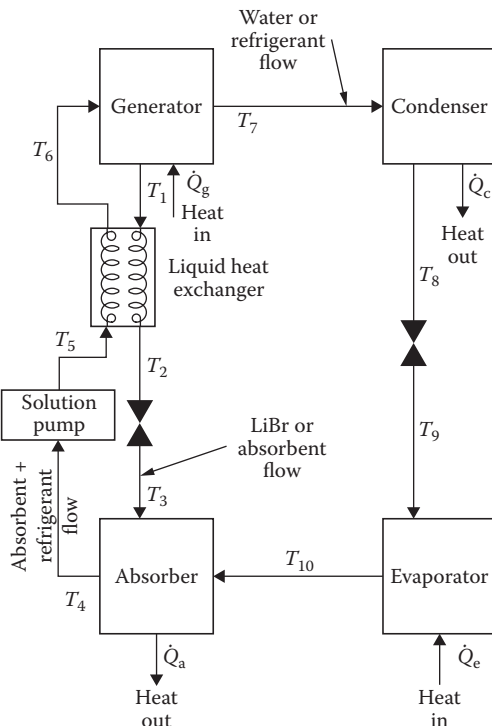


FIGURE 6.5

Lithium bromide–water, absorption refrigeration cycle (see Table 6.3). (From Kreider, J.F. and F. Kreith, *Solar Heating and Cooling*, Revised 1st Ed. Washington, DC: Hemisphere Publ. Corp., 1977.)

1. The machine is to provide 352 kW of refrigeration with an evaporator temperature of 5°C, an absorber outlet temperature of 32°C, and a condenser temperature of 43°C.
2. The approach at the low-temperature end of the liquid heat exchanger is to be 6°C.
3. The generator is heated by a flat-plate solar collector capable of providing a temperature level of 90°C.

Determine the COP, absorbent and refrigerant flow rates, and heat input.

Solution

For analytical evaluation of the LiBr–H₂O cycle, the following simplifying assumptions are made:

1. At those points in the cycle for which temperatures are specified, the refrigerant and absorbent phases are in equilibrium.
2. With the exception of pressure reductions across the expansion device between points 2 and 3 and points 8 and 9 in Figure 6.5, pressure reductions in the lines and heat exchangers are neglected.
3. Pressures at the evaporator and condenser are equal to the vapor pressure of the refrigerant, that is, water, as found in steam tables.
4. Enthalpies for LiBr–H₂O mixtures are given in Figure 6.6.

As a first step in solving the problem, set up a table (Table 6.3) of properties; for example, given

$$\begin{aligned}\text{Generator temperature} &= 90^\circ\text{C} = T_1 = T_7 \\ \text{Evaporator temperature} &= 5^\circ\text{C} = T_9 = T_{10} \\ \text{Condenser temperature} &= 43^\circ\text{C} = T_8 \\ \text{Absorber temperature} &= 32^\circ\text{C} = T_4 \\ \text{Neglecting the pump work, } T_5 &\approx T_4 = 32^\circ\text{C.}\end{aligned}$$

Since the approach at the low-temperature end of the heat exchanger is 6°C,

$$T_2 = T_5 + 6^\circ\text{C} = 38^\circ\text{C, and}$$

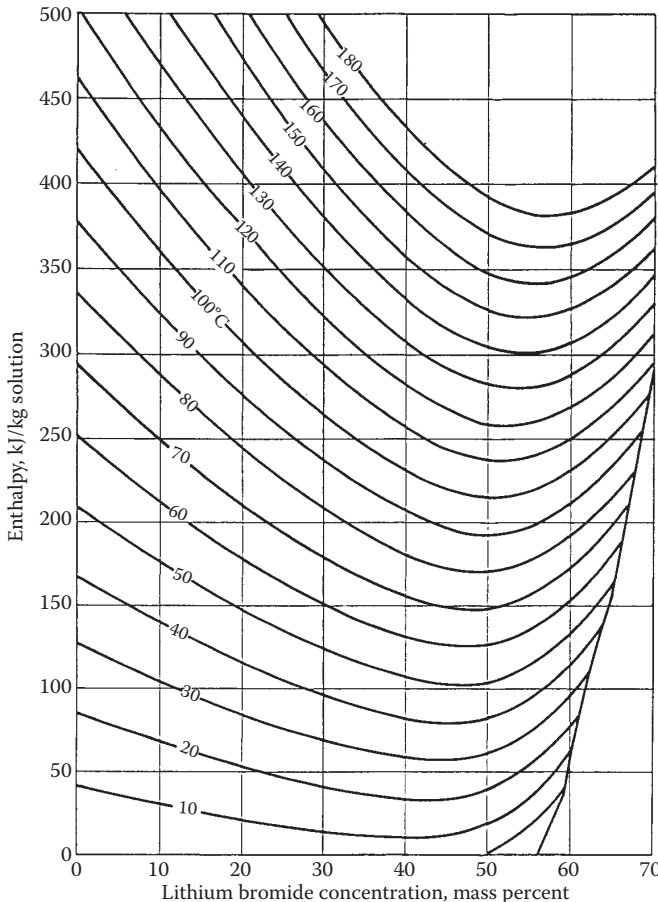
$$T_3 \simeq T_2 = 38^\circ\text{C.}$$

Since the fluid at conditions 7, 8, 9, and 10 is pure water, the properties can be found from the steam tables. Therefore,

$$P_7 = P_8 = \text{Saturation pressure of H}_2\text{O at } 43^\circ\text{C} = 8.65 \text{ kPa}$$

and

$$P_9 = P_{10} = \text{Saturation pressure of H}_2\text{O at } 5^\circ\text{C} = 0.872 \text{ kPa.}$$



Equations	Concentration range $40 < X < 70\%$ LiBr	Temperature range $15 < t < 165^\circ\text{C}$
$h = \sum_0^4 A_n X^n + t \sum_0^4 B_n X^n + t^2 \sum_0^4 C_n X^n$ in kJ/kg, where $t = {}^\circ\text{C}$ and $X = \% \text{LiBr}$		
$A_0 = -2024.33$	$B_0 = 18.2829$	$C_0 = -3.7008214 \text{ E-}2$
$A_1 = 163.309$	$B_1 = -1.1691757$	$C_1 = 2.8877666 \text{ E-}3$
$A_2 = -4.88161$	$B_2 = 3.248041 \text{ E-}2$	$C_2 = -8.1313015 \text{ E-}5$
$A_3 = 6.302948 \text{ E-}2$	$B_3 = -4.034184 \text{ E-}4$	$C_3 = 9.9116628 \text{ E-}7$
$A_4 = -2.913705 \text{ E-}4$	$B_4 = 1.8520569 \text{ E-}6$	$C_4 = -4.4441207 \text{ E-}9$

FIGURE 6.6
Enthalpy-concentration diagram for lithium–water bromide solutions.

Therefore,

$$P_1 = P_2 = P_5 = P_6 = P_7 = 8.65 \text{ kPa}$$

and

$$P_3 = P_4 = P_{10} = 0.872 \text{ kPa.}$$

TABLE 6.3

Thermodynamic Properties of Refrigerant and Absorbent for Figure 6.5

Condition No. in Figure 6.5	Temperature (°C)	Pressure (kPa)	LiBr Weight Fraction	Flow (kg/kg H ₂ O)	Enthalpy (kJ/kg)
1	90	8.65	0.605	7.07	215
2	38	8.65	0.605	7.07	110
3	38	0.872	0.605	7.07	110
4	32	0.872	0.53	8.07	70
5	32	8.65	0.53	8.07	70
6	74	8.65	0.53	8.07	162
7	90	8.65	0	1.0	2670
8	43	8.65	0	1.0	180
9	5	0.872	0	1.0	180
10	5	0.872	0	1.0	2510

Enthalpy,

$$h_9 = h_g = 180 \text{ kJ/kg} \text{ (Saturated liquid at } 43^\circ\text{C}),$$

$$h_{10} = 2510 \text{ kJ/kg} \text{ (Saturated vapor enthalpy at } 5^\circ\text{C}), \text{ and}$$

$$h_7 = 2670 \text{ kJ/kg} \text{ (Superheated vapor at } 8.65 \text{ kPa, } 90^\circ\text{C}).$$

For the LiBr–H₂O mixture, conditions 1 and 4 may be considered equilibrium saturation conditions, which may be found from Figures 6.6 and 6.7 as follows:

For

$$T_4 = 32^\circ\text{C} \text{ and } P_4 = 0.872 \text{ kPa}$$

$$X_s = 0.53, h_4 = 70 \text{ kJ/kg · Sol.}$$

Therefore,

$$h_5 \approx 70 \text{ kJ/kg · Sol.}$$

And for

$$T_1 = 90^\circ\text{C} \text{ and } P_1 = 8.65 \text{ kPa}, X_{ab} = 0.605, h_1 = 215 \text{ kJ/kg · Sol.,}$$

for

$$T_3 = 38^\circ\text{C}, X_3 = 0.605, h_3 = 110 \text{ kJ/kg · Sol.,}$$

$$h_2 = h_3 = 110 \text{ kJ/kg.}$$

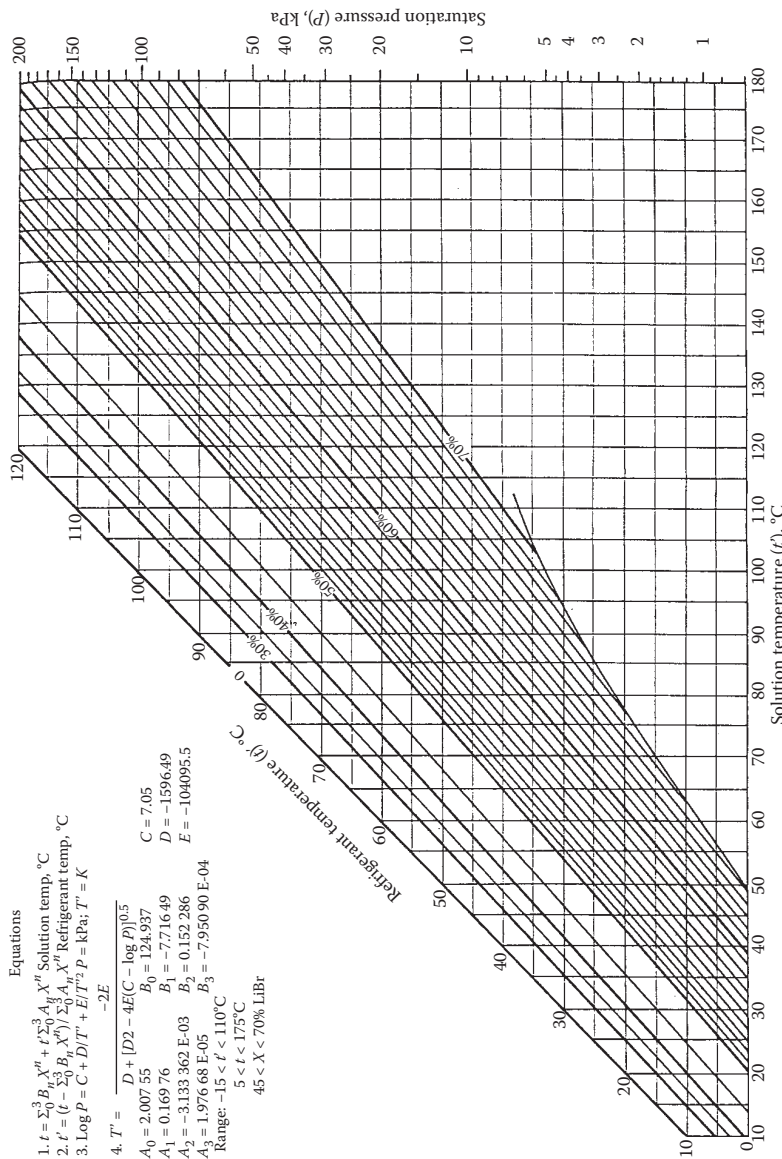


FIGURE 6.7
Equilibrium chart for lithium bromide–water solutions.

6.1.4 Mass Balance Equations

Relative flow rates for the absorbent (LiBr) and the refrigerant (H_2O) are obtained from material balances. A total material balance on the generator gives

$$\dot{m}_6 = \dot{m}_1 + \dot{m}_7,$$

while a LiBr balance gives

$$\dot{m}_6 X_s = \dot{m}_1 X_{ab},$$

where X_{ab} is the concentration of LiBr in absorbent solution and X_s is the concentration of LiBr in refrigerant-absorbent solution.

Substituting $(\dot{m}_1 + \dot{m}_7)$ for \dot{m}_6 gives

$$\dot{m}_1 X_s + \dot{m}_7 X_s = \dot{m}_1 X_{ab}.$$

Since the fluid entering the condenser is pure refrigerant, that is, water, \dot{m}_7 is the same as the flow rate of the refrigerant \dot{m}_r :

$$\frac{\dot{m}_1}{\dot{m}_7} = \frac{X_s}{X_{ab} - X_s} = \frac{\dot{m}_{ab}}{\dot{m}_r},$$

where \dot{m}_{ab} is the flow rate of absorbent and \dot{m}_r is the flow rate of refrigerant.

Substituting for X_s and X_{ab} from the table gives the ratio of absorbent-to-refrigerant flow rate:

$$\frac{\dot{m}_{ab}}{\dot{m}_r} = \frac{0.53}{0.605 - 0.53} = 7.07.$$

The ratio of the refrigerant-absorbent solution flow rate \dot{m}_s to the refrigerant solution flow rate \dot{m}_r is

$$\frac{\dot{m}_s}{\dot{m}_r} = \frac{\dot{m}_{ab} + \dot{m}_r}{\dot{m}_r} = 7.07 + 1 = 8.07.$$

Now, Table 6.3 is complete except for T_6 and h_6 , which may be found from an energy balance at the heat exchanger.

$$\dot{m}_s h_5 + \dot{m}_{ab} h_1 = \dot{m}_{ab} h_2 + \dot{m}_s h_6.$$

Hence,

$$h_6 = h_5 + \frac{\dot{m}_{ab}}{\dot{m}_s} (h_1 - h_2) = 70 + \frac{7.07}{8.07} [215 - 110] = 162 \text{ kJ/kg of solution.}$$

The temperature corresponding to this value of enthalpy and a LiBr mass fraction of 0.53 is found from Figure 6.6 to be 74°C.

The flow rate of refrigerant required to produce the desired 352 kW of refrigeration is

$$\dot{Q}_e = \dot{m}_r(h_{10} - h_9),$$

where \dot{Q}_e is the cooling effect produced by the refrigeration unit and

$$\dot{m}_r = \frac{352}{2510 - 180} = 0.15 \text{ kg/s.}$$

The flow rate of the absorbent is

$$\dot{m}_{ab} = \frac{\dot{m}_{ab}}{\dot{m}_r} \dot{m}_r = 7.07 \times 0.15 = 1.06 \text{ kg/s,}$$

while the flow rate of the solution is

$$\dot{m}_s = \dot{m}_{ab} + \dot{m}_r = 1.06 + 0.15 = 1.21 \text{ kg/s.}$$

The rate at which heat must be supplied to the generator \dot{Q}_g is obtained from the heat balance

$$\begin{aligned}\dot{Q}_g &= \dot{m}_r h_7 + \dot{m}_{ab} h_1 - \dot{m}_s h_6 \\ &= [(0.15 \times 2670) + (1.06 \times 215)] - (1.21 \times 162) \\ &= 432 \text{ kW.}\end{aligned}$$

This requirement, which determines the size of the solar collector, probably represents the maximum heat load that the collector unit must supply during the hottest part of the day.

The coefficient of performance COP is

$$\text{COP} = \frac{\dot{Q}_e}{\dot{Q}_g} = \frac{352}{432} = 0.81.$$

The rate of heat transfer in the other three heat-exchanger units—the liquid heat exchanger, the water condenser, and the absorber—is obtained from heat balances. For the liquid heat exchanger, this gives

$$\dot{Q}_{1-2} = \dot{m}_{ab}(h_1 - h_2) = 1.06[215 - 110] = 111 \text{ kW,}$$

where \dot{Q}_{1-2} is the rate of heat transferred from the absorbent stream to the refrigerant-absorbent stream. For the water condenser, the rate of heat transfer \dot{Q}_{7-8} rejected to the environment is

$$\dot{Q}_{7-8} = \dot{m}_r(h_7 - h_8) = 0.15(2670 - 180) = 374 \text{ kW.}$$

The rate of heat removal from the absorber can be calculated from an overall heat balance on this system:

$$\dot{Q}_a = \dot{Q}_{7-8} - \dot{Q}_g - \dot{Q}_e = 374 - 432 - 352 = -410 \text{ kW.}$$

Explicit procedures for the mechanical and thermal design as well as the sizing of the heat exchangers are presented in standard heat-transfer texts. In large commercial units, it may be possible to use higher concentrations of LiBr, operate at a higher absorber temperature, and thus save on heat-exchanger cost. In a solar-driven unit, this approach would require concentrator-type or high efficiency flat-plate solar collectors.

6.1.5 Ammonia–Water Refrigeration System

The main difference between an ammonia–water system and a water–lithium bromide system is that the ammonia–water system has a rectifier (also called dephlegmator) after the boiler to condense as much water vapor out of the mixture vapor as possible. Figure 6.8 shows a schematic of an $\text{NH}_3\text{-H}_2\text{O}$ absorption refrigeration system. Since ammonia has a much lower boiling point than water, a very high fraction of ammonia and a very small

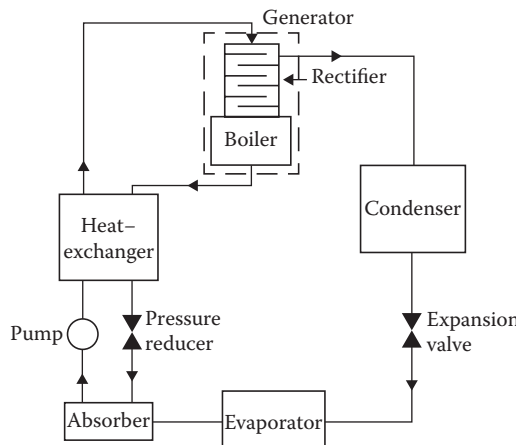


FIGURE 6.8
Schematic of an ammonia–water absorption refrigeration system.

fraction of water are boiled off in the boiler. The vapor is cooled, as it rises in the rectifier, by the countercurrent flow of the strong $\text{NH}_3\text{-H}_2\text{O}$ solution from the absorber; therefore, some moisture is condensed. The weak ammonia–water solution from the boiler goes through a pressure-reducing valve to the absorber, where it absorbs the ammonia vapor from the evaporator. The high-pressure, high-temperature ammonia from the rectifier is condensed by rejecting heat to the atmosphere. It may be further subcooled before expanding in a throttle valve. The low-pressure, low-temperature ammonia from the throttle valve provides refrigeration in the evaporator. The vapor from the evaporator is reunited with the weak ammonia solution in the absorber. Operating pressures are primarily controlled by the ambient air temperature for an air-cooled condenser, the evaporator temperature, and the concentration of the ammonia solution in the absorber. Thermodynamic analysis of an ammonia–water absorption cooling system will become clear from the following example.

Example 6.4

A 10.5 kW, gas-fired, ammonia–water absorption chiller is shown schematically in Figure 6.9. The chiller is operating with the following conditions:

Evaporator temperature: 2°C

Evaporator pressure: 4.7 bar

Condenser and generator pressure: 21.7 bar

Concentration of ammonia in refrigerant (X_r) = 0.985

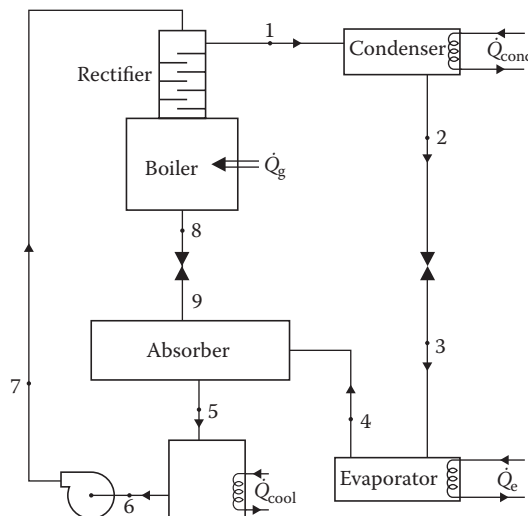


FIGURE 6.9

Schematic of a 10.5-kW, gas-fired, aqua–ammonia absorption chiller for Example 6.4.

Concentration of ammonia in strong solution (X_s) = 0.415
 Concentration of ammonia in weak solution (X_w) = 0.385

Find the mass flow rates, temperatures, and enthalpies at various points in the cycle, and find the COP of the cycle.

Solution

States are defined using Figure 6.10. Properties at all the points are summarized in Table 6.4 and they are calculated as follows.

State Point 2: Assume equilibrium saturated liquid condition

$$\begin{aligned} P_2 &= 21.7 \text{ bar}, & h_2 &= 250 \text{ kJ/kg}, \\ X_2 &= 0.985, & T_2 &= 54^\circ\text{C}. \end{aligned}$$

State Point 3: From an isenthalpic process at the valve,

$$h_3 = h_2 = 250 \text{ kJ/kg}.$$

State Point 4: Assume equilibrium saturated vapor condition,

$$\begin{aligned} P_4 &= 4.7 \text{ bar}, & h_4 &= 1425 \text{ kJ/kg}, \\ X_4 &= 0.985, & T_4 &= 2^\circ\text{C}. \end{aligned}$$

Energy balance at the evaporator,

$$\begin{aligned} \dot{Q}_e &= \dot{m}_r(h_4 - h_3) \\ \dot{m}_r &= \frac{\dot{Q}_e}{(h_4 - h_3)} = \frac{10.5 \text{ kW}}{(1425 - 250) \text{ kJ/kg}} = 0.01 \text{ kg/s}. \end{aligned}$$

Ammonia mass balance at the absorber,

$$\begin{aligned} \dot{m}_s X_s &= \dot{m}_r X_r + \dot{m}_w X_w, \text{ and } \dot{m}_w = \dot{m}_s - \dot{m}_r, \\ \dot{m}_s &= \dot{m}_r \frac{(X_r - X_w)}{(X_s - X_w)} = 0.01 \frac{(0.985 - 0.385)}{0.415 - 0.385} = 0.2 \text{ kg/s}, \\ \dot{m}_w &= \dot{m}_s - \dot{m}_r = 0.2 - 0.01 = 0.19 \text{ kg/s}. \end{aligned}$$

State Point 1: Assume equilibrium saturated vapor condition,

$$\begin{aligned} P_1 &= 21.7 \text{ bar}, & h_1 &= 1430 \text{ kJ/kg}, \\ X_1 &= 0.985, & T_1 &= 90^\circ\text{C}. \end{aligned}$$

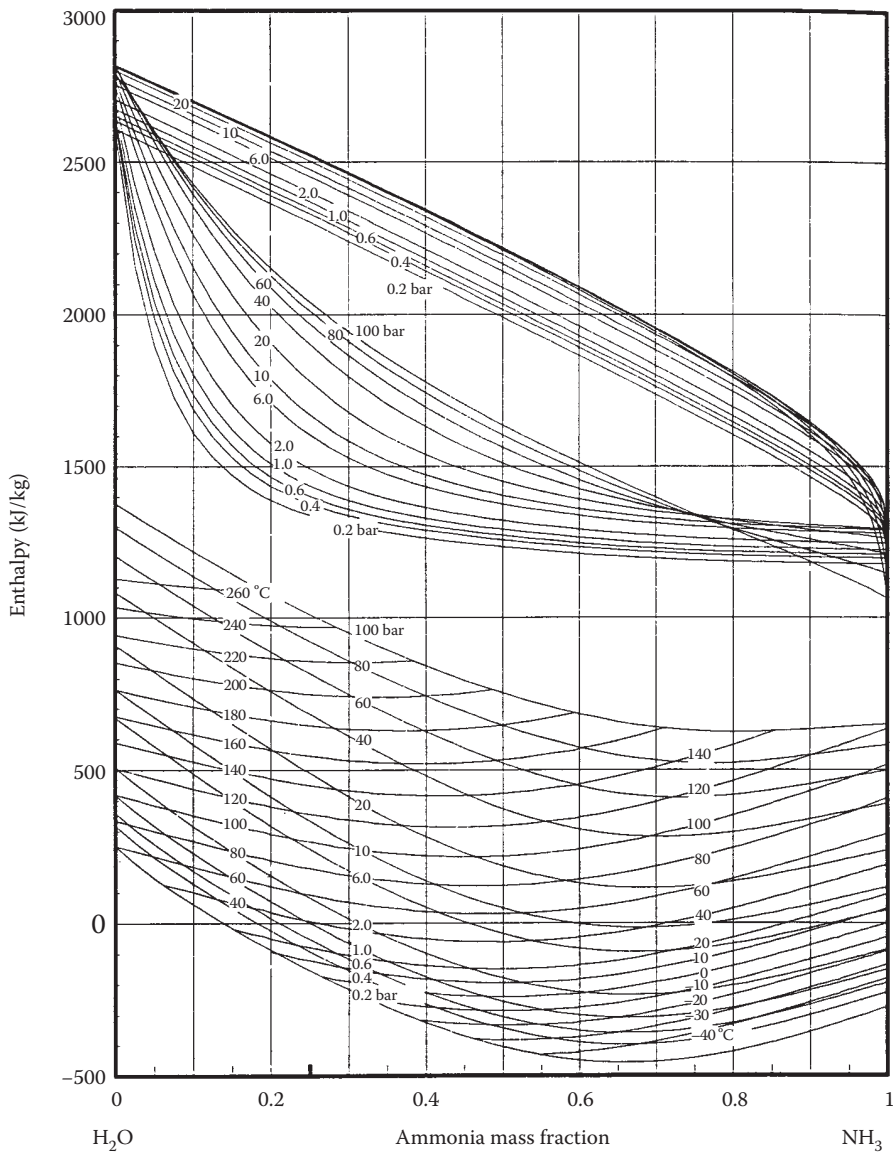


FIGURE 6.10
Enthalpy-concentration diagram for ammonia-water.

TABLE 6.4

Thermodynamic Properties of Ammonia–Water in Example 6.4

State Point	Pressure, P (bar)	Temperature, T (°C)	Enthalpy, h (kJ/kg)	Concentration, X (kg NH ₃ /kg mix)	Flow Rate, \dot{m} (kg/s)	Equilibrium Saturated Condition	Quality (\dot{m}_g/\dot{m}_r)
1	21.7	90	1430	0.985	0.01	✓	1
2	21.7	≈54	≈250	0.985	0.01	✓	0
3	4.7	2	250	0.985	0.01		
4	4.7	2	1265	0.985	0.01	✓	1
5	4.7	52	361	0.415	0.2		
6	4.7	52	0	0.415	0.2	✓	0
7	21.7	≈52	≈0	0.415	0.2		
8	21.7	120	305	0.385	0.19	✓	0
9	4.7	59	305	0.385	0.19		

State Point 6: Assume equilibrium saturated liquid condition,

$$P_6 = 4.7 \text{ bar}, \quad h_6 = 0 \text{ kJ/kg}, \\ X_6 = 0.415, \quad T_6 = 52^\circ\text{C}.$$

State Point 7: Neglecting the pump work,

$$P_7 = 21.7 \text{ bar}, \quad h_7 \approx h_6 = 0 \text{ kJ/kg}, \\ X_7 = 0.415, \quad T_7 \approx T_6 = 52^\circ\text{C}.$$

State Point 8: Assume equilibrium saturated liquid condition,

$$P_8 = 21.7 \text{ bar}, \quad h_8 = 305 \text{ kJ/kg}, \\ X_8 = 0.385, \quad T_8 = 120^\circ\text{C}.$$

Energy balance at the generator,

$$\dot{Q}_g = \dot{m}_r h_1 + \dot{m}_w h_8 - \dot{m}_s h_7 \\ \dot{Q}_g = 0.01 \times 1430 + 0.19 \times 305 - 0.2 \times 0 = 72.3 \text{ kW}.$$

Coefficient of performance,

$$\text{COP} = \frac{\dot{Q}_e}{\dot{Q}_g} = \frac{10.5 \text{ kW}}{72.3 \text{ kW}} = 0.15.$$

State Point 9: From an isoenthalpic process at the valve,

$$h_9 = h_8 = 305 \text{ kJ/kg.}$$

Energy balance at the absorber,

$$h_5 = \frac{\dot{m}_r h_4 + \dot{m}_w h_9}{\dot{m}_s} = \frac{0.01 \times 1425 + 0.19 \times 305}{0.2} = 361 \text{ kJ/kg.}$$

Example 6.5

It is proposed to convert the gas-fired chiller of Example 6.4 to a solar-based chiller. Propose the modifications and analyze the performance.

Solution

Assuming that we can use a flat-plate solar collector system to provide heat for the generator, which will operate at 75°C, the high pressure in the cycle would have to be reduced. Taking the high pressure to be 17 bar and following the procedure of Example 6.4, the properties are as in Table 6.5.

Note that the values of concentration in the cycle must change in order to obtain reasonable values of temperatures. For example, in order to achieve condensation (State 2) at a temperature above the ambient (we choose 40°C), the concentration at State 8 must be increased to 0.55. This will allow us to get ammonia vapor of concentration 0.99 at 70°C at State 1 (pressure 17 bars), which, in turn, will condense at 40°C. The concentration of 0.55 at State 8 is found by an iterative procedure.

$$\dot{Q}_g = 51.2 \text{ kW, and COP} = 0.205.$$

TABLE 6.5

Thermodynamic Properties of Ammonia–Water in Example 6.5

State Point	Pressure, P (bar)	Temperature, T (°C)	Enthalpy, H (kJ/kg)	Concentration, X (kg NH ₃ /kg mix)	Flow Rate, \dot{m} (kg/s)	Equilibrium Saturated Condition	Quality (\dot{m}_g/\dot{m}_r)
1	17	70	1400	0.99	0.0086	✓	1
2	17	≈40	≈180	0.99	0.0086	✓	0
3	4.7	2	180	0.99	0.0086		
4	4.7	2	1400	0.99	0.0086	✓	1
5	4.7	28	156	0.57	0.2		
6	4.7	28	-100	0.57	0.2	✓	0
7	17	≈28	≈-100	0.57	0.2		
8	17	75	100	0.55	0.1914	✓	0
9	4.7	25	100	0.55	0.1914		

6.2 Solar Desiccant Dehumidification

In hot and humid regions of the world experiencing significant latent cooling demand, solar energy may be used for dehumidification using liquid or solid desiccants. Rengarajan et al. (1989) compared a number of strategies for ventilation air conditioning for Miami, Florida, and found that a conventional vapor-compression system could not even meet the increased ventilation requirements of ASHRAE Standard 62-1989. By pretreating the ventilation air with a desiccant system, proper indoor humidity conditions could be maintained and significant electrical energy could be saved. A number of researchers have shown that a combination of a solar desiccant and a vapor-compression system can save from 15% to 80% of the electrical energy requirements in commercial applications, such as supermarkets (Meckler 1994, 1995, 1988; Meckler et al. 1993; Oberg and Goswami 1998a,b; Spears and Judge 1997; Thombloom and Nimmo 1994, 1995).

In a desiccant air-conditioning system, moisture is removed from the air by bringing it in contact with the desiccant and followed with sensible cooling of the air by a vapor-compression cooling system, vapor absorption cooling systems, or an evaporative cooling system. The driving force for the process is the water vapor pressure. When the vapor pressure in air is higher than that on the desiccant surface, moisture is transferred from the air to the desiccant until an equilibrium is reached (see Figure 6.11). In order to regenerate the desiccant for reuse, the desiccant is heated, which increases the water

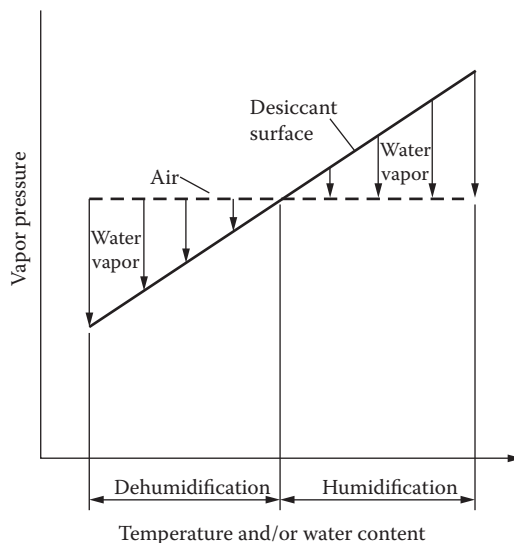


FIGURE 6.11

Vapor pressure versus temperature and water content for dessicant and air.

vapor pressure on its surface. If air with lower vapor pressure is brought in contact with this desiccant, the moisture passes from the desiccant to the air (Figure 6.11). Two types of desiccants are used: solids, such as silica gel and lithium chloride, or liquids, such as salt solutions and glycols.

6.2.1 Solid Desiccant Cooling System

The two solid desiccant materials that have been used in solar systems are silica gel and the molecular sieve, a selective absorber. Figure 6.12 shows the equilibrium absorption capacity of several substances. Note that the molecular sieve has the highest capacity up to 30% humidity, and silica gel is optimal between 30% and 75%—the typical humidity range for buildings.

Figure 6.13 is a schematic diagram of a desiccant cooling ventilation cycle (also known as Pennington cycle), which achieves both dehumidification and cooling. The desiccant bed is normally a rotary wheel of a honeycomb-type substrate impregnated with the desiccant. As the air passes through the rotating wheel, it is dehumidified while its temperature increases (processes 1 and 2) owing to the latent heat of condensation. Simultaneously, a hot air stream passes through the opposite side of the rotating wheel, which removes moisture from the wheel. The hot and dry air at state 2 is cooled in a heat-exchanger wheel to condition 3 and further cooled by evaporative cooling to condition 4. Air at condition 3 may be further cooled by vapor-compression or vapor-absorption systems instead of evaporative cooling. The return air from the conditioned space is cooled by evaporative cooling (processes 5 and 6), which in turn cools the heat-exchanger

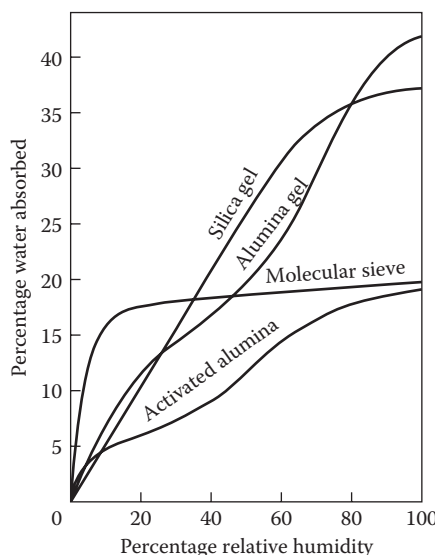
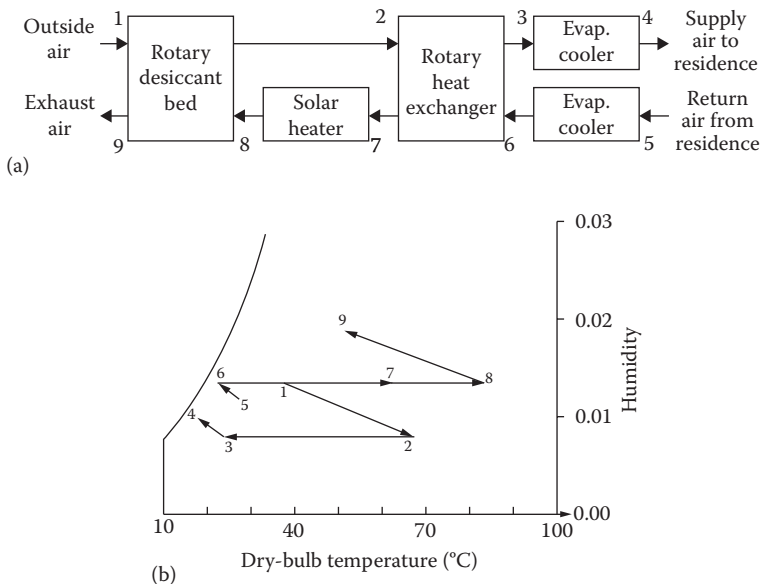


FIGURE 6.12
Equilibrium capacities of common water absorbents.

**FIGURE 6.13**

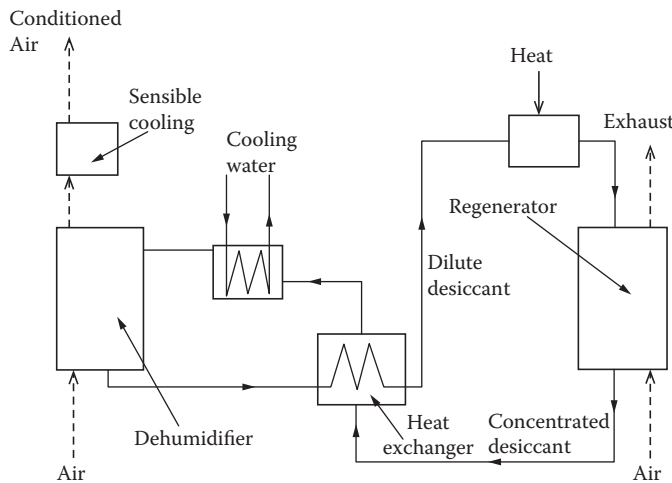
Schematic of a desiccant cooling ventilation cycle: (a) schematic of airflow, (b) process on a psychrometric chart.

wheel. This air is then heated to condition 7. Using solar heat, it is further heated to condition 8 before going through the desiccant wheel to regenerate the desiccant. A number of researchers have studied this cycle, or an innovative variation of it, and have found thermal COPs in the range of 0.5 to 2.58 (Pesaran et al. 1992).

6.2.2 Liquid Desiccant Cooling System

Liquid desiccants offer a number of advantages over solid desiccants. The ability to pump a liquid desiccant makes it possible to use solar energy for regeneration more efficiently. It also allows several small dehumidifiers to be connected to a single regeneration unit. Since a liquid desiccant does not require simultaneous regeneration, the liquid may be stored for later regeneration when solar heat is available. A major disadvantage is that the vapor pressure of the desiccant itself may be enough to cause some desiccant vapors to mix with the air. This disadvantage, however, may be overcome by proper choice of the desiccant material.

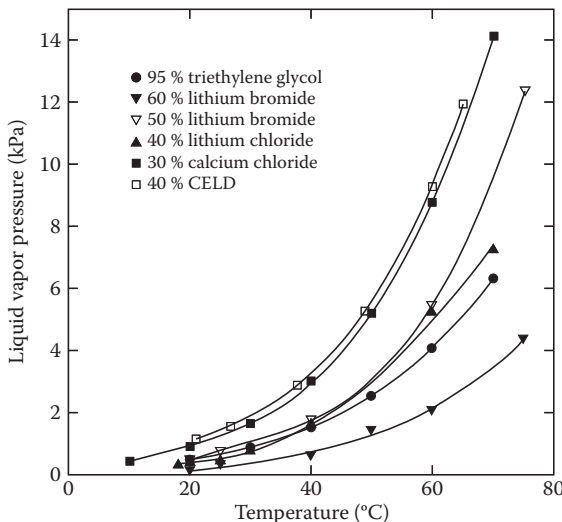
A schematic of a liquid desiccant system is shown in Figure 6.14. Air is brought in contact with concentrated desiccant in a countercurrent flow in a dehumidifier. The dehumidifier may be a spray column or packed bed. The packings provide a very large area for heat and mass transfer between the air and the desiccant. After dehumidification, the air is sensibly cooled before entering the conditioned space. The dilute desiccant exiting the dehumidifier

**FIGURE 6.14**

A conceptual liquid desiccant cooling system.

is regenerated by heating and exposing it to a countercurrent flow of a moisture scavenging air stream.

Liquid desiccants commonly used are aqueous solutions of lithium bromide, lithium chloride, calcium chloride, mixtures of these solutions, and triethylene glycol (TEG) (see Oberg and Goswami 1998b). Vapor pressures of these common desiccants are shown in Figure 6.15 as a function

**FIGURE 6.15**

Vapor pressures of liquid desiccants.

of concentration and temperature, based on a number of references (Dow Chemical Company 1992, 1996; Ertas et al. 1992; Zaytsev and Aseyev 1992). Other physical properties important in the selection of desiccant materials are listed in Table 6.6. Although salt solutions and TEG have similar vapor pressures, the salt solutions are corrosive and have higher surface tension. The disadvantage of TEG is that it requires higher pumping power because of higher viscosity.

Oberg and Goswami (1998b) have presented an in-depth review of liquid desiccant cooling systems. Based on an extensive numerical modeling and on experimental studies, they have presented correlations for the performance of a packed bed liquid desiccant dehumidifier and a regenerator.

The performance of a packed bed dehumidifier or a regenerator may be represented by a humidity effectiveness ϵ_y defined as the ratio of the actual change in humidity of the air to the maximum possible for the operating conditions (Chung 1989; Khan 1994; Ullah et al. 1988).

$$\epsilon_y = \frac{Y_{in} - Y_{out}}{Y_{in} - Y_{eq}}, \quad (6.19)$$

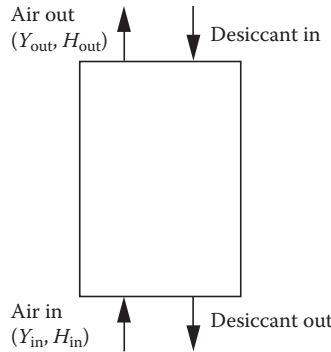
where Y_{in} and Y_{out} are the humidity ratios of the air inlet and outlet, respectively, and Y_{eq} is the humidity ratio in equilibrium with the desiccant solution at the local temperature and concentration (see Figure 6.16).

TABLE 6.6

Physical Properties of Liquid Desiccants at 25°C

Dessicant	Density, $\rho \cdot 10^{-3}$ (kg/nV)	Viscosity, $\mu \cdot 10^3$ (Ns/m ²)	Surface Tension, $\gamma \cdot 10^3$ (N/m)	Specific Heat, c_p (kJ/kg·°C)	Reference
95% by weight triethylene glycol	1.1	28	46	2.3	Kreider and Kreith (1977)
55% by weight lithium bromide	1.6	6	89	2.1	Kettleborough and Waugaman (1995) and Zaytsev and Aseyev (1992)
40% calcium chloride	1.4	7	93	2.5	Close (1965), Khan (1994), and Zaytsev and Aseyev (1992)
40% by weight lithium chloride	1.2	9	96	2.5	Zaytsev and Aseyev (1992)
40% by weight CELD	1.3	5	—	—	Löf and Tybout (1974)

Source: Oberg, V. and D.Y. Goswami, *Advances in Solar Energy*, ASES 12: 431–470, 1998.

**FIGURE 6.16**

Exchange of humidity and moisture between desiccant and air in the tower.

In addition to the humidity effectiveness, an enthalpy effectiveness ε_H is also used as a performance parameter (Kettleborough and Waugaman 1995; Khan 1994):

$$\varepsilon_H = \frac{H_{a,in} - H_{a,out}}{H_{a,in} - H_{a,eq}}, \quad (6.20)$$

where $H_{a,in}$, $H_{a,out}$, and $H_{a,eq}$ are the enthalpies of the air at the inlet and outlet, and in equilibrium with the desiccant, respectively. Oberg and Goswami (1998a) found the following correlation for ε_y and ε_H :

$$\varepsilon_y, \varepsilon_H = 1 - C_1 \left(\frac{L}{G} \right)^a \left(\frac{H_{a,in}}{H_{L,in}} \right)^b (aZ)^c, \quad (6.21)$$

where

$$a = k_1 \frac{\gamma_L}{\gamma_c} + m_1 \quad \text{and} \quad c = k_2 \frac{\gamma_L}{\gamma_c} + m_2.$$

Here, C_1 , b , k_1 , m_1 , and m_2 are constants listed in Table 6.7. L and G are the liquid and air mass flow rates, respectively; a is the packing surface area per unit volume for heat and mass transfer in m^2/m^3 ; Z is the tower height in

TABLE 6.7

Constants for Performance Correlations

	C_1	b	k_1	m_1	k_2	m_2
ε_y	48.345	-0.751	0.396	-1.573	0.033	-0.906
ε_H	3.766	-0.528	0.289	-1.116	-0.004	-0.365

meters; γ_L is the surface tension of the liquid desiccant; and γ_c is the critical surface tension for the packing material.

6.3 Summary

The techniques useful for active solar cooling, refrigeration, and dehumidification have been described in this chapter. The absorption method provides a suitable thermodynamic match of flat-plate collector to cooling machine because of the usability of low temperatures by the H_2O -LiBr and NH_3 - H_2O absorption methods.

Air dehumidification by desiccants and solar regeneration of desiccants is also a method whereby a large part of the cooling load can be met by solar energy. Both solid and liquid desiccants have been described.

PROBLEMS

1. The following table gives the characteristics of a building in Houston, Texas. Determine the cooling load for July 30 at solar noon. Any information regarding the load not given may be assumed or neglected.

Factor	Description or Specification
Roof	
Type	Flat, shaded
Area, $A_{rf,sh}$ (m^2)	250
U factor ($W/m^2 \cdot K$)	$U_{rf} = 0.35$
Walls	
Type	Vertical, painted white
Orientation, size ($m \times m$)	North, south, 3×10 ; east, west, 3×25
U factor ($W/m^2 \cdot K$)	$U_{wa} = 1.08$
Windows	
Orientation, area (m^2)	North, 8; south, 8; east, 20; west, 25
U factor ($W/m^2 \cdot K$)	$U_{wi} = 6.2$
Insolation transmittance	$\bar{\tau}_{b,wi} = 0.60; \bar{\tau}_{d,wi} = 0.80; \bar{\tau}_{r,wi} = 0.55$
Temperature	
Inside, outside ($^{\circ}C$)	$T_{in} = 24; T_{out} = 37$
Insolation	
Beam, diffuse, reflected (W/m^2)	$I_{h,b} = 580; I_{h,d} = 250; I_r = 200$

2. An air-conditioning system working in a vapor-compression cycle is used to manage the load for the building in Problem 1. If the high pressure and low pressure in the cycle are 915 and 290 kPa,

respectively, and the efficiency of the compressor is 90%, find the flow rate of R-134a used for the equipment and the COP of the cycle.

3. Consider the absorption refrigeration cycle, shown in the line diagram below, that uses lithium bromide as carrier and water as refrigerant to provide cooling. By using steam tables and the chart giving the properties of lithium bromide and water, calculate first:

- Heat removed from the absorber
- Heat removed from the condenser
- Heat added to the evaporator
- COP of the cycle

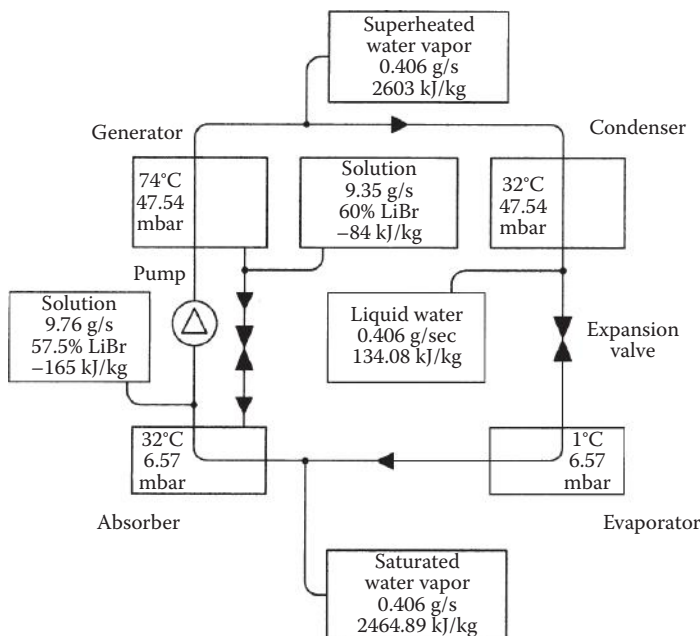
Then calculate, for a flat-plate collector with an $F_R(\tau\alpha)$ intercept of 0.81 and an $F_R U_c$ of 3 W/m²·K, the area required for operation in Arizona at noon in August for a 3-ton unit. Assume that the enthalpy of the water vapor leaving the evaporator can be approximated by the equation

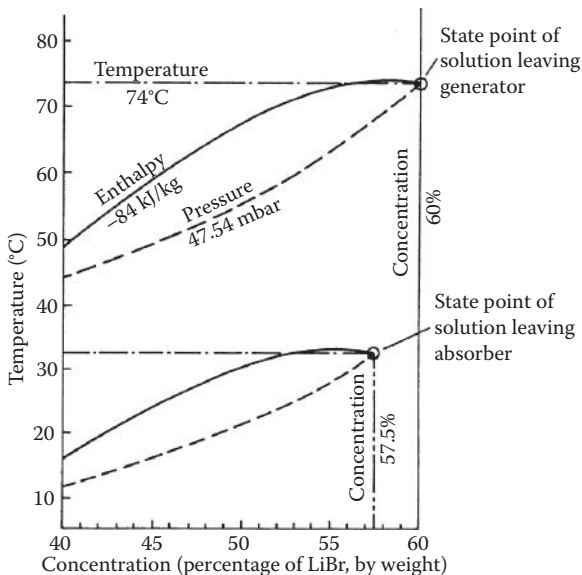
$$h_{ve} = 2463 + 1.9T_e \text{ kJ/kg}$$

and that the enthalpy of the liquid water is

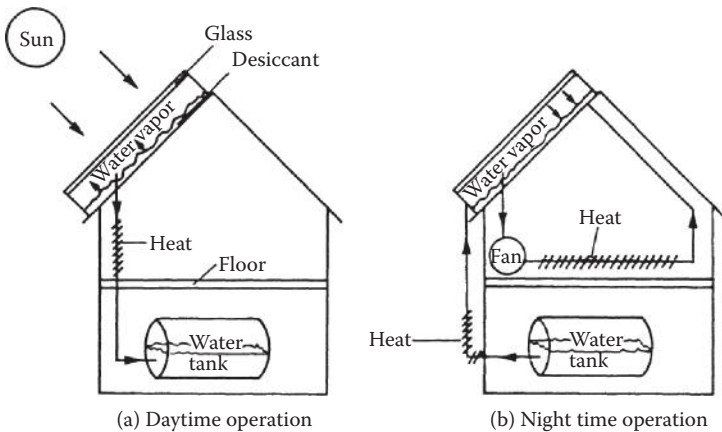
$$h_{le} = 4.2T_e \text{ kJ/kg},$$

where T_e is the temperature of the evaporator in °C. In the analysis, assume that evaporation occurs at 1°C and condensation occurs at 32°C.





4. Make a preliminary design for a solar-driven Rankine refrigeration machine to provide the temperature environment required below the surface of a 20×40 m ice skating rink that is to operate all year in the vicinity of Denver, Colorado. State all your assumptions.
5. An inventor has proposed a desiccant heat pump to augment the heat delivered by a solar collector, and a sketch of the system is shown below. The collector bottom is covered with a desiccant, such as silica gel or zeolite, that contains water, and during the day, the solar radiation heats up the desiccant bed and vaporizes a significant fraction of the water. The water vapor thus driven off passes through a heat exchanger in the building, and the vapor condenses with the release of heat into the building. At night, the liquid water stored in a tank passes through a heat exchanger outside the building where it absorbs heat and evaporates. The vapor produced then condenses in the desiccant at a temperature of 150°F , and air from the building is circulated between the building and collector to supply heat to the building at night. Comment on the feasibility of the system proposed and estimate the effective COP.



6. A 5-ton, ammonia–water refrigeration system as shown in Figure 6.9 was designed to work with solar energy. The low and high pressures are 3 and 15 bar, respectively. The concentrations are $X_r = 0.98$, $X_s = 0.6$, and $X_w = 0.58$, and the COP is expected to be 0.3. Determine the area and the required minimum temperature for a flat-plate solar collector system. Choose a site of interest to you.
 7. The table below shows data from a dehumidification process using aqueous solution of lithium chloride (LiCl) in a packed tower. The desiccant leaving the dehumidifier is passed through another packed tower for regeneration. For the regeneration process, it is known that the rate of evaporation of water as a function of the concentration X ($\text{kg}_{\text{LiCl}}/\text{kg}_{\text{sol}}$) and temperature, T (°C), of the desiccant is given by the following equation:

$$m_{\text{evap}} = (a_0 + a_1 T + a_2 T^2) + (b_0 + b_1 T + b_2 T^2)X + (c_0 + c_1 T + c_2 T^2)X^2 \text{ (g/s)},$$

where

$$\begin{aligned} a_0 &= 285,077, & b_0 &= -1,658,652, & c_0 &= 2,412,282, \\ a_1 &= -8992, & b_1 &= 52,326, & c_1 &= -76,112, \text{ and} \\ a_2 &= 70.88, & b_2 &= -412, & c_2 &= 600. \end{aligned}$$

Find the temperature to which a flat-plate collector must raise the temperature of the desiccant for the regeneration process. Assume that the flow rate of liquid desiccant in both processes (dehumidification and regeneration) is the same.

Variable	Air		Desiccant		Variable
	Inlet	Outlet	Inlet	Outlet	
Temp (°C)	30.4	32.6	30	33.1	Temp (°C)
RH (%)	66.7	36.7	35	—	Concent. (%)
Mass (kg/h)	260	—	850	—	Mass (kg/h)

References

- ASHRAE. 2013. *Handbook of Fundamentals*. American Society of Heating, Refrigerating and Air-Conditioning Engineers, Atlanta, GA.
- Chinnappa, J.C.V., and N.E. Wijeyesundara. 1992. Simulation of solar-powered ammonia-water integrated hybrid cooling system. *J. Sol. Energy Eng., Trans. ASME* 114: 125–127.
- Chung, T.-W. 1989. Predictions of the moisture removal efficiencies for packed-bed dehumidification systems. *Solar Engineering—1989, Proc. of the 11th Annual ASME Solar Energy Conf*, San Diego, CA, pp. 371–377.
- Close, D.J. 1965. Rock pile thermal storage for comfort air conditioning. *Mech. Chem. Eng. Trans. Inst. Eng. (Australia)* MC-1: 11.
- Dow Chemical Company. 1992. *A Guide to Glycols*. Dow Chemical Company, Midland, MI.
- Dow Chemical Company. 1996. *Calcium Chloride Handbook*. Dow Chemical Company, Midland, MI.
- Ertas, A., E.E. Anderson, and I. Kiris. 1992. Properties of a new liquid desiccant solution—Lithium chloride and calcium chloride mixture. *Sol. Energy* 49: 205–212.
- Kettleborough, C.F., and D.G. Waugaman. 1995. An alternative desiccant cooling cycle. *J. Sol. Energy Eng.* 117: 251–255.
- Khan, A.Y. 1994. Sensitivity analysis and component modeling of a packed-type liquid desiccant system at partial load operating conditions. *Int. J. Energy Res.* 18: 643–655.
- Kochhar, G.S. 1982. Optimum thermal performance of a flat plate solar collector driven ammonia-water absorption system. *Alternative Energy Sources 4 (Proceedings of the 4th Miami International Conference on Alternative Energy)*, Miami Beach, FL, USA, Vol. 8, pp. 333–343.
- Kreider, J.F., and F. Kreith. 1977. *Solar Heating and Cooling*, revised 1st ed. Hemisphere Publ. Corp, Washington, DC.
- Löf, G.O.G., and R.A. Tybout. 1974. Design and cost of optimal systems for residential heating and cooling by solar energy. *Sol. Energy* 16: 9.
- Macriss, R.A., and T.S. Zawacki. 1989. Absorption fluid data survey: 1989 update. Oak Ridge National Laboratory Report, Oak Ridge, TN, ORNL/Sub84-47989/4.
- Manrique, J.A. 1991. Thermal performance of ammonia-water refrigeration system. *Int. Comm., Heat Mass Transfer* 19(6): 779–789.
- Meckler, M. 1988. Off-peak desiccant cooling and cogeneration combine to maximize gas utilization. *ASHRAE Trans.* 94(Pt 1): 575–596.

- Meckler, M. 1994. Desiccant-assisted air conditioner improves IAQ and comfort. *Heating/Piping/Air Conditioning* 66(10): 75–84.
- Meckler, M. 1995. Desiccant outdoor air preconditioners maximize heat recovery ventilation potentials. *ASHRAE Trans.* 101(Pt 2): 992–1000.
- Meckler, M., Y.O. Parent, and A.A. Pesaran. 1993. Evaluation of dehumidifiers with polymeric desiccants. Gas Institute Report, Contract No. 5091-246-2247. Gas Research Institute, Chicago, IL.
- Oberg, V., and D.Y. Goswami. 1998a. Experimental study of heat and mass transfer in a packed bed liquid desiccant air dehumidifier. In *Solar Engineering*, J.H. Morehouse, and R.E. Hogan, eds., pp. 155–166.
- Oberg, V., and D.Y. Goswami. 1998b. A review of liquid desiccant cooling. In *Advances in Solar Energy*, K. Boer, ed., ASES, Boulder, CO, Vol. 12, pp. 431–470.
- Pesaran, A.A., T.R. Penney, and A.W. Czanderna. 1992. Desiccant cooling: State-of-the art assessment. NREL, Report No. NREL/TP-254-4147. National Renewable Laboratory, Golden, CO.
- Rengarajan, K., D.B. Shirley, III, and R.A. Raustad. 1989. Cost-effective HVAC technologies to meet ASHRAE Standard 62-1989 in hot and humid climates. *ASHRAE Trans.* (Pt 1): 166–182.
- Siddiqui, A.M. 1993. Optimum generator temperatures in four absorption cycles using different sources of energy. *Energy Convers. Mgmt.* 34(4): 251–266.
- Spears, J.W., and J. Judge. 1997. Gas-fired desiccant system for retail super center. *ASHRAE J.* 39: 65–69.
- Thombloom, M., and B. Nimmo. 1994. Modification of the absorption cycle for low generator firing temperatures. *Joint Solar Engineering Conf.*, ASME, American Solar Energy Society, Boulder, CO.
- Thombloom, M., and B. Nimmo. 1995. An economic analysis of a solar open cycle desiccant dehumidification system. *Solar Engineering—1995, Proc. of the 13th Annual ASME Conference*, Hawaii, Vol. 1, pp. 705–709.
- Thombloom, M., and B. Nimmo. 1996. Impact of design parameters on solar open cycle liquid desiccant regenerator performance. *SOLAR '96, Proc. of 1996 Annual Conf. of the American Solar Energy Society*, Asheville, NC, pp. 107–111.
- Ullah, M.R., C.F. Kettleborough, and P. Gandhidasan. 1988. Effectiveness of moisture removal for an adiabatic counterflow packed tower absorber operating with CaCl_2 -air contact system. *J. Sol. Energy Eng.* 110: 98–101.
- Zaytsev, I.O., and G.G. Aseyev. 1992. *Properties of Aqueous Solutions of Electrolytes*. CRC Press, Boca Raton, FL.

7

Passive Solar Heating, Cooling, and Daylighting

7.1 Introduction

Passive systems are defined, quite generally, as systems in which the thermal energy flow is by natural means: by conduction, radiation, and natural convection. Passive features increase the use of solar energy, ambient conditions, and earth and deep space to meet the heating, cooling, and lighting loads of buildings. For example, window placement can enhance solar gains to meet winter heating loads, provide daylighting, or do both. Using a solar chimney to draw air through a building directly or via an earth air tunnel is an example of passive cooling.

A *passive solar heating system* is one in which the sun's radiant energy is converted to heat upon absorption by the building. The absorbed heat can be transferred to thermal storage by natural means or used to directly heat the building. *Passive cooling systems* use natural energy flows to transfer heat to the environmental sinks: the ground, air, and sky (space).

A distinction is made between energy conservation techniques and passive solar measures. Energy conservation features are designed to reduce the heating and cooling energies required to thermally condition a building, for example, the use of insulation to reduce either heating or cooling loads or the use of window shading or window placement to reduce solar gains, reducing summer cooling loads.

If one of the major heat transfer paths employs a pump or fan to force flow of a heat transfer fluid, then the system is referred to as having an *active* component or subsystem. *Hybrid systems* use both passive and active energy flows. The use of the sun's radiant energy for the natural illumination of a building's interior spaces is called *daylighting*.

7.1.1 Current Applications and Costs

There are many examples of ancient buildings with passive heating, cooling, and daylighting. However, most building designs in the past century neglected passive features to provide a part of the energy needs of the

buildings. That began to change in the late last century as the cost of energy increased rapidly. A typical passive heating design in a favorable climate might supply up to one-third of a home's original load at a cost of 2–4¢/kWh energy saved. An appropriately designed daylighting system can supply lighting at a cost of 2.5–5¢/kWh (ASES [American Solar Energy Society] 1992).

The distinction between passive systems and energy conservation is not critical for economic calculations. An important consideration is the trade-off between the life-cycle costs of the energy saved (performance) and the initial investment and the operating and maintenance costs (cost). The other significant part of the economic trade-off involves determining the difference between the cost of construction of a passive building and that of a conventional building against which it is to be compared, that is, the "solar add-on cost."

Passive solar water heaters are described in Chapter 5. This chapter describes passive space heating and cooling systems and daylighting.

7.2 Passive Space Heating Systems

Passive heating systems contain the five basic components of all solar systems, as described in Chapters 4 and 5. Typical passive realizations of these components are as follows:

1. Collector—windows, walls, and floors
2. Storage—walls and floors, large interior masses (often these are integrated with the collector absorption function)
3. Distribution system—radiation, free convection, simple circulation fans
4. Controls—moveable window insulation, vents both to other inside spaces and to ambient
5. Backup system—any nonsolar heating system

The design of passive systems requires the strategic placement of windows, storage masses, and the occupied spaces themselves. The fundamental principles of solar radiation geometry and availability are instrumental in the proper location and sizing of the system's "collectors" (windows). Storage devices are usually more massive than those used in active systems and are frequently an integral part of the collection and distribution system.

7.2.1 Types of Passive Heating Systems

A commonly used method of cataloging the various passive system concepts is to distinguish three general categories: direct, indirect, and isolated gain.

Most of the physical configurations of passive heating systems are seen to fit within one of these three categories.

For direct gain systems (Figure 7.1), sunlight enters the heated space and is converted to heat at absorbing surfaces. This heat is then distributed throughout the space and to the various enclosing surfaces and room contents.

For indirect gain systems, sunlight is absorbed and stored by a mass interposed between the glazing and the conditioned space. The conditioned space is partially enclosed and bounded by this thermal storage mass; hence, a natural thermal coupling is achieved. Examples of the indirect approach are the thermal storage wall, the thermal storage roof, and the northerly room of an attached sunspace.

In the thermal storage wall (Figure 7.2a), sunlight penetrates the glazing and is absorbed and converted to heat at a wall surface interposed between the glazing and the heated space. The wall is usually masonry (Trombe wall) or containers filled with water (water wall), although it might contain phase-change material. The attached sunspace (Figure 7.2b) is actually a two-zone combination of direct gain and thermal storage wall. Sunlight enters and heats a direct gain southerly *sunspace* and a mass wall separating the northerly buffered space, which is heated indirectly. The *sunspace* is frequently used as a greenhouse, in which case the system is called an *attached greenhouse*. The thermal storage roof (Figure 7.2c) is similar to the thermal storage wall except that the interposed thermal storage mass is located on the building roof. A thermal storage roof using water for storage and movable insulation on the top was developed by Hay (Hay and Yellott 1969), which is also known as the *roof-pond* system.

The isolated gain category concept is an indirect system except that there is a distinct thermal separation (by means of either insulation or physical separation) between the thermal storage and the heated space. The convective

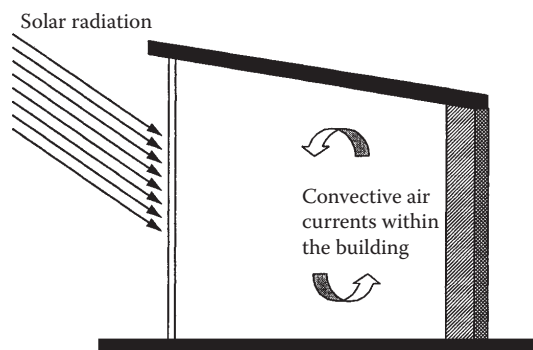
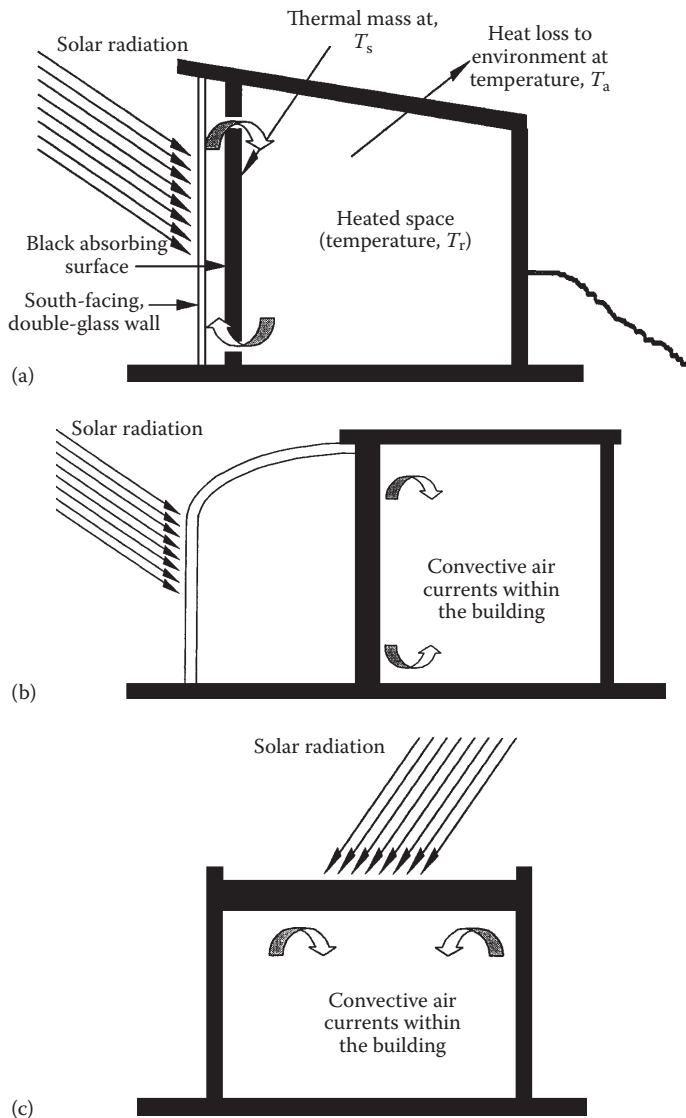


FIGURE 7.1
Concept of a direct gain passive heating system.

**FIGURE 7.2**

(a) Thermal storage wall. (b) Attached sunspace. (c) Thermal storage roof.

(thermosyphon) loop, as depicted in Figure 7.3, is in this category and is often used to heat domestic water. It is most akin to conventional active systems in that there is a separate collector and separate thermal storage. The thermal storage wall, thermal storage roof, and attached sunspace approaches can also be made into isolated systems by insulating between the thermal storage and the heated space.

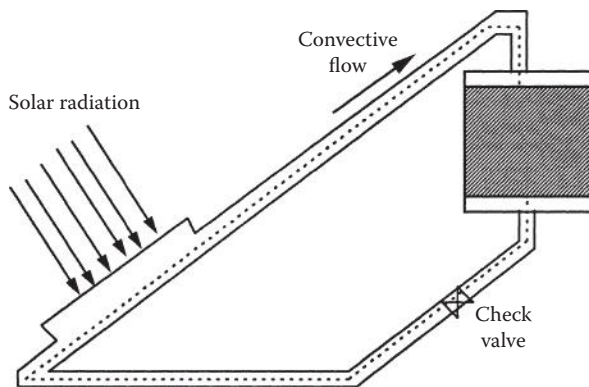


FIGURE 7.3
Convective loop.

7.2.2 Fundamental Concepts for Passive Heating Design

Figure 7.4 is an equivalent thermal circuit for the building illustrated in Figure 7.2a, the Trombe wall-type system. For the heat transfer analysis of the building, three temperature nodes can be identified—room temperature, storage wall temperature, and the ambient temperature. The circuit responds to climatic variables represented by a current injection I_s (solar radiation) and by the ambient temperature T_a . The storage temperature T_s and room temperature T_r are determined by current flows in the equivalent circuit. By using seasonal and annual climatic data, the performance of a passive structure can be simulated, and the results of many such simulations correlated to give the design approaches described in the following.

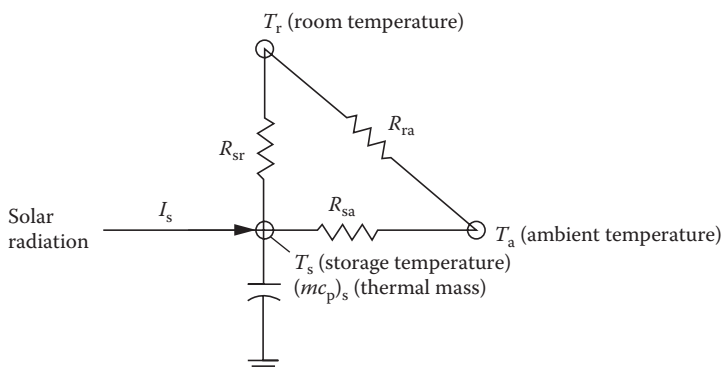


FIGURE 7.4
Equivalent thermal circuit for passively heated solar building in Figure 7.2a.

7.2.3 Generalized Passive Design Methods

Design of a passive heating system involves selection and sizing of the passive feature type(s), determination of thermal performance, and cost estimation. Ideally, a cost/performance optimization would be performed by the designer. Owner and architect ideas usually establish the passive feature type, with general size and cost estimation available. However, the thermal performance of a passive heating system has to be calculated.

There are several “levels” of methods that can be used to estimate the thermal performance of passive designs. First-level methods involve a rule of thumb or generalized calculation to get a starting estimate for size or annual performance. A second-level method involves climate, building, and passive system details, which allow annual performance determination, plus some sensitivity to passive system design changes. Third-level methods involve periodic calculations (hourly, monthly) of performance and permit more detailed variations of climatic, building, and passive solar system design parameters.

These three levels of design methods have a common basis in that they all are derived from correlations of a multitude of computer simulations of passive systems (PSDH [*Passive Solar Design Handbook*] 1980, 1984). As a result, a similar set of defined terms is used in many passive design approaches:

- A_p , solar projected area, m^2 (ft^2): The net south-facing passive solar glazing area projected onto a vertical plane.
- NLC, net building load coefficient, kJ/CDD (Btu/FDD): Net load of the nonsolar portion of the building per day per degree of indoor-outdoor temperature difference. The C-day and F-day terms refer to centigrade and Fahrenheit degree days, respectively.
- Q_{net} , net reference load, Wh (Btu): Heat loss from nonsolar portion of building is calculated by

$$Q_{\text{net}} = \text{NLC} \times (\text{no. of degree days}). \quad (7.1)$$

- LCR, load collector ratio, $\text{kJ}/\text{m}^2\cdot\text{C-day}$ ($\text{Btu}/\text{ft}^2\cdot\text{F-day}$): Ratio of NLC to A_p ,

$$\text{LCR} = \frac{\text{NLC}}{A_p}. \quad (7.2)$$

- SSF, solar savings fraction, is the fractional reduction in required auxiliary heating relative to net reference load,

$$\text{SSF} = 1 - \frac{Q_{\text{aux}}}{Q_{\text{net}}}. \quad (7.3)$$

Hence, using Equation 7.1,

$$\text{Auxiliary heat required, } Q_{\text{aux}} = (1 - \text{SSF}) \times \text{NLC} \times (\text{no. of degree days}). \quad (7.4)$$

The amount of auxiliary heat required is often a basis of comparison between possible solar designs as well as the basis for determining building energy operating costs. Thus, many of the passive design methods are based on determining SSF, NLC, and the number of degree days in order to calculate the auxiliary heat required for a particular passive system by using Equation 7.4.

7.2.4 First Level: Rule of Thumb

A first estimate or starting value is needed to begin the overall passive system design process. Rules of thumb have been developed to generate initial values for solar aperture size, storage size, SSF, auxiliary heat required, and other size and performance characteristics. The following rules of thumb are meant to be used with the defined terms presented previously.

7.2.4.1 Load

A rule of thumb used in conventional building design is that a design heating load of 120–160 kJ/C-day per m² of floor area (6–8 Btu/F-day·ft²) is considered an energy-conservative design. Reducing these nonsolar values by 20% to solarize the proposed south-facing solar wall gives rule-of-thumb NLC values per unit of floor area:

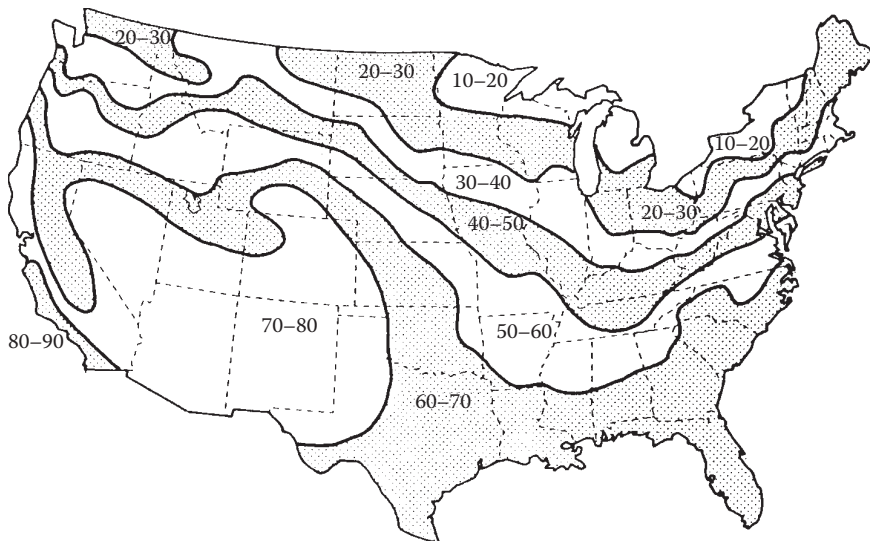
$$\frac{\text{NLC}}{\text{Floor area}} = 100 - 130 \text{ kJ/C-day} \cdot \text{m}^2 (4.8 - 6.4 \text{ Btu/F-day} \cdot \text{ft}^2). \quad (7.5)$$

7.2.4.2 Solar Savings Fraction

A method of getting starting-point values for the SSF is presented in Figure 7.5 (PSDH 1984). The map values represent optimum SSF in percentage for a particular set of conservation and passive solar costs for different climates across the United States. With the Q_{net} generated from the NLC rule of thumb above and the SSF read from the map, the Q_{aux} can be determined.

7.2.4.3 Load Collector Ratio

The A_p can be determined using the NLC from above, if the LCR is known. The rule of thumb associated with “good” values of LCR (Robbins 1986) differs depending on whether the design is for a “cold” or “warm” climate:

**FIGURE 7.5**

Starting-point values of SSF in percentage. (From PSDH, *Passive Solar Design Handbook*, Van Nostrand Reinhold Co., New York, 1984.)

$$\begin{aligned}
 \text{Good LCR} = & \quad \text{For cold climate: } 410 \text{ kJ/m}^2 \cdot \text{C-day} \quad (20 \text{ Btu/ft}^2 \cdot \text{F-day}) \\
 & \quad \text{For warm climate: } 610 \text{ kJ/m}^2 \cdot \text{C-day} \quad (30 \text{ Btu/ft}^2 \cdot \text{F-day})
 \end{aligned} \tag{7.6}$$

7.2.4.4 Storage

Rules of thumb for thermal mass storage relate storage material total heat capacity to the solar projected area (PSDH 1984). The use of the storage mass is to provide for heating on cloudy days and to regulate sunny day room air temperature swing. When the thermal mass directly absorbs the solar radiation, each square meter of the projected glazing area requires enough mass to store 613 kJ/C. If the storage material is not in direct sunlight, but heated from room air only, then four times as much mass is needed. In a room with a direct sunlight heated storage mass, the room air temperature swing will be approximately one-half the storage mass temperature swing. For room air heated storage, the air temperature swing is twice that of the storage mass.

A more location-dependent set of rules of thumb is presented in PSDH (1980). Comparing the results of that method to those of the method presented above, the two rules of thumb are seen to produce roughly similar answers. General system cost and performance information can be generated

with results from rule-of-thumb calculations, but a more detailed level of information is needed to determine design-ready passive system type (direct gain, thermal wall, sunspace), size, performance, and costs.

Example 7.1

A 200-m² residential building in Nashville, Tennessee, is designed to have an NLC of 20,000 kJ/°C-day. Using rule of thumb, find the projected passive area, SSF, and the auxiliary heat required.

Solution

Using the LCR for cold climate, the projected passive solar area can be found from Equation 7.2.

$$A_p = \frac{NLC}{LCR} = \frac{(20,000 \text{ kJ/C-day})}{410 \text{ kJ/m}^2 \cdot \text{C-day}} \\ = 48.8 \text{ m}^2$$

Figure 7.5 shows that Nashville, Tennessee, is at the border of 40%–50% and 50%–60% regions. Therefore, a value of 50% would be a good guess.

Table A7.2 gives 3696 F-days for Nashville, Tennessee, which is equivalent to 2053 C-days. Therefore, the auxiliary heat required, Q_{aux} , may be found from Equation 7.4:

$$Q_{aux} = (1 - 0.50)(20,000 \text{ kJ/C-day})(2053 \text{ C-days}) \\ = 20,530 \text{ MJ annually.}$$

7.2.5 Second Level: LCR Method

The LCR method is useful for making estimates of the annual performance of specific types of passive system(s) combinations. The LCR method was developed by calculating the annual SSF for 94 reference passive solar systems for 219 US and Canadian locations over a range of LCR values. Table A7.1 includes the description of these 94 reference systems for use both with the LCR method and with the solar load ratio (SLR) method described in the following. Tables were constructed for each city with LCR versus SSF listed for each of the 94 reference passive systems. (Note: The SLR method was used to make the LCR calculations, and this SLR method is described in Section 7.2.6 as the third-level method.) While the complete LCR tables (PSDH 1984) include 219 locations, Table A7.2 only includes six “representative” cities (Albuquerque, Boston, Madison, Medford, Nashville, and Santa

Maria), purely owing to space restrictions. The LCR method consists of the following:

1. Determine the building parameters:
 - a. Building load coefficient, NLC.
 - b. Solar projected area, A_p .
 - c. Load collector ratio, $LCR = NLC/A_p$.
2. Find the short designation of the reference system closest to the passive system design (Table A7.1).
3. Enter the LCR Tables (Table A7.2):
 - a. Find the city.
 - b. Find the reference system listing.
 - c. Determine annual SSF by interpolation using the LCR value from above.
 - d. Note the annual heating degree days (no. of degree of days).
4. Calculate the annual auxiliary heat required:

$$\text{Auxiliary heat required} = (1 - \text{SSF}) \times \text{NLC} \times (\text{no. of degree days}).$$

If more than one reference solar system is being used, then find the “aperture area weighted” SSF for the combination. Determine each individual reference system SSF using the total aperture area LCR, then take the “area weighted” average of the individual SSFs.

The LCR method allows no variation from the 94 reference passive designs. To treat off-reference designs, sensitivity curves have been produced that illustrate the effect on SSF of varying one or two design variables. These curves were produced for the six “representative” cities, chosen for their wide geographical and climatological ranges. Several of these SSF “sensitivity curves” are presented in Figure A7.1.

7.2.6 Third Level: SLR Method

The SLR method calculates monthly performance, and the terms and values used are monthly based. The method allows the use of specific location weather data and the 94 reference design passive systems (Table A7.1). In addition, the sensitivity curves (Figure A7.1) can again be used to define performance outside the reference design systems. The result of the SLR method is the determination of the monthly heating auxiliary energy required, which is then summed to give the annual requirement for auxiliary heating energy. Generally, the SLR method gives annual values within $\pm 3\%$ of detailed simulation results, but the monthly values may vary more (Duffie and Beckman 1991; PSDH 1984). Thus, the monthly SLR method is more “accurate” than the

rule-of-thumb methods and provides the designer with system performance on a month-by-month basis.

The SLR method uses equations and correlation parameters for each of the 94 reference systems combined with the insolation absorbed by the system, the monthly degree days, and the system's LCR to determine the monthly SSF. These correlation parameters are listed in Table A7.3 as A , B , C , D , R , G , H , and LCRs for each reference system (PSDH 1984). The correlation equations are as follows:

$$\text{SSF} = 1 - K(1 - F), \quad (7.7)$$

where

$$K = 1 + \frac{G}{\text{LCR}}, \quad (7.8)$$

$$F = \begin{cases} AX, & \text{when } X < R \\ B - C \exp(-DX), & \text{when } X > R, \end{cases} \quad (7.9)$$

$$X = \frac{S/\text{DD} - (\text{LCR}_s)H}{(\text{LCR})K}, \quad (7.10)$$

and X is called the generalized SLR. The DD term is the monthly number of degree-days. The term S is the monthly insolation absorbed by the system per unit of solar projected area. Monthly average daily insolation data on a vertical south-facing surface can be found or calculated using various sources (McQuiston and Parker 1994; PSDH 1984). The S term can be determined by multiplying by a transmission and an absorption factor and the number of days in the month. Absorption factors for all systems are close to 0.96 (McQuiston and Parker 1994), whereas the transmission is approximately 0.9 for single glazing, 0.8 for double glazing, and 0.7 for triple glazing.

Example 7.2

For a vented, 180-ft², double-glazed with night insulation, 12-in.-thick Trombe wall system (TWD4) in an NLC = 11,800 Btu/FDD house in Medford, Oregon, determine the auxiliary energy required in January.

Solution

Weather data for Medford, Oregon (PSDH 1984) yields for January ($N = 31$ days): daily vertical surface insolation = 565 Btu/ ft^2 and 880 FDD; thus, $S = (31)(565)(0.8)(0.96) = 13,452 \text{ Btu}/\text{ft}^2\text{-month}$.

$$\text{LCR} = \frac{\text{NLC}}{A_p} = \frac{11,800}{180} = 65.6 \text{ Btu/FDD ft}^2.$$

From Table A7.3 at TWD4: $A = 0$, $B = 1$, $C = 1.0606$, $D = 0.977$, $R = -9$, $G = 0$, $H = 0.85$, LCRs = 5.8 Btu/FDD ft^2 .

Substituting into Equation 7.8 gives

$$K = 1 + \frac{0}{65.6} = 1.$$

Equation 7.10 gives

$$X = \frac{13,452/880 - (5.8 \times 0.85)}{65.6 \times 1} = 0.16.$$

Equation 7.9 gives

$$F = 1 - 1.0606e^{-0.977 \times 0.16} = 0.09.$$

Equation 7.7 gives

$$\text{SSF} = 1 - 1(1 - 0.09) = 0.09.$$

The January auxiliary energy required can be calculated using Equation 7.4:

$$\begin{aligned} Q_{\text{aux}}(\text{January}) &= (1 - \text{SSF}) \times \text{NLC} \times (\text{no. of degree days}) \\ &= (1 - 0.09) \times 11,800 \times 880 \\ &= 9,450,000 \text{ Btu}. \end{aligned}$$

As mentioned, the use of sensitivity curves (PSDH 1984) as in Figure A7.1 will allow SSF to be determined for many off-reference system design conditions involving storage mass, number of glazings, and other more esoteric parameters. Also, the use of multiple passive system types within one building would be approached by calculating the SSF for each system type individually using a combined area LCR, and then a weighted area (aperture) average SSF would be determined for the building.

7.3 Passive Space Cooling Systems

Passive cooling systems are designed to use natural means to transfer heat from buildings, including convection/ventilation, evaporation, radiation, and conduction. However, the most important element in both passive and conventional cooling design is to prevent heat from entering the building in the first place. Cooling conservation techniques involve building surface colors, insulation, special window glazings, overhangs and orientation, and numerous other architectural/engineering features.

7.3.1 Controlling the Solar Input

Controlling the solar energy input to reduce the cooling load is usually considered a passive (vs. conservation) design concern because solar input may be needed for other purposes, such as daylighting throughout the year or heating during the winter. Basic architectural solar control is normally “designed in” via the shading of the solar windows, where direct radiation is desired for winter heating and needs to be excluded during the cooling season.

The shading control of the windows can be of various types and “controllability,” ranging from drapes and blinds, use of deciduous trees, to the commonly used overhangs and vertical louvers. A rule-of-thumb design for determining proper south-facing window overhang for both winter heating and summer shading is presented in Table 7.1. Technical details on calculating shading from various devices and orientations are found in ASHRAE (American Society of Heating, Refrigerating and Air-Conditioning Engineers) (2011) and Haggard et al. (2010).

7.3.2 Movement of Air

Air movement provides cooling comfort through convection and evaporation from human skin. ASHRAE places the comfort limit at 79°F (26°C) for an air velocity of 50 ft/min (0.25 m/s), 82°F for 160 ft/min, and 85°F for 200 ft/min. To determine whether or not comfort conditions can be obtained, a designer must calculate the volumetric flow rate, Q , which is passing through the occupied space. Using the cross-sectional area, A_x , of the space and the room air velocity, V_a , required, the flow is determined by

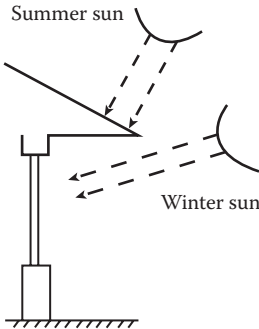
$$Q = A_x V_a. \quad (7.11)$$

The proper placement of windows, “narrow” building shape, and open landscaping can enhance natural wind flow to provide ventilation. The air flow rate through open windows for wind-driven ventilation is given by ASHRAE (2013):

$$Q = C_v V_w A_w, \quad (7.12)$$

TABLE 7.1

South-Facing Window Overhang Rule of Thumb

		Length of the Overhang = $\frac{\text{Window Height}}{F}$
(a) Overhang Factors		
North Latitude	F^a	(b) Roof Overhang Geometry
28	5.6–11.1	
32	4.0–6.3	
36	3.0–4.5	
40	2.5–3.4	
44	2.0–2.7	
48	1.7–2.2	
52	1.5–1.8	
56	1.3–1.5	

Properly sized overhangs shade out hot summer sun but allow winter sun (which is lower in the sky) to penetrate windows.

Source: Halacy, D.S., *Home Energy*, Rodale Press, Inc., Emmaus, PA, 1984.

^a Select a factor according to your latitude. High values provide complete shading at noon on June 21; lower values, until August 1.

where Q is the air flow rate (m^3/s), A_w is the free area of inlet opening (m^2), V_w is the wind velocity (m/s), and C_v is the effectiveness of opening = 0.5–0.6 for wind perpendicular to opening and 0.25–0.35 for wind diagonal to opening.

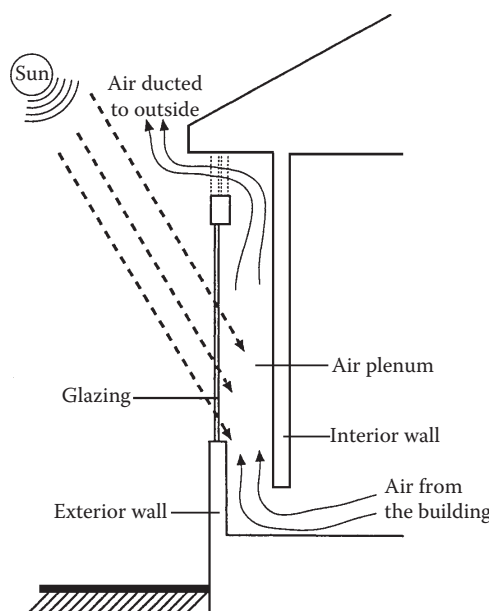
The stack effect can induce ventilation when warm air rises to the top of a structure and exhausts outside, while cooler outside air enters the structure to replace it. Figure 7.6 illustrates the solar chimney concept, which can easily be adapted to a thermal storage wall system.

The greatest stack-effect flow rate is produced by maximizing the stack height and the air temperature in the stack, as given by

$$Q = 0.116 A_j \sqrt{h(T_s - T_o)}, \quad (7.13)$$

where Q is the stack flow rate (m^3/s), A_j is the area of inlets or outlets (whichever is smaller) (m^2), h is the inlet-to-outlet height (m), T_s is the average temperature in stack ($^\circ\text{C}$), and T_o is the outdoor air temperature ($^\circ\text{C}$).

If inlet or outlet area is twice the other, the flow rate will increase by 25%, and by 35% if the areas' ratio is 3:1 or larger.

**FIGURE 7.6**

The stack-effect/solar chimney concept to induce convection/ventilation. (From PSDH, *Passive Solar Design Handbook*, Volume One: *Passive Solar Design Concepts*, DOE/CS-0127/1, March; Volume Two: *Passive Solar Design Analysis*, DOE/CS-0127/2, January. Washington, DC: U.S. Department of Energy, 1980.)

Example 7.3

A two-story (5 m) solar chimney is being designed to produce a flow of $0.25 \text{ m}^3/\text{s}$ through a space. The preliminary design features include a $25 \text{ cm} \times 1.5 \text{ m}$ inlet, a $50 \text{ cm} \times 1.5 \text{ m}$ outlet, and an estimated 35°C average stack temperature on a sunny 30°C day. Can this design produce the desired flow?

Solution

Substituting the design data into Equation 7.13,

$$\begin{aligned} Q &= 0.116(0.25 \times 1.5)[5(5)]^{1/2} \\ &= 0.2 \text{ m}^3/\text{s}. \end{aligned}$$

Since the outlet area is twice the inlet area, the 25% flow increase can be used:

$$Q = 0.2(1.25) = 0.25 \text{ m}^3/\text{s}. \quad (\text{Answer: Yes, the proper flow rate is obtained.})$$

7.3.3 Evaporative Cooling

When air with less than 100% relative humidity moves over a water surface, the evaporation of water causes both the air and the water to cool. The lowest temperature that can be reached by this direct evaporative cooling effect is the wet-bulb temperature of the air, which is directly related to the relative humidity, with lower wet-bulb temperature associated with lower relative humidity. Thus, dry air (low relative humidity) has a low wet-bulb temperature and will undergo a large temperature drop with evaporative cooling, while humid air (high relative humidity) can only be slightly cooled evaporatively. The wet-bulb temperature for various relative humidity and air temperature conditions can be found via the “psychrometric chart” available in most thermodynamic texts. Normally, an evaporative cooling process cools the air only part of the way down to the wet-bulb temperature. To get the maximum temperature decrease, it is necessary to have a large water surface area in contact with the air for a long time, and interior ponds and fountain sprays are often used to provide this air–water contact area.

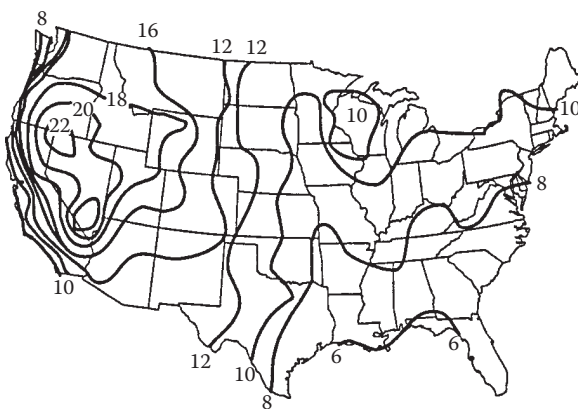
The use of water sprays and open ponds on roofs provides cooling primarily via evaporation. The hybrid system involving a fan and wetted mat, the “swamp cooler,” is by far the most widely used evaporative cooling technology. Direct, indirect, and combined evaporative cooling system design features are described in ASHRAE (2011, 2013).

7.3.4 Nocturnal and Radiative Cooling Systems

Another approach to passive convective/ventilative cooling involves using cooler night air to reduce the temperature of the building or a storage mass. Thus, the building/storage mass is prepared to accept part of the heat load during the hotter daytime. This type of convective system can also be combined with evaporative and radiative modes of heat transfer, utilizing air or water as the convective fluid. Work in Australia (Close et al. 1968) investigated rock storage beds that were chilled using evaporatively cooled night air. Room air was then circulated through the bed during the day to provide space cooling. The use of encapsulated roof ponds as a thermal cooling mass has been tried by several investigators (Hay and Yellott 1969; Marlatt et al. 1984) and is often linked with nighttime radiative cooling.

All warm objects emit thermal infrared radiation; the hotter the body, the more energy it emits. A passive cooling scheme is to use the cooler night sky as a sink for thermal radiation emitted by a warm storage mass, thus chilling the mass for cooling use the next day. The net radiative cooling rate, Q_r , for a horizontal unit surface (ASHRAE 2013) is

$$Q_r = \epsilon\sigma(T_{\text{body}}^4 - T_{\text{sky}}^4), \quad (7.14)$$

**FIGURE 7.7**

Average monthly sky temperature depression ($T_{\text{air}} - T_{\text{sky}}$) for July in Fahrenheit. (Adapted from Martin, M. and P. Berdahl, *Solar Energy*, 33(314): 321–336, 1984.)

where Q_r is the net radiative cooling rate, W/m^2 ($\text{Btu/h}\cdot\text{ft}^2$); ε is the surface emissivity fraction (usually 0.9 for water); $\sigma = 5.67 \times 10^{-8} \text{ W/m}^2\text{K}^4$ ($1.714 \times 20^{-9} \text{ Btu/h}\cdot\text{ft}^2\text{R}^4$); T_{body} is the warm body temperature, Kelvin (Rankine); and T_{sky} is the effective sky temperature, Kelvin (Rankine).

The monthly average air-sky temperature difference has been determined (Martin and Berdahl 1984) and Figure 7.7 presents these values for July (in Fahrenheit) for the United States.

Example 7.4

Estimate the overnight cooling possible for a 10-m², 30°C water thermal storage roof during July in Los Angeles.

Solution

Assume that the roof storage unit is black with $\varepsilon = 0.9$. From Figure 7.7, $T_{\text{air}} - T_{\text{sky}}$ is approximately 10°F for Los Angeles. From weather data for Los Angeles airport (ASHRAE 2013; Robbins 1986), the July average temperature is 20°C with a range of 8°C. Assuming night temperatures vary from the average (20°C) down to half the daily range (8 0/2°F), the average nighttime temperature is chosen as $20 - (1/2)(8/2) = 18^\circ\text{C}$. Hence, $T_{\text{sky}} = 18 - (10/1.8) = 12.5^\circ\text{C}$. From Equation 7.14,

$$\begin{aligned} Q_r &= 0.9(5.67 \times 10^{-8})[(273 + 30)^4 - (273 + 12.5)^4] \\ &= 91.1 \text{ W/m}^2. \end{aligned}$$

For a 10-h night and a 10-m² roof area,

$$\begin{aligned}\text{Total radiative cooling} &= 91.1 (10)(10) \\ &= 9110 \text{ Wh} = 9.11 \text{ kWh.}\end{aligned}$$

Note: This does not include the convective cooling possible, which can be approximated (at its maximum rate) for still air (Table A5.1) by

$$\begin{aligned}\text{Maximum total } Q_{\text{conv}} &= hA(T_{\text{roof}} - T_{\text{air}})(\text{Time}) \\ &= 5(129)(85 - 65)(10) \\ &= (1.63 \times 5.678)(10) (30 - 18)(10) \\ &= 11,110 \text{ Wh} = 11.1 \text{ kWh.}\end{aligned}$$

This is a maximum since the 30°C storage temperature will drop as it cools—which is also the case for the radiative cooling calculation. However, convection is seen to usually be the more dominant mode of nighttime cooling.

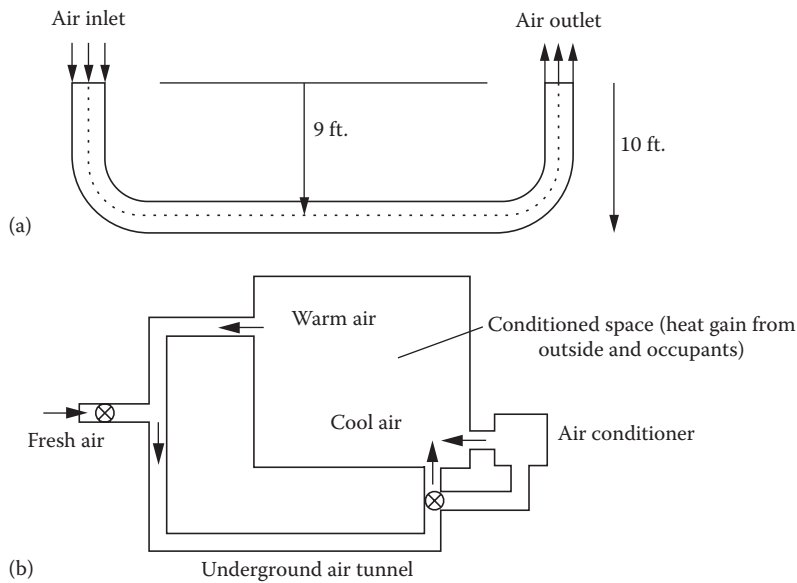
7.3.5 Earth Contact Cooling (or Heating)

Earth contact cooling or heating is a passive summer cooling and winter heating technique that utilizes underground soil as the heat sink or source. By installing a pipe underground and passing air through the pipe, the air will be cooled or warmed depending on the season. A schematic of an open loop system and that of a closed loop air-conditioning system are presented in Figure 7.8a and b, respectively (Goswami and Dhaliwal 1985).

The use of this technique can be traced back to 3000 BC when Iranian architects designed some buildings to be cooled by natural resources only. In the 19th century, Wilkinson (in USDA [US Department of Agriculture] 1960) designed a barn for 148 cows where a 500-ft-long underground passage was used for cooling during the summertime. Since that time, a number of experimental and analytical studies of this technique have continued to appear in the literature. Goswami and Dhaliwal (1985) have given a brief review of the literature, as well as presented an analytical solution to the problem of transient heat transfer between the air and the surrounding soil as the air is made to pass through a pipe buried underground. More recently, Krarti and Kreider (1996) have also presented an analytical model for heat transfer in an underground air tunnel.

7.3.5.1 Heat Transfer Analysis

The transient thermal analysis of the air and soil temperature fields (Goswami and Ileslamlou 1990) is conducted using finite elements with the convective heat transfer between the air and the pipe and using semi-infinite cylindrical

**FIGURE 7.8**

(a) Open loop underground air tunnel system. (b) Schematic of closed loop air-conditioning system using air tunnel.

conductive heat transfer to the soil from the pipe. It should be noted that the thermal resistance of the pipe (whether metal, plastic, or ceramic) is negligible relative to the surrounding soil.

7.3.5.1.1 Air and Pipe Heat Transfer

The pipe is divided into a large number of elements and a psychrometric energy balance written for each, depending on whether the air leaves the element (a) unsaturated or (b) saturated. Assuming that air with a flow rate, m , and temperature T_1 enters the element and leaves at a temperature T_2 :

- If the air leaves an element as unsaturated, the energy balance on the element is

$$mC_p(T_1 - T_2) = hA_p(T_{\text{air}} - T_{\text{pipe}}). \quad (7.15)$$

T_{air} can be taken as $(T_1 + T_2)/2$.

Substituting and simplifying, we get

$$T_2 = \frac{[(1 - U/2)T_1 + UT_{\text{pipe}}]}{(1 + U/2)}, \quad (7.16)$$

where U is defined as

$$U = \frac{A_p h}{m C_p}$$

- b. If the air leaving the element is saturated and the specific humidity at the entry and exit is W_1 and W_2 respectively, the energy balance is

$$mC_p T_1 + m(W_1 - W_2)H_{fg} = mC_p T_2 + hA_p(T_{\text{air}} - T_{\text{pipe}}). \quad (7.17)$$

Simplifying, we get

$$T_2 = \frac{1 - \frac{U}{2} T_1 + \frac{W_1 - W_2}{C_p} H_{fg} + U T_{\text{pipe}}}{(1 + U/2)}. \quad (7.18)$$

The convective heat transfer coefficient h in the preceding equations depends on Reynolds number, the shape, and roughness of the pipe. Using the exit temperature from the first element as the inlet temperature for the next element, the exit temperature for the element can be calculated in a similar way. Continuing this way from one element to the next, the temperature of air at the exit from the pipe can be calculated.

7.3.5.1.2 Soil Heat Transfer

The heat transfer from the pipe to the soil is analyzed by considering the heat flux at the internal radius of a semi-infinite cylinder formed by the soil around the pipe. For a small element, the problem can be formulated as

$$\frac{\partial^2 T(r, t)}{\partial r^2} + \frac{1}{r} \frac{\partial T(r, t)}{\partial r} = \frac{1}{\alpha} \frac{\partial T(r, t)}{\partial t}, \quad (7.19)$$

with initial and boundary conditions as

$$T(r, 0) = T_e \quad (7.20)$$

$$T(\infty, t) = T_e \quad (7.21)$$

$$-K \frac{\partial T}{\partial r}(r, t) = q'' , \quad (7.22)$$

where T_e is the bulk earth temperature and q'' is also given by the amount of heat transferred to the air from the pipe by convection; that is, $q'' = h(T_{\text{air}} - T_{\text{pipe}})$.

7.3.5.2 Soil Temperatures and Properties

Labs (1981) studied the earth temperatures in the United States. According to both of these studies, temperature swings in the soil during the year are damped with depth below the ground. There is also a phase lag between the soil temperature and the ambient air temperature, and this phase lag increases with depth below the surface. For example, the soil temperature for light dry soil at a depth of approximately 10 ft (3.05 m) varies by approximately $\pm 5^{\circ}\text{F}$ (2.8°C) from the mean temperature (approximately equal to mean annual air temperature) and has a phase lag of approximately 75 days behind ambient air temperature (Labs 1981).

The thermal properties of the soil are difficult to determine. The thermal conductivity and diffusivity both change with the moisture content of the soil itself, which is directly affected by the temperature of and heat flux from and to the buried pipe. Most researchers have found that using constant property values for soil taken from standard references gives reasonable predictive results (Goswami and Biseli 1994).

7.3.5.3 Generalized Results from Experiments

Figure 7.9 presents data from Goswami and Biseli (1994) for an open system, 100-ft-long, 12-in.-diameter pipe, buried 9 ft deep. The figure shows the relationship between pipe inlet-to-outlet temperature reduction ($T_{\text{in}} - T_{\text{out}}$) and the initial soil temperature with ambient air inlet conditions of 90°F and 55% relative humidity for various pipe flow rates.

Other relations from this same report that can be used with the Figure 7.9 data include the following: (1) the effect of increasing pipe/tunnel length on

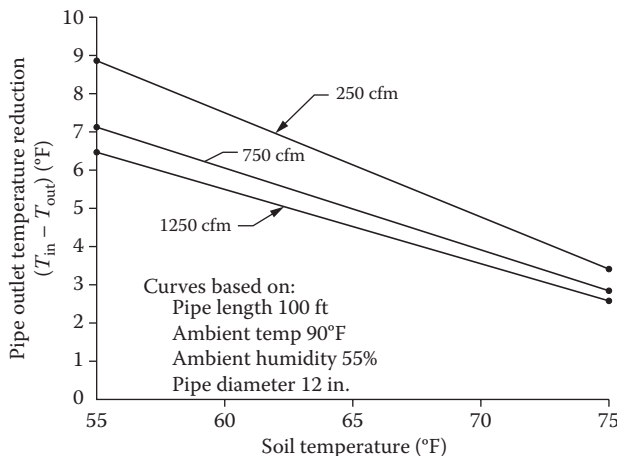


FIGURE 7.9

Air temperature drop through a 100-ft-long, 12-in.-diameter pipe buried 9 ft underground.

increasing the inlet-to-outlet air temperature difference is fairly linear up to 250 ft and (2) the effect of decreasing pipe diameter on lowering the outlet air temperature is slight and only marginally effective for pipes less than 12-in.-diameter.

Example 7.5

Provide the necessary 12-in.-diameter pipe length(s) that will deliver 1500 cfm of 75°F air if the ambient temperature is 85°F and the soil at 9 ft is 65°F.

Solution

From Figure 7.9, for 100 ft of pipe at 65°F soil temperature, the pipe temperature reduction is

$$\begin{aligned}T_{\text{in}} - T_{\text{out}} &= 6^\circ \text{ (at 250 cfm)} \\&= 5^\circ\text{F (at 750 cfm)} \\&= 4.5^\circ\text{F (at 1250 cfm).}\end{aligned}$$

Since the “length versus temperature reduction” is linear (see text above), the 10°F reduction required (85 down to 75) would be met by the 750 cfm case (5°F for 100 ft) if 200 ft of pipe is used. Then, two 12-in.-diameter pipes would be required to meet the 1500-cfm requirement.

Answer

Two 12-in.-diameter pipes, each 200 ft long. (*Note:* See what would be needed if the 250-cfm or the 1250-cfm cases had been chosen. Which of the three flow rate cases leads to the “cheapest” installation?)

7.4 Daylighting Design Fundamentals

Daylighting is the use of the sun’s radiant energy to illuminate the interior spaces in a building. In the last century, electric lighting was considered an alternative technology to daylighting. Today, the situation is reversed, primarily attributed to the economics of energy use and conservation. However, there are good physiological reasons for using daylight as an illuminant. The quality of daylight matches the human eye’s response, thus permitting lower light levels for task comfort, better color rendering, and clearer object discrimination (Robbins 1986).

7.4.1 Lighting Terms and Units

Measurement of lighting level is based on the “standard candle,” where the *lumen* (lm), the unit of *luminous flux* (ϕ), is defined as the rate of luminous energy passing through a 1-m² area located 1 m from the candle. Thus, a standard candle generates 4π lumens, which radiate away in all directions. The *illuminance* (E) on a surface is defined as the luminous flux on the surface divided by the surface area, $E = \phi/A$. Illuminance is measured in either *lux* (lx), as lumens per square meter, or *footcandles* (fc), as lumens per square foot.

Determination of the daylighting available at a given location in a building space at a given time is important to evaluate the reduction possible in electric lighting and the associated impact on heating and cooling loads. Daylight provides approximately 110 lm/W of solar radiation, fluorescent lamps provide approximately 75 lm/W of electrical input, and incandescent lamps provide approximately 20 lm/W; thus, daylighting generates only 1/2 to 1/5 the heating that equivalent electric lighting does, significantly reducing the building cooling load.

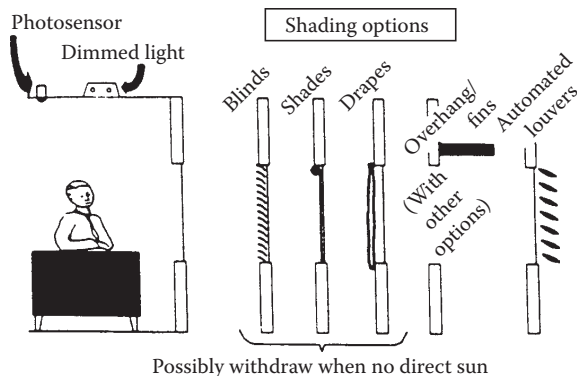
7.4.2 Economics of Daylighting

The economic benefit of daylighting is directly tied to the reduction in lighting electrical energy operating costs. Also, lower cooling system operating costs are possible because of the reduction in heating caused by the reduced electrical lighting load. The reduction in lighting and cooling system electrical power during peak demand periods could also beneficially affect demand charges.

The reduction of the design cooling load through the use of daylighting can also lead to the reduction of installed or first-cost cooling system dollars. Normally, economics dictate that an automatic lighting control system must take advantage of the reduced lighting/cooling effect, and the control system cost, minus any cooling system cost, savings should be expressed as a net first cost. A payback timer for the lighting control system (net or not) can be calculated from the ratio of first costs to yearly operating savings. In some cases, these paybacks for daylighting controls have been found to be in the range of 1 to 5 years for office building spaces (Rundquist 1991).

Controls, both aperture and lighting, directly affect the efficacy of the daylighting system. As shown in Figure 7.10, aperture controls can be architectural (overhangs, lightshelves, etc.) or window shading devices (blinds, automated louvers, etc.). The aperture controls generally moderate the sunlight entering the space to maximize or minimize solar thermal gain, permit the proper amount of light for visibility, and prevent glare and beam radiation onto the workplace. Photosensor control of electric lighting allows the dimming (or shutting off) of the lights in proportion to the amount of available daylighting luminance.

In most cases, using daylighting controls to increase the solar gain for daylighting purposes saves more in electrical lighting energy and in cooling

**FIGURE 7.10**

Daylighting system controls. (From Rundquist, R.A., *ASHRAE Journal* 11: 30–34, November, 1991.)

energy associated with the lighting than is incurred with the added solar gain (Rundquist 1991). In determining the annual energy savings from daylighting (ES_T), the annual lighting energy saved from daylighting (ES_L) is added with the reduction in cooling system energy (∇ES_C) and with the negative of the heating system energy increase (∇ES_H):

$$ES_T = ES_L + \nabla ES_C - \nabla ES_H. \quad (7.23)$$

A simple approach to estimating the heating and cooling energy changes associated with lighting energy reduction is to use the fraction of the year associated with the cooling or heating season (f_c, f_H) and the seasonal COP of the cooling or heating equipment. Thus, Equation 7.23 can be expressed as

$$\begin{aligned} ES_T &= ES_L + \frac{f_c ES_L}{COP_c} - \frac{f_c ES_L}{COP_H} \\ &= ES_L \left(1 + \frac{f_c}{COP_c} - \frac{f_H}{COP_H} \right). \end{aligned} \quad (7.24)$$

It should be noted that the increased solar gain attributed to daylighting has not been included here but would reduce summer savings and increase winter savings. If it is assumed that the increased wintertime daylighting solar gain approximately offsets the reduced lighting heat gain, then the last term in Equation 7.24 becomes negligible.

7.4.3 Daylighting Design Fundamentals

As mentioned, aperture controls such as blinds and drapes are used to moderate the amount of daylight entering the space, as are the architectural features of the building itself (glazing type, area, and orientation; overhangs and wing-walls; lightshelves; etc.). Dimming controls are used to adjust the electric light level on the basis of the quantity of the daylighting. With these two types of controls (aperture and lighting), the electric lighting and cooling energy use and demand, as well as cooling system size, can be reduced. However, the determination of the daylighting position and time *illuminance* value within the space is required before energy usage and demand reduction calculations can be made.

7.4.3.1 Architectural Features

Daylighting design approaches use both solar beam radiation (*sunlight*) and the diffuse radiation scattered by the atmosphere (*skylight*) as sources for interior lighting, with historical design emphasis being on utilizing skylight. Daylighting is provided through a variety of glazing features, which can be grouped as *sidelighting* (light entering via the side of the space) and *toplighting* (light entering from the ceiling area). Figure 7.11 illustrates several architectural forms producing sidelighting and toplighting. The dashed lines represent the illuminance distribution within the space. The calculation of work-plane illuminance depends on whether sidelighting or toplighting features are used, and the combined illuminance values are additive.

7.4.3.2 Daylighting Geometry

The solar illuminance on a vertical or horizontal window depends on the position of the sun relative to that window. In the method described here, the sun and sky illuminance values are determined using the sun's altitude angle (α) and the sun–window azimuth angle difference (a_{sw}). These angles need to be determined for the particular time of day, day of year, and window placement under investigation.

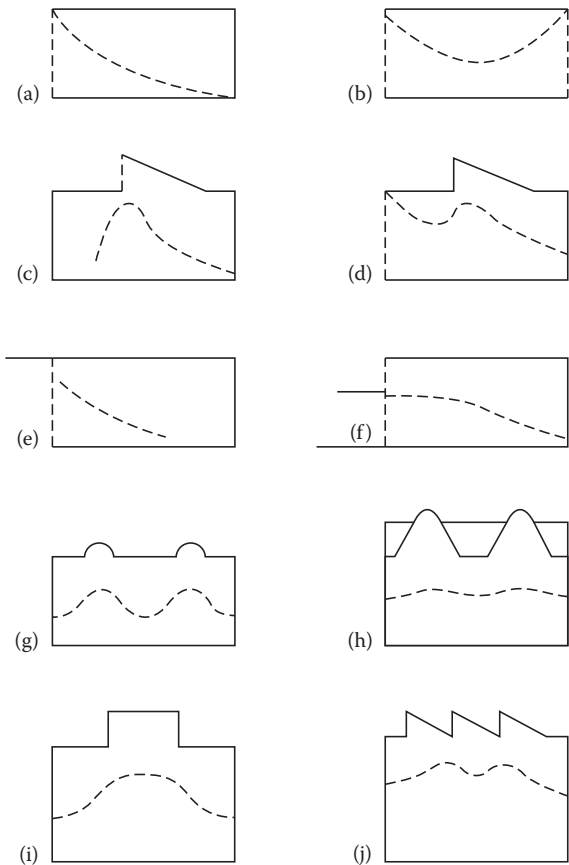
7.4.3.2.1 Solar Altitude Angle (α)

The solar altitude angle is the angle swept out by a person's arm when pointing to the horizon directly below the sun and then raising the arm to point at the sun. Equation 2.28 can be used to calculate solar altitude, α , as

$$\sin \alpha = \cos L \cos \delta_s \cos h_s + \sin L \sin \delta_s. \quad (2.28)$$

7.4.3.2.2 Sun–Window Azimuth Angle Difference (a_{sw})

The difference between the sun's azimuth and the window's azimuth needs to be calculated for vertical window illuminance. The window's azimuth

**FIGURE 7.11**

Example of sidelighting and toplighting architectural features (dashed lines represent illuminance distributions). (a) Unilateral. (b) Bilateral. (c) Clerestory. (d) Clerestory + unilateral. (e) Overhang. (f) Overhang + ground reflection. (g) Skylight. (h) Skylight + well. (i) Roof monitor. (j) Sawtooth. (Reprinted by permission from Macmillan Publishers Ltd. *Illumination Engineering—From Edison's Lamp to the Laser*, Murdoch, J.B., copyright 1985.)

angle, a_w , is determined by which way it faces, as measured from south (east of south is negative, westward is positive). The solar azimuth angle, a_s , is calculated using Equation 2.29:

$$\sin a_s = \cos \delta_s \sin h_s / \cos \alpha. \quad (2.29)$$

The sun–window azimuth angle difference, a_{sw} , is given by the absolute value of the difference between a_s and a_w :

$$a_{sw} = |a_s - a_w|. \quad (7.25)$$

7.4.4 Design Methods

To determine the annual lighting energy saved (ES_L), for the space under investigation, calculations using the lumen method described in the following should be performed on a monthly basis for both clear and overcast days. Monthly weather data for the site would then be used to prorate clear and overcast lighting energy demands each month. Subtracting the calculated daylighting illuminance from the design illuminance leaves the supplementary lighting needed, which determines the lighting energy required.

The approach in the following method is to calculate the sidelighting and the skylighting of the space separately and then combine the results. This procedure has been computerized and includes many details of controls, daylighting methods, weather, and heating and cooling load calculations. ASHRAE (2013) lists many of the methods and simulation techniques currently used with daylighting and its associated energy effects.

7.4.5 Lumen Method of Sidelighting (Vertical Windows)

The lumen method of sidelighting calculates interior horizontal illuminance at three points, as shown in Figure 7.12, at the 30-in. (0.76-m) work plane on the room-and-window centerline. A vertical window is assumed to extend from 36 in. (0.91-m) above the floor to the ceiling. The method accounts for both direct and ground-reflected sunlight and skylight; thus, both horizontal and vertical illuminances from sun and sky are needed. The steps in the lumen method of sidelighting are presented next.

The incident direct and ground-reflected window illuminances are normally calculated for both a cloudy and a clear day for representative days during the year (various months), as well as for clear or cloudy times during a given day.

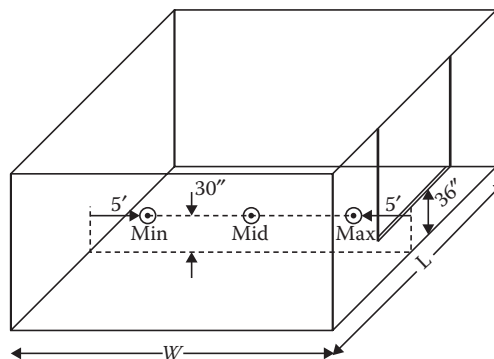


FIGURE 7.12

Location of illumination points within the room (along centerline of window) determined by the lumen method of sidelighting.

Thus, the interior illumination owing to sidelighting and skylighting can then be examined for effectiveness throughout the year.

Step 1: Incident direct sky and sun illuminances. The solar altitude and sun–window azimuth angle difference are calculated for the desired latitude, date, and time using Equations 2.28 and 7.25, respectively. Using these two angles, the total illuminance on the window (E_{sw}) can be determined by summing the direct sun illuminance (E_{uw}) and the direct sky illuminance (E_{kw}), each determined from the appropriate graph in Figure 7.13.

Step 2: Incident ground-reflected illuminance. The sun illuminance on the ground (E_{ug}) plus the overcast or clear sky illuminance (E_{kg}) on the ground make up the total horizontal illuminance on the ground surface (E_{sg}). A fraction of the ground surface illuminance is then considered diffusely reflected onto the vertical window surface (E_{gw}), where “gw” indicates from the ground to the window.

The horizontal ground illuminances can be determined using Figure 7.14, where the clear sky plus sun case and the overcast sky case are functions of solar altitude. The fractions of the ground illuminance diffusely reflected onto the window depend on the reflectivity (ρ) of the ground surface (see Table 7.2) and the window-to-ground surface geometry.

If the ground surface is considered uniformly reflective from the window outward to the horizon, then the illuminance on the window from ground reflection is

$$E_{gw} = \frac{\rho E_{sg}}{2}. \quad (7.26)$$

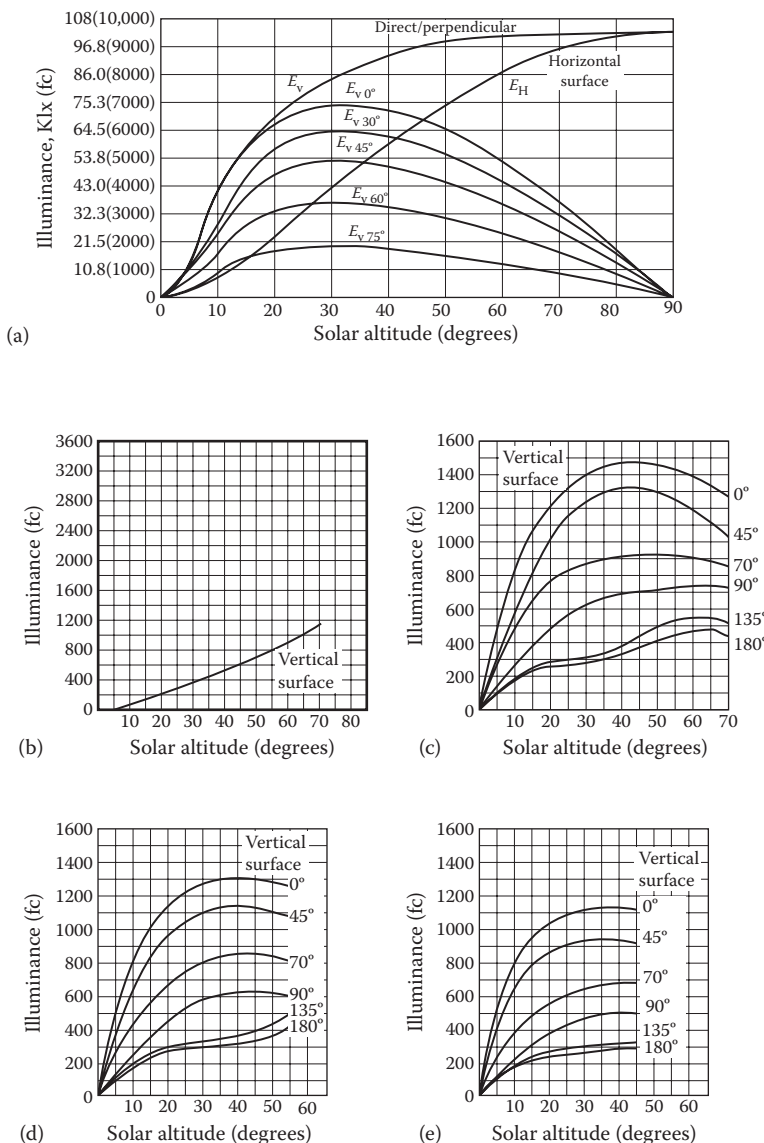
A more complicated ground-reflection case is illustrated in Figure 7.15, with multiple strips of differently reflecting ground being handled using the angles to the window, where a strip’s illuminance on a window is calculated:

$$E_{gw(\text{strip})} = \frac{\rho_{\text{strip}} E_{sg}}{2} (\cos \theta_1 - \cos \theta_2). \quad (7.27)$$

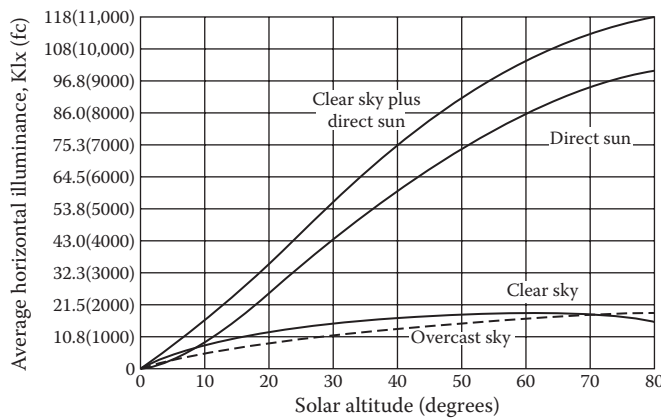
And the total reflected onto the window is the sum of the strip illuminances:

$$E_{gw} = \frac{E_{sg}}{2} [\rho_1(\cos \theta_0 - \cos \theta_1) + \rho_2(\cos \theta_1 - \cos \theta_2) + \dots + \rho_n(\cos \theta_{n-1} - \cos 90)]. \quad (7.28)$$

Step 3: Luminous flux entering space. The direct sky–sun and ground-reflected luminous fluxes entering the building are attenuated by the transmissivity of the window. Table 7.3 presents the transmittance fraction (τ) of several window glasses. The fluxes entering the space are calculated from

**FIGURE 7.13**

Vertical illuminance from (a) direct sunlight. (b) Overcast skylight. (c) Clear summer skylight. (d) Clear autumn/spring skylight. (e) Clear winter skylight, for various sun–window azimuth angle differences. (From IES, *Lighting Handbook, Applications Volume*, Illumination Engineering Society, New York, 1979.)

**FIGURE 7.14**

Horizontal illuminance for overcast sky, clear sky, direct sun, and clear sky plus direct sun. (Reprinted by permission from Macmillan Publishers Ltd. *Illumination Engineering—From Edison's Lamp to the Laser*, Murdoch, J.B., copyright 1985.)

the total sun-sky and the ground-reflected illuminances by using the area of the glass, A_w :

$$\begin{aligned}\phi_{sw} &= E_{sw} \tau A_w \\ \phi_{gw} &= E_{gw} \tau A_w.\end{aligned}\tag{7.29}$$

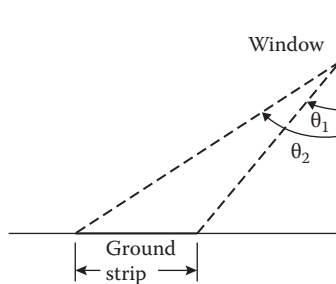
Step 4: Light loss factor. The light loss factor (K_m) accounts for the attenuation of luminous flux owing to dirt on the window (window dirt depreciation [WDD])

TABLE 7.2

Ground Reflectivities

Material	ρ (%)
Cement	27
Concrete	20–40
Asphalt	7–4
Earth	10
Grass	6–20
Vegetation	25
Snow	70
Red brick	30
Gravel	15
White paint	55–75

Source: Reprinted by permission from Macmillan Publishers Ltd. *Illumination Engineering—From Edison's Lamp to the Laser*, Murdoch, J.B., copyright 1985.

**FIGURE 7.15**

Geometry for ground strips. (Reprinted by permission from Macmillan Publishers Ltd. *Illumination Engineering—From Edison's Lamp to the Laser*, Murdoch, J.B., copyright 1985.)

TABLE 7.3

Glass Transmittances

Glass	Thickness (in.)	τ (%)
Clear	$\frac{1}{8}$	89
Clear	$\frac{3}{16}$	88
Clear	$\frac{1}{4}$	87
Clear	$\frac{5}{16}$	86
Gray	$\frac{1}{8}$	61
Gray	$\frac{3}{16}$	51
Gray	$\frac{1}{4}$	44
Gray	$\frac{5}{16}$	35
Bronze	$\frac{1}{8}$	68
Bronze	$\frac{3}{16}$	59
Bronze	$\frac{1}{4}$	52
Bronze	$\frac{5}{16}$	44
Thermopane	$\frac{1}{8}$	80
Thermopane	$\frac{3}{16}$	79
Thermopane	$\frac{1}{4}$	77

Source: Reprinted by permission from Macmillan Publishers Ltd. *Illumination Engineering—From Edison's Lamp to the Laser*, Murdoch, J.B., copyright 1985.

and on the room surfaces (room surface dirt depreciation [RSDD]). WDD depends on how often the window is cleaned, but a 6-month average for offices is 0.83 and that for factories is 0.71.

The RSDD is a more complex calculation involving time between cleanings, the direct–indirect flux distribution, and room proportions. However, for rooms cleaned regularly, RSDD is around 0.94, and for once-a-year-cleaned dirty rooms, the RSDD would be around 0.84.

The light loss factor is the product of the preceding two fractions:

$$K_m = (\text{WDD})(\text{RSDD}). \quad (7.30)$$

Step 5: Work-plane illuminances. As discussed earlier, Figure 7.12 illustrates the location of the work-plane illuminances determined with this lumen method of sidelighting. The three illuminances (max, mid, min) are determined using two coefficients of utilization, the C factor and the K factor. The C factor depends on room length, width, and wall reflectance. The K factor depends on ceiling–floor height, room width, and wall reflectance. Table 7.4 presents C and K values for the three cases of incoming fluxes: (a) sun plus clear sky, (b) overcast sky, and (c) ground reflected. Assumed ceiling and floor reflectances are given for this last case with no window controls (shades, blinds, overhangs, etc.). These further window control complexities can be found in IES (Illumination Engineering Society) (1987), LOF (Libbey–Owens–Ford Co.) (1976), and others. A reflectance of 70% represents light-colored walls, with 30% representing darker walls.

The work-plane max, mid, and min illuminance are each calculated by adding the sun–sky and ground-reflected illuminances, which are given by

$$\begin{aligned} E_{sp} &= \phi_{sw} C_s K_s K_m \\ E_{gp} &= \phi_{gw} C_g K_g K_m, \end{aligned} \quad (7.31)$$

where “sp” and “gp” refer to the sky-to-work-plane and ground-to-work-plane illuminances.

7.4.6 Lumen Method of Skylighting

The lumen method of skylighting calculates the average illuminance at the interior work plane provided by horizontal skylights mounted on the roof. The procedure for skylighting is generally the same as that described above for sidelighting. As with windows, the illuminance from both overcast sky and clear sky plus sun cases are determined for specific days in different seasons and for different times of the day, and a judgment is then made as to the number and size of skylights and any controls needed.

TABLE 7.4
 C and K Factors for No Window Controls for (a) Overcast Sky, (b) Clear Sky, and (c) Ground Illumination (Ceiling Reflectance, 80%;
 Floor Reflectance, 20%)

C: Coefficient of Utilization						K: Coefficient of Utilization							
Room Length	20 ft		30 ft		40 ft		Ceiling Height	8 ft		10 ft		12 ft	14 ft
	Wall Reflectance	70%	30%	70%	30%	70%		Wall Reflectance	70%	30%	70%	30%	
Room Width (ft)							Room Width (ft)						
<i>(a) Illumination by Overcast Sky</i>													
Max	20	0.0276	0.0251	0.0191	0.0173	0.0143	0.0137	Max	20	0.125	0.129	0.121	0.123
	30	0.0272	0.0248	0.0188	0.0172	0.0137	0.0131		30	0.122	0.131	0.122	0.121
	40	0.269	0.246	0.0182	0.0171	0.0133	0.0130		40	0.145	0.133	0.131	0.126
Mid	20	0.0159	0.0177	0.0101	0.0087	0.0081	0.0071	Mid	20	0.0908	0.0982	0.107	0.115
	30	0.0058	0.0050	0.0054	0.0040	0.0034	0.0033		30	0.156	0.102	0.0939	0.113
	40	0.0039	0.0027	0.0030	0.0023	0.0022	0.0019		40	0.106	0.0948	0.123	0.107
Min	20	0.0087	0.0053	0.0033	0.0043	0.0050	0.0037	Min	20	0.0908	0.102	0.0951	0.114
	30	0.0032	0.0019	0.0029	0.0017	0.0020	0.0014		30	0.0924	0.119	0.101	0.114
	40	0.0019	0.0009	0.0016	0.0009	0.0012	0.0008		40	0.111	0.0926	0.125	0.109
<i>(b) Illumination by Clear Sky</i>													
Max	20	0.0206	0.0173	0.0143	0.0123	0.0110	0.0098	Max	20	0.145	0.155	0.129	0.132
	30	0.0203	0.0173	0.0137	0.0120	0.0098	0.0092		30	0.141	0.149	0.125	0.130
	40	0.0200	0.0168	0.0131	0.0119	0.0096	0.0091		40	0.157	0.157	0.135	0.134

(Continued)

TABLE 7.4 (CONTINUED)

C and K Factors for No Window Controls for (a) Overcast Sky, (b) Clear Sky, and (c) Ground Illumination (Ceiling Reflectance, 80%; Floor Reflectance, 20%)

C: Coefficient of Utilization							K: Coefficient of Utilization																		
Room Length	20 ft			30 ft			40 ft			Ceiling Height			8 ft			10 ft			12 ft			14 ft			
	Wall Reflectance	70%			70%			70%			Wall Reflectance			70%			70%			70%			70%		
		Room Width (ft)	Room Width (ft)	Room Width (ft)	Room Width (ft)	Room Width (ft)	Room Width (ft)	Room Width (ft)	Room Width (ft)	Room Width (ft)	Room Width (ft)	Room Width (ft)	Room Width (ft)	Room Width (ft)	Room Width (ft)	Room Width (ft)	Room Width (ft)	Room Width (ft)	Room Width (ft)						
<i>(b) Illumination by Clear Sky</i>																									
Mid	20	0.0153	0.0104	0.0100	0.0079	0.0083	0.0067	Mid	20	0.110	0.128	0.116	0.126	0.111	0.111	0.103	0.108	0.111	0.111	0.111	0.111	0.111	0.111		
	30	0.0082	0.0054	0.0062	0.0043	0.0046	0.0037		30	0.106	0.125	0.110	0.129	0.111	0.111	0.112	0.120	0.111	0.111	0.111	0.111	0.111	0.111		
	40	0.0052	0.0032	0.0040	0.0028	0.0029	0.0023		40	0.117	0.118	0.122	0.118	0.111	0.111	0.123	0.122	0.111	0.111	0.111	0.111	0.111	0.116		
Min	20	0.0106	0.060	0.0079	0.0049	0.0067	0.0043	Min	20	0.105	0.129	0.112	0.130	0.111	0.111	0.111	0.116	0.111	0.111	0.111	0.111	0.111	0.116		
	30	0.0054	0.0028	0.0047	0.0023	0.0032	0.0021		30	0.0994	0.144	0.107	0.126	0.111	0.111	0.107	0.124	0.111	0.111	0.111	0.111	0.111	0.118		
	40	0.0031	0.0014	0.0027	0.0013	0.0021	0.0012		40	0.119	0.116	0.130	0.118	0.111	0.111	0.120	0.118	0.111	0.111	0.111	0.111	0.111	0.118		
<i>(c) Ground Illumination (Ceiling Reflectance, 80%; Floor Reflectance, 20%)</i>																									
Max	20	0.0147	0.0112	0.0102	0.0088	0.0081	0.0071	Max	20	0.124	0.206	0.140	0.135	0.111	0.111	0.0909	0.0859	0.111	0.111	0.111	0.111	0.111	0.111		
	30	0.0141	0.0012	0.0098	0.0088	0.0077	0.0070		30	0.182	0.188	0.140	0.143	0.111	0.111	0.0918	0.0878	0.111	0.111	0.111	0.111	0.111	0.111		
	40	0.0137	0.0112	0.0093	0.0086	0.0072	0.0069		40	0.124	0.182	0.140	0.142	0.111	0.111	0.0936	0.0879	0.111	0.111	0.111	0.111	0.111	0.111		
Mid	20	0.0128	0.0090	0.0094	0.0071	0.0073	0.0060	Mid	20	0.123	0.145	0.122	0.129	0.111	0.111	0.100	0.0945	0.111	0.111	0.111	0.111	0.111	0.105		
	30	0.0083	0.0057	0.0062	0.0048	0.0050	0.0041		30	0.0966	0.104	0.107	0.112	0.111	0.111	0.110	0.105	0.111	0.111	0.111	0.111	0.111	0.105		
	40	0.0055	0.0037	0.0044	0.0033	0.0042	0.0026		40	0.0790	0.0786	0.0999	0.106	0.111	0.111	0.118	0.118	0.111	0.111	0.111	0.111	0.111	0.118		
Min	20	0.0106	0.0071	0.0082	0.0054	0.0067	0.0044	Min	20	0.0994	0.108	0.110	0.114	0.111	0.111	0.107	0.104	0.111	0.111	0.111	0.111	0.111	0.116		
	30	0.0051	0.0026	0.0041	0.0023	0.0033	0.0021		30	0.0816	0.0822	0.0984	0.105	0.111	0.111	0.121	0.116	0.111	0.111	0.111	0.111	0.111	0.132		
	40	0.0029	0.0018	0.0026	0.0012	0.0022	0.0011		40	0.0700	0.0656	0.0946	0.0986	0.111	0.111	0.125	0.132	0.111	0.111	0.111	0.111	0.111	0.118		

Source: IES, *Lighting Handbook, Applications Volume*, Illumination Engineering Society, New York, 1987.

The procedure is presented in four steps: (1) finding the horizontal illuminance on the outside of the skylight, (2) calculating the effective transmittance through the skylight and its well, (3) figuring the interior space light loss factor and the utilization coefficient, and, finally, (4) calculating illuminance on the work plane.

Step 1: Horizontal sky and sun illuminances. The horizontal illuminance value for an overcast sky or a clear sky plus sun situation can be determined from Figure 7.14 knowing only the solar altitude (see Equation 2.28).

Step 2: Net skylight transmittance. The transmittance of the skylight is determined by the transmittance of the skylight cover(s), the reflective efficiency of the skylight well, the net-to-gross skylight area, and the transmittance of any light-control devices (lenses, louvers, etc.).

The transmittance for several flat-sheet plastic materials used in skylight domes is presented in Table 7.5. To get the effective dome transmittance (T_D) from the flat-plate transmittance (T_F) value (AAMA [Architectural Aluminum Manufacturers Association] 1977), use

$$T_D = 1.25T_F(1.18 - 0.416T_F). \quad (7.32)$$

If a double-domed skylight is used, then the single-dome transmittances are combined as follows (Pierson 1962):

$$T_D = \frac{T_{D_1}T_{D_2}}{T_{D_1} + T_{D_2} - T_{D_1}T_{D_2}}. \quad (7.33)$$

TABLE 7.5

Flat-Plate Plastic Material Transmittance for Skylights

Type	Thickness (in.)	Transmittance (%)
Transparent	$\frac{1}{8} - \frac{3}{16}$	92
Dense translucent	$\frac{1}{8}$	32
Dense translucent	$\frac{3}{16}$	24
Medium translucent	$\frac{1}{8}$	56
Medium translucent	$\frac{3}{16}$	52
Light translucent	$\frac{1}{8}$	72
Light translucent	$\frac{3}{16}$	68

Source: Reprinted by permission from Macmillan Publishers Ltd. *Illumination Engineering—From Edison's Lamp to the Laser*, Murdoch, J.B., copyright 1985.

If the diffuse and direct transmittances for solar radiation are available for the skylight glazing material, it is possible to follow this procedure and determine diffuse and direct dome transmittances separately. However, this difference is usually not a significant factor in the overall calculations.

The efficiency of the skylight well (N_w) is the fraction of the luminous flux from the dome that enters the room from the well. The well index (WI) is a geometric index (height, h ; length, l ; width, w) given by

$$\text{WI} = \frac{h(w+l)}{2wl}, \quad (7.34)$$

and WI is used with the well-wall reflectance value in Figure 7.16 to determine well efficiency, N_w .

With T_D and N_w determined, the net skylight transmittance for the skylight and well is given by

$$T_n = T_D N_w R_A T_C, \quad (7.35)$$

where R_A is the ratio of net to gross skylight areas and T_C is the transmittance of any light-controlling devices.

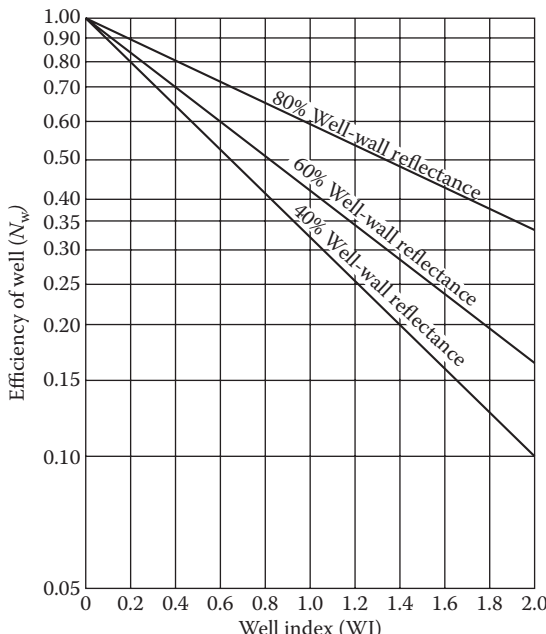


FIGURE 7.16

Efficiency of well versus well index. (From IES, *Lighting Handbook, Applications Volume*, Illumination Engineering Society, New York, 1987.)

Step 3: Light loss factor and utilization coefficient. The light loss factor (K_m) is again defined as the product of the RSDD and the skylight direct depreciation (SDD) fractions, similar to Equation 7.30. Following the reasoning for the sidelighting case, the RSDD value for clean rooms is around 0.94 and that for dirty rooms is 0.84. Without specific data indicating otherwise, the SDD fraction is often taken as 0.75 for office buildings and 0.65 for industrial areas.

The fraction of the luminous flux on the skylight that reaches the work plane (K_u) is the product of the net transmittance (T_n) and the room coefficient of utilization (RCU). Dietz et al. (1981) developed RCU equations for office and warehouse interiors with ceiling, wall, and floor reflectances of 75%, 50%, and 30%, and 50%, 30%, and 20%, respectively.

$$\text{RCU} = \frac{1}{1 + A(\text{RCR})^B}, \quad \text{if } \text{RCR} < 8, \quad (7.36)$$

where

$$A = 0.0288 \text{ and } B = 1.560 \text{ (offices)}$$

$$A = 0.0995 \text{ and } B = 1.087 \text{ (warehouses)}$$

and room cavity ratio (RCR) is given by

$$\text{RCR} = \frac{5h_c(l+w)}{lw}, \quad (7.37)$$

with h_c being the ceiling height above the work plane and l and w being room length and width, respectively.

The RCU is then multiplied by the previously determined T_n to give the fraction of the external luminous flux passing through the skylight and incident on the workplace:

$$K_u = T_n(\text{RCU}). \quad (7.38)$$

Step 4: Work-plane illuminance. The illuminance at the work plane (E_{TWP}) is given by

$$E_{\text{TWP}} = E_H \frac{A_T}{A_{\text{wp}}} K_u K_m, \quad (7.39)$$

where E_H is the horizontal overcast or clear sky plus sun illuminance from Step 1, A_T is total gross area of the skylights (number of skylights times

skylight gross area), and A_{WP} is the work-plane area (generally room length times width).

Note that in Equation 7.39, it is also possible to fix the E_{TWP} at some desired value and determine the skylight area required.

Rules of thumb for skylight placement for uniform illumination include 4%–8% of roof area and spacing less than 1 1/2 times ceiling-to-work-plane distance between skylights.

Example 7.6

Determine the work-plane clear sky plus sun illuminance for a 30' × 30' × 10' office with 75% ceiling, 50% wall, and 30% floor reflectance with four 4' × 4' double-domed skylights at 2 p.m. on January 15 at 32° latitude. The skylight well is 1' deep with 60% reflectance walls, and the outer and inner dome flat-plastic transmittances are 0.85 and 0.45, respectively. The net skylight area is 90%.

Solution

Follow the four steps in the lumen method for skylighting.

Step 1: Use Figure 7.14 with the solar altitude of 41.7° (calculated from Equation 2.28) for the clear sky plus sun curve to get horizontal illuminance:

$$E_H = 7400 \text{ fc.}$$

Step 2: Use Equation 7.32 to get domed transmittances from the flat-plate plastic transmittances given,

$$T_{D_1} = 1.25(0.85)[1.18 - 0.416(0.85)] = 0.89$$

$$T_{D_2} (T_F = 0.45) = 0.56,$$

and Equation 7.33 to get total dome transmittance from the individual dome transmittances:

$$T_D = \frac{(0.89)(0.56)}{(0.89) + (0.56) - (0.89)(0.56)} = 0.52.$$

To get well efficiency, use $WI = 0.25$ from Equation 7.34 with 60% wall reflectance in Figure 7.16 to give $N_w = 0.80$. With $R_A = 0.90$, use Equation 7.35 to calculate net transmittance:

$$T_n = (0.52)(0.80)(0.90)(1.0) = 0.37.$$

Step 3: The light loss factor is assumed to be from typical values: $K_m = (0.75)(0.94) = 0.70$. The room utilization coefficient is determined using Equations 7.36 and 7.37:

$$\text{RCR} = \frac{5(7.5)(30 + 30)}{(30)(30)} = 2.5$$

$$\text{RCU} = [1 + 0.0288(2.5)^{1.560}]^{-1} = 0.89$$

and Equation 7.38 yields $K_u = (0.37)(0.89) = 0.33$.

Step 4: The work-plane illuminance is calculated by substituting the above values into Equation 7.39:

$$E_{\text{TWP}} = 7400 \frac{4(16)2}{30(30)} 0.33(0.70) = 122 \text{ fc.}$$

7.5 Further Information

7.5.1 General Background Information

The most complete basic reference for passive system heating design is still the 1980 Los Alamos Lab's *Passive Solar Design Handbook*, all three parts of it. The *ASHRAE Handbook of Fundamentals* is a good general introduction to passive cooling techniques and calculations, with an emphasis on evaporative cooling. *Passive Solar Buildings* and *Passive Cooling*, both published by MIT Press, contain a large variety of techniques and details concerning passive system designs and economics. All the major building energy simulation codes (DOE-2, EnergyPlus, TRNSYS, TSB13, etc.) now include passive heating and cooling technologies.

The Illumination Engineering Society's *Lighting Handbook* presents the basis for and details of daylighting and artificial lighting design techniques. However, most texts on illumination present simplified format daylighting procedures. Currently used daylighting computer programs include various versions of *Lumen Micro*, *Lightscape*, and *Radiance*.

Solar Today magazine, published by the American Solar Energy Society (ASES), is a readily available source for current practice designs and economics, as well as a source for passive system equipment suppliers.

7.5.2 Technical Publication Information

Many of the current and archival passive solar technical papers are found from the conference proceedings and journals associated with the International Solar Energy Society, its affiliated ASES, the American Society of Mechanical Engineering, and ASHRAE. Also, many of the early passive solar practitioners

were architects and builders who published in their specific industry trade journals, as is still the case today. As an Internet search for passive solar articles today will reveal, there are several “new” energy/solar/sustainable technical journals that publish passive solar-related articles.

PROBLEMS

1. Explain how window placement in a building could be defined as (a) a passive solar feature, (b) an energy conservation technique, and (c) both of the above.
2. Write an equation for calculating the cost of savings life-cycle economics of a proposed passive solar system. Explain why it is important to be able to determine the auxiliary energy required for any given passive (or active) system design.
3. Referring to the thermal circuit diagram of Figure 7.4 for the thermal storage (Trombe) wall building, construct appropriate thermal circuits for (a) attached sunspace, (b) thermal storage, and (c) direct gain buildings.
4. Using rules of thumb for a 200-m² floor area Denver residence, determine (a) the auxiliary heating energy required, (b) the solar projected area, and (c) the concrete storage mass needed for a maximum 10°C daily temperature swing.
5. A 2000-ft² house in Boston is being designed with NLC = 12,000 Btu/F-day and 150 ft² of direct gain. The direct gain system includes double glazing, nighttime insulation, and 30 Btu/ft²°F thermal storage capacity. Using the LCR method, determine (a) the annual auxiliary heating energy needed by this design and (b) the storage mass and dimensions required.
6. Compare the annual SSF for 150 ft² of the following passive systems for the house in Problem 5: (a) direct gain (DGA3), (b) vented Trombe wall (TWD4), (c) unvented Trombe wall (TW14), (d) water wall (WWB4), and (e) sunspace (SSB4).
7. A design modification to the house in Problem 5 is desired. A 200-ft², vented, 12"-thick Trombe wall is to be added to the direct gain system. Assuming the same types of glazing and storage as described above, determine (a) the annual heating auxiliary energy needed and (b) the Trombe wall mass.
8. Using the SLR method, calculate the auxiliary energy required in March for a 2000-ft², NLC 12,000 Btu/F-day house in Boston with a 150-ft², night-insulated double-glazed direct gain system with 6-in.-thick storage floors of 45 Btu/ft²°F capacity.
9. Calculate the heating season auxiliary energy required for the Boston house in Problem 8.

10. Determine the length of the overhang needed to shade a south-facing 2-m-high window in Dallas, Texas (latitude $32^{\circ}51'$), to allow for both winter heating and summer shading.
11. A 10-mph wind is blowing directly into an open $3\text{ ft} \times 5\text{ ft}$ window, which is mounted in a room's 8-ft-high by 12-ft-wide wall. If the wind's temperature is 80°F , are the room's occupants thermally comfortable?
12. Design a stack-effect/solar chimney (vented Trombe wall) to produce an average velocity of 0.3 m/s within a 4-m-wide by 5-m-long by 3-m-high room. Justify your assumptions.
13. Estimate the overnight radiant cooling possible from an open, 30°C , 8-m-diameter water tank during July in Chicago. What would you expect for convective and evaporative cooling values?
14. Calculate the overnight cooling possible by radiation for a 10-m^2 water thermal storage roof with water as the storage medium, when the ambient air temperature decreases linearly from 20°C to 15°C during the first 5 h and then increases to 20°C in the next 5 h. The equivalent sky temperature is given by the following equation: Equivalent sky temperature, $T_{\text{sky}}(\text{K}) = T_{\text{air}}(\text{K}) \times e_{\text{sky}}^{0.25}$, where e_{sky} is the sky emissivity, given as $e_{\text{sky}} = 0.741 + 0.0062 \times (T_{\text{air}}(\text{C}) - 10)$.
Assume the initial temperature of storage water as 25°C and emissivity of the storage as 0.9.
15. For the buried pipe example (7.4) in Chapter 7, determine which of the three flow rate cases leads to the least expensive installation.
16. Using data from Figure 79, design a 9-ft-deep ground-pipe system for Dallas in June to deliver 1000 cfm at 75°F when the outside air temperature is 90°F .
17. A $30\text{ ft} \times 20\text{ ft}$ office space has a photosensor dimmer control working with installed lighting of 2 W/ft^2 . The required workplace illuminance is 60 fc and the available daylighting is calculated as 40 fc on the summer peak afternoon. Determine the payback period for the dimmer control system assuming the following: 1-1/2 ton cooling installed for 600 ft^2 at $\$2200/\text{ton}$, lighting control system cost at $\$/\text{ft}^2$, 30% reduction in annual lighting owing to daylighting, $\$0.10/\text{kWh}$ electricity cost, and cooling for 6 months at a $\text{COP}_c = 2.5$.
18. Determine the illuminances (sun, sky, and ground-reflected) on a vertical, south-facing window at solar noon at 36°N latitude on June 21 and December 21 for (a) a clear day and (b) an overcast day.
19. Determine the sidelighting workplace illuminances for a 20-ft-long, 15-ft-wide (deep), 8-ft-high light-colored room with a 15-ft-long by 5-ft-high window. Assume the direct sun plus clear sky illuminance is 3000 fc and the ground-reflected illuminance is 200 fc.
20. Determine the clear sky day and the cloudy day work-plane illuminances for a 30-ft-long, 30-ft-wide, 10-ft-high light-colored room. A

20-ft-long by 7-ft-high window with 1/4-in clear glass faces 10°E of south, the building is at 32°N latitude, and it is January 15 at 2 p.m. solar. The ground outside is covered by dead grass!

21. Determine the clear day and cloudy day illuminances on a horizontal skylight at noon on June 21 and December 21 in (a) Miami, (b) Los Angeles, (c) Denver, (d) Boston, and (e) Seattle.
 22. A 3 ft × 5 ft double-domed skylight has outer and inner flat-plate plastic transmittances of 0.8 and 0.7, respectively; a 2-ft-deep well with 80% reflectance walls; and a 90% net skylight area. Calculate the net transmittance of the skylight.
 23. Determine the number and roof placement of 10 ft × 4 ft skylights needed for a 50 ft × 50 ft × 10 ft high office when the horizontal illuminance is 6000 fc, the skylight has 45% net transmittance, and the required workplace illuminance is 100 fc.
 24. What would be the procedure for producing uniform workplace illumination when both sidelighting and skylighting are used simultaneously?
-

References

- AAMA. 1977. *Voluntary Standard Procedure for Calculating Skylight Annual Energy Balance*. Architectural Aluminum Manufacturers Association Publication 1602.1.1977, Chicago, IL.
- ASES. 1992. *Economics of Solar Energy Technologies*, R. Larson, F. Vignola, and R. West, eds. American Solar Energy Society.
- ASHRAE Handbook. 2011. *Heating, Ventilating, and Air-Conditioning Applications*. American Society of Heating, Refrigerating and Air-Conditioning Engineers, Atlanta, GA.
- ASHRAE Handbook. 2013. *Fundamentals*. American Society of Heating, Refrigerating and Air-Conditioning Engineers, Atlanta, GA.
- Close, D.J., R.V. Dunkle, and K.A. Robeson. 1968. Design and performance of a thermal storage air conditioning system. *Mech. Chem. Eng. Trans., Institute Eng. Australia* MC4: 45.
- Dietz, P. et al. 1981. A skylight energy balance analysis procedure. *J. Illum. Eng. Soc.* 11(1): 27–34.
- Duffie, J.A., and W.A. Beckman. 1991. *Solar Engineering of Thermal Processes*, 2nd ed. John Wiley and Sons, New York.
- Goswami, D.Y., and K.M. Biseli. 1994. Use of underground air tunnels for heating and cooling agricultural and residential buildings. Report EES-78. Florida Energy Extension Service, University of Florida, Gainesville, FL.
- Goswami, D.Y., and A.S. Dhaliwal. 1985. Heat transfer analysis in environmental control using and underground air tunnel. *J. Sol. Energy Eng.* 107: 141–145.

- Goswami, D.Y., and S. Ileslamlou. 1990. Performance analysis of a closed-loop climate control system using underground air tunnel. *J. Sol. Energy Eng.* 112: 76–81.
- Haggard, K., D. Bainbridge, and R. Aljilani. 2010. *Passive Solar Architecture Pocket Reference*, D.Y. Goswami, ed. International Solar Energy Society, Freiburg, Germany.
- Halacy, D.S. 1984. *Home Energy*. Rodale Press, Inc. Emmaus, PA.
- Hay, H., and J. Yellott. 1969. Natural air conditioning with roof ponds and movable insulation. *ASHRAE Trans.* 75(1): 165–177.
- IES. 1979. *Lighting Handbook, Applications Volume*. Illumination Engineering Society, New York.
- IES. 1987. *Lighting Handbook, Applications Volume*. Illumination Engineering Society, New York.
- Krarti, M., and J.F. Kreider. 1996. Analytical model for heat transfer in an underground air tunnel. *Energy Convers. Mgmt.* 37(10): 1561–1574.
- Labs, K. 1981. Regional analysis of ground and above ground climate. Report ORNAL/Sub-81/40451/1. Oak Ridge National Laboratory, Oak Ridge, TN.
- LOF. 1976. *How to Predict Interior Daylight Illumination*. Libbey–Owens–Ford Co., Toledo, OH.
- Marlatt, W., C. Murray, and S. Squire. 1984. Roof pond systems energy technology engineering center. Rockwell International Report No. ETEC 6.
- Martin, M., and P. Berdahl. 1984. Characteristics of infrared sky radiation in the United States. *Sol. Energy* 33(314): 321–336.
- McQuiston, P.C., and J.D. Parker. 1994. *Heating, Ventilating, and Air Conditioning*, 4th ed. Wiley, New York.
- Murdoch, J.B. 1985. *Illumination Engineering—From Edison's Lamp to the Laser*. Macmillan Publishing, New York.
- Pierson, O. 1962. *Acrylics for the Architectural Control of Solar Energy*. Rohm and Haas, Philadelphia, PA.
- PSDH. 1980. *Passive Solar Design Handbook, Volume One: Passive Solar Design Concepts*, DOE/CS-0127/1, March; *Volume Two: Passive Solar Design Analysis*, DOE/CS-0127/2, January. U.S. Department of Energy, Washington, DC.
- PSDH. 1984. *Passive Solar Design Handbook*. Van Nostrand Reinhold Co., New York.
- Robbins, C.L. 1986. *Daylighting: Design and Analysis*. Van Nostrand, New York.
- Rundquist, R.A. 1991. Daylighting controls: Orphan of HVAC design. *ASHRAE J.* 11: 30–34.
- USDA. 1960. *Power to Produce, 1960 Yearbook of Agriculture*. U.S. Department of Agriculture, Washington, DC.

Suggested Readings

- Kreith, F., and R. West. 2007. *CRC Handbook of Energy Efficiency and Renewable Energy*. CRC Press, Boca Raton, FL.
- Kusuda, T., and P.R. Achenbach. 1965. Earth temperature and thermal diffusivity at selected stations in the United States. *ASHRAE Trans.* 71(1): 965.

8

Solar Thermal Power

8.1 Historical Perspective

Attempts to harness the sun's energy for power production date back to at least 1774 (Trombe 1956) when the French chemist Lavoisier and the English scientist Joseph Priestley discovered oxygen and developed the theory of combustion by concentrating the rays of the sun on mercuric oxide in a test tube, collecting the gas produced with the aid of solar energy, and burning a candle in the gas. Also, during the same year, an impressive picture of Lavoisier was published in which he stands on a platform near the focus of a large glass lens and is carrying out other experiments with focused sunlight (see schematic, Figure 8.1).

A century later, in 1878, a small solar power plant was exhibited at the World's Fair in Paris (Figure 8.2). To drive this solar steam engine, sunlight was focused from a parabolic reflector onto a steam boiler located at its focus; this produced the steam that operated a small reciprocating steam engine that ran a printing press. In 1901, a 10-hp solar steam engine was operated by A.G. Eneas in Pasadena, California (Daniels 1964). It used a 700-ft² focusing collector the shape of a truncated cone as shown in Figure 8.3. Between 1907 and 1913, the American engineer F. Shuman developed solar-driven hydraulic pumps; in 1913, he built, jointly with C.V. Boys, a 50-hp solar engine for pumping irrigation water from the Nile near Cairo in Egypt (Figure 8.4). This device used long parabolic troughs that focused solar radiation onto a central pipe with a concentration ratio of 4.5:1.

With the increasing availability of low-cost oil and natural gas, interest in solar energy for power production waned. Except for C.G. Abbott, who exhibited in 1936 a 1/2-hp solar-powered engine at an International Power Conference in Washington, D.C., and in 1938 in Florida, an improved, somewhat smaller version with a flash boiler, there was very little activity in the field of solar power between 1915 and 1950. Interest in solar power revived in 1949 when, at the centennial meeting of the American Association for the Advancement of Science in Washington, D.C., one session was devoted to future energy sources. At that time, the potentials as well as the economic problems of solar energy utilization were clearly presented by Daniels (1949).



FIGURE 8.1

Solar furnace used by Lavoisier in 1774. (Courtesy of Bibliotheque Nationale de Paris. Lavoisier, Oeuvres, vol. 3.)

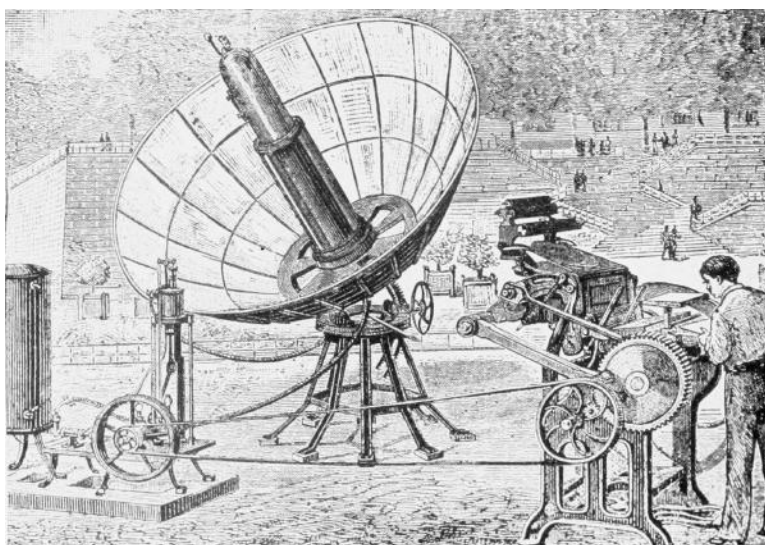
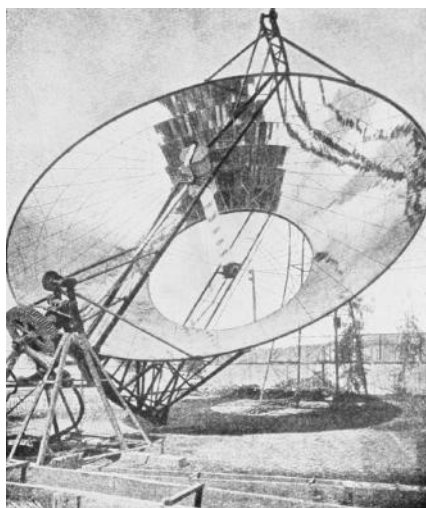
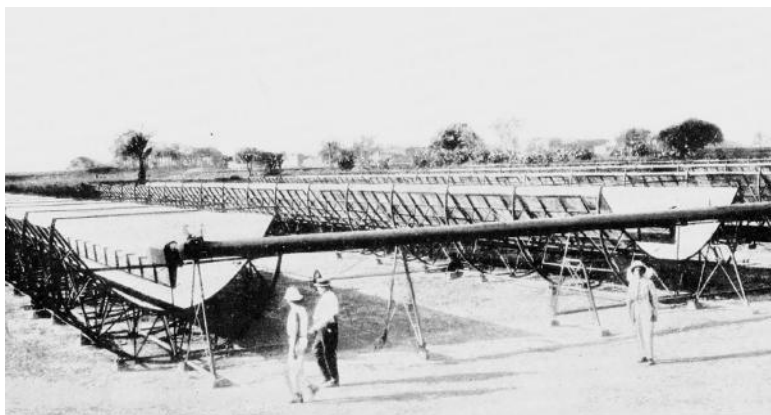


FIGURE 8.2

Parabolic collector powered a printing press at the 1878 Paris Exposition. (From Abbot, C.G., *The Sun and the Welfare of Man*, Washington, DC: Smithsonian Institution, 1929.)

**FIGURE 8.3**

Irrigation pumps were run by a solar-powered steam engine in Arizona in the early 1900s. The system consisted of an inverted cone that focused rays of the sun on the boiler. (From Abbot, C.G., *The Sun and the Welfare of Man*, Washington, DC: Smithsonian Institution, 1929.)

**FIGURE 8.4**

Solar irrigation pump (50 hp) operating in 1913 in Egypt. (From Abbot, C.G., *The Sun and the Welfare of Man*, Washington, DC: Smithsonian Institution, 1929.)

Some important conferences that considered solar power generation were held by UNESCO in 1954, the Association for Applied Solar Energy in 1955, the US National Academy of Sciences in 1961, and the United Nations in 1961. In addition, a research and development program supported by the National Aeronautics and Space Administration to build a solar electric power system capable of supplying electricity for the US space program was undertaken in the 1960s. However, widespread interest developed only after research funds

TABLE 8.1

Characteristics of CSP Systems

System	Peak Efficiency (%)	Annual Efficiency (%)	Annual Capacity Factor (%)
Parabolic trough/LFR	21	10–12 (d) 14–18 (p)	24 (d)
Power tower	30	14–25 (p)	25–70 (p)
Dish/engine	29	18–25 (p)	25 (p)

Source: Adapted from Romero-Alvarez, M. and E. Zarza, Concentrating solar thermal power, In *Energy Conversion*, D.Y. Goswami and F. Kreith (eds.), CRC Press, Boca Raton, FL, 2008.

Note: d, demonstrated; p, projected, based on pilot-scale testing.

became available for the development of earth-bound solar electric power and process heat after the oil embargo in 1973. Pace of development increased in the 1980s with the development of commercial parabolic trough collector (PTC)–based power plants SEGS I to SEGS IX totaling 354 MW_e capacity and the 1-MW_e Solar I central receiver tower demonstration plant in California. However, the progress stalled after that until a commercial 75-MW_e parabolic trough power plant started operating near Las Vegas, Nevada, in 2007. Since then, commercial and research activity in concentrated solar thermal power, also known as CSP, has increased tremendously in Europe, the United States, Asia, and Australia.

Currently, four different CSP technologies are in use based on the type of solar collection system: (1) PTC, (2) linear Fresnel reflector (LFR) system, (3) power tower or central receiver system (CRS), and (4) parabolic dish system. Of these, the PTC-based plants are the most in operation since 1985. The LFR system is in principle the same as the PTC except that the parabolic concentration is achieved via LFRs. CRS systems have the potential to achieve the highest efficiencies, which is why most of the present research activity in CSP is focused on CRS-based systems. Table 8.1 summarizes the characteristics of each solar technology.

8.2 Thermodynamic Power Cycles

There are two basic approaches to solar electric power generation. One is by photovoltaic process, a direct energy conversion, which is described in detail in Chapter 9. The other approach is to convert sunlight to heat at high temperatures and then heat to mechanical energy by a thermodynamic power cycle and, finally, convert the mechanical energy to electricity. This

indirect approach, called solar thermal power or CSP, is based on well-established principles of thermal power. A vast majority of electricity in the world is produced by thermal power conversion. Most of the thermal power production in the world is based on Rankine cycle and, to a smaller extent, Brayton cycle. Both of these are applicable to solar thermal power conversion, with Rankine cycle being the most popular. Normally, water is the working fluid for the Rankine cycle. However, for lower-temperature solar collection systems (70°C to approximately 300°C), organic fluids are used, in which case the cycle is commonly referred to as the organic Rankine cycle (ORC). When a Rankine cycle is operated under supercritical conditions of the working fluid, the cycle is usually referred to as the supercritical Rankine cycle (SRC). The Stirling cycle has also shown great potential, and solar thermal power systems based on this cycle are under development. More recently, researchers have been developing modifications of these cycles or entirely new cycles or combined cycles to increase the conversion efficiencies and to make them more applicable to the solar collection systems.

8.2.1 Rankine Cycle

Most of the existing thermal power plants are based on the Rankine cycle. The basic ideal Rankine cycle is shown in Figure 8.5, which also shows a temperature–entropy (T - s) diagram for steam as a working fluid. The ideal cycle consists of the following process:

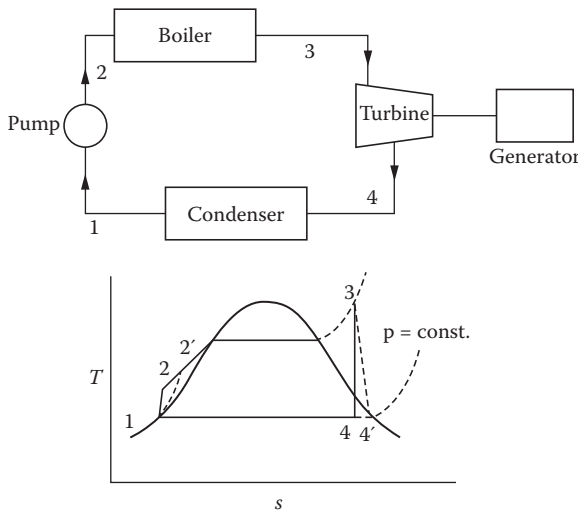


FIGURE 8.5
Basic Rankine power cycle.

Process

- 1–2 Saturated liquid from the condenser at state 1 is pumped to the boiler at state 2 isentropically.
- 2–3 Liquid is heated in the boiler at constant pressure. The temperature of the liquid rises until it becomes a saturated liquid. Further addition of heat vaporizes the liquid at constant temperature until all of the liquid turns into saturated vapor. Any additional heat superheats the working fluid to state 3.
- 3–4 Steam expands isentropically through a turbine to state 4.
- 4–1 Steam exiting the turbine is condensed at constant pressure until it returns to state 1 as saturated liquid.

In an actual Rankine cycle, the pumping and the turbine expansion processes are not ideal. The actual processes are 1–2' and 3–4', respectively. For the above cycle,

$$\text{Turbine efficiency } \eta_{\text{turbine}} = \frac{h_3 - h_4}{h_3 - h_4} \quad (8.1)$$

$$\text{Pump efficiency } \eta_{\text{pump}} = \frac{h_1 - h_2}{h_1 - h_2} \quad (8.2)$$

$$\text{Net work output} = (h_3 - h_4) - (h_{2'} - h_1) \quad (8.3)$$

$$\text{Heat input} = h_3 - h_{4'} \quad (8.4)$$

$$\text{Pump work} = h_2 - h_1 = \frac{v(P_2 - P_1)}{\eta_{\text{pump}}} \quad (8.5)$$

$$\text{Cycle efficiency} = \frac{\text{Net work output}}{\text{Heat input}} = \frac{(h_3 - h_4) - (h_{2'} - h_1)}{h_3 - h_2}, \quad (8.6)$$

where h represents enthalpy and v is the specific volume at state 1.

Example 8.1

In a simple steam Rankine cycle, steam exits the boiler at 7.0 MPa and 540°C. The condenser operates at 10 kPa and rejects heat to the atmosphere at 40°C. Find the Rankine cycle efficiency and compare it to

the Carnot cycle efficiency. Both pump and turbine operate at 85% efficiencies.

The cycle is shown in Figure 8.5.

The Rankine cycle efficiency:

$$\eta_R = \frac{(h_3 - h_4) - (h_2 - h_1)}{h_3 - h_2},$$

$$\eta_{\text{turbine}} = \frac{h_3 - h_4}{h_3 - h_2},$$

and

$$\eta_{\text{pump}} = \frac{h_2 - h_1}{h_2 - h_1} = \frac{v_1(P_2 - P_1)}{h_2 - h_1}.$$

The enthalpies at the state points are found as follows:

$$h_1 = h_f(10 \text{ kPa}) = 191.8 \text{ kJ/kg.}$$

Pump work from 1 to 2:

$$\begin{aligned} W_2 &= \frac{v_1(P_2 - P_1)}{\eta_{\text{pump}}} = h_2 - h_1 \\ h_2 &= h_1 + \frac{v_1(P_2 - P_1)}{\eta_{\text{pump}}} \\ &= 191.8 \text{ kJ/kg} + \frac{(0.00101 \text{ m}^3/\text{kg})(7000 - 10) \text{ kPa}}{0.85} \\ &= 200.1 \text{ kJ/kg} \\ h_3(540^\circ\text{C}, 7 \text{ MPa}) &= 3506.9 \text{ kJ/kg.} \end{aligned}$$

States 3 and 4 have the same entropy.
Therefore,

$$s_3 = 6.9193 \text{ kJ/kg}\cdot\text{K} = s_4.$$

Saturated vapor entropy at state 4 (10 kPa):

$$s_{4g} = 8.1502 \text{ kJ/kg}\cdot\text{K.}$$

Since s_4 is less than s_{4g} , 4 is a wet state:

$$s_4 = s_f + Xs_{fg} \text{ or } s_g - Ms_{fg},$$

where X is the vapor quality and M is the moisture.

$$M_4 = \frac{s_g - s_4}{s_{fg}} = \frac{8.1502 - 6.9193}{7.5009} = 0.1641 \text{ or } 16.41\%.$$

$$h_4 = h_g - M_4 h_{fg} = 2584.7 - 0.1641(2392.8) = 2192 \text{ kJ/kg.}$$

Therefore,

$$\begin{aligned} h_4 &= h_3 - \eta_{\text{turbine}}(h_3 - h_4) \\ &= 3507 - 0.85(3507 - 2192) = 2389 \text{ kJ/kg.} \end{aligned}$$

Actual moisture at the turbine exhaust:

$$h_{4'} = h_g - M_4 h_{fg}.$$

$$\begin{aligned} M_4 &= \frac{h_g - h_4}{h_{fg}} = \frac{2584.7 - 2389}{2391} \\ &0.0817 \text{ or } 8.17\%. \end{aligned}$$

$$\text{Net work} = (h_3 - h_4) - (h_2 - h_1) = 1109 \text{ kJ/kg.}$$

$$\eta = \frac{\text{Net work}}{h_3 - h_2} = \frac{1109}{3507 - 200} = 0.3354 \text{ or } 33.54\%.$$

$$\eta_{\text{Carnot}} = \frac{813K - 313K}{813K} = 0.615 \text{ or } 61.5\%.$$

Several improvements can be made to the basic Rankine cycle in order to improve the cycle efficiency. The efficiency of the Rankine cycle may be increased by increasing the pressure in the boiler. However, that will result in increased moisture in the steam exiting the turbine. In order to avoid this problem, the steam is expanded to an intermediate pressure and reheated in the boiler. The reheated steam is expanded in the turbine until the exhaust pressure is reached. Figure 8.6 shows the Rankine cycle with reheat.

The cycle efficiency of the Rankine cycle with reheat:

$$\eta = \frac{(h_3 - h_4) + (h_s - h_6) - (h_2 - h_1)}{(h_3 - h_2) + (h_5 - h_4)}. \quad (8.7)$$

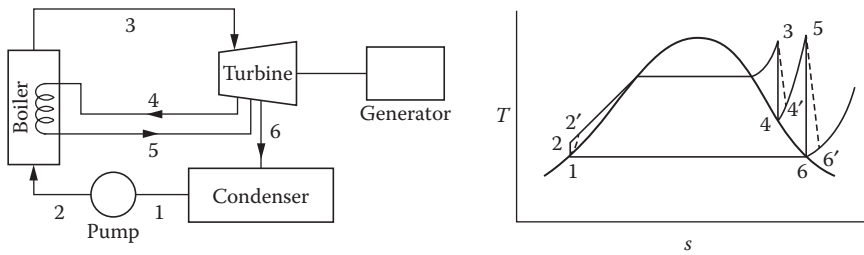


FIGURE 8.6
Rankine cycle with reheat.

Example 8.2

A reheat Rankine cycle uses steam as a working fluid. The steam leaves the boiler and enters the turbine at 5 MPa and 350°C, and it leaves the condenser as a saturated liquid. After expansion in the turbine to $P = 1.4$ MPa, the steam is reheated to 350°C and then expands in the low-pressure turbine to 20 kPa. If the efficiencies of the pump and turbine are 0.9 each, determine the cycle efficiency.

Solution

Point 3

$$P_3 = 5 \text{ MPa}, T_3 = 350^\circ\text{C}.$$

From steam tables,

$$h_3 = 3068 \text{ kJ/kg},$$

$$s_3 = 6.449 \text{ kJ/kg}\cdot\text{K}.$$

Point 4

$$s_4 = s_3 = 6.449 \text{ kJ/kg}\cdot\text{K}, P_4 = 1.4 \text{ MPa}.$$

From steam tables,

$$h_4 = 2781 \text{ kJ/kg}.$$

Using h_4 and turbine efficiency to find h_4' ,

$$\eta_T = \frac{h_3 - h_4}{h_3 - h_4'},$$

$$h_4' = h_3 - \eta_T(h_3 - h_4) = 3082 - 0.9(3082 - 2781) = 2811.1 \text{ kJ/kg}.$$

Point 5

$$P_5 = 1.4 \text{ MPa}, T_5 = 350^\circ\text{C}.$$

From steam tables,

$$h_5 = 3149 \text{ kJ/kg},$$

$$s_5 = 7.136 \text{ kJ/kg}\cdot\text{K}.$$

Point 6

$$P_6 = 20 \text{ kPa},$$

$$s_6 = s_5 = 7.136 \text{ kJ/kg}\cdot\text{K}.$$

$$x = \frac{7.136 - 0.8319}{7.908 - 0.8319} = 0.89,$$

$$h_6 = h_f + xh_{fg} = 251.4 + 0.89(2610 - 251.4) = 2352.$$

Using the turbine efficiency to find h_6' ,

$$h_6' = h_5 - \eta_T(h_5 - h_6) = 3149 - 0.9(3149 - 2352) = 2432 \text{ kJ/kg}.$$

Point 1

$$P_1 = 20 \text{ kPa},$$

Saturated liquid:

$$v_1 = 0.001017 \text{ m}^3/\text{kg},$$

$$h_1 = 251.4 \text{ kJ/kg}.$$

Point 2

Pump work, 1 to 2,

$$w_2 = h_2 - h_1 = v(P_2 - P_1),$$

Pump efficiency,

$$\eta_p = \frac{h_2 - h_1}{h_2 - h_1},$$

$$h_2 - h_1 = \frac{h_2 - h_1}{\eta_p}.$$

But $h_2 - h_1 = v(P_2 - P_1)$,

$$h_2 - h_1 = \frac{v(P_2 - P_1)}{\eta_p} = \frac{0.001017(5000 - 20)}{0.9} = 5.6274,$$

and

$$h_2 = 257.03 \text{ kJ/kg.}$$

Computing the cycle efficiency,

$$\eta = \frac{(h_3 - h_4) + (h_5 - h_6) - (h_2 - h_1)}{(h_3 - h_2) + (h_5 - h_4)} = 0.3075 = 30.75\%.$$

Another improvement to the basic Rankine cycle is the regenerative cycle in which expanded steam is extracted at various points in the turbine and mixed with the condensed water to preheat it in the feedwater heaters. Figure 8.7 shows a schematic diagram and a $T-s$ diagram of a Rankine cycle with regeneration.

If a fraction f of the steam in the turbine is bled at state 5 to mix with the feedwater, the efficiency of the Rankine cycle with regeneration as shown in Figure 8.7 is

$$\eta = \frac{(h_5 - h_6) + (1-f)(h_6 - h_7) - (1-f)(h_2 - h_1) - (h_4 - h_3)}{h_5 - h_4}, \quad (8.8)$$

h_3 can be found from the energy balance

$$mh_3 = f mh_6 + (1-f)m h_2$$

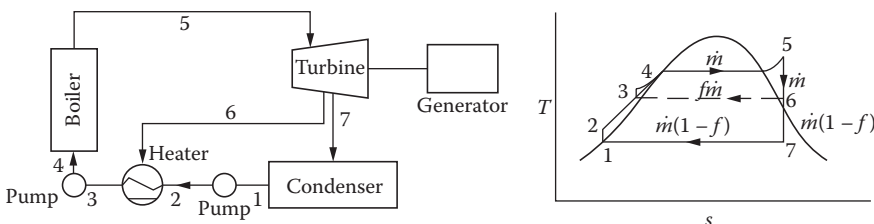


FIGURE 8.7
Rankine cycle with regeneration.

or

$$h_3 = f(h_6 - h_2) + h_2. \quad (8.9)$$

Example 8.3

A regenerative Rankine cycle uses steam as the working fluid. Steam leaves the boiler and enters the turbine at $P = 5 \text{ MPa}$, $T = 500^\circ\text{C}$. After expansion to 400 kPa, a part of the steam is extracted from the turbine for the purpose of heating the feedwater in the feedwater heater. The pressure in the feedwater heater is 400 kPa and the water leaving it is saturated liquid at 400 kPa. The steam that is not extracted expands to 10 kPa. Assuming the efficiencies of the turbine and the two pumps are 100% each, determine the fraction of the steam extracted to the feedwater heater (f) and the cycle efficiency (η).

Solution

Point 5

$$P_5 = 5 \text{ MPa}, T_5 = 500^\circ\text{C}$$

From the steam table, steam is superheated.

$$s_5 = 6.976 \text{ kJ/kg}\cdot\text{K},$$

$$h_5 = 3434 \text{ kJ/kg}.$$

Point 6

$$s_6 = s_5 = 6.976 \text{ kJ/kg}\cdot\text{K},$$

$$P_6 = 400 \text{ kPa}.$$

From the steam table, steam is superheated.

Using s_6 , we can interpolate for h_6 :

$$h_6 = 2773 \text{ kJ/kg}.$$

Point 7

$P_7 = 10 \text{ kPa}$. Again, $s_7 = s_5 = 6.976 \text{ kJ/kg}\cdot\text{K}$, mixture.

Computing,

$$x = \frac{6.976 - 0.6492}{8.1501 - 0.6492} = 0.84,$$

$$h_7 = h_f + xh_{fg} = 191.81 + 0.84(2392.8) = 2210 \text{ kJ/kg.}$$

Point 1

$$P_1 = 10 \text{ kPa.}$$

Saturated liquid,

$$h_1 = 191.81 \text{ kJ/kg.}$$

Point 2

$$P_2 = 400 \text{ kPa,}$$

$$h_2 - h_1 = v_1(P_2 - P_1) = 0.00101(400 - 10) = 0.3939 \text{ kJ/kg,}$$

$$h_2 = (191.81 + 0.3939) = 192.2 \text{ kJ/kg.}$$

Point 3

$$P = 400 \text{ kPa.}$$

Saturated liquid,

$$v_3 = 0.001084 \text{ m}^3/\text{kg,}$$

$$h_3 = 604.73 \text{ kJ/kg.}$$

Using the energy balance of feedwater heater, f may be computed as

$$\begin{aligned} h_3 &= fh_6 + (1-f)h_2 \\ f &= \frac{h_3 - h_2}{h_6 - h_2} = \frac{604.73 - 192.2}{2773 - 192.2} = 0.16. \end{aligned}$$

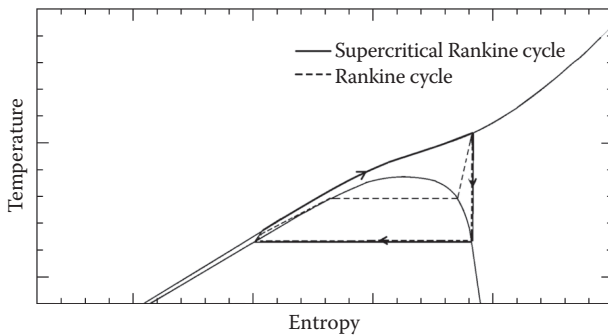
Point 4

$$w_{p2} = h_4 - h_3 = v_3(P_4 - P_3) = 0.001084(5000 - 400) = 4.9864 \text{ kJ/kg.}$$

$$h_4 = h_3 + 4.9864 = 609.72 \text{ kJ/kg.}$$

Efficiency (η) may be computed from Equation 8.8 as

$$\eta = \frac{(h_5 - h_6) - (1-f)(h_6 - h_7) - (1-f)(h_2 - h_1) - (h_4 - h_3)}{(h_5 - h_4)} = 0.399 = 39.9\%.$$

**FIGURE 8.8**

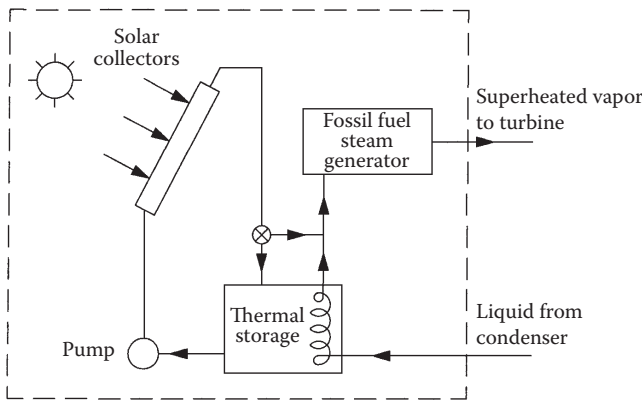
A supercritical Rankine cycle on a T - s diagram.

8.2.2 Supercritical Rankine Cycle

Conventional Rankine cycles work under subcritical conditions and generally use pure working fluids. Since a pure fluid boils at a constant temperature (Figure 8.8), it results in a mismatch with the temperature profile of the heat source. This mismatch results in higher losses in the heat exchange process, which can be reduced by the use of an SRC. In an SRC, shown in Figure 8.8, the working fluid is pressurized beyond its critical pressure and then heated isobarically directly to supercritical vapor phase. The supercritical vapor then expands in the turbine producing mechanical work. The turbine exhaust is then cooled to the liquid state in a condenser and the condensed fluid is pumped back to high pressure. A steam Rankine cycle can be operated under supercritical conditions; however, the critical pressure of steam is very high, which introduces corresponding material requirements, thus increasing the cost. On the other hand, organic fluids such as hydrocarbons and refrigerants have lower critical temperatures and pressures; therefore, they are being actively considered for SRC for low- and medium-temperature heat sources. These fluids give better efficiency in SRCs than the conventional ORC.

8.2.3 Components of a Rankine Power Plant

Major components of a Rankine power plant include boiler, turbine, condenser, pumps (condensate pump, feedwater booster, and boiler feed pump), and heat exchangers (open heaters and closed heaters). All of the components of a solar thermal power plant are the same as those in a conventional thermal power plant except the boiler. The boiler in a solar thermal power plant includes a solar collection system, a storage system, an auxiliary fuel heater and heat exchangers. Figure 8.9 shows a schematic representation of a solar boiler. The maximum temperature from the solar system depends on the type of solar collection system (PTCs, central receiver with heliostat field, parabolic dishes, etc.). Parabolic trough and parabolic dish collectors are described in detail in Chapter 3, while

**FIGURE 8.9**

Schematic of a solar boiler.

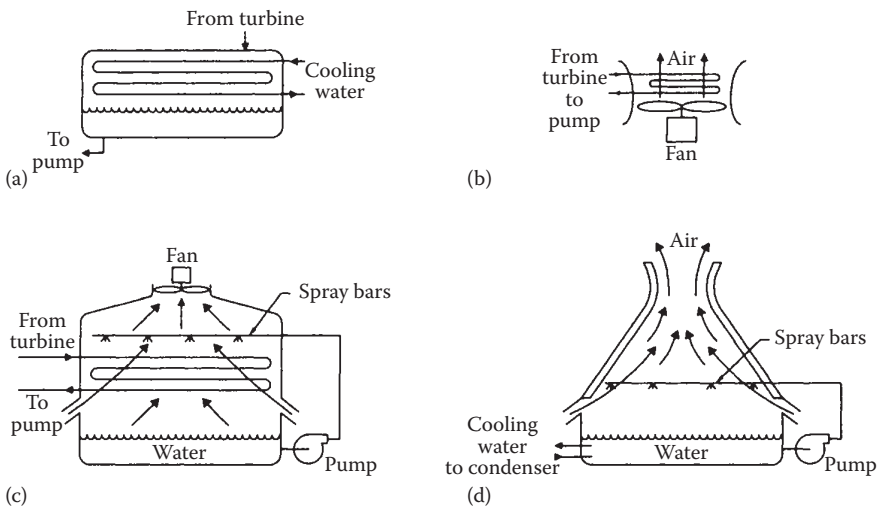
central receiver systems are described later in this chapter. If the temperature of the fluid from the solar system/storage is less than the required temperature for the turbine, an auxiliary fuel is used to boost the temperature. A fossil fuel or a biomass fuel may be used as the auxiliary fuel.

A condenser is a large heat exchanger that condenses the exhaust vapor from the turbine. Steam turbines employ surface-type condensers, mainly shell and tube heat exchangers operating under vacuum. The vacuum in the condenser reduces the exhaust pressure at the turbine blade exit to maximize the work in the turbine. The cooling water from either a large body of water such as a river or a lake, or from cooling tower, circulates through the condenser tubes. The cooling water is cooled in the cooling tower by evaporation. The air flow in the cooling tower is either natural draft (hyperbolic towers) or forced draft (see Figure 8.10). The condensate and feedwater pumps are motor-driven centrifugal pumps, while the boiler feed pumps may be motor- or turbine-driven centrifugal pumps.

Steam turbines and generators are described in detail in a number of books (Fitzgerald et al. 1971; Japikse and Nicholas 1994; Kreith and Goswami 2004; Salisbury 1950; Goswami and Kreith 2007) and will not be discussed here.

8.2.4 Choice of Working Fluid

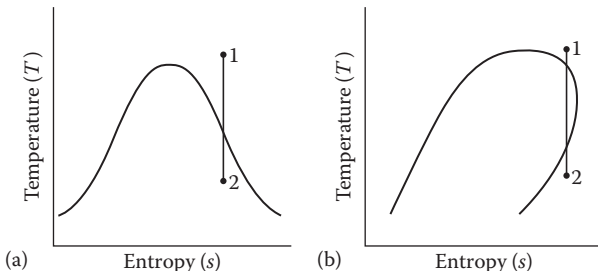
Working fluid in a solar Rankine cycle is chosen on the basis of the temperature from the solar collection system. The working fluid must be such that it optimizes the cycle efficiency based on the expected temperature from the source. Steam is the most common working fluid in a Rankine cycle. Its critical temperature and pressure are 374°C and 22.1 MPa, respectively. Therefore, it can be used for systems operating at fairly high temperatures. Systems employing parabolic trough, parabolic dish, or central receiver collection systems can use steam as a working fluid. Other major advantages of

**FIGURE 8.10**

Types of condenser or heat rejection used in Rankine cycle solar power systems: (a) tube-and-shell condenser, (b) dry cooling tower, (c) wet cooling tower, and (d) natural-draft cooling tower. (Stine, W.B. and R.W. Harrigan: *Solar Energy Fundamentals and Design: With Computer Applications*. 1985. Copyright Wiley-VCH Verlag GmbH & Co. KGaA. Reproduced with permission.)

steam are that it is nontoxic, environmentally safe, and inexpensive. Its major disadvantage is its low molecular weight, which requires very high turbine speeds in order to get high turbine efficiencies.

Steam is a wetting fluid; that is, as it is expanded in a turbine, once it reaches saturation, any further expansion increases the moisture content. In other words, steam becomes wetter as it expands as shown in Figure 8.11a. On the other hand, a fluid that has a T - s (temperature–entropy) diagram similar to that shown in Figure 8.11b is called a drying fluid. As seen from this figure, even though the working fluid passes through the two-phase region, it may exit the turbine as superheated. Normally, the turbine speed is so high that,

**FIGURE 8.11**

T - s characteristics of (a) wetting and (b) drying types of working fluids.

in such a case, there is no condensation in the turbine. Examples of drying fluids include hydrocarbons (toluene, methanol, isobutane, pentane, and hexane) and chlorofluorocarbons (CFCs such as R-11 and R-113). Since a drying fluid does not get wetter on expansion from a saturated vapor condition in an ideal or real process, it does not have to be superheated. Therefore, a Rankine cycle using a drying fluid may be more efficient than the cycle using a wetting fluid. In fact, a drying fluid may be heated above its critical point so that upon expansion, it may pass through the two-phase dome. Because of the T - s characteristics, the fluid may pass through the two-phase region and still exit from the turbine as superheated. These characteristics can be used to increase the resource effectiveness of a cycle by as much as 8% (Goswami et al. 1991). Chen et al. (2010) have given a comprehensive review of the potential working fluids for the Rankine cycle.

It has been mentioned that a working fluid can be classified as a dry, isotropic, or wet fluid depending on the slope of the saturation vapor curve on a T - s diagram (dT/ds) (Figure 8.12). Since the value of dT/ds leads to infinity for isentropic fluids, the inverse of the slope, (i.e., ds/dT) is used to express how "dry" or "wet" a fluid is. If we define $\xi = \frac{ds}{dT}$, the working fluid can be classified by the value of ξ ; that is, $\xi > 0$: a dry fluid (e.g., pentane), $\xi \approx 0$: an isentropic fluid (e.g., R11), and $\xi < 0$: a wet fluid (e.g., water). Figure 8.12 shows the three types of fluids in a T - s diagram.

Liu et al. (2004) derived an expression to compute ξ , which is

$$\xi = \frac{C_p}{T_H} - \frac{\frac{n \cdot T_{rH}}{1 - T_{rH}} + 1}{\Delta H_{H_2}} \quad (8.10)$$

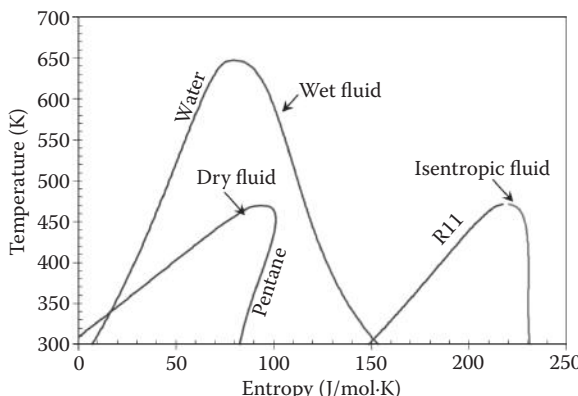


FIGURE 8.12

Three types of working fluids: dry, isentropic, and wet.

where ξ (ds/dT) denotes the inverse of the slope of saturated vapor curve on the $T-s$ diagram, n is suggested to be 0.375 or 0.38 (Poling et al. 2000), $T_{rH} = (T_H/T_C)$ denotes the reduced evaporation temperature, and ΔH_H is the enthalpy of vaporization.

Table 8.2 gives some characteristics of candidate working fluids for Rankine cycles (Chen et al. 2010) including their ξ values. Figure 8.13a and b show the ξ values of the fluids. Before selecting any of these fluids, one needs to look at their chemical stability under the conditions of operation and their environmental aspects, including the ozone depletion potential (ODP), the global warming potential (GWP), and the atmospheric lifetime. The ODP and GWP represent substance's potential to contribute to ozone degradation and global warming. Because of environmental concerns, some working fluids have been phased out, such as R-11, R-12, R-113, R-114, and R-115, while some others are being phased out in 2020 or 2030 (such as R-21, R-22, R-123, R-124, R-141b, and R-142b). Water is the most common working fluid for power plants based on solar energy, nuclear energy, and fossil fuels, while hydrocarbons and R134a and R245fa are commonly used for geothermal power. At present, CO_2 is being actively investigated as a working fluid in a supercritical cycle for high-temperature central receiver tower-based plants (Besarati and Goswami 2013). Chen et al. (2010) proposed using zeotropic mixtures of working fluids instead of pure fluids. They showed that using mixtures reduces the irreversibilities in a cycle, since the condensation process is not isothermal and there is no sharp pinch point during boiling, and improves the efficiency of conversion.

8.3 Design of Parabolic Trough-Based Power Plants

Design of a PTC-based CSP plant involves sizing and layout of the solar field, selection of the heat-transfer fluid (HTF), designing thermal energy storage (if any), design of the power block, and integration of the solar field with the power block and the control system. Vasquez-Padilla (2011) has presented a detailed methodology of the design of PTC-based CSP power plants. The following Sections 8.31 through 8.35 are based on Vasquez-Padilla (2011).

8.3.1 Sizing and Layout of the Solar Field

Details of a PTC and its performance parameters are described earlier in Chapter 3. Normally, PTC collectors are oriented N–S horizontally and they track the sun from E to W. Beam solar radiation per unit area of the tracking PTC is estimated for the selected location on the basis of the models described in Chapter 2. This is followed by a preliminary area of the solar

TABLE 8.2
Properties of Potential Working Fluids for Rankine Power Cycle

ASHRAE Number	Name	Molecular Weight	T _c (K)	P _c (MPa)	Vapor C _p (J/kg·K)	Latent heat L (kJ/kg)	ξ (J/kg·K ²)
R-21	Dichlorofluoromethane	102.92	451.48	5.18	339.85	216.17	-0.78
R-22	Chlorodifluoromethane	86.47	369.30	4.99	1069.13	158.46	-1.33
R-23 ^a	Trifluoromethane	70.01	299.29	4.83	3884.02	89.69	-6.49
	Difluoromethane	52.02	351.26	5.78	2301.61	218.59	-4.33
R-41 ^a	Fluoromethane	34.03	317.28	5.90	3384.66	270.04	-7.20
	Hexafluoroethane	138.01	293.03	3.05	4877.91	30.69	-5.54
R-116 ^a	2,2-Dichloro-1,1,1-trifluoroethane	152.93	456.83	3.66	738.51	161.82	0.26
R-123	2-Chloro-1,1,1,2-tetrafluoroethane	136.48	395.43	3.62	908.70	132.97	0.26
R-124	Pentafluoroethane	120.02	339.17	3.62	1643.89	81.49	-1.08
R-125	1,1,1,2-Tetrafluoroethane	102.03	374.21	4.06	1211.51	155.42	-0.39
R-134a	1,1-Dichloro-1-fluoroethane	116.95	477.50	4.21	848.37	215.13	0.00
R-141b	1-Chloro-1,1-difluoroethane	100.50	410.26	4.06	1036.52	185.69	0.00
R-142b	1,1,1-Trifluoroethane	84.04	345.86	3.76	1913.97	124.81	-1.49
R-143a	1,1-Difluoroethane	66.05	386.4	4.52	1456.02	249.67	-1.14
R-152a	Ethane	30.07	305.33	4.87	5264.72	223.43	-8.28
R-170 ^a	Octafluoropropane	188.02	345.02	2.64	1244.87	58.29	0.45
R-218	1,1,1,2,3,3-Hexafluoropropane	170.03	375.95	3.00	1013.00	97.14	0.76
R-227ea	1,1,1,2,3,3-Hexafluoropropane	152.04	412.44	3.50	973.69	142.98	0.76
R-236ea							

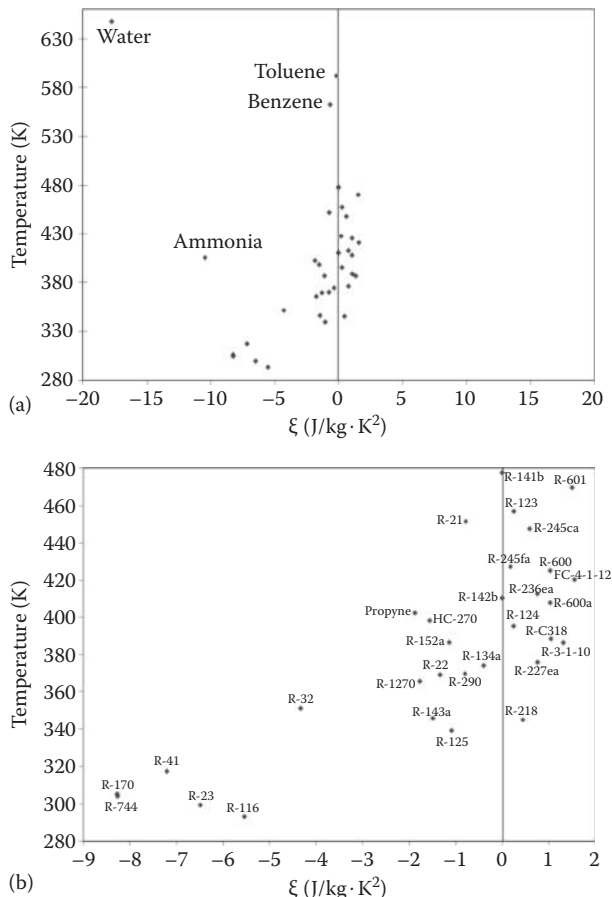
(Continued)

TABLE 8.2 (CONTINUED)
Properties of Potential Working Fluids for Rankine Power Cycle

ASHRAE Number	Name	Molecular Weight	T _c (K)	P _c (MPa)	Vapor C _p (J/kg·K)	Latent heat L (kJ/kg)	ξ (J/kg·K ²)
R-245ca	1,1,2,2,3-Pentafluoropropane	134.05	447.57	3.93	1011.26	188.64	0.60
R-245fa	1,1,1,3,3-Pentafluoropropane	134.05	427.20	3.64	980.90	177.08	0.19
HC-270	Cyclopropane	42.08	398.30	5.58	1911.81	366.18	-1.54
R-290	Propane	44.10	369.83	4.25	2395.46	292.13	-0.79
R-C318	Octafluoroclobutane	200.03	388.38	2.78	896.82	93.95	1.05
R-3-10	Decafluorobutane	238.03	386.33	2.32	928.83	77.95	1.32
FC-4-1-12	Dodecafluoropentane	288.03	420.56	2.05	884.25	86.11	1.56
R-600	Butane	58.12	425.13	3.80	1965.59	336.82	1.03
R-600a	Isobutane	58.12	407.81	3.63	1981.42	303.44	1.03
R-601	Pentane	72.15	469.70	3.37	1824.12	349.00	1.51
R-717	Ammonia	17.03	405.40	11.33	3730.71	1064.38	-10.48
R-718	Water	18.00	647.10	22.06	1943.17	2391.79	-17.78
R-744 ^a	Carbon dioxide	44.01	304.13	7.38	3643.72	167.53	-8.27
R-1270	Propene	42.08	365.57	4.66	2387.36	284.34	-1.77
	Propyne	40.06	402.38	5.63	2100.54	431.61	-1.87
	Benzene	78.11	562.05	4.89	1146.72	418.22	-0.70
	Toluene	92.14	591.75	4.13	1223.90	399.52	-0.21
	Sodium						
	Potassium						
	Mercury						

Source: Chen H. et al., *Renewable and Sustainable Energy Reviews*, 14 (9), 3059–3067, 2010.

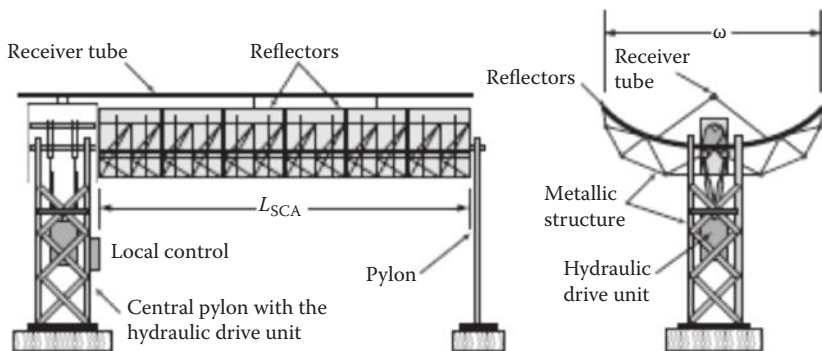
^a The critical temperature of the fluid is below 320 K, and the data are given based on 290 K.

**FIGURE 8.13**

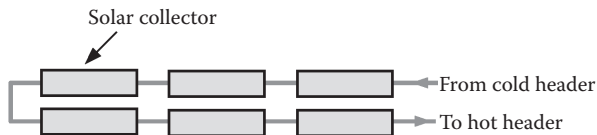
Distribution of the screened 35 working fluids in the $T-\xi$ chart: (a) all 35 fluids, (b) enlarged view of 31 fluids.

collectors determining for the design of the solar field. A solar field consists of a number of solar collector assemblies (SCAs) connected in a series parallel arrangement as described later. Each SCA consists of metallic support structure, parabolic mirrors, receiver/absorber tube, hydraulic drive unit, and pylon supports as shown in Figure 8.14. In order to reach the operational conditions of temperature, these SCAs are connected in series to form a solar collector loop. The number of SCAs in series, N , is calculated from the nominal design temperature rise, ΔT , in a loop and the temperature rise, ΔT_c , in an SCA.

$$N = \Delta T / \Delta T_c. \quad (8.11)$$

**FIGURE 8.14**

A solar collector assembly (SCA) for an LS-3 PTC. (Adapted from Romero-Alvarez, M. and E. Zarza, Concentrating solar thermal power, In *Energy Conversion*, D.Y. Goswami and F. Kreith (eds.), Boca Raton, FL: CRC Press, 2008.)

**FIGURE 8.15**

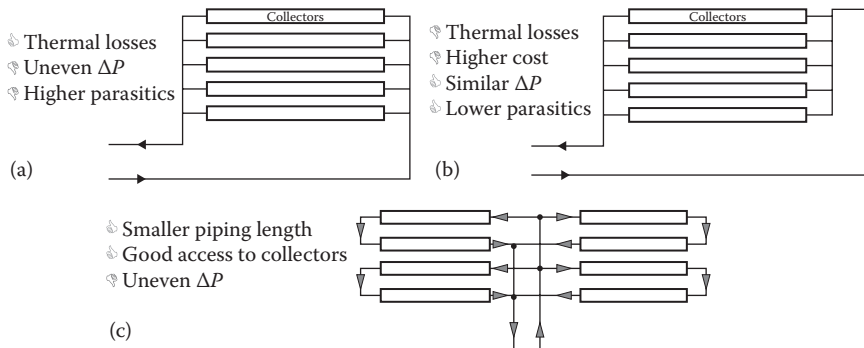
Schematic of a solar collector loop. (Adapted from Romero-Alvarez, M. and E. Zarza, Concentrating solar thermal power, In *Energy Conversion*, D.Y. Goswami and F. Kreith (eds.), Boca Raton, FL: CRC Press, 2008.)

Figure 8.15 shows a schematic of a solar collector loop.

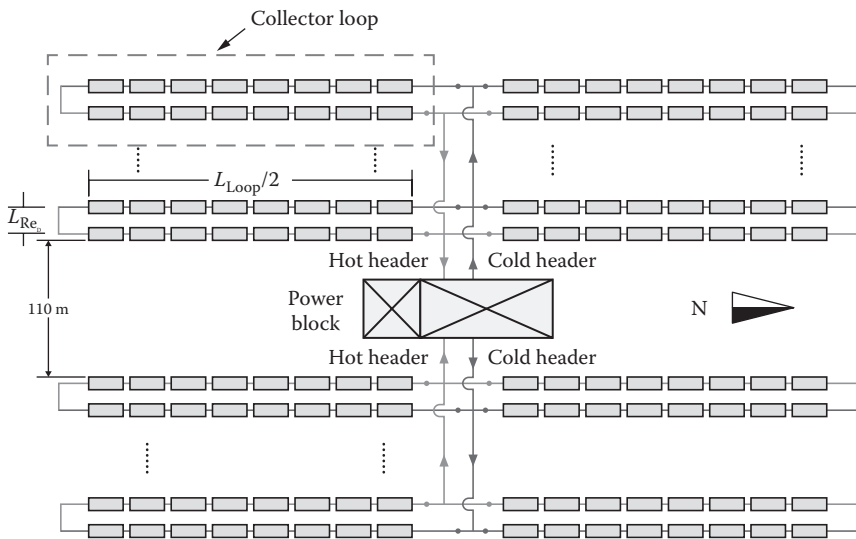
The number of parallel loops is then calculated from the thermal energy output from each loop and the total thermal energy needed from the total field. The parallel loops can be connected in three different ways as shown in Figure 8.16. The direct return layout has uneven pressure drops in each loop, therefore requiring flow-balancing valves. In contrast, the inverse return has similar pressure drops in all the loops; however, it requires longer pipe lengths. These two layouts are normally used in smaller industrial process heat applications, while much larger fields needed for CSP plants use a central feed and return. Therefore, the power block for the CSP plants is generally located in the center. The central feed can be an H-type or an I-type field layout as shown in Figures 8.17 and 8.18.

8.3.1.1 I Field Layout

As shown in Figure 8.17, the solar field is divided into two header pairs, with the power block located at the center of the field. Each collector loop consists of two rows connected in series, and the cold and hot headers run in the E-W direction. Because of uneven pressure drops in the loops, flow balancing valves are required.

**FIGURE 8.16**

Solar field layout loops. (a) Direct return. (b) Inverse return. (c) Central feed. (Adapted from Romero-Alvarez, M. and E. Zarza, Concentrating solar thermal power, In *Energy Conversion*, D.Y. Goswami and F. Kreith (eds.), Boca Raton, FL: CRC Press, 2008.)

**FIGURE 8.17**

I solar field layout. (Adapted from Vasquez-Padilla, R., Simplified methodology for designing parabolic through solar power plants. PhD dissertation, University of South Florida, Tampa, FL, 2011.)

8.3.1.2 H Field Layout

As shown in Figure 8.18, this field layout is divided into four header pairs, two on each side of the central power block. All four headers are in the E-W direction. In a solar collector loop, the SCAs may be connected by ball joints or flexible hoses to allow for independent rotation. Ball joints are preferred

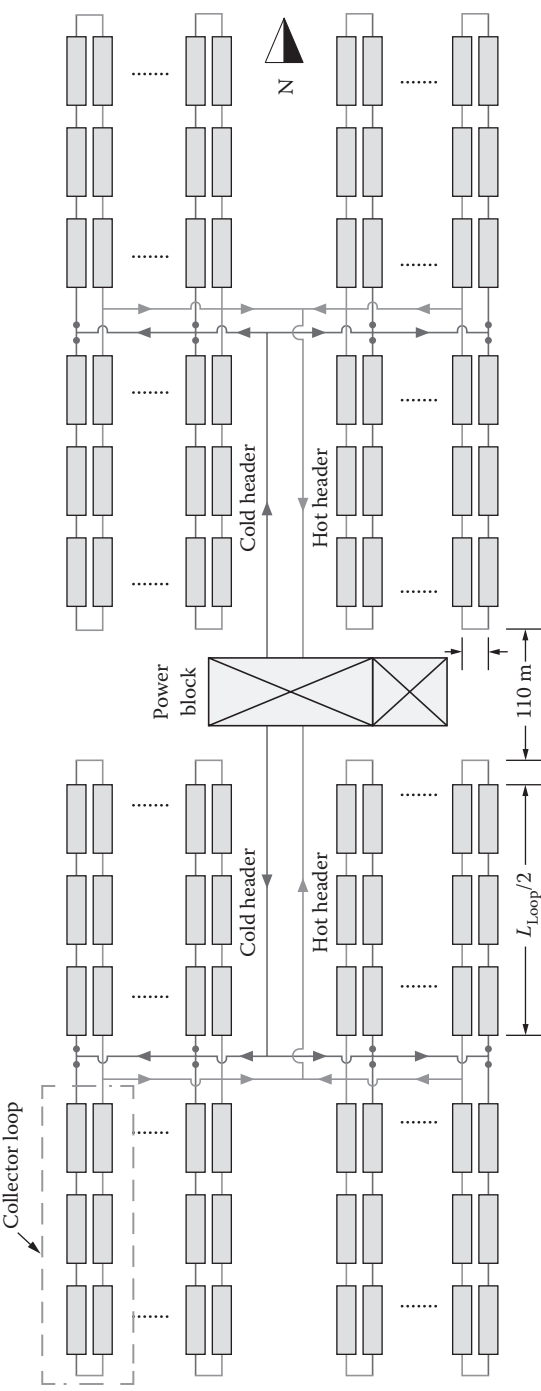


FIGURE 8.18
 H solar field layout. (Adapted from Vasquez-Padilla, R., Simplified methodology for designing parabolic through solar power plants, PhD dissertation, University of South Florida, Tampa, FL, 2011.)

over flexible hoses because of their lower cost, reduced pressure drop, and reduced heat losses (Romero-Alvarez and Zarza 2008).

8.3.2 Pressure Drop in the Solar Field

The pressure drop in the solar field depends on the HTF mass flow rate, inner diameter of the pipes, and fittings (elbow, cross, reduction, expansion, valves, etc.). Initially, it is necessary to determine the optimum diameter for each section. According to Kelly and Kearney (2006), the optimum flow velocity is in the range of 2–4 m/s. For the pressure requirements, the required wall thickness of the pipe is calculated as (Megyesy 2004)

$$t_{\text{wall}} = \frac{(P_{\text{abs}} - P_{\text{atm}})D_0}{2S_y + 0.4(P_{\text{abs}} - P_{\text{atm}})}, \quad (8.12)$$

where P_{abs} is the absolute pressure of HTF in pounds per square inch (psi), P_{atm} is the atmospheric pressure in psi, D_0 is the outside diameter in inches, and S_y is the allowable stress in psi. Kelly and Kearney (2006) recommend three different pipe materials: ASTM A106, Grade B, Seamless Carbon Steel; ASTM A335 P9, Intermediate Alloy Steel; and ASTM TP347, Stainless Steel. The allowable stress for each material is shown in Table 8.3. The inner diameter and wall thickness for different pipe schedules and nominal diameters are shown in Appendix 4 (Figure A4.5).

Once the diameter is selected, the flow friction loss is calculated using the Darcy–Weisbach equation:

$$h_i = 2C_f \frac{L_i}{D_i} \frac{V_i^2}{g}, \quad (8.13)$$

where C_f is the friction coefficient (Fanning friction factor), L_i is the length of the pipe section in meters, and V_i is the flow velocity in meters per second. The friction coefficient can be calculated from the correlation given in Kakaç et al. (1987):

$$\frac{1}{\sqrt{C_f}} = 3.48 - 1.7372 \ln 2 \frac{\epsilon}{D_t} - \frac{16.2426}{\text{Re}_D} \ln A_2 \quad (8.14)$$

$$A_2 = \frac{(2\epsilon/D_t)^{1.1098}}{6.0983} + \frac{7.149}{\text{Re}_D}^{0.8981},$$

where Re_D is the Reynolds number and ϵ is the pipe roughness in meters. This correlation is valid for $4000 \leq \text{Re}_D \times 10^8$ and $2 \times 10^{-8} \leq \epsilon/a \leq 0.1$.

TABLE 8.3

Maximum Allowable Stress (ksi) for Different Materials

Temperature (°F)	Maximum Allowable Stress (ksi)		
	A106	TP347	A335
400	—	15.5	—
500	—	14.9	14.4
600	—	14.7	14.2
650	15	14.7	13.9
700	14.4	14.7	13.7
750	13.0	14.7	13.2
800	10.8	14.7	12.8
850	—	14.7	12.1
900	—	14.7	11.4
950	—	14.6	10.6
1000	—	14.0	7.4
1050	—	12.1	5.0
1100	—	9.1	3.3
1150	—	6.1	2.2
1200	—	4.4	1.5

Source: Adapted from ASME, ASME B31.1-2004, American National Standard, ASME Code for Pressure Piping, 2004.

The pressure drop in a section is given by

$$\Delta P_{Li} = \rho_i g h_i. \quad (8.15)$$

The additional pressure loss owing to the pipe fittings is accounted by calculating the equivalent pipe length for each fitting, L_f , as

$$L_f = K \frac{D_i}{2 C_f}. \quad (8.16)$$

The K factors for various fittings are given in Table 8.4. To calculate the total pressure drop, L_f is added to L_i before applying Equations 8.13 through 8.16.

The pressure drop through the solar field is calculated for the longest path traveled by the HTF. The HTF is circulated in a closed loop by using a variable speed pump (Turchi 2010). The pump power is the highest parasitic load in the solar plant and therefore a variable speed pump is used to reduce the power requirements when the solar field requires flow rates less than the nominal rate. The pumping power is calculated as

$$\dot{W}_{p,nom} = \rho_{HTF} T_{cold} g \Delta P_{total} \quad (8.17)$$

TABLE 8.4

K Values for Different Pipe Fittings Used in the Solar Field

Fitting	K
Gate valve	0.19
Globe valve	10.00
Check valve	2.50
Standard elbow	0.90
Medium elbow	0.75
Long elbow	0.60
Weldolet	1.80
Ball joint	4.73
Flexible hose	20.60

Source: Adapted from Kelly, B. and D. Kearney, Parabolic trough solar system piping model. Tech. Rep., National Renewable Laboratory, NREL/SR-550-40165, July, Golden, CO, 2006.

At different speeds, the pump law is used and the pump work is given by (Logan 1993)

$$\dot{W}_p = \dot{W}_{p,nom} \left(\frac{\dot{m}_{SF}}{\dot{m}_{SF,nom}} \right)^3, \quad (8.18)$$

where \dot{m}_{SF} is the actual HTF flow rate in the solar field and $\dot{m}_{SF,nom}$ is the nominal flow rate. Finally, the pumping power is calculated with the pump efficiency, which is affected by the flow rate through the pump.

$$\dot{W}_{p,actual} = \dot{W}_p / \eta_p. \quad (8.19)$$

All pipes are insulated and the heat losses from the pipes are calculated as explained in Chapter 4. During nights, the HTF flow is kept at approximately 20% of the nominal flow rate to keep the pipes and the solar collectors warm and avoid thermal shock. If the temperature of the HTF falls below the minimum allowable, auxiliary heaters heat the fluid.

8.3.3 Expansion Tank

An expansion tank is provided in the solar loop to account for expansion of the HTF as it heats up. It is normally installed at the highest point in the field close to the pump. The expansion tank is sized to be approximately 25% full at the cold conditions and approximately 75% full at normal operating conditions. The open space is filled with nitrogen at positive pressure to provide a nonreactive atmosphere and to keep the air and moisture from the atmosphere from entering the HTF loop.

8.3.4 Power Block

The power block commonly used in PTC-based CSP plants is a regenerative-reheat Rankine cycle as explained in Section 8.2.1 and Example 8.3. Figure 8.19 shows a schematic of a power block with a regenerative-reheat Rankine cycle configuration.

The HTF passes through three heat exchangers to heat the working fluid: preheater, boiler, and superheater. All of them are generally shell- and tube-type heat exchangers. The HTF flows through the tube side while the working fluid being heated flows through the shell side. The preheater heats the high-pressure working fluid to a saturated liquid condition, the boiler heats it to a saturated vapor condition while changing phase, and finally the superheater heats it to the high temperature of the cycle. The equations for sizing the heat exchangers and for calculating the exit temperatures of the two fluids based on the heat-exchanger effectiveness are given in Chapter 4.

There are normally two multistage turbines in the PTC power plants: high-pressure and low-pressure turbines. Reheat is normally applied between the high-pressure turbine and the low-pressure turbines. Closed feedwater heaters are used to heat the feedwater by extracting a small quantity of steam at various stages in the turbine. The closed feedwater heaters are shell- and tube-type heaters. Open feedwater heaters simply mix the extracted steam with the feedwater. The open feedwater heaters are also used as deaerators to remove any air and other dissolved gases from the working fluids.

8.3.5 Condenser

The condenser is a two-phase heat exchanger to condense the working fluid vapor from the turbine exhaust to saturated liquid. It is normally a shell- and tube-type heat exchanger where the cooling water flows through the tube while the steam flows through the shell side. The efficiency of the Rankine cycle depends on the condenser pressure, which should be designed to be as low as possible to obtain a condensing temperature that is as low as possible. Wet-bulb temperature of the ambient air is the minimum ambient temperature available to condense the working fluid. Normally, cooling towers are used to evaporate some of the cooling water to cool the water down to the wet-bulb temperature. However, this method uses a lot of water that cannot be recovered. Shortages of clean water around the globe require that the cooling water use be reduced to as small as possible. While fossil- or nuclear-based power plants can be located where the cooling water is available, solar power plants are often located in desert areas where cooling water may not be available.

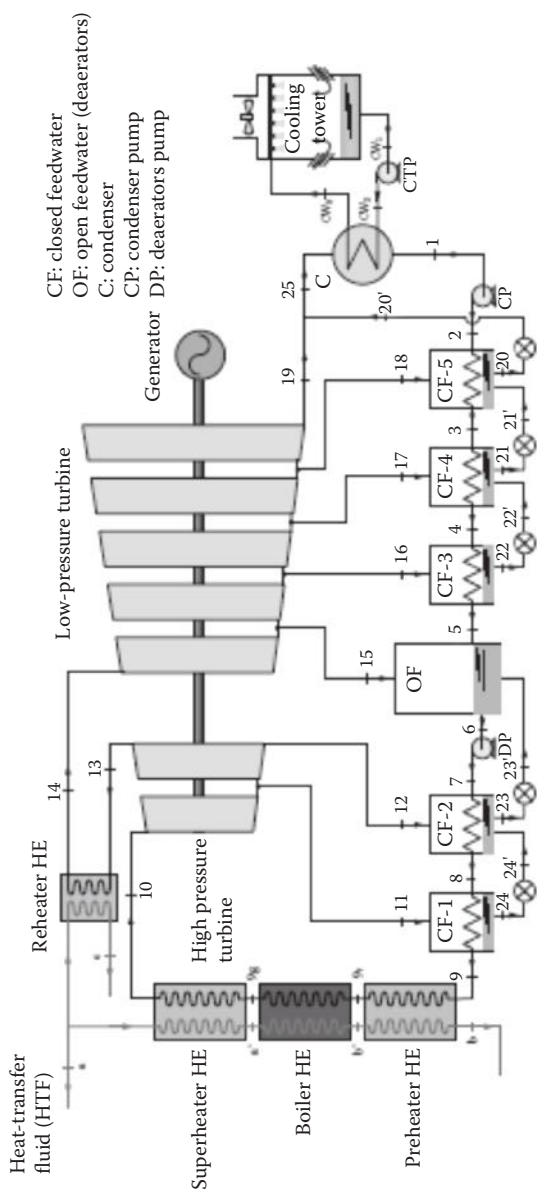


FIGURE 8.19
Schematic of a solar power block based on a regenerative-reheat Rankine cycle.

8.3.5.1 Air-Cooled Condensers

The air-cooled (also called dry-cooled) condensers become necessary for solar thermal power plants because of the scarcity of water where the solar radiation is the most attractive. There are many advantages of dry-cooled condensers:

- Reduced maintenance costs (no chemical additives or periodic cleaning required)
- Elimination of the cooling tower plume
- Reduction of condensation on the mirrors—no reduction in the optical efficiency of PTC
- Plant siting flexibility
- Emission of only warm and clean air reducing adverse environmental impact

On the other hand, the disadvantages of dry cooling are:

- Lower heat-transfer coefficients; therefore, larger heat exchanger area is needed.
- Greater fan power is required to achieve the same heat transfer.

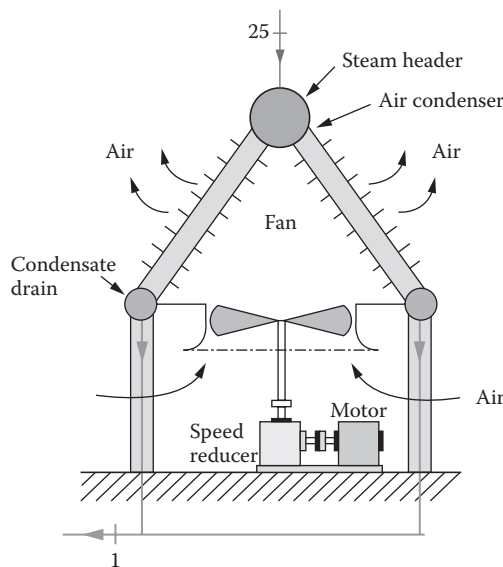


FIGURE 8.20

Configuration of an A frame air-cooled condenser. (Adapted from Kröger, D., *Air-Cooled Heat Exchangers and Cooling Towers: Thermal-Flow Performance Evaluation and Design*, Vol. 2. Pennwell Corp., Tulsa, OK, 2004.)

- Performance is strongly influenced by the ambient temperatures that change with the time of the day and the season.
- Lower power plant efficiency.

In dry-cooled condensers, the steam flows through finned coils over which the ambient air is blown. Figure 8.20 shows an A frame condenser in which the steam flows through the finned coils oriented at angles of 45°–60° to the horizontal. Figure 8.21 shows horizontal frame air-cooled condensers using forced flow and induced flow on the finned coil. Kröger (2004) gives detailed information about air-cooled condensers for power plants.

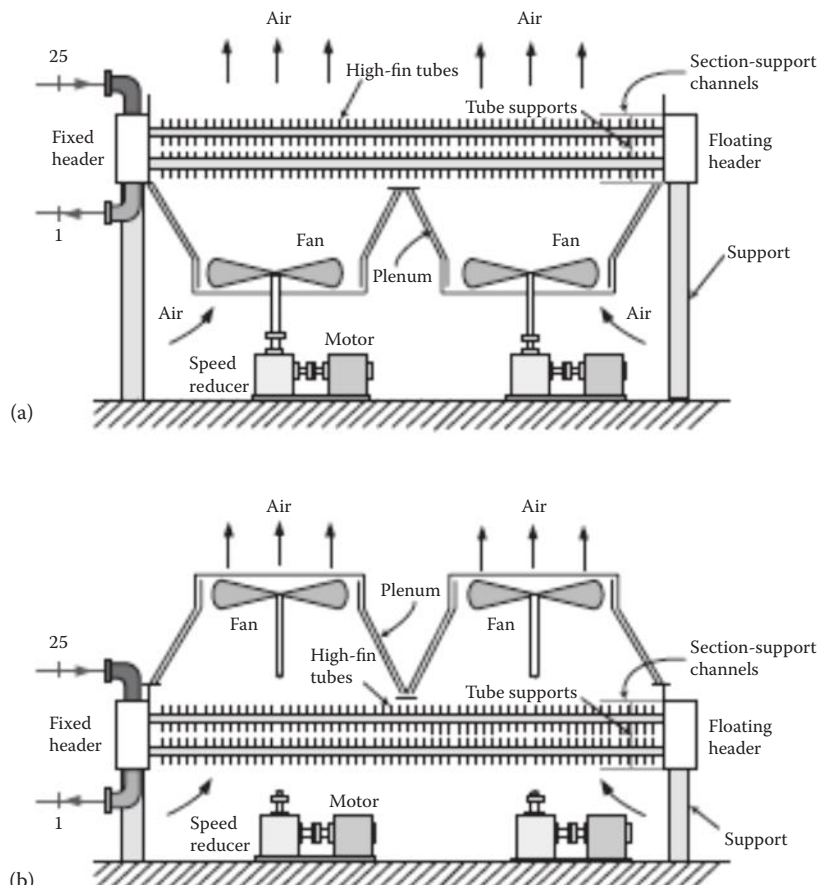


FIGURE 8.21

Configuration of horizontal frame air-cooled condenser: (a) forced flow; (b) induced flow. (Adapted from Serth, R.W., *Process Heat Transfer: Principles, Applications and Rules of Thumb*, Academic Press, 2007.)

8.4 Examples of PTC Solar Thermal Power Plants

There are successful examples of solar thermal power plants working on Rankine cycle and using parabolic troughs. An example of each type is given in the following.

Luz Corporation developed components and commercialized PTC-based solar thermal power by constructing a series of such power plants from 1984 to 1991. Starting with their first 14-MW_e Solar Electric Generating Station (SEGS I) in Southern California, they added a series of SEGS power plants with a total generating capacity of 354 MW_e. Figure 8.22 shows a schematic of the SEGS VIII and IX plants. Table 8.5 provides information about the solar field, power block, and other general information about SEGS I and SEGS IX plants. All of these plants use natural gas as the auxiliary fuel so that, on average, 75% of the energy is supplied from the sun and 25% is from natural gas. With power plant electrical conversion efficiencies of the order of 40% and solar field efficiencies of 40% to 50%, overall efficiencies for solar to electricity conversion of the order of 15% are being achieved in these plants. The cost of electricity from these plants has been decreased from approximately 30¢/kWh to less than 10¢/kWh. The SEGS plants have been operating successfully since 1990; however, the development of CSP plants stopped, mainly for policy reasons, until the construction and operation of the Nevada Solar One in 2007, a 64-MW nominal capacity PTC plant. Since then, a number of PTC power plants have been built or are under construction. Table 8.6 gives a list of the

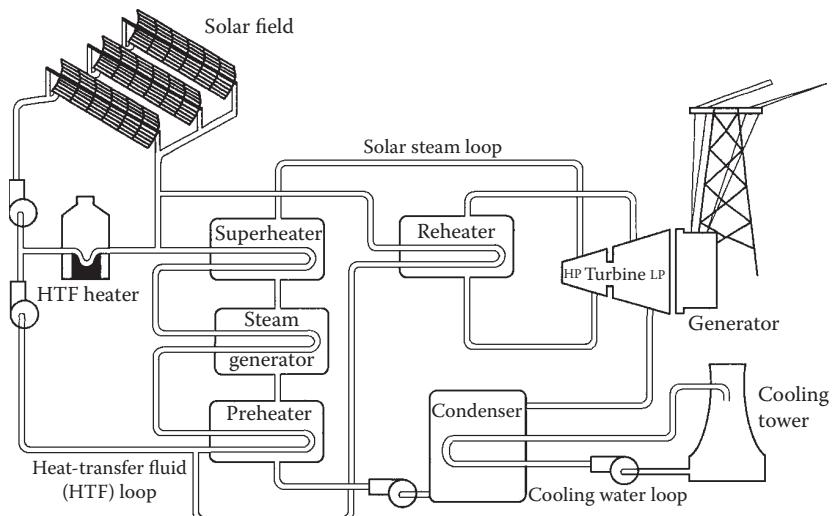


FIGURE 8.22

Flow of heat-transfer fluid through the SEGS VIII and IX plants. (Adapted from Fitzgerald, A.E. et al., *Electric Machinery*, 3rd ed., New York: McGraw-Hill, 1971.)

TABLE 8.5
Important Characteristics of SEGS I to SEGS IX Parabolic Trough Plants

	Units	I	II	III	IV	V	VI	VII	VIII	IX
<i>Power Block</i>										
Turbine-generator output	Gross MW _e	14.7	33	33	33	33	33	33	88	88
Output to utility	Net MW _e	13.8	30	30	30	30	30	30	80	80
<i>Turbine-Generator Set</i>										
Solar Steam Conditions										
Inlet pressure	Bar	35.3	27.2	43.5	43.5	43.5	100	100	100	100
Reheat pressure	Bar	0	0	0	0	0	17.2	17.2	17.2	17.2
Inlet temperature	°C	415	360	327	327	327	371	371	371	371
Reheat temperature	°C	na	na	na	na	na	371	371	371	371
Gas Mode Steam Conditions ^a										
Inlet pressure	Bar	0	105	105	105	105	100	100	100	100
Reheat pressure	Bar	0	0	0	0	0	17.2	17.2	17.2	17.2
Inlet temperature	°C	0	510	510	510	510	510	510	510	510
Reheat temperature	°C	na	na	na	na	na	371	371	371	371
<i>Electrical Conversion Efficiency</i>										
Solar mode ^b	%	31.5	29.4	30.6	30.6	30.6	37.5	37.5	37.6	37.6
Gas mode ^c	%	0	37.3	37.3	37.3	37.3	39.5	39.5	37.6	37.6
<i>Solar Field</i>										
Solar Collector Assemblies										
LS 1 (128 m ²)										

(Continued)

TABLE 8.5 (CONTINUED)
Important Characteristics of SEGS I to SEGS IX Parabolic Trough Plants

	Units	I	II	III	IV	V	VI	VII	VIII	IX
LS 2 (235 m ²)		560	536	0	0	0	0	0	0	0
LS 3 (545 m ²)		48	518	980	980	992	800	400	0	0
Number of mirror segments		0	0	0	0	32	0	184	852	888
Field aperture area	m ²	41,600	96,464	117,600	117,600	126,208	96,000	89,216	190,848	198,912
Field inlet temperature	°C	82,960	190,338	230,300	230,300	250,560	188,000	194,280	464,340	483,960
Field outlet temperature	°C	240	231	248	248	248	293	293	293	293
Annual thermal efficiency	%	307	321	349	349	349	390	390	390	390
Peak optical efficiency	%	35	43	43	43	43	42	43	53	50
System thermal losses	% of peak	71	71	73	73	73	76	76	80	80
		17	12	14	14	14	15	15	15	15
<i>Heat-Transfer Fluid</i>										
Type		Esso 500	VP-1							
Inventory	m ³	3213	416	403	403	461	416	416	1289	1289
Thermal storage capacity	MWh _t	110	0	0	0	0	0	0	0	0
<i>General</i>										
Annual power outlet	Net MWh/ year	30,100	80,500	91,311	91,311	99,182	90,850	92,646	252,842	256,125
Annual gas power use	10 ⁹ m ³ / year	4.76	9.46	9.63	9.63	10.53	8.1	8.1	24.8	25.2

^a Gas superheating contributes 18% of turbine inlet energy.

^b Generator gross electrical output divided by solar field thermal input.

^c Generator gross electrical output divided by thermal input from gas-fired boiler or HTF heater.

TABLE 8.6
PTC Solar Power Plants in Operation in 2012

Project Name	Country	Capacity (MW)	Power Block	HTF	Thermal Storage	Fossil Backup	Additional Description	Start Year
Andasol-1	Spain	50	STR	D/B/O	2-t-i-m, 7.5 h	HTF heater	η: 16%	2008
Andasol-2	Spain	50	STR	D/B/O	2-t-i-m, 7.5 h	HTF heater	η: 16%	2009
Andasol-3	Spain	50	STR	Thermal oil	2-t-i-m, 7.5 h	—	—	2011
Archimede	Italy	134.74	ISCC	Molten salt	2-t-d-m, 8 h	—	5 MW solar	2010
Arcosol-50	Spain	50	STR	D/B/O	2-t-i-m, 7.5 h	Natural gas	—	2011
Aste 1A	Spain	50	STR	Thermal oil	2-t-i-m, 8 h	HTF boiler	η: 15%	2012
Aste 1B	Spain	50	STR	Thermal oil	2-t-i-m, 8 h	HTF boiler	η: 15%	2012
Astexol II	Spain	50	STR	Thermal oil	2-t-i-m, 8 h	HTF boiler	η: 15%	2012
Cameo	United States	2 (solar)	STR	Food-grade mineral oil	None	—	Hybrid CSP/coal	2010
Extresol-1	Spain	50	STR	D/B/O	2-t-i-m, 7.5 h	HTF heater (12%)	η: 16%	2010
Extresol-2	Spain	50	STR	D/B/O	2-t-i-m, 7.5 h	HTF heater (12%)	η: 16%	2010
Helioenergy 1	Spain	50	STR	Thermal oil	None	HTF boiler	—	2011
Helioenergy 2	Spain	50	STR	Thermal oil	None	HTF boiler	—	2012
Helios I	Spain	50	STR	Thermal oil	None	—	—	2012
Holaniku	United States	2	STR	Xceltherm 600	2 h	—	η: 2%	2009
Ibersol Ciudad Real (Puertollano)	Spain	50	STR	D/B/O	—	HTF heater (gas fired)	—	2009
Hassi R'mel	Algeria	150	ISCC	Thermal oil	None	—	25 MW solar	2011
Kuraymat	Egypt	140	ISCC	Therminol VP-1	None	—	20 MW solar	2011
Morocco	Morocco	470	ISCC	Thermal oil	None	—	20 MW solar	2010

(Continued)

TABLE 8.6 (CONTINUED)
PTC Solar Power Plants in Operation in 2012

Project Name	Country	Capacity (MW)	Power Block	HTF	Thermal Storage	Fossil Backup	Additional Description	Start Year
La Dehesa	Spain	50	STR	D/DO	2-t-i-m, 7.5 h	HTF heater (12%)	η: 13.81%	2011
La Florida	Spain	50	STR	D/DO	2-t-i-m, 7.5 h	HTF heater (12%)	η: 13.81%	2010
Alvarado I	Spain	50	STR	D/BO	None	HTF heater (35 MWt)		2009
Lebrija 1	Spain	50	STR	VPI	None	HTF heater (12%)		2011
Majadas I	Spain	50	STR	D/BO	—	—		2010
Manchasol-1	Spain	50	STR	D/DO	2-t-i-m, 7.5 h	HTF heater (12%)	η: 16%	2011
Manchasol-2	Spain	50	STR	D/DO	2-t-i-m, 7.5 h	HTF heater (12%)	η: 16%	2011
Martin	United States	75	STR	Thermal oil	None	—		2010
Morón	Spain	50	STR	Thermal oil	None	HTF boiler		2012
Nevada Solar One	United States	75	STR	DOWTHERM A	0.5 h	—		2007
Palma del Río I	Spain	50	STR	D/BO	None	—		2011
Palma del Río II	Spain	50	STR	D/BO	None	—		2010
Saguaro	United States	1	ORC	Xceltherm 600	—	—	η: 7.5%-working fluid: <i>n</i> -pentane	2006
Solabén 3	Spain	50	STR	Thermal oil	None	HTF boiler		2012
Solacor 1	Spain	50	STR	Thermal oil	None	HTF boiler		2012
Solacor 2	Spain	50	STR	Thermal oil	None	HTF boiler		2012
SEGS I	United States	13.8	STR	Caloria	2-t-d-m, 3 h	None	Storage system was damaged by fire	1984

SEGS II	United States	30	STR	STR	None	Natural gas	Natural gas-fired superheater	1985
SEGS III	United States	30	STR	Thermolin	None	Natural gas	Natural gas-fired superheater	1985
SEGS IV	United States	30	STR	Thermolin	None	Natural gas	Natural gas-fired superheater	1989
SEGS V	United States	30	STR	Thermolin	None	Natural gas	Natural gas-fired superheater	1989
SEGS VI	United States	30	STR	Thermolin	None	Natural gas	Natural gas-fired superheater	1989
SEGS VII	United States	30	STR	Thermolin	None	Natural gas	Natural gas-fired superheater	1989
SEGS VIII	United States	80	STR	Thermolin	None	Natural gas	Natural gas-fired superheater	1989
SEGS IX	United States	80	STR	Thermolin	None	Natural gas	Natural gas-fired superheater	1990
Solnova 1	Spain	50	STR	Thermal oil	None	HTF boiler	HTF boiler	2009
Solnova 3	Spain	50	STR	Thermal oil	None	HTF boiler	HTF boiler	2009
Solnova 4	Spain	50	STR	Thermal oil	None	HTF boiler	HTF boiler	2009
Termesol 50	Spain	50	STR	D/DO	2-t-i-m, 7.5 h	Natural gas	Natural gas	2011
Thai Solar	Thailand	5	DSG	Water/steam	None	None	n: 12%	2012

Note: 2-t-d-m, 2 tank direct molten salt; 2-t-i-m, 2 tank indirect molten salt; DSG, direct steam generation; D/B O, diphenyl/biphenyl oxide; ISCC, integrated solar combined cycle; STR, steam Rankine cycle.

PTC-based CSP plants operating in the world and Table 8.7 gives a list of the PTC plants under construction. Table 8.8 shows the plants based on LFR.

The design of all CSP power plants is complex and is usually accomplished using computer modeling. Ho (2008) lists a number of computer programs available for the design of CSP plants, including TRNSYS, DELSOL,

TABLE 8.7

PTC Solar Power Plants under Construction

Project Name	Country	Capacity (MW)	Power Block	HTF	Thermal Storage	Fossil Backup Type	Start Year
Abengoa Mojave	United States	250	STR		None		2013
Agua Prieta II Arenales	Mexico Spain	478 50	ISCC STR	Thermal oil Thermal oil	None 2-t-i-m, 7 h	HTF heater	2013 2013
Borges Termosolar Casablanca	Spain	25 50	STR	Thermal oil	None	Biomass	2012
Enerstar (Villena)	Spain	50	STR	D/B O	2-t-i-m, 7.5 h	HTF heater (12%)	2013
Extresol-3 (EX-3)	Spain	50	STR	D/B O	2-t-i-m, 7.5 h	HTF heater (12%)	2012
Genesis Solar Energy Project	United States	250	STR	Theminol VP-1	None		2014
Godawari Solar Project	India	50	STR	Dowtherm	None		2013
Guzmán	Spain	50	STR	Thermal oil	None	HTF heater (12%)	2012
Helios II	Spain	50	STR	Thermal oil	None		2012
KaXu Solar one	South Africa	100	STR		2-t-i-m, 3 h		2014
La Africana	Spain	50	STR		2-t-i-m, 7.5 h		2012
NextEra Beacon	United States	250	STR		None		2014
Olivenza 1	Spain	50	STR	Thermal oil	None	HTF boiler	2012
Orellana	Spain	50	STR	Thermal oil	None		2012
Palen Solar Power Project	United States	500	STR		None		2014
Palmdale Hybrid Power Plant	United States	50	STR				2013

TABLE 8.8

Operational Fresnel Reflectors Power Plants

Project Name	Country	Capacity (MW)	Power Block	HTF	Thermal Storage	Start Year
Augustin Fresnel 1	France	0.25	STR	Water	Ruths tank, 0.25 h	2012
Kimberlina	United States	5	STR	Water	None	2008
Puerto Errado 1 (PE1)	Spain	1.4	STR	Water	Ruths tank, single-tank thermocline	2009
Puerto Errado 2 (PE2)	Spain	30	STR	Water	Ruths tank, single-tank thermocline, 0.5 h	2012

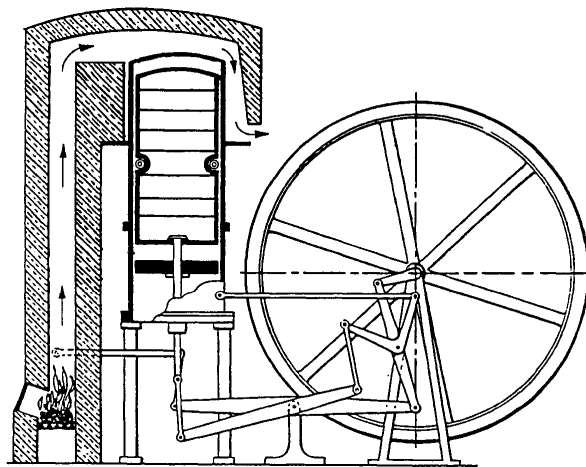
SAM, IPSEpro, DELSOL, GATECYCLE, SOLERGY, and HELIOS. Systems Advisor Model (SAM) was developed by NREL under contract with the US Department of Energy and is available for free.

8.5 Parabolic Dish Systems

Parabolic dishes, as explained in Chapter 3, can achieve very high concentration ratios and temperatures as high as 700°C. Therefore, CSP plants based on parabolic dishes can achieve very high thermodynamic efficiencies. One of the advantages of dish-based power plants is that they can be modular; that is, one dish could produce from approximately 10 kW_e to approximately 100 kW_e, which could be combined to give higher output. The Rankine cycle and the Stirling cycle are appropriate for dish systems. Since a Stirling cycle is one of the most efficient thermodynamic cycles, integration of the Stirling engine with a dish can be a very efficient solar power system. Even though a dish type of system has all of these advantages, somehow, these systems have not found commercial success. However, it is a matter of time before these systems will find commercial success. The dish systems, especially with a Stirling cycle, are described in detail in this chapter.

8.6 Stirling Cycle

The Stirling cycle has become very important in recent years because of its potential to operate at very high efficiency. In fact, theoretically, its efficiency is the same as the Carnot efficiency. It was proposed by Rev. Robert Stirling, a

**FIGURE 8.23**

The original patented Stirling engine of Rev. Robert Stirling.

Scottish minister, as a solar alternative to a steam engine (Figure 8.23). In the 1930s, Phillips Research Laboratory in Eindhoven, The Netherlands, developed the technology to commercialize it. More recently, interest in Stirling engines has increased with increased interest in solar and biomass energy sources (Stine and Diver 1994). The first solar application of a Stirling engine was conducted by John Ericsson, a Swedish engineer who spent a long and productive career in the United States. A Stirling cycle engine can use air as the working fluid; therefore, it is also called a hot air engine. Since it is an external combustion engine, it can use any fuel or concentrated sunlight. High-performance Stirling engines operate at very high temperatures, typically 600°C to 800°C, resulting in conversion efficiencies of 30% to 40% (Stine 2004). Stirling engines are being developed in small power capacities, typically 10 to 100 kW.

8.6.1 Thermodynamics of Stirling Cycle

Figure 8.24 shows thermodynamic diagrams of an ideal Stirling cycle. A gas is used as the working fluid. The cycle consists of two isothermal and two constant volume processes. The working gas is compressed isothermally (constant temperature) from state 1 to state 2. This process is accomplished by heat rejection at the low temperature of the cycle, T_L . It is then heated at constant volume to state 3. The gas is then expanded isothermally from 3 to 4. This process is accompanied by heat addition at the high temperature in the cycle, T_H . Finally, the gas is cooled at constant volume from temperature T_H to T_L (process 4–1). The hatched area under process 2–3 represents the heat addition to the working gas while raising its temperature from T_L to T_H .

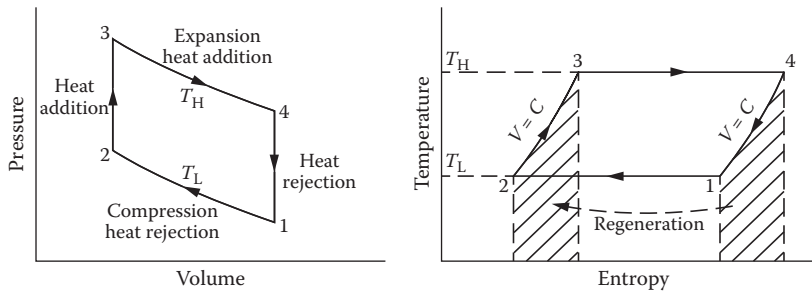


FIGURE 8.24
Thermodynamic diagrams of an ideal Stirling engine.

and the hatched area under process 4–1 represents heat rejection while the gas goes from T_H to T_L . The heat addition from 2 to 3 is equal to the heat rejection from 4 to 1, and they are between the same temperature limits:

$$Q_{2-3} = mC_v(T_H - T_L) \quad (8.20)$$

and

$$Q_{4-1} = mC_v(T_H - T_L). \quad (8.21)$$

Ideally, if the heat rejected in process 4–1 could be stored and transferred to the gas later in process 2–3 (perfect regeneration), the only external heat addition in the cycle would be in process 3–4:

$$Q_{3-4} = -W_{3-4} = \int_3^4 p dV = mRT_H \ln \frac{V_4}{V_3}. \quad (8.22)$$

The work input for compression from 1–2 is

$$\begin{aligned} W_{1-2} &= -\int_1^2 p dV = mRT_L \ln \frac{V_1}{V_2} \\ &= -mRT_L \ln \frac{V_2}{V_1} \end{aligned} \quad (8.23)$$

since

$$\frac{V_2}{V_1} = \frac{V_3}{V_4}.$$

The net work output is

$$mR \ln \frac{V_3}{V_4} (T_H - T_L). \quad (8.24)$$

Therefore, the cycle efficiency

$$\eta = \frac{\text{Net work out}}{\text{Heat input}} = \frac{T_H - T_L}{T_H}. \quad (8.25)$$

This efficiency, which is equal to the Carnot cycle efficiency, is based on the assumption that regeneration is perfect, which is not possible in practice. Therefore, the cycle efficiency would be lower than that indicated by the above equation. For a regeneration effectiveness e as defined below, the efficiency is given by (Stine and Harrigan 1985)

$$\eta = \frac{T_H - T_L}{T_H + [(1-e)/(k-1)][(T_H - T_L)/\ln(V_1/V_2)]}, \quad (8.26)$$

where $e = \frac{T_R - T_L}{T_H - T_L}$, T_R is the regenerator temperature, and $k = C_p/C_v$ for the gas.

For perfect regeneration ($e = 1$), the above expression reduces to the Carnot efficiency. It is also seen from the above equation that regeneration is not necessary for the cycle to work, because even for $e = 0$, the cycle efficiency is not zero.

Example 8.4

A Stirling engine with air as the working fluid operates at a source temperature of 400°C and a sink temperature of 80°C. The compression ratio is 5.

Assuming perfect regeneration, determine the following:

1. Expansion work
2. Heat input
3. Compression work
4. Efficiency of the machine

If the regenerator temperature is 230°C, determine the following:

5. Regenerator effectiveness
6. Efficiency of the machine
7. If the regeneration effectiveness is zero, what is the efficiency of the machine?

Solution

1. Expansion work per unit mass of the working fluid. Assuming air as an ideal gas,

$$w_{34} = - \int_3^4 P dv = RT_H \ln \frac{v_4}{v_3} = (0.287)(400 + 273) \ln 5 = -310.9 \text{ kJ/kg.}$$

The minus sign shows work output.

2. Heat input per unit mass of the working fluid:

$$q_{34} = w_{34} = 310.9 \text{ kJ/kg.}$$

3. Compression work per unit mass of the working fluid:

$$w_{12} = - \int_1^2 P dv = RT_L \ln \frac{v_2}{v_1} = -(0.287)(80 + 273) \ln \frac{1}{5} = 163.1 \text{ kJ/kg.}$$

4. Efficiency of the machine:

$$\eta = \frac{T_H - T_L}{T_H} = \frac{400 - 80}{(400 + 273)} = 0.475 = 47.5\%.$$

5. Regenerator effectiveness:

$$e = \frac{T_R - T_L}{T_H - T_L} = \frac{230 - 80}{400 - 80} = 0.469.$$

6. Efficiency of the machine:

$$\eta = \frac{T_H - T_L}{T_H + \frac{(1-e)(T_H - T_L)}{(k-1)\ln(v_1/v_2)}} = \frac{400 - 800}{(400 + 273) + \frac{(1-0)}{(1.4 - 1)} \frac{(400 - 80)}{\ln(5)}} = 0.341,$$

$$\eta = 34.1\%.$$

7. If the regeneration effectiveness is zero, the efficiency of the machine:

$$\eta = \frac{T_H - T_L}{T_H + \frac{(1-e)(T_H - T_L)}{(k-1)\ln(v_1/v_2)}} = \frac{400 - 800}{(400 + 273) + \frac{(1-0)}{(1.4 - 1)} \frac{(400 - 80)}{\ln(5)}} = 0.273,$$

$$\eta = 27.3\%.$$

In order to understand how the Stirling cycle shown in Figure 8.24 may be achieved, in practice, the simple arrangement and sequence of processes shown in Figure 8.25 is helpful. In the proposed arrangement, two cylinders with pistons are connected via a porous medium, which allows gas to pass through from one cylinder to the other. As the gas passes through the porous medium, it exchanges heat with the medium. The porous medium, therefore, serves as the regenerator. In practice, this arrangement can be realized in three ways as shown in Figure 8.26 (alpha, beta, and gamma types).

The choice of a working fluid for Stirling engine depends mainly on the thermal conductivity of the gas in order to achieve high heat-transfer rates. Air has traditionally been used as the working fluid. Since hydrogen has 40% higher thermal conductivity at 500°C, it is preferable over

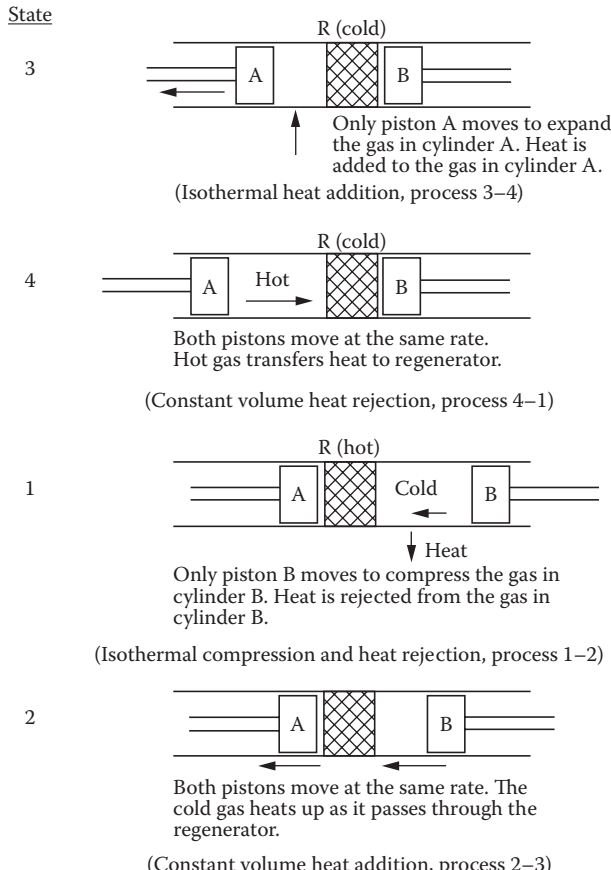
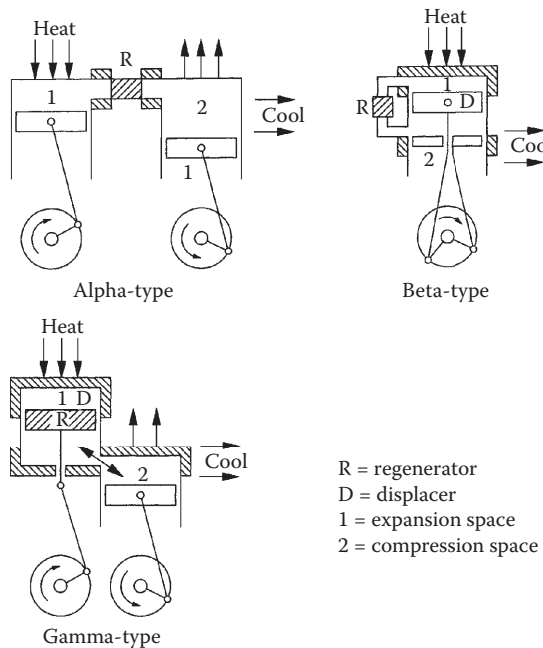


FIGURE 8.25

Stirling cycle states and processes with reference to Figure 8.24.

**FIGURE 8.26**

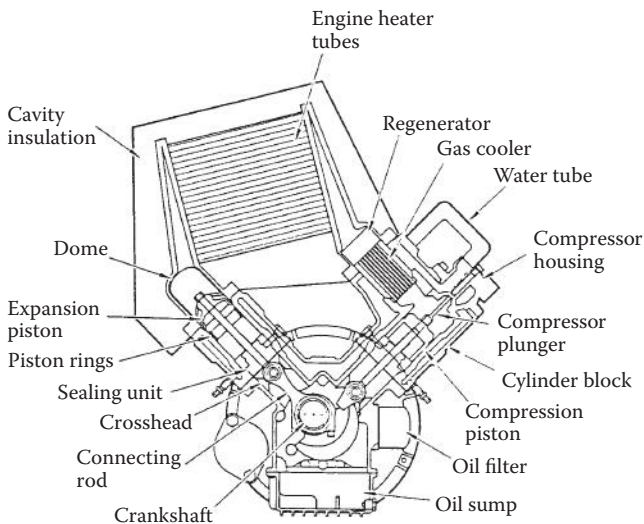
Three basic types of Stirling engine arrangements.

air. Helium has a higher ratio of specific heats (k), which lessens the impact of imperfect regeneration.

In the alpha configuration, there are two cylinders and pistons on either side of a regenerator. Heat is supplied to one cylinder and cooling is provided to the other. The pistons move at the same speed to provide constant volume processes. When all the gas has moved to one cylinder, the piston of that cylinder moves with the other remaining fixed to provide expansion or compression. Compression is done in the cold cylinder and expansion is done in the hot cylinder. The Stirling Power Systems V-160 engine (Figure 8.27) is based on an alpha configuration.

The beta configuration has a power piston and a displacer piston that divides the cylinder into hot and cold sections. The power piston is located on the cold side and compresses the gas when the gas is in the cold side and expands it when it is in the hot side. The original patent of Robert Stirling was based on beta configuration, as are free-piston engines.

The gamma configuration also uses a displacer and a power piston. In this case, the displacer is also the regenerator, which moves gas between the hot and cold ends. In this configuration, the power piston is in a separate cylinder.

**FIGURE 8.27**

Stirling Power Systems/Solo Kleinmotoren V-160 alpha-configuration Stirling engine. (Adapted from Stine, W.B., Stirling engines. In *The CRC Handbook of Mechanical Engineering*, D.Y. Goswami, ed., Boca Raton, FL: CRC Press, 2004.)

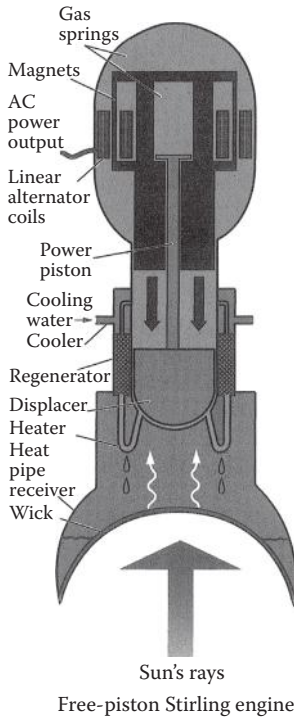
8.6.2 Piston/Displacer Drives

The power and displacer pistons are designed to move according to a simple harmonic motion to approximate the Stirling cycle. This is done by a crankshaft or a bouncing spring/mass second-order mechanical system (Stine 2004).

8.6.3 Kinematic or Free-Piston Engines

Stirling engines are designed as kinematic or free piston depending on how power is removed. In a kinematic engine, the power piston is connected to the output shaft by a connecting rod/crankshaft arrangement.

Free-piston arrangement is an innovative way to realize the Stirling cycle. In this arrangement, the power piston is not connected physically to an output shaft. The piston bounces between the working gas space and a spring (usually a gas spring). The displacer is also usually free to bounce. This configuration is called the Beale free-piston Stirling engine after its inventor, William Beale (Stine 2004). Since a free-piston Stirling engine has only two moving parts, it offers the potential of simplicity, low cost, and reliability. Moreover, if the power piston is made magnetic, it can generate current in the stationary conducting coil around the engine as it moves. This is the principle of the free-piston/linear alternator in which the output from the engine is electricity. Figure 8.28 shows a schematic of a free-piston Stirling engine with a linear alternator.

**FIGURE 8.28**

Basic components of a Beale free-piston Stirling converter incorporating a sodium heat pipe receiver for heating with concentrated solar energy.

8.6.4 Examples of Solar Stirling Power Systems

Stirling engines can provide very high efficiencies with high-concentration solar collectors. Since practical considerations limit the Stirling engines to small sizes (5 to 100 kW), a Stirling engine fixed at the focal point of a parabolic dish provides an optimum match. Therefore, all of the commercial developments to date have been in parabolic dish–Stirling engine combination. The differences in the commercial systems have been in the construction of the dish and the type of Stirling engine.

Advanco Corporation developed and tested a 25-kW_e dish Stirling system (called Vanguard I) in Rancho Mirage, California, in 1984 and achieved net conversion efficiency of approximately 30% (Gupta 1985). The system consisted of an 11-m-diameter parabolic dish with a concentration ratio of 2100 and a United Stirling Mark II engine operating at 800°C. Despite the technical success, the effort had to be abandoned by Advanco because of an exclusive agreement between McDonnell Douglas Corporation and United Stirling AB of Sweden.

McDonnell Douglas and United Stirling jointly developed a 25-kW_e dish Stirling system and tested it in California. The concentrator was

made from glass mirror facets on a structure to approximate a parabolic dish. Figure 8.29 shows a picture of the system. Tests showed the system efficiency to be in the same range as the Vanguard I system. McDonnell Douglas built six prototypes but decided to abandon the commercialization efforts.

In the 1990s, Cummins Power Generation and Stirling Technology Company developed a 25-kW_e free-piston, linear alternator engine. Cummins Power also developed a 5-kW_e dish Stirling power system for remote power applications with a view to mass produce the system (see Figure 8.30). The company, however, abandoned the effort in 1996.

Schlach Bergermann and Partner also developed a 7.7-kW_e dish Stirling power system using a V-160 two-cylinder Stirling engine developed by Stirling Power Systems and a stretched-membrane dish. Stirling engine development in Japan includes a 3-kW_e engine developed by Toshiba Corp. for residential heat pump applications and a 2.4-kW_e engine developed for space testing by Aisin Seiki Company (Kagawa et al. 1989; Proctor and Morse 1975).

Stirling Engine Systems, Inc. developed a Dish Stirling System and planned to build large-scale power plants with their 25-kW dishes (Figure 8.31). However, the company filed for bankruptcy in 2011. Its technology and

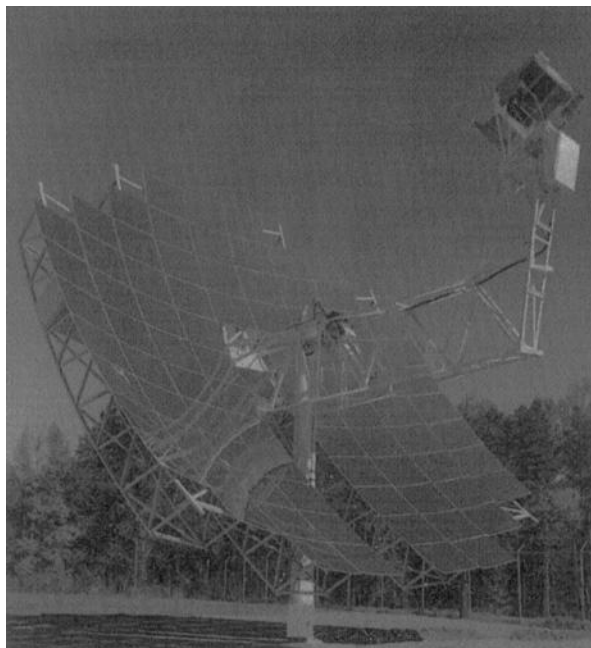


FIGURE 8.29

The McDonnell Douglas/United Stirling dish-Stirling 25 kW_e module.

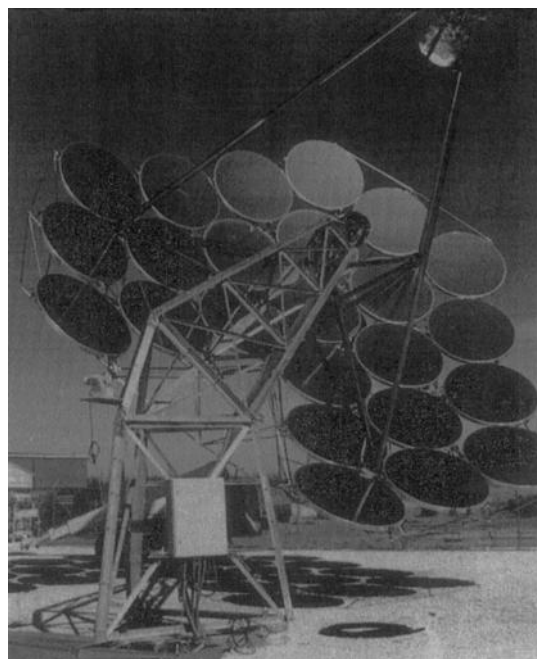


FIGURE 8.30

The Cummins Power Generation dish-Stirling engine power system.



FIGURE 8.31

A 25-kW_e dish Stirling system by Stirling Energy Systems, Inc., USA.

planned projects were bought by a British company, United Sun Systems International, headquartered in Gothenburg, Sweden, which plans to build large-scale plants in China in collaboration with its Chinese partners.

8.7 Central Receiver Tower Systems

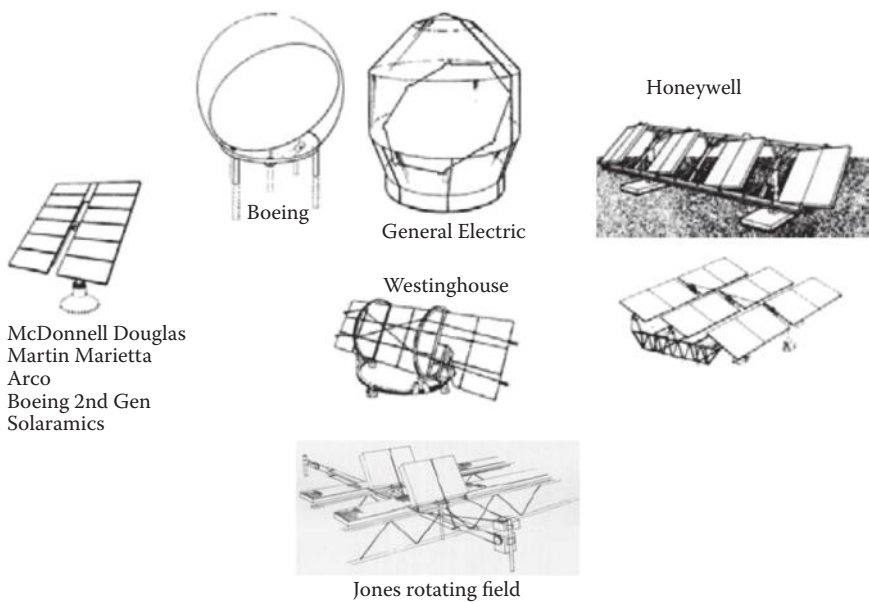
A central receiver collector consists of a large field of mirrors on the ground that track the sun in such a way that the reflected radiation is concentrated on a receiver/absorber on top of a tower. The mirrors are called *heliostats*. Central receivers can achieve temperatures of the order of 1000°C. Therefore, a central receiver concentrator is suitable for thermal electric power production in the range of 1–1000 MW. The concept of a central receiver solar thermal power, also known as *power tower*, has been known for a long time. Francia (1968) built a pilot model of a solar power tower plant in 1967 at the University of Genoa, Italy. Since the early 1970s, when the power tower concept was first proposed by Hildebrandt and Vant-Hull (1974), the central receiver technology has been actively developed in the United States. Since then, the technology has been pursued in Germany, Spain, Switzerland, France, Russia, Italy, and Japan (DeLaquil et al. 1993) and more recently in South Africa, India, and China.

A central receiver collector consists of a heliostat field, a receiver/absorber, and the tracking controls for the heliostats. Sections 8.7.1 and 8.7.2 briefly describe the heliostats and the receiver.

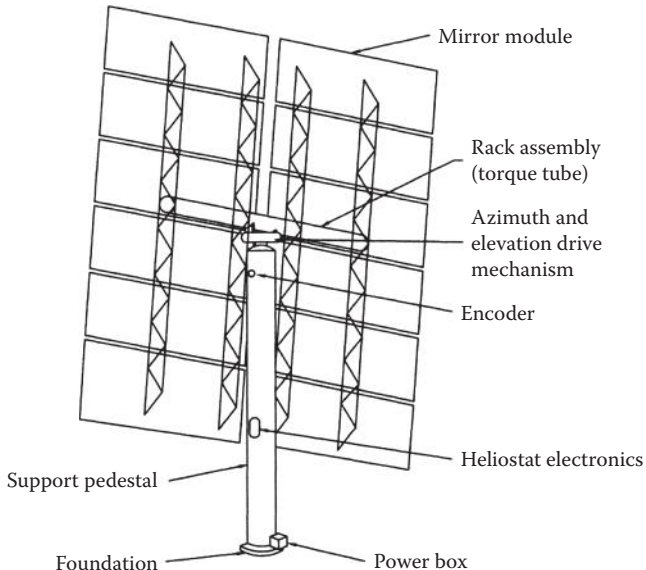
8.7.1 Heliostats

Developing cost-effective and optically efficient heliostats in the United States was initiated in the late 1970s. A number of designs were examined to be used in Solar One, the first 10-MW solar power tower plant in the Mojave Desert, which are shown in Figure 8.32. Five different concepts including seven different designs are shown in the figure: (1) pedestal mounted (left), (2) bubble-enclosed membrane (top), (3) ganged (right), (4) carousel (center), and (5) rotating field (bottom). Ultimately, the pedestal-mounted concept was found as the most cost-effective option and was selected for the Solar One plant in 1982 (Kolb et al. 2007).

Figure 8.33 shows the back side of a heliostat used at the Solar One plant. It consists of several mirror panels supported on a steel structure so that it forms a slightly concave mirror surface. The heliostat focal length is approximately equal to the distance of the heliostat from the receiver. Recent research and development of heliostats has been concentrated on using stretched-membrane reflectors in order to reduce the cost. A stretched-membrane heliostat consists of two polymer membranes stretched over a metal ring support

**FIGURE 8.32**

Heliostat designs developed in the United States between 1975 and 1982. (From Kolb, G.J. et al., Heliostat cost reduction study, Sandia Report, SAND2007-3293, June, Sandia National Lab., Albuquerque, NM, 2007.)

**FIGURE 8.33**

A heliostat consisting of glass mirrors supported on a structure (back view).

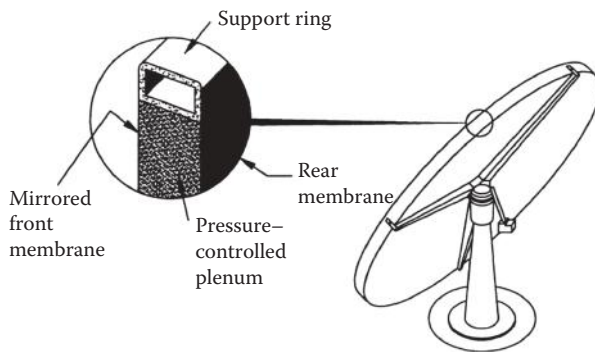


FIGURE 8.34

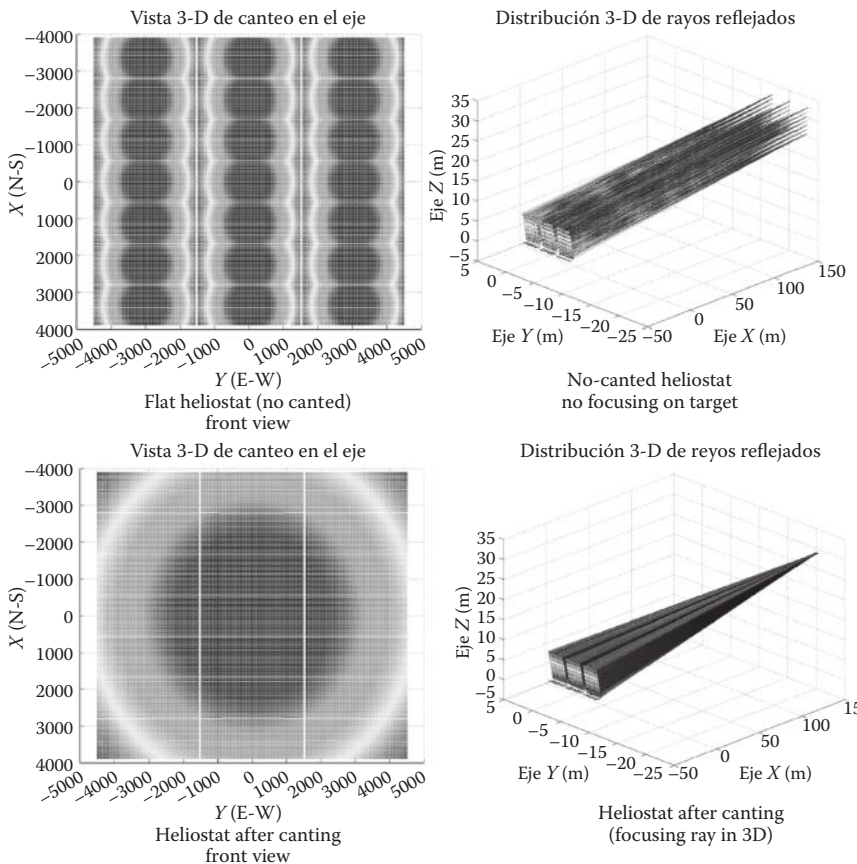
Stretched-membrane heliostat consists of two membranes, a mirror front one and supporting rear one, which are stretched across a support structure. Curvature of the heliostat is adjusted by changing the vacuum pressure of the space between the membranes. (Adapted from Colorado State University and Westinghouse Electric Corporation, *Solar Thermal Electric Power Systems*, 1974.)

structure. The front polymer is laminated with a silvered polymer reflector. The space between the two membranes is evacuated. The vacuum pressure is adjusted to achieve the desired focal length. Figure 8.34 shows a stretched-membrane heliostat developed by Science Applications International Corp. These heliostats have the potential to reduce the cost of the central receiver systems; however, the problems include uncertainties regarding their durability and lifetimes.

Another option for cost reduction is increasing the size of the heliostats. Therefore, the overall number of the required heliostats for power plant decreases, which consequently reduces other costs associated with each heliostat such as the drives. On the other hand, the performance of the heliostat might be affected by increasing the size. For example, mirror imperfections have higher impact on the reflected image when the heliostat is large. Moreover, the wind load is higher at a larger heliostat because of the larger surface area. A report by Sandia National Laboratory has predicted that the low-cost heliostats are most likely to be more than 150 m^2 (Kolb et al. 2007).

As can be seen from Figure 8.33, each heliostat consists of a number of mirrors (facets) that are mounted on a supporting structure. Mirror alignment or canting of the heliostats considerably influences the performance of the heliostat field. All the mirror modules of a heliostat have to be arranged in a specific orientation to achieve highly concentrated solar flux on the receiver surface. The effect of canting the facets is clearly shown in Figure 8.35.

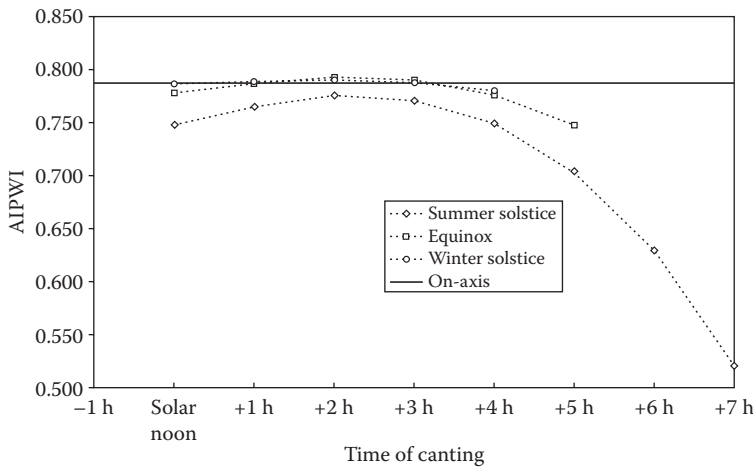
There are different on-axis and off-axis canting methods, which are extensively described in the literature (Buck and Teufel 2009; Jones 1996; Sproul et al. 2011; Landman and Gauché 2013). On-axis canting refers to the alignment adjustment when the heliostat center, target, and the sun all fall along a line. In this case, the facets are aligned to reflect the sun rays that are parallel to

**FIGURE 8.35**

Effect of canting facets in a glass metal heliostat. (From Jones, S.A., A comparison of on-axis and off-axis heliostat alignment strategies, Report SAND96-0566C, Sandia National Lab., Albuquerque, NM, 1996.)

the surface normal of the heliostat. On the other hand, in off-axis canting, the facets are aligned for a specific time in a specific day of the year. Therefore, both methods provide optimal performance only for specific times of the year. At other times of the year, the performance of the heliostat field is less than optimal.

Figure 8.36 compares the on-axis canting with off-axis canting for three different days of the year for a group of heliostats located at a certain location of the field. AIPWI represents the annual incident power weighted intercept, which is the fraction of the annual beam power reflected by the heliostats that is intercepted by the receiver surface (Jones 1996). As can be seen, on-axis canting leads to a uniform high-performance field. Although the off-axis canting performance could theoretically exceed that of on-axis, it

**FIGURE 8.36**

Effect of different canting methods on the annual performance of the heliostats. (From Jones, S.A., A comparison of on-axis and off-axis heliostat alignment strategies. Report SAND96-0566C. Sandia National Lab., Albuquerque, NM, 1996.)

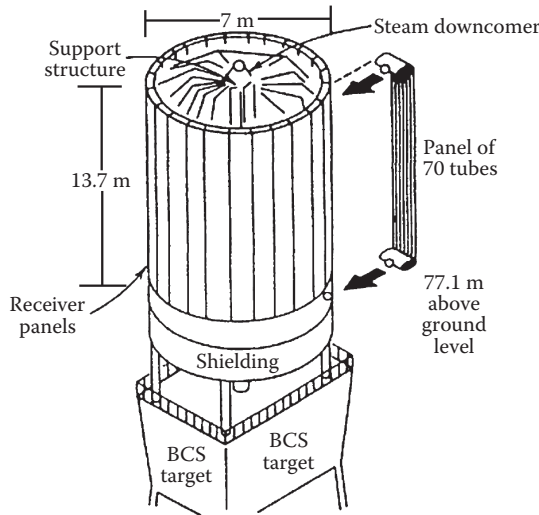
is very dependent on the time of day and varies at different seasons. It must be pointed out that the results in Figure 8.36 are based on a specific location on the field. Hence, one cannot conclude from this figure that performance on winter solstice is the best for all locations on the field. There is no single optimal approach for canting the heliostats and one needs to do a detailed performance analysis and consider the budget before selecting the canting method.

8.7.2 Receiver

Receivers are designed to accept and absorb very high solar flux and to transfer the heat to a fluid at a very high temperature. The HTF may be indirectly or directly irradiated depending on whether it is flowing through tubes irradiated by concentrated radiation or being directly exposed to solar radiation. External and cavity receivers are two types of indirectly irradiated receivers. Volumetric receivers are directly irradiated receivers.

8.7.2.1 External Receiver

External receivers consist of several panels of vertical tubes connected at the top and the bottom by the welded headers. The tubes are generally made of a stainless steel alloy. The panels are connected with each other to approximate a vertical cylinder. The number of tubes per panel, the number of panels, length of the tube, tube diameter, and receiver diameter are important

**FIGURE 8.37**

The receiver of the Solar One central receiver facility at Barstow, California. This is an external-type receiver.

parameters that need to be carefully determined. The Solar One central receiver facility used this type of receiver absorber as shown in Figure 8.37. It consists of 24 panels, each containing 70 tubes of 12.7 mm diameter. The tubes were made of Incoloy 800 and coated with high-absorptance black paint. The overall dimensions of the receiver were 7 m diameter and 13.7 m height.

The main drawback of external receivers is the heat loss from the high-temperature surface of the panels, which are exposed to the environment. Therefore, it is necessary to keep the area of the receiver as small as possible. On the other hand, the cylindrical shape of the receiver accommodates a heliostat field with 360° azimuth angle.

Heat loss from an external receiver can be approximated by

$$Q_{\text{loss}} = Q_{\text{loss rad}} + Q_{\text{loss conv}} + Q_{\text{loss ref}} \quad (8.27)$$

where $Q_{\text{loss rad}}$, $Q_{\text{loss conv}}$, and $Q_{\text{loss ref}}$ are losses due to radiation, convection, and reflection, respectively. The radiation loss can be calculated as

$$Q_{\text{loss rad}} = \varepsilon \sigma A (T_{\text{wall}}^4 - T_{\infty}^4), \quad (8.28)$$

where ε is the emissivity of the receiver surface, σ is the Stefan–Boltzmann constant, A is the receiver surface area, T_{wall} is the receiver surface temperature, and T_{∞} is the ambient temperature. The convective heat loss is the

combined loss by natural convection based on the temperature difference between the receiver surface and the ambient air, and forced convection due to wind at the receiver level. It can be found using a combined convective heat-transfer coefficient h_{mix} by

$$Q_{\text{loss conv}} = h_{\text{mix}} A (T_{\text{wall}} - T_{\infty}), \quad (8.29)$$

where h_{mix} can be estimated from (Siebers and Kraabel 1984)

$$h_{\text{mix}} = \left(h_{\text{forced}}^{3.2} + h_{\text{natural}}^{3.2} \right)^{\frac{1}{3.2}}. \quad (8.30)$$

The Nusselt numbers for natural and forced convection for smooth surfaces are given as

$$Nu_{\text{natural}} = \frac{h_{\text{natural}} H}{k} = 0.098 \text{ Gr}_H^{\frac{1}{3}} \left(\frac{T_{\text{wall}}}{T_{\infty}} \right)^{-0.14} \quad (8.31)$$

$$Nu_{\text{forced}} = \frac{h_{\text{forced}} D}{k} = 0.00239 \text{ Re}^{0.98} + 0.000945 \text{ Re}^{0.89}, \quad (8.32)$$

where H is the receiver height, D is the receiver diameter, and k is the thermal conductivity. Re and Gr are Reynolds and Grashof numbers respectively, which are given as

$$Re = \frac{VD}{\nu} \quad (8.33)$$

$$Gr = \frac{g\beta(T_{\text{wall}} - T_{\infty})H^3}{\nu^2}, \quad (8.34)$$

where ν is the kinematic viscosity and β is the bulk expansion coefficient, which can be approximated as $1/T$. The fluid properties are calculated at the film temperature, which is the average of the ambient and receiver surface temperatures. The correlation for the forced convection is valid for Reynolds numbers between 3.7×10^4 and 10^7 . The heat-transfer coefficients obtained from the above equations can be modified to account for the effect of surface roughness by multiplying by a $\frac{\pi}{2}$ factor.

Example 8.5

The following information is given for an external receiver. Determine the total heat loss and the receiver efficiency if the conduction heat loss is negligible.

- Receiver diameter (D) = 7 m
- Receiver height (H) = 13.7 m
- Ambient temperature (T_{∞}) = 20°C
- Receiver average surface temperature (T_{wall}) = 480°C
- Mean flux density at the receiver surface (q) = 200 $\frac{\text{kW}}{\text{m}^2}$
- Receiver surface absorptivity (α) = 0.95
- Mean wind velocity (V) = 8 m/s
- Thermal conductivity at 250°C = $42.17 \times 10^{-3} \frac{\text{W}}{\text{mK}}$
- Kinematic viscosity of air at 250°C = $41.90 \times 10^{-6} \frac{\text{m}^2}{\text{s}}$

Solution

$$\text{Receiver area } A = \pi \times 7 \times 13.7 = 301.28 \text{ m}^2$$

$$Q_{\text{in}} = q \times A = 200 \times 301.28 = 60.26 \text{ MW.}$$

$$Q_{\text{loss rad}} = \epsilon \sigma A (T_{\text{wall}}^4 - T_{\infty}^4) = 0.95 \times 5.67 \times 10^{-8} \times 301.28 \times (753^4 - 293^4) = 5.10 \text{ MW}$$

$$\text{Reflectivity } (\rho) = 1 - \alpha = 0.05.$$

$$Q_{\text{loss ref}} = \rho \times Q_{\text{in}} = 3.01 \text{ MW.}$$

$$T_f = \frac{T_{\text{wall}} + T_{\infty}}{2} = 523 \text{ K.}$$

At this temperature, the bulk expansion coefficient of air is equal to

$$\beta = \frac{1}{523} = 0.0019 \frac{1}{K}.$$

The dimensionless numbers are calculated as

$$\text{Re} = \frac{VD}{\nu} = \frac{8 \times 7}{41.90 \times 10^{-6}} = 1.336 \times 10^6,$$

$$\text{Gr} = \frac{g\beta(T_{\text{wall}} - T_{\infty})H^3}{v^2} = \frac{9.81 \times 0.0019 \times (480 - 20) \times 13.7^3}{(41.90 \times 10^{-6})^2} = 1.256 \times 10^{13}.$$

$$\begin{aligned} h_{\text{natural}} &= 0.098 \times \frac{k}{H} \times \text{Gr}_H^{\frac{1}{3}} \left(\frac{T_{\text{wall}}}{T_{\infty}} \right)^{-0.14} h_{\text{natural}} \\ &= 0.098 \times \frac{42.17 \times 10^{-3}}{13.7} \times (1.256 \times 10^{13})^{\frac{1}{3}} \times (2.57)^{-0.14} = 6.144 \frac{\text{W}}{\text{m}^2 \cdot \text{K}} \\ h_{\text{natural rough}} &= \frac{\pi}{2} h_{\text{natural}} = 9.651 \frac{\text{W}}{\text{m}^2 \cdot \text{K}}. \end{aligned}$$

$$\begin{aligned} h_{\text{forced}} &= \frac{k}{D} (0.00239 \text{ Re}^{0.98} + 0.000945 \text{ Re}^{0.89}) = \frac{42.17 \times 10^{-3}}{7} \\ &\times (0.00239 \times (1.336 \times 10^6)^{0.98} + 0.000945 \times (1.336 \times 10^6)^{0.89}) = 16.119 \frac{\text{W}}{\text{m}^2 \cdot \text{K}} \\ h_{\text{forced rough}} &= \frac{\pi}{2} h_{\text{forced}} = 25.32 \frac{\text{W}}{\text{m}^2 \cdot \text{K}}. \end{aligned}$$

$$h_{\text{mix}} = \left(h_{\text{forced}}^{3.2} + h_{\text{natural}}^{3.2} \right)^{\frac{1}{3.2}} = (23.32^{3.2} + 9.651^{3.2})^{\frac{1}{3.2}} = 23.744 \frac{\text{W}}{\text{m}^2 \cdot \text{K}}.$$

$$Q_{\text{loss conv}} = h_{\text{mix}} A (T_{\text{wall}} - T_{\infty}) = 23.744 \times 301.28 \times (480 - 20) = 3.29 \text{ MW}.$$

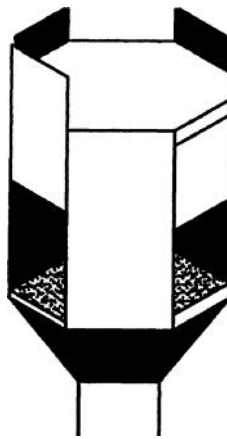
$$Q_{\text{loss}} = Q_{\text{loss rad}} + Q_{\text{loss ref}} + Q_{\text{loss conv}} = 5.10 + 3.01 + 3.29 = 11.4 \text{ MW}.$$

$$\eta = \frac{Q_{\text{in}} - Q_{\text{loss}}}{Q_{\text{in}}} = \frac{60.26 - 11.4}{60.26} = 0.81.$$

8.7.2.2 Cavity Receivers

A cavity receiver receives the concentrated flux inside a small insulated cavity in order to reduce the radiative and convective losses. Typical designs have an aperture area approximately one-third to one-half of the internal absorbing surface area. The acceptance angles range from 60° to 120°. There may be more than one cavity in a receiver, each receiving energy from a sector of the heliostat field (Batteson 1981). Figure 8.38 shows an example of a cavity receiver.

The optimal size of the cavity aperture is defined by a compromise between minimizing the thermal loss and maximizing the radiation capture. For an insulated cavity receiver with circular aperture, neglecting conduction,

**FIGURE 8.38**

A cavity-type receiver-type receiver design incorporating four apertures. It would operate in the 510°C–565°C temperature with steam, molten salt, or sodium. (From Battleson, K.W., Solar power tower design guide: Solar thermal central receiver power systems. A source of electricity and/or process heat, NASA STI/Recon Tech. Report N81, 31670, 1981.)

and convection losses, the absorption efficiency is given as (Steinfeld and Schubnell 1993)

$$\eta_{\text{absorption}} = \frac{\alpha_{\text{eff}} P_{\text{ap}} - \varepsilon_{\text{eff}} \pi r^2 \sigma T^4}{P_{\text{in}}} , \quad (8.35)$$

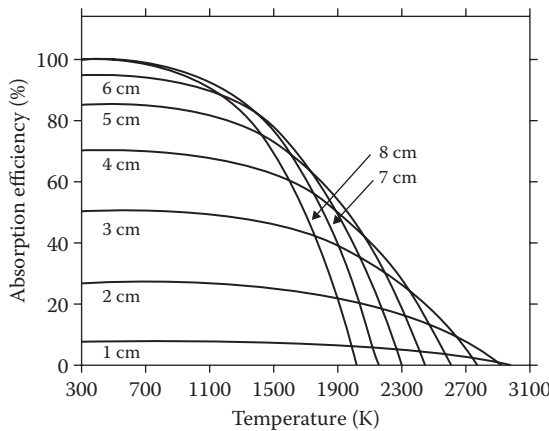
where P_{in} is the total power coming from the heliostat field, P_{app} is the power intercepted by the aperture, α_{eff} and ε_{eff} are the effective absorptance and emittance of the receiver, r is the radius of the circular aperture, σ is the Stefan–Boltzmann constant, and T is the nominal cavity temperature. The maximum cavity temperature can be obtained by setting the absorption efficiency equal to zero, which results in

$$T_{\text{max}} = \left(\frac{\alpha_{\text{eff}} I C}{\varepsilon_{\text{eff}} \sigma} \right)^{0.25} , \quad (8.36)$$

where I is the beam normal radiation and C is the concentration ratio, which is defined as

$$C = \frac{P_{\text{ap}}}{A_{\text{ap}} I} . \quad (8.37)$$

In order to capture solar energy at a reasonable efficiency, the operating temperature of the receiver should be significantly lower than the T_{max} value.

**FIGURE 8.39**

Absorption efficiency of a circular cavity receiver as a function of receiver temperature and aperture radius. (From Steinfeld, A. and M. Schubnell, *Solar Energy*, 50 (1), 19–25, 1993.)

Figure 8.39 depicts the variations of absorption efficiency versus receiver temperature and aperture size. At low temperatures where the radiation loss is negligible, the larger aperture has higher absorption efficiency as more power is intercepted. However, by increasing the temperature and consequently the radiation loss, the efficiency decreases with steeper slopes for larger apertures.

Similar to external receivers, the convective heat loss in cavity receivers is a combined effect of natural and forced convection. Siebers and Kraabel (1984) proposed using a mixed heat-transfer coefficient as the sum of the individual natural and forced heat-transfer coefficients. However, finding the coefficients is not straightforward and depends on the details of the receiver design, such as aperture area relative to that of the absorbing surfaces, tilt angle of the aperture, and wind velocities and directions (Winter et al. 1991). Kistler (1986) suggested the following equations that directly estimate the heat loss:

$$Q_{\text{loss conv}} = Q_{\text{forced}} + Q_{\text{natural}} \quad (8.38)$$

$$Q_{\text{forced}} = 7631 \frac{A_{\text{ap}}}{W_{\text{ap}}^{0.2}} \text{ Watts} \quad (8.39)$$

$$Q_{\text{natural}} = 5077 A_{\text{cav}} \text{ Watts} \quad (8.40)$$

where A_{ap} is the aperture area (m^2), W_{ap} is the aperture width (m), and A_{cav} is the total area inside of cavity (m^2).

8.7.2.3 Volumetric Receivers

Volumetric receivers usually use highly porous structures to absorb concentrated solar radiation substantially inside the structure rather than on the surface. While the HTF is passing through the porous media, it is heated by forced convection. In a good volumetric receiver, the temperature on the irradiated side of the absorber is lower than the outlet temperature, which tends to decrease the radiative losses at the inlet. This is the so-called volumetric effect (Ávila-Marín 2011). Figure 8.40 compares the temperature profiles of air as an HTF in a tube and a volumetric receiver. As can be seen, the temperature difference between the absorber surface and air vanishes in the middle of the volumetric receiver. On the other hand, the temperature of the outer surface of an external tube receiver is much higher than the air, which increases the heat loss. Moreover, the maximum flux that a tube receiver can sustain is significantly lower than a volumetric receiver.

A volumetric receiver may be open to the ambient or enclosed by a highly transparent window depending on the type of the HTF and the operating pressure. Open volumetric receivers are used to heat air at atmospheric pressure. The high-temperature air can be used to generate steam for steam power plants. The maximum operating temperature of a volumetric receiver is limited by the type of the material that is used to absorb solar radiation. With metal absorbers, air outlet temperatures between 800°C and 1000°C are achievable, while silicon-based ceramics are able to operate at higher temperatures. Figure 8.41 shows ceramic foams with different pore sizes and materials manufactured by Institut für Keramische Technologien und Sinterwerkstoffe (IKTS) in Dresden, Germany.

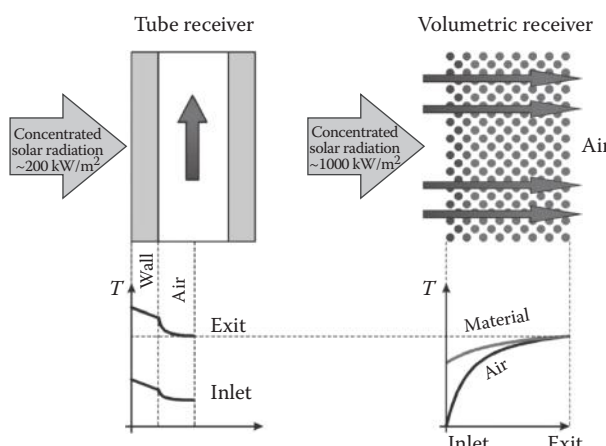
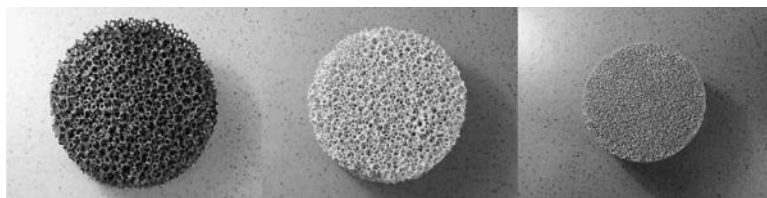


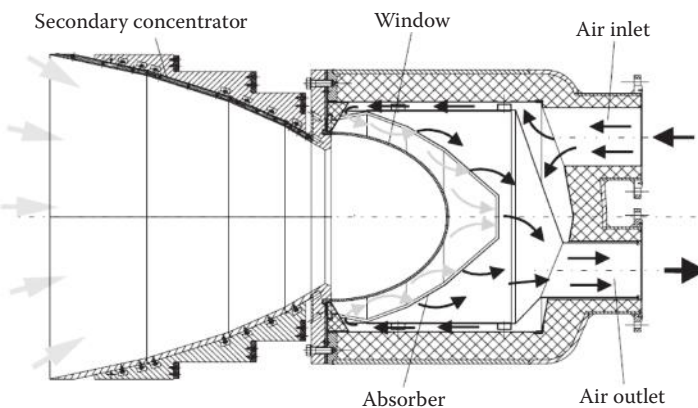
FIGURE 8.40

Comparison of a tube and a volumetric receiver. (From Fend, T., *Optica Applicata*, 11 (2), 271–284, 2010.)

**FIGURE 8.41**

Ceramic foams manufactured by IKTS. (From Fend, T. et al., *Energy*, 29 (5–6), 823–833, 2004.)

Volumetric receivers can be used to heat up the working fluid of a gas turbine. In this case, the receiver operates under elevated pressure and a window is used to separate the receiver cavity from the ambient air. Figure 8.42 shows a schematic of a pressurized volumetric receiver module called REFOS, which was installed in the CESA-1 solar tower test facility of the Plataforma Solar de Almería (PSA), Spain. A secondary concentrator is installed in front of the receiver to further concentrate the solar radiation. A domed quartz window is used to transmit the solar radiation. The pressurized air enters the plenum between the window and the absorber and is heated by passing through the absorber. Air exit temperatures up to 815°C and receiver efficiency in the range of 70% were achieved (Buck et al. 2002). The design of a window for a pressurized receiver is very challenging as it has to be highly transparent, yet strong and durable at high pressures and temperatures. Quartz windows (SiO_2) are widely used, which have a maximum operating temperature limit of 1000°C. A window made of fused silica was tested at the Weizmann Institute of Science in Israel, which successfully

**FIGURE 8.42**

REFOS volumetric receiver module. (From Buck, R. et al., *Journal of Solar Energy Engineering*, 124 (1), 2, 2002.)

**FIGURE 8.43**

Local melting in a honeycomb absorber. (From Karni, J. et al., *Journal of Solar Energy Engineering*, 120 (2), 85, 1998b.)

sustained an operating pressure and peak absorber temperature of 30 bar and 1700°C, respectively (Karni et al. 1998a).

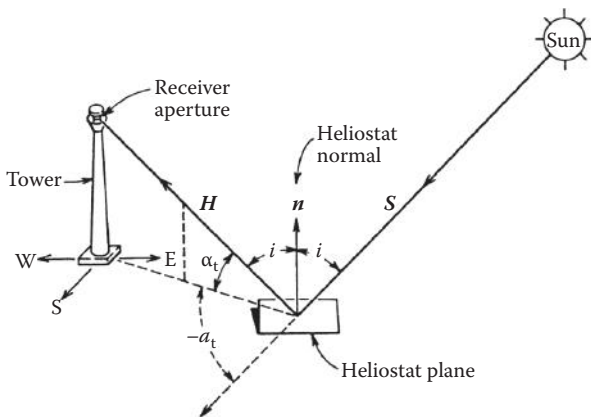
One of the main problems in the operation of the volumetric receivers is the relationship between local solar flux and the flow speed. High local solar flux increases the viscosity of air leading to a lower mass flow rate and, consequently, a higher material temperature. On the other hand, a low solar flux causes higher mass flow rate and lower material temperature. Therefore, it is possible for the material temperature to exceed the maximum allowable temperature at some points while the average air outlet temperature is still low. This may lead to local failures, such as melting or cracking (Becker et al. 2006). Local melting in a honeycomb absorber owing to high local temperature is shown in Figure 8.43.

A volumetric particle receiver is another type of directly irradiated receiver in which the HTF is seeded by small particles that act as absorbers. Carbon particles with sizes less than a micron have been suggested for absorbing solar energy (Fend 2010; Fend et al. 2004). If air is used as the HTF with carbon particles as the absorbers, carbon could be oxidized at the high temperatures in the receiver, which would provide additional heat to the fluid, although the additional heat is very small (Bertocchi et al. 2004). This type of receiver has a high surface-to-volume ratio, which minimizes the temperature difference between the absorber and the HTF. Moreover, a small-particle receiver can withstand higher fluxes and is immune to hotspots (Fend 2010; Fend et al. 2004).

8.7.3 Design of Heliostat Field

A detailed design of the heliostat field is beyond the scope of this book. However, some macroscale features are described here.

A heliostat is oriented in such a way that a solar ray incident on the heliostat is reflected toward the receiver as shown in Figure 8.44. In vector notation,

**FIGURE 8.44**

Sun-heliostat-tower geometry for calculating tracking requirements. Tower unit vector \mathbf{H} altitude and azimuth angles are shown.

the angle between a heliostat to receiver vector \mathbf{H} and the heliostat normal \mathbf{n} is given by the scalar product

$$\cos i = \frac{\mathbf{n} \cdot \mathbf{H}}{|\mathbf{n}| |\mathbf{H}|}. \quad (8.41)$$

This equation, along with Equation 2.48, gives the incidence angle between a solar ray \mathbf{S} and the heliostat normal \mathbf{n} . The second equation relating the two heliostat rotation angles (surface tilt and azimuth angles) is the requirement that the incident ray \mathbf{S} , heliostat normal \mathbf{n} , and the reflected ray \mathbf{H} all be coplanar; that is,

$$(\mathbf{S} \times \mathbf{n}) \cdot \mathbf{H} = 0. \quad (8.42)$$

Unit vectors \mathbf{S} , \mathbf{n} , and \mathbf{H} are shown in Figure 8.44.

Using a Cartesian coordinate system in which (x,y,z) correspond to east, north, and vertical, the components of \mathbf{n} , \mathbf{H} , and \mathbf{S} are

$$\begin{aligned} \mathbf{n} = & \begin{pmatrix} \cos \alpha_n \sin \alpha_n \\ -\cos \alpha_n \cos \alpha_n \\ \sin \alpha_n \end{pmatrix} \end{aligned} \quad (8.43)$$

$$\begin{aligned} \mathbf{H} = & \begin{pmatrix} \cos \alpha_t \sin \alpha_t \\ -\cos \alpha_t \cos \alpha_t \\ \sin \alpha_t \end{pmatrix} \end{aligned} \quad (8.44)$$

$$\begin{aligned} S = & \frac{\cos \alpha \sin a_s}{-\cos \alpha \cos a_s}, \\ & \sin \alpha \end{aligned} \quad (8.45)$$

where α and a_s are the solar altitude and azimuth angles, α_t and a_t are the altitude and azimuth angles of the reflected ray vector to the fixed tower shown in Figure 8.44, and α_n and a_n are the heliostat normal altitude and azimuth angles measured in the same way as α and a_s .

Optimal design of the heliostat field has been the subject of many studies because it typically accounts for approximately 50% of the total cost of the plant (Kolb et al. 2007) and 40% of energy losses (Sargent and Lundy LLC Consulting Group 2003). Several codes have been developed over the last few decades, which are well documented in Garcia et al. (2008). Different approaches are used in these codes to maximize the overall field efficiency, which is defined as

$$\eta_{\text{field}} = \eta_{\text{reflection}} \times \eta_{\text{cosine}} \times \eta_{\text{attenuation}} \times \eta_{\text{interception}} \times \eta_{\text{shading \& blocking}}, \quad (8.46)$$

where $\eta_{\text{reflection}}$ represents the reflectivity of the heliostats, η_{cosine} is the cosine factor, $\eta_{\text{attenuation}}$ is the atmospheric attenuation factor, $\eta_{\text{interception}}$ is the interception factor that accounts for the fraction of the reflected rays that hit the target, and $\eta_{\text{shading \& blocking}}$ is the shading and blocking factor.

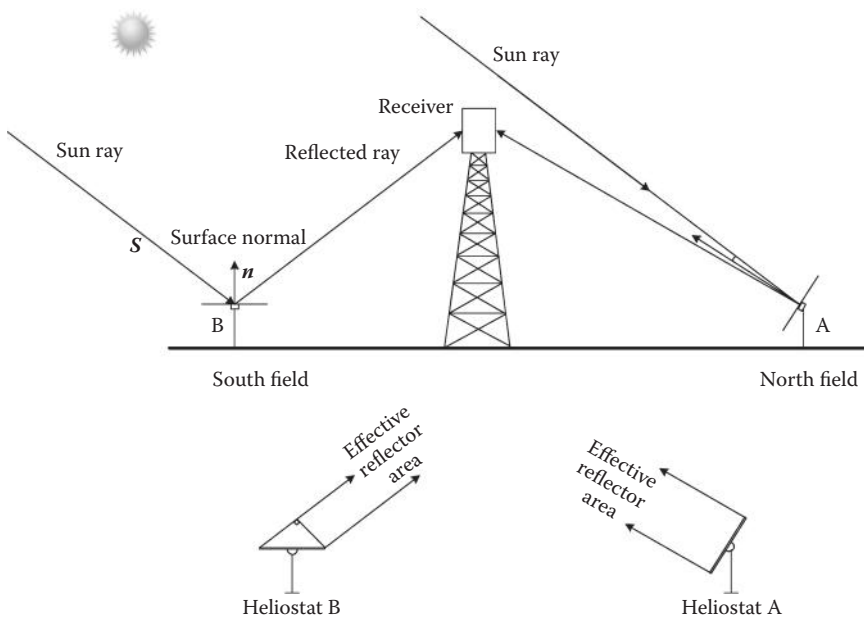
8.7.3.1 Reflection Factor ($\eta_{\text{reflection}}$)

A part of the incident radiation on a heliostat is absorbed by the surface. The fraction that is reflected depends on the absorptivity of the heliostat surface coating and the incidence angle.

8.7.3.2 Cosine Factor (η_{cosine})

This is the most significant loss in the heliostat field that is due to the angle between the incident solar beam and the surface normal (incidence angle). Therefore, it depends on both sun and heliostat positions. The reflected radiation from the heliostat is proportional to the cosine of this angle, which is why it is called the cosine effect. As shown in Figure 8.45, for a field located in the Northern Hemisphere, a heliostat situated in the south field has a higher incidence angle and, consequently, less effective reflector area and cosine factor. Knowing the sun ray vector S and surface normal n , the cosine factor is defined as

$$\eta_{\text{cosine}} = \frac{\mathbf{S} \cdot \mathbf{n}}{|\mathbf{S}| |\mathbf{n}|}. \quad (8.47)$$

**FIGURE 8.45**

The cosine effect for a heliostat field located at the Northern Hemisphere. (Stine, W.B. and R.W. Harrigan: *Solar Energy Fundamentals and Design: With Computer Applications*. 1985. Copyright Wiley-VCH Verlag GmbH & Co. KGaA. Reproduced with permission.)

8.7.3.3 Atmospheric Attenuation Factor ($\eta_{\text{attenuation}}$)

The reflected beam radiation from the surface of a heliostat may be scattered, depending on the distance between the heliostat and the receiver, ambient humidity, and particulate matter in the air. This atmospheric attenuation factor can be calculated by (Schmitz et al. 2006)

$$\eta_{\text{attenuation}} = 0.99321 - 0.000176 \times d + 1.97 \times 10^{-8} \times d^2 \quad (8.48)$$

for $d \leq 1000 \text{ m}$

$$\eta_{\text{attenuation}} = \exp(-0.0001106 \times d) \quad (8.49)$$

for $d > 1000 \text{ m}$,

where d is the distance between the heliostat surface and the receiver.

8.7.3.4 Interception Factor ($\eta_{\text{interception}}$)

A portion of the reflected image from the heliostat may fail to intercept the receiver aperture, which is the cumulative result of several factors such as tracking precision, shape of the sun, nonuniformity of mirror surface, and so

on. There are two general approaches to find the interception factor (spillage factor), that is, ray tracing method and analytical integration of the image shape produced by the mirror over the receiver domain. Two well-known analytical methods that are extensively used are the UNIZAR model from Universidad de Zaragoza (Collado et al. 1986; Collado and Turegano 1989) and the HFCAL model from the German Aerospace Center (Schwarzbözl et al. 2009). Collado (2010) compared the two models and concluded that both of them are appropriate tools while the HFCAL model is much simpler and slightly more accurate. In the HFCAL model, the flux density on the receiver aperture is given as (Collado 2010)

$$F(x, y) = \frac{P}{2\pi\sigma_{\text{tot}}^2} \exp \left(-\frac{x^2 + y^2}{2\sigma_{\text{tot}}^2} \right), \quad (8.50)$$

where P is the total power reflected from an individual heliostat on the receiver plane and σ_{tot} is the total dispersion of the flux distribution. The total power is calculated as

$$P = I \times A_m \times \eta_{\text{cosine}} \times \eta_{\text{attenuation}} \times \eta_{\text{reflection}}, \quad (8.51)$$

where I is the direct solar radiation and A_m is the mirror surface area. The total dispersion can be calculated as

$$\sigma_{\text{tot}} = \frac{\sqrt{d^2 \left(\sigma_{\text{sun}}^2 + \sigma_{\text{ast}}^2 + \sigma_t^2 + (2\sigma_s)^2 \right)}}{\cos i}, \quad (8.52)$$

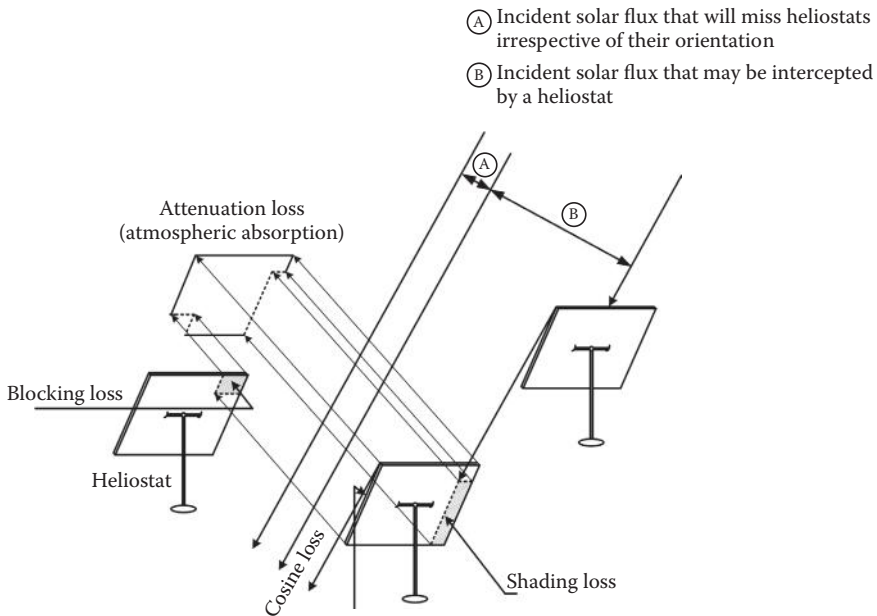
where σ_{sun} , σ_{ast} , σ_t , and σ_s are the standard deviations due to sun shape error, astigmatic effect, tracking error, and mirror slope error, respectively. Here, d represents the actual distance between the heliostat surface center and the aim point on the receiver while $\cos i$ is the cosine of the angle between the reflected central ray from the heliostat and the receiver surface normal.

The intercepted power is obtained by integrating the flux distribution along the receiver aperture. The interception factor can be obtained as

$$\eta_{\text{interception}} = \frac{1}{2\pi\sigma_{\text{tot}}^2} \iint_{x, y} \exp \left(-\frac{x^2 + y^2}{2\sigma_{\text{tot}}^2} \right) dy dx. \quad (8.53)$$

8.7.3.5 Shading and Blocking Factor ($\eta_{\text{shading \& blocking}}$)

The shading and blocking factor not only depends on the sun's position and the individual location of the analyzed heliostat but also is a function of the

**FIGURE 8.46**

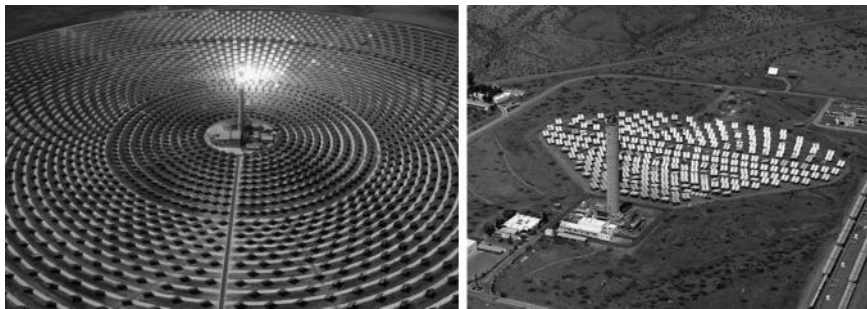
Shading and blocking losses in a heliostat field. (Stine, W.B. and R.W. Harrigan: *Solar Energy Fundamentals and Design: With Computer Applications*. 1985. Copyright Wiley-VCH Verlag GmbH & Co. KGaA. Reproduced with permission.)

location of the neighboring heliostats. Shading occurs when the incoming solar radiation is obstructed by a neighboring heliostat. On the other hand, blocking occurs when the reflected image from a heliostat is partially blocked by an adjacent heliostat from reaching the receiver (Figure 8.46). The shading and blocking factor of a heliostat is defined as the area not shaded or blocked divided by the total heliostat area.

The shading and blocking loss can be minimized by increasing the distance between the heliostats. On the other hand, increasing the size of the field leads to other consequences such as higher atmospheric attenuation and higher land costs. Therefore, an optimization study needs to be carried out to find the optimal field layout. A number of codes have been developed for this purpose, which are well documented in Garcia et al. (2008).

8.7.4 Field Layout

Heliostat field layout depends on the choice of the receiver. The north field layout (in the Northern Hemisphere) is commonly used for cavity receivers. The north field is more effective at a midday design point and consequently leads to a lower system cost. On the other hand, the surrounding field is used

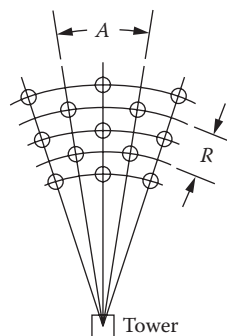
**FIGURE 8.47**

Aerial views of the plants Gemasolar (19.9 MW) and CESA-1 (1.2 MW) in Spain.

for cylindrical receivers, which allows the use of a smaller tower. In this case, the south field performs very well in the morning and evening while it is less effective at midday. Figure 8.47 shows a surrounding and a north field for the power plants in Spain.

The radial stagger layout (Lipps and Vant-Hull 1978) proposed by Lipps and Vant-Hull is commonly used for heliostat field design as it requires minimal computational effort and is well tested over time. There are two parameters that need to be optimally defined, that is, radial spacing R and azimuth spacing, which are depicted in Figure 8.48. The correlations for these parameters determined by curve fits to the optimized layouts are given for high reflectance heliostats in a large field as

$$R = h \left(1.44 \cot \alpha_t - 1.094 + 3.068\alpha_t - 1.1256\alpha_t^2 \right) \quad (8.54)$$

**FIGURE 8.48**

The radial stagger heliostat layout pattern developed by the University of Houston.

and

$$A = w \cdot 1.749 + 0.6396\alpha_t + \frac{0.2873}{\alpha_t - 0.04902} , \quad (8.55)$$

where h and w are the height and width of the heliostat and α_t is the tower altitude angle measured from the center of the front heliostat.

8.8 Central Receiver System (CRS) Design

The design of a CRS is complicated, involving the use of computer programs. There are many commercial computer programs that can be used to design the solar field and the receiver. The System Analyzer Model (SAM) is one of the programs that can be used for a preliminary design and economic analysis. Commercial computer models such as TRNSYS, GATECYCLE, and IPSEpro can be used to design the power block for a central receiver power plant.

The following example shows a preliminary design of the solar field of a CRS.

Example 8.6

A preliminary estimate of the power plant size can be helpful before performing a detailed system design. Provide a preliminary size of the solar field and the receiver for a 50-MW_e central receiver plant in Barstow, California, with a design point insolation of 950 W/m².

Solution

The method used here follows the approach proposed by Vant-Hull and Izgyon (2003) where the parameters are estimated from rules of thumb or prior experience. A solar multiple (SM) of 1.8 and an average receiver surface temperature of 700 K are considered. The calculation procedure is described step by step.

1. Receiver Design

The receiver thermal rating (RTR) can be found by knowing the power cycle efficiency (η_{cycle}), parasitics, and SM as

$$\begin{aligned} RTR &= \frac{SM \times (\text{Design point power} + \text{Parasitics})}{\eta_{cycle}} \\ &= \frac{1.8 \times (50 \text{ MW}_e + 5 \text{ MW}_e)}{0.4} = 248 \text{ MW}_{th}. \end{aligned}$$

It is assumed that the parasitics are 10% of the design point power and the cycle efficiency is 40%. Now, the receiver absorbing area (RAA) can be found from the average flux density. Typically, the average flux density is equal to allowable flux density $\times 0.53$. It is assumed that the allowable flux density is 0.825 MW/m². Therefore,

$$\text{RAA} = \frac{248}{0.825 \times 0.53} = 568 \text{ m}^2.$$

Receiver thermal losses (RTLs) can be found by the following correlation:

$$\text{RTL} = 30 \frac{\text{kW}}{\text{m}^2} \times \left(\frac{T}{800 \text{ K}} \right)^2 \times \text{RAA} = 30 \times \left(\frac{700}{800} \right)^2 \times 568 = 13 \text{ MW}_{\text{th}}.$$

Therefore, the total energy that needs to be provided by the field is $248 + 13 = 261 \text{ MW}_{\text{th}}$. However, absorptivity of the receiver surface as well as interception and atmospheric attenuation efficiencies need to be taken into account. Therefore, field rating (FR) is given as

$$\text{FR} = \frac{261}{\text{Absorptivity} \times \eta_{\text{int}} \times \eta_{\text{att}}} = \frac{261}{0.92 \times 0.98 \times 0.95} = 305 \text{ MW}_{\text{th}}.$$

2. Field Design

As previously described in Chapter 3, there are also other efficiency factors that need to be taken into consideration such as reflectivity, cosine factor, and shading and blocking efficiency. Assuming 99% availability, the field efficiency (FE) is obtained as

$$\text{FE} = \eta_{\text{ref}} \times \eta_{\text{cosine}} \times \eta_{\text{shading \& blocking}} \times \text{availability} = 0.88 \times 0.83 \times 0.92 \times 0.99 = 0.665.$$

Therefore, the reflector area (RA) is given as

$$\text{RA} = \frac{\text{FR}}{(\text{FE} \times \text{Insolation})} = \frac{305 \text{ MW}_{\text{th}}}{0.665 \times 950} = 483,000 \text{ m}^2.$$

The field area (FA) can be calculated by considering ground coverage (GC) and exclusion factor (EF), which accounts for the areas restricted for roads, power block, drainage, and so on.

$$\text{FA} = \frac{\text{RA}}{\text{GC} \times \text{EF}} = \frac{0.483 \text{ km}^2}{0.25 \times 0.97} = 1.99 \text{ km}^2.$$

The field radius to the north, east, and west for the surround field can be obtained by

$$R_{\text{surround}} = \frac{FA \times 1.25}{\pi}^{0.5}$$

Considering the reduced southern field, the radius of the south part of the field is given as

$$R_{\text{south}} = \frac{2}{3} \times R.$$

Moreover, the field radius for the north-only field is given as

$$R_{\text{north only}} = \frac{FA \times 2.25}{\pi}^{0.5}$$

Therefore,

$$R_{\text{surround}} = 0.89 \text{ km}$$

$$R_{\text{north only}} = 1.19 \text{ km.}$$

Tower focal height (HT) can be obtained by

$$HT = R \tan (8.8^\circ) = R \times 0.154.$$

HT is the distance from the plane of the reflector to the center of the receiver. In an optimized surround field, 8.8° is the typical elevation angle from the most distant heliostat. Therefore,

$$HT = 0.89 \times 0.154 = 137 \text{ m (surround field)}$$

$$HT = 1.19 \times 0.154 = 183 \text{ m (north field).}$$

8.9 Recent Developments in Solar Thermal Power Cycles

Solar thermal power technologies were successfully demonstrated in the 1980s, as noted in Section 8.4 in this chapter. In fact, SEGS thermal power plants built in the 1980s are still producing power commercially. With that

learning experience, a number of new CSP plants have been built or are under construction. However, the capital costs of \$2500–\$3500/kW for a solar power plant is still three to four times higher than the natural gas combustion turbines, and the plant efficiency of 12% to 14% has the potential to improve by as much as three times (Goswami 1998). This potential has drawn the interest of researchers to fundamental thermodynamic improvements in power cycles for solar energy.

8.9.1 Hybrid and Combined Cycles

The SEGS plants and the CPG dish/Stirling power plants were designed to use natural gas as a supplemental fuel. It has also been suggested that natural gas be used as a supplemental fuel for the CRS (Bohn et al. 1995). If the supplemental natural gas flows in the power system are large enough, it makes sense to use the natural gas in a combined-cycle mode. With the present-day technology of natural gas combustion turbines, a combined combustion turbine/steam Rankine cycle power plant can achieve a cycle efficiency as high as 58%. Figure 8.49 shows a schematic of a combined-cycle solar/natural gas power plant (Washam et al. 1993). In 2012, Florida Power & Light built a 75-MW parabolic trough-based solar thermal power plant

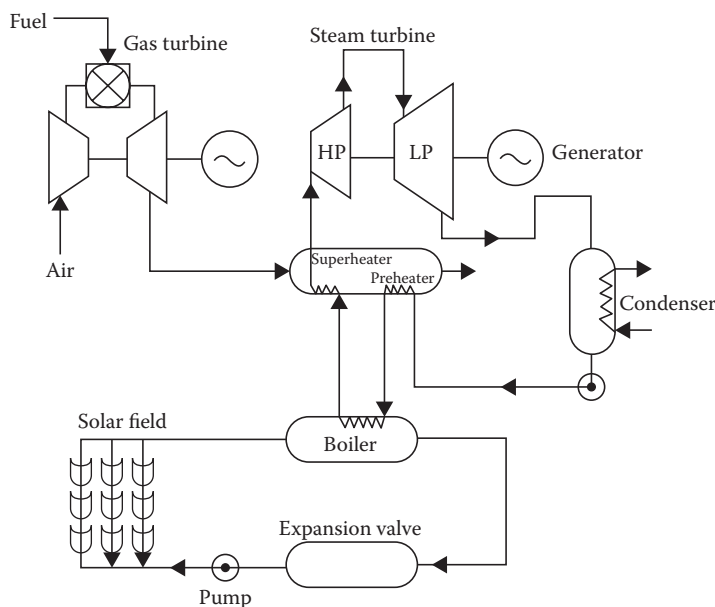


FIGURE 8.49

Concept of an integrated solar combination–cycle power system. (From Washam, B.M. et al., *Integrated Solar Combined Cycle Systems [ISCCS] Utilizing Solar Parabolic Trough Technology—Golden Opportunities for the '90s*, Diablo, CA: Spencer Management Associates, 1993.)

in Martin County as a preheater for a 1000-MW natural gas combined-cycle power plant. With the present cost of the commercially available, aeroderivative combustion turbines as low as \$500/kW, and the cost of a solar power plant being approximately \$2500–\$3000/kW, the capital costs of a combined-cycle solar/natural gas power plant could be as low as \$1000–\$2000/kW, depending on the natural gas fraction. This idea seems very attractive, especially where natural gas is to be used as a backup fuel anyway.

8.9.2 Kalina Cycle

Kalina (1984) proposed a novel bottoming cycle for a combined-cycle power plant that improves the overall performance of the cycle. This novel cycle, now known as the Kalina cycle, uses a mixture of ammonia and water as the working fluid for the bottoming cycle expansion turbine. Using a two-component working fluid and multipressure boiling, one can reduce heat transfer-related irreversibilities and therefore improve the resource effectiveness (Figure 8.50). Also, the ammonia–water mixture can be used as a working fluid for a lower-temperature (250°C) solar energy system employing lower-cost parabolic trough technology. According to Kalina and Tribus (1992), it is possible to improve the efficiency of the bottoming cycle by more than 45% over the steam Rankine cycle for a lower temperature resource ($\sim 250^{\circ}\text{C}$). Therefore, if the Kalina cycle is used for solar thermal power in place of the Rankine cycle, the capital cost could be reduced by at least 45% because of the higher efficiency and the possibility of using cheaper concentrating collectors owing to the lower temperature

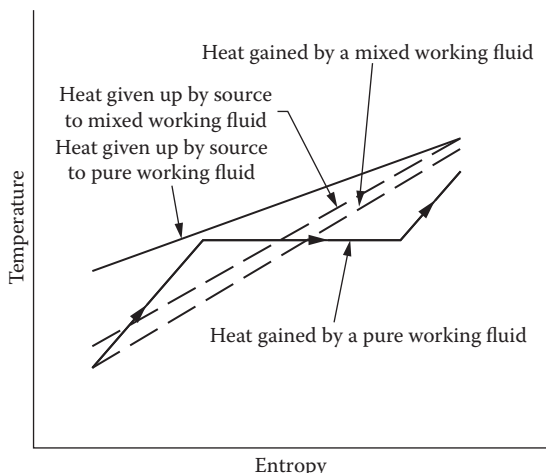


FIGURE 8.50
Heat transfer between a heat source and a working fluid.

requirement. These improvements may be enough to make solar thermal power economically competitive by itself and not a burden on natural gas for combined-cycle power plants. This offers an opportunity for research in solar thermal power utilizing the Kalina cycle.

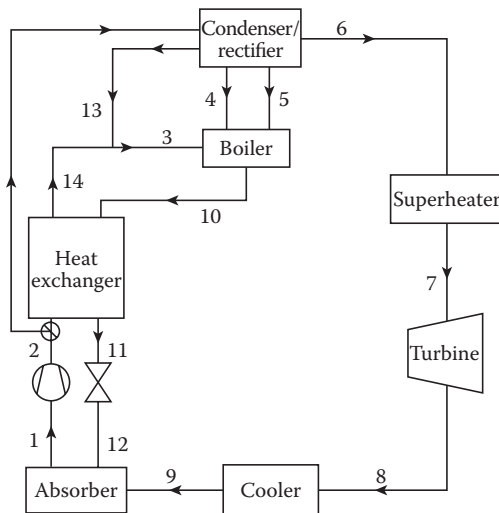
Although the use of mixed working fluids such as ammonia–water provides a big advantage in utilizing sensible heat sources in a boiler, they present a disadvantage in the condenser, since condensation must also take place with change in temperature. This disadvantage could be overcome if the normal condensation process is replaced by the absorption condensation process as proposed by Rogdakis and Antonopoulos (1991) and Kouremenos et al. (1994) as a modification of the Kalina cycle and, more recently, by Goswami (1995) as an ammonia-based combined power/cooling cycle.

8.9.3 Aqua–Ammonia Combined Power/Absorption Cycle

Kouremenos et al. (1994) showed an analysis of an aqua–ammonia power cycle that is similar to the Kalina cycle; however, it replaces the conventional condensation process of the aqua–ammonia mixture coming out of the low-pressure turbine with an absorption condensation process. They showed that with an ammonia concentration of 72.86% in the mixed working fluid in the turbine, cycle efficiencies of the order of 25%–45% could be achieved for a source temperature of 500°C and pressure ratios from 25 to 100.

8.9.4 Combined Power/Cooling Cycle

Goswami (1995) has proposed a new thermodynamic cycle that improves the cycle efficiency and, therefore, resource utilization by producing power and refrigeration in the same cycle. The new cycle, also known as the Goswami cycle, was developed to use ammonia as the working fluid in an innovative combination of an ammonia-based Rankine cycle and an ammonia–water absorption refrigeration cycle. The use of any mixture of fluids was later allowed provided that one is much more volatile than the other and the more volatile component could be condensed by absorption in the other. The ammonia–water mixture is an obvious example, but other examples include mixtures of hydrocarbons such as isobutane and heptane or pentane and decane. Figure 8.51 shows a schematic of the cycle. By boiling a mixture, for example, ammonia–water, this cycle reduces the irreversibilities associated with the heat transfer from a sensible heat source. Also, by expanding almost pure ammonia in the last-stage turbine, it allows the working fluid to go down to a much lower temperature, providing refrigeration. The working fluid is condensed by absorption in the water. The net effect lowers the sink temperature of the cycle. The cycle can use source temperatures as low as 100°C, thereby making it a useful power cycle for low-cost solar thermal collectors, geothermal resources, and waste heat from existing power plants.

**FIGURE 8.51**

A schematic diagram of the Goswami combined power/cooling cycle.

8.9.5 Supercritical CO₂ Power Cycle

Carbon dioxide, as a nontoxic, abundant, inexpensive, nonflammable, and highly stable compound with low critical properties, has been the subject of interest for many researchers to be used as a working fluid for thermodynamic power cycle for high-temperature solar fields such as a central receiver tower. Design of the first supercritical CO₂ (S-CO₂) cycle dates back to late 1960s when Feher (1967) and Angelino (1967, 1968) began their separate investigations on replacing the conventional working fluids with S-CO₂. However, the main problem about using CO₂ is the low critical temperature (30.98°C) that requires low-temperature cooling water, which is not available in many locations. This limitation led to studies on the CO₂ cycle in gas state only. It was reported by Angelino (1969) that compressing CO₂ around its critical point results in lower compression work and consequently higher cycle efficiency, which is mainly due to the reduction of the specific volume at critical condition. Since then, S-CO₂ power cycles have drawn attention for nuclear power generation in gas reactors (Dostal et al. 2006; Moisseytsev and Sienicki 2009).

On the other hand, there is a growing interest in deploying S-CO₂ in concentrated solar power plants owing to limitations of the current HTFs. Oil, molten salt, and steam are the common HTFs, which are used to absorb solar energy in the solar receiver. However, the maximum operating temperature of the oil is 400°C, which limits the overall performance of the plant. Although molten salt operates at higher temperatures (around 560°C), the high freezing point becomes a major challenge, which requires elaborate freeze protection systems. As the phase of the fluid changes in the receiver in direct steam

generation plants, complex control systems are required while the storage capacity is also limited (Turchi 2009). On the other hand, there is no maximum or minimum temperature limits for CO₂, and it is nontoxic, inexpensive, and nonflammable. Moreover, by employing an appropriate power cycle, it can be used as both heat transfer and working fluids, eliminating the need for a heat exchanger in between. It has been shown by Turchi et al. (2012) that the S-CO₂ Brayton cycle can achieve more than 50% efficiency under dry cooling conditions. The main advantages of the S-CO₂ Brayton cycle are its high efficiency, high power density, compactness, and low cost.

There are different S-CO₂ configurations, for example, recompression and partial cooling (Turchi et al. 2012), but all of them have been derived from the simple cycle that is shown in Figure 8.52. The CO₂ is pressurized in the

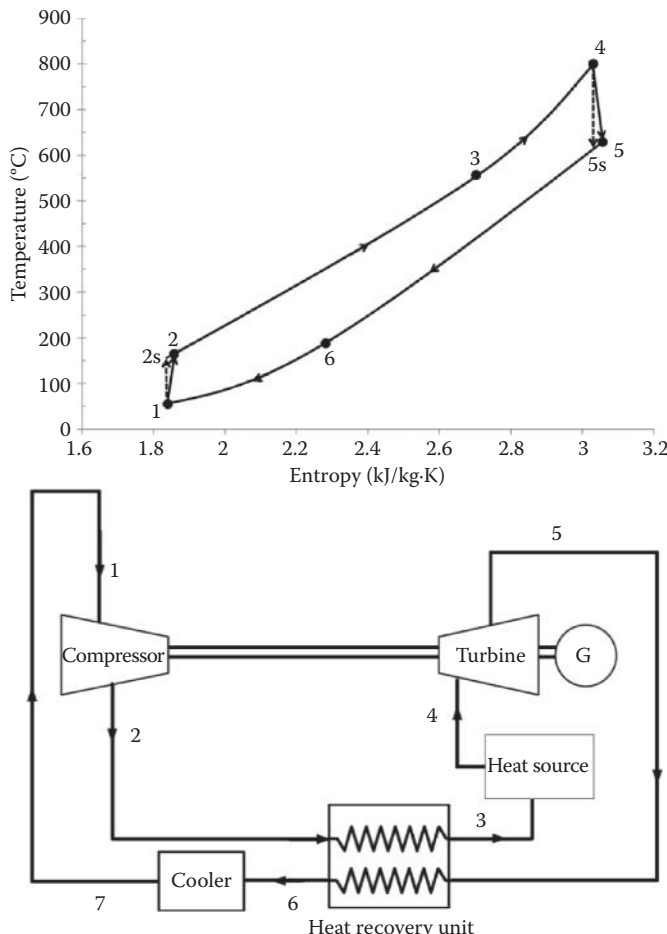


FIGURE 8.52
Basic S-CO₂ Brayton cycle.

compressor to above its critical pressure. The S-CO₂ is then heated by the heat source, for example, solar receiver, to the required turbine inlet temperature. After expansion in the turbine, the flow goes through the recuperator and transfers energy to the fluid exiting the compressor. The cycle is completed by cooling the working fluid in the cooler and rejecting heat to the cold sink. The cycle efficiency can be increased by dividing the compression into two stages and using an intercooler in between. Similarly, using two stages of expansion and a reheater can also increase the efficiency.

Example 8.7

In a closed-loop Brayton cycle (Figure 8.52), S-CO₂ enters the compressor at 7.5 MPa and exits at 25 MPa. The turbine inlet temperature is set at 750°C and the temperature of the fluid leaving the cooler is 32°C. The turbine and compressor efficiencies are 93% and 89%, respectively. If the heat exchanger effectiveness is 0.95, find the cycle efficiency assuming the pressure drop in the pipes is negligible and there is no heat loss to the environment.

Solution

Properties of S-CO₂ may be found from REFPROP database (Lemmon et al. 2002). Table A8.3 lists some of the properties needed for analyzing the S-CO₂ cycle.

State 1. Using the table of properties for S-CO₂ (Table A8.3) the enthalpy and entropy values can be found for 7.5 MPa by interpolation between 30°C and 40°C as:

$$P_1 = 7.5 \text{ MPa}, T_1 = 32^\circ\text{C} \rightarrow h_1 = 362.21 \text{ kJ/kg}, s_1 = 1.5310 \text{ kJ/kg}\cdot\text{K}$$

State 2. For an isentropic process between states 1 and 2s, and using Table A8.3:

$$P_2 = 25 \text{ MPa}, s_{2s} = s_1 = 1.5310 \text{ kJ/kg}\cdot\text{K} \rightarrow h_{2s} = 396.83 \text{ kJ/kg}$$

The enthalpy at state 2 can be determined using the compressor isentropic efficiency, η_c , as:

$$h_2 = h_1 + \frac{h_{2s} - h_1}{\eta_c} = 362.21 + \frac{396.83 - 362.21}{0.89} = 401.11 \text{ kJ/kg}$$

From Table A8.3, for the enthalpy, h_2 and pressure, $P_2 = 25$ MPa, by interpolation:

$$s_2 = 1.5426 \text{ kJ/kg}\cdot\text{K}$$

$$T_2 = 98.51^\circ\text{C}$$

State 4. The turbine inlet condition can be found from Table A8.3:
For

$$P_4 = 25 \text{ MPa}, T_4 = 750^\circ\text{C}$$

we find

$$h_4 = 1285.6 \text{ kJ/kg}, s_4 = 2.9691 \text{ kJ/kg}\cdot\text{K}.$$

State 5. For an isentropic expansion from 4 to 5s, using Table A8.3:

$$P_5 = 7.5 \text{ MPa}, s_{5s} = s_4 = 2.9691 \text{ kJ/kg}\cdot\text{K}, \text{ which gives } h_{5s} = 1067.6 \text{ kJ/kg}.$$

The enthalpy at state 5 can be determined using the turbine isentropic efficiency, η_t :

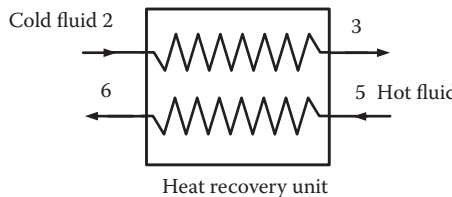
$$h_5 = h_4 - \eta_t(h_4 - h_{5s}) = 1285.6 - 0.93 \times (1285.6 - 1067.6) = 1082.86 \text{ kJ/kg}$$

From Table A8.3, for the enthalpy, h_5 and pressure, $P_5 = 7.5 \text{ MPa}$, by interpolation:

$$s_5 = 2.9871 \text{ kJ/kg}\cdot\text{K}$$

$$T_5 = 581.25^\circ\text{C}$$

Heat-Exchanger Calculation



The effectiveness of a heat exchanger is defined as the ratio between the actual heat transfer rate and the maximum possible heat transfer rate. The maximum heat transfer rate is determined from the fluid with the lower heat capacity, which undergoes the maximum possible temperature change. In order to find which fluid (cold or hot) has the lower heat capacity, we find the enthalpy change in the two fluids for the maximum possible temperature change (temperature difference between the inlets of the hot and cold fluids)

Cold fluid: h at $(T_5, P_3) = h_3$ at $(581.25^\circ\text{C}, 25 \text{ MPa}) = 1071.1 \text{ kJ/kg}$
Therefore, enthalpy change for cold fluid between 98.51°C and 581.25°C :

$$Q_{\max,\text{cold}} = h \text{ at } (T_5, P_3) - h_2 = 669.99 \text{ kJ/kg}.$$

Hot fluid: h at $(T_2, P_6) = h_6$ at $(98.51^\circ\text{C}, 7.5 \text{ MPa}) = 521.74 \text{ kJ/kg}$
Therefore, enthalpy change for cold fluid between 581.25°C and 98.51°C :

$$Q_{\max,\text{hot}} = h_5 - h \text{ at } (T_2, P_6) = 561.12 \text{ kJ/kg}.$$

Therefore, the hot fluid has lower heat capacity and $Q_{\max} = Q_{\max,\text{hot}} = 561.12 \text{ kJ/kg}$.

$$\text{The heat-exchanger effectiveness } = \frac{h_3 - h_2}{Q_{\max}} = \frac{h_5 - h_6}{Q_{\max}} = 0.95$$

$$h_3 = Q_{\max} \times 0.95 + h_2 = 934.17 \text{ kJ/kg}$$

$$h_6 = h_5 - Q_{\max} \times 0.95 = 1082.86 - 561.12 \times 0.95 = 549.79 \text{ kJ/kg}$$

Other properties can be found from Table A8.3.

State 3. $P_3 = 25 \text{ MPa}$, $h_3 = 934.17 \text{ kJ/kg}\cdot^\circ\text{C} \rightarrow T_3 = 471.91^\circ\text{C}$, $s_3 = 2.5686 \text{ kJ/kg}\cdot\text{K}$

State 6. $P_6 = 7.5 \text{ MPa}$, $h_6 = 521.74 \text{ kJ/kg}\cdot^\circ\text{C} \rightarrow T_6 = 120.84^\circ\text{C}$, $s_6 = 2.0934 \text{ kJ/kg}\cdot\text{K}$

The heat input to the cycle is:

$$Q_{\text{in}} = h_4 - h_3 = 351.43 \text{ kJ/kg.}$$

The work output from the turbine is:

$$W_t = h_4 - h_5 = 202.74 \text{ kJ/kg.}$$

The energy input to the compressor is:

$$W_c = h_2 - h_1 = 38.91 \text{ kJ/kg.}$$

The thermal efficiency is:

$$\eta_{\text{thermal}} = \frac{W_t - W_c}{Q_{\text{in}}} = 0.466.$$

8.10 Solar Distillation of Saline Water

Solar distillation for the production of potable water from saline water has been practiced for many years. A solar distillation plant, covering 4740 m² of land, was built in Las Salinas, Chile, in 1872, to provide fresh water from salt water for use at a nitrate mine (Talbert et al. 1970). Single-glass-covered flat-plate collectors with salt water flowing downward over slanting roofs were used to vaporize some of the water, which was then condensed on the air-cooled underside of the roof. This plant ran effectively for over 40 years and produced up to 23,000 liters of fresh water per day until the nitrate mine was exhausted.

Solar stills have been extensively studied and there are many different solar still configurations, as illustrated in Figure 8.53. Combining solar stills

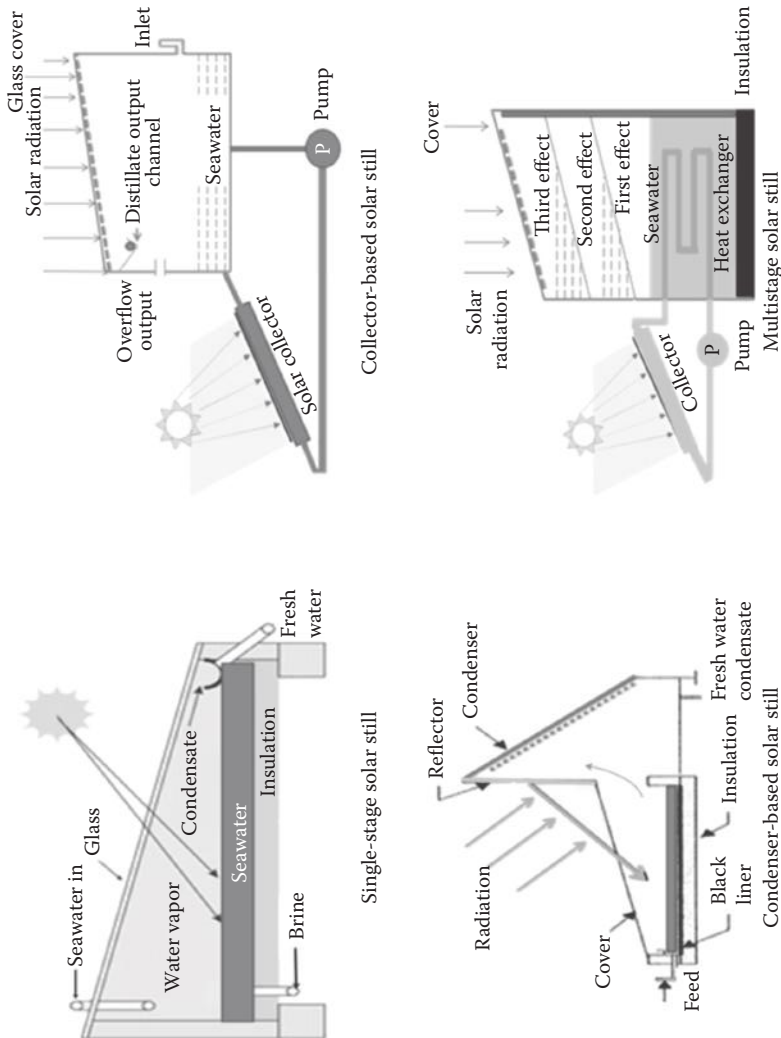


FIGURE 8.53
Different types of solar stills. (From Abutayeh, M. et al., Desalination: Water from water, In *Chapter 11: Solar Desalination*, J. Kucera (ed.), Scrivener/Wiley, Hoboken, NJ, 2014; Li, C. et al., *Renewable and Sustainable Energy Review*, 19, 136–163, 2013a.)

with flat-plate or concentrating solar collectors and integrating the passive vacuum method into solar stills provide different techniques to increase the feasibility of solar stills. Solar stills are relatively inexpensive and easy to maintain, which makes them a viable option for underdeveloped communities with good solar resource.

The stills used to date are called shallow basin-type stills and Figure 8.54 illustrates their method of operation. The still is irradiated by direct and diffuse solar radiation I_s as well as some infrared radiation I_i from the surroundings. The long-wavelength radiation is absorbed by the glass, but $\tau_{s,g}I_s$ of the solar radiation reaches the saline water; $\tau_{s,w}\tau_{s,g}I_s$ reaches the bottom of the trough where $\alpha_{s,t}\tau_{s,g}\tau_{s,w}I_s$ is absorbed per unit still area. A value of 0.8 has been suggested as a reasonable approximation for $\alpha_{s,t}\tau_{s,w}\tau_{s,g}$ if good glass, a blackened tray surface, and a 0.2-m-thick layer of water are used (Dunkle 1961). Typical shallow basin stills are 1.5 m wide, 2–25 m long, and approximately 0.2 m deep; the glass roof should have a slope of 10°–15°.

Of the energy absorbed at the bottom, one part $q_{k,s}$ is lost through the insulation by conduction, while the other part will be transferred to the saline water in the still tray above. Of the latter portion, some will heat the water, if the water temperature is less than the tray temperature, while the rest is transferred from the surface of the water by free convection, radiation, and evaporation to the underside of the glass cover. Some of this heat passes through the glass by conduction and is transferred from the outer surface of the glass cover by convection and radiation to the surrounding atmosphere. The thermal circuit for this system is shown in Figure 8.55.

To obtain the greatest yield, the rate of evaporation of water, which is proportional to q_e , should be as large as possible. An inspection of the thermal circuit shows that to achieve large values of q_e , $\tau_{s,g}\tau_{s,w}\alpha_{s,t}I_s$ should be as large as possible, while $q_{c,s}$, $q_{r,s}$, and $q_{k,s}$ should be as small as possible. To achieve these results, the transmittance of the glass cover and the absorptance of the tray surface must be large, and the bottom of the tray should be well

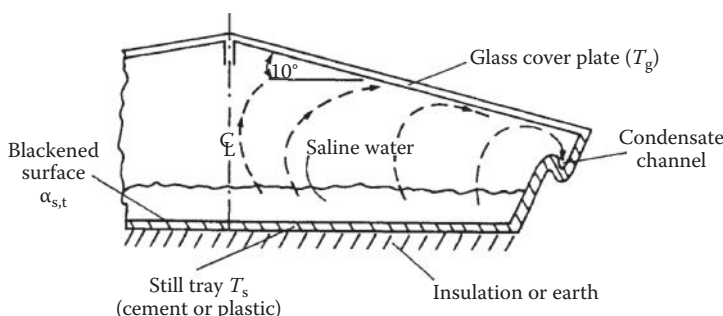


FIGURE 8.54

Sketch of shallow basic-type solar still.

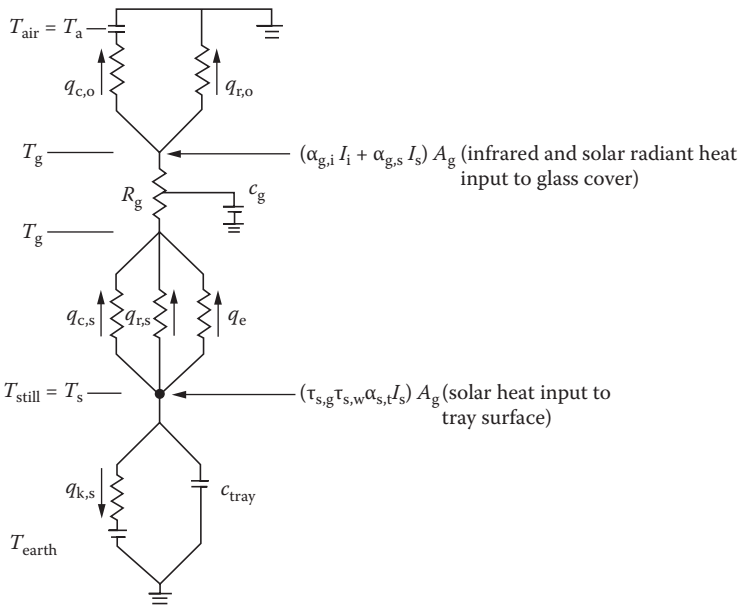


FIGURE 8.55
Thermal circuit for solar still.

insulated. Obviously, the amount of solar irradiation should be as large as possible.

In order to analyze the thermal performance, heat balances must be written for the glass cover and the tray, and the resulting equations must be solved simultaneously to obtain the tray and glass cover temperatures. The objective is to obtain the thermal efficiency, defined as the ratio of the energy used in evaporating saline water to the incident solar radiation.

If steady-state conditions prevail, the glass resistance R_g is neglected, and the water temperature is assumed equal to the tray temperature, a heat balance on the glass cover gives

$$q_e + q_{r,s} + q_{c,s} + \alpha_{g,i} I_i A_g + \alpha_{g,s} I_s A_g = q_{c,o} + q_{r,o}, \quad (8.56)$$

where

$q_{r,s}$ = rate of heat transfer by radiation from the water in the tray to the inner surface of the glass = $A \bar{h}_{r,s} (T_s - T_g)$,

$$\bar{h}_{r,s} = \sigma (T_s^2 + T_g^2) (T_s + T_g) / (1/\varepsilon_w + 1/\varepsilon_g - 1),$$

$q_{c,s}$ = rate of heat transfer by convection from water to the inner surface of the glass = $A \bar{h}_{r,s} (T_s - T_g)$,

$q_{c,o}$ = rate of convection heat loss from the glass to the ambient air = $A\bar{h}_{c,o}(T_g - T_a)$,

$q_{r,o}$ = rate of radiation heat loss from the glass = $A\bar{h}_{r,o}(T_g - T_a)$, and
 $\bar{h}_{r,o} \approx \epsilon_g \sigma(T_g^2 + T_a^2)(T_g + T_a)$.

Similarly, a heat balance on the saline water gives

$$\alpha_{s,t}\tau_{s,g}\tau_{s,w}I_s = q_k + q_{c,s} + q_{r,s} + q_e \quad (8.57)$$

In the enclosed space between the water surface and the glass cover, heat and mass transfer occur simultaneously as brine is evaporated, condenses on the lower surface of the cooler glass, and finally flows into the condensate channel. Since the glass cover is nearly horizontal, the correlations developed in Chapter 3 for free convection between parallel plates can be used to calculate the Nusselt number and heat-transfer coefficient. However, because heat and mass transfer occur simultaneously in the still, the buoyancy term in the Grashof number must be modified to take account of the density gradient resulting from composition as well as temperature. As shown in Battleson (1981), in horizontal enclosed air spaces in the range $3 \times 10^5 < \text{Gr}_L < 10^7$, the relationship

$$\text{Nu} = \frac{\bar{h}_c L}{k} = 0.075 \left(\frac{L^3 \rho^2 g \beta_T \Delta T}{2} \right)^{\frac{1}{3}}, \quad (8.58)$$

can be used to calculate the heat-transfer coefficient if ΔT is considered an equivalent temperature difference between the water and the glass cover and includes the molecular weight difference resulting from the change in vapor concentration in evaluating the buoyancy. For an air–water system, $\Delta T'$ is given by Dunkle (1961) in English units.

$$\Delta T' = (T_s - T_g) + \frac{p_{w,s} - p_{w,g}}{39 - p_{w,s}} T_s, \quad (8.59)$$

where $p_{w,s}$ is the partial pressure of water (in psia) at the temperature of the water surface T_s and $p_{w,g}$ is the vapor pressure of water in psia at the temperature of the glass cover T_g .

Since the size of the still does not affect the heat-transfer coefficient in the Grashof number range of interest, \bar{h}_c in Equation 8.58 can be approximated by evaluating all physical constants at an average still temperature or

$$h_c = 0.13 (T_s - T_g) + \frac{p_{w,s} - p_{w,g}}{39 - p_{w,s}} T_s^{\frac{1}{3}}. \quad (8.60)$$

The rate of heat transfer by convection between the water and the glass is then

$$q_c = \bar{h}_c A_s (T_s - T_g), \quad (8.61)$$

and, using the analogy between heat and mass transfer, the rate of mass transfer q_m (in lb/h) is

$$q_m = 0.2 \bar{h}_c A_s (p_{w,s} - p_{w,g}). \quad (8.62)$$

The heat-transfer rate resulting from evaporation q_e (in Btu/h) equals the rate of mass transfer times h_{fg} , the latent heat of evaporation at T_g , or

$$q_e = 0.2 \bar{h}_c A_s (p_{w,s} - p_{w,g}) h_{fg}. \quad (8.63)$$

If the tray of the still is resting on the ground, the conduction loss is difficult to estimate because it depends on the conductivity of the earth, which varies considerably with moisture content. If the bottom of the tray is insulated and raised above the ground, the preferable arrangement, unless too expensive, the bottom heat loss is given by

$$q_k = U_b A_s (T_s - T_a), \quad (8.64)$$

where the bottom conductance U_b is composed of the tray insulation and the free convection elements in series and can be calculated by the methods given in Chapter 3.

Since $p_{w,s}$ and $p_{w,g}$ in Equations 8.59 and 8.60 are functions of T_s and T_g , respectively, Equations 8.56 and 8.57 can be solved simultaneously for T_s and T_g , provided I_s and all the physical properties are known. However, this approach is more complex than assuming a still temperature and solving for T_g and I_s .

Example 8.8

For a solar still operating at a brine temperature of 155°F (410 K) in ambient air at 76°F (298 K) with a bottom conductance $U_b = 0.3 \text{ Btu/h}\cdot\text{ft}^2\cdot^\circ\text{F}$ (1.7 W/m²°C), and $(1/\epsilon_g + 1/\epsilon_w - 1) = 0.9$, calculate the rates of heat transfer by convection q_c , radiation q_r , and conduction q_k , and the rate of evaporation per unit still area q_e . Then, calculate the still efficiency.

Solution

First, the temperature of the glass cover is calculated from Equation 8.56 (the partial pressure of water vapor was obtained from Keenan and Keys

1956). This temperature is found to be 135°F (390.5 K) and the various heat fluxes are shown below:

$$\begin{aligned} q_{c,s}/A_s & \text{ convection flux from brine} = 10 \text{ Btu/h}\cdot\text{ft}^2 (31.5 \text{ W/m}^2). \\ q_e/A_s & \text{ rate of evaporation per unit area} = 158 \text{ Btu/h}\cdot\text{ft}^2 (497 \text{ W/m}^2). \\ q_{r,s}/A_s & \text{ radiation flux from brine} = 28 \text{ Btu/h}\cdot\text{ft}^2 (88 \text{ W/m}^2). \\ q_{k,x}/A_s & \text{ conduction back loss flux} = 23 \text{ Btu/h}\cdot\text{ft}^2 (72 \text{ W/m}^2). \\ \alpha_{s,t} \tau_{s,g} \tau_{s,w} I_s & = 219 \text{ Btu/h}\cdot\text{ft}^2 (689 \text{ W/m}^2). \\ I_s & = 219/0.8274 \text{ Btu/h}\cdot\text{ft}^2 (863 \text{ W/m}^2). \end{aligned}$$

The thermal efficiency is then

$$\eta = \frac{q_e}{I_s} = \frac{158}{274} = 58\%.$$

A potentially important factor omitted in the preceding analysis is the effect of air leakage. It increases with increasing temperature and can also be accelerated by high wind. Leakage should be minimized for good performance.

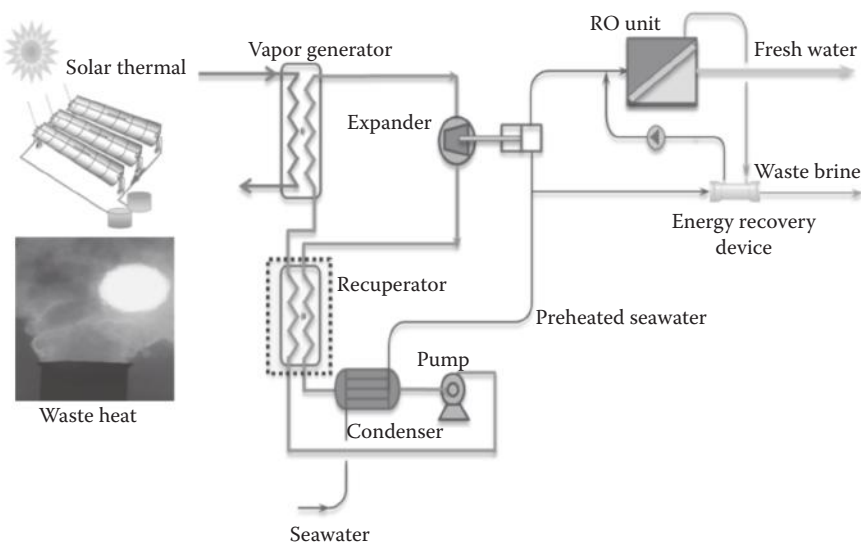
The maximum performance of a still is limited by the heat of vaporization of water and the solar insolation. Under favorable conditions with $I_s = 250 \text{ Btu/h}\cdot\text{ft}^2 (789 \text{ W/m}^2)$, $\eta_s = 40\%$, and $h_{fg} = 1000 \text{ Btu/lb (2326 kJ/kg)}$, 1 ft² of still can provide 0.1 lb of water per hour, or approximately 1 lb/day. Thus, approximately 10 ft² (1 m²) is required for a production rate of 1 gal/day (~3.8 L/day) and 27 ft² (~2.5 m²) of still would be required to produce 1000 gal/year (~3800 L/year).

8.10.1 Solar-Driven Reverse Osmosis

Osmosis is a natural phenomenon in which water passes through a membrane from a lower-concentration to a higher-concentration solution. The flow of water can be reversed if a pressure larger than the osmotic pressure is applied on the lower-concentration side. Reverse osmosis (RO) is the most common desalination process because of its superior energy efficiency compared to thermal desalination systems (Childs et al. 1999; Li et al. 2013a). However, RO uses mechanical energy/electricity as the energy source, which has to be generated by either PV arrays or solar heat engines.

PV-powered RO desalination is common in demonstration plants because of the modularity and scalability of both PV and RO systems (Alajlan and Smiai 1996; Alawaji et al. 1995; Hasnain and Alajlan 1998). Economic and reliability considerations are the main challenges to improving PV-powered RO desalination systems (Thomson and Infield 2005; Tzen et al. 2008). Solar thermal-assisted RO desalination is even further away from commercialization (Li et al. 2012).

However, the advantage of coupling a power cycle with RO is that seawater provides a heat sink for the power cycle condenser while it is being pre-heated to increase the RO membrane permeability leading to reduced power

**FIGURE 8.56**

Schematic of solar power cycle–driven RO system. (From Li, C. et al., *Applied Energy*, 102, 1071–1080, 2012; Li, C. et al., *Desalination*, 318, 107–117, 2013b.)

consumption and reduced thermal pollution (Li et al. 2013b). Furthermore, waste heat from a conventional power cycle could be used at night while solar energy is used during the day, so that the power cycle–RO system could provide consistent power and water, which are crucial for many remote areas, as shown in Figure 8.56.

Flat-plate, evacuated tube, or concentrating solar collectors may be used to heat the working fluid of the power cycle and a fraction of the mechanical energy generated by the power cycle could be used to drive the attached RO desalination system. The energy recovery device (ERD) recovers a part of the pressure head of the remaining brine to prepressurize the feedwater, which would otherwise be wasted.

8.10.2 RO Mathematical Model

The work required for the RO process with an ERD may be estimated by (Li et al. 2012)

$$W_{SWRO} = \frac{V_{\text{fresh}} * P_{\text{sea}}}{\eta_{\text{pump}}} + \Delta P * 1 + \frac{1}{\alpha} - 1 * (1 - \eta_{\text{ERD}}) , \quad (8.65)$$

where α is the seawater desalination system recovery ratio and ΔP is the overpressure above the osmotic pressure that drives the water flow through

the membrane. P_{sea} is the osmotic pressure given by the van't Hoff equation: $P_{\text{sea}} = cRT$, where c is the ionic molar concentration, R is the gas constant, and T is the absolute temperature. $\frac{P_{\text{sea}}}{1-\alpha}$ is the pressure used to overcome the concentrated brine osmotic pressure. The units of W , P , and V are kilojoules, kilopascals, cubic meters (or m^3/s if using flow rate), respectively; η_{pump} is the high-pressure pump efficiency, V_{fresh} is the fresh water volume, $\frac{V_{\text{fresh}}}{\alpha}$ is the total seawater pumped by the pump, and η_{ERD} is the efficiency of the ERD. The recovery rate ranges from 30% to 60% for RO.

Example 8.9

Consider a small RO desalination system driven by a series of solar collectors that provide heat. Preheated seawater is desalinated with a 50% recovery rate, which implies that 50% of the seawater turns to potable water and the rest is rejected into the sea. Assume that the organic working fluid of the power cycle is condensed at 37°C by the feed seawater that heats up from 25°C to 32°C .

Solution

The small RO system is simulated with the Dow Chemical Reverse Osmosis System Analysis (ROSA72). The simulated system is a single-stage RO system using 10 pressure vessels in each stage and seven elements in each vessel. Details of the small RO unit are not required to be understood but are available in Table 8.9. The feed seawater peak flow rate is 22.08 L/s and the Dow Chemical's FILMTEC SW30XHR-400i RO membrane is used. When the feed seawater temperature rises, the permeated total dissolved solids (TDS) of the RO increase. In this study, effluents with a TDS level higher than that of US average tap water TDS (approximately 350 mg/L) were not considered. The temperature correction factor (TCF) for the membrane is

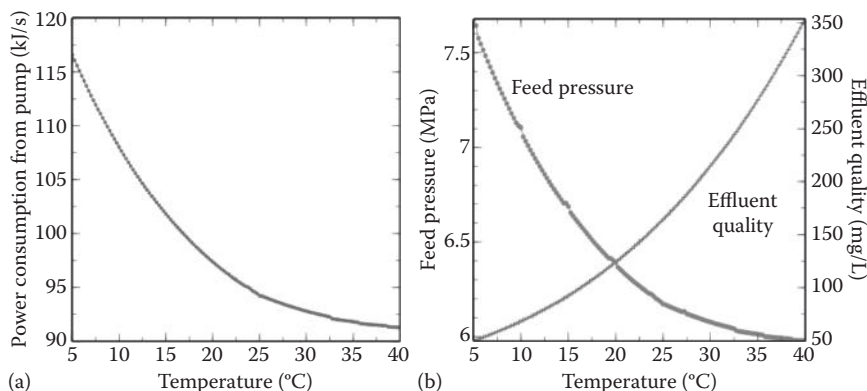
$$\text{TCF} = \text{EXP}[2640^* \frac{1}{298} - \frac{1}{T + 273.15}] ; \text{ when } T \geq 25^\circ\text{C} \quad (8.66)$$

$$\text{TCF} = \text{EXP}[3020^* \frac{1}{298} - \frac{1}{T + 273.15}] ; \text{ when } T \leq 25^\circ\text{C} \quad (8.67)$$

The energy consumption of the RO system with respect to the seawater temperature is shown in Figure 8.57a. The required RO pressure and effluent water quality are shown in Figure 8.57b. It can be seen that both the RO pressure and the energy consumption decrease when the seawater temperature increases, which is due to the increased flux through the membranes at higher temperatures. With the increased flux, the effluent

TABLE 8.9
Design Parameters of the RO Unit

Seawater TDS	35,240 mg/L
Water classification	Seawater (well/MF) SDI < 3
RO feedwater temperature	32°C
Seawater recovery	50.00%
Element type	SW30XHR-440i
Maximum operating pressure	8.3 MPa
Stage	1
Pressure vessels per stage	10
Elements per pressure vessel	7
Average flux	0.23 L/m ² ·min
Power consumption with ERD	92.356 kJ/s
Raw seawater flow to the system	22.08 L/s
Feed pressure	6.048 MPa
Total active area	2861 m ²
Concentrate pressure	5.96 MPa
Concentrate TDS	70,244.42 mg/L
High-pressure efficiency	0.8
Energy recovery device efficiency	0.9

**FIGURE 8.57**

(a) Power consumption of the designed RO versus seawater temperature; (b) RO system pressure and effluent TDS versus seawater temperature.

water quality decreases; nevertheless, the effluent TDS still meets the average US tap water quality. The changes in RO pressure and energy consumption are more dramatic at lower seawater temperatures, indicating the necessity of seawater preheating at low temperatures. Heated from 5°C to 32°C, the energy consumption is reduced by as much as 26.23%, while heated from 25°C to 32°C, the reduction is only 2.02%.

Note that with seawater preheated to 32°C, the RO system's pressure requirement is 6.048 MPa, the energy consumption is 8.365 kJ/L fresh water generated, and the effluent TDS is 238 mg/L. Both the RO fresh water and discharged brine are at 0.137 MPa.

8.11 Nonconvecting Solar Ponds

The nonconvecting solar pond is a horizontal-surfaced solar collector using the absorption of solar radiation at the bottom of a 1- or 2-m-deep body of water to generate low-temperature heat. Since heat storage is an integral part of ponds, they have promise in some parts of the world for continuous energy delivery to process or space-conditioning systems. Modern solar ponds were first studied scientifically in Israel by Tabor (1963, 1966). This section describes ponds in which a temperature substantially above ambient—by 50 K or more—may be achieved.

8.11.1 Introduction

When solar energy enters a pond, the infrared component is absorbed within a few centimeters, near the surface, since water is opaque to long-wave radiation. The visible and ultraviolet components of sunlight can penetrate clear water to a depth of several meters. These radiation components can be absorbed at the bottom of the pond by a dark-colored surface. The lowest layer of water is then the hottest and would tend to rise because of its relatively lower density if measures were not taken to prevent it.

In nonconvecting solar ponds, the water at the bottom is made heavier than that at the top by dissolving salt in the water as shown in Figure 8.58. The concentration of salt is decreased from bottom to top so that the natural

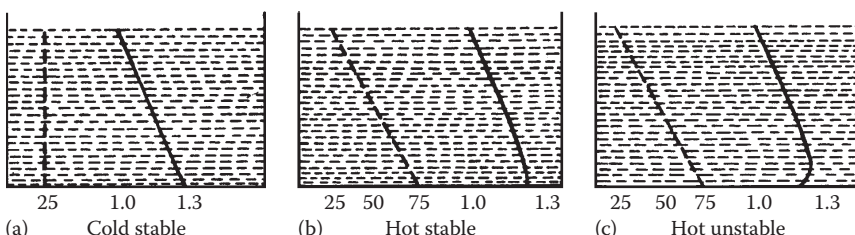
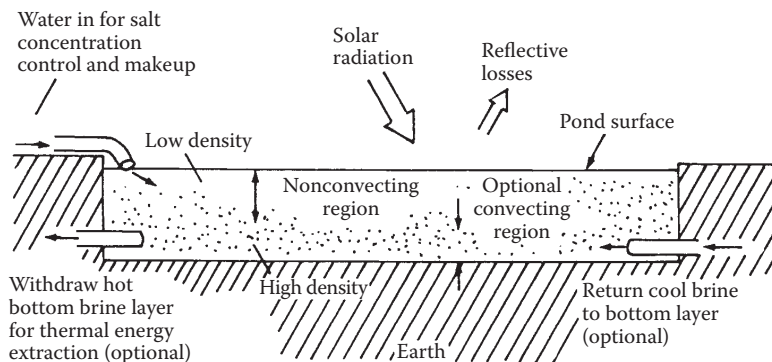


FIGURE 8.58

Density gradients in a solar pond. If the gradient is positive when cold (a), it becomes less positive when heated (b); if the lowest layers become too hot, the density profile may reverse (c) and the onset of convection will follow. Dashed lines represent temperature profiles and the solid lines represent density profiles (units are °C and g/cm³).

**FIGURE 8.59**

Schematic diagram of a nonconvection solar pond showing conduits for heat withdrawal, surface washing, and an optional convecting zone near the bottom.

tendency of ponds to mix by the creation of convection currents is effectively eliminated if the density gradient is adequate.

Since stationary water is quite an effective insulator, it is possible for the lowest layers of a well-designed solar pond to boil. Boiling, of course, must be avoided, for it destroys the stable density gradient. Therefore, the design of a solar pond for heat generation must involve a mechanism for useful heat removal in sufficient quantity to avoid boiling (Figure 8.59).

Since solar ponds are usually envisioned to be on the order of hectares in size, a heat-exchanger pipe network using a separate working fluid is impractical. However, hydrodynamic principles predict that a layer of fluid could be removed slowly from the bottom of the pond without disturbing the main body of water. This is evidenced on a large scale by the ability of ocean currents—Gulf Stream, Benguela Current, and so on—to retain their identity over thousands of miles. The fluid in the removed layer of a pond is then passed through a heat exchanger for useful heat removal and returned to the bottom of the pond. Since the returned fluid is cooler than the extracted fluid, the required density gradient is maintained. In practice, the horizontal flows can disturb the hydrostatic equilibrium somewhat, depending on the Reynolds and Froude numbers, and a mixed layer can exist at the pond's bottom. In this layer, convection can occur, although it can be confined to a zone on the order of centimeters. Nielsen (1976) has described a pond in which a convective zone is an intentional feature of the design proposed for space heating.

Several practical difficulties arise during long-term use of solar ponds in the field. Since a salinity gradient exists, diffusion of salt from regions of high concentration to low concentration occurs naturally. Hence, the density gradient required for hydrostatic stability tends to destroy itself. This diffusion can amount to 60 tons/km²xd (Tabor 1966). To maintain the gradient, it is necessary to supply salt to the bottom of the pond and to wash the surface with a weak brine solution. The supply of salt to a pond is a major

maintenance cost for this type of solar collector. Tabor (1966) has suggested an idea whereby the bottom layer of a pond is decanted, partially evaporated, and returned to the pond bottom. Simultaneously, water is added to the top of the pond to replace that evaporated from the layer. As a result, the net flow of water is downward, and the *relative* flow (diffusion) of salt is upward. By proper matching of these rates, the salt can remain stationary in a fixed frame of reference.

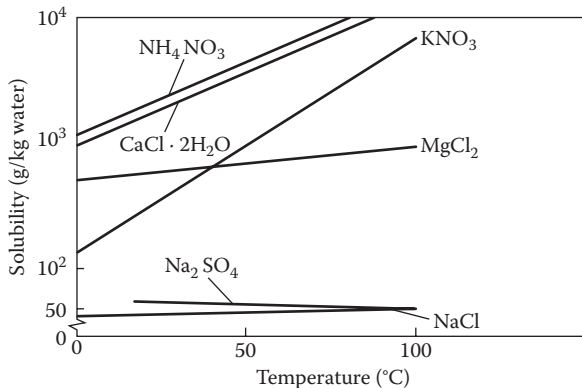
The replacement of water that evaporates naturally from the surface of a pond is a second practical consideration. If water is not replaced at the top, a local reversal of the stable salinity gradient will occur and a convective layer will form at the surface. This is to be avoided, since it destroys a part of the insulation effect of the stagnant pond. Nielsen (1976) proposed the use of a plastic cover over the pond to help maintain the proper gradient. Since reflection of solar radiation from plastic is greater than that for water (see Chapter 3), they also suggest maintaining a thin water layer over the plastic cover.

Other practical matters that must be considered are the effects of wind, waves, rain, and leaks on the pond gradient (halocline). Waves can destroy the halocline and therefore must be controlled. An economical and effective method for this task has yet to be developed. Very severe rainstorms and wind can destroy the surface gradient to a depth of 35–50 cm (Nogawa et al. 1989). A plastic cover could presumably avoid the problem if it could stay intact during severe storms. The problem of dirt in a pond depends on the location of the particles. Either on the surface or suspended within the pond, they reduce solar transmittance and must be removed by withdrawing, filtering, and replacing a layer of the pond. Dirt on the bottom can likewise be removed but may not cause a major problem if left in place. Leaves in a pond should be avoided, since they may float, may lose their color to the water, and may plug fluid circulation machinery and conduits. Algae growth in ponds should be readily controllable by chemical means.

A final feature of a solar pond determines its geographic limits. Since the ponds are horizontal and the sun is low in the sky north or south of the mid-latitudes in winter, ponds must be used near the equator if winter yields are not to be curtailed sharply. Other climatic effects in the tropic—monsoons or storms—must also be considered in finding the best sites for large-scale pond usage.

8.11.2 Solar Pond Stability Criteria

One of the principal costs of a solar pond is the dissolved salt required to establish a stable density gradient. For economical applications, it is essential that no more salt be used than necessary to assure hydrostatic stability. Figure 8.60 shows the solubility of several common salts in water as a function of temperature. Salts like NH_4 , NO_3 , or KNO_3 , whose solutions are as transparent as water, are best for solar ponds, since solubility increases significantly with temperature, thereby ensuring a significant density gradient.

**FIGURE 8.60**

Solubility of some common inorganic salts usable in solar ponds.

Salts such as Na₂SO₄ with the opposite solubility characteristic would not be suitable for ponds.

Weinberger (1964) has established the criteria for the hydrostatic and hydrodynamic stability of large solar ponds. To avoid convection, the fluid density must decrease upward from the bottom; that is,

$$\frac{d\rho}{dz} = \frac{\partial \rho}{\partial s} \frac{ds}{dz} + \frac{\partial \rho}{\partial T} \frac{dT}{dz} \geq 0, \quad (8.68)$$

where s is the salt concentration, ρ is the density, T is the temperature, and z is the vertical coordinate, increasing downward.

However, to avoid the growth of oscillatory motion, a stronger condition is required (Nielsen 1976):

$$\frac{v + K_s}{\rho} \frac{\partial \rho}{\partial s} \frac{ds}{dz} + \frac{v + K_T}{\rho} \frac{\partial \rho}{\partial T} \frac{dT}{dz} \geq 0, \quad (8.69)$$

where v , K_s , and K_T are momentum, salt, and thermal diffusivities, respectively. On the basis of this condition, a convective layer of thickness h will grow if (Nielsen 1976)

$$q_{\text{net}} > 0.89h(\rho c)\sqrt{\frac{K_T}{t}} - \frac{dT}{dz} - \frac{(v + K_s)}{(v + K_T)} \frac{(\partial \rho / \partial s)}{(\partial \rho / \partial T)} \frac{ds}{dz}, \quad (8.70)$$

where t is the time during which heat is absorbed at rate q_{net} in a region of heat capacity (ρc) per unit volume.

If the net heat rate is above that required for convective layer growth, the layer grows in thickness as (Leshuk et al. 1976)

$$h^2 = Cq_{\text{net}} + h^2 (t = 0), \quad (8.71)$$

where

$$C = \frac{2}{(\rho c)[(ds/dz)(\partial p/\partial s)/(\partial p/\partial T) + dT/dz]} . \quad (8.72)$$

If the heat rate q_{net} is less than the critical value from Equation 8.70, the convective layer may not decrease, as is the case in many other hydrodynamic phenomena. This is a result of the much greater numerical value of thermal diffusivity compared with salt diffusivity. Nielsen and Rabl (1976) have shown that the salinity gradient needed to stabilize a convective zone is about five times that required to maintain a stagnant zone. A density difference of 25% has successfully stabilized ponds in practice.

8.11.3 Thermal Performance of Solar Ponds

In a solar pond, solar radiation is partially reflected at the surface, partially absorbed in the water, and partially absorbed at the bottom. The absorption of solar energy by water does not follow a simple Bouguer's law since the absorption phenomena differ widely with wavelength. Table 8.10 is a summary of absorption of sunlight in water as a function of wavelength. Absorption in solutions of inorganic salts used in solar ponds is expected to be nearly the same.

The data from Table 8.10 are plotted in Figure 8.61. An adequate curve fit of these data is represented by the sum of several exponential terms. If $\tau(x)$ is the transmittance of water of depth x , it can be related to x by (Nielsen 1976)

$$\tau(x) = \sum_{i=1}^4 a_i e^{-b_i x}, \quad (8.73)$$

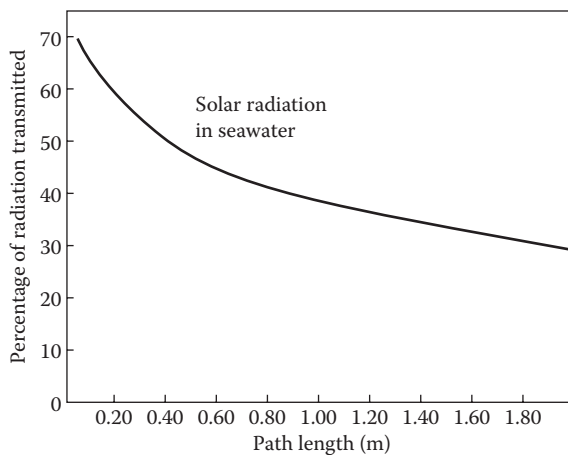
where the regression coefficients a_i and b_i are given in Table 8.11.

Equation 8.73 does not include the infrared spectrum ($\lambda > 1.2 \mu\text{m}$), since it is of no interest in solar pond analysis. As shown in Hipser and Roehm (1976),

TABLE 8.10
Spectral Absorption of Sunlight in Water

Wavelength (μm)	Layer Depth				
	0	1 cm	10 cm	1 m	10 m
0.2–0.6	23.7	23.7	23.6	22.9	17.2
0.6–0.9	36.0	35.3	36.0	12.9	0.9
0.9–1.2	17.9	12.3	0.8	0.0	0.0
1.2 and over	22.4	1.7	0.0	0.0	0.0
Total	100.0	73.0	54.9	35.8	18.1

Note: Numbers in the table show the percentage of sunlight in the wavelength band passing through water of the indicated thickness.

**FIGURE 8.61**

Transmittance of water to solar radiation as a function of the thickness of the water layer. See Table 8.10 for numerical values.

TABLE 8.11

Regression Coefficients a_i and b_i for
Transmittance of Solar Pond (Equation 8.73)

Wavelength (μm)	a_i	$b_i (\times 10^{-3} \text{ cm}^{-1})$
0.2–0.6	0.237	0.32
0.6–0.75	0.193	4.5
0.75–0.90	0.167	30.0
0.90–1.20	0.179	350.0

Reddy (1987), and Washam et al. (1993), a detailed analysis of heat transfer in a solar pond is very complex and must include effects of volumetric absorption, variation of density, and conductivity with salinity.

Figure 8.61 shows that approximately 30% of the incident radiation reaches the absorbing bottom surface of a 2-m solar pond. This represents the upper limit of collection efficiency of a pond. But since the bottom is an imperfect absorber and heat losses occur from the top and bottom surfaces, the thermal efficiency is an inadequate index of solar system viability; economics must be considered. Since solar ponds are presently not in commercial use, their economic analyses are not reliable. However, Rabl and Nielsen (1975) have predicted that solar ponds for building heating may be more economical than fuel oil heating in some areas. Styris et al. (1976) have analyzed solar ponds for process heat as well.

An additional consequence of the data shown in Figure 8.61 should be noted. The insulating effect of the nonconvecting layer in a solar pond increases linearly with depth. In most practical cases (Hipser and Roehm 1976; Reddy 1987; Washam et al. 1993), this insulating effect increases more rapidly than does the attenuation of sunlight because of increased depth. For

example, a 1-m-deep pond that can achieve a no-load temperature of 100°C could achieve a temperature of approximately 180°C if it were 2 m deep. Of course, brine costs increase with pond depth and pond depth should therefore be selected to match the task for which the heat is required.

PROBLEMS

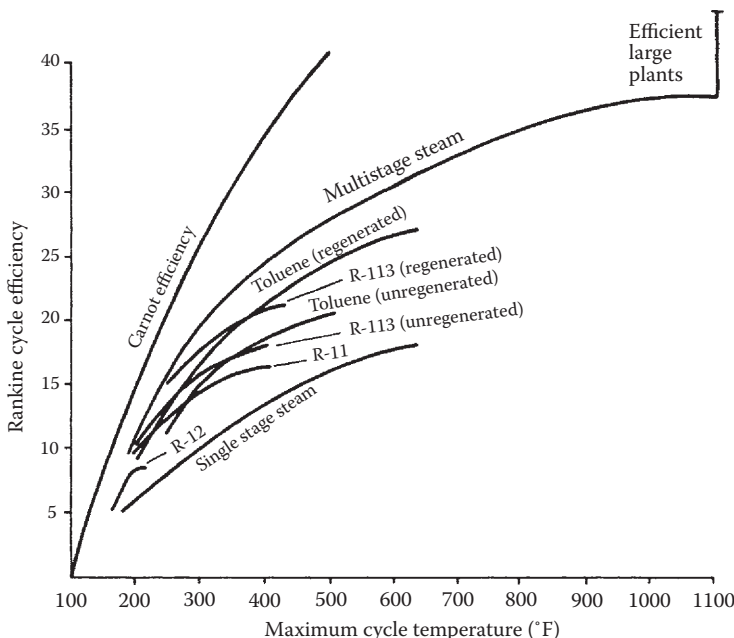
1. A reheat Rankine cycle uses steam as a working fluid. The steam leaves the condenser as saturated liquid. The steam leaves the boiler and enters the turbine at 5 MPa, 350°C. After expansion in the turbine to $P = 1.2$ MPa, the steam is reheated to 350°C and then expands in the low-pressure turbine to $P = 10$ kPa. If the efficiencies of the pump and turbine are 0.9, determine the following:
 - a. Work output from high-pressure turbine per unit mass of working fluid
 - b. Work output from low-pressure turbine per unit mass of working fluid
 - c. Work input to the pump per unit mass of working fluid
 - d. Heat added to the boiler
 - e. Quality of vapor at the exit of high-pressure turbine and low-pressure turbine
 - f. Cycle efficiency
2. A regenerative Rankine cycle uses steam as the working fluid. Steam leaves the boiler and enters the turbine at $P = 5$ MPa, $T = 500^\circ\text{C}$. After expansion to 400 kPa, a part of steam is extracted from the turbine for the purpose of heating the feedwater in the feedwater heater. The pressure in the feedwater heater is 400 kPa and the water leaving it is saturated liquid at 400 kPa. The steam not extracted expands to 10 kPa. Assuming the efficiencies of the turbine and two pumps are 90%, determine the following:
 - a. The fraction of steam extracted to the feedwater heater (f)
 - b. Heat added to the boiler per unit mass of working fluid
 - c. Work obtained from the turbine
 - d. Work for both pumps per unit mass of working fluid
 - e. The cycle efficiency (η)
3. Consider a Stirling cycle from Example 8.4 with imperfect regenerator ($T_R = 230^\circ\text{C}$). Assume ideal gas.
 - a. Compute the efficiency from

$$\eta = \frac{\text{work}_{\text{net}}}{\text{Heat}_{\text{input}}},$$

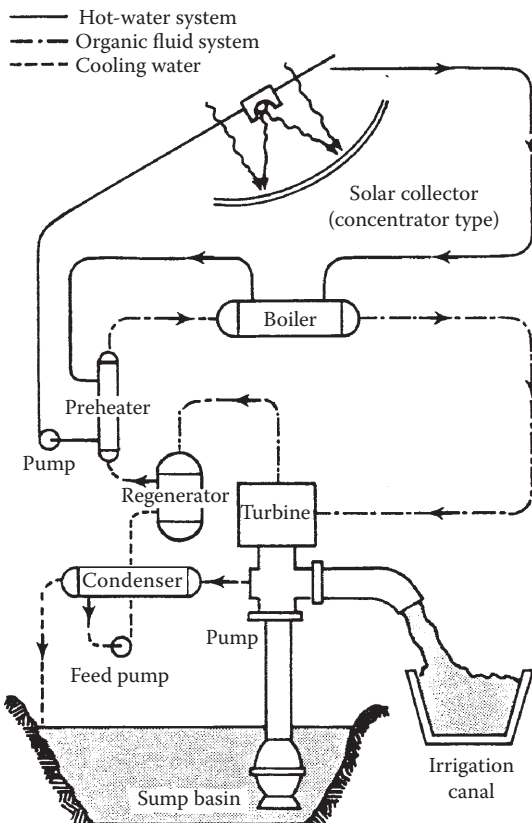
where $\text{Heat}_{\text{input}} = q_{34} + mC_v(T_H - T_R)$.

Verify that the efficiency you get is the same as the efficiency obtained by Equation 8.26.

- b. Start from the efficiency equation above. Derive the efficiency in Equation 8.26.
4. A solar electric engine operating between 5°C and 95°C has an efficiency equal to one-half the Carnot efficiency. This engine is to drive a 4-kW pump. If the collector has an efficiency of 50%, calculate the area needed for operation in Egypt where the insolation averages approximately 2800 kJ/m²×h during the day. State any additional assumptions.
5. The graph below shows the Rankine cycle efficiency as a function of maximum cycle temperature for different working fluids. Prepare a thermal analysis matching a line focusing collector, a paraboloid dish collector, and a CPC collector with a concentration ratio of 3:1 to a suitable working fluid in Washington, D.C., and Albuquerque, New Mexico. Comment on storage needs in both locations. Low-temperature organic and steam efficiencies were computed with the following assumptions: expander efficiency, 80%; pump efficiency, 50%; mechanical efficiency, 95%; condensing temperature, 95°F; regeneration efficiency, 80%; high side pressure loss, 5%; low side pressure loss, 8%.



6. The schematic diagram shown below for a solar-driven irrigation pump was developed by Battelle Memorial Institute and uses tracking PTCs. Solar energy is to heat the water in the collectors to 423 K, which then vaporizes an organic working fluid that powers the pump turbine. Calculate the surface area needed to power a 50-hp pump capable of delivering up to 38,000 L/min of water at noon in Albuquerque, New Mexico. (Answer: 510 m².)



7. Write a closed-form expression for the work output of a solar-powered heat engine if the energy delivery of the solar collector at high temperature is given approximately by the expression

$$q_u = (\tau\alpha)_{\text{eff}} I_c - \frac{\sigma\epsilon\bar{T}_f^4}{\text{CR}},$$

(convection and conduction losses are neglected), where \bar{T}_f is the average fluid temperature and CR is the concentration ratio. Two heat engines are to be evaluated:

a. Carnot cycle:

$$\text{Cycle efficiency } \eta_c = 1 - \frac{T_\infty}{T_f}$$

b. Brayton cycle:

$$\text{Cycle efficiency } \eta_B = 1 - \frac{C_B T_\infty}{T_f}, \quad C_B \geq 1,$$

where $C_B = (r_p)^{(k-1)/k}$ (r_p is the compressor pressure ratio and k is the specific heat ratio of the working fluid).

Write an equation with \bar{T}_f as the independent variable that, when solved, will specify the value of \bar{T}_f to be used for maximum work output as a function of concentration ratio, surface emittance and $(\tau\alpha)_{\text{eff}}$ product, insolation level, and C_B . Optional: solve the equation derived above for $CR = 100$, $\epsilon = 0.5$, and $(\tau\alpha)_{\text{eff}} = 0.70$, at an insolation level of 1 kW/m^2 . What is the efficiency of a solar-powered Carnot cycle and a Brayton cycle for which $C_B = 2$?

8. In a closed-loop S-CO₂ Brayton cycle, CO₂ enters the compressor at 8 MPa and exits at 20 MPa. The turbine inlet temperature is set at 700°C and the temperature of the fluid leaving the cooler is 35°C. The turbine and compressor efficiencies are 90%. If the heat exchanger effectiveness is 0.90, find the cycle efficiency assuming the pressure drop in the pipes is negligible and there is no heat loss to the environment.
9. An external receiver with the following information is used for a central receiver solar thermal power system. Determine the total heat loss and the receiver efficiency if the conduction heat loss is negligible.

Receiver diameter (D) = 5 m

Receiver height (H) = 12 m

Ambient temperature (T_∞) = 35°C

Receiver average surface temperature (T_{wall}) = 520°C

Mean flux density at the receiver surface $q = 300 \frac{\text{kW}}{\text{m}^2}$

Average receiver surface absorptivity (α) = 0.9

Average receiver emissivity (ϵ) = 0.9

Mean wind velocity (V) = 4 m/s

Thermal conductivity at 250°C = $42.363 \times 10^{-3} \frac{\text{W}}{\text{m}\cdot\text{K}}$

Kinematic viscosity at 250°C = $45.37 \times 10^{-6} \text{ m}^2/\text{s}$

10. The optical performance of a heliostat is evaluated in a solar power tower plant at PSA in Almeria, Spain (Lat. 37.43°N). The heliostat is 6.7 m wide and 6.8 m high. The target is a flat plate that is placed at $X = 0$ m, $Y = 0.74$ m, and $Z = 35.16$ m with respect to the origin of the coordinate system at the base of the tower (X pointing to East, Y to North, and Z to the zenith). The plate is 8 m wide and 7.2 m high. The test is performed at 12:53 p.m. on September 7. The coordinates of the heliostat with respect to the tower are as follows: $X = -50.60$ m, $Y = 155.44$ m, and $Z = 6.23$ m. If tracking error and astigmatic effect are negligible, sun shape error is 2.51 mrad, and mirror slope error is 1 mrad, find the optical efficiency of the heliostat. Reflectivity of the heliostat is 90%.
-

References

- Abutayeh, M. et al. 2014. Desalination: Water from water. In Chapter 11: *Solar Desalination*, Ed. J. Kucera. Scrivener/Wiley, Hoboken, NJ.
- Alajlan, S.A., and M.S. Smiai. 1996. Performance and development of PV—Plant for water pumping and desalination for remote area in Saudi Arabia. *Renew. Energy* 8(1–4): 441–446.
- Alawaji, S. et al. 1995. PV-powered water pumping and desalination plant for remote areas in Saudi Arabia. *Applied Energy* 52(2–3): 283–289.
- American Society of Mechanical Engineers (ASME). 2004. ASME B31.1-2004. American National Standard, ASME Code for Pressure Piping.
- Angelino, G. 1967. Perspectives for the liquid phase compression gas turbine. *J. Eng. Power Trans. ASME* 89: 229–237.
- Angelino, G. 1968. Carbon dioxide condensation cycles for power production. *J. Eng. Power* 90: 287–295.
- Angelino, G. 1969. Real gas effects in carbon dioxide cycles. ASME Paper No. 69-GT-103, ASME, New York.
- Ávila-Marín, A.L. 2011. Volumetric receivers in solar thermal power plants with central receiver system technology: A review. *Sol. Energy* 85(5): 891–910.
- Batteson, K.W. 1981. Solar power tower design guide: Solar thermal central receiver power systems. A source of electricity and/or process heat. NASA STI/Recon Tech. Report N81(1981): 31670.
- Becker, M. et al. 2006. Theoretical and numerical investigation of flow stability in porous materials applied as volumetric solar receivers. *Sol. Energy* 80(10): 1241–1248.
- Bertocchi, R., J. Karni, and A. Kribus. 2004. Experimental evaluation of a non-isothermal high temperature solar particle receiver. *Energy* 29(5–6): 687–700.
- Besarati, S.M., and D.Y. Goswami. 2013. Analysis of advanced supercritical carbon dioxide power cycles with a bottoming cycle for concentrating solar power applications. *J. Sol. Energy Eng., Trans. ASME* Vol. 136, No. 1. doi:10.1115/1.4025700.
- Bohn, M.S., T. Williams, and H.W. Price. 1995. Combined cycle power tower. *Solar Engineering*. ASME Solar Energy Conference. ASME, New York, pp. 597–606.
- Buck, R. et al. 2002. Solar-hybrid gas turbine-based power tower systems (REFOS). *J. Sol. Energy Eng.* 124(1): 2.

- Buck, R., and E. Teufel. 2009. Comparison and optimization of heliostat canting methods. *J. Sol. Energy Eng.* 131(1): 011001.
- Chen, H., D.Y. Goswami, and E. Stefanakos. 2010. A review of thermodynamic cycles and working fluids for the conversion of low grade heat. *Renew. Sustain. Energy Rev.* 14(9): 3059–3067.
- Childs, W.D. et al. 1999. VARI-RO solar-powered desalting technology. *Desalination* 125(1–3): 155–166.
- Collado, F.J. 2010. One-point fitting of the flux density produced by a heliostat. *Sol. Energy* 84: 673–684.
- Collado, F.J., A. Gomez, and J.A. Turegano. 1986. An analytic function for the flux density due to sunlight reflected from a heliostat. *Sol. Energy* 37(3): 215–234.
- Collado, F.J., and J.A. Turegano. 1989. Calculation of the annual thermal energy supplied by a defined heliostat at field. *Sol. Energy* 42(2): 149–165.
- Daniels, F. 1949. Solar energy. *Science* 109: 51–57.
- Daniels, F. 1964. *Direct Use of the Sun's Energy*. Yale University Press, New Haven, CT.
- DeLaquil, III, P. et al. 1993. Solar thermal electric technology. In *Renewable Energy-Sources for Fuels and Electricity*, Eds. T. Johansson et al. Island Press, Washington, DC, pp. 213–296.
- Dostal, V., P. Hejzlar, and M.J. Driscoll. 2006. The supercritical carbon dioxide power cycle: Comparison to other advanced power cycles. *Nucl. Technol.* 154(3): 283–301.
- Dunkle, R.V. 1961. Solar water distillation: The roof type still and a multiple effect diffusion still. *Proc. 1961 International Heat Transfer Conf.*, American Society of Mechanical Engineers, New York.
- Feher, E.G. 1967. Supercritical thermodynamic power cycle. *Proceeding of the IECEC*, Florida.
- Fend, T. 2010. High porosity materials as volumetric receivers for solar energetics. *Opt. Appl.* 11(2): 271–284.
- Fend, T. et al. 2004. Porous materials as open volumetric solar receivers: Experimental determination of thermophysical and heat transfer properties. *Energy* 29(5–6): 823–833.
- Fitzgerald, A.E., C.F. Kingsley, and A. Kusko. 1971. *Electric Machinery*, 3rd edition. McGraw-Hill, New York.
- Francia, G. 1968. Pilot plants of solar steam generating stations. *Sol. Energy* 12: 51–64.
- Garcia, P., A. Ferriere, and J.-J. Bezan. 2008. Codes for solar flux calculation dedicated to central receiver. *Sol. Energy* 82: 189–197.
- Goswami, D.Y. 1995. Solar thermal power: Status of technologies and opportunities for research. *Proc. of ASME Heat and Mass Transfer Conference*, Surathkal, India, December.
- Goswami, D.Y. 1998. Solar thermal power technology: Present status and ideas for the future. *Energy Sources* 20: 137–145.
- Goswami, D.Y., and F. Kreith (eds.). 2007. *Energy Conversion*. CRC Press, Boca Raton, FL.
- Goswami, D.Y., S. Hingorani, and G. Mines. 1991. A laser-based technique for particle sizing to study two-phase expansion in turbines. *J. Sol. Energy Eng., Trans ASME* 113(3): 211–218.
- Gupta, B.P. 1985. Status and progress in solar thermal research and technology. In *Progress in Solar Engineering*, Ed. D.Y. Goswami. Hemisphere Publishing Corporation, Washington, DC.

- Hasnain, S.M., and S.A. Alajlan. 1998. Coupling of PV-powered RO brackish water desalination plant with solar stills. *Desalination* 116(1): 57–64.
- Hildebrandt, A.F., and L.L. Vant-Hull. 1974. Tower top focus solar energy collector. *Mech. Eng.* 23(9): 23–27.
- Hipser, M.S., and R.F. Roehm. 1976. Heat transfer considerations of a non-convecting solar pond heat exchanger. ASME Paper 76-WA/Sol-4, ASME, New York.
- Ho, C. 2008. Software and codes for analysis of concentrating solar power technologies. SAND2008-8053. Sandia National Lab., Albuquerque, NM.
- Japikse, D., and C.B. Nicholas. 1994. *Introduction to Turbomachinery Concepts*. ETI, Norwich, VT.
- Jones, S.A. 1996. A comparison of on-axis and off-axis heliostat alignment strategies. Report SAND96-0566C. Sandia National Lab., Albuquerque, NM.
- Kagawa, N. et al. 1989. Mechanical analysis and durability for a 3KW Stirling engine. *Proc. of the 24th IECEC Conference*, Vol. 5, IEEE, NY, August 6–11, pp. 2369–2374.
- Kakaç, S., R.K. Shah, and W. Aung. 1987. *Handbook of Single-Phase Convective Heat Transfer*. John Wiley & Sons, New York.
- Kalina, A.I. 1984. Combined cycle system with novel bottoming cycle. *J. Eng. Gas Turbines Power* 106: 737–742.
- Kalina, A.I., and M. Tribus. 1992. Advances in Kalina cycle technology (1980–91), Part I: Development of a practical cycle, energy for the transition age. *Proc. of FLOWERS '92*, Nova Science Publishers, pp. 97–109.
- Karni, J. et al. 1998a. A high-pressure window for volumetric solar receivers. *J. Sol. Energy Eng.* 120(2): 101.
- Karni, J. et al. 1998b. The “porcupine”: A novel high-flux absorber for volumetric solar receivers. *J. Sol. Energy Eng.* 120(2): 85.
- Keenan, J.H., and F.G. Keys. 1956. *Thermodynamic Properties of Steam*. John Wiley & Sons, New York.
- Kelly, B., and D. Kearney. 2006. Parabolic trough solar system piping model. Tech. Rep., National Renewable Energy Laboratory, NREL/SR-550-40165, July, Golden, CO.
- Kistler, B.L. 1986. A user’s manual for DELSOL3: A computer code for calculating the optical performance and optimal system design for solar thermal central receiver plants. Sandia Report, SABD86-8018, Sandia National Lab., Albuquerque, NM.
- Kolb, G.J. et al. 2007. Heliostat cost reduction study. Sandia Report, SAND2007-3293, June, Sandia National Lab., Albuquerque, NM.
- Kouremenos, D.A., E.D. Rogdakis, and K.A. Antonopoulos. 1994. Cogeneration with combined gas and aqua-ammonia absorption cycles. In *Thermodynamics and the Design, Analysis, and Improvement of Energy Systems*, Vol. 33. American Society of Mechanical Engineers, Advanced Energy Systems Division (Publication) AES, ASME, New York, pp. 231–238.
- Kreith, F., and D.Y. Goswami (eds.). 2004. *The CRC Handbook of Mechanical Engineering*. CRC Press, Boca Raton, FL.
- Kröger, D. 2004. *Air-Cooled Heat Exchangers and Cooling Towers: Thermal-Flow Performance Evaluation and Design*, Vol. 2. Pennwell Corp., Tulsa, OK.
- Landman, W., and P. Gauché. 2013. Influence of canting mechanism and facet profile on heliostat field performance. *Energy Procedia* 49(2014): 126–135.
- Lemmon, E.W., M.O. McLinden, and M.L. Huber. 2002. NIST reference fluid thermodynamic and transport properties—REFPROP, NIST standard reference database 23. NIST, Boulder CO.

- Leshuk, J.P. et al. 1976. Solar pond stability experiments. In *Sharing the Sun*, Vol. 5. ISES, Winnipeg, pp. 188–202.
- Li, C. et al. 2012. Reverse osmosis desalination driven by low-temperature supercritical organic Rankine cycle. *Applied Energy* 102: 1071–1080.
- Li, C., Y. Goswami, and E. Stefanakos. 2013a. Solar-assisted seawater desalination: A review. *Renew. Sustain. Energy Rev.* 19: 136–163.
- Li, C. et al. 2013b. Performance investigation of concentrating solar collectors coupled with a transcritical organic Rankine cycle for power and seawater desalination co-generation. *Desalination* 318: 107–117.
- Lipps, F.W., and L.L. Vant-Hull. 1978. A cellwise method for the optimization of large central receiver systems. *Sol. Energy* 20: 505–516.
- Liu, B., K. Chien, and C. Wang. 2004. Effect of working fluids on organic Rankine cycle for waste heat recovery. *Energy* 29(8): 1207–1217.
- Logan, E. 1993. *Turbomachinery: Basic Theory and Applications*. CRC Press, Boca Raton, FL.
- Megyesy, E.F. 2004. *Pressure Vessel Handbook*, 13th edition. Pressure Vessel Publishing, Tulsa, OK.
- Moisseytsev, A., and J.J. Sienicki. 2009. Investigation of alternative layouts for the supercritical carbon dioxide Brayton cycle for a sodium-cooled fast reactor. *Nucl. Eng. Des.* 239(7): 1362–1371.
- Nielsen, C.E. 1976. Experience with a prototype solar pond for space heating. In *Sharing the Sun*, Vol. 5. ISES, Winnipeg, pp. 169–182.
- Nielsen, C.E., and A. Rabl. 1976. Salt requirement and stability of solar ponds. In *Sharing the Sun*, Vol. 5. ISES, Winnipeg, pp. 183–187.
- Nogawa, M. et al. 1989. Development of solar Stirling engine alternator for space experiments. *Proc. of the 24th IECEC Conference*, Vol. 5, IEEE, NY, August 6–11, pp. 2375–2378.
- Poling, B., J. Prausnitz, and J.O. Connell. 2000. *The Properties of Gases and Liquids*. McGraw-Hill.
- Proctor, D., and R.N. Morse. 1975. *Solar Energy for Australian Food Processing Industry*. CSIRO Solar Energy Studies, East Melbourne, Victoria, Australia.
- Rabl, A., and C.E. Nielsen. 1975. Solar ponds for space heating. *Sol. Energy* 17: 1–12.
- Reddy, T.A. 1987. *The Design and Sizing of Active Solar Thermal Systems*. Oxford University Press, Oxford.
- Rogdakis, E.D., and K.A. Antonopoulos. 1991. High efficiency NH₃/H₂O absorption power cycle. *Heat Recovery Syst. CHP* 11(4): 263–275.
- Romero-Alvarez, M., and E. Zarza. 2008. Concentrating solar thermal power. In *Energy Conversion*, Eds. D.Y. Goswami, and F. Kreith. CRC Press, Boca Raton, FL.
- Salisbury, J.K. 1950. *Steam Turbines and Their Cycles*. Robert K. Krieger Publishing, Malabar, FL. Reprint 1974.
- Sargent and Lundy LLC Consulting Group. 2003. Assessment of parabolic trough and power tower solar technology cost and performance forecasts. NREL/SR-550-34440, Golden, CO.
- Schmitz, M. et al. 2006. Assessment of the potential improvement due to multiple apertures in central receiver systems with secondary concentrators. *Sol. Energy* 80(1): 111–120.
- Schwarzbözl, P., M. Schmitz, and R. Pitz-Paal. 2009. Visual HFLCAL- A software tool for layout and optimization of heliostat fields. *SolarPACES*, 2009.
- Siebers, D.L., and J.S. Kraabel. 1984. Estimating convective energy losses from solar central receivers. SAND84-8717. Sandia National Laboratories, Livermore, CA.

- Sproul, E., K. Chavez, and J. Yellowhair. 2011. The development of the heliostat focusing and canting enhancement technique: An optical heliostat alignment tool for the national solar thermal test facility. *Proceedings of the ASME 2011, 5th International Conference on Energy Sustainability*, pp. 1–9.
- Steinfeld, A., and M. Schubnell. 1993. Optimum aperture size and operating temperature of a solar cavity-receiver. *Sol. Energy* 50(1): 19–25.
- Stine, W.B. 2004. Stirling engines. In *The CRC Handbook of Mechanical Engineering*, Eds. F. Kreith, and D.Y. Goswami. CRC Press, Boca Raton, FL.
- Stine, W.B., and R.E. Diver. 1994. A compendium of solar dish/Stirling technology. SAND93-7026. Sandia National Laboratory, Albuquerque, NM.
- Stine, W.B., and R.W. Harrigan. 1985. *Solar Energy Fundamentals and Design: With Computer Applications*. Wiley-Interscience, Hoboken, NJ.
- Styris, D.L. et al. 1976. The nonconvecting solar pond applied to building and process heating. *Sol. Energy* 18: 245–251.
- Tabor, H. 1963. Solar ponds. *Solar Energy* 7: 189–194.
- Tabor, H. 1966. Solar ponds. *Sci. J.* 21: 66–71.
- Talbert, S.G., J.A. Eibling, and G.O.G. Löf. 1970. Manual on solar distillation of saline water. Office of Saline Water, Research and Development Progress Rept. 546. U.S. Department of Interior, Washington, DC.
- Thomson, M., and D. Infield. 2005. Laboratory demonstration of a photovoltaic-powered seawater reverse-osmosis system without batteries. *Desalination* 183(1–3): 105–111.
- Trombe, F. 1956. High temperature furnaces. *Proc. World Symposium on Applied Solar Energy*, Phoenix, Arizona, 1955, Stanford Research Institute, Menlo Park, CA.
- Turchi, C.S. 2009. Supercritical CO₂ for application in concentrating solar power systems. *Proceedings of SCCO₂ Power Cycle Symposium, 2009*, no. Figure 1, pp. 1–5.
- Turchi, C. 2010. Parabolic trough reference plant for cost modeling with the Solar Advisor Model (SAM). Tech. Rep., National Renewable Energy Laboratory (NREL), Golden, CO.
- Turchi, C.S. et al. 2012. Thermodynamic study of advanced supercritical carbon dioxide power cycles for high performance concentrating solar power systems. *Proceedings of the ASME 2012, 6th International Conference on Energy Sustainability ES2012*.
- Tzen, E., D. Theofiloyianakos, and Z. Kologios. 2008. Autonomous reverse osmosis units driven by RE sources experiences and lessons learned. *Desalination* 221(1–3): 29–36.
- Vant-Hull, L.L., and M.E. Izgyon. 2003. Guideline to central receiver system heliostat field optimization. *Adv. Solar Energy* 15: 1–42.
- Vasquez-Padilla, R. 2011. Simplified methodology for designing parabolic trough solar power plants. PhD dissertation, University of South Florida, Tampa, FL.
- Washam, B.M. et al. 1993. *Integrated Solar Combined Cycle Systems (ISCCS) Utilizing Solar Parabolic Trough Technology—Golden Opportunities for the '90s*. Spencer Management Associates, Diablo, CA.
- Weinberger, H. 1964. The physics of the solar pond. *Sol. Energy* 8: 45–56.
- Winter, C.-J., R.L. Sizmann, and L.L. Vant-Hull. 1991. *Solar Power Plants: Fundamentals, Technology, Systems, Economics*. Springer, New York.

9

Photovoltaics

Photovoltaic (PV) conversion is the direct conversion of sunlight into electricity with no intervening heat engine. PV devices are solid state; therefore, they are rugged and simple in design and require very little maintenance. Perhaps the biggest advantage of solar PV devices is that they can be constructed as stand-alone systems to give outputs from microwatts to megawatts. That is why they have been used as the power sources for calculators, watches, water pumping, remote buildings, communications, satellites and space vehicles, and even megawatt-scale power plants. PV panels can be made to form components of a building skin, such as roof shingles and wall panels. With such a vast array of applications, the demand for photovoltaics is increasing every year. In 2012, global PV installations were approximately 32 GW with a cumulative global total of more than 100 GW.

In the early days of solar cells in the 1960s and 1970s, more energy was required to produce a cell than it could ever deliver during its lifetime (Nijs et al. 1997). Since then, dramatic improvements have taken place in the efficiencies and manufacturing methods. In 2008, the energy payback periods were reduced to approximately 2 to 5 years, depending on the location of use (http://en.wikipedia.org/wiki/File:SEPIC_Schematic.gif), while panel lifetimes were increased to more than 30 years. The costs of PV panels have come down to less than \$1.00 per peak watt by 2012.

Historically, the photoelectric effect was first noted by Becquerel in 1839 when light was incident on an electrode in an electrolyte solution (Angrist 1976). Adams and Day first observed the effect in solids in 1877 while working with selenium. Early work was done with selenium and copper oxide by pioneers such as Schottkey, Lange, and Grandahl. In 1954, researchers at RCA and Bell Laboratories reported achieving efficiencies of approximately 6% by using devices made of *p* and *n* types of semiconductors. The space race between the United States and the Soviet Union resulted in dramatic improvements in PV devices. Bube (1960) gives a review of the early developments in PV conversion.

9.1 Semiconductors

A basic understanding of the atomic structure is quite helpful in understanding the behavior of semiconductors and their use as PV energy conversion devices. Any fundamental book on physics or chemistry generally gives adequate background for basic understanding. Böer (1990) presents an in-depth treatment of a number of topics in semiconductor physics.

For any atom, the electrons arrange themselves in orbitals around the nucleus so as to result in the minimum amount of energy. Figure 9.1 shows the distribution of the electrons in various shells and subshells in light elements. In elements that have electrons in multiple shells, the innermost electrons have minimum energy and, therefore, require the maximum amount of externally imparted energy to overcome the attraction of the nucleus and become free. Electrons in the outermost band of subshells are the only ones that participate in the interaction of an atom with its neighboring atoms. If these electrons are very loosely attached to the atom, they may attach themselves with a neighboring atom to give that atom a negative charge, leaving the original atom as a positive charged ion. The positive and negatively charged ions become attached by the force of attraction of the charges, thus forming *ionic bonds*. If the electrons in the outermost band do not fill the band completely but are not loosely attached either, they arrange themselves so that neighboring atoms can share them to make the outermost bands full. The bonds thus formed between the neighboring atoms are called *covalent bonds*.

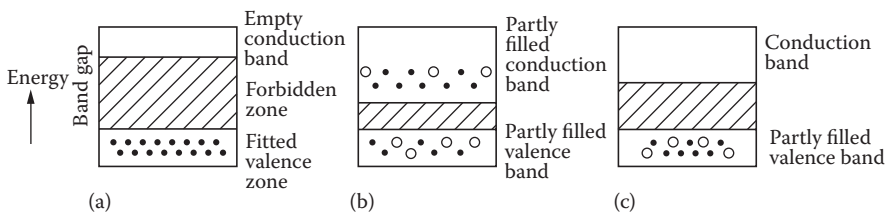
Since electrons in the outermost band of an atom determine how an atom will react or join with a neighboring atom, the outermost band is called the *valence band*. Some electrons in the valence band may be so energetic that they jump into a still higher band and are so far removed from the nucleus that a small amount of impressed force would cause them to move away from the atom. Such electrons are responsible for the conduction of heat and electricity, and this remote band is called a *conduction band*. The difference in the energy of an electron in the valence band and the innermost subshell of the conduction band is called the *band gap*, or the forbidden gap.

Materials whose valence bands are full have very high band gaps (>3 eV). Such materials are called *insulators*. Materials, on the other hand, that have relatively empty valence bands and may have some electrons in the conduction band are good *conductors*. Metals fall in this category. Materials with valence bands partly filled have intermediate band gaps (≤ 3 eV). Such materials are called *semiconductors* (Figure 9.2). Pure semiconductors are called *intrinsic semiconductors*, while semiconductors doped with very small amounts of impurities are called *extrinsic semiconductors*. If the dopant material has more electrons in the valence band than the semiconductor, the doped material is called an *n-type* of semiconductor. Such a material seems to have excess electrons available for conduction even though the material is

Principal quantum number n				1	2		3		4		5				
Azimuthal quantum number l				0	0	1	0	1	2	0	1				
Letter designation of state				1s	2s	2p	3s	3p	3d	4s	4p				
Z	Symbol	Element	V_i Volts												
1	H	Hydrogen	13.60	1											
2	He	Helium	24.58	2											
3	Li	Lithium	5.39	Helium core	1										
4	Be	Beryllium	9.32		2										
5	B	Boron	8.30		2	1									
6	C	Carbon	11.26		2	2									
7	N	Nitrogen	14.54		2	3									
8	O	Oxygen	13.61		2	4									
9	F	Fluorine	17.42		2	5									
10	Ne	Neon	21.56		2	6									
11	Na	Sodium	5.14				1								
12	Mg	Magnesium	7.64				2								
13	Al	Aluminum	5.98	Neon core			2	1							
14	Si	Silicon	8.15				2	2							
15	P	Phosphorus	10.55				2	3							
16	S	Sulfur	10.36				2	4							
17	Cl	Chlorine	13.01				2	5							
18	A	Argon	15.76				2	6							
19	K	Potassium	4.34						1						
20	Ca	Calcium	6.11						2						
21	Sc	Scandium	6.56						1	2					
22	Ti	Titanium	6.83						2	2					
23	V	Vanadium	6.74						3	2					
24	Cr	Chromium	6.76						5	1					
25	Mn	Manganese	7.43						5	2					
26	Fe	Iron	7.90						6	2					
27	Co	Cobalt	7.86	Argon core					7	2					
28	Ni	Nickel	7.63						8	2					
29	Cu	Copper	7.72						10	1					
30	Zn	Zinc	9.39						10	2					
31	Ga	Gallium	6.00						10	2	1				
32	Ge	Germanium	7.88						10	2	2				
33	As	Arsenic	9.81						10	2	3				
34	Se	Selenium	9.75						10	2	4				
35	Br	Bromine	11.84						10	2	5				
36	Kr	Krypton	14.00						10	2	6				

FIGURE 9.1

Electronic structure of atoms. (From Moore, C.E., *Atomic Energy Levels*, Vol. 2. Washington, D.C.: National Bureau of Standards Circular 467, 1952.)

**FIGURE 9.2**

Electrical conduction is described in terms of allowed and forbidden energy bands. Band gap for insulators (a) is the highest, followed by semiconductors (c) and metals (b), respectively.

electronically neutral. For example, silicon has four electrons in the valence band. Atoms of pure silicon arrange themselves in such a way that, to form a stable structure, each atom shares two electrons with each neighboring atom with covalent bonds. If phosphorus, which has five valence electrons (one more than Si), is introduced as an impurity in silicon, the doped material seems to have excess electrons even though it is electrically neutral. Such a doped material is called *n*-type silicon. If, on the other hand, silicon is doped with boron, which has three valence electrons (one less than Si), there seems to be a positive hole (missing electrons) in the structure, even though the doped material is electrically neutral. Such material is called *p*-type silicon. Thus, *n*- and *p*-type semiconductors make it easier for the electrons and holes, respectively, to move in the semiconductors.

9.1.1 *p–n* Junction

As explained earlier, an *n*-type material has some impurity atoms with more electrons than the rest of the semiconductor atoms. If those excess electrons are removed, the impurity atoms will fit more uniformly in the structure formed by the main semiconductor atoms; however, the atoms will be left with positive charges. On the other hand, a *p*-type material has some impurity atoms with fewer electrons than the rest of the semiconductor atoms. Therefore, these atoms seem to have holes that could accommodate excess electrons even though the atoms are electrically neutral (Figure 9.3). If additional electrons could be brought to fill the holes, the impurity atoms would fit more uniformly in the structure formed by the main semiconductor atoms; however, the atoms will be negatively charged.

The above scenario occurs at the junction when a *p* and an *n* type of material are joined together as shown in Figure 9.4. As soon as the two materials are joined, “excess” electrons from the *n* layer jump to fill the “holes” in the *p* layer. Therefore, close to the junction, the material has positive charges on the *n* side and negative charges on the *p* side. The negative charges on the *p* side restrict the movement of additional electrons from the *n* side to the *p* side, while the movement of additional electrons from the *p* side to the

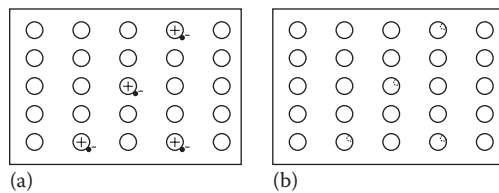


FIGURE 9.3

Representation of n - and p -type semiconductors: (a) n type showing "excess" electrons as dots; (b) p type showing "excess" positive holes as \odot .

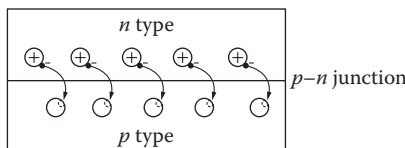


FIGURE 9.4

"Excess" electrons from n -material jump to fill "excess" holes on the p side of a $p-n$ junction, leaving the n side of the junction positively charged and the p side negatively charged.

n side is made easier because of the positive charges at the junction on the n side. This restriction makes the $p-n$ junction behave like a diode. This diode character of a $p-n$ junction is made use of in solar PV cells as explained in the following.

9.1.2 PV Effect

When a photon of light is absorbed by a valence electron of an atom, the energy of the electron is increased by the amount of energy of the photon. If the energy of the photon is equal to or more than the band gap of the semiconductor, the electron with excess energy will jump into the conduction band where it can move freely. If, however, the photon energy is less than the band gap, the electron will not have sufficient energy to jump into the conduction band. In this case, the excess energy of the electrons is converted to excess kinetic energy of the electrons, which manifests in increased temperature. If the absorbed photon had more energy than the band gap, the excess energy over the band gap simply increases the kinetic energy of the electron. It must be noted that a photon can free up only one electron even if the photon energy is a lot higher than the band gap. This fact is a big reason for the low conversion efficiency of PV devices. The key to using the PV effect for generating useful power is to channel the free electrons through an external resistance before they recombine with the holes. This is achieved with the help of the $p-n$ junction.

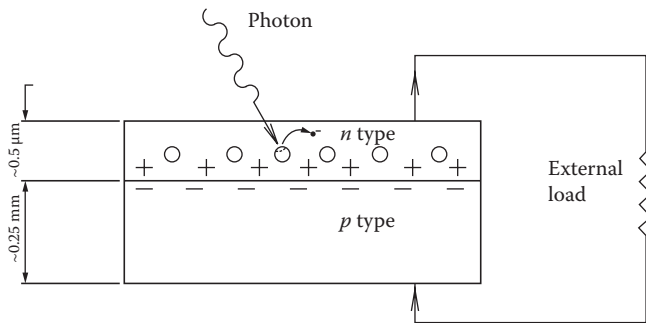


FIGURE 9.5
Schematic of a PV device.

Figure 9.5 shows a schematic of a PV device. As free electrons are generated in the *n* layer by the action of photons, they can pass through an external circuit, recombine with positive holes in the lateral direction, or move toward the *p* layer. The negative charges in the *p* layer at the *p-n* junction restrict their movement in that direction. If the *n* layer is made extremely thin, the movement of the electrons and, therefore, the probability of recombination within the *n* layer is greatly reduced unless the external circuit is open. If the external circuit is open, the electrons generated by the action of photons eventually recombine with the holes, resulting in an increase in the temperature of the device.

In a typical crystalline silicon cell, the *n* layer is approximately $0.5\text{ }\mu\text{m}$ thick and the *p* layer is approximately 0.25 mm thick. As explained in Chapter 2, energy contained in a photon E_p is given by

$$E_p = h\nu, \quad (9.1)$$

where h is Planck's constant ($6.625 \times 10^{-34}\text{ J}\cdot\text{s}$) and ν is the frequency that is related to the wavelength λ and the speed of light c as

$$\nu = \frac{c}{\lambda}.$$

Therefore,

$$E_p = hc/\lambda. \quad (9.2)$$

For silicon, which has a band gap of 1.11 eV , the following example shows that photons of solar radiation of wavelength $1.12\text{ }\mu\text{m}$ or less are useful in creating electron-hole pairs. This spectrum represents a major part of the solar radiation. Table 9.1 lists some candidate semiconductor materials for PV cells along with their band gaps.

TABLE 9.1

Energy Gap for Some Candidate Materials
for PV Cells

Material	Band Gap (eV)
Si	1.11
SiC	2.60
CdAs ₂	1.00
CdTe	1.44
CdSe	1.74
CdS	2.42
CdSnO ₄	2.90
GaAs	1.40
GaP	2.24
Cu ₂ S	1.80
CuO	2.00
Cu ₂ Se	1.40
CuInS ₂	1.50
CuInSe ₂	1.01
CuInTe ₂	0.90
InP	1.27
In ₂ Te ₃	1.20
In ₂ O ₃	2.80
Zn ₃ P ₂	1.60
ZnTe	2.20
ZnSe	2.60
AlP	2.43
AlSb	1.63
As ₂ Se ₃	1.60
Sb ₂ Se ₃	1.20
Ge	0.67
Se	1.60

Source: Garg, H.P. *Advances in Solar Energy Technology*, vol. 3, Dordrecht, Holland: D. Reidel Publishing Company, 1987.

Example 9.1

Calculate the wavelength of light capable of forming an electron–hole pair in silicon.

Solution

The band gap energy of silicon is 1.11 eV. From Equation 9.2, we can write

$$\lambda = \frac{hc}{E}$$

For $c = 3 \times 10^8 \text{ m/s}$, $h = 6.625 \times 10^{-34} \text{ J}\cdot\text{s}$, and $1 \text{ eV} = 1.6 \times 10^{-19} \text{ J}$, the above equation gives the required wavelength as

$$\lambda = \frac{(6.625 \times 10^{-34} \text{ J}\cdot\text{s})(3 \times 10^8 \text{ m/s})}{(1.11)(1.6 \times 10^{-19} \text{ J})} = 1.12 \text{ m.}$$

Example 9.2

A monochromatic red laser beam emitting 1 mW at a wavelength of 638 nm is incident on a silicon solar cell. Find the following:

- The number of photons per second incident on the cell
- The maximum possible efficiency of conversion of this laser beam to electricity

Solution

- The intensity of light in the laser beam (I_p) is equal to the energy of all the photons in it. If the number of photons is N_{ph} , then

$$I_p = N_{ph} \cdot E_p \quad (9.3)$$

$$1 \times 10^{-3} \text{ W} = N_{ph} \cdot E_p \quad (1 \text{ W} = 1 \text{ J/s})$$

$$E_p = hc/\lambda$$

$$= \frac{(6.625 \times 10^{-34} \text{ J}\cdot\text{s}) \cdot 3 \times 10^8 \text{ m/s}}{638 \times 10^{-9} \text{ m}}$$

$$= 3.12 \times 10^{-19} \text{ J}$$

$$\therefore N_{ph} = \frac{1 \times 10^{-3} \text{ J/s}}{3.12 \times 10^{-19} \text{ J}} = 3.21 \times 10^{15} \text{ photons/s.}$$

- Assuming that each photon is able to generate an electron, a total number of N_{ph} electrons will be generated. Therefore, the electrical output will be equal to $N_{ph} \cdot (\text{Band Gap})$. Therefore, the maximum possible efficiency is

$$\eta_{max} = \frac{(N_{ph}) \cdot (\text{B.G.})}{(N_{ph}) \cdot E_p} = \frac{\text{B.G.}}{E_p} \quad (9.4)$$

$$= \frac{1.11 \times 1.6 \times 10^{-19} \text{ J}}{3.12 \times 10^{-19} \text{ J}} = 0.569 \text{ or } 56.9\%.$$

From the above examples, it is clear that for a silicon solar cell, none of the photons of the sunlight over 1.12 μm wavelength will produce any electricity. However, photons of sunlight at a wavelength of 1.12 μm may be converted to electricity at a maximum efficiency of 100%, while photons at lower wavelengths will be converted at lower efficiencies. The overall maximum efficiency of a cell can be found by integrating the efficiency at each wavelength over the entire solar spectrum:

$$\eta = \frac{\int \eta_\lambda I_\lambda d\lambda}{\int I_\lambda d\lambda} \quad (9.5)$$

In addition, other factors such as probability of electron–hole recombination reduce the theoretical maximum achievable efficiency of a solar cell.

In 1961, William Shockley and Hans Queisser conducted a detailed analysis of the maximum possible solar cell efficiency based on possible electron–hole recombination. By assuming the solar spectrum as a smooth black-body spectrum at 6000 K, they plotted the efficiency limit of solar cells on the basis of the band gap (Shockley and Queisser 1961). When applied to a nonconcentrated real solar spectrum at AM1.5, the Shockley–Queisser (SQ) efficiency limit is shown in Figure 9.6. According to this figure, the maximum efficiency limit for a AM 1.5 solar spectrum (1000 W/m^2) at 25°C is 33.7% for a single p – n junction solar cell with a band gap of 1.34 eV. Figure 9.6 also shows the maximum efficiencies achieved so far for a few cells.

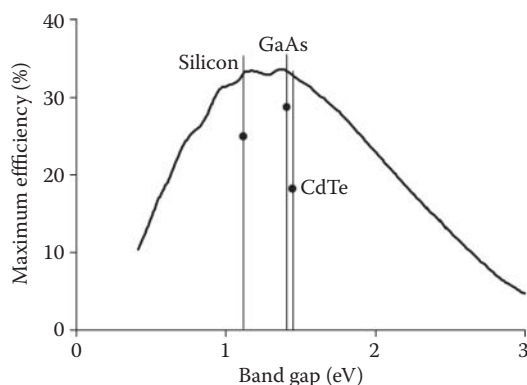


FIGURE 9.6

The maximum solar energy conversion efficiency as a function of the energy gap of the semiconductor calculated according to the SQ efficiency limit for a 1.5 AM solar spectrum (1000 W/m^2) at 25°C . Actual achieved efficiency of some of the materials is also shown. Actual efficiencies achieved as of 2012 are also given in Table 9.2.

The SQ limit can be exceeded by multi-junction cells, high-concentration sunlight, and other methods, which are still under research. On the basis of a theoretical analysis, the limit for a two-junction cell is 42%, and for a three-junction cell, it is 49%. For an infinite junction cell, the maximum limit is 68% (De Vos 1980). Other methods of exceeding the SQ limit include

TABLE 9.2

Confirmed Terrestrial Cell and Submodule Efficiencies Measured under the Global AM1.5 Spectrum (1000 W/m²) at 25°C

Classification	Efficiency (%)	Area (cm ²) ^a	V _{oc} (V)	J _{sc} (mA/cm ²)	FF (%)
<i>Silicon</i>					
Si (crystalline)	25.0 ± 0.5	4.00 (da)	0.706	42.7	82.8
Si (multicrystalline)	20.4 ± 0.5	1.002 (ap)	0.664	38.0	80.9
Si (thin-film transfer)	20.1 ± 0.4	242.6 (ap)	0.682	38.14	77.4
SI (thin-film submodule)	10.5 ± 0.3	94.0 (ap)	0.492	29.7	72.1
<i>III–V Cells</i>					
GaAs (thin film)	28.8 ± 0.9	0.9927 (ap)	1.122	29.68	86.5
GaAs (multicrystalline)	18.4 ± 0.5	4.011 (t)	0.994	23.2	79.7
InP (crystalline)	22.1 ± 0.7	4.02 (t)	0.878	29.5	85.4
<i>Thin-Film Chalcogenide</i>					
CIGS (cell)	19.6 ± 0.6	0.996 (ap)	0.713	34.8	79.2
CIGS (submodule)	17.4 ± 0.5	15.993 (da)	0.6815	33.84	75.5
CdTe (cell)	18.3 ± 0.5	1.005 (ap)	0.857	26.95	77.0
<i>Amorphous/Nanocrystalline Si</i>					
Si (amorphous)	10.1 ± 0.3	1.036 (ap)	0.886	16.75	67.8
Si (nanocrystalline)	10.1 ± 0.2	1.199 (ap)	0.539	24.4	76.6
<i>Photochemical</i>					
Dye sensitized	11.9 ± 0.4	1.005 (da)	0.744	22.47	71.2
Dye sensitized (submodule)	9.9 ± 0.4	17.11 (ap)	0.719	19.4	71.4
<i>Organic</i>					
Organic thin film	10.7 ± 0.3	1.013 (da)	0.872	17.75	68.9
Organic (submodule)	6.8 ± 0.2	395.9 (da)	0.798	13.50	62.8
<i>Multijunction Devices</i>					
InGaP/GaAs/InGaAs	37.7 ± 1.2	1.047 (ap)	3.014	14.57	86.0
<i>a</i> -Si/nc-Si/nc-Si (thin film) ^b	13.4 ± 0.4	1.006 (ap)	1.963	9.52	71.9
<i>a</i> -Si/nc-Si (thin-film cell)	12.3 ± 0.3	0.962 (ap)	1.365	12.93	69.4
<i>a</i> -Si/nc-Si (thin-film submodule)	11.7 ± 0.4	14.23 (ap)	5.462	2.99	71.3

Source: Adapted from Green, M.A. et al., *Prog. Photovolt: Res. Appl.*, 21, 1–11, 2013.

^a ap, aperture area; t, total area; da, designated illumination area.

^b nc-Si, nano-crystalline or microcrystalline silicon.

TABLE 9.3

Terrestrial Concentrator Cell Efficiencies Measured under ASTM G-173-03 Direct Beam AM1.5 Spectrum at a Cell Temperature of 25°C

Classification	Efficiency (%)	Area (cm ²) ^a	Intensity (suns)
<i>Single Cells</i>			
GaAs	29.1 ± 1.3	0.505 (da)	117
Si	27.6 ± 1.0	1.00 (da)	92
<i>Multijunction Cells (Monolithic)</i>			
GaInP/GaAs/GaInNAs	44.0 ± 3	0.3104 (ap)	942
InGaP/GaAs/InGaAs	43.5 ± 2.6	0.167 (da)	306
GaInP/GaInAs/Ge	41.6 ± 2.5	0.3174 (da)	364
<i>Submodule</i>			
GaInP/GaAs; GaInAsP/GaInAs	38.5 ± 1.9	0.202 (ap)	20
<i>Modules</i>			
Si	20.5 ± 0.8	1875 (ap)	79
Triple junction	33.5 ± 0.5	10,674.8 (ap)	N/A
<i>"Notable exceptions"</i>			
Si (large area)	21.7 ± 0.7	20.0 (da)	11

Source: Adapted from Green, M.A. et al., *Prog. Photovolt: Res. Appl.*, 21, 1–11, 2013.

^a ap, aperture area; t, total area; da, designated illumination area.

photon up-conversion (absorption of more than one photon of less energy than the band gap and emitting a photon of more energy than the band gap), hot electron capture, and photon down-conversion (capturing a photon of higher energy than the band gap and emitting more than one photon). Use of quantum dots is an example of research in this direction (Semonin 2011).

Table 9.2 gives the maximum efficiencies achieved by various solar cells around the world for global AM1.5 solar spectrum. Table 9.3 gives the maximum achieved efficiencies for concentrated solar radiation.

9.2 Analysis of PV Cells

This section presents an electrical analysis of PV cells, which will be useful in the design of PV devices for various applications. The physics leading to the expressions for the number density of electrons and holes in *n* and *p* materials at a temperature *T* will not be presented here. For such details, the reader is referred to books such as those by Angrist (1976) and Böer (1990). It would suffice to point out here that at the *p*-*n* junction, a current is generated, called the *junction current*. The junction current *J_j* is the net current owing to

the J_o from the p side to the n side (called the *dark current* or the *reverse saturation current*) and a *light-induced recombination current* J_r from the n side to the p side. On the basis of the temperature T , a certain number of electrons in the p material exist in the conduction band. These electrons can easily move to the n side to fill the holes created at the $p-n$ junction, generating a current J_o . Normally, the electrons occupying the conduction band owing to the temperature in the n material do not have enough potential energy to cross the $p-n$ junction to the p side. However, if a forward bias voltage V is applied, which in a PV cell is due to the action of the photons of light, some of the electrons thus generated have enough energy to cross over and recombine with the holes in the p region. This gives rise to a light-induced recombination current J_r , which is proportional to J_o , and is given by

$$J_r = J_o \exp(e_o V / kT), \quad (9.6)$$

where e_o is the charge of an electron = 1.602×10^{-19} coulombs or J/V and k is Boltzmann's constant = $1.381 \times 10^{-23} \text{ J/K}$.

The junction current J_j is the net current due to J_r and J_o .

$$\begin{aligned} J_j &= J_r - J_o \\ &= J_o [\exp(e_o V / kT) - 1]. \end{aligned} \quad (9.7)$$

Referring to Figure 9.7, it is clear that the current generated in the cell has two parallel paths, one through the junction and the other through the external resistance R_L . Figure 9.7 shows an equivalent circuit of a PV cell. It must be pointed out here that the current generated in a PV cell, including the junction current, is proportional to the area of the cell. Therefore, it

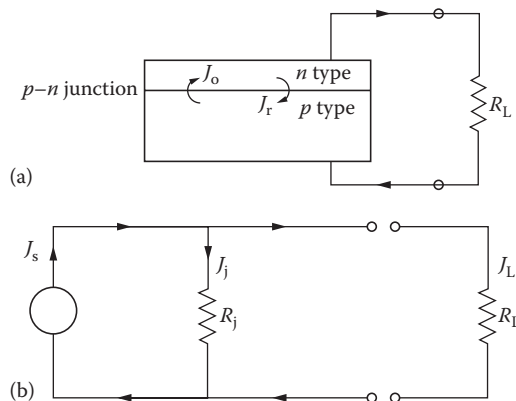


FIGURE 9.7
Equivalent circuit of a PV cell.

is appropriate to analyze in terms of the current density J (current per unit area) instead of the current I . The relationship between the two is

$$I = J \cdot A. \quad (9.8)$$

Referring to Figure 9.7, we can write

$$\begin{aligned} J_L &= J_s - J_j \\ &= J_s - J_o[\exp(e_o V/kT) - 1], \end{aligned} \quad (9.9)$$

where J_s is the *short-circuit current*.

For short circuit, $V = 0$ and $J_L = J_s$.

For open circuit, $J_L = 0$ and $V = V_{oc}$,

which gives

$$0 = J_s - J_o[\exp(e_o V_{oc}/kT) - 1], \quad (9.10)$$

or

$$V_{oc} = \frac{kT}{e_o} \ln \frac{J_s}{J_o} + 1.$$

Figure 9.8 shows a typical performance curve ($I-V$) of a solar cell. The power output is the product of the load current and voltage and is a function of the load resistance

$$\begin{aligned} P_L &= AJ_L V = I_L V \\ &= I_L^2 R_L, \end{aligned} \quad (9.11)$$

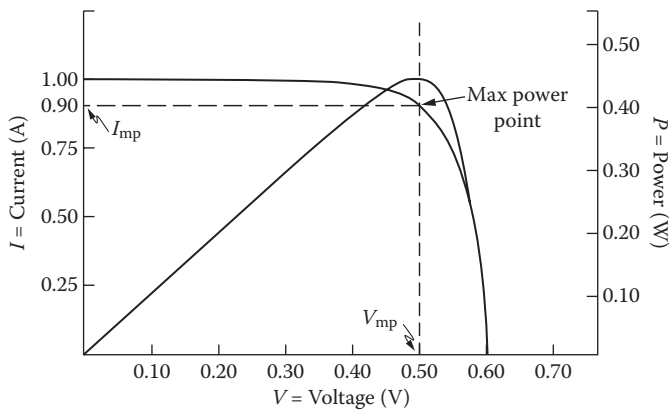
where A is the area of the cell.

The power output exhibits a maximum. To find the condition for the maximum power output (P_{max}), differentiate P_L with respect to V and equate it to zero:

$$\exp(e_o V_m/kT) \cdot 1 + \frac{e_o V_m}{kT} = 1 + \frac{J_s}{J_o}, \quad (9.12)$$

where V_m stands for voltage at maximum power. The current at max power condition $J_{L,m}$ and the maximum power P_{max} can be found from Equations 9.9 and 9.11, respectively.

$$J_{L,m} = J_s - J_o[\exp(e_o V_m/kT) - 1]. \quad (9.13)$$

**FIGURE 9.8**

Typical current, voltage, and power characteristics of a solar cell. (Adapted from Florida Solar Energy Center. Photovoltaic system design. FSEC-GP-31-86. Cocoa Beach, FL: Florida Solar Energy Center, 1991.)

Combining Equations 9.12 and 9.13, $J_{L,m}$ is found to be

$$J_{L,m} = \frac{e_o V_m / kT}{1 + (e_o V_m / kT)} (J_s + J_o) \quad (9.14)$$

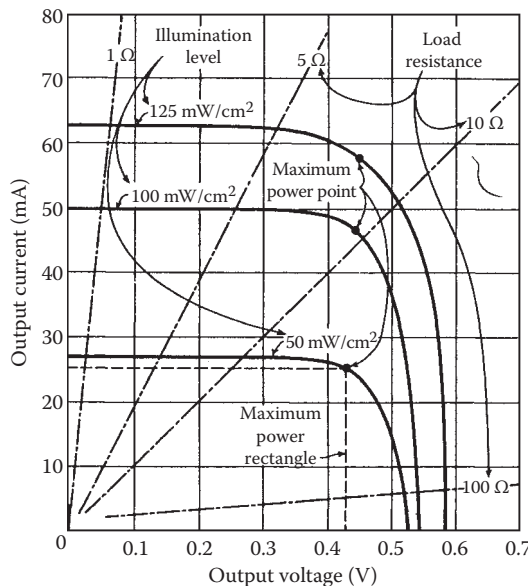
$$P_{\max} = \frac{e_o V_m^2 / kT}{1 + (e_o V_m / kT)} (J_s + J_o) \cdot A. \quad (9.15)$$

Figure 9.9 shows the effect of illumination intensity and the load resistance on the performance of a silicon cell. Temperature also affects the performance in such a way that the voltage and thus the power output decreases with increasing temperature.

Example 9.3

The dark current density for a silicon solar cell at 40°C is $1.8 \times 10^{-8} \text{ A/m}^2$ and the short-circuit current density is 200 A/m^2 . Calculate the following:

- Open circuit voltage
- Voltage at maximum power
- Current density at maximum power
- Maximum power
- Maximum efficiency
- The cell area required for an output of 25 W when exposed to a solar radiation of 900 W/m^2

**FIGURE 9.9**

Typical current–voltage characteristics of a silicon cell showing the effects of illumination level and load resistance.

Solution

Given:

$$J_o = 1.8 \times 10^{-8} \text{ A/m}^2$$

$$J_s = 200 \text{ A/m}^2,$$

and

$$T = 40^\circ\text{C} = 313 \text{ K.}$$

a. Using Equation 9.10,

$$V_{oc} = \frac{kT}{e_o} \ln \frac{J_s}{J_o} + 1 .$$

Since e_o/kT will be needed for other parts also, it can be evaluated separately as

$$e_o/kT = \frac{1.602 \times 10^{-19} \text{ J/V}}{(1.381 \times 10^{-23} \text{ J/K})(313 \text{ K})} = 37.06 \text{ V}^{-1}.$$

Therefore,

$$V_{oc} = \frac{1}{37.06} \ln \frac{200}{1.8 \times 10^{-8}} + 1 \\ = 0.624 \text{ V.}$$

b. Voltage at maximum power condition can be found from Equation 9.12 by an iterative or trial-and-error solution:

$$\exp(37.06 V_m)(1 + 37.06 V_m) = 1 + \frac{200}{1.8 \times 10^{-8}} \\ \text{or } V_m = 0.542 \text{ V.}$$

c. Current density at maximum power can be found from Equation 9.14:

$$J_{L,m} = \frac{e_o V_m / kT}{1 + (e_o V_m / kT)} (J_s + J_o) \\ = \frac{(37.06) \cdot (0.542)}{1 + (37.06) \cdot (0.542)} (200 + 1.8 \times 10^{-8}) \text{ A/m}^2 \\ = 190.5 \text{ A/m}^2.$$

d. $P_{max} = V_m \cdot J_m \cdot A$

$$\frac{P_{max}}{A} = (0.542 \text{ V}) \cdot (190.5 \text{ A/m}^2) \\ = 103.25 \text{ W/m}^2.$$

e. $\eta_{max} = \frac{103.25 \text{ W/m}^2}{900 \text{ W/m}^2} = 11.5\%.$

f. Cell area required:

$$A = \frac{P_{out}}{P_{max}/A} = \frac{25 \text{ W}}{103.25 \text{ W/m}^2} \\ = 24.2 \text{ cm}^2.$$

9.2.1 Efficiency of Solar Cells

Theoretical limitation on the efficiency of a solar cell can be calculated using Equation 9.5. These efficiency limitations and the practical efficiencies of some of the cells are shown in Figure 9.6. Some of the reasons for the actual efficiency being lower than the theoretical limitation are as follows:

1. Reflection of light from the surface of the cell. This can be minimized by antireflection (AR) coating. For example, AR coatings can reduce the reflection from a Si cell to 3% from more than 30% from an untreated cell.
2. Shading of the cell due to current collecting electrical contacts. This can be minimized by reducing the area of the contacts or making them transparent; however, both of these methods will increase the resistance of the cell to current flow.
3. Internal electrical resistance of the cell.
4. Recombination of electrons and holes before they can contribute to the current. This effect can be reduced in polycrystalline and amorphous cells by using hydrogen alloys.

9.2.2 Maximum Power Point Tracking

It is important to ensure that the solar cells in a system are operating at the “maximum power point (MPP)” as seen in Figures 9.8 and 9.9. There are several methods that can be used for maximum power point tracking (MPPT). They include simple methods (e.g., method of determining V_{mp} as equal to kV_{oc} or determining I_{mp} as equal to kI_{sc}) as well as more involved methods (perturb and observe [P&O], incremental conductance [IC], artificial neural networks, and fuzzy logic methods). Each method uses a DC–DC converter consisting of inductors and capacitors in a parallel circuit to measure the operating point of the cell and to change the output voltage to V_{mp} using a control algorithm. The parallel circuit consists of either a DC/DC single-ended primary inductor converter (SEPIC) or a buck–boost converter or a modification of these. Figure 9.10 shows a schematic of a SEPIC converter and Figure 9.11 shows a schematic of a buck–boost converter.

Although a detailed analysis of these converters is outside the scope of this book, opening and closing the switches allows the current to pass from the source through the inductor or from the capacitor to the load. The switching speed determines the output voltage seen by the load.

The differences in the MPPT methods consist of how the V_{mp} is determined. The simplest methods use a fixed constant “ k ” to determine it either from V_{oc} or I_{sc} . Both V_{oc} and I_{sc} change with insulation and the temperature of the cell

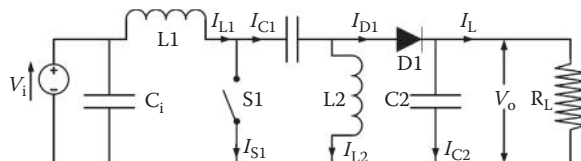
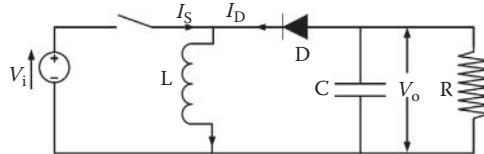


FIGURE 9.10

Schematic of a SEPIC DC/DC converter. (Adapted from http://en.wikipedia.org/wiki/File:SEPIC_Schematic.gif.)

**FIGURE 9.11**

Schematic of a buck-boost converter. (Adapted from http://en.wikipedia.org/wiki/File:Buckboost_conventions.svg.)

and therefore will not always give the best values of V_{mp} . The P&O method is much more accurate and more common in use. In a P&O algorithm, the output voltage is increased or decreased (perturbed) and the output power is compared with the power before perturbation. If the power increases ($dP/dV > 0$), then the voltage is increased more and vice versa. The method runs into problems if the insolation changes rapidly during a perturbation. IC is a similar method in which current I and voltage V are measured before and after a perturbation and dI/dV is compared with I/V .

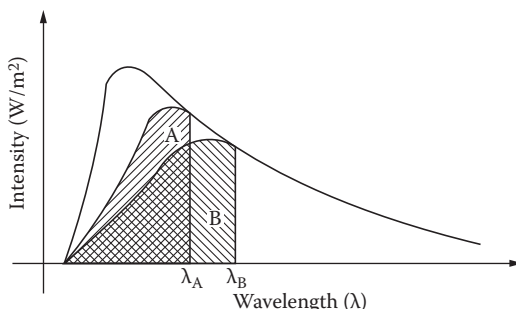
At MPP

$$(dI/dV + I/V) = 0.$$

If the MPP is to the right of the perturbed point, then $(dI/dV + I/V) > 0$ and vice versa.

9.2.3 Multijunction Solar Cells

The limits imposed on solar cells owing to band gap can be partially overcome by using multiple layers of solar cells stacked on top of each other, each layer with a band gap higher than the layer below it. For example (Figure 9.12), if the top layer is made from a cell of material A (band gap corresponding to λ_A), solar radiation with wavelengths less than λ_A would be absorbed to give an output equal to the hatched area A. The solar radiation with wavelength greater than λ_A would pass through A and be converted

**FIGURE 9.12**

Energy conversion from a two-layered stacked cell.

Band gap (eV)	Material	Deposition process	Thickness (nm)
Glass			
~1.95	SnO ₂ : F	Textured tin oxide	APCVD
P ₁	<i>a</i> -SiC: H: B	PECVD	500–800
~1.72	i ₁	<i>a</i> -Si: H, H ₂ diluted	PECVD
1.72	n ₁	<i>μc</i> -Si: H: P	PECVD
~1.95	P ₂	<i>a</i> -SiC: H: B	PECVD
~1.72	i ₂	<i>a</i> -Si: H, H ₂ diluted	PECVD
1.72	n ₂	<i>μc</i> -Si: H: P	PECVD
~1.95	P ₃	<i>a</i> -SiC: H: B	PECVD
~1.44	i ₃	<i>a</i> -SiGe: H, H ₂ diluted	PECVD
1.72	n ₃	<i>μc</i> -Si: H: P	PECVD
	ZnO:F	Reactive magnetron sputtered or LPCVD	80–100
	Ag or Al	Sputtered	
Polyurethane			

FIGURE 9.13

Typical triple-junction *a*-Si cell structure. (From Crandall, R., and W. Luft. The future of amorphous silicon photovoltaic technology. NREL/TP-441-8019. Golden, CO: National Renewable Energy Laboratory, 1995.)

by the bottom layer cell B (band gap corresponding to λ_B) to give an output equal to the hatched area B. The total output and therefore the efficiency of this tandem cell would be higher than the output and the efficiency of each single cell individually. The efficiency would increase with the number of layers. For this concept to work, each layer must be as thin as possible, which puts a very difficult if not an insurmountable constraint on crystalline and polycrystalline cells to be made multijunction. As a result, this concept is being investigated mainly for thin-film amorphous solar cells.

At present, a triple-junction *a*-Si solar cell is under development. This cell consists of layers of cells made from *a*-Si_xC:H (an amorphous silicon, carbon, and hydrogen alloy) with a band gap of 2.0 eV, *a*-Si:H (an amorphous silicon and hydrogen alloy) with a band gap of 1.75 eV, and *a*-Si_xGe:H (an amorphous silicon, germanium, and hydrogen alloy) with a band gap of 2.3 eV. The efficiency of a multijunction cell can be approximately 50% higher than a corresponding single cell. Figure 9.13 shows a conceptual device structure of a triple-junction *a*-Si cell (Crandall and Luft 1995).

9.2.4 Thin-Film Solar Cells

Thin-film solar cells based on cadmium telluride (CdTe), copper indium gallium diselenide (CIGS), and gallium arsenide (GaAs) have been the most developed and have become commercially available in the last 10–15 years mainly

because of their potential highest efficiencies on the basis of their band gaps (see Table 9.1 and Figure 9.6). Among these, CdTe panels achieved the most commercial success because of their low cost of production. However, since 2010, silicon cells achieved the same cost reductions because of improved manufacturing technologies and high efficiencies. Multijunction GaAs cells have achieved efficiencies of 44% under concentrated sunlight (see Table 9.3). Achievement of high efficiencies under highly concentrated sunlight has given rise to a kind of PV device, known as concentrated PV or CPV. Figure 9.14 shows general schematics of CdTe and CIGS solar cells. Figure 9.15 shows a schematic of a triple-junction GaAs solar cell.

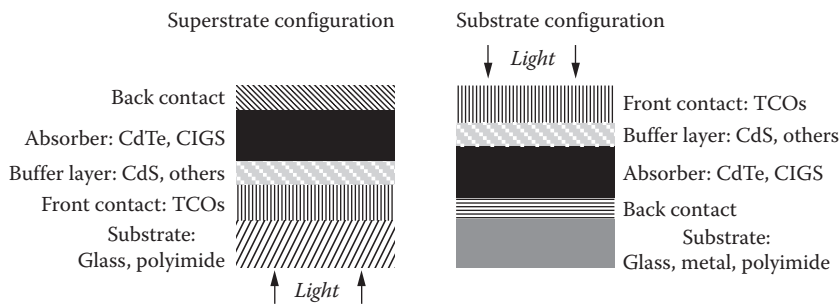


FIGURE 9.14

Schematic structure of a CdTe or a CIGS solar cell. (Adapted from Romeo, A.M. et al., *Prog. Photovolt: Res. Appl.*, 12, 93–111, 2004.)

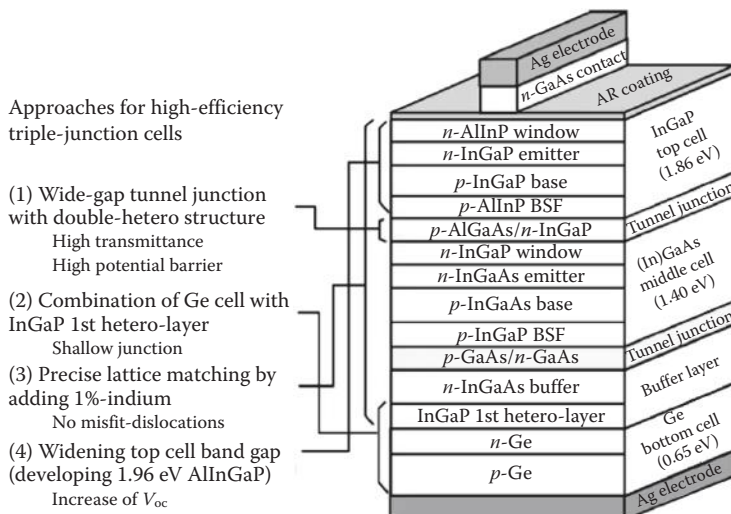


FIGURE 9.15

Schematic structure of a triple-junction GaAs solar cell. (Adapted from Yamaguchi, M. et al., *Solar Energy*, 79, 78–85, 2005.)

9.2.5 Dye-Sensitized Solar Cells and Polymer Solar Cells

Research over the last 30 years has resulted in the development of a new class of PV devices that are essentially photoelectrochemical cells and operate differently from the conventional *p-n* junction solar cells. Since they use cheap and abundant materials, the pace of research picked up after the publication of the seminal paper by O'Regan and Grätzel (1991). Since then, efficiencies greater than 12% have been reported (Grätzel 2009). Jena et al. (2012) and Hagfeldt et al. (2010) provide comprehensive reviews of the progress in this technology.

Figure 9.16 shows a schematic of a dye-sensitized solar cell (DSSC). The basic construction (Hagfeldt et al. 2010; Jena et al. 2012) of a DSSC consists of the following:

1. A photoanode consisting of a porous thick film ($\sim 10 \mu\text{m}$) of a wide-band semiconductor, such as TiO_2 (10–30 nm diameter) coated with a dye, which absorbs in the visible wavelength range. The film is deposited on a transparent conducting oxide (TCO) coated on a transparent glass substrate. The porosity of the TiO_2 film is around 50%.
2. An electrolyte, usually an organic solvent containing iodide/triiodide redox system.
3. A cathode consisting of a TCO coated on a glass substrate and containing a catalyst, such as platinum.
4. A sealant to seal the cell assembly.

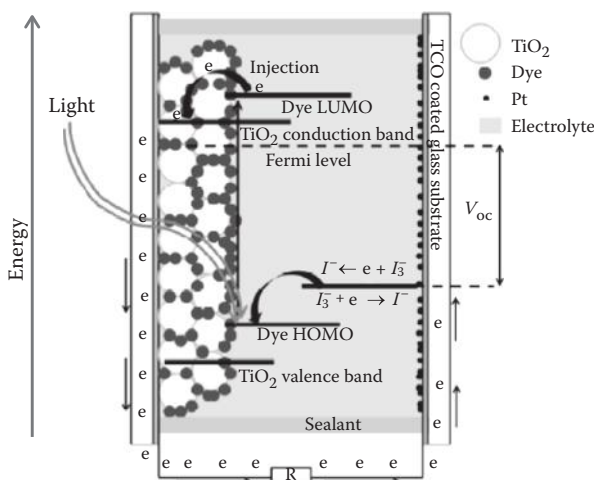


FIGURE 9.16

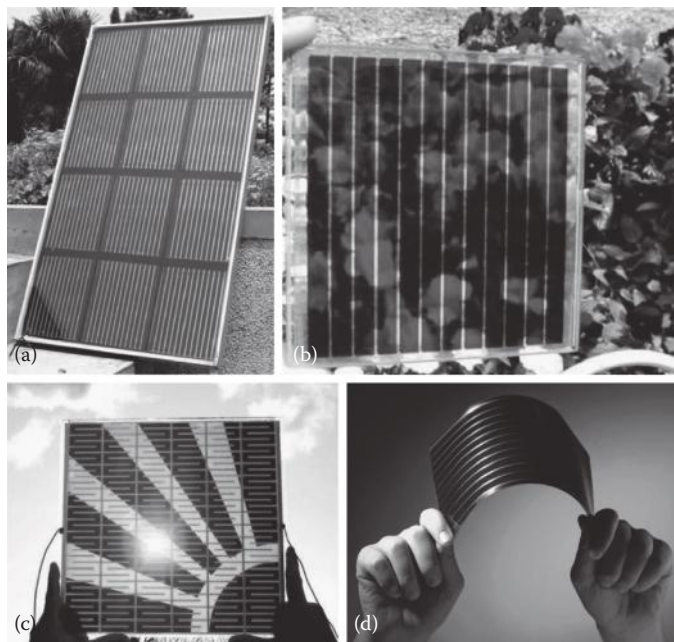
Schematic of a dye-sensitized solar cell. (Adapted from Jena, A. et al., *Transactions of the Indian Ceramic Society*, 71 (1), 1–16, 2012; Hagfeldt, A. et al., *Chem. Rev.* 110, 6595–6663, 2010.)

As the dye absorbs the visible light photons, with energy equal to or greater than the difference between its highest occupied molecular orbital (HOMO) and the lowest unoccupied molecular orbital (LUMO), the electrons from the ground state of the dye (S) get energized to an excited state (S^*), which is known as the photoexcitation of the dye. The energized electrons from the photoexcited dye are injected into the conduction band of TiO_2 . The dye in turn gets electrons from the electrolyte, thereby becoming electrically neutral. The excess electrons in the TiO_2 conduction band pass through the TCO to the external circuit returning through the cathode to the electrolyte. In the electrolyte, the I^- ions close to the dye transfer electrons to the dye, bringing it to the ground state and themselves being oxidized to I_3^- . The oxidized I_3^- ions diffuse a short distance ($>50\ \mu\text{m}$) to the cathode and get reduced to I^- with the injection of the electrons. The concentration of iodine (I_2) in the electrolyte is typically less than $1\ \mu\text{M}$. The transfer of electrons from the dye to the conduction band of TiO_2 is an extremely fast process (picoseconds); however, the speed of diffusion of electrons from TiO_2 to the anode depends on the crystallinity of TiO_2 . Higher crystallinity results in faster diffusion and therefore higher current density.

A number of dyes have been investigated for use as the photosensitizer (Hagfeldt et al. 2010). The classic dyes that have given the highest efficiencies are the ruthenium-based N3 dye that starts to absorb around 800 nm and the black N4 dye that starts to absorb around 900 nm.

9.2.5.1 Fabrication of DSSC

A number of inexpensive and established techniques may be used to fabricate DSSC cells and panels. These include screen printing, spray coating, doctor blading, and spin coating, among others. Since clear plastics could be used as substrates instead of glass, DSSCs could be made as flexible panels. A DSSC panel may be fabricated by thoroughly mixing nanoparticles of TiO_2 in water or an organic solvent, such as ethanol, and an organic binder, such as polyethylene glycol, making it into a paste that is then coated as a thick film on a TCO-coated transparent substrate, such as glass or a clear plastic. The film is then dried, followed by sintering at around 450°C to remove the organic binder and partially crystallize the TiO_2 to allow conduction of electrons through it. The film is then soaked in a dye for approximately 24 h to allow the dye molecules to cover and get adsorbed on the TiO_2 surface. A TCO- and catalyst-coated glass or clear plastic is then attached to it with a spacer around the edges to provide a uniform gap in between. The assembly is sealed around the sides with a hole to inject the iodine-containing electrolyte followed by sealing of the hole. Various groups around the world and commercial manufacturing companies have developed more sophisticated versions of the above simple method. Figure 9.17 shows some of the DSSCs made by various companies and research groups around the world. Latest research on DSSCs includes finding natural and organic dyes, which would

**FIGURE 9.17**

DSSC panels made by various companies and research groups. (a) Institute of Plasma Physics in Hefei, China; (b) Fraunhofer ISE, Germany; (c) Toyota Central R&D Laboratories., Inc. and Aisin Seiki Co., Ltd., Japan; (d) G24i Innovations Ltd., UK.

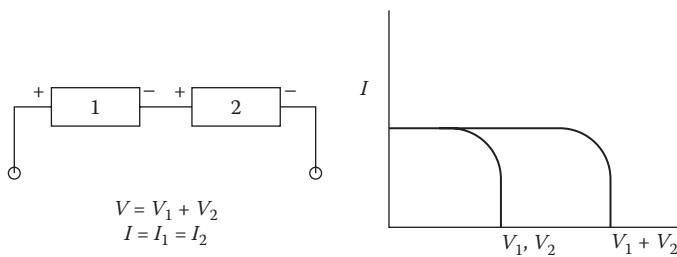
be much cheaper, solid and semisolid electrolytes, and improving the lifetimes of the cells.

9.2.6 Design of a PV System

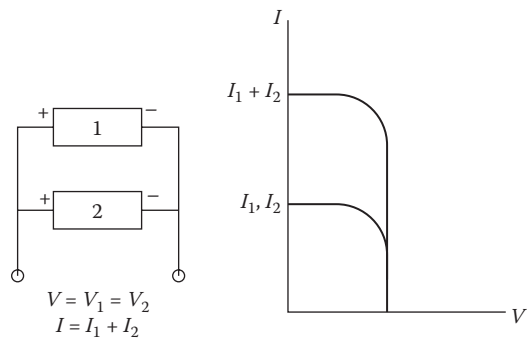
Solar cells may be connected in series, parallel, or both to obtain the required voltage and current. When similar cells or devices are connected in series, the output voltages and current are as shown in Figure 9.18. A parallel connection results in the addition of currents as shown in Figure 9.19. If the cells or devices 1 and 2 have dissimilar characteristics, the output characteristics will be as shown in Figure 9.20. Cells are connected to form modules, modules are connected to form panels, and panels are connected to form arrays. Principles shown in Figures 9.18 and 9.19 apply to all of these connections.

Example 9.4

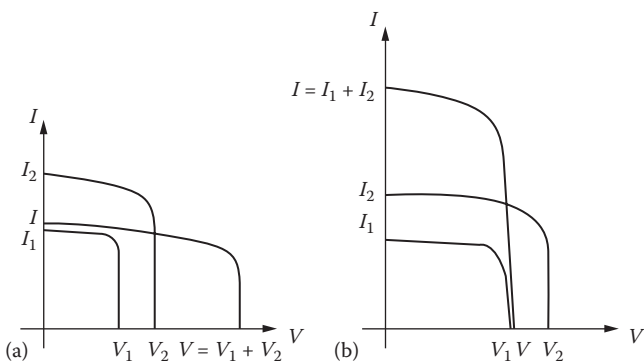
An application requires 300 W at 28 V. Design a PV panel using solar cells from Example 9.3 each with an area of 6 cm^2 .

**FIGURE 9.18**

Characteristics of two similar cells connected in series.

**FIGURE 9.19**

Characteristics of two similar cells connected in parallel.

**FIGURE 9.20**

Characteristics of two dissimilar cells connected in (a) series and (b) parallel.

Solution

Assuming that the cell will be operated at maximum power conditions, the voltage and current from each cell are

$$V_m = 0.542 \text{ V}, I_m = 190.5 \frac{\text{A}}{\text{m}^2} (6 \times 10^{-4} \text{ m}^2)$$

$$= 0.1143 \text{ A},$$

$$\text{Power/cell} = 0.542 \times 0.1143 = 0.062 \text{ W},$$

$$\text{Number of cells required} = \frac{300 \text{ W}}{0.062 \text{ W/cell}} = 4840,$$

$$\text{Number of cells in series} = \frac{\text{System voltage}}{\text{Voltage/cell}} = \frac{28 \text{ V}}{0.542 \text{ V}} = 52,$$

$$\text{Number of rows of 52 cells connected in parallel} = \frac{4840}{52} \approx 93.1.$$

Since the number of rows must be a whole number, we may increase the number to 94 rows, which will give a 303-W output (Figure 9.21).

A blocking diode is used in series with a module or an array to prevent the current from flowing backward, for example, from the battery to the cells under dark conditions. A bypass diode is used in parallel with a module in an array to bypass the module if it is shaded. A PV system may be connected to a DC or an AC load as shown in Figure 9.22.

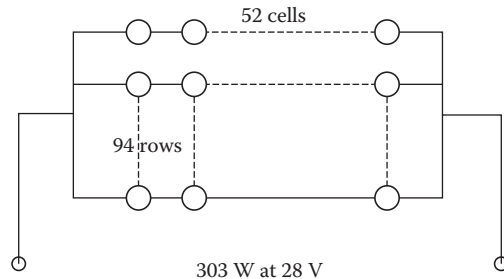


FIGURE 9.21

Connection of cells in rows and columns for Example 9.4.

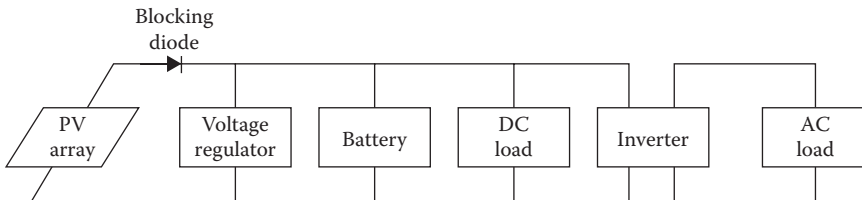


FIGURE 9.22

Schematic of a PV system.

9.3 Manufacture of Solar Cells and Panels

Manufacture of crystalline silicon solar cells is an outgrowth of the manufacturing methods used for microprocessors. A major difference is that silicon used in microprocessors is ultrapure, which is not needed for PV cells. Therefore, a major source of feedstock for silicon solar cells has been the waste material from the microelectronics industry. Solar cells are also manufactured as polycrystalline and thin films. The following are some of the common methods of manufacture of silicon solar cells.

9.3.1 Single-Crystal and Polycrystalline Cells

Single-crystal silicon cells are produced by a series of processes: (1) growing crystalline ingots of *p*-silicon, (2) slicing wafers from the ingots, (3) polishing and cleaning the surface, (4) doping with *n* material to form the *p–n* junction, (5) deposition of electrical contacts, (6) application of AR coating, and (7) encapsulation. Figure 9.23 illustrates the process.

The *Czochralski method* (Figure 9.24a) is the most common method of growing single-crystal ingots. A seed crystal is dipped in molten silicon doped with a *p*-material (boron) and drawn upward under tightly controlled conditions of linear and rotational speed and temperature. This process produces cylindrical ingots of typically 10 cm diameter, although ingots of 20 cm diameter and more than 1 m long can be produced for other applications. An alternative method is called the *float zone* method (Figure 9.24b). In this method, a polycrystalline ingot is placed on top of a seed crystal and the interface is melted by a heating coil around it. The ingot is moved linearly and rotationally, under controlled conditions. This process has the potential to reduce the cell cost.

Polycrystalline ingots are produced by casting silicon in a mold of preferred shape (rectangular) as shown in Figure 9.25. Molten silicon is cooled slowly in a mold along one direction in order to orient the crystal structures and grain boundaries in a preferred direction. In order to achieve efficiencies

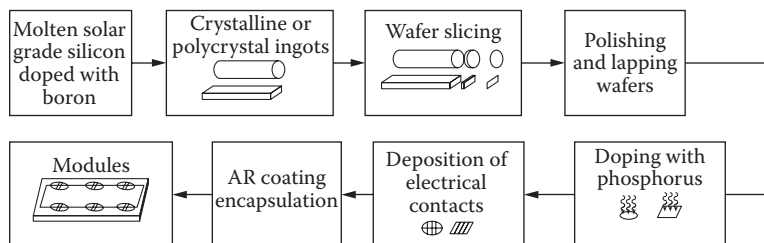


FIGURE 9.23

Series of processes for the manufacture of crystalline and polycrystalline cells.

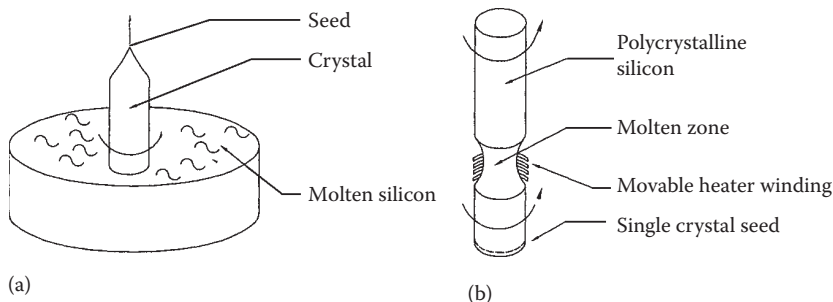


FIGURE 9.24
Crystalline silicon ingot production methods. (a) Czochralski method. (b) Float zone method.

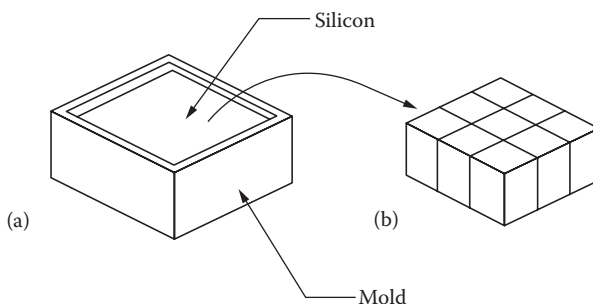


FIGURE 9.25
Polycrystalline ingot production: (a) mold, (b) ingots.

of greater than 10%, grain sizes greater than 0.5 mm are needed and the grain boundaries must be oriented perpendicular to the wafer. Ingots as large as 40 cm × 40 cm × 400 cm can be produced by this method.

Ingots are sliced into wafers by internal diameter saws or multiwire saws impregnated with diamond abrasive particles. Both of these methods result in high wastage of valuable crystalline silicon.

Alternative methods that reduce wastage are those that grow polycrystalline *thin films*. Some of the thin-film production methods include dendritic web growth (Figure 9.26), edge-defined film-fed growth (EFG) (Figure 9.27), ribbon against drop (RAD) method, supported web method, and ramp-assisted foil casting technique (RAFT) (Figure 9.28).

A *p-n* junction is formed in the cell by diffusing a small amount of *n* material (phosphorus) in the top layer of a *p*-silicon wafer. The most common method is diffusion of phosphorus in the vapor phase. In this case, the back side of the wafer must be covered to prevent the diffusion of vapors from that side. An alternate method is to deposit a solid layer of the dopant material on the top surfaces followed by high-temperature (800°C–900°C) diffusion.

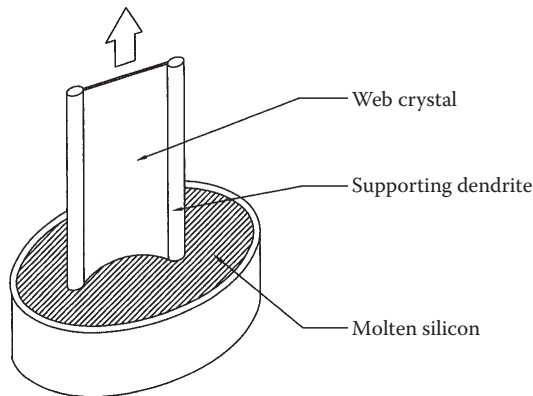


FIGURE 9.26
Thin-film production by dendritic web growth.

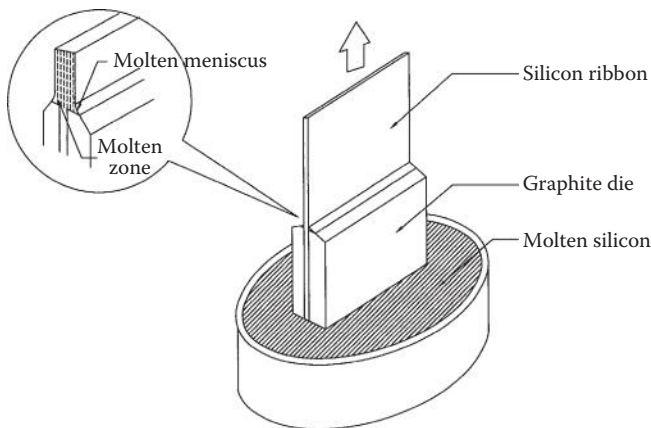


FIGURE 9.27
Thin-film production by edge-defined film-fed growth.

Electrical contacts are attached to the top surface of the cell in a grid pattern to cover no more than 10% of the cell surface and a solid metallic sheet is attached to the back surface. The front grid pattern is made by either vacuum metal vapor deposition through a mask or by screen printing. Figure 9.29 shows how cells are connected to form modules.

AR coatings of materials such as silicon dioxide (SiO_2), titanium dioxide (TiO_2), and tantalum pentoxide (Ta_2O_5) are deposited on the cell surface to reduce reflection from more than 30% for untreated Si to less than 3%. AR coatings are deposited by vacuum vapor deposition, sputtering, or chemical spraying. Finally, the cells are encapsulated in a transparent material to

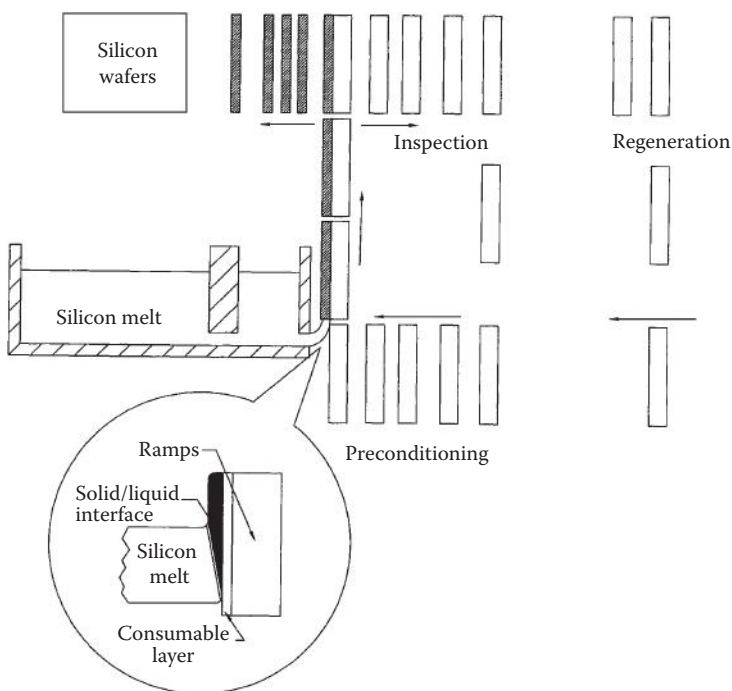


FIGURE 9.28
Schematic of RAFT processing.

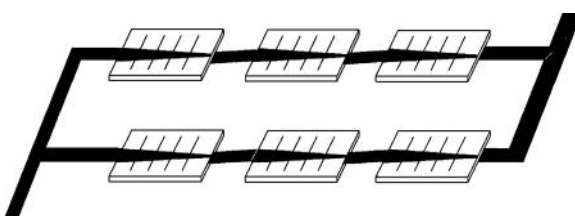
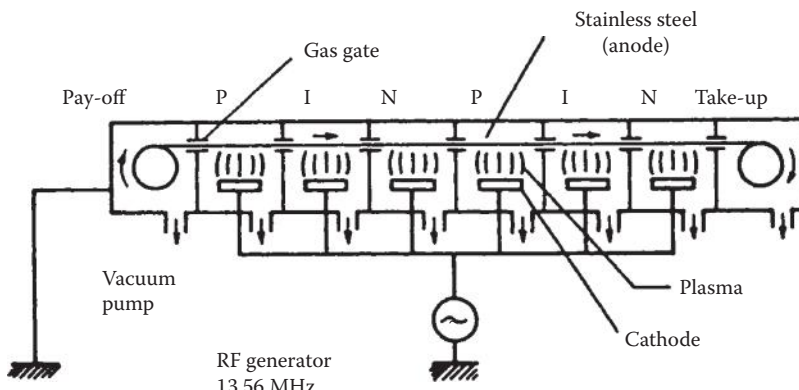


FIGURE 9.29
Assembly of solar cells to form a module.

protect them from the environment. Encapsulants usually consist of a layer of either polyvinyl butyryl or ethylene vinyl acetate and a top layer of low-iron glass.

9.3.2 Amorphous Silicon and Thin-Film Fabrication

Amorphous silicon (α -Si) cells are made as thin films of α -Si:H alloy doped with phosphorus and boron to make n and p layers, respectively. The atomic structure of an α -Si cell does not have any preferred orientation. The cells are manufactured by depositing a thin layer of α -Si on a substrate (glass,

**FIGURE 9.30**

A schematic diagram of a roll-to-roll plasma CVD machine. (From Lasnier, F. and T.G. Ang, *Photovoltaic Engineering Handbook*, New York: A. Hilger Publishing, 1990.)

metal, or plastic) from glow discharge, sputtering, or chemical vapor deposition (CVD) methods. The most common method is by an RF glow discharge decomposition of silane (SiH_4) on a substrate heated to a temperature of 200°C – 300°C . To produce *p*-silicon, diborane (B_2H_6) vapor is introduced with the silane vapor. Similarly, phosphene (PH_3) is used to produce *n*-silicon. The cell consists of an *n* layer, an intermediate undoped *a*-Si layer, and a *p* layer on a substrate. The cell thickness is approximately $1 \mu\text{m}$. The manufacturing process can be automated to produce rolls of solar cells from rolls of substrate. Figure 9.30 shows an example of roll-to-roll *a*-Si cell manufacturing equipment using a plasma CVD method. This machine can be used to make multifunction or tandem cells by introducing the appropriate materials at different points in the machine.

9.4 Design for Remote PV Applications

PV power may be ideal for a remote application requiring a few watts to hundreds of kilowatts of electrical power. Even where a conventional electrical grid is available, for some applications, where uninterruptible or emergency standby power is necessary, PV power would be appropriate. Some examples of remote PV applications include water pumping for potable water supply and irrigation, power for remote houses, street lighting, battery charging, telephone and radio communication relay stations, and weather stations. Examples of some other applications include electrical utility switching stations, peak electrical utility power where environmental quality is a concern, data acquisition systems, and speciality applications such as ventilation fans and vaccine refrigeration.

The design of a PV system is based on some basic considerations for the application.

1. Which is more important, the daily energy output or the power (average or peak)?
2. Is a backup energy source needed or available?
3. Is energy storage important? What type—battery, pumped water, and so on?
4. Is the power needed as AC or DC? What voltage?

There are three basic steps in the design of a PV system:

1. Estimation of load and load profile
2. Estimation of available solar radiation
3. Design of PV system, including area of PV panels, selection of other components, and electrical system schematic

Each of these steps will be explained in the following examples. These examples are based on the work of Post and Risser (1995) and Taylor and Kreider (1998).

9.4.1 Estimation of Loads and Load Profiles

Precise estimation of loads and their timings (load profile) are important for PV systems since the system is sized as the minimum required to satisfy the demand over a day. For example, if power is needed for five different appliances requiring 200, 300, 500, 1000, and 1500 W, respectively, so that only one appliance is on at any one time and each appliance is on for an average of 1 h a day, the PV system would be sized based on 1500 W peak power and 3500 watt hours (Wh) of daily energy requirement. The multiple loads on a PV system are intentionally staggered to use the smallest possible system, since the capital costs of a PV system are the most important as opposed to the energy costs in a conventional fuel-based system.

Example 9.5

Daily load calculations. How much energy per day is used by a remote weather station given the following load characteristics?

Load	Load Power (W)	Run Time (h/day)
Charge controller	2.0	8
Data gathering	4.0	3
Modem (standby)	1.5	22.5
Modem (send/receive)	30.0	1.5

Solution

$$\begin{aligned}\text{Daily energy} &= (2.0 \text{ W})(8 \text{ h}) + (4.0 \text{ W})(3 \text{ h}) + (1.5 \text{ W})(22.5 \text{ h}) \\ &\quad + (30 \text{ W})(2.5 \text{ h}) \\ &= 106.75 \text{ Wh.}\end{aligned}$$

Daily energy use is approximately 107 Wh/day.

Example 9.6

Load calculations. An owner of a remote cabin wants to install a PV power system. The loads in the home are described in the following. Assume that all lights and electronics are powered by AC. Find the daily and weekly peak and average energy use estimates. The system used is a 24-V DC system with an inverter.

Lights	Four, 23-W compact fluorescent bulbs	On at night for 5 h
Lights	Six 13-W compact fluorescent bulbs	2 h each (daytime)
Stereo	110 W (amplifier), 15 W (other)	On for 8 h per week
Water pump	55 W (3.75 amp start current)	Runs for 2 h per day
Computer	250 W (monitor included)	On for 1 1/2 h daily (weekend nights only)
Bathroom fan	40 W (3.5 amp start current)	On for 1 h per day
Microwave	550 W (AC)–1000 W surge	On for 30 min per day

Solution

Loads need to be broken down according to (1) run time, (2) peak power, (3) night or day use, and (4) AC or DC loads. The load profile is as follows:

Load Name Description	Power (W)		Run Time (h)		Energy (Wh)	
	Average	Peak	Day	Week	Day	Week
Lights (AC)	(4)(23)	(4)(23)	5.0	35	460	3220
Lights (AC)	(6)(13)	(6)(13)	2.0	14	156	1092
Stereo (AC)	(1)(110)	(1)(110)	—	8	—	880
Pump (DC)	(1)(55)	(3.75 A)(24 V)	2.0	14	110	770
Computer (AC)	(1)(250)	(1)(250)	1.5	3	—	750
Fan (DC)	(1)(40)	(3.5 A)(24 V)	1.0	7	40	280
Microwave (AC)	(1)(550)	(1)(1000)	0.5	3.5	275	1925

Average DC load: $[770 + 280]/7 = 150 \text{ Wh/day.}$

Average AC load: $[3220 + 1092 + 880 + 750 + 1925]/7 = 1124 \text{ Wh/day.}$

Peak DC load: $\max \{[(3.5)(24) + 55] :: [(3.75)(24) + 40]\} = 139 \text{ W.}^*$

Peak AC load: $(1000) + \max \{[(4)(23) :: (6)(13)] + 250 + 100\} = 1442 \text{ W.}^{\dagger}$

* It can be assumed that the pump and fan will not start precisely at the same instant.

[†] It is assumed that the night and day lighting loads will not be on simultaneously.

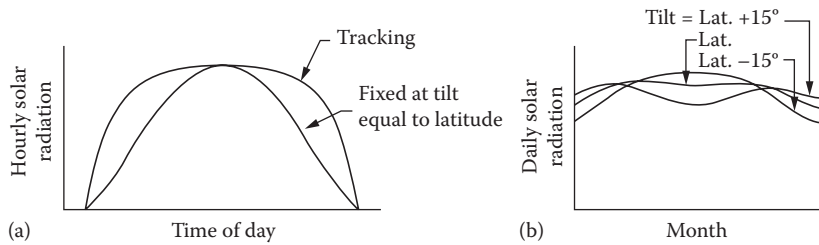


FIGURE 9.31
Solar radiation on panels at different tilt angles.

9.4.2 Estimation of Available Solar Radiation

Methods of estimation of available solar radiation are described in Chapter 2. If long-term measured solar radiation values are available at a location, Equations 2.56 through 2.65 can be used to estimate the average solar radiation per day. Otherwise, data for clear day can be used along with percent sunshine data (if available). For designing a PV system, a decision is made whether the PV panel will be operated as tracking the sun or will be fixed at a certain tilt and azimuth angle. For fixed panels, a tilt angle of latitude $+15^\circ$ works best for winter and latitude -15° works best for summer. To keep the panel fixed year round, an angle equal to the latitude provides the maximum yearly energy (see Figure 9.31).

9.4.3 PV System Sizing

If meeting the load at all times is not critical, PV systems are usually sized on the basis of the average values of energy and power needed, available solar radiation, and component efficiencies. This is known as the *heuristic approach*. It is important to note that a system designed by this approach will not give the best design but may provide a good start for a detailed design. A detailed design accounts for the changes in the efficiencies of the components depending on the load and the solar radiation availability and whether the system is operating in a PV-to-load, PV-to-storage, or storage-to-load mode.

Example 9.7

Heuristic approach to PV system sizing. A PV system using 50-W, 12-V panels with 6-V, 125 Ah batteries is needed to power a home in Farmington, New Mexico, with a daily load of 1700 Wh. System voltage is 24 V.

There is an average of 5 daylight hours in the winter. Specify the collector and storage values for the system using the heuristic approach.

Solution

Load = 1700 Wh/day.
 Daylight hours = 5 h/day.
 Average panel output = 50 W.

$$\text{Number of panels} = \frac{1700 \text{ Wh/day}}{(5 \text{ h/day})(50 \text{ W/panel})} = 6.8, \text{ round off to 7 panels.}$$

Since the system voltage is 24 V, but each panel produces only 12 V, an even number of panels will be needed. Therefore, the number of panels is equal to 8.

Farmington, New Mexico, is a very sunny location; thus, 3 days of storage is plenty. Assuming a battery efficiency of 75% and a maximum depth of discharge 70%,

$$\text{Storage} = (1700)(3)/(0.75 \times 0.7) = 9714 \text{ Wh}$$

$$\begin{aligned}\text{Number of batteries} &= (9714/\text{Wh})/(125 \text{ Ah} \times 6 \text{ V}) \\ &= 13 \text{ (rounded off to the next whole number).}\end{aligned}$$

Since the system voltage is 24 V, and each battery provides 6 V, the number of batteries is increased to 16. In a detailed design, the efficiencies of battery storage, inverter, and the balance of system (BOS) must be accounted for. The following example shows how these efficiencies increase the energy requirements of the PV panel.

Example 9.8

System operating efficiency. Using the cabin electrical system from Example 9.6, calculate the overall system efficiency for each operating mode possible for the system. Estimate the amount of energy required per day for the system. When load timing (day or night), assume half of the load runs during the day and half runs at night. The inverter used has an efficiency of 91%, the battery efficiency is 76%, and the distribution system efficiency is 96%.

Solution

From the example, the loads are as follows:

Average DC load: 150 Wh/day,
 Average AC load: 1124 Wh/day.

The various system efficiencies are as follows:

PV to load (DC):	0.96	(day, DC),
Battery to load (DC):	$(0.76)(0.96) = 0.73$	(night, DC),
PV to load (AC):	$(0.96)(0.91) = 0.874$	(day, AC),
Battery to load (AC):	$(0.76)(0.91)(0.96) = 0.664$	(night/AC).

Expected day and night loads are as follows:

$$\text{Day (DC): } (0.5)(110) + (0.5)(40) = 75 \text{ Wh/day},$$

$$\text{Night (DC): } (0.5)(110) + (0.5)(40) = 75 \text{ Wh/day},$$

$$\text{Day (AC): } (156) + (0.5)(880 + 750)/7 + (0.5)(275) = 409.9 \text{ Wh/day},$$

$$\text{Night (AC): } (460) + (0.5)(880 + 750)/7 + (0.5)(275) = 713.9 \text{ Wh/day}.$$

Without considering system efficiency, the daily energy requirement is

$$E_{\text{day}} = (150) + (1124) = 1274 \text{ Wh/day}.$$

The expected daily energy requirement is

$$E_{\text{day}} = (75)/(0.96) + (75)/(0.73) + (409.9)/(0.874) + (713.9)/(0.664)$$

$$E_{\text{day}} = 1725 \text{ Wh/day}$$

The actual energy requirement is 35% higher than simple calculation.

9.4.4 Water Pumping Applications

Water pumping for drinking water or irrigation at remote locations is an important application of PV. For a simple schematic shown in Figure 9.32, the power needed to pump water at a volumetric rate \dot{V} is given by $P = \rho \dot{V} g H / \eta_p$, where ρ is the density of water, g is the acceleration due to gravity, and η_p is the pump efficiency. The static head H_s is $(A + B)$. In case the water level is

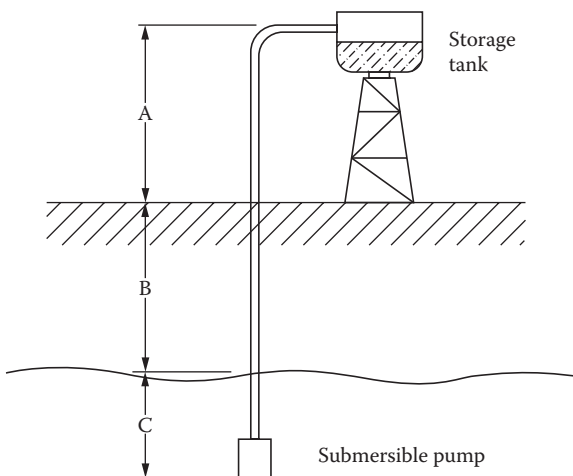


FIGURE 9.32

Water pumping using a submersible pump.

TABLE 9.4

Typical Range of Pump Performance Parameters

Head (m)	Pump Type	Wire-to-Water Efficiency (%)
0–5	Centrifugal	15–25
6–20	Centrifugal with jet	10–20
	Submersible	20–30
21–100	Submersible	30–45
	Jack pump	
>100	Jack pump	35–50

drawn down, the static head would be $(A + B + C)$. The pump must work against the total head H , which includes the dynamic head H_d also,

$$H_d = H_f + \frac{v^2}{2g},$$

where H_f is the frictional head loss in the pipe and the bends and v is the velocity of the water at the pipe outlet. The pump efficiency η_p is a function of the load (head and flowrate) and is available as a characteristic curve from the manufacturer. For general design purposes, typical values given in Table 9.4 may be used. The table lists two basic types of pumps, centrifugal and positive displacement. These pumps can be driven by AC or DC motors. DC motors are preferable for the PV applications, because they can be directly coupled to the PV array output. Centrifugal pumps with submersible motors are the optimum for PV applications because of their efficiency, reliability, and economy. However, for deep wells, jack pumps may be necessary. Jack pumps are the piston type of positive displacement pumps that move chunks of water with each stroke. They require very large currents; therefore, they are connected through batteries.

Example 9.9

A PV system is designed to pump water for livestock in the vicinity of El Paso, Texas. The following information is available:

Site:	Near El Paso, Texas 32°20'N, 106°40'W, 1670 m
Ambient temperature:	-5°C to 45°C
Water source:	Cased borehole 15 cm
Static head:	106 m
Maximum drawdown:	8 m
Water required:	8325 L/day, June to August

Solution

Since the required head is very high, a deep well jack pump with DC motor is needed. Assuming a friction factor of 0.05, the total head = 106 + 8 + (106) (0.05) = 122 m. We select a 75-V DC jack pump with an average efficiency of 0.45.

$$\begin{aligned}\text{Daily energy required} &= \rho \dot{V} g H / \eta_p \\ &= (8325 \text{ L/day}) \frac{1 \text{ kg}}{\text{L}} 9.81 \frac{\text{m}}{\text{s}^2} (122 \text{ m}) \frac{1}{0.45} \\ &= 22.14 \times 10^6 \text{ J/day} \\ &= 6150 \text{ Wh/day}\end{aligned}$$

Since the system will be used from June to August, a tilt angle of lat. -15° would be optimum. Daily solar radiation at El Paso for 1 axis tracking and a tilt angle of 17° is as follows:

June	11.51	$\text{kWh/m}^2\cdot\text{day}$
July	10.58	$\text{kWh/m}^2\cdot\text{day}$
August	10.02	$\text{kWh/m}^2\cdot\text{day}$

Since August has the minimum insolation, the panel area will be based on insolation for this month. We select PV panels with the following specifications (this information may be obtained from a manufacturer):

Voltage	$V_{oc} = 21.7 \text{ V}$	$V_m \text{ at } 25^\circ = 17.4 \text{ V}$
Current	$I_s = 3.5 \text{ A}$	$I_{L,m} = 3.1 \text{ A}$
Temperature correction factor for voltage = $1 - 0.0031 (T_c - T_{ref})$		

Assuming that the panels will operate at a maximum temperature of $45^\circ\text{C} + 15^\circ\text{C} = 60^\circ\text{C}$, the voltage at the highest expected temperature

$$\begin{aligned}&= 17.4 [1 - 0.0031 (60 - 25)] \\ &= 15.5 \text{ V} \\ \text{Voltage required} &= 75 \text{ V.}\end{aligned}$$

Therefore, the number of panels in series = $75/15.5 \approx 5$.

Power output/panel = $3.1 \text{ A} \times 15.5 \text{ V} = 48.05 \text{ W}$ at a standard insolation of 1000.

$$\begin{aligned}\text{Power output/panel/day} &= 48.05 \text{ W} \times \frac{10.02 \text{ kWh/m}^2 \cdot \text{day}}{1 \text{ kW/m}^2} \\ &= 481.5 \text{ Wh/day.}\end{aligned}$$

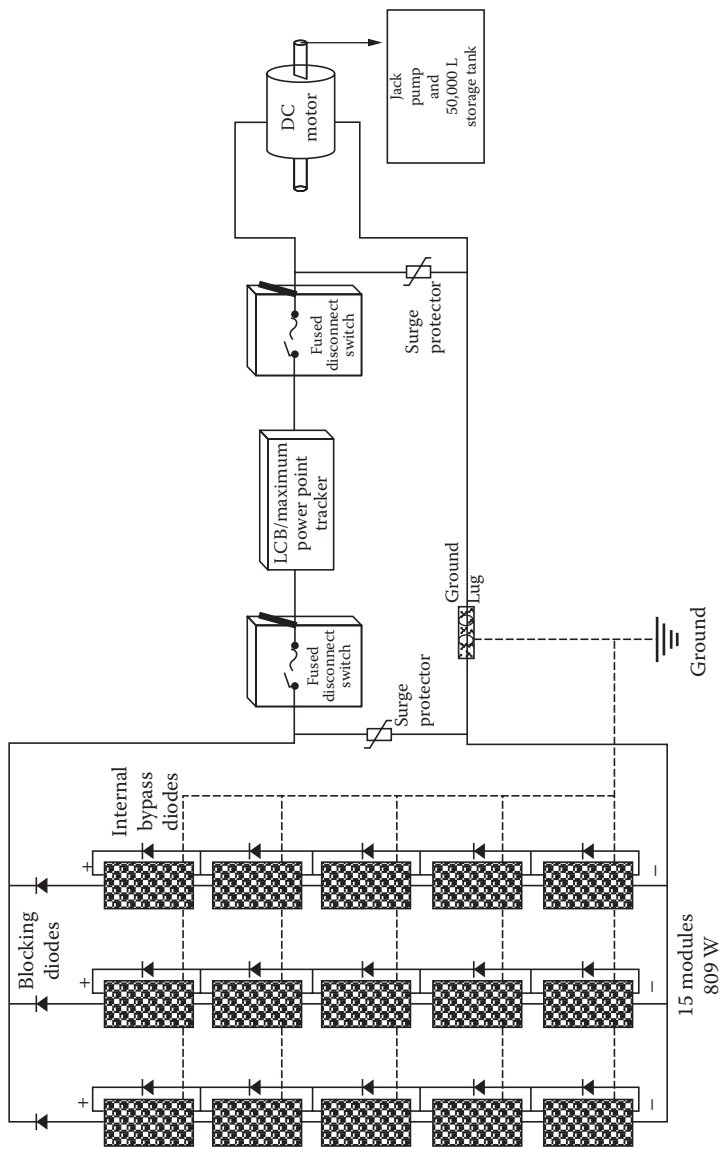


FIGURE 9.33
A system schematic for Example 9.9.

Assuming an overall efficiency of 90% owing to insolation times, wiring, and so on,

$$\text{Number of panels required} = \frac{6150 \text{ Wh/day}}{0.9 \times 481.5 \text{ Wh/day}} \approx 15$$

The array will consist of 3 parallel rows of 5 panels each in series. As a check, the daily water pumping rate for August

$$\begin{aligned} &= \frac{15 \times 481.5 \times 0.9 \text{ Wh/day} \cdot 3600 \text{ s/h}}{9.81 \frac{\text{m}}{\text{s}^2} (1 \text{ kg/L})(122 \text{ m})} \times 0.45 \\ &= 8798 \text{ L/day} \end{aligned}$$

Therefore, the system will meet the requirement. A system schematic is shown in Figure 9.33.

PROBLEMS

- Find the wavelength of radiation whose photons have energy equal to the band gap of GaAs.
- What is the theoretical maximum efficiency of conversion if blue light of wavelength 0.45 μm is incident on a GaAs solar cell?
- Find the theoretical maximum overall efficiency of GaAs solar cells in space.
- The reverse saturation current I_o of a silicon cell at 40°C is 1.8×10^{-7} A/m². The short-circuit current when exposed to sunlight is 5 A/m². From this information, compute the following:
 - Open circuit voltage
 - Maximum power output of the cell
 - The number of 4 cm × 4 cm cells needed to supply 100 W at 12 V. How must the cells be arranged? (Number of rows and number of panels in a row?)
- At what efficiency is a PV array running if insolation on the collector is 650 W/m², the total collector area is 10 m², the voltage across the array is 50 V, and the current being delivered is 15 A?
- If a PV array has a maximum power output of 10 W under an insolation level of 600 W/m², what must the insolation be to achieve a power output of 17 W? Would you expect the open circuit voltage to increase or decrease? Would you expect the short-circuit current to increase or decrease?

7. A PV battery system has an end-to-end efficiency of 77%. The system is used to run an all-AC load that is run only at night. The charge controller efficiency is 96% and the inverter efficiency is 85%. How much energy will need to be gathered by the PV array if the load is 120 W running for 4 h per night?
8. If the average output of the PV system in Problem 7 is 200 W, the load is changed to run during the day, how much PV output energy is needed for the same load conditions? Assume that the battery bank is at 100% charge and that input efficiency is equal to output efficiency.
9. For the system in Problem 7, how many hours of sunlight are needed to ensure that the battery bank is at 100% charge at the end of the day assuming the same load?

Problems 10–14. The owner of a small cabin would like to convert her home to PV power. She has the following equipment and associated run times:

Household Equipment	Power (W)	Run Time, day (h)	Run Time, night (h)
Lighting (DC)	25	2	4
Stereo (AC)	40	3	2
Refrigerator (DC)	125	3 ^a	3 ^a
Water pump (DC)	400	1.5	0.5
Alarm clock (DC)	8	12	12
Computer (AC)	250	3	0
Printer	175	0.25	0
Outdoor safety lights	48	0	8
Answering machine (AC)	7	12	12
Coffee pot (AC)	1200	0.25	0

^a The refrigerator is assumed to run 25% of the time.

10.
 - a. What is the homeowner's daily energy requirement as measured from the load?
 - b. If she replaces her alarm clock with a wind-up clock, how much energy per day will she avoid using?
 - c. What would you suggest she do to cut back her daily load?
11. How many 50-W panels will the owner require assuming battery storage is 75% efficient and all loads are DC (no inverter)?
 - a. For a stationary system "seeing" 5 h of sunlight per day?
 - b. For a tracking system "seeing" 8 h of sunlight per day?

12. For the loads listed:
- What size inverter (peak watts) should she purchase?
 - If the inverter is 88% efficient, how much more daily energy is required from the PV array as compared to an all-DC system?
13. The homeowner decides to hire you to design a system for her. She has cut a deal with a local solar supplier for the following equipment. Specify the system and provide a line diagram showing system connection.

PV panels:	42 W, nominal 12 V
Batteries:	125 Ah, 6 V, end-to-end efficiency = 72%
Charge controller:	95% efficient, 12 V
Inverter:	90% efficient; sizes of 500, 1000, 2000, and 4000 W available; 12 V input

14. Through your connections, you have the following equipment available. Redesign the system.

PV panels:	51 W, nominal 12 V
Batteries:	200 Ah, 12 V, end-to-end efficiency = 78%
Charge controller:	97% efficient, 24 V
Inverter:	91% efficient; sizes of 500, 1200, 2500, and 5000 W available; 24 V input

15. A flashing beacon is mounted on a navigation buoy in the shipping channel at a port at 30°N latitude. The load consists of a single lamp operating 1.0 s on and 3.6 s off during the hours of darkness. Hours of darkness vary from 9.8 h in July to 13.0 h in December. The lamp draws 2 A at 12 V when lighted. A flasher controls the lamp and draws 0.22 A when the lamp is on. There is a surge current of 0.39 A each time the flasher turns on. This current flows approximately 1/10 of the time the flasher is on. The design has 14 days of battery capacity. Provision has to be made to disconnect the load if the battery voltage drops below 11 V.

The available module has a rated voltage of 17.2 V at 25°C (15 V at 55°C) and 2.3 A at 1 kW/m². The available battery has a rated capacity of 105 Ah at 12 V. Assume maximum depth of discharge 30%. Design the PV system.

16. Design a PV system for the following application: A refrigerator/freezer unit for vaccine storage in a remote island of Roatan, Honduras (16°N latitude, 86°W longitude, temperature range, 15°C–30°C).

Two compressors—one each for refrigerator and freezer.
Each compressor draws 5 A at 12 V.

Compressors remain on for	Summer	Winter
Refrigerator	9 h/day	5 h/day
Freezer	7 h/day	4 h/day

Design the PV system using the panels and the batteries described in Problem 15.

17. A village in Antigua (17°N , 61°W , 15°C – 30°C temperature range), West Indies, requires 20,000 liters of water per day for community water supply. Assuming a year-round average insolation of 8 kWh/ $\text{m}^2\text{-day}$, design the system using the following components:

PV panels:	Solarex panels 17.5 V and 3.6 A at 1000 W/ m^2 and 25°C
Pump:	Grundfos multistage pump input 105 V DC, 9 A, 30% efficiency

18. The energy required to produce the PV panels and BOS of a grid-connected PV system (GCPVS) was estimated to be (Perpinan et al. 2009) as follows:

Energy Required by the Main Components of Different GCPVS

Component	Double Axis		Horizontal N-S Axis		Fixed	
	(MJ _p /kW _p)	(%)	(MJ _p /kW _p)	(%)	(MJ _p /kW _p)	(%)
Module	41,819	69.54	41,819	78.67	41,819	81.99
Support structure	9329	15.51	6108	11.49	4459	8.74
Tracking mechanisms	248	0.41	58	0.11	0	0.00
Foundation (steel)	3371	5.61	1536	2.89	0	0.00
Foundation (concrete)	2445	4.07	1281	2.41	2352	4.61
Transport	1339	2.23	900	1.69	1037	2.03
Inverter	1.091	1.81	1091	2.05	1091	2.14
Wiring	497	0.83	364	0.68	248	0.49
Total	60,140	100	53,157	100	51,005	100

All the amounts are referred to a nominal PV power of 1 kW_p.

Estimate the energy payback time in years for this system operating in

- Tampa, Florida, USA
- Las Vegas, Nevada, USA
- Sydney, Australia
- Madrid, Spain
- New Delhi, India
- Beijing, China

19. Find the IRR of the following investment in a 15-MW_p PV system planned for Tampa, Florida (you may choose another location for which solar radiation data are available):

Total initial cost of the system: \$1.7 M/MW_p

Annual O&M costs: 2% of the initial costs

Equity investment: 30% of the initial costs

Debt financed by a bank: 70% of the initial costs at 10%/year

Annual reduction in performance: 0.2%/year

Electricity tariff for the plant: \$0.30/kWh_e for the first 20 years

Salvage value after 20 years: 20% of the initial costs

20. The investor in Problem 19 is able to get a preferential debt rate from a government-backed bank at a rate of 4%/year. What is the new IRR?

References

- Angrist, S.W. 1976. *Direct Energy Conversion*, 3rd ed. Allyn and Bacon, Inc., Boston.
- Böer, K.W. 1990. *Survey of Semiconductor Physics*. Van Nostrand Reinhold, New York.
- Bube, R.H. 1960. *Photoconductivity of Solids*. John Wiley & Sons, Inc., New York.
- Crandall, R., and W. Luft. 1995. The future of amorphous silicon photovoltaic technology. NREL/TP-441-8019. Golden, CO: National Renewable Energy Laboratory.
- De Vos, A. 1980. Detailed balance limit of the efficiency of tandem solar cells. *J. Phys. D: Appl. Phys.* 13(5): 839–846.
- Florida Solar Energy Center. 1991. Photovoltaic system design. FSEC-GP-31-86. Florida Solar Energy Center, Cocoa Beach, FL.
- Garg, H.P. 1987. *Advances in Solar Energy Technology*, Vol. 3. D. Reidel Publishing Company, Dordrecht, Holland.
- Grätzel, M. 2009. Recent advances in sensitized mesoscopic solar cells. *Acc. Chem. Res.* 42: 1788.
- Green, M.A. et al. 2013. Solar cell efficiency tables. *Prog. Photovolt.: Res. Appl.* 21: 1–11.
- Hagfeldt, A. et al. 2010. Dye sensitized solar cells. *Chem. Rev.* 110: 6595–6663.
- Jena, A. et al. 2012. Dye sensitized solar cells—A review. *Trans. Indian Ceram. Soc.* 71(1): 1–16.
- Lasnier, F., and T.G. Ang. 1990. *Photovoltaic Engineering Handbook*. A. Hilger Publishing, New York.
- Moore, C.E. 1952. *Atomic Energy Levels*, Vol. 2. National Bureau of Standards Circular 467, NIST, Gaithersburg, MD.
- Nijs, J. et al. 1997. Energy payback time of crystalline silicon solar modules, Chapter 6. In *Advances in Solar Energy*, Vol. 11, K.W. Böer, ed., ASES, Boulder, CO, pp. 291–327.

- O'Regan, B., and M. Grätzel. 1991. A low cost, high-efficiency solar cell based on dye-sensitized colloidal TiO_2 films. *Nature* 353: 737.
- Perpinan, O. et al. 2009. Energy payback time of grid connected PV systems: Comparison between tracking and fixed systems. *Prog. Photovolt.: Res. Appl.* 17: 137–147.
- Post, H.N., and V.V. Risser. 1995. *Stand-Alone Photovoltaic Systems—A Handbook of Recommended Design Practices*. Report SAND-87-7023. Sandia National Lab, Albuquerque, NM.
- Romeo, A.M. et al. 2004. Development of thin-film Cu(In,Ga)Se₂ and CdTe solar cells. *Prog. Photovolt.: Res. Appl.* 12: 93–111. doi: 10.1002/pip.527.
- Semonin, O.E. 2011. Peak external photocurrent quantum efficiency exceeding 100% via MEG in a quantum dot solar cell. *Science* 334: 1530–1533.
- Shockley, W., and H.J. Queisser. 1961. Detailed balance limit of efficiency of p–n junction solar cells. *J. Appl. Phys.* 32: 510–519.
- Taylor, M., and J. Kreider. 1998. *Solar Energy Applications*, 3rd ed. Univ. of Colorado Bookstore, Boulder, CO.
- Yamaguchi, M. et al. 2005. Multi-junction III–V solar cells: Current status and future potential. *Sol. Energy* 79: 78–85.

10

Solar Photochemical Applications

The use of solar energy for the production of food, fiber, and heat has been known to mankind for a long time. Research over the last five decades has also made it possible to produce mechanical and electrical power with solar energy. Although the potential of solar radiation for disinfection and environmental mitigation has been known for years, only recently has this technology been scientifically recognized and researched.

For anyone who has observed colors fading over long exposure to sunlight, certain materials deteriorating in the sunlight, or skin getting sunburned, it is not hard to imagine sunlight causing reactions that could be used beneficially to break up toxic chemicals. Older civilization considered it essential that human dwellings be designed to allow sunshine in. This may have been for disinfection or to keep the growth of microorganisms in check.

Research over the last three decades has not only confirmed the capability of sunlight for detoxification and disinfection but also accelerated the natural process by the use of catalysts. When sunlight is used to cause a chemical reaction by direct absorption, the process is called *photolysis*. If the objective is achieved by the use of catalysts, it is known as *photocatalysis*. Recent research has concentrated mainly on photocatalytic reactions for detoxification, disinfection, and production of hydrogen. Hydrogen energy systems, especially fuel cells, are being considered as a clean solution to transportation needs. Hydrogen can also provide solar energy storage that can be transported over long distances using pipelines and supertankers, and regionally in special containers via road and rail (Sherif et al. 1999, 2014).

10.1 Photocatalytic Reactions

The fundamentals of how photons affect molecules when absorbed have been described in Chapter 9. Basically, if a photon has more energy than the band gap of a material, it will free up an electron when absorbed. The band gap of a material represents the difference in the energy of the electrons in the valence band of the atom and the conduction band. As an electron moves up from the valence band to the conduction band and becomes free, it leaves a positive hole behind. The positive hole and the negative electron may recombine with the release of thermal energy, unless they interact with

neighboring atoms of other materials to cause chemical reactions. Such reactions are known as *photoreactions*, since they are initiated by photons. If the reaction involves atoms or molecules that act as catalysts, the reaction is known as *photocatalytic*. Sunlight may be used in both photolytic and photocatalytic reactions that could result in useful applications, such as the oxidation of toxic organic chemicals or production of hydrogen.

As noted in Chapter 9, the energy ϵ of a photon is

$$\epsilon = h\nu = \frac{hc}{\lambda}, \quad (10.1)$$

where h is Planck's constant ($6.625 \times 10^{-34} \text{ J}\cdot\text{s}$), ν is the frequency, λ is the wavelength, and c is the speed of light ($3 \times 10^8 \text{ m/s}$).

Titanium dioxide (TiO_2) has a band gap of 3.2 eV; therefore, the wavelength λ of a photon with energy equal to the band gap of TiO_2 is

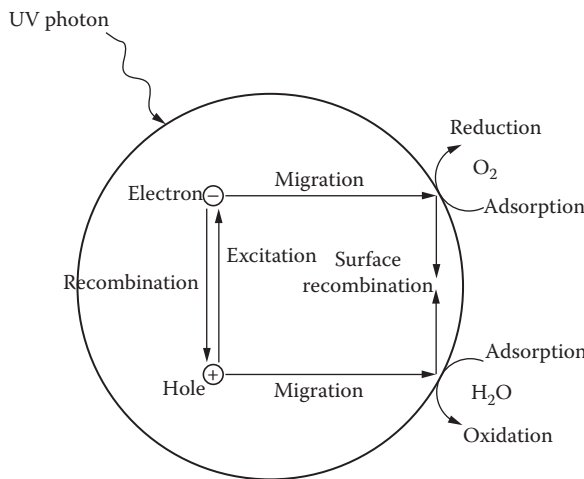
$$\begin{aligned} \lambda &= \frac{hc}{\epsilon} \\ &= \frac{(6.625 \times 10^{-34} \text{ J}\cdot\text{s}) \times (3 \times 10^8 \text{ m/s})}{3.2 \text{ eV}} \times \frac{1 \text{ eV}}{(1.6 \times 10^{-19} \text{ J})} \\ &= 0.388 \times 10^{-6} \text{ m or } 0.388 \text{ m or } 388 \text{ nm.} \end{aligned}$$

Therefore, a photon of sunlight with a wavelength of 388 nm or less (i.e., energy 3.2 eV or higher) will excite an electron from a valence band (vb) to a conduction band (cb) when absorbed, resulting in a free electron (e^-) and a positive hole (hole^+) (Bard 1979; Heller 1981).



The holes (hole^+) and the electrons (e^-) are both highly energetic and mobile. They may recombine and release heat or migrate to the surface. On the surface, they may react with adsorbed molecules of other species and cause a reduction or oxidation of that species.

Since recombination, in the bulk or near the surface, is the most common reaction, the *quantum yields* (molecules reacted/photons absorbed) of most photolytic reactions are low. Separation of the electron–hole pairs is aided by formation of a potential gradient near the surface of the semiconductor. This “space charge region” results from the different electrical potential of the solid semiconductor and the liquid phase of the ambient solution. For TiO_2 , this potential drives valance band holes toward the particle surface and conduction band electrons away from the surface. The electrons and holes at the surface become active sites for oxidation and reduction of adsorbed molecules, as illustrated in Figure 10.1.

**FIGURE 10.1**

Oxidation–reduction reaction occurring at the TiO_2 surface upon irradiation.

The positive holes cause oxidation of the surface-adsorbed species while the electrons cause reduction. Both reactions must take place in order to maintain electro-neutrality. Thus, if the objective is the oxidation of organics, the electrons must be consumed in a reduction reaction such as absorption by oxygen molecules to form superoxide, in order to keep the holes available for oxidation. On the other hand, if the objective is the reduction and recovery of metals, all other reducible species such as oxygen must be eliminated or kept away. The following equations (Bahnemann et al. 1991; Blake et al. 1991; Prairie et al. 1992) describe the oxidation and reduction reactions:



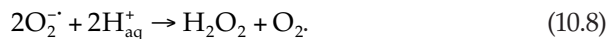
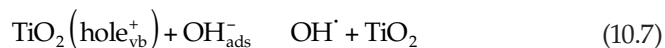
If the objective is oxidation of an organic pollutant, the electron is consumed by an adsorbed compound/molecule:



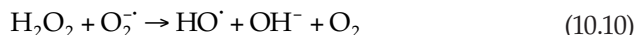
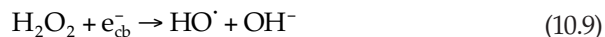
If a water molecule is adsorbed on the surface of TiO_2 , it may exist as hydroxyl and hydrogen ions.



The negatively charged hydroxyl ion adsorbed on the surface of TiO_2 gives up its negative charge (electron) to the positive hole to regenerate the neutral TiO_2 and it in turn becomes a neutral hydroxyl radical (OH^\cdot).



H_2O_2 may yield additional hydroxyl radicals by any of the following reactions:



The hydroxyl radical is a very potent oxidizing agent that can oxidize a pollutant organic molecule $\text{C}_l\text{H}_m\text{X}_n$ into CO_2 and H_2O , directly or through intermediate compounds as

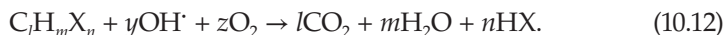


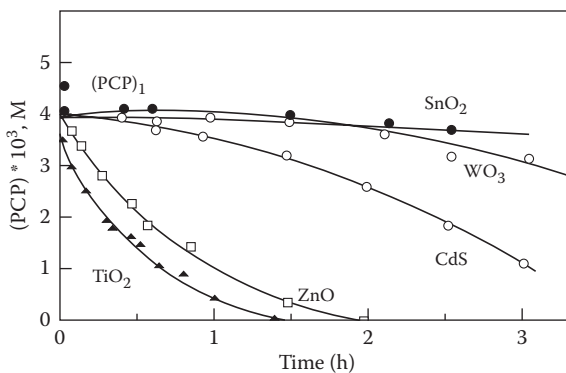
Table 10.1 shows the relative oxidation power of various species relative to that of chlorine. The oxidation power of the hydroxyl radical is ranked

TABLE 10.1

Oxidation Power for Various Species Relative to Chlorine

Species	Relative Oxidation Power
Fluorine	2.23
Hydroxyl radical	2.06
Atomic oxygen (singlet)	1.78
Hydrogen peroxide	1.31
Hydroxyl radical	1.25
Permanganate	1.24
Hypobromous acid	1.17
Chlorine dioxide	1.15
Hypochlorous acid	1.10
Chlorine	1.00
Bromine	0.80
Iodine	0.54

Source: Elizardo, K., Pollution Engineering, 106–109, 1991.

**FIGURE 10.2**

Photodegradation of pantachlorophenol (PCP) in the presence of various semiconductors. (From Barbeni, M. et al., *Chromosphere*, 14(2): 195–208, 1985.)

second among these known strong oxidizing agents. This demonstrates the hydroxyl radical's potential for oxidizing pollutants that normally are hard to destroy, like halogenated organics, surfactants, herbicides, and pesticides.

If the objective is to reduce and precipitate a metal from a metal compound, the electron is consumed by the metal compound as



Although the above photocatalytic reactions have been explained based on TiO_2 , almost all of the semiconductors may be used with varying degrees of usefulness. Figure 10.2 shows a comparison of some of the catalysts for photodegradation of a hazardous organic compound.

10.2 Solar Photocatalytic Detoxification

Solar photocatalytic detoxification refers to the destruction of hazardous pollutants from the environment by solar photocatalytic oxidation or reduction reactions. Solar detoxification has shown great promise for the treatment of groundwater, industrial wastewater, and contaminated air and soil. In recent years, the process has also shown great potential for disinfection of air and water, making possible a number of applications. Research studies on the photocatalytic oxidation process have been conducted over at least the last three decades (Blake 1994a). Blake (1994a) published a bibliography listing 660 publications, and even this long list is incomplete. He compiled a list of organic and inorganic compounds with references that shows over

300 compounds including approximately 100 on the US Environmental Protection Agency priority pollutant list that can be treated by the photocatalytic process. Blake (1994a) also lists 42 review articles including Blake et al. (1992), Kamat (1993), Legrini et al. (1993), Ollis et al. (1989a,b), and Venkatadri and Peters (1993) that cover various aspects of photocatalytic chemistry and technology.

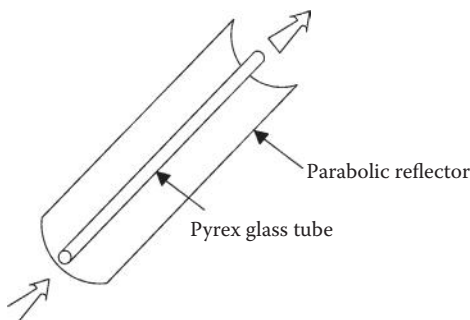
TiO₂ has been the most commonly used photocatalyst. The use of TiO₂ in water detoxification was first demonstrated by Carey et al. (1976). They showed that polychlorinated biphenyls were dechlorinated in aqueous suspensions of TiO₂. Other semiconductors have also been investigated as alternatives to TiO₂; however, TiO₂ has generally been shown to be the most active (Barbeni et al. 1985). Figure 10.2 shows a typical result from such a comparative study. Only ZnO has an activity similar to TiO₂. However, zinc oxides dissolve in acidic solutions, which make them inappropriate for technical applications. Titanium dioxide, on the other hand, is insoluble under most conditions, photostable, and nontoxic.

The energy needed to activate TiO₂ is 3.2 eV or more, which corresponds to near-ultraviolet (UV) radiation of a wavelength of 388 nm or less. As 4%–6% of sunlight reaching the earth's surface is characterized by these wavelengths, the sun can be used as the illumination source (Goswami et al. 1993). However, since UV radiation forms just 4%–6% of the usable solar spectrum, recent research has been aimed at improving the catalyst's performance by improving the reaction kinetics, increasing the useful wavelength range to utilize larger portions of the solar spectrum, developing appropriate reactors, and finding new engineering applications of the process for practical problems.

The following sections describe the engineering aspects of solar detoxification applications, including reactor design, modeling of kinetic reactions, system design, and industrial and commercial applications.

10.3 Solar Reactors

Designs of solar photocatalytic reactors have followed the well-known designs of solar thermal collectors including concentrating and nonconcentrating designs. The key differences are as follows: (1) the fluid to be treated must be exposed to UV solar radiation; therefore, the absorber must be transparent to UV solar radiation; and (2) no insulation is needed, since temperature does not play a role in the photoreaction. Therefore, the first engineering-scale outdoor reactor developed was a simple conversion of a parabolic trough solar thermal collector by replacing its absorber/glazing tube combination with a simple Pyrex glass tube through which contaminated water can flow (Figure 10.3).

**FIGURE 10.3**

Parabolic trough solar photocatalytic reactor.

Pacheco and Tyner (1990) used this reactor to treat water contaminated with trichloroethylene (TCE). The catalyst, TiO_2 powder, was mixed with contaminated water to form a slurry, which was passed through the Pyrex glass tube (reactor tube) located at the focal line of the parabolic trough. Since that time, a number of reactor concepts and designs have been advanced by researchers all over the world. Basically, all these reactors fall into the following categories:

- A. Reactor configuration
 - 1. Concentrating reactors
 - 2. Nonconcentrating reactors
- B. Catalyst deployment
 - 1. Fixed catalyst
 - 2. Slurry
 - 3. Neutral density large particles

10.3.1 Concentrator Reactors

As mentioned before, Pacheco and Tyner (1990) developed a simple modification of the parabolic trough solar thermal collector that worked successfully. They used this reactor in experiments with the catalyst deployed as a slurry. Since then, another configuration of this reactor has been developed and used by researchers at the Sandia National Laboratory (SNL) and at the National Renewable Energy Laboratory (NREL), in which the catalyst is fixed on a loosely woven fiberglass matrix that is inserted into the reactor tube. Both of these configurations have worked well. Parabolic concentrating type of reactors have been used for applications such as groundwater remediation (Mehos and Turchi 1993) and metal removal from water (Prairie et al. 1992).

A disadvantage of concentrating reactors is their inability to use diffuse solar radiation. For solar thermal applications, this limitation is not a major

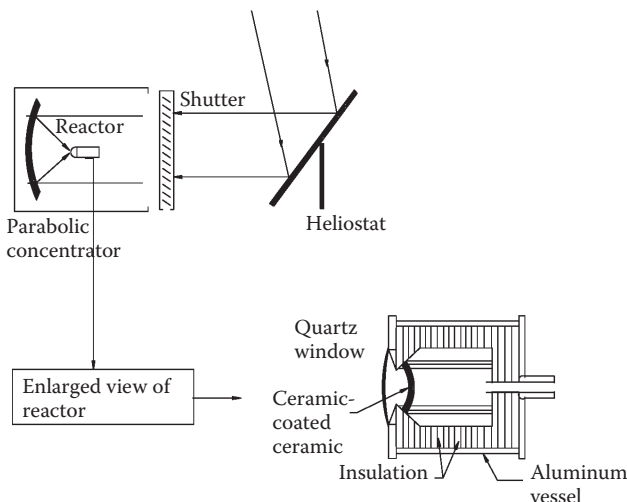
problem since diffuse radiation forms a small fraction of the total solar radiation. However, solar photocatalytic detoxification with TiO_2 as a catalyst uses only the UV portion of the solar radiation, approximately 4%–6% of the total spectrum. As much as 50% or more of the UV radiation can be diffuse, especially at locations with high humidity or during cloudy or partly cloudy periods. Therefore, concentrating reactors would be more useful at dry, high direct insolation locations. Another disadvantage of the concentrating reactors is low quantum efficiency (Bahnemann et al. 1991; Link and Turchi 1991), resulting in a reaction rate constant dependence on the intensity of UV radiation as

$$k \propto I^{1/2}. \quad (10.14)$$

These disadvantages tend to favor the use of nonconcentrating reactors. However, a big advantage of the concentrating reactors is that the reactor tube area is very small, which allows the use of high-quality UV transmitting materials, such as Pyrex glass, without increasing the cost too much, while also improving the lifetime of use of these reactors. Ultimately, the choice of these types of reactors or any other type will be based on the overall economics of the solar detoxification system. As explained later in this chapter, under certain conditions, the reactor capital cost may be a small portion of the overall costs, in which case the balance of the system costs, the catalyst costs, and the operation and maintenance costs dictate the economics of the solar detoxification process.

Other concentrating reactors that have been constructed and tested include very high concentration, high-temperature solar furnaces (Figure 10.4) and a heliostat concentration system with a vertical falling film reactor (Tyner et al. 1989). The high-concentration, high-temperature solar furnaces combine solar photolytic and thermal effects and have been demonstrated to work well for gas-phase detoxification as well as other applications.

The solar catalytic steam reforming furnace shown in Figure 10.4 uses a parabolic dish to concentrate the sunlight into a reactor through a quartz window, where it heats the reactor absorber to 700°C–1000°C. The toxic organic waste is destroyed by a steam reforming process over a rhodium catalyst supported by a porous ceramic absorber. A version of this direct catalytic absorption receiver reactor has been tested at the SNL solar furnace for engineering-scale experiments to demonstrate various steam reforming reactions including CO_2 /methane, steam/methane, steam/propanol, and steam/TCE (Skocypec and Hogan 1990). Another version of this system was built in Germany by a joint collaboration involving the SNL of the United States and the *Deutsche Forschungsanstalt für Luft- und Raumfahrt* (DLR) of Germany. A concentrating furnace has been built at NREL, which has been used for detoxification tests for various hazardous chemicals (Glatzmaier and Bohn 1993; Glatzmaier et al. 1990a,b). Although the high-concentration, high-temperature solar furnaces have worked well, the major impediment to their widespread use is the high capital cost.

**FIGURE 10.4**

Direct catalytic absorption steam reforming furnace. A furnace based on a similar concept was also built at NREL. (From Glatzmaier, G.C. et al., *J. Environ. Sci. Health A25(5)*: 571–581, 1990a; Glatzmaier, G.C. et al., *Solar Engineering 1990, Proceedings of the ASME International Solar Energy Conference*, pp. 153–158, 1990b.)

10.3.2 Nonconcentrating Reactors

Nonconcentrating reactors have a major advantage over concentrating reactors because they can utilize the diffuse part of solar UV radiation in addition to the beam part. While diffuse solar radiation forms only approximately 10%–15% of the total solar radiation over the whole solar spectrum, that is not the case for UV solar radiation. Since UV is not absorbed by water vapor, it can be as much as 50% of the total solar radiation at certain locations, especially locations with high atmospheric humidities (Saltiel et al. 1992). Moreover, the quantum efficiency of the photocatalytic process due to non-concentrated incident radiation is also higher than that due to a concentrated beam. In addition, nonconcentrating reactors have the potential to be simple in design and low in cost. A disadvantage of the nonconcentrating reactors is the requirement of a much larger reactor area (although the total solar aperture would be less) than the concentrating reactors. Researchers have proposed a number of different designs of nonconcentrating solar reactors. They are

1. Flat plate
2. Tubular
3. Falling film
4. Shallow solar pond

Researchers at the University of Florida have developed a number of non-concentrating solar reactors including trickle-down flat plate, pressurized flat plate, tubular (rigid and inflatable), free-falling film, and shallow solar pond.

10.3.3 Flat-Plate Reactors

Figure 10.5 shows a trickle-down flat-plate reactor with a thin film glazing (Wyness et al. 1994). This reactor consists of a back plate on which water trickles down from a spray bar at the top. A woven mesh (fiberglass) covers the back plate in order to damp out surface waves as the water trickles down and to even out the flow. This allows a thin even film of water to flow on the plate. A UV transparent glazing prevents any evaporation from the flow. This design allows contaminated water, mixed with the catalyst particles as a slurry, to be treated as the water trickles down when exposed to the sun. The reactor can be operated in a fixed catalyst configuration by replacing the plain woven mesh with a mesh with the catalyst fixed on it.

10.3.4 Tubular Reactors

Because of the weight of water, the glazing of the pressurized flat plate requires additional structural support. A simple concept of such a reactor is shown in Figure 10.6 (Goswami 1995). In this system, the contaminated water flows through the small channels between the lower and the upper headers. A variation of this concept is to substitute rigid transparent tubes in place of rectangular channels (Figure 10.7). Such tubular reactors were tested at the University of Florida to treat water contaminated by volatile organic compounds (Oberg et al. 1993). These reactors were also tested in the field

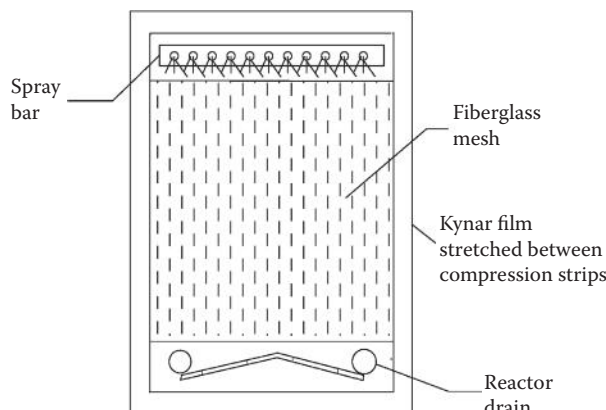
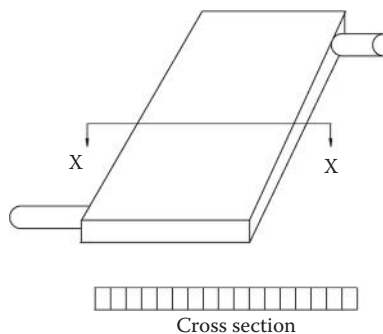
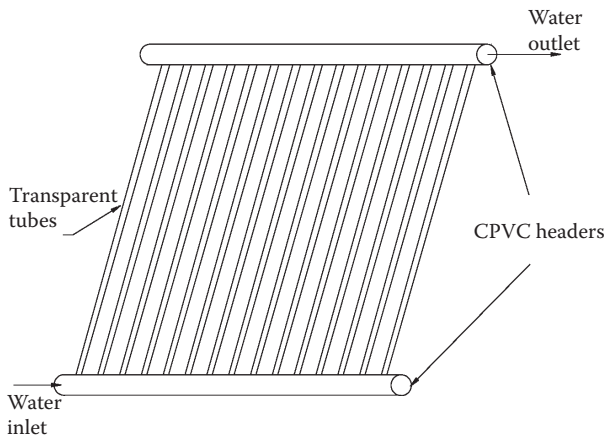


FIGURE 10.5

Trickle-down flat plate reactor. (From Wyness, P. et al., *J. Sol. Energy Eng.*, ASME 116(1): 2–7, 1994.)

**FIGURE 10.6**

Pressurized flat plate reactor. (From Goswami, D.Y., *Adv. Solar Energy* 13: 208, 1995.)

**FIGURE 10.7**

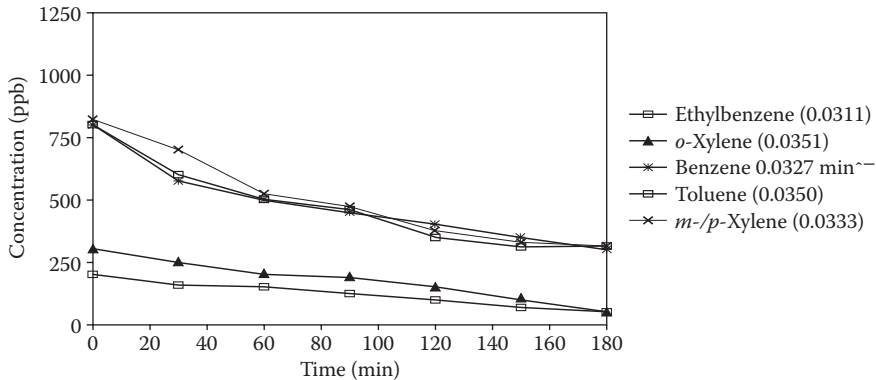
Flat plate reactor with rigid transparent tubes.

at Tyndall Air Force Base (TyAFB) to treat groundwater contaminated with fuel, oil, and lubricants (Goswami et al. 1993). Figure 10.8 shows the performance of this system.

A simple reactor concept consists of transparent inflatable tubes connected in parallel between two headers (Goswami 1995). As the water flows through the reactors under pressure, the tubes inflate. Large areas of this reactor can be rolled or folded into a small volume for portability and transported for on-site use.

10.3.5 Shallow Solar Ponds

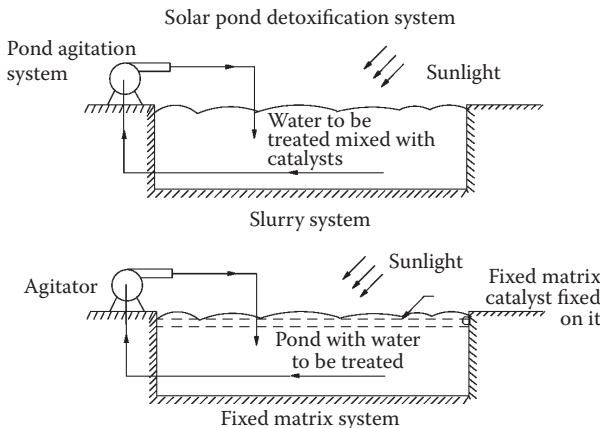
Shallow pond-type reactors, developed at the University of Florida, may be constructed on-site especially for industrial wastewater treatment (Bedford

**FIGURE 10.8**

Destruction of BTEX in groundwater at Tyndall AFB using nonconcentrating tubular reactors. (From Goswami, D.Y. et al., Solar photocatalytic treatment of groundwater at Tyndall AFB, field test results. *Solar* 1993, *Proceedings of the American Solar Energy Society Annual Conference*, pp. 235–239, 1993.)

et al. 1994). Since industries already use holding ponds for microbiological treatment of wastewater, shallow solar ponds can be used for the front end or the back end of a combined solar/microbiological treatment of wastewater. Therefore, these reactors would be ideal for wastewater treatment in industries such as pulp and paper, textiles, pharmaceuticals, and chemicals.

The reactor concept is simple, as shown in Figure 10.9. The reactor can be operated in a slurry or fixed catalyst configuration. If TiO_2 is used as a catalyst in a slurry configuration, it settles down to the bottom, if it is not continuously mixed. While the disadvantage of this configuration is that

**FIGURE 10.9**

Shallow solar pond reactors. (From Bedford, J. et al., *J. Sol. Energy Eng.*, ASME 116(1): 8–13, 1994.)

continuous mechanical mixing is needed, the advantage is that after the catalyst settles down, the treated water can be removed from the top without filtration. Bedford et al. (1994) tested shallow pond reactors in both slurry and fixed configuration, and various area-to-depth ratios, for treating contaminated water. The reactors worked extremely well under various insolation conditions (sunny, partly cloudy, and cloudy).

10.3.6 Falling Film

Some of the other nonconcentrating reactors developed include a vertically free-falling film reactor developed by Goswami (1995). The vertical film of this reactor is open to the atmosphere on both sides, which allows it to make maximum use of the diffuse atmospheric radiation. The integrity of the film is maintained by means of vertical strings appropriately spaced apart.

Finally, solar detoxification would work just as well, on-site, if the application involves treatment of large bodies of contaminated water, such as spills in lake, or the sea. Heller and Brock (1991) developed neutral density spheres coated with TiO_2 , which can be floated in large bodies of water to treat the contamination *in situ* in the presence of the sun (Heller et al. 1992).

10.4 Kinetic Models

An understanding of reaction rates and how the reaction rate is influenced by different parameters is important for the design and optimization of an industrial system. The rate of photolytic degradation depends on several factors including illumination intensity, catalyst type, oxygen concentration, pH, presence of inorganic ions, and the concentration of organic reactant. As is typical of many photo-assisted reactions, the effect of temperature is small. Figure 10.10 shows a typical change in pollutant concentration C with time t .

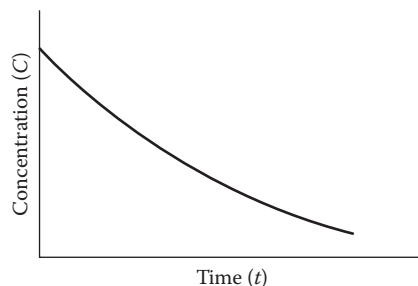


FIGURE 10.10

Typical concentration–time history.

The destruction rates of organics in photocatalytic oxidation have been modeled by different kinetic models. Langmuir–Hinshelwood (L–H) kinetics seems to describe many of the reactions fairly well.

The rate of destruction is given by

$$-\frac{dC}{dt} = \frac{K_1 K_2 C}{(1 + K_2 C)}. \quad (10.15)$$

In the ideal case for which the L–H model is derived, C is the bulk solute concentration, K_1 is the reaction rate constant, K_2 is the equilibrium adsorption constant, and t represents time. In the photocatalytic system, these definitions are less clear because of the importance of reactive radical species.

The L–H reaction rate constants are useful for comparing the reaction rate under different experimental conditions. Once the reaction constants K_1 and K_2 have been evaluated, the disappearance of reactant can be estimated if all other factors are held constant.

For low solute concentrations, C is almost equal to zero, which makes the denominator in the L–H expression equal to 1. This reduces the L–H expression to a pseudo-first-order expression:

$$-\frac{dC}{dt} = K_1 K_2 C = kC. \quad (10.16)$$

This equation has been shown to apply to many photocatalyzed reactions (Bahnemann et al. 1991). Industrial pollutant levels are typically on the order of parts per million (ppm), which are low enough for the reaction rate to follow pseudo-first-order kinetics.

For the design of a system, the reaction rate constant k can be determined from experimental data as described here. Figure 10.11 shows a simplified schematic of a batch-type solar photocatalytic detoxification facility. The

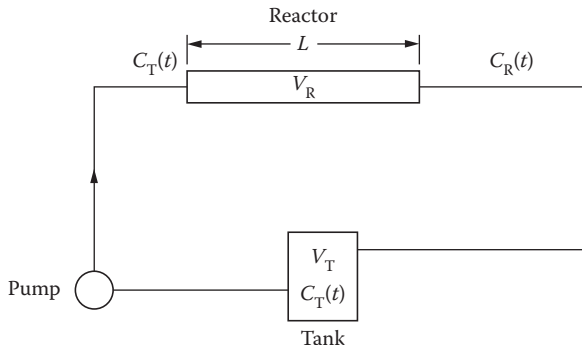


FIGURE 10.11

Simplified schematic diagram of a batch-type solar detoxification facility.

contaminated water is stored in a containment tank and pumped through a reactor, which is illuminated by the sun or another light source. The partially treated water coming out of the reactor is mixed with the water in the containment tank. The process continues until the mixed concentration in the containment tank reaches an acceptable level. Laboratory treatment studies normally employ such a facility to determine reaction rate constants that can be used in the design of treatment systems.

If the reaction rate constant is determined from Equation 10.15 or 10.16 by simply using the concentration–time history in the tank, the results would be in error, unless the tank volume (V_T) is negligible as compared to the reactor volume (V_R), which is usually not the case. Wolfrum and Turchi (1992) suggested that an apparent reaction rate constant k_{app} may be calculated using Equation 10.16 and the concentration–time history in the tank, from which actual reaction rate constants may be approximated by

$$k = k_{app} \frac{1 + \gamma}{\gamma}, \text{ where } \gamma = \frac{V_R}{V_T}. \quad (10.17)$$

From a rigorous analysis, Klausner et al. (1994) determined that the approximation given by Equation 10.17 gives reaction rate constants that are accurate to within 5% for

$$\frac{\gamma + 0.79}{\kappa^{0.62}} > 3.30, \text{ where } \kappa = \frac{V_R k}{Q} \quad (10.18)$$

and Q is the volume flow rate through the reactor, V_R is the volume of the reactor and V_T is the tank volume.

For $\kappa < 0.1$, Equation 10.16 is in error by less than 5%, regardless of γ .

Example 10.1

Assuming that pseudo-first-order kinetics can model the destruction of benzene as shown by the experimental concentration history data in Figure 10.8, determine the apparent and actual reaction rate constants if the reactor volume is 20 gal and the tank volume is 500 gal (neglect volume in pipes). If the solution flows at 30 gal/min, comment on the accuracy of the calculated actual reaction rate. What happens when the tank volume becomes much smaller than the reactor volume?

Solution

Using Equation 10.16,

$$\frac{-dC}{dt} = k_{app} C$$

$$\int_{c_i}^{c_f} \frac{dC}{C} = -k_{app} \int_0^{\Delta t} dt$$

$$k_{app} = \frac{\ln C_i/C_f}{\Delta t}.$$

From Figure 10.8 for benzene, $C_i = 800$ ppb, $C_f = 350$ ppb, and $\Delta t = 180$ min. Plugging into the above equation, we get

$$k_{app} = 0.00459 \text{ min}^{-1}.$$

From Equation 10.17,

$$k = k_{app} \frac{1 + \gamma}{\gamma} = k_{app} \frac{V_T}{V_R} + 1$$

or

$$k = 0.119 \text{ min}^{-1}.$$

Note that the actual reaction rate is faster than the apparent one, since no reaction occurs in the large tank where the concentration is measured.

From Equation 10.18,

$$\frac{\gamma + 0.79}{K^{0.62}} = \frac{\frac{V_R}{V_T} + 0.79}{\frac{V_R k}{Q}^{0.62}} = 3.99 > 3.30.$$

The inequality of Equation 10.18 holds, indicating that the actual reaction rate constant is accurate to within 5%.

As the tank volume decreases,

$$V_T \ll V_R \quad \text{or} \quad \gamma \gg 1;$$

with $\gamma \gg 1$, Equation 10.17 reduces to

$$k = k_{app}.$$

This indicates all the solution is in the reactor; hence, the reaction rate measured is the actual reaction rate.

It should be noted here that the reaction rate constant k determined herein is not the traditional rate constant used in reactor engineering. Because of the nature of the photocatalytic reaction, it is a function of external system parameters such as UV irradiation intensity, pH, catalyst loading, and possible degree of mixing in the fluid. It may also depend

on the geometry of the photoreactor. Of these parameters, the intensity of the solar UV radiation cannot be controlled; therefore, the experimentally determined reaction rate constant, k_o , must be adjusted for the actual UV intensity according to the following equations:

Concentrating reactors (Link and Turchi 1991):

$$\frac{k}{k_o} = a \left(\frac{I}{I_o} \right)^x, \quad (10.19)$$

where a is a constant given as A/V (Link and Turchi 1991) and x is an intensity-dependent exponent, which varies between 0.5 and 1. A value of 0.5 is recommended for x (Bahnemann et al. 1991).

Nonconcentrating tubular or channel-type reactors (Goswami et al. 1993):

$$\frac{k}{k_o} = a \left(\frac{I}{I_o} \right), \quad (10.20)$$

where $a = 0.88$ for 0.1% TiO_2 and 1.14 for 0.01% TiO_2 (Wyness et al. 1994).

Trickle-film flat-plate reactors (Wyness et al. 1994):

$$\frac{k}{k_o} = a \left(\frac{I}{I_o} \right) \frac{\delta_o}{\delta}. \quad (10.21)$$

Here, δ represents the film thickness and the value of a is 0.97 (Wyness et al. 1994). δ_o is the reference film thickness corresponding to k_o and I_o .

Shallow pond reactor (Bedford et al. 1994):

$$\frac{k}{k_o} = m \left(\frac{I(A/V)}{I_o(A/V)_o} \right)^n. \quad (10.22)$$

Values of m and n are given in Table 10.2 (Bedford et al. 1994). It can be seen from the above equations that the liquid film thickness (δ) is an important parameter for a trickle bed reactor, while the ratio of the area to volume (A/V) is critical for the shallow ponds.

Example 10.2

Three reactors—a flat-plate, a parabolic trough concentrator, and a shallow solar pond—were tested for effectiveness in treating a water stream contaminated with 4CP. Using 0.1% TiO_2 solution, all three gave

TABLE 10.2

Empirical Constants m and n for Destruction of 4-Chlorophenol in a Shallow Pond Reactor

% TiO ₂	$C_o \times 10^{-4}$ (M)	m	n
0.01	1	0.28	0.50
0.1	1	0.66	0.70
0.3	1	0.95	1.00
0.01	4	0.52	0.44
0.1	4	0.95	0.65
0.3	4	1.23	0.66

Source: Bedford, J. et al., *Journal of Solar Energy Engineering*, ASME, 116 (1): 8–13, 1994.

a reaction rate constant k_o of 0.0172 min^{-1} for an incident UV radiation of 31 W/m^2 .

- Determine the reaction rate for a 0.1% TiO₂ solution of the contaminated water passing through each reactor experiencing a steady UV insolation of 43 W/m^2 .
- Determine the depth of a rectangular shallow pond reactor to give (a) the reaction rate found in part (i) and (b) double the reaction rate found in part (i).

Use the following reference values:

$$(A/V)_o = 19.7 \text{ m}^{-1} \text{ (for shallow pond reactor)}$$

$$a = 1.0 \text{ (for concentrating reactor).}$$

Solution

- From Equation 10.20, for a flat-plate reactor,

$$k = k_o a \frac{I}{I_o} = (0.0172 \text{ min}^{-1})(0.88) \frac{43 \text{ W/m}^2}{31 \text{ W/m}^2}$$

$$k = 0.021 \text{ min}^{-1}.$$

For a concentrating reactor, Equation 10.19 yields

$$k = k_o a \frac{I}{I_o}^x \quad \text{where } x = 0.5$$

$$k = (0.0172)(1.0)(43/31)^{0.5} = 0.0203 \text{ min}^{-1}.$$

For a shallow solar pond, Equation 10.22 yields

$$k = k_o \cdot m \cdot \frac{I(A/V)}{I_o(A/V)_o}^n.$$

For the same A/V ratio,

$$k = (0.0172)(0.66)(43/31)^{0.7} = 0.0143 \text{ min}^{-1}.$$

ii. For the same reaction rate constant, it was assumed that

$$(A/V) = (A/V_o) = 19.7 \text{ m}^{-1}.$$

For a rectangular pond, $V = A \cdot D$, where D is the depth of the pond,

$$\text{Therefore, } 1/D = 19.7 \text{ m}^{-1}$$

or

$$D = 0.051 \text{ m or } 5.1 \text{ cm.}$$

For double the reaction rate constant $k = 0.0143 \times 2 = 0.0286 \text{ min}^{-1}$ for the same insolation, from Equation 10.22,

$$\begin{aligned} (A/V) &= (A/V)_o \cdot (I_o/I)(k/mk_o)^{1/n} \\ &= (19.7 \text{ m}^{-1})(1)(2/0.66)^{1/0.7} \\ &= 96 \text{ m}^{-1} \end{aligned}$$

$$\text{Therefore, } D = 1/96 = 0.0104 \text{ m or } 1.04 \text{ cm.}$$

10.5 Useful Insolation

Photocatalytic detoxification using TiO_2 as catalyst requires photons of UV radiation with wavelength less than 388 nm. The extraterrestrial radiation supplied by the sun contains approximately 10% UV radiation when it first reaches the earth's atmosphere, which is reduced to approximately 4%–6% as the solar radiation travels to the surface (ground level). Typically, the maximum value of UV radiation is approximately 50 W/m^2 for a south-facing surface in the Northern Hemisphere or a north-facing surface in the Southern Hemisphere tilted at an angle equal to the latitude of the location. Typical solar radiation data available for most locations in the world represent the

insolation values for the entire spectrum. However, utilization of these data for modeling detoxification processes requires the estimation of the UV component. Riordan et al. (1990) developed correlations that related measured UV to measured total values. Based on their study, global horizontal and direct normal UV radiation can be calculated as

$$\frac{I_{uv,h}}{I_t} = 0.14315K_t^2 - 0.20445K_t + 0.135544 \quad (10.23)$$

$$\frac{I_{uv,b}}{I_{t,b}} = 0.0688e^{-0.575m} = 0.688 \exp \left(\frac{-0.575}{\sin \alpha} \right), \quad (10.24)$$

where K_t is the cloudiness index and m is the air mass. These correlations were based on limited measurements at only a few locations (Cape Canaveral, Florida; San Ramon, California; and Denver, Colorado) with an uncertainty greater than 20%.

The functional form of irradiance on the reactor aperture varies according to the reactor type. For a flat-plate reactor, UV irradiance can be calculated by using the following equation (Saltiel et al. 1992), which is a modified form of an equation given by Rabl (1981) for total solar radiation:

$$I_{uv} = I_{uv,b} K(i) \max\{\cos i, 0\} + 0.5K(i)[I_{uv,d}(1 + \cos \beta) + \rho_{uv,gr} I_{uv,h}(1 - \cos \beta)], \quad (10.25)$$

where i is the incident angle of the reactor aperture (calculated at the midpoint of each hour), $K(i)$ is the incident angle modifier, β is the reactor tilt, and $\rho_{uv,gr}$ is the UV reflectance of the ground. Ground reflectance values in the UV region are determined for various ground covers using a data fit developed by Green (1983). Ground cover may be assumed to be farmland, where reflectance is approximately 4%, unless covered by snow, where reflectance is approximately 29% (Green 1983). The incident angle modifier $K(i)$, defined as the ratio of the UV transmittance-absorbance product for the reactor at an angle i to the normal, is dependent on the materials used for reactors. Actual values of $K(i)$ for the reactor under consideration must be used whenever possible. In the absence of actual values, the following expression for a solar thermal collector may be used, although reactor receiver covers and the useful solar spectrum are generally not the same as those for solar thermal collectors.

$$K(i) = 1 - 0.10 \frac{1}{\cos i} - 1. \quad (10.26)$$

March et al. (1995) demonstrated the use of above-described reaction kinetic models and solar insolation models to simulate the performance of solar detoxification systems.

10.6 Catalyst Development

At present, TiO_2 in anatase form is the most common catalyst used in solar photocatalytic detoxification. As explained earlier, this limits the useful range of the solar spectrum to wavelengths of less than approximately 388 nm. Only approximately 4%–6% of the solar radiation is available in this wavelength range. Therefore, the catalyst improvement research is concentrated on

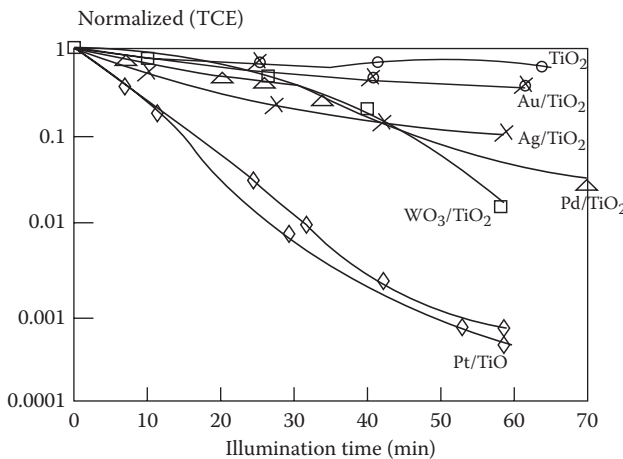
1. Physical and chemical modification of TiO_2 to improve the catalyst performance
2. Dye sensitization to increase the useful wavelength range of the solar radiation
3. Development of homogenous catalysts

Figure 10.12 shows the results of the comparative tests conducted on modified catalysts. It can be seen that several methods, by themselves or in combination, can be used to improve the performance of the TiO_2 catalyst.

According to Magrini et al. (1994), thermal treatment at 550°C–600°C can double the reaction rates. Manipulating the surface area and particle size can also improve the catalyst performance. Metallization of TiO_2 particles with Pt can improve the performance five times, while Pd, Ag, and WO_3 can improve it by factors of 2 to 3.*

Another improvement being investigated by researchers is the use of photosensitizer (dye) molecules on the surface of a semiconductor. In dye sensitization, a dye molecule absorbs visible light, gets excited to a higher energy state, and interacts with the semiconductor molecule (TiO_2), water, and oxygen to produce hydroxyl radicals. The result is an extension of the photoresponse of the semiconductor photocatalyst, making it capable of using a broader spectrum of solar radiation than the semiconductor alone (Dieckmann et al. 1994; Kamat 1993). Dye sensitization of TiO_2 photocatalyst has the potential to reduce the overall cost of treatment. Methylene blue and Rose Bengal have been the most common dyes investigated so far. The results have been inconclusive.

* For detailed data on the catalyst improvement research, see Crittendon et al. (1995), Linder et al. (1995), and Magrini et al. (1994, 1995).

**FIGURE 10.12**

Concentration vs. illumination time data for metallized TiO₂. The metal-containing catalyst contained 1–2 wt% metal, and the WO₃/TiO₂ contained 3 wt% WO₃. All reactions were conducted in a 0.51 circulating batch reactor with 0.05 wt% catalyst at 22°C, 25 ppm initial TCE, and illuminated with a 1000 W Xe source. (From Magrini, K.A. et al., *Solar Engineering* 1994. *Proceedings of the 1994 ASME International Solar Engineering Conference*, pp. 163–170, 1994.)

10.7 System Design Methodology

The effectiveness of solar detoxification systems has been demonstrated commercially (Goswami 1995). Goswami and Anheden (1994) have developed a methodology that can be used for the design of simple solar detoxification systems.

The procedure for designing a solar detoxification system requires the selection of the reactor, reactor operational mode (slurry or fixed matrix), reactor field configuration (series or parallel), treatment system mode (once through or batch), flow rate, pressure drop, pretreatment, catalyst and oxidant loading, pH control, and catalyst reuse system. For the treatment of groundwater or industrial wastewater, the following must be known or determined a priori:

1. Complete analysis of the water to be treated to determine pretreatments
2. Target chemicals and their initial and final desired concentrations
3. Amount of water to be treated daily

The following steps describe a design procedure:

A. Laboratory Treatment Study

A laboratory treatment study must be conducted to determine the following parameters for optimum treatment:

1. Reaction rate constant
2. Catalyst loading
3. Oxidant (H_2O_2 , O_3 , etc.) loading, if any
4. Required pH
5. Pre- and posttreatment

Indoor reactors, with simulated radiation similar to the expected solar radiation and reactor geometry similar to the chosen outdoor reactor, may be used for the laboratory treatment study.

Experiments are conducted to find the concentration–time history of the pollutant chemical under consideration from which the reaction rate constant k may be calculated as explained earlier. If more than one target chemical is present, reaction rate constants for all the chemicals must be determined. In this case, the lowest value of k should be used for the reactor design.

B. Treatment Facility Operational Mode

A solar detoxification facility may be operated in the following modes:

1. Batch mode (Figure 10.13a): In this mode, the effluent is stored in a tank and is continuously recirculated through the reactors until the desired destruction is achieved. Operation in this mode requires one or more storage tanks. If the desired destruction of the contaminated water is not achieved in a single day, the system is operated the following day until the desired destruction is obtained. Shallow solar ponds that combine reactor and storage fall in this category.

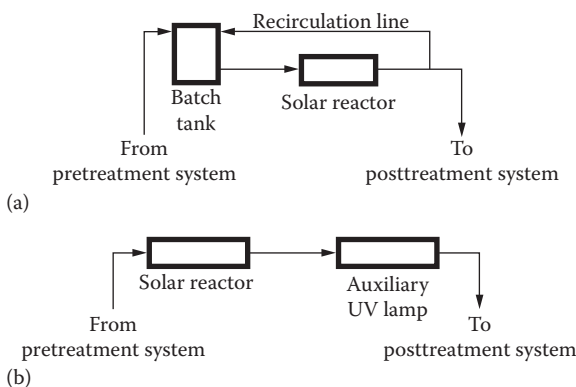


FIGURE 10.13

Schematics of treatment facility operational modes: (a) batch mode; (b) single pass mode. (From Blake, D.M. et al., Solar photocatalytic detoxification of water. In *Advances in Solar Energy*, Vol. 7, K.W. Boer, ed. American Solar Energy Society, Boulder, CO, pp. 167–210, 1992.)

2. Single-pass mode (once through) (Figure 10.13b): In this mode, the reactor area and the flow rates are designed such that the desired destruction is achieved in a single pass. The flow rates in this case are normally lower. The solar insolation varies throughout the day, and hence, the flow rate through the reactors should be varied with the intensity of the solar insolation. As the UV intensity decreases, the flow rate through the reactor should be decreased in order to maintain the same final concentration.

C. Residence Time

For the first-order reaction kinetics, the required residence time t is calculated by using Equation 10.16 as

$$\frac{C_f}{C_i} = e^{-kt} \quad (10.27)$$

or

$$t = \frac{\ln(C_i/C_f)}{k}, \quad (10.28)$$

where C_f is the final concentration of the contaminant, C_i is the initial concentration of the contaminant, and k is the rate constant (min^{-1}).

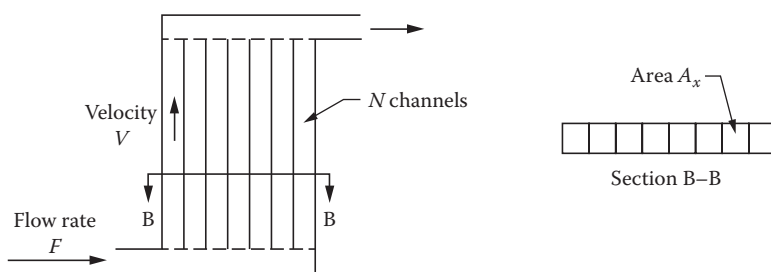
The rate constant k is obtained from k_o (which is the measured rate constant for the intensity I_o) by adjusting it for the actual intensity, I , according to Equations 10.19 through 10.22. Since the intensity I changes throughout the day, k would require continuous adjustment. An approximate and simplified value can be used by adjusting k_o for an average value of I for the useful part of the day.

The time needed for the detoxification of the wastewater depends on the desired amount of destruction of the contaminant. As can be seen from the above equation, the time increases exponentially for destruction approaching 100%.

D. Reactor Area

For a given amount of wastewater to be treated per day, q , an average useful time of operation per day, T , and the reactor geometry, the fluid velocity in the reactor can be calculated. For a reactor with N parallel tubes/channels that are connected between two headers, the flow velocity can be calculated as (Figure 10.14)

$$\text{Total flow rate } F = \frac{q}{T} \quad (10.29)$$

**FIGURE 10.14**

Flow through a reactor with N channels.

$$\text{Velocity in one channel } v = \frac{F}{(NA_x)}, \quad (10.30)$$

where A_x is the cross-sectional area of a channel.

From the required residence time t as calculated from Equation 10.28, the flow velocity v as calculated from Equation 10.30, and the length of one reactor L , the total number of reactors for a once-through system can be calculated as follows:

$$\text{Residence time for one reactor } t_r = \frac{L}{v}. \quad (10.31)$$

Total number of reactors = t/t_r (rounded off to the next integer number).

The following is given as an example of the reactor design using the experimental data from field tests conducted at TyAFB (Goswami et al. 1993).

Example 10.3

Using the experimental data for treatment of groundwater at TyAFB in Florida (Table 10.3), find (1) the residence time for 99.75% destruction of the contaminants and (2) the number of reactors required to treat 36,000 L of contaminated groundwater per day, using tubular reactors.

Each reactor is 2.44 m \times 1.83 m (nominal) and contains 132 tubes that are 2.44 m long and 6.4 mm in diameter. The volume capacity of each reactor is 25 L. Assume a yearly average UV radiation value of 28 W/m² for an average of 6 h each day.

TABLE 10.3

Experimental Parameters and Results for TyAFB Field Tests

Test No.	UV (W/m ²)	TiO ₂ %	pH	H ₂ O ₂	Rate Constants, K (min ⁻¹)			
					Benzene	Toluene	Ethylbenzene	<i>m</i> , <i>p</i> -Xylene
1	45.3	0.1	6	100	0.0327	0.0350	0.0311	0.0333
2	47.7	0.05	6	100	0.0263	0.321	0.0304	0.0337
3	47.2	0.1	5	100	0.364	0.364	0.364	0.364

Source: Goswami, D.Y. et al., Solar photocatalytic treatment of groundwater at Tyndall AFB, field test results, *Solar 1993, Proceedings of the American Solar Energy Society Annual Conference*, pp. 235–239, 1993.

Note: Test 3 consisted of city water spiked with BTEX.

Solution

From Table 10.3, the minimum *k* value is selected for the residence time and the design of the reactor. For example, for Test 1, the minimum *k* value is 0.0311 (min⁻¹). The solar UV intensity for this test data is 45.3 W/m². Since the *k* value depends on the UV intensity, it needs to be adjusted for the design UV intensity. In this case, we assume the design for yearly average conditions when the average UV intensity is 28 W/m². Thus, the adjusted *k* value is given by the following equation:

$$k = k_o \frac{I}{I_o} \quad (10.32)$$

or

$$k = 0.0311 \times \frac{28}{45.3} = 0.0192(\text{min}^{-1}). \quad (10.33)$$

Assuming first-order reaction kinetics, for a 99.75% destruction (*C_f/C_i* = 0.0025), the residence time can be found from Equation 10.28 as

$$t = \frac{\ln(C_i/C_f)}{k} \quad \text{or} \quad t = \frac{\ln(1/(0.0025))}{0.0192} = 312 \text{ min}$$

or

$$t = 312 \text{ min (approximately 5.2 h).}$$

The time that is needed for detoxification increases exponentially for destruction rates approaching 100%. For example, for the above kinetics, the residence time increases from 72.2 min for 75% destruction, to 156 min for 95% destruction, to 312 min for 99.75% destruction rate.

For a single-pass (once-through) system, number of reactors depends upon several parameters, such as the amount of material to be treated, residence time required, and the size and configuration of reactors. In this example, we have to treat 36,000 L of wastewater per day.

Assuming the length of a day as 6 h, the volume of water to be treated per minute would equal $36,000/(6 \times 60) = 100$ Lpm. Knowing the flow rate, we can now determine the residence time of wastewater in one reactor as follows:

$$\text{Total flow rate} = 100 \text{ Lpm}$$

$$\text{Flow in one tube} = 100/132 = 0.76 \text{ Lpm} = 760 \text{ cm}^3/\text{min}$$

$$\text{Cross-sectional area of one tube} = (\pi/4) d^2 = 0.32 \text{ cm}^2$$

Hence, velocity = $760/0.32 = 2375 \text{ cm/min} = 0.39 \text{ m/s}$ and residence time for one reactor = length of tube/velocity = $2.44 \text{ m}/0.39 \text{ m/s} = 6.26 \text{ s}$.

Therefore, the number of reactors required = total residence time/(residence time in one reactor) = $(5.2 \text{ h} \times 3600)/6.26 = 2990$ reactors.

The number of reactors strongly depends upon the reaction rate constant k . For example, the k value for the city water—spiked with the same amount of BTEX (benzene, toluene, ethylbenzene, and xylene) as found in the groundwater—was determined to be 0.361 in comparison to an average of 0.031 for the groundwater. The residence time required for the k value of 0.361 will be only 27 min, as compared to 5.2 h for a k value of 0.031. Following the above procedure in this case, the number of reactors required will be only 262 as compared to 2990 for the groundwater.

10.7.1 Catalyst Life

Catalyst life and the fraction of the catalyst useful after each run are important parameters in the process economics. Catalyst may be poisoned by contaminants and particles or washed away in the discharge water, reducing the catalyst's life and requiring additional catalysts for each run. Useful catalyst life can be estimated by conducting tests with actual contaminated water a number of times and determining the reduction in reaction rate constant each time. In the field tests conducted at TyAFB, Goswami et al. (1993) found that approximately 10% of the catalyst was lost in each run.

10.8 Gas-Phase Photocatalytic Detoxification

Since air contains approximately 21% oxygen and that contaminant levels are often in the range of 0.1 to 100 ppm, it follows that contaminated air has a great deal of excess oxidant available versus that needed for total oxidation

of impurities (Ollis 1994). Published literature shows that gas-phase photocatalytic oxidation can be used successfully to oxidize paraffins, olefins, and alcohol (Dibble and Raupp 1990); TCE (Anderson et al. 1993; Dibble and Raupp 1990; Nishida et al. 1993); *trans*-dichloroethylene (*trans*-DCE) and *cis*-dichloroethylene (*cis*-DCE) (Nimlos et al. 1993); toluene (Ibusuki and Takeuchi 1986); airborne nitroglycerin (Raissi and Muradov 1993); and 3-chlorosalicylic acid (Sabate et al. 1991; Tunesi and Anderson 1991).

10.8.1 Photoreactors

Many photoreactors have been successfully studied for liquid-phase photocatalysis, but reactor design information for gas-phase photocatalytic processes is scarce. There are two major differences between gas-phase systems and aqueous systems that affect the performance of the reactor. First, the concentration of oxygen in a gas-phase reactor, which is 20% by volume, provides a sufficient supply of electron acceptors. Second, the concentration of water vapor present in gas-phase reactors can vary considerably, unlike aqueous photoreactors in which water molecules are always the predominant species in contact with the catalyst (Anderson et al. 1993).

Because of intense commercial interest in using photocatalysis to clean indoor air and industrial emissions, very little information is available in the open literature on gas-phase reactors.

Figure 10.15 shows an off-gas photocatalytic treatment system based on a commercial system (Miller and Fox 1993; Turchi et al. 1994). This system is

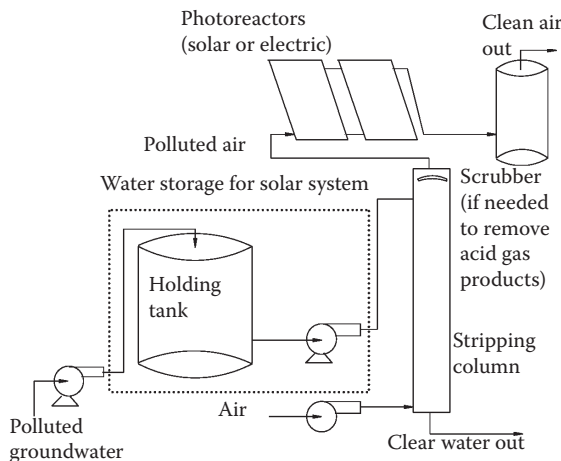


FIGURE 10.15

Schematic of an air stripper with photocatalytic off-gas treatment. (From Turchi, C.S. et al., Off-gas treatment by photocatalytic oxidation: Concepts and economics. *Proceedings of the First International Conference on Advanced Oxidation Technologies for Water and Air Remediation*, London, Ontario, Canada, Book of Abstracts, pp. 125–128, 1994.)

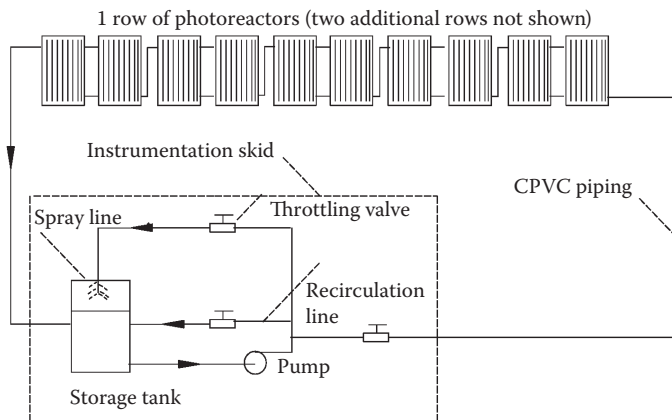
designed to transfer volatile contaminants from the groundwater to air in an air stripper tower. The contaminants transferred to air are then treated by solar radiation or UV lamps in photoreactors.

10.9 Commercial/Industrial Applications

Solar photocatalytic detoxification research to date has shown great potential for the application of this technology to treatment of groundwater and soils contaminated with toxic organic chemicals, as well as treatment of certain industrial wastewaters. Recent research also shows the potential of this technology for gas-phase detoxification and for disinfection of water and air. However, to date, there has been very little commercial/industrial use of this technology. Published literature shows only three engineering-scale applications for groundwater treatment in the United States and one industrial wastewater treatment in Spain. Field demonstrations of this technology for groundwater remediation took place at the Lawrence Livermore National Laboratory (LLNL) and TyAFB. Engineering-scale field experiments were conducted by NREL at LLNL to treat groundwater contaminated with TCE. The field system consisted of 158 m² of parabolic trough reactors, as described earlier, and used Degussa P25 TiO₂ particles as catalyst in a slurry flow configuration. With 0.1% TiO₂ concentration in the slurry, the TCE concentration was reduced from 200 ppb to less than 5 ppb. The field experiment is detailed in Blake (1994b).

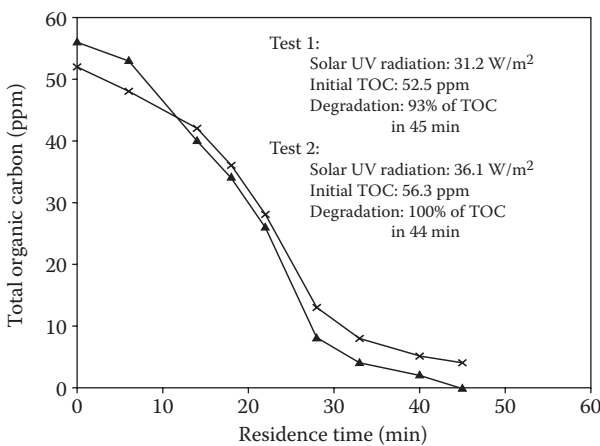
Engineering-scale demonstration of the nonconcentrating solar reactor technology was conducted at TyAFB in 1992 (Goswami et al. 1993). A "one-sun" solar detoxification facility was constructed to treat groundwater contaminated with fuel, oil, and lubricants leaking from the underground storage tanks. The contaminants of interest included BTEX, although there were other chemicals also present in the groundwater. The facility shown in Figure 10.16 consisted of three rows of five-each series connected 2.4 m × 3.1 m (nominal) photoreactors developed by the University of Florida and an equipment skid from NREL containing storage tanks and metering pumps for the addition of acid, base, H₂O₂, and TiO₂ to the contaminated water.

The field tests were successful in destroying the BTEX in the groundwater as seen from the results shown earlier in Figure 10.8. However, in a laboratory test using the same reactors in similar sunlight conditions and city water spiked with the same amounts of BTEX as in the groundwater, the reaction rates were an order of magnitude faster. These results suggest that a careful site treatability study and establishment of appropriate pretreatment methods are extremely important in the successful field deployment of solar photocatalytic processes.

**FIGURE 10.16**

Schematic diagram of solar groundwater treatment test facility at TyAFB.

Blanco and Malato (1994) have described an engineering-scale field demonstration of treatment of industrial wastewater from a resins factory containing organic contaminants such as phenols, fornol, phthalic acid, fumaric acid, maleic acid, glycols, xylene, toluene, methanol, butanol, and phenylethylene, amounting to 600 ppm TOC. They used 12 two-axis tracking parabolic troughs of total aperture area of 384 m², with borosilicate glass tube absorber reactors. One hundred milligrams per liter of TiO₂ was used as the catalyst and 0.007 molar concentration of sodium peroxydisulphate (Na₂S₂O₈) was used as an oxidizing additive. Figure 10.17

**FIGURE 10.17**

Treatment of industrial wastewater containing organic contaminants. (From Blanco, J., and S. Malato., Solar photocatalytic mineralization of real hazardous waste water at pre-industrial level. In *Solar Engineering 1994*, D.E. Klett, R.E. Hogan, and T. Tanaka, eds. pp. 103–109, 1994.)

shows 100% degradation of TOC in 44 min, amounting to 1.25 mg/L/min degradation rate of the mixed contaminants. On the basis of this rate, they estimated treatment costs of \$19.3/m³ of industrial wastewater treating 10 m³/day.

Other investigations of treatment of real industrial wastewater, although not to engineering scale, do show the potential of the solar treatment process where conventional treatment methods have been unsuccessful. Goswami and Anheden (1994) demonstrated the potential for solar photocatalytic oxidation for decolorization and COD reduction of wastewater from a 5-fluorouracil (a cancer drug) manufacturing plant. They showed that using 0.1% TiO₂ as the catalyst and 2400 ppm H₂O₂ as an oxidizing additive, the color of the wastewater is reduced by 80% in 1 h and the COD of the wastewater was reduced by 70% in 16 h. All of the conventional (nonsolar) treatments tried by the manufacturers for the reduction of color and COD failed (Anheden et al. 1995). Zaidi (1993) showed the potential of the solar photocatalytic technology to reduce color and COD of distillery wastewater pretreated by anaerobic microbiological methods. Figure 10.18 shows that both color and COD can be reduced successfully by the solar process where conventional methods have failed to work.

Both of the above studies report that the solar treatment works much better if the wastewater is first diluted with clean water to approximately 10%–20% of the initial concentration. Although this method increases the volume of water to be pumped, a continuous system can be designed by recirculating a fraction of the treated water for dilution.

In a laboratory study, Turchi et al. (1989) showed the potential of photocatalytic treatment of the wastewater from pulp and paper mills. Although no studies have been published on the potential use of the solar process for the cleanup of textile mill wastewater, preliminary studies indicate that the solar process can be very successful in treating textile plant wastewater, namely, dyehouse wastewater. Since many manufacturing plants, such as textiles, pulp and paper, and chemicals, are located in areas where a large part of the solar UV is diffuse and where large open areas with solar access are available, the shallow solar pond reactors may be used.

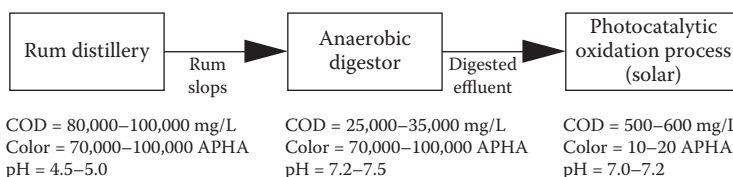


FIGURE 10.18

Treatment of distillery effluent by anaerobic digestion and post-treatment by solar photocatalytic oxidation process. (From Zaidi, A., Solar photocatalytic post-treatment of anaerobically digested distillery effluent. M.S. thesis, University of Florida, Gainesville, FL, 1993.)

10.10 Solar Disinfection of Water and Air

UV disinfection has been widely used in the past to destroy biological contaminants by using UV radiation from germicidal lamps primarily at 254 nm wavelength. Solar UV, which is primarily at 290–400 nm wavelength, is much less active as a germicide. However, a review of the literature has shown that photocatalytic disinfection has been demonstrated in Japan by Matsunaga (1985) and later by others (Ireland et al. 1993; Morioka et al. 1988; Nagame et al. 1989; Onoda et al. 1988). In a recent study, Block and Goswami (1995) have studied the antibacterial effect of solar photocatalytic reaction and the conditions that affect it. Their study showed that several common bacteria (*Serratia marcescens*, *Escherichia coli*, and *Streptococcus aureus*) were killed in just a few minutes on solar exposure in the presence of TiO_2 , whereas without TiO_2 , it took over an hour to destroy them (Figure 10.19). A concentration of 0.01% TiO_2 was most effective in killing bacteria and even 0.001% was quite effective. However, bactericidal activity went down at 0.1% and higher concentrations of TiO_2 .

Recently, some studies have appeared in the literature that report disinfection and deodorization of air (Goswami et al. 1995). Goswami et al. (1995) demonstrated the antibacterial effect of titanium dioxide in indoor air. They used a TiO_2 -coated fiberglass matrix reactor to kill *S. marcescens* bacteria in air. Recently, Dalrymple et al. (2010, 2011) conducted a detailed analysis of the disinfection mechanisms of photocatalytic oxidation and developed a model. Results indicated that the photocatalytic process can be a viable technique for controlling indoor air quality.

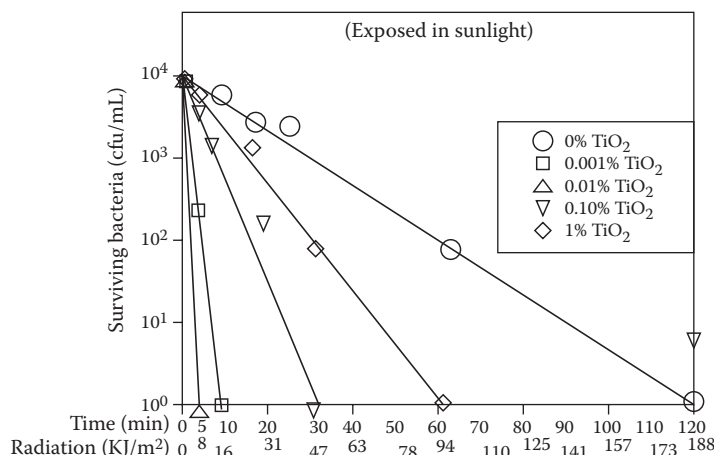


FIGURE 10.19

Effect of concentration of TiO_2 on survival of *Serratia marcescens* bacteria. (From Block, S.S., and D.Y. Goswami, Chemically enhanced sunlight for killing bacteria. *Solar Engineering, Proceedings of the ASME International Solar Energy Conference*, Hawaii, March, pp. 431–438, 1995.)

10.11 Summary

Solar photocatalytic detoxification and disinfection processes have shown great promise for the treatment of contaminated groundwater, industrial wastewater, air, and soil. Development of these processes has reached a point where the solar technology can be competitive with the conventional treatment methods. In some cases requiring decolorization and reduction of COD, the photocatalytic technology may be the only effective treatment technology. The next logical step is the commercial demonstration of the technology. Although only a few commercial demonstrations have been reported to date, it is expected and hoped that activity will pick up considerably in the future.

PROBLEMS

1.
 - i. A laboratory test with TiO_2 as the catalyst produced a concentration time plot of *o*-xylene destruction identical to that shown in Figure 10.8. The reactor used was of 40 gal while the storage tank contained 100 gal, with minimal volume in piping. Determine the reaction rate constant corrected for the finite volumes of the system.
 - ii. A single reactor is to be designed to decontaminate water with the same initial concentration of *o*-xylene as above to acceptable levels of 10 ppb. If the reaction rate is the same as found above, what is the required residence time for this process? What is the residence time for 99.9% destruction? 100% destruction?
 - iii. Each of 250 nonconcentrating channel-type reactors connected in series and parallel sets is composed of 140 channels 3 m long, 1 cm wide, and 3 cm deep. The system is designed to treat 1000 L of *o*-xylene-contaminated water per day. If the system operates for 7 h each day, what is average reaction rate constant? At what velocity does the solution flow? Use the residence time for destruction to acceptable levels of contaminant. Assume 90% destruction levels are achieved.
 - iv. A similar reactor tested with 35 W/m^2 insolation in a controlled indoor laboratory experiment yielded a reaction rate constant of 0.283 min^{-1} . What must be the insolation in the field trials based on these tests. A 0.01% TiO_2 catalyst solution is used? Can the field reactor site dictate which catalyst to use?
2. Discuss the effects of the following factors on the photocatalytic destruction of organic contaminants. How are the concentration–time histories of the contaminant affected?

- i. Illumination intensity
 - ii. Catalyst type
 - iii. Addition of inorganic and organic particles
 - iv. Dissolved oxygen concentration
 - v. pH of the solution
 - vi. Temperature
 - vii. Metallization of the catalyst
 - viii. Dye sensitization
-

References

- Anderson, M., S. Nishiida, and S. Cervera-March. 1993. Photodegradation of trichlorethylene in the gas phase using TiO₂ porous ceramic membrane. *Photocat. Purific. Water Air* 1: 405–420.
- Anheden, M., D.Y. Goswami, and G. Svedberg. 1995. Photocatalytic treatment of wastewater from 5-fluorouracil manufacturing. *Solar Engineering 1995, Proceedings of the 1995 ASME International Solar Energy Conference*.
- Bahnemann, D., D. Bockelmann, and R. Goslich. 1991. Mechanistic studies of water detoxification in illuminated TiO₂ suspensions. *Sol. Energy Mater.* 24: 564–583.
- Barbeni, M. et al. 1985. Photodegradation of pentachlorophenol catalyzed by semiconductor particles. *Chromosphere* 14(2): 195–208.
- Bard, A.J. 1979. Photoelectrochemistry and heterogeneous photocatalysis at semiconductors. *J. Photochem.* 10(1): 59–75.
- Bedford, J. et al. 1994. Performance of non-concentrating solar photocatalytic oxidation reactors, part II: Shallow pond configuration. *J. Sol. Energy Eng., ASME* 116(1): 8–13.
- Blake, D.M. 1994a. Bibliography of work on the photocatalytic removal of hazardous compounds from water and air. NREL Report #NREL/TP-430-6084. NTIS, Springfield, VA.
- Blake, D.M. 1994b. Solar processes for the destruction of hazardous chemicals, Chapter 10. In *Alternative Fuels and the Environment*, F.S. Sterrett, ed. Lewis Publishers, Boca Raton, FL.
- Blake, D.M. et al. 1991. Kinetic and mechanistic overview of TiO₂-photocatalyzed oxidation reactions in aqueous solution. *Sol. Energy Mater.* 24: 584–593.
- Blake, D.M., H.F. Link, and K. Eber. 1992. Solar photocatalytic detoxification of water. In *Advances in Solar Energy*, Vol. 7, K.W. Boer, ed. American Solar Energy Society, Boulder, CO, pp. 167–210.
- Blanco, J., and S. Malato. 1994. Solar photocatalytic mineralization of real hazardous waste water at pre-industrial level. In *Solar Engineering 1994*, D.E. Klett, R.E. Hogan, and T. Tanaka, eds. ASME, New York, pp. 103–109.
- Block, S.S., and D.Y. Goswami. 1995. Chemically enhanced sunlight for killing bacteria. *Solar Engineering, Proceedings of the ASME International Solar Energy Conference, Hawaii, March*, pp. 431–438.

- Carey, J.H., J. Lawrence, and H.M. Tosine. 1976. Photodechlorination of polychlorinated biphenyls in the presence of titanium dioxide in aqueous solution. *Bull. Environ. Contam. Toxicol.* 16(6): 697–701.
- Crittendon, J.C. et al. 1995. Destruction of organic compounds in water using fixed bed photocatalysts. *Solar Engineering 1995. Proceedings of the 1995 ASME International Solar Engineering Conference*, pp. 449–457.
- Dalrymple, O.K., E. Stefanakos, M.A. Trotz, and D.Y. Goswami. 2010. A review of the mechanisms and modeling of photocatalytic disinfection. *Appl. Catal. B: Environ.*, 98(1–2): 27–38.
- Dalrymple, O.K., W. Isaacs, E. Stefanakos, M.A. Trotz, and D.Y. Goswami. 2011. Lipid vesicles as model membranes in photocatalytic disinfection studies. *J. Photochem. Photobiol. A: Chemistry*, 221(1): 64–70.
- Dibble, L.A., and G.B. Raupp. 1990. Kinetics of the gas-solid heterogeneous photocatalytic oxidation of trichlorethylene by near UV illuminated titanium dioxide. *Catal. Lett.* 4: 345–354.
- Dieckmann, M.S., K.A. Gray, and R.G. Zepp. 1994. The sensitized photocatalysis of azo dyes in a solid system: A feasibility study. *Chemosphere* 28(4): 1021–1034.
- Elizardo, K. 1991. Fighting pollution with hydrogen peroxide. *Pollut. Eng.* 23: 106–109.
- Glatzmaier, G.C., and M.S. Bohn. 1993. Solar assisted combustion of 1,2 dichlorobenzene. *Proceedings of the AIChE/ASME National Heat Transfer Conference*, August.
- Glatzmaier, G.C., M.S. Mehos, and R.G. Nix. 1990a. Solar destruction of hazardous chemicals. *J. Environ. Sci. Health* A25(5): 571–581.
- Glatzmaier, G.C., M.S. Mehos, and R.G. Nix. 1990b. Solar destruction of hazardous chemicals. *Solar Engineering 1990, Proceedings of the ASME International Solar Energy Conference*, pp. 153–158.
- Goswami, D.Y. 1995. Engineering of solar photocatalytic detoxification and disinfection processes. *Adv. Solar Energy* 13: 208.
- Goswami, D.Y., and M. Anheden. 1994. Preliminary study of photocatalytic oxidation of wastewater from 5-fluorouracil manufacturing. Report #UFME/SEECL-9402. Solar Energy and Energy Conversion Laboratory, University of Florida, FL, February.
- Goswami, D.Y. et al. 1993. Solar photocatalytic treatment of groundwater at Tyndall AFB, field test results. *Solar 1993, Proceedings of the American Solar Energy Society Annual Conference*, pp. 235–239.
- Goswami, D.Y., D. Trivedi, and S.S. Block. 1995. Photocatalytic disinfection of indoor air. *Solar Engineering, Proceedings of the ASME International Solar Energy Conference*, Hawaii, March, pp. 421–430.
- Green, A.E.S. 1983. The penetration of ultraviolet radiation to the ground. *Phys. Plant* 58: 351.
- Heller, A. 1981. Conversion of sunlight into electrical power and photoassisted electrolysis of water in photoelectrochemical cells. *Acc. Chem. Res.* 14: 154–162.
- Heller, A., and J.R. Brock. 1991. Materials and methods for photocatalyzing oxidation of organic compounds in water. United States Patent 4,997,576, March 5.
- Heller, A. et al. 1992. Photoassisted oxidation of oil and organic spill on water. *Proceedings of the First International Conference on TiO₂ Photocatalytic Purification and Treatment of Water and Air*, London, Ontario, pp. 39–155.
- Ibusuki, T., and K. Takeuchi. 1986. Toluene oxidation on UV-irradiated titanium dioxide with and without O₂, NO₂ or H₂O at ambient temperature. *Atmos. Environ.* 20: 1711–1715.

- Ireland, J.S. et al. 1993. Inactivation of *Escherichia coli* by titanium dioxide photocatalytic oxidation. *Appl. Environ. Microbiol.* 59: 1668–1670.
- Kamat, P.V. 1993. Photochemistry on nonreactive and reactive (semiconductor) surfaces. *Chem. Rev.* 93: 267–300.
- Klausner, J.F. et al. 1994. On the accurate determination of reaction rate constants in batch-type solar photocatalytic oxidation facilities. *J. Sol. Energy Eng., ASME* 116(1): 19–24.
- Legrini, O., E. Oliveros, and A.M. Braun. 1993. Photochemical processes for water treatment. *Chem. Rev.* 93: 671–698.
- Linder, M. et al. 1995. Solar water detoxification: Novel TiO₂ powders as highly active photocatalysts. *Solar Engineering 1995. Proceedings of the ASME International Solar Engineering Conference*, pp. 399–408.
- Link, H., and C.S. Turchi. 1991. Cost and performance projections for solar water detoxification system. *Solar Engineering 1991. Proceedings of the ASME International Solar Energy Conference*, pp. 289–294.
- Magrini, K.A. et al. 1994. Improving catalyst performance for the solar based photocatalytic oxidation of organics. *Solar Engineering 1994. Proceedings of the 1994 ASME International Solar Engineering Conference*, pp. 163–170.
- Magrini, K.A., A. Watt, and B. Rinehart. 1995. Photocatalyst evaluation for solar based aqueous organic oxidation. *Solar Engineering 1995. Proceedings of the 1995 ASME International Solar Engineering Conference*, pp. 415–420.
- March, M., A. Martin, and C. Saltiel. 1995. Performance modelling of nonconcentrating solar detoxification systems. *Sol. Energy* 54(3): 143–151.
- Matsunaga, T. 1985. Sterilization with particulate photosemiconductor. *J. Antibact. Antifung. Agents* 13: 211–220.
- Mehos, M.S., and C.S. Turchi. 1993. Field testing solar photocatalytic detoxification on TCE-contaminated groundwater. *Environ. Prog.* 12: 194–199.
- Miller, R.A., and R. Fox. 1993. Treatment of organic contaminants in air by photocatalytic oxidation: A commercialization perspective. In *Photocatalytic Purification and Treatment of Water and Air*, D.F. Ollis, and H. El-Akabi, eds. Elsevier Publishers, pp. 573–578.
- Morioka, T. et al. 1988. Antibacterial action of powdered semiconductor on a Serotype g *Streptococcus mutans*. *Caries Res.* 22: 230–231.
- Nagame, S. et al. 1989. Antibacterial effect of the powdered semiconductor TiO₂ on the viability of oral microorganisms. *J. Dent. Res.* 68(Special Issue): 1696–1697.
- Nimlos, M. et al. 1993. Direct mass spectrometric studies of the destruction of hazardous wastes: Gas-phase photocatalytic oxidation of trichloroethylene over TiO₂. *Environ. Sci. Technol.* 27: 732–740.
- Nishida, S. et al. 1993. Photocatalytic degradation of trichlorethylene in the gas-phase using titanium dioxide pellets. *J. Photochem. Photobiol. A: Chem.* 70(1): 95–99.
- Oberg, V., D.Y. Goswami, and G. Svedberg. 1993. On photocatalytic detoxification of water containing volatile organic compounds. *Solar Engineering 1993. Proceedings of the ASME International Solar Engineering Conference*, pp. 147–153.
- Ollis, D.F. 1994. *Photoreactors for Purification and Decontamination of Air*. Department of Chemical Engineering, North Caroline State University, Raleigh, NC.
- Ollis, D.F., E. Pelizzetti, and N. Serpone. 1989a. Heterogeneous photocatalysis in the environment: Application to water purification. In *Photocatalysis Fundamentals and Applications*, N. Serpone, and E. Pelizzetti, eds. Wiley-Interscience, New York, pp. 603–637.

- Ollis, D.F., E. Pelizzetti, and N. Serpone. 1989b. Chapter 18. In *Photocatalysis Fundamentals and Applications*, N. Serpone, and E. Pelizzetti, eds. Wiley & Sons, New York.
- Onoda, K. et al. 1988. Photocatalytic bactericidal effect of powdered TiO₂ on *Streptococcus mutans*. *Denki Kagaku* 56(12): 1108–1109.
- Pacheco, J.E., and C.E. Tyner. 1990. Enhancement of processes for solar photocatalytic detoxification of water. *Solar Engineering 1990, Proceedings of the ASME Solar Energy Conference*, pp. 163–166.
- Prairie, M.R., J.E. Pacheco, and L.R. Evans. 1992. Solar detoxification of water containing chlorinated solvents and heavy metals via TiO₂ photocatalysis. *Solar Engineering 1992, Proceedings of the ASME International Solar Energy Conference*, Vol. 1, pp. 1–8.
- Rabl, A. 1981. Yearly average performance of the principal solar collector types. *Sol. Energy* 27: 215.
- Raiissi, A., and N. Muradov. 1993. Flow reactor studies of TiO₂ photocatalytic treatment of airborne nitroglycerin. *Photocat. Purific. Treat. Water Air* 1: 435–454.
- Riordan, C.J., R.L. Hustrom, and D.R. Myers. 1990. Influences of atmospheric conditions and air mass on the ratio of ultraviolet to total solar radiation. SERI Report SERI/TP-215-3895. NREL, Golden, Co.
- Sabate, J. et al. 1991. A kinetic study of the photocatalytic degradation of 3-chlorosalicylic acid over TiO₂ membranes supported on glass. *J. Catal.* 127: 167–177.
- Saltiel, C., A. Martin, and D.Y. Goswami. 1992. Performance analysis of solar water detoxification systems by detailed simulation. *ASME International Solar Energy Conference*, Maui, Hawaii.
- Sherif, S.A., F. Barbir, and T.N. Veziroglu. 1999. Hydrogen energy system. In *Wiley Encyclopedia of Electrical and Electronics Engineering*, J.G. Webster, ed. John Wiley & Sons, Inc., New York.
- Sherif, S.A., D.Y. Goswami, E.K. Stefanakos, and A. Steinfeld. 2014. *Handbook of Hydrogen Energy*. CRC Press, Boca Raton, FL.
- Skocypec, R.D., and R.E. Hogan. 1990. Investigation of a direct catalytic absorption reactor for hazardous waste destruction. *Solar Engineering 1990, Proceedings of the ASME International Solar Energy Conference*, pp. 167–173.
- Tunesi, S., and M. Anderson. 1991. Influence of chemisorption on the photodecomposition of salicylic acid and related compounds using suspended TiO₂ ceramic membranes. *J. Phys. Chem.* 95: 3399–3405.
- Turchi, C.S., L. Edmundson, and D.F. Ollis. 1989. Application of heterogeneous photocatalysis for the destruction of organic contaminants from a paper mill alkali extraction process. Presented at *TAPPI 5th International Symposium on Wood and Pulping Chemistry*, Raleigh, NC.
- Turchi, C.S., E.J. Wolfrum, and R.A. Miller. 1994. Off-gas treatment by photocatalytic oxidation: Concepts and economics. *Proceedings of the First International Conference on Advanced Oxidation Technologies for Water and Air Remediation*, London, Ontario, Canada, Book of Abstracts, pp. 125–128.
- Tyner, C.E. et al. 1989. Rapid destruction of organic chemicals in groundwater using sunlight. Paper presented at the *Hazardous Materials Management Conference/HASMAT CENTRAL*.
- Venkatadri, R., and R.W. Peters. 1993. Chemical oxidation technologies: Ultraviolet light/hydrogen peroxide, Fenton's reagent and titanium dioxide-assisted photocatalysis. *Hazard. Waste Hazard. Mater.* 10: 107–149.

- Wolfrum, E.J., and C.S. Turchi. 1992. Comments on "Reactor dynamics in the evaluation of photocatalytic oxidation kinetics." *J. Catal.* 136: 626–628.
- Wyness, P. et al. 1994. Performance of non-concentrating solar photocatalytic oxidation reactors. Part I: Flat plate configuration. *J. Sol. Energy Eng., ASME* 116(1): 2–7.
- Zaidi, A. 1993. Solar photocatalytic post-treatment of anaerobically digested distillery effluent. M.S. thesis, University of Florida, Gainesville, FL.

Appendix 1: International System of Units, Fundamental Constants, and Conversion Factors

The International System of Units (SI) is based on seven base units. Other derived units can be related to these base units through governing equations. The base units with the recommended symbols are listed in Table A1.1. Derived units of interest in solar engineering are given in Table A1.2.

Standard prefixes can be used in the SI system to designate multiples of the basic units and thereby conserve space. The standard prefixes are listed in Table A1.3.

Table A1.4 lists some physical constants that are frequently used in solar engineering, together with their values in the SI system of units.

Conversion factors between the SI and English systems for commonly used quantities are given in Table A1.5.

TABLE A1.1

The Seven SI Base Units

Quantity	Name of Unit	Symbol
Length	Meter	m
Mass	Kilogram	kg
Time	Second	s
Electric current	Ampere	A
Thermodynamic temperature	Kelvin	K
Luminous intensity	Candela	cd
Amount of a substance	Mole	mol

TABLE A1.2

SI Derived Units

Quantity	Name of Unit	Symbol
Acceleration	Meters per second squared	m/s^2
Area	Square meters	m^2
Density	Kilogram per cubic meter	kg/m^3
Dynamic viscosity	Newton-second per square meter	$\text{N}\cdot\text{s}/\text{m}^2$
Force	Newton (= 1 $\text{kg}\cdot\text{m}/\text{s}^2$)	N
Frequency	Hertz	Hz
Kinematic viscosity	Square meter per second	m^2/s
Plane angle	Radian	rad
Potential difference	Volt	V

(Continued)

TABLE A1.2 (CONTINUED)

SI Derived Units

Quantity	Name of Unit	Symbol
Power	Watt (= 1 J/s)	W
Pressure	Pascal (= 1 N/m ²)	Pa
Radiant intensity	Watts per steradian	W/sr
Solid angle	Steradian	sr
Specific heat	Joules per kilogram-Kelvin	J/kg·K
Thermal conductivity	Watts per meter-Kelvin	W/m·K
Velocity	Meters per second	m/s
Volume	Cubic meter	m ³
Work, energy, heat	Joule (= 1 N·m)	J

TABLE A1.3

English Prefixes

Multiplier	Symbol	Prefix	Multiplier	Symbol
10 ¹²	T	Tera	10 ³	M (thousand)
10 ⁹	G	Giga	10 ⁶	MM (million)
10 ⁶	m	Mega		
10 ³	k	Kilo		
10 ²	h	Hecto		
10 ¹	da	Deka		
10 ⁻¹	d	Deci		
10 ⁻²	c	Centi		
10 ⁻³	m	Milli		
10 ⁻⁶	μ	Micro		
10 ⁻⁹	n	Nano		
10 ⁻¹²	p	Pico		
10 ⁻¹⁵	f	Femto		
10 ⁻¹⁸	a	Atto		

TABLE A1.4

Physical Constants in SI Units

Quantity	Symbol	Value
Avogadro constant	N	6.022169 × 10 ²⁶ kmol ⁻¹
Boltzmann constant	k	1.380622 × 10 ⁻²³ J/K
First radiation constant	C ₁ = 2πhc ²	3.741844 × 10 ⁻¹⁶ W·m ²
Gas constant	R	8.31434 × 10 ³ J/kmol·K
Planck constant	h	6.626196 × 10 ⁻³⁴ J·s
Second radiation constant	C ₂ = hc/k	1.438833 × 10 ⁻² m·K
Speed of light in a vacuum	c	2.997925 × 10 ⁸ m/s
Stefan–Boltzmann constant	σ	5.66961 × 10 ⁻⁸ W/m ² ·K ⁴

TABLE A1.5

Conversion Factors

Physical Quantity	Symbol	Conversion Factor
Area	A	1 ft ² = 0.0929 m ² 1 acre = 43,560 ft ² = 4047 m ² 1 hectare = 10,000 m ² 1 square mile = 640 acres
Density	ρ	1 lb _m /ft ³ = 16.018 kg/m ³
Heat, energy, or work	Q or W	1 Btu = 1055.1 J 1 kWh = 3.6 MJ 1 Therm = 105.506 MJ 1 cal = 4.186 J 1 ft·lb _f = 1.3558 J
Force	F	1 lb _f = 4.448 N
Heat flow rate, refrigeration	q	1 Btu/h = 0.2931 W 1 ton (refrigeration) = 3.517 kW 1 Btu/s = 1055.1 W
Heat flux	q/A	1 Btu/h·ft ² = 3.1525 W/m ²
Heat-transfer coefficient	h	1 Btu/h·ft ² ·F = 5.678 W/m ² ·K
Length	L	1 ft = 0.3048 m 1 in = 2.54 cm 1 mi = 1.6093 km
Mass	m	1 lb _m = 0.4536 kg 1 ton = 2240 lb _m 1 tonne (metric) = 1000 kg
Mass flow rate	\dot{m}	1 lb _m /h = 0.000126 kg/s
Power	\dot{W}	1 hp = 745.7 W 1 kW = 3415 Btu/h 1 ft·lb _f /s = 1.3558 W 1 Btu/h = 0.293 W
Pressure	p	1 lb _f /in ² (psi) = 6894.8 Pa (N/m ²) 1 in. Hg = 3386 Pa
Radiation	I	1 atm = 101,325 Pa (N/m ²) = 14.696 psi 1 langley = 41,860 J/m ² 1 langley/min = 697.4 W/m ²
Specific heat capacity	c	1 Btu/lb _m ·°F = 4187 J/kg·K
Internal energy or enthalpy	e or h	1 Btu/lb _m = 2326.0 J/kg 1 cal/g = 4184 J/kg
Temperature	T	T(°R) = (9/5)T(K) T(°F) = [T(°C)](9/5) + 32 T(°F) = [T(K) - 273.15](9/5) + 32
Thermal conductivity	k	1 Btu/h·ft·°F = 1.731 W/m·K
Thermal resistance	R_{th}	1 h·°F/Btu = 1.8958 K/W

(Continued)

TABLE A1.5 (CONTINUED)

Conversion Factors

Physical Quantity	Symbol	Conversion Factor
Velocity	V	$1 \text{ ft/s} = 0.3048 \text{ m/s}$ $1 \text{ mi/h} = 0.44703 \text{ m/s}$
Viscosity, dynamic	μ	$1 \text{ lb}_m/\text{ft}\cdot\text{s} = 1.488 \text{ N}\cdot\text{s}/\text{m}^2$ $1 \text{ cP} = 0.00100 \text{ N}\cdot\text{s}/\text{m}^2$
Viscosity, kinematic	ν	$1 \text{ ft}^2/\text{s} = 0.09029 \text{ m}^2/\text{s}$ $1 \text{ ft}^2/\text{h} = 2.581 \times 10^{-5} \text{ m}^2/\text{s}$
Volume	V	$1 \text{ ft}^3 = 0.02832 \text{ m}^3 = 28.32 \text{ liters}$ $1 \text{ barrel} = 42 \text{ gal (U.S.)}$ $1 \text{ gal (U.S. liq.)} = 3.785 \text{ liters}$ $1 \text{ gal (U.K.)} = 4.546 \text{ liters}$
Volumetric flow rate	\dot{Q}	$1 \text{ ft}^3/\text{min (cfm)} = 0.000472 \text{ m}^3/\text{s}$ $1 \text{ gal/min (GPM)} = 0.0631 \text{ l/s}$

Appendix 2: Solar Radiation Data

DESCRIPTION OF METHOD*

To find the solar altitude and azimuth:

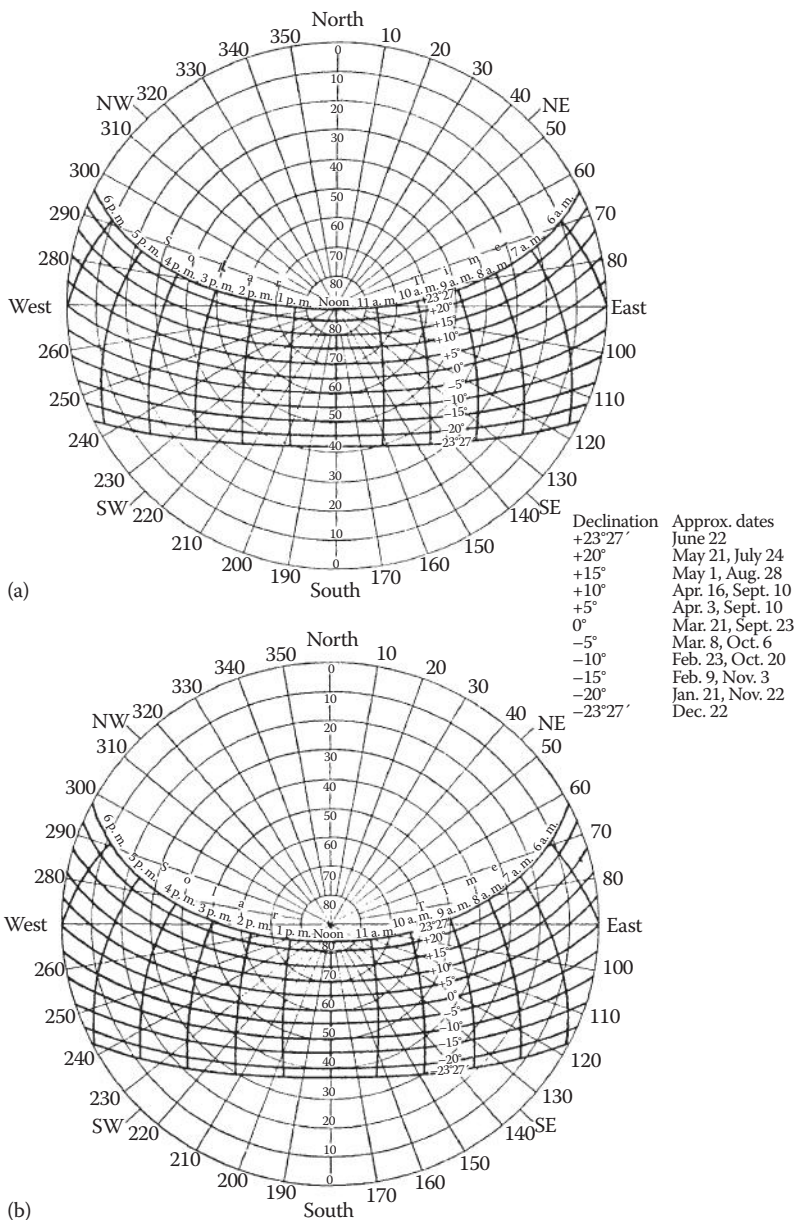
1. Select the chart or charts in Figure A2.1 that are appropriate to the latitude.
2. Find the solar declination δ corresponding to the date.
3. Determine the *true solar time* as follows:
 - a. To the *local standard time* (zone time), add 4' for each degree of longitude the station is east of the standard meridian or subtract 4' for each degree west of the standard meridian to get the *local mean solar time*.
 - b. To the *local mean solar time*, add algebraically the equation of time; the sum is the required *true solar time*.
4. Read the required altitude and azimuth at the point determined by the declination and the true solar time. Interpolate linearly between two charts for intermediate latitudes.

It should be emphasized that the solar altitude determined from these charts is the true geometric position of the center of the sun. At low solar elevations, terrestrial refraction may considerably alter the apparent position of the sun. Under average atmospheric refraction, the sun will appear on the horizon when it actually is approximately 34' below the horizon; the effect of refraction decreases rapidly with increasing solar elevation. Since sunset or sunrise is defined as the time when the upper limb of the sun appears on the horizon, and the semidiameter of the sun is 16', sunset or sunrise occurs under average atmospheric refraction when the sun is 50' below the horizon. In polar regions especially, unusual atmospheric refraction can make considerable variation in the time of sunset or sunrise.

The 90°N chart is included for interpolation purposes; the azimuths lose their directional significance at the pole.

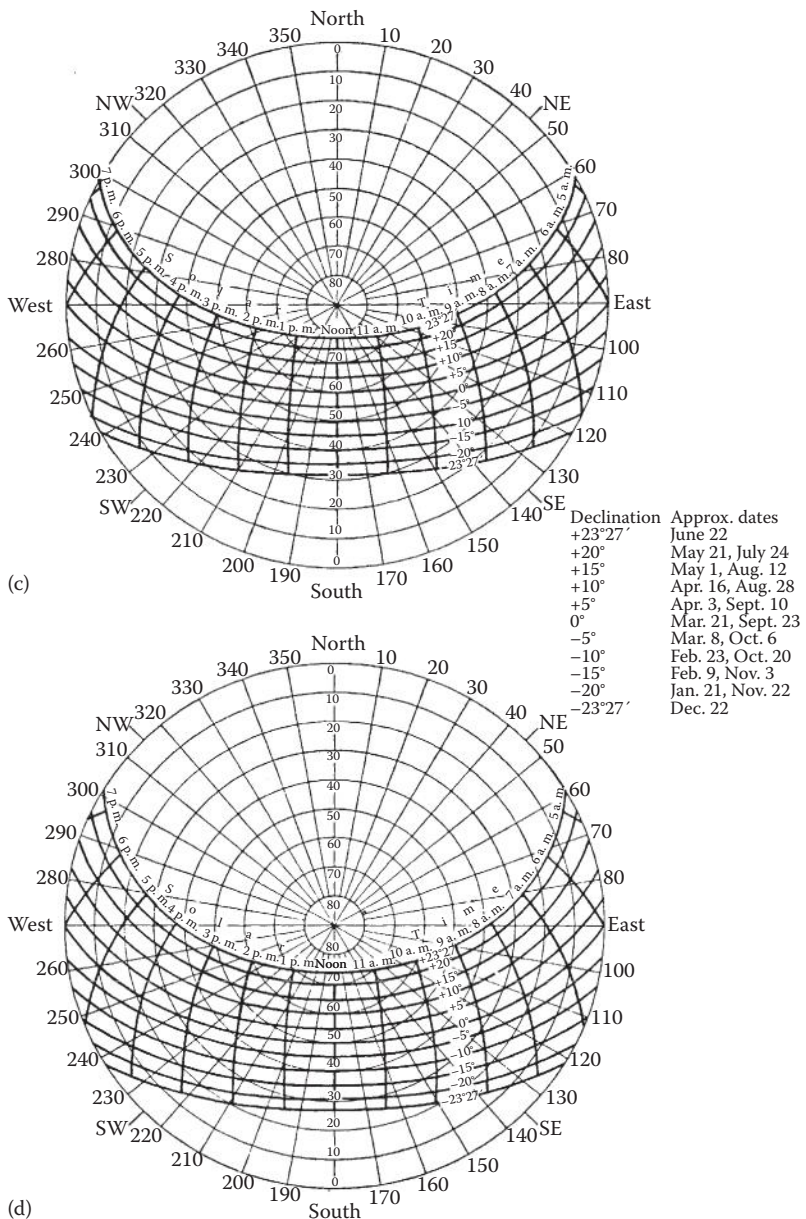
Altitude and azimuth in southern latitudes. To compute solar altitude and azimuth for southern latitudes, change the sign of the solar declination and proceed as above. The resulting azimuths will indicate angular distance from *south* (measured eastward) rather than from north.

* Description and charts in Figure A2.1 from *Smithsonian Meteorological Tables*, Smithsonian Institution, Washington, D.C.

**FIGURE A2.1**

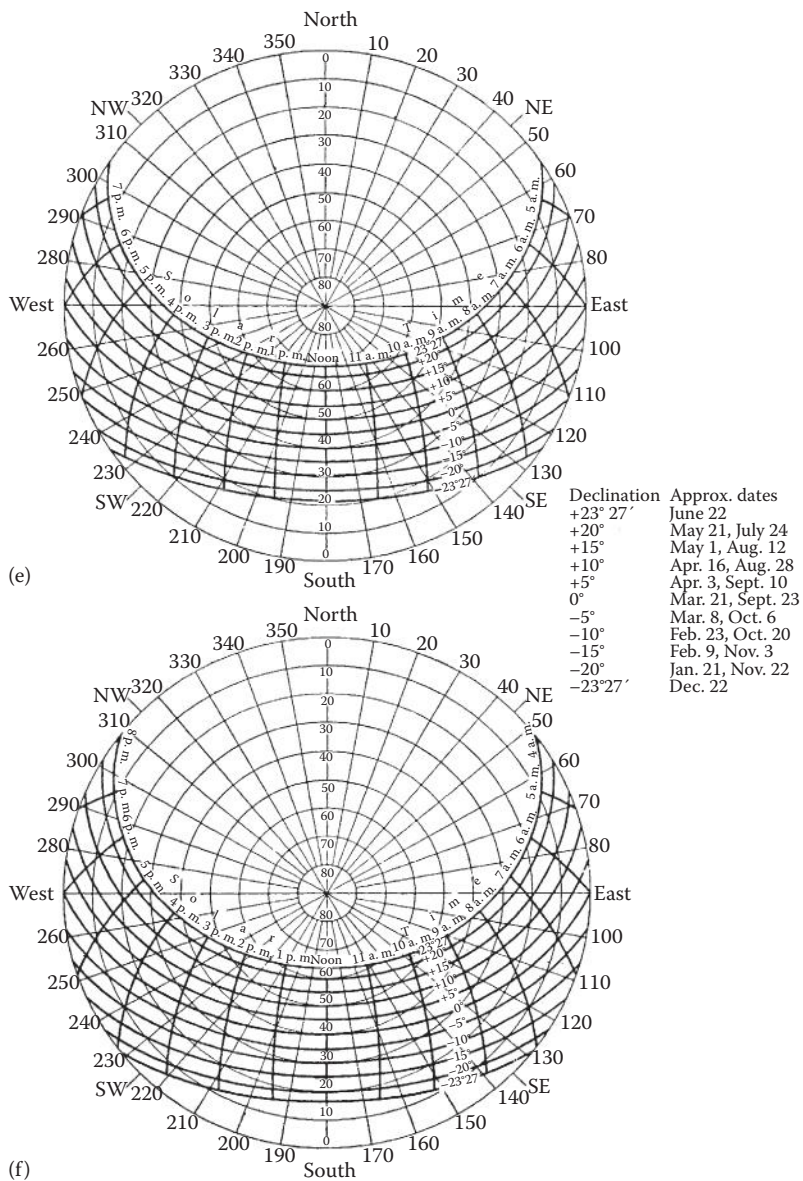
Meteorological charts for computing solar altitude and azimuth angles. (a) 25°N latitude; (b) 30°N latitude.

(Continued)

**FIGURE A2.1 (CONTINUED)**

Meteorological charts for computing solar altitude and azimuth angles. (c) 35°N latitude; (d) 40°N latitude.

(Continued)

**FIGURE A2.1 (CONTINUED)**

Description of method for calculating true solar time, together with accompanying meteorological charts, for computing solar altitude and azimuth angles. (e) 45°N latitude; (f) 50°N latitude.

TABLE A2.1
Monthly Averaged, Daily Extraterrestrial Insolation on a Horizontal Surface (Wh/m²)

Latitude (°)	Jan	Feb	Mar	Apr	May	Jun	Jul	Aug	Sep	Oct	Nov	Dec
-65	11,248	8502	5126	2199	570	96	286	1438	3903	7284	10,486	12,135
-60	11,398	9006	5897	3023	1237	596	871	2214	4713	7891	10,737	12,133
-55	11,589	9485	6628	3844	1986	1257	1575	3015	5490	8461	11,005	12,215
-50	11,765	9918	7310	4651	2774	1997	2337	3819	6227	8982	11,248	12,299
-45	11,901	10,295	7939	5431	3578	2779	3128	4611	6919	9445	11,445	12,350
-40	11,980	10,607	8508	6177	4380	3580	3929	5382	7559	9844	11,583	12,352
-35	11,995	10,848	9014	6881	5170	4385	4725	6121	8142	10,174	11,654	12,292
-30	11,940	11,016	9452	7538	5937	5182	5505	6823	8664	10,431	11,655	12,164
-25	11,811	11,107	9819	8141	6672	5959	6261	7479	9121	10,613	11,582	11,967
-20	11,608	11,120	10,111	8685	7368	6709	6984	8084	9509	10,718	11,433	11,697
-15	11,331	11,054	10,327	9166	8019	7423	7667	8634	9824	10,745	11,208	11,354
-10	10,980	10,909	10,465	9580	8618	8095	8304	9122	10,066	10,693	10,909	10,941
-5	10,556	10,686	10,524	9924	9161	8720	8888	9546	10,231	10,562	10,536	10,459
0	10,064	10,386	10,504	10,195	9642	9290	9416	9901	10,319	10,354	10,092	9911
5	9507	10,012	10,403	10,390	10,059	9803	9883	10,186	10,329	10,069	9581	9302
10	8888	9566	10,225	10,509	10,408	10,255	10,286	10,398	10,260	9711	9007	8635
15	8214	9053	9968	10,550	10,687	10,642	10,621	10,535	10,114	9281	8373	7918
20	7490	8475	9637	10,0514	10,895	10,962	10,888	10,597	9891	8784	7687	7155
25	6722	7839	9232	10,400	11,030	11,214	11,085	10,583	9594	8223	6953	6355
30	5919	7149	8758	10,211	11,092	11,399	11,213	10,495	9224	7603	6179	5525
35	5088	6412	8218	9948	11,084	11,518	11,272	10,334	8784	6929	5372	4675
40	4240	5635	7617	9614	11,008	11,573	11,266	10,103	8278	6208	4542	3816
45	3386	4826	6958	9211	10,869	11,572	11,199	9805	7710	5445	3700	2961
50	2541	3994	6248	8746	10,673	11,523	11,081	9445	7084	4649	2858	2127
55	1725	3150	5491	8224	10,432	11,443	10,925	9032	6406	3827	2033	1338
60	969	2309	4696	7653	10,166	11,365	10,756	8575	5682	2992	1251	633
65	334	1493	3869	7045	9915	11,366	10,631	8095	4917	2158	560	101

TABLE A2.2a
Worldwide Values of τ_b and τ_d for Solar Radiation Modeling

Position	Lat	Long	Jan	Feb	Mar	Apr	May	Jun	Jul	Aug	Sep	Oct	Nov	Dec	
<i>Argentina</i>															
Buenos Aires	34.57°S	58.42°W	τ_b	0.387	0.378	0.367	0.349	0.339	0.338	0.332	0.381	0.391	0.362	0.389	
			τ_d	2.329	2.377	2.438	2.474	2.455	2.412	2.448	2.196	2.176	2.369	2.298	
<i>Australia</i>															
Adelaide	34.95°S	138.53°E	τ_b	0.345	0.336	0.324	0.317	0.309	0.305	0.307	0.316	0.332	0.334	0.333	0.343
			τ_d	2.529	2.602	2.683	2.665	2.718	2.701	2.653	2.590	2.513	2.536	2.567	2.536
Brisbane	27.38°S	153.13°E	τ_b	0.391	0.380	0.368	0.352	0.339	0.324	0.322	0.330	0.355	0.379	0.384	0.383
			τ_d	2.435	2.515	2.542	2.589	2.644	2.658	2.670	2.608	2.486	2.387	2.398	2.446
Canberra	35.30°S	149.20°E	τ_b	0.363	0.340	0.326	0.313	0.299	0.291	0.292	0.297	0.315	0.318	0.334	0.342
			τ_d	2.403	2.559	2.606	2.638	2.730	2.747	2.702	2.678	2.582	2.609	2.520	2.519
Darwin	12.42°S	130.88°E	τ_b	0.410	0.411	0.401	0.368	0.369	0.364	0.359	0.375	0.418	0.451	0.458	0.434
			τ_d	2.446	2.445	2.491	2.717	2.610	2.581	2.607	2.492	2.294	2.171	2.149	2.291
Hobart	42.83°S	147.50°E	τ_b	0.361	0.359	0.340	0.334	0.322	0.319	0.323	0.325	0.340	0.339	0.345	0.353
			τ_d	2.415	2.445	2.533	2.515	2.554	2.504	2.484	2.511	2.443	2.491	2.461	2.440
Laverton	37.87°S	144.75°E	τ_b	0.374	0.353	0.339	0.327	0.311	0.312	0.309	0.316	0.333	0.336	0.342	0.364
			τ_d	2.360	2.499	2.555	2.573	2.698	2.611	2.630	2.589	2.510	2.514	2.497	2.390
Sydney	33.93°S	151.18°E	τ_b	0.401	0.388	0.359	0.340	0.323	0.316	0.314	0.322	0.346	0.351	0.374	0.386
			τ_d	2.301	2.368	2.516	2.577	2.671	2.635	2.627	2.572	2.475	2.479	2.373	2.355
<i>Austria</i>															
Wien	48.20°N	16.37°E	τ_b	0.326	0.363	0.435	0.473	0.469	0.491	0.509	0.479	0.418	0.398	0.351	0.331
			τ_d	2.280	2.072	1.876	1.810	1.876	1.861	1.827	1.919	2.089	2.084	2.236	2.291
Innsbruck	47.27°N	11.35°E	τ_b	0.306	0.367	0.423	0.427	0.454	0.456	0.461	0.443	0.413	0.366	0.345	0.319
			τ_d	2.268	1.923	1.799	1.836	1.867	1.950	1.973	2.043	2.078	2.178	2.131	2.226

Barbados												
Grantley Adams	13.07°N	59.48°W	τ_b	0.390	0.397	0.423	0.450	0.516	0.589	0.547	0.488	
airport			τ_d	2.414	2.390	2.279	2.182	1.949	1.753	1.860	2.075	
<i>Belgium</i>												
Brussels	50.90°N	4.53°E	τ_b	0.334	0.365	0.418	0.426	0.464	0.480	0.470	0.456	
Oostende	51.20°N	2.87°E	τ_d	2.297	2.128	1.958	1.953	1.867	1.855	1.919	1.957	
<i>Brunei</i>				τ_b	0.342	0.373	0.433	0.437	0.459	0.471	0.473	0.451
Brunei	4.93°N	114.93°E	τ_d	2.238	2.111	1.920	1.939	1.911	1.910	1.933	1.997	
<i>Bulgaria</i>				τ_b	0.427	0.441	0.446	0.453	0.438	0.436	0.444	0.523
Chirpan	42.20°N	25.33°E	τ_d	2.341	0.382	0.420	0.462	0.447	0.488	0.500	0.502	
Sofia	42.65°N	23.38°E	τ_b	0.331	0.375	0.414	0.456	0.443	0.466	0.473	0.471	
<i>Canada</i>				τ_d	2.201	1.980	1.912	1.831	1.964	1.941	1.942	1.938
Montreal	45.47°N	73.75°W	τ_b	0.268	0.290	0.393	0.409	0.449	0.471	0.465	0.440	
Ottawa	45.32°N	75.67°W	τ_d	2.467	2.265	1.867	1.951	1.915	1.910	1.966	2.044	
Toronto	43.63°N	79.40°W	τ_b	0.273	0.293	0.387	0.377	0.401	0.431	0.444	0.424	
Vancouver	49.20°N	123.18°W	τ_d	2.457	2.277	1.908	2.110	2.122	2.072	2.050	2.125	

(Continued)

TABLE A2.2a (CONTINUED)
 Worldwide Values of τ_b and τ_d for Solar Radiation Modeling

Position	Lat	Long	Jan	Feb	Mar	Apr	May	Jun	Jul	Aug	Sep	Oct	Nov	Dec
<i>Chile</i>														
Antofagasta	23.43°S	70.45°W	τ_b	0.390	0.399	0.372	0.326	0.315	0.312	0.318	0.320	0.326	0.331	0.359
La Serena	29.92°S	71.20°W	τ_d	2.269	2.239	2.376	2.633	2.653	2.593	2.595	2.614	2.567	2.545	2.399
China	39.93°N	116.28°E	τ_b	0.362	0.415	0.498	0.733	0.771	0.747	0.697	0.623	0.546	0.415	0.358
Beijing	39.93°N	113.33°E	τ_d	2.020	1.864	1.691	1.336	1.336	1.273	1.448	1.510	1.571	1.640	1.931
Guangzhou	23.17°N	113.33°E	τ_b	0.714	0.719	0.841	0.903	0.779	0.824	0.839	0.850	0.828	0.821	0.687
Harbin	45.75°N	126.77°E	τ_b	0.254	0.285	0.361	0.401	0.461	0.545	0.499	0.440	0.423	0.401	0.326
Kunming	25.02°N	102.68°E	τ_b	0.334	0.344	0.448	0.435	0.445	0.495	0.544	0.562	0.515	0.426	0.356
Lanzhou	36.05°N	103.88°N	τ_b	0.352	0.406	0.497	0.595	0.636	0.669	0.666	0.654	0.578	0.507	0.398
Shanghai	31.40°N	121.47°E	τ_b	0.741	0.818	0.931	0.961	0.996	1.006	0.882	0.784	0.758	0.807	0.797
Colombia	10.88°N	74.78°W	τ_b	0.416	0.470	0.581	0.576	0.506	0.488	0.486	0.475	0.472	0.455	0.439
Barranquilla	4.70°N	74.13°W	τ_d	2.291	2.071	1.748	1.776	1.991	2.055	2.064	2.118	2.136	2.195	2.237
Bogota	0.329	0.374	0.412	0.383	0.339	0.339	0.332	0.338	0.363	0.362	0.354	0.340	0.331	0.263

(Continued)

TABLE A2.2a (CONTINUED)
 Worldwide Values of τ_b and τ_d for Solar Radiation Modeling

Position	Lat	Long	Jan	Feb	Mar	Apr	May	Jun	Jul	Aug	Sep	Oct	Nov	Dec
<i>France</i>														
Agen	44.18°N	0.6°E	τ_b	0.313	0.342	0.383	0.402	0.434	0.469	0.457	0.447	0.393	0.369	0.336
Nice	43.65°N	7.20°E	τ_d	2.476	2.279	2.113	2.051	1.996	1.922	2.001	2.036	2.219	2.261	2.351
Paris	48.82°N	2.33°E	τ_b	0.343	0.387	0.421	0.447	0.469	0.495	0.476	0.479	0.438	0.427	0.376
			τ_d	2.181	2.100	2.003	1.950	1.948	1.903	1.999	1.985	2.093	2.048	2.324
<i>Germany</i>														
Bremen	53.05°N	8.80°E	τ_b	0.343	0.374	0.417	0.430	0.432	0.449	0.487	0.450	0.412	0.370	0.349
Hamburg	53.63°N	10.00°E	τ_d	2.229	2.088	1.957	1.948	1.987	1.967	1.869	1.991	2.094	2.217	2.165
Stuttgart	48.83°N	9.20°E	τ_b	0.355	0.361	0.406	0.431	0.420	0.428	0.479	0.451	0.408	0.366	0.356
Nuremberg	49.50°N	11.08°E	τ_d	2.280	2.141	1.989	1.940	2.030	2.043	1.892	1.983	2.105	2.229	2.218
			τ_b	0.322	0.373	0.413	0.408	0.428	0.442	0.449	0.433	0.398	0.369	0.337
			τ_d	2.309	2.040	1.961	2.025	2.004	1.998	2.004	2.061	2.145	2.203	2.289
<i>Great Britain</i>														
Belfast	54.65°N	6.22°W	τ_b	0.311	0.331	0.397	0.389	0.406	0.403	0.424	0.400	0.364	0.353	0.327
Jersey	49.22°N	2.20°W	τ_d	2.451	2.330	2.029	2.108	2.072	2.129	2.076	2.168	2.297	2.277	2.356
London	51.52°N	0.12°W	τ_b	0.342	0.365	0.403	0.407	0.427	0.423	0.428	0.416	0.387	0.383	0.346
			τ_d	0.334	0.345	0.412	0.409	0.437	0.452	0.471	0.443	0.397	0.373	0.348
			τ_b	2.270	2.239	1.974	2.009	1.951	1.942	1.912	2.001	2.142	2.171	2.222

(Continued)

TABLE A2.2a (CONTINUED)
Worldwide Values of τ_b and τ_d for Solar Radiation Modeling

Position	Lat	Long	Jan	Feb	Mar	Apr	May	Jun	Jul	Aug	Sep	Oct	Nov	Dec	
Nagpur	21.10°N	79.05°E	τ_b	0.491	0.490	0.533	0.549	0.610	0.710	0.771	0.650	0.572	0.498	0.480	
New Delhi	28.58°N	77.20°E	τ_d	1.841	1.854	1.765	1.754	1.652	1.506	1.419	1.607	1.766	1.920	1.913	
				0.552	0.576	0.598	0.714	0.940	1.021	1.066	0.906	0.711	0.878	0.783	
<i>Iran</i>				1.650	1.596	1.579	1.413	1.208	1.179	1.167	1.282	1.483	1.244	1.616	
Abadan	30.37°N	48.25°E	τ_b	0.418	0.688	0.702	0.815	0.898	0.827	0.965	0.924	0.773	0.772	0.645	0.441
			τ_d	1.925	1.346	1.340	1.235	1.166	1.217	1.128	1.159	1.281	1.273	1.419	1.840
Anzali	37.47°N	49.47°E	τ_b	0.380	0.422	0.495	0.557	0.598	0.566	0.580	0.573	0.526	0.458	0.402	0.380
			τ_d	2.005	1.860	1.710	1.635	1.600	1.712	1.713	1.723	1.774	1.902	2.027	2.041
Esfahan	32.47°N	51.67°E	τ_b	0.331	0.350	0.424	0.633	0.741	0.725	0.771	0.683	0.600	0.446	0.381	0.337
			τ_d	2.089	2.047	1.820	1.397	1.275	1.311	1.287	1.387	1.469	1.777	1.937	2.094
Mashhad	36.27°N	59.63°E	τ_b	0.354	0.443	0.613	0.709	0.735	0.744	0.745	0.672	0.581	0.532	0.458	0.365
			τ_d	2.021	1.731	1.425	1.338	1.328	1.335	1.349	1.425	1.537	1.603	1.746	2.011
Shiraz	29.53°N	52.53°E	τ_b	0.330	0.395	0.449	0.596	0.653	0.658	0.731	0.771	0.661	0.483	0.433	0.385
			τ_d	2.217	1.935	1.795	1.486	1.401	1.407	1.354	1.294	1.389	1.692	1.810	1.951
Tabriz	38.08°N	46.28°E	τ_b	0.334	0.410	0.481	0.578	0.568	0.578	0.650	0.602	0.536	0.479	0.404	0.357
			τ_d	1.972	1.702	1.609	1.485	1.554	1.577	1.473	1.541	1.620	1.715	1.865	1.914
Tehran	35.68°N	51.32°E	τ_b	0.335	0.359	0.661	0.731	0.686	0.698	0.752	0.672	0.583	0.593	0.393	0.340
			τ_d	2.072	1.981	1.319	1.269	1.356	1.369	1.326	1.424	1.523	1.476	1.933	2.081
<i>Ireland</i>															
Dublin	53.43°N	6.25°W	τ_b	0.316	0.326	0.389	0.379	0.404	0.395	0.431	0.396	0.367	0.350	0.327	0.328
			τ_d	2.407	2.382	2.074	2.157	2.082	2.176	2.057	2.208	2.294	2.293	2.360	2.326

<i>Israel</i>	Tel Aviv	32.10°N	34.78°E	τ_b	0.404	0.451	0.547	0.650	0.696	0.455	0.496	0.507	0.477	0.475	0.447	0.445
<i>Italy</i>	Milan	45.43°N	9.28°E	τ_d	2.010	1.864	1.632	1.459	1.416	1.981	1.870	1.836	1.915	1.874	1.912	1.868
<i>Japan</i>	Rome	41.78°N	12.58°E	τ_b	0.340	0.395	0.499	0.561	0.579	0.578	0.515	0.495	0.504	0.495	0.392	0.338
	Fukuoka	33.58°N	130.38°E	τ_d	2.248	1.977	1.693	1.588	1.596	1.640	1.818	1.876	1.799	1.759	2.036	2.261
	Tokyo	35.68°N	139.77°E	τ_b	0.340	0.376	0.415	0.428	0.448	0.477	0.470	0.475	0.434	0.404	0.381	0.353
	Yonago	35.43°N	133.33°E	τ_d	2.292	2.113	1.989	1.992	1.980	1.924	1.975	1.963	2.070	2.122	2.127	2.226
<i>Kenya</i>	Mombasa	4.03°S	39.62°E	τ_b	0.423	0.422	0.421	0.388	0.405	0.424	0.433	0.419	0.422	0.411	0.399	0.407
	Nairobi	1.32°S	36.92°E	τ_d	2.294	2.283	2.326	2.564	2.430	2.263	2.221	2.296	2.297	2.360	2.443	2.399
<i>Lithuania</i>	Kaunas	54.88°N	23.88°E	τ_b	0.283	0.312	0.353	0.383	0.362	0.355	0.389	0.383	0.365	0.324	0.296	0.285
<i>Madagascar</i>	Antananarivo	18.80°S	47.48°E	τ_d	2.436	2.195	2.054	2.034	2.191	2.306	2.151	2.164	2.191	2.315	2.392	2.440

(Continued)

TABLE A2.2a (CONTINUED)
Worldwide Values of τ_b and τ_d for Solar Radiation Modeling

Position	Lat	Long	Jan	Feb	Mar	Apr	May	Jun	Jul	Aug	Sep	Oct	Nov	Dec
<i>Malaysia</i>														
Kuala Lumpur	3.12°N	101.55°E	τ_b	0.498	0.514	0.544	0.510	0.519	0.552	0.572	0.618	0.662	0.535	0.475
			τ_d	1.987	1.948	1.870	1.980	1.947	1.838	1.783	1.684	1.692	1.597	1.879
<i>Martinique</i>														
Le Lamentin	14.60°N	61.00°W	τ_b	0.383	0.386	0.409	0.438	0.501	0.589	0.567	0.491	0.456	0.417	0.401
			τ_d	2.447	2.439	2.339	2.231	1.999	1.749	1.803	2.061	2.213	2.213	2.466
<i>Mexico</i>														
Mexico City	19.43°N	99.13°W	τ_b	0.393	0.403	0.414	0.487	0.519	0.486	0.461	0.449	0.464	0.424	0.383
			τ_d	2.031	2.016	2.003	1.804	1.724	1.859	1.949	1.992	1.962	2.022	2.125
<i>Cancun</i>	21.03°N	86.87°W	τ_b	0.381	0.394	0.427	0.456	0.472	0.488	0.495	0.454	0.430	0.419	0.398
			τ_d	2.439	2.351	2.212	2.132	2.092	2.062	2.028	2.204	2.341	2.354	2.388
<i>Mongolia</i>														
Ulaanbaatar	47.92°N	106.87°E	τ_b	0.208	0.218	0.281	0.352	0.404	0.425	0.412	0.387	0.342	0.298	0.245
airport			τ_d	2.617	2.560	2.212	2.019	1.933	1.946	2.077	2.157	2.244	2.313	2.445
<i>Uliastai</i>	47.75°N	96.85°E	τ_b	0.198	0.205	0.244	0.325	0.381	0.406	0.409	0.382	0.332	0.298	0.238
			τ_d	2.553	2.513	2.318	2.044	1.948	1.966	2.017	2.079	2.203	2.159	2.383
<i>Morocco</i>														
Casablanca	33.57°N	7.67°W	τ_b	0.353	0.329	0.378	0.416	0.461	0.517	0.502	0.497	0.462	0.366	0.336
			τ_d	2.312	2.531	2.238	2.087	1.954	1.801	1.860	1.882	1.988	2.416	2.547
<i>Mozambique</i>														
Maputo	25.92°S	32.57°E	τ_b	0.406	0.401	0.393	0.378	0.353	0.349	0.355	0.412	0.443	0.465	0.423
			τ_d	2.330	2.364	2.381	2.388	2.480	2.441	2.415	2.151	2.075	2.027	2.210

(Continued)

TABLE A2.2a (CONTINUED)
 Worldwide Values of τ_b and τ_d for Solar Radiation Modeling

Position	Lat	Long	Jan	Feb	Mar	Apr	May	Jun	Jul	Aug	Sep	Oct	Nov	Dec
<i>Pakistan</i>														
Karachi	24.90°N	67.13°E	τ_b	0.403	0.448	0.701	0.824	0.932	1.035	1.164	1.026	0.810	0.705	0.583
			τ_d	2.089	1.918	1.399	1.269	1.191	1.142	1.094	1.167	1.326	1.416	1.580
Islamabad	33.62°N	73.10°E	τ_b	0.337	0.400	0.449	0.688	0.735	0.920	0.974	0.912	0.630	0.433	0.384
			τ_d	2.271	1.981	1.866	1.397	1.371	1.214	1.193	1.243	1.556	1.959	2.070
<i>Peru</i>														
Lima	12.00°S	77.12°W	τ_b	0.603	0.610	0.601	0.546	0.484	0.457	0.446	0.507	0.586	0.611	0.612
			τ_d	1.715	1.710	1.734	1.862	2.042	2.117	2.150	1.953	1.760	1.705	1.676
<i>Poland</i>														
Warszawa	52.17°N	20.97°E	τ_b	0.348	0.380	0.455	0.471	0.457	0.467	0.506	0.454	0.428	0.393	0.363
			τ_d	2.191	2.002	1.787	1.815	1.906	1.925	1.819	1.994	2.026	2.096	2.163
Kolobrzeg	54.18°N	15.58°E	τ_b	0.363	0.373	0.415	0.429	0.429	0.425	0.454	0.441	0.411	0.387	0.378
			τ_d	2.138	2.091	1.965	1.983	2.037	2.118	2.017	2.059	2.120	2.136	2.102
<i>Portugal</i>														
Evora	38.57°N	7.90°W	τ_b	0.306	0.324	0.358	0.353	0.386	0.393	0.389	0.399	0.382	0.348	0.322
			τ_d	2.543	2.424	2.232	2.319	2.202	2.205	2.253	2.198	2.251	2.380	2.495
Lisbon	38.77°N	9.13°W	τ_b	0.327	0.349	0.390	0.371	0.404	0.411	0.404	0.413	0.399	0.372	0.345
			τ_d	2.425	2.312	2.124	2.274	2.163	2.163	2.207	2.172	2.215	2.297	2.381
<i>Romania</i>														
Bucuresti	44.48°N	26.12°E	τ_b	0.320	0.357	0.410	0.437	0.431	0.491	0.502	0.500	0.442	0.384	0.353
			τ_d	2.280	2.074	1.984	1.943	2.026	1.883	1.868	1.860	1.997	2.176	2.243
Constanta	44.22°N	28.65°E	τ_b	0.348	0.382	0.403	0.428	0.431	0.455	0.484	0.488	0.435	0.392	0.366
			τ_d	2.192	2.021	2.038	1.997	2.063	2.037	1.950	1.928	2.051	2.173	2.195

Galati	45.48°N	28.03°E	τ_b	0.315	0.344	0.383	0.419	0.412	0.458	0.484	0.486	0.426	0.370	0.344	0.317
			τ_d	2.340	2.163	2.088	2.004	2.105	1.993	1.924	1.908	2.052	2.240	2.273	2.381
<i>Russia</i>															
Aleksandrovskoe	60.43°N	77.87°E	τ_b	0.242	0.257	0.299	0.331	0.392	0.400	0.409	0.400	0.408	0.325	0.273	0.257
			τ_d	2.684	2.501	2.195	2.096	2.041	2.117	2.157	2.140	1.973	2.283	2.513	2.761
Moscow	55.83°N	37.62°E	τ_b	0.297	0.320	0.361	0.439	0.435	0.411	0.437	0.446	0.442	0.370	0.326	0.296
St. Petersburg	59.97°N	30.30°E	τ_b	0.294	0.304	0.326	0.403	0.390	0.395	0.413	0.408	0.378	0.341	0.328	0.319
Singapore			τ_d	2.491	2.349	2.209	1.968	2.118	2.194	2.146	2.143	2.186	2.278	2.330	2.597
Singapore	1.37°N	103.98°E	τ_b	0.500	0.507	0.523	0.486	0.485	0.494	0.508	0.571	0.610	0.678	0.515	0.489
			τ_d	1.983	1.967	1.930	2.072	2.076	2.030	1.984	1.810	1.722	1.577	1.952	2.028
<i>South Korea</i>															
Seoul	37.57°N	126.97°E	τ_b	0.409	0.483	0.571	0.631	0.712	0.789	0.682	0.560	0.503	0.479	0.441	0.387
			τ_d	1.844	1.669	1.529	1.476	1.397	1.343	1.526	1.771	1.845	1.808	1.861	1.982
<i>South Africa</i>															
Cape Town	33.97°S	18.60°E	τ_b	0.335	0.341	0.333	0.334	0.323	0.311	0.316	0.327	0.335	0.345	0.329	0.336
			τ_d	2.613	2.599	2.652	2.575	2.616	2.661	2.595	2.521	2.522	2.479	2.608	2.600
Port Elizabeth	33.98°S	25.62°E	τ_b	0.372	0.378	0.368	0.355	0.339	0.331	0.327	0.357	0.373	0.385	0.368	0.369
Pretoria	25.73°S	28.18°E	τ_b	0.379	0.381	0.378	0.350	0.308	0.307	0.295	0.352	0.374	0.396	0.361	0.364
			τ_d	2.279	2.272	2.242	2.308	2.526	2.445	2.563	2.221	2.190	2.138	2.331	2.338
<i>Spain</i>															
Barcelona	41.28°N	2.07°E	τ_b	0.333	0.364	0.402	0.421	0.467	0.505	0.511	0.492	0.449	0.404	0.361	0.337
			τ_d	2.394	2.221	2.075	2.041	1.934	1.863	1.862	1.927	2.030	2.137	2.266	2.364
Madrid	40.45°N	3.55°W	τ_b	0.307	0.329	0.376	0.372	0.424	0.457	0.446	0.453	0.408	0.368	0.328	0.318
			τ_d	2.446	2.306	2.075	2.140	1.976	1.895	1.933	1.906	2.048	2.189	2.357	2.378

(Continued)

TABLE A2.2a (CONTINUED)
Worldwide Values of τ_b and τ_d for Solar Radiation Modeling

Position	Lat	Long	Jan	Feb	Mar	Apr	May	Jun	Jul	Aug	Sep	Oct	Nov	Dec
<i>Sweden</i>														
Goteborg	57.72°N	12.00°E	τ_b	0.332	0.335	0.349	0.392	0.400	0.402	0.421	0.413	0.377	0.361	0.374
			τ_d	2.276	2.263	2.243	2.089	2.103	2.158	2.110	2.136	2.243	2.214	2.102
Stockholm	59.65°N	17.95°E	τ_b	0.307	0.313	0.337	0.384	0.388	0.390	0.395	0.393	0.361	0.354	0.349
			τ_d	2.403	2.323	2.247	2.094	2.126	2.199	2.220	2.214	2.295	2.203	2.226
<i>Switzerland</i>														
Geneva	46.25°N	6.13°E	τ_b	0.311	0.354	0.417	0.412	0.440	0.440	0.439	0.424	0.394	0.373	0.330
			τ_d	2.311	2.077	1.880	1.937	1.927	2.002	2.054	2.110	2.177	2.175	2.267
Zurich	47.48°N	8.53°E	τ_b	0.304	0.347	0.399	0.407	0.413	0.436	0.430	0.401	0.393	0.360	0.330
			τ_d	2.309	2.051	1.924	1.941	2.022	1.997	2.057	2.186	2.148	2.202	2.217
<i>Thailand</i>														
Bangkok	13.73°N	100.57°E	τ_b	0.612	0.762	0.827	0.666	0.612	0.619	0.629	0.585	0.612	0.653	0.566
			τ_d	1.654	1.429	1.366	1.598	1.701	1.684	1.663	1.764	1.700	1.605	1.762
<i>Trinidad and Tobago</i>														
Crown Point	11.15°N	60.83°W	τ_b	0.401	0.411	0.449	0.474	0.519	0.564	0.533	0.461	0.446	0.415	0.422
			τ_d	2.387	2.349	2.174	2.097	1.947	1.828	1.916	2.201	2.280	2.444	2.378

<i>Tunisia</i>	36.83°N	10.23°E	τ_b	0.360	0.406	0.436	0.490	0.510	0.515	0.545	0.541	0.505	0.466	0.406	0.384
Tunis			τ_d	2.214	2.013	1.934	1.803	1.794	1.815	1.731	1.764	1.847	1.905	2.052	2.097
<i>Ukraine</i>															
Kiev	50.40°N	30.57°E	τ_b	0.318	0.338	0.402	0.426	0.415	0.434	0.459	0.454	0.411	0.356	0.331	0.321
			τ_d	2.285	2.093	1.941	1.960	2.057	2.054	1.980	1.981	2.074	2.259	2.285	2.280
<i>Uzbekistan</i>															
Tashkent	41.27°N	69.27°E	τ_b	0.378	0.415	0.478	0.508	0.535	0.556	0.600	0.536	0.499	0.495	0.455	0.380
<i>Venezuela</i>															
Caracas	10.60°N	66.98°W	τ_b	0.395	0.413	0.472	0.539	0.528	0.525	0.505	0.457	0.444	0.432	0.427	0.409
			τ_d	2.418	2.341	2.079	1.877	1.913	1.925	1.995	2.201	2.273	2.317	2.320	2.372
<i>St. Antonio</i>	7.85°N	72.45°W	τ_b	0.443	0.510	0.671	0.641	0.501	0.484	0.485	0.492	0.483	0.484	0.471	0.449
			τ_d	2.227	1.981	1.601	1.654	2.021	2.080	2.085	2.071	2.114	2.095	2.124	2.199
<i>Zimbabwe</i>															
Harare	17.92°S	31.13°E	τ_b	0.350	0.360	0.351	0.316	0.297	0.302	0.312	0.346	0.397	0.400	0.364	0.362
			τ_d	2.532	2.434	2.447	2.656	2.716	2.613	2.544	2.341	2.113	2.138	2.347	2.412
<i>Masvingo</i>	20.07°S	30.87°E	τ_b	0.351	0.359	0.346	0.324	0.303	0.309	0.310	0.344	0.389	0.397	0.372	0.369
			τ_d	2.555	2.484	2.524	2.615	2.697	2.612	2.610	2.386	2.178	2.187	2.333	2.402

TABLE A2.2b Values of τ_b and τ_d for Solar Radiation Modeling for Sites in the United States

Position	Latitude	Longitude	Jan	Feb	Mar	Apr	May	Jun	Jul	Aug	Sep	Oct	Nov	Dec
Alabama Birmingham	33.56 N	86.75 W	τ_b 0.327	0.346	0.377	0.404	0.439	0.483	0.583	0.584	0.439	0.370	0.340	0.322
Montgomery	32.30 N	86.39 W	τ_b 0.332	0.352	0.382	0.399	0.438	0.490	0.573	0.581	0.441	0.372	0.344	0.328
Alaska Fairbanks	64.82 N	147.86 W	τ_b τ_d 0.186	0.250	0.251	0.281	0.350	0.380	0.387	0.403	0.309	0.269	0.226	0.171
Anchorage	61.18 N	149.99 W	τ_b τ_d 0.265	0.258	0.260	0.292	0.389	0.370	0.387	0.372	0.323	0.284	0.273	0.220
Nome	64.51 N	165.44 W	τ_b τ_d 0.195	0.240	0.241	0.286	0.387	0.369	0.408	0.455	0.318	0.292	0.232	0.183
St. Paul Island	57.16 N	170.22 W	τ_b τ_d 0.281	0.317	0.316	0.373	0.410	0.378	0.413	0.390	0.364	0.333	0.318	0.288
Yakutat	59.51 N	139.63 W	τ_b τ_d 0.266	0.280	0.280	0.333	0.397	0.389	0.371	0.370	0.333	0.307	0.279	0.282
Arizona Phoenix	33.44 N	111.99 W	τ_b τ_d 0.306	0.317	0.339	0.366	0.419	0.465	0.588	0.547	0.456	0.393	0.318	0.298
Tucson	32.13 N	110.96 W	τ_b τ_d 0.296	0.306	0.327	0.361	0.431	0.473	0.555	0.510	0.434	0.372	0.309	0.287
Arkansas Little Rock	34.75 N	92.23 W	τ_b τ_d 0.325	0.348	0.378	0.399	0.418	0.472	0.517	0.514	0.422	0.363	0.341	0.319
Adams Field			τ_b τ_d 0.457	2.319	2.218	2.175	2.183	2.028	1.901	1.895	2.205	2.386	2.410	2.503

Fort Smith	35.33 N	94.37 W	τ_b	0.320	0.339	0.361	0.387	0.420	0.465	0.490	0.482	0.416	0.359	0.336	0.314
<i>California</i>															
Bakersfield	35.43 N	119.06 W	τ_b	0.313	0.334	0.345	0.372	0.391	0.388	0.438	0.445	0.382	0.377	0.331	0.315
Fresno	36.78 N	119.72 W	τ_d	2.468	2.363	2.298	2.226	2.159	2.040	1.983	2.006	2.235	2.411	2.439	2.528
Long Beach	33.83 N	118.16 W	τ_b	0.304	0.323	0.337	0.371	0.388	0.378	0.428	0.428	0.379	0.370	0.328	0.310
Sacramento	38.51 N	121.49 W	τ_d	2.632	2.460	2.431	2.251	2.251	2.375	2.152	2.150	2.371	2.303	2.497	2.540
San Diego Lindbergh Field	32.74 N	117.17 W	τ_b	0.319	0.329	0.344	0.364	0.364	0.389	0.389	0.462	0.450	0.395	0.387	0.340
San Francisco	37.62 N	122.40 W	τ_d	2.583	2.518	2.458	2.351	2.272	2.301	2.159	2.214	2.401	2.360	2.536	2.601
Los Angeles	33.94 N	118.41 W	τ_b	0.326	0.334	0.362	0.368	0.368	0.353	0.371	0.365	0.352	0.335	0.320	0.318
Santa Maria Public Airport	34.92 N	120.47 W	τ_d	2.703	2.568	2.565	2.423	2.406	2.480	2.357	2.414	2.531	2.496	2.630	2.637
Colorado Springs	38.81 N	104.71 W	τ_b	0.247	0.269	0.292	0.343	0.370	0.391	0.408	0.387	0.328	0.297	0.261	0.244
Connecticut	41.94 N	72.68 W	τ_b	0.315	0.335	0.370	0.393	0.415	0.459	0.486	0.462	0.393	0.361	0.335	0.312
Hartford	2.350	2.235	2.130	2.119	2.105	2.003	1.943	2.020	2.271	2.315	2.358	2.438			

(Continued)

TABLE A2.2b (CONTINUED)
 Values of τ_b and τ_d for Solar Radiation Modeling for Sites in the United States

Position	Latitude	Longitude	Jan	Feb	Mar	Apr	May	Jun	Jul	Aug	Sep	Oct	Nov	Dec	
<i>Delaware</i>															
Wilmington	39.67 N	75.60 W	τ_b	0.319	0.358	0.428	0.423	0.493	0.567	0.567	0.419	0.373	0.352	0.317	
			τ_d	2.369	2.155	1.929	2.010	1.829	1.693	1.755	1.711	2.164	2.264	2.284	2.458
<i>Florida</i>															
Daytona Beach	29.18 N	81.06 W	τ_b	0.350	0.371	0.394	0.405	0.468	0.477	0.512	0.498	0.445	0.396	0.362	0.348
			τ_d	2.468	2.346	2.259	2.255	2.042	2.066	1.951	2.002	2.196	2.364	2.475	2.495
Jacksonville	30.49 N	81.69 W	τ_b	0.351	0.366	0.390	0.411	0.482	0.504	0.541	0.523	0.450	0.397	0.361	0.342
			τ_d	2.420	2.343	2.244	2.199	1.979	1.957	1.863	1.912	2.156	2.323	2.444	2.488
Tallahassee	30.39 N	84.35 W	τ_b	0.344	0.357	0.383	0.397	0.450	0.493	0.537	0.536	0.441	0.388	0.353	0.337
			τ_d	2.461	2.386	2.274	2.255	2.098	1.995	1.879	1.874	2.200	2.366	2.480	2.510
Miami	25.82 N	80.30 W	τ_b	0.368	0.388	0.418	0.433	0.501	0.520	0.528	0.505	0.473	0.425	0.389	0.370
			τ_d	2.439	2.306	2.190	2.160	1.945	1.929	1.905	1.987	2.095	2.257	2.362	2.400
Key West	24.55 N	81.75 W	τ_b	0.375	0.386	0.421	0.434	0.466	0.477	0.488	0.461	0.437	0.414	0.390	0.381
			τ_d	2.443	2.365	2.217	2.200	2.115	2.119	2.077	2.194	2.308	2.375	2.416	2.387
Tampa	27.96 N	82.54 W	τ_b	0.344	0.364	0.391	0.403	0.470	0.473	0.509	0.493	0.445	0.398	0.360	0.346
			τ_d	2.531	2.403	2.271	2.272	2.029	2.070	1.950	2.010	2.190	2.356	2.488	2.512
<i>Georgia</i>															
Athens	33.95 N	83.33 W	τ_b	0.320	0.341	0.375	0.390	0.438	0.492	0.539	0.570	0.426	0.371	0.336	0.317
			τ_d	2.507	2.371	2.215	2.199	2.062	1.934	1.828	1.734	2.177	2.331	2.454	2.550
Atlanta	33.64 N	84.43 W	τ_b	0.325	0.349	0.383	0.395	0.448	0.505	0.556	0.593	0.431	0.373	0.339	0.320
			τ_d	2.461	2.316	2.176	2.175	2.028	1.892	1.779	1.679	2.151	2.317	2.422	2.514
Columbus	32.52 N	84.94 W	τ_b	0.330	0.348	0.379	0.398	0.439	0.481	0.564	0.593	0.438	0.375	0.343	0.326
			τ_d	2.497	2.380	2.238	2.197	2.096	1.998	1.778	1.699	2.158	2.366	2.477	2.545

Macon	32.69 N	83.65 W	τ_b	0.328	0.348	0.381	0.395	0.442	0.481	0.549	0.595	0.434	0.377	0.341	0.324
Savannah	32.12 N	81.20 W	τ_d	2.498	2.367	2.220	2.200	2.078	1.995	1.812	1.686	2.172	2.345	2.481	2.548
Hawaii			τ_b	0.340	0.356	0.391	0.409	0.481	0.517	0.558	0.554	0.442	0.387	0.352	0.335
Honolulu	21.33 N	157.94 W	τ_d	2.461	2.353	2.199	2.173	1.956	1.899	1.811	1.811	2.173	2.338	2.456	2.506
Idaho			τ_b	0.332	0.350	0.370	0.401	0.391	0.385	0.385	0.382	0.371	0.373	0.359	0.346
Boise	43.57 N	116.22 W	τ_d	2.773	2.614	2.491	2.316	2.407	2.463	2.489	2.521	2.620	2.565	2.645	2.673
Illinois			τ_b	0.279	0.287	0.305	0.346	0.371	0.363	0.398	0.394	0.352	0.315	0.289	0.277
Chicago	41.99 N	87.91 W	τ_d	2.419	2.446	2.420	2.238	2.181	2.301	2.125	2.124	2.282	2.435	2.542	2.493
Rockford	39.85 N	89.68 W	τ_b	0.302	0.343	0.390	0.417	0.438	0.458	0.455	0.452	0.412	0.365	0.337	0.307
Springfield	39.85 N	89.68 W	τ_d	0.312	0.347	2.149	2.030	1.998	1.999	2.001	2.050	2.048	2.146	2.259	2.303
Indiana	39.71 N	86.27 W	τ_b	0.330	0.377	0.427	0.422	0.470	0.484	0.480	0.472	0.418	0.370	0.345	0.326
Iowa			τ_d	2.217	2.010	1.901	1.986	1.890	1.909	1.954	1.971	2.124	2.243	2.273	2.288
Mason City	43.16 N	93.33 W	τ_b	0.272	0.298	0.340	0.358	0.381	0.398	0.409	0.412	0.386	0.340	0.307	0.278
Waterloo	42.55 N	92.40 W	τ_b	0.286	0.331	2.491	2.243	2.191	2.234	2.227	2.241	2.210	2.171	2.209	2.329
			τ_d	2.381	2.082	0.417	0.371	0.380	0.400	0.417	0.427	0.430	0.394	0.347	0.325

(Continued)

TABLE A2.2b (CONTINUED)
 Values of τ_b and τ_d for Solar Radiation Modeling for Sites in the United States

Position	Latitude	Longitude	Jan	Feb	Mar	Apr	May	Jun	Jul	Aug	Sep	Oct	Nov	Dec
<i>Kansas</i>														
Dodge City	37.77 N	99.97 W	τ_b	0.273	0.301	0.328	0.356	0.384	0.422	0.419	0.414	0.370	0.326	0.289
Goodland	39.37 N	101.69 W	τ_d	2.618	2.374	2.305	2.226	2.187	2.086	2.142	2.165	2.294	2.409	2.577
<i>Kentucky</i>														
Lexington	38.04 N	84.61 W	τ_b	0.321	0.358	0.390	0.389	0.461	0.468	0.503	0.500	0.410	0.357	0.329
Louisville	38.18 N	85.73 W	τ_d	2.334	2.159	2.067	2.144	1.925	1.972	1.885	1.882	2.180	2.332	2.410
Standiford Field														
<i>Louisiana</i>														
New Orleans	29.99 N	90.25 W	τ_b	0.372	0.392	0.410	0.438	0.477	0.526	0.568	0.553	0.475	0.396	0.371
Lake Charles	30.13 N	93.23 W	τ_d	2.275	2.185	2.153	2.084	2.004	1.885	1.788	1.821	2.045	2.301	2.342
<i>Maine</i>														
Portland	43.64 N	70.30 W	τ_b	2.480	2.339	2.256	2.163	2.010	1.970	2.103	2.304	2.374	2.368	2.470
<i>Maryland</i>														
Baltimore	39.17 N	76.68 W	τ_b	0.319	0.353	0.411	0.417	0.474	0.546	0.552	0.580	0.421	0.370	0.342

Massachusetts		Boston		71.01 W		τ_b		0.318		0.335		0.374		0.400		0.425		0.472		0.488		0.470		0.391		0.361		0.340		0.313					
Michigan		Detroit		83.35 W		τ_b		0.303		0.374		0.437		0.447		0.476		0.519		0.470		0.454		0.416		0.369		0.345		0.318					
Lansing		42.78 N		84.58 W		τ_b		0.301		0.325		0.396		0.395		0.427		0.462		0.462		0.429		0.428		0.395		0.348		0.327		0.308			
Minnesota		Duluth		92.19 W		τ_b		0.249		0.263		0.302		0.338		0.363		0.382		0.398		0.387		0.362		0.316		0.289		0.262		0.231			
Minneapolis		44.88 N		93.23 W		τ_b		0.263		0.282		0.356		0.374		0.393		0.409		0.416		0.411		0.385		0.337		0.301		0.280		0.237			
Rochester		43.90 N		92.49 W		τ_b		0.268		0.287		0.361		0.364		0.381		0.398		0.404		0.401		0.377		0.334		0.305		0.276		0.231			
Mississippi		Jackson		32.32 N		90.08 W		τ_b		0.332		0.353		0.380		0.399		0.426		0.465		0.534		0.531		0.439		0.369		0.343		0.329		0.299	
Missouri		Columbia		38.82 N		92.22 W		τ_b		0.311		0.344		0.377		0.388		0.406		0.438		0.448		0.462		0.391		0.348		0.320		0.304		0.278	
Kansas City		39.30 N		94.72 W		τ_b		0.303		0.349		0.393		0.395		0.405		0.427		0.438		0.448		0.387		0.345		0.319		0.298		0.270			
Springfield		37.24 N		93.39 W		τ_b		0.304		0.337		0.357		0.374		0.404		0.434		0.448		0.452		0.389		0.342		0.317		0.301		0.276			
St. Louis		38.75 N		90.37 W		τ_b		0.316		0.351		0.385		0.406		0.427		0.455		0.470		0.478		0.406		0.359		0.329		0.313		0.286			
Boston		42.36 N		71.01 W		τ_d		2.372		2.277		2.131		2.094		2.068		1.964		1.950		1.992		2.284		2.321		2.339		2.452		2.414			
Detroit		42.22 N		83.35 W		τ_d		2.302		1.947		1.827		1.875		1.843		1.784		1.978		2.027		2.103		2.216		2.237		2.264		2.470			
Lansing		42.78 N		84.58 W		τ_d		2.282		2.137		1.967		2.063		2.015		1.960		2.133		2.125		2.193		2.340		2.347		2.315		2.414			
Duluth		46.84 N		92.19 W		τ_d		2.728		2.559		2.353		2.284		2.276		2.279		2.218		2.265		2.316		2.474		2.519		2.637		2.470			
Minneapolis		44.88 N		93.23 W		τ_d		2.570		2.346		2.053		2.128		2.158		2.183		2.190		2.220		2.357		2.463		2.472		2.470		2.414			
Rochester		43.90 N		92.49 W		τ_d		2.490		2.297		2.041		2.178		2.208		2.224		2.226		2.225		2.254		2.361		2.427		2.499		2.528			
Jackson		32.32 N		90.08 W		τ_d		2.482		2.350		2.247		2.205		2.168		2.073		1.869		1.861		2.157		2.401		2.462		2.528		2.470			
Columbia		38.82 N		92.22 W		τ_d		2.407		2.218		2.123		2.149		2.158		2.100		2.098		2.029		2.285		2.394		2.467		2.470		2.414			
Kansas City		39.30 N		94.72 W		τ_d		2.427		2.142		2.040		2.107		2.164		2.151		2.146		2.091		2.307		2.402		2.455		2.469		2.414			
Springfield		37.24 N		93.39 W		τ_d		2.460		2.272		2.228		2.225		2.168		2.120		2.097		2.072		2.299		2.426		2.485		2.477		2.414			
St. Louis		38.75 N		90.37 W		τ_d		2.377		2.195		2.091		2.072		2.067		2.031		2.004		1.966		2.203		2.324		2.406		2.414		2.414			

(Continued)

TABLE A2.2b (CONTINUED)
 Values of τ_b and τ_d for Solar Radiation Modeling for Sites in the United States

Position	Latitude	Longitude	Jan	Feb	Mar	Apr	May	Jun	Jul	Aug	Sep	Oct	Nov	Dec
<i>Montana</i>														
Helena	46.61 N	111.96 W	τ_b	0.253	0.252	0.296	0.341	0.370	0.375	0.380	0.416	0.362	0.299	0.269
			τ_d	2.529	2.583	2.310	2.177	2.149	2.222	2.232	2.044	2.215	2.505	2.568
Lewistown	47.05 N	109.47 W	τ_b	0.265	0.265	0.284	0.332	0.362	0.360	0.382	0.418	0.358	0.292	0.257
			τ_d	2.579	2.399	2.418	2.240	2.164	2.262	2.178	1.992	2.186	2.503	2.647
<i>Nebraska</i>														
Lincoln	40.83 N	96.76 W	τ_b	0.286	0.321	0.362	0.376	0.392	0.403	0.414	0.418	0.375	0.337	0.312
			τ_d	2.431	2.167	2.147	2.163	2.186	2.229	2.224	2.187	2.311	2.383	2.420
Omaha	41.31 N	95.90 W	τ_b	0.288	0.323	0.388	0.391	0.406	0.407	0.421	0.423	0.382	0.343	0.315
			τ_d	2.396	2.146	2.011	2.092	2.128	2.222	2.196	2.170	2.272	2.341	2.398
<i>Nevada</i>														
Elko	40.83 N	115.79 W	τ_b	0.249	0.278	0.306	0.332	0.358	0.373	0.446	0.431	0.358	0.319	0.275
			τ_d	2.489	2.292	2.282	2.230	2.177	2.165	1.888	1.919	2.195	2.315	2.524
Las Vegas	36.08 N	115.16 W	τ_b	0.314	0.333	0.355	0.382	0.404	0.412	0.550	0.560	0.407	0.380	0.317
			τ_d	2.386	2.277	2.211	2.099	2.062	2.059	1.674	1.654	2.084	2.096	2.388
Reno	39.48 N	119.77 W	τ_b	0.277	0.291	0.314	0.336	0.344	0.337	0.398	0.389	0.329	0.311	0.282
			τ_d	2.504	2.422	2.366	2.267	2.319	2.437	2.123	2.152	2.464	2.470	2.597
<i>New Hampshire</i>														
Concord	43.20 N	71.50 W	τ_b	0.292	0.319	0.351	0.382	0.412	0.439	0.459	0.441	0.383	0.350	0.323
			τ_d	2.506	2.284	2.175	2.136	2.090	2.059	2.014	2.072	2.289	2.346	2.416
<i>New Jersey</i>														
Atlantic City	39.46 N	74.46 W	τ_b	0.331	0.340	0.376	0.411	0.458	0.522	0.557	0.549	0.413	0.373	0.350
			τ_d	2.353	2.324	2.180	2.073	1.966	1.830	1.774	1.773	2.224	2.292	2.318

Newark	40.72 N	74.17 W	τ_b	0.327	0.366	0.406	0.431	0.464	0.526	0.528	0.516	0.413	0.376	0.352	0.323
New Mexico			τ_d	2.306	2.108	2.008	1.981	1.924	1.802	1.831	1.848	2.189	2.246	2.274	2.387
Albuquerque	35.04 N	106.62 W	τ_b	0.264	0.279	0.296	0.333	0.372	0.405	0.463	0.433	0.365	0.320	0.278	0.259
New York			τ_d	2.584	2.498	2.428	2.244	2.117	2.025	1.887	2.005	2.225	2.329	2.551	2.646
Albany	42.75 N	73.80 W	τ_b	0.308	0.332	0.388	0.392	0.407	0.457	0.490	0.456	0.400	0.362	0.338	0.309
Buffalo	42.94 N	78.74 W	τ_b	2.340	2.171	1.997	2.099	2.137	2.007	1.923	2.037	2.220	2.290	2.325	2.416
New York City	40.66 N	73.80 W	τ_b	0.331	0.362	0.401	0.439	0.476	0.534	0.541	0.527	0.418	0.362	0.332	0.306
Rochester	43.12 N	77.68 W	τ_b	0.307	0.323	0.373	0.404	0.413	0.469	0.463	0.440	0.401	0.362	0.336	0.308
North Carolina			τ_d	2.307	2.210	2.059	2.038	2.085	1.941	2.001	2.080	2.187	2.259	2.297	2.361
Charlotte	35.21 N	80.94 W	τ_b	0.318	0.338	0.373	0.411	0.435	0.488	0.557	0.567	0.421	0.359	0.331	0.314
Wilmington	34.27 N	77.91 W	τ_b	0.345	0.357	0.390	0.417	0.472	0.524	0.584	0.542	0.440	0.380	0.353	0.335
North Dakota			τ_d	2.384	2.325	2.181	2.113	1.973	1.869	1.738	1.841	2.163	2.345	2.414	2.462
Bismarck	46.77 N	100.75 W	τ_b	0.252	0.266	0.309	0.383	0.381	0.376	0.393	0.422	0.363	0.316	0.279	0.259
Fargo	46.93 N	96.81 W	τ_b	0.244	0.261	0.302	0.340	0.363	0.389	0.396	0.405	0.365	0.316	0.283	0.257
Ohio			τ_d	2.609	2.458	2.356	2.316	2.307	2.260	2.253	2.185	2.302	2.476	2.538	2.588
Cleveland	41.41 N	81.85 W	τ_b	0.308	0.368	0.435	0.427	0.464	0.488	0.471	0.455	0.413	0.364	0.338	0.313
			τ_d	2.337	2.023	1.852	1.960	1.897	1.886	1.988	2.035	2.147	2.269	2.295	2.339

(Continued)

TABLE A2.2b (CONTINUED)Values of τ_b and τ_d for Solar Radiation Modeling for Sites in the United States

Position	Latitude	Longitude	Jan	Feb	Mar	Apr	May	Jun	Jul	Aug	Sep	Oct	Nov	Dec	
Columbus	39.99 N	82.88 W	τ_b	0.329	0.359	0.419	0.405	0.469	0.487	0.484	0.482	0.410	0.364	0.343	0.320
			τ_d	2.200	2.087	1.928	2.057	1.887	1.898	1.943	1.931	2.166	2.271	2.285	2.330
Dayton	39.91 N	84.22 W	τ_b	0.338	0.376	0.436	0.427	0.498	0.490	0.478	0.475	0.409	0.367	0.349	0.328
			τ_d	2.122	1.988	1.858	1.959	1.790	1.879	1.955	1.944	2.150	2.234	2.234	2.253
Youngstown	41.25 N	80.67 W	τ_b	0.305	0.362	0.411	0.396	0.437	0.462	0.456	0.446	0.403	0.354	0.321	0.301
			τ_d	2.331	2.013	1.914	2.072	1.974	1.958	2.022	2.044	2.171	2.302	2.392	2.410
<i>Oklahoma</i>															
Oklahoma City	35.39 N	97.60 W	τ_b	0.305	0.324	0.339	0.361	0.401	0.430	0.426	0.431	0.393	0.345	0.317	0.300
			τ_d	2.478	2.389	2.371	2.310	2.211	2.157	2.214	2.179	2.298	2.430	2.484	2.524
<i>Oregon</i>															
Eugene	44.13 N	123.21 W	τ_b	0.299	0.311	0.324	0.356	0.362	0.355	0.357	0.352	0.346	0.329	0.317	0.303
			τ_d	2.742	2.624	2.565	2.366	2.397	2.515	2.559	2.603	2.576	2.606	2.635	2.668
Medford	42.39 N	122.87 W	τ_b	0.297	0.305	0.327	0.363	0.363	0.347	0.356	0.360	0.341	0.332	0.314	0.305
			τ_d	2.693	2.662	2.516	2.324	2.390	2.590	2.582	2.534	2.601	2.577	2.646	2.586
Portland	45.59 N	122.60 W	τ_b	0.296	0.309	0.324	0.356	0.371	0.368	0.364	0.358	0.349	0.330	0.315	0.298
			τ_d	2.719	2.600	2.507	2.328	2.316	2.401	2.503	2.549	2.529	2.558	2.591	2.687
<i>Pennsylvania</i>															
Philadelphia	39.87 N	75.23 W	τ_b	0.322	0.357	0.419	0.421	0.482	0.552	0.550	0.552	0.417	0.374	0.352	0.319
			τ_d	2.357	2.166	1.965	2.021	1.865	1.734	1.776	1.750	2.178	2.266	2.292	2.443
Pittsburgh	40.50 N	80.23 W	τ_b	0.307	0.336	0.386	0.379	0.440	0.474	0.479	0.473	0.401	0.352	0.319	0.305
			τ_d	2.357	2.184	2.037	2.159	1.963	1.913	1.937	1.936	2.175	2.307	2.420	2.417
<i>Rhode Island</i>															
Providence	41.72 N	71.43 W	τ_b	0.323	0.334	0.372	0.402	0.426	0.471	0.507	0.466	0.393	0.364	0.343	0.319
			τ_d	2.350	2.302	2.156	2.091	2.066	1.963	1.885	2.007	2.281	2.311	2.328	2.414

South Carolina			
Charleston	32.90 N	80.04 W	τ_b
			τ_d
		0.343	0.361
		2.319	2.165
		0.316	0.335
		2.513	2.388
South Dakota			
Pierre	44.38 N	100.29 W	τ_b
			τ_d
		0.266	0.286
		2.546	2.354
		0.259	0.276
		2.590	2.407
Rapid City			
		0.266	0.286
		2.314	2.026
		0.300	0.383
		2.393	2.037
Tennessee			
Memphis	35.06 N	89.99 W	τ_b
			τ_d
		0.336	0.362
		2.220	2.122
		0.331	0.357
		2.357	2.225
Nashville			
		0.336	0.362
		2.122	2.087
		0.387	0.392
		2.130	2.172
Texas			
Austin	30.18 N	97.68 W	τ_b
			τ_d
		0.340	0.357
		2.404	2.328
		0.385	0.396
		2.258	2.242
		0.286	0.303
Brownsville			
		0.340	0.357
		2.291	2.204
		0.527	0.482
		2.137	1.969
		0.303	0.317
El Paso			
		0.336	0.351
		2.313	2.250
		0.410	0.436
		2.190	2.181
Houston			
		0.336	0.351
		2.308	2.223
San Antonio			
		0.449	0.441
		2.144	2.174
		0.345	0.368

(Continued)

TABLE A2.2b (CONTINUED)
 Values of τ_b and τ_d for Solar Radiation Modeling for Sites in the United States

Position	Latitude	Longitude	Jan	Feb	Mar	Apr	May	Jun	Jul	Aug	Sep	Oct	Nov	Dec	
Utah Salt Lake City	40.79 N	111.97 W	τ_b	0.270	0.319	0.326	0.374	0.368	0.377	0.440	0.418	0.372	0.335	0.293	0.270
Vermont Burlington	44.47 N	73.15 W	τ_b	2.426	2.115	2.197	2.039	2.184	2.199	1.968	2.037	2.185	2.259	2.394	2.445
Virginia Norfolk	36.90 N	76.19 W	τ_b	0.332	0.348	0.386	0.427	0.463	0.536	0.590	0.566	0.428	0.373	0.342	0.326
Washington Olympia	46.97 N	122.90 W	τ_b	0.295	0.300	0.328	0.349	0.377	0.373	0.364	0.359	0.345	0.328	0.310	0.297
Seattle	47.46 N	122.31 W	τ_b	2.686	2.652	2.437	2.346	2.263	2.367	2.492	2.536	2.558	2.548	2.607	2.645
Yakima	46.56 N	120.53 W	τ_b	0.278	0.288	0.326	0.391	0.419	0.416	0.395	0.397	0.373	0.342	0.310	0.284

TABLE A2.3a
Worldwide Global Horizontal Average Solar Radiation (MJ/m².day)

Position	Lat	Long	Jan	Feb	Mar	Apr	May	Jun	Jul	Aug	Sep	Oct	Nov	Dec
<i>Argentina</i>														
Buenos Aires	34.58°S	58.48°W	24.86	21.75	18.56	11.75	8.71	7.15	7.82	8.75	14.49	16.66	24.90	21.93
<i>Australia</i>														
Adelaide	34.93°S	138.52°E	20.99	17.50	20.15	18.27	17.98	—	18.81	19.64	20.11	20.88	20.57	20.72
Brisbane	27.43°S	153.08°E	25.36	22.22	13.25	16.61	12.23	11.52	9.70	15.10	17.61	19.89	—	—
Canberra	35.30°S	148.18°E	28.20	24.68	20.56	14.89	10.29	6.62	—	12.33	16.88	24.06	26.00	25.77
Darwin	12.47°S	130.83°E	26.92	23.40	18.13	13.62	9.30	7.89	9.41	11.15	14.85	18.87	23.43	22.34
Hobart	42.88°S	147.32°E	—	—	—	10.09	7.26	6.04	5.72	9.21	13.54	18.12	—	—
Laverton	37.85°S	114.08°E	22.96	20.42	15.59	13.40	7.48	6.10	6.54	10.43	13.24	18.76	—	—
Sydney	33.87°S	151.20°E	21.09	21.75	17.63	13.63	9.78	8.79	7.62	12.84	16.93	22.10	—	—
<i>Austria</i>														
Wien	48.20°N	16.57°E	3.54	7.10	8.05	14.72	16.79	20.87	19.89	17.27	12.55	8.45	3.51	2.82
Innsbruck	47.27°N	11.38°E	5.57	9.28	10.15	15.96	14.57	17.65	18.35	17.26	12.98	9.08	4.28	3.50
<i>Barbados</i>														
Husbands	13.15°N	59.62°W	19.11	20.23	—	21.80	19.84	20.86	21.55	22.14	—	—	18.30	16.56
<i>Belgium</i>														
Ostende	51.23°N	2.92°E	2.82	5.75	9.93	15.18	16.74	16.93	18.21	18.29	11.71	6.15	2.69	1.97
Melle	50.98°N	3.83°E	2.40	4.66	8.41	13.55	14.23	13.28	15.71	15.61	10.63	5.82	2.40	1.59
<i>Brunei</i>														
Brunei	4.98°N	114.93°E	19.46	20.12	22.71	20.54	19.74	18.31	19.38	20.08	20.83	17.51	17.39	18.12
<i>Bulgaria</i>														
Chirpan	42.20°N	25.33°E	6.72	6.79	8.54	13.27	17.25	17.39	19.85	14.61	12.53	8.52	5.08	5.09
Sofia	42.65°N	23.38°E	4.05	6.23	7.93	9.36	12.98	19.73	19.40	17.70	14.71	6.44	—	3.14

TABLE A2.3a (CONTINUED)
Worldwide Global Horizontal Average Solar Radiation (MJ/m²·day)

Position	Lat	Long	Jan	Feb	Mar	Apr	May	Jun	Jul	Aug	Sep	Oct	Nov	Dec
<i>Egypt</i>														
Cairo	30.08°N	31.28°E	10.06	12.96	18.49	23.04	21.91	26.07	25.16	23.09	21.01	—	11.74	9.85
Mersa Matruh	31.33°N	27.22°E	8.38	11.92	18.47	24.27	24.17	—	26.67	26.27	21.92	18.28	11.71	8.76
<i>Ethiopia</i>														
Addis Ababa	8.98°N	38.80°E	—	11.39	—	12.01	—	—	—	6.33	9.35	11.71	11.69	11.50
<i>Fiji</i>														
Nandi	17.75°S	177.45°E	20.82	20.65	20.25	18.81	15.68	14.18	15.08	16.71	19.37	20.11	21.78	25.09
Suva	48.05°S	178.57°E	20.37	17.74	16.22	13.82	10.81	12.48	11.40	—	—	18.49	19.96	20.99
<i>Finland</i>														
Helsinki	60.32°N	24.97°E	1.13	2.94	5.59	11.52	17.60	16.81	20.66	15.44	8.44	3.31	0.97	0.63
<i>France</i>														
Agen	44.18°N	0.60°E	4.83	7.40	10.69	17.12	19.25	20.42	21.63	20.64	15.56	8.41	5.09	5.01
Nice	43.65°N	7.20°E	6.83	—	11.37	17.79	20.74	24.10	24.85	24.86	15.04	10.99	7.08	6.73
Paris	48.97°N	2.45°E	2.62	5.08	7.21	12.90	14.84	13.04	15.54	16.30	10.17	5.61	3.14	2.20
<i>Germany</i>														
Bonn	50.70°N	7.15°E	2.94	5.82	8.01	14.27	15.67	14.41	18.57	17.80	11.70	6.15	3.42	1.90
Nuremberg	53.33°N	13.20°E	3.23	6.92	9.08	15.69	15.71	18.21	21.14	17.98	12.43	8.15	2.79	2.51
Bremen	53.05°N	8.80°E	2.36	4.93	8.53	14.52	14.94	14.52	19.40	15.02	10.48	6.27	2.80	1.66
Hamburg	53.63°N	10.00°E	1.97	3.96	7.59	12.32	14.11	12.69	19.00	14.11	10.29	6.45	2.33	1.43
Stuttgart	48.83°N	9.20°E	3.59	7.18	9.22	15.81	17.72	17.44	22.21	19.87	12.36	7.81	3.19	2.54
<i>Ghana</i>														
Bole	9.03°N	2.48°W	18.29	19.76	19.71	19.15	16.61	—	—	13.68	16.29	17.27	17.33	15.93
Accra	5.60°N	0.17°W	14.82	16.26	18.27	16.73	18.15	13.96	13.86	13.49	15.32	19.14	18.16	14.23
<i>Great Britain</i>														
Belfast	54.65°N	6.22°W	2.00	3.60	6.85	12.00	15.41	15.09	15.46	13.56	11.49	4.63	2.34	1.24

<i>Jersey</i>	49.22°N	2.20°W	2.76	5.65	9.51	14.98	18.51	17.83	18.14	18.62	12.98	6.16	3.26	2.83
<i>London</i>	51.52°N	0.12°W	2.24	3.87	7.40	12.01	12.38	13.24	16.59	16.23	12.59	5.67	2.87	1.97
<i>Greece</i>														
Athens	37.97°N	23.72°E	9.11	10.94	15.70	20.91	23.85	25.48	24.21	23.08	19.03	13.29	5.98	6.64
Sikiwna	37.98°N	22.73°E	7.60	8.16	11.99	21.06	22.62	24.32	23.56	21.73	17.30	11.75	9.45	6.35
<i>Guadeloupe</i>														
Le Raizet	16.27°N	61.52°W	14.88	18.10	20.55	19.69	20.26	20.65	20.24	18.47	17.79	13.49	14.38	
<i>Guyana</i>														
Cayenne	4.83°N	52.37°W	14.46	14.67	16.28	17.57	—	14.92	17.42	18.24	20.52	—	22.69	17.04
<i>Hong Kong</i>														
King's Park	22.32°N	114.17°E	12.34	7.39	6.94	9.50	11.38	13.60	16.70	17.06	15.91	16.52	14.19	10.09
<i>Hungary</i>														
Budapest	47.43°N	19.18°E	2.61	7.46	11.14	14.46	20.69	19.47	21.46	19.72	12.88	7.96	2.95	2.47
<i>Iceland</i>														
Reykjavík	64.13°N	21.90°W	0.52	2.02	6.25	11.77	13.07	14.58	16.83	11.35	9.70	3.18	1.00	0.65
<i>India</i>														
Mumbai	19.12°N	72.85°E	18.44	21.00	22.72	24.52	24.86	19.75	15.84	16.00	18.19	20.38	19.18	17.81
Calcutta	22.53°N	88.33°E	15.69	18.34	20.09	22.34	22.37	17.55	17.07	16.55	16.52	16.90	16.35	15.00
Chennai	13.00°N	80.18°E	19.09	22.71	25.14	24.88	23.89	—	18.22	19.68	19.81	16.41	14.76	15.79
Nagpur	21.10°N	79.05°E	18.08	21.01	22.25	24.08	24.79	19.84	15.58	15.47	17.66	20.10	18.98	17.33
New Delhi	28.58°N	77.20°E	14.62	18.25	20.15	23.40	23.80	19.16	20.20	19.89	20.08	19.74	16.95	14.22
<i>Ireland</i>														
Dublin	53.43°N	6.25°W	2.51	4.75	7.48	11.06	17.46	19.11	15.64	13.89	9.65	5.77	2.93	—
<i>Israel</i>														
Jerusalem	31.78°N	35.22°E	10.79	13.01	18.08	23.79	29.10	31.54	31.83	28.79	25.19	20.26	12.61	10.71
<i>Italy</i>														
Milan	45.43°N	9.28°E	—	6.48	10.09	13.17	17.55	16.32	18.60	16.86	11.64	5.40	3.52	2.41

(Continued)

TABLE A2.3a (CONTINUED)
 Worldwide Global Horizontal Average Solar Radiation (MJ/m².day)

Position	Lat	Long	Jan	Feb	Mar	Apr	May	Jun	Jul	Aug	Sep	Oct	Nov	Dec
Rome	41.80°N	12.55°E	—	9.75	13.38	15.82	18.89	22.27	21.53	16.08	8.27	6.41	4.49	
<i>Japan</i>														
Fukuoka	33.58°N	130.38°E	8.11	8.72	10.95	13.97	14.36	12.81	13.84	16.75	13.92	11.86	10.05	7.30
Tateno	36.05°N	140.13°E	9.06	12.17	11.00	15.78	16.52	15.26	—	—	—	9.60	8.55	8.26
Yonago	35.43°N	133.35°E	6.25	7.16	10.87	17.30	16.72	15.44	17.06	19.93	12.41	10.82	7.50	5.51
<i>Kenya</i>														
Mombasa	4.03°S	39.62°E	22.30	22.17	22.74	18.49	18.31	17.41	—	18.12	21.03	22.97	21.87	21.25
Nairobi	1.32°S	36.92°E	—	24.10	21.20	18.65	14.83	15.00	13.44	14.12	19.14	19.38	16.90	18.27
<i>Lithuania</i>														
Kaunas	54.88°N	23.88°E	1.89	4.43	7.40	12.97	18.88	18.74	21.41	15.79	10.40	5.64	1.80	1.10
<i>Madagascar</i>														
Antananarivo	18.80°S	47.48°E	15.94	13.18	13.07	11.53	9.25	8.21	9.32	—	—	16.43	15.19	15.62
<i>Malaysia</i>														
Kuala Lumpur	3.12°N	101.55°E	15.36	17.67	18.48	16.87	15.67	16.24	15.32	15.89	14.62	14.13	13.54	11.53
Penang	5.30°N	100.27°E	19.47	21.35	23.24	20.52	18.63	19.32	17.17	16.96	15.93	16.01	18.35	17.37
<i>Martinique</i>														
Le Lamentin	14.60°N	61.00°W	17.76	20.07	22.53	21.95	22.42	21.23	20.86	21.84	20.23	19.87	14.08	16.25
<i>Mexico</i>														
Chihuahua	28.63°N	106.08°W	14.80	—	—	26.94	26.28	24.01	24.22	20.25	19.55	10.57	15.79	
Orizabita	20.58°N	99.20°E	19.49	23.07	27.44	27.35	26.04	25.05	—	27.53	21.06	17.85	15.48	12.93
<i>Mongolia</i>														
Ulan Bator	47.93°N	106.98°E	6.28	9.22	14.34	18.18	20.50	19.34	16.34	16.65	14.08	11.36	7.19	5.35
Ulaanbaatar	47.75°N	96.85°E	6.43	10.71	14.83	20.32	23.86	20.46	21.66	17.81	15.97	10.92	7.32	5.08

<i>Morocco</i>	33.57°N	7.67°E	11.46	12.70	15.93	21.25	24.45	25.27	25.53	23.60	19.97	14.68	11.61	9.03
Casablanca														
<i>Mozambique</i>														
Maputo	25.97°S	32.60°E	26.35	23.16	19.33	20.54	16.33	14.17	—	—	—	22.55	25.48	26.19
<i>Netherlands</i>														
Maastricht	50.92°N	5.78°E	3.20	5.43	8.48	14.82	14.97	14.32	18.40	17.51	11.65	6.51	3.01	1.72
<i>New Caledonia</i>														
Koumac	20.57°S	164.28°E	24.89	21.15	16.96	18.98	15.67	14.55	15.75	17.62	22.48	15.83	27.53	26.91
<i>New Zealand</i>														
Wilmington	41.28°S	174.77°E	22.59	19.67	14.91	9.52	6.97	4.37	5.74	7.14	12.50	16.34	19.07	24.07
Christchurch	43.48°S	172.55°E	23.46	19.68	13.98	8.96	6.47	4.74	5.38	6.94	13.18	17.45	18.91	24.35
<i>Nigeria</i>														
Benin City	6.32°N	5.60°E	14.89	17.29	19.15	17.21	16.97	15.04	10.24	12.54	14.37	15.99	17.43	15.75
<i>Norway</i>														
Bergen	60.40°N	5.32°E	0.46	1.33	3.18	8.36	19.24	16.70	16.28	10.19	6.53	3.19	1.36	0.35
<i>Oman</i>														
Seeb	23.58°N	58.28°E	12.90	14.86	21.22	22.22	25.30	24.02	23.46	21.66	20.07	18.45	15.49	13.12
Salalah	17.03°N	54.08°E	16.52	16.92	18.49	20.65	21.46	16.92	8.52	11.41	17.14	18.62	16.42	—
<i>Pakistan</i>														
Karachi	24.90°N	67.13°E	13.84	—	—	19.69	20.31	16.62	—	—	—	—	12.94	11.07
Multan	30.20°N	71.43°E	12.29	15.86	18.33	22.35	22.57	21.65	20.31	20.44	20.57	15.91	12.68	10.00
Islamabad	33.62°N	73.10°E	10.38	12.42	16.98	22.65	—	25.49	20.64	18.91	14.20	15.30	10.64	8.30
<i>Peru</i>														
Puno	15.83°S	70.02°W	14.98	12.92	16.08	20.03	17.45	17.42	15.74	15.32	16.11	16.18	14.24	13.90
<i>Poland</i>														
Warszawa	52.28°N	20.97°E	1.73	3.83	7.81	10.53	19.22	17.11	20.18	15.00	10.65	4.95	2.39	1.68
Kolobrzeg	54.18°N	15.58°E	2.50	3.25	8.86	15.21	20.79	20.50	17.19	16.46	7.95	5.75	1.78	1.18

(Continued)

TABLE A2.3a (CONTINUED)

Worldwide Global Horizontal Average Solar Radiation (MJ/m²-day)

Position	Lat	Long	Jan	Feb	Mar	Apr	May	Jun	Jul	Aug	Sep	Oct	Nov	Dec
<i>Portugal</i>														
Evora	38.57°N	7.90°W	9.92	12.43	17.81	18.69	23.57	29.23	28.75	23.77	20.17	—	6.81	4.57
Lisbon	38.72°N	9.15°W	9.24	11.60	17.52	18.49	24.64	29.02	28.14	22.20	19.76	13.56	7.18	4.83
<i>Romania</i>														
Bucharest	44.50°N	26.13°E	7.05	10.22	12.04	16.53	18.97	22.16	23.19	—	17.17	9.55	4.82	—
Constanta	44.22°N	28.63°E	5.62	9.28	14.31	20.59	23.23	25.80	27.98	24.22	16.91	11.89	6.19	5.10
Galati	45.50°N	28.02°E	6.09	9.33	14.31	17.75	21.77	22.74	25.55	19.70	14.05	11.26	6.32	5.38
<i>Russia</i>														
Alexandrovsk	60.38°N	77.87°E	1.34	4.17	9.16	17.05	21.83	21.34	20.26	13.05	10.16	4.68	1.71	0.68
Moscow	55.75°N	37.57°E	1.45	3.96	8.09	11.69	18.86	18.12	17.51	14.17	10.92	4.03	2.28	1.29
St. Petersburg	59.97°N	30.30°E	1.03	3.11	4.88	12.24	20.59	21.55	20.43	13.27	7.83	2.93	1.16	0.59
Verkhoyansk	67.55°N	133.38°E	0.21	2.25	7.61	15.96	19.64	—	—	14.12	7.59	3.51	0.54	—
<i>St. Pierre and Miquelon</i>														
St. Pierre	46.77°N	56.17°W	4.43	6.61	12.50	17.57	18.55	17.84	19.95	16.46	12.76	8.15	3.69	3.33
<i>Singapore</i>														
Singapore	1.37°N	103.98°E	19.08	20.94	20.75	18.20	14.89	15.22	13.92	16.66	16.51	15.82	13.81	12.67
<i>South Korea</i>														
Seoul	37.57°N	126.97°E	6.24	9.40	10.34	13.98	16.35	17.49	10.65	12.94	11.87	10.35	6.47	5.14
<i>South Africa</i>														
Cape Town	33.98°S	18.60°E	27.47	25.57	—	15.81	11.44	9.08	8.35	13.76	17.30	22.16	26.37	27.68
Port Elizabeth	33.98°S	25.60°E	27.22	22.06	19.01	15.29	11.79	11.13	10.73	13.97	18.52	23.09	23.15	27.26
Pretoria	25.73°S	28.18°E	26.06	22.43	20.52	16.09	15.67	13.67	15.19	18.65	21.62	21.75	24.82	23.43
<i>Spain</i>														
Madrid	40.45°N	3.72°W	7.73	10.53	15.35	21.74	22.81	22.05	26.27	22.90	18.89	10.21	8.69	5.56

(Continued)

TABLE A2.3a (CONTINUED)
 Worldwide Global Horizontal Average Solar Radiation ($MJ/m^2\text{-day}$)

Position	Lat	Long	Jan	Feb	Mar	Apr	May	Jun	Jul	Aug	Sep	Oct	Nov	Dec
<i>Vietnam</i>														
Hanoi	21.03°N	105.85°E	5.99	7.48	8.73	13.58	19.10	21.26	19.85	19.78	20.67	14.78	12.44	13.21
<i>Yugoslavia</i>														
Beograd	44.78°N	20.53°E	4.92	6.27	10.64	14.74	20.95	22.80	22.09	20.27	15.57	11.24	6.77	4.99
Kopaonik	43.28°N	20.80°E	7.03	10.93	14.75	12.78	13.54	20.43	22.48	—	20.14	11.61	6.26	4.64
Portoroz	45.52°N	13.57°E	5.11	7.84	13.75	17.30	23.66	22.31	25.14	21.34	13.40	8.98	6.04	3.92
<i>Zambia</i>														
Lusaka	15.42°S	28.32°W	16.10	18.02	20.24	19.84	17.11	16.37	19.45	20.72	21.68	23.83	23.85	20.52
<i>Zimbabwe</i>														
Bulawayo	20.15°S	28.62°N	20.03	22.11	21.03	18.09	17.15	15.36	16.46	19.49	21.55	23.44	25.08	23.46
Harare	17.83°S	31.02°N	19.38	19.00	19.22	17.67	18.35	16.10	14.55	17.87	21.47	23.98	19.92	21.88

Source: Voeikov Main Geophysical Observatory, Russia (http://wrdc-mgo.nrel.gov/html/get_data-ap.html). Data for 872 locations are available from these sources in 68 countries. Source for Canadian data: Environment Canada (<http://www.ec.gc.ca/~envhome.html>).

TABLE A2.3b
Average Daily Solar Radiation on a Horizontal Surface in the United States (MJ/m²·day)

Position	Jan	Feb	Mar	Apr	May	June	July	Aug	Sep	Oct	Nov	Dec	Average
<i>Alabama</i>													
Birmingham	9.20	11.92	15.67	19.65	21.58	22.37	21.24	20.21	17.15	14.42	10.22	8.40	16.01
Montgomery	9.54	12.49	16.24	20.33	22.37	23.17	21.80	20.56	17.72	14.99	10.90	8.97	16.58
<i>Alaska</i>													
Fairbanks	0.62	2.77	8.31	14.66	17.98	19.65	16.92	12.36	7.02	3.20	1.01	0.23	8.74
Anchorage	1.02	3.41	8.18	13.06	15.90	17.72	16.69	12.72	8.06	3.97	1.48	0.56	8.63
Nome	0.51	2.95	8.29	15.22	18.97	19.65	16.69	11.81	7.72	3.63	0.99	0.09	8.86
St. Paul Island	1.82	4.32	8.52	12.72	14.08	14.42	12.83	10.33	7.84	4.54	2.16	1.25	7.95
Yakutat	1.36	3.63	7.72	12.61	14.76	15.79	14.99	12.15	7.95	3.97	1.82	0.86	8.18
<i>Arizona</i>													
Phoenix	11.58	15.33	19.87	25.44	28.85	30.09	27.37	25.44	21.92	17.60	12.95	10.56	20.56
Tucson	12.38	15.90	20.21	25.44	28.39	29.30	25.44	24.08	21.58	17.94	13.63	11.24	20.44
<i>Arkansas</i>													
Little Rock	9.09	11.81	15.56	19.19	21.80	23.51	23.17	21.35	17.26	14.08	9.77	8.06	16.24
Fort Smith	9.31	12.15	15.67	19.31	21.69	23.39	23.85	24.46	17.26	13.97	9.88	8.29	16.35
<i>California</i>													
Bakersfield	8.29	11.92	16.69	22.15	26.57	28.96	28.73	26.01	21.35	15.90	10.33	7.61	18.74
Fresno	7.61	11.58	16.81	22.49	27.14	29.07	28.96	25.89	21.12	15.56	9.65	6.70	18.62
Long Beach	9.99	12.95	17.03	21.60	23.17	24.19	26.12	24.08	19.31	14.99	11.24	9.31	17.83
Sacramento	6.93	10.68	15.56	21.24	25.89	28.28	28.62	25.32	20.56	14.54	8.63	6.25	17.72
San Diego	11.02	13.97	17.72	21.92	22.49	23.28	24.98	23.51	19.53	15.79	12.26	10.22	18.06
San Francisco	7.72	10.68	15.22	20.44	24.08	25.78	26.46	23.39	19.31	13.97	8.97	7.04	16.92
Los Angeles	10.11	13.06	17.26	21.80	23.05	23.74	25.67	23.51	18.97	14.99	11.36	9.31	17.72

(Continued)

TABLE A2.3b (CONTINUED)
Average Daily Solar Radiation on a Horizontal Surface in the United States (MJ/m²/day)

Position	Jan	Feb	Mar	Apr	May	June	July	Aug	Sep	Oct	Nov	Dec	Average
Santa Maria	10.22	13.29	17.49	22.26	25.10	26.57	26.91	24.42	20.10	15.67	11.47	9.54	18.62
<i>Colorado</i>													
Boulder	7.84	10.45	15.64	17.94	20.47	20.28	17.12	16.07	12.09	8.66	7.10	14.31	
Colorado Springs	9.09	12.15	16.13	20.33	22.26	24.98	23.96	21.69	18.51	14.42	9.99	8.18	16.81
<i>Connecticut</i>													
Hartford	6.70	9.65	13.17	16.69	19.53	21.24	21.12	18.51	14.76	10.68	6.59	5.45	13.74
<i>Delaware</i>													
Wilmington	7.27	10.22	13.97	17.60	20.33	22.49	21.80	19.65	15.79	11.81	7.84	6.25	14.65
<i>Florida</i>													
Daytona Beach	11.24	13.85	17.94	22.15	23.17	22.03	21.69	20.44	17.72	14.99	12.15	10.33	17.38
Jacksonville	10.45	13.17	17.03	21.12	22.03	21.58	21.01	19.42	16.69	14.20	11.47	9.65	16.47
Tallahassee	10.33	13.29	16.92	21.24	22.49	22.03	20.90	19.65	17.72	15.56	11.92	9.77	16.81
Miami	12.72	15.22	18.51	21.58	21.46	20.10	21.10	20.10	17.60	15.67	13.17	11.81	17.38
Key West	13.17	16.01	19.65	22.71	22.83	22.03	22.03	21.01	18.74	16.47	13.85	15.79	18.40
Tampa	11.58	14.42	18.17	22.26	23.05	21.92	20.90	19.65	17.60	16.01	12.83	11.02	17.49
<i>Georgia</i>													
Athens	9.43	12.38	16.01	20.21	22.03	22.83	21.80	20.21	17.26	14.42	10.45	8.40	16.29
Atlanta	9.31	12.26	16.13	20.33	22.37	23.17	22.15	20.56	17.49	14.54	10.56	8.52	16.43
Columbus	9.77	12.72	16.47	20.67	22.37	22.83	21.58	20.33	17.60	14.99	11.02	9.09	16.62
Macon	9.54	12.61	16.35	20.56	22.37	22.83	21.58	20.21	17.26	14.88	10.90	8.86	16.50
Savanna	9.99	12.72	16.81	21.01	22.37	22.60	21.80	19.76	16.92	14.65	11.13	9.20	16.58
<i>Hawaii</i>													
Honolulu	14.08	16.92	19.42	21.24	22.83	23.51	23.74	23.28	21.35	18.06	14.88	13.40	19.42

(Continued)

TABLE A2.3b (CONTINUED)
 Average Daily Solar Radiation on a Horizontal Surface in the United States (MJ/m²·day)

Position	Jan	Feb	Mar	Apr	May	June	July	Aug	Sep	Oct	Nov	Dec	Average
<i>Michigan</i>													
Detroit	5.91	8.86	12.38	16.47	20.33	22.37	21.92	18.97	14.76	10.11	6.13	4.66	13.63
Lansing	5.91	8.86	12.49	16.58	20.21	22.26	21.92	18.85	14.54	9.77	5.91	4.66	13.51
<i>Minnesota</i>													
Duluth	5.68	9.31	13.74	17.38	20.10	21.46	21.80	18.28	13.29	8.86	5.34	4.43	13.29
Minneapolis	6.36	9.77	13.51	16.92	20.56	22.49	22.83	19.42	14.65	9.99	6.13	4.88	13.97
Rochester	6.36	9.65	13.17	16.58	20.10	22.15	22.15	19.08	14.54	10.11	6.25	5.11	13.74
<i>Mississippi</i>													
Jackson	9.43	12.38	16.13	19.87	22.15	23.05	22.15	19.08	14.54	10.11	6.25	5.11	13.74
<i>Missouri</i>													
Columbia	8.06	10.90	14.31	18.62	21.58	23.62	23.85	21.12	16.69	12.72	8.29	6.70	15.56
Kansas City	7.95	10.68	14.08	18.28	21.24	23.28	23.62	20.78	16.58	12.72	8.40	6.70	15.44
Springfield	8.52	11.02	14.65	18.62	21.24	23.05	23.62	21.24	16.81	13.17	8.86	7.27	15.67
St. Louis	7.84	10.56	13.97	18.06	21.12	23.05	22.94	20.44	16.58	12.49	8.18	6.59	15.22
<i>Montana</i>													
Helena	5.22	8.29	12.61	17.15	20.67	23.28	25.21	21.24	15.79	10.45	6.02	4.43	14.20
Lewistown	5.22	8.40	12.72	17.15	20.33	23.05	24.53	20.78	15.10	10.22	5.91	4.32	13.97
<i>Nebraska</i>													
Omaha	7.50	10.33	13.97	18.06	21.24	2.40	23.51	20.56	16.01	11.81	7.61	6.13	15.10
Lincoln	7.33	10.10	13.65	16.22	19.26	21.21	22.15	18.87	15.44	11.54	7.76	6.20	14.16
<i>Nevada</i>													
Elko	7.61	10.56	14.42	18.85	22.71	25.67	26.69	23.62	19.31	13.63	8.29	6.70	16.58
Las Vegas	10.79	14.42	19.42	24.87	28.16	30.09	28.28	25.89	22.15	17.03	12.15	9.88	20.33
Reno	8.29	11.58	16.24	21.24	25.10	27.48	28.16	24.98	20.56	14.88	9.31	7.38	17.94

	New Hampshire	Concord	10.11	13.97	16.92	20.21	21.80	19.08	14.99	10.45	6.47	5.45	14.08
<i>New Jersey</i>													
Atlantic City	7.38	10.22	13.97	17.49	20.21	21.92	21.24	19.19	15.79	11.92	8.06	6.36	14.54
Newark	6.93	9.77	13.51	17.26	19.76	21.35	21.01	18.85	15.33	11.36	7.27	5.68	13.97
<i>New Mexico</i>													
Albuquerque	11.47	14.99	19.31	24.53	27.60	29.07	27.03	24.76	21.12	17.03	12.49	10.33	19.99
<i>New York</i>													
Albany	6.36	9.43	12.95	16.69	19.53	21.46	21.58	18.51	14.65	10.11	6.13	5.00	13.51
Buffalo	5.68	8.40	12.15	16.35	19.76	22.03	21.69	18.62	14.08	9.54	5.68	4.54	13.29
New York City	6.93	9.88	13.85	17.72	20.44	22.03	21.69	19.42	15.56	11.47	7.27	5.79	14.31
Rochester	5.68	8.52	12.26	16.58	19.87	21.92	21.69	18.51	14.20	9.54	5.68	4.54	13.29
<i>North Carolina</i>													
Charlotte	8.97	11.81	15.67	19.76	21.58	22.60	21.92	19.99	16.92	13.97	9.99	8.06	16.01
Wilmington	9.31	12.15	16.24	20.44	21.92	22.60	21.58	19.53	16.69	14.08	10.56	8.52	16.13
<i>North Dakota</i>													
Fargo	5.79	9.09	13.17	16.92	20.56	22.37	23.17	19.87	14.31	9.54	5.68	4.54	13.74
Bismarck	6.12	9.75	13.88	17.43	21.45	23.01	24.06	20.12	15.21	10.61	6.28	4.84	14.39
<i>Ohio</i>													
Cleveland	5.79	8.63	12.04	16.58	20.10	22.15	21.92	18.97	14.76	10.22	6.02	4.66	13.51
Columbus	6.47	9.09	12.49	16.58	19.76	21.58	21.12	18.97	15.44	11.24	6.81	5.34	13.74
Dayton	6.81	9.43	12.83	17.03	20.33	22.37	22.37	19.65	15.90	11.47	7.04	5.45	14.20
Youngstown	5.79	8.40	11.92	15.90	19.19	21.24	20.78	18.06	14.31	10.11	6.02	4.77	13.06
<i>Oklahoma</i>													
Oklahoma City	9.88	1.25	16.47	20.33	22.26	24.42	24.98	22.49	18.17	14.54	10.45	8.74	17.15
<i>Oregon</i>													
Eugene	4.54	7.04	11.24	15.79	19.99	22.37	24.19	21.01	15.90	9.65	5.11	3.75	13.40
Medford	5.34	8.52	13.17	18.62	23.39	26.23	27.82	23.96	18.62	11.92	6.02	4.43	15.67

(Continued)

TABLE A2.3b (CONTINUED)
 Average Daily Solar Radiation on a Horizontal Surface in the United States (MJ/m²/day)

Position	Jan	Feb	Mar	Apr	May	June	July	Aug	Sep	Oct	Nov	Dec	Average
Portland	4.20	6.70	10.68	15.10	18.97	21.24	22.60	19.53	14.88	9.20	4.88	3.52	12.61
<i>Pacific Islands</i>													
Guam	16.35	17.38	19.65	20.78	20.56	19.76	18.28	17.49	17.49	16.58	15.79	15.10	17.94
<i>Pennsylvania</i>													
Philadelphia	7.04	9.88	13.63	17.26	19.99	22.03	21.46	19.42	15.67	11.58	7.72	6.02	14.31
Pittsburgh	6.25	8.97	12.61	16.47	19.65	21.80	21.35	18.85	15.10	10.90	6.59	5.00	13.63
<i>Rhode Island</i>													
Providence	6.70	9.65	13.40	16.92	19.99	21.58	21.24	18.85	15.22	11.02	6.93	5.56	13.97
<i>South Carolina</i>													
Charleston	9.77	12.72	16.81	21.12	22.37	22.37	21.92	19.65	16.92	14.54	11.02	9.09	16.58
Greenville	9.20	12.04	15.90	19.99	21.58	22.60	21.58	19.87	16.81	14.08	10.22	8.18	16.01
<i>South Dakota</i>													
Pierre	6.47	9.54	13.85	17.94	21.46	24.08	24.42	21.46	16.35	11.24	7.04	5.45	14.99
Rapid City	6.70	9.88	14.20	18.28	21.46	24.19	24.42	21.80	16.92	11.81	7.50	5.79	15.33
<i>Tennessee</i>													
Memphis	8.86	11.58	15.22	19.42	22.03	23.85	23.39	21.46	17.38	14.20	9.65	7.84	16.24
Nashville	8.29	11.13	14.65	19.31	21.69	23.51	22.49	20.56	16.81	13.51	8.97	7.15	15.67
<i>Texas</i>													
Austin	10.68	13.63	17.03	19.53	21.24	23.74	24.42	22.83	18.85	15.67	11.92	9.99	17.49
Brownsville	10.33	13.17	16.47	19.08	20.78	22.83	23.28	21.58	18.62	16.13	12.38	9.88	17.03
El Paso	12.38	16.24	20.90	25.44	28.05	28.85	26.46	24.30	21.12	17.72	13.63	11.47	20.56
Houston	9.54	12.26	15.22	18.06	20.21	21.69	21.35	20.21	17.49	15.10	11.02	8.97	15.90
San Antonio	10.88	13.53	16.26	17.35	21.10	23.87	24.92	22.81	19.22	15.52	11.50	9.98	17.24

<i>Utah</i>	Salt Lake City	6.93	10.45	14.76	19.42	23.39	26.46	26.35	23.39	18.85	13.29	8.06	6.02	16.47
<i>Vermont</i>	Burlington	5.79	9.20	13.06	16.47	19.87	21.69	21.80	18.74	14.42	9.43	5.56	4.43	13.40
<i>Virginia</i>	Norfolk	8.06	10.90	14.65	18.51	20.78	22.15	21.12	19.42	16.13	12.49	9.09	7.27	15.10
<i>Richmond</i>	Richmond	8.06	10.90	14.76	18.62	20.90	22.49	21.58	19.53	16.24	12.61	8.97	7.15	15.22
<i>Washington</i>	Olympia	3.63	6.02	9.99	14.20	18.06	20.10	21.12	18.17	13.63	7.95	4.32	3.07	11.70
<i>Seattle</i>	Seattle	3.52	5.91	10.11	14.65	19.08	20.78	21.80	18.51	13.51	7.95	4.20	2.84	11.92
<i>Yakima</i>	Yakima	4.88	7.95	12.83	17.83	22.49	24.87	25.89	22.26	16.92	10.68	5.56	4.09	17.76
<i>West Virginia</i>	Charleston	7.04	9.65	13.40	17.15	20.21	21.69	20.90	18.97	15.56	11.81	7.72	6.02	14.20
<i>Elkins</i>	Elkins	6.93	9.43	12.83	16.35	19.08	20.56	19.99	18.06	14.88	11.13	7.27	5.79	13.51
<i>Wisconsin</i>	Green Bay	6.25	9.31	13.17	16.81	20.56	22.49	22.03	18.85	14.20	9.65	5.79	4.88	13.74
<i>Madison</i>	Madison	6.59	9.88	13.29	16.92	20.67	22.83	22.37	19.42	14.76	3.41	6.25	5.22	14.08
<i>Milwaukee</i>	Milwaukee	6.47	9.31	12.72	16.69	20.78	22.94	22.60	19.42	14.88	10.22	6.25	5.11	13.97
<i>Wyoming</i>	Rock Springs	7.61	10.90	15.10	19.42	23.17	26.01	25.78	22.94	18.62	13.40	8.40	6.70	16.58
<i>Sheridan</i>	Sheridan	6.47	9.77	13.97	17.94	20.90	23.85	24.64	21.69	16.47	11.24	7.15	5.56	14.99

Source: National Renewable Energy Laboratory, USA (<http://rredc.nrel.gov/solar>).

TABLE A2.4Regression Coefficients a and b for Page Model for Solar Radiation (Equation 2.52) for Worldwide Locations

Country	Station	Lat.	Alt. (m)	Climate (Khogai et al. 1983)	a	b	Ref.
Egypt	Bahtim	30.13°N	200	BWh	0.220	0.550	Ibrahim (1985)
	Cairo	30.08°N	112	BWh	0.140	0.610	Ibrahim (1985)
	Giza	30.05°N	19	BWh	0.230	0.540	Ibrahim (1985)
	Kharga Oasis	25.45°N	78	BWh	0.520	0.230	Ibrahim (1985)
	Mersa M.	31.33°N	20	BWh	0.170	0.590	Ibrahim (1985)
	Tahrir	30.65°N	16	BWh	0.290	0.460	Ibrahim (1985)
Ghana	Accra	5.33°N	~20	BS	0.290	0.470	Anane-Fenin (1986)
	Bole	9.02°N	~350	Aw	0.280	0.440	Anane-Fenin (1986)
	Ho	6.35°N	~300	Aw	0.210	0.460	Anane-Fenin (1986)
	Kumasi	6.41°N	~400	Aw	0.250	0.440	Anane-Fenin (1986)
	Saltpond	5.12°N	~50	BS	0.260	0.450	Anane-Fenin (1986)
	Takoradi	4.59°N	~20	BS	0.250	0.470	Anane-Fenin (1986)
	Tamale	9.25°N	~250	Aw	0.270	0.470	Anane-Fenin (1986)
	Wenchi	7.42°N	~300	Aw	0.280	0.360	Anane-Fenin (1986)
	Yendi	9.26°N	~300	Aw	0.320	0.410	Anane-Fenin (1986)
	Greece	38.63°N	60	Csa	0.240	0.520	Zabara (1986)
	Athens	37.97°N	~300	Csa	0.230	0.460	Zabara (1986)
	Chania	35.50°N	50	Csa	0.220	0.580	Zabara (1986)
	Kavala	40.93°N	150	Csa	0.250	0.460	Zabara (1986)
	Larissa	39.63°N	65	Csa	0.230	0.560	Zabara (1986)
	Mytilene	39.15°N	65	Csa	0.240	0.510	Zabara (1986)
	Rhodes	36.37°N	5	Csa	0.260	0.520	Zabara (1986)
	Hong Kong	Hong Kong	22.37°N	Caf	0.214	0.514	Leung (1980)
			~5				

India	Ahmedabad	22.37°N	55	Aw	0.302	0.464	Garg and Garg (1985)
	Bombay (Mumbai)	19.12°N	14	Aw	0.292	0.464	Garg and Garg (1985)
	Calcutta	22.65°N	6	Aw	0.327	0.399	Garg and Garg (1985)
	Goa	15.48°N	55	Am	0.279	0.514	Garg and Garg (1985)
	Jodhpur	26.30°N	224	BSh	0.309	0.439	Garg and Garg (1985)
	Madras	13.00°N	16	Aw	0.340	0.399	Garg and Garg (1985)
	Nagpur	21.10°N	310	Aw	0.293	0.460	Garg and Garg (1985)
	New Delhi	28.63°N	216	Caw	0.341	0.446	Garg and Garg (1985)
	Poona	18.53°N	559	Bs	0.330	0.453	Garg and Garg (1985)
	Trivandrum	8.48°N	64	Am	0.393	0.357	Garg and Garg (1985)
Italy	Vizagapatnam	17.72°N	3	Aw	0.286	0.467	Garg and Garg (1985)
	Alghero	40.63°N	40	Csa	0.118	0.765	Jain (1986)
	Amendola	41.53°N	56	Csa	0.212	0.635	Jain (1986)
	Ancona	43.63°N	105	Csa	0.197	0.679	Jain (1986)
	Balzano	46.47°N	241	Csa	0.192	0.719	Jain (1986)
	Bologna	44.53°N	49	Csa	0.216	0.639	Jain (1986)
	Brindisi	40.65°N	10	Csa	0.183	0.706	Jain (1986)
	Cagliari	39.25°N	18	Csa	0.175	0.679	Jain (1986)
	Cape Mele	43.95°N	221	Csa	0.129	0.779	Jain (1986)
	Cape Palinurus	40.02°N	185	Csa	0.213	0.604	Jain (1986)
Italy	Crotone	39.07°N	158	Csa	0.266	0.546	Jain (1986)
	Gela	37.09°N	33	Csa	0.105	0.851	Jain (1986)
	Genova	44.42°N	3	Csa	0.089	0.821	Jain (1986)
	M. Cimone	44.20°N	2137	H	0.104	0.755	Jain (1986)
	M. Terminillo	42.47°N	1875	H	0.246	0.482	Jain (1986)
	Messina	38.20°N	59	Csa	0.199	0.689	Jain (1986)

(Continued)

TABLE A2.4 (CONTINUED)Regression Coefficients *a* and *b* for Page Model for Solar Radiation (Equation 2.52) for Worldwide Locations

Country	Station	Lat.	Alt. (m)	Climate (Khogali et al. 1983)	<i>a</i>	<i>b</i>	Ref.
Milano	45.43°N	103	Csa	0.148	0.775	Jain (1986)	
Napoli	40.85°N	72	Csa	0.181	0.709	Jain (1986)	
Olbia	40.93°N	2	Csa	0.183	0.633	Jain (1986)	
Pantelleria	36.82°N	170	Csa	0.191	0.679	Jain (1986)	
Pescara	42.43°N	18	Csa	0.188	0.669	Jain (1986)	
Pianosa	42.58°N	27	Csa	0.143	0.771	Jain (1986)	
Pisa	43.67°N	1	Csa	0.205	0.614	Jain (1986)	
Roma	41.80°N	131	Csa	0.148	0.722	Jain (1986)	
Torino	45.18°N	282	Daf	0.161	0.780	Jain (1986)	
Trapani	37.92°N	14	Csa	0.204	0.662	Jain (1986)	
Trieste	45.65°N	20	Csa	0.157	0.701	Jain (1986)	
Udine	46.03°N	92	Csa	0.167	0.666	Jain (1986)	
Ustica	38.70°N	251	Csa	0.254	0.586	Jain (1986)	
Venezia	45.50°N	6	Csa	0.144	0.782	Jain (1986)	
Vigna Diwali	42.08°N	270	Csa	0.154	0.689	Jain (1986)	
Kota Bharu	6.17°N	5	Af	0.340	0.490	Chuah and Lee (1981)	
Kuala Lumpur	3.12°N	19	Af	0.340	0.490	Chuah and Lee (1981)	
Penang	5.33°N	35	Af	0.350	0.570	Chuah and Lee (1981)	
Enugu	6.47°N	137	Af	0.228	0.492	Eze and Ododo (1988)	
Makurdi	7.70°N	76	Aw	0.288	0.472	Eze and Ododo (1988)	
Nsukka	6.80°N	147	Af	0.217	0.490	Eze and Ododo (1988)	
Port Harcourt	4.85°N	6	Af	0.246	0.488	Eze and Ododo (1988)	
Lungi Free	8.61°N	25	Am	0.260	0.440	Massaquoi (1988)	
Abu Naama	12.73°N	445	BShw	0.433	0.271	Khogali (1983)	
Sierra L.							
Sudan							

Aroma	15.83°N	430	BWh	0.460	0.208	Khogali (1983)
Dongola	19.17°N	225	BWh	0.211	0.572	Khogali (1983)
El Fasher	13.63°N	773	BShw	0.361	0.366	Khogali (1983)
El Showak	14.22°N	380	BWh	0.325	0.423	Khogali (1983)
G. Ghawazat	11.47°N	480	Aw	0.350	0.353	Khogali (1983)
Hudeiba	17.57°N	350	BWh	0.208	0.544	Khogali (1983)
Jubo	4.87°N	460	Aw	0.402	0.234	Khogali (1983)
Kadugli	11.00°N	501	Aw	0.237	0.463	Khogali (1983)
Malakai	9.55°N	387	Aw	0.339	0.359	Khogali (1983)
Port Sudan	19.58°N	5	BWh	0.315	0.402	Khogali (1983)
Shambat	15.67°N	376	BWh	0.278	0.467	Khogali (1983)
Wadi Medani	14.38°N	405	BWh	0.357	0.374	Khogali (1983)
Zalingei	12.90°N	900	BShw	0.325	0.456	Khogali (1983)
Yemen	15.73°N	2100	H	0.331	0.385	Khogali et al. (1983)
El Khabar	14.38°N	2100	H	0.342	0.372	Khogali et al. (1983)
El Macca	13.25°N	10	BWh	0.358	0.346	Khogali et al. (1983)
Hodeidah	14.75°N	33	BWh	0.374	0.321	Khogali et al. (1983)
Sana	15.52°N	2210	BSh	0.347	0.364	Khogali et al. (1983)
Taiz	13.58°N	1400	H	0.364	0.335	Khogali et al. (1983)
Kasama	10.22°S	1384	Aw	0.268	0.454	Jain and Jain (1985)
Livingstone	17.82°S	986	Aw	0.187	0.613	Jain and Jain (1985)
Luangwa	13.27°S	570	Aw	0.253	0.588	Jain and Jain (1985)
Lusaka	15.32°S	1154	Aw	0.198	0.551	Jain and Jain (1985)
Mansa	11.10°S	1259	Aw	0.265	0.476	Jain and Jain (1985)
Mbala	8.37°S	1673	Aw	0.245	0.505	Jain and Jain (1985)
Mongu	15.25°S	1053	Aw	0.188	0.556	Jain and Jain (1985)
Ndolo	13.00°S	1270	Aw	0.288	0.386	Jain and Jain (1985)

Source: Data compiled from Akinoglu, B.G., A review of sunshine-based models used to estimate monthly average global solar radiation. *Renewable Energy*, 1 (3), 479–499, 1991.

TABLE A2.5Solar Collector Tilt Factor (\bar{R}_b) for South-Facing Collectors

Month	$L = 20^\circ$		$L = 30^\circ$		$L = 40^\circ$		$L = 50^\circ$	
	$\beta = 20^\circ$	$\beta = 40^\circ$	$\beta = 30^\circ$	$\beta = 50^\circ$	$\beta = 40^\circ$	$\beta = 60^\circ$	$\beta = 50^\circ$	$\beta = 70^\circ$
Jan	1.36	1.52	1.68	1.88	2.28	2.56	3.56	3.94
Feb	1.22	1.28	1.44	1.52	1.80	1.90	2.49	2.62
Mar	1.08	1.02	1.20	1.15	1.36	1.32	1.65	1.62
Apr	1.00	0.83	1.00	0.84	1.05	0.90	1.16	1.00
May	0.92	0.70	0.87	0.66	0.88	0.66	0.90	0.64
Jun	0.87	0.63	0.81	0.58	0.79	0.60	0.80	0.56
Jul	0.89	0.66	0.83	0.62	0.82	0.64	0.84	0.62
Aug	0.95	0.78	0.93	0.76	0.96	0.78	1.02	0.83
Sep	1.04	0.95	1.11	1.00	1.24	1.12	1.44	1.32
Oct	1.17	1.20	1.36	1.36	1.62	1.64	2.10	2.14
Nov	1.30	1.44	1.60	1.76	2.08	2.24	3.16	3.32
Dec	1.39	1.60	1.76	1.99	2.48	2.80	4.04	4.52

Source: Kreider, J.F. and F. Kreith, *Solar Heating and Cooling*, Revised 1st ed., Hemisphere Publ. Corp., 1977.

Note: The solar collector tilt factor is the ratio of monthly beam insolation on a tilted surface to monthly beam insolation on a horizontal surface. Here, β = collector tilt angle and L = collector latitude.

Date	Solar time		Solar position		Total insolation on surface (W/m ²)						
	a.m.	p.m.	Alt	Azm	Direct normal	Horiz.	South-facing surface angle with horizon				
Jan 21							14°	24°	34°	44°	90°
7	5	4.8	65.6	224	32	54	66	79	88	98	
8	4	16.9	58.3	753	262	347	397	432	457	400	
9	3	27.9	48.8	908	476	593	652	697	719	555	
10	2	37.2	36.1	971	643	775	845	889	905	652	
11	1	43.6	19.6	999	747	892	965	1005	1021	712	
12		46	0	1009	785	933	690	1046	1059	731	
		Surface daily totals					8718	5113	6254	6852	7250
Feb 21	7	5	9.3	74.6	498	110	139	154	167	177	145
	8	4	22.3	67.2	829	366	426	457	473	476	322
	9	3	34.4	57.6	939	589	671	709	725	719	444
	10	2	45.1	44.2	990	760	860	901	917	905	530
	11	1	53	25	1012	870	977	1021	1034	1018	583
	12		56	0	1021	908	1018	1062	1075	1056	602
	Surface daily totals					9569	6298	7174	7552	7678	7640
Mar 21	7	5	13.7	83.3	611	189	199	202	195	186	85
	8	4	27.2	76.8	842	444	473	479	470	448	202
	9	3	40.2	67.9	930	668	712	722	709	675	299
	10	2	52.3	54.8	974	838	898	908	892	851	378
	11	1	61.9	33.4	993	946	1015	1028	1009	961	426
	12		66	0	999	983	1053	1069	1050	999	441
	Surface daily totals					9702	7155	7653	7741	7603	7243
Apr 21	6	6	4.7	100.6	126	22	16	13	13	9	6
	7	5	18.3	94.9	640	262	243	221	195	161	32
	8	4	32	89	807	504	495	470	432	385	50
	9	3	45.6	81.9	883	716	716	693	649	586	145
	10	2	59	71.8	920	876	889	867	816	842	192
	11	1	71.1	51.6	939	977	996	974	924	848	233
	12		77.6	0	942	1012	1034	1012	961	883	249
Surface daily totals					9569	7735	7748	7483	7023	6354	1538
May 21	6	6	8	108.4	271	69	47	32	28	28	16
	7	5	21.2	103.2	640	309	268	230	186	139	38
	8	4	34.6	98.5	782	539	501	457	400	334	47
	9	3	48.3	93.6	848	734	706	662	599	520	50
	10	2	62	87.7	883	886	867	823	753	665	69
	11	2	75.5	76.9	901	980	968	924	851	756	107
	12		86	0	908	1015	999	958	886	788	117
Surface daily totals					9557	8057	7713	7205	6531	5674	769

FIGURE A2.2a

Solar position and insolation values for 24°N latitude.

(Continued)

Date	Solar time		Solar position		Total insolation on surface (W/m ²)							
	a.m.	p.m.	Alt	Azm	Direct Normal	Horiz.	South-facing surface angle with horizon					
							14°	24°	34°	44°	90°	
Jun 21	6	6	9.3	111.6	306	91	63	38	38	35	22	
	7	5	22.3	106.8	634	325	274	230	183	129	41	
	8	4	35.5	102.6	763	545	498	448	385	312	50	
	9	3	49	98.7	829	738	697	643	574	489	57	
	10	2	62.6	98	864	883	848	797	722	627	57	
	11	1	76.3	90.8	879	974	946	892	816	716	60	
	12		89.4	0	886	1005	977	927	848	744	69	
	Surface daily totals				9437	8113	7599	7029	6279	5358	643	
	Surface daily totals				9242	7962	7603	7092	6417	5566	775	
	Surface daily totals				9027	7590	7571	7300	6834	6172	1481	
Jul 21	6	6	8.2	109	255	72	50	35	32	28	19	
	7	5	21.4	103.8	615	309	268	230	186	139	41	
	8	4	34.8	99.2	753	533	495	451	394	328	50	
	9	3	48.4	94.5	823	728	697	652	589	507	57	
	10	2	62.1	89	857	876	851	807	741	649	66	
	11	1	75.7	79.2	876	968	952	905	835	741	101	
	12		86.6	0	883	999	983	939	867	772	113	
	Surface daily totals				9242	7962	7603	7092	6417	5566	775	
	Surface daily totals				9027	7590	7571	7300	6834	6172	1481	
	Surface daily totals				9027	7590	7571	7300	6834	6172	3127	
Aug 21	6	6	5	101.3	110	22	16	13	13	13	6	
	7	5	18.5	95.6	586	258	240	217	189	158	35	
	8	4	32.2	89.7	760	498	485	460	422	372	50	
	9	3	45.9	82.9	835	703	700	675	630	571	123	
	10	2	59.3	73	876	860	867	845	794	725	183	
	11	1	71.6	53.2	895	958	974	949	898	823	224	
	12		78.3	0	901	993	1009	987	933	857	236	
	Surface daily totals				9027	7590	7571	7300	6834	6172	1481	
	Surface daily totals				9027	7590	7571	7300	6834	6172	3127	
	Surface daily totals				9027	7590	7571	7300	6834	6172	3127	
Sep 21	7	5	13.7	83.8	545	180	189	189	186	177	82	
	8	4	27.2	76.8	782	429	454	460	451	429	195	
	9	3	40.2	67.9	876	646	687	697	684	649	293	
	10	2	52.3	54.8	920	813	867	876	860	823	366	
	11	1	61.9	33.4	942	917	980	993	974	930	413	
	12		66	0	949	952	1018	1031	1012	965	429	
	Surface daily totals				9027	6915	7382	7458	7319	6972	3127	
Oct 21	7	5	9.1	74.1	435	101	126	142	151	158	129	
	8	4	22	66.7	779	350	407	438	454	457	312	
	9	3	34.1	57.1	895	567	649	684	703	697	435	
	10	2	44.7	43.8	949	738	835	873	889	879	520	
	11	1	52.5	24.7	974	845	949	993	1005	990	574	
	12		55.5	0	980	879	990	1034	1046	1031	593	
	Surface daily totals				9040	6077	6928	7294	7451	7395	4545	

FIGURE A2.2a (CONTINUED)

Solar position and insolation values for 24°N latitude.

(Continued)

Date	Solar time		Solar position		Total insolation on surface (W/m ²)						
	a.m.	p.m.	Alt	Azm	Direct normal	Horiz.	South-facing surface angle with horizon				
Nov 21							14°	24°	34°	44°	90°
7	5	4.9	65.8	211	32	50	63	76	85	91	
8	4	17	58.4	794	258	340	388	426	448	391	
9	3	28	48.9	889	473	586	646	684	706	542	
10	2	37.3	36.3	955	640	769	835	876	892	643	
11	1	43.8	19.7	983	744	883	952	996	1009	700	
12		46.2	0	993	779	924	993	1034	1046	719	
		Surface daily totals					8529	5075	6184	6764	7149
Dec 21	7	5	3.2	62.6	95	9	22	28	35	38	44
	8	4	14.9	55.3	709	224	312	366	407	438	410
	9	3	25.5	46	886	432	555	624	675	703	580
	10	2	34.3	33.7	958	596	738	813	867	892	684
	11	1	40.4	18.2	990	697	851	930	983	1009	744
	12		42.6	0	999	731	889	971	1024	1046	766
	Surface daily totals					8271	4646	5838	6487	6947	7205

FIGURE A2.2a (CONTINUED)

Solar position and insolation values for 24°N latitude.

Date	Solar Time		Solar Position		Total Insolation on Surface (W/m ²)						
	a.m.	p.m.	Alt	Azm	Direct Normal	Horiz.	South-facing surface angle with horizon				
Jan 21							22°	32°	42°	52°	90°
7	5	1.4	65.2	3	0	0	0	0	3	9	
8	4	12.5	56.5	640	177	293	334	366	388	362	
9	3	22.5	46	848	372	552	608	649	668	571	
10	2	30.6	33.1	930	526	741	807	848	864	697	
11	1	36.1	17.5	965	624	860	930	971	983	772	
12		38	0	977	0	898	971	1012	1021	797	
		Surface daily totals					7748	4060	5797	6329	6676
Feb 21	7	5	7.1	73.5	381	69	107	117	126	132	120
	8	4	19	64.4	779	299	400	429	441	444	340
	9	3	29.9	53.4	908	507	649	684	700	693	498
	10	2	39.1	39.4	965	668	838	876	892	879	608
	11	1	45.6	21.4	993	769	958	999	1012	993	675
	12		48	0	999	804	996	1040	1053	1034	700
	Surface daily totals					9053	5434	6897	7250	7391	7319

FIGURE A2.2b

Solar position and insolation values for 32°N latitude.

(Continued)

Date	Solar time		Solar position		Total insolation on surface (W/m^2)						
	a.m.	p.m.	Alt	Azm	Direct normal	Horiz.	South-facing surface angle with horizon				
Mar 21							22°	32°	42°	52°	90°
7	5	12.7	81.9	583	170	189	189	186	177	101	
8	4	25.1	73	820	407	460	463	454	432	246	
9	3	36.8	62.1	914	611	700	706	693	659	375	
10	2	47.3	47.5	958	772	883	892	876	835	473	
11	1	55	26.8	980	873	999	1012	993	946	536	
12		58	0	987	905	1037	1050	1031	983	558	
		Surface daily totals					9494	6569	7495	7574	7432
Apr 21	6	6	61.1	99.9	208	44	28	19	19	16	9
	7	5	18.8	92.2	649	271	246	224	195	161	32
	8	4	31.5	84	804	498	492	466	429	378	110
	9	3	43.9	74.2	876	693	709	684	640	577	214
	10	2	55.7	60.3	914	842	879	857	807	738	299
	11	1	65.4	37.5	930	936	987	965	914	835	353
	12		69.6	0	936	968	1024	1002	949	870	372
Surface daily totals					9696	7533	7703	7426	6953	6285	2408
May 21	6	6	10.4	107.2	375	113	66	41	41	38	22
	7	5	22.8	100.1	665	337	277	236	189	139	41
	8	4	35.4	92.9	788	552	501	457	400	331	47
	9	3	48.1	74.7	848	734	703	659	593	514	104
	10	2	60.6	73.3	883	873	860	816	747	656	177
	11	2	72	51.9	898	961	961	914	845	842	227
	12		78	0	901	993	993	949	876	779	243
Surface daily totals					9809	8138	7735	7199	6506	5636	1478
Jun 21	6	6	12.2	110.2	413	142	82	50	47	44	28
	7	5	24.3	103.4	662	362	287	240	186	129	44
	8	4	36.9	96.8	775	567	501	451	385	312	50
	9	3	49.6	89.4	832	744	697	643	571	482	60
	10	2	62.2	79.7	864	879	845	791	716	621	129
	11	1	74.2	60.9	879	965	942	889	810	706	177
	12		81.5	0	883	993	974	920	842	738	189
Surface daily totals					9721	8302	7678	7042	6272	5327	1166
Jul 21	6	6	10.7	107.7	356	117	69	44	41	38	25
	7	5	23.1	100.6	640	337	274	236	189	139	44
	8	4	35.7	93.6	760	548	498	451	394	328	50
	9	3	48.4	85.5	823	728	693	646	583	501	98
	10	2	60.9	74.3	854	864	848	801	731	643	170
	11	1	72.4	53.3	873	952	946	898	8258	826	217
	12		78.6	0	879	980	977	933	860	763	233
Surface daily totals					9494	8063	7634	7092	6399	5529	1444

FIGURE A2.2b (CONTINUED)

Solar position and insolation values for 32°N latitude.

(Continued)

Date	Solar time		Solar position		Total insolation on surface (W/m ²)						
	a.m.	p.m.	Alt	Azm	Direct Normal	Horiz.	South-facing surface angle with horizon				
							22°	32°	42°	52°	90°
Aug 21	6	6	6.5	100.5	186	44	28	22	19	19	13
	7	5	19.1	92.8	599	268	243	217	189	158	38
	8	4	31.8	84.7	756	492	479	454	416	366	104
	9	3	44.3	75	829	681	693	668	621	561	205
	10	2	56.1	61.3	870	826	857	832	785	744	287
	11	1	66	38.4	889	920	961	939	886	810	337
	12		70.3	0	895	952	999	974	920	845	356
Surface daily totals					9147	7414	7527	7237	6758	6096	2320
Sep 21	7	5	12.7	81.9	514	161	177	177	173	164	95
	8	4	25.1	73	756	391	441	444	435	413	236
	9	3	36.8	62.1	857	593	671	678	665	634	359
	10	2	47.3	47.5	905	747	851	860	845	804	457
	11	1	55	26.8	927	845	965	974	955	911	517
	12		58	0	933	876	1002	1012	993	946	539
	Surface daily totals					8851	6348	7212	7275	7136	6789
Oct 21	7	5	6.8	73.1	312	60	91	101	107	113	101
	8	4	18.7	64	722	284	378	403	419	422	328
	9	3	29.5	53	860	489	624	656	671	668	482
	10	2	38.7	39.1	924	643	810	848	860	851	593
	11	1	45.1	21.1	952	744	927	968	980	965	659
	12		47.5	0	958	779	965	1009	1021	1002	684
	Surface daily totals					8498	5213	6619	6960	7098	7035
Nov 21	7	5	1.5	65.4	6	0	0	0	3	3	3
	8	4	12.7	56.6	618	173	287	328	356	375	350
	9	3	22.6	46.1	829	372	545	599	637	656	555
	10	2	30.8	33.2	911	523	734	794	835	851	684
	11	1	36.2	17.6	949	621	851	917	955	968	760
	12		38.2	0	958	652	889	958	996	1009	785
	Surface daily totals					7584	4035	5724	6241	6569	6714
Dec 21	8	4	10.3	53.8	555	129	243	284	318	340	337
	9	3	19.8	43.6	810	322	507	567	615	643	577
	10	2	27.6	31.2	908	473	697	769	816	842	712
	11	1	32.7	16.4	949	567	813	889	939	961	791
	12		34.6	0	958	599	854	930	980	1002	816
	Surface daily totals					7401	3581	5371	5951	6354	6575

FIGURE A2.2b (CONTINUED)

Solar position and insolation values for 32°N latitude.

Date	Solar time		Solar position		Total insolation on surface (W/m^2)						
	a.m.	p.m.	Alt	Azm	Direct normal	Horiz.	South-facing surface angle with horizon				
Jan 21							30°	40°	50°	60°	90°
8	4	8.1	55.3	448	88	205	233	255	268	265	
9	3	16.8	44	753	262	489	539	574	589	539	
10	2	23.8	30.9	864	400	66	747	785	801	703	
11	1	28.4	16	911	485	810	873	914	924	797	
12		30	0	927	517	851	917	955	965	829	
		Surface daily totals					6878	2988	5232	5705	6008
Feb 21	7	5	4.8	72.7	217	32	60	66	72	76	69
	8	4	15.4	62.2	706	230	359	385	397	400	337
	9	3	25	50.2	864	416	615	646	659	656	526
	10	2	32.8	35.9	930	561	807	842	854	842	662
	11	1	38.1	18.9	961	649	924	965	977	958	744
	12		40	0	971	681	965	1005	1018	999	772
Surface daily totals					8321	4457	6493	6815	6941	6859	5453
Mar 21	7	5	11.4	80.2	539	145	173	173	170	161	110
	8	4	22.5	69.6	788	359	441	444	435	413	281
	9	3	32.8	57.3	889	545	678	684	671	637	435
	10	2	41.6	41.9	936	687	860	870	854	813	555
	11	1	47.7	22.6	961	779	977	987	968	924	630
	12		50	0	968	810	1015	1028	1009	961	656
Surface daily totals					9191	5838	7275	7344	7199	6852	4678
Apr 21	6	6	7.4	98.9	281	63	35	25	22	22	13
	7	5	18.9	89.5	649	274	243	221	192	158	38
	8	4	30.3	79.3	794	479	482	457	419	369	167
	9	3	41.3	67.2	864	652	697	671	627	564	293
	10	2	51.2	51.4	901	788	867	842	794	722	397
	11	1	58.7	29.2	920	873	971	949	898	820	463
Surface daily totals					924	905	1009	987	933	854	485
May 21	Surface daily totals				9746	7168	7603	7313	6834	6165	3221
	5	7	1.9	114.7	3	0	0	0	0	0	0
	6	6	12.7	105.6	454	154	79	47	44	41	28
	7	5	24	96.6	681	675	281	240	189	139	41
	8	4	35.4	87.2	788	552	498	454	394	328	79
	9	3	46.8	76	842	716	697	649	586	504	189
Surface daily totals					873	842	851	804	734	646	281
	10	2	57.5	60.9	892	924	949	905	832	738	340
	11	1	66.2	37.1	895	949	983	936	864	766	359
	12		70	0	895	949	983	936	864	766	359
	Surface daily totals					9960	8044	7697	7136	6430	5548

FIGURE A2.2c

Solar position and insolation values for 40°N latitude.

(Continued)

Date	Solar time		Solar position		Total insolation on surface (W/m^2)						
	a.m.	p.m.	Alt	Azm	Direct normal	Horiz.	South-facing surface angle with horizon				
							30°	40°	50°	60°	90°
Jun 21	5	7	4.2	117.3	69	13	9	9	6	6	3
	6	6	14.8	108.4	489	189	95	57	54	50	32
	7	5	26	99.7	681	388	290	243	186	129	44
	8	4	37.4	90.7	775	574	501	448	381	306	50
	9	3	48.8	80.2	829	734	690	637	564	476	148
	10	2	59.8	65.8	857	857	838	782	706	611	233
	11	1	69.2	41.9	873	933	933	876	797	697	290
	12		73.5	0	879	958	965	911	829	725	309
	Surface daily totals				10,023	8346	7672	7010	6222	5264	1923
Jul 21	5	7	2.3	115.2	6	0	0	0	0	0	0
	6	6	13.1	106.1	435	158	82	54	47	44	28
	7	5	24.3	97.2	656	359	281	236	189	139	44
	8	4	35.8	87.8	760	548	495	448	391	322	76
	9	3	47.2	76.7	816	709	687	640	574	495	183
	10	2	57.9	61.7	848	835	838	791	722	630	271
	11	1	66.7	37.9	867	914	933	886	813	719	328
	12		70.6	0	870	939	968	920	848	750	350
	Surface daily totals				9651	7987	7593	7029	6323	5447	2213
Aug 21	6	6	7.9	99.5	255	66	38	28	25	22	16
	7	5	19.3	90.9	602	274	240	217	189	154	38
	8	4	30.7	79.9	747	473	473	444	407	356	158
	9	3	41.8	67.9	820	646	681	652	608	545	281
	10	2	51.7	52.1	857	775	842	816	769	697	378
	11	1	59.3	29.7	876	860	946	920	870	794	441
	12		62.3	0	883	889	980	955	905	826	463
	Surface daily totals				9191	7073	7420	7117	6632	5970	3083
Sep 21	7	5	11.4	80.2	470	136	161	161	154	148	101
	8	4	22.5	69.6	725	344	419	422	413	391	265
	9	3	32.8	57.3	829	526	649	656	640	608	416
	10	2	41.6	41.9	883	665	826	835	820	779	530
	11	1	47.7	22.6	905	753	939	949	930	886	605
	12		50	0	914	785	977	987	968	920	630
	Surface daily totals				8536	5636	6966	7023	6878	6537	4463
Oct 21	7	5	4.5	72.3	151	22	44	47	54	54	50
	8	4	15	61.9	643	214	334	356	369	372	315
	9	3	24.5	49.8	810	397	583	615	630	624	504
	10	2	32.4	35.6	883	536	772	810	823	810	640
	11	1	37.6	18.7	917	627	892	930	942	927	722
	12		39.5	0	927	656	930	971	983	965	750
	Surface daily totals				7735	4249	6184	6493	6613	6537	5213

FIGURE A2.2c (CONTINUED)

Solar position and insolation values for 40°N latitude.

(Continued)

Date	Solar time		Solar position		Total insolation on surface (W/m^2)						
	a.m.	p.m.	Alt	Azm	Direct normal	Horiz.	South-facing surface angle with horizon				
							30°	40°	50°	60°	90°
Nov 21	8	4	8.2	55.4	429	88	199	227	246	258	255
	9	3	17	44.1	731	258	479	526	561	577	526
	10	2	24	31	845	397	678	734	772	785	690
	11	1	28.6	16.1	892	482	801	860	898	908	782
	12		30.2	0	908	514	842	905	939	949	813
	Surface daily totals				6707	2969	5157	5604	5894	6014	5314
Dec 21	8	4	5.5	53	281	44	123	142	158	170	177
	9	3	14	41.9	684	205	426	479	517	539	514
	10	2	20	29.4	823	337	630	697	741	763	697
	11	1	25	15.2	883	422	753	826	870	892	794
	12		26.6	0	898	451	797	867	914	933	829
	Surface daily totals				6235	2465	4665	5150	5484	5661	5188

FIGURE A2.2c (CONTINUED)

Solar position and insolation values for 40°N latitude.

Date	Solar time		Solar position		Total insolation on surface (W/m^2)						
	a.m.	p.m.	Alt	Azm	Direct normal	Horiz.	South-facing surface angle with horizon				
							38°	48°	58°	68°	90°
Jan 21	8	4	3.5	54.6	117	13	54	60	66	69	69
	9	3	11	42.6	583	145	378	416	441	457	438
	10	2	16.9	29.4	753	262	599	649	681	693	649
	11	1	20.7	15.1	823	337	728	785	820	829	766
	12		22	0	842	362	772	832	867	876	804
	Surface daily totals				5390	1879	4287	4659	4886	4974	4659
Feb 21	7	5	2.4	72.2	38	3	9	13	13	13	13
	8	4	11.6	60.5	593	154	299	322	331	334	303
	9	3	19.7	47.7	791	315	561	589	602	599	526
	10	2	26.2	33.3	876	438	756	791	804	791	684
	11	1	30.5	17.2	914	520	876	914	927	908	779
	12		32	0	924	545	917	958	968	949	813
Surface daily totals				7344	3404	5926	6216	6380	6235	5421	

FIGURE A2.2d

Solar position and insolation values for 48°N latitude.

(Continued)

Date	Solar time		Solar position		Total insolation on surface (W/m^2)						
	a.m.	p.m.	Alt	Azm	Direct normal	Horiz.	South-facing surface angle with horizon				
Mar 21									38°	48°	58°
7	5	10	78.7	482	117	154	154	148	142	110	
8	4	19.5	66.8	744	303	413	416	407	385	303	
9	3	28.2	53.4	851	463	646	652	640	608	479	
10	2	35.4	37.8	905	589	829	838	823	782	615	
11	1	40.3	19.8	930	668	946	955	936	892	703	
12		42	0	939	693	983	993	974	927	731	
Apr 21	Surface daily totals				8763	4974	6960	7023	6878	6537	5144
	6	6	8.6	97.8	340	85	41	28	25	22	16
	7	5	18.6	86.7	646	268	240	217	186	151	66
	8	4	28.5	74.9	779	448	470	444	407	356	217
	9	3	37.8	61.2	845	602	681	656	611	548	362
	10	2	45.8	44.6	883	719	845	820	772	703	479
	11	1	51.5	24	901	794	949	927	876	801	558
May 21	12		53.6	0	908	820	987	961	911	832	583
	Surface daily totals				9696	6638	7432	7142	6663	5995	3978
	5	7	5.2	114.3	129	28	13	13	13	9	6
	6	6	14.7	103.7	416	192	85	50	47	41	32
	7	5	24.6	93	690	372	281	236	189	136	41
	8	4	34.7	81.6	782	539	492	448	388	318	142
	9	3	44.3	68.3	832	684	684	637	574	492	271
Jun 21	10	2	53	51.3	864	794	835	791	722	630	378
	11	1	59.5	28.6	785	864	933	886	813	719	444
	12		62	0	883	886	965	920	848	750	470
	Surface daily totals				11,108	7823	7622	7042	6336	5447	3095
	5	7	7.9	116.5	243	66	28	28	25	22	16
	6	6	17.2	106.2	542	233	104	60	57	50	38
	7	5	27	95.8	693	407	293	243	186	123	47
Jul 21	8	4	37.1	84.6	775	571	495	441	375	299	110
	9	3	46.9	71.6	823	709	681	624	552	463	233
	10	2	55.8	54.8	848	816	826	769	693	596	331
	11	1	62.7	31.2	864	883	917	860	782	681	397
	12		65.5	0	867	905	949	892	813	709	419
	Surface daily totals				10,439	8277	7628	6947	6146	5182	2755
	5	7	5.7	114.7	136	32	16	16	13	13	9
	6	6	15.2	104.1	492	195	88	57	50	47	35
	7	5	25.1	93.5	665	372	281	236	186	132	44
	8	4	35.1	82.1	756	539	485	441	381	312	136
	9	3	44.8	68.8	807	678	675	627	561	482	262
	10	2	53.5	51.9	838	788	823	775	706	615	366
	11	1	60.1	29	854	857	917	870	797	703	432
	12		62.6	0	857	879	949	901	829	731	454
Surface daily totals				9954	7798	7521	6934	6222	5339	3013	

FIGURE A2.2d (CONTINUED)

Solar position and insolation values for 48°N latitude.

(Continued)

Date	Solar time		Solar position		Total insolation on surface (W/m^2)									
	a.m.	p.m.	Alt	Azm	Direct normal	Horiz.	South-facing surface angle with horizon				38°	48°	58°	68°
Aug 21														
6	6	9.1	98.3	312	88	44	32	28	25	19				
7	5	19.1	87.2	599	268	236	211	183	148	63				
8	4	29	75.4	731	444	457	432	394	344	205				
9	3	38.4	61.8	801	596	662	634	589	530	347				
10	2	46.4	45.1	838	709	820	794	747	675	460				
11	1	52.2	24.3	857	782	924	898	845	769	533				
12		54.3	0	864	807	958	933	879	804	558				
		Surface daily totals				9134	6575	7250	6934	6449	5787	3808		
Sep 21	7	5	10	78.7	413	110	139	139	136	126	98			
	8	4	19.5	66.8	678	290	391	391	381	362	284			
	9	3	28.2	53.4	791	448	618	621	608	577	451			
	10	2	35.4	37.8	848	571	791	801	782	744	583			
	11	1	40.3	19.8	876	646	905	911	895	848	668			
	12		42	0	883	671	942	952	933	886	697			
	Surface daily totals				8094	4797	6626	6676	6525	6197	4873			
Oct 21	7	5	2	71.9	13	0	3	3	3	3	3			
	8	4	11.2	60.2	426	139	271	287	299	299	274			
	9	3	19.3	47.4	734	296	526	555	567	561	495			
	10	2	25.7	33.1	826	419	719	753	763	753	652			
	11	1	30	17.1	864	495	838	873	886	870	747			
	12		31.5	0	876	523	879	917	927	908	779			
	Surface daily totals				6789	3221	5592	5863	5957	5882	5125			
Nov 21	8	4	3.6	54.7	113	16	54	60	66	69	69			
	9	3	11.2	42.7	564	145	369	407	432	444	426			
	10	2	17.1	29.5	734	262	586	637	668	678	634			
	11	1	20.9	15.1	804	337	716	772	804	813	845			
	12		22.2	0	823	362	760	816	851	857	788			
	Surface daily totals				5258	1879	4211	4564	4785	4867	4545			
	Surface daily totals				4551	1406	3581	3940	4180	4299	4110			

FIGURE A2.2d (CONTINUED)

Solar position and insolation values for 48°N latitude.

Date	Solar time		Solar position		Total insolation on surface (W/m^2)							
	a.m.	p.m.	Alt	Azm	Direct normal	Horiz.	South-facing surface angle with horizon					
							46°	56°	66°	76°	90°	
Jan 21	9	3	5	41.8	246	35	158	173	186	189	189	
	10	2	9.9	28.5	536	123	426	460	485	492	482	
	11	1	12.9	14.5	652	183	577	621	649	656	634	
	12		14	0	684	205	624	675	700	709	684	
	Surface daily totals				3549	889	2944	3184	3335	3385	3291	
Feb 21	8	4	7.6	59.4	407	79	205	217	227	227	217	
	9	3	14.2	45.9	675	205	476	501	511	507	476	
	10	2	19.4	31.5	788	309	678	709	719	706	656	
	11	1	22.8	16.1	838	375	801	835	845	829	766	
	12		24	0	851	397	845	879	889	870	804	
Surface daily totals				6260	2332	5169	5409	5491	5409	5037		
Mar 21	7	5	8.3	77.5	403	88	126	126	123	117	101	
	8	4	16.2	64.4	678	236	375	378	369	350	306	
	9	3	23.3	50.3	797	372	605	608	596	567	485	
	10	2	29	34.9	857	476	785	791	775	738	646	
	11	1	32.7	17.9	889	542	898	908	889	845	744	
12				34	0	895	564	936	946	927	883	775
Surface daily totals				8151	3997	6512	6569	6430	6109	5358		
Apr 21	5	7	1.4	108.8	0	0	0	0	0	0	0	
	6	6	9.6	96.5	385	101	44	28	25	22	19	
	7	5	18	84.1	634	255	233	208	180	145	91	
	8	4	26.1	70.9	753	407	451	426	388	340	258	
	9	3	33.6	56.3	820	533	656	630	586	526	419	
10				29	857	634	816	791	744	675	548	
11				44.1	20.7	876	693	920	895	845	772	630
12				45.6	0	883	716	955	930	879	804	659
Surface daily totals				9532	5964	7193	6890	6424	5768	4596		
May 21	4	8	1.2	125.5	0	0	0	0	0	0	0	
	5	7	8.5	113.4	293	79	32	28	25	22	19	
	6	6	16.5	101.4	552	224	88	54	47	41	35	
	7	5	24.8	89.3	690	375	277	233	183	129	50	
	8	4	33.1	76.3	769	514	482	435	375	309	199	
9				40.9	61.6	816	634	668	621	555	476	344
10				47.6	44.2	845	728	816	769	700	611	460
11				52.3	23.4	860	785	908	864	791	700	536
12				54	0	867	804	942	895	823	728	561
Surface daily totals				10,528	7483	7483	6897	6184	5302	3839		

FIGURE A2.2e

Solar position and insolation values for 40°N latitude.

(Continued)

Date	Solar time		Solar position		Total insolation on surface (W/m^2)							
	a.m.	p.m.	Alt	Azm	Direct normal	Horiz.	South-facing surface angle with horizon					
Jun 21							46°	56°	66°	76°	90°	
4	8	4.2	127.2	66	13	6	6	6	6	3		
5	7	11.4	115.3	385	126	44	41	35	32	25		
6	6	19.3	103.6	583	271	107	60	54	47	38		
7	5	27.6	91.7	700	416	290	240	180	120	47		
8	4	35.9	78.8	766	552	485	432	366	290	173		
9	3	43.8	64.1	810	668	665	608	536	451	309		
10	2	50.7	46.4	835	756	804	750	675	580	419		
11	1	55.6	24.9	848	813	895	842	763	662	492		
12		57.5	0	854	832	927	870	791	690	517		
Surface daily totals				10,837	7962	7527	6827	6020	5062	3530		
Jul 21	4	8	1.7	125.8	0	0	0	0	0	0	0	
	5	7	9	113.7	287	85	35	32	28	25	19	
	6	6	17	101.9	533	227	95	57	142	44	38	
	7	5	25.3	89.7	668	375	277	233	328	129	47	
	8	4	33.6	76.7	747	514	476	429	504	303	192	
	9	3	41.4	62	794	634	656	608	545	463	334	
	10	2	48.2	44.6	823	725	801	753	684	596	448	
	11	1	52.9	23.7	835	782	892	845	772	681	520	
	12		54.6	0	842	801	924	876	804	709	545	
	Surface daily totals				10,212	7477	7382	6783	6071	5188	3738	
Aug 21	5	7	2	109.2	3	0	0	0	0	0	0	
	6	6	10.2	97	353	107	50	35	32	28	22	
	7	5	18.5	84.5	589	258	230	205	177	142	88	
	8	4	26.7	71.3	709	403	441	413	375	328	246	
	9	3	34.3	56.7	775	530	637	608	564	189	397	
	10	2	40.5	40	813	627	791	763	716	649	523	
	11	1	44.8	20.9	832	687	889	864	813	741	602	
	12		46.3	0	838	709	924	898	848	772	630	
	Surface daily totals				8983	5938	6991	6676	6197	5548	4388	
Sep 21	7	5	8.3	77.5	337	79	113	113	107	101	88	
	8	4	16.2	64.4	611	227	350	340	322	322	281	
	9	3	23.3	50.3	734	359	571	574	561	530	463	
	10	2	29	34.9	797	460	744	747	731	697	608	
	11	1	32.7	17.9	829	523	854	860	842	801	703	
	12		34	0	838	545	892	898	879	835	734	
	Surface daily totals				7464	3845	6146	6184	6046	5737	5024	
Oct 21	8	4	7.1	59.1	328	63	167	180	186	186	180	
	9	3	13.8	45.7	608	189	435	457	466	463	435	
	10	2	19	31.3	728	290	634	662	671	662	615	
	11	1	22.3	16	782	353	756	788	797	782	725	
	12		23.5	0	797	375	797	829	838	823	760	
	Surface daily totals				5686	2169	4778	4999	5081	5005	4665	

FIGURE A2.2e (CONTINUED)

Solar position and insolation values for 56°N latitude.

(Continued)

Date	Solar time		Solar position		Total insolation on surface (W/m^2)						
	a.m.	p.m.	Alt	Azm	Direct normal	Horiz.	South-facing surface angle with horizon				
Nov 21							46°	56°	66°	76°	90°
9	3	5.2	41.9	240	38	154	170	180	186	183	
10	2	10	28.5	520	123	416	422	470	479	466	
11	1	13.1	14.5	634	183	564	608	634	640	618	
12		14.2	0	665	205	611	659	684	690	665	
		Surface daily totals					3448	895	2881	1217	3253
Dec 21	9	3	1.9	40.5	16	0	9	13	13	13	13
	10	2	6.6	27.5	356	60	271	299	318	328	325
	11	1	9.5	13.9	523	117	444	485	514	526	517
	12		10.6	0	567	136	501	545	574	586	574
	Surface daily totals					2358	492	1954	2137	2257	2314

FIGURE A2.2e (CONTINUED)

Solar position and insolation values for 56°N latitude.

Date	Solar time		Solar position		Total insolation on surface (W/m^2)						
	a.m.	p.m.	Alt	Azm	Direct normal	Horiz.	South-facing surface angle with horizon				
Jan 21							54°	64°	74°	84°	90°
10	2	2.8	28.1	69	6	54	60	63	63	63	
11	1	5.2	14.1	255	38	227	243	252	255	255	
12		6	0	315	50	287	309	322	325	325	
Surface daily totals					965	142	845	914	952	965	958
Feb 21	8	4	3.4	58.7	110	13	54	60	60	60	60
	9	3	8.6	44.8	463	98	325	340	350	347	337
	10	2	12.6	30.3	627	173	536	561	571	561	545
	11	1	15.1	15.3	700	224	668	693	703	690	671
	12		16	0	719	243	709	741	747	731	712
Surface daily totals					4514	1261	3877	4053	4104	4041	3946
Mar 21	7	5	6.5	76.5	299	57	95	91	91	85	79
	8	4	20.7	62.6	583	170	318	322	312	296	281
	9	3	18.1	48.1	716	274	539	542	533	504	482
	10	2	22.3	32.7	785	353	716	722	706	671	640
	11	1	25.1	16.6	820	407	826	835	816	775	741
	12		26	0	829	422	864	873	854	813	775
Surface daily totals					7237	2938	5850	5894	5768	5472	5220

FIGURE A2.2f

Solar position and insolation values for 64°N latitude.

(Continued)

Date	Solar time		Solar position		Total insolation on surface (W/m^2)						
	a.m.	p.m.	Alt	Azm	Direct normal	Horiz.	South-facing surface angle with horizon				
Apr 21							54°	64°	74°	84°	90°
5	7	4	108.5	85	16	6	6	6	3	3	
6	6	10.4	95.1	419	117	47	28	25	22	19	
7	5	17	81.6	611	240	221	199	170	136	117	
8	4	23.3	67.5	719	353	429	403	366	322	287	
9	3	29	52.3	782	454	621	596	555	498	457	
10	2	33.5	36	820	533	775	753	706	640	593	
11	1	36.5	18.4	838	580	876	851	804	734	681	
12		37.6	0	845	599	911	886	838	766	709	
Surface daily totals				9399	5182	6859	6562	6102	5472	5024	
May 21	4	8	5.8	125.1	161	35	16	13	13	9	9
	5	7	11.6	112.1	416	132	41	35	32	28	25
	6	6	17.9	99.1	583	249	91	50	44	38	35
	7	5	24.5	85.7	687	369	271	227	177	123	88
	8	4	30.9	71.5	753	479	466	419	362	296	252
	9	3	36.8	56.1	794	574	643	599	536	457	403
	10	2	41.6	38.9	823	646	785	741	671	586	526
	11	1	44.9	20.1	835	690	876	832	763	671	608
	12		46	0	842	706	719	864	791	700	634
	Surface daily totals				10,937	7048	7297	6695	5982	5119	4526
Jun 21	3	9	4.2	139.4	66	13	6	6	6	3	
	4	8	9	126.4	293	85	32	28	25	22	19
	5	7	14.7	113.6	485	189	50	47	41	35	32
	6	6	21	100.8	611	303	107	60	54	44	41
	7	5	27.5	87.5	697	416	287	233	173	113	72
	8	4	34	73.3	753	523	473	419	353	277	230
	9	3	39.9	57.8	791	615	643	589	517	432	375
	10	2	44.9	40.4	813	684	779	725	649	558	495
	11	1	48.3	20.9	826	728	867	813	734	637	571
	12		49.5	0	829	741	895	842	763	665	596
Jul 21	Surface daily totals				11,505	7842	7382	6676	5869	4911	4274
	4	8	6.4	125.3	167	41	19	16	16	13	13
	5	7	12.1	112.4	403	139	44	41	35	32	28
	6	6	18.4	99.4	564	255	95	54	50	41	38
	7	5	25	86	665	372	271	227	177	120	88
	8	4	31.4	71.8	728	479	460	413	356	287	243
	9	3	37.3	56.3	772	574	634	586	523	444	391
	10	2	42.2	39.2	797	643	772	725	656	571	511
	11	1	45.4	20.2	810	687	860	813	744	652	589
	12		46.6	0	816	703	889	842	772	681	615
Surface daily totals				10,629	7086	7187	6588	5875	5005	4413	

FIGURE A2.2f (CONTINUED)

Solar position and insolation values for 64°N latitude.

(Continued)

Date	Solar time		Solar position		Total insolation on surface (W/m^2)						
	a.m.	p.m.	Alt	Azm	Direct normal	Horiz.	South-facing surface angle with horizon				
							54°	64°	74°	84°	90°
Aug 21	5	7	4.6	108.8	91	19	9	9	6	6	6
	6	6	11	95.5	388	123	50	35	32	25	22
	7	5	17.6	81.9	571	243	217	192	164	132	110
	8	4	23.9	67.8	675	356	416	388	353	306	274
	9	3	29.6	52.6	738	454	599	574	533	473	435
	10	2	34.2	36.2	775	530	747	722	678	611	564
	11	1	37.2	18.5	794	577	845	820	769	700	646
	12		38.3	0	801	593	876	851	804	731	678
Surface daily totals					8851	5188	6644	3177	5863	5239	4797
Sep 21	7	5	6.5	76.5	243	50	79	79	76	72	66
	8	4	12.7	72.6	514	161	290	290	284	268	255
	9	3	18.1	48.1	649	262	501	501	492	463	444
	10	2	22.3	32.7	722	340	668	671	659	624	596
	11	1	25.1	16.6	756	391	775	782	766	725	693
	12		26	0	769	407	813	820	801	760	725
	Surface daily totals					6537	2812	5440	5472	5346	5068
Oct 21	8	4	3	58.5	54	6	28	28	32	32	32
	9	3	8.1	44.6	385	82	271	287	293	290	284
	10	2	12.1	30.2	555	158	479	501	507	501	489
	11	1	14.6	15.2	634	205	608	634	640	630	615
	12		15.5	0	656	224	652	678	684	671	656
	Surface daily totals					3902	1128	3429	3581	3631	3574
Nov 21	10	2	3	28.1	72	9	57	63	66	66	66
	11	1	5.4	14.2	249	38	221	240	249	252	249
	12		6.2	0	306	54	281	303	315	318	315
	Surface daily totals					952	145	838	901	939	952
Dec 21	11	1	1.8	13.7	13	0	9	13	13	13	13
	12		2.6	0	50	6	44	47	50	54	54
	Surface daily totals					76	6	63	69	76	76

FIGURE A2.2f (CONTINUED)

Solar position and insolation values for 64°N latitude.

TABLE A2.6

Reflectivity Values for Characteristic Surfaces (Integrated over Solar Spectrum and Angle of Incidence)

Surface	Average Reflectivity
Snow (freshly fallen or with ice film)	0.75
Water surfaces (relatively large incidence angles)	0.07
Soils (clay, loam, etc.)	0.14
Earth roads	0.04
Coniferous forest (winter)	0.07
Forests in autumn, ripe field crops, plants	0.26
Weathered blacktop	0.10
Weathered concrete	0.22
Dead leaves	0.30
Dry grass	0.20
Green grass	0.26
Bituminous and gravel roof	0.13
Crushed rock surface	0.20
Building surfaces, dark (red brick, dark paints, etc.)	0.27
Building surfaces, light (light brick, light paints, etc.)	0.60

Source: Hunn, B.D. and D.O. Calafell, Determination of average ground reflectivity for solar collectors, *Sol. Energy*, 19, 87, 1977; see also List, R.J., *Smithsonian Meteorological Tables*, 6th ed., Smithsonian Institution Press, 442–443, 1949.

References

- Anane-Fenin, K. 1986. Estimating solar radiation in Ghana. *International Centre for Theoretical Physics*. Internal Report No. IC/86/68, Trieste, Italy.
- Chuah, D.G.S., and S.L. Lee. 1981. Solar radiation estimates in Malaysia. *Sol. Energy* 26: 33.
- Eze, A.E., and S.C. Ododo. 1988. Solar radiation prediction from sunshine in eastern Nigeria. *Energy Convers. Manage.* 28: 69.
- Ibrahim, S.M.A. 1985. Predicted and measured global solar radiation in Egypt. *Sol. Energy* 35: 185.
- Jain, P.C. 1986. Irradiation estimation for Italian localities. *Sol. Wind Technol.* 3: 323.
- Jain, S., and P.G. Jain. 1985. A comparison of the angstrom type correlations and the estimation of monthly average daily global irradiation. Internal Report, No. IC85-269, Trieste, Italy, International Centre for Theoretical Physics.
- Khogali, A. 1983. Star radiation over Sudan: Comparison of measured and predicted data. *Sol. Energy* 31: 45.
- Khogali, A. et al. 1983. Global and diffuse star irradiance in Yemen. *Sol. Energy* 31: 55.
- Leung, C.T. 1980. The fluctuation of solar irradiance in Hong Kong. *Sol. Energy* 25: 485.
- Massaquoi, J.G.M. 1988. Global solar radiation in Sierre Leone (West Africa). *Sol. Wind Technol.* 5: 281.
- Zabara, K. 1986. Estimation of the global solar radiation in Greece. *Sol. Wind Technol.* 3: 267.

Appendix 3: Supplementary Material for Chapter 3

TABLE A3.1

Properties of Dry Air at Atmospheric Pressures between 250 and 1000 K

T (K)	ρ (kg/m ³)	c_p (kJ/kg·K)	μ (kg/m·s × 10 ⁵)	ν (m ² /s × 10 ⁶)	k (W/m·K)	α (m ² /s × 10 ⁴)	Pr
250	1.4128	1.0053	1.488	9.49	0.02227	0.13161	0.722
300	1.1774	1.0057	1.983	15.68	0.02624	0.22160	0.708
350	0.9980	1.0090	2.075	20.76	0.03003	0.2983	0.697
400	0.8826	1.0140	2.286	25.90	0.03365	0.3760	0.689
450	0.7833	1.0207	2.484	28.86	0.03707	0.4222	0.683
500	0.7048	1.0295	2.671	37.90	0.04038	0.5564	0.680
550	0.6423	1.0392	2.848	44.34	0.04360	0.6532	0.680
600	0.5879	1.0551	3.018	51.34	0.04659	0.7512	0.680
650	0.5430	1.0635	3.177	58.51	0.04953	0.8578	0.682
700	0.5030	1.0752	3.332	66.25	0.05230	0.9672	0.684
750	0.4709	1.0856	3.481	73.91	0.05509	1.0774	0.686
800	0.4405	1.0978	3.625	82.29	0.05779	1.1951	0.689
850	0.4149	1.1095	3.765	90.75	0.06028	1.3097	0.692
900	0.3925	1.1212	3.899	99.3	0.06279	1.4271	0.696
950	0.3716	1.1321	4.023	108.2	0.06525	1.5510	0.699
1000	0.3524	1.1417	4.152	117.8	0.06752	1.6779	0.702

Source: Natl. Bureau Standards (U.S.) Circ. 564, 1955.

Note: K = absolute temperature, degrees Kelvin; $\nu = \mu/\rho$; ρ = density; c_p = specific heat capacity; $\alpha = c_p\rho/k$; μ = viscosity; k = thermal conductivity; Pr = Prandtl number, dimensionless. The values of μ , k , c_p , and Pr are not strongly pressure dependent and may be used over a fairly wide range of pressures.

TABLE A3.2

Properties of Water (Saturated Liquid) between 273 and 533 K

K	°F	°C	c_p (kJ/kg·°C)	ρ (kg/m ³)	μ (kg/m·s)	k (W/m·°C)	Pr	$g\beta\rho^2c_p$
								μk (m ⁻³ ·°C ⁻¹)
273	32	0	4.225	999.8	1.79×10^{-3}	0.566	13.25	
277.4	40	4.44	4.208	999.8	1.55	0.575	11.35	1.91×10^9
283	50	10	4.195	999.2	1.31	0.585	9.40	6.34×10^9
288.6	60	15.56	4.186	998.6	1.12	0.595	7.88	1.08×10^{10}
294.1	70	21.11	4.179	997.4	9.8×10^{-4}	0.604	6.78	1.46×10^{10}
299.7	80	26.67	4.179	995.8	8.6	0.614	5.85	1.91×10^{10}
302.2	90	32.22	4.174	994.9	7.65	0.623	5.12	2.48×10^{10}
310.8	100	37.78	4.174	993.0	6.82	0.630	4.53	3.3×10^{10}
316.3	110	43.33	4.174	990.6	6.16	0.637	4.04	4.19×10^{10}
322.9	120	48.89	4.174	988.8	5.62	0.644	3.64	4.89×10^{10}
327.4	130	54.44	4.179	985.7	5.13	0.649	3.30	5.66×10^{10}
333.0	140	60	4.179	983.3	4.71	0.654	3.01	6.48×10^{10}
338.6	150	65.55	4.183	980.3	4.3	0.659	2.73	7.62×10^{10}
342.1	160	71.11	4.186	977.3	4.01	0.665	2.53	8.84×10^{10}
349.7	170	76.67	4.191	973.7	3.72	0.668	2.33	9.85×10^{10}
355.2	180	82.22	4.195	970.2	3.47	0.673	2.16	1.09×10^{11}
360.8	190	87.78	4.199	966.7	3.27	0.675	2.03	
366.3	200	93.33	4.204	963.2	3.06	0.678	1.90	
377.4	220	104.4	4.216	955.1	2.67	0.684	1.66	
388.6	240	115.6	4.229	946.7	2.44	0.685	1.51	
399.7	260	126.7	4.250	937.2	2.19	0.685	1.36	
410.8	280	137.8	4.271	928.1	1.98	0.685	1.24	
421.9	300	148.9	4.296	918.0	1.86	0.684	1.17	
449.7	350	176.7	4.371	890.4	1.57	0.677	1.02	
477.4	400	204.4	4.467	859.4	1.36	0.665	1.00	
505.2	450	232.2	4.585	825.7	1.20	0.646	0.85	
533.0	500	260	4.731	785.2	1.07	0.616	0.83	

Source: Adapted from Brown, A.I. and S.M. Marco, *Introduction to Heat Transfer*, 3rd ed., McGraw-Hill Book Company, New York, 1958.

TABLE A3.3
Emittances and Absorptances of Materials

Substance	Short-Wave Absorptance	Long-Wave Emittance	$\frac{\alpha}{\epsilon}$
<i>Class I Substances: Absorptance-to-Emittance Ratios Less than 0.5</i>			
Magnesium carbonate, MgCO ₃	0.025–0.04	0.79	0.03–0.05
White plaster	0.07	0.91	0.08
Snow, fine particles, fresh	0.13	0.82	0.16
White paint, 0.017 in, on aluminum	0.20	0.91	0.22
Whitewash on galvanized iron	0.22	0.90	0.24
White paper	0.25–0.28	0.95	0.26–0.29
White enamel on iron	0.25–0.45	0.9	0.28–0.5
Ice, with sparse snow cover	0.31	0.96–0.97	0.32
Snow, ice granules	0.33	0.89	0.37
Aluminum oil base paint	0.45	0.90	0.50
White powdered sand	0.45	0.84	0.54
<i>Class II Substances: Absorptance-to-Emittance Ratios between 0.5 and 0.9</i>			
Asbestos felt	0.25	0.50	0.50
Green oil base paint	0.5	0.9	0.56
Bricks, red	0.55	0.92	0.60
Asbestos cement board, white	0.59	0.96	0.61
Marble, polished	0.5–0.6	0.9	0.61
Wood, planed oak	—	0.9	—
Rough concrete	0.60	0.97	0.62
Concrete	0.60	0.88	0.68
Grass, green, after rain	0.67	0.98	0.68
Grass, high and dry	0.67–0.69	0.9	0.76
Vegetable fields and shrubs, wilted	0.70	0.9	0.78
Oak leaves	0.71–0.78	0.91–0.95	0.78–0.82
Frozen soil	—	0.93–0.94	—
Desert surface	0.75	0.9	0.83
Common vegetable fields and shrubs	0.72–0.76	0.9	0.82
Ground, dry plowed	0.75–0.80	0.9	0.83–0.89
Oak woodland	0.82	0.9	0.91
Pine forest	0.86	0.9	0.96
Earth surface as a whole (land and sea, no clouds)	0.83	—	—

(Continued)

TABLE A3.3 (CONTINUED)

Emittances and Absorptances of Materials

Substance	Short-Wave Absorptance	Long-Wave Emittance	$\frac{\alpha}{\epsilon}$
<i>Class III Substances: Absorptance-to-Emittance Ratios between 0.8 and 1.0</i>			
Gray paint	0.75	0.95	0.79
Red oil base paint	0.74	0.90	0.82
Asbestos, slate	0.81	0.96	0.84
Asbestos, paper		0.93–0.96	—
Linoleum, red-brown	0.84	0.92	0.91
Dry sand	0.82	0.90	0.91
Green roll roofing	0.88	0.91–0.97	0.93
Slate, dark gray	0.89	—	—
Old gray rubber	—	0.86	—
Hard black rubber	—	0.90–0.95	—
Asphalt pavement	0.93	—	—
Black cupric oxide on copper	0.91	0.96	0.95
Bare moist ground	0.9	0.95	0.95
Wet sand	0.91	0.95	0.96
Water	0.94	0.95–0.96	0.98
Black tar paper	0.93	0.93	1.0
Black gloss paint	0.90	0.90	1.0
Small hole in large box, furnace, or enclosure	0.99	0.99	1.0
"Hohlraum," theoretically perfect black body	1.0	1.0	1.0
<i>Class IV Substances: Absorptance-to-Emittance Ratios Greater than 1.0</i>			
Black silk velvet	0.99	0.97	1.02
Alfalfa, dark green	0.97	0.95	1.02
Lampblack	0.98	0.95	1.03
Black paint, 0.017 in, on aluminum	0.94–0.98	0.88	1.07–1.11
Granite	0.55	0.44	1.25
Graphite	0.78	0.41	1.90
High ratios, but absorptances less than 0.80			
Dull brass, copper, lead	0.2–0.4	0.4–0.65	1.63–2.0
Galvanized sheet iron, oxidized	0.8	0.28	2.86
Galvanized iron, clean, new	0.65	0.13	5.0
Aluminum foil	0.15	0.05	3.00
Magnesium	0.3	0.07	4.3
Chromium	0.49	0.08	6.13
Polished zinc	0.46	0.02	23.0
Deposited silver (optical reflector) un tarnished	0.07	0.01	

TABLE A3.3 (CONTINUED)

Emittances and Absorptances of Materials

Substance	Short-Wave Absorptance	Long-Wave Emittance	$\frac{\alpha}{\epsilon}$
<i>Class V Substances: Selective Surfaces^a</i>			
Plated metals:			
Black sulfide on metal	0.92	0.10	9.2
Black cupric oxide on sheet aluminum	0.08–0.93	0.09–0.21	
Copper (5×10^{-5} cm thick) on nickel or silver-plated metal			
Cobalt oxide on platinum			
Cobalt oxide on polished nickel	0.93–0.94	0.24–0.40	3.9
Black nickel oxide on aluminum	0.85–0.93	0.06–0.1	14.5–15.5
Black chrome	0.87	0.09	9.8
Particulate coatings:			
Lamblack on metal			
Black iron oxide, 47 μm grain size, on aluminum			
Geometrically enhanced surfaces ^b :			
Optimally corrugated grays	0.89	0.77	1.2
Optimally corrugated selectives	0.95	0.16	5.9
Stainless-steel wire mesh	0.63–0.86	0.23–0.28	2.7–3.0
Copper, treated with NaClO_2 and NaOH	0.87	0.13	6.69

Source: Anderson, B., *Solar Energy*, McGraw-Hill Book Company, 1977. With permission.

^a Selective surfaces absorb most of the solar radiation between 0.3 and 1.9 μm and emit very little in the 5–15 μm range—the infrared.

^b For a discussion of how surface selectivity can be enhanced through surface geometry, see K.G.T. Hollands, Directional selectivity emittance and absorptance properties of vee corrugated specular surfaces, *J. Sol. Energy Sci. Eng.*, vol. 3, July 1963.

TABLE A3.4

Thermal Properties of Metals and Alloys

Material	<i>k</i> , Btu/(h)(ft)(°F)				<i>c</i> , Btu/(lb _m)(°F)	<i>ρ</i> , lb _m /ft ³	<i>α</i> , ft ² /h
	32°F	212°F	572°F	932°F			
Metals							
Aluminum	117	119	133	155	0.208	169	3.33
Bismuth	4.9	3.9	0.029	612	0.28
Copper, pure	224	218	212	207	0.091	558	4.42
Gold	169	170	0.030	1203	4.68
Iron, pure	35.8	36.6	0.104	491	0.70
Lead	20.1	19	18	...	0.030	705	0.95
Magnesium	91	92	0.232	109	3.60
Mercury	4.8	0.033	849	0.17
Nickel	34.5	34	32	...	0.103	555	0.60
Silver	242	238	0.056	655	6.6
Tin	36	34	0.054	456	1.46
Zinc	65	64	59	...	0.091	446	1.60
Alloys							
Admiralty metal	65	64					
Brass, 70% Cu, 30% Zn	56	60	66	...	0.092	532	1.14
Bronze, 75% Cu, 25% Sn	15	0.082	540	0.34
Cast iron							
Plain	33	31.8	27.7	24.8	0.11	474	0.63
Alloy	30	28.3	27	...	0.10	455	0.66
Constantan, 60% Cu, 40% Ni	12.4	12.8	0.10	557	0.22
18-8 Stainless steel,							
Type 304	8.0	9.4	10.9	12.4	0.11	488	0.15
Type 347	8.0	9.3	11.0	12.8	0.11	488	0.15
Steel, mild, 1%C	26.5	26	25	22	0.11	490	0.49

Source: Kreith, F., *Principles of Heat Transfer*, PWS Publishing Co., Boston, 1997.

Note: 1 Btu/h·ft·°F = 1.731 W/m·K.

1 Btu/lb_m·°F = 4187 J/kg·K.

1 lb_m/ft³ = 16.018 kg/m³.

1 ft²/h = 2.581 × 10⁻⁵ m²/s.

TABLE A3.5

Thermal Properties of Some Nonmetals

Material	Average Temperature, °F	k , Btu/(h) (ft)(°F)	c , Btu/(lb _m) (°F)	ρ , lb _m /ft ³	α , ft ² /h
Insulating materials					
Asbestos	32	0.087	0.25	36	~0.01
	392	0.12	...	36	~0.01
Cork	86	0.025	0.04	10	~0.006
Cotton, fabric	200	0.046			
Diatomaceous earth, powdered	100	0.030	0.21	14	~0.01
	300	0.036	...		
	600	0.046	...		
Molded pipe covering	400	0.051	...	26	
	1600	0.088	...		
Glass wool					
Fine	20	0.022	...		
	100	0.031	...	1.5	
	200	0.043	...		
Packed	20	0.016	...		
	100	0.022	...	6.0	
	200	0.029	...		
Hair felt	100	0.027	...	8.2	
Kaolin insulating brick	932	0.15	...	27	
	2102	0.26	...		
Kaolin insulating firebrick	392	0.05	...	19	
	1400	0.11	...		
85% magnesia	32	0.032	...	17	
	200	0.037	...	17	
Rock wool	20	0.017	...	8	
	200	0.030	...		
Rubber	32	0.087	0.48	75	0.0024
Building materials					
Brick					
Fire-clay	392	0.58	0.20	144	0.02
	1832	0.95			
Masonry	70	0.38	0.20	106	0.018
Zirconia	392	0.84	...	304	
	1832	1.13	...		
Chrome brick	392	0.82	...	246	
	1832	0.96	...		

(Continued)

TABLE A3.5 (CONTINUED)

Thermal Properties of Some Nonmetals

Material	Average Temperature, °F	k , Btu/(h) (ft)(°F)	c , Btu/(lb _m) (°F)	ρ , lb _m /ft ³	α , ft ² /h
Concrete					
Stone	~70	0.54	0.20	144	0.019
10% moisture	~70	0.70	...	140	~0.025
Glass, window	~70	~0.45	0.2	170	0.013
Limestone, dry	70	0.40	0.22	105	0.017
Sand					
Dry	68	0.20	...	95	
10% H ₂ O	68	0.60	...	100	
Building materials					
Soil					
Dry	70	~0.20	0.44	...	~0.01
Wet	70	~1.5	~0.03
Wood					
Oak ⊥ to grain	70	0.12	0.57	51	0.0041
Oak to grain	70	0.20	0.57	51	0.0069
Pine ⊥ to grain	70	0.06	0.67	31	0.0029
Pine to grain	70	0.14	0.67	31	0.0067
Ice	32	1.28	0.46	57	0.048

Source: Kreith, F. *Principles of Heat Transfer*, PWS Publishing Co., 1997.

TABLE A3.6
Thermal and Radiative Properties of Collector Cover Materials

Material Name	Index of Refraction (n)	τ (Solar) ^a (%)	τ (Solar) ^b (%)	τ (Infrared) ^c (%)	Expansion Coefficient (in/in. $^{\circ}$ F)	Temperature Limits (°F)	Weatherability (Comment)	Chemical Resistance (Comment)
Lexan (polycarbonate)	1.586 (D 542) ^d	125 mil 64.1 (± 0.8)	125 mil 72.6 (± 0.1)	125 mil 2.0 (est) ^e	3.75 (10^{-5}) (H 696)	250–270 service temperature	Good; 2 years exposure in Florida caused yellowing; 5 years caused 5% loss in τ	Good; comparable to acrylic
Plexiglas (acrylic)	1.49 (D 542)	125 mil 89.6 (± 0.3)	125 mil 79.6 (± 0.8)	125 mil 2.0 (est) ^f	3.9 (10^{-9}) at 60°F; 4.6 (10^{-9}) at 100°F	180–200 service temperature	Average to good; based on 20-year testing in Arizona, Florida, and Pennsylvania	Good to excellent; resists most acids and alkalis
Teflon F.E.P. (fluorocarbon)	1.343 (D 542)	5 mil 92.3 (± 0.2)	5 mil 89.8 (± 0.4)	5 mil 25.6 (± 0.5)	5.9 (10^{-5}) at 160°F; 9.0 (10^{-5}) at 212°F	400 continuous use; 475 short-term use	Good to excellent; based on 15-year exposure in Florida environment	Excellent; chemically inert
Tedlar PVF. (fluorocarbon)	1.46 (D 542)	4 mil 92.2 (± 0.1)	4 mil 88.3 (± 0.9)	4 mil 20.7 (± 0.2)	2.8 (10^{-5}) (D 696)	225 continuous use; 350 short-term use	Good to excellent; 10-year exposure in Florida with slight yellowing	Excellent; chemically inert
Mylar (polyester)	1.64–1.67 (D 542)	5 mil 86.9 (± 0.3)	5 mil 80.1 (± 0.1)	5 mil 17.8 (± 0.5)	0.94 (10^{-5}) (D 696–44)	300 continuous use; 400 short-term use	Poor; ultraviolet degradation great	Good to excellent; comparable to Tedlar

(Continued)

TABLE A3.6 (CONTINUED)
Thermal and Radiative Properties of Collector Cover Materials

Material Name	Index of Refraction (n)	τ (Solar) ^a (%)	τ (Solar) ^b (%)	τ (Infrared) ^c (%)	Expansion Coefficient (in/in. $^{\circ}$ F)	Temperature Limits (°F)	Weatherability (Comment)	Chemical Resistance (Comment)
Sunlite® (fiberglass)	1.54 (D 542)	25 mil (P) 86.5 (\pm 0.2)	25 mil (P) 75.4 (\pm 0.1)	25 mil (P) 7.6 (\pm 0.1)	1.4 (10^{-5}) (D 696)	200 continuous use causes 5% loss in τ	Fair to good; regular, 7-year solar life; premium, 20-year solar life	Good: inert to chemical atmospheres
Float glass (glass)	1.518 (D 542)	125 mil 84.3 (\pm 0.1)	125 mil 78.6 (\pm 0.2)	125 mil 2.0 (est) ^e	4.8 (10^{-5}) (D 696)	1350 softening point; 100 thermal shock	Excellent: time proved	Good to excellent: time proved
Temper glass (glass)	1.518 (D 542)	125 mil 84.3 (\pm 0.1)	125 mil 78.6 (\pm 0.2)	125 mil 2.0 (est) ^e	4.8 (10^{-5}) (D 696)	450–500 continuous use; 500–550 short-term use	Excellent: time proved	Good to excellent: time proved
Clear lime sheet glass (low iron oxide glass)	1.51 (D 542)	Insufficient data provided by ASG	125 mil 87.5 (\pm 0.5)	125 mil 2.0 (est)	5.0 (10^{-5}) (D 696)	400 for continuous operation	Excellent: time proved	Good to excellent: time proved

Clear lime temper glass (low iron oxide glass)	1.51 (D 542)	Insufficient data provided by ASG	125 mil 87.5 (± 0.5) 2.0 (est)	125 mil 5.0 (10^{-6}) (D 696)	400 for continuous operation	Excellent: time proved	Good to excellent: time proved
Sunadex white crystal glass (0.01% iron oxide glass)	1.50 (D 542)	Insufficient data provided by ASG	125 mil 91.5 (± 0.2) 2.0 (est)	125 mil 4.7 (10^{-6}) (D 696)	400 for continuous operation	Excellent: time proved	Good to excellent: time proved

Source: Abstracted from Ratzel, A.C. and R.B. Bannerot, Optimal Material Selection for Flat-Plate Solar Energy Collectors Utilizing Commercially Available Materials, presented at ASME-AICHE Natl. Heat Transfer Conf., 1976.

^a Compiled data based on ASTM Code E 424 Method B.

^b Numerical integration ($\sum \tau_{avg} F_{1,17-227}$) for $\lambda = 0.2\text{--}4.0 \mu\text{M}$.

^c Numerical integration ($\sum \tau_{avg} F_{1,17-227}$) for $\lambda = 3.0\text{--}50.0 \mu\text{M}$.

^d All numbers in parentheses refer to ASTM test codes.

^e Data not provided; estimate of 2% to be used for 125 mil samples.

^f Degrees differential to rupture $2 \times 2 \times \frac{1}{4}$ in samples. Glass specimens heated and then quenched in water bath at 70°F.

^g Sunlite premium data denoted by (P); Sunlite regular data denoted by (R).

TABLE A3.7
Saturated Steam and Water—SI Units

Temperature (K)	Pressure (MN/m ²)	Specific Volume (m ³ /kg)				Specific Internal Energy (kJ/kg)		Specific Enthalpy (kJ/kg)		Specific Entropy (kJ/kg·K)	
		<i>v_f</i>	<i>v_g</i>	<i>u_f</i>	<i>u_g</i>	<i>h_f</i>	<i>h_g</i>	<i>s_f</i>	<i>s_g</i>		
273.15	0.0006109	0.0010002	206.278	-0.030	2375.3	-0.02	2501.4	2501.3	-0.0001	9.1565	
273.16	0.0006113	0.0010002	206.136	0	2375.3	+0.01	2501.3	2501.4	0	9.1562	
278.15	0.0008721	0.0010001	147.120	+20.97	2382.3	20.98	2489.6	2510.6	+0.0761	9.0257	
280.13	0.0010000	0.0010002	129.208	29.30	2385.0	29.30	2484.9	2514.2	0.1059	8.975	
283.15	0.0012276	0.0010004	106.379	42.00	2389.2	42.01	2477.7	2519.8	0.1510	8.9008	
286.18	0.0015000	0.0010007	87.980	54.71	2393.3	54.71	2470.6	2525.3	0.1957	8.8279	
288.15	0.0017051	0.0010009	77.926	62.99	2396.1	62.99	2465.9	2528.9	0.2245	8.7814	
290.65	0.0020000	0.0010013	67.004	73.48	2399.5	73.48	2460.0	2533.5	0.2607	8.7737	
293.15	0.002339	0.0010018	57.791	83.95	2402.9	83.96	2454.1	2538.1	0.2966	8.6672	
297.23	0.0030000	0.0010027	45.665	101.04	2408.5	101.05	2444.5	2545.5	0.3545	8.5776	
298.15	0.003169	0.0010029	43.360	104.88	2409.8	104.89	2442.3	2547.2	0.3674	8.5580	
302.11	0.0040000	0.0010040	34.800	121.45	2415.2	121.46	2432.9	2554.4	0.4226	8.4746	
303.15	0.0042446	0.0010043	32.894	125.78	2416.6	125.79	2430.5	2556.3	0.4369	8.4533	
306.03	0.0050000	0.0010053	28.192	137.81	2420.5	137.82	2423.7	2561.5	0.4764	8.3951	
308.15	0.005628	0.0010060	25.216	146.67	2423.4	146.68	2418.6	2565.3	0.5053	8.3531	
309.31	0.0060000	0.0010064	23.739	151.53	2425.0	151.53	2415.9	2567.4	0.5210	8.3304	
312.15	0.0070000	0.0010074	20.530	163.39	2428.8	163.40	2409.1	2572.5	0.5592	8.2758	
313.15	0.007384	0.0010078	19.523	167.56	2430.1	167.57	2406.7	2574.3	0.5725	8.2570	
314.66	0.0080000	0.0010084	18.103	173.87	2432.2	173.88	2403.1	2577.0	0.5926	8.2287	
316.91	0.0090000	0.0010094	16.203	183.27	2435.2	183.29	2397.7	2581.0	0.6224	8.1872	

318.15	0.009593	0.0010099	15.258	188.44	2436.8	188.45	2394.8	2583.2	0.6387	8.1648
318.96	0.010000	0.0010102	14.674	191.82	2437.9	191.83	2392.8	2584.7	0.6493	8.1502
323.15	0.012349	0.0010121	12.032	209.32	2443.5	209.33	2382.7	2592.1	0.7038	8.0763
327.12	0.015000	0.0010141	10.022	225.92	2448.7	225.94	2373.1	2599.1	0.7549	8.0085
328.15	0.015758	0.0010146	9.568	230.21	2450.1	230.23	2370.7	2600.9	0.7679	7.9913
333.15	0.019940	0.0010172	7.671	251.11	2456.6	251.13	2358.5	2609.6	0.8312	7.9096
333.21	0.020000	0.0010172	7.649	251.38	2456.7	251.40	2358.3	2609.7	0.8320	7.9085
338.15	0.025030	0.0010199	6.197	272.02	2463.1	272.06	2346.2	2618.3	0.8935	7.8310
342.25	0.030000	0.0010223	5.229	289.20	2468.4	289.23	2336.1	2625.3	0.9439	7.7686
343.15	0.031190	0.0010228	5.042	292.95	2469.6	292.98	2333.8	2626.8	0.9549	7.7553
348.15	0.038580	0.0010259	4.131	313.90	2475.9	313.93	2221.4	2635.3	1.0155	7.6824
349.02	0.040000	0.0010265	3.993	317.53	2477.0	317.58	2319.2	2636.8	1.0259	7.6700
353.15	0.047390	0.0010291	3.407	334.86	2482.2	334.91	2308.8	2643.7	1.0753	7.6122
354.48	0.050000	0.0010300	3.240	340.44	2483.9	340.49	2305.4	2645.9	1.0910	7.5939
358.15	0.057830	0.0010325	2.828	355.84	2488.4	355.90	2296.0	2651.9	1.1343	7.5445
359.09	0.060000	0.0010331	2.732	359.79	2489.6	359.86	2293.6	2653.5	1.1453	7.5320
363.10	0.070000	0.0010360	2.365	376.63	2494.5	376.70	2283.3	2660.0	1.1919	7.4797
363.15	0.070140	0.0010360	2.361	376.85	2494.5	376.92	2283.2	2660.1	1.1925	7.4791
366.65	0.080000	0.0010386	2.087	391.58	2498.8	391.66	2274.1	2665.8	1.2329	7.4346
368.15	0.084550	0.0010397	1.9819	397.88	2500.6	397.96	2270.2	2668.1	1.2500	7.4159

Source: Bolz, R.E. and G.L. Tuve, eds., CRC Handbook of Tables for Applied Engineering Science, 2nd ed., Chemical Rubber Co., Cleveland, Ohio, 1973.

Note: Subscripts: "f" refers to a property of liquid in equilibrium with vapor; "g" refers to a property of vapor in equilibrium with liquid; "fg" refers to a change by evaporation.

TABLE A3.8
Superheated Steam—SI Units

Pressure (MN/m ²)		Temperature								
(Saturation Temperature)	50°C 323.15 K	100°C 373.15 K	150°C 423.15 K	200°C 473.15 K	300°C 573.15 K	400°C 673.15 K	500°C 773.15 K	700°C 973.15 K	1000°C 1273.15 K	1300°C 1573.15 K
0.001 (6.98°C) (280.13 K)	<i>v</i>	149.093	172.187	195.272	218.352	264.508	310.661	356.814	449.117	587.571
	<i>u</i>	2445.4	2516.4	2588.4	2661.6	2812.2	2969.0	3132.4	3479.6	4053.0
	<i>h</i>	2594.5	2688.6	2783.6	2880.0	3076.8	3279.7	3489.2	3928.7	4640.6
0.002 (17.50°C) (290.65 K)	<i>s</i>	9.2423	9.5129	9.7520	9.9671	10.3443	10.6705	10.9605	11.4655	12.1019
	<i>v</i>	74.524	86.081	97.628	109.170	132.251	155.329	178.405	224.558	293.785
	<i>u</i>	2445.2	2516.3	2588.3	2661.6	2812.2	2969.0	3132.4	3479.6	4053.0
0.004 (28.96°C) (302.11 K)	<i>h</i>	2594.3	2688.4	2793.6	2879.9	3076.7	3279.7	3489.2	3928.7	4640.6
	<i>s</i>	8.9219	9.1928	9.4320	9.6471	10.0243	10.3506	10.6406	11.1456	11.7820
	<i>v</i>	37.240	43.028	48.806	54.580	66.122	77.662	89.201	112.278	146.892
0.006 (36.16°C) (309.31 K)	<i>u</i>	2444.9	2516.1	2588.2	2661.5	2812.2	2969.0	3132.3	3479.6	4053.0
	<i>h</i>	2593.9	2688.2	2783.4	2879.8	3076.7	3279.6	3489.2	3928.7	4640.6
	<i>s</i>	8.6009	8.8724	9.1118	9.3271	9.7044	10.0307	10.3207	10.8257	11.4621
0.008 (41.51°C) (314.66 K)	<i>v</i>	24.812	28.676	32.532	36.383	44.079	51.774	59.467	74.852	97.928
	<i>u</i>	2444.6	2515.9	2588.1	2661.4	2812.2	2969.0	3132.3	3479.6	4053.0
	<i>h</i>	2593.4	2688.0	2783.3	2879.7	3076.6	3279.6	3489.1	3928.7	4640.6
0.008 (41.51°C) (314.66 K)	<i>s</i>	8.4128	8.6847	8.9244	9.1398	9.5172	9.8435	10.1336	10.6386	11.2750
	<i>v</i>	18.598	21.501	24.395	27.284	33.058	38.829	44.599	56.138	73.446
	<i>u</i>	2444.2	2515.7	2588.0	2661.4	2812.1	2969.0	3132.3	3479.6	4053.0
<i>h</i>	2593.0	2687.7	2783.1	2879.6	3076.6	3279.6	3489.1	3928.7	4640.6	5409.7
	<i>s</i>	8.5514	8.7914	9.0069	9.3844	9.7107	10.0008	10.5058	11.1422	11.6841

0.010 (45.81°C) (318.96 K)	<i>v</i>	14.869	17.196	19.512	21.825	26.445	31.063	35.679	44.911	58.757	72.602
	<i>u</i>	2443.9	2515.5	2587.9	2661.3	2812.1	2968.9	3132.3	3479.6	4053.0	4663.7
	<i>h</i>	2592.6	2687.5	2783.0	2879.5	3076.5	3279.6	3489.1	3928.7	4640.6	5409.7
0.020 (60.06°C) (333.21 K)	<i>s</i>	8.1749	8.4479	8.6882	8.9038	9.2813	9.6077	9.8978	10.4028	11.0393	11.5811
	<i>v</i>	7.412	8.585	9.748	10.907	13.219	15.529	17.838	22.455	29.378	36.301
	<i>u</i>	2442.2	2514.6	2587.3	2660.9	2811.9	2968.8	3132.2	3479.5	4053.0	4663.7
0.040 (75.87°C) (349.02 K)	<i>h</i>	2590.4	2686.2	2782.3	2879.1	3076.3	3279.4	3489.0	3928.6	4640.6	5409.7
	<i>s</i>	7.8498	8.1255	8.3669	8.5831	8.9611	9.2876	9.5778	10.0829	10.7193	11.2612
0.060 (85.94°C) (359.09 K)	<i>v</i>	3.683	4.279	4.866	5.448	6.606	7.763	8.918	11.227	14.689	18.151
	<i>u</i>	2438.8	2512.6	2586.2	2660.2	2811.5	2968.6	3132.1	3479.4	4052.9	4663.6
	<i>h</i>	2586.1	2683.8	2780.8	2878.1	3075.8	3279.1	3488.8	3928.5	4640.5	5409.6
0.080 (93.50°C) (366.65 K)	<i>s</i>	7.5192	7.8003	8.0444	8.2617	8.6406	8.9674	9.2577	9.7629	10.3994	10.9412
	<i>v</i>	2.440	2.844	3.238	3.628	4.402	5.174	5.944	7.484	9.792	12.100
	<i>u</i>	2435.3	2510.6	2585.1	2659.5	2811.2	2968.4	3131.9	3479.4	4052.9	4663.6
	<i>h</i>	2581.7	2681.3	2779.4	2877.2	3075.3	3278.8	3488.6	3928.4	4640.4	5409.6
0.100 (99.63°C) (372.78 K)	<i>s</i>	7.3212	7.6079	7.8546	8.0731	8.4528	8.7799	9.0704	9.5757	10.2122	10.7541
	<i>v</i>	1.8183	2.127	2.425	2.718	3.300	3.879	4.458	5.613	7.344	9.075
	<i>u</i>	2431.7	2508.7	2583.9	2658.8	2810.8	2968.1	3131.7	3479.3	4052.8	4663.5
	<i>h</i>	2577.2	2678.8	2777.9	2876.2	3074.8	3278.5	3488.3	3928.3	4640.4	5409.5
	<i>s</i>	7.1775	7.4698	7.7191	7.9388	8.3194	8.6468	8.9374	9.4428	10.0794	10.6213
	<i>v</i>	1.4450	1.6958	1.9364	2.172	2.639	3.103	3.565	4.490	5.875	7.260
	<i>u</i>	2428.2	2506.7	2582.8	2658.1	2810.4	2967.9	3131.6	3479.2	4052.8	4663.5
	<i>h</i>	2572.7	2676.2	2776.4	2875.3	3074.3	3278.2	3488.1	3928.2	4640.3	5409.5
	<i>s</i>	7.0633	7.3614	7.6134	7.8343	8.2158	8.5435	8.8342	9.3398	9.9764	10.5183

(Continued)

TABLE A3.8 (CONTINUED)
Superheated Steam—SI Units

Pressure (MN/m ²)		Temperature										
(Saturation Temperature)	50°C	100°C	150°C	200°C	300°C	400°C	500°C	700°C	1000°C	1273.15 K	1300°C	1573.15 K
0.200 (120.23°C) (393.38 K)	v	0.6969	0.8340	0.9596	1.0803	1.3162	1.5493	1.7814	2.244	2.937	3.630	
	u	2409.5	2496.3	2576.9	2654.4	2808.6	2966.7	3130.8	3478.8	4052.5	4683.2	
	h	2548.9	2663.1	2768.8	2870.5	3071.8	3276.6	3487.1	3927.6	4640.0	5409.3	
0.300 (133.55°C) (406.70 K)	s	6.6844	7.0135	7.2795	7.5066	7.8926	8.2218	8.5133	9.0194	9.6563	10.1982	
	v	0.4455	0.5461	0.6339	0.7163	0.8753	1.0315	1.1867	1.4957	1.9581	2.4201	
	u	2389.1	2485.4	2570.8	2650.7	2806.7	2965.6	3130.0	3478.4	4052.3	4683.0	
0.400 (143.63°C) (416.78 K)	h	2522.7	2649.2	2761.0	2865.6	3069.3	3275.0	3486.0	3927.1	4639.7	5409.0	
	s	6.4319	6.7965	7.0778	7.3115	7.7022	8.0330	8.3251	8.8319	9.4690	10.0110	
	v	0.3177	0.4017	0.4708	0.5342	0.6548	0.7726	0.8893	1.1215	1.4685	1.8151	
0.500 (151.86°C) (425.01 K)	u	2366.3	2473.8	2564.5	2646.8	2804.8	2964.4	3129.2	3477.9	4052.0	4682.8	
	h	2493.4	2634.5	2752.8	2860.5	3066.8	3273.4	3484.9	3926.5	4639.4	5408.8	
	s	6.2248	6.6319	6.9299	7.1706	7.5662	7.8985	8.1913	8.6987	9.3360	9.8780	
v	v	0.3146	0.3729	0.4249	0.5226	0.6173	0.7109	0.8969	1.1747	1.4521		
	u	2461.5	2557.9	2642.9	2802.9	2963.2	3128.4	3477.5	4051.8	4682.5		
	h	2618.7	2744.4	2855.4	3064.2	3271.9	3483.9	3925.9	4639.1	5408.6		
s	s	6.4945	6.8111	7.0592	7.4599	7.7938	8.0873	8.5952	9.2328	9.7749		

Source: Bolz, R.E. and G.I. Tuve, eds, *CRC Handbook of Tables for Applied Engineering Science*, 2nd ed., Chemical Rubber Co., Cleveland, Ohio, 1973.
Note: v = specific volume, m³/kg; u = specific internal energy, kJ/kg; h = specific enthalpy, kJ/kg; s = specific entropy, kJ/K·kg.

TABLE A3.9

Normal Distribution Function

$$F(z) = \frac{1}{\sqrt{2\pi}} \int_{-\infty}^z e^{-1/2t^2} dt$$

Appendix 4: Supplementary Material for Chapter 4

TABLE A4.1

Toxicological Properties of Common Glycols Used as Antifreeze in Solar Systems

	Single Oral LD ₅₀ Dose in Rats (ml/kg)	Repeated Oral Feeding in Rats Acceptable Level in Diet and Duration	Single Skin Penetration LD ₅₀ Dose in Rabbits (ml/kg)	Single Inhalation Concentrated Vapor (8 h) in Rats	Primary Skin Irritation in Rabbits	Eye Injury in Rabbits
Ethylene glycol	7.40 ^a	0.18 g/kg/day (30 days)	>20	Killed none of 6	None	None
Diethylene glycol	28.3	0.18 g/kg/day (30 days)	11.9	Killed none of 6	None	None
Triethylene glycol	28.2	0.83 g/kg/day (30 days)	>20	Killed none of 6	None	None
Tetraethylene glycol	28.9	1.88 g/kg/day (2 years)	>20	Killed none of 6	None	None
Propylene glycol	34.6	2.0 g/kg/day (2 years) ^b	>20	Killed none of 6	None	Trace
Dipropylene glycol	14.8	—	>20	Killed none of 6	None	Trace
Hexylene glycol	4.06	0.31 g/kg/day (90 days)	8.56	Killed none of 6	Trace	Minor
2-Ethyl-1,3-hexanediol	6.50	0.48 g/kg/day (90 days)	15.2	Killed none of 6	Trace	Moderate
1,5-Pentanediol	5.89 ^c	—	>20	Killed none of 6	None	Trace

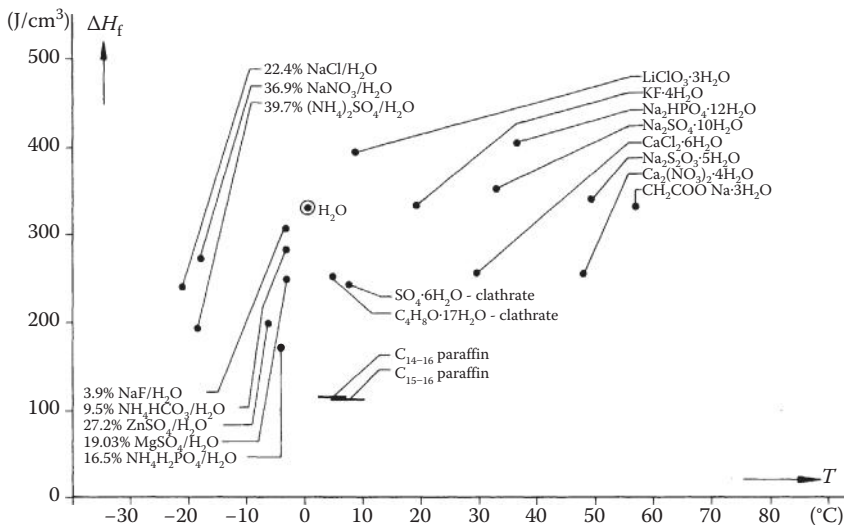
Source: Union Carbide, Glycols, F-41515A 7/71-12M, p. 68, 1971.

Note: The term LD₅₀ refers to that quantity of chemical that kills 50% of dosed animals within 14 days. For uniformity, dosage is expressed in grams or milliliters per kilogram of body weight. Single skin penetration refers to a 24-h covered skin contact with the liquid chemical. Single inhalation refers to the continuous breathing of a certain concentration of chemical for the stated period. Primary irritation refers to the skin response 24 h after application of 0.01-ml amounts to uncovered skin. Eye injury refers to surface damage produced by the liquid chemical.

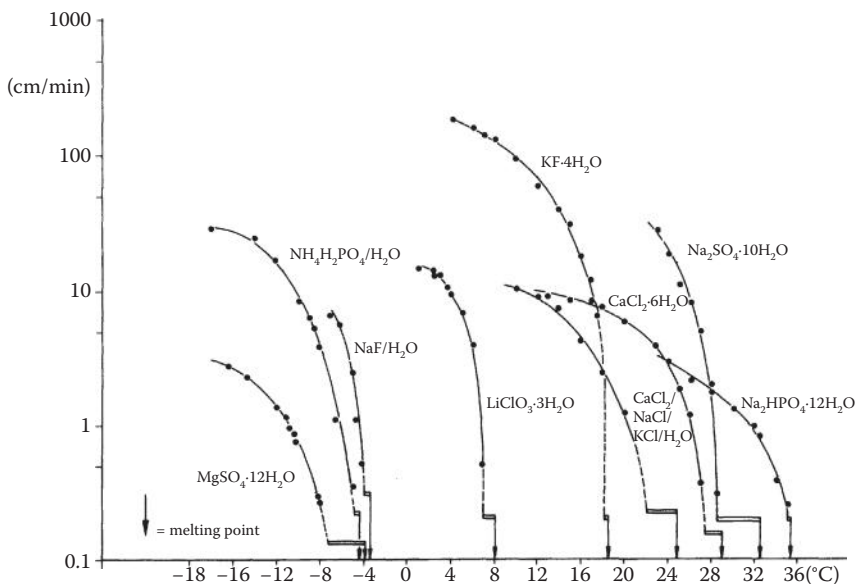
^a Single dose oral toxicity to humans is greater.

^b Dogs.

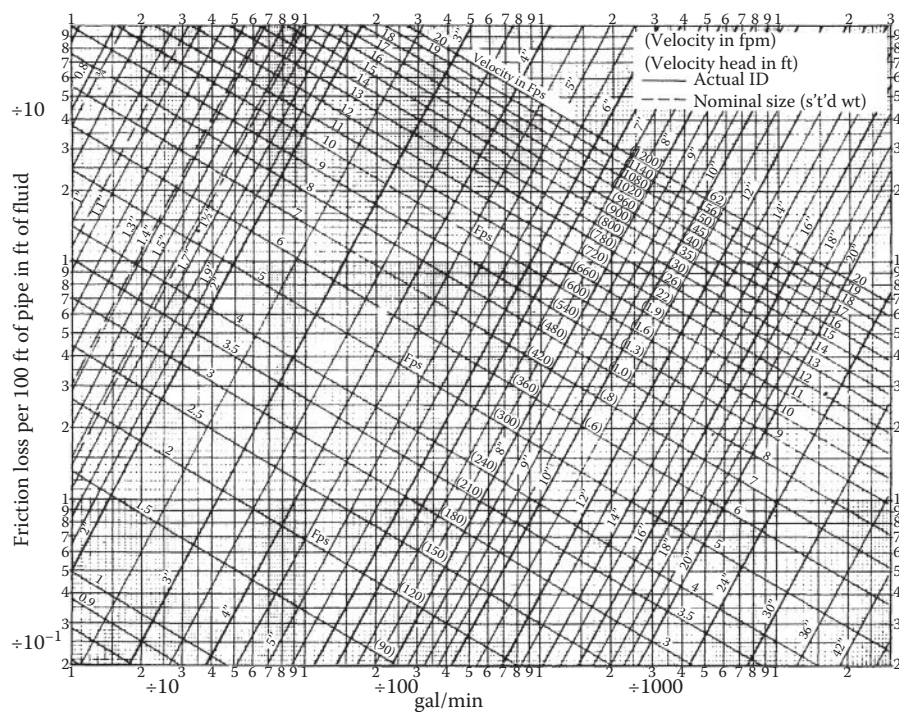
^c g/kg.

**FIGURE A4.1**

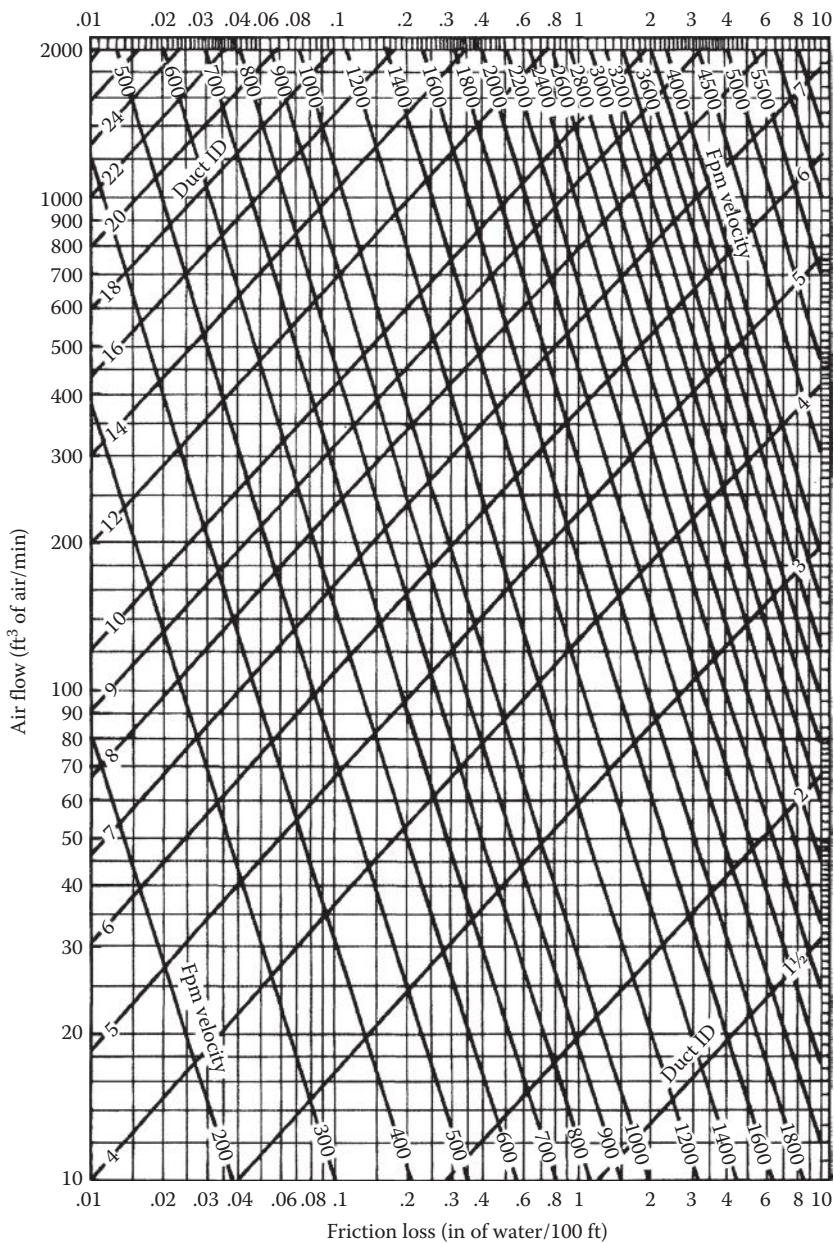
Enthalpy of fusion and phase change temperatures of low-temperature phase-change storage media. (From Schröder, J., Philips GmbH Forschungslaboratorium [Aachen] Report, 1977)

**FIGURE A4.2**

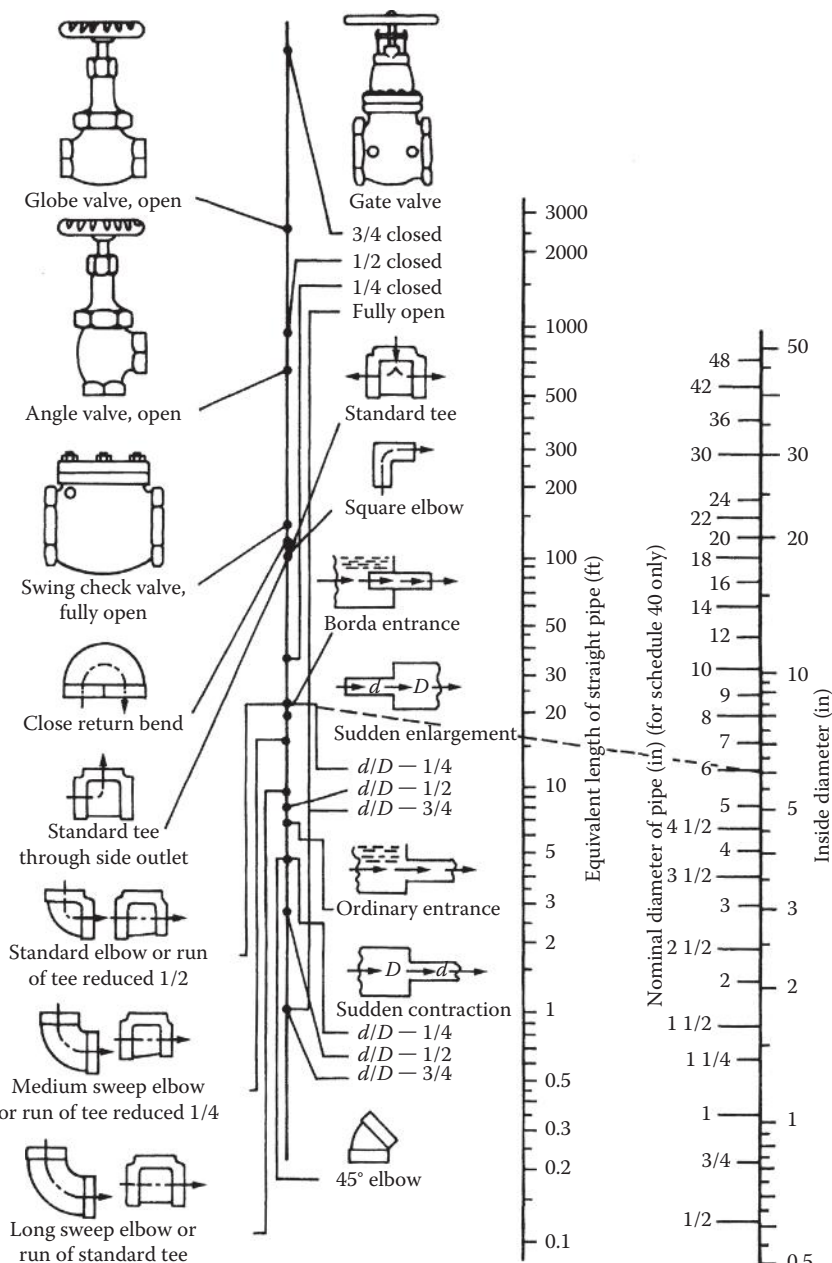
Rate of crystallization of several low-temperature hydrates and eutectics. Note that Na₂SO₄·10H₂O and CaCl₂/NaCl/KCl/H₂O have very inadequate rates without substantial subcooling. (From Schröder, J., Philips GmbH Forschungslaboratorium [Aachen] Report, 1977)

**FIGURE A4.3**

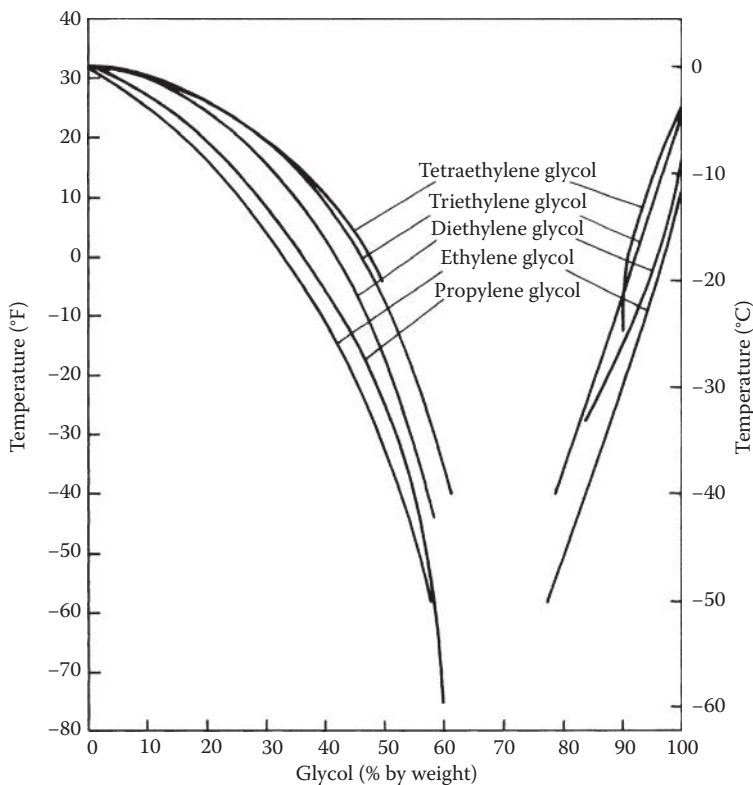
Pressure drop of water in turbulent flow for standard pipe sizes. ($1 \text{ gal/min} = 3.79 \times 10^{-3} \text{ m}^3/\text{min}$; $1 \text{ ft} = 0.305 \text{ m}$; $1 \text{ in} = 2.54 \text{ cm}$) (From Potter, P.J., *Power Plant Theory and Design*, 2nd ed. Copyright © 1959. The Ronald Press Company, New York.)

**FIGURE A4.4**

Pressure drop of air flowing in ducts; velocities shown for circular ducts. ($1 \text{ in H}_2\text{O} = 249 \text{ N/m}^2$; $1 \text{ ft}^3 = 2.83 \times 10^{-2} \text{ m}^3$; $1 \text{ in} = 2.54 \text{ cm}$; $1 \text{ ft}^3 = 0.305 \text{ m}^3$) (From ASHRAE, *Handbook of Fundamentals*, American Society of Heating, Refrigerating, and Air Conditioning Engineers, New York, 1972.)

**FIGURE A4.5**

Equivalent lengths of pipe, standard pipe fittings. (1 ft = 0.305 m; 1 in = 2.54 cm.) For sudden enlargements and sudden contractions, the equivalent length is in feet of pipe of the smaller diameter d . Dashed line shows determination of equivalent length of a 6-in standard elbow. (From Crane Co., Flow of fluids, Technical Paper 410, 1957.)

**FIGURE A4.6**

Freezing-point depression of aqueous solutions of common glycol antifreezes. (From Union Carbide, Glycols, F-41515A 7/71-12M, p. 17, 1971.)

*Appendix 5: Supplementary
Material for Chapter 5*

TABLE A5.1
Conductance and Resistance Values for External Air Surfaces

Wind Condition		Type of Surface					
Position of Surface	Direction of Heat Flow	Foil		Aluminum-Coated Paper		Nonreflective Building Materials	
		Conductance $C, \text{Btu}/(\text{h})(\text{ft}^2)(^\circ\text{F})$	Resistance R, $1/\text{Btu}/(\text{h})(\text{ft}^2)(^\circ\text{F})$	Conductance $C, \text{Btu}/(\text{h})(\text{ft}^2)(^\circ\text{F})$	Resistance R, $1/\text{Btu}/(\text{h})(\text{ft}^2)(^\circ\text{F})$	Conductance $C, \text{Btu}/(\text{h})(\text{ft}^2)(^\circ\text{F})$	Resistance R, $1/\text{Btu}/(\text{h})(\text{ft}^2)(^\circ\text{F})$
<i>Still Air</i>							
Horizontal	Up	0.76	1.32	0.91	1.10	1.63	0.61
45° slope	Up	0.73	1.37	0.88	1.14	1.60	0.62
Vertical	Horizontal	0.59	1.70	0.74	1.35	1.46	0.68
45° slope	Down	0.45	2.22	0.60	1.67	1.32	0.76
Horizontal	Down	0.22	4.55	0.37	2.70	1.08	0.92
<i>7.5-mph Wind</i>							
Any position	Any direction (for summer calculations)	4.00	0.25
<i>15-mph Wind</i>							
Any position	Any direction (for winter calculations)	6.00	0.17

Source: Adapted from Johns-Mansville, Denver, Colorado.

TABLE A5.2
Conductance and Resistance Values for Internal Air Surfaces

		Type of Surface									
Position of Airspace	Direction of Heat Flow ^a	Thickness, in.	Temp. Cond.	Foil and Nonreflective Building Materials		Aluminum-Coated Paper and Nonreflective Building Materials		Both Surfaces Nonreflective Building Materials			
				Conductance $C, \text{Btu}/(\text{h})(\text{ft}^2)(^\circ\text{F})$	Resistance $R, \text{I}[\text{Btu}/(\text{h})(\text{ft}^2)(^\circ\text{F})]$	Conductance $C, \text{Btu}/(\text{h})(\text{ft}^2)(^\circ\text{F})$	Resistance $R, \text{I}[\text{Btu}/(\text{h})(\text{ft}^2)(^\circ\text{F})]$	Conductance $C, \text{Btu}/(\text{h})(\text{ft}^2)(^\circ\text{F})$	Resistance $R, \text{I}[\text{Btu}/(\text{h})(\text{ft}^2)(^\circ\text{F})]$		
				Up	3/4	W	0.45	2.23	0.59	1.71	1.15
45° slope	Up	3/4	S	0.44	2.26	0.61	1.63	1.32	0.76	0.76	0.76
		4	W	0.37	2.73	0.50	1.99	1.07	0.94	0.94	0.94
		4	S	0.36	2.75	0.53	1.87	1.24	0.80	0.80	0.80
	Horizontal	3/4	W	0.36	2.78	0.50	2.02	1.06	0.94	0.94	0.94
		3/4	S	0.36	2.81	0.53	1.90	1.24	0.81	0.81	0.81
		4	W	0.33	3.00	0.47	2.13	1.04	0.96	0.96	0.96
Vertical	Horizontal	4	S	0.33	3.00	0.51	1.98	1.21	0.82	0.82	0.82
		3/4	W	0.29	3.48	0.42	2.36	0.99	0.99	0.99	0.99
		3/4	S	0.31	3.28	0.48	2.10	1.19	0.84	0.84	0.84
	45° slope	4	W	0.29	3.45	0.43	2.34	0.99	0.99	0.99	0.99
		4	S	0.29	3.44	0.46	2.16	1.17	0.91	0.91	0.91
		3/4	W	0.28	3.57	0.42	2.40	0.98	1.02	1.02	1.02
Horizontal	Down	3/4	S	0.31	3.24	0.48	2.09	1.19	0.84	0.84	0.84
	Down	4	W	0.23	4.41	0.36	2.75	0.93	1.08	1.08	1.08
	Down	4	S	0.23	4.36	0.40	2.50	1.11	0.90	0.90	0.90
	Down	3/4	W	0.28	3.55	0.42	2.39	0.98	1.02	1.02	1.02

(Continued)

TABLE A5.2 (CONTINUED)
Conductance and Resistance Values for Internal Air Surfaces

Position of Airspace	Direction of Heat Flow ^a	Thickness, in.	Temp. Cond.	Type of Surface			
				Foil and Nonreflective Building Materials		Aluminum-Coated Paper and Nonreflective Building Materials	
				Conductance $C, \text{Btu}/(\text{ft}^2)\text{°F}$	Resistance $R, \text{h}/(\text{Btu}/(\text{ft}^2)\text{°F})$	Conductance $C, \text{Btu}/(\text{ft}^2)\text{°F}$	Resistance $R, \text{h}/(\text{Btu}/(\text{ft}^2)\text{°F})$
1 1/2	W	0.17	5.74	0.31	3.21	0.88	1.14
4	W	0.11	8.94	0.25	4.02	0.81	1.23
3/4	S	0.31	3.25	0.48	2.08	1.19	0.84
1 1/2	S	0.19	5.24	0.36	2.76	1.07	0.93
4	S	0.12	8.08	0.30	3.38	1.01	0.99

Source: Adapted from Johns-Manville, Denver, Colorado.

Note: W = winter; S = summer.

^a Heat flows from hot to cold. For ceiling instillation, the direction of heat flow would normally be "up" for winter and "down" for summer. In a floor the direction of heat flow would be "down" in winter and "up" in summer. Heat flow in walls would be in a horizontal direction.

TABLE A5.3

Conductance and Resistance Values for Exterior Siding Materials

Material	Description	Conductivity <i>k</i> , Btu/(h)(ft ²) (°F/in.)	Thickness, in.	Conductance <i>C</i> , Btu/(h) (ft ²)(°F)	Resistance <i>R</i> , l/[Btu/(h) (ft ²)(°F)]
Brick	Common	5.0	4	1.25	0.80
Brick	Face	9.0	4	2.27	0.44
Stucco		5.0	1	5.0	0.20
Asbestos cement shingles				4.76	0.21
Wood shingles	16–7 1/2-in. exposure			1.15	0.87
Wood shingles	Double 16–12 in. exposure			0.84	1.19
Wood shingles	Plus 5/16 in. insulated backerboard			0.71	1.40
Asbestos cement siding	1/4 in. lapped			4.76	0.21
Asphalt roll siding				6.50	0.15
Asphalt insulating siding			1/2	0.69	1.46
Wood	Drop siding, 1 × 8 in.			1.27	0.79
Wood	Bevel, 1/2 × 8 in. lapped			1.23	0.81
Wood	Bevel, 3/4 × 10 in. lapped			0.95	1.05
Wood	Plywood, 3/8 in. lapped			1.59	0.59
Hardboard	Medium density	0.73	1/4	2.94	0.34
	Tempered	1.00	1/4	4.00	0.25
Plywood lap siding			3/8	1.79	0.56
Plywood flat siding			3/8	2.33	0.43

Source: Adapted from Johns-Mansville, Denver, Colorado.

TABLE A5.4

Conductance and Resistance Values for Sheathing and Building Paper

Material	Description	Conductivity k , Btu/(h)(ft ²) (°F/in.)	Thickness, in.	Conductance C , Btu/(h) (ft ²)(°F)	Resistance R , l/[Btu/(h) (ft ²)(°F)]
Gypsum	...	1.11	3/8	3.10	0.32
			1/2	2.25	0.45
			5/8	1.75	0.57
Plywood	...	0.80	1/4	3.20	0.31
			3/8	2.13	0.47
			1/2	1.60	0.62
			5/8	1.28	0.78
			3/4	1.07	0.93
Nail-base sheathing	...	0.44	1/2	0.88	1.14
Wood sheathing	Fir or pine	0.80	3/4	1.06	0.94
Sheathing paper	Vapor- permeable			16.70	0.06
Vapor barrier	2 layers mopped 15-lb felt			8.35	0.12
	Plastic film			Negl.	Negl.

Source: Adapted from Johns-Mansville, Denver, Colorado.

TABLE A5.5
Conductance and Resistance Values for Masonry Materials

Material	Description	Conductivity <i>k</i> , Btu/(h) (ft ²)°F/in.)	Thickness, in.	Conductance <i>C</i> , Btu/(h) (ft ²)°F)	Resistance <i>R</i> , l/[Btu/(h) (ft ²)°F)]
Concrete blocks, three-oval core	Sand and gravel aggregate	...	4	1.40	0.71
			8	0.90	1.11
			12	0.78	1.28
	Cinder aggregate	...	4	0.90	1.11
			8	0.58	1.72
			12	0.53	1.89
	Lightweight aggregate	...	4	0.67	1.50
			8	0.50	2.00
			12	0.44	2.27
Hollow clay tile	1 cell deep	...	4	0.90	1.11
	2 cells deep	...	8	0.54	1.85
	3 cells deep	...	12	0.40	2.50
Gypsum partition tile	3 × 12 × 30 in. solid	...	3	0.79	1.26
	3 × 12 × 30 in. 4-cell	...	3	0.74	1.35
	4 × 12 × 30 in. 3-cell	...	4	0.60	1.67
Cement mortar		5.0	1	5.0	0.20
Stucco		5.0	1	5.0	0.20
Gypsum	Poured	1.66	1	1.66	0.60
	Precast	2.80	2	1.40	0.71
Concrete	Sand and gravel or stone	12.0	1	12.0	0.08
Lightweight concrete	Perlite or zonolite mixture				
	1:4 mix, 36 lb/ft ³	0.72–0.75	1	0.74	1.35
	1:5 mix, 30 lb/ft ³	0.61–0.72	1	0.67	1.49
	1:6 mix, 27 lb/ft ³	0.54–0.61	1	0.58	1.72
	1:8 mix, 22 lb/ft ³	0.47–0.54	1	0.51	1.96
Stone	...	12.5	1	12.5	0.08

Source: Adapted from Johns-Mansville, Denver, Colorado.

TABLE A5.6
Conductance and Resistance Values for Woods

Material	Description	Conductivity k , Btu/(h) (ft ²)(°F/in.)	Thickness, in.	Conductance C , Btu/(h) (ft ²)(°F)	Resistance R , I/[Btu/(h) (ft ²)(°F)]
Maple, oak, and similar hardwoods	45 lb/ft ³	1.10	3/4	1.47	0.68
Fir, pine, and similar softwoods	32 lb/ft ³	C.80	3/4	1.06	0.94
			1 1/2	0.53	1.89
			2 1/2	0.32	3.12
			3 1/2	0.23	4.35

Source: Adapted from Johns-Mansville, Denver, Colorado.

TABLE A5.7

Conductance and Resistance Values for Wall-Insulation Materials

Material	Description	Conductivity k , Btu/(h) (ft ²)(°F/in.)	Thickness, in.	Conductance C , Btu/(h) (ft ²)(°F)	Resistance R , l/[Btu/(h)] (ft ²)(°F)]
Fiber glass roof insulation	... Thickness includes membrane roofing on both sides	0.13	15/16	0.27	3.70
			1 1/16	0.24	4.17
			1 5/16	0.19	5.26
			1 5/8	0.15	6.67
			1 7/8	0.13	7.69
			2 1/4	0.11	9.09
Urethane roof insulation	Thickness includes membrane roofing on both sides	0.13	4/5	0.19	5.26
			1	0.15	6.67
			1 1/5	0.12	8.33
Styrofoam SM & TG	2.1 lb/ft ³	0.19	3/4	0.25	3.93
			1	0.19	5.26
			1 1/2	0.13	7.89
			2	0.95	10.52
Wood shredded	Cemented in preformed slabs	0.60	1	0.60	1.67
Insulating board	Building and service board, decorative ceiling panels	0.38	3/8	1.01	0.99
			1/2	0.76	1.32
			9/16	0.68	1.48
			3/4	0.51	1.98
Thermal, acoustical fiber glass	... 0.39 0.36 0.34	0.39	2 3/4	0.14	7.00
			4	0.09	11.00
			6 1/2	0.05	19.00
Corkboard	6.4 lb/ft ³	0.26	1	0.26	3.85
Expanded polystyrene	Extruded Molded beads	1.8 lb/ft ³ 1.0 lb/ft ³	0.25	1	0.25
			1	0.26	3.85
Urethane foam	1.9 lb/ft ³	0.17	3/4	0.23	4.41
			1 1/2	0.11	8.82
			2	0.09	11.76
Fiber glass perimeter insulation	1	0.23	4.30
Fiber glass form board	1 1/4	0.19	5.40
			1	0.25	4.00

Source: Adapted from Johns-Mansville, Denver, Colorado.

TABLE A5.8

Conductance and Resistance Values for Roofing Materials

Material	Description	Conductivity k , Btu/(h) (ft ²)°F/in.)	Thickness, in.	Conductance C , Btu/(h) (ft ²)°F)	Resistance R , l/[Btu/(h) (ft ²)°F)]
Asbestos cement shingles	120 lb/ft ³	4.76	0.21
Asphalt shingles	70 lb/ft ³	2.27	0.44
Wood shingles	1.06	0.94
Slate	1/2	20.0	0.05
Asphalt roll roofing	70 lb/ft ³	6.50	0.15
Built-up roofing	Smooth or gravel surface	...	3/8	3.00	0.33
Sheet metal	Negl.	Negl.

Source: Adapted from Johns-Mansville, Denver, Colorado.

TABLE A5.9

Conductance and Resistance Values for Flooring Materials

Material	Description	Conductivity k , Btu/(h) (ft ²)°F/in.)	Thickness, in.	Conductance C , Btu/(h) (ft ²)°F)	Resistance R , l/[Btu/(h) (ft ²)°F)]
Asphalt, vinyl, rubber, or linoleum tile	20.0	0.05
Cork tile	...	0.45	1/8	3.60	0.28
Terrazzo	...	12.5	1	12.50	0.08
Carpet and fibrous pad	0.48	2.08
Carpet and rubber pad	0.81	1.23
Plywood subfloor	...	0.80	5/8	1.28	0.78
Wood subfloor	...	0.80	3/4	1.06	0.94
Wood, hardwood finish	...	1.10	3/4	1.47	0.68

Source: Adapted from Johns-Mansville, Denver, Colorado.

TABLE A5.10

Conductance and Resistance Values for Interior Finishes

Material	Description	Conductivity k , Btu/(h) (ft ²)(°F/in.)	Thickness, in.	Conductance C , Btu/(h) (ft ²)(°F)	Resistance R , l/[Btu/(h) (ft ²)(°F)]
Gypsum board		1.11	3/8	3.10	0.32
			1/2	2.25	0.45
Cement plaster	Sand aggregate	5.0	1/2	10.00	0.10
			3/4	6.66	0.15
Gypsum plaster	Sand aggregate	5.6	1/2	11.10	0.09
			5/8	9.10	0.11
Gypsum plaster	Lightweight aggregate	1.6	1/2	3.12	0.32
			5/8	2.67	0.39
Gypsum plaster on Metal lath	Sand aggregate		3/4	7.70	0.13
Metal lath	Lightweight aggregate		3/4	2.13	0.47
Gypsum board, 3/8 in.	Sand aggregate		7/8	2.44	0.41
Insulating board		0.38	1/2	0.74	1.35
Plywood		0.80	3/8	2.13	0.47

Source: Adapted from Johns-Mansville, Denver, Colorado.

TABLE A5.11

Conductance and Resistance Values for Glass

Material	Description	Conductivity k , Btu/(h) (ft ²)(°F/in.)	Thickness, in.	Conductance $C (U)$, Btu/(h) (ft ²)(°F)	Resistance R (1/ U), l/[Btu/ (h)(ft ²)(°F)]
Single plate				1.13	0.88
Double plate	Air space, 3/16 in.	0.69	1.45
Storm windows	Air space, 1–4 in.	0.56	1.78
Solid-wood door	Actual thickness, 1 1/2 in.	0.49	2.04
Storm door, wood and glass	With wood and glass storm door	0.27	3.70
Storm door, metal and glass	With metal and glass storm door	0.33	3.00

Source: Adapted from Johns-Mansville, Denver, Colorado.

TABLE A5.12

Internet Sources of World Climatic Data

The following climatic data, useful for solar energy system design, are available for various locations in the countries listed below.

- *Temperature (Max., Min., Mean)*
- *Precipitation*
- *Wind Speed*
- *Dew Point (Mean)*
- *Pressure*

Additional information about national weather data for some countries is available from the internet. For websites, see the National Oceanic and Atmospheric Administration (NOAA) website [<http://www.ncdc.noaa.gov/cgi-bin/res40?page=climvisgsod.html>]

Additional data available for the United States from the National Oceanic and Atmospheric Administration (NOAA) [<http://www.ncdc.noaa.gov/ol/documentlibrary/hc/hcs.html>] include:

- *Heating Degree Days*
- *Cooling Degree Days*

Countries (Numbers in Parentheses Denote the Number of Sites for Which Data Are Available)

Africa

Algeria (55)	Angola (19)
Benin (6)	Botswana (17)
Bouvet Island (1)	Burkina Faso (11)
Burundi (2)	Cameroon (10)
Cape Verde (3)	Central African Republic (8)
Chad/Tchad (12)	Comoros (4)
Congo (14)	Cote D'Ivoire/Ivory Coast (12)
Democratic Republic of the Congo (73)	Djibouti (2)
Egypt (39)	Equatorial Guinea (2)
Eritrea (3)	Ethiopia (14)
Gabon (9)	Gambia (12)
Ghana (23)	Guinea (7)
Guinea-Bissau (4)	Kenya (11)
Lesotho (3)	Liberia (2)
Libyan Arab Jamahiriya (17)	Madagascar (9)
Madeira (2)	Malawi (7)
Mali (6)	Mauritania (6)
Morocco (24)	Mozambique (16)
Namibia (11)	Niger (7)
Nigeria (21)	Ocean Islands (12)
Rwanda (5)	Senegal (6)
Seychelles (5)	Sierra Leone (6)
Somalia (7)	South Africa (101)
Spain (Canary Islands) (7)	Sudan (8)
Swaziland (1)	Uganda (9)
Tunisia (17)	Togo (5)
United Republic of Tanzania (12)	Western Sahara (2)
Zambia (31)	Zimbabwe (27)

TABLE A5.12 (CONTINUED)

Internet Sources of World Climatic Data

Countries (Numbers in Parentheses Denote the Number of Sites for Which Data Are Available)

Asia

Afghanistan (17)	Bahrain (1)
Bangladesh (14)	Cambodia (9)
China (414)	North Korea (15)
Hong Kong (18)	India (540)
Iran (81)	Iraq (31)
Japan (315)	Kazakhstan (76)
Kuwait (19)	Kyrgyzstan (6)
Lao (19)	Macau (4)
Maldives (5)	Mongolia (38)
Myanmar (51)	Nepal (9)
Oman (12)	Pakistan (72)
Qatar (3)	South Korea (68)
Russian Federation (in Asia) (576)	Saudi Arabia (87)
Sri Lanka (26)	Tajikistan (9)
Thailand (73)	Turkmenistan (29)
United Arab Emirates (5)	Uzbekistan (36)
Vietnam (21)	Yemen (17)

Europe

Albania (8)	Armenia (36)
Austria (174)	Azerbaijan (72)
Belarus (23)	Belgium (19)
Bosnia and Herzegovina (10)	Bulgaria (34)
Croatia (47)	Cyprus (4)
Czech Republic (32)	Denmark (70)
Estonia (27)	Finland (49)
France (180)	Georgia (17)
Germany (306)	Gibraltar (2)
Greece (52)	Greenland (43)
Hungary (33)	Iceland (58)
Ireland (17)	Israel (8)
Italy (140)	Jordan (9)
Kazakhstan (Europe) (3)	Latvia (22)
Lebanon (6)	Lithuania (17)
Luxembourg (3)	Malta (1)
Netherlands (54)	Norway (198)
Poland (72)	Portugal (33)
Republic of Moldova (3)	Romania (42)
Russian Federation (in Europe) (342)	Slovakia (25)
Slovenia (23)	Spain (79)

(Continued)

TABLE A5.12 (CONTINUED)

Internet Sources of World Climatic Data

Countries (Numbers in Parentheses Denote the Number of Sites for Which Data Are Available)

Europe

Sweden (96)	Switzerland (70)
Syrian Arab Republic (35)	Macedonia (22)
Turkey (102)	Ukraine (117)
United Kingdom and No. Ireland (344)	Yugoslavia (47)

North and South America

Anguilla (1)	Antigua and Barbuda (2)
Argentina (90)	Bolivia (36)
Bahamas (7)	Barbados (2)
Belize (4)	Bermuda (1)
Brazil (342)	British Virgin Islands (1)
Canada (324)	Cayman Islands (2)
Chile (35)	Clipperton (1)
Columbia (54)	Costa Rica (5)
Cuba (69)	Curacao (3)
Dominica (18)	Ecuador (37)
El Salvador (6)	French Guyana (5)
Grenada (1)	Guatemala (7)
Guyana (8)	Haiti (6)
Honduras (7)	Islands (7)
Jamaica (4)	Martinique (2)
Mexico (89)	Paraguay (49)
Peru (54)	Suriname (7)
Uruguay (17)	Venezuela (33)
Nicaragua (13)	Panama (7)
Puerto Rico (5)	Saint Kitts (2)
Saint Lucia (2)	Saint Vincent (1)
St. Martin, St. Eustatius (5)	St. Pierre (1)
Trinidad and Tobago (2)	Turks and Caicos Islands (2)
United States of America (756)	Venezuela (1)

South-West Pacific

Australia (Additional Islands) (828)	Brunei (2)
Cook Islands (5)	Detached Islands (6)
East Timor/Timor Oriental (7)	Fiji (15)
French Polynesia (Austral Islands) (16)	Indonesia (198)
Islands (157)	Kiribati (6)
Malaysia (18)	Nauru (2)
New Caledonia (8)	New Zealand (126)
Niue (2)	Papua New Guinea (54)
Philippines (72)	Samoa and American Samoa (5)

TABLE A5.12 (CONTINUED)

Internet Sources of World Climatic Data

Countries (Numbers in Parentheses Denote the Number of Sites for Which Data Are Available)

South-West Pacific

Singapore (5)	Solomon Islands (7)
Southern Line Islands (3)	Tokelau (4)
Tonga (9)	Tuvalu (5)
Vanuatu (7)	

Appendix 6: Thermodynamic Data for Cooling Systems

TABLE A6.1a

Saturated Refrigerant-134a—Temperature Table

Temp., <i>T</i> °C	Press., <i>P</i> _{sat} MPa	Specific Volume, m ³ /kg		Enthalpy, kJ/kg			Entropy, kJ/(kg·K)	
		Sat. Liquid, <i>v</i> _f	Sat. Vapor, <i>v</i> _g	Sat. Liquid, <i>h</i> _f	Evap., <i>h</i> _{fg}	Sat. Vapor, <i>h</i> _g	Sat. Liquid, <i>s</i> _f	Sat. Vapor, <i>s</i> _g
-40	0.05164	0.0007055	0.3569	0.00	222.88	222.88	0.0000	0.9560
-36	0.06332	0.0007113	0.2947	4.73	220.67	225.40	0.0201	0.9506
-32	0.07704	0.0007172	0.2451	9.52	218.37	227.90	0.0401	0.9456
-28	0.09305	0.0007233	0.2052	14.37	216.01	230.38	0.0600	0.9411
-26	0.10199	0.0007265	0.1882	16.82	214.80	231.62	0.0699	0.9390
-24	0.11160	0.0007296	0.1728	19.29	213.57	232.85	0.0798	0.9370
-22	0.12192	0.0007328	0.1590	21.77	212.32	234.08	0.0897	0.9351
-20	0.13299	0.0007361	0.1464	24.26	211.05	235.31	0.0996	0.9332
-18	0.14483	0.0007395	0.1350	26.77	209.76	236.53	0.1094	0.9315
-16	0.15748	0.0007428	0.1247	29.30	208.45	237.74	0.1192	0.9298
-12	0.18540	0.0007498	0.1068	34.39	205.77	240.15	0.1388	0.9267
-8	0.21704	0.0007569	0.0919	39.54	203.00	242.54	0.1583	0.9239
-4	0.25274	0.0007644	0.0794	44.75	200.15	244.90	0.1777	0.9213
0	0.29282	0.0007721	0.0689	50.02	197.21	247.23	0.1970	0.9190
4	0.33765	0.0007801	0.0600	55.35	194.19	249.53	0.2162	0.9169
8	0.38756	0.0007884	0.0525	60.73	191.07	251.80	0.2354	0.9150
12	0.44294	0.0007971	0.0460	66.18	187.85	254.03	0.2545	0.9132
16	0.50416	0.0008062	0.0405	71.69	184.52	256.22	0.2735	0.9116
20	0.57160	0.0008157	0.0358	77.26	181.09	258.35	0.2924	0.9102
24	0.64566	0.0008257	0.0317	82.90	177.55	260.45	0.3113	0.9089
26	0.68530	0.0008309	0.0298	85.75	175.73	261.48	0.3208	0.9082
28	0.72675	0.0008362	0.0281	88.61	173.89	262.50	0.3302	0.9076
30	0.77006	0.0008417	0.0265	91.49	172.00	263.50	0.3396	0.9070
32	0.81528	0.0008473	0.0250	94.39	170.09	264.48	0.3490	0.9064
34	0.86247	0.0008530	0.0236	97.31	168.14	265.45	0.3584	0.9058

(Continued)

TABLE A6.1a (CONTINUED)

Saturated Refrigerant-134a—Temperature Table

Temp., $T^{\circ}\text{C}$	Press., P_{sat} MPa	Specific Volume, m^3/kg		Enthalpy, kJ/kg			Entropy, kJ/(kg·K)	
		Sat. Liquid, v_f	Sat. Vapor, v_g	Sat. Liquid, h_f	Evap., h_{fg}	Sat. Vapor, h_g	Sat. Liquid, s_f	Sat. Vapor, s_g
36	0.91168	0.0008590	0.0223	100.25	166.15	266.40	0.3678	0.9053
38	0.96298	0.0008651	0.0210	103.21	164.12	267.33	0.3772	0.9047
40	1.0164	0.0008714	0.0199	106.19	162.05	268.24	0.3866	0.9041
42	1.0720	0.0008780	0.0188	109.19	159.94	269.14	0.3960	0.9035
44	1.1299	0.0008847	0.0177	112.22	157.79	270.01	0.4054	0.9030
48	1.2526	0.0008989	0.0159	118.35	153.33	271.68	0.4243	0.9017
52	1.3851	0.0009142	0.0142	124.58	148.66	273.24	0.4432	0.9004
56	1.5278	0.0009308	0.0127	130.93	143.75	274.68	0.4622	0.8990
60	1.6813	0.0009488	0.0114	137.42	138.57	275.99	0.4814	0.8973
70	2.1162	0.0010027	0.0086	154.34	124.08	278.43	0.5302	0.8918
80	2.6324	0.0010766	0.0064	172.71	106.41	279.12	0.5814	0.8827
90	3.2435	0.0011949	0.0046	193.69	82.63	276.32	0.6380	0.8655
100	3.9742	0.0015443	0.0027	224.74	34.40	259.13	0.7196	0.8117

Source: Wilson, D.P. and R.S. Basu. Thermodynamic properties of a new stratospherically safe working fluid-refrigerant-134a. *ASHRAE Trans.* 94(2):2095–2118, 1988.

TABLE A6.1b

Saturated Refrigerant-134a—Pressure Table

Press., P (MPa)	Temp., T_{sat} ($^{\circ}\text{C}$)	Specific Volume, m^3/kg		Enthalpy, kJ/kg			Entropy, kJ/(kg·K)	
		Sat. Liquid, v_f	Sat. Vapor, v_g	Sat. Liquid, h_f	Evap., h_{fg}	Sat. Vapor, h_g	Sat. Liquid, s_f	Sat. Vapor, s_g
0.06	-37.07	0.0007097	0.3100	3.46	221.27	224.72	0.0147	0.9520
0.08	-31.21	0.0007184	0.2366	10.47	217.92	228.39	0.0440	0.9447
0.10	-26.43	0.0007258	0.1917	16.29	215.06	231.35	0.0678	0.9395
0.12	-22.36	0.0007323	0.1614	21.32	212.54	233.86	0.0879	0.9354
0.14	-18.80	0.0007381	0.1395	25.77	210.27	236.04	0.1055	0.9322
0.16	-15.62	0.0007435	0.1229	29.78	208.18	237.97	0.1211	0.9295
0.18	-12.73	0.0007485	0.1098	33.45	206.26	239.71	0.1352	0.9273
0.20	-10.09	0.0007532	0.0993	36.84	204.46	241.30	0.1481	0.9253
0.24	-5.37	0.0007618	0.0834	42.95	201.14	244.09	0.1710	0.9222
0.28	-1.23	0.0007697	0.0719	48.39	198.13	246.52	0.1911	0.9197

TABLE A6.1b (CONTINUED)

Saturated Refrigerant-134a—Pressure Table

Press., <i>P</i> (MPa)	Temp., <i>T</i> _{sat} (°C)	Specific Volume, m ³ /kg		Enthalpy, kJ/kg			Entropy, kJ/(kg·K)	
		Sat. Liquid, <i>v</i> _f	Sat. Vapor, <i>v</i> _g	Sat. Liquid, <i>h</i> _f	Evap., <i>h</i> _{fg}	Sat. Vapor, <i>h</i> _g	Sat. Liquid, <i>s</i> _f	Vapor, <i>s</i> _g
0.32	2.48	0.0007770	0.0632	53.31	195.35	248.66	0.2089	0.9177
0.36	5.84	0.0007839	0.0564	57.82	192.76	250.58	0.2251	0.9160
0.4	8.93	0.0007904	0.0509	62.00	190.32	252.32	0.2399	0.9145
0.5	15.74	0.0008056	0.0409	71.33	184.74	256.07	0.2723	0.9117
0.6	21.58	0.0008196	0.0341	79.48	179.71	259.19	0.2999	0.9097
0.7	26.72	0.0008328	0.0292	86.78	175.07	261.85	0.3242	0.9080
0.8	31.33	0.0008454	0.0255	93.42	170.73	264.15	0.3459	0.9066
0.9	35.53	0.0008576	0.0226	99.56	166.62	266.18	0.3656	0.9054
1.0	39.39	0.0008695	0.0202	105.29	162.68	267.97	0.3838	0.9043
1.2	46.32	0.0008928	0.0166	115.76	155.23	270.99	0.4164	0.9023
1.4	52.43	0.0009159	0.0140	125.26	148.14	273.40	0.4453	0.9003
1.6	57.92	0.0009392	0.0121	134.02	141.31	275.33	0.4714	0.8982
1.8	62.91	0.0009631	0.0105	142.22	134.60	276.83	0.4954	0.8959
2.0	67.49	0.0009878	0.0093	149.99	127.95	277.94	0.5178	0.8934
2.5	77.59	0.0010562	0.0069	168.12	111.06	279.17	0.5687	0.8854
3.0	86.22	0.0011416	0.0053	185.30	92.71	278.01	0.6156	0.8735

Source: Wilson, D. P. and R. S. Basu. Thermodynamic properties of a new stratospherically safe working fluid-refrigerant-134a. *ASHRAE Trans.* 94(2):2095–2118, 1988.

T (°C)	v (m³/kg)	h (kJ/kg)	s [kJ/(kg·K)]	$P = 0.10 \text{ MPa}$ ($T_{\text{sat}} = -26.43^\circ\text{C}$)		$P = 0.14 \text{ MPa}$ ($T_{\text{sat}} = -18.80^\circ\text{C}$)		$P = 0.14 \text{ MPa}$ ($T_{\text{sat}} = -18.80^\circ\text{C}$)	
Sat.	0.31003	224.72	0.9520	0.19170	231.35	0.9395	0.13945	236.04	0.9322
-20	0.33536	237.98	1.0062	0.19770	236.54	0.9602	0.14549	243.40	0.9606
-10	0.34992	245.96	1.0371	0.20686	244.70	0.9918	0.15219	251.86	0.9922
0	0.36433	254.10	1.0675	0.21587	252.99	1.0227	0.1531	0.15875	1.0230
10	0.37861	262.41	1.0973	0.22473	261.43	1.0531	0.16520	269.13	1.0532
20	0.39279	270.89	1.1267	0.23349	270.02	1.0829	0.17155	277.97	1.0828
30	0.40688	279.53	1.1557	0.24216	278.76	1.1122	0.17833	286.96	1.1120
40	0.42091	288.35	1.1844	0.25076	287.66	1.1411	0.18404	296.09	1.1407
50	0.43487	297.34	1.2126	0.25930	296.72	1.1696	0.19020	305.37	1.1690
60	0.44879	306.51	1.2405	0.26779	305.94	1.1977	0.19633	314.80	1.1969
70	0.46266	315.84	1.2681	0.27623	315.32	1.2254	0.20241	324.39	1.2244
80	0.47650	325.34	1.2954	0.28464	324.87	1.2528	0.20846	334.14	1.2516
90	0.49031	335.00	1.3224	0.29302	334.57	1.2799	0.21449	344.04	1.2785
100									
Sat.	0.10983	239.71	0.9273	0.09933	241.30	0.9253	0.08343	244.09	0.9222
-10	0.11135	242.06	0.9362	0.09938	241.38	0.9256	0.08574	248.89	0.9399
0	0.11678	250.69	0.9684	0.10438	250.10	0.9582	0.08993	257.84	0.9721
10	0.12207	259.41	0.9998	0.10922	258.89	0.9898	0.09339	266.85	1.0034
20	0.12723	268.23	1.0304	0.11394	267.78	1.0206	0.09794	275.95	1.0339
30	0.13230	277.17	1.0604	0.11856	276.77	1.0508	0.10181	285.16	1.0637
40	0.13730	286.24	1.0898	0.12311	285.88	1.0804	0.10562	294.47	1.0930
50	0.14222	295.45	1.1187	0.12758	295.12	1.1094			

FIGURE A6.1
Superheated refrigerant-134a.

(Continued)

$P = 0.28 \text{ MPa}$ ($T_{\text{sat}} = -1.23^\circ\text{C}$)							$P = 0.32 \text{ MPa}$ ($T_{\text{sat}} = -2.48^\circ\text{C}$)							$P = 0.40 \text{ MPa}$ ($T_{\text{sat}} = 8.93^\circ\text{C}$)											
Sat.	0.07193	246.52	0.9197	0.06322	248.66	0.9177	0.05089	252.32	0.9145																
0	0.07240	247.64	0.9238																						
10	0.07613	256.76	0.9566	0.06576	255.65	0.9427	0.05119	253.35	0.9182																
20	0.07972	265.91	0.9883	0.06901	264.95	0.9749	0.05397	262.96	0.9515																
30	0.08320	275.12	1.0192	0.07214	274.28	1.0062	0.05662	272.54	0.8937																
40	0.08660	284.42	1.0494	0.07518	283.67	1.0367	0.05917	282.14	1.0148																
50	0.08992	293.81	1.0789	0.07815	293.15	1.0665	0.06164	291.79	1.0452																
60	0.09319	303.32	1.1079	0.08106	302.72	1.0957	0.06405	301.51	1.0748																
70	0.09641	312.95	1.1364	0.08392	312.41	1.1243	0.06641	311.32	1.1038																
80	0.09960	322.71	1.1644	0.08674	322.22	1.1525	0.06873	321.23	1.1322																
90	0.10275	332.60	1.1920	0.08953	332.15	1.1802	0.07102	331.25	1.1602																
100	0.10587	342.62	1.2193	0.09229	342.21	1.1076	0.07327	341.38	1.1878																
110	0.10897	352.78	1.2461	0.09503	352.40	1.2345	0.07550	351.64	1.2149																
120	0.11205	363.08	1.2727	0.09774	362.73	1.2611	0.07771	362.03	1.2417																
130										0.07991	372.54	1.2681													
140										0.08208	383.18	1.2941													
$P = 0.50 \text{ MPa}$ ($T_{\text{sat}} = 15.74^\circ\text{C}$)							$P = 0.60 \text{ MPa}$ ($T_{\text{sat}} = 21.58^\circ\text{C}$)							$P = 0.70 \text{ MPa}$ ($T_{\text{sat}} = 26.72^\circ\text{C}$)											
Sat.	0.04086	256.07	0.9117	0.03408	259.19	0.9097	0.02918	261.85	0.9080																
20	0.04188	260.34	0.9264	0.03581	267.89	0.9388	0.02979	265.37	0.9197																
30	0.04416	270.28	0.9597																						

FIGURE A6.1 (CONTINUED)
Superheated refrigerant-134a.

(Continued)

T (°C)	ν (m ³ /kg)	h (kJ/kg)	s [kJ/(kg·K)]	$P = 0.50 \text{ MPa } (T_{\text{sat}} = 15.74^\circ\text{C})$		$P = 0.60 \text{ MPa } (T_{\text{sat}} = 21.58^\circ\text{C})$		$P = 0.70 \text{ MPa } (T_{\text{sat}} = 26.72^\circ\text{C})$	
40	0.04633	280.16	0.9918	0.03774	278.09	0.9719	0.03157	275.93	0.9539
50	0.04842	290.04	1.0229	0.03958	288.23	1.0037	0.03324	286.35	0.9867
60	0.05043	299.95	1.0531	0.04134	298.35	1.0346	0.03482	296.69	1.0182
70	0.05240	309.92	1.0825	0.04304	308.48	1.0645	0.03634	307.01	1.0487
80	0.05432	319.96	1.1114	0.04469	318.67	1.0938	0.03781	317.35	1.0784
90	0.05620	330.10	1.1397	0.04631	328.93	1.1225	0.03924	327.74	1.1074
100	0.05805	340.33	1.1675	0.04790	339.27	1.1505	0.04064	338.19	1.1358
110	0.05988	350.68	1.1949	0.04946	349.70	1.1781	0.04201	348.71	1.1637
120	0.06168	361.14	1.2218	0.05099	360.24	1.2053	0.04335	359.33	1.1910
130	0.06347	371.72	1.2484	0.05251	370.88	1.2320	0.04468	370.04	1.2179
140	0.06524	382.42	1.2746	0.05402	381.64	1.2584	0.04599	380.86	1.2444
150				0.05550	392.52	1.2844	0.04729	391.79	1.2706
160				0.05698	403.51	1.3100	0.04857	402.82	1.2963
$P = 0.80 \text{ MPa } (T_{\text{sat}} = 31.33^\circ\text{C})$				$P = 0.90 \text{ MPa } (T_{\text{sat}} = 35.53^\circ\text{C})$		$P = 1.00 \text{ MPa } (T_{\text{sat}} = 39.39^\circ\text{C})$		$P = 1.00 \text{ MPa } (T_{\text{sat}} = 39.39^\circ\text{C})$	
Sat.	0.02547	264.15	0.9066	0.02255	266.18	0.9054	0.02020	267.97	0.9043
40	0.02691	273.66	0.9374	0.02325	271.25	0.9217	0.02029	268.68	0.9066
50	0.02846	284.39	0.9711	0.02472	282.34	0.9566	0.02171	280.19	0.9428
60	0.02992	294.98	1.0034	0.02609	293.21	0.9897	0.02301	291.36	0.9768
70	0.03131	305.50	1.0345	0.02738	303.94	1.0214	0.02423	302.34	1.0093
80	0.03264	316.00	1.0647	0.02861	314.62	1.0521	0.02538	313.20	1.0405
90	0.03393	326.52	1.0940	0.02980	325.28	1.0819	0.02649	324.01	1.0707
100	0.03519	337.08	1.1227	0.03095	335.96	1.1109	0.02755	334.82	1.1000
110	0.03642	347.71	1.1508	0.03207	346.68	1.1392	0.02858	345.65	1.1286

FIGURE A6.1 (CONTINUED)
Superheated refrigerant-134a.

(Continued)

				$P = 1.20 \text{ MPa}$ ($T_{\text{sat}} = 46.32^\circ\text{C}$)	$P = 1.40 \text{ MPa}$ ($T_{\text{sat}} = 52.43^\circ\text{C}$)	$P = 1.60 \text{ MPa}$ ($T_{\text{sat}} = 57.92^\circ\text{C}$)
Sat.	0.01663	270.99	0.9023	0.01405	273.40	0.9003
50	0.01712	275.52	0.9164			
60	0.01835	287.44	0.9527	0.01495	283.10	0.9297
70	0.01947	298.96	0.9868	0.01603	295.31	0.9658
80	0.02051	310.24	1.0192	0.01701	307.10	0.9997
90	0.02150	321.39	1.0503	0.01792	318.63	1.0319
100	0.02244	332.47	1.0804	0.01878	330.32	1.0628
110	0.02335	343.52	1.1096	0.01960	341.32	1.0927
120	0.02423	354.58	1.1381	0.02039	352.59	1.1218
130	0.02508	365.68	1.1660	0.02115	363.86	1.1501
140	0.02592	376.83	1.1933	0.02189	375.15	1.1777
150	0.02674	388.04	1.2201	0.02262	386.49	1.2048
160	0.02754	399.33	1.2465	0.02333	397.89	1.2315
170	0.02834	410.70	1.2724	0.02403	409.36	1.2576
180	0.02912	422.16	1.2980	0.02472	420.90	1.2834
190				0.02541	432.53	1.3088
200				0.02608	444.24	1.3338

FIGURE A6.1 (CONTINUED)
Superheated refrigerant-134a. (From Wilson, D.P. and R.S. Basu. Thermodynamic properties of a new stratospherically safe working fluid-refrigerant-134a. *ASHRAE Trans.* 94(2):2095-2118, 1988.)

TABLE A6.2Properties of Ammonia, NH₃

<i>t</i>	<i>p</i>	Saturated					Degrees of Superheat			
		<i>v_g</i>	<i>h_f</i>	<i>h_g</i>	<i>s_f</i>	<i>s_g</i>	100°F		200°F	
							<i>h</i>	<i>s</i>	<i>h</i>	<i>s</i>
-70	3.94	61.65	-31.1	584.4	-0.0771	1.5026	635.6	1.6214	686.2	1.7151
-65	4.69	52.34	-26.0	586.6	-0.0642	1.4833	638.0	1.6058	688.7	1.6990
-60	5.55	44.73	-20.9	588.8	-0.0514	1.4747	640.3	1.5907	691.1	1.6834
-55	6.54	38.38	-15.7	591.0	-0.0381	1.4614	642.6	1.5761	693.6	1.6683
-50	7.67	33.08	-10.5	593.2	-0.0254	1.4487	644.9	1.5620	696.1	1.6537
-45	8.95	28.62	-5.3	595.4	-0.0128	1.4363	647.2	1.5484	698.6	1.6395
-40	10.41	24.86	0	597.6	0	1.4242	649.4	1.5353	701.0	1.6260
-35	12.05	21.68	5.3	599.5	0.0126	1.4120	651.7	1.5226	703.4	1.6129
-30	13.90	18.97	10.7	601.4	0.0250	1.4001	653.9	1.5103	705.9	1.6002
-25	15.98	16.66	16.0	603.2	0.0374	1.3886	656.1	1.4983	708.3	1.5878
-20	18.30	14.68	21.4	605.0	0.0497	1.3774	658.3	1.4868	710.8	1.5759
-15	20.88	12.97	26.7	606.7	0.0618	1.3664	660.5	1.4756	713.2	1.5644
-10	23.74	11.50	32.1	608.5	0.0738	1.3558	662.6	1.4647	715.5	1.5531
-5	26.92	10.23	37.5	610.1	0.0857	1.3454	664.7	1.4541	717.9	1.5423
0	30.42	9.116	42.9	611.8	0.0975	1.3352	666.8	1.4438	720.3	1.5317
5	34.27	8.150	48.3	613.3	0.1092	1.3253	668.9	1.4338	722.7	1.5214
10	38.51	7.304	53.8	614.9	0.1208	1.3157	670.9	1.4241	725.0	1.5115
15	43.14	6.562	59.2	616.3	0.1323	1.3062	672.9	1.4147	727.3	1.5018
20	48.21	5.910	64.7	617.8	0.1437	1.2969	675.0	1.4055	729.6	1.4924
25	53.73	5.334	70.2	619.1	0.1551	1.2879	677.0	1.3966	731.9	1.4833
30	59.74	4.825	75.7	620.5	0.1663	1.2790	678.9	1.3879	734.2	1.4744
35	66.26	4.373	81.2	621.7	0.1775	1.2704	680.8	1.3794	736.4	1.4658
40	73.32	3.971	86.8	623.0	0.1885	1.2618	682.7	1.3711	738.6	1.4575
45	80.96	3.614	92.3	624.1	0.1996	1.2535	684.5	1.3630	740.9	1.4493
50	89.19	3.294	97.9	625.2	0.2105	1.2453	686.4	1.3551	743.1	1.4413
55	98.06	3.008	103.5	626.3	0.2214	1.2373	688.2	1.3474	745.2	1.4335
60	107.6	2.751	109.2	627.3	0.2322	1.2294	689.9	1.3399	747.4	1.4260
65	117.8	2.520	114.8	628.2	0.2430	1.2216	691.6	1.3326	749.5	1.4186
70	128.8	2.312	120.5	629.1	0.2537	1.2140	693.3	1.3254	751.6	1.4114
75	140.5	2.125	126.2	629.9	0.2643	1.2065	694.9	1.3184	753.7	1.4044
80	153.0	1.955	132.0	630.7	0.2749	1.1991	696.6	1.3115	755.8	1.3976
85	166.4	1.801	137.8	631.4	0.2854	1.1918	698.1	1.3048	757.9	1.3909
90	180.6	1.661	143.5	632.0	0.2958	1.1846	699.7	1.2982	759.9	1.3843

TABLE A6.2 (CONTINUED)Properties of Ammonia, NH₃

<i>t</i>	<i>p</i>	Saturated					Degrees of Superheat			
		<i>v_g</i>	<i>h_f</i>	<i>h_g</i>	<i>s_f</i>	<i>s_g</i>	100°F		200°F	
							<i>h</i>	<i>s</i>	<i>h</i>	<i>s</i>
95	195.8	1.534	149.4	632.6	0.3062	1.1775	701.2	1.2918	761.8	1.3779
100	211.9	1.419	155.2	633.0	0.3166	1.1705	702.7	1.2855	763.8	1.3717
105	228.9	1.313	161.1	633.4	0.3269	1.1635	704.2	1.2793	765.7	1.3656
110	247.0	1.217	167.0	633.7	0.3372	1.1566	705.6	1.2732	767.6	1.3596
115	266.2	1.128	173.0	633.9	0.3474	1.1497	706.9	1.2672	769.5	1.3538
120	286.4	1.047	179.0	634.0	0.3576	1.1427	708.2	1.2613	771.3	1.3480
125	307.8	0.973	185.1	634.0	0.3679	1.1358	709.5	1.2555	773.1	1.3423

Note: *t*, °F; *p*, psia; *v_g*, ft³/lb; *h_f*, Btu/lb; *h_g*, Btu/lb; *s_f*, Btu/lb·°R; *s_g*, Btu/lb·°R; *h*, Btu/lb; *s*, Btu/lb·°R.

TABLE A6.3Psychrometric Table—SI Units; Properties of Moist Air at 101,325 N/m²

Temperature			Properties ^a						
°C	K	°F	<i>P_s</i>	<i>W_s</i>	<i>V_a</i>	<i>V_s</i>	<i>h_a</i>	<i>h_s</i>	<i>s_s</i>
-40	233.15	-40	12.838	0.00007925	0.65961	0.65968	-22.35	-22.16	-90.659
-30	243.15	-22	37.992	0.0002344	0.68808	0.68833	-12.29	-11.72	-46.732
-25	248.15	-13	63.248	0.0003903	0.70232	0.70275	-7.265	-6.306	-24.706
-20	253.15	-4	103.19	0.0006371	0.71649	0.71724	-2.236	-0.6653	-2.2194
-15	258.15	+5	165.18	0.001020	0.73072	0.73191	+2.794	5.318	21.189
-10	263.15	14	259.72	0.001606	0.74495	0.74683	7.823	11.81	46.104
-5	268.15	23	401.49	0.002485	0.75912	0.76218	12.85	19.04	73.365
0	273.15	32	610.80	0.003788	0.77336	0.77804	17.88	27.35	104.14
5	278.15	41	871.93	0.005421	0.78759	0.79440	22.91	36.52	137.39
10	283.15	50	1227.2	0.007658	0.80176	0.81163	27.94	47.23	175.54
15	288.15	59	1704.4	0.01069	0.81600	0.82998	32.97	59.97	220.22
20	293.15	68	2337.2	0.01475	0.83017	0.84983	38.00	75.42	273.32
25	298.15	77	3167.0	0.02016	0.84434	0.87162	43.03	94.38	337.39
30	303.15	86	4242.8	0.02731	0.85851	0.89609	48.07	117.8	415.65
35	308.15	95	5623.4	0.03673	0.87274	0.92406	53.10	147.3	512.17
40	313.15	104	7377.6	0.04911	0.86692	0.95665	58.14	184.5	532.31
45	318.15	113	9584.8	0.06536	0.90115	0.99535	63.17	232.0	783.06
50	323.15	122	12339	0.08678	0.91532	1.0423	68.21	293.1	975.27
55	328.15	131	15745	0.1152	0.92949	1.1007	73.25	372.9	1221.5
60	333.15	140	19925	0.1534	0.94372	1.1748	78.29	478.5	1543.5

(Continued)

TABLE A6.3 (CONTINUED)Psychrometric Table—SI Units; Properties of Moist Air at 101,325 N/m²

Temperature			Properties ^a						
°C	K	°F	P_s	W_s	V_a	V_s	h_a	h_s	s_s
65	338.15	149	25014	0.2055	0.95790	1.2721	83.33	621.4	1973.6
70	343.15	158	31167	0.2788	0.97207	1.4042	88.38	820.5	2564.8
75	348.15	167	38554	0.3858	0.98630	1.5924	93.42	1110	3412.8
80	353.15	176	47365	0.5519	1.0005	1.8791	98.47	1557	4710.9
85	358.15	185	57809	0.8363	1.0146	2.3632	103.5	2321	6892.6
90	363.15	194	70112	1.416	1.0288	3.3409	108.6	3876	11281

Source: Abstracted from Bolz, R.E. and G.L. Tuve, eds., *CRC Handbook of Tables for Applied Engineering Science*, 2nd ed., Chemical Rubber Co., Cleveland, Ohio, 1973.

Note: P_s = pressure of water vapor at saturation, N/m²; W_s = humidity ratio at saturation, mass of water vapor associated with unit mass of dry air; V_a = specific volume of dry air, m³/kg; V_s = specific volume of saturated mixture, m³/kg dry air; h_a = specific enthalpy of dry air, kJ/kg; h_s = specific enthalpy of saturated mixture, kJ/kg dry air; s_s = specific entropy of saturated mixture, J/K·kg dry air.

^a The P_s column gives the vapor pressure of pure water at temperature intervals of 5°C. For the latest data on vapor pressures at intervals of 0.1°C, from 0°C to 100°C, see Wexler, A. and L. Greenspan, Vapor pressure equation for water, *J. Res. Natl. Bur. Stand. Sect. A*, 75(3):213–229, May–June 1971. For very low barometric pressures and wet-bulb temperatures, the values of h_a here are somewhat low; for corrections, see the *Handbook of Fundamentals*, American Society of Heating, Refrigerating, and Air-Conditioning Engineers, 1972.

TABLE A6.4
Refrigerant Temperature ($t' = ^\circ\text{C}$) and Enthalpy ($h = \text{kJ/kg}$) of Lithium Bromide Solutions

Temp (t = °C)	Percent LiBr						
	0	10	20	30	40	45	50
20	<i>t'</i>	20	19.1	17.7	15.0	9.8	5.8
	<i>h</i>	84.0	67.4	52.6	40.4	33.5	38.9
30	<i>t'</i>	30.0	29.0	27.5	24.6	19.2	15.0
	<i>h</i>	125.8	103.3	84.0	68.6	58.3	56.8
40	<i>t'</i>	40.0	38.9	37.3	34.3	28.5	24.1
	<i>h</i>	167.6	139.5	115.8	96.0	82.5	79.7
50	<i>t'</i>	50.0	48.8	47.2	44.0	37.9	33.3
	<i>h</i>	209.3	175.2	147.0	123.4	106.7	102.6
60	<i>t'</i>	60.0	58.8	57.0	53.6	47.3	42.5
	<i>h</i>	251.1	211.7	179.1	151.4	131.7	125.8
70	<i>t'</i>	70.0	68.7	66.8	63.3	56.6	51.6
	<i>h</i>	293.0	247.7	210.5	178.8	155.7	148.9
80	<i>t'</i>	80.0	78.6	76.7	73.0	66.0	60.8
	<i>h</i>	334.9	287.8	243.6	207.3	181.0	172.8
90	<i>t'</i>	90.0	88.6	86.5	82.6	75.4	70.0
	<i>h</i>	376.9	321.1	275.6	235.4	206.1	195.8
100	<i>t'</i>	100.0	98.5	96.3	92.3	84.7	79.1
	<i>h</i>	419.0	357.6	307.9	263.8	231.0	219.9
110	<i>t'</i>	110.0	108.4	106.2	101.9	94.1	88.3
	<i>h</i>	461.3	394.3	340.1	292.4	255.9	243.3
120	<i>t'</i>	120.0 ^b	118.3 ^b	116.0 ^b	111.6	103.4	97.5

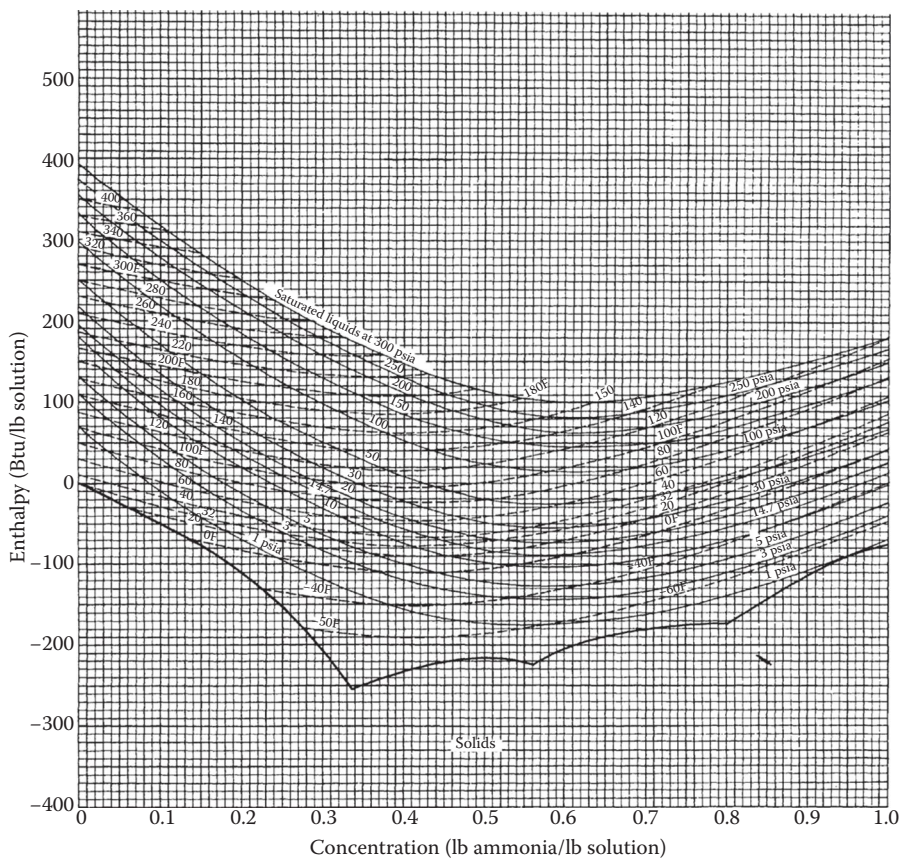
(Continued)

TABLE A6.4 (CONTINUED)
Refrigerant Temperature ($t' = {}^\circ\text{C}$) and Enthalpy ($h = \text{kJ/kg}$) of Lithium Bromide Solutions

Temp ($t = {}^\circ\text{C}$)	Percent LiBr											
	0	10	20	30	40	50	60					
130	h	503.7 ^b	431.0 ^b	372.5 ^b	320.9	281.0	267.0	259.0	260.0	270.2	289.5	313.4
	t'	130.0 ^b	128.3 ^b	125.8 ^b	121.3 ^b	112.8	106.7	92.8	88.7	78.4	67.1	55.0
140	h	546.5 ^b	468.4 ^b	404.5 ^b	349.6 ^b	306.2	290.7	281.0	280.4	289.1	306.9	330.2
	t'	140.0 ^b	138.2 ^b	135.7 ^b	130.9 ^b	122.2 ^b	115.8	107.1	97.4	87.0	75.3	62.7
150	h	589.1 ^b	505.6 ^b	437.8 ^b	377.9 ^b	331.3 ^b	314.2	303.2	301.1	308.1	324.7	346.9
	t'	150.0 ^b	148.1 ^b	145.5 ^b	140.6 ^b	131.5 ^b	125.0 ^b	116.1 ^b	106.2	95.5	83.5	70.3
160	h	632.2 ^b	542.7 ^b	470.5 ^b	406.8 ^b	356.6 ^b	337.8 ^b	325.5 ^b	321.6	327.3	342.7	363.6
	t'	160.0 ^b	158.1 ^b	155.3 ^b	150.3 ^b	140.9 ^b	134.2 ^b	125.0 ^b	115.0	104.1	91.8	78.9
170	h	675.6 ^b	580.8 ^b	503.1 ^b	435.4 ^b	381.9 ^b	361.2 ^b	347.7 ^b	342.2	346.1	360.3	380.1
	t'	170.0 ^b	168.0 ^b	165.2 ^b	159.9 ^b	150.3 ^b	143.3 ^b	134.0 ^b	123.7	112.7	100.0	85.7
180	h	719.2 ^b	618.9 ^b	536.1 ^b	464.3 ^b	406.8 ^b	384.9 ^b	369.9 ^b	362.9	365.4	378.3	396.0
	t'	180.0 ^b	177.9 ^b	175.0 ^b	169.6 ^b	159.6 ^b	152.5 ^b	142.9 ^b	132.5 ^b	121.2 ^b	108.2	93.3
h	h	763.2 ^b	657.1 ^b	569.4 ^b	493.4 ^b	432.1 ^b	408.8 ^b	392.1 ^b	383.4 ^b	384.3 ^b	395.8	411.3

^a Supersaturated solution.

^b Extensions of data above 115°C are well above the original data and should be used with care.

**FIGURE A6.2**

Thermodynamic properties of ammonia–water mixtures used for absorption air conditioning.

Appendix 7: Supplementary Material for Chapter 7

TABLE A7.1

Designations and Characteristics for 94 Reference Passive Systems

(a) Overall System Characteristics

<i>Masonry Properties</i>	
Thermal conductivity (<i>k</i>)	
Sunspace floor	0.5 Btu/h/ft/°F
All other masonry	1.0 Btu/h/ft/°F
Density (<i>Q</i>)	150 lb/ft ³
Specific heat (<i>c</i>)	0.2 Btu/lb/°F
Infrared emittance of normal surface	0.9
Infrared emittance of selective surface	0.1
<i>Solar Absorptances</i>	
Waterwall	1.0
Masonry, Trombe wall	1.0
Direct gain and sunspace	0.8
Sunspace: water containers	0.9
Lightweight common wall	0.7
Other lightweight surfaces	0.3
<i>Glazing Properties</i>	
Transmission characteristics	Diffuse
Orientation	Due south
Index of refraction	1.526
Extinction coefficient	0.5 inch ⁻¹
Thickness of each pane	1/8 inch
Gap between panes	1/2 inch
Infrared emittance	0.9
<i>Control Range</i>	
Room temperature	65°F to 75°F
Sunspace temperature	45°F to 95°F
Internal heat generation	0
<i>Thermocirculation Vents (When Used)</i>	
Vent area/projected area (sum of both upper and lower vents)	0.06
Height between vents	8 ft
Reverse flow	None

(Continued)

TABLE A7.1 (CONTINUED)

Designations and Characteristics for 94 Reference Passive Systems

<i>Nighttime Insulation (When Used)</i>						
Thermal resistance					R9	
In place, solar time					5:30 p.m. to 7:30 a.m.	
<i>Solar Radiation Assumptions</i>						
Shading					None	
Ground diffuse reflectance					0.3	
<i>(b) Direct-Gain (DG) System Types</i>						
Designation	Thermal Storage Capacity ^a (in Btu/ ft ² /°F)	Mass Thickness ^a (inches)	Mass-Area-to-Glazing-Area Ratio	No. of Glazings	Nighttime Insulation	
A1	30	2	6	2	No	
A2	30	2	6	3	No	
A3	30	2	6	2	Yes	
B1	45	6	3	2	No	
B2	45	6	3	3	No	
B3	45	6	3	2	Yes	
C1	60	4	6	2	No	
C2	60	4	6	3	No	
C3	60	4	6	2	Yes	
<i>(c) Vented Trombe-Wall (TW) System Types</i>						
Designation	Thermal Storage Capacity ^a (Btu/ft ² /°F)	Wall Thickness ^a (inches)	ρck (Btu ² /h/ ft ⁴ /°F ²)	No. of Glazings	Wall Surface	Nighttime Insulation
A1	15	6	30	2	Normal	No
A2	22.5	9	30	2	Normal	No
A3	30	12	30	2	Normal	No
A4	45	18	30	2	Normal	No
B1	15	6	15	2	Normal	No
B2	22.5	9	15	2	Normal	No
B3	30	12	15	2	Normal	No
B4	45	18	15	2	Normal	No
C1	15	6	7.5	2	Normal	No
C2	22.5	9	7.5	2	Normal	No

TABLE A7.1 (CONTINUED)

Designations and Characteristics for 94 Reference Passive Systems

(c) Vented Trombe-Wall (TW) System Types

Designation	Thermal Storage Capacity ^a (Btu/ft ² /°F)	Wall Thickness ^a (inches)	ρck (Btu ² /h/ ft ⁴ /°F ²)	No. of Glazings	Wall Surface	Nighttime Insulation
C3	30	12	7.5	2	Normal	No
C4	45	18	7.5	2	Normal	No
D1	30	12	30	1	Normal	No
D2	30	12	30	3	Normal	No
D3	30	12	30	1	Normal	Yes
D4	30	12	30	2	Normal	Yes
D5	30	12	30	3	Normal	Yes
E1	30	12	30	1	Selective	No
E2	30	12	30	2	Selective	No
E3	30	12	30	1	Selective	Yes
E4	30	12	30	2	Selective	Yes

(d) Unvented Trombe-Wall (TW) System Types

Designation	Thermal Storage Capacity ^a (Btu/ft ² /°F)	Wall Thickness ^a (inches)	ρck (Btu ² /h/ ft ⁴ /°F ²)	No. of Glazings	Wall Surface	Nighttime Insulation
F1	15	6	30	2	Normal	No
F2	22.5	9	30	2	Normal	No
F3	30	12	30	2	Normal	No
F4	45	18	30	2	Normal	No
G1	15	6	15	2	Normal	No
G2	22.5	9	15	2	Normal	No
G3	30	12	15	2	Normal	No
G4	45	18	15	2	Normal	No
H1	15	6	7.5	2	Normal	No
H2	22.5	9	7.5	2	Normal	No
H3	30	12	7.5	2	Normal	No
H4	45	18	7.5	2	Normal	No
I1	30	12	30	1	Normal	No
I2	30	12	30	3	Normal	No
I3	30	12	30	1	Normal	Yes
I4	30	12	30	2	Normal	Yes
I5	30	12	30	3	Normal	Yes
J1	30	12	30	1	Selective	No
J2	30	12	30	2	Selective	No

(Continued)

TABLE A7.1 (CONTINUED)

Designations and Characteristics for 94 Reference Passive Systems

(d) Unvented Trombe-Wall (TW) System Types

Designation	Thermal Storage Capacity ^a (Btu/ft ² /°F)	Wall Thickness ^a (inches)	ρck (Btu ² /h/ ft ⁴ /°F ²)	No. of Glazings	Wall Surface	Nighttime Insulation
J3	30	12	30	1	Selective	Yes
J4	30	12	30	2	Selective	Yes

(e) Waterwall (WW) System Types

Designation	Thermal Storage Capacity ^a (in Btu/ft ² /°F)	Wall Thickness (inches)	No. of Glazings	Wall Surface	Nighttime Insulation
A1	15.6	3	2	Normal	No
A2	31.2	6	2	Normal	No
A3	46.8	9	2	Normal	No
A4	62.4	12	2	Normal	No
A5	93.6	18	2	Normal	No
A6	124.8	24	2	Normal	No
B1	46.8	9	1	Normal	No
B2	46.8	9	3	Normal	No
B3	46.8	9	1	Normal	Yes
B4	46.8	9	2	Normal	Yes
B5	46.8	9	3	Normal	Yes
C1	46.8	9	1	Selective	No
C2	46.8	9	2	Selective	No
C3	46.8	9	1	Selective	Yes
C4	46.8	9	2	Selective	Yes

(f) Sunspace (SS) System Types

Designation	Type	Tilt (°)	Common Wall	End Walls	Nighttime Insulation
A1	Attached	50	Masonry	Opaque	No
A2	Attached	50	Masonry	Opaque	Yes
A3	Attached	50	Masonry	Glazed	No
A4	Attached	50	Masonry	Glazed	Yes
A5	Attached	50	Insulated	Opaque	No
A6	Attached	50	Insulated	Opaque	Yes
A7	Attached	50	Insulated	Glazed	No
A8	Attached	50	Insulated	Glazed	Yes
B1	Attached	90/30	Masonry	Opaque	No

TABLE A7.1 (CONTINUED)

Designations and Characteristics for 94 Reference Passive Systems

(f) *Sunspace (SS) System Types*

Designation	Type	Tilt (°)	Common Wall	End Walls	Nighttime Insulation
B2	Attached	90/30	Masonry	Opaque	Yes
B3	Attached	90/30	Masonry	Glazed	No
B4	Attached	90/30	Masonry	Glazed	Yes
B5	Attached	90/30	Insulated	Opaque	No
B6	Attached	90/30	Insulated	Opaque	Yes
B7	Attached	90/30	Insulated	Glazed	No
B8	Attached	90/30	Insulated	Glazed	Yes
C1	Semienclosed	90	Masonry	Common	No
C2	Semienclosed	90	Masonry	Common	Yes
C3	Semienclosed	90	Insulated	Common	No
C4	Semienclosed	90	Insulated	Common	Yes
D1	Semienclosed	50	Masonry	Common	No
D2	Semienclosed	50	Masonry	Common	Yes
D3	Semienclosed	50	Insulated	Common	No
D4	Semienclosed	50	Insulated	Common	Yes
E1	Semienclosed	90/30	Masonry	Common	No
E2	Semienclosed	90/30	Masonry	Common	Yes
E3	Semienclosed	90/30	Insulated	Common	No
E4	Semienclosed	90/30	Insulated	Common	Yes

Source: PSDH, *Passive Solar Design Handbook*, Van Nostrand Reinhold Co., New York, 1984.

^a The thermal storage capacity is per unit of projected area, or, equivalently, the quantity $\rho c k$. The wall thickness is listed only as an appropriate guide by assuming $\rho c = 30 \text{ Btu}/\text{ft}^3/\text{°F}$.

TABLE A7.2

LCR Tables for Six Representative Cities (Albuquerque, Boston, Madison, Medford, Nashville, and Santa Maria) LCR Units (Btu/ft²·F-day)

SSF	0.10	0.20	0.30	0.40	0.50	0.60	0.70	0.80	0.90
<i>Santa Maria, California</i>									
WW A1	1776	240	119	73	50	35	25	18	12
WW A2	617	259	154	103	74	54	39	28	19
WW A3	523	261	164	114	82	61	45	33	22
WW A4	482	260	169	119	87	65	48	35	24
WW A5	461	263	175	125	92	69	52	38	26
WW A6	447	263	177	128	95	72	54	40	27
WW B1	556	220	128	85	60	43	32	23	15
WW B2	462	256	168	119	88	66	49	36	25
WW B3	542	315	211	151	112	85	64	47	32
WW B4	455	283	197	144	109	83	63	47	32
WW B5	414	263	184	136	103	79	60	45	31
WW C1	569	330	221	159	118	89	67	49	33
WW C2	478	288	197	143	107	81	61	45	31
WW C3	483	318	228	170	130	100	77	57	40
WW C4	426	280	200	149	114	88	68	51	35
TW A1	1515	227	113	70	48	34	24	17	11
TW A2	625	234	134	89	63	46	33	24	16
TW A3	508	231	140	95	68	50	37	27	18
TW A4	431	217	137	95	69	51	38	28	19
TW B1	859	212	112	71	49	35	25	18	12
TW B2	502	209	124	83	59	43	32	23	15
TW B3	438	201	123	84	60	44	33	24	16
TW B4	400	184	112	76	55	40	30	22	14
TW C1	568	188	105	69	48	35	25	18	12
TW C2	435	178	105	70	50	36	27	19	13
TW C3	413	165	97	64	46	33	25	18	12
TW C4	426	146	82	54	38	27	20	14	10
TW D1	403	170	101	67	48	35	25	18	12
TW D2	488	242	152	105	76	57	42	31	21
TW D3	509	271	175	123	90	67	50	36	25
TW D4	464	266	177	127	94	71	53	39	27
TW D5	425	250	169	122	91	69	52	38	26
TW E1	581	309	199	140	102	76	57	42	28
TW E2	512	283	186	132	97	73	55	40	27
TW E3	537	328	225	164	123	94	71	53	36
TW E4	466	287	199	145	109	83	63	47	32
TW F1	713	198	107	68	47	34	25	18	12
TW F2	455	199	120	81	58	42	31	22	15

TABLE A7.2 (CONTINUED)

LCR Tables for Six Representative Cities (Albuquerque, Boston, Madison, Medford, Nashville, and Santa Maria) LCR Units (Btu/ft²·F-day)

SSF	0.10	0.20	0.30	0.40	0.50	0.60	0.70	0.80	0.90
<i>Santa Maria, California</i>									
TW F3	378	190	120	83	60	45	33	24	16
TW F4	311	169	110	77	57	42	32	23	16
TW G1	450	170	98	65	46	33	24	17	12
TW G2	331	163	102	70	51	38	28	20	14
TW G3	278	147	94	66	48	36	27	20	13
TW G4	222	120	78	55	40	30	22	16	11
TW H1	295	137	84	57	41	30	22	16	11
TW H2	226	118	75	52	38	28	21	15	10
TW H3	187	99	64	44	33	24	18	13	9
TW H4	143	75	48	33	24	18	14	10	7
TW I1	318	144	88	59	42	31	23	16	11
TW I2	377	203	132	93	68	51	38	28	19
TW I3	404	226	149	106	78	58	44	32	22
TW I4	387	230	156	113	84	64	48	36	24
TW I5	370	226	155	113	85	65	49	36	25
TW J1	483	271	179	127	94	71	53	39	26
TW J2	422	246	165	119	88	67	50	37	25
TW J3	446	283	199	146	111	85	65	48	33
TW J4	400	254	178	132	100	77	58	43	30
DG A1	392	188	117	79	55	38	26	16	7
DG A2	389	190	121	85	61	45	32	22	14
DG A3	443	220	142	102	77	58	44	31	19
DG B1	384	191	122	86	64	48	35	24	13
DG B2	394	196	127	91	69	53	40	29	19
DG B3	445	222	145	105	80	62	49	37	25
DG C1	451	225	146	104	78	61	47	34	21
DG C2	453	226	148	106	80	63	49	37	25
DG C3	509	254	167	121	92	73	58	45	31
SS A1	1171	396	220	142	98	69	49	34	22
SS A2	1028	468	283	190	135	98	71	50	33
SS A3	1174	380	209	133	91	64	45	31	20
SS A4	1077	481	289	193	136	98	71	50	32
SS A5	1896	400	204	127	86	60	42	29	18
SS A6	1030	468	283	190	135	97	71	50	32
SS A7	2199	359	178	109	72	50	35	24	15
SS A8	1089	478	285	190	133	96	69	48	31
SS B1	802	298	170	111	77	55	40	28	18
SS B2	785	366	224	152	108	79	57	41	27

(Continued)

TABLE A7.2 (CONTINUED)

LCR Tables for Six Representative Cities (Albuquerque, Boston, Madison, Medford, Nashville, and Santa Maria) LCR Units (Btu/ft²·F-day)

SSF	0.10	0.20	0.30	0.40	0.50	0.60	0.70	0.80	0.90
<i>Santa Maria, California</i>									3053 DD
SS B3	770	287	163	106	74	52	37	26	17
SS B4	790	368	224	152	108	78	57	40	26
SS B5	1022	271	144	91	62	44	31	22	14
SS B6	750	356	219	149	106	77	56	40	26
SS B7	937	242	127	80	54	38	27	19	12
SS B8	750	352	215	146	103	75	55	39	25
SS C1	481	232	144	99	71	52	39	28	19
SS C2	482	262	170	120	88	66	49	36	24
SS C3	487	185	107	71	50	36	27	19	13
SS C4	473	235	147	102	74	55	41	30	20
SS D1	1107	477	282	188	132	95	68	48	31
SS D2	928	511	332	232	169	125	92	66	43
SS D3	1353	449	248	160	110	78	56	39	25
SS D4	946	500	319	222	160	117	86	61	40
SS E1	838	378	227	153	108	78	56	40	26
SS E2	766	419	272	190	138	102	75	54	36
SS E3	973	322	178	115	79	56	40	28	18
SS E4	780	393	247	170	122	89	65	47	31
<i>Albuquerque, New Mexico</i>									4292 DD
WW A1	1052	130	62	38	25	18	13	9	6
WW A2	354	144	84	56	39	29	21	15	10
WW A3	300	146	90	62	45	33	24	18	12
WW A4	276	146	93	65	47	35	26	19	13
WW A5	264	148	97	69	50	38	28	21	14
WW A6	256	148	99	70	52	39	30	22	15
WW B1	293	111	63	41	28	20	15	11	7
WW B2	270	147	96	67	49	37	28	20	14
WW B3	314	179	119	84	62	47	35	26	18
WW B4	275	169	116	85	64	49	37	28	19
WW B5	252	159	110	81	61	47	36	27	19
WW C1	333	190	126	89	66	50	38	28	19
WW C2	287	171	115	83	62	47	36	27	18
WW C3	293	191	136	101	77	59	46	34	24
WW C4	264	172	122	91	69	54	41	31	22
TW A1	900	124	60	37	25	17	12	9	6
TW A2	361	130	73	48	33	24	18	13	8
TW A3	293	129	77	52	37	27	20	15	10

TABLE A7.2 (CONTINUED)

LCR Tables for Six Representative Cities (Albuquerque, Boston, Madison, Medford, Nashville, and Santa Maria) LCR Units (Btu/ft²·F-day)

SSF	0.10	0.20	0.30	0.40	0.50	0.60	0.70	0.80	0.90
<i>Albuquerque, New Mexico</i>									
TW A4	249	123	76	52	38	28	21	15	10
TW B1	502	117	60	38	26	18	13	9	6
TW B2	291	118	68	45	32	23	17	12	8
TW B3	254	114	68	46	33	24	18	13	9
TW B4	233	104	63	42	30	22	16	12	8
TW C1	332	106	58	37	26	19	14	10	6
TW C2	255	101	58	39	27	20	15	11	7
TW C3	243	94	54	36	25	18	13	10	7
TW C4	254	84	46	30	21	15	11	8	5
TW D1	213	86	50	33	23	17	12	9	6
TW D2	287	139	86	59	43	32	24	17	12
TW D3	294	153	97	68	49	37	27	20	14
TW D4	281	158	104	74	55	41	31	23	16
TW D5	260	151	101	73	54	41	31	23	16
TW E1	339	177	113	78	57	43	32	23	16
TW E2	308	168	109	77	56	42	32	23	16
TW E3	323	195	133	96	72	55	42	31	21
TW E4	287	175	120	88	66	50	38	28	20
TW F1	409	108	57	36	24	17	13	9	6
TW F2	260	110	65	43	31	22	17	12	8
TW F3	216	106	66	45	33	24	10	13	9
TW F4	178	95	61	42	31	23	17	13	9
TW G1	256	93	53	34	24	17	13	9	6
TW G2	189	91	56	38	27	20	15	11	7
TW G3	159	82	52	36	26	20	15	11	7
TW G4	128	68	43	30	22	16	12	9	6
TW H1	168	76	45	31	22	16	12	9	6
TW H2	130	66	41	29	21	15	11	8	6
TW H3	108	56	35	25	8	13	10	7	5
TW H4	83	42	27	19	13	10	7	5	4
TW I1	166	73	43	29	20	15	11	8	5
TW I2	221	117	75	52	30	28	21	16	11
TW I3	234	128	83	59	43	32	24	10	12
TW I4	234	137	92	66	49	37	28	21	14
TW I5	226	136	93	67	50	38	29	22	15
TW J1	282	156	102	72	53	40	30	22	15
TW J2	254	146	97	69	51	39	29	22	15
TW J3	269	169	118	86	65	50	38	29	20

(Continued)

TABLE A7.2 (CONTINUED)

LCR Tables for Six Representative Cities (Albuquerque, Boston, Madison, Medford, Nashville, and Santa Maria) LCR Units (Btu/ft²·F-day)

SSF	0.10	0.20	0.30	0.40	0.50	0.60	0.70	0.80	0.90
<i>Albuquerque, New Mexico</i>									
TW J4	247	155	106	80	60	46	35	26	18
DG A1	211	97	57	36	22	13	5	—	—
DG A2	227	107	67	46	32	23	16	10	5
DG A3	274	131	83	59	44	34	25	18	10
DG B1	210	97	60	42	30	21	13	6	—
DG B2	232	110	69	49	37	28	21	14	8
DG B3	277	134	85	61	47	37	28	21	14
DG C1	253	120	74	53	39	30	22	14	—
DG C2	271	130	82	59	45	35	26	19	12
DG C3	318	155	96	71	54	43	34	26	18
SS A1	591	187	101	64	44	31	22	16	10
SS A2	531	232	137	92	65	47	34	25	16
SS A3	566	170	90	56	38	27	19	13	8
SS A4	537	230	135	89	63	45	33	23	15
SS A5	980	187	92	56	37	26	18	13	8
SS A6	529	231	136	91	64	47	34	24	16
SS A7	1103	158	74	44	29	20	14	10	6
SS A8	540	226	131	87	61	44	32	23	15
SS B1	403	141	78	50	35	25	18	13	8
SS B2	412	186	111	75	53	39	28	20	14
SS B3	372	130	71	46	31	22	16	11	7
SS B4	403	181	106	72	51	37	27	20	13
SS B5	518	127	65	40	27	19	13	9	6
SS B6	390	179	106	73	52	38	28	20	13
SS B7	457	108	54	33	22	16	11	8	5
SS B8	379	171	102	69	49	35	26	19	12
SS C1	270	126	77	52	37	27	20	15	10
SS C2	282	150	97	68	49	37	28	20	14
SS C3	276	101	57	37	26	19	14	10	7
SS C4	277	135	83	57	41	31	23	17	11
SS D1	548	225	130	85	59	43	31	22	14
SS D2	474	253	162	113	82	61	45	33	22
SS D3	683	212	113	72	49	35	25	17	11
SS D4	484	248	156	107	77	57	42	30	20
SS E1	410	176	103	68	48	35	25	18	12
SS E2	390	208	133	92	67	50	37	27	18
SS E3	487	151	80	51	35	25	18	12	8
SS E4	400	195	120	82	59	43	32	23	15

TABLE A7.2 (CONTINUED)

LCR Tables for Six Representative Cities (Albuquerque, Boston, Madison, Medford, Nashville, and Santa Maria) LCR Units (Btu/ft²·F-day)

SSF	0.10	0.20	0.30	0.40	0.50	0.60	0.70	0.80	0.90
<i>Nashville, Tennessee</i>									3696 DD
WW A1	588	60	24	13	8	5	3	2	1
WW A2	192	70	38	23	15	11	7	5	3
WW A3	161	72	42	27	18	13	9	6	4
WW A4	148	72	43	29	20	14	10	7	5
WW A5	141	74	46	31	22	16	11	8	5
WW A6	137	74	47	32	22	16	12	8	5
WW B1	135	41	19	10	6	3	2	—	—
WW B2	152	78	48	33	23	17	12	9	6
WW B3	179	97	61	42	30	22	16	12	8
WW B4	164	97	65	46	34	25	19	14	9
WW B5	153	93	63	45	33	25	19	14	9
WW C1	193	105	67	46	33	24	18	13	8
WW C2	169	97	63	44	32	24	18	13	8
WW C3	181	115	79	58	43	33	25	18	12
WW C4	164	104	72	53	39	30	23	17	11
TW A1	509	59	25	13	8	5	3	2	1
TW A2	199	64	33	20	13	9	6	4	3
TW A3	160	65	36	23	15	11	8	5	3
TW A4	136	62	36	23	16	11	8	6	4
TW B1	282	57	26	15	9	6	4	3	2
TW B2	161	59	32	20	13	9	6	4	3
TW B3	141	58	32	21	14	10	7	5	3
TW B4	131	54	30	19	13	9	7	5	3
TW C1	188	53	27	16	10	7	5	3	2
TW C2	144	52	28	18	12	8	6	4	2
TW C3	139	49	27	17	11	8	5	4	2
TW C4	149	45	23	14	9	7	5	3	2
TW D1	99	33	16	9	5	3	2	1	—
TW D2	164	75	44	29	20	14	10	7	5
TW D3	167	82	49	33	23	17	12	8	5
TW D4	168	91	58	40	29	21	15	11	7
TW D5	160	89	58	40	29	22	16	12	8
TW E1	198	98	59	40	28	20	15	10	7
TW E2	182	95	59	40	29	21	15	11	7
TW E3	197	115	76	54	39	29	22	16	11
TW E4	178	105	70	50	37	27	20	15	10
TW F1	221	50	23	13	8	5	4	2	1
TW F2	139	53	29	18	12	8	6	4	2

(Continued)

TABLE A7.2 (CONTINUED)

LCR Tables for Six Representative Cities (Albuquerque, Boston, Madison, Medford, Nashville, and Santa Maria) LCR Units (Btu/ft²·F-day)

SSF	0.10	0.20	0.30	0.40	0.50	0.60	0.70	0.80	0.90
<i>Nashville, Tennessee</i>									
TW F3	116	52	30	19	13	9	7	5	3
TW F4	96	47	28	19	13	9	7	5	3
TW G1	137	44	22	13	9	6	4	3	2
TW G2	101	44	25	16	11	8	5	4	2
TW G3	86	41	24	16	11	8	6	4	2
TW G4	69	34	21	14	10	7	5	3	2
TW H1	89	36	20	13	8	6	4	3	2
TW H2	69	33	19	12	9	6	4	3	2
TW H3	59	28	17	11	8	5	4	3	2
TW H4	46	22	13	9	6	4	3	2	1
TW I1	74	26	13	7	4	2	1	—	—
TW I2	125	62	38	25	18	13	9	7	4
TW I3	133	69	43	29	20	15	11	8	5
TW I4	139	78	51	35	26	19	14	10	7
TW I5	137	80	53	37	27	20	15	11	7
TW J1	164	86	54	36	26	19	14	10	6
TW J2	150	82	53	36	26	19	14	10	7
TW J3	165	101	68	49	36	27	20	15	10
TW J4	153	93	63	46	34	25	19	14	10
DG A1	98	34	—	—	—	—	—	—	—
DG A2	130	55	31	19	11	6	—	—	—
DG A3	173	78	47	32	23	16	11	7	2
DG B1	100	36	17	—	—	—	—	—	—
DG B2	134	58	33	22	15	10	6	—	—
DG B3	177	81	49	33	24	18	14	10	6
DG C1	131	52	28	17	9	—	—	—	—
DG C2	161	71	42	28	20	14	10	6	—
DG C3	205	94	57	39	29	22	17	12	8
SS A1	351	100	50	29	19	13	9	6	4
SS A2	328	135	76	49	33	24	17	12	8
SS A3	330	87	41	24	15	10	6	4	2
SS A4	331	133	74	47	32	22	16	11	7
SS A5	595	98	43	24	15	10	7	4	2
SS A6	324	132	75	48	32	23	16	11	7
SS A7	668	79	32	17	10	6	4	2	1
SS A8	330	129	71	45	30	21	15	10	6
SS B1	236	74	38	23	15	10	7	5	3
SS B2	258	110	63	41	28	20	14	10	6

TABLE A7.2 (CONTINUED)

LCR Tables for Six Representative Cities (Albuquerque, Boston, Madison, Medford, Nashville, and Santa Maria) LCR Units (Btu/ft²·F-day)

SSF	0.10	0.20	0.30	0.40	0.50	0.60	0.70	0.80	0.90
<i>Nashville, Tennessee</i>									3696 DD
SS B3	212	65	32	19	12	8	5	3	2
SS B4	251	105	60	39	27	19	13	9	6
SS B5	307	65	30	17	10	7	4	3	2
SS B6	241	104	60	39	27	19	14	10	6
SS B7	264	52	23	12	7	5	3	2	—
SS B8	233	98	56	36	25	17	12	9	5
SS C1	141	60	33	21	14	10	7	5	3
SS C2	161	81	50	33	23	17	12	9	6
SS C3	149	48	25	15	10	7	4	3	2
SS C4	160	73	43	28	19	14	10	7	5
SS D1	317	119	64	39	26	18	13	8	5
SS D2	287	147	90	61	43	31	23	16	10
SS D3	405	113	55	33	21	14	10	6	4
SS D4	295	144	87	58	40	29	21	15	10
SS E1	229	89	48	29	19	13	9	6	4
SS E2	233	118	72	48	34	24	18	12	8
SS E3	283	77	37	22	14	9	6	4	2
SS E4	242	111	65	43	29	21	15	11	7
<i>Medford, Oregon</i>									4930 DD
WW A1	708	64	24	11	—	—	—	—	—
WW A2	212	73	38	22	13	7	3	—	—
WW A3	174	75	41	25	16	9	5	2	—
WW A4	158	74	43	27	17	11	6	3	1
WW A5	149	75	45	29	19	12	7	4	2
WW A6	144	75	46	30	20	13	8	4	2
WW B1	154	43	16	—	—	—	—	—	—
WW B2	162	80	48	31	21	14	9	6	3
WW B3	190	100	62	41	28	19	13	8	5
WW B4	171	99	65	45	32	23	16	11	7
WW B5	160	95	63	45	32	23	17	12	7
WW C1	205	108	67	45	31	21	15	10	6
WW C2	178	99	63	43	30	22	15	10	6
WW C3	189	117	80	57	42	31	23	16	10
WW C4	170	106	72	52	38	28	21	15	9
TW A1	607	63	25	12	5	—	—	—	—
TW A2	222	68	33	19	11	6	2	—	—
TW A3	175	67	36	21	13	8	4	2	—
TW A4	147	64	36	22	14	9	5	3	1

(Continued)

TABLE A7.2 (CONTINUED)

LCR Tables for Six Representative Cities (Albuquerque, Boston, Madison, Medford, Nashville, and Santa Maria) LCR Units (Btu/ft²·F-day)

SSF	0.10	0.20	0.30	0.40	0.50	0.60	0.70	0.80	0.90
<i>Medford, Oregon</i>									4930 DD
TW B1	327	61	27	14	7	3	—	—	—
TW B2	178	62	32	19	12	7	4	2	—
TW B3	154	60	33	20	12	8	4	2	1
TW B4	143	56	31	19	12	8	5	2	1
TW C1	212	56	27	15	9	5	2	—	—
TW C2	159	55	28	17	11	7	4	2	—
TW C3	154	52	27	16	10	6	4	2	1
TW C4	167	48	24	14	9	5	3	2	—
TW D1	112	34	14	—	—	—	—	—	—
TW D2	177	77	44	28	18	12	8	5	3
TW D3	180	85	50	32	21	14	9	6	3
TW D4	177	93	58	39	27	19	13	9	5
TW D5	168	92	58	40	28	20	14	10	6
TW E1	213	101	60	39	26	18	12	8	4
TW E2	194	98	59	39	27	19	13	9	5
TW E3	208	118	77	53	38	27	20	13	8
TW E4	186	108	71	49	36	26	19	13	8
TW F1	256	53	23	12	5	—	—	—	—
TW F2	153	56	29	17	10	5	2	—	—
TW F3	125	54	30	18	11	7	3	1	—
TW F4	102	48	28	18	11	7	4	2	1
TW G1	153	46	22	12	7	—	—	—	—
TW G2	109	46	25	15	9	5	3	1	—
TW G3	92	42	24	15	9	6	3	2	—
TW G4	74	35	20	13	8	5	3	2	—
TW H1	97	38	20	12	7	4	1	—	—
TW H2	75	34	19	12	7	5	3	1	—
TW H3	63	29	17	10	7	4	3	1	—
TW H4	49	23	13	8	5	3	2	1	—
TW I1	83	27	10	—	—	—	—	—	—
TW I2	133	64	38	24	16	11	7	4	2
TW I3	142	71	43	28	19	13	9	5	3
TW I4	146	80	51	35	25	17	12	8	5
TW I5	144	82	53	37	26	19	13	9	6
TW J1	175	89	54	36	24	17	11	7	4
TW J2	158	85	53	36	25	18	12	8	5
TW J3	173	103	69	48	35	26	18	13	8
TW J4	160	96	64	45	33	24	17	12	8

TABLE A7.2 (CONTINUED)

LCR Tables for Six Representative Cities (Albuquerque, Boston, Madison, Medford, Nashville, and Santa Maria) LCR Units (Btu/ft²·F-day)

SSF	0.10	0.20	0.30	0.40	0.50	0.60	0.70	0.80	0.90
<i>Medford, Oregon</i>									4930 DD
DG A1	110	35	—	—	—	—	—	—	—
DG A2	142	58	32	18	9	—	—	—	—
DG A3	187	82	48	32	22	15	9	5	—
DG B1	110	40	15	—	—	—	—	—	—
DG B2	146	61	35	21	13	7	—	—	—
DG B3	193	84	51	34	24	17	12	7	3
DG C1	144	57	29	13	—	—	—	—	—
DG C2	177	75	44	28	19	12	6	—	—
DG C3	224	98	60	41	29	21	14	10	5
SS A1	415	110	51	28	16	9	4	2	—
SS A2	372	146	79	48	31	21	14	8	5
SS A3	397	96	42	21	10	—	—	—	—
SS A4	379	144	76	46	29	19	12	7	4
SS A5	732	111	45	23	12	5	—	—	—
SS A6	368	143	77	47	30	20	13	8	4
SS A7	846	90	33	14	—	—	—	—	—
SS A8	379	140	73	44	27	17	11	6	3
SS B1	274	81	38	21	12	6	3	—	—
SS B2	288	117	65	40	26	18	12	7	4
SS B3	249	71	33	17	8	—	—	—	—
SS B4	282	113	62	38	25	16	11	7	4
SS B5	368	72	30	15	7	—	—	—	—
SS B6	269	111	62	30	25	17	11	7	4
SS B7	323	58	23	10	—	—	—	—	—
SS B8	262	106	57	35	23	15	9	6	3
SS C1	153	62	33	19	11	5	—	—	—
SS C2	172	83	50	32	22	15	10	6	3
SS C3	166	51	24	13	7	3	—	—	—
SS C4	173	76	43	27	18	12	8	5	3
SS D1	367	129	65	37	22	13	7	3	1
SS D2	318	156	92	60	40	27	18	12	7
SS D3	480	124	57	31	18	10	5	2	—
SS D4	328	153	89	57	38	26	17	11	6
SS E1	262	95	48	27	15	7	—	—	—
SS E2	257	124	73	47	31	21	14	9	5
SS E3	334	84	38	20	10	4	—	—	—
SS E4	269	118	67	42	27	18	12	7	4

(Continued)

TABLE A7.2 (CONTINUED)

LCR Tables for Six Representative Cities (Albuquerque, Boston, Madison, Medford, Nashville, and Santa Maria) LCR Units (Btu/ft²·F-day)

SSF	0.10	0.20	0.30	0.40	0.50	0.60	0.70	0.80	0.90
<i>Boston, Massachusetts</i>									5621 DD
WW A1	368	28	9	—	—	—	—	—	—
WW A2	119	41	20	12	7	5	3	2	—
WW A3	101	43	24	15	10	6	4	3	1
WW A4	93	44	26	16	11	7	5	3	2
WW A5	89	45	27	18	12	8	6	4	2
WW A6	87	46	28	19	13	9	6	4	3
WW B1	59	—	—	—	—	—	—	—	—
WW B2	103	52	31	21	15	10	7	5	3
WW B3	123	66	41	28	20	14	10	7	5
WW B4	118	70	46	33	24	18	13	9	6
WW B5	113	69	46	33	25	18	14	10	7
WW C1	135	72	46	31	22	16	12	8	5
WW C2	121	68	44	31	22	16	12	9	6
WW C3	136	86	60	44	33	25	19	14	9
WW C4	124	78	54	40	30	23	17	12	8
TW A1	324	30	11	4	—	—	—	—	—
TW A2	126	37	18	10	6	4	2	1	—
TW A3	102	39	21	13	8	5	3	2	1
TW A4	88	38	22	14	9	6	4	3	2
TW B1	180	32	13	7	4	2	—	—	—
TW B2	104	36	19	11	7	5	3	2	1
TW B3	92	36	19	12	8	5	3	2	1
TW B4	86	34	19	12	8	5	4	2	1
TW C1	122	32	15	9	5	3	2	1	—
TW C2	95	33	17	10	7	4	3	2	1
TW C3	93	31	16	10	6	4	3	2	1
TW C4	102	29	15	9	6	4	3	2	1
TW D1	45	—	—	—	—	—	—	—	—
TW D2	112	49	28	18	12	9	6	4	3
TW D3	113	54	32	21	15	10	7	5	3
TW D4	121	64	41	28	20	15	11	8	5
TW D5	118	66	42	30	21	16	12	8	6
TW E1	138	67	40	27	18	13	9	7	4
TW E2	130	66	41	28	20	14	10	7	5
TW E3	146	84	56	39	29	21	16	11	8
TW E4	133	78	52	37	27	20	15	11	7
TW F1	134	25	10	4	—	—	—	—	—
TW F2	86	30	16	9	5	3	2	1	—

TABLE A7.2 (CONTINUED)

LCR Tables for Six Representative Cities (Albuquerque, Boston, Madison, Medford, Nashville, and Santa Maria) LCR Units (Btu/ft²·F-day)

SSF	0.10	0.20	0.30	0.40	0.50	0.60	0.70	0.80	0.90
<i>Boston, Massachusetts</i>									5621 DD
TW F3	72	31	17	11	7	4	3	2	1
TW F4	61	29	17	11	7	5	3	2	1
TW G1	83	24	11	6	3	2	—	—	—
TW G2	63	26	14	9	5	4	2	1	—
TW G3	54	25	14	9	6	4	3	2	1
TW G4	45	21	12	8	5	4	3	2	1
TW H1	54	21	11	6	4	2	1	—	—
TW H2	44	20	11	7	5	3	2	1	—
TW H3	38	17	10	6	4	3	2	1	—
TW H4	30	14	8	5	3	2	2	1	—
TW I1	30	—	—	—	—	—	—	—	—
TW I2	84	41	24	16	11	8	6	4	2
TW I3	91	46	28	19	13	9	7	5	3
TW I4	100	56	36	25	18	13	10	7	5
TW I5	101	58	38	27	20	15	11	8	5
TW J1	114	59	37	25	17	12	9	6	4
TW J2	107	58	37	25	18	13	10	7	4
TW J3	123	75	51	36	27	20	15	11	7
TW J4	115	70	47	34	25	19	14	10	7
DG A1	43	—	—	—	—	—	—	—	—
DG A2	85	34	18	9	—	—	—	—	—
DG A3	125	56	33	22	16	11	7	4	—
DG B1	44	—	—	—	—	—	—	—	—
DG B2	87	36	20	12	7	—	—	—	—
DG B3	129	58	35	24	17	13	9	6	3
DG C1	71	23	—	—	—	—	—	—	—
DG C2	109	47	27	17	12	8	4	—	—
DG C3	151	68	41	28	21	16	12	8	5
SS A1	230	61	29	16	10	6	4	2	1
SS A2	231	93	52	33	22	15	11	7	5
SS A3	205	48	20	10	4	—	—	—	—
SS A4	229	90	49	31	20	14	9	6	4
SS A5	389	58	23	11	6	3	—	—	—
SS A6	226	91	50	32	21	15	10	7	4
SS A7	420	40	12	—	—	—	—	—	—
SS A8	226	86	46	28	19	12	8	6	3
SS B1	151	44	21	12	7	4	2	1	—
SS B2	183	77	43	28	19	13	9	6	4

(Continued)

TABLE A7.2 (CONTINUED)

LCR Tables for Six Representative Cities (Albuquerque, Boston, Madison, Medford, Nashville, and Santa Maria) LCR Units (Btu/ft²·F-day)

SSF	0.10	0.20	0.30	0.40	0.50	0.60	0.70	0.80	0.90
<i>Boston, Massachusetts</i>									5621 DD
SS B3	129	36	16	8	3	—	—	—	—
SS B4	176	73	41	26	17	12	8	6	4
SS B5	193	36	15	7	3	—	—	—	—
SS B6	169	72	41	26	18	12	9	6	4
SS B7	157	25	7	—	—	—	—	—	—
SS B8	160	66	37	23	16	11	7	5	3
SS C1	84	33	17	10	6	4	2	1	—
SS C2	110	54	33	22	15	11	8	5	3
SS C3	91	26	12	7	4	2	—	—	—
SS C4	109	48	28	18	12	9	6	4	3
SS D1	206	73	38	22	14	9	5	3	2
SS D2	203	103	63	42	29	21	15	10	6
SS D3	264	69	32	18	10	6	4	2	1
SS D4	208	100	60	39	27	19	14	9	6
SS E1	140	51	25	14	8	4	2	—	—
SS E2	161	80	48	32	22	15	11	7	5
SS E3	177	44	19	10	5	2	—	—	—
SS E4	166	75	43	28	19	13	9	6	4
<i>Madison, Wisconsin</i>									7730 DD
WW A1	278	—	—	—	—	—	—	—	—
WW A2	91	27	12	—	—	—	—	—	—
WW A3	77	30	15	8	3	—	—	—	—
WW A4	72	32	17	10	5	—	—	—	—
WW A5	69	33	19	11	7	4	—	—	—
WW A6	67	34	19	12	7	4	2	—	—
WW B1	—	—	—	—	—	—	—	—	—
WW B2	84	41	24	15	10	7	5	3	2
WW B3	102	53	32	21	15	10	7	5	3
WW B4	101	59	39	27	19	14	10	7	5
WW B5	98	59	39	28	20	15	11	8	5
WW C1	113	59	37	25	17	12	8	6	3
WW C2	103	57	37	25	18	13	9	6	4
WW C3	119	75	51	37	28	21	15	11	7
WW C4	109	68	47	34	25	19	14	10	7
TW A1	249	16	—	—	—	—	—	—	—
TW A2	97	26	11	4	—	—	—	—	—
TW A3	79	28	13	7	3	—	—	—	—
TW A4	69	28	15	9	5	3	—	—	—

TABLE A7.2 (CONTINUED)

LCR Tables for Six Representative Cities (Albuquerque, Boston, Madison, Medford, Nashville, and Santa Maria) LCR Units (Btu/ft²·F-day)

SSF	0.10	0.20	0.30	0.40	0.50	0.60	0.70	0.80	0.90
<i>Madison, Wisconsin</i>									7730 DD
TW B1	139	20	5	—	—	—	—	—	—
TW B2	81	26	12	6	3	—	—	—	—
TW B3	72	27	13	7	4	2	—	—	—
TW B4	69	26	13	8	5	3	1	—	—
TW C1	96	23	10	4	—	—	—	—	—
TW C2	76	25	12	7	4	2	—	—	—
TW C3	75	24	12	7	4	2	1	—	—
TW C4	84	23	11	6	4	2	1	—	—
TW D1	—	—	—	—	—	—	—	—	—
TW D2	91	39	22	13	9	6	4	2	1
TW D3	93	43	25	16	10	7	5	3	1
TW D4	103	54	34	23	16	12	8	6	4
TW D5	102	56	36	25	18	13	10	7	4
TW E1	115	54	32	21	14	10	7	4	3
TW E2	110	55	34	22	16	11	8	5	3
TW E3	126	72	47	33	24	18	13	9	6
TW E4	116	68	45	32	23	17	13	9	6
TW F1	99	13	—	—	—	—	—	—	—
TW F2	65	20	8	—	—	—	—	—	—
TW F3	55	22	11	5	—	—	—	—	—
TW F4	47	21	11	7	4	2	—	—	—
TW G1	61	14	—	—	—	—	—	—	—
TW G2	47	18	8	4	—	—	—	—	—
TW G3	42	18	9	5	3	—	—	—	—
TW G4	35	16	9	5	3	2	—	—	—
TW H1	41	13	6	—	—	—	—	—	—
TW H2	34	14	7	4	2	—	—	—	—
TW H3	29	13	7	4	2	1	—	—	—
TW H4	24	10	6	3	2	1	—	—	—
TW I1	—	—	—	—	—	—	—	—	—
TW I2	68	32	18	12	8	5	3	2	1
TW I3	75	37	22	14	10	7	4	3	2
TW I4	85	47	30	21	15	11	8	5	3
TW I5	87	50	33	23	16	12	9	6	4
TW J1	95	48	29	19	13	9	6	4	3
TW J2	91	48	30	21	14	10	7	5	3
TW J3	106	65	43	31	23	17	12	9	6
TW J4	100	61	41	29	21	16	12	9	6

(Continued)

TABLE A7.2 (CONTINUED)

LCR Tables for Six Representative Cities (Albuquerque, Boston, Madison, Medford, Nashville, and Santa Maria) LCR Units (Btu/ft²·F-day)

SSF	0.10	0.20	0.30	0.40	0.50	0.60	0.70	0.80	0.90
<i>Madison, Wisconsin</i>									7730 DD
DG A1	—	—	—	—	—	—	—	—	—
DG A2	68	25	11	—	—	—	—	—	—
DG A3	109	47	28	18	12	8	5	—	—
DG B1	—	—	—	—	—	—	—	—	—
DG B2	70	27	14	6	—	—	—	—	—
DG B3	114	50	30	20	14	10	7	4	—
DG C1	47	—	—	—	—	—	—	—	—
DG C2	91	37	21	13	7	—	—	—	—
DG C3	133	59	35	24	17	13	9	6	3
SS A1	192	47	20	9	3	—	—	—	—
SS A2	200	78	42	26	17	12	8	5	3
SS A3	166	32	—	—	—	—	—	—	—
SS A4	197	74	39	23	15	10	6	4	2
SS A5	329	42	13	—	—	—	—	—	—
SS A6	195	75	40	25	16	11	7	5	3
SS A7	349	22	—	—	—	—	—	—	—
SS A8	192	69	36	21	13	8	5	3	2
SS B1	122	32	13	5	—	—	—	—	—
SS B2	158	64	36	22	15	10	7	5	3
SS B3	100	22	—	—	—	—	—	—	—
SS B4	150	60	33	29	13	9	6	4	2
SS B5	156	24	—	—	—	—	—	—	—
SS B6	145	59	33	20	13	9	6	4	2
SS B7	122	—	—	—	—	—	—	—	—
SS B8	136	54	29	18	11	7	5	3	2
SS C1	61	20	7	—	—	—	—	—	—
SS C2	90	43	25	16	11	7	5	3	2
SS C3	67	16	—	—	—	—	—	—	—
SS C4	90	38	22	13	9	6	4	2	1
SS D1	169	56	26	13	6	—	—	—	—
SS D2	175	86	51	34	23	16	11	7	5
SS D3	221	52	21	10	—	—	—	—	—
SS D4	179	84	49	32	21	15	10	7	4
SS E1	108	34	12	—	—	—	—	—	—
SS E2	135	65	38	24	16	11	7	5	3
SS E3	141	29	8	—	—	—	—	—	—
SS E4	140	61	34	21	14	9	6	4	2

Source: PSDH, *Passive Solar Design Handbook*, Van Nostrand Reinhold Co., New York, 1984.

TABLE A7.3

SLR Correlation Parameters for the 94 Reference Systems

Type	A	B	C	D	R	G	H	LCRs	STDV
WW A1	0.0000	1.0000	0.9172	0.4841	-9.0000	0.00	1.17	13.0	0.053
WW A2	0.0000	1.0000	0.9833	0.7603	-9.0000	0.00	0.92	13.0	0.046
WW A3	0.0000	1.0000	1.0171	0.8852	-9.0000	0.00	0.85	13.0	0.040
WW A4	0.0000	1.0000	1.0395	0.9569	-9.0000	0.00	0.81	13.0	0.037
WW A5	0.0000	1.0000	1.0604	1.0387	-9.0000	0.00	0.78	13.0	0.034
WW A6	0.0000	1.0000	1.0735	1.0827	-9.0000	0.00	0.76	13.0	0.033
WW B1	0.0000	1.0000	0.9754	0.5518	-9.0000	0.00	0.92	22.0	0.051
WW B2	0.0000	1.0000	1.0487	1.0851	-9.0000	0.00	0.78	9.2	0.036
WW B3	0.0000	1.0000	1.0673	1.0087	-9.0000	0.00	0.95	8.9	0.038
WW B4	0.0000	1.0000	1.1028	1.1811	-9.0000	0.00	0.74	5.8	0.034
WW B5	0.0000	1.0000	1.1146	1.2771	-9.0000	0.00	0.56	4.5	0.032
WW C1	0.0000	1.0000	1.0667	1.0437	-9.0000	0.00	0.62	12.0	0.038
WW C2	0.0000	1.0000	1.0846	1.1482	-9.0000	0.00	0.59	8.7	0.035
WW C3	0.0000	1.0000	1.1419	1.1756	-9.0000	0.00	0.28	5.5	0.033
WW C4	0.0000	1.0000	1.1401	1.2378	-9.0000	0.00	0.23	4.3	0.032
TW A1	0.0000	1.0000	0.9194	0.4601	-9.0000	0.00	1.11	13.0	0.048
TW A2	0.0000	1.0000	0.9680	0.6318	-9.0000	0.00	0.92	13.0	0.043
TW A3	0.0000	1.0000	0.9964	0.7123	-9.0000	0.00	0.85	13.0	0.038
TW A4	0.0000	1.0000	1.0190	0.7332	-9.0000	0.00	0.79	13.0	0.032
TW B1	0.0000	1.0000	0.9364	0.4777	-9.0000	0.00	1.01	13.0	0.045
TW B2	0.0000	1.0000	0.9821	0.6020	-9.0000	0.00	0.85	13.0	0.038
TW B3	0.0000	1.0000	0.9980	0.6191	-9.0000	0.00	0.80	13.0	0.033
TW B4	0.0000	1.0000	0.9981	0.5615	-9.0000	0.00	0.76	13.0	0.028
TW C1	0.0000	1.0000	0.9558	0.4709	-9.0000	0.00	0.89	13.0	0.039
TW C2	0.0000	1.0000	0.9788	0.4964	-9.0000	0.00	0.79	13.0	0.033
TW C3	0.0000	1.0000	0.9760	0.4519	-9.0000	0.00	0.76	13.0	0.029
TW C4	0.0000	1.0000	0.9588	0.3612	-9.0000	0.00	0.73	13.0	0.026
TW D1	0.0000	1.0000	0.9842	0.4418	-9.0000	0.00	0.89	22.0	0.040
TW D2	0.0000	1.0000	1.0150	0.8994	-9.0000	0.00	0.80	9.2	0.036
TW D3	0.0000	1.0000	1.0346	0.7810	-9.0000	0.00	1.08	8.9	0.036
TW D4	0.0000	1.0000	1.0606	0.9770	-9.0000	0.00	0.85	5.8	0.035
TW D5	0.0000	1.0000	1.0721	1.0718	-9.0000	0.00	0.61	4.5	0.033
TW E1	0.0000	1.0000	1.0345	0.8753	-9.0000	0.00	0.68	12.0	0.037
TW E2	0.0000	1.0000	1.0476	1.0050	-9.0000	0.00	0.66	8.7	0.035
TW E3	0.0000	1.0000	1.0919	1.0739	-9.0000	0.00	0.61	5.5	0.034
TW E4	0.0000	1.0000	1.0971	1.1429	-9.0000	0.00	0.47	4.3	0.033
TW F1	0.0000	1.0000	0.9430	0.4744	-9.0000	0.00	1.09	13.0	0.047
TW F2	0.0000	1.0000	0.9900	0.6053	-9.0000	0.00	0.93	13.0	0.041
TW F3	0.0000	1.0000	1.0189	0.6502	-9.0000	0.00	0.86	13.0	0.036
TW F4	0.0000	1.0000	1.0419	0.6258	-9.0000	0.00	0.80	13.0	0.032

(Continued)

TABLE A7.3 (CONTINUED)

SLR Correlation Parameters for the 94 Reference Systems

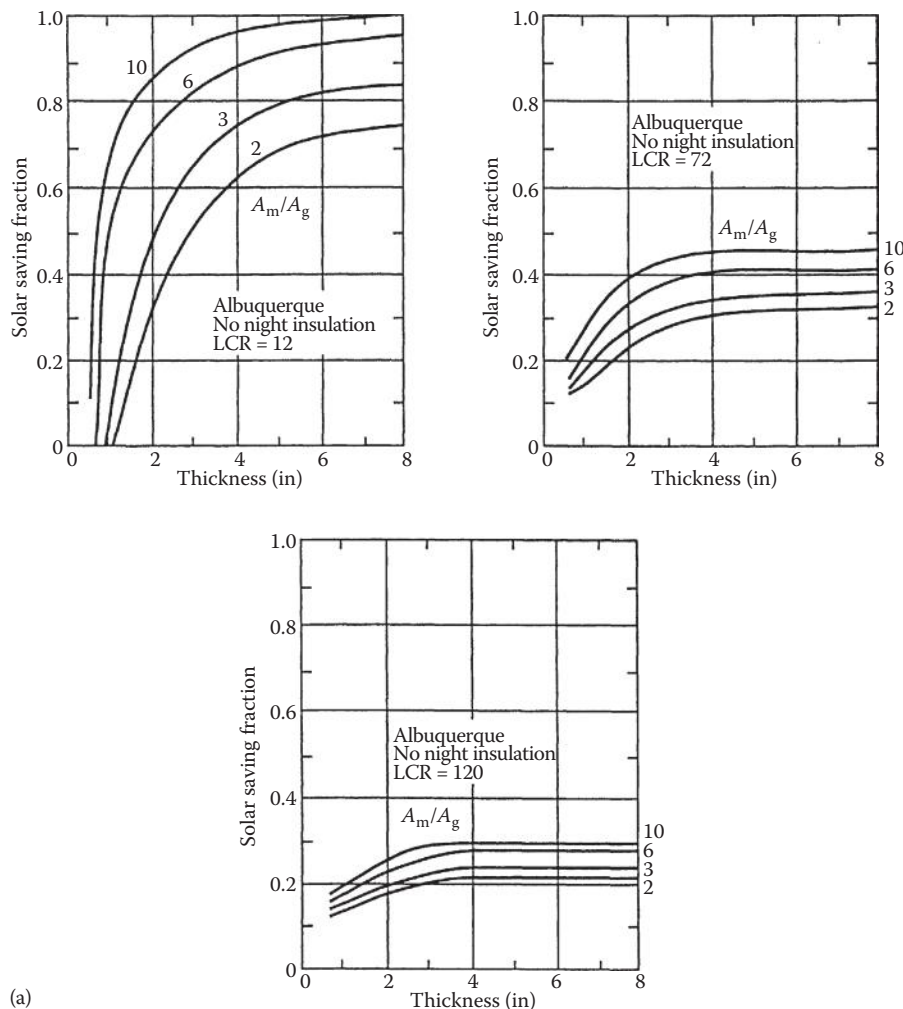
Type	A	B	C	D	R	G	H	LCRs	STDV
TW G1	0.0000	1.0000	0.9693	0.4714	-9.0000	0.00	1.01	13.0	0.042
TW G2	0.0000	1.0000	1.0133	0.5462	-9.0000	0.00	0.88	13.0	0.035
TW G3	0.0000	1.0000	1.0325	0.5269	-9.0000	0.00	0.82	13.0	0.031
TW G4	0.0000	1.0000	1.0401	0.4400	-9.0000	0.00	0.77	13.0	0.030
TW H1	0.0000	1.0000	1.0002	0.4356	-9.0000	0.00	0.93	13.0	0.034
TW H2	0.0000	1.0000	1.0280	0.4151	-9.0000	0.00	0.83	13.0	0.030
TW H3	0.0000	1.0000	1.0327	0.3522	-9.0000	0.00	0.78	13.0	0.029
TW H4	0.0000	1.0000	1.0287	0.2600	-9.0000	0.00	0.74	13.0	0.024
TW I1	0.0000	1.0000	0.9974	0.4036	-9.0000	0.00	0.91	22.0	0.038
TW I2	0.0000	1.0000	1.0386	0.8313	-9.0000	0.00	0.80	9.2	0.034
TW I3	0.0000	1.0000	1.0514	0.6886	-9.0000	0.00	1.01	8.9	0.034
TW I4	0.0000	1.0000	1.0781	0.8952	-9.0000	0.00	0.82	5.8	0.032
TW I5	0.0000	1.0000	1.0902	1.0284	-9.0000	0.00	0.65	4.5	0.032
TW J1	0.0000	1.0000	1.0537	0.8227	-9.0000	0.00	0.65	12.0	0.037
TW J2	0.0000	1.0000	1.0677	0.9312	-9.0000	0.00	0.62	8.7	0.035
TW J3	0.0000	1.0000	1.1153	0.9831	-9.0000	0.00	0.44	5.5	0.034
TW J4	0.0000	1.0000	1.1154	1.0607	-9.0000	0.00	0.38	4.3	0.033
DG A1	0.5650	1.0090	1.0440	0.7175	0.3931	9.36	0.00	0.0	0.046
DG A2	0.5906	1.0060	1.0650	0.8099	0.4681	5.28	0.00	0.0	0.039
DG A3	0.5442	0.9715	1.1300	0.9273	0.7068	2.64	0.00	0.0	0.036
DG B1	0.5739	0.9948	1.2510	1.0610	0.7905	9.60	0.00	0.0	0.042
DG B2	0.6180	1.0000	1.2760	1.1560	0.7528	5.52	0.00	0.0	0.035
DG B3	0.5601	0.9839	1.3520	1.1510	0.8879	2.38	0.00	0.0	0.032
DG C1	0.6344	0.9887	1.5270	1.4380	0.8632	9.60	0.00	0.0	0.039
DG C2	0.6763	0.9994	1.4000	1.3940	0.7604	5.28	0.00	0.0	0.033
DG C3	0.6182	0.9859	1.5660	1.4370	0.8990	2.40	0.00	0.0	0.031
SS A1	0.0000	1.0000	0.9587	0.4770	-9.0000	0.00	0.83	18.6	0.027
SS A2	0.0000	1.0000	0.9982	0.6614	-9.0000	0.00	0.77	10.4	0.026
SS A3	0.0000	1.0000	0.9552	0.4230	-9.0000	0.00	0.83	23.6	0.030
SS A4	0.0000	1.0000	0.9956	0.6277	-9.0000	0.00	0.80	12.4	0.026
SS A5	0.0000	1.0000	0.9300	0.4041	-9.0000	0.00	0.96	18.6	0.031
SS A6	0.0000	1.0000	0.9981	0.6660	-9.0000	0.00	0.86	10.4	0.028
SS A7	0.0000	1.0000	0.9219	0.3225	-9.0000	0.00	0.96	23.6	0.035
SS A8	0.0000	1.0000	0.9922	0.6173	-9.0000	0.00	0.90	12.4	0.028
SS B1	0.0000	1.0000	0.9683	0.4954	-9.0000	0.00	0.84	16.3	0.028
SS B2	0.0000	1.0000	1.0029	0.6802	-9.0000	0.00	0.74	8.5	0.026
SS B3	0.0000	1.0000	0.9689	0.4685	-9.0000	0.00	0.82	19.3	0.029
SS B4	0.0000	1.0000	1.0029	0.6641	-9.0000	0.00	0.76	9.7	0.026
SS B5	0.0000	1.0000	0.9408	0.3866	-9.0000	0.00	0.97	16.3	0.030
SS B6	0.0000	1.0000	1.0068	0.6778	-9.0000	0.00	0.84	8.5	0.028
SS B7	0.0000	1.0000	0.9395	0.3363	-9.0000	0.00	0.95	19.3	0.032

TABLE A7.3 (CONTINUED)

SLR Correlation Parameters for the 94 Reference Systems

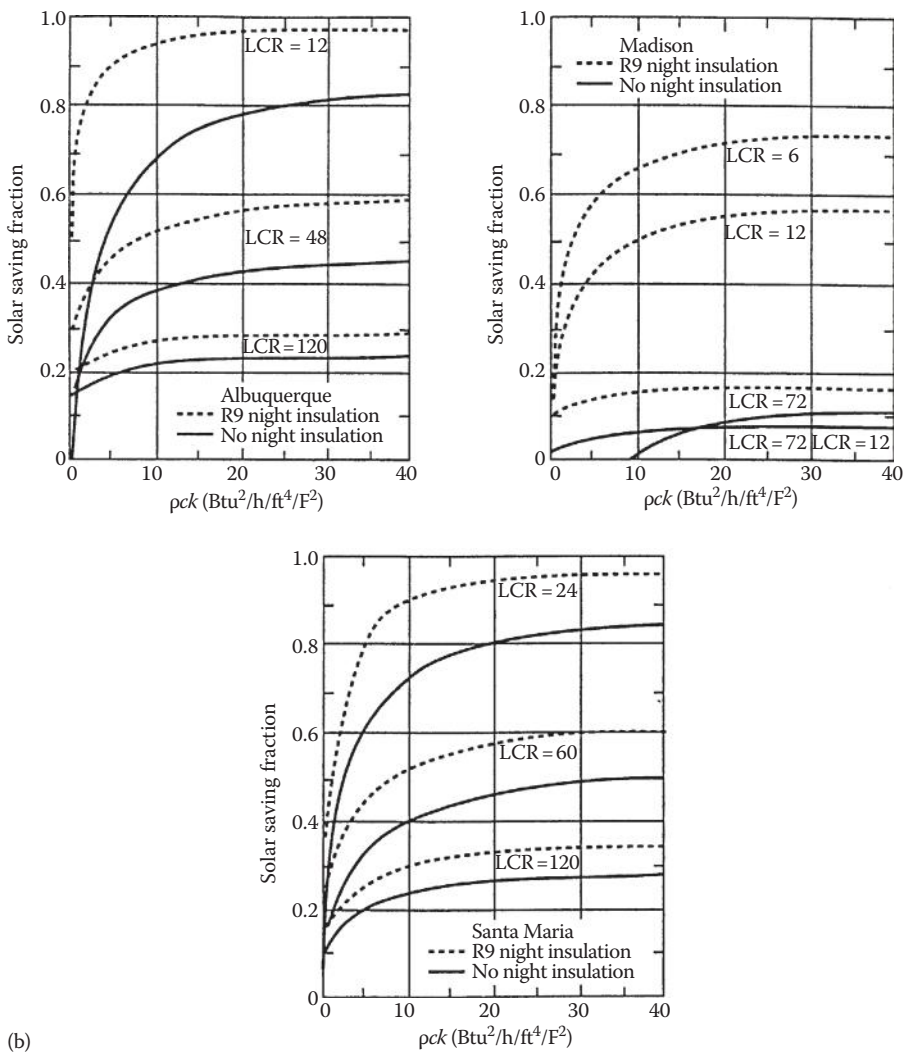
Type	A	B	C	D	R	G	H	LCRs	STDV
SS B8	0.0000	1.0000	1.0047	0.6469	-9.0000	0.00	0.87	9.7	0.027
SS C1	0.0000	1.0000	1.0087	0.7683	-9.0000	0.00	0.76	16.3	0.025
SS C2	0.0000	1.0000	1.0412	0.9281	-9.0000	0.00	0.78	10.0	0.027
SS C3	0.0000	1.0000	0.9699	0.5106	-9.0000	0.00	0.79	16.3	0.024
SS C4	0.0000	1.0000	1.0152	0.7523	-9.0000	0.00	0.81	10.0	0.025
SS D1	0.0000	1.0000	0.9889	0.6643	-9.0000	0.00	0.84	17.8	0.028
SS D2	0.0000	1.0000	1.0493	0.8753	-9.0000	0.00	0.70	9.9	0.028
SS D3	0.0000	1.0000	0.9570	0.5285	-9.0000	0.00	0.90	17.8	0.029
SS D4	0.0000	1.0000	1.0356	0.8142	-9.0000	0.00	0.73	9.9	0.028
SS E1	0.0000	1.0000	0.9968	0.7004	-9.0000	0.00	0.77	19.6	0.027
SS E2	0.0000	1.0000	1.0468	0.9054	-9.0000	0.00	0.76	10.8	0.027
SS E3	0.0000	1.0000	0.9565	0.4827	-9.0000	0.00	0.81	19.6	0.028
SS E4	0.0000	1.0000	1.0214	0.7694	-9.0000	0.00	0.79	10.8	0.027

Source: PSDH, *Passive Solar Design Handbook*, Van Nostrand Reinhold Co., New York, 1984.

**FIGURE A7.1**

(a) Storage wall: mass thickness sensitivity of SSF to off-reference conditions.

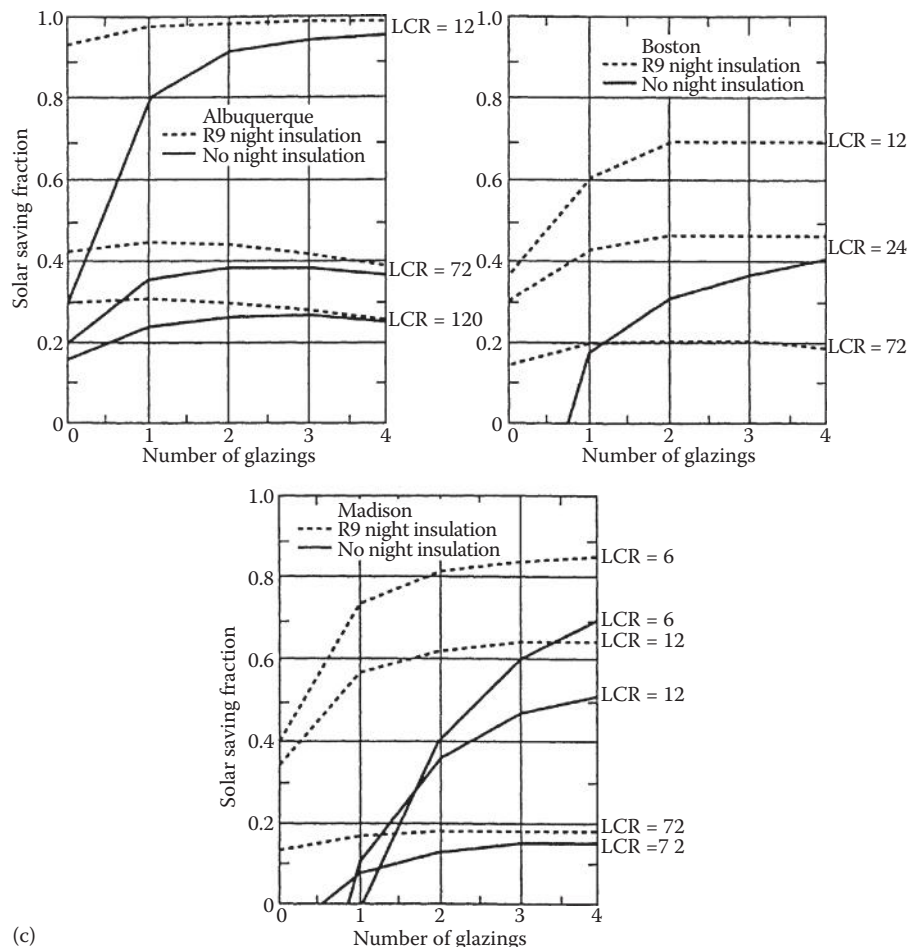
(Continued)



(b)

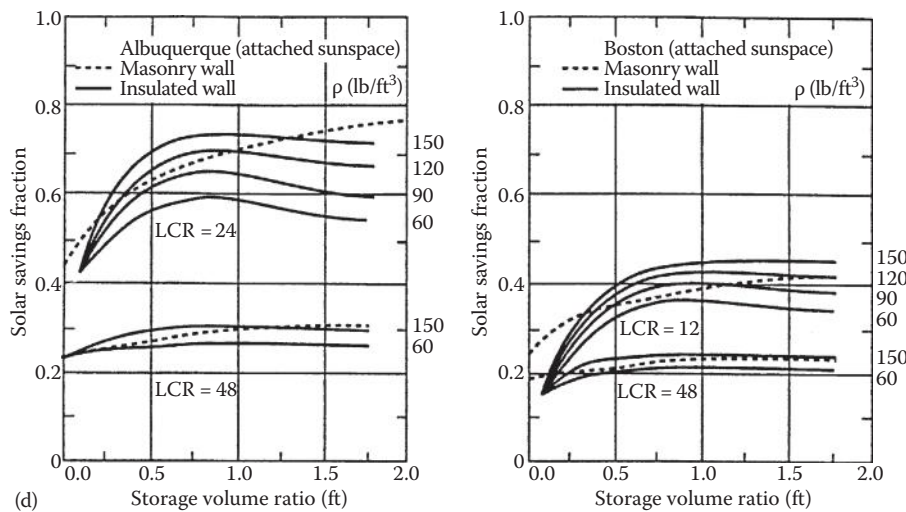
FIGURE A7.1 (CONTINUED)
 (b) Storage wall: pck product.

(Continued)

**FIGURE A7.1 (CONTINUED)**

(c) Storage wall: number of glazings.

(Continued)

**FIGURE A7.1 (CONTINUED)**

(d) Sunspace: storage volume to projected area ratio. (From PSDH, *Passive Solar Design Handbook*, Van Nostrand Reinhold Co., New York, 1984.)

Appendix 8: Supplementary Material for Chapter 8

TABLE A8.1a

Wall Thickness, in Millimeters, for Different Nominal Pipe Sizes
(Pipe Schedule A–G)

Nominal Pipe Size, in	Pipe Schedule						
	A	B	C	D	E	F	G
2.5	2.11	3.05	5.16	7.01	9.53	14.02	...
3	2.11	3.05	5.49	7.62	11.13	15.24	...
4	2.11	3.05	3.96	4.78	6.02	8.56	11.13
6	2.77	3.40	4.78	7.11	10.97	14.27	18.26
8	2.77	3.76	6.35	7.04	8.18	10.31	12.70
10	3.40	4.19	4.78	6.35	7.80	9.27	12.70
12	3.96	4.57	6.35	8.38	9.53	10.31	12.70
14	4.78	6.35	7.92	9.53	11.13	12.70	15.09
16	4.78	6.35	7.92	9.53	12.70	14.35	21.44
18	4.78	6.35	7.92	9.53	11.13	12.70	14.27
20	5.54	6.35	9.53	12.70	15.09	20.62	26.19
22	6.35	9.53	12.70	22.23	28.58	34.93	41.28
24	6.35	9.53	12.70	14.27	17.48	24.61	30.96
26	7.92	9.53	12.70
28	7.92	9.53	12.70	15.88
30	7.92	9.53	12.70	15.88
32	7.92	9.53	12.70	15.88	17.48
34	7.92	9.53	12.70	15.88	17.48
36	7.92	9.53	12.70	15.88	19.05
42	9.53	12.70	15.88	19.05
48	9.53	12.70	19.05	25.40
54	9.53	12.70	19.05	25.40
60	9.53	12.70	19.05	25.40
66	9.53	12.70	19.05	25.40
72	9.53	12.70	19.05	25.40

Source: Adapted from Kelly, B. and D. Kearney, Parabolic trough solar system piping model. Tech. Rep., National Renewable Laboratory, NREL/SR-550-40165, July, 2006.

TABLE A8.1b

Wall Thickness, in Millimeters, for Different Nominal Pipe Sizes
(Pipe Schedule H–M)

Nominal Pipe Size, in	Pipe Schedule					
	H	I	J	K	L	M
2.5
3
4	13.49	17.12
6	21.95
8	15.09	18.26	20.62	22.23	23.01	...
10	15.09	18.26	21.44	25.40	28.58	...
12	14.27	17.48	21.44	25.40	28.58	33.32
14	19.05	23.83	27.79	31.75	35.71	...
16	26.19	30.96	36.53	40.49
18	19.05	23.83	29.36	34.93	39.67	45.24
20	32.54	38.10	44.45	50.01
22	47.63	53.98
24	38.89	46.02	52.37	59.54
26
28
30
32
34
36
42
48
54
60
66
72

Source: Adapted from Kelly, B. and D. Kearney, Parabolic trough solar system piping model. Tech. Rep., National Renewable Laboratory, NREL/SR-550-40165, July, 2006.

TABLE A8.1c

Inside Diameter, in Millimeters, for Different Nominal Pipe Sizes
(Pipe Schedule A–G)

Nominal Pipe Size, in	Pipe Schedule						
	A	B	C	D	E	F	G
2.5	68.8	66.9	62.7	59.0	54.0	45.0	...
3	84.7	82.8	77.9	73.7	66.6	58.4	...
4	110.1	108.2	106.4	104.7	102.3	97.2	92.0
6	162.7	161.5	158.7	154.1	146.3	139.7	131.7
8	213.5	211.6	206.4	205.0	202.7	198.5	193.7
10	266.2	264.7	263.5	260.4	257.5	254.5	247.7
12	315.9	314.7	311.2	307.1	304.8	303.2	298.5
14	346.0	342.9	339.8	336.6	333.3	330.2	325.4
16	396.8	393.7	390.6	387.4	381.0	377.7	363.5
18	447.6	444.5	441.4	438.2	434.9	431.8	428.7
20	496.9	495.3	489.0	482.6	477.8	466.8	455.6
22	546.1	539.8	533.4	514.4	501.7	489.0	476.3
24	596.9	590.6	584.2	581.1	574.6	560.4	547.7
26	644.6	641.4	635.0
28	695.4	692.2	685.8	679.5
30	746.2	743.0	736.6	730.3
32	797.0	793.8	787.4	781.1	777.8
34	847.8	844.6	838.2	831.9	828.6
36	898.6	895.4	889.0	882.7	876.3
42	1047.8	1041.4	1035.1	1028.7
48	1200.2	1193.8	1181.1	1168.4
54	1352.6	1346.2	1333.5	1320.8
60	1505.0	1498.6	1485.9	1473.2
66	1657.4	1651.0	1638.3	1625.6
72	1809.8	1803.4	1790.7	1778.0

Source: Adapted from Kelly, B. and D. Kearney, Parabolic trough solar system piping model. Tech. Rep., National Renewable Laboratory, NREL/SR-550-40165, July, 2006.

TABLE A8.1d

Inside Diameter, in Millimeters, for Different Nominal Pipe Sizes (Pipe Schedule H–M)

Nominal Pipe Size, in	Pipe Schedule					
	H	I	J	K	L	M
2.5
3
4	87.3	80.1
6	124.4
8	188.9	182.5	177.8	174.6	173.1	...
10	242.9	236.5	230.2	222.3	215.9	...
12	295.3	288.9	281.0	273.1	266.7	257.2
14	317.5	307.9	300.0	292.1	284.2	...
16	354.0	344.5	333.3	325.4
18	419.1	409.5	398.5	387.4	377.9	366.7
20	442.9	431.8	419.1	408.0
22	463.6	450.9
24	531.8	517.6	504.9	490.5
26
28
30
32
34
36
42
48
54
60
66
72

Source: Adapted from Kelly, B. and D. Kearney, Parabolic trough solar system piping model. Tech. Rep., National Renewable Laboratory, NREL/SR-550-40165, July, 2006.

TABLE A8.2

Commercial Software and Codes for Solar Power Plant Design

Power Plant Type	Components	Software/Codes Used
Power tower	Optical design and performance of heliostat	ASAP [1], DELSOL [2], HELIOS, MIRVAL [3], SOLTRACE [4], Stress Analysis Codes such as ANSYS® [5] and CosmosWorks® [6], HFLCAL [7]
	Central receiver performance	FLUENT [8], Thermal Stress Analysis Codes such as ANSYS® [5] and CosmosWorks® [6]
	Heat transfer fluid transport, exchange, and storage	FLUENT [8], SAM [9], SOLERGY [10], TRNSYS [11]
	Power cycle	GATECYCLE [12], IPSEPRO [13], STEAM PRO [14], Epsilon [15]
	Total system performance	DELSOL [2], SAM [9], SOLERGY [10], TRNSYS [11]
Linear concentrator systems (troughs and linear reflectors)	Solar collectors	ASAP [1], CIRCE [16], FLUENT [8], SOLTRACE [17]
	Dish receiver	AAETES [18], FLUENT [8]
	Power cycle	GATECYCLE [12], IPSEPRO [13], STEAM PRO [14]
	Total system performance	SAM [9], SOLERGY [10], TRNSYS [11]
Dish engine systems	Dish solar collector	ASAP [1], CIRCE [16], SOLTRACE [17]
	Heat transfer fluid transport, exchange, and storage	FLUENT [8], SAM [9], SOLERGY [10], TRNSYS [11]
	Dish field system performance	Dish Field System Model [19] (an Excel-based model)

TABLE A8.3Properties of Supercritical CO₂ at Different Pressures and Temperatures

T (°C)	<i>h</i> (kJ/kg)	<i>s</i> (kJ/kg · K)	T (°C)	<i>h</i> (kJ/kg)	<i>s</i> (kJ/kg · K)
<i>Properties of Carbon Dioxide at P = 7.5 MPa</i>					
30	291.65	1.2994	420	891.33	2.7388
40	419.41	1.7169	430	902.97	2.7555
50	445.65	1.7994	440	914.65	2.772
60	465.04	1.8586	450	926.35	2.7883
70	481.57	1.9075	460	938.09	2.8044
80	496.51	1.9504	470	949.86	2.8204
90	510.44	1.9893	480	961.66	2.8361
100	523.67	2.0252	490	973.5	2.8517
110	536.41	2.0589	500	985.36	2.8672
120	548.77	2.0908	510	997.25	2.8825
130	560.85	2.1211	520	1009.2	2.8976
140	572.72	2.1502	530	1021.1	2.9126
150	584.42	2.1782	540	1033.1	2.9274
160	595.99	2.2052	550	1045.1	2.9421
170	607.46	2.2314	560	1057.2	2.9566
180	618.86	2.2568	570	1069.2	2.971
190	630.19	2.2816	580	1081.3	2.9853
200	641.48	2.3057	590	1093.5	2.9994
210	652.74	2.3292	600	1105.6	3.0134
220	663.98	2.3523	610	1117.8	3.0273
230	675.21	2.3748	620	1130	3.0411
240	686.43	2.3969	630	1142.3	3.0547
250	697.65	2.4185	640	1154.5	3.0682
260	708.87	2.4398	650	1166.8	3.0816
270	720.11	2.4607	660	1179.1	3.0949
280	731.35	2.4812	670	1191.5	3.108
290	742.62	2.5014	680	1203.9	3.1211
300	753.9	2.5212	690	1216.3	3.134
310	765.21	2.5408	700	1228.7	3.1468
320	776.53	2.56	710	1241.1	3.1596
330	787.89	2.579	720	1253.6	3.1722
340	799.26	2.5977	730	1266.1	3.1847
350	810.67	2.6162	740	1278.6	3.1971
360	822.1	2.6344	750	1291.1	3.2094
370	833.56	2.6523	760	1303.7	3.2216
380	845.06	2.6701	770	1316.3	3.2338
390	856.58	2.6876	780	1328.9	3.2458
400	868.13	2.7049	790	1341.5	3.2577
410	879.71	2.7219	800	1354.2	3.2696

TABLE A8.3 (CONTINUED)Properties of Supercritical CO₂ at Different Pressures and Temperatures

T (°C)	<i>h</i> (kJ/kg)	<i>s</i> (kJ/kg · K)	T (°C)	<i>h</i> (kJ/kg)	<i>s</i> (kJ/kg · K)
<i>Properties of Carbon Dioxide at P = 14 MPa</i>					
30	261.62	1.1727	420	882.44	2.608
40	288.21	1.259	430	894.41	2.6251
50	319.07	1.3559	440	906.4	2.642
60	355.38	1.4665	450	918.41	2.6588
70	392.61	1.5767	460	930.44	2.6753
80	423.79	1.6663	470	942.48	2.6916
90	449.04	1.7368	480	954.55	2.7077
100	470.38	1.7948	490	966.64	2.7237
110	489.21	1.8446	500	978.75	2.7394
120	506.35	1.8888	510	990.88	2.755
130	522.29	1.9288	520	1003	2.7704
140	537.37	1.9658	530	1015.2	2.7857
150	551.78	2.0003	540	1027.4	2.8008
160	565.69	2.0327	550	1039.6	2.8157
170	579.2	2.0636	560	1051.9	2.8305
180	592.39	2.093	570	1064.1	2.8452
190	605.32	2.1212	580	1076.4	2.8596
200	618.05	2.1484	590	1088.7	2.874
210	630.6	2.1747	600	1101.1	2.8882
220	643.02	2.2001	610	1113.4	2.9023
230	655.32	2.2248	620	1125.8	2.9162
240	667.53	2.2488	630	1138.2	2.93
250	679.66	2.2722	640	1150.6	2.9437
260	691.73	2.2951	650	1163.1	2.9573
270	703.74	2.3174	660	1175.6	2.9707
280	715.72	2.3393	670	1188.1	2.984
290	727.67	2.3607	680	1200.6	2.9972
300	739.59	2.3817	690	1213.1	3.0103
310	751.49	2.4023	700	1225.7	3.0233
320	763.39	2.4225	710	1238.2	3.0361
330	775.27	2.4424	720	1250.8	3.0489
340	787.15	2.4619	730	1263.4	3.0615
350	799.04	2.4811	740	1276.1	3.074
360	810.92	2.5	750	1288.7	3.0865
370	822.81	2.5187	760	1301.4	3.0988
380	834.71	2.537	770	1314.1	3.111
390	846.63	2.5551	780	1326.8	3.1232
400	858.55	2.573	790	1339.6	3.1352
410	870.49	2.5906	800	1352.3	3.1471

(Continued)

TABLE A8.3 (CONTINUED)Properties of Supercritical CO₂ at Different Pressures and Temperatures

T (°C)	<i>h</i> (kJ/kg)	<i>s</i> (kJ/kg · K)	T (°C)	<i>h</i> (kJ/kg)	<i>s</i> (kJ/kg · K)
<i>Properties of Carbon Dioxide at P = 20 MPa</i>					
30	255	1.128	420	875.03	2.5294
40	277.02	1.1994	430	887.28	2.5469
50	300.13	1.2721	440	899.54	2.5643
60	324.5	1.3463	450	911.8	2.5813
70	350.07	1.4219	460	924.08	2.5982
80	376.23	1.4971	470	936.36	2.6148
90	401.91	1.5688	480	948.66	2.6313
100	426.19	1.6348	490	960.97	2.6475
110	448.67	1.6942	500	973.29	2.6636
120	469.36	1.7475	510	985.63	2.6794
130	488.49	1.7956	520	997.98	2.6951
140	506.35	1.8394	530	1010.3	2.7106
150	523.19	1.8796	540	1022.7	2.7259
160	539.21	1.9171	550	1035.1	2.7411
170	554.57	1.9521	560	1047.5	2.756
180	569.39	1.9852	570	1060	2.7709
190	583.77	2.0166	580	1072.4	2.7856
200	597.79	2.0465	590	1084.9	2.8001
210	611.51	2.0752	600	1097.4	2.8145
220	624.98	2.1028	610	1109.9	2.8287
230	638.25	2.1295	620	1122.4	2.8428
240	651.34	2.1552	630	1135	2.8568
250	664.28	2.1802	640	1147.5	2.8706
260	677.09	2.2045	650	1160.1	2.8843
270	689.8	2.2281	660	1172.7	2.8979
280	702.42	2.2511	670	1185.3	2.9113
290	714.97	2.2736	680	1197.9	2.9247
300	727.45	2.2956	690	1210.6	2.9379
310	739.88	2.3171	700	1223.3	2.951
320	752.27	2.3381	710	1236	2.9639
330	764.62	2.3588	720	1248.7	2.9768
340	776.94	2.379	730	1261.4	2.9895
350	789.24	2.3989	740	1274.1	3.0022
360	801.52	2.4185	750	1286.9	3.0147
370	813.78	2.4377	760	1299.7	3.0271
380	826.04	2.4566	770	1312.5	3.0395
390	838.29	2.4752	780	1325.3	3.0517
400	850.54	2.4935	790	1338.1	3.0638
410	862.78	2.5116	800	1350.9	3.0758

TABLE A8.3 (CONTINUED)Properties of Supercritical CO₂ at Different Pressures and Temperatures

T (°C)	<i>h</i> (kJ/kg)	<i>s</i> (kJ/kg · K)	T (°C)	<i>h</i> (kJ/kg)	<i>s</i> (kJ/kg · K)
<i>Properties of Carbon Dioxide at P = 25 MPa</i>					
30	252.25	1.1007	420	869.47	2.4786
40	272.65	1.1669	430	881.93	2.4964
50	293.58	1.2327	440	894.4	2.514
60	315.07	1.2982	450	906.86	2.5314
70	337.11	1.3634	460	919.32	2.5485
80	359.57	1.4279	470	931.79	2.5654
90	382.13	1.4909	480	944.26	2.5821
100	404.4	1.5514	490	956.74	2.5985
110	426.04	1.6086	500	969.23	2.6148
120	446.8	1.6621	510	981.72	2.6308
130	466.6	1.7118	520	994.23	2.6467
140	485.42	1.758	530	1006.7	2.6624
150	503.34	1.8008	540	1019.3	2.6779
160	520.45	1.8408	550	1031.8	2.6932
170	536.86	1.8782	560	1044.4	2.7083
180	552.67	1.9135	570	1056.9	2.7233
190	567.98	1.947	580	1069.5	2.7382
200	582.87	1.9787	590	1082.1	2.7528
210	597.38	2.0091	600	1094.7	2.7674
220	611.59	2.0382	610	1107.3	2.7817
230	625.53	2.0662	620	1119.9	2.796
240	639.25	2.0932	630	1132.6	2.81
250	652.77	2.1193	640	1145.3	2.824
260	666.13	2.1446	650	1157.9	2.8378
270	679.35	2.1692	660	1170.6	2.8515
280	692.44	2.1931	670	1183.3	2.865
290	705.43	2.2163	680	1196.1	2.8784
300	718.33	2.239	690	1208.8	2.8917
310	731.16	2.2612	700	1221.6	2.9049
320	743.91	2.2829	710	1234.4	2.918
330	756.61	2.3041	720	1247.1	2.9309
340	769.26	2.3249	730	1260	2.9438
350	781.87	2.3453	740	1272.8	2.9565
360	794.45	2.3654	750	1285.6	2.9691

(Continued)

TABLE A8.3 (CONTINUED)Properties of Supercritical CO₂ at Different Pressures and Temperatures

T (°C)	<i>h</i> (kJ/kg)	<i>s</i> (kJ/kg·K)	T (°C)	<i>h</i> (kJ/kg)	<i>s</i> (kJ/kg·K)
<i>Properties of Carbon Dioxide at P = 25 MPa</i>					
370	807	2.385	760	1298.5	2.9816
380	819.52	2.4043	770	1311.3	2.994
390	832.03	2.4233	780	1324.2	3.0063
400	844.52	2.442	790	1337.1	3.0185
410	857	2.4604	800	1350	3.0306

Note: These properties were found from the REFPROP database from Lemmon, E.W., M.O. McLinden, and M.L. Huber, NIST reference fluid thermodynamic and transport properties—REFPROP, NIST Standard Reference Database 23. NIST, Boulder, CO, 2002. Additional properties may be found from the REFPROP database as needed.

References

1. <http://www.breault.com/software/asap.php>.
2. Kistler BL, A user's manual for DELSOL3: A computer code for calculating the optical performance and optimal system design for solar thermal central receiver plants, Sandia National Laboratories, Livermore, CA, 1987.
3. Leary PL, Hankins JD, User's guide for MIRVAL—A computer code for modeling the optical behavior of reflecting solar concentrators, Sandia National Laboratories, Livermore, CA, 1979.
4. http://www.nrel.gov/csp/troughnet/models_tools.html.
5. <http://www.ansys.com>.
6. <http://www.solidworks.com/sw/products/fea-cfd-simulation-software.htm>.
7. Schmitz M, Schwarzbozl P, Buck R, Pitz-Paal R, Assessment of the potential improvement due to multiple apertures in central receiver systems with secondary concentrators, *Solar Energy*, 80, 111–20, 2006.
8. <http://www.ansys.com/Products/Simulation+Technology/Fluid+Dynamics>.
9. <https://sam.nrel.gov>.
10. Stoddard MC, Faas SE, Chiang CJ, Dirks JA, SOLERGY—A computer code for calculating the annual energy from central receiver power plants, Sandia National Laboratories, Livermore, CA, 1987.
11. <http://sel.me.wisc.edu/trnsys>.
12. http://www.ge-energy.com/solutions/generation_solutions.jsp.
13. <http://www.simtechnology.com/IPSEpro/english/IPSEpro.php>.
14. http://www.thermoflow.com/ConvSteamCycle_STP.htm.
15. http://www.steag-systemtechnologies.com/ebsilon_professional+M5208_7573ab0.html.
16. Ratzel AC, Boughton BD, CIRCE.001: A computer code for analysis of point-focus concentrators with flat targets, Sandia National Laboratories, Albuquerque, 1987.

17. http://www.nrel.gov/csp/troughnet/models_tools.html.
18. Hogan J, R.E. AEETES—A solar reflux receiver thermal performance numerical model, *Proceedings of the 1992 ASME International Solar Energy Conference*, Maui, HI, 1992.
19. Igo J, Andraka CE, Solar dish field system model for spacing optimization, *Proceedings of the Energy Sustainability Conference*, Long Beach, CA, 2007.

Appendix 9: Economic Data Tables

TABLE A9.1

Capital-Recovery Factors

<i>n</i>	Annual Mortgage Interest Rate										
	7	7 1/2	8	8 1/2	9	9 1/2	10	10 1/2	11	11 1/2	12
1	1.070	1.075	1.080	1.085	1.090	1.095	1.100	1.105	1.110	1.115	1.120
2	0.553	0.557	0.561	0.565	0.568	0.572	0.576	0.580	0.584	0.588	0.592
3	0.381	0.385	0.388	0.392	0.395	0.399	0.402	0.406	0.409	0.413	0.416
4	0.295	0.299	0.302	0.305	0.309	0.312	0.315	0.319	0.322	0.326	0.329
5	0.244	0.247	0.250	0.254	0.257	0.260	0.264	0.267	0.271	0.274	0.277
6	0.210	0.213	0.216	0.220	0.223	0.226	0.230	0.233	0.236	0.240	0.243
7	0.186	0.189	0.192	0.195	0.199	0.202	0.205	0.209	0.212	0.216	0.219
8	0.167	0.171	0.174	0.177	0.181	0.184	0.187	0.191	0.194	0.198	0.201
9	0.153	0.157	0.160	0.163	0.167	0.170	0.174	0.177	0.181	0.184	0.188
10	0.142	0.146	0.149	0.152	0.156	0.159	0.163	0.166	0.170	0.173	0.177
11	0.133	0.137	0.140	0.143	0.147	0.150	0.154	0.158	0.161	0.165	0.168
12	0.126	0.129	0.133	0.136	0.140	0.143	0.147	0.150	0.154	0.158	0.161
13	0.120	0.123	0.127	0.130	0.134	0.137	0.141	0.144	0.148	0.152	0.156
14	0.114	0.118	0.121	0.125	0.128	0.132	0.136	0.139	0.143	0.147	0.151
15	0.110	0.113	0.117	0.120	0.124	0.128	0.131	0.135	0.139	0.143	0.147
16	0.106	0.109	0.113	0.117	0.120	0.124	0.128	0.132	0.136	0.139	0.143
17	0.102	0.106	0.110	0.113	0.117	0.121	0.125	0.129	0.132	0.136	0.140
18	0.099	0.103	0.107	0.110	0.114	0.118	0.122	0.126	0.130	0.134	0.138
19	0.097	0.100	0.104	0.108	0.112	0.116	0.120	0.124	0.128	0.132	0.136
20	0.094	0.098	0.102	0.106	0.110	0.113	0.117	0.121	0.126	0.130	0.134

Note: *n* is the mortgage term in years.

TABLE A9.2

Interest Fraction of Mortgage Payment

Years Left on Mortgage	Annual Mortgage Interest Rate										
	7	7 1/2	8	8 1/2	9	9 1/2	10	10 1/2	11	11 1/2	12
20	0.742	0.765	0.785	0.804	0.822	0.837	0.851	0.864	0.876	0.887	0.896
19	0.723	0.747	0.768	0.788	0.806	0.822	0.836	0.850	0.862	0.874	0.884
18	0.704	0.728	0.750	0.770	0.788	0.805	0.820	0.834	0.847	0.859	0.870
17	0.683	0.708	0.730	0.750	0.769	0.786	0.802	0.817	0.830	0.843	0.854
16	0.661	0.686	0.708	0.729	0.748	0.766	0.782	0.798	0.812	0.825	0.837
15	0.638	0.662	0.685	0.706	0.725	0.744	0.761	0.776	0.791	0.805	0.817
14	0.612	0.637	0.660	0.681	0.701	0.719	0.737	0.753	0.768	0.782	0.795
13	0.585	0.609	0.632	0.654	0.674	0.693	0.710	0.727	0.742	0.757	0.771
12	0.556	0.580	0.603	0.624	0.644	0.663	0.681	0.698	0.714	0.729	0.743
11	0.525	0.549	0.571	0.592	0.612	0.631	0.650	0.667	0.683	0.698	0.713
10	0.492	0.515	0.537	0.558	0.578	0.596	0.614	0.632	0.648	0.663	0.678
9	0.456	0.478	0.500	0.520	0.540	0.558	0.576	0.593	0.609	0.625	0.639
8	0.418	0.439	0.460	0.479	0.498	0.516	0.533	0.550	0.566	0.581	0.596
7	0.377	0.397	0.417	0.435	0.453	0.470	0.487	0.503	0.518	0.533	0.548
6	0.334	0.352	0.370	0.387	0.404	0.420	0.436	0.451	0.465	0.480	0.493
5	0.287	0.303	0.319	0.335	0.350	0.365	0.379	0.393	0.407	0.420	0.433
4	0.237	0.251	0.265	0.278	0.292	0.304	0.317	0.329	0.341	0.353	0.364
3	0.184	0.195	0.206	0.217	0.228	0.238	0.249	0.259	0.269	0.279	0.288
2	0.127	0.135	0.143	0.151	0.158	0.166	0.174	0.181	0.188	0.196	0.203
1	0.065	0.070	0.074	0.078	0.083	0.087	0.091	0.095	0.099	0.103	0.107

TABLE A9.3
Present-Worth Factors

Year	Discount Rate (%)													
	0	1	2	3	4	5	6	7	8	9	10	11	12	13
1	1.000	0.990	0.980	0.971	0.962	0.952	0.943	0.935	0.926	0.917	0.909	0.901	0.893	0.885
2	1.000	0.980	0.961	0.943	0.925	0.907	0.890	0.873	0.857	0.842	0.826	0.812	0.797	0.783
3	1.000	0.971	0.942	0.915	0.889	0.864	0.840	0.816	0.794	0.772	0.751	0.731	0.712	0.693
4	1.000	0.961	0.924	0.888	0.855	0.823	0.792	0.763	0.735	0.708	0.683	0.659	0.636	0.613
5	1.000	0.951	0.906	0.863	0.822	0.784	0.747	0.713	0.681	0.650	0.621	0.593	0.567	0.543
6	1.000	0.942	0.888	0.837	0.790	0.746	0.705	0.666	0.630	0.596	0.564	0.535	0.507	0.480
7	1.000	0.933	0.871	0.813	0.760	0.711	0.665	0.623	0.583	0.547	0.513	0.482	0.452	0.425
8	1.000	0.923	0.853	0.789	0.731	0.677	0.627	0.582	0.540	0.502	0.467	0.434	0.404	0.376
9	1.000	0.914	0.837	0.766	0.703	0.645	0.592	0.544	0.500	0.460	0.424	0.391	0.361	0.333
10	1.000	0.905	0.820	0.744	0.676	0.614	0.558	0.508	0.463	0.422	0.386	0.352	0.322	0.295
11	1.000	0.896	0.804	0.722	0.650	0.585	0.527	0.475	0.429	0.388	0.350	0.317	0.287	0.261
12	1.000	0.887	0.788	0.701	0.625	0.557	0.497	0.444	0.397	0.356	0.319	0.286	0.257	0.231
13	1.000	0.879	0.773	0.681	0.601	0.530	0.469	0.415	0.368	0.326	0.290	0.258	0.229	0.204
14	1.000	0.870	0.758	0.661	0.577	0.505	0.442	0.388	0.340	0.299	0.263	0.232	0.205	0.181
15	1.000	0.861	0.743	0.642	0.555	0.481	0.417	0.362	0.315	0.275	0.239	0.209	0.183	0.160
16	1.000	0.853	0.728	0.623	0.534	0.458	0.394	0.339	0.292	0.252	0.218	0.188	0.163	0.141
17	1.000	0.844	0.714	0.605	0.513	0.436	0.371	0.317	0.270	0.231	0.198	0.170	0.146	0.125
18	1.000	0.836	0.700	0.587	0.494	0.416	0.350	0.296	0.250	0.212	0.180	0.153	0.130	0.111
19	1.000	0.828	0.686	0.570	0.475	0.396	0.331	0.277	0.232	0.194	0.164	0.138	0.116	0.098
20	1.000	0.820	0.673	0.554	0.456	0.377	0.312	0.258	0.215	0.178	0.149	0.124	0.104	0.087

"The authors have done a nice job updating this edition of their classic textbook by enhancing the chapter on photovoltaics and by including more recent advances in solar thermal power technologies such as the supercritical Rankine cycle and the supercritical CO₂ power cycle."

—Dr. Kevin Anderson, Cal Poly Pomona, Mechanical Engineering, California, USA

"The organization of the book seems much better than the second edition... The present chapter eight is a great piece of work, which provides many details in solar thermal power design. To my best knowledge, no other textbook on solar engineering can compete with this book regarding this topic."

—Yuan Zheng, University of Wyoming, Laramie, USA

AN ENGINEERING-BASED SURVEY OF MODERN SOLAR ENERGY CONCEPTS AND PRACTICAL APPLICATIONS

Reflecting major developments in solar energy since the publication of the last edition, **Principles of Solar Engineering, Third Edition** follows the changes in energy policies that have led to the rapid growth of solar energy systems. This latest edition focuses on the fundamentals and the design of systems for various applications including building, heating and cooling, industrial process heat, electric power plants (including PV and CSP), and environmental systems.

WHAT'S NEW IN THE THIRD EDITION:

The revised edition introduces new topics that include organic and dye sensitized solar cells in the photovoltaics chapter, advanced thermodynamic power cycles such as supercritical CO₂ cycle and information on design software packages. The chapters on solar radiation and solar thermal collectors have been completely changed. Because of its increased importance, solar thermal power is covered in much more depth than in the previous edition.

The book contains increased coverage of high temperature thermal storage for CSP in the chapter for energy storage and transport. It changes many end-of-chapter problems, provides examples and problems for both northern and southern hemispheres and countries around the world, includes a solutions manual, and corrects all errors in the retained material. A significant change in the new edition is the addition of economic analysis in the first chapter, which includes a number of solved examples, and allows the students to analyze the applications in the later chapters from an economic stand point.

Principles of Solar Engineering, Third Edition addresses the need for solar resource assessment and highlights improvements and advancements involving photovoltaics and solar thermal technologies, grid power, and energy storage.



CRC Press

Taylor & Francis Group
an informa business

WWW.CRPCPRESS.COM

6000 Broken Sound Parkway, NW
Suite 300, Boca Raton, FL 33487
711 Third Avenue
New York, NY 10017
2 Park Square, Milton Park
Abingdon, Oxon OX14 4RN, UK

K16006

ISBN: 978-1-4665-6378-0
90000



9 781466 563780

